Proceedings of the conference

Stars and their variability, observed from space

held in Vienna on August 19-23, 2019

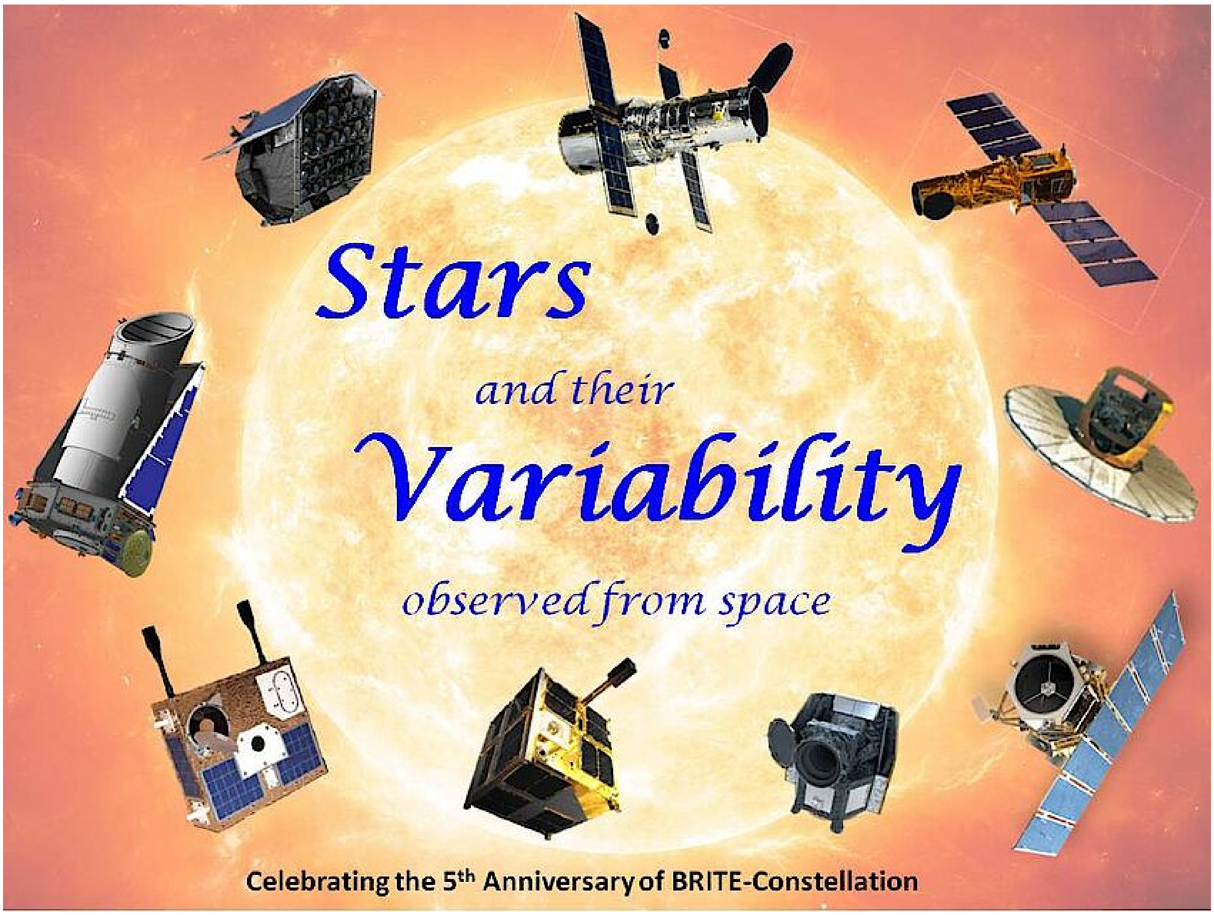

Credit: University of Vienna

Contents

Preface

Motivation for this conference

Stars are the most visible components of the Universe. They are crucial elements for understanding many problem areas in astrophysics, e.g., the history and evolution of our Universe, of galaxies and of our local solar system, and stars host zillions of planets (which we expect to discover in the near future). The variability of stars provides powerful access to their structure, environment and evolution.

Stars represent laboratory sites for physical processes that cannot be tested experimentally on Earth. They are crucial for understanding basic physics, such as nuclear physics, particle physics, statistical physics, hydrodynamics, atomic physics and opacities, and many more such topics. In theoretical modelling we are facing the limitations of the basic radiation, plasma and other physics, which oversimplify (or ignore) the treatment of radiation–matter coupling, magnetic fields, dynamical processes, etc. Experience tells us that once the physics is properly accounted for, our picture of how stars work has frequently to be changed.

Observing stars from satellites has increased significantly the data volume and parameter space for realistic modelling of these most prominent objects in the Universe. Variability can now be traced down to incredibly low noise levels and long time-intervals, through the availability of satellites. New observing capabilities have improved precision and accuracy, which in turn have uncovered new populations of stars and revealed limits in our physical understanding of their structure and evolution. In particular, the BRITE-Constellation has demonstrated the unique advantage of nano-satellites for exploring stars which are bright (and close) enough to allow access to fundamental techniques like interferometry, highly accurate parallaxes, direct imaging, very high spectral and temporal resolution, etc. These are the advantages that led us in 2009 to the funding of the first BRITE satellites.

All this considered, it does not come as a surprise that the Canadian Astronomy Data Centre (CADC) lists for 2019 a total of 345 conferences, meetings and workshops, of which about 60% deal with stars and usually last several days. In other words, on average there is at least one meeting *every day* somewhere in the world dedicated to stars. Our conference of 261 participants from 44 different countries world-wide and occupying a full week confirms the enthusiasm for this topic in the community.

Concept

During our conference, which was nicknamed "Stars and Space", our plan was to discuss issues in stellar modelling which are still undecided owing to discrepancies between theory and observation, to highlight the physics needed to describe their structure, in particular convection, rotation, magnetic fields, and evolution (from genesis to end of life), to elaborate on the interaction of stars with their environments (winds out and in, outbursts, magnetic fields, etc.), and to discuss their properties as isolated objects but also being members of ensembles (from binaries to clusters). What are the most recent achievements in space observations and theory? We also aimed to attract the younger generation, and to develop a strategy for the future.

This concept is reflected in the structure of our conference. Six short "flashlight" presentations give examples of the impact of space observations on our understanding of stars. The following seven sections focussed on the wide parameter space needed to describe stellar properties, on pulsations (asteroseismology), on variabilities other than pulsations, on modelling of stars, on ensembles of stars (binaries and clusters) and on stellar spheres of influence. A special section was devoted to the lessons we have learned so far, and the final session to future activities.

The video streaming of the entire conference is available via:
https://starsandspace.univie.ac.at/home/conference-streams/

Team

To organise such a conference without serious problems would not be possible without a dedicated science and local organisation team. Members of the SOC were Conny Aerts, Jadwiga Daszynska-Daskiewicz, Marc-Antoine Dupret (co-chair), Laurent Eyer, Luca Fossati, Martin Groenewegen, Hans Kjeldsen, Franz Kerschbaum, Coralie Neiner, Hiromoto Shibahashi, Nicole St.Louis, Werner Weiss (chair) and Konstanze Zwintz. Members of the LOC were Luca Fossati, Anneliese Haika, Shelley-Anne Harrisberg, Patrick Harnisch, Gabor Herbst-Kiss, Dorothea Holzschuh, Bernhard Hörl, Thomas Kallinger, Theresa Lueftinger, Lina Rummler, Stefanie Schauer, Sarah Stidl, Stefan Wallner, Werner Weiss (chair) and Konstanze Zwintz, who all did an excellent job. In addition, I express my thanks also to Dietrich Baade, Otto Koudelka, Anthony Moffat, Andrzej Pigulski and Gregg Wade for their continuous support.

Last, but certainly not least, the enormous efforts of the editorial team with Coralie Neiner as editor-in-chief have to be acknowledged. We hope that these Proceedings will serve as a powerful reference for future projects.

Acknowledgements

Manpower is one important aspect of the organisation of a conference; funding is another. Funding was crucial, in particular for supporting students, pre-docs and young post-docs. We are therefore grateful to the following sponsors:

- University of Vienna (Rectorate and Faculty of Earth Sciences, Geography and Astronomy)
- Austrian Research Promotion Agency (FFG)
- RUAG Space GmbH, Vienna Conference Service
- Ströck-Brot GmbH
- Josef Manner & Comp.

W. W. Weiss
University of Vienna, Department of Astrophysics, 1180 Vienna, Austria

List of participants

Conny Aerts, Institute of Astronomy, KU Leuven, Belgium
Felix Ahlborn, Max Planck Institute for Astrophysics, Germany
Rudolf Albrecht, Austrian Space Forum, Austria
Georges Alecian, CNRS, Observatoire de Paris, France
Richard I. Anderson, European Southern Observatory, Germany
Hasmik Andreasyan, Byurakan Astrophysical Observatory, Armenia
Victoria Antoci, Stellar Astrophysics Centre, Denmark
Emmanuel Ariyibi, Obafemi Awolowo University, Ile-Ife, Nigeria
Victor Atisele, Vacubeg Aluminium, Nigeria
Kyle Augustson, CEA Paris-Saclay DRF/IRFU/DAp, France
Elias Aydi, Michigan State University, USA
Thomas Ayres, University of Colorado, USA
Dietrich Baade, ESO, Germany
Timo Bachmann, Student at University of Vienna, Austria
Annie Baglin, Observatoire de Paris, France
Karolina Bakowska, Nicolaus Copernicus Astron. Centre, Polish Academy of Sciences, Poland
Sebastia Barcelo-Forteza, Centro de Astrobiología (CAB, CSIC-INTA), United Kingdom
Alexander Batrakov, Saint Petersburg State University, Russia
Matthew Battley, University of Warwick, United Kingdom
Paul Beck, Instituto de Astrofisica de Canarias, Spain
Mansour Benbakoura, CEA Saclay, France
Willy Benz, University of Bern, Switzerland
Sopia Beradze, Abastumani Astrophysical Observatory, Ilia State University , Giorgia
Emanuele Bertone, INAOE, Mexico
Martin Blažek, Masaryk University, Czech Republic
Zsófia Bognár, Konkoly Observatory, MTA CSFK, Hungary
Kevin Bouchaud, LESIA, Paris observatory, France
Dominic Bowman, Institute of Astronomy, Belgium
Ana Brito, CENTRA - Center for Astrophysics and Gravitation, Portugal
David Brown, Specola Vaticana, Vatican City
Emily Brunsden, University of York, United Kingdom
Gaël Buldgen, Observatoire de Genéve, Switzerland
Siemen Burssens, Institute of Astronomy, KU Leuven, Belgium
Derek Buzasi, Florida Gulf Coast University, USA
Juan Cabrera, Deutsches Zentrum für Luft- und Raumfahrt, Germany
Matteo Cantiello, Flatiron Institute, USA
Alex Carciofi, Universidade de São Paulo, Brasilia
Pradip Kumar Chattopadhyay, Dept. of Phys., Coochbehar Panchanan Barma Univ., India
Mohamed Imad Chouaf, Kali Trading, Qatar
Steven Christophe, Observatoire de Paris, France
Vera Chubenko, ÖGAA/WAA, Austria
Vyacheslav Chubenko, ÖGAA/WAA, Austria
Gisella Clementini, INAF Osservatorio di Astrofisica e Scienza dello Spazio, Italy
Thomas Constantino, University of Exeter, United Kingdom
Alejandro Hugo Córsico, University of La Plata, Argentina
Borbála Cseh, Konkoly Observatory, MTA CSFK, Hungary

Min Cui, Institut Polytechnique des Sciences Avancées (IPSA), France
Natasa Cvetkovic, University of Vienna, Austria
Hasan Ali Dal, Ege University, Turkey
Fatemeh Danesh Manesh, Ferdowsi University of Mashhad, Iran
Alexandre David-Uraz, University of Delaware, USA
Bartlomiej Debski, Jagiellonian University, Poland
Jacqueline den Hartogh, Konkoly Observatory, MTA CFSK, Hungary
Aliz Derekas, ELTE Gothard Astrophysical Observatory, Hungary
Maria Pia Di Mauro, INAF, IAPS, Italy
Ernst Dorfi, Institut für Astrophysik, Austria
Marc-Antoine Dupret, University Liège, Belgium
Sylvia Ekström, University of Geneva, Switzerland
Nancy R, Evans, SAO, USA
Laurent Eyer, Observatoire de Genève, Switzerland
Damian Fabbian, Institut für Astrophysik Göttingen, Georg-August-Universität, Germany
Martin Farnir, Université de Liège, Belgium
Gilles Fontaine, Université de Montréal, Canada
Adrienn Forró, MTA CSFK, Hungary
Luca Fossati, Austrian Academy of Sciences, SRI, Austria
Jim Fuller, California Institute of Technology, USA
Alfred Gautschy, CBmA, Switzerland
Elizabeth Griffin, Dominion Astrophysical Observatory, Canada
Martin Groenewegen, Koninklijke Sterrenwacht van België, Belgium
Desmond H. Grossmann, University of Graz, Austria
Franz Gruber, ÖGAA, Austria
Eike Guenther, Thüringer Landessternwarte Tautenburg, Germany
fei guo, Yunnan Observatories, Chinese Academy of Sciences, China
Yanxin Guo, NAOC, China
Zhao Guo, Pennsylvania State University, USA
Eka Gurgenashvili, Ilia State University, University of Goettingen, Giorgia
Anneliese Haika, Institut für Astrophysik, Austria
Franz-Josef Hambsch, ROAD Observatory, Belgium
Gerald Handler, Nicolaus Copernicus Astronomical Center, Poland
Patrick Harnisch, Universität Wien, Austria
Shelley Anne Harrisberg, Institut für Astrophysik, Austria
Erich Hartig, University of Vienna, Astrophysics, Austria
Artie Hatzes, Thüringer Landessternwarte Tautenburg, Germany
Saskia Hekker, Max Planck Institute for Solar system research, Germany
Susanne Hoffmann, FSU Jena, Faculty of Physics and Astronomy, Germany
Erik Høg, Copenhagen University, Denmark
Daniel Holdsworth, University of Central Lancashire, United Kingdom
Dorothea Holzschuh, Institut für Astrophysik, Austria
Bernhard Hörl, Universität Wien, Austria
Günter Houdek, Dept. of Physics and Astronomy, Aarhus University, Denmark
Daniel Huber, University of Hawaii, USA
Nikoleta Ilic, Leibniz Institut für Astrophysik Potsdam, Germany
Gabor Imre-Kiss, University of Vienna, Austria
Andreas Irrgang, Dr. Karl Remeis-Observatory, Germany
Ing-Guey Jiang, National Tsing Hua University, Taiwan
Liping Jin, Jilin University, China
Meridith Joyce, Australian National University, Australia
Simon Joyce, University of Leicester, United Kingdom
Monika I. Jurkovic, Astronomical Observatory Belgrade, Serbia
Filiz Kahraman Alicavus, Nicolaus Copernicus Astronomical Center, Poland
Thomas Kallinger, Institut für Astrophysik, Austria
Emma Kalokoh, Hendry Fergusson Junior Secondary School, Sierra Leone
Ifeanyi Kalu, Vacubeg Aluminium, Nigeria

Csilla Kalup, Konkoly Observatory, Hungary
Amit Kashi, Ariel University, Israel
Steven Kawaler, Iowa State University, USA
Nathaniel Dylan Kee, Institute of Astronomy, KU Leuven, Belgium
Franz Kerschbaum, Institut für Astrophysik, Austria
Pierre Kervella, Observatoire de Paris, France
Laura Ketzer, Universität Innsbruck, Austria
Maxim Khodachenko, SRI, Austrian Academy of Sciences, Austria
René Kiefer, University of Warwick, United Kingdom
Nino Kochiashvili, Abastumani Observatory, Ilia University, Giorgia
Oleg Kochukhov, Uppsala University, Sweden
Piotr Kolaczek-Szymanski, Astronomical Institute of University of Wroclaw, Poland
Dmitry Kolesnikov, Sternberg Astronomical Institute, Russia
Krzysztof Kotysz, Uniwersytet Wroclawski, Poland
Otto Koudelka, Graz University of Technology, Austria
Gábor Kovács, CSFK MTA, Hungary
Jirí Krticka, Masaryk University, Czech Republic
Iva Krticková, Masaryk University, Czech Republic
Friedrich Kupka, MPI for Solar System Research, Germany
Rainer Kuschnig, Graz University of Technology, Austria
James Kuszlewicz, Max-Planck-Institut für Sonnensystemforschung, Germany
Jonathan Labadie-Bartz, Universidade de São Paulo, Brasilia
Patricia Lampens, Koninklijke Sterrenwacht van België, Belgium
John Landstreet, Physics & Astronomy, Univ. of Western Ontario, Canada
Antonino Francesco Lanza, INAF-Osservatorio Astrofisico di Catania, Italy
JaeWoo Lee, Korea Astronomy and Space Science Institute, South Korea
Holger Lehmann, Thüringer Landessternwarte Tautenburg, Germany
Guillaume Lenoir-Craig, Université de Montréal, Canada
Patrick Lenz, Ronin Institute, USA
Siqi Liu, University of Toronto, Canada
Catherine Lovekin, Department of Physics, Mount Allison University, Canada
Theresa Lüftinger, Institut für Astrophysik, Austria
Carla Maceroni, INAF, IAPS, Italy
Ekaterina I. Makarenko, Saint Petersburg State University, Russia
Faisal Maqsood, University of the Punjab, Lahore Pakistan, Pakistan
Chinedu Marcel, Vacubeg Aluminium, Nigeria
Olga Maryeva, Astronomical Institute of Academy of Sciences, Czech Republic
Stephane Mathis, CEA, Department of Astrophysics, France
Gautier Mathys, ESO, Chile
Jaymie Matthews, University of British Columbia, Canada
Maria Messineo, University of Science and Technology of China, China
Mathias Michielsen, KU Leuven, Belgium
Przemyslaw Mikolajczyk, Astronomical Institute, University of Wroclaw, Poland
Zdenek Mikulasek, DTPA, Faculty of Science, Masaryk University Brno, Czech Republic
Amadeusz Miszuda, Astronomical Institute, University of Wroclaw, Poland
David Mkrtichian, National Astronomical Research Institute of Thailand, Thailand
Anthony Moffat, Univ. de Montréal, Canada
László Molnár, Konkoly Observatory, MTA CSFK, Hungary
Joey Mombarg, Institute of Astronomy, Belgium
Dawid Mozdzierski, University of Wroclaw, Poland
Marco Müllner, University Innsbruck, Austria
Melissa Munoz, Queen's University, Canada
Simon Murphy, University of Sydney, Australia
Mahdieh Navabi, Alzahra University, Iran
Coralie Neiner, Observatoire de Paris, France
Henryka Netzel, Nicolaus Copernicus Astronomical Centre, Poland
Daisaku Nogami, Kyoto University, Japan

Jürgen Öhlinger, Technisches Museum Wien, Austria
Rhita-Maria Ouazzani, LESIA, Paris Observatory, France
Dogus Ozuyar, Ankara University, Turkey
Bert Pablo, AAVSO, USA
Alexey Pamyatnykh, Copernicus Astronomical Centre, Poland
Sankar Narayan Patra, Jadavpur Unversity, India
Ernst Paunzen, Institut für Astrophysik, Austria
Michal Pawlak, Charles University in Prague, Czech Republic
Volker Perdelwitz, Hamburger Sternwarte, Germany
Frank Pertermann, Thüringer Landessternwarte Tautenburg, Germany
Jordan Philidet, LESIA, Observatoire de Paris, France
Andrzej Pigulski, Instytut Astronomiczny, Uniwersytet Wroclawski, Poland
Bogumil Pilecki, Nicolaus Copernicus Astronomical Center, Poland
Charly Pinçon, STAR Institute, University of Liège, Belgium
Olga Pintado, Centro de Tecnología Disruptiva, Univ. de San Pablo Tucuman, Argentina
Emese Plachy, Konkoly Observatory, MTA CSFK, Hungary
Ernst Pollmann, ASPA, Active Spectroscopy in Astronomy, Germany
Andrew Pollock, University of Sheffield, United Kingdom
Augustus Porter, University of Oxford, United Kingdom
Vincent Prat, AIM/CEA, France
Judith Provencal, University of Delaware and Mt. Cuba Observatory, USA
Daniel Reese, LESIA, Observatoire de Paris, France
Thomas Rivinius, ESO, Chile
Monika Rode-Paunzen, Österreichische Akademie der Wissenschaften, Austria
Iosif Romanyuk, Special Astrophysical Observatory, Russia
Lina Rummler, Universität Wien, Austria
Tatiana Ryabchikova, Institute of Astronomy, Russian Academy of Sciences, Russia
Mikhail Sachkov, Institute of Astronomy RAS, Russia
Hideyuki Saio, Astronomical Institute, Tohoku University, Japan
Takahito Sakaue, Kyoto University, Japan
Réza Samadi, LESIA, Observatoire de Paris, France
Gaetano Scandariato, INAF, OACt, Italy
Stefanie Schauer, Universität Wien, Austria
Gerd Schmid, JKU, Austria
Thomas Schobesberger, Institut für Astrophysik, Austria
Carla Nicolin Schoder, University of Vienna, Austria
Jesper Schou, Max Planck Institute for Solar System Research, Germany
Manfred Schwarz, BAA, Austria
Evgeni Semkov, Institute of Astronomy and NAO, Bulgaria
Shanmugha Sundaram G A, Amrita University, India
Sami Gauchan Sherchan, Tribhuvan University, Prithvi Narayan Campus, Nepal
Hiromoto Shibahashi, University of Tokyo, Japan
Matthew Shultz, University of Delaware, USA
Aaron Sigut, The University of Western Ontario, Canada
James Sikora, Queen's University, Canada
Marek Skarka, Dept. of Theoretical Physics and Astrophysics, Masaryk University, Czech Republic
Radoslaw Smolec, Nicolaus Copernicus Astronomical Center, Poland
Ádám Sódor, Konkoly Observatory, MTA CSFK, Hungary
John Southworth, Keele University, United Kingdom
Federico Spada, Max-Planck-Institut für Sonnensystemforschung, Germany
Sitara Srinivasan, RNS Institute Of Technoogy, India
Thomas Steindl, University Innsbruck, Austria
Sarah Stidl, University of Vienna, Austria
Nicole St-Louis, Université de Montréal, Canada
Klaus Strassmeier, AIP, Germany
Jie Su, Yunnan Observatories, Chinese Academy of Sciences, China
Nofoz Suleiman, Eötvös Loránd University, Hungary

Hyun-Il Sung, Korea Astronomy and Space Science Institute, South Korea
Wojciech Szewczuk, Astronomical Institute of the Wroclaw University, Poland
Ali Taani, Al-Balqa Applied University, Jordan
Koh Takahashi, Albert-Einstein-Institut, Germany
Monica Taormina, Nicolaus Copernicus Astronomical Centre (CAMK), Poland
Dóra Tarczay-Nehéz, Hungarian Academy of Sciences Research, Centre for Astronomy, Hungary
Grazina Tautvaisiene, Vilnius University, Lithuania
Nathalie Themeßl, Max Planck Institute for Solar System Research, Germany
Anne Thoul, FNRS, University of Liège, Belgium
Giovanna Tinetti, University College London, United Kingdom
Andrew Tkachenko, Institute of Astronomy, KU Leuven, Belgium
Michele Trabucchi, Univ. of Padova, Dept. of Physics and Astronomy, Italy
Regner Trampedach, Space Science Institute, USA
Otto Trust, Mbarara University of Science and Technology, Uganda
Dmytro Tvardovskyi, Odessa I.I. Mechnikov National University, Ukraine
Asif ud-Doula, Penn State Scranton, USA
Devendra Raj Upadhyay, Amrit Campus (ASCOL), Tribhuvan University, Nepal
Murat Uzundag, Universidad de Valparaiso, Chile
Valerie Van Grootel, Université de Liège, Belgium
Manana Vardosanidze, Abastumani Observatory, Iliauni, Giorgia
Laura Venuti, NASA Ames Research Center, USA
Ethan Vishniac, Johns Hopkins University, USA
Irina Voloshina, Sternberg Astronomical Institute, Moscow State university, Russia
Eduard Vorobyov, Institut für Astrophysik, Austria
Gregg Wade, RMC, Canada
Przemyslaw Walczak, Astronomical Institute, Wroclaw University, Poland
Stefan Wallner, Institut für Astrophysik, Austria
Roman Wawrzaszek, Centrum Badan Kosmicznych PAN, Poland
Werner Wolfgang Weiss, Institut für Astrophysik, Austria
Manuela Wenger, Graz University of Technology, Austria
David Wöckel, Thüringer Landessternwarte Tautenburg, Germany
Li-Chin Yeh, National Tsing Hua University, Taiwan
Ezgi Yoldas, Ege University, Turkey
Jiri Zak, Masaryk University, Czech Republic
Teimuraz Zaqarashvili, Ilia State University, Giorgia
Milan Zboril, Slovakia, Slovakia
Miloslav Zejda, Masaryk University, Czech Republic
Qian-Sheng Zhang, Yunnan Observatories, Chinese Academy of Sciences, China
xinyi zhang, Yunnan Observatories, Chinese Academy of Sciences, China
Sebastian Zieba, Universität Innsbruck, Inst. für Astro- und Teilchenphysik, Austria
Elzbieta Zoclonska, Nicolaus Copernicus Astronomical Center, Poland
Fang Zuo, National Astronomical Observatories, Academy of Sciences, China
Zhao-Yu Zuo, Xi an Jiao Tong University, China
Konstanze Zwintz, Universität Innsbruck, Institut für Astro- und Teilchenphysik, Austria

Fig. 1. Conference Participants

Introduction

Stars and their variability observed from space
C. Neiner, W. W. Weiss, D. Baade, R. E. Griffin, C. C. Lovekin, A. F. J. Moffat (eds)

THE SPACE PHOTOMETRY REVOLUTION

F. Kerschbaum[1]

Abstract. We look back to more than half a century of photometric measurements from space. They provided us with access to the full electromagnetic spectrum, atmospherically undisturbed spatial resolution and photometric quality as well as uninterrupted, high cadence measurements. By this our picture of the universe as a whole and its constituents changed drastically. This success story was not without setbacks but the future is promising.

Keywords: Space vehicles: instruments, Stars: variables, Asteroseismology

1 Introduction

The late 1960s and early 1970s saw the first space photometry focussed on the infrared and ultraviolet spectral ranges. Missions like OAO-2, ANS, TD1, COPERNICUS, and later IUE or HST, must be mentioned in that context. Some experiments were connected to manned missions like Spacelab. The expectations included the avoidance of atmospheric extinction, emission, seeing, scintillation, a much better sky coverage, the absence of day/night interruptions and favourable thermal conditions.

Reality was different: Low and short orbits reduced continuous viewing zones, reslted in short missions and did not allow for long-term studies, while uncertainties with technical and financial constraints did not allow reliable planning. The extremely strong competition prevented early space astronomy from becoming a regular tool for observational astronomy.

2 Great ambitions

Motivated by the great success of helioseismology in the 1970s and 1980s, similar approaches on stars became desirable. Ground-based work using world-wide telescope networks (e.g. Breger et al. (1990) demonstrated the potential, but it was clear that space-based observatories could have great advantages from their potentially uninterrupted and their atmospherically undisturbed time-series. Consequently, the 1990s saw several national attempts for devoted space instruments, like EVRIS (Baglin et al. 1993) on MARS96 or MONS (Kjeldsen et al. 2000). Several increasingly big proposals (40 to 120 cm apertures!) were submitted to ESA's Horizon 2000 programme, namely PRISMA (Appourchaux et al. 1993), STARS (Fridlund et al. 1995) and Eddington (Roxburgh & Favata 2004) While not successful for various reasons, the efforts built up a strong European community interested in space photometry. Several critical technical components were pre-developed, and the scientific interest in such missions broadened after detections of the first exoplanets around normal stars (Mayor & Queloz 1995).

3 The revolution starts

The first really successful demonstration of high-precision photometry from space was that of the WIRE 5 cm startracker (Schember et al. 1996) an (unfortunately) otherwise failed infrared mission. Then, with Canadian-led MOST (Matthews et al. 2000), asteroseismology becomes routine in a "suitcase" form factor with a 15-cm aperture and its revolutionary attitude control. The French-led CoRoT (Catala et al. 1995) with its 25-cm telescope initiated the final revolution. To put their first results in perspective: to find (e.g.) 10 modes in a δ-Scuti star Breger et al. (1995) needed 170 hrs of photometric data from a world-wide coordinated observational campaign. CoRoT enabled the identification to be made of several hundred modes in two months (Poretti et al. 2009). The next big step was *Kepler* (Borucki et al. 2010), which enabled a revolutionary census by monitoring some 150,000 (typically distant) stars with a 95-cm aperture.

[1] Department of Astrophysics, University of Vienna, Türkenschanzstr. 17, 1180 Vienna, Austria

4 Now and then

Today, the ongoing *Gaia* (Gaia Collaboration et al. 2016) provides parallaxes, radial velocities, spectroscopy and long-term variability/activity monitoring for up to one billion stars. What an advance from the early days! With BRITE constellation (Handler et al. 2017), the first nanosats with miniaturized gyros, cheap fabrication using mostly off-the-shelf components and comparatively cheap launch and operation, provide hig- precision photometry for apparently bright stars in two filter bands. At present TESS (Ricker et al. 2016), a small 2-year explorer-class mission, is performing an all-sky survey of 200,000 stars within about 200 pc. In common with BRITE, the stars observed by TESS are bright and are therefore relatively easy to follow up at high spectral or spatial resolution than in the case of *Kepler*.

The future for space photometry is bright! After its launch on 2019 December 17,CHEOPS (Broeg et al. 2013), an fast and small ESA mission, will build on the significant CoRoT heritage and will enable detailed characterizations of both individual planets and host stars. After 2026 PLATO (Rauer et al. 2016), an ESA M-class mission, will carry out a census for up to 6 years (some 10^6 stars) down to earth-sized planets and accurate stellar and planetary masses, radii and ages, with a strong focus on more nearby objects in order to enable follow-ups with high-resolution spectroscopy and interferometry. Together with *Gaia* (see above) it is a perfect complement to carrying out galactic archaeology – many revolutions to come. We live in great times!

References

Appourchaux, T., Gough, D. O., Catala, C., et al. 1993, ASPCS, Vol. 42, Prisma - the First Space Mission to See Inside the Stars (ASP), 411

Baglin, A., Weiss, W. W., & Bisnovatyi-Kogan, G. 1993, ASPCS, Vol. 40, E. V. R. I. S on board MARS 94: the first space experiment devoted to stellar seismology (ASP), 758

Borucki, W. J., Koch, D., Basri, G., et al. 2010, Science, 327, 977

Breger, M., Handler, G., Nather, R. E., et al. 1995, A&A, 297, 473

Breger, M., McNamara, B. J., Kerschbaum, F., et al. 1990, A&A, 231, 56

Broeg, C., Fortier, A., Ehrenreich, D., et al. 2013, in EPJ Web of Conferences, Vol. 47, EPJ Web of Conferences, 03005

Catala, C., Mangeney, A., Gautier, D., et al. 1995, ASPCS, Vol. 76, COROT: A Proposal to Study Stellar Convection and Internal Rotation (ASP, San Francisco), 426

Fridlund, M., Gough, D. O., Jones, A., et al. 1995, ASPCS, Vol. 76, STARS: A Proposal for a Dedicated Space Mission to Study Stellar Structure and Evolution (ASP, San Francisco), 416

Gaia Collaboration, Prusti, T., de Bruijne, J. H. J., et al. 2016, A&A, 595, A1

Handler, G., Pigulski, A., Weiss, W. W., et al. 2017, in EPJ Web of Conferences, Vol. 160, EPJ Web of Conferences, 01001

Kjeldsen, H., Bedding, T. R., & Christensen-Dalsgaard, J. 2000, ASPCS, Vol. 203, MONS: Measuring Oscillations in Nearby Stars (ASP), 73

Matthews, J. M., Kuschnig, R., Walker, G. A. H., et al. 2000, ASPCS, Vol. 203, Ultraprecise Photometry from Space: The MOST Microsat Mission (ASP), 74–75

Mayor, M. & Queloz, D. 1995, Nature, 378, 355

Poretti, E., Michel, E., Garrido, R., et al. 2009, A&A, 506, 85

Rauer, H., Aerts, C., Cabrera, J., & PLATO Team. 2016, AN, 337, 961

Ricker, G. R., Vanderspek, R., Winn, J., et al. 2016, SPIE Conference Series, Vol. 9904, The Transiting Exoplanet Survey Satellite (SPIE), 99042B

Roxburgh, I. & Favata, F. 2004, in IAU Symposium, Vol. 215, Stellar Rotation, ed. A. Maeder & P. Eenens, 323

Schember, H. R., Kemp, J. C., Ames, H. O., et al. 1996, SPIE Conference Series, Vol. 2744, Wide-field Infrared Explorer (WIRE) (SPIE), 751–760

Stars and their variability observed from space
C. Neiner, W. W. Weiss, D. Baade, R. E. Griffin, C. C. Lovekin, A. F. J. Moffat (eds)

PUTTING STARS INTO BOXES

R. E. Griffin[1]

Abstract.
The approaches which researchers follow can be subdivided into two simple but quite distinct categories: (A) "broad sweepers", and (B) "ultimate refiners". The first look at the wide picture and extract the kind of statistics upon which stellar physics was founded. The second look at the outliers – the ones that don't fit that wide picture, and spend a lifetime showing that the wide picture doesn't fit.

In researching a sample of nearly 50 northern composite-spectrum binaries I have succeeded in identifying some norms, but some of those systems "just can't be like that". Two will be summarized: (1) a triple system containing a pair of similar early-A stars in a 3.8-day orbit which are both traveling at over 100 km/s and yet show no rotation at all, and (2) an SB2 system that shows no evidence of a third body or of mass loss, and yet the SB2 orbit finds that the mass of the secondary is more than twice that of the primary. These two alone challenge theories of stellar evolution, or need to be re-observed thoroughly and sorted out - but who will do high-dispersion spectroscopy on 6th-mag systems when the rest of the world is after 23rd mag? I have presented these cases to conferences, but I not been able to frighten any theoretician sufficiently into investigating closely. The only one who was at all interested claimed that the observational data were wrong, and proceeded to alter them.

Other systems cry out for more attention too. Epsilon Aurigae ($V = 2.9$, $P = 27$ years) was centre stage while it was in eclipse in 2010; it still baffled everyone, and it was left unsolved. It is obscured by something opaque – we know not what, and during egress (and only then) it emits a thin stream of gas that is rich in rare-earths. Then those Am stars – a significant fraction – seem to have low rotation and to be in binary systems, often with Am companions and quite possibly tidally locked in synchronous rotation, but the more cautious see room for doubt as to whether the slow rotation is the cause of the Am characteristics, since not all Am stars are members of short-period binaries, and several are known to fall outside that particular box. Surveys like *LSST* and *Gaia* predict the volumes of their discoveries by extrapolation. We can extrapolate too; the four brightest stars in the northern sky (Arcturus, Vega, Sirius and Capella) are all curiously odd in some way. What does that say, then, for the rest of the stars in our Galaxy? Have the ultimate refiners been in the shadow of the broad sweepers for too long?

Keywords: stars: classification, stars: binaries, stars: rotation, stars: evolution

1 Two Distinct Boxes

Researchers in astrophysics can be divided broadly into two types: *broad sweepers* and *ultimate refiners*. The phrases were invented by the late Bernard Pagel, of stellar abundance fame, and aptly describe participants at this conference: those whose work requires them to assign stars to specific boxes and to attribute to each box a generic set of parameters, and those who find such an approach anathema, are deeply disturbed by the oddballs that do not fit, and spend a lifetime working out why they don't fit.

1.1 Avoiding Bias

At the outset, it is important to identify one's own natural tendency in terms of broad sweeper or ultimate refiner, because one's natural leaning can colour, influence or bias the approaches one adopts in research, and how much weight or credence one gives to solutions, whether from one's own work or from that published by others. Identifying one's own specific position also helps discussions between those of the two opposite camps to flow more productively.

Modelling stars – whether to simulate spectra, pulsations, rotation, velocities or whatever – commences with the assumption of some particular set of parameters, and if those parameters were merely derived as

[1] Herzberg Astronomy & Astrophysics Research Centre, Dominion Astrophysical Observatory, 5071 West Saanich Road, Victoria, BC, V9E 2E7, Canada

average representatives of objects within some 'box' then the purity of the output will be compromised and the significance of any deviations by members of that set will not be recognized, or not correctly. Some of these problems are already being faced in early efforts to characterize large volumes of spectra recorded in surveys, where it is tempting to dismiss oddballs as glitches in the data.

2 Oddities from the Start

Because these two different approaches are fully complementary, even orthogonal, they are essential to any scientific field, not least astrophysics (where direct experiment is of course not possible). Broad sweepers generated the statistics which laid the foundations of stellar science as we know it today, beginning with the classification of some 10,000 stars in the HD Catalogue 100+ years ago, while ultimate refiners find there are many more exceptions to the rule than conformers, and have largely been responsible for designing ingenious space experiments, questioning every definition of so-called normality, and challenging theories of stellar evolution. From the very beginnings of astrophysics it has therefore been felt necessary (and very important) to put stars into boxes, each with a well-defined label, though – thanks to the insistence of the ultimate refiners – also allowing one box to be labelled "odd". But even while the Harvard classifiers were busily putting stars into boxes, Antonia Maury was equally busy taking some of them out again. She noticed that some cool stars had unusually narrow spectral lines, and that their Balmer lines had distinct, narrow, cores (Maury & Pickering 1897): she had discovered the signatures of the low pressure that prevails in the atmospheres of giants and supergiants. Nancy Roman was later to point out that the dominant molecular bands of CN and CH in the mid-blue were stronger in some stars than 'normal' in the same 'box' (Roman 1965), a characteristic that could be explained as a consequence of stellar evolution.

3 Examples from Composite-Spectrum Binaries . . .

In researching a sample of some 45 northern composite-spectrum binaries I have met interesting examples of these problems. A composite-spectrum binary is a detached system containing a G-K-M giant and a B-A dwarf, clearly of unequal masses and of correspondingly different luminosities. Their SEDs are of course also quite different, but in such a way that both spectra are easily visible in the blue-UV region, though superimposed and thus somewhat tangled, making it difficult to measure one spectrum faithfully in the presence of the other. In this situation it is necessary to separate the component spectra digitally so that the individual spectra can be handled uncontaminated by the features of the other star, and measured as though they were single stars. One can thus obtain accurate SB2 orbits, and thence the mass ratios of the component stars, yielding some of the most precise results possible for any binary system. Ten members of this class also undergo eclipses, so in those cases the masses of both components can be derived absolutely.

Many of my sample of composite-spectrum binaries appear to conform to familiar norms, but some simply do not. One is a hierarchical triple system (HR 6497), whose inner orbit consists of a pair of similar early-A stars in a 3.8-day orbit; the pair are both traveling at over 100 km/s *and yet show no rotation at all* (Griffin & Griffin 2012). Another is an SB2 system that shows no evidence of a third body or of mass loss, and yet Griffin & Griffin (2018) find that the SB2 orbit gives a mass for the secondary that is more than twice that of the primary. If a merger has taken place, there is no spectroscopic evidence for such an event in the blue-visible spectral region. These two cases alone challenge theories of stellar evolution, or need to be re-observed thoroughly and sorted out - but who will do high-dispersion spectroscopy on 6th-mag systems when the rest of the world is after 23rd mag? I have presented these cases to conferences, but I have not been able to frighten any theoretician sufficiently into investigating closely. The only one who was at all interested claimed that the observational data were wrong, and proceeded to alter them.

4 . . . and Throughout Astrophysics

Other systems cry out, too, for more attention. Epsilon Aurigae ($V = 2.9$, $P = 27$ years) was centre stage while it was in eclipse in 2010, yet it still baffled everyone, *and it was left unsolved*. Its bright F-supergiant primary is nearly completely obscured by something opaque – we still know not what – and during egress (and only then) it emits a thin stream of gas that is rich in rare-earths. Perfectly fascinating, yet where in stellar evolution does it fit in, and if not, why not?

Then those Am stars, confidently postulated by someone once as being so formed because they are members of fairly close but detached binaries, a hypothesis that has become adopted as theory by being repeated so frequently. But can we really be so sure that they are all members of short-period binaries when that 75-year system HD 88021 has a secondary that is clearly Am but is also quite clearly *single*, as Griffin & Griffin (1988) demonstrated? What about Sirius, too, an Am star whose only companion (Sirius B) is a white dwarf, and whose orbit has $P = 50$ years? And why are those two scarcely-rotating, early-A dwarfs that comprise the double secondary of HR 6497 (Griffin & Griffin 2012) *not* Am stars? Indeed, the detailed study by the ultimate refiners Carquillat & Prieur (2007) shows that there is no simple correlation between binarity and aspects of the Am phenomenon. Moreover, if not all Am stars have been formed by the same process as once so confidently asserted, how is that being explained where astrophysics is taught, and where does it leave stellar evolution theory?

One final note: Broad-sweeping surveys like LSST and Gaia predict the volumes of their discoveries by extrapolation. Ultimate refiners can extrapolate too. The four brightest stars in the northern sky (Arcturus, Vega, Sirius and Capella) are all curiously odd in some way; what does that say, then, for the rest of the stars in our Galaxy?

Have the ultimate refiners been in the shadow of the broad sweepers for too long?

I am very grateful to the Local Organizing Committee and also to the DAO/NRC Canada for generous travel grants that enabled me to attend this conference.

References

Carquillat, J. M. & Prieur, J. L. 2007, MNRAS, 380, 1064

Griffin, R. & Griffin, R. 1988, JA&A, 9, 193

Griffin, R. E. M. & Griffin, R. F. 2012, AN, 333, 613

Griffin, R. E. M. & Griffin, R. F. 2018, AN, 339, 586

Maury, A. C. & Pickering, E. C. 1897, Annals of HCO, 28, 1

Roman, N. G. 1965, High-Velocity Stars, in Galactic structure, edited by Adriaan Blaauw and Maarten Schmidt, (The University of Chicago press), 345

Parameter space and pattern

GAIA'S REVOLUTION IN STELLAR VARIABILITY

L. Eyer[1], L. Rimoldini[2], L. Rohrbasser[2], B. Holl[1], M. Audard[1,2], D.W. Evans[3], P. Garcia-Lario[4], P. Gavras[4], G. Clementini[5], S. T. Hodgkin[2], G. Jevardat de Fombelle[2,6], A. C. Lanzafame[7,8], T. Lebzelter[9], I. Lecoeur-Taibi[2], N. Mowlavi[1,2], K. Nienartowicz[2,7], V. Ripepi[10] and L. Wyrzykowski[11]

Abstract. Stellar variability studies are now reaching a completely new level thanks to ESA's Gaia mission, which enables us to locate many variable stars in the Hertzsprung-Russell diagram and determine the various instability strips/bands. Furthermore, this mission also allows us to detect, characterise and classify many millions of new variable stars thanks to its very unique nearly simultaneous multi-epoch survey with different instruments (photometer, spectro-photometer, radial velocity spectrometer). An overview of what can be found in the literature mostly in terms of data products by the Gaia consortium is given. This concerns the various catalogues of variable stars derived from the Gaia time series and also the location and motion of variable stars in the observational Hertzsprung-Russell diagram. In addition, we provide a list of a few thousands of variable white dwarf candidates derived from the published DR2 data, among them probably many hundreds of new pulsating white dwarfs. On a very different topic, we also show how Gaia allows us to reveal the 3D structure of the Milky Way and its environment thanks to the RR Lyrae stars.

Keywords: stars: general, stars: variables: general, stars: oscillations, stars: white dwarfs, Stars: distances, surveys, methods: data analysis

1 Introduction

The time-domain revolution for "large" sky surveys *from space* keeps advancing strongly since the 1990s, with the Hipparcos mission (ESA 1997), CoRoT (Baglin 2003), and the Kepler/K2 survey (Koch et al. 2010; Howell et al. 2014). Today, we are experiencing a major advance in global space-based surveys thanks to Gaia (Gaia Collaboration et al. 2016) and TESS (Ricker et al. 2015). However, we are still at the stage where each space mission is unique, and we can claim that Gaia benefits from very unique features. One obvious feature is the exceptional astrometric precision, but it is not the only one. Gaia's (spectro)photometric survey with its G band photometry, integrated BP and RP photometry, and BP and RP low resolution spectra is very singular. Gaia remains unique even without its photometry and astrometry, thanks to its spectroscopic survey that covers more than one hundred million objects (Sartoretti et al. 2018). In addition, since the entire sky is measured with one set of instruments and their measurements are made nearly simultaneously, the physical interpretation of the data is facilitated. The uniqueness of Gaia is also revealed by its stunning numbers accumulated during 5 years: nearly 1.3 trillions of astrometric CCD measurements, close to 1.5 trillion G-band/BP/RP photometric CCD data and more than 25 billion spectroscopic measurements.

From all these data of different nature, we can perform large-scale statistical descriptions of the stellar populations of variable stars in the Milky Way and its neighbourhood.

[1] Department of Astronomy, University of Geneva, Chemin des Maillettes 51, 1290 Versoix, Switzerland
[2] Department of Astronomy, University of Geneva, Chemin d'Ecogia, 1290 Versoix, Switzerland
[3] Institute of Astronomy, University of Cambridge, Madingley Road, 10 Cambridge CB3 0HA, UK
[4] European Space Astronomy Centre (ESA/ESAC), Villanueva de la Canada, 28692 Madrid, Spain
[5] Osservatorio di Astrofisica e Scienza dello Spazio di Bologna, Via Piero Gobetti 93/3, 40129 Bologna, Italy
[6] SixSq, Route de Meyrin 267, 1217 Meyrin, Switzerland
[7] Universit di Catania, Dipartimento di Fisica e Astronomia, Sezione Astrofisica, Via S. Sofia 78, 95123 Catania, Italy
[8] Osservatorio Astrofisico di Catania, Via S. Sofia 78, 95123 Catania, Italy
[9] University of Vienna, Department of Astrophysics, Trkenschanzstrae 17, 1180 Vienna, Austria
[10] Osservatorio Astronomico di Capodimonte, Via Moiariello 16, 80131, Napoli, Italy
[11] Astronomical Observatory, University of Warsaw, Al. Ujazdowskie 4, 00-478 117 Warszawa, Poland

2 A few examples of Gaia results

2.1 Science alerts

While scanning the entire sky, Gaia continuously reports alerts* to astronomical events whose scientific potential could be missed if they were not followed up promptly by the community. As of mid-November 2019, the Gaia Photometric Science Alerts team have released more than 10,000 alerts, at a current rate of more than 10 alerts per day. About 25% of the alerts are classified, and out of these about two-thirds turn out to be supernovae (e.g., Kangas et al. 2017). Gaia has also discovered almost 300 cataclysmic variables, and perhaps most excitingly the eclipsing AM CVn system Gaia14aae (Campbell et al. 2015). Thanks to significant community involvement, Gaia has also found in excess of 30 confirmed microlensing events (from >100 candidates, most of which are awaiting confirmation), located mostly outside of the Galactic bulge (e.g. Wyrzykowski et al. 2019).

2.2 Variable stars in the first Gaia data release

Variable-star data were published in the first Gaia data release. The release was small since its main goal was to demonstrate Gaia's photometric capabilities, and to expose the general approach/methodology to analyse the photometric time series of Gaia (Eyer et al. 2017). We released 3,194 G-band time series of Cepheids and RR Lyrae stars from the first 14 month solution and concentrated on stars sampled with the ecliptic pole scanning law (Clementini et al. 2016). There was also a science demonstration article on the period-luminosity (PL) relation for Cepheids and infrared PL and optical luminosity-metallicity relations for RR Lyrae stars (Gaia Collaboration et al. 2017) calibrated with parallaxes of the Tycho-Gaia astrometric solution (TGAS, Lindegren et al. 2016).

2.3 Variable stars in the second Gaia data release

As part of the second data release, "only" half a million stars with Gaia variability information were published (Holl et al. 2018). The resulting catalogues are among the largest catalogues of RR Lyrae (Clementini et al. 2019; Rimoldini et al. 2019), δ Scuti and SX Phoenicis stars (Rimoldini et al. 2019), Long Period variable stars (Mowlavi et al. 2018; Rimoldini et al. 2019), and rotationally modulated variable stars (Lanzafame et al. 2018, 2019). We further published a catalogue of Cepheids in the Galaxy and the Magellanic Clouds (Clementini et al. 2019; Rimoldini et al. 2019; Ripepi et al. 2019) and of short-timescale (< 1 day) variables (Roelens et al. 2018). For all these sources, more than 1.6 million photometric time series (G-band, integrated BP and RP bands) were published as well as statistical attributes and specific parameters for specific groups.

Another product is the science demonstration article (Gaia Collaboration et al. 2019), in which we show where stars of certain variability types are located and how they move in the observational Hertzsprung-Russell diagram. This description is totally unprecedented. It was given for pulsating, cataclysmic, and eruptive stars, eclipsing binaries/exo-planet transit hosts, and rotationally-induced variable stars. For cataclysmic variables, the samples have been cleaned and sub-classified in Pala et al. (2019) and Abril et al. (2019). We also shown how the stars are moving in the Hertzsprung-Russell diagram in several movies, e.g. on YouTube†.

We also derived the fraction of variable stars as detected with the Gaia precision of DR2 over the entire Hertzsprung-Russell diagram. It is quite striking that, in the instability strip at the location of the δ Scuti stars, the fraction of variable stars is not so different than that of Murphy et al. (2019) which is based on Kepler data.

We were also surprised to see the fraction of variables along the white-dwarf sequence which prompted us to analyse further this region of the Hertzsprung-Russell diagram using the published DR2 data (see Section 3).

2.4 Images of the week

There are also examples which are published in the Gaia Image of the Week series at the ESA website‡, which demonstrate the capabilities of Gaia in many different domains, including features of photometric/spectroscopic time series. In that way, astronomers can get an early view of what Gaia is capable of. A few of them are mentioned below.

*http://gsaweb.ast.cam.ac.uk/alerts/home

†https://www.youtube.com/watch?v=Pcy4U5uvL8I

‡https://www.cosmos.esa.int/web/gaia/image-of-the-week

- 29/05/2019: The time series of spectra of X Per (a member of the Be/X-ray class of binaries) from Gaia's Radial Velocity Spectrometer (RVS) was visualised by an animation that shows clear variability of the emission lines of the Be star, linked also to the accretion of the circumstellar matter around the Be star on the neutron star companion. Animations of spectral time series of other stars are also shown, for example one related to the RS CVn system SZ Psc which shows strongly variable chromospheric activity in the calcium lines.
- 24/05/2019: The period-amplitude diagram of rotational-modulation-variability candidates shows a multi-modal structure that is interpreted as different regimes in surface inhomogeneities as function of age, see Lanzafame et al. (2019).
- 18/12/2018: The outburst of a rare FU Orionis star showed the extreme changes in brightness and spectral type that are typical of this type of young stellar objects.
- 15/11/2018: Epoch (or phased dynamical) RP spectra were used to determine if the atmosphere of an evolved star is carbon or oxygen rich (as also described in Mowlavi et al. 2019).
- 24/03/2017: The median colour-magnitude diagram of fundamental-mode RR Lyrae stars was shown to be able to identify the location of these variable stars, from the Galactic halo to the direction towards the bulge, from the Sagittarius dwarf spheroidal galaxy to its tidal streams, and from the Large to the Small Magellanic Cloud.
- 09/10/2015: The radial velocity of a spectroscopic double-lined binary (SB2) was derived for each binary component as a function of time from the epoch RVS spectra.

2.5 Other results on variable stars

The Gaia data have been used for many purposes in relation to variable stars. Here, we highlight a few studies that developed a virtuous circle between Gaia and these topics. We have a stunning improvement of the RR Lyrae luminosity properties (Muraveva et al. 2018) thanks to the high relative precision of Gaia parallaxes for a large number of stars. There is an an interplay with other distance-determination methods based on asteroseimology (Zinn et al. 2019), Cepheids (Riess et al. 2018), and eclipsing binaries (Graczyk et al. 2019), although all of these studies have a larger parallax offset term than the one resulting from quasars (Lindegren et al. 2018; Arenou et al. 2018).

3 New pulsating white dwarf candidates

We detected a whole new set of variable white dwarf candidates from a Gaia DR2-based selection by Gentile Fusillo et al. (2019). To this end, we used the published Gaia DR2 data (Gaia Collaboration et al. 2018), which contain averaged quantities for the photometry of all sources, with the exception of the released variable objects which include also time series, see Holl et al. (2018). We used the uncertainty on the mean and the number of per-CCD measurements to estimate the standard deviation of the (unpublished) photometric time series. This proxy of the amplitude was then used to detect variable white dwarfs as a function of magnitude (e.g., Eyer 1998), as described in Fig. 1. A colour-absolute magnitude diagram of the variable white dwarf candidates is presented in Fig. 2 and the known locations of pulsating white dwarfs are clearly visible. We see the very distinctive clump of ZZ Ceti stars at BP−RP = 0.05 and $M_G = 12.2$, an elongated structure of V777 Her stars at BP−RP = −0.25 and $M_G = 11.2$ and an even more elongated region of GW Vir stars at BP−RP = −0.5 and $M_G = 9$. The low-density general background points are very probably false detections. A sky map of these variable candidates is shown in Fig. 3 and highlights problematic regions with likely contaminants (from over-density-induced correlations in the sky). Such spurious features are well known to the consortium. Such problematic data are also apparent in the quasar map of Bailer-Jones et al. (2019); it is probably coming from their variability indicator. The list of sources is made available along with this publication and also at `https://www.unige.ch/sciences/astro/variability/en/data/`. The list contains 5837 candidates, among them many new true pulsating white dwarfs.

4 The Galaxy in 3D with RR Lyrae stars

We can obtain a view of the structures in and around the Milky Way thanks to the RR Lyrae stars (from DR2, Clementini et al. 2019). For this, we used the simplistic assumption that the RR Lyrae stars from this catalogue

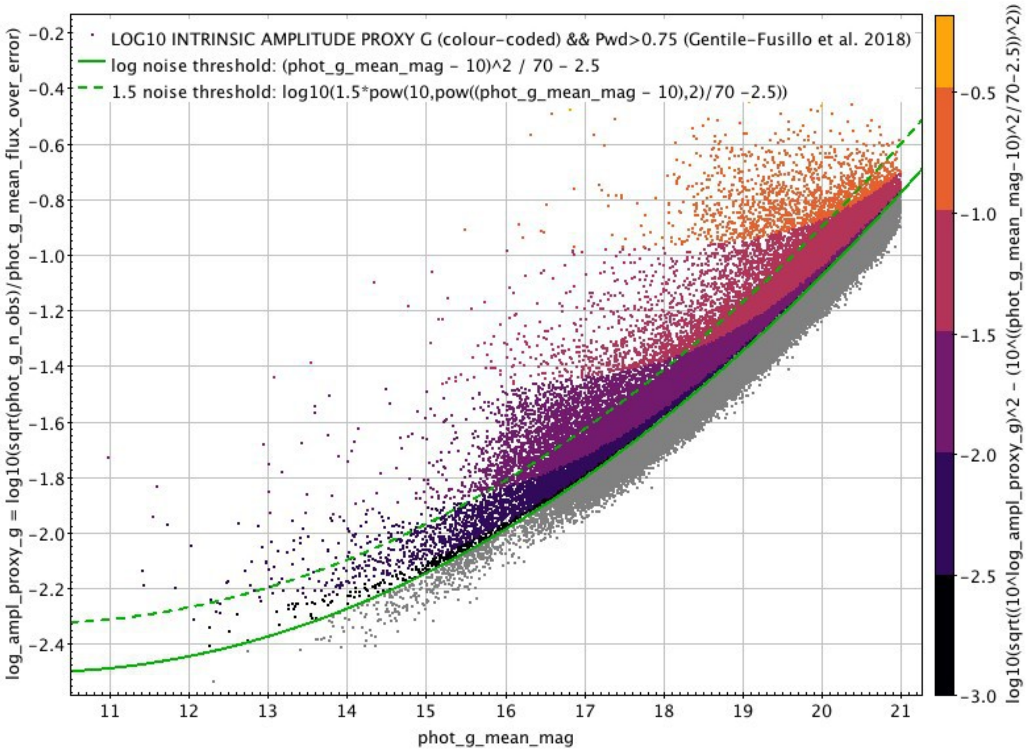

Fig. 1. An amplitude proxy (defined in terms of published quantities) is shown for a selection of white dwarf candidates (with probability greater than 0.75 in Gentile Fusillo et al. 2019) as a function of the mean G-band magnitude. Intrinsic variation amplitudes were computed with respect to the assumed noise level (solid line, which represents an indicative average for constant objects). They are colour-coded as shown in the legend. Most of the white dwarfs above the dashed green line are expected to be intrinsically variable.

have an absolute magnitude of $M_G = 0.6$, and derived their distance from the distance modulus only, without taking into account the dependencies on extinction and metallicity. The 3-dimensional view in Fig. 4 shows the Large and Small Magellanic Clouds, the Sagittarius dwarf galaxy and the associated Sagittarius stream. We can also see small 'streaks' corresponding to globular clusters. The precision of the distances is reduced by the assumptions mentioned above which cause visible radial tails, though the location of the sources in the sky is very precise. This figure can be seen as an online animation using the Chrome browser (only) at the following address: `https://obswww.unige.ch/~eyer/lroro/presentation/`. This animation can be also rolled back and stopped at any time, and it can be interactively explored.

5 Future and other data releases

The first Gaia data release occurred in September 2016 and the second one in April 2018. The work during these data releases was extremely intense and it became clear that an interval of 2 years between successive releases was too short. Currently, the next foreseen release is the third data release (DR3) based on 33/34 months of data. This data release will be split into:

- an early data release (EDR3) in 2020, containing improved astrometry (positions, parallaxes, proper motions) and mean photometry (integrated G, G_{BP}, G_{RP}),
- the full DR3 release in 2021, including 5-10 million variable stars, with a classification, and the associated photometric time series. This release will also include: object classification and astrophysical parameters, together with BP/RP spectra and/or RVS spectra on which they are based; mean radial velocities for stars with available atmospheric parameter estimates; solar-system results with preliminary orbital solutions and individual epoch observations; non-single stars; quasars and results for extended objects. In addition, we proposed to release a pencil beam with epoch photometry for all sources (variable and non-variable), centered on the Andromeda Galaxy.

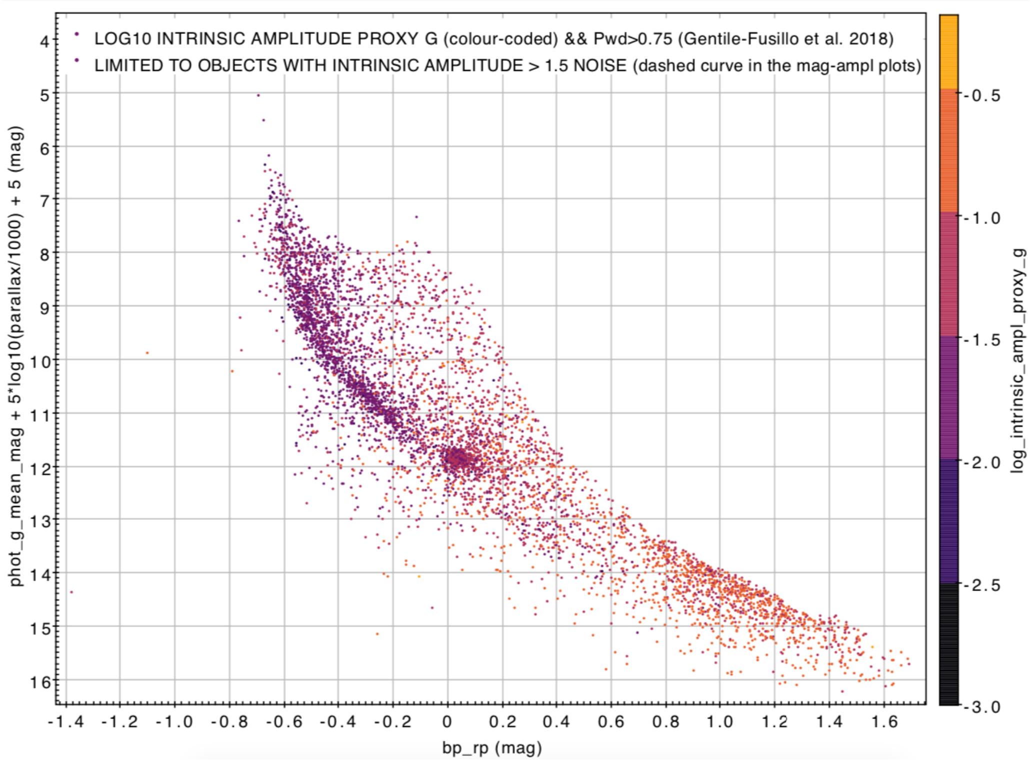

Fig. 2. The observational Hertzsprung-Russell diagram of the variable white dwarf candidates. We note the presence of several regions of over-densities: those that correspond to the known ZZA, ZZB, and ZZO types (from $G_{BP}-G_{RP} \sim 0.1$ mag to bluer objects) and one at the red end of the sequence that is associated with high astrometric excess noise (and thus likely spurious).

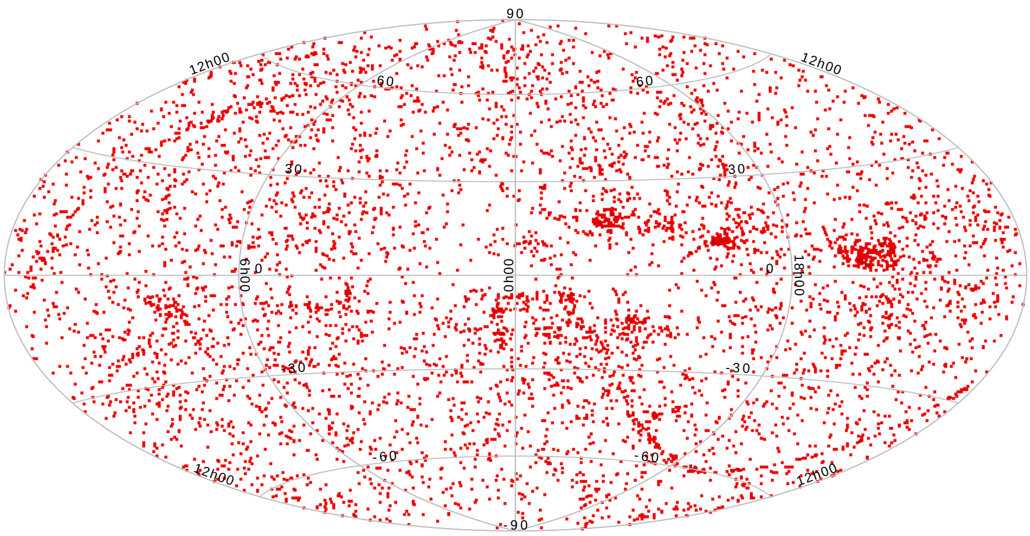

Fig. 3. The sky map of variable white dwarf candidates (in Galactic coordinates). We notice some filamentary features related to the scanning law (owing to outliers within given time intervals). There are also clumps of candidates in regions of low interstellar extinction, most of which correspond to the (likely spurious) over-density at the red end of the sequence in Fig. 2.

.

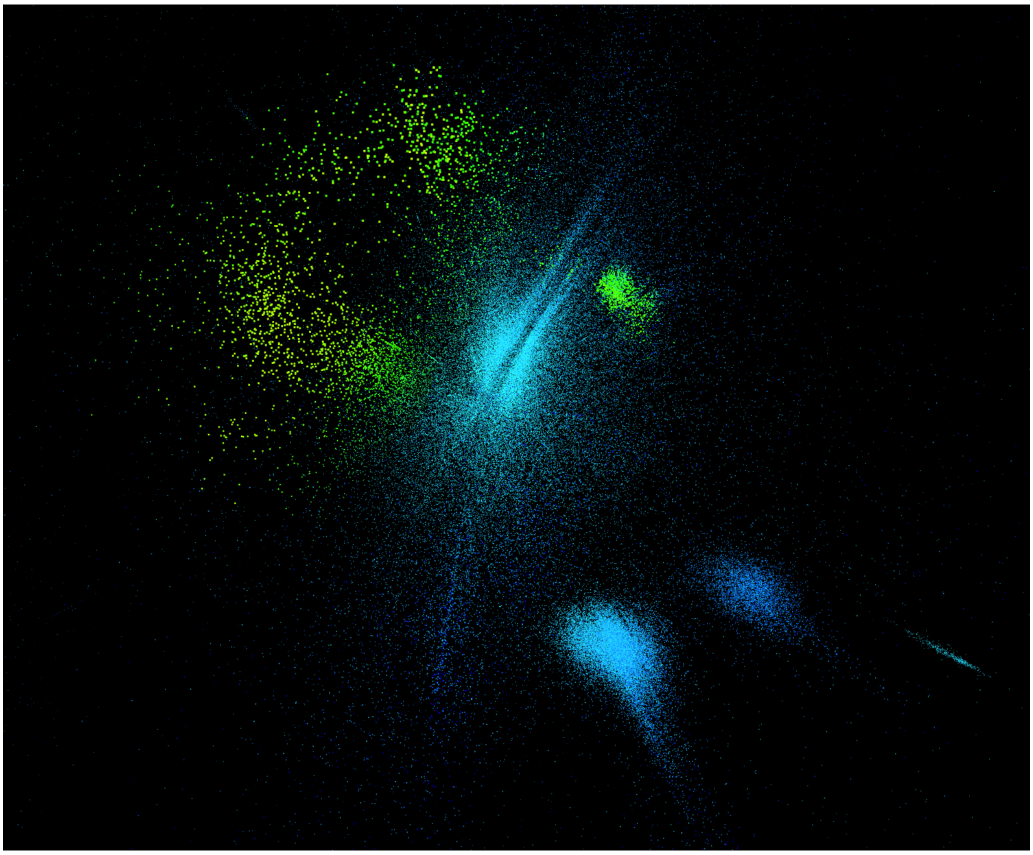

Fig. 4. Distribution of 141,000 RR Lyrae stars from Clementini et al. (2019) in Gaia DR2 as viewed from an unspecified point in space with the animation tool described in Sect. 4. The green points are from a region selected in parallax and proper-motion parameter space. They trace the Sagittarius galaxy and stream.

The latest updates and details on the data releases are available at the ESA website[§].

The time of the 4th data release is not fixed but may happen in 2024, the schedule is currently being discussed within the consortium. This release should contain the first 5 years of data (the nominal mission) and possibly a part of the data from the extended mission.

A final data release containing the nominal mission and the data from the extension (at most 5 years) will also be made (though it is too early to specify a date).

6 Conclusion

By essence/design, Gaia is a time-domain space machine. Gaia time series analysis produces the parallaxes, proper motions, and various photometrically and spectroscopically variable signals. Their nature can be periodic, quasi-periodic, transient or stochastic. These signals from Gaia animate directly many diagrams as shown in this contribution, however they are just the shiny tip of the iceberg of Gaia's contribution to astronomy — Gaia has and will have a staggering impact in nearly all domains of astrophysics, also thanks to its content of variable celestial objects.

Acknowledgement: We would like to thank the late Prof. Gilles Fontaine for the interactions and encouragements on the variable white dwarf candidates from Gaia. This work has made use of data from the European Space Agency (ESA) mission *Gaia* (`https://www.cosmos.esa.int/gaia`), processed by the *Gaia* Data Processing and Analysis Consortium (DPAC, `https://www.cosmos.esa.int/web/gaia/dpac/consortium`). Funding for the DPAC has been provided by national institutions, in particular the institutions participating in the *Gaia* Multilateral Agreement.

[§] `https://www.cosmos.esa.int/web/gaia/release`

References

Abril, J., Schmidtobreick, L., Ederoclite, A. r., & López-Sanjuan, C. 2019, arXiv e-prints, arXiv:1912.01531
Arenou, F., Luri, X., Babusiaux, C., et al. 2018, A&A, 616, A17
Baglin, A. 2003, Advances in Space Research, 31, 345
Bailer-Jones, C. A. L., Fouesneau, M., & Andrae, R. 2019, MNRAS, 490, 5615
Campbell, H. C., Marsh, T. R., Fraser, M., et al. 2015, MNRAS, 452, 1060
Clementini, G., Ripepi, V., Leccia, S., et al. 2016, A&A, 595, A133
Clementini, G., Ripepi, V., Molinaro, R., et al. 2019, A&A, 622, A60
ESA. 1997, The Hipparcos and Tycho Catalogues (ESA), ESA SP-1200
Eyer, L. 1998, PhD thesis, University of Geneva, Switzerland
Eyer, L., Mowlavi, N., Evans, D. W., et al. 2017, arXiv e-prints, arXiv:1702.03295
Gaia Collaboration, Brown, A. G. A., Vallenari, A., et al. 2018, A&A, 616, A1
Gaia Collaboration, Clementini, G., Eyer, L., et al. 2017, A&A, 605, A79
Gaia Collaboration, Eyer, L., Rimoldini, L., et al. 2019, A&A, 623, A110
Gaia Collaboration, Prusti, T., de Bruijne, J. H. J., et al. 2016, A&A, 595, A1
Gentile Fusillo, N. P., Tremblay, P.-E., Gänsicke, B. T., et al. 2019, MNRAS, 482, 4570
Graczyk, D., Pietrzyński, G., Gieren, W., et al. 2019, ApJ, 872, 85
Holl, B., Audard, M., Nienartowicz, K., et al. 2018, A&A, 618, A30
Howell, S. B., Sobeck, C., Haas, M., et al. 2014, PASP, 126, 398
Kangas, T., Blagorodnova, N., Mattila, S., et al. 2017, MNRAS, 469, 1246
Koch, D. G., Borucki, W. J., Basri, G., et al. 2010, ApJ, 713, L79
Lanzafame, A. C., Distefano, E., Barnes, S. A., & Spada, F. 2019, ApJ, 877, 157
Lanzafame, A. C., Distefano, E., Messina, S., et al. 2018, A&A, 616, A16
Lindegren, L., Hernández, J., Bombrun, A., et al. 2018, A&A, 616, A2
Lindegren, L., Lammers, U., Bastian, U., et al. 2016, A&A, 595, A4
Mowlavi, N., Lecoeur-Taïbi, I., Lebzelter, T., et al. 2018, A&A, 618, A58
Mowlavi, N., Trabucchi, M., & Lebzelter, T. 2019, in The Gaia Universe, 62
Muraveva, T., Delgado, H. E., Clementini, G., Sarro, L. M., & Garofalo, A. 2018, MNRAS, 481, 1195
Murphy, S. J., Hey, D., Van Reeth, T., & Bedding, T. R. 2019, MNRAS, 485, 2380
Pala, A. F., Gänsicke, B. T., Breedt, E., et al. 2019, arXiv e-prints, arXiv:1907.13152
Ricker, G. R., Winn, J. N., Vanderspek, R., et al. 2015, JATIS, 1, 014003
Riess, A. G., Casertano, S., Yuan, W., et al. 2018, ApJ, 861, 126
Rimoldini, L., Holl, B., Audard, M., et al. 2019, A&A, 625, A97
Ripepi, V., Molinaro, R., Musella, I., et al. 2019, A&A, 625, A14
Roelens, M., Eyer, L., Mowlavi, N., et al. 2018, A&A, 620, A197
Sartoretti, P., Katz, D., Cropper, M., et al. 2018, A&A, 616, A6
Wyrzykowski, Ł., Mróz, P., Rybicki, K. A., et al. 2019, arXiv e-prints, arXiv:1901.07281
Zinn, J. C., Pinsonneault, M. H., Huber, D., & Stello, D. 2019, ApJ, 878, 136

Stars and their variability observed from space
C. Neiner, W. W. Weiss, D. Baade, R. E. Griffin, C. C. Lovekin, A. F. J. Moffat (eds)

WHAT WE CAN LEARN FROM CONSTANT STARS, AND WHAT DOES CONSTANT MEAN?

E. Paunzen[1], J. Janík[1], J. Krtička[1], Z. Mikulášek[1] and M. Zejda[1]

Abstract. In this paper we postulate the need for a homogeneous sample of non-variable stars for various astrophysical applications. Although there are almost 1 000 000 high-quality space-based photometric light-curves publicly available, such a comprehensive sample still does not exist. We review the needed steps to achieve this goal, the possible pitfalls and present the first results of our corresponding project.

Keywords: Stars: variables: general, Methods: numerical, Techniques: photometric

1 Introduction

Theory predicts that if we look very closely on the brightness of any arbitrarily chosen star, we will find variability. The detection limit of the corresponding amplitude only depends on the instrumentation and accuracy of the measurements. This means that variable stars can be found at all locations across the Hertzsprung-Russell diagram (HRD). Countless papers over the last 150 years have been dedicated to the search and detection of new variable stars. Most astrophysical theories including stellar formation and evolution can be tested with variable stars because they allow a look deep into the stellar interior (e.g. Asteroseimology).

In the following, the term "non-variability" is defined as a given upper limit of variability in a certain wavelength range for a given time base and frequency domain.

Nowadays, we know of millions of variable stars in our Milky Way and other galaxies, especially due to large photometric surveys. In such a situation, it is more and more difficult to find really stable (constant), non-variable stars. However, do we need such stars? Just as an example, non-variable stars can be counted as boundary conditions of stellar models such as evolutionary tracks. It is therefore necessary to know the distribution of non-variable stars across the HRD answering questions like why there are variable together with non-variable stars in the classical instability strip.

In this paper, the need of such objects, the definition of non-variability, some time-series analysis techniques and first results of our dedicated project are reviewed.

2 Why do we need non-variable stars?

First of all, one has to keep in mind that if a star is not listed as variable within one of the various catalogues, this does not mean that it actually is non-variable. It might not be analysed in this respect or the amplitude is below the given detection limit. A photometric colour (index) of a variable object is then measured at a certain phase of the corresponding period. We know that colours and absolute magnitudes can vary significantly for different kinds of variable star groups. In Fig. 1 (adopted from Gaia Collaboration et al. 2019) those changes are shown for several groups. It is obvious that these shifts have to be taken into account when calibrating the effective temperature, mass, and age, for example.

But also studying amplitudes of variables is interesting for several fields of Astrophysics. For example, there exists an amplitude-period-metallicity relation for Cepheids and RR-Lyrae stars (Szabados & Klagyivik 2012). The question if all stars in the corresponding instability strips indeed show pulsations, is still not answered. There is also a clear correlation of the amplitude with the flare activity and spot filling-factor for M-type dwarfs (Yang et al. 2017).

Non-variable stars are very much needed for calibrations of observations as well as theories and models describing the stellar behaviour. Such calibration stars across the HRD are necessary for ground based and also satellite observations, in order to define flux standards, for example. Here, possible applications are listed:

[1] Department of Theoretical Physics and Astrophysics, Masaryk University, Brno, Czech Republic (eMail: epaunzen@physics.muni.cz)

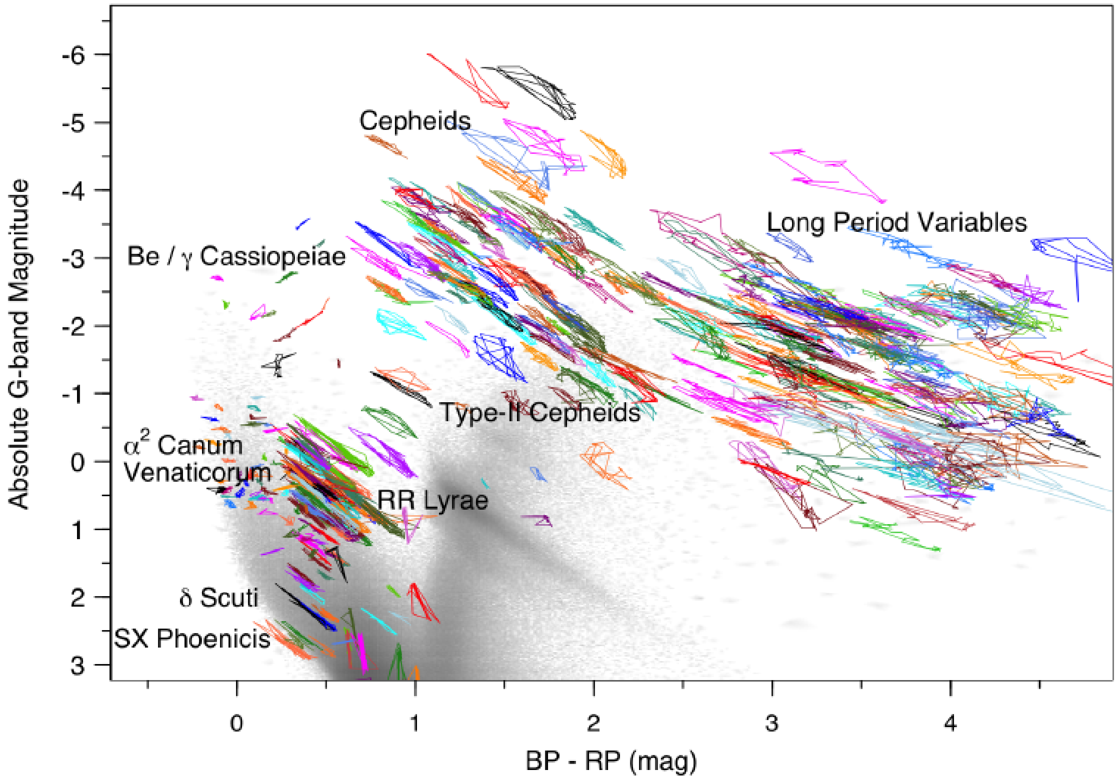

Fig. 1. The changes within the HRD for several variable star groups as adopted from Gaia Collaboration et al. (2019)

- Flux standards (Bohlin 2007)
- Radial velocity standards (Soubiran et al. 2018)
- Calibration of stellar formation and evolutionary tracks (Claret 1995)
- Testing pulsation models (Yadav & Glatzel 2017; Trabucchi et al. 2019)
- Photometric calibration of effective temperature, surface gravity, and metallicity (Netopil 2017)

Finally, the question which astrophysical parameters discriminate a variable and non-variable object in the identical [$T_{\rm eff}$,log $L/{\rm L}_\odot$] or [dereddened colour, absolute magnitude] space is still not answered. One can think of the following parameters which might play a significant role:

- Rotation
- Metallicity
- Binarity
- Stellar Magnetic Field
- Circumstellar Material
- Inclination

A definite conclusion can only be drawn by comparing objects in the same astrophysical parameter space. Thus, generating a sample of non-variable stars (such a sample does not yet exist) will be useful in the wide community for many applications.

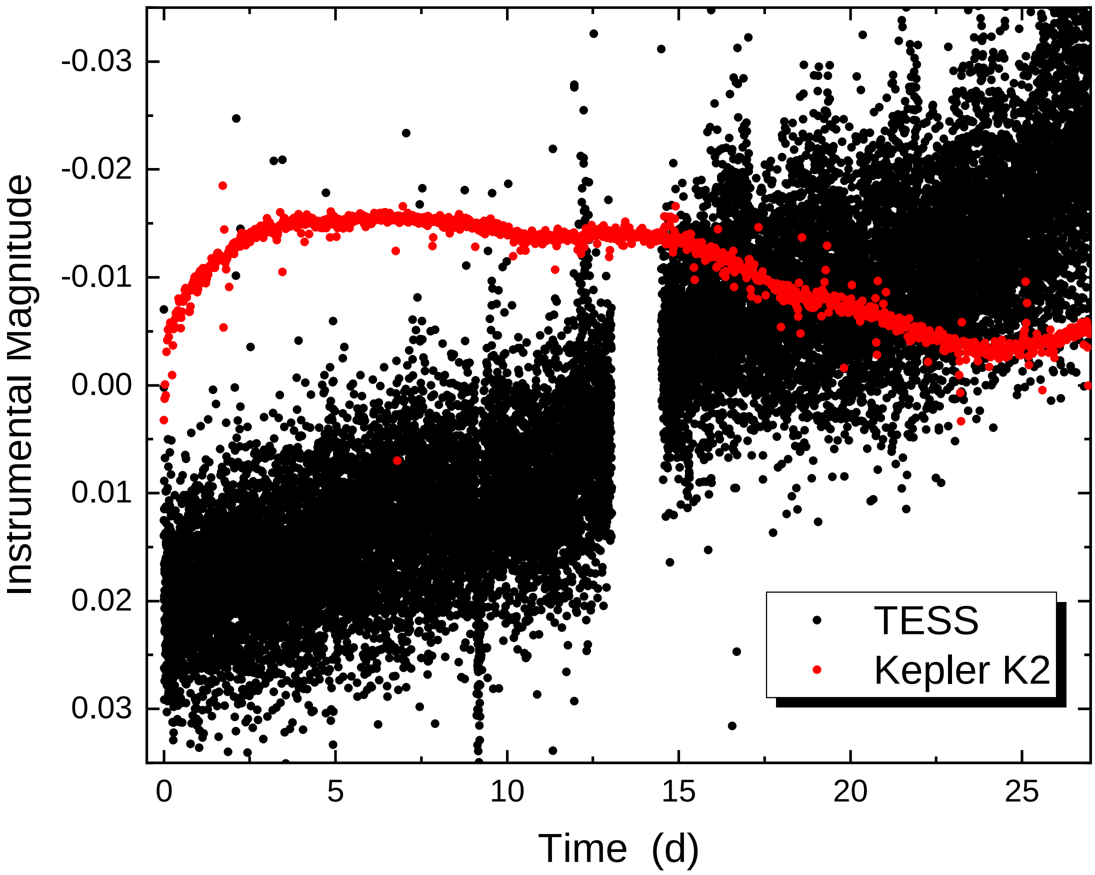

Fig. 2. The photometric data of Kepler K2 and TESS for one selected star. The light curves were shifted to the same zero points, i.e. the scales of the relative instrumental magnitudes were not changed. It is left to the reader to judge if this object is variable or not.

3 What does non-variability mean?

The classical approach is to search for a periodical (usually sinusoidal) signal in a time-series. Different criteria have been established in which frequency and amplitude range such a signal can be detected (Schwarzenberg-Czerny 1989). However, there is also a variety of other methods available, such as string-length (Schwarzenberg-Czerny 1997; Paunzen & Vanmunster 2016) and bootstrap (Paunzen et al. 2013; Mikulášek et al. 2015) methods. To define the (non-)variability, i.e. the significance of a peak in the periodogram, the False Alarm Probability (FAP) as defined in Horne & Baliunas (1986) can be used. If the usage of an automatic routine is intended, only a strict mathematical/statistical test can be applied. However, depending on the data set, the level of non-variability depends on

- Frequency range
- Time basis of the observations
- Amplitude – noise level
- Wavelength region – filter
- Applied "reduction pipeline software"
- Applied time-series analysis method

These characteristics should always be specified when publishing a corresponding analysis. In Fig. 2, the photometric time series of the Kepler K2 and TESS satellite missions for one selected star are shown. The light

Table 1. Characteristics of different data sets including the number of available light curves N_{lc}, which is not necessarily the number of observed stars. Notice that the TESS measurements are still ongoing.

Name	Type	Cadence (d)	Time Basis (d)	Mag. range (mag)	N_{lc}	Filter/Wavelength (nm)
CoRoT		0.00041/0.022	20 – 150	6 – 9/11 – 16	170 000	360 – 950
Kepler		0.00069/0.2083	1500	8 – 19	200 000	420 – 900
K2	Long Cadence	0.2083	80	8 – 19	490 000	420 – 900
	Short Cadence	0.00069	80	8 – 19	2 000	420 – 900
TESS		0.00139/0.02083	27 – 351	4 – 17	250 000	600 – 1 000

curves were shifted to the same zero points, i.e. the scales of the relative instrumental magnitudes were not changed. It is left to the reader to judge if this object is variable or not. However, this star is not listed in the latest version of the The International Variable Star Index (VSX, Watson et al. 2006). But it is obvious that an automatic analysis for such an object is very difficult to interpret in an astrophysical context.

4 How to determine non-variability

The number of available space-based photometric time-series, i.e. photometric light curves, which are publicly available for a significant number of stars is already huge (Table 1). For most of these data sources, an extensive analysis of the instrumental effects and thus introduced false periods is already available. The knowledge of these effects is very important for any time-series analysis (see Fig. 2).

The individual data sets have a different quality due to the processing pipelines. For example, the CoRoT data show small jumps and spurious trends (Paunzen et al. 2015). Before a time series analyses can be applied, an automatic cleaning and pre-processing of the data sets has to be performed. This procedure includes subtracting off the known instrumentally and orbitally introduced frequencies. Also a detrending has to be done.

Depending on the cadence and overall time basis of the data sets (see Table 1), the measurements have to be binned for analysing the desired frequency range. For example, if looking for periods of a few days, bins of one hour and one day should guarantee the search for possible variability in the most convenient way, smoothing out possible short-term variations.

From our experience, we wish to point out a few critical issues which are important in order to generate an automatic way of detecting (non-)variability

- Learning all about the "instrumental frequencies"
- Studying known variable stars in the used data set
- Being aware of the time basis
- Being aware of the frequencies removed by your method/algorithm
- Dividing the investigated frequency range, for example in a low- and high-frequency region
- Frequencies in an "uninteresting" domain may also affect the "interesting" domain
- Being aware of irregular (non-sinusoidal) variability
- Using more than one time series analysis method, i.e. Fourier and String based techniques
- Comparing measurements of objects from common data sets helps learning about the pitfalls

5 What is the current status of non-variable stars?

The status of non-variable stars from different data sources is very unsatisfying. Normally, their characteristics and statistical occurrence compared to the variable stars in the same [T_{eff},$\log L/\mathrm{L}_{\odot}$] or [dereddened colour, absolute magnitude] space are widely neglected and even not known.

One exception is, for example, the paper by Adelman (2001) who investigated time series from the Hipparcos mission. He found many objects reported as variable but turned out to be constant and vice versa.

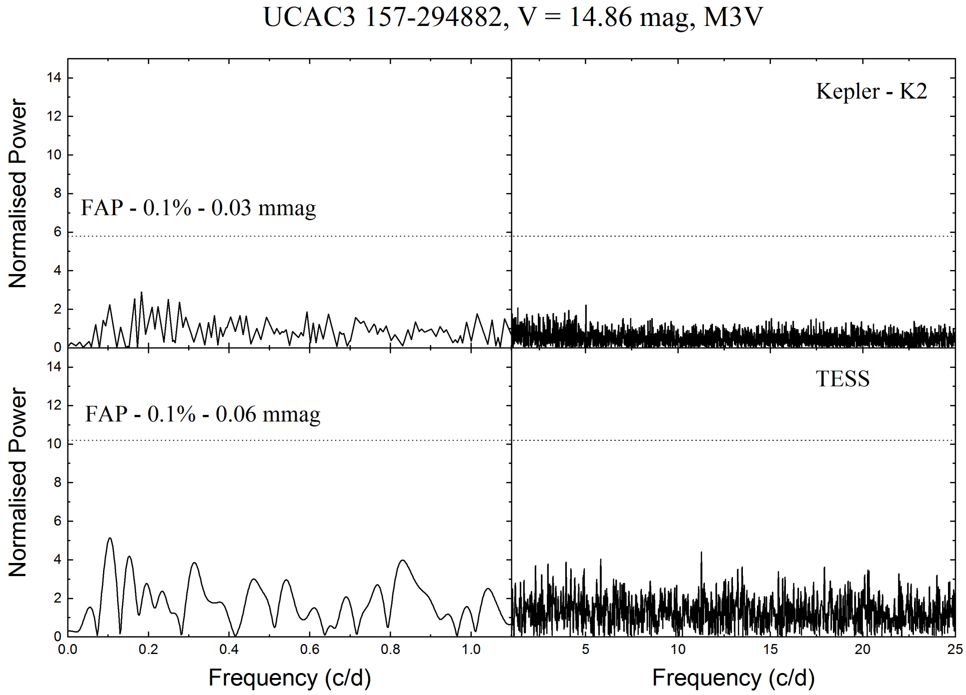

Fig. 3. An example of the result from our automatic algorithm analysing the Kepler K2 and TESS light curves for M3 V star UCAC3 157-294882. It shows two different frequency domains which were analysed.

Recently, a first basic study in this respect entitled "Gaia Data Release 2 – Variable stars in the colour–absolute magnitude diagram" (Gaia Collaboration et al. 2019) was published which we want to discuss in more detail in the following way. On the basis of the available Gaia observations, they searched for (non-)variable stars for which more than 20 observations in the three different bands are available and which have a relative parallax uncertainty of less than 5%. This transforms to a precision level of approximately 5 to 10 mmag. Furthermore, the reddening for all stars was neglected, which excludes the Galactic disk within $\pm 5^{\circ}$. Therefore, they have introduced a bias in their analysis because it is well known that especially young and massive stars are concentrated in the Galactic disk (Carraro 2014). These stars are missing in the published colour-absolute magnitude diagram. In summary, the paper by the Gaia consortium is an excellent guide-line and comparison for any new comprehensive study, but the given accuracy can be significantly improved using other data sets.

We have started a project for automatically analysing photometric light curves in order to define upper limits for non-variability. The algorithm is built such that any data set can be analysed with input parameters, such as known instrumental frequencies and trends, for example.

In Fig. 3, the example of the M3 V star UCAC3 157-294882 is shown. We used the Kepler K2 and TESS light curves for this object and the FAP as defined in Sect. 3 for two different frequency domains. The established non-variability for this 15th magnitude stars is in the sub-mmag region. Such an amplitude limit is need for testing the available pulsation models, for example.

The next step is now to analyse all available light curves from the data sets listed in Table 1 in a homogeneous way. The programs and results will be publicly available to the whole community.

This work was supported by Masaryk University Institutional Support of Research.

References

Adelman, S. J. 2001, A&A, 367, 297

Bohlin, R. C. 2007, ASPCS, Vol. 364, HST Stellar Standards with 1% Accuracy in Absolute Flux (San Francisco: ASP), 315

Carraro, G. 2014, in IAU Symposium, Vol. 298, Setting the scene for Gaia and LAMOST, ed. S. Feltzing, G. Zhao, N. A. Walton, & P. Whitelock, 7–16

Claret, A. 1995, A&AS, 109, 441

Gaia Collaboration, Eyer, L., Rimoldini, L., et al. 2019, A&A, 623, A110

Horne, J. H. & Baliunas, S. L. 1986, ApJ, 302, 757

Mikulášek, Z., Paunzen, E., Netopil, M., & Zejda, M. 2015, ASPCS, Vol. 494, New Tools for Finding and Testing Weak Periodic Variability (San Francisco: ASP), 320

Netopil, M. 2017, MNRAS, 469, 3042

Paunzen, E., Fröhlich, H. E., Netopil, M., Weiss, W. W., & Lüftinger, T. 2015, A&A, 574, A57

Paunzen, E., Mikulášek, Z., Poleski, R., et al. 2013, A&A, 556, A12

Paunzen, E. & Vanmunster, T. 2016, AN, 337, 239

Schwarzenberg-Czerny, A. 1989, MNRAS, 241, 153

Schwarzenberg-Czerny, A. 1997, ApJ, 489, 941

Soubiran, C., Jasniewicz, G., Chemin, L., et al. 2018, A&A, 616, A7

Szabados, L. & Klagyivik, P. 2012, A&A, 537, A81

Trabucchi, M., Wood, P. R., Montalbán, J., et al. 2019, MNRAS, 482, 929

Watson, C. L., Henden, A. A., & Price, A. 2006, Society for Astronomical Sciences Annual Symposium, 25, 47

Yadav, A. P. & Glatzel, W. 2017, MNRAS, 471, 3245

Yang, H., Liu, J., Gao, Q., et al. 2017, ApJ, 849, 36

Stars and their variability observed from space
C. Neiner, W. W. Weiss, D. Baade, R. E. Griffin, C. C. Lovekin, A. F. J. Moffat (eds)

PRE-TESS OBSERVATIONS OF PULSATING WHITE DWARF STARS AT KONKOLY OBSERVATORY

Zs. Bognár[1, 2], Cs. Kalup[1, 3] and Á. Sódor[1,2]

Abstract. The *TESS* (Transiting Exoplanet Survey Satellite) all-sky survey space mission provides a unique opportunity to study the pulsations of white dwarf variables with its 120-second cadence mode. We performed survey observations at the Piszkstető mountain station of Konkoly Observatory, Hungary, to find new bright white dwarf pulsators, which could be potentially interesting targets for *TESS* observations. We successfully identified two new ZZ Ceti pulsators, WD 1310+583 and PM J22299+3024. We also performed extended observations of other proposed *TESS* targets, LP 119-10 and HS 1625+1231, respectively. With the one-season long measurements of these stars, we determined a set of eigenmodes for all targets. We present here the results of our measurements on these four ZZ Ceti variables.

Keywords: techniques: photometric, stars: oscillations, white dwarfs

1 Introduction

The most populous group of the pulsating white dwarf stars is that of ZZ Ceti. ZZ Ceti (or DAV) stars are short-period (P ∼ 100–1500 s) and low-amplitude ($A \sim 0.1\%$) pulsators with 10 500–13 000 K effective temperatures. Pulsation modes detected in these objects are low spherical degree ($\ell = 1$ and 2), low-to-mid radial order g-modes.

The main goal of the almost all-sky survey *TESS* space mission (Ricker et al. 2015) is to detect exoplanets at nearby and bright stars with the transit method. However, with the time sampling of 120 s of the short-cadence mode available for selected targets, it is also possible to study the light variations of several different types of short-period pulsating variable stars, including white dwarf pulsators.

We performed observations with the 1-m Ritchey–Chrétien–Coudé telescope located at the Piszkéstető mountain station of Konkoly Observatory, Hungary. We obtained data with an FLI Proline 16803 CCD camera in white light. The exposure times were 30–60 s. Raw data frames were treated the standard way utilizing IRAF tasks, then we performed standard Fourier analysis of the reduced data sets with the photometry modules of the Frequency Analysis and Mode Identification for Asteroseismology (FAMIAS) software package (Zima 2008).

2 WD 1310+583

WD 1310+583 (B = 13.9 mag) was observed on eight nights during the 2017 March–July term, and we determined 17 significant frequencies in the complete data set (Bognár et al. 2018). Seven of them seem to be independent pulsation modes. The additional, closely spaced frequencies to these modes suggest the presence of amplitude and/or phase variations, frequently observed in ZZ Ceti stars in the middle of the instability strip or close to its red edge. This newly discovered relatively bright WD variable is an excellent target for 1-m-class telescopes.

3 HS 1625+1231

HS 1625+1231 (B = 16.1 mag) was reported as a new ZZ Ceti variable by Voss et al. (2006). They detected three pulsation periods at 385.2, 533.6, and 862.9 s. We observed this star on 14 nights in the 2019 observing season (March–July), and our frequency analysis resulted in the determination of six pulsation modes between 514 − 881 s.

[1] Konkoly Observatory, Research Centre for Astronomy and Earth Sciences, Konkoly Thege Miklós út 15-17, H–1121 Budapest
[2] MTA CSFK Lendület Near-Field Cosmology Research Group
[3] Eötvös University, Department of Astronomy, Pázmány Péter sétány 1/A, H–1117 Budapest

4 PM J22299+3024

We discovered the variability of PM J22299+3024 ($g = 15.9$ mag) in July 2018. At that time we considered it as a variable candidate, as only one night of observations was available on this target (Bognár et al. 2019). However, the subsequent observations proved that PM J22299+3024 is indeed a new, bright ZZ Ceti star, laying close to the red edge of the instability strip. Based on 14 nights of observations (2018 July–November), we accepted eight modes between 967 – 1335 s, which can be inputs for asteroseismic fittings. However, its complex frequency structure suggests that further modes may be present in the data set. Additional observations will hopefully clear this situation up.

5 LP 119-10

LP 119-10 ($B = 15.3$ mag) was discovered to be a variable star by Green et al. (2015). They presented one frequency at 873.6 s in the discovery publication. We collected data on this star altogether on 20 nights between October 2018 and April 2019. Our data analysis revealed an even more complex frequency structure than in the case of PM J22299+3024, and we have determined ten pulsation modes between 768 – 1005 s.

6 Ongoing observations and future plans

All four stars are amongst the targets proposed for *TESS* observations. However, because of the unexpected field shifts, the space telescope did not observe PM J22299+3024 in the planned cycle. Therefore, we decided to collect more data on this target from the ground until December, 2019. We also plan to analyse the *TESS* data on the remaining three targets, correct the periods if needed, complete the list of known eigenmodes with the ones detected by the space-based measurement (if any), and perform asteroseismic fits utilizing the modes derived this way.

ZsB acknowledges the support provided from the National Research, Development and Innovation Fund of Hungary, financed under the PD_{17} funding scheme, project no. PD-123910. This project has been supported by the Lendület Program of the Hungarian Academy of Sciences, project No. LP2018-7/2019.

References

Bognár, Z., Kalup, C., & Sódor, Á. 2019, Acta Astron., 69, 55

Bognár, Z., Kalup, C., Sódor, Á., Charpinet, S., & Hermes, J. J. 2018, MNRAS, 478, 2676

Green, E. M., Limoges, M. M., Gianninas, A., et al. 2015, in ASPCS, Vol. 493, 19th European Workshop on White Dwarfs, ed. P. Dufour, P. Bergeron, & G. Fontaine, 237

Ricker, G. R., Winn, J. N., Vanderspek, R., et al. 2015, JATIS, 1, 014003

Voss, B., Koester, D., Østensen, R., et al. 2006, A&A, 450, 1061

Zima, W. 2008, Communications in Asteroseismology, 155, 17

Stars and their variability observed from space
C. Neiner, W. W. Weiss, D. Baade, R. E. Griffin, C. C. Lovekin, A. F. J. Moffat (eds)

A PRE-MAIN SEQUENCE VARIABILITY CLASSIFIER FOR TESS

M. Müllner[1] and K. Zwintz[1]

Abstract. We present a new variability classifier to identify pre-main sequence (pre-MS) stars observed by the Transiting Exoplanet Survey Satellite (TESS) mission. We present 4 indicators to characterize this type of star and briefly suggest how this classifier can be used in the future.

Keywords: Stars: pre-main sequence, Methods: statistical, Stars: variables: T Tauri, Herbig Ae/Be

1 Introduction

The identification of pre-MS stars is a notoriously hard task, as young stars are indistinguishable from their post-MS counterparts in the HR-diagram. The distinction of these two types of evolutionary stages is usually done by including observational features typical for the pre-MS phase to associate stars to young star forming regions, assuming that the members of these regions formed at the same time. We present an alternative methodology which takes into account four indicators of pre-MS nature as part of the classification scheme in the TASOC* collaboration. In the following we describe the individual indicators used in the classification scheme.

2 Identifying T-Tauri objects

T-Tauri objects are low-mass pre-MS stars with a unique light-curve (LC) morphology. These objects generally show either regular variability, semi-regular variability or irregular variability. For this work we consider only the semi-regular variable T-Tauri stars. If we can identify and find this type of variability in a given star, we can conclude that it is a pre-MS object. The indicator consists of a three-step algorithm (as indicated by box **1.** in Fig. 1):

1. Initially, we smooth the high-frequency variation in the LC. We then count the number of zero crossings, giving an initial approximation for the period in the variability P'_{var}.
2. We apply the phase dispersion minimization (PDM) technique (Stellingwerf 1978) to the LC. Using P'_{var} from step one, we search for the closest dominant period in the PDM, P_{var}, which we apply in step three.
3. The light curve is phase-folded with P_{var}. We then count the number of minima N_m in the phases, and if that number is equal for all periods we define this star as a semi-regular T-Tauri object.

3 Gaia astrometry and young stellar clusters

We also use the classical approach for the identification of pre-MS stars by their association with young clusters. To find young clusters and their member stars, we use the catalogues of visible clusters from Dias, W. S. et al. (2002), Cantat-Gaudin et al. (2018) and Sampedro et al. (2017). Each individual star is assigned a pre-MS probability according to its position in its evolution, taking the age of the cluster into account as well as the different evolution time-scales for different masses. This is indicated as box **2.** in Fig. 1.

4 Gaia flux uncertainty as a proxy for variability

Applying the methodology from Vioque et al. (in prep.), one can use the Gaia (Gaia Collaboration et al. 2016) flux error as a variability indicator and as a proxy for pre-MS stars. With a specifically trained neural network (indicated by box **3.** in Fig. 1), we can assign pre-MS probabilities to stars based on the Gaia flux error as well as on some other parameters available from Gaia.

---

[1] Institut für Astro- und Teilchenphysik, Universität Innsbruck
*`https://tasoc.dk/`

5 Variability tree classifier

Many pre-MS stars show strong irregular variability during the early phases of their evolution. We can make use of that by applying the methodology from Valenzuela & Pichara (2018). In their work they describe an algorithm to create a variability tree classifier; it is described there in detail.

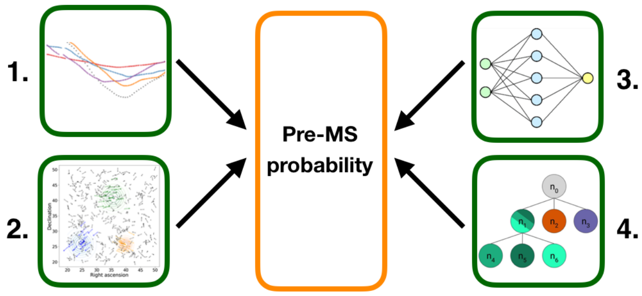

Fig. 1. Overview over the four indicators used in the classification scheme. Box 1. illustrates the identification of T-Tauri objects, 2. the use of Gaia astrometry and cluster association, 3. shows a schematic neural network used to identify pre-MS stars by considering the Gaia flux error, and 4. shows the populated variability tree.

6 Conclusion

We have presented a novel way to distinguish pre-MS stars from their more evolved counterparts. We showed four distinct ways to classify pre-MS stars, each with their unique strengths. This classifier will be a part of the TASOC classification scheme, and will be applied to all the stars in the TASOC catalogue.

References

Cantat-Gaudin, T., Jordi, C., Vallenari, A., et al. 2018, A&A, 618, A93

Dias, W. S., Alessi, B. S., Moitinho, A., & Lépine, J. R. D. 2002, A&A, 389, 871

Gaia Collaboration, Prusti, T., de Bruijne, J. H. J., et al. 2016, A&A, 595, A1

Sampedro, L., Dias, W. S., Alfaro, E. J., Monteiro, H., & Molino, A. 2017, MNRAS, 470, 3937

Stellingwerf, R. F. 1978, ApJ, 224, 953

Valenzuela, L. & Pichara, K. 2018, MNRAS, 474, 3259

Stars and their variability observed from space
C. Neiner, W. W. Weiss, D. Baade, R. E. Griffin, C. C. Lovekin, A. F. J. Moffat (eds)

CLASSIFICATION OF VARIABLE STARS

D. Tarczay-Nehéz[1,2], R. Szabó[1,2] and Z. Szeleczky[3]

Abstract. The most recent space telescopes (e.g. Kepler, K2, Gaia, TESS) and sky surveys (e.g. SSDS, and the forthcoming LSST) provide huge amounts of data, and creating challenges of data processing. These huge amounts of data need to be analyzed with fast and effective robotic computer programming techniques. Machine learning algorithms are becoming popular in astronomy, as they can play a key role in the automatic classification of variable stars. In this work, we present our machine learning algorithm for searching variable stars; it is based on statistical data of light-curves that represent the brightness variability of the Cepheid variables observed by Gaia (see Gaia Data Release 2 in Gaia Collaboration et al. 2018)*.

Keywords: Stars: variables: Cepheids, Methods: data analysis

1 Introduction

The most recent rapid increase in the amount (and quality) of data reveals the importance of applying new automated classification and data processing techniques to the observations. Machine learning techinques have been used for classifications of time-series data since the early 2000s (see e.g. Belokurov et al. 2003; Mahabal et al. 2008; Richards et al. 2011, and the references therein).

To classify variable stars, we have used supervised machine learning techniques, and have compared the accuracy against the Cepheid variables listed in the Gaia DR2. The Gaia archive provides an easy access to all classified variable stars. The Gaia DR2 archive consists of 9575 Cepheid variables (8890 classical, 585 Type II, 100 anomalous Cepheids; see the distribution in Fig. 1)

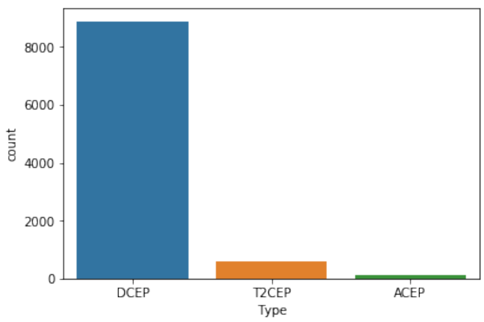

Fig. 1. The distribution of three types of Cepheid variables in the Gaia DR2 archive.

To carry out classifications, we used the Fourier parameters of the folded light-curves listed in the data base:

- period values (fundamental (PF), first overtone (P1O), second overtone (P2O), third overtone (P3O));
- peak-to-peak amplitude (in G band);
- phase differences (ϕ_{21} and ϕ_{31});
- amplitude ratios (R_{21}, R_{31}).

[1] Konkoly Observatory, Research Centre for Astronomy and Earth Science, Konkoly-Thege Miklós 15-17, H-1121
[2] MTA CSFK Lendület Near-Field Cosmology Research Group
[3] University of Liverpool, Liverpool, UK
*https://www.cosmos.esa.int/web/gaia/dr2

2 Classification

We compared the precision of 5 different supervised machine learning algorithms to classify Cepheid variables. For the classification process, we used the scikit-learn Python machine learning library†. In each case, the first step is to split our data into training sets and test sets. We then investigated 3 cases (see Table 1):

- 90% training + 10% test set (T10);
- 85% training + 15% test set (T15);
- 80% training + 20% test set (T20).

Table 1. Accuracy of the machine learning algorithms in the test sample of the Gaia DR2 Cepheids.

Algorithm	**Accuracy**		
	T10	**T15**	**T20**
Logistic regression	0.93	0.93	0.94
Decision tree (depth = 3)	0.93	0.94	0.94
K-Nearest Neighbor	0.93	0.94	0.95
Support Vector Machine	0.93	0.93	0.94
Gaussian Naive Bayes	0.33	0.26	0.26

Fig. 2 shows the scatterplot-matrix of the Fourier parameters of the Cepheid variables used for the classification, which shows the correlations in each parameter, i.e., there is a weak correlation between the amplitude ratios.

3 Example: decision tree

Figure 3 shows the decision tree for our test sample of Gaia DR2 Cepheids. In this case we have set a depth of only 3, meaning that the longest path from the "root" to the "leaf" is 3.

The first step in the decision tree algorithm is to analyze one of the given parameters (e.g. X_0 in Fig. 3): is this value smaller than 0.029? The decision can be either true or false. The algorithm moves forward, checking different parameters at each depth. The gini score describes the purity of each leaf/node. If gini = 0, it means that only 1 single class exists in that leaf/node and the decision is pure.

The example describes the number of test sample elements in each node. In the beginning, for the T10 case, our test sample contains 8617 Cepheids. That value represents the number of test sample elements in each category. In fact it contained 91 anomalous Cepheids, 8004 classical Cepheids and 522 Type II Cepheids. The decision tree algorithm may suffer from overfitting if the depth is too large. To minimize errors, one should use a Random Forest method, which is a collection of decision trees.

Technical help from Attila Bódi, László Molnár is gratefully acknowledged. We also acknowledge financial support from the Momentum grant No. LP2018-7/2019 of the Hungarian Academy of Sciences, the Hungarian OTKA Grant No. 119993 and from the Hungarian NKFIH project K-115709.

References

Belokurov, V., Evans, N. W., & Du, Y. L. 2003, MNRAS, 341, 1373

Gaia Collaboration, Brown, A. G. A., Vallenari, A., et al. 2018, A&A, 616, A1

Mahabal, A., Djorgovski, S. G., Turmon, M., et al. 2008, AN, 329, 288

Richards, J. W., Starr, D. L., Butler, N. R., et al. 2011, ApJ, 733, 10

† `https://scikit-learn.org/`

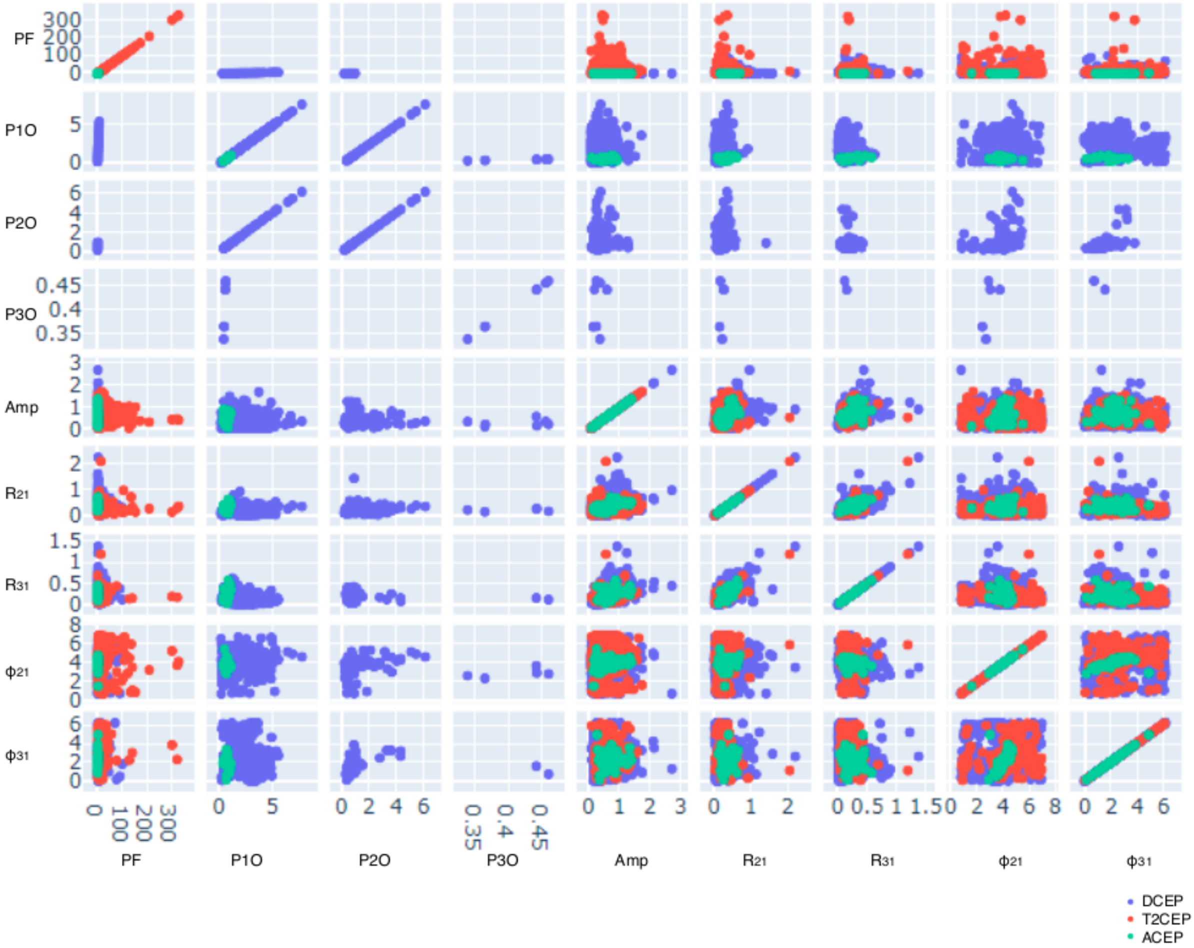

Fig. 2. Scatterplot-matrix of the Fourier parameters on GDR2 Cepheids.

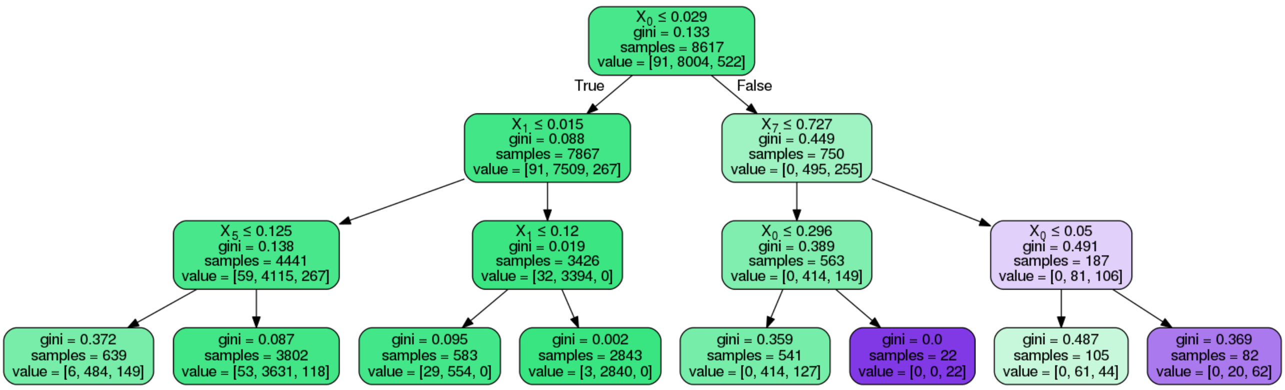

Fig. 3. Decision tree for Gaia DR2 Cepheid variables (with depth = 3) in the case of T10.

Pulsation

THE DEMYSTIFICATION OF CLASSICAL Be STARS THROUGH SPACE PHOTOMETRY

D. Baade[1] and T. Rivinius[2]

Abstract. All optical high-cadence space photometers have observed Be stars and achieved some of their most prominent results with them. Single-object highlights from five different satellites are selected to delineate the progress made for Be stars. Multi-mode nonradial pulsation (NRP) is the most universal photometric signature of Be stars, and variations on timescales from days to years can be traced back to them. Nested multi-instance NRP frequency differences explain regularly repeating outbursts of Be stars, which probably are the building blocks of the formation process of the gaseous disks around Be stars. During outbursts, frequency spectra can differ drastically from those at quiescence. Observations by TESS of hundreds of Be stars may (i) pulsationally distinguish Be stars from the also rapidly rotating but diskless Bn stars and (ii) discriminate between different evolutionary paths towards Be stars. Conceivably, the angular-momentum loss incurred by pulsation-driven outbursts enables Be stars to escape rotational rupture. This process may also govern the selection of frequency differences involved in the mass loss.

Keywords: Stars: emission-line, Be, Stars: oscillations, Stars: mass loss, Stars: individual: ζ Oph, α Eri, HD 49330, KIC 11971405, 25 Ori

1 Introduction

γ Cas was the first B-type star discovered to exhibit emission lines (Secchi 1866). In the $1\frac{1}{2}$ centuries elapsed since then, new myths popped up from time to time, trying to explain complex, often coupled variabilities on timescales from hours to decades. Careful analysis of high-quality data ultimately overcame them all. Long-term space photometry made particularly valuable contributions. For broad reviews of Be stars see Porter & Rivinius (2003) and Rivinius et al. (2013).

Already in 1931, Struve (1931) realized that Be stars form a rapidly rotating sub-population of B-type stars that are surrounded by a gaseous disk. Extreme rotation is difficult to characterize quantitatively from spectra only (Townsend et al. 2004) so that the scarcity of critically rotating Be stars might be due to a bias. On the other hand, Achernar, one of the interferometrically best-studied Be stars (Domiciano de Souza et al. 2014) is probably rotating slightly sub-critically. With these caveats, it seems reasonably safe to state that rotational instability is not the mechanism by which Be stars eject matter into the disk. Even safer is the conclusion that it is viscosity that transforms $\sim$1% of the ejecta into a Keplerian disk (for the Viscous Decretion Disk [VDD] model, see Labadie-Bartz & Carciofi, these proceedings and references therein).

Very few other long-standing issues of stellar physics have benefited more from space photometry than the understanding of the mass-ejection mechanism of Be stars. After first spectroscopic detections of nonradial pulsations (NRPs), space photometry established the ubiquity of NRPs in Be stars. As elaborated below, multi-mode NRP seems to be at the core of the mass-loss process. The observed frequencies straddle the domain of plausible rotation frequencies. Therefore, it is sometimes still speculated that the variability of Be stars is due to rotational modulation of some usually undisclosed quantity (e.g., Smith et al. 2016; Balona & Ozuyar 2019). Such beliefs are only possible if the spectroscopic proof of highly structured large-scale surface-velocity fields (Rivinius et al. 2003) is ignored. Rotational modulation cannot accommodate such velocity fields whereas NRP produces them. Of course, it is impossible to exclude rotational modulation as a higher-order effect. However, given the difficulty of reliably determining the rotation rate of Be stars, it is extremely hard to identify the rotation frequency with any confidence among the often large number of peaks in power spectra.

[1] European Organisation for Astronomical Research in the Southern Hemisphere (ESO), Garching b. München, Germany
[2] European Organisation for Astronomical Research in the Southern Hemisphere (ESO), Santiago, Chile

2 Discoveries by space photometry of specific variability properties of Be stars

All high-cadence optical space photometers observed Be stars, each made specific discoveries, and the results concatenate such that multi-mode NRP is the strongest contender for the driver of the star-to-disk mass-transfer process in Be stars. The following subsections describe the progress satellite by satellite, ordered by the start of their operations. Because of the limited space, observations of only one Be star each are highlighted.

2.1 Microvariability and Oscillations of Stars Telescope (MOST)

MOST (2003-2011, Walker et al. 2003) pioneered the photometric monitoring of stars from space. So far it was the last point-source space photometer without a dedication to exoplanets in its name. The showcase Be star was ζ Oph (O9.5 Ve, Walker et al. 2005). MOST detected at least a dozen frequencies from observations spanning 24 days. This was a significant step forward from the two groups of frequencies detected in μ Cen (B2Ve, Rivinius et al. 1998). Parallel spectroscopy from three sites with high cadence, spectral resolution, and S/N confirmed the NRP nature for 6 of the 12+ frequencies. While none of the details found in ζ Oph had not been seen before, MOST established the complexity of Be stars to be at par with other pulsating early-type stars.

2.2 Solar Mass Ejection Imager (SMEI)

The mission of SMEI (2003-2011, Jackson et al. 2004) was to monitor space weather in the inner solar system. For clean maps of the light scattered by electrons ejected by the Sun, stars down to $\sim$10th magnitude had to be removed. The community owes the SMEI responsibles much gratitude for not scrapping these snippets on a rubbish tip but making them available in an online database*. By the example of α Eri (B6 Ve, Achernar), SMEI established for the first time the long-term coherence (over 5+ years) of a variability in a Be star (Goss et al. 2011), another important requirement if variability is to be assigned a high diagnostic value.

2.3 Convection, Rotation and planetary Transits (CoRoT)

The nominal dedication of CoRoT (2006-2012, Baglin et al. 2006) to exoplanet transits did not prevent its usage for observations of, and important discoveries in, Be stars. Most spectacular was the serendipitously captured detailed light curve of a small outburst of the B0.5 IVe star HD 49330 (Huat et al. 2009). Almost since the discovery of mass loss from Be stars, there had been indications of the now well-established fact that a large part of this process consists of a discontinuous, event-like component. The CoRoT observations of HD 49330 illustrated for the first time substantial changes in the photometric power spectrum during the course of a Be outburst. In the low-to-intermediate frequency domain, numerous features grew above the detection threshold while others lost the prominence they had during quiescence. The causality, though, remained ambiguous: Did the outburst change the pulsation pattern, or did changes in the pulsation cause the outburst? Also, were the additional frequencies stellar or circumstellar?

2.4 Kepler

The impact on Be stars of Kepler (2009-2018, Borucki et al. 2010), the most powerful space photometer to date, was limited by the selection of a patrol field with a high content of sun-like stars. However, this resulted in the data for the just three, moreover marginal, observed Be stars being analyzed by three different teams. In KIC 11971405, Kurtz et al. (2015) could reconstruct only five frequencies from, partly not particularly simple, linear relations between some of a total of 15 base frequencies, but speculated that many more such constructs should exist so that outbursts would be powered by multi-mode beating. The wavelet analysis of the light curves by Rivinius et al. (2016) identified several frequency groups and revealed variable correlated as well as anticorrelated group amplitudes. In the latest investigation of KIC 11971405, Pápics et al. (2017) realized that the top-level clustering of frequencies is probably explained by the scheme more broadly described in Sect. 2.6. Baade et al. (2018) added that the spacing in time of the outbursts noted by Kurtz et al. (2015) and Pápics et al. (2017) corresponds to the frequency difference between two of the highest-amplitude variations.

---

*http://smei.ucsd.edu/new_smei/data&images/stars/timeseries.html

2.5 Bright Target Explorer (BRITE)

Being nano(= dwarf)-spacecraft, the five BRITE satellites (2014-2020+, Weiss et al. 2014) easily stand on the shoulders of giants. However, with the exception of SMEI, which reached much worse single-measurement accuracy, and the few Kepler Be stars, the BRITEs spread their wings over more time than their predecessors. The resulting higher frequency resolution enabled the discovery in 25 Ori (B1 Vn, Baade et al. 2018) of outbursts apparently pumping matter into the disk with a difference frequency corresponding to multiple frequency differences of the same value ('multi-instance frequency differences'). Another, but lower, difference frequency governs the timing of the mass-loss-valve opening events. Further difference frequencies at the same or higher levels of nesting may exist. The appearance in the frequency spectra of such difference frequencies may be partly caused by the concomitant amplitude modulation with the difference frequency but is a useful empirical indicator. In power spectra, the difference frequencies appear with high power so that they are not due to a beating process. Multi-instance frequency differences would also remove the ambiguity in the CoRoT observations of the outburst of HD 49330: It is the pulsations that drive the outburst. Moreover, such tight relations are not likely to exist between stellar and disk variations or disk variations only so that they are all of stellar origin. However, one ambiguity remains: Is the increased photometric amplitude associated with the higher difference frequency the result of increased pulsation amplitudes or a nonlinear atmospheric/circumstellar response or both. Temporarily reduced amplitudes may be due to obscuration by ejecta (Maintz et al. 2003; Balona & Ozuyar 2019).

2.6 Transiting Exoplanet Survey Satellite (TESS)

At the time of this conference, TESS (2018-2020+, Ricker et al. 2016) had accumulated half of its prospected data harvest, which will include precision light curves of many hundred Be stars covering between 1 and 12 months. Even at the upper end of this range, observations with other satellites do not predict three periodically repeating outbursts as a standard feature, placing the slow periodicity, which could be the 'secret' of many Be-stars, out of reach. Accordingly, TESS will probably make its biggest impact by exploiting the vast superiority of its statistics. Two applications not so far observationally accessible jump to mind:

- Do Bn stars, which are rapidly rotating B stars without disk, pulsate differently than Be stars as unpublished spectroscopy reportedly suggested (Penrod 1986)? If yes, this would support the conclusion that pulsations are at the root of the Be phenomenon.
- Do *bona fide* single and binary Be stars pulsate differently? If yes, there might be (at least) two evolutionary paths towards Be stars: If single Be stars are not the result of mergers, their formation process (Martayan et al. 2007) and the evolutionary contraction of the core (Granada et al. 2013) could combine and lead to the observed rapid surface rotation. Competing models (cf. Langer et al. 2019, and references therein) attribute the rapid rotation to mass and angular-momentum transfer in a binary. Bimodal pulsation properties could hint at both evolutionary paths having been followed.

As a byproduct, the clustering of frequencies could be studied in more detail. Preliminary evidence suggests (Pápics et al. 2017; Baade et al. 2018) that many Be-star frequency spectra exhibit three major clusters. The main one is around 1 c/d, a second one consists mostly of difference frequencies built from the main one, and the third one comprises mainly sum frequencies and second harmonics from the main cluster. In this scheme, the main (middle) cluster would host the stellar eigenfrequencies. The location, width, total population, internal spacing etc. of these clusters should be investigated for links to spectral type, rotation rate, etc.

In addition, some Be stars also exhibit higher frequencies that occupy the range of p-modes in β Cephei stars. The dependence of such frequencies on spectral type, $v \sin i$, and other parameters as well as any correlation with the slower variations in the three clusters mentioned could provide important global asteroseismological indicators of the structure and, by implication, formation process of Be stars.

3 Conclusions

Two developments have removed the veil of alleged mysteriousness from Be stars: the VDD model and the satellite-boosted quality of light curves. Together they have laid the foundation to an incipient ability to crudely 'read' the observed variability of many classical Be stars. Nonlinear coupling of multi-instance frequency differences is the key process. In the simplest case, one such difference frequency opens and closes the mass-loss valve of a Be star and another, lower difference frequency triggers these events on timescales that can be arbitrarily long. Conventional beating and stochastic processes do not seem to play major general roles.

Compared to amplitudes of individual modes, group amplitudes of coupled modes can be huge, thereby probably enabling sufficient star-to-disk mass-transfer rates even in significantly sub-critical rotators. However, it is not clear whether the amplification concerns pulsation amplitudes, some atmospheric response, or circumstellar reprocessing of stellar light. In any event, most historical (ground-based + Gaia) Be-star photometry only pertains to the circumstellar response and carries no information about the underlying mass-loss process.

Future work will answer the following questions:

- Is the difference between the open and the closed state of the mass-loss valve simply the difference between the respective total (nonlinear) sums of the pulsation-amplitudes?
- Can pulsation spectra distinguish Be stars according to their provenience from single-star evolution or mass transfer in a binary? What is the binary status of Bn stars?

Because only differential analyses are required, the answers will be unambiguous.

A daunting task will it be to explain how seemingly arbitrary multi-instance frequency differences are selected in a continuum of eigenfrequencies. Perhaps, their involvement in mass loss gives a first hint: The upward rising angular momentum (due to core contraction and mixing) might be the frequency matchmaker so that pulsation-driven angular-momentum loss in outbursts can prevent rotational rupture (see Krtička et al. 2011). If the lower activity of late-type Be stars signals lower mass loss, the also observed higher fractional critical rotation of late-type Be stars (Cranmer 2005) could be the consequence. However, the slower evolution of lower-mass stars can have the same effect. A tantalizing speculation could be whether the episodic mass loss from Be stars is a quasi-real time observable of stellar evolution.

References

Baade, D., Rivinius, T., Pigulski, A., et al. 2018, in Polish Astron. Soc., Vol. 8, 3rd BRITE Science Conference, ed. G. A. Wade, D. Baade, J. A. Guzik, & R. Smolec, 69–76

Baglin, A., Auvergne, M., Boisnard, L., et al. 2006, in COSPAR Meeting, Vol. 36, 36th COSPAR Scientific Assembly

Balona, L. A. & Ozuyar, D. 2019, arXiv e-prints, arXiv:1911.03068

Borucki, W. J., Koch, D., Basri, G., et al. 2010, Science, 327, 977

Cranmer, S. R. 2005, ApJ, 634, 585

Domiciano de Souza, A., Kervella, P., Moser Faes, D., et al. 2014, A&A, 569, A10

Goss, K. J. F., Karoff, C., Chaplin, W. J., Elsworth, Y., & Stevens, I. R. 2011, MNRAS, 411, 162

Granada, A., Ekström, S., Georgy, C., et al. 2013, A&A, 553, A25

Huat, A.-L., Hubert, A.-M., Baudin, F., et al. 2009, A&A, 506, 95

Jackson, B. V., Buffington, A., Hick, P. P., et al. 2004, Sol. Phys., 225, 177

Krtička, J., Owocki, S. P., & Meynet, G. 2011, A&A, 527, A84

Kurtz, D. W., Shibahashi, H., Murphy, S. J., Bedding, T. R., & Bowman, D. M. 2015, MNRAS, 450, 3015

Langer, N., Baade, D., Bodensteiner, J., et al. 2019, arXiv e-prints, arXiv:1911.06508

Maintz, M., Rivinius, T., Štefl, S., et al. 2003, A&A, 411, 181

Martayan, C., Frémat, Y., Hubert, A.-M., et al. 2007, A&A, 462, 683

Pápics, P. I., Tkachenko, A., Van Reeth, T., et al. 2017, A&A, 598, A74

Penrod, G. D. 1986, PASP, 98, 35

Porter, J. M. & Rivinius, T. 2003, PASP, 115, 1153

Ricker, G. R., Vanderspek, R., Winn, J., et al. 2016, in SPIE Conference Series, Vol. 9904, Proc. SPIE, 99042B

Rivinius, T., Baade, D., & Carciofi, A. C. 2016, A&A, 593, A106

Rivinius, T., Baade, D., & Štefl, S. 2003, A&A, 411, 229

Rivinius, T., Baade, D., Štefl, S., et al. 1998, A&A, 336, 177

Rivinius, T., Carciofi, A. C., & Martayan, C. 2013, A&A Rev., 21, 69

Secchi, A. 1866, AN, 68, 63

Smith, M. A., Lopes de Oliveira, R., & Motch, C. 2016, Advances in Space Research, 58, 782

Struve, O. 1931, ApJ, 73, 94

Townsend, R. H. D., Owocki, S. P., & Howarth, I. D. 2004, MNRAS, 350, 189

Walker, G., Matthews, J., Kuschnig, R., et al. 2003, PASP, 115, 1023

Walker, G. A. H., Kuschnig, R., Matthews, J. M., et al. 2005, ApJ, 623, L145

Weiss, W. W., Rucinski, S. M., Moffat, A. F. J., et al. 2014, PASP, 126, 573

Stars and their variability observed from space
C. Neiner, W. W. Weiss, D. Baade, R. E. Griffin, C. C. Lovekin, A. F. J. Moffat (eds)

POTENTIAL AND CHALLENGES OF PRE-MAIN SEQUENCE ASTEROSEISMOLOGY

K. Zwintz[1]

Abstract.
Studying the pulsational properties of pre-main sequence (pre-MS) stars carries the potential to improve our concept of early stellar evolution and our descriptions of the input physics for theoretical models. At the same time, both the observational and the theoretical investigation of stars in their earliest evolutionary phases needs to deal with certain challenges connected to the stars' youth. In this article, I describe some of the most important challenges, suggest ways to deal with them, and summarize the potential of pre-MS asteroseismology.

Keywords: Stars: pre-main sequence, Asteroseismology, Stars: variables: delta Scuti, Stars: variables: general

1 Introduction

The properties that describe stars during their formation (such as initial mass, chemical composition and angular momentum) define how they will continue to evolve. Physical effects also influence stellar evolution even in the earliest phases after birth, and let the stars develop their characteristic properties that we detect during their later phases. For example, some stars on the zero-age main sequence (ZAMS) and in later stages possess chemical inhomogeneities in their atmospheres that cause spots to appear. But it is not clear why only a certain fraction of stars shows chemical peculiarities, nor when they are formed. It is also not understood at present how the angular momentum evolves between the birth of stars and their arrival on the ZAMS; on the main sequence and post-main sequence, stars seem to rotate rigidly and the rotation of their cores and envelopes are coupled. The question of how stars rotate near their cores during the pre-MS stages currrently remains open. It is therefore obvious that we need to improve our understanding about the processes acting in a star's pre-MS stages if we are to be able to explain the behaviour we observe in later stages.

Other open questions in the context of early stellar evolution include: How can we describe precisely the interplay between the different physical processes (e.g., convection, diffusion, rotation, angular momentum transport, magnetic fields, accretion, ...) acting in the early evolutionary stages? Can we provide more reliable age estimates for young stars? Currently, an age value of (say) five million years for a young object has a typical error of a few million years, which can translate into a relative error of up to 100%. What is the origin of the sometimes strong magnetic fields observed in some stars? What is the influence of the circumstellar environment on early stellar evolution?

Asteroseismology of pre-MS objects has the potential to contribute to finding answers to these questions. The necessary prerequisites are observational data of sufficient precision, and reliable theoretical models. Photometric time series for pre-MS pulsators are currently available from the MOST (Walker et al. 2003), the CoRoT (Auvergne et al. 2009), the Kepler K2 (Gilliland et al. 2010) and the TESS (Ricker 2014) space telescopes, where the maximum time-base available is $\sim$80 days. With these data it was possible to describe the pulsational properties of the class of pre-MS δ Scuti stars quite well based on 34 well-studied stars (Zwintz et al. 2014) and at least two dozen additional candidates. The first g-mode pulsating pre-MS γ Doradus stars were identified from CoRoT data of NGC 2264 (Zwintz et al. 2013), and first attempts to find Slowly Pulsating B (SPB) g-mode oscillators in their pre-MS stages were conducted, illustrating the statistical challenge to find B-type pulsators that are still in their pre-MS stage (Gruber et al. 2012; Zwintz et al. 2017).

2 Challenges for pre-main sequence asteroseismology

If we want to study pre-MS stars, we are faced with some challenges.

[1] Universität Innsbruck, Institut für Astro- und Teilchenphysik, Technikerstraße 25, A-6020 Innsbruck

2.1 Circumstellar matter

Quite often, Pre-MS stars are still surrounded by the remnants of their birth clouds. Their circumstellar disks can be a sign of the stars' youth, but at the same time they also strongly shape observational measurements. Photometric time-series show irregular variations of the order of a magnitude or more, while pulsational variability lies at the millimagnitude level and below. Fig. 1 shows the light curve of the Herbig Ae star HD 142666 as observed by Kepler; the circumstellar disk is seen edge-on and causes the large irregular variations, but HD 142666 is also a δ Scuti type pulsator with 12 detected frequeicncies in the range 5.77–28.05 d^{-1} and with amplitudes less than 3 mmag (Zwintz et al. 2009). In spectroscopic observations, the presence of a circumstellar disk is evident through strong emission lines that complicate the determination of fundamental parameters. Spectral energy distributions of pre-MS stars are typically characterized by an increased flux in the infrared, i.e., an infrared exhcess.

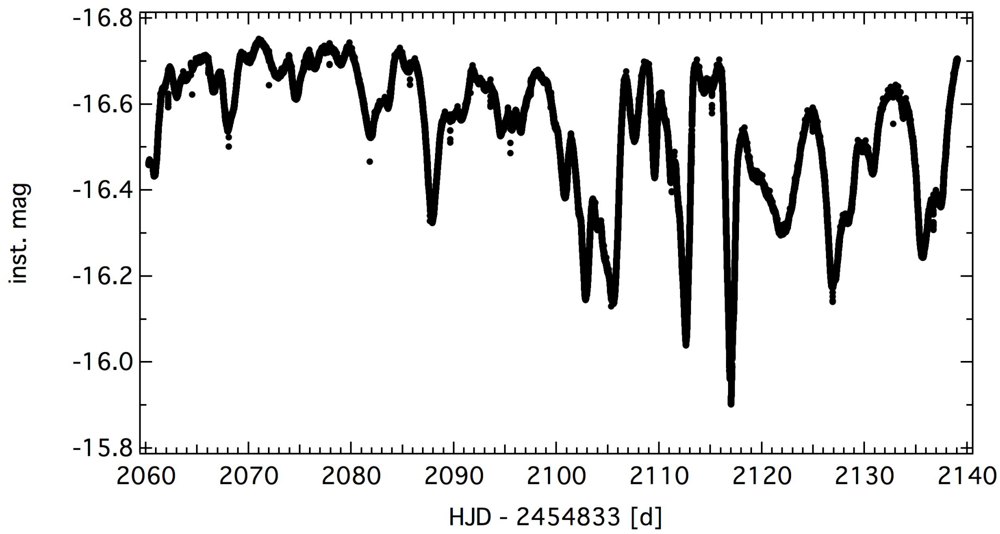

Fig. 1. Light curve of HD 142666 obtained with Kepler K2, illustrating the influence of circumstellar disks on photometric time-series of pre-MS stars.

2.2 Evolutionary stage and ages

The analysis of stars on the main sequence and in later stages can use different methods to determine the respective evolutionary stages of the objects and their ages. Apart from comparing the fundamental parameters derived from spectroscopy to the theoretically calculated evolutionary tracks or fitting isochrones, asteroseismology enables us to use the fraction of the core hydrogen, X_c, as a measure of relative age on the main sequence (e.g., Kurtz et al. 2014). For pre-MS stars it is more challenging because evolutionary tracks of pre- and post-main sequence stars of same mass, effective temperature and luminosity intersect, and isochrone fitting is usually affected by large errors even when applied to well-studied young regions like NGC 2264. Moreover, the fraction of core hydrogen, X_c, is not applicable as pre-MS stars have not processed hydrogen significantly enough yet. Hence, the identification of a pre-MS object is ambiguous, can only be based on features typical for stellar youth, and is a challenge in some cases.

2.3 Age determination

We are also faced with querying the actual zero age of a star when dealing with stars in their youngest phases. Do we set age zero at the formation of the second Larson's core (e.g., Baraffe et al. 2012), at the birthline, at the ignition of Deuterium burning, at the first hydrostatic pre-MS model, at a specified point on the Hayashi track, at the ZAMS, or at any other possible point? All of these points in early stellar evolution rely on the underlying theoretical stellar model, and thence on the corresponding input physics, and are currently used by different state-of-the-art theoretical stellar models. The effect which the choice of a given age zero-point has on stars on the main sequence – and in later stages – might be insignificant, but it has a huge impact on the determination of the ages of pre-MS stars.

2.4 Observational material and theoretical models

As mentioned above, current observational data for pre-MS stars have time-bases of up to only ~80 days, which limits the analyses compared to what would be possible with data from (say) half a year (as for BRITE-Constellation observations) to several years (in the case of Kepler).

Theoretical models for pre-MS stars use a lot of assumptions, and trying to improve on those leads to some simple-sounding questions like, "What is the definition of the ZAMS as seen from the pre-MS side?" (for more information on a new way to define the ZAMS, see T. Steindl (PAGE). It is also not clear how the choice of the input physics influences the theoretical description of pre-MS stars. These challenges need to be tackled.

3 Potential of pre-main sequence asteroseismology

Every challenge can also be regarded as a potential invitation to overcome difficulties. The most striking potentials for the asteroseismology of pre-MS stars from my personal view are:

3.1 Pulsations on top of irregular variability

Despite the high degree of activity leading to irregular variations in the light from pre-MS stars, it was shown that disentangling irregular variability caused by circumstellar dust and gas from pulsational variability works successfully for p-mode oscillators (Zwintz et al. 2009). With a (simple) theoretical representation of the variability caused by the disk, pulsations can be identified clearly when their frequency values are higher than the frequencies induced overall by the disk (i.e., these are typically lower-range frequencies, between about 0–3 d^{-1}). It is more challenging to disentangle the two types of variability when the pulsations lie in the same frequency range as the variations from the disk (as in the case of g-modes with periods between ~0.3–3 days; Aerts et al. 2010).

3.2 Discovery of empirical scaling relations

Asteroseismic scaling relations are powerful tools that connect the masses and radii of stars theoretically to their asteroseismic properties (e.g., frequency separations or frequency of maximum power), and are mostly tuned to the Sun and solar-like oscillators (e.g., Kjeldsen & Bedding 1995). With a large enough number of pre-MS pulsators that have well-studied pulsational frequencies and a reliable determination of fundamental parameters (effective temperature, $\log g$, $v \sin i$), group properties can be studied. For the pre-MS δ Scuti stars, an empirical relation between the p-mode oscillation properties and the evolutionary stage can be identified, illustrating that the highest excited p-mode frequency is smallest close to the birthline and increases towards the ZAMS (Zwintz et al. 2014). It illustrates that finding new pre-MS pulsators, in particular for the γ Doradus and SPB classes and populating the HR diagram with them, has the potential to investigate whether similar relations exist for the other types of stars as well. Consequently, asteroseismic scaling relations for pre-MS stars can connect the pulsational properties of young stars to their fundamental parameters, enabling us to test theoretical models of early stellar evolution; they therefore have a power similar to that for more evolved solar-like oscillators.

3.3 g-mode period spacings in pre-main sequence stars

By detecting g-mode period spacings, it is possible to study the angular momentum transport near the stellar core and to investigate whether the envelope and the core rotate rigidly or not (Aerts et al. 2017). This was done quite successfully for main-sequence and post-main sequence objects (e.g., Van Reeth et al. 2015). For pre-MS stars, the first g-mode period spacings have recently been discovered using Kepler K2 data of the Lagoon Nebula (see L. Ketzer, PAGE). In particular, g-mode period spacings in pre-MS stars have the potential to extend earlier studies of angular-momentum transport from the main sequence to the earlier evolutionary phases and to investigate when the strong coupling occurs between the surface and the core of a star.

3.4 What was our Sun like in its youth?

The presence of stochastic, solar-like oscillations in pre-MS stars has been predicted by theory (Samadi et al. 2005; Pinheiro 2008). As pre-MS stars in this mass regime are characterized by high degrees of activity and mostly fall into the class of T Tauri stars, the observational detection of solar-like oscillations is even more challenging. The amplitudes of solar-like oscillations are generally smaller than those driven by the heat engine mechanism (such as δ Scuti and γ Doradus pulsations). And although we are faced by several of the previously mentioned challenges (including a lack of sufficient observational material), searching for pre-MS solar like oscillators has the potential of recognizing what the Sun was like in its early phases and investigating how its interior structure changed with time.

3.5 Automated selection of pre-MS stars

The identification of the pre-MS nature of a given star can be quite challenging and ambiguous (see Section 2.2). Pre- and post-main sequence evolutionary tracks for masses lower than ~ 6 solar masses intersect several times, and there is no unique identifier that enables us to distinguish a pre- from a post-main sequence star. Several features that are attributed to an early evolutionary stage must therefore be used for a possible identification of stellar youth. This process is typically carried out manually on a case-by-case basis.

In the context of space missions like TESS or (in the future)PLATO (Rauer et al. 2014), where thousands of stars will be measured, such a selection of potential pre-MS stars has to be done in an automatic way. An appropriate variability classifier is currently being developed for application to TESS data, with an additional possibility of an extension to PLATO data in the future. It combines known catalogues of young stellar objects, features attributed to pre-MS stars and information provided by *Gaia* (Gaia Collaboration et al. 2016). It applies machine learning to carry out automatic classification of a pre-MS object. More information can be found in the article by Müllner (PAGE).

4 Conclusions: The power of pre-MS asteroseismology

Despite the challenges we face when applying asteroseismic methods to pre-MS stars (e.g., influences of the circumstellar disk and accretion), the subsequent power of asteroseismology of the youngest pulsating stars is evident.

- The evolutionary stage of a given pulsating star, i.e., if it is a pre- or a post-main sequence object, can be identified from its frequency pattern *only*.
- The oscillation properties of pre-MS stars are related to their relative evolutionary stage during their pre-MS phase (i.e., between the birthline and the ZAMS).
- When we overcome the lack of long enough photometric time series for pre-MS pulsators - e.g., through observations with TESS and in the future with PLATO - we will reveal many more oscillatory features typical for the pre-MS stages similar as it was possible in red giant asteroseismology. Consequently, we will be able to find the "young Sun", i.e., pre-MS solar like oscillators that are currently only theoretically predicted.
- Current work concentrates on improving the input physics for starsu in their pre-MS phases, e.g. by modelling warm and cold accretion (Vorobyov et al. 2017). With the expected advances in our theoretical concept of early stellar evolution together with theoretical models of pre-MS oscillations, we will test the influences of the choice of the input physics and learn more about the physical effects acting in young stars.

Pre-MS asteroseismology allows to connect the early stages of stellar evolution with the later evolutionary phases and has the potential to improve our descriptions of the physical effects acting in young stars. This is essential because only if we understand how stars pass through their pre-MS stages, we will be able to derive a complete picture of stellar evolution.

References

Aerts, C., Christensen-Dalsgaard, J., & Kurtz, D. W. 2010, Asteroseismology (Springer)
Aerts, C., Van Reeth, T., & Tkachenko, A. 2017, ApJ, 847, L7
Auvergne, M., Bodin, P., Boisnard, L., et al. 2009, A&A, 506, 411
Baraffe, I., Vorobyov, E., & Chabrier, G. 2012, ApJ, 756, 118
Gaia Collaboration, Prusti, T., de Bruijne, J. H. J., et al. 2016, A&A, 595, A1
Gilliland, R. L., Brown, T. M., Christensen-Dalsgaard, J., et al. 2010, PASP, 122, 131
Gruber, D., Saio, H., Kuschnig, R., et al. 2012, MNRAS, 420, 291
Kjeldsen, H. & Bedding, T. R. 1995, A&A, 293, 87

Kurtz, D. W., Saio, H., Takata, M., et al. 2014, MNRAS, 444, 102
Pinheiro, F. J. G. 2008, A&A, 478, 193
Rauer, H., Catala, C., Aerts, C., et al. 2014, Experimental Astronomy, 38, 249
Ricker, G. R. 2014, Journal of the AAVSO, 42, 234
Samadi, R., Goupil, M. J., Alecian, E., et al. 2005, JA&A, 26, 171
Van Reeth, T., Tkachenko, A., Aerts, C., et al. 2015, ApJS, 218, 27
Vorobyov, E. I., Elbakyan, V., Hosokawa, T., et al. 2017, A&A, 605, A77
Walker, G., Matthews, J., Kuschnig, R., et al. 2003, PASP, 115, 1023
Zwintz, K., Fossati, L., Ryabchikova, T., et al. 2014, Science, 345, 550
Zwintz, K., Fossati, L., Ryabchikova, T., et al. 2013, A&A, 550, A121
Zwintz, K., Kallinger, T., Guenther, D. B., et al. 2009, A&A, 494, 1031
Zwintz, K., Moravveji, E., Pápics, P. I., et al. 2017, A&A, 601, A101

Stars and their variability observed from space
C. Neiner, W. W. Weiss, D. Baade, R. E. Griffin, C. C. Lovekin, A. F. J. Moffat (eds)

OBSERVATIONS OF INTERNAL STRUCTURES OF LOW-MASS MAIN-SEQUENCE STARS AND RED GIANTS

S. Hekker[1, 2]

Abstract. Over the past years, asteroseismic observations have been able to probe the internal structures of stars. In this review, I highlight some of the results that have been presented and some open questions that are still being addressed.

Keywords: asteroseismology, stars: interiors, stars: oscillations (including pulsations), stars: solar-type

1 Introduction

Following the advent of the space observatories CoRoT and *Kepler*, the number of stars in which solar-like oscillations have been detected has grown rapidly, and this growth is predicted to continue with data from the current TESS mission and the future Plato mission (see Fig. 1, for a schematic overview of the order of magnitude of the number of red-giant stars with asteroseismic time-series observations versus time). The different space observatories provide data with different duration and hence different resolutions in the frequency domain. These differing frequency resolutions determine the amount of information as well as the accuracy and precision with which the information regarding the stellar structure can be extracted. This in turn determines the science questions that can be answered with a specific set of observations. The data of many stars with short time series are of importance for more statistical studies where global stellar parameters are required for a large number of stars. This is, for instance, the case for galactic archaeology and planet abundance studies. The high resolution data can be used to infer information regarding the internal structure of stars. In particular, the *Kepler* data spanning nearly four years of data are suitable to study stellar internal structures. Here, I present an overview of some of the recent results in this regard and some topics that require further studies to reveal stellar internal structures.

2 Datasets

With the *Kepler* mission a couple of hundred main-sequence stars with solar-like oscillations have been observed (Chaplin et al. 2011). Out of this sample there are nearly a hundred stars that have been considered for further investigations using their individual frequencies, the so-called KAGES (Silva Aguirre et al. 2015; Davies et al. 2016) and LEGACY (Lund et al. 2017; Silva Aguirre et al. 2017) samples. In the following sections, I highlight a few examples of stellar structure information that have been obtained from (subsamples) of the KAGES and LEGACY stars.

Red-giant stars were well represented among the stars observed with *Kepler*. Catalogues of red giants with detected solar-like oscillations are presented in several papers starting with early results by Hekker et al. (2011) to the most recent public catalogue by Yu et al. (2018). These catalogues contain stars with observations of different lengths. The stars with observations covering the full timespan of the *Kepler* mission (about four years) are the ones of interest for stellar structure studies. A subset of these stars have been selected for complementary observation with the SDSS-APOGEE spectrograph and are known as the APOKASC sample (Pinsonneault et al. 2014, 2018). This sample of 6661 stars is currently one of the best studied samples of red-giant stars.

[1] Max Planck Institute for Solar system research, Justus-von-Liebig Weg 3, 37077 Göttingen, Germany
[2] Stellar Astrophysics Centre, Department of Physics and Astronomy, Aarhus University, Ny Munkegade 120, DK-8000 Aarhus C, Denmark

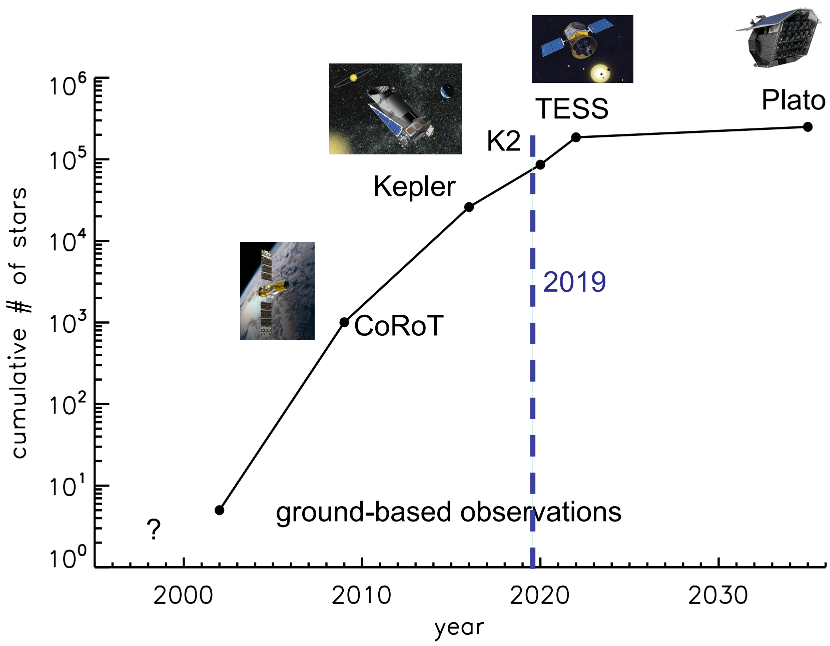

Fig. 1. The approximate cumulative numbers of red-giant stars with asteroseismic timeseries observations versus time in years. These are based on current data releases and rough estimates for K2, TESS and Plato. The blue dashed line indicates the time of the *Stars and their Variability Observed from Space* meeting in Vienna.

3 Inferences from solar-like oscillations

Solar-like oscillations can be trapped in a cavity in the outer layers of a star where the restoring force is pressure and the oscillations have the nature of standing acoustic waves. These oscillation modes are referred to as p-mode oscillations. Solar-like oscillations can also be trapped in a cavity in the inner radiative region of the stars where the restoring force is buoyancy and the oscillations have the character of standing gravity waves. These are called g-mode oscillations. I shall first discuss internal structure results obtained from pure p-modes and then, I will present some of the results for more evolved subgiant and red-giant stars where non-radial modes have a mixed p-g nature as a result of the coupling, or resonance interaction, between an oscillation in the p-mode cavity and an oscillation in the g-mode cavity (e.g. Osaki 1975; Aizenman et al. 1977; Deheuvels & Michel 2010; Hekker & Mazumdar 2014).

3.1 Inferences from pressure modes

Solar-like oscillations in low-mass main-sequence stars are all p-mode oscillations. For more evolved stars the radial modes have a pure p-mode character, while for the non-radial modes, the pure p mode nature gives way to a mixed p-g nature as the effects of the buoyancy increases with evolution.

3.1.1 Acoustic depth of the HeII ionisation zone and the base of the convection zone

Stellar structure changes that occur at a length scale that is short compared to the local wavelength of the oscillations cause a ‘glitch’ in the wave. This glitch is apparent as small periodic changes in the oscillation frequencies and can be seen in the second difference ($\Delta_2\nu(n,l)$) measurements:

$$\Delta_2\nu(n,l) = \nu(n-1,l) - 2\nu(n,l) + \nu(n+1,l) \tag{3.1}$$

where $\nu(n,l)$ is the frequency of a mode with radial order n and degree l. Note that a 5 point difference is used in some cases.

Two well-known glitches in main-sequence stars are the HeII ionisation zone and the base of the convection zone. Each of these glitches leaves a sinusoidal trace in the second differences, which can be fitted with the following function:

$$\Delta_2\nu = a_0 + \frac{b_2}{\nu^2}\sin(4\pi\nu\tau_{\rm bcz} + 2\phi_{\rm bcz}) + c_0\nu e^{-c_2\nu^2}\sin(4\pi\nu\tau_{\rm HeII} + 2\phi_{\rm HeII}) \quad (3.2)$$

where a_0,b_2, c_0, c_2, $\tau_{\rm bcz}$, $\phi_{\rm bcz}$, $\tau_{\rm HeII}$, $\phi_{\rm HeII}$ are eight free parameters of the fit (Mazumdar et al. 2014, showed some alternative ways to extract information from the glitches). The parameters $\tau_{\rm bcz}$ and $\tau_{\rm HeII}$ are the acoustic depths of the base of the convection zone and HeII ionisation zone, respectively. In this way, these model-independent observables directly provide information on the stellar internal structure. For more details regarding the acoustic depth of the HeII ionisation zone and base of the convection zone, I refer the reader to e.g. Houdek & Gough (2007), Mazumdar et al. (2014), Verma et al. (2014a,b), Vrard et al. (2015), where the latter study concerned red-giant stars, while earlier studies were focussed on main-sequence stars.

3.1.2 Surface helium abundance

Solar-like oscillators are too cool to have helium absorption lines visible in their spectra and therefore the helium abundance can not be determined through spectroscopic observations of these stars. The prospect of determining the helium abundance from the HeII signature in the oscillation frequencies was first investigated by Basu et al. (2004) and by Broomhall et al. (2014) who specifically looked at red-giant stars. Both studies concluded that the oscillatory signal in the frequencies caused by the depression in the adiabatic index Γ_1 in the HeII ionisation zone can be used to determine the envelope helium abundance of these stars, though relative errors in the frequencies need to be small, i.e. of the order of 10^{-4} (Basu et al. 2004).

Indeed, Verma et al. (2019) could determine the envelope helium abundance of 38 stars in the *Kepler* seismic LEGACY sample. This led them to confirm that atomic diffusion does take place in solar-type stars. These authors subsequently used the measured surface abundances in combination with the settling predicted by stellar models to determine the initial abundances, which were then used to obtain preliminary estimates of the primordial helium abundance to be 0.244 ± 0.019.

3.1.3 Sound speed profiles

Structure inversions can be used to reveal the sound-speed profile in the stellar internal structure. In the early days, the only star for which enough data were available to perform structure inversions was the Sun. In recent years, some of the issues such as the less accurate determinations of mass and radius for stars other than the Sun and the limitations of only observing low-degree modes from the integrated light of stars have been mitigated. First inversion results for main-sequence stars other than the Sun, were presented based on inversions using global quantities in a series of papers by G. Buldgen and collaborators (e.g. Buldgen et al. 2015, 2016, 2019). These results were subsequently followed by structure inversions for the squared isothermal sound speed using an algorithm called ‘inversions for agreement’ (Bellinger et al. 2017, 2019). These results tentatively show that for stars that have similar parameters as the Sun the best-fit model shows reasonable agreement with the sound speed profile determined through inversions. On the other hand, if the structure is very different from that of the Sun, for instance owing to a convective core, the inversion results show significant differences compared to the best fit model (Bellinger et al. 2019). The cause of these discrepancies is still unknown, and is not remedied by known physics in the form of convective overshooting or elemental diffusion, thereby showing that other physical processes should be included in the models.

3.2 Inferences from mixed pressure-gravity modes

In more evolved stars with expanded envelopes and denser cores compared to main-sequence stars, the frequencies in the p-mode and g-mode cavities have similar values, which allows non-radial modes to couple and form mixed modes. These mixed modes have p-mode like properties in the outer layers and g-mode like properties in the deep layers, and hence, these mixed modes are sensitive to the stellar cores. This feature is increasingly being used to extract stellar internal structure information for evolved solar-like oscillators. For an in-depth review of giant-star seismology, I refer the reader to Hekker & Christensen-Dalsgaard (2017).

3.2.1 Distinguishing red-giant and red-clump stars

The first detection of mixed dipole modes in red-giant stars (Beck et al. 2011) was subsequently followed by the finding that the typical spacing in period between mixed dipole modes can discriminate between stars that have hydrogen-shell burning as their sole nuclear energy supply and stars that also burn helium in their core (Bedding et al. 2011; Mosser et al. 2011, 2014; Elsworth et al. 2019). The difference in the period spacing is due to the fact that the core-helium burning stars have a convective core, whilst the inert helium core in hydrogen-shell burning stars is radiative (Christensen-Dalsgaard 2014).

In addition to the spacing in period, the mixed modes also provide input on the coupling between the mode in the p and g cavity and the phase offset of the gravity modes (Mosser et al. 2017b, 2018; Hekker et al. 2018; Pinçon et al. 2019). These works reveal that the coupling is directly related to the width of the evanescent zone between the p and g cavity and therefore have different values for red-giant branch (RGB) and core-helium burning (CHeB) stars (Mosser et al. 2017b; Hekker et al. 2018). Additionally, the phase offset of gravity modes may probe the local density contrast of the core (see Fig. 10 of Hekker et al. 2018), and also appears to be related to the evolutionary phase (Mosser et al. 2018; Pinçon et al. 2019). Hence these features provide further prospects to study the internal structures of red giants.

3.2.2 Core properties

Cunha et al. (2015, 2019) showed that mixed modes in red-giant stars are affected by structural glitches near the cores of these stars. Along the red-giant branch, glitch-induced variations occur only at the luminosity bump. For the post-helium-ignition stages, glitches are only expected in the early phases of helium-core burning and at the beginning of helium-shell burning. This is due to the requirement that the structural change has to be sharp compared to the local wavelength. The local wavelength is short in the core regions and hence only in these particular phases the shell-burning feature is seen as sharp by the oscillation modes. Thus, the detection of a glitch in the mixed modes already allows us to determine the evolutionary state of the star to unprecedented detail, while extracting details of the structure of the cores awaits further development of analysis techniques.

3.2.3 Radial differential rotation

Different mixed modes have different sensitivities to the p or g cavity, which allows for probing radial differential rotation in case the mixed modes are also rotationally split. Beck et al. (2012); Deheuvels et al. (2012, 2014); Di Mauro et al. (2016); Triana et al. (2017); Di Mauro et al. (2018) analysed a small set of stars and showed that the cores of subgiants and red giant branch stars rotate faster than their surfaces (see also Marques et al. 2013; Goupil et al. 2013). Furthermore, Deheuvels et al. (2015) reported only weak radial differential rotation in six intermediate-mass core helium-burning stars. The results of individual stars are complemented by ensemble results for both red-giant branch and core helium-burning stars by (Mosser et al. 2012; Gehan et al. 2018). The latter works show that the core rotation rate is almost constant along the RGB, while cores of CHeB stars rotate about six time slower. Sills & Pinsonneault (2000) showed that this change in core rotation rate can't be fully explained by the expansion of the core indicating that internal momentum has been transferred from the core to the envelope.

Angular momentum transport in stellar interiors (see for a recent review Aerts et al. 2019, and references therein) continues to be difficult to understand. As shown by, e.g., Cantiello et al. (2014) reproducing the observed rotation rates requires some new physics to be included in the modelling. Recent suggestions, such as extraction of angular momentum from the core by mixed modes (Belkacem et al. 2015a,b), magnetic instabilities (Eggenberger et al. 2019) or the magnetic Tayler instability (Fuller et al. 2019) could bring the models more in line with the observations.

4 The road ahead

As the state-of-the-art results show, we are now inferring information on the stellar structure through the global oscillation modes, in other words asteroseismology is effective. Despite the achievements, there are still many open questions. One of the issues that is currently being worked on is measuring and identifying oscillation modes in the thousands of red-giant stars that have time-series data. Kallinger (2019) released frequencies and mode identifications of all stars in the APOKASC sample based on the AʙʙA code. Additionally, Themeßl et al. (these proceedings contribution 5o12) provide first results from the TACO (Tools for Automated Characterisation of Oscillations) code that has been developed to analyse the power spectra of solar-like oscillations in an automated way. The parameters of the identified oscillation modes are essential inputs for further stellar structure studies.

One of these further studies involves the (unusual) structure of red-giant stars with suppressed dipole modes (e.g. Fuller et al. 2015; Stello et al. 2016; Cantiello et al. 2016; Loi & Papaloizou 2018). One of the current hypotheses is that these could be caused by large magnetic fields in the cores of stars with masses larger than the Sun which rotated faster during their main-sequence phase. The scenario proposed by Fuller et al. (2015) was based on the presence of a poloidal magnetic field in the core of red-giant stars which would completely damp the mixed modes. However, Mosser et al. (2017a) refuted this argument by showing that some mixed modes are still present in the observed spectra. Loi & Papaloizou (2018) proposed to mitigate this by adding a toroidal field. Since it is not possible to observe these magnetic fields in the core directly, the cause of the suppressed dipole modes is still debated. One of the alternative hypotheses could be a connection to binarity as indicated by Themeßl et al. (2017).

Another ingredient of stellar structure that is still under investigation is the convection which drives and damps solar-like oscillations. Progress, partly using 3-D simulations, has recently been made by, e.g., Samadi et al. (2012), Belkacem et al. (2019), Houdek et al. (2019), Zhou et al. (2019). Additionally, overshooting at convective boundaries is also still being actively investigated using solar-like oscillations. It is generally believed that overshoot is a necessary ingredient in models in order to match observational constraints. Angelou et al. (submitted) have shown that overshooting can be estimated from seismic data using frequency ratios. These again may lead to interesting findings regarding the internal structures of stars with solar-like oscillations.

5 Final remarks

About 10 years after the launch of *Kepler* the asteroseismic revolution may be over, however asteroseismology of solar-like oscillators has just begun. Inferences about the internal structures of these stars are ongoing and with the current data from MOST (Matthews et al. 2000), CoRoT (Baglin et al. 2007), *Kepler* (Borucki et al. 2009), K2 (Howell et al. 2014), BRITE-Constellation (Weiss et al. 2014), SONG (Grundahl et al. 2008) and TESS (Ricker et al. 2016) and the data that we still expect from BRITE-Constellation, SONG, the TESS extended mission as well as the planned Plato (Rauer et al. 2014) mission, we will be able to increase our knowledge and understanding further.

I am grateful for comments by Sarbani Basu and Yvonne Elsworth on earlier versions of this manuscript, which improved it significantly.

References

Aerts, C., Mathis, S., & Rogers, T. M. 2019, ARA&A, 57, 35

Aizenman, M., Smeyers, P., & Weigert, A. 1977, A&A, 58, 41

Baglin, A., Auvergne, M., Barge, P., et al. 2007, in AIPCS, Vol. 895, Fifty Years of Romanian Astrophysics, ed. C. Dumitrache, N. A. Popescu, M. D. Suran, & V. Mioc, 201–209

Basu, S., Mazumdar, A., Antia, H. M., & Demarque, P. 2004, MNRAS, 350, 277

Beck, P. G., Bedding, T. R., Mosser, B., et al. 2011, Science, 332, 205

Beck, P. G., Montalban, J., Kallinger, T., et al. 2012, Nature, 481, 55

Bedding, T. R., Mosser, B., Huber, D., et al. 2011, Nature, 471, 608

Belkacem, K., Kupka, F., Samadi, R., & Grimm-Strele, H. 2019, A&A, 625, A20

Belkacem, K., Marques, J. P., Goupil, M. J., et al. 2015a, A&A, 579, A31

Belkacem, K., Marques, J. P., Goupil, M. J., et al. 2015b, A&A, 579, A30

Bellinger, E. P., Basu, S., Hekker, S., & Ball, W. H. 2017, ApJ, 851, 80

Bellinger, E. P., Basu, S., Hekker, S., & Christensen-Dalsgaard, J. 2019, ApJ, 885, 143

Borucki, W., Koch, D., Batalha, N., et al. 2009, in IAU Symposium, Vol. 253, Transiting Planets, ed. F. Pont, D. Sasselov, & M. J. Holman, 289–299

Broomhall, A. M., Miglio, A., Montalbán, J., et al. 2014, MNRAS, 440, 1828

Buldgen, G., Farnir, M., Pezzotti, C., et al. 2019, A&A, 630, A126

Buldgen, G., Reese, D. R., Dupret, M. A., & Samadi, R. 2015, A&A, 574, A42

Buldgen, G., Salmon, S. J. A. J., Reese, D. R., & Dupret, M. A. 2016, A&A, 596, A73

Cantiello, M., Fuller, J., & Bildsten, L. 2016, ApJ, 824, 14

Cantiello, M., Mankovich, C., Bildsten, L., Christensen-Dalsgaard, J., & Paxton, B. 2014, ApJ, 788, 93

Chaplin, W. J., Kjeldsen, H., Christensen-Dalsgaard, J., et al. 2011, Science, 332, 213

Christensen-Dalsgaard, J. 2014, Asteroseismology of red giants (Cambridge University Press, pages = 194, adsurl = https://ui.adsabs.harvard.edu/abs/2014aste.book..194C, adsnote = Provided by the SAO/NASA Astrophysics Data System)

Cunha, M. S., Avelino, P. P., Christensen-Dalsgaard, J., et al. 2019, MNRAS, 490, 909

Cunha, M. S., Stello, D., Avelino, P. P., Christensen-Dalsgaard, J., & Townsend, R. H. D. 2015, ApJ, 805, 127

Davies, G. R., Silva Aguirre, V., Bedding, T. R., et al. 2016, MNRAS, 456, 2183

Deheuvels, S., Ballot, J., Beck, P. G., et al. 2015, A&A, 580, A96

Deheuvels, S., Doğan, G., Goupil, M. J., et al. 2014, A&A, 564, A27

Deheuvels, S., García, R. A., Chaplin, W. J., et al. 2012, ApJ, 756, 19

Deheuvels, S. & Michel, E. 2010, Ap&SS, 328, 259

Di Mauro, M. P., Ventura, R., Cardini, D., et al. 2016, ApJ, 817, 65

Di Mauro, M. P., Ventura, R., Corsaro, E., & Lustosa De Moura, B. 2018, ApJ, 862, 9

Eggenberger, P., Buldgen, G., & Salmon, S. J. A. J. 2019, A&A, 626, L1

Elsworth, Y., Hekker, S., Johnson, J. A., et al. 2019, MNRAS, 489, 4641

Fuller, J., Cantiello, M., Stello, D., Garcia, R. A., & Bildsten, L. 2015, Science, 350, 423

Fuller, J., Piro, A. L., & Jermyn, A. S. 2019, MNRAS, 485, 3661

Gehan, C., Mosser, B., Michel, E., Samadi, R., & Kallinger, T. 2018, A&A, 616, A24

Goupil, M. J., Mosser, B., Marques, J. P., et al. 2013, A&A, 549, A75

Grundahl, F., Christensen-Dalsgaard, J., Arentoft, T., et al. 2008, Communications in Asteroseismology, 157, 273

Hekker, S. & Christensen-Dalsgaard, J. 2017, A&A Rev., 25, 1

Hekker, S., Elsworth, Y., & Angelou, G. C. 2018, A&A, 610, A80

Hekker, S., Gilliland, R. L., Elsworth, Y., et al. 2011, MNRAS, 414, 2594

Hekker, S. & Mazumdar, A. 2014, in IAU Symposium, Vol. 301, Precision Asteroseismology, ed. J. A. Guzik, W. J. Chaplin, G. Handler, & A. Pigulski, 325–331

Houdek, G. & Gough, D. O. 2007, MNRAS, 375, 861

Houdek, G., Lund, M. N., Trampedach, R., et al. 2019, MNRAS, 487, 595

Howell, S. B., Sobeck, C., Haas, M., et al. 2014, PASP, 126, 398

Kallinger, T. 2019, arXiv e-prints, arXiv:1906.09428

Loi, S. T. & Papaloizou, J. C. B. 2018, MNRAS, 477, 5338

Lund, M. N., Silva Aguirre, V., Davies, G. R., et al. 2017, ApJ, 835, 172

Marques, J. P., Goupil, M. J., Lebreton, Y., et al. 2013, A&A, 549, A74

Matthews, J. M., Kuschnig, R., Walker, G. A. H., et al. 2000, ASPCS, Vol. 203, Ultraprecise Photometry from Space: The MOST Microsat Mission (ASP Conference Series), 74–75

Mazumdar, A., Monteiro, M. J. P. F. G., Ballot, J., et al. 2014, ApJ, 782, 18

Mosser, B., Barban, C., Montalbán, J., et al. 2011, A&A, 532, A86

Mosser, B., Belkacem, K., Pinçon, C., et al. 2017a, A&A, 598, A62

Mosser, B., Benomar, O., Belkacem, K., et al. 2014, A&A, 572, L5

Mosser, B., Gehan, C., Belkacem, K., et al. 2018, A&A, 618, A109

Mosser, B., Goupil, M. J., Belkacem, K., et al. 2012, A&A, 548, A10

Mosser, B., Pinçon, C., Belkacem, K., Takata, M., & Vrard, M. 2017b, A&A, 600, A1

Osaki, Y. 1975, PASJ, 27, 237

Pinçon, C., Takata, M., & Mosser, B. 2019, A&A, 626, A125

Pinsonneault, M. H., Elsworth, Y., Epstein, C., et al. 2014, ApJS, 215, 19

Pinsonneault, M. H., Elsworth, Y. P., Tayar, J., et al. 2018, ApJS, 239, 32

Rauer, H., Catala, C., Aerts, C., et al. 2014, Experimental Astronomy, 38, 249

Ricker, G. R., Vanderspek, R., Winn, J., et al. 2016, SPIE Conference Series, Vol. 9904, The Transiting Exoplanet Survey Satellite (SPIE), 99042B

Samadi, R., Belkacem, K., Dupret, M. A., et al. 2012, A&A, 543, A120

Sills, A. & Pinsonneault, M. H. 2000, ApJ, 540, 489

Silva Aguirre, V., Davies, G. R., Basu, S., et al. 2015, MNRAS, 452, 2127

Silva Aguirre, V., Lund, M. N., Antia, H. M., et al. 2017, ApJ, 835, 173

Stello, D., Cantiello, M., Fuller, J., et al. 2016, Nature, 529, 364

Themeßl, N., Hekker, S., & Elsworth, Y. 2017, in EPJ Web of Conferences, Vol. 160, EPJ Web of Conferences, 05009

Triana, S. A., Corsaro, E., De Ridder, J., et al. 2017, A&A, 602, A62

Verma, K., Antia, H. M., Basu, S., & Mazumdar, A. 2014a, ApJ, 794, 114
Verma, K., Faria, J. P., Antia, H. M., et al. 2014b, ApJ, 790, 138
Verma, K., Raodeo, K., Basu, S., et al. 2019, MNRAS, 483, 4678
Vrard, M., Mosser, B., Barban, C., et al. 2015, A&A, 579, A84
Weiss, W. W., Rucinski, S. M., Moffat, A. F. J., et al. 2014, PASP, 126, 573
Yu, J., Huber, D., Bedding, T. R., et al. 2018, ApJS, 236, 42
Zhou, Y., Asplund, M., & Collet, R. 2019, ApJ, 880, 13

Stars and their variability observed from space
C. Neiner, W. W. Weiss, D. Baade, R. E. Griffin, C. C. Lovekin, A. F. J. Moffat (eds)

WHAT PHYSICS IS MISSING IN THEORETICAL MODELS OF HIGH-MASS STARS: NEW INSIGHTS FROM ASTEROSEISMOLOGY

D. M. Bowman[1]

Abstract. Asteroseismology of massive stars has recently begun a revolution thanks to high-precision time series photometry from space telescopes. This has allowed accurate and robust constraints on interior physical processes, such as mixing and rotation in the near-core region of stars, to be determined across different masses and ages. In this review, I discuss recent advances in our knowledge of massive star interiors made by means of gravity-mode asteroseismology, and highlight some new observational discoveries of variability in some of the most massive stars in our universe.

Keywords: asteroseismology, stars: early-type, stars: evolution, stars: rotation

1 Introduction

The lives and energetic deaths of massive stars play a pivotal role in shaping the Universe (Maeder 2009; Langer 2012). Massive stars are significant metal factories and provide energy and chemical feedback to the interstellar environment when they end their lives as a supernova. Hence, understanding how massive stars evolve is of paramount importance for the chemical and dynamical evolution of the host galaxy (Bromm et al. 2009; de Rossi et al. 2010). Despite the importance of massive stars, the physics of their interiors is currently not well constrained, which in turn strongly impacts their post-main sequence evolution (Ekström et al. 2012; Chieffi & Limongi 2013). Specifically, the interior mixing, rotation and angular momentum transport mechanisms inside massive stars are controlled by uncalibrated free parameters in evolution models (Aerts et al. 2019). When combined with the significant effects of binarity and metallicity (e.g. Sana et al. 2012 and Georgy et al. 2013), these represent large theoretical uncertainties in massive-star evolution theory which need to be mitigated (Martins & Palacios 2013; Aerts et al. 2019).

A powerful method for probing stellar interiors is asteroseismology (Aerts et al. 2010), which uses stellar oscillations to probe the physics of stellar structure. Different types of pulsation modes can be excited within a massive star. Gravity modes are standing waves restored by buoyancy (i.e. gravity) and are extremely sensitive to the physics of near-core region in massive stars (Miglio et al. 2008). For rotating stars, the Coriolis force is also a dominant restoring force, such that stars exhibit gravito-inertial modes which probe rotation in the near-core region (Bouabid et al. 2013). Massive stars can also pulsate in pressure modes, which probe the envelope and near-surface layers (Aerts et al. 2010). The successful application of asteroseismology requires long-term, continuous and high-precision photometric time series data to resolve individual pulsation-mode frequencies, such that a quantitative comparison of observed and predicted pulsation-mode frequencies reveals the physics that best represents the observed star.

Since massive stars have convective cores and radiative envelopes during the main sequence, the physics of convection and convective-boundary mixing is crucial in determining their core masses and ultimate evolutionary fate (Ekström et al. 2012; Chieffi & Limongi 2013; Georgy et al. 2013). The mixing profile at the interface of the convective core and radiative envelope, and the mixing profile within the envelope itself directly impact the amount of hydrogen available for nuclear burning. With more internal mixing, a massive star experiences a longer main sequence lifetime and produces a larger helium core at the terminal age main sequence. The relative abundance of pulsating B stars compared to O stars means that the majority of constraints on massive star interiors currently come from β Cep and slowly-pulsating B (SPB) stars (Aerts et al. 2019). Together these two types of main sequence and post-main sequence pulsators span a wide range in mass between approximately 3 and 20 $M_{\odot}$. Hence these pulsators provide invaluable potential to constrain interior mixing and rotation in stars that span the boundary between intermediate- and high-mass stars – i.e. the boundary between stars that end their lives as white dwarfs and those that explode as supernovae and become neutron stars or black holes (Langer 2012).

[1] Institute of Astronomy, KU Leuven, Celestijnenlaan 200D, B-3001 Leuven, Belgium

2 New insights of stellar interiors from asteroseismology

Even though the pressure-mode pulsations in β Cep stars provide constraints on the interior properties of massive stars (see e.g. Aerts et al. 2003; Handler et al. 2004, 2006; Briquet et al. 2007; Daszyńska-Daszkiewicz et al. 2013), the focus of recent asteroseismic studies has been on gravity-mode pulsators (see Aerts et al. 2019 for a review). A powerful diagnostic in interpreting the oscillation spectrum of a star pulsating in gravity modes is its period spacing pattern, which is defined as the period differences of consecutive radial order (n) gravity modes of the same angular degree (ℓ) and azimuthal order (m) as a function of the pulsation mode period. Under the asymptotic approximation, gravity modes in a non-rotating, chemically homogenous star are equally spaced in period, yet rotation and a chemical gradient left behind from a receding convective core introduce perturbations in the form of a tilt and dips, respectively (Miglio et al. 2008; Bouabid et al. 2013; Van Reeth et al. 2016). Higher rotation rates induce a larger tilt with the gradient being negative for prograde modes and positive for retrograde modes. On the other hand, the dips caused by mode trapping are diminished with increased mixing (Miglio et al. 2008).

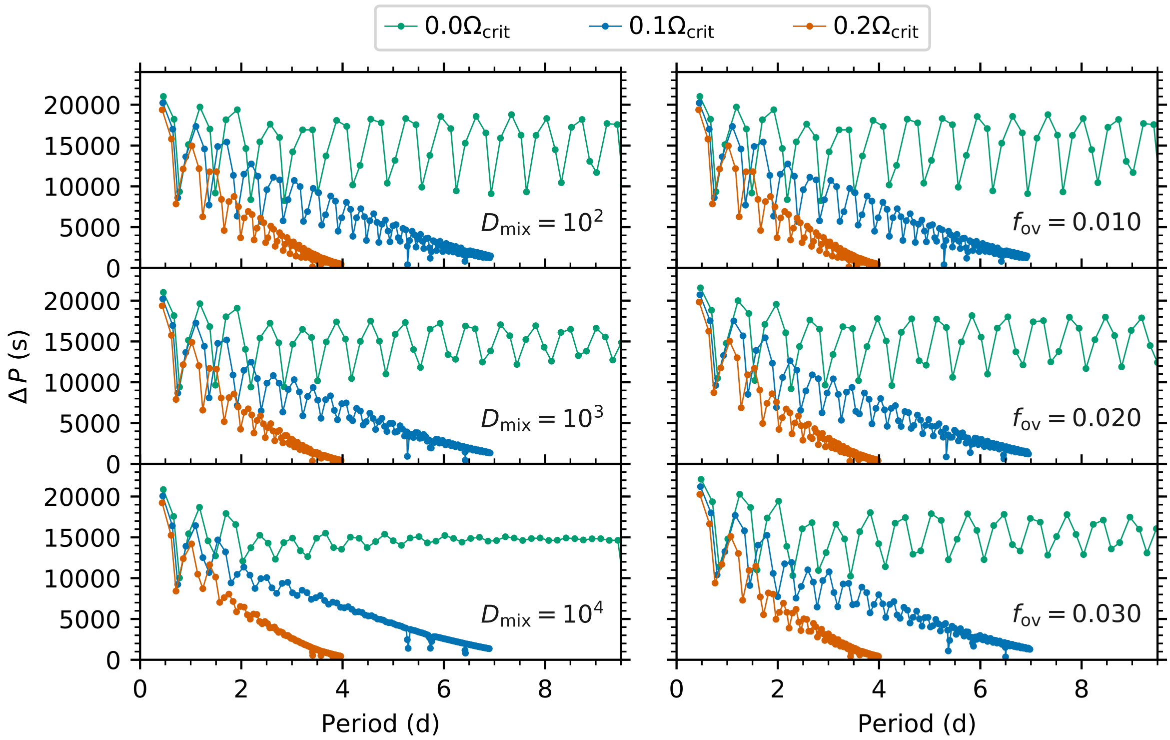

Fig. 1. Theoretical gravity-mode period spacing patterns for prograde dipole modes of a 12 $M_\odot$ star about halfway through the main sequence (i.e. $X_c = 0.4$). The left and right columns are for different envelope mixing ($D_{\rm mix}$) in $\rm cm^2\,s^{-1}$, and exponential convective-boundary mixing ($f_{\rm ov}$) expressed in local pressure scale height, respectively, calculated using the MESA stellar evolution code (Paxton et al. 2011, 2019). For each panel, three rotation rates calculated using the Traditional Approximation for Rotation (TAR) using the GYRE pulsation code (Townsend & Teitler 2013) are shown.

An illustration of the effect of different amounts of interior mixing and rotation rates for a 12 $M_\odot$ star about halfway through the main sequence is shown in Figure 1. Since a non-negligible rotation rate has a significant impact on stellar structure (see e.g. Ouazzani et al. 2015), it also strongly affects the oscillation spectrum of a pulsating star (Bouabid et al. 2013; Van Reeth et al. 2016; Aerts et al. 2019). Therefore, the effect of rotation is critical when calculating and interpreting the oscillation spectrum of a massive star (Aerts et al. 2018), which includes slowly-rotating stars. The effect of (slow-to-moderate) rotation on gravity-mode frequencies, and also the corresponding period spacing pattern, is illustrated in Figure 1, which is calculated using the Traditional Approximation for Rotation (TAR) with the GYRE pulsation code (Townsend & Teitler 2013; Townsend et al. 2018). Hence, the morphology of an observed gravity-mode period spacing pattern facilitates mode identification and offers a direct measurement of the near-core rotation and chemical mixing within a star.

2.1 Interior mixing and rotation

The high-precision space photometry assembled by the CoRoT (Auvergne et al. 2009) and Kepler missions (Borucki et al. 2010; Koch et al. 2010) heralded the birth of gravity-mode asteroseismology for massive stars. Although earlier studies primarily based on pressure modes extracted using ground-based photometry and/or spectroscopy provided valuable insights of massive star interiors, space photometry has opened the door to studying the deep interiors of many more stars across a wider parameter space in the Hertzsprung–Russell (HR) diagram than before. Gravity-mode asteroseismology of massive stars typically employs a data-driven approach, in which observations are used to calibrate models of stellar structure and evolution. In turn, this allows new insight of the physics currently missing within models.

The 4-yr Kepler photometric dataset has unprecedented photometric precision and was the first dataset to provide dozens of SPB stars to test theory. Amongst the first examples was the SPB star KIC 10526294. From a series of rotationally-split gravity modes in KIC 10526294, Pápics et al. (2014) determined a near-core rotation period of approximately 188 d, which was in turn used by Triana et al. (2015) to compute a near-rigid interior rotation profile by means of an inversion. Later, the in-depth modelling of the 19 zonal dipole gravity-modes detected in KIC 10526294, allowed Moravveji et al. (2015) to conclude that a non-zero amount of envelope mixing ($D_{\rm mix} \simeq 100$ cm^2 s^{-1}) was needed to accurately explain the pulsation modes in this star. Furthermore, Moravveji et al. (2015), demonstrated that a non-negligible amount of extra mixing in the near-core region (also known as convective-core overshooting) was required to reproduce the oscillation spectrum of KIC 10526294 – i.e. the best fitting models revealed $0.017 \leq f_{\rm ov} \leq 0.018$. Similar conclusions for needing extra mixing in a moderately rotating SPB star, KIC 7760680, were obtained by Moravveji et al. (2016) with the best-fitting models yielding $D_{\rm mix} \simeq 10$ cm^2 s^{-1} and $f_{\rm ov} = 0.024 \pm 0.001$. At higher masses, moderate values of convective-core overshooting were also found for the 6-M$_\odot$ SPB star KIC 3240411 by Szewczuk & Daszyńska-Daszkiewicz (2018), and a non-zero amount of overshooting in the magnetic, rapidly-rotating SPB star HD 43317 by Buysschaert et al. (2018). These pioneering asteroseismic studies demonstrated the power and importance of constraining the properties of convective cores using gravity modes in the era of space photometry, especially given the relatively large variance in measured overshooting values from only a small sample. In particular, observations clearly show that mixing, and hence core masses and main-sequence lifetimes of stars with convective cores are underestimated in current state-of-the-art models.

Asteroseismology has since been applied to thousands of intermediate-mass stars observed by Kepler, covering masses between approximately 1 and 8 M$_\odot$, rotation rates up to 80% of critical, and evolutionary stages from the main sequence through to the red giant branch. An important conclusion from such a large number of stars has been that current angular momentum transport theory is erroneous by more than an order of magnitude (Aerts et al. 2019). The situation is less clear for massive stars owing to the much smaller sample size currently available, but significant progress has already been made in recent years because of space telescope data and gravity-mode asteroseismology.

In addition to demonstrating the need for larger convective cores in main sequence stars than currently predicted by models, asteroseismology also has the capability to ascertain the *shape* of the mixing profile within the convective-core overshooting region (Pedersen et al. 2018; Mombarg et al. 2019). Typical shapes available in models include the "step" and "exponential" overshooting prescription, but there is currently little consensus as to the correct amount and shape of the mixing profile for massive stars, the temperature gradient within the overshooting region (see e.g. Michielsen et al. 2019), and how these may change as a function of mass and age.

In addition to the need for convective-boundary mixing in massive stars, the origin of mixing within their radiative envelopes is also unconstrained within evolutionary models. Direct evidence for needing increased envelope mixing comes from enhanced surface nitrogen abundances in massive stars (Hunter et al. 2009; Brott et al. 2011). Since nitrogen is a by-product of the CNO cycle of nuclear fusion in a massive star, an efficient mixing mechanism in the stellar envelope must bring it to the surface. Rotationally-induced mixing has been proposed as a possible mechanism (Maeder & Meynet 2000), but it is currently unable to explain observed surface nitrogen abundances in slowly-rotating massive stars in the Milky Way and low-metallicity Large Magellanic Cloud (LMC) galaxies (Hunter et al. 2009; Brott et al. 2011). Furthermore, there was no statistically-significant relationship between the observed rotation and surface nitrogen abundance in a sample of galactic massive stars studied by Aerts et al. (2014). In fact, the only robust correlation with surface nitrogen abundance in the sample was the dominant pulsation frequency (Aerts et al. 2014), which suggests that pulsational mixing is important in massive stars (Townsend et al. 2018). This clearly motivates ongoing work to constrain the origin, amount and shape of envelope mixing in massive stars using gravity-mode asteroseismology given the clear impact of interior mixing and rotation on spectroscopic surface abundances and stellar evolution.

2.2 Diverse photometric variability in massive star photospheres

With the successful delivery of TESS mission photometry (Ricker et al. 2015), we are now entering a new and exciting era in which asteroseismology can be applied to hundreds of pulsating massive stars (Pedersen et al. 2019). The TESS mission is providing a large photometric data set, which also includes hundreds of massive stars in the low-metallicity environment of the Large Magellanic Cloud galaxy (Bowman et al. 2019a). The diversity of photometric variability in hundreds of massive stars – i.e. those known to have spectral types O or B – has already been demonstrated by Pedersen et al. (2019), a sample which also includes (eclipsing) binaries, pulsating stars and magnetic stars (see also, e.g., Handler et al. 2019 and David-Uraz et al. 2019).

A recent discovery made using TESS mission photometry combined with data from the K2 mission (Howell et al. 2014) was that the vast majority of stars with spectral types O or B have significant low-frequency variability in their light curves and amplitude spectra in addition to coherent pressure and/or gravity modes (Bowman et al. 2019b). Such stochastic variability is not predicted from pulsation excitation mechanisms commonly associated with coherent pressure and gravity modes in massive stars. However, convectively-driven gravity waves excited at the boundary of convective regions are predicted by 3D hydrodynamical simulations to produce low-frequency gravity waves and stochastic variability near the surface of a massive star (Edelmann et al. 2019). An example of the temperature fluctuations caused by gravity waves driven by core convection within a massive star from a numerical simulation is shown in Figure 2.

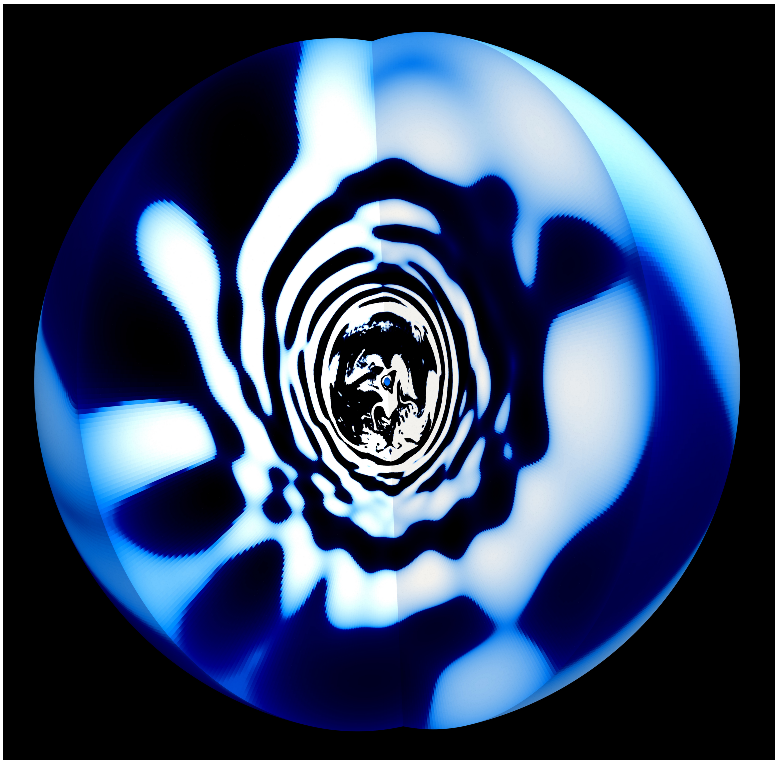

Fig. 2. Snapshot of a 3D numerical simulation of internal gravity waves in a main-sequence massive star, with a white-blue colour scale for temperature fluctuations. Simulation courtesy of Edelmann et al. (2019).

The morphology of the low-frequency variability in more than 160 OB stars was found to be similar across a large range in stellar mass and age and, most importantly, the morphologies were also similar between metal-rich galactic and metal-poor LMC stars (Bowman et al. 2019b). The insensitivity of the low-frequency variability to the apparent metallicity of the host star and the fact that evolutionary timescales predicted that most of the stars in the sample were likely to be in the main sequence phase of evolution led Bowman et al. (2019b) to conclude that the low-frequency variability was evidence of gravity waves excited by core convection. Two examples of massive stars with observed low-frequency variability after coherent pressure and gravity modes have been removed using iterative pre-whitening (Bowman et al. 2019b) are shown in Figure 3, in which the left panel corresponds to the B0 Ia(n) galactic star EPIC 223956110 observed by the K2 mission and the right panel corresponds to the B0.5 Ia LMC star TIC 31105740 observed by the TESS mission.

At present, there are four excitation mechanisms known to trigger waves in OB stars: coherent pressure and/or gravity modes excited by a heat-engine mechanism (Szewczuk & Daszyńska-Daszkiewicz 2017), stochastic wave generation at the interface of the convective core and the radiative envelope (Edelmann et al. 2019), stochastic wave generation by thin sub-surface convection zones (Cantiello et al. 2009; Lecoanet et al. 2019), and tidal excitation in binary systems (Fuller 2017). The identification of standing gravity waves within the observed low-frequency variability is essential to calibrate and constrain numerical simulations of convectively driven waves in terms of wave excitation, propagation and dissipation (Edelmann et al. 2019), and ultimately facilitate asteroseismology in stars for which the heat-engine mechanism may not be the dominant excitation mechanism (Bowman et al. 2019b).

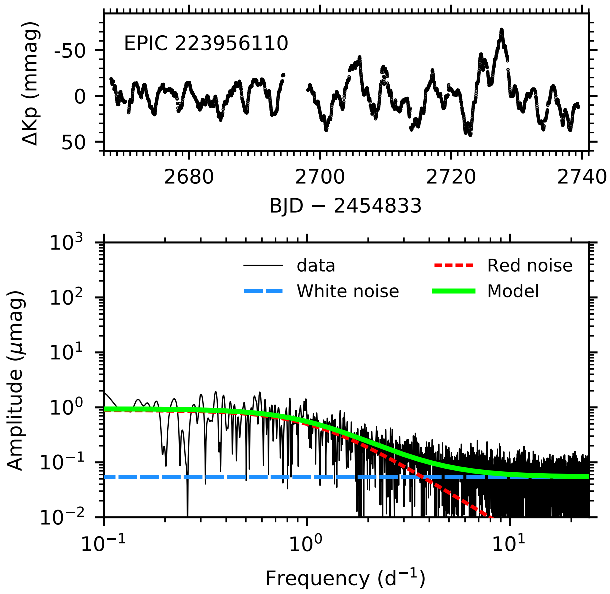

Fig. 3. Observed light curves and amplitude spectra of two pulsating massive stars, which show significant low-frequency variability indicative of an entire spectrum of low-frequency gravity waves after coherent gravity and/or pressure modes have been removed by iterative pre-whitening (Bowman et al. 2019b). The left panel is the B0 Ia(n) star EPIC 223956110 and the right panel is the B0.5 Ia star TIC 31105740.

3 Conclusions and future prospects

Today, thanks to space missions including Kepler/K2 (Borucki et al. 2010; Howell et al. 2014), TESS (Ricker et al. 2015) and BRITE-Constellation (Weiss et al. 2014), there is huge asteroseismic potential for massive stars. The long-term and high-photometric precision provided by space telescopes is unrivalled by ground-based telescopes, and the sample of massive stars is growing significantly larger thanks to the ongoing all-sky TESS mission. Crucially, TESS is also observing massive stars in different metallicity regimes because its southern continuous viewing zone includes the LMC galaxy, which will allow pulsation excitation models to be tested for metal-rich and metal-poor stars. The diverse variability of massive stars, which includes both coherent pulsators and those with low-frequency gravity waves (Pedersen et al. 2019; Bowman et al. 2019b), enables asteroseismology for a sample of massive stars larger by two orders of magnitude compared to any that came before the TESS mission.

An important future goal of asteroseismology is to constrain the near-core and envelope mixing profiles, interior rotation profiles and angular momentum transport mechanisms inside massive stars, since insight of the physics in the near-core region of stars above approximately 8 $M_\odot$ is currently lacking compared to intermediate- and low-mass stars (Aerts et al. 2019). In turn this will mitigate the currently large uncertainties in stellar evolution theory and lead to improved predictions of supernova chemical yields and remnant masses. The future is bright from massive stars, and the goal to calibrate stellar structure and evolution models of massive stars using gravity-mode asteroseismology is now within reach.

DMB thanks the SOC and LOC for their organisation of a productive and enjoyable conference. Some of the research leading to these results has received funding from the European Research Council (ERC) under the European Unions Horizon 2020 research and innovation programme (grant agreement No. 670519: MAMSIE). The K2 and TESS data discussed here are obtainable from the Mikulski Archive for Space Telescopes (MAST) at the Space Telescope Science Institute (STScI), which is operated by the Association of Universities for Research in Astronomy, Inc., under NASA contract NAS5-26555. Funding for the K2 mission is provided by NASAs Science Mission Directorate. Support to MAST for TESS data is provided by the NASA Office of Space Science via grant NAG5-7584 and by other grants and contracts. Funding for the TESS mission is provided by the NASA Explorer Program. The research presented here made use of the SIMBAD database, operated at CDS, Strasbourg, France; the SAO/NASA Astrophysics Data System; and the VizieR catalog access tool, CDS, Strasbourg, France.

References

Aerts, C., Christensen-Dalsgaard, J., & Kurtz, D. W. 2010, Asteroseismology (Springer)
Aerts, C., Mathis, S., & Rogers, T. M. 2019, ARA&A, 57, 35
Aerts, C., Molenberghs, G., Kenward, M. G., & Neiner, C. 2014, ApJ, 781, 88
Aerts, C., Molenberghs, G., Michielsen, M., et al. 2018, ApJS, 237, 15
Aerts, C., Thoul, A., Daszyńska, J., et al. 2003, Science, 300, 1926
Auvergne, M., Bodin, P., Boisnard, L., et al. 2009, A&A, 506, 411
Borucki, W. J., Koch, D., Basri, G., et al. 2010, Science, 327, 977
Bouabid, M.-P., Dupret, M.-A., Salmon, S., et al. 2013, MNRAS, 429, 2500
Bowman, D. M., Aerts, C., Johnston, C., et al. 2019a, A&A, 621, A135
Bowman, D. M., Burssens, S., Pedersen, M. G., et al. 2019b, Nature Astronomy, 3, 760
Briquet, M., Morel, T., Thoul, A., et al. 2007, MNRAS, 381, 1482
Bromm, V., Yoshida, N., Hernquist, L., & McKee, C. F. 2009, Nature, 459, 49
Brott, I., Evans, C. J., Hunter, I., et al. 2011, A&A, 530, A116
Buysschaert, B., Aerts, C., Bowman, D. M., et al. 2018, A&A, 616, A148
Cantiello, M., Langer, N., Brott, I., et al. 2009, A&A, 499, 279
Chieffi, A. & Limongi, M. 2013, ApJ, 764, 21
Daszyńska-Daszkiewicz, J., Szewczuk, W., & Walczak, P. 2013, MNRAS, 431, 3396
David-Uraz, A., Neiner, C., Sikora, J., et al. 2019, MNRAS, 487, 304
de Rossi, M. E., Tissera, P. B., & Pedrosa, S. E. 2010, A&A, 519, A89
Edelmann, P. V. F., Ratnasingam, R. P., Pedersen, M. G., et al. 2019, ApJ, 876, 4
Ekström, S., Georgy, C., Eggenberger, P., et al. 2012, A&A, 537, A146
Fuller, J. 2017, MNRAS, 472, 1538
Georgy, C., Ekström, S., Eggenberger, P., et al. 2013, A&A, 558, A103
Handler, G., Jerzykiewicz, M., Rodríguez, E., et al. 2006, MNRAS, 365, 327
Handler, G., Pigulski, A., Daszyńska-Daszkiewicz, J., et al. 2019, ApJ, 873, L4
Handler, G., Shobbrook, R. R., Jerzykiewicz, M., et al. 2004, MNRAS, 347, 454
Howell, S. B., Sobeck, C., Haas, M., et al. 2014, PASP, 126, 398
Hunter, I., Brott, I., Langer, N., et al. 2009, A&A, 496, 841
Koch, D. G., Borucki, W. J., Basri, G., et al. 2010, ApJ, 713, L79
Langer, N. 2012, ARA&A, 50, 107
Lecoanet, D., Cantiello, M., Quataert, E., et al. 2019, ApJ, 886, L15
Maeder, A. 2009, Physics, Formation and Evolution of Rotating Stars (Springer)
Maeder, A. & Meynet, G. 2000, ARA&A, 38, 143
Martins, F. & Palacios, A. 2013, A&A, 560, A16
Michielsen, M., Pedersen, M. G., Augustson, K. C., Mathis, S., & Aerts, C. 2019, A&A, 628, A76
Miglio, A., Montalbán, J., Eggenberger, P., & Noels, A. 2008, AN, 329, 529
Mombarg, J. S. G., Van Reeth, T., Pedersen, M. G., et al. 2019, MNRAS, 485, 3248
Moravveji, E., Aerts, C., Pápics, P. I., Triana, S. A., & Vandoren, B. 2015, A&A, 580, A27
Moravveji, E., Townsend, R. H. D., Aerts, C., & Mathis, S. 2016, ApJ, 823, 130
Ouazzani, R.-M., Roxburgh, I. W., & Dupret, M.-A. 2015, A&A, 579, A116
Pápics, P. I., Moravveji, E., Aerts, C., et al. 2014, A&A, 570, A8
Paxton, B., Bildsten, L., Dotter, A., et al. 2011, ApJS, 192, 3
Paxton, B., Smolec, R., Schwab, J., et al. 2019, ApJS, 243, 10
Pedersen, M. G., Aerts, C., Pápics, P. I., & Rogers, T. M. 2018, A&A, 614, A128

Pedersen, M. G., Chowdhury, S., Johnston, C., et al. 2019, ApJ, 872, L9
Ricker, G. R., Winn, J. N., Vanderspek, R., et al. 2015, JATIS, 1, 014003
Sana, H., de Mink, S. E., de Koter, A., et al. 2012, Science, 337, 444
Szewczuk, W. & Daszyńska-Daszkiewicz, J. 2017, MNRAS, 469, 13
Szewczuk, W. & Daszyńska-Daszkiewicz, J. 2018, MNRAS, 478, 2243
Townsend, R. H. D., Goldstein, J., & Zweibel, E. G. 2018, MNRAS, 475, 879
Townsend, R. H. D. & Teitler, S. A. 2013, MNRAS, 435, 3406
Triana, S. A., Moravveji, E., Pápics, P. I., et al. 2015, ApJ, 810, 16
Van Reeth, T., Tkachenko, A., & Aerts, C. 2016, A&A, 593, A120
Weiss, W. W., Rucinski, S. M., Moffat, A. F. J., et al. 2014, PASP, 126, 573

Stars and their variability observed from space
C. Neiner, W. W. Weiss, D. Baade, R. E. Griffin, C. C. Lovekin, A. F. J. Moffat (eds)

CEPHEIDS UNDER THE MAGNIFYING GLASS – NOT SO SIMPLE, AFTER ALL!

R. I. Anderson[1]

Abstract. Classical Cepheids are blue loop stars that have famously been dubbed "magnifying glasses of stellar evolution" and have been studied for a long time. As more and more precise observations of Cepheids are secured over ever-increasing temporal baselines, our ignorance of the physics governing these crucial stars is becoming increasingly clear. Thus, it is time to turn up the magnification and investigate the limitations of our understanding of classical pulsators. Of course, classical Cepheids are also standard candles thanks to the Leavitt law that allows one to measure distances in the nearby Universe. Nowadays, Cepheids serve as the backbone of a precisely calibrated distance ladder, that allows one to measure Hubble's constant (H_0) to better than 2%, thus providing crucial constraints for precision cosmology. The recently established discord among H_0 values measured in the late-time Universe and inferred from observations of the early Universe requires utmost diligence in estimating systematic uncertainties in order to strengthen the significance of the results. In this presentation I focus on two main aspects of recent Cepheid-related research. First, I present the Geneva Cepheid Radial Velocity survey (GE-CeRVS) and an update on the modulated spectroscopic variability exhibited by the 4 d Cepheid QZ Normae based on 8 years of monitoring. Then, I discuss some efforts directed towards a 1% H_0 measurement needed for understanding the cosmological implications of discordant H_0 values. Finally, I argue that now is a particularly opportune time to leverage the synergies between stellar physics and observational cosmology.

Keywords: Stars: variables: Cepheids, Stars: oscillations, Line: profiles, Methods: observational, Techniques: radial velocities, distance scale

1 Introduction

Classical Cepheids (henceforth: Cepheids) are evolved intermediate-mass high-amplitude radially pulsating stars with important applications for stellar astrophysics and cosmology. The variability of these very luminous stars provides insights into a stellar evolutionary phase that is notoriously difficult to model — the blue loop during core He burning — and allows one to determine precise (extragalactic) distances thanks to the Leavitt law (Leavitt & Pickering 1912). Importantly, Cepheids form the backbone of the currently most precise distance ladder used for measuring the local expansion rate of the Universe, H_0, which has become a focus of observational cosmologists, since recent precise measurements of H_0 differ by approximately 9% depending on whether they are based on the late Universe ("today") or the early Universe as it was 13.8 billion years ago (Riess et al. 2019, and cf. Verde et al. 2019 for a recent conference summary).

Despite the long history of astronomical research involving Cepheids (Goodricke 1786) and the precision of the modern distance ladder, recent research has increasingly identified a wealth of phenomena that defy explanation and are relevant for many different sub-fields of astronomy & astrophysics, including the evolution of multiple stars, the effects of rotation, convection, and other internal mixing processes, the relation between mass and luminosity, and the variability content of Cepheids, in particular concerning the regularity of Cepheid pulsations. Hence, I would argue that the adjective "classical" should not be considered synonymous with "well-understood", and that digging deeper to identify and understand these issues will help to progress to a better understanding of how stars and the cosmos evolve. Additionally, a reinforced astrophysical basis for the objects that calibrate the distance ladder is required for strengthening the interpretation of discordant H_0 values as an indication of new physics beyond the concordance model of cosmology, that is, flat ΛCDM.

2 Modulated Spectroscopic Variability

2.1 *The Geneva Cepheid Radial Velocity Survey*

The Geneva Cepheid Radial Velocity Survey (*GE-CeRVS*, Anderson et al. in prep.) is a large ongoing survey dedicated to measuring high-precision radial velocities of Galactic classical Cepheids. Since 2011, *GE-CeRVS*

[1] European Southern Observatory, Karl-Schwarzschild-Str. 2, 85748 Garching b. München, Germany

has gathered > 19000 observations of > 300 candidate Cepheids. *GE-CeRVS* operates on two 1m-class telescopes that provide access to the full sky: the Flemish Mercator telescope located at the Roque de los Muchachos Observatory on the island of La Palma, Spain, and the Swiss Euler telescope at the La Silla site of the European Southern Observatory in Chile. Both telescopes feature efficient fiber-fed high-resolution optical echelle spectrographs (Queloz et al. 2001; Raskin et al. 2011). While RVs measured with Hermes reach approximately $10 - 15\,\mathrm{m\ s^{-1}}$ precision, the simultaneous wavelength reference provided by Coralie's Fabry-Pérot etalon affords a precision of $1 - 2\,\mathrm{m\ s^{-1}}$ for bright objects. Thanks to their high precision, dense pulsation phase coverage, and multi-year baseline, *GE-CeRVS* data provide an unprecedented view of the spectroscopic variability of Cepheids. Additionally, they provide a crucial reference for understanding RV variability measured by the RVS instrument on-board the *Gaia* spacecraft (Wallerstein et al. 2019). Among other things, *GE-CeRVS* data have shown that Cepheid RV signals are modulated on different timescales. Specifically, Anderson (2014) showed that the short-period (overtone?) Cepheids QZ Nor and V335 Pup exhibit long-term changes in their RV amplitudes, whereas the long-period Cepheids ℓ Car and RS Pup exhibit cycle-to-cycle variations in pulsation period, RV amplitude, and line profiles (cf. also Anderson 2016).

The following subsection provides a work-in-progress update on this initial discovery 5 years ago and illustrates this surprising long-term behavior for the short-period Cepheid QZ Nor. In addition to RV measurements, it considers the Bisector Inverse Span (BIS) (for a visualization, see e.g. Anderson 2016, their Fig. 2), which provides a useful and precise measure of spectral line asymmetry.

2.2 Monitoring QZ Nor for 8 years

Figure 1 shows the *GE-CeRVS* time series RV and BIS measurements of the 3.79 d Cepheid QZ Nor, whose modulated RV curve was first reported by Anderson (2014). As is clear from the figure, both the RV amplitude and the line profile asymmetry traced by the BIS quantity exhibit long-term changes throughout the 8-year time scale of the observations.

Figure 2 separates the RV variability into epochs of 16.1 d duration and illustrates that each epoch is reasonably well sampled, exhibiting fairly simple variability curves that can be represented by low-order Fourier series. However, Fig. 3 shows that the pulsation-averaged RV (v_γ) and the RV amplitude (A_{RV}) exhibit correlated changes over time. This is important because the top panel in Fig. 3 resembles a low-amplitude high-eccentricity orbit, and would likely be interpreted as such if the bottom panel did not imply a contemporaneous change in A_{RV}. In other words, Fig. 3 cautions us against interpreting all temporal variations on the order of even $1\,\mathrm{km\ s^{-1}}$ as signs of orbital motion, contradicting the typical interpretation of such signals. At present, it remains unclear whether these changes are (quasi-)periodic or repeating, not to mention what causes these phenomena. (Derekas et al. 2017) reported the previously longest modulation seen in a Cepheid for the only classical Cepheid in the original *Kepler* field, V1154 Cyg, with a period of 1160 d based on a light curve spanning 1470 d. Unfortunately, we do not yet know whether photometric and spectroscopic modulations correspond to each other. This is mostly because precise long-timescale photometric monitoring of bright stars is not available, whereas spectroscopic observations do not exist in sufficient quantity for fainter Cepheids, e.g. in the OGLE fields (e.g. Soszyński et al. 2019). However, Anderson et al. (2016) showed that interferometric observations suggest that ℓ Car exhibits cycle-to-cycle changes in its maximum diameter. High-quality contemporaneous photometric and spectroscopic time series are required for understanding these phenomena and casting open these exciting windows into stellar pulsations.

As explained in Anderson (2018), different ways of measuring RV in Cepheids have different merits and potential issues. In *GE-CeRVS*, RV is defined as the center of a Gaussian line fitted to the cross-correlation profile, which is the standard in precision RV measurements of stable stars (Baranne et al. 1996; Pepe et al. 2002). Astrophysical effects can change the shape of line profiles over time, out of sync with the dominant radial mode pulsation. Such effects can lead to spurious changes in the mean velocity by introducing time-dependence in the bias of RVs measured using Gaussian fits to asymmetric line profiles. Although this complicates the interpretation of v_γ as an indicator for spectroscopic binary motion, this is useful for identifying previously unknown hydrodynamical effects, such as coupling between pulsations and convection (Anderson 2016). Another particularly puzzling, and potentially telling, signal is the 40.2 d periodic BIS variation seen in the North Star, Polaris (Anderson 2019a), whose light curve and RV variations are dominated by periodic variability on a timescale of 3.97 d.

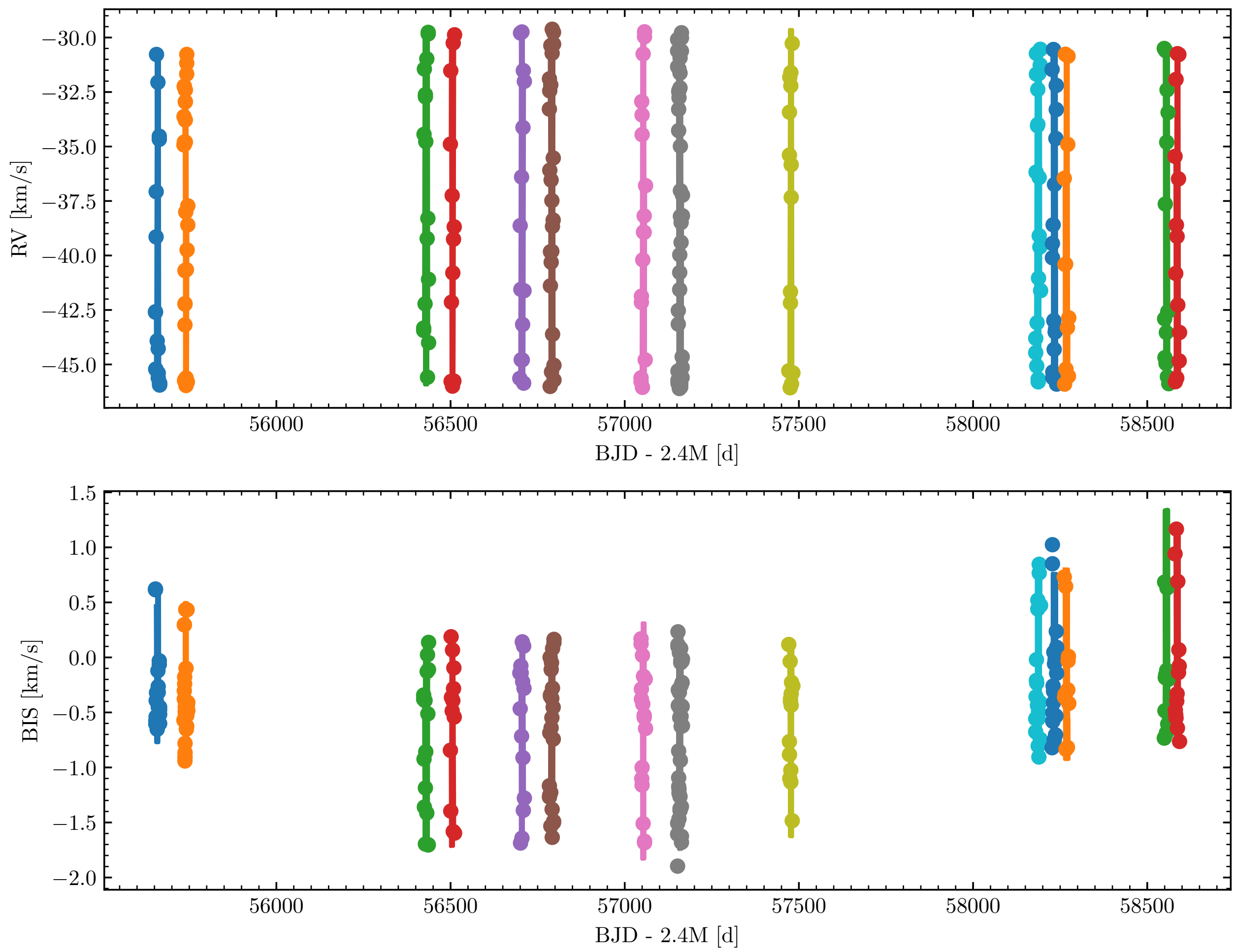

Fig. 1. GE-CeRVS data of the 3.79 d (overtone?) Cepheid QZ Nor. **top:** RV against observation date. **bottom:** Line asymmetry as measured by BIS against observation date

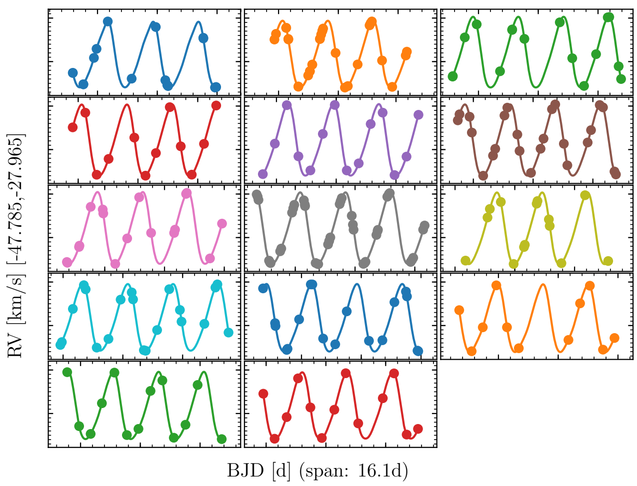

Fig. 2. QZ Nor's RV curves per epoch

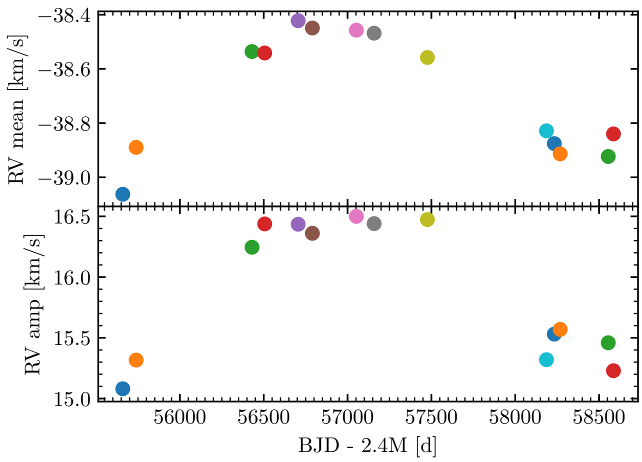

Fig. 3. QZ Nor's mean RV and RV amplitude variations over time

3 Towards a 1% measurement of Hubble's Constant

Very large efforts are under way to measure the local expansion rate of the Universe, Hubble's constant H_0, to within 1%. Until recently, a prime motivation for pursuing this factor of 10 improvement over the Hubble

Space Telescope (*HST*) Key Project (Freedman et al. 2001) was an improved ability to elucidate the nature of dark energy. Indeed, a 1% H_0 measurement used as prior for determining the equation of state of dark energy would optimally support future developments in observational cosmology Weinberg et al. (2013). In as much as it is acceptable to use H_0 as a prior for the analysis of the Cosmic Microwave Background (CMB), this motivation remains true and important. However, recent works have found a conspicuous disagreement between measurements of H_0 based on the late-time Universe (as it is "today" by cosmic standards) and the value of H_0 inferred from observations of early Universe physics, such as the CMB or Big Bang Nucleosynthesis (cf. Verde et al. 2019, for an overview). Notably, there is a $\sim 9\%$ difference (at 4.4σ significance) between a faster late-Universe H_0 and a slower early-Universe value based on an extragalactic distance scale composed of classical Cepheids and type-Ia supernovae (Riess et al. 2019) and observations of the CMB by the *Planck* satellite (Planck Collaboration 2018). This *Hubble tension* challenges the adequacy of the concordance cosmological model, which connects the present-day Universe with the oldest observed radiation and describes the Universe as flat, consisting of dark energy in the form of a cosmological constant, dark matter, and ordinary matter (ΛCDM). If it can be shown that new physics are required to solve this conundrum, then we may well be near a breakthrough in our understanding of the Universe and its evolution.

Classical Cepheids play a crucial role for increasing the precision of H_0 measurements for several reasons. As easily recognizable and very luminous stars, Cepheids provide the absolute calibration of type-Ia supernovae, whose distance-redshift relation defines the Hubble-Lemaître law. Although Cepheid alternatives such as Mira stars (Huang et al. 2019) and stars near the Tip of the Red Giant Branch (Freedman et al. 2019, TRGB) have made tremendous progress over the last few years, they have not yet reached the same precision as that currently offered by Cepheids and it remains to be seen which type of primary standard candle will first be limited by systematic uncertainties. Hence, it is crucial to determine the systematic "error floor" of Cepheids (and other standard candles) and to pay particular attention to previously neglected or overlooked systematic effects.

Anderson & Riess (2018) recently examined a frequently mentioned, albeit poorly quantified, systematic uncertainty of the distance ladder: stellar association bias. In particular, we considered the effect of stellar multiplicity and cluster membership on the modern H_0 measurements as implemented by Riess et al. (2016), rather than describing the effects on the Leavitt law (or period-luminosity relation). The latter exercise provides a valuable test of stellar physics, that is whether stellar models correctly predict observed Leavitt laws. In terms of a systematic error or bias of H_0, however, it is most important to consider the equivalence between Leavitt laws observed in nearby and more distant Cepheid populations.

The bias arises because Cepheids are relatively young (30-300 Myr old) evolved supergiant stars that occasionally occur in open star clusters or loose associations (e.g. Turner et al. 2010; Anderson et al. 2013). On Local Group scales, star clusters are easily recognized and spatially resolved. At the average supernova host galaxy distance of 23 Mpc, however, the typical physical cluster scale of 4 pc is equal to the plate scale of *HST*'s WFC3 in UVIS mode (0.04"). Thus, stars physically associated with Cepheids do not contribute to the calibration of the Leavitt law, which is done locally, but do contribute light to distant Cepheids on the second rung of the distance ladder. Figure 4 illustrates this. Stellar association bias is different from chance blending of field stars because the latter is corrected using artificial star tests, whereas cluster light contributions cannot be easily corrected in distant galaxies.

Using M31 as a supernova-host analog for its high metallicity, spiral structure, and external view, Anderson & Riess (2018) measured the light contributions for 9 cluster Cepheids using *HST* photometry from the PHAT project (Dalcanton et al. 2012). Cluster positions were known from the Andromeda Project (Johnson et al. 2015) and Cepheid positions from the PanSTARRS survey (Kodric et al. 2018), M31's cluster Cepheids were highlighted by Senchyna et al. (2015).

Interested readers are referred to Anderson & Riess (2018) for the details of the analysis. Suffice it here to state that the bias was estimated as the product of the clustered Cepheid fraction times the average bias measured using curve-of-growth analysis of 9 M31 cluster Cepheids. We find that on average a Cepheid's distance is underestimated by 7.4 mmag using a reddening-free Wesenheit magnitude that combines V, I, and H-band photometry, and by 9.8 mmag when using H-band only. Corrections for these light contributions are now included in the H_0 measurements by Riess et al. (2019). Further work in this direction will clarify the adequacy of the adopted clustered Cepheid fraction and the effects of selection criteria applied to extragalactic Cepheid samples on this bias.

Of course, Cepheids very frequently occur in multiple star systems (e.g. Evans et al. 2015; Kervella et al. 2019b,a). However, companion stars contribute a bias of $< 0.004\%$ because most configurations of companion stars are rarely spatially resolved (Anderson & Riess 2018). This estimate was based on the Geneva stellar evolution models (Ekström et al. 2012; Georgy et al. 2013; Anderson et al. 2016) and the properties of Cepheid orbits (Moe & Di Stefano 2017).

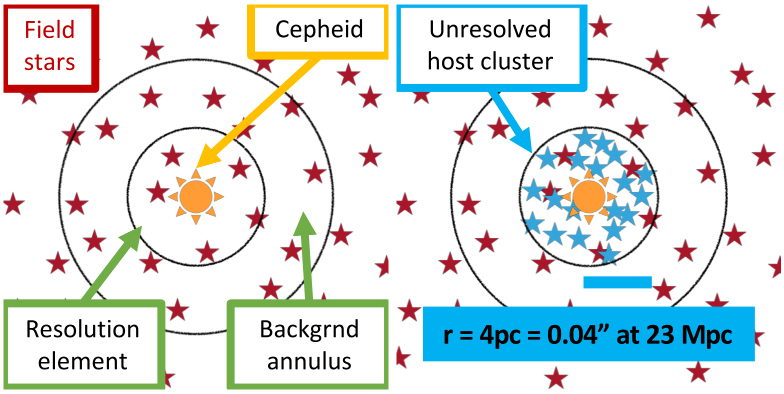

Fig. 4. Distinction between chance blending (left) and blending of physically associated stars that leads to biased extragalactic measurements and H_0 (right). Chance blending can be corrected statistically by measuring field star contributions. However, blending of physically associated stars cannot be corrected in this way, since the physical scale of stellar association in clusters is unresolved at typical supernova-host galaxy distances.

Another bias affecting the distance scale due to inherent differences between near and far Cepheid populations concerns the dilation of variability periods due to cosmological redshift. As shown in Anderson (2019b), time dilation has previously led to a 0.3% underestimate of H_0. However, this bias will increase as future work will focus on more and more distant Cepheids in order to increase the number of supernova-host galaxies, which is limited by the rate of supernova explosions in the nearby Universe. For reference, Leavitt law distances to pulsating stars at 100 Mpc would be biased by 2% if redshift is not accounted for. Thus, future distance scale work aimed at a 1% measurement of H_0 must account for dilated variability periods, for example using observed host galaxy redshifts.

4 Synergies between precision cosmology and stellar physics

Extragalactic pulsating stars (e.g. Cepheids & Miras) provide the backbone of the extragalactic distance ladder and the associated measurement of H_0 sets the scale and age of the Universe. As we are pursuing a 1% H_0 measurement (or better), additional scrutiny is required to ensure that systematic uncertainties that could shift the center value of H_0 are under control at the same level, or better. Given that the primary distance ladder rungs dominate the uncertainty budget of the H_0 measurement (cf. Riess et al. 2019), further scrutiny is required to identify and mitigate systematics affecting Cepheid distances. This leads to wonderful opportunities for studying populations of extragalactic Cepheids in different environments (star formation, galactic potentials, chemical composition, etc.) that can provide new insights into stellar pulsations and the evolution of stellar populations.

At the same time, precision observations of the closest Cepheids reveal surprising new phenomena, such as multi-periodic variability (cf. above) or difficult-to-explain circumstellar environments (Hocdé et al. 2019). Moreover, long-term photometric monitoring of Cepheid pulsation periods challenges the canonical interpretation of observed rates of period change as indicative of secular evolution (e.g. Poleski 2008; Süveges & Anderson 2018). These are fundamental new insights into stellar astrophysics, which ultimately explain the mechanisms upon which the distance ladder rests. Of course, mmag-level non-radial pulsations and short-term period fluctuations do not immediately lead to biases in measuring H_0. However, such work may allow us to select cleaner samples of Cepheids exhibiting tighter Leavitt laws that ultimately increase distance ladder precision and accuracy. With large time-domain surveys such as *Gaia* and LSST (cf. contributions by L. Eyer and G. Clementini in these proceedings) gathering unprecedented data for classical pulsators, and even small telescopes providing high-quality datasets (such as GE-CeRVS), now is a great time to leverage the synergies between precision cosmology and detailed stellar physics.

I would like to thank the organizers, and Werner Weiss in particular, for this wonderful and inspiring meeting and my collaborators, especially everyone involved with GE-CeRVS, incl. L. Eyer and N. Mowlavi.

References

Anderson, R. I. 2014, A&A, 566, L10

Anderson, R. I. 2016, MNRAS, 463, 1707

Anderson, R. I. 2018, in The RR Lyrae 2017 Conference. Revival of the Classical Pulsators: from Galactic Structure to Stellar Interior Diagnostics, ed. R. Smolec, K. Kinemuchi, & R. I. Anderson, Vol. 6, 193–200

Anderson, R. I. 2019a, A&A, 623, A146

Anderson, R. I. 2019b, A&A, 631, A165

Anderson, R. I., Eyer, L., & Mowlavi, N. 2013, MNRAS, 434, 2238

Anderson, R. I., Mérand, A., Kervella, P., et al. 2016, MNRAS, 455, 4231

Anderson, R. I. & Riess, A. G. 2018, ApJ, 861, 36

Anderson, R. I., Saio, H., Ekström, S., Georgy, C., & Meynet, G. 2016, A&A, 591, A8

Baranne, A., Queloz, D., Mayor, M., et al. 1996, A&AS, 119, 373

Dalcanton, J. J., Williams, B. F., Lang, D., et al. 2012, ApJS, 200, 18

Derekas, A., Plachy, E., Molnár, L., et al. 2017, MNRAS, 464, 1553

Ekström, S., Georgy, C., Eggenberger, P., et al. 2012, A&A, 537, A146

Evans, N. R., Berdnikov, L., Lauer, J., et al. 2015, AJ, 150, 13

Freedman, W. L., Madore, B. F., Gibson, B. K., et al. 2001, ApJ, 553, 47

Freedman, W. L., Madore, B. F., Hatt, D., et al. 2019, ApJ, 882, 34

Georgy, C., Ekström, S., Granada, A., et al. 2013, A&A, 553, A24

Goodricke, J. 1786, Philosophical Transactions of the Royal Society of London Series I, 76, 48

Hocdé, V., Nardetto, N., Lagadec, E., et al. 2019, arXiv e-prints

Huang, C. D., Riess, A. G., Yuan, W., et al. 2019, arXiv e-prints

Johnson, L. C., Seth, A. C., Dalcanton, J. J., et al. 2015, ApJ, 802, 127

Kervella, P., Gallenne, A., Evans, N. R., et al. 2019a, A&A, 623, A117

Kervella, P., Gallenne, A., Remage Evans, N., et al. 2019b, A&A, 623, A116

Kodric, M., Riffeser, A., Seitz, S., et al. 2018, ApJ, 864, 59

Leavitt, H. S. & Pickering, E. C. 1912, HCO Circular, 173, 1

Moe, M. & Di Stefano, R. 2017, ApJS, 230, 15

Pepe, F., Mayor, M., Galland, F., et al. 2002, A&A, 388, 632

Planck Collaboration. 2018, arXiv e-prints

Poleski, R. 2008, Acta Astron., 58, 313

Queloz, D., Mayor, M., Udry, S., et al. 2001, The Messenger, 105, 1

Raskin, G., van Winckel, H., Hensberge, H., et al. 2011, A&A, 526, A69

Riess, A. G., Casertano, S., Yuan, W., Macri, L. M., & Scolnic, D. 2019, ApJ, 876, 85

Riess, A. G., Macri, L. M., Hoffmann, S. L., et al. 2016, ApJ, 826, 56

Senchyna, P., Johnson, L. C., Dalcanton, J. J., et al. 2015, ApJ, 813, 31

Soszyński, I., Udalski, A., Szymański, M. K., et al. 2019, Acta Astron., 69, 87

Süveges, M. & Anderson, R. I. 2018, A&A, 610, A86

Turner, D. G., Majaess, D. J., Lane, D. J., Rosvick, J. M., & Henden, A. A. B. D. D. 2010, Odessa Astronomical Publications, 23, 119

Verde, L., Treu, T., & Riess, A. G. 2019, Nature Astronomy, 3, 891

Wallerstein, G., Anderson, R. I., Farrell, E. M., et al. 2019, PASP, 131, 094203

Weinberg, D. H., Mortonson, M. J., Eisenstein, D. J., et al. 2013, Phys. Rep., 530, 87

Stars and their variability observed from space
C. Neiner, W. W. Weiss, D. Baade, R. E. Griffin, C. C. Lovekin, A. F. J. Moffat (eds)

ASTEROSEISMOLOGY OF RAPIDLY ROTATING STARS WITH ACOUSTIC MODES

D. R. Reese[1]

Abstract.
Recent observations of mixed modes in red giants has revealed the shortcomings of current theory for explaining stellar rotation and angular momentum transport. Such shortcomings become more acute in the case of rapidly rotating stars, where the relevant physical processes such as baroclinicity are amplified. A series of recent stellar models based on 1D and 2D numerical approaches are starting to provide insights into these questions, but require observational constraints. Stellar pulsations potentially provide the tightest constraints on internal stellar structure but need to be identified correctly. The present contribution focusses on acoustic pulsations of rapidly rotating stars. After recalling the asymptotic behaviour of so-called island modes, the rotating counterparts to low-degree modes, it describes generalized rotational splittings and the insights they provide for the stellar rotation profile. It then describes recent efforts at interpreting observed pulsations, in particular searches for regular frequency patterns in different stars, and also multi-colour mode identification in β Pictoris using observations from various instruments, including the BRITE constellation.

Keywords: Stars: oscillations (including pulsations), rotation, interiors, evolution, fundamental parameters, stars: individual: 38 Eridani, β Pictoris, Rasalhague, Altair

1 Introduction

Many early-type main sequence stars rotate rapidly (*e.g.* Royer 2009). They include g-mode pulsating classes of stars, namely γ Dor stars and SPBs, as well as acoustic pulsators, namely δ Scuti and β Cep stars. Gravity-mode pulsators are described by Ouazzani (PAGE), but this contribution focusses on acoustic pulsators.

Currently, exquisite space photometry of pulsating stars has been, or will be, provided by the missions *MOST, CoRoT, Kepler* and *K*2 for a single photometric band, and by BRITE and PLATO for multiple colours. In parallel, the ground-based network SONG is starting to provide high-quality spectroscopic time-series for these stars. However, in the case of rapidly rotating acoustic pulsators, theoretical interpretations of asteroseismic data are lagging behind. There is a number of theoretical hurdles to overcome in modelling such stars, such as centrifugal deformation and baroclinicity. Furthermore, mode identification, i.e., matching observed pulsations with theoretically calculated modes, is very challenging. Nonetheless, gaining a better understanding of these stars would provide insights into baroclinic flows, transport processes of angular momentum and chemical species, and the effects of these phenomena on stellar lifetime and chemical yields. It would lead to a better modelling of the precursors to supernovæ and γ-ray bursts. This contribution will therefore describe recent insights in the theoretical modelling of acoustic pulsations of such stars, (Sect. 2) and also some of the latest asteroseismic investigations that have been carried out (Sect. 3).

2 Rotation and pulsations

Acoustic modes are high-frequencies modes for which the restoring force is pressure. They are especially affected by the centrifugal force. Those effects can be characterised by the ratio of the stellar flattening $\epsilon = 1-R_{\mathrm{p}}/R_{\mathrm{eq}} \propto \Omega^2$, where R_{p} and R_{eq} are the polar and equatorial radii, and Ω the rotation rate, to the mode wavelength $\lambda \propto \omega^{-1}$, where ω is the pulsation frequency. Accordingly, high-requency modes are affected more quickly than low-frequency modes for increasing rotation rates (*e.g.* Reese et al. 2006).

At high rotation rates, different classes of acoustic pulsation modes appear, as shown by ray dynamics (Lignières & Georgeot 2008, 2009), which are characterised by distinct mode geometries and frequency organisation in the pulsation spectrum. These classes include island modes, chaotic modes and whispering gallery modes, and are the rotating counterparts to modes with low, intermediate, and high values of $\ell - |m|$. Mirouh et al. (2019) recently put together a convolution neural network to classify theoretically calculated modes automatically according to these different classes, thus avoiding laborious manual classification.

[1] LESIA, Observatoire de Paris, Université PSL, CNRS, Sorbonne Université, Université de Paris, 5 place Jules Janssen, 92195 Meudon, France

2.1 *Island modes*

Of these different classes, island modes are probably the most interesting, as they are the most visible of the regular modes (Lignières & Georgeot 2009; Reese et al. 2013). They are characterised by the quantum numbers $\tilde{n}$, the number of nodal lines which are perpendicular to the underlying periodic orbit, $\tilde{\ell}$, the number of nodal lines parallel to the orbit, and m, the azimuthal order. By using these quantum numbers, one can obtain an asymptotic expression for their frequencies in an inertial frame (*e.g.* Reese et al. 2009):

$$\omega \simeq \Delta_{\tilde{n}}\tilde{n} + \Delta_{\tilde{\ell}}\tilde{\ell} + \frac{\Delta_{\tilde{m}} m^2}{\tilde{n}^2} - m\Omega + \tilde{\alpha} \tag{2.1}$$

The quantity $\Delta_{\tilde{n}}$ is deduced from the acoustic travel time along the underlying orbit (Lignières & Georgeot 2008, 2009), and is roughly proportional to $\sqrt{\bar{\rho}}$, where $\bar{\rho}$ is the mean density (Reese et al. 2008; García Hernández et al. 2015). A semi-analytical formula for $\Delta_{\tilde{\ell}}$ has also been obtained by Pasek et al. (2011, 2012).

An important question is whether it is possible to probe the rotation profile using island modes. In order to answer it, we can already investigate the forward problem, i.e., how do different rotation profiles affect the pulsation frequencies. Reese et al. (2009, submitted) derived a formula that relates the generalised rotational splittings, defined as the splitting between a prograde mode and its retrograde counterpart, to weighted integrals of the rotation profile, where the weighting is mode-dependant:

$$\frac{\omega_{-\mathrm{m}} - \omega_{\mathrm{m}}}{2m} \simeq \frac{\Omega_{\mathrm{m}}^{\mathrm{eff}} + \Omega_{-\mathrm{m}}^{\mathrm{eff}}}{2} + \frac{\mathcal{C}_{\mathrm{m}} + \mathcal{C}_{-\mathrm{m}}}{2} \tag{2.2}$$

with

$$\Omega_{\mathrm{eff}} = \frac{\int_V \Omega\rho_o\|\vec{\xi}\|^2 dV}{\int_V \rho_o\|\vec{\xi}\|^2 dV} \tag{2.3}$$

$$\mathcal{C} = \frac{i}{m}\frac{\int_V \rho_o\vec{\Omega}\cdot\left(\vec{\xi}^* \times \vec{\xi}\right) dV}{\int_V \rho_o\|\vec{\xi}\|^2 dV}, \tag{2.4}$$

where $-m$ corresponds to prograde modes, ρ_o is the equilibrium density profile, and $\vec{\xi}$ the Lagrangian displacement. Applying this formula to the profiles shown in the left part of Fig. 1 using $\tilde{\ell} = 0$ modes leads to the splittings in the right panel of the figure. A clear distinction can be seen between profiles with a radial gradient but only a small horizontal gradient (ESTER and Shellular) and those with a stronger horizontal gradient (Cylindrical and Conical). Also shown in the right panel are the true splittings, which should be compared with those deduced for the ESTER profile using the above formula (thus giving an idea of the accuracy of the formula).

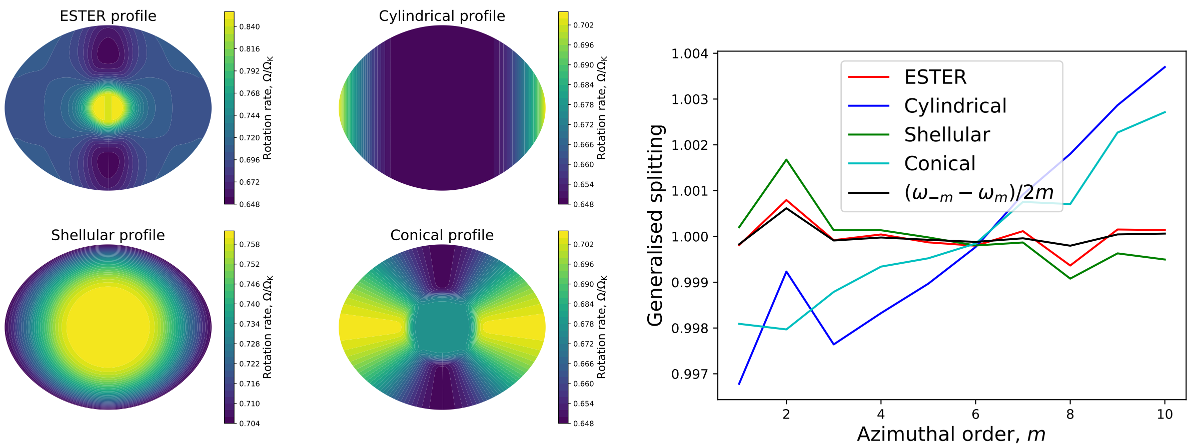

Fig. 1. Four different rotation profiles (**left**) and the resultant generalised rotational splittings for a set of $\tilde{\ell} = 0$ modes with m ranging from 1 to 10 using Eq. (2.2) (**right**). The true splittings are also shown in black in the right panel.

2.2 Chaotic modes

Chaotic modes are characterised by a chaotic mode structure (as expected, based on the relevant ray trajectories) and a statistical distribution of pulsation frequencies rather than an asymptotic formula. Nonetheless, Evano et al. (2019a,b) recently showed that these modes also display partial regularities. As revealed through peaks in the autocorrelation functions of their pulsation spectra, a characteristic spacing close to the large frequency separation is present – as can be seen in the echelle diagram shown in the left panel of Fig. 2. The modes associated with a given ridge in the echelle diagram also have a similar geometric structure, as illustrated in the right panel of Fig. 2.

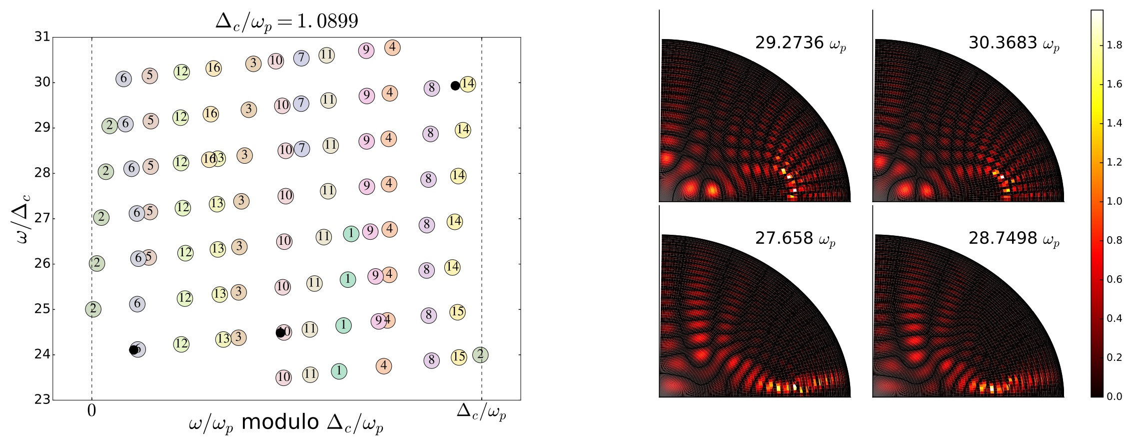

Fig. 2. (**Left**:) Echelle diagram with chaotic modes. The colours and numbers highlight different ridges composed of modes with a similar geometric structure. (**Right**:) Meridional cross sections of consecutive chaotic modes from series 8 (upper row) and 3 (lower row). From Evano et al. (2019b), reproduced with permission ©ESO.

Such regularities are not expected in the context of quantum chaos theory, i.e., the theory which provides the link between eigenvalue spectra and chaotic ray trajectories. As argued in Evano et al. (2019a,b), the cause behind this behaviour is the strong stratification in sound velocity in the radial direction which leads to a fairly regular structure in that direction, even if the latitudinal structure is chaotic.

3 Interpreting observations

Various approaches have been used to interpret the acoustic pulsations of rapidly rotating stars. They include the search for frequency patterns, multi-colour mode identification, and combining asteroseismic constraints with other constraints, in particular those from interferometry.

3.1 Frequency patterns

As was shown in various theoretical calculations (*e.g.* Lignières et al. 2006; Reese et al. 2008), the large frequency separation, $\Delta\nu$, continues to exist at high rotation rates and to scale with the mean density. Accordingly, García Hernández et al. (2013, 2015); García Hernández et al. (2017) have identified $\Delta\nu$ through Fourier transforms of the pulsation spectra and used it to constrain $\bar{\rho}$ and $\log(g)$, the surface gravity, in δ Scuti stars. Michel et al. (2017) stacked the pulsation spectra from multiple main-sequence δ Scuti stars observed by *CoRoT*, thus revealing the presence of similar frequency spacings in these stars. Bowman & Kurtz (2018) repeated the same exercise for *Kepler* stars but their results were less clear.

Once a recurrent frequency separation has been found, it is possible to construct echelle diagrams with the pulsation frequencies. That has been done by García Hernández et al. (2013); Paparó et al. (2016a,b) for *CoRoT* stars, and more recently by Bedding et al. (2020) for TESS stars. Ridges appear in the echelle diagrams and have been interpreted as axisymmetric $\ell = 0$ and 1 modes in Bedding et al. (2020). Indeed, up to rapid rotation rates, the normalised frequencies for axisymmetric $\ell = 0$ and 1 modes vary little, apart from the occasional avoided crossing, as illustrated in Fig. 3.

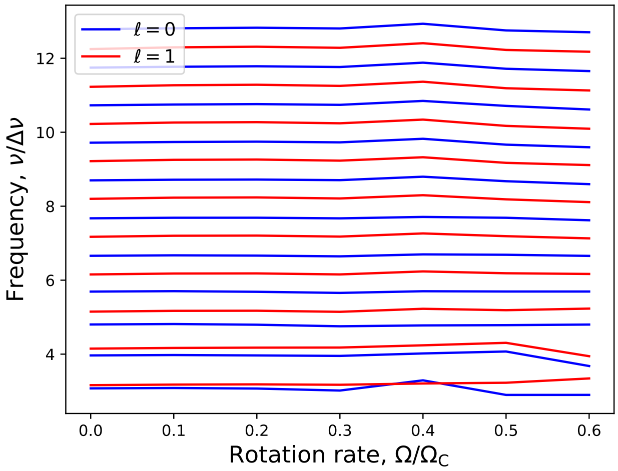

Fig. 3. Axisymmetric $\ell = 0$ and 1 mode frequencies, normalised by the large separation for $1.8\,M_\odot$ ZAMS models ranging from $0 - 0.6\Omega_C$ calculated with the Self-Consistent Field (SCF) method (Jackson et al. 2005; MacGregor et al. 2007). Ω_C is the critical rotation rate and is very close to the Keplerian break-up rotation rate (see Table 1 of Reese et al. 2013).

3.2 Multi-colour mode identification

For a given pulsation mode, the amplitude ratios and phase differences between different photometric bands depends only on its geometric characteristics. Hence, measuring these quantities provides constraints on the identification of the observed modes. Although quite popular for slowly rotating stars, this method has not been applied extensively to rapid rotators; in fact, in the rotating case, amplitude ratios depend on the inclination of the star and the azimuthal order (Daszyńska-Daszkiewicz et al. 2002; Townsend 2003), thus complicating the identification process.

Recently, Paparó et al. (2018) studied 38 Eri, a δ Scuti star with $v \sin i = 98\,\mathrm{km\ s^{-1}}$, using ground-based observations in multiple photometric bands from the Strömgren and Johnson systems, and also space photometry data from the MOST satellite, and found 18 pulsation frequencies corresponding to low order p and g modes. They went on to carry out mode identification using amplitude ratios (without including the effects of rotation) and what appears to be g-mode rotational splittings. However, the two approaches produced conflicting results, thus pointing to a need for further analysis including full 2D-mode visibility calculations when interpreting the results.

More recently, Zwintz et al. (2019) studied β Pic, a δ Scuti star rotating at $v \sin i = 124 \pm 3, \mathrm{km\ s^{-1}}$ and with a disk and an exoplanet (Lagrange et al. 2010), and found 15 pulsation frequencies in 2 to 5 photometric bands from multiple instruments, namely the BRITE blue and red satellites, bRing*, SMEI†, and ASTEP. They carried out a detailed asteroseismic analysis using $1.8\,M_\odot$ ZAMS models with rotation rates from $0 - 0.6\,\Omega_C$ based on the Self-Consistent Field (SCF) method (Jackson et al. 2005; MacGregor et al. 2007). Multi-colour mode visibility calculations including an approximate treatment of non-adiabatic effects were carried out following Reese et al. (2013, 2017b). An MCMC fit to the amplitude ratios and pulsation frequencies, including various classic constraints, was performed, and led to a variety of solutions depending on the weight factors for the different constraints. Figure 4 shows a comparison between observed and theoretical amplitude ratios and frequencies, for a near-equator-on configuration of the star (which is what would be expected if the star were aligned with the disk and exoplanet orbit). It illustrates the challenges in reproducing the observations and the need for developing theoretical predictions further.

3.3 Combining asteroseismology and interferometry

When stars rotate rapidly, it can be particularly interesting to combine the constraints from interferometry with those from asteroseismology. Indeed, interferometry provides constraints on the stellar radius (when combined with the parallax), the rotation rate (by measuring the amount of centrifugal deformation), and inclination (thanks to gravity darkening). Those in turn narrow down the possibilities when searching for models which reproduce the asteroseismic constraints.

*The β Pictoris b Ring project.
†Solar Mass Ejection Image

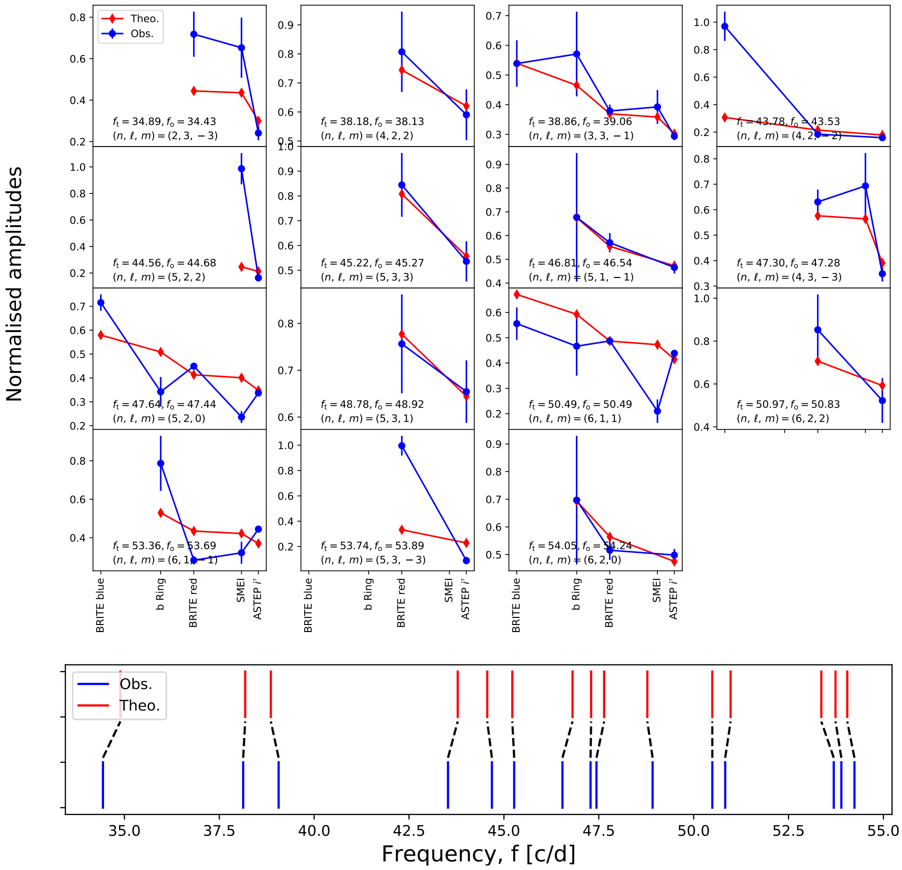

Fig. 4. A comparison between observed and theoretical amplitude ratios (**upper panel**) and frequencies (**lower panel**) for β Pic. From Zwintz et al. (2019).

The δ Scuti star α Ophiuchi ('Rasalhague') has been observed interferometrically, and led to a precise determination of its inclination, polar and equatorial radii (Zhao et al. 2009). 57 pulsation frequencies have been detected, thanks to MOST photometry (Monnier et al. 2010). Deupree (2011); Deupree et al. (2012) carried out asteroseismic studies of this star using a 2D approach. However, a precise mode identification remained elusive owing to the multitude of theoretical pulsation modes which could potentially match the observed frequencies. More recently, Mirouh et al. (2017) studied this star using 2D ESTER models (Espinosa Lara & Rieutord 2013; Rieutord et al. 2016) which fit the interferometric constraints. They carried out an asteroseismic fit taking into account mode visibilities and excitation, and using the non-adiabatic version of the 2D pulsation code TOP (Reese et al. 2006, 2017a). The results were not conclusive, owing to the lack of excited island modes; that points towards limitations in the models and/or the pulsation calculations.

More recently still, Bouchaud et al. (submitted) carried out an in-depth study of the star α Aquilae ('Altair'). As a first step, they fitted the interferometric constraints from the PIONIER and GRAVITY instruments at the VLTI and also some spectroscopic constraints, using Roche Models with the gravity darkening prescription from Espinosa Lara & Rieutord (2011) and full 2D ESTER models. That led to well-constrained values for the equatorial radius, the rotation rate, the inclination and position angle. However, a degeneracy appeared between the mass, the metallicity, the envelope and the core hydrogen content. Using the pulsation frequencies obtained with WIRE (Buzasi et al. 2005), and assuming they were the rotating counterparts to $\ell = 0$ and 1 modes, they were able to constrain the mass to $1.86 \pm 0.03\,M_{\odot}$, and thence narrow down the other parameters as well, thus showing that Altair is close to the ZAMS. The theoretical mode visibilities were also shown to behave qualitatively in a manner similar to the observed amplitudes, as illustrated in Fig. 5.

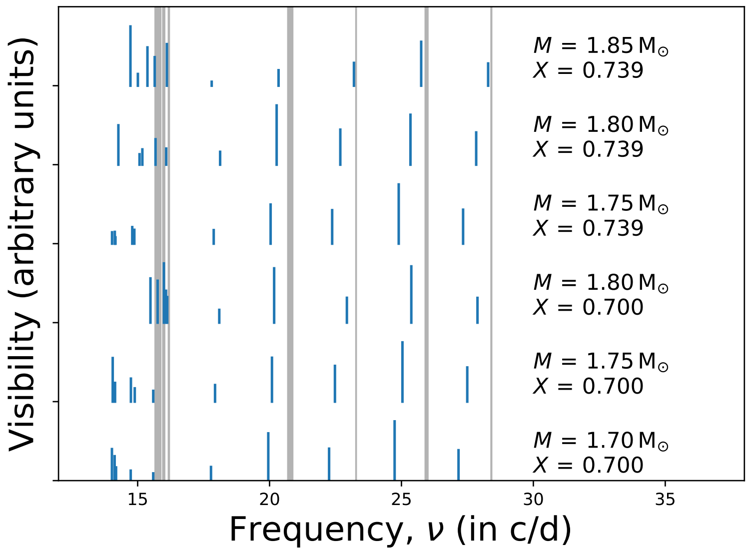

Fig. 5. A comparison between observed and theoretical pulsation spectra for Altair. The vertical grey lines correspond to observed pulsations; their thicknesses indicate the amplitudes. The blue segments correspond to theoretical modes from six ESTER models (1 per row). Their lengths correspond to mode visibilities. From Bouchaud et al. (submitted).

4 Conclusions

As can be seen, much progress has been made both in terms of theoretical developments for acoustic modes in rapidly rotating stars and in terms of interpreting observations. One can, for instance, cite the unexpected regularity in the pulsation spectra of chaotic modes, the discovery of frequency patterns in a number of δ Scuti stars, or the finding of plausible identifications for individual modes. This opens up various prospects, such as the possibility of constraining global stellar parameters for these stars, probing their internal rotation profiles, or providing insights into the different transport processes occurring in them as a result of rotation.

DRR gratefully acknowledges support of the French Agence Nationale de la Recherche (ANR) for the ESRR project under grant ANR-16-CE31-0007, and financial support from the Programme National de Physique Stellaire (PNPS) of the CNRS/INSU co-funded by the CEA and the CNES. DRR benefited from the hospitality of ISSI as part of the SoFAR team early in 2018 and 2019.

References

Bedding, T. R., Murphy, S. J., Hey, D. R., et al. 2020

Bouchaud, K., Domiciano de Souza, A., Rieutord, M., Reese, D. R., & Kervella, P. submitted, A&A

Bowman, D. M. & Kurtz, D. W. 2018, MNRAS, 476, 3169

Buzasi, D. L., Bruntt, H., Bedding, T. R., et al. 2005, ApJ, 619, 1072

Daszyńska-Daszkiewicz, J., Dziembowski, W. A., Pamyatnykh, A. A., & Goupil, M.-J. 2002, A&A, 392, 151

Deupree, R. G. 2011, ApJ, 742, 9

Deupree, R. G., Castañeda, D., Peña, F. o., & Short, C. I. 2012, ApJ, 753, 20

Espinosa Lara, F. & Rieutord, M. 2011, A&A, 533, A43

Espinosa Lara, F. & Rieutord, M. 2013, A&A, 552, A35

Evano, B., Georgeot, B., & Lignières, F. 2019a, EPL (Europhysics Letters), 125, 49002

Evano, B., Lignières, F., & Georgeot, B. 2019b, A&A, 631, A140

García Hernández, A., Martín-Ruiz, S., Monteiro, M. J. P. F. G., et al. 2015, ApJ Letter, 811, L29

García Hernández, A., Moya, A., Michel, E., et al. 2013, A&A, 559, A63

García Hernández, A., Suárez, J. C., Moya, A., et al. 2017, MNRAS, 471, L140

Jackson, S., MacGregor, K. B., & Skumanich, A. 2005, ApJS, 156, 245

Lagrange, A. M., Bonnefoy, M., Chauvin, G., et al. 2010, Science, 329, 57

Lignières, F. & Georgeot, B. 2008, Phys. Rev. E, 78, 016215

Lignières, F. & Georgeot, B. 2009, A&A, 500, 1173

Lignières, F., Rieutord, M., & Reese, D. 2006, A&A, 455, 607

MacGregor, K. B., Jackson, S., Skumanich, A., & Metcalfe, T. S. 2007, ApJ, 663, 560

Michel, E., Dupret, M.-A., Reese, D., et al. 2017, in EPJ Web of Conferences, Vol. 160, EPJ Web of Conferences, 03001

Mirouh, G. M., Angelou, G. C., Reese, D. R., & Costa, G. 2019, MNRAS, 483, L28

Mirouh, G. M., Reese, D. R., Rieutord, M., & Ballot, J. 2017, in SF2A-2017: Proceedings of the Annual meeting of the French Society of Astronomy and Astrophysics, Di

Monnier, J. D., Townsend, R. H. D., Che, X., et al. 2010, ApJ, 725, 1192

Paparó, M., Benkő, J. M., Hareter, M., & Guzik, J. A. 2016a, ApJ, 822, 100

Paparó, M., Benkő, J. M., Hareter, M., & Guzik, J. A. 2016b, ApJS, 224, 41

Paparó, M., Kolláth, Z., Shobbrook, R. R., et al. 2018, MNRAS, 477, 4362

Pasek, M., Georgeot, B., Lignières, F., & Reese, D. R. 2011, Physical Review Letters, 107, 121101

Pasek, M., Lignières, F., Georgeot, B., & Reese, D. R. 2012, A&A, 546, A11

Reese, D., Lignières, F., & Rieutord, M. 2006, A&A, 455, 621

Reese, D., Lignières, F., & Rieutord, M. 2008, A&A, 481, 449

Reese, D. R., Dupret, M.-A., & Rieutord, M. 2017a, in EPJ Web of Conferences, Vol. 160, EPJ Web of Conferences, 02007

Reese, D. R., Lignières, F., Ballot, J., et al. 2017b, A&A, 601, A130

Reese, D. R., MacGregor, K. B., Jackson, S., Skumanich, A., & Metcalfe, T. S. 2009, A&A, 506, 189

Reese, D. R., Mirouh, G. M., Espinosa Lara, F., Rieutord, M., & Putigny, B. submitted, A&A

Reese, D. R., Prat, V., Barban, C., van 't Veer-Menneret, C., & MacGregor, K. B. 2013, A&A, 550, A77

Rieutord, M., Espinosa Lara, F., & Putigny, B. 2016, Journal of Computational Physics, 318, 277

Royer, F. 2009, On the Rotation of A-Type Stars, Vol. 765 (Berlin: Springer), 207–230

Townsend, R. H. D. 2003, MNRAS, 343, 125

Zhao, M., Monnier, J. D., Pedretti, E., et al. 2009, ApJ, 701, 209

Zwintz, K., Reese, D. R., Neiner, C., et al. 2019, A&A, 627, A28

Stars and their variability observed from space
C. Neiner, W. W. Weiss, D. Baade, R. E. Griffin, C. C. Lovekin, A. F. J. Moffat (eds)

THE BRITE-SONG OF ALDEBARAN – STELLAR MUSIC IN THREE VOICES

P. G. Beck[1,2,3], R. Kuschnig[4], G. Houdek[5], T. Kallinger[6], W. W. Weiss[6], P. L. Palle[2,3], F. Grundahl[5], A. Hatzes[7], H. Parviainen[2,3], C. Allende Prieto[2,3], H. J. Deeg[2,3], A. Jiménez[2,3], S. Mathur[2,3], R. A. Garcia[8], T. R. White[5,9], T. R. Bedding[9,5], D. H. Grossmann[1], S. Janisch[1], T. Zaqarashvili[1], A. Hanslmeier[1], K. Zwintz[10] and the BRITE & SONG teams

Abstract. Solar-like oscillations in red-giant stars are now commonly detected in thousands of stars with space telescopes such as *Kepler.* Parallel radial-velocity and photometric measurements would help us understand better the physics governing the amplitudes of solar-like oscillators, but most stars targetted for space photometry are too faint for light-demanding ground-based spectroscopy. The *BRITE*-Constellation provides a unique opportunity of monitoring in two colours the flux variations of bright luminous red giants. Those stars are also bright enough to be monitored with high-resolution spectrographs on small telescopes, such as the *SONG* Network. This contribution provided a first overview of our comprehensive, multi-year campaign to use both *BRITE* and *SONG* to characterize Aldebaran (one of the brightest red giants in the sky) seismically. Because luminous red giants can be seen at large distances, when characterized well they will serve as valuable benchmark stars for Galactic archeology.

Keywords: stars: pulsation, evolution, individual: Aldebaran

1 Introduction

Space missions such as NASA's *Kepler* or *TESS* (Borucki et al. 2010; Ricker et al. 2015, respectively) have enabled the detection of solar-like oscillations in tens of thousands of main-sequence and red-giant stars (e.g. Hon et al. 2018; García & Ballot 2019; SilvaAguirre et al. 2019). While such satellites can provide ultra-precise monochromatic photometry, typical target stars are too faint for light-demanding ground-based complementary techniques. Simultaneous multi-colour photometry and parallel radial-velocity (RV) monitoring of solar-like oscillating stars would provide crucial information for understanding the physics governing the oscillations and their amplitudes. So far, the only solar-like oscillators for which such simultaneous data have been acquired and analysed are the Sun itself (Jiménez et al. 1999) and the mid-F sub-giant Procyon (Arentoft et al. 2008).

The 3-cm telescopes of the five *BRITE*-Constellation satellites (BRIght Target Explorer, Weiss et al. 2014), with their blue and red photometric filters, have enabled multi-colour space photometry of very bright targets since the launch of the the first pair in 2013. While the primary science case for BRITE satellites does not include solar-like oscillations on the main sequence, or evolved stars, it was shown by Kallinger et al. (2019) that red-giant stars with oscillation frequencies below 10 μHz ($R_\star > \sim 25 R_\odot$) exhibit oscillation amplitudes that are large enough to be detected by the *BRITE* satellites. Such targets are also accessible by spectrographs mounted on 1-m-class telescopes, such as SONG (Stellar Observations Network Group, Grundahl et al. 2017), which was designed for the acquisition of high-quality spectroscopic time-series for asteroseismology. The first telescope of that telescope network was commissioned in 2014 and is installed at the Teide observatory (Tenerife). It is

[1] Institute of Physics, University of Graz, NAWI Graz, Universitätsplatz 5/II, 8010 Graz, Austria
[2] Instituto de Astrofísica de Canarias, 38205 La Laguna, Tenerife, Spain
[3] Departamento de Astrofísica, Universidad de La Laguna, 38206 La Laguna, Tenerife, Spain
[4] Inst. of Communication Networks & Satellite Communications, Graz University of Technology, Infeldgasse 12, 8010 Graz, Austria
[5] Aarhus University, Department of Physics and Astronomy, Ny Munkegade 120, 8000 Aarhus C, Denmark
[6] Institut für Astrophysik der Universität Wien, Tärkenschanzstr. 17, 1180 Vienna, Austria
[7] Thüringen Landessternwarte Tautenburg, Sternwarte 5, D-07778 Tautenburg, Germany;
[8] AIM, CEA, CNRS, Université Paris-Saclay, Université Paris Diderot, Sorbonne Paris Cité, F-91191 Gif-sur-Yvette, France
[9] Sydney Institute for Astronomy (SIfA), School of Physics, University of Sydney, NSW 2006, Australia
[10] Institut fur Astro- und Teilchenphysik, Universität Innsbruck, Technikerstrasse 25, A-6020 Innsbruck, Austria

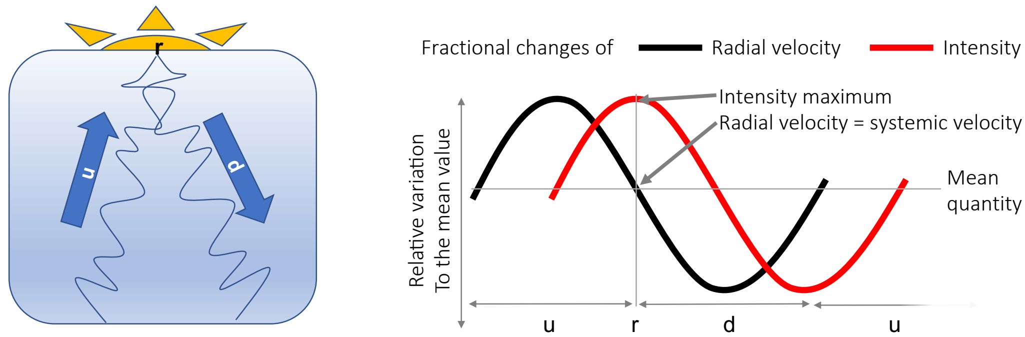

Fig. 1. Conceptual illustration of the behaviour of an oscillation mode near the surface of a star. **Left panel:** A wave coming from the interior (u) reaches regions of lower density and gets reflected back (r) into the deeper and denser layers again (d). **Right panel:** Two sine curves approximate the variations in radial velocity and intensity field (black and red, respectively). This sketch assumes ideal adiabatic conditions in the outer atmosphere, with the velocity field leading to an intensity variation shifted by 90^o.

equipped with a high-resolution spectrograph (with a resolving power of $77000 \leq \mathrm{R} \leq 112000$) and is capable of simultaneous wavelength calibration providing metre/sec RV precision.

This project is using a combination of multi-colour *BRITE* photometry and *SONG* spectroscopy to investigate solar-like oscillations in the luminous red-giant star Aldebaran (α Tau) wwhich has a visual brightness of $+0.9$ mag and a luminosity of $439 \pm 17\,\mathrm{L}_{\odot}$ (Heiter et al. 2015). Photometry obtained for Aldebaran by Farr et al. (2018) with *Kepler* shows intensity variations of $\sim$5.7days, corresponding to an oscillation frequency of $\sim 2\ \mu$Hz. They concluded that the star has a mass of $1.16 \pm 0.07\,\mathrm{M}_{\odot}$. Interferometric radii are also available (Richichi & Roccatagliata 2005), thus providing an opportunity to test seismic scaling relations for luminous RGBs, which are suspected to depart significantly from well-established seismic scaling relations (Yu et al. 2020). More technical details are provided in Section 3. More than three decades of RV measurements (Hatzes et al. 2015) have revealed the presence a quasi-periodic modulation with a period of $\sim$700 days, which is not reflected in the variation of the strength of the emission lines in the cores of the Ca II H & K lines, which are a classic activity indicator in cool stars. The authors suggested that this signal could originate from a planetary companion of 6 Jupiter masses, but also urged caution as the signal is not stable over decades as expected for a planet, and over-stable convection could serve as an alternative explanation. As is discussed further in Section 4, this candidate planet has been debated heavily in the literature.

2 Variations in the intensity *vs.* velocity field

When an oscillation mode reaches the near surface layers, it is reflected back to deeper, denser layers. Such modes at the surface lead to periodic distortions of the surface temperature and velocity field, described typically by the degree ℓ of the spherical harmonics (see Aerts et al. 2010, and references therein). The surface temperature variations lead to fractional variations of the stellar luminosity. Spectroscopy measures the surface field component along the line of sight. Oscillation modes therefore manifest themselves observationally as variations in the mean brightness and the systemic radial velocity of the star, respectively. At the point of reflection an oscillation mode exhibits its maximum brightness, as it is then least obscured by overlying layers. Coincidentally, the perturbation of the velocity field is changing its direction of propagation. The velocity field for a given mode therefore shows no perturbation and is equal to the systemic radial velocity of the star. As illustrated in Fig. 1, that leads to a phase shift of –90 deg in the ideal case.

The two parameters describing the differences between the velocity and intensity variations in Fourier space are (i) amplitude ratio and (ii) the phase difference. The quantities provide two important diagnostic constraints. The information contained in these parameters allows us to test stellar oscillation and atmospheric models beyond the possibilities of classic asteroseismology. Nevertheless, owing to the lack of appropriate simultaneous data, such studies have only been carried out for two solar-like oscillators.

As demonstrated by Houdek & Gough (2002) and Houdek (2010), a calibrated amplitude ratio between intensity and velocity variations provides strong constraints on the stellar atmosphere that are independent of the excitation model. While the RV amplitude is determined by the velocity fluctuations from oscillations and granulation along the line of sight, and therefore enables a direct comparison with models, the case of photometric variations remains challenging Kjeldsen & Bedding (2011). The intensity variations correspond primarily to the temperature fluctuations of the atmosphere over the whole oscillation cycle, but need to be

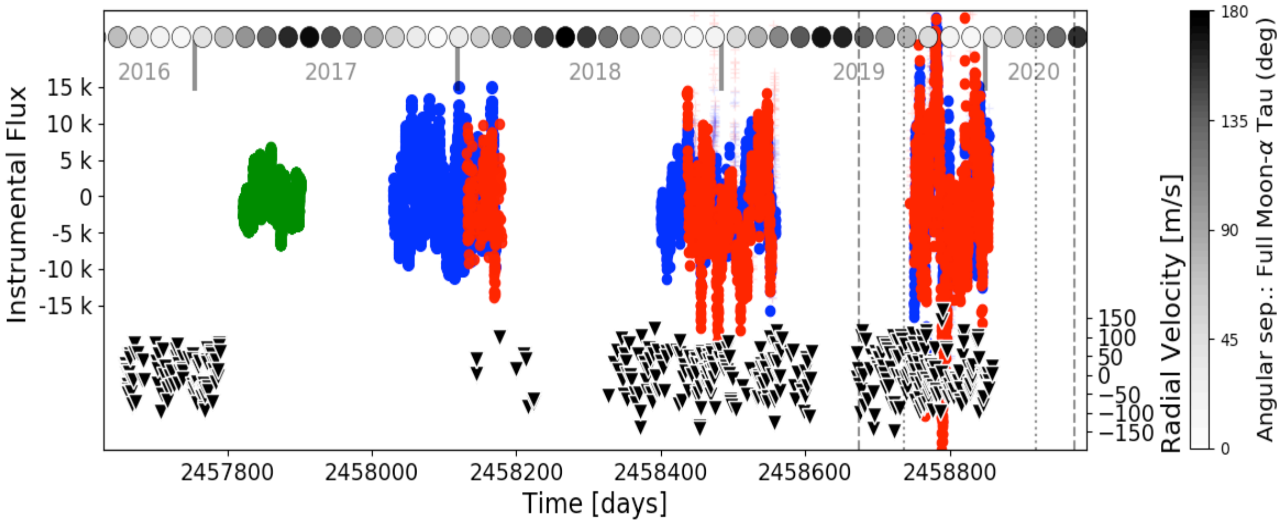

Fig. 2. Data from the ongoing observing campaign on Aldebaran. The red and blue points depict the mean orbital values of the photometric flux measured by *BRITE*/Lem (blue filter) and *BRITE*/Toronto (red filter), respectively. The 80 days of *K2* photometry (Farr et al. 2018) are shown in green. Radial velocities measured with SONG are depicted as black triangles; the long-period trend has been removed. The duration of the ongoing *SONG* and *BRITE* observations in the 2019/20 season are indicated by dashed and dotted lines, respectively. Years are noted at the top, and are juxtaposed with measures of the angular distance between the star and the Moon at the moment of full moon (indicated in the grey scale on the right). Owing to stray-light contamination, data points taken with the Moon closer than 35 degrees are shown as semi-transparent plusses.

translated into fractional changes of the bolometric luminosity. However, to compare observations and models, observational aspects such as the photometric passband and the colour-dependent quantum efficiency of the detector of the space telescope need to be taken into account. In that respect, simultaneous multi-colour photometry provides different measures of the same quantity and increases the robustness of the experiment.

The phase shift between oscillation modes seen in these two observables is a relevant parameter for constraining pulsation eigenfunctions and eventually models of stochastic excitation (Houdek 2010). Were the oscillations purely adiabatic, the RVs would be expected to lead the intensity variations with a phase shift of −90 deg when normalised by the oscillation period. The solar case has been found to be close to this value (Jiménez et al. 1999). Any departure from it reveals heat transfer between the stellar background and the oscillation modes (Christensen-Dalsgaard & Frandsen 1984; Jiménez et al. 1999), with a maximal lag of −180 deg in the isothermal case.

3 Experimental data: 2016–2020

The multi-technique campaign described in this contribution (see Fig. 2) was started in the visibility season 2017/18 of Aldebaran, with observations from *BRITE*/Lem, which is equipped with a blue photometric filter (λ 4000–4500 AA). At the end of the same observing season, Aldebaran was added to the observing programme of *BRITE*/Toronto, which is equipped with a red filter (λ 5000–7000 AA). Each data point shown in Fig. 2 represents the mean of all the individual measurements obtained during a satellite orbit; we discard orbits with less than 15 individual measurements. The orbital period of the *BRITE* satellites is about 90 minutes, resulting in 14–15 photometric measurements per day.

Towards the end of that season we also attempted simultaneous spectroscopic observations with *SONG*. The standard observing programme was comprised of 1 or 2 pointings a night, taking three consecutive spectra with a resolving power of 90,000 and an iodine cell for simultaneous wavelength calibration. However, unfortunately we experienced adverse weather conditions that were extreme in both intensity and duration for Tenerife.

Since observing season 2018/19, all three instruments have become well coordinated. A typical observing season with *BRITE* lasts for about 140 days (September–March), while *SONG* can obtain at least one set of spectra per night for about 300 consecutive days; That time series is only interrupted between May and July, though periodic gaps are introduced into the dataset by the Moon. Given the low ecliptic latitude of Aldebaran of about 5 deg, photometric observations are contaminated by, and eventually interrupted by, the full moon once every $\sim$28 days. Scattered light from the Moon is not an issue for spectroscopic observations.

The complete dataset of the ongoing campaign is depicted in Fig. 2. It also shows the complementary dataset of 80 days of *K2* photometry, obtained by Farr et al. (2018) using the photometric technique of Halo-photometry to counteract the effects of partial saturation White et al. (2017). In 2016 and prior to *K2* photometry, Farr et al. (2018) obtained 125 days of RV with *SONG*, which is also included in our analysis.

4 The controversy over the planet orbiting Aldebaran

The possibility of the presence of a planetary companion around Aldebaran was originally proposed by Hatzes et al. (2015), who interpreted the long-period trend present in the RV signal as a possible indication of a massive Jupiter-like planetary companion. However, they were cautious about declaring it firmly as a planet, as the RV signal was not as stable as would be expected from an exoplanet. They also considered an alternative possibility that the signal originated from overstable convection, which can occur under extreme non-adiabatic conditions in a stellar atmosphere (Saio et al. 2015).

Three years later (and parallel to the start of our campaign), numerous studies on Aldebaran or the nature of the long-period variations were published. First, Hatzes et al. (2018) showed that the RV in the luminous red giant γ Draconis initially exhibited a similar behaviour. However, the RV signals disappeared in 2013–16 and then reappeared with a phase-shift, so were not compatible with a planetary origin. The authors concluded that the finding also supported a non-planetary explanation for the long-period signal in Aldebaran. Farr et al. (2018), who presented a first seismic analysis based on *K2* photometry and *SONG* RVs, used their results to improve the parameters of the planetary companion. In addition, they argued that both Aldebaran b and γ Draconis b must be planets, stating that: *"it would be a cruel conspiracy of nature if red giants support a type of oscillation that is common and closely resembles a planetary signal. We believe this cannot be the case"*, (Farr et al. 2018, incipit of paragraph 3, Appendix D). Reichert et al. (2019) then presented an analysis of the stability of the dataset of Hatzes et al. (2015), complemented with their own spectroscopic observations from Lick Observatory. They tested a two-planet model, which reduced significantly the large RV scatter in the residuals, but found that such solution was very unlikely to be stable dynamically.

5 Current status of the analysis, conclusions & Outlook

The ongoing photometric and spectroscopic observations obtained by the *BRITE* satellites and the *SONG* telescope are building a unique, multi-year data set for studying amplitude and phase differences between velocity and intensity variations. Combining the RV from *SONG* with multi-colour space photometry from *BRITE* offers a rare possibility to characterise the outermost layers of luminous red giants and to provide crucial diagnostics to test the physics of the stellar atmosphere. Those parameters give access to layers in the star that are not well probed by normal oscillation modes. Luminous red giants like Aldebaran are of added interest in that they enable us to study the asteroseismic scaling relations and the stellar structure of objects with increasing departure from the adiabatic conditions in the atmosphere (Yu et al. 2020; Kallinger et al. 2018).

As is visible in Fig. 2, the observing project is still ongoing and the data we have shown for analysis are only preliminary. That affectsthe photometric amplitudes in particular We therefore refrain from quantifying the parameters discussed above.

The comparison of photometric and spectroscopic datasets shows clearly that the variation in RV is leading the variation in intensity. Visual inspection in the time domain suggests a phase difference which is much larger than the –90 degrees predicted in the adiabatic case. This is not surprising, but one needs to be cautious because the interference from granulation, which has amplitudes and periods comparabe to the oscillation signal of Aldebaran, could lead to an overestimated phase difference. The final value will therefore be determined from the frequency domain. However, the frequency resolution of a full season of *BRITE* observations is not sufficient to resolve individual oscillation modes.

The long-period modulations previously reported in the literature are also present in the *SONG* dataset. However, it is too early to arrive at concrete conclusions about their origin. The long time-base and the high sampling rate of the RV measurements will help us decide if those variations are caused by a planetary companion or by an unidentified physical process. We note that they are on different times-scales than were found for secondary clump stars of the Hyades and which were likely to originate from rotational modulation (Beck et al. 2015; Arentoft et al. 2019).

Constraining the origin of the signal is essential for disentangling actual planets around red giants from spurious detections due to intrinsic effects and activity. The observations reported clearly demonstrate that a firm detection of planets around red giants requires RV monitoring that extends over at least several decades.

Understanding benchmark stars like Aldebaran, γ Draconis or Arcturus is of high importance, since luminous red giants can also be seen at greater distances in the Milky Way (e.g. Mathur et al. 2016). Such stars can therefore serve as highly-needed probes for understanding extreme phases of stellar evolution, the distribution of exoplanets, and (eventually) the evolutionary history of our Galaxy.

The authors gratefully acknowledge the work of the *BRITE*-constellation and *SONG* science and technical teams. This work was based on data collected by the *BRITE* Constellation satellite mission, designed, built, launched, operated and supported by the Austrian Research Promotion Agency (FFG), the University of Vienna, the Technical University of Graz, the University of Innsbruck, the Canadian Space Agency (CSA), the University of Toronto Institute for Aerospace Studies (UTIAS), the Foundation for Polish Science & Technology (FNiTP MNiSW), and National Science Centre (NCN). We would like to acknowledge the Villum Foundation, The Danish Council for Independent Research – Natural Science, and the Carlsberg Foundation for support to build the *SONG* prototype on Tenerife. We thank the SOC/LOC of the *"Stars and their Variability"* conference for organizing an inspiring meeting.

References

Aerts, C., Christensen-Dalsgaard, J., & Kurtz, D. W. 2010, Asteroseismology (Springer)
Arentoft, T., Grundahl, F., White, T. R., et al. 2019, A&A, 622, A190
Arentoft, T., Kjeldsen, H., Bedding, T. R., et al. 2008, ApJ, 687, 1180
Beck, P. G., Kambe, E., Hillen, M., et al. 2015, A&A, 573, A138
Borucki, W. J., Koch, D., Basri, G., et al. 2010, Science, 327, 977
Christensen-Dalsgaard, J. & Frandsen, S. 1984, Mem. Soc. Astron. Italiana, 55, 285
Farr, W. M., Pope, B. J. S., Davies, G. R., et al. 2018, ApJ, 865, L20
García, R. A. & Ballot, J. 2019, Living Reviews in Solar Physics, 16, 4
Grundahl, F., Fredslund Andersen, M., Christensen-Dalsgaard, J., et al. 2017, ApJ, 836, 142
Hatzes, A. P., Cochran, W. D., Endl, M., et al. 2015, A&A, 580, A31
Hatzes, A. P., Endl, M., Cochran, W. D., et al. 2018, AJ, 155, 120
Heiter, U., Jofré, P., Gustafsson, B., et al. 2015, A&A, 582, A49
Hon, M., Stello, D., & Yu, J. 2018, MNRAS, 476, 3233
Houdek, G. 2010, Ap&SS, 328, 237
Houdek, G. & Gough, D. O. 2002, MNRAS, 336, L65
Jiménez, A., Roca Cortés, T., Severino, G., & Marmolino, C. 1999, ApJ, 525, 1042
Kallinger, T., Beck, P. G., Hekker, S., et al. 2019, A&A, 624, A35
Kallinger, T., Beck, P. G., Stello, D., & Garcia, R. A. 2018, A&A, 616, A104
Kjeldsen, H. & Bedding, T. R. 2011, A&A, 529, L8
Mathur, S., García, R. A., Huber, D., et al. 2016, ApJ, 827, 50
Reichert, K., Reffert, S., Stock, S., Trifonov, T., & Quirrenbach, A. 2019, A&A, 625, A22
Richichi, A. & Roccatagliata, V. 2005, A&A, 433, 305
Ricker, G. R., Winn, J. N., Vanderspek, R., et al. 2015, JATIS, 1, 014003
Saio, H., Wood, P. R., Takayama, M., & Ita, Y. 2015, MNRAS, 452, 3863
SilvaAguirre, V., Stello, D., Stokholm, A., et al. 2019, arXiv e-prints, arXiv:1912.07604
Weiss, W. W., Rucinski, S. M., Moffat, A. F. J., et al. 2014, PASP, 126, 573
White, T. R., Pope, B. J. S., Antoci, V., et al. 2017, MNRAS, 471, 2882
Yu, J., Bedding, T. R., Stello, D., et al. 2020, MNRAS (subm.)

THE COMPLEX ASTEROSEISMOLOGY OF SX PHOENICIS

J. Daszyńska-Daszkiewicz[1], P. Walczak[1], A. Pamyatnykh[2], W. Szewczuk[1] and W. Dziembowski[2]

Abstract. This paper presented a seismic analysis of the prototype SX Phoenicis, and was aimed at fitting the two radial-mode frequencies and the corresponding values of the bolometric flux amplitude (the parameter f), whose empirical values were derived from multi-coulor photometric observations. A seismic model that meets those conditions is of low mass ($M = 1.05 M_{\odot}$), has moderately effective convection in the outer layers and described by the mixing-length parameter $\alpha_{\rm MLT} \approx 0.7$, and a microturbulent velocity in the atmospheres of about $\xi_{\rm t} \approx 8$ km s^{-1}. These seismic studies of a star like SX Phe are very important for deriving constraints on outer-layer convection because the object is borderline between very effective and ineffective convection.

Keywords: Stars: evolution, atmospheres, asteroseismology, convection

1 Introduction

SX Phoenicis (HD 223065) is A3-type star of Population II discovered to be variable almost seven decades ago by Eggen (1952a,b). This is a prototype for the whole class of high-amplitude and usually metal-poor pulsators located inside the δ Scuti instability region. SX Phe was a target of several studies based on photometric and spectroscopic observations. Analyses of photometric data revealed two frequencies and their combinations (e.g., by Coates et al. 1979; Rolland et al. 1991; Garrido & Rodriguez 1996). The frequency ratio indicated that SX Phe pulsates in two radial modes: fundamental and first overtone ones. These two periodicities are also present in the radial-velocity variations (Kim et al. 1993). Interestingly, the recent analysis of high-precision data from *TESS* confirmed the former results that these two frequencies alone dominate the light-curve of SX Phe (Antoci et al. 2019). The frequencies extracted from the *TESS* light-curve were $\nu_1 = 18.193565(6)$ d^{-1} and $\nu_2 = 23.37928(2)$ d^{-1}.

There was also some evidence that both pulsation periods change on a time-scale of decades (Landes et al. 2007). Moreover, for the dominant pulsational period the effective temperature varies in a huge range (7210–8120 K) and the surface gravity from 3.63–4.23. The corresponding mean values are 7640 K and 3.89 (Kim et al. 1993). A recent determination of the effective temperature from spectroscopy gives $T_{\rm eff} = 7500 \pm 150$ K and the luminosity derived from the Gaia DR2 data is $\log L/L_{\odot} = 0.844 \pm 0.009$ (Antoci et al. 2019). The metallicity of SX Phe is low, and amounts to about [Fe/H] = –1.4 (McNamara 1997).

SX Phe has been also a subject of seismic modelling. In the first attempts, Dziembowski & Kozłowski (1974) derived a small mass of about $0.2\,M_{\odot}$. However, modelling by Petersen & Christensen-Dalsgaard (1996) with the recomputed OPAL opacity data (Iglesias et al. 1992) showed that the period ratio of the two radial modes is best reproduced by a model with parameters mass $M = 1.0 M_{\odot}$, metallicity $Z = 0.001$, initial hydrogen abundance $X_0 = 0.70$ and age = 4.07 Gyr.

The aim of this paper is to repeat the seismic modelling of SX Phe and to extend it by employing the bolometric flux amplitude (the parameter f), which is very sensitive to physical conditions in sub-photospheric layers.

2 Fitting models to the two radial-mode frequencies

Using the Warsaw–New Jersey evolutionary code (e.g., Pamyatnykh et al. 1998; Pamyatnykh 1999) and a non-adiabatic pulsational code (Dziembowski 1977), we computed models of SX Phe with the specific aim of fitting ν_1 and ν_2 as the radial fundamental and first overtone modes, respectively. Part of these results have been already published in Antoci et al. (2019).

[1] Astronomical Institute, Wrocław University, ul. Kopernika 11, 51–622 Wrocław, Poland
[2] Nicolaus Copernicus Astronomical Center, Polish Academy of Sciences, Bartycka 18, 00–716 Warsaw, Poland

We searched the whole range of effective temperatures for SX Phe reported in the literature, i.e., from about 7000–9000 K. The OPAL opacity tables and the solar abundance mixture of Asplund et al. (2009) were adopted. We considered different values of metallicity (Z) and initial hydrogen abundance (X_0), from the range (0.0005, 0.003) and (0.66, 0.74), respectively. Different values of the mixing-length padrameter were investigated: $\alpha_{\mathrm{MLT}} \in (0,\ 2.5)$; overshooting from the convective core was not included. At such low metallicity and effective temperatures $T_{\mathrm{eff}} > 7000\,\mathrm{K}$, the effect of α_{MLT} on mode frequencies would be negligible, but it strongly affects the values of the parameter f, as discussed in the next section.

We started by re-calculating the seismic model of Petersen & Christensen-Dalsgaard (1996), which had constraints of mass $M = 1.0\ M_{\odot}$, metallicity $Z = 0.001$ and initial hydrogen $X_0 = 0.70$. Our best seismic model with those parameters had an effective temperature $\log T_{\mathrm{eff}} = 3.88427$, luminosity $\log L/L_{\odot} = 0.811$, and a frequency ratio (of the radial fundamental mode to the first overtone) of $\nu_1/\nu_2 = 0.780014$. The observed counterpart was 0.778192. The theoretical values of the frequencies were $\nu_1 = 18.193565\ \mathrm{d}^{-1}$ (the model was interpolated at that frequency) and $\nu_2 = 23.324654\ \mathrm{d}^{-1}$. Both radial modes in this model were excited. However, as one can see, the difference between the theoretical and observed value of ν_1/ν_2 is significant, and amounted to 0.001822. The age given by the model was about 3.93 Gyr, which is slightly less than for the model of Petersen & Christensen-Dalsgaard (1996), who obtained about 4.07 Gyr, and may result from different versions of the OPAL opacity tables and from using slightly differentr evolutionary and pulsational codes.

The next step was to change the value of the metallicity, and we found that the model for $Z = 0.0014$ with a mass $M = 1.15\ M_{\odot}$ fitted the observed frequency ratio better. It had the following parameters: $\log T_{\mathrm{eff}} = 3.91770$, luminosity $\log L/L_{\odot} = 0.984$, and a frequency ratio of $\nu_1/\nu_2 = 0.778412$; individual frequencies were $\nu_1 = 18.193565\ \mathrm{d}^{-1}$ and $\nu_2 = 23.372681\ \mathrm{d}^{-1}$. It was also much younger than the previous model we derived, having an age of about 2.45 Gyr. The fundamental and first overtone radial modes were both stable. Increasing the metallicity slightly, to $Z = 0.002$, enabled us to find a model with a mass of $M = 1.05\ M_{\odot}$, $\log T_{\mathrm{eff}} = 3.87152$, $\log L/L_{\odot} = 0.770$, and a frequency ratio matching the two radial modes considered: $\nu_1/\nu_2 = 0.778073$. This models was about 3.42 Gyr old; both radial fundamental and first overtone modes were excited. As we could see, the models with a higher metallicity gave much better fit to the frequencies, but there was still room for improvement, so in the next step we changed the initial abundance of hydrogen.

We managed to find a model that reproduced the observed frequency ratio up to the fifth place of decimals (which we adopted as the numerical accuracy). It had the following parameters: $M = 1.05\ M_{\odot}$, $X_0 = 0.67$, $Z = 0.002$, $\log T_{\mathrm{eff}} = 3.88979$, $\log L/L_{\odot} = 0.844$; it was interpolated at the dominant frequency $\nu_1 = 18.193565\ \mathrm{d}^{-1}$. The value of the second frequency was $\nu_2 = 23.379761\ \mathrm{d}^{-1}$, which differed by $0.00048\ \mathrm{d}^{-1}$ from the observed value. The theoretical value of the frequency ratio was therefore 0.778176, compared to the observed value 0.778192. Taking into account the numerical accuracy, which was not better than five decimal places, we could conclude that this model reproduced perfectly the observed frequencies of the two radial modes of SX Phe. Moreover, it predicted instability (excitation) of both the radial fundamental and the first overtone modes. It gave an age of about 2.85 Gyr. Another advantage of the model was the fact that it had a luminosity which agreed with the value derived from the *Gaia* DR2 data.

The lower hydrogen abundance (higher helium abundance) was also quite probable because, like other SX Phoenicis variables, SX Phe itself can be a blue straggler. Such objects are presumably formed by the merger of two stars, or by interactions in a binary system and as a consequence they may have enhanced helium abundances (e.g., McNamara 2011; Nemec et al. 2017).

The left panel of Fig. 1 shows the evolution of the frequency ratio as a function of the dominant frequency (the "Petersen diagram") for the 4 best seismic models that we derived. The observed value is marked as a solid square. The right panel of Fig. 1 depicts the corresponding evolutionary tracks on the H–R diagram and the position of SX Phe.

3 Complex seismic modeling

The next step was to extend the seismic analysis by including the parameter which describes the relative amplitude of the radiative flux perturbations at the photosphere level. This amplitude is the so-called nonadiabatic parameter f, defined by:

$$\frac{\delta \mathcal{F}_{\mathrm{bol}}}{\mathcal{F}_{\mathrm{bol}}} = \mathrm{Re}\{\varepsilon f Y_\ell^m(\theta, \varphi) \mathrm{e}^{-\mathrm{i}\omega t}\}, \tag{3.1}$$

where $\mathcal{F}_{\mathrm{bol}}$ is the bolometric flux, ε is the mode intrinsic amplitude, Y_ℓ^m is the spherical harmonic with degree ℓ and azimuthal order m. Other quantities have their usual meanings. The value of f is complex and is associated with a given mode. The theoretical values of f are very sensitive to the subphotospheric layers from which

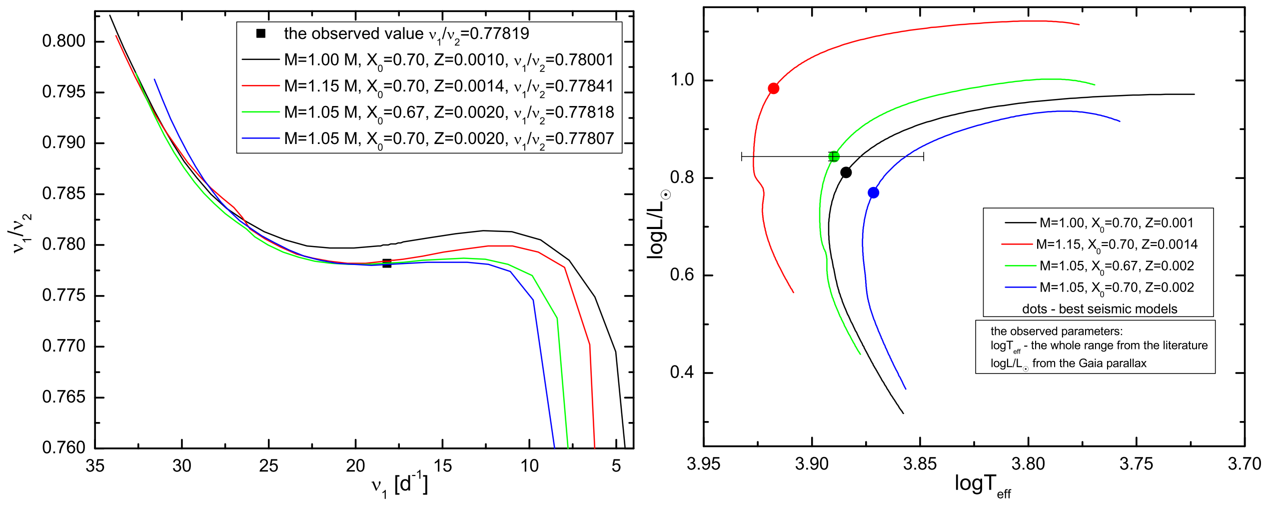

Fig. 1. Left: Petersen diagram for the 4 best seismic models suitable for SX Phoenicis. The solid square marks the observed value. The theoretical values of ν_1/ν_2 are given in the legend along with the mass and chemical composition (X, Z). **Right:** Corresponding evolutionary tracks of the seismic models with the observed position of SX Phe.

pulsation is driven. In the case of B-type pulsators, these values depend mainly on the adopted opacity data and their modifications around the Z-bump (Daszyńska-Daszkiewicz et al. 2005a). In the case of cooler pulsators like δ Scuti or SX Phoenicis stars, the values of f are affected by convection in the envelope (Daszyńska-Daszkiewicz et al. 2003).

One aim of this paper was to obtain some constraints on the efficiency of convective transport in the outer layers of SX Phe. Semi-empirical values of f can be derived from multi-colour light variations and radial-velocity measurements (e.g., Daszyńska-Daszkiewicz et al. 2003, 2005a). To that end, we used the Strömgren amplitudes and phases for the two radial mode frequencies as determined by Rolland et al. (1991). The atmospheric flux derivatives over the effective temperature and gravity and also limb darkening were derived from the Vienna model atmospheres (NEMO, see, e.g., Nendwich et al. 2004).

Fig. 2 compares the theoretical and empirical values of f for our best seismic model (its parameters were $M = 1.05\ M_\odot$, $\log T_{\rm eff} = 3.889793$, $\log L/L_\odot = 0.84375$ and $X_0 = 0.67$ and $Z = 0.002$). The theoretical values were computed for different values of the mixing-length parameter $\alpha_{\rm MLT}$, and their empirical counterparts for different values of the microturbulent velocity, ξ_t. The left panel shows the results for the dominant frequency ν_1 (the radial fundamental mode), and the right panel for the frequency ν_2 (the first overtone radial mode).

In the case of the frequency, ν_1, there is a fairly good agreement with an MLT parameter $\alpha_{\rm MLT} \approx 0.7$ and a microturbulent velocity of $\xi_{\rm t} \approx 8$ km s^{-1}. The results for the second mode frequency, ν_2, are less unambiguous. While the imaginary part of f suggests a lower value for the MLT parameter ($\alpha_{\rm MLT} < 1.5$), the real part of it does not agree with any theoretical value. that can result from a much smaller light amplitude of ν_2, which is determined with much lower accuracy. For example, the amplitude in the Strömgren v filter is almost three times lower for ν_2 than for ν_1.

4 Conclusions

We carried out a seismic analysis of the prototype star SX Phoenicis. We started by fitting the two radial mode frequencies and constrained the mass, luminosity and chemical composition. Our best seismic model to reproduce those two frequencies has the parameters $M = 1.05\ M_\odot$, $\log T_{\rm eff} = 3.889793$, $\log L/L_\odot = 0.84375$, and a chemical composition of $X_0 = 0.67$ and $Z = 0.002$. The effective temperature was within the allowed observational range, and the luminosity agreed completely with the determination from *Gaia* DR2 data. The ages of the other seismic models which we generated were in the range 2.5–3.9 Gyr. Further studies are needed to determine the age more accurately, because it would give a clue to the star's evolutionary past and its origin.

In the next step we tried to reproduce the bolometric flux amplitude f corresponding to each mode. The aim was to get further constraints on (e.g.) convection and atmospheric conditions. The (semi)empirical values of f were derived from the Strömgren amplitudes and phases, by adopting the Vienna model atmospheres. We found that the microturbulent velocity, ξ_t, had a very strong effect on the empirical values of f; that had already

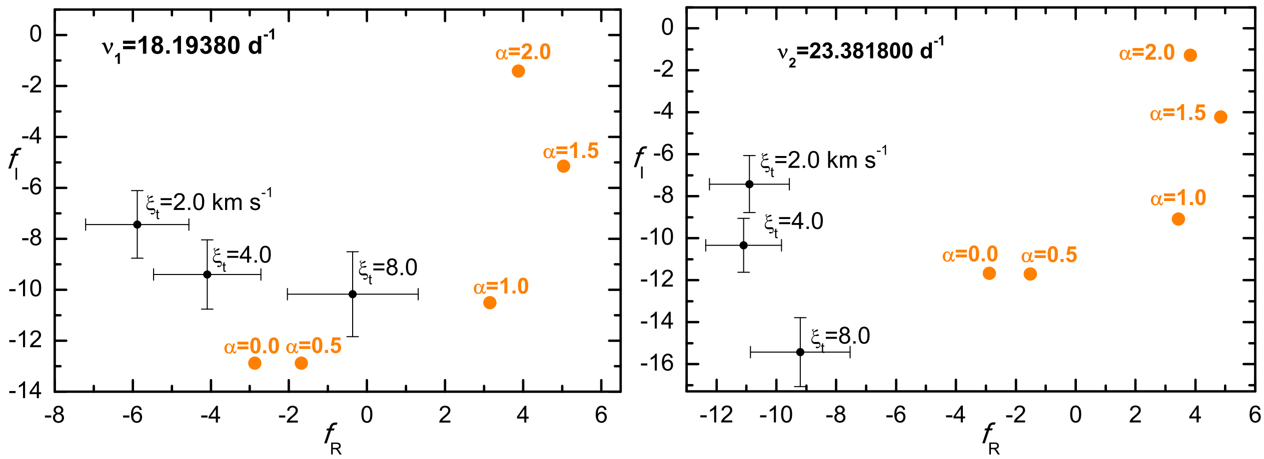

Fig. 2. Comparison of the theoretical and empirical values of f on the complex plane, for the radial fundamental mode (**left panel**) and for the first overtone mode (**right panel**). The theoretical values were computed for our best seismic model (see text) by considering different values of the mixing-length parameter $\alpha_{\rm MLT}$. Their (semi)empirical counterparts were determined from the Strömgren photometry and the Vienna model atmospheres assuming different values of the microturbulent velocity ξ_t.

been announced by Daszyńska-Daszkiewicz et al. (2005b) and Daszyńska-Daszkiewicz (2007). In the case of the fundamental radial mode, the empirical and theoretical values of f agreed if the MLT parameter was about $\alpha_{\rm MLT} = 0.7$ and the microturbulent velocities in the atmospheres were about $\xi_t = 8$ km s^{-1}. It would mean that the efficiency of convective transport in the outer layers of SX Phe is rather moderate. In the case of the first overtone mode the agreement was poor, and further studies are needed. It might have resulted from some interaction between the two modes, or a need of additional modification in pulsational and/or atmospheric modellinig. Another reason could be that smaller photometric amplitudes are determined with much lower accuracy.

We plan to extend these studies by re-computing atmospheric models for a higher helium abundance and higher microturbulent velocities. The effects of modifying the mean opacities will also be examined.

New simultaneous multi-colour photometric and spectroscopic time-series observations would definitely lead to more plausible seismic constraints on the parameters of the model and the theory.

The research was supported financially by the Polish NCN grant 2018/29/B/ST9/02803.

References

Antoci, V., Cunha, M. S., Bowman, D. M., & et al. 2019, MNRAS, 490, 4040
Asplund, M., Grevesse, N., Sauval, A. J., & Scott, P. 2009, ARA&A, 47, 481
Coates, D. W., Dale, M., Halprin, L., & et al. 1979, MNRAS, 187, 83
Daszyńska-Daszkiewicz, J. 2007, Comm. in Asteroseismology, 150, 32
Daszyńska-Daszkiewicz, J., Dziembowski, W. A., & Pamyatnykh, A. A. 2003, A&A, 407, 999
Daszyńska-Daszkiewicz, J., Dziembowski, W. A., & Pamyatnykh, A. A. 2005a, A&A, 441, 641
Daszyńska-Daszkiewicz, J., Dziembowski, W. A., Pamyatnykh, A. A., & et al. 2005b, A&A, 438, 653
Dziembowski, W. & Kozłowski, M. 1974, Acta Astr., 24, 245
Dziembowski, W. A. 1977, Acta Astr., 27, 95
Eggen, O. J. 1952a, PASP, 64, 31
Eggen, O. J. 1952b, PASP, 64, 305
Garrido, R. & Rodriguez, E. 1996, MNRAS, 281, 696
Iglesias, C. A., Rogers, F. J., & Wilson, B. G. 1992, ApJ, 397, 717
Kim, C., McNamara, D. H., & Christensen, C. G. 1993, AJ, 106, 2493
Landes, H., Bambery, K. R., Coates, D. W., & et al. 2007, PASAustral., 24, 41
McNamara, D. H. 1997, PASP, 109, 1221
McNamara, D. H. 2011, AJ, 142, 110

Nemec, J. M., Balona, L. A., Murphy, S. J., & et al. 2017, MNRAS, 466, 1290
Nendwich, J., Heiter, U., Kupka, F., & et al. 2004, Comm. in Asteroseismology, 144, 43
Pamyatnykh, A. A. 1999, Acta Astr., 49, 119
Pamyatnykh, A. A., Dziembowski, W. A., Handler, G., & et al. 1998, A&A, 333, 141
Petersen, J. O. & Christensen-Dalsgaard, J. 1996, A&A, 312, 463
Rolland, A., Rodriguez, E., Lopez de Coca, P., & et al. 1991, A&A Suppl., 91, 347

Stars and their variability observed from space
C. Neiner, W. W. Weiss, D. Baade, R. E. Griffin, C. C. Lovekin, A. F. J. Moffat (eds)

MODELLING LONG-PERIOD VARIABLES IN THE GAIA ERA

M. Trabucchi[1], T. Lebzelter[2], N. Mowlavi[3], P. R. Wood[4], P. Marigo[1], G. Pastorelli[1] and I. Lecoeur-Taïbi[3]

Abstract. Luminous red giant stars exhibit variability due to stellar pulsation, that is interconnected with uncertain processes (convection, mass loss and dust formation) and results in observable features that are strongly related to stellar properties. These so-called long-period variables (LPVs) provide us with a powerful tool to infer global stellar parameters and constrain the physics of late evolutionary phases in intermediate- and old-age stellar populations. Moreover, their period-luminosity relations represent a highly promising distance indicator. Large-scale optical microlensing surveys carried out during the last few decades made ideal laboratories out of the Magellanic Clouds to investigate the ensemble properties of LPVs with low impact from distance and interstellar extinction. Building on those results, the second data release (DR2) from the *Gaia* mission is providing new insight on these objects and novel methods to exploit them in the study of the evolution of stars and stellar populations. These results, together with related developments, are summarized here.

Keywords: Stars: AGB and post-AGB, Stars: oscillations, Galaxies: Magellanic Clouds

1 Introduction

After the pioneering discovery of the multiple period-luminosity (PL) relations of LPVs, achieved by Wood et al. (1999) with data from the MACHO survey, the most important observational source of information for the study of bright, pulsating red giants has been the still-operating Optical Gravitational Microlensing Experiment (OGLE). With about eight years of observations, the extensive catalogs of LPVs from the OGLE-III data releases (Soszyński et al. 2009, 2011) allows us to study these objects to an unprecedented level of detail, mainly focusing on the Magellanic Clouds to effectively remove biases related to distance and interstellar reddening. Among the most important outcomes it is worth mentioning the discoveries of an additional PL relation at short periods (sequence A′ in Fig. 1, according to the nomenclature used by Wood (2015)) and of the fine structure of PL sequences, as well as the identification of a potential new variability sub-type labelled OSARG (OGLE Small Amplitude Red Giants Wray et al. 2004).

Two relevant features that made such an important source of the OGLE-III data sets are the high photometric sensitivity (to identify LPVs with amplitudes as small as a few milli-mags) and the inclusion of multi-periodicity information. In comparison, the *Gaia* DR2 catalog of LPV candidates (Mowlavi et al. 2018) provides a single period per star, limited to amplitudes larger than 0.2 mag in the *Gaia G* band. While improvement with respect to these aspects is expected from the upcoming data releases, *Gaia* is already enabling new science in the context of LPVs. This is clearly due to its full-sky coverage (Fig. 1, right panel), as well as its providing access to the variability of optically bright asymptotic giant branch (AGB) and red supergiant (RSG) stars that suffer from saturation in OGLE.

2 The Gaia-2MASS diagram

Using *Gaia* DR2 data together with 2MASS near-infrared (NIR) photometry for stars in the Large Magellanic Cloud (LMC), Lebzelter et al. (2018) constructed a diagram in which LPVs occupy different regions according to their initial mass and surface chemistry. This "*Gaia*-2MASS diagram" shows the K_s magnitude versus

[1] Department of Physics and Astronomy, University of Padova, Vicolo dell'Osservatorio 3, I-35122 Padova, Italy
[2] University of Vienna, Department of Astrophysics, Tuerkenschanzstrasse 17, A1180 Vienna, Austria
[3] Department of Astronomy, University of Geneva, Ch. des Maillettes 51, CH-1290 Versoix, Switzerland
[4] Research School of Astronomy and Astrophysics, Australian National University, Canberra, ACT 2611, Australia

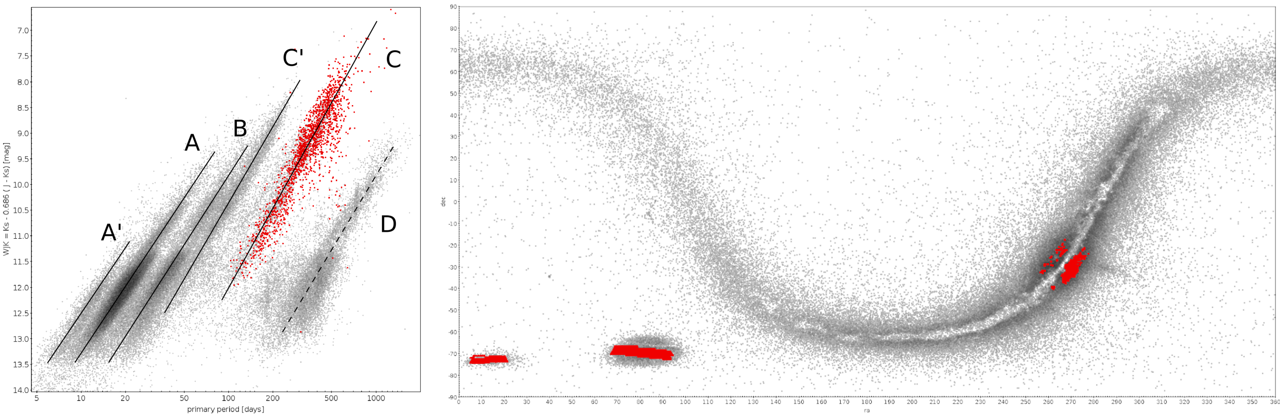

Fig. 1. Left: period-luminosity diagram of LPVs in the LMC as a function of the 2MASS K_{s} band. Red symbols are Mira variables identified by their variability amplitude larger than 0.8 mag in the I band. **Right:** sky coverage comparison between the OGLE-III catalogues of LPVs and the *Gaia* DR2 catalog of LPV candidates.

the difference between the Wesenheit indices obtained from 2MASS [$W_{\mathrm{J,K_s}} = K_{\mathrm{s}} - 0.686(J - K_{\mathrm{s}})$] and *Gaia* [$W_{\mathrm{BP,RP}} = G_{\mathrm{RP}} - 1.3(G_{\mathrm{BP}} - G_{\mathrm{RP}})$] photometry (Fig. 2, left panel).

Carbon-rich stars lie in the right side of the diagram, while the left side is populated by O-rich LPVs, a result confirmed by a classification based on low-resolution *Gaia* spectra*, as well as with the guide of state-of-the art stellar evolution models (Marigo et al. 2017). This dichotomy is due to the increased molecular abundance (and associated absorption) with decreasing surface temperature, combined with the different spectral ranges affected by oxygen-bearing molecules with respect to carbon-based ones. In contrast with ordinary colour-magnitude diagrams (CMDs), in which cool stars reside in the right (red) side of the diagram, LPVs move towards either side of the *Gaia*-2MASS diagram as they cool down, depending on their surface chemistry.

A convenient side effect of this splitting is the formation of a "gap" in the O-rich star distribution at $K_{\mathrm{s}} \sim 10$ mag, the brightness level corresponding to the initial mass range associated with the formation of C-stars (roughly 1.5 to 3.0 $\mathrm{M}_{\odot}$). In combination with the fact that the brightest, most massive O-rich stars are also relatively warm and unaffected by molecular formation, thus remaining in the central part of the diagram, this effect results in a splitting of O-rich stars into three branches, according their initial mass.

3 Application to the period-luminosity diagram

Building on the potential of the *Gaia*-2MASS diagram, Lebzelter et al. (2019) investigated the location of these different groups of LPVs in the PL diagrams (PLDs) obtained with different luminosity indicators, namely the K_{s} magnitude and the two Wesenheit indices $W_{\mathrm{J,K_s}}$ and $W_{\mathrm{BP,RP}}$ (Fig. 2, right panel), and extended the analysis to the Small Magellanic Cloud (SMC), finding consistent results. Thanks to the inclusion of a larger sample of bright O-rich LPVs with respect to the OGLE-III catalog, they were able to identify a systematic shift of these massive objects towards the left side of the corresponding K_{s}-log(P) PL relation, confirming the theoretical predictions of Wood (2015).

The same effect is found using $W_{\mathrm{J,K_s}}$, but no such displacement is observed with $W_{\mathrm{BP,RP}}$. This difference is due to the fact that the more massive stars are also warmer, and less affected by molecular absorption. As far as O-rich stars are concerned, the colour term involved in the $W_{\mathrm{J,K_s}}$ index is effectively insensitive to temperature. Hence the similarity between the K_{s}-log(P) and $W_{\mathrm{J,K_s}}$-log(P) diagrams. In contrast, both the magnitude and colour used in $W_{\mathrm{BP,RP}}$ are temperature-dependent, but the colour term is slightly more sensitive: at fixed mass, a cooler star is actually brighter in $W_{\mathrm{BP,RP}}$ than a hotter one.

Incidentally, this trend compensates almost exactly for the mass-related shift seen using NIR photometry. As a result, the $W_{\mathrm{BP,RP}}$-log(P) PL relation of LPVs, including the brightest objects up to $M_{K_{\mathrm{s}}} \sim -11.5$ mag, is considerably narrow and better defined than with IR photometry. These features represent a likely advantage in the promising application as distance indicator. However, due to this "compensation", the most massive LPVs (including RSGs), that lie on sequence C′ in the NIR PLDs, are actually found on sequence C in the $W_{\mathrm{BP,RP}}$-

* *Gaia* Image of the Week, 15/11/2018 (cosmos.esa.int/web/gaia/iow_20181115).

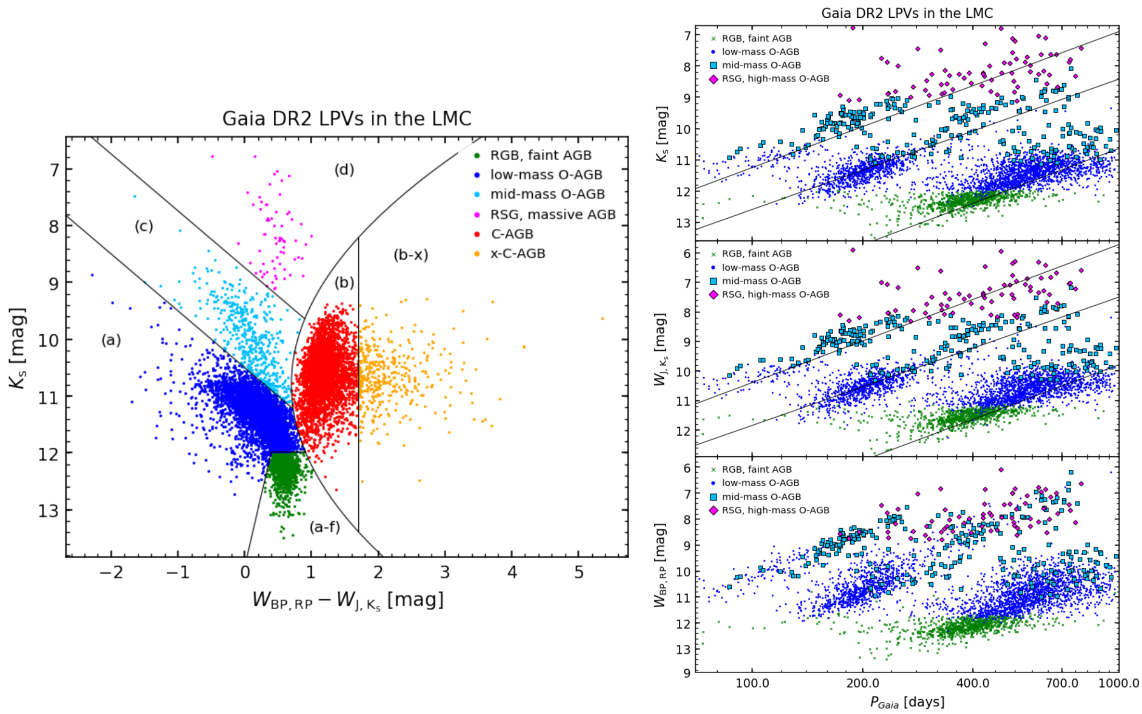

Fig. 2. Left: LMC stars from the *Gaia* DR2 catalog of LPV candidates in the *Gaia*-2MASS diagram, with the corresponding photometric classification of stars with different surface chemistry and initial mass range. **Right:** the same sample, limited to stars classified as O-rich, in the K_s, W_{J,K_s}, and $W_{BP,RP}$ PLDs. (Adapted from Lebzelter et al. (2019).)

$\log(P)$ PLD. This clearly complicates the use of the PL relations to identify the pulsation modes responsible for the observed periods.

4 The role of pulsation

Given the important role played by pulsation in the mass-loss and dust-formation processes that terminate the AGB evolution, contributing significantly to the chemical enrichment of the interstellar medium, a better understanding of LPVs is definitely crucial. This is true not only for individual stars, but also for their collective properties. Recently, McDonald & Trabucchi (2019) have pointed out the connection between an increased mass-loss rate and the transition of a star between sequences B and C′ in the PLD, which Trabucchi et al. (2017) had previously linked with the unexplained long-secondary periods (LSPs) on sequence D (see Fig. 1).

The detailed analysis made possible by the *Gaia* DR2 suggests that future data releases, as well as planned ground- and space-based surveys (such as the Large Synoptic Survey Telescope and the James Webb Space Telescope) will revolutionize the way we investigate LPVs and their PL relations. A proper modelling framework will be necessary to exploit the full potential of such an upcoming wealth of data. Recently, Trabucchi et al. (2017) (see also Trabucchi et al. (2019)) have shown how the combination of pulsation models with stellar population synthesis tools is able to take up this challenge, but also pointed out some of the main shortcomings of current pulsation models of LPVs, that systematically overestimate the fundamental mode period of the brightest stars. This is exemplified in Fig. 3, showing an attempt to reproduce the PL relations of LPVs using theoretical period-mass-radius relations from several authors.

To address such issues is highly desirable in order for theory to keep up with observation, and a great opportunity to achieve a better understanding of stellar interiors.

We acknowledge the support from the ERC Consolidator Grant funding scheme (*project STARKEY*, G.A. n. 615604).

References

Fox, M. W. & Wood, P. R. 1982, ApJ, 259, 198

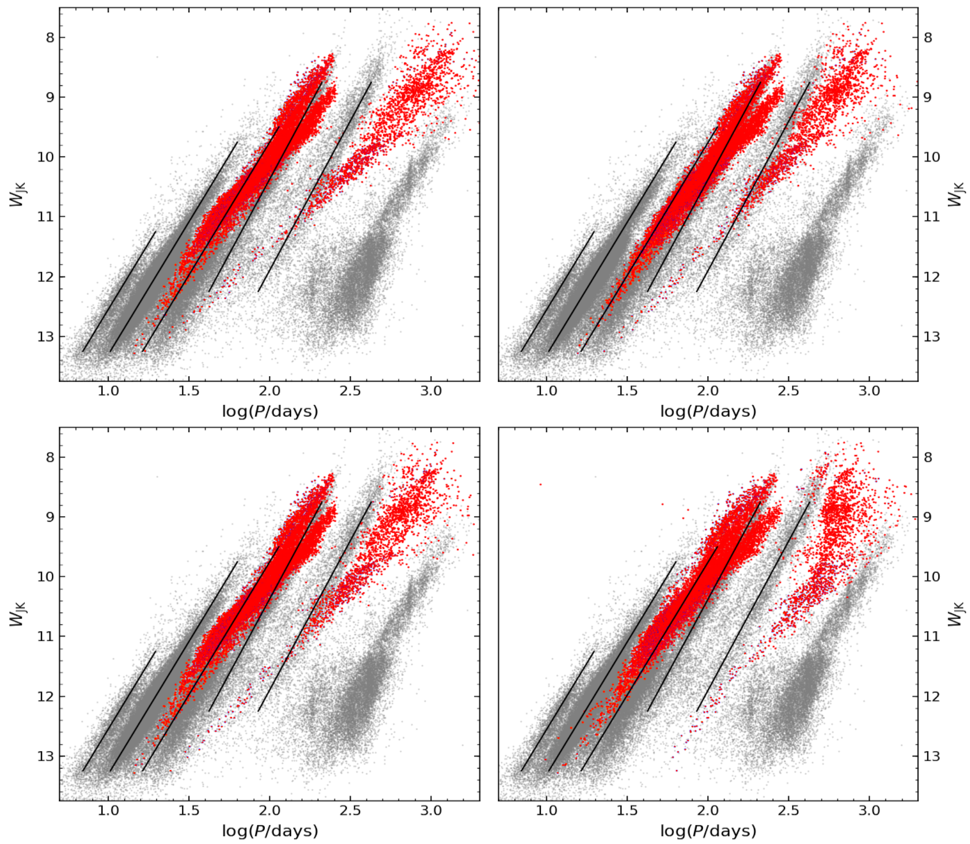

Fig. 3. Synthetic PLDs obtained by combining a LMC population model with prescriptions from the pulsation models by (clockwise from the upper left panel) Fox & Wood (1982), Ostlie & Cox (1986), Xiong & Deng (2007), and Wood (1990). Theoretical fundamental periods (right sequence of red points in each panel) are systematically longer than observed ones (grey points, from OGLE-III).

Lebzelter, T., Mowlavi, N., Marigo, P., et al. 2018, A&A, 616, L13

Lebzelter, T., Trabucchi, M., Mowlavi, N., et al. 2019, A&A, 631, A24

Marigo, P., Girardi, L., Bressan, A., et al. 2017, ApJ, 835, 77

McDonald, I. & Trabucchi, M. 2019, MNRAS, 484, 4678

Mowlavi, N., Lecoeur-Taïbi, I., Lebzelter, T., et al. 2018, A&A, 618, A58

Ostlie, D. A. & Cox, A. N. 1986, ApJ, 311, 864

Soszyński, I., Udalski, A., Szymański, M. K., et al. 2009, Acta Astron., 59, 239

Soszyński, I., Udalski, A., Szymański, M. K., et al. 2011, Acta Astron., 61, 217

Trabucchi, M., Wood, P. R., Montalbán, J., et al. 2017, ApJ, 847, 139

Trabucchi, M., Wood, P. R., Montalbán, J., et al. 2019, MNRAS, 482, 929

Wood, P. R. 1990, in From Miras to Planetary Nebulae: Which Path for Stellar Evolution?, ed. M. O. Mennessier & A. Omont, 67

Wood, P. R. 2015, MNRAS, 448, 3829

Wood, P. R., Alcock, C., Allsman, R. A., et al. 1999, in IAU Symposium, Vol. 191, Asymptotic Giant Branch Stars, ed. T. Le Bertre, A. Lebre, & C. Waelkens, 151

Wray, J. J., Eyer, L., & Paczyński, B. 2004, MNRAS, 349, 1059

Xiong, D. R. & Deng, L. 2007, MNRAS, 378, 1270

Stars and their variability observed from space
C. Neiner, W. W. Weiss, D. Baade, R. E. Griffin, C. C. Lovekin, A. F. J. Moffat (eds)

THE PLANET-HOST PULSATING STAR HR 8799 AS SEEN BY BRITE

Á. Sódor[1,2] and Zs. Bognár[1,2]

Abstract. HR 8799 is a well-known planet-host star with at least 4 planets discovered by direct imaging. HR 8799 is also a gamma Doradus pulsator, target of several previous photometric studies. BRITE observed this target in 2017 for 140 days, obtaining the most extended photometric data on this pulsator to date. We analyse these data in comparison with the results of previous space- and ground-based photometric observations. We confirm our earlier conclusion that resonances in the sparse frequency content of this pulsator might render the astreroseismic investigations rather difficult, if not impossible.

Keywords: techniques: photometric, stars: oscillations

1 Introduction

HR 8799 is a well-known planet-host star with at least 4 planets discovered by direct imaging (Marois et al. 2010). HR 8799 is also a gamma Doradus pulsator (Zerbi et al. 1999), target of several previous ground-based variability studies (Zerbi et al. 1999; Cuypers et al. 2009; Mathias et al. 2004; Wright et al. 2011). Asteroseismic studies are important for age and mass determination of the planetary-mass companions (Moro-Martín et al. 2010).

BRITE (Weiss et al. 2014) observed HR 8799 in 2017 for 140 days, obtaining the most extended photometric data on this pulsator to date. Previously, the MOST satellite also observed the target in 2009 for 48 days (Sódor et al. 2014, S14 hereafter).

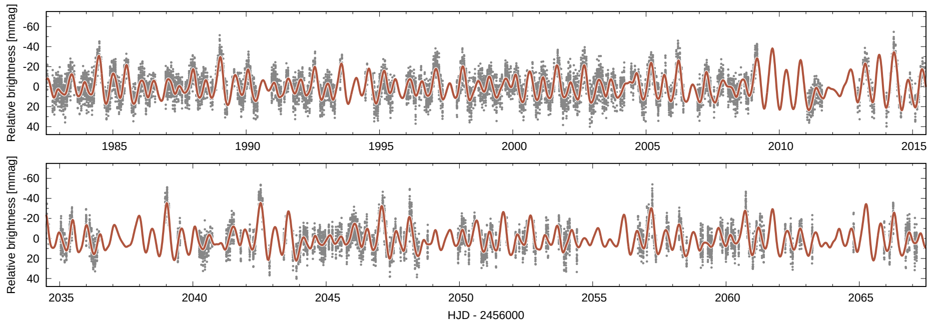

Fig. 1. The BRITE photometry along with the 31-frequency Fourier-solution (red curve; see Fig. 2).

2 Quick Look at the BRITE Data

We identified 31 significant pulsation frequencies in the BRITE data of HR 8799. Most of these correspond closely to those detected in the MOST data (see S14). The same f_3 and f_5 peak groups indicate frequency variability, and the same $n : 9$ resonances emerge. The 3 times longer BRITE observations permit 3 times better frequency precision that confirms the earlier detected resonance ratios (see details in S14). Fig 1 shows the BRITE light curve along with the 31-frequency Fourier-solution. The Fourier amplitude spectrum and the extracted frequency components of the BRITE photometry are shown in Fig. 2.

[1] Konkoly Observatory, Research Centre for Astronomy and Earth Sciences, Konkoly Thege Miklós út 15-17, H–1121 Budapest
[2] MTA CSFK Lendület Near-Field Cosmology Research Group

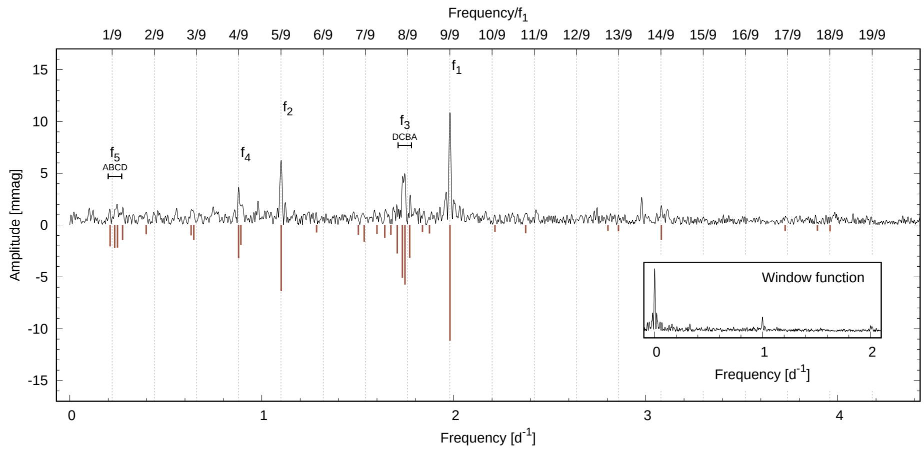

Fig. 2. The Fourier amplitude spectrum and the extracted frequency components (red bars with negative amplitudes) of the BRITE photometry.

3 Conclusion

The MOST and BRITE data have similar overall accuracy. Even though the individual BRITE observations are more noisy, the larger number of data points (25 590 BRITE vs. 5370 MOST observations) greatly compensate for it.

Even though earlier ground-based observations and MOST data indicated short time-scale variations in the frequency content of HR 8799, the data from the two spacecrafts show remarkable agreement. Comparing Figs 1 and 2 with the similar plots on the MOST data (Figs. 1 and 2 in S14) we see that the same dominant frequencies were identified within the frequency resolution limit. The stability of some of these (f_1, f_2), the variability of others (f_3, f_5), and even their relative amplitudes agree between the two observations taken 8 years apart.

With the exception of several marginally significant light-variation peaks, the large majority of the pulsation frequencies are resonantly coupled with the dominant mode (f_1), which render the astreroseismic investigations rather difficult, if not impossible.

ZsB acknowledges the support provided from the National Research, Development and Innovation Fund of Hungary, financed under the PD_{17} funding scheme, project no. PD-123910. This project has been supported by the Lendület Program of the Hungarian Academy of Sciences, project No. LP2018-7/2019. This work benefited a lot from the discussions within the SoFAR international team (`http://www.issi.unibe.ch/teams/sofar/`) supported by the International Space Science Institute. The study is based on data collected by the BRITE Constellation satellite mission, designed, built, launched, operated, and supported by the Austrian Research Promotion Agency (FFG), the University of Vienna, the Technical University of Graz, the University of Innsbruck, the Canadian Space Agency (CSA), the University of Toronto Institute for Aerospace Studies (UTIAS), the Foundation for Polish Science & Technology (FNiTP MNiSW), and Polish National Science Centre (NCN).

References

Cuypers, J., Aerts, C., De Cat, P., et al. 2009, A&A, 499, 967
Marois, C., Zuckerman, B., Konopacky, Q. M., Macintosh, B., & Barman, T. 2010, Nature, 468, 1080
Mathias, P., Le Contel, J. M., Chapellier, E., et al. 2004, A&A, 417, 189
Moro-Martín, A., Rieke, G. H., & Su, K. Y. L. 2010, ApJ, 721, L199
Sódor, Á., Chené, A. N., De Cat, P., et al. 2014, A&A, 568, A106
Weiss, W. W., Rucinski, S. M., Moffat, A. F. J., et al. 2014, PASP, 126, 573
Wright, D. J., Chené, A. N., De Cat, P., et al. 2011, ApJ, 728, L20
Zerbi, F. M., Rodríguez, E., Garrido, R., et al. 1999, MNRAS, 303, 275

Stars and their variability observed from space
C. Neiner, W. W. Weiss, D. Baade, R. E. Griffin, C. C. Lovekin, A. F. J. Moffat (eds)

THE NON-RADIAL PULSATION PATTERN OF THE ALGOL STAR RZ CAS

H. Lehmann[1], F. Pertermann[1], V. Tsymbal[2], A. Tkachenko[3] and D. E. Mkrtichian[4]

Abstract. We have introduced a Python-based computer programme that extends the capabilities of the pixel-by-pixel method of the FAMIAS package to perform an automated frequency search when there is a large number of non-radial pulsation modes. It also determines the error estimates of the frequencies detected, which has not been possible with the pixel-by-pixel method. We applied the programme to time-series of spectra obtained for the short-period Algol-type star RZ Cas in different epochs, to search for changes in its pulsation pattern indicative of active and inactive phases of mass transfer. We present here the first results.

Keywords: Stars: variables: delta Scuti, Asteroseismology, Methods: data analysis

1 Introduction

The oscillating eclipsing Algol stars (oEA stars) were introduced as a subclass of variable stars by Mkrtichian et al. (2002). They are active, semi-detached Algol-type systems in which the mass gainer shows δ Sct-like oscillations. Stars of this type enable one to investigate the interaction between episodes of rapid mass-transfer and excited oscillations. RZ Cas is the best-studied object within the group (see e.g., Mkrtichian et al. (2018) for a review). We monitored the star spectroscopically over more than a decade with the aim of investigating correlations between changes in its amplitudes of excited pulsations modes, $v \sin(i)$, orbital period, and the occurrence of episodes of mass-transfer. From time-series of spectra we could determine pulsation modes of low l degree from measured radial velocities (RVs), while high-degree modes can be found from line-profile variations (LPV). In the latter case, the FAMIAS package (Zima 2008) provides a useful tool by its pixel-by-pixel method. However, a large effort in interactive data handling (pre-whitening data for successively found frequencies) is necessary when applying it to stars that show a rich frequency spectrum, like the δ Sct stars. It has not been possible so far to estimate errors for the frequencies determined. We tried to rectify those limitations by writing our own Python code that is compatible with FAMIAS, adopting its basic methods but extending its capabilities.

2 Observations, Methods and Application

Spectra of RZ Cas were obtained with the TCES spectrograph at the 2-m telescope of the Thüringer Landessternwarte Tautenburg in 2001, 2006, 2008, 2013, and 2014 with a resolving power of $R = 30\,000$, and in 2015 and 2016 at $R = 58\,000$; more were obtained in 2009 with the HERMES spectrograph at the 1.25-m Mercator telescope on La Palma at $R = 85\,000$. We used the LSDbinary package (Lehmann et al. 2018) to calculate the individual least-squares decomposed (LSD) profiles of the two components, together with their RVs. We cleaned the RVs of the primary component for orbital motion and nightly trends, and used the residuals to search for frequencies of low-degree modes with PERIOD04 Lenz & Breger (2005). For the high-degree modes we used our Python-based extension of FAMIAS. It works similarly to the pixel-by-pixel method in FAMIAS but performs the alternating steps of Fourier analysis, least-squares fitting, and pre-whitening of data completely automatically in a cyclic way until all significant contributions have been found. The cut-off criterion that it applied is therefore similar to that made by Breger et al. (1993). In addition, it optimizes all frequencies in each step, and contains a least-squares fitting method that optimizes the final set of frequencies to find their uncertainties as well. We used the programme, together with the LSD profiles of the primary component shifted for orbital motion, for frequency searches, and FAMIAS for subsequent mode identification.

[1] Thüringer Landessternwarte, D-07778 Tautenburg, Germany
[2] Institute of Astronomy, Russian Academy of Sciences, Moscow, Russia; V. I. Vernadsky Crimea Federal University, Simferopol
[3] Instituut voor Sterrenkunde, KU Leuven, Belgium
[4] National Astronomical Research Institute of Thailand, Chiang Mai, Thailand

3 Preliminary Results

LSDbinary enabled us to decompose the RVs and LSD profiles of the two components of RZ Cas. The LPV of the primary component shows a rich frequency spectrum. Low frequencies are dominated by the rotation frequency and up to six of its harmonics, i.e., we see time-varying surface structures, possibly caused by spots and/or an accretion disk of varying density. In the high-frequency domain we see rapidly changing non-radial pulsation patterns. Different modes are excited in different epochs and with different amplitudes (Fig. 1, left). The main mode at $f_1 = 64.2\,\mathrm{c\,d^{-1}}$, which also dominates the photometric variations (e.g. Mkrtichian et al. 2018), was present in the RV variations in all the years, and could also be found from LPV in 2014–2016. We derived $l, m = 1, 0$, which gave a distinctly better fit to the observed amplitude across line-profile variations than did $l, m = 2, 1$ as deduced from photometry (Fig. 1, right). We found further high l-degree modes with FAMIAS that could not be detected in the RV variations. In the 2006 and 2009 data we observed strong contributions close to $70\,\mathrm{c\,d^{-1}}$, and weak ones in the 2001 and 2013 data; we identified them as high l-degree sectoral modes. From the different l numbers and the small difference in frequency we concluded that we had observed two different modes, one in 2001 and 2006, and one in 2009 and 2013.

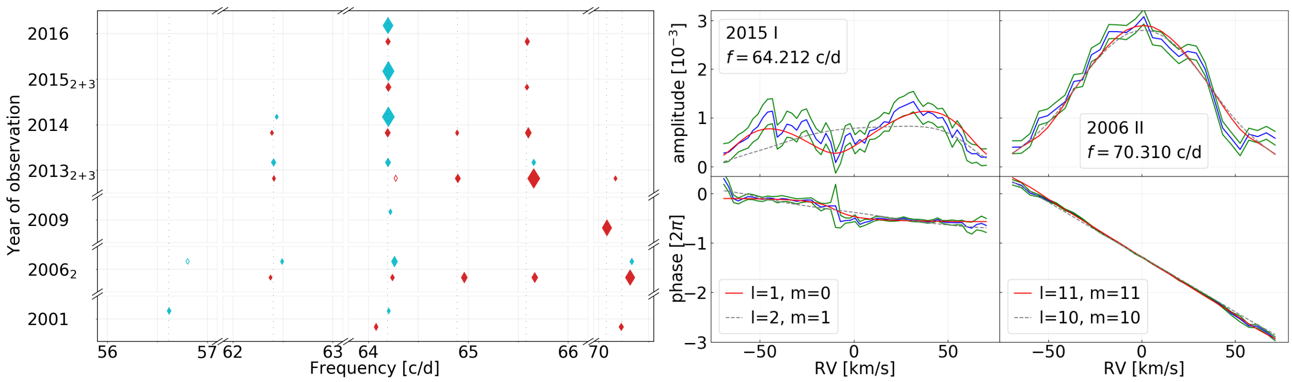

Fig. 1. Left: Frequencies found in different epochs from RV (blue) and LPV (red). The sizes of diamonds scale with the pulsation amplitudes (separately for the two methods). Right: Examples of observed amplitudes and phases across the line-profile contributions (blue), with errors (green) and the best-fitting theoretical curves (red and dotted grey).

4 Conclusions

Our results showed the capabilities of the new methods like LSDbinary and our Python-based FAMIAS extension. We confirmed the seasonal changes of frequencies of pulsation modes in RZ Cas found by Mkrtichian et al. (2018) from light-curve analysis, and interpreted them as acceleration and braking of surface rotation of the mass-accreting star. Relations obtained between changes in pulsation frequencies and amplitudes, the orbit-to-rotation synchronisation factor, and $v\sin(i)$ of the primary component of RZ Cas, will be published in a forthcoming paper, together with a detailed pulsation mode analysis.

HL and FP acknowledge support from DFG grant LE1102/3-1. VT acknowledges support by the RF Ministry of Science and Higher Education (project no. 3.7126.2017/8.9). AT acknowledges funding from the European Research Council (ERC) under the EU's Horizon 2020 research and innovation programme (grant agreement N°670519: MAMSIE).

References

Breger, M., Stich, J., Garrido, R., et al. 1993, A&A, 271, 482

Lehmann, H., Tsymbal, V., Pertermann, F., et al. 2018, A&A, 615, A131

Lenz, P. & Breger, M. 2005, Communications in Asteroseismology, 146, 53

Mkrtichian, D. E., Kusakin, A. V., Gamarova, A. Y., & Nazarenko, V. 2002, in ASPCS, Vol. 259, IAU Colloq. 185, ed. C. Aerts, T. R. Bedding, & J. Christensen-Dalsgaard, 96

Mkrtichian, D. E., Lehmann, H., Rodríguez, E., et al. 2018, MNRAS, 475, 4745

Zima, W. 2008, Communications in Asteroseismology, 157, 387

PRE-MAIN SEQUENCE GRAVITY-MODE PULSATORS IN K2

L. Ketzer[1] and K. Zwintz[1]

Abstract.
Campaigns 2, 9, 13 and 15 in the extended *Kepler* mission (K2) pointed towards young star forming regions, which host pre-main sequence (pre-MS) stars. Currently only a handful of pre-MS gravity (g-)mode pulsators of the γ Doradus and Slowly Pulsating B (SPB) types are known. We used archived K2 data to search for additional members of these two classes of young oscillators, and discovered 13 previously unknown pre-MS g-mode pulsators. In one of our targets we detect a period spacing sequence, which made this one a prime candidate for future asteroseismic modelling efforts. By increasing the known sample size of young gravity-mode pulsators we laidthe groundwork for future studies aimed at probing the location and extent of the pre-MS instability strips, and also an investigation into a possible observable relation between the g-mode pulsation properties and the evolutionary state of a star.

Keywords: Asteroseismology, Stars: oscillations, Stars: pre-main sequence

1 The power of gravity-mode pulsators

Gravity-mode pulsations have great probing power for deep stellar interiors because observations of them enable us to probe indirectly the physical conditions close to the core. That makes g-mode pulsators sought-after targets in the field of asteroseismology. Much information can be extracted from the detection of period-spacing sequences, in which consecutive modes are evenly spaced in period. Chemical composition gradients in the stellar interior, however, induce periodic dips in these period-spacing patterns (Miglio et al. 2008), and stellar rotation causes the spacings of certain pulsation modes to be sloped (Ouazzani et al. 2017). Those deviations can be used to measure the near-core rotation rate, and they give hints about the evolutionary state of the star. Bouabid et al. (2011) showed that no strong mean molecular-weight gradient is expected in pre-MS stars, and thus the period-spacing patterns should not present any of the periodic dips that are observed for many more evolved stars (see e.g., Van Reeth et al. 2015; Pápics et al. 2017). Consequently, period-spacing sequences can present a way of distinguishing between very young stars and more evolved ones, an achievement which often proves ambiguous when tackled from atmospheric properties alone.

2 Pre-main sequence pulsators in the K2 data

Up to now, only 15 pre-MS gravity-mode pulsators have been identified (Gruber et al. 2012; Zwintz et al. 2013, 2017; Ripepi et al. 2015). One key challenge is the short pre-MS lifetime of these intermediate mass B-, A- and F-type γ Dor and SPBs. FUrthermore, their pulsation periods, which are of the order of 0.3–3 days, make them challenging to find with ground-based equipment. We therefore examined the three well-known regions with ages less than ~ 10 Myr within the K2 fields for young pulsating stars. Campaigns 2 and 15 pointed to the Upper Scorpius region and the embedded ρ Ophiuchus star-forming region; Campaign 9 observed the open cluster NGC 6530 within the Lagoon Nebula, and Campaign 13 contained the Taurus–Auriga star-forming region. We conducted a literature search to compile a sample of roughly 500 stars associated with the regions of interest. We then downloaded several different light-curve products available in the MAST archive, and searched for pulsations using a tool called SMURFS*, which performs a quick frequency analysis of a time-series based on the Lomb–Scargle periodogram. If a star in our sample showed multiple significant frequencies in the g-mode regime that cannot be explained as rotational modulation or binarity, we conducted a thorough literature search on this individual target and compiled a list of additional criteria of 'youth'. If a star had been associated as a member (usually from kinematics), and shows additional youth indicators like an X-ray, IR or UV excess, Hα emission or a high lithium abundance, we could be confident that that target was likely to be still in its pre-MS stage. Additional spectroscopic follow-up observations are then required to determine if a pre-MS candidate is indeed located above the the zero-age main-sequence on the spectroscopic Kiel diagram.

[1] University of Innsbruck, Institute for Astro- and Particle Physics, Technikerstr. 25, 6020 Innsbruck, Austria
*`https://smurfs.readthedocs.io/en/master/`

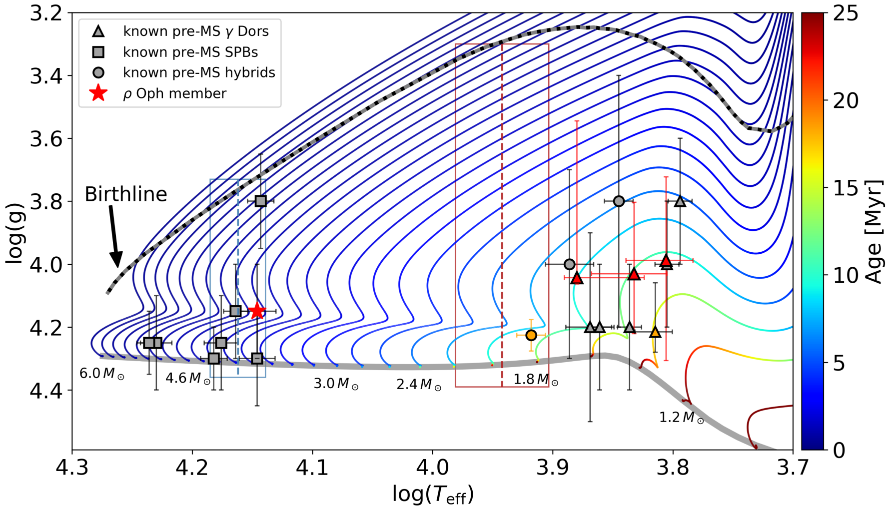

Fig. 1. Kiel diagram, showing all known pre-MS pulsators before K2 (grey), together with 8 candidates discovered in the K2 data (colour). SPBs are marked as squares, γ Dors as triangles and the hybrid stars as circles. The evolutionary tracks (T.Steindl, priv. communication) are colour-coded to indicate stellar age along the pre-MS.

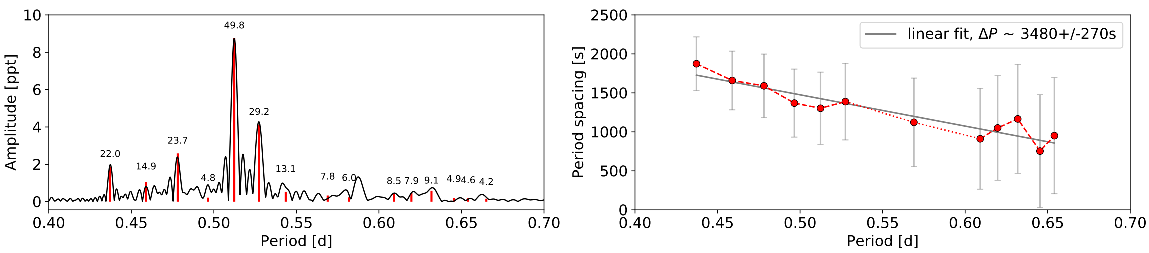

Fig. 2. Left: Periodogram with all frequencies identified as part of the period spacing pattern marked in red, together with the corresponding SNR values. **Right**: Plot of ΔP vs. P, illustrating the extracted period spacing sequence. A linear fit to the pattern is shown in grey.

3 Results and Outlook

Among our sample of $\sim$500 young stars we found 13 promising candidates for pre-MS γ Dor or SPB pulsators. In another 13 either we could not rule out the presence of pulsations, or we were uncertain about the pre-MS nature of the candidate. For one of our 13 prime candidates we found archived spectra, which enabled us to place the star in the Kiel diagram and confirm its pre-MS SPB nature. For two other targets we have only spectroscopic temperature estimates available, and for another three we used the EPIC temperature and surface gravity estimates to place them on the Kiel diagram (see Fig 1). Our next step is to conduct follow-up spectroscopic observations of our candidates in order to obtain reliable constraints on their atmospheric parameters. One of our young g-mode pulsators in the Lagoon Nebula shows strong indications of a sloped period-spacing pattern (see Fig 2), making it a promising target for future asteroseismic modelling. If this star turns out to be a γ Doradus type, it would be the first pre-MS star in this pulsator class with a period-spacing detection. With almost 30 known pre-MS gravity-mode pulsators now, it is becoming feasible to probe the location and extent of the pre-MS instability strips, and investigate whether an observable relation exists between the g-mode pulsation properties and the evolutionary state of a star, similar to the one found for pre-MS δ Scuti stars (Zwintz et al. 2014).

References

Bouabid, M. P., Montalbán, J., Miglio, A., et al. 2011, A&A, 531, A145
Gruber, D., Saio, H., Kuschnig, R., et al. 2012, MNRAS, 420, 291
Miglio, A., Montalbán, J., Noels, A., & Eggenberger, P. 2008, MNRAS, 386, 1487

Ouazzani, R.-M., Salmon, S. J. A. J., Antoci, V., et al. 2017, MNRAS, 465, 2294
Pápics, P. I., Tkachenko, A., Van Reeth, T., et al. 2017, A&A, 598, A74
Ripepi, V., Balona, L., Catanzaro, G., et al. 2015, MNRAS, 454, 2606
Van Reeth, T., Tkachenko, A., Aerts, C., et al. 2015, A&A, 574, A17
Zwintz, K., Fossati, L., Ryabchikova, T., et al. 2014, Science, 345, 550
Zwintz, K., Fossati, L., Ryabchikova, T., et al. 2013, A&A, 550, A121
Zwintz, K., Moravveji, E., Pápics, P. I., et al. 2017, A&A, 601, A101

ASTEROSEISMOLOGY OF THE β CEN SYSTEM

C. Lovekin[1] and J. Tompkins[1]

Abstract. The triple system β Centauri has been observed with the *BRITE*-Constellation. These photometric observations detected 19 periods, of which 8 are probably g modes and 9 are identified as p modes. As both the Aa and Ab components of the system are identified as early B-type stars, the pulsations could belong to either or both components. Preliminary asteroseismic modelling of the system has been attempted, but the rapid rotation meant that no final seismic model was produced. We have expanded that modelling, using a 2D stellar-evolution code and a 2D pulsation code to calculate models of the Aa and Ab components of the system. The 2D nature of these codes enables us to account more fully for the effects of rotation on both the structure and the pulsation frequencies of the stars. We appied the known binary constraints of the system to limit the range of the models we calculated, and to constrain our fit further. This article presents the preliminary results of our fit; it includes our conclusion as to which star produces the pulsation frequencies; we have also given the absolute rotation rates, convective core overshoot parameters, and the absolute age of the system.

Keywords: Stars: oscillations, interiors, binaries: spectroscopic, visual, individual: β Centauri, HD 122451

1 Introduction

Convective core overshoot is an important process in the structure and evolution of stars, but is poorly understood. Observations suggest overshoot is required, but the quantity remains uncertain (e.g., Rosenfield et al. 2017). It is also not clear how core overshoot changes with mass, age and metallicity of a star. Asteroseismology has proved to be a useful tool for probing the interior structure of stars across the H–R diagram, and constraints on core overshoot and rotation can be determined for many low-mass stars and evolved stars. Many B stars pulsate either in p modes as β Cep stars or in g modes as Slowly Pulsating B (SPB) stars; a few hybrid pulsators have also been observed (Pápics et al. 2012). Recent space missions, including *Kepler, TESS, CoRoT* and *BRITE*, have increased greatly the number of β Cep and SPB stars that have well known frequencies, and detailed seismic modelling of those stars is now possible.

A recent observing campaign using the *BRITE* Constellation observed the β Centaurus system for nearly 146 days, providing a detailed light-curve. Using those data, Pigulski et al. (2016) were able to detect 19 periods in the data, corresponding to 17 unique frequencies. The β-Cen system is a triple system, and contains a pair of non-eclipsing early-B stars (components Aa and Ab) with a fainter B-type companion in a wide orbit. Radial velocities from Ausseloos et al. (2006), combined with the *BRITE* photometry, enabled Pigulski et al. (2016) to derive strict constraints on the orbital parameters of the system, including the stellar masses.

2 Results

We calculated a grid of models using ROTORC (Deupree 1990, 1995) and including step overshoot (0.1, 0.15 and 0.2) and rotation (100-300 km s^{-1}). We held the masses fixed at 10.5 M$_\odot$ and 12 M$_\odot$. Pulsation frequencies were calculated with NRO (Clement 1998; Lovekin et al. 2009) for 5 points along the evolutionary track.

From the resulting grid of models we created a suite of synthetic binary systems by selecting one 10.5 M$_\odot$ model and one 12 M$_\odot$ model. Models in each synthetic binary were constrained to have the same age. We then compared the individualfrequencies observed with the model frequencies in order to determine whether each frequency was a better fit for the 10.5 M$_\odot$ or 12 M$_\odot$ model based on χ^2 statistics. Once all frequencies had been compared, the χ^2s were summed to give a total χ^2 for the synthetic binary. The frequency assignment for the synthetic binary with the lowest χ^2 are presented in columns 2 and 3 of Table 1.

Observational constraints have suggested that frequencies f_2 and f_3 must be associated with the primary star of the system. We therefore re-fitted the system, this time forcing those two frequencies to be assigned to the primary star in each synthetic binary. The results of this fit are presented in columns 4 and 5 of Table 1.

[1] Physics Department, Mount Allison University, Sackville, NB, E4L 1E6, Canada

	Unconstrained		Constrained	
Frequency (c/d)	Aa	Ab	Aa	Ab
$f_2 = 5.54517$		X	X	
$f_3 = 6.41350$		X	X	
$f_4 = 1.59815$		X		X
$f_5 = 0.35367$		X	X	
$f_6 = 4.04180$		X		X
$f_7 = 1.19867$	X			X
$f_8 = 4.44439$	X			X
$f_9 = 1.52100$	X			X
$f_{10} = 1.32022$		X	X	
$f_{11} = 5.61725$		X	X	
$f_{12} = 4.88617$		X	X	
$f_{13} = 4.16793$		X		X
$f_{14} = 4.10357$	X			X
$f_{15} = 0.67907$		X	X	
$f_{16} = 1.63040$	X			X
$f_{17} = 1.34157$	X		X	
$f_{18} = 4.36444$	X			X

Table 1. Best fit frequency assignments

	Unconstrained		Constrained	
Parameter	Aa	Ab	Aa	Ab
L ($L/L_\odot$)	19 500	12 700	24 900	16 200
M_V	-3.65	-3.18	- 4.00	-3.71
$T_{\rm eff}$ (K)	24 100	22 600	23 200	21 500
$\log g$	3.70	3.72	3.52	3.53
$v_{\rm ZAMS}$ (km s^{-1})	100	150	250	150
$v_{\rm eq}$ (km s^{-1})	27	55	114	67
age (years)	14×10^6		17×10^6	
X_c	0.21	0.21	0.0015	0.0035
$\alpha_{\rm ov}$	0.1	0.15	0.15	0.2
$n_{\rm freqs}$	7	10	8	9

Table 2. Best fitting model parameters

The parameters of the best fitting models in the unconstrained and constrained fits are summarized in Table 2. We found that the constrained fit produces a better fit to the observational constraints than did the unconstrained fit. Both models correspond to a relatively old stellar age; the constrained fit model has reached the TAMS. This is consistent with studies of g mode excitation (Pigulski et al. 2016). In both cases, our fit shows that the Aa and Ab components of β Cen are hybrid SPB/β Cep pulsators, which signals them as good candidates for future study. The Ab component has been identified previously as a magnetic star (Alecian et al. 2011), which means that these stars could be adapted for probing interactions between convection, rotation and magnetic fields in stellar interiors.

3 Conclusions

We are able to find a good fit to the system by using the binary mass and observed frequencies as initial constraints. We have presented tentative frequency assignments for each star; the resulting fits are in good agreement with the observational constraints on the system.

This work was supported by a grant from the Natural Sciences and Engineering Research Council of Canada.

References

Alecian, E., Kochukhov, O., Neiner, C., et al. 2011, A&A, 536, L6

Ausseloos, M., Aerts, C., Lefever, K., Davis, J., & Harmanec, P. 2006, A&A, 455, 259

Clement, M. J. 1998, ApJSS, 116, 57

Deupree, R. G. 1990, ApJ, 357, 175

Deupree, R. G. 1995, ApJ, 439, 357

Lovekin, C. C., Deupree, R. G., & Clement, M. J. 2009, ApJ, 693, 677

Pápics, P. I., Briquet, M., Baglin, A., et al. 2012, A&A, 542, A55

Pigulski, A., Cugier, H., Popowicz, A., et al. 2016, A&A, 588, A55

Rosenfield, P., Girardi, L., Williams, B. F., et al. 2017, ApJ, 841, 69

Stars and their variability observed from space
C. Neiner, W. W. Weiss, D. Baade, R. E. Griffin, C. C. Lovekin, A. F. J. Moffat (eds)

THE PROTOTYPE STAR γ DORADUS OBSERVED BY *TESS*

S. Christophe[1], V. Antoci[2], E. Brunsden[3], R.-M. Ouazzani[1] and S.J.A.J. Salmon[4]

Abstract. γ Doradus is the prototype star for the eponymous class of pulsating stars that consists of late A to early F main-sequence stars oscillating in low-frequency gravito-inertial modes. Being among the brightest stars of its kind ($V = 4.2$ mag), γ Dor benefits from a large set of observational data that has recently been completed by high-quality space photometry from the *TESS* mission. With these new data, we propose to study γ Dor as an example of possibilities offered by synergies between multi-technical ground and space-based observations. We present here the preliminary results of our investigations.

Keywords: Asteroseismology, stars: oscillations, rotation, individual: gamma Doradus

1 *TESS* photometry

TESS observed γ Dor during Sectors 3, 4, and 5, representing 80 days of nearly uninterrupted data. Being bright, the star saturated the CCDs and left bleeding trails along CCD columns. That is shown on the Full Frame Image (FFI) cutout on the left panel of Fig. 1. The light-curve was extracted by performing simple aperture photometry on FFI cutouts with a custom mask chosen to include most of the target flux. Data downlink or scattered light from the Earth or the Moon are responsible for gaps in the data, but overall a duty cycle of 87% was achevied.

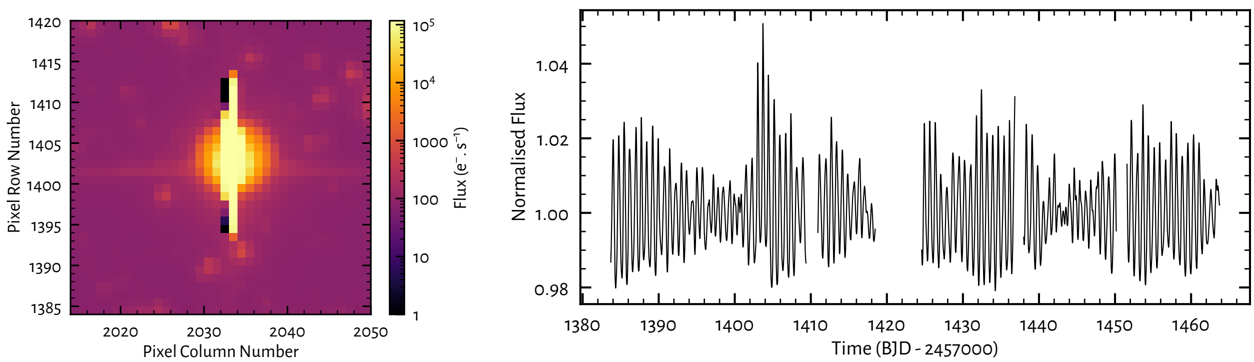

Fig. 1. Left: Example of *TESS* Full Frame Image (FFI) cutout for γ Dor. **Right:** Light-curve of γ Dor extracted from *TESS* FFI cutouts.

2 Asteroseismology from ground and space

We carried out the frequency analysis of the *TESS* light-curve by iterative prewhitening. We found 21 frequencies with S/N > 4 (see Fig. 2). The 6 previously known frequencies from ground-based observations (Brunsden et al. 2018) are all confirmed in the *TESS* data. Based on line profile variations, Brunsden et al. (2018) identified the

[1] LESIA, Observatoire de Paris, Université PSL, CNRS, Sorbonne Université, Université de Paris, 5 place Jules Janssen, 92195 Meudon, France
[2] Stellar Astrophysics Centre, Department of Physics and Astronomy, Aarhus University, Ny Munkegade 120, DK-8000 Aarhus C, Denmark
[3] Department of Physics, University of York, Heslington, York, YO10 5DD, UK
[4] STAR Institute, Université de Liège, Allée du 6 Août 19, 4000 Liège, Belgium

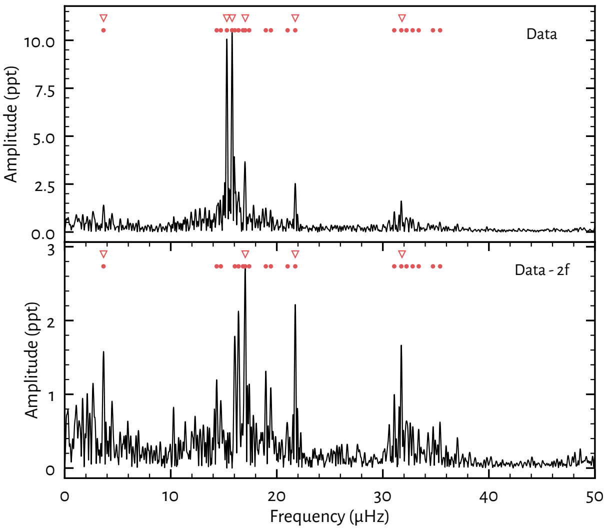

Fig. 2. Amplitude periodograms before (top) and after pre-whitening (bottom) of the first two frequencies of high amplitude. Red circles represent frequencies extracted from the *TESS* light-curve. Upside down triangles indicate frequencies found by Brunsden et al. (2018) from ground-based photometry and spectroscopy.

three frequencies at 15.3, 15.8 and 21.7 μHz to be prograde gravity modes of $(\ell, m) = (1, -1)$. Assuming the frequency group at $\sim$16 μHz is mostly consisting of $(1, -1)$ modes, we applied the method of Christophe et al. (2018) to estimate the near-core rotation rate of γ Dor. The mode frequencies are compatible with rotation rates in the 9–12 μHz range, but the limited resolution of the periodogram prevented us from obtaining a more precise value. The second frequency group around $\sim$32 μHz can be interpreted as either combination frequencies or $(\ell, m) = (2, -2)$ modes.

3 Surface rotation

In order to determine the surface rotation rate, we need the luminosity L, the effective temperature $T_{\rm eff}$, the projected surface velocity $v \sin i$, and the inclination angle i. The luminosity is taken from Gaia DR2 ($L = 6.99 \pm 0.06\ L_\odot$, Gaia Collaboration et al. 2018). We derived $T_{\rm eff} \approx 7145 \pm 150$ K by averaging the photometric and spectroscopic estimates available in the literature. The projected velocity, $v \sin i = 59.5 \pm 3$ km s^{-1} was taken from Ammler-von Eiff & Reiners (2012). γ Dor hosts a debris disk that has been observed with *Herschel* and modelled by Broekhoven-Fiene et al. (2013), who found $i \approx 70°$. Assuming the rotation axis of γ'Dor is aligned with its disk axis, we estimated the surface rotation rate to be 8.4 ± 0.8 μHz. That is close to the range of near-core rotation rates estimated from seismology, and suggesting a nearly uniform rotation profile.

This research made use of Lightkurve, a Python package for *Kepler* and *TESS* data analysis (Lightkurve Collaboration et al. 2018); Period04 (Lenz & Breger 2005) and Astroquery (Ginsburg et al. 2019). S.C. acknowledges support from the Programme National de Physique Stellaire (PNPS) of the CNRS/INSU co-funded by CEA and CNES.

References

Ammler-von Eiff, M. & Reiners, A. 2012, A&A, 542, A116

Broekhoven-Fiene, H., Matthews, B. C., Kennedy, G. M., et al. 2013, ApJ, 762, 52

Brunsden, E., Pollard, K. R., Wright, D. J., De Cat, P., & Cottrell, P. L. 2018, MNRAS, 475, 3813

Christophe, S., Ballot, J., Ouazzani, R. M., Antoci, V., & Salmon, S. J. A. J. 2018, A&A, 618, A47

Gaia Collaboration, Brown, A. G. A., Vallenari, A., et al. 2018, A&A, 616, A1

Ginsburg, A., Sipőcz, B. M., Brasseur, C. E., et al. 2019, AJ, 157, 98

Lenz, P. & Breger, M. 2005, Communications in Asteroseismology, 146, 53

Lightkurve Collaboration, Cardoso, J. V. d. M., Hedges, C., et al. 2018, Lightkurve: Kepler and TESS time series analysis in Python, Astrophysics Source Code Library

Stars and their variability observed from space
C. Neiner, W. W. Weiss, D. Baade, R. E. Griffin, C. C. Lovekin, A. F. J. Moffat (eds)

THE EXISTENCE OF HOT γ DORADUS AND A–F-TYPE HYBRID STARS

F. Kahraman Aliçavuş[1,2], E. Poretti[3,4], G. Catanzaro[5], B. Smalley[6], E. Niemczura[7], M. Rainer[3,8] and G. Handler[1]

Abstract. The γ Dor-type pulsations are thought to be driven by a convective blocking mechanism within a convective envelope in a sufficient depth. However, there are several hot γ Dor and hybrid star candidates in which there should not be an adequate convective envelope to excite the γ Dor-type oscillations. In this study we presented the result of examinong these hot variables by spectroscopic and photometric analyses.

Keywords: stars: general, abundances, atmospheres, variables, individual: γ Doradus

1 Introduction

The existence of the hot γ Dor stars was first discussed by Balona (2014); Balona et al. (2016). These stars have been thought to be either binary systems, or rapidly rotating and slowly pulsating B (SPB) stars seen equator-on. In an attempt to sort out these problems we carried out detailed spectroscopic and photometric studies. Twenty-four hot γ Dor and hybrid candidates were selected from the study of Uytterhoeven et al. (2011); they have T_{eff} values higher than 7500 K in the Huber et al. (2014) catalogue, and have no high-resolution spectroscopy. Our spectroscopic observations were carried out with the FIES spectrograph at medium resolution (R=46000). To examine the binary nature of the targets, we took at least two spectra per star on different nights. The average S/N ratio of the spectra was 70.

2 Spectroscopic and photometric analyses

In our spectroscopic analyses we used ATLAS9 model atmospheres (Kurucz 1993) and the SYNTHE code (Kurucz & Avrett 1981), and carried out spectral synthesis. The atmospheric parameters (T_{eff}, $\log g$, ξ) were determined by comparing the strengths of Fe lines having a range of excitation and ionization potentials. The resulting atmospheric parameters were adopted as input for determining the chemical abundances of the stars. Values of $v \sin i$ were also derived. Photometric analyses were carried out using the long- and short-cadence *Kepler* data. Through these analyses we identified 2 non-pulsating, 9 δ Sct, 8 γ Dor and 5 hybrid stars in our sample.

3 Conclusions

In this study we found 5 hot γ Dor and 2 hot hybrid stars in our sample but no binary systems amojng them. If hot γ Dor stars are SPB variables, they should show high rotational velocities. However, the average $v \sin i$ value for these systems was 126 km s^{-1}, while an average $v \sin i$ value for stars having the spectral types similar to the SPB stars is 144 km s^{-1} (Balona et al. 2016; Głebocki & Gnaciński 2005).

We could not confirm any SPB properties in these hot objects. If the hot γ Dor stars are rapidly rotating SPB systems, they should show B-type spectral features. However, no such features were seen, though this

[1] Nicolaus Copernicus Astronomical Center, Bartycka 18, PL-00-716 Warsaw, Poland
[2] Çanakkale Onsekiz Mart University, Faculty of Sciences and Arts, Physics Department, 17100, Çanakkale, Turkey
[3] INAF – Osservatorio Astronomico di Brera, via E. Bianchi 46, 23807 Merate (LC), Italy
[4] INAF – Fundación Galileo Galilei, Rambla José Ana Fernandez Pérez 7, 38712 Breña Baja, TF, Spain
[5] INAF – Osservatorio Astrofisico di Catania, Via S. Sofia 78, I-95123 Catania, Italy
[6] Astrophysics Group, Keele University, Staffordshire, ST5 5BG, UK
[7] Instytut Astronomiczny, Uniwersytet Wrocławski, ul. Kopernika 11, 51-622 Wrocław, Poland
[8] INAF – Osservatorio Astrofisico di Arcetri Largo E. Fermi 5, 50125 Firenze, Italy

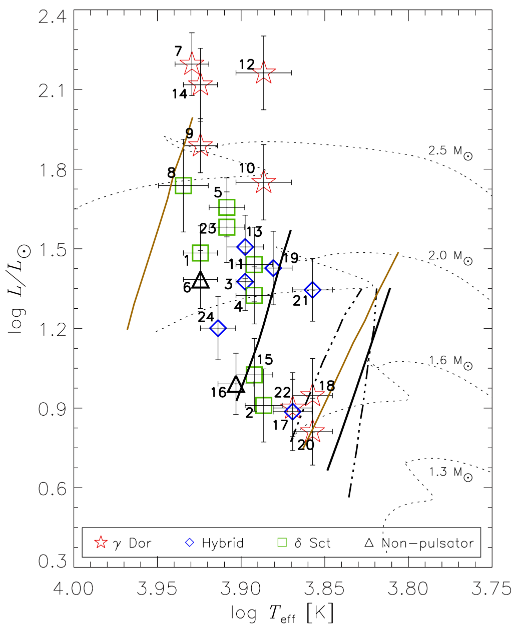

Fig. 1. Positions of the stars in the H–R diagram. The theoretical instability strips of the γ Dor (dashedlines) and δ Sct (solid black lines) stars were taken from Dupret et al. (2005). The recently suggested δ Sct instability strip (Murphy et al. 2019), which had recently been defined, is shown by solid brown lines. The evolutionary tracks (Z=0.02) were adopted from Kahraman Aliçavuș et al. (2016).

result should be checked with higher S/N spectra. The positions of the stars in the Hertzsprung-Russell (H–R) diagram (Fig. 1) use Gaia paralaxes (Gaia Collaboration et al. 2018). As can be seen from that figure, all hot γ Dor stars show higher luminosity values, and imply larger radii. We also calculated the luminosities of the other hot γ Dor stars given in Balona et al. (2016). It turned out that 70% of these stars also have higher luminosities, and consequently larger radii, compared to the theoretically calculated values for their range of spectral types.

Observations made with the Nordic Optical Telescope (La Palma, Spain) under the proposal 54-003 (P.I. E. Poretti). FKA, GH, and EN thank the Polish National Center for Science (NCN) through grant no. grant 2015/18/A/ST9/00578 and 2014/13/B/ST9/00902. The calculations have been carried out in Wrocław Centre for Networking and Super computing (http://www.wcss.pl), grant No. 214.

References

Balona, L. A. 2014, MNRAS, 437, 1476

Balona, L. A., Engelbrecht, C. A., Joshi, Y. C., et al. 2016, MNRAS, 460, 1318

Dupret, M. A., Grigahcène, A., Garrido, R., Gabriel, M., & Scuflaire, R. 2005, A&A, 435, 927

Gaia Collaboration, Brown, A. G. A., Vallenari, A., et al. 2018, A&A, 616, A1

Głebocki, R. & Gnaciński, P. 2005, in ESA Special Publication, Vol. 560, 13th Cambridge Workshop on Cool Stars, Stellar Systems and the Sun, ed. F. Favata, G. A. J. Hussain, & B. Battrick, 571

Kahraman Aliçavuș, F., Niemczura, E., De Cat, P., et al. 2016, MNRAS, 458, 2307

Kurucz, R. 1993, ATLAS9 Stellar Atmosphere Programs and 2 km/s grid. Kurucz CD-ROM No. 13. Cambridge, 13

Kurucz, R. L. & Avrett, E. H. 1981, SAO Special Report, 391

Murphy, S. J., Hey, D., Van Reeth, T., & Bedding, T. R. 2019, MNRAS, 485, 2380

Uytterhoeven, K., Moya, A., Grigahcène, A., et al. 2011, A&A, 534, A125

Stars and their variability observed from space
C. Neiner, W. W. Weiss, D. Baade, R. E. Griffin, C. C. Lovekin, A. F. J. Moffat (eds)

EFFECT OF THE MAGNETIC FIELD ON PERIOD SPACINGS OF GRAVITY MODES IN RAPIDLY ROTATING STARS

V. Prat[1], S. Mathis[1,2], B. Buysschaert[2,3], J. Van Beeck[3], D. M. Bowman[3], C. Aerts[3,4] and C. Neiner[2]

Abstract. Stellar magnetic fields play a crucial role in the evolution of the angular momentum of stars and in their interactions with stellar/planetary companions. Spectropolarimetric surveys provide us with observational constraints on surface magnetic fields, but we have very few direct constraints on internal magnetic fields. Asteroseismology allows us to probe stellar interiors and is thus an excellent candidate to obtain new constraints on this magnetism. In this context, we developed a perturbative treatment of a large-scale fossil-like mixed magnetic field (i.e. poloidal and toroidal) in the traditional approximation of rotation (which neglects the horizontal component of the rotation vector) to investigate its effect on the period spacing patterns of gravity modes in rapidly rotating stars. We then applied it to a representative model of the slowly pulsating B-type star HD 43317 and show how the magnetic signatures are different from those of rotation and chemical mixing.

Keywords: asteroseismology, waves, stars: magnetic field, stars: oscillations, stars: rotation

1 Introduction

Gravity waves are crucial in stellar physics. First, they allow us to probe the internal properties of intermediate-mass and massive stars (see e.g. Van Reeth et al. 2018). Second, they redistribute angular momentum and chemical elements across the whole Hertzsprung-Russell diagram (Talon & Charbonnel 2005; Mathis et al. 2013; Rogers 2015). Finally, they contribute to tidal dissipation in close-in multiple stars and planetary systems (Ogilvie & Lin 2007).

Surface stellar magnetic fields can be detected using spectropolarimetric measurements of the Zeeman effect. In contrast, there are no direct constraints on the internal properties of stellar magnetic fields. Asteroseismology is a promising way to obtain such new constraints.

Internal magnetic fields can modify the propagation of waves and the frequency of eigenmodes. When the rotation is slow and the field is weak enough to be considered as a perturbation of the non-magnetic system, their main effect is to generate splittings of modes of same radial order and angular degree, but different azimuthal orders. This effect has been studied for pressure modes in rapidly oscillating Ap stars with an oblique dipolar field (Shibahashi & Takata 1993), and for gravity modes in slowly pulsating B-type (SPB) stars with an axisymmetric dipolar field (Hasan et al. 2005). When the field is stronger, it has been proposed as a possible explanation for depressed mixed modes in red giant stars (Fuller et al. 2015; Loi & Papaloizou 2018).

Typical intermediate-mass and massive stars, such as γ Doradus, δ Scuti, SPB, β Cephei, or Be stars, rotate rapidly, and thus require a non-perturbative treatment of rotation (Ballot et al. 2010). The traditional approximation of rotation (TAR), which neglects the horizontal component of the rotation vector, allows to efficiently compute gravity and Rossby modes for seismic modelling (Van Reeth et al. 2016). In the present work, we investigate the perturbative effect of a dipolar magnetic field with both poloidal and toroidal components, which correspond to a stable fossil magnetic field (Duez et al. 2010), on gravity modes computed in the TAR.

[1] AIM, CEA, CNRS, Universit Paris-Saclay, Universit Paris Diderot, Sorbonne Paris Cit, F-91191 Gif-sur-Yvette, France
[2] LESIA, Observatoire de Paris, PSL University, CNRS, Sorbonne Université, Univ. Paris Diderot, Sorbonne Paris Cité, 5 place Jules Janssen, 92195 Meudon, France
[3] Instituut voor Sterrenkunde, KU Leuven, Celestijnenlaan 200D, 3001 Leuven, Belgium
[4] Dept. of Astrophysics, IMAPP, Radboud University Nijmegen, 6500 GL Nijmegen, The Netherlands

2 Magnetic frequency shifts

The formalism used to compute the magnetic frequency shifts is presented in Prat et al. (2019). This formalism is applied to a representative model of HD 43317, which is a magnetic, rapidly rotating, SPB star (Buysschaert et al. 2018). Figure 1 shows that the magnetic field generates sawtooth-like signatures on period spacing patterns. The key result is that these signatures are different from rotational or chemical signatures and can

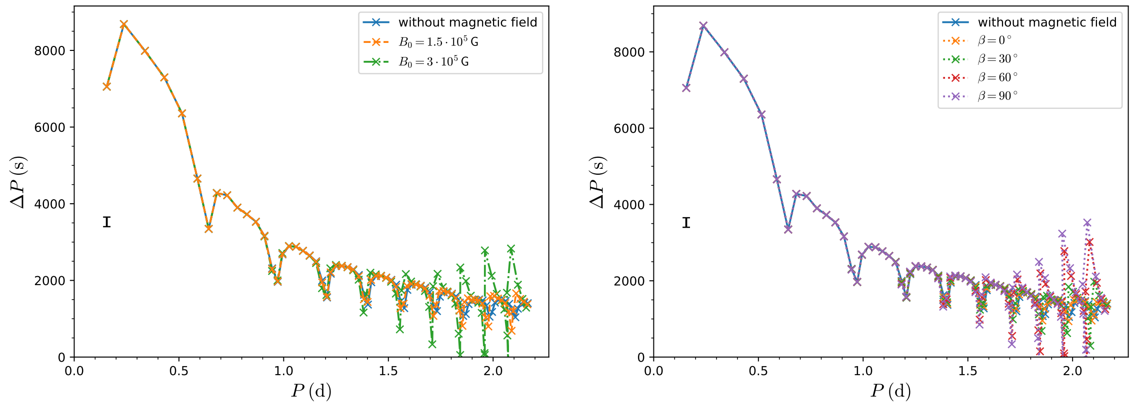

Fig. 1. Period spacings of dipole ($\ell = 1$) zonal ($m = 0$) gravity modes. **Left:** axisymmetric case with different magnetic field strengths. **Right:** oblique case with different obliquity angles for $B_0 = 10^5$ G. The error bar corresponds to typical uncertainties from a nominal Kepler light curve with a duration of 4 years.

thus be used to detect internal magnetic fields. As illustrated in Fig. 1, magnetic signatures scale with the square of the magnetic field strength, and they are also stronger for oblique fields, with a maximum for an obliquity angle of 90°.

3 Conclusions

This work shows that it should be possible to detect internal magnetic fields from asteroseismic measurements. To be able to constrain the properties of such fields, it is necessary to observe and identify a large number of low-frequency gravity modes. A similar technique could be used to extract additional information from Rossby modes. Future work will be dedicated to more complex magnetic configurations.

The research leading to these results received funding from the European Research Council (ERC) under the European Union's Horizon 2020 research and innovation program (grant agreements No. 647383: SPIRE with PI S.M. and No. 670519: MAMSIE with PI C.A.). V.P. and S.M. acknowledge support from the CNES PLATO grant at CEA/DAp.

References

Ballot, J., Lignières, F., Reese, D. R., & Rieutord, M. 2010, A&A, 518, A30
Buysschaert, B., Aerts, C., Bowman, D. M., et al. 2018, A&A, 616, A148
Duez, V., Braithwaite, J., & Mathis, S. 2010, ApJ, 724, L34
Fuller, J., Cantiello, M., Lecoanet, D., & Quataert, E. 2015, ApJ, 810, 101
Hasan, S. S., Zahn, J.-P., & Christensen-Dalsgaard, J. 2005, A&A, 444, L29
Loi, S. T. & Papaloizou, J. C. B. 2018, MNRAS, 477, 5338
Mathis, S., Decressin, T., Eggenberger, P., & Charbonnel, C. 2013, A&A, 558, A11
Ogilvie, G. I. & Lin, D. N. C. 2007, ApJ, 661, 1180
Prat, V., Mathis, S., Buysschaert, B., et al. 2019, A&A, 627, A64
Rogers, T. M. 2015, ApJ, 815, L30
Shibahashi, H. & Takata, M. 1993, PASJ, 45, 617
Talon, S. & Charbonnel, C. 2005, A&A, 440, 981
Van Reeth, T., Mombarg, J. S. G., Mathis, S., et al. 2018, A&A, 618, A24
Van Reeth, T., Tkachenko, A., & Aerts, C. 2016, A&A, 593, A120

Stars and their variability observed from space
C. Neiner, W. W. Weiss, D. Baade, R. E. Griffin, C. C. Lovekin, A. F. J. Moffat (eds)

DYNAMICAL MASS OF A TYPE II CEPHEID AND A DISK AROUND ITS BE STAR COMPANION

B. Pilecki[1]

Abstract. We present the main results of an analysis of a peculiar W Virginis (pWVir) type II Cepheid, OGLE-LMC-T2CEP-211 (P_{puls} = 9.393 d), in an SB2 binary system (P_{orb} = 242 d), which sheds light on the evolutionary status and structure of pWVir stars. We make the first-ever determination of the dynamical mass of a type-II Cepheid, M=0.64 ± 0.02 $M_{\odot}$, and its radius R=25.1 ± 0.3 $R_{\odot}$. The companion is a massive (5.67 $M_{\odot}$) main-sequence star that is partially obscured by a disk. Such a configuration suggests mass transfer in the system's history. We deduced that the system (P_{init}=12 d) was originally composed of stars of 3.5 $M_{\odot}$ and 2.8 $M_{\odot}$, the current Cepheid being the more massive. The system's age is now ∼200 Myr and the Cepheid is almost completely stripped of hydrogen, its helium mass being ∼92% of the total mass. The companion is most probably a Be main-sequence star with T=22000 K and R=2.5 $R_{\odot}$. The observations are consistent with our model of a three-ring disk (∼ 120 $R_{\odot}$) around the companion; however, a more complex structure of the disk, including a spiral formation, cannot be excluded. The disk probably originates from a combination of material from a past mass transfer, the mass being lost by the Cepheid through wind and pulsations, and a decretion disk around the rapidly-rotating secondary.

Keywords: Stars: variables: Cepheids, Stars: binaries: eclipsing, emission-line, Be, accretion, accretion disks

1 Introduction

Type II Cepheids are low-mass pulsating stars that belong to the disk and halo populations (Wallerstein 2002). They are a much older counterpart of the more massive classical Cepheids, which have periods and amplitudes in a similar range but are about 1.5–2 mag fainter. They exhibit a well-defined period–luminosity (P–L) relation (Leavitt 1908), enabling a measurement of distances both inside and outside our Galaxy (Groenewegen & Jurkovic 2017; Soszyński et al. 2018). Since the work of Gingold (1976, 1985), type II Cepheids have usually been divided into three subgroups (BL Her, W Vir and RV Tau); they are distinguished by different ranges of pulsation periods, observational properties and evolutionary status, but they obey a similar period–luminosity relation. However, Gingold did not explain either their occurrence rates or the values of their basic parameters, including their masses. The evolutionary status of W Vir stars is somewhat mysterious; some authors contradict the popular explanation (e.g. Pietrinferni et al. 2004).

It is clearly important to obtain direct measurements of the masses of a sample of type-II Cepheids in order to pinpoint their evolutionary status. The best sources of such measurements are observations of eclipsing binary systems in which one or both components are pulsating stars. We have applied this method to eclipsing binaries containing classical Cepheids, and obtained very precise masses (e.g. Pilecki et al. 2013, 2018b).

The OGLE project Soszyński et al. (2008, 2018) identified a group of W Virginis stars that had similar periods but different-looking light-curves, and called them "peculiar WVirginis stars" (hereafter pWVir). Since a significant fraction of pWVir stars shows eclipses and ellipsoidal modulations, it has been suggested that they are all members of binary systems.

The evolution of binary stars is also one of the most important channels for the formation of Be stars, as a lot of angular momentum has to be transferred to spin them up (Klement et al. 2019). The presence of a companion is also a crucial factor that shapes the disk around a Be star (Panoglou et al. 2019).

Up to now we have observed and analyzed two pWVir type II Cepheids that exhibit eclipses. OGLE-LMC-T2CEP-098 turned out to be an outlier that did not fit any known type of pulsating star, having a mass of 1.5 $M_{\odot}$ and a brightness in between those expected for classical and type II Cepheids (Pilecki et al. 2017). Below is a summary of the results published by Pilecki et al. (2018a) regarding a genuine type II Cepheid of a peculiar W Virginis type, OGLE-LMC-T2CEP-211. A complex disk structure (ringed or spiral) was also detected round it.

[1] Centrum Astronomiczne im. Mikołaja Kopernika, PAN, Bartycka 18, 00-716 Warsaw, Poland

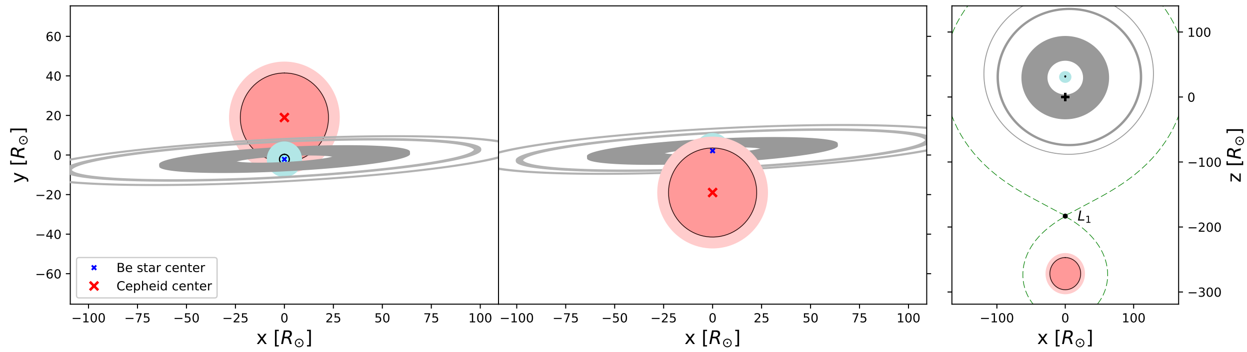

Fig. 1. Schematic model of the system. The Cepheid is in red, the companion in blue, and the rings of the disk in grey. The Roche lobe contours are plotted in the right panel.

2 Analysis of OGLE-LMC-T2CEP-098

2.1 *Detached binary: Cepheid + Be shell star with a disk.*

From the analysis of the light-curve and spectra of this Cepheid, we concluded that it is a giant (R=25.1 $R_\odot$) that undergoes a significant radius change during its pulsational cycle (light red area in Fig. 1), while its smaller companion is surrounded by a very extended (R $\sim$ 120 $R_\odot$) complex disk structure; our models suggest two or more rings, or a spiral structure. If we adopt the ring model, we find that the disk is tilted and slightly eccentric. The system is detached, so there is no fast mass transfer currently in the system, but accretion of the matter being lost through a wind from the companion is possible.

With the help of evolutionary theory, we also found that the companion is most probably a B-type dwarf (R=2.5 $R_\odot$) embedded in a bright shell ($\sim$9 $R_\odot$), suggesting a Be shell star and a decretion origin for the disk – or at least of its inner part.

2.2 *Hα and Hβ lines and the disk*

The broad Hα emission line clearly corresponds to the disk around the companion, and the absorption line to the companion itself, as can be seen in Fig. 2. The Cepheid seems relatively weak in Hα but stronger in Hβ, where both absorption and emission features of the disk are also seen.

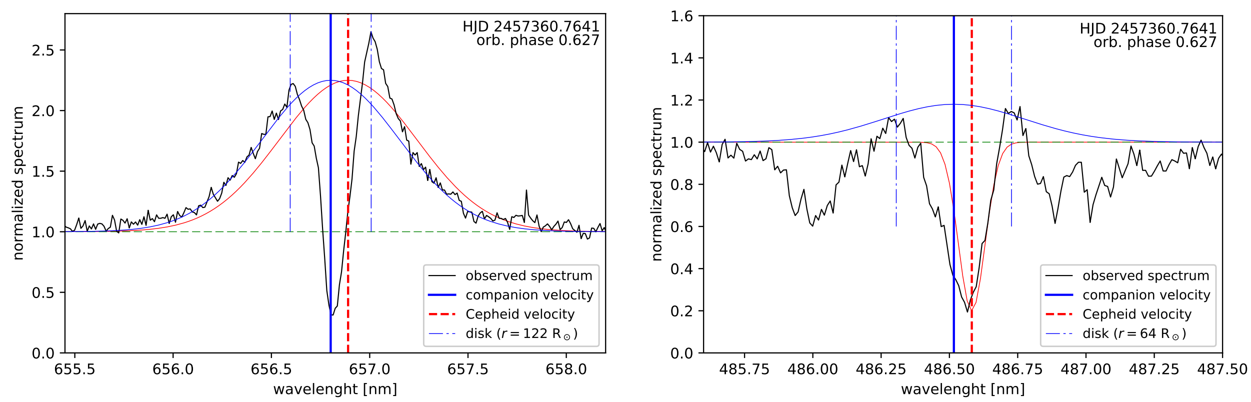

Fig. 2. The maxima of disk emission in Hα correspond roughly to the radius of the outer ring, while the maxima in Hβ correspond to the outer radius of the inner ring.

2.3 *The evolution*

The high mass ratio of the system indicates binary interaction (mass transfer) during its evolution. We performed a binary evolution analysis using the STARS code, with different initial conditions.

Table 5
Results from Binary Evolution Analysis

Parameter	Initial	Current	Measured
System			
Mass ratio	0.8 ± 0.03	7.87 ± 0.05	8.92 ± 0.05
Orbital period (days)	12.0 ± 0.7	180.8 ± 1.7	242.14 ± 0.04
β	⋯	0.0 ± 0.04	⋯
Primary Component/Currently Cepheid			
Spectral type	B5V	GIII	GIII
M_1 ($M_\odot$)	3.52 ± 0.12	0.715 ± 0.004	0.643 ± 0.015
R_1 ($R_\odot$)	1.91 ± 0.13	25.12 ± 0.12	25.1 ± 0.3
$\log g$ (cgs)	4.42 ± 0.06	1.491 ± 0.005	1.446 ± 0.015
T1 (K)	15700 ± 450	5410 ± 370	5400 ± 200
$\log L_1/L_\odot$	2.30 ± 0.05	2.65 ± 0.06	2.68 ± 0.07
Secondary Component			
Spectral type	B7V	B2V	⋯
M_2 ($M_\odot$)	2.82 ± 0.19	5.625 ± 0.005	5.67 ± 0.06
R_2 ($R_\odot$)	1.68 ± 0.12	2.51 ± 0.17	9 ± 2
$\log g$ (cgs)	4.44 ± 0.07	4.39 ± 0.06	⋯
T2 (K)	13700 ± 530	22000 ± 450	7000 ± 1000
$\log L_2/L_\odot$	1.95 ± 0.10	3.117 ± 0.011	⋯

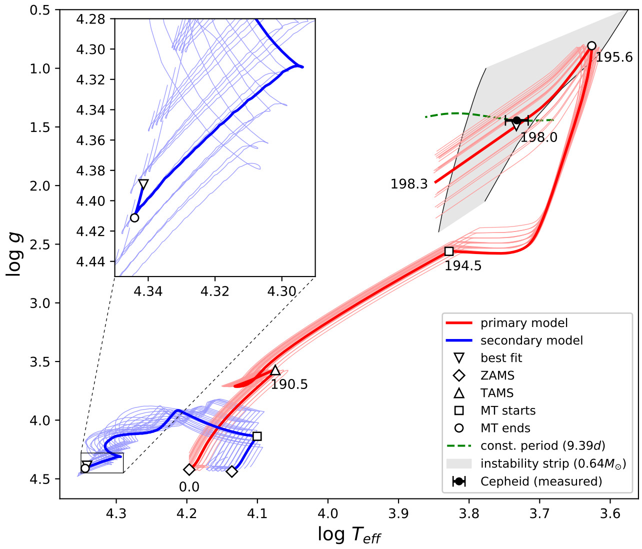

Fig. 3. Left: Table with the model, initial and current, and measured parameters. **Right:** Temperature *vs.* $\log g$ diagram, showing the evolutionary tracks of the primary (the current Cepheid) in red and the secondary (now probably a Be star) in blue. The Cepheid is now crossing the instability strip (grey area).

The analysis suggested that the system was initially composed of stars with masses of 3.5 $M_\odot$ and 2.8 $M_\odot$ and an orbital period of ∼12 days. Mass transfer started about 4 Myr after the Cepheid progenitor completed its main-sequence evolution. Mass transfer ceased about 2.5 Myr ago, and the Cepheid is now evolving towards lower temperatures and passing through the instability strip. In losing most of its mass, it has become almost completely depleted of hydrogen.

The companion never evolved from the main sequence, and should now be a B2 star with a radius of 2.5 $R_\odot$. According to the light-curve analysis, the bright component of the companion is much larger (∼9 $R_\odot$), which – together with the observed spectral features – indicates that the companion is a Be shell star.

Our evolutionary model suggests that this may be typical of the early stages of existence of Be stars, not long after the accretion from the previously more massive star has finished.

More information about this work is available at `https://users.camk.edu.pl/pilecki/`, where the data are also provided. See also the original publication, Pilecki et al. (2018a).

We gratefully acknowledge financial support for this work from the Polish National Science Center grant SONATA 2014/15/D/ST9/02248.

References

Gingold, R. A. 1976, ApJ, 204, 116
Gingold, R. A. 1985, Mem. Soc. Astron. Italiana, 56, 169
Groenewegen, M. A. T. & Jurkovic, M. I. 2017, A&A, 604, A29
Klement, R., Carciofi, A. C., Rivinius, T., et al. 2019, arXiv e-prints, arXiv:1909.12413
Leavitt, H. S. 1908, Annals of HCO, 60, 87
Panoglou, D., Borges Fernandes, M., Baade, D., et al. 2019, MNRAS, 486, 5139
Pietrinferni, A., Cassisi, S., Salaris, M., & Castelli, F. 2004, ApJ, 612, 168
Pilecki, B., Dervişoğlu, A., Gieren, W., et al. 2018a, ApJ, 868, 30
Pilecki, B., Gieren, W., Pietrzyński, G., et al. 2018b, ApJ, 862, 43
Pilecki, B., Gieren, W., Smolec, R., et al. 2017, ApJ, 842, 110
Pilecki, B., Graczyk, D., Pietrzyński, G., et al. 2013, MNRAS, 436, 953
Soszyński, I., Udalski, A., Szymański, M. K., et al. 2008, Acta Astron., 58, 293
Soszyński, I., Udalski, A., Szymański, M. K., et al. 2018, Acta Astron., 68, 89
Wallerstein, G. 2002, PASP, 114, 689

Stars and their variability observed from space
C. Neiner, W. W. Weiss, D. Baade, R. E. Griffin, C. C. Lovekin, A. F. J. Moffat (eds)

GALACTIC RED SUPERGIANTS IN GAIA DR2

M. Messineo[1] and A.G.A. Brown[2]

Abstract. We present the recently published catalogue of known Galactic late-type stars of luminosity class I that have a counterpart in the *Gaia* DR2 catalog.

Keywords: infrared: stars, stars: supergiants, evolution

1 Introduction

By the term "red supergiant" (RSG) astronomers usually refer to a star with a specific type of internal structure, and not just to its surface temperature or luminosity. RSG stars are cold massive stars "which do not develop a strongly electron-degenerate core until all exoergic reactions have run to completion at the centre" (Iben 1974). Temperatures are below 4200 K (K0), and may be even colder than 3000 K (e.g., μ Cep, whose spectral type is M7.5). Luminosities are typically above $\log(\frac{L}{L_\odot})= 4$, though the lower limit deepends on the treatment of rotation and convection; it can be as faint as $\log(\frac{L}{L_\odot})= 3.5$ (Ekström et al. 2012). RSGs are the brightest stars of a galaxy at infrared wavelengths being luminous and intrinsically cold, they are easily detectable at distances of a few megaparsecs. Their nucleosynthesis, stellar winds, and ultimate explosions as supernovae are fundamental processes for understanding a galaxy's chemical enrichment; they are tracers of star-formation episodes dating back 4.5–30 Myr. Despite their importance, we know only a small fraction of galactic RSGs; a census of them is seriously incomplete. Indeed, even though the Milky Way is the closest laboratory of resolved stellar populations, their detections are hampered by our location in the Disk, by dust obscuration in observations, and by uncertainties in distances. Furthermore, astronomical luminosity classes are observational quantities that cannot necessarily be translated into internal stellar structures, the major problem being the overlap in luminosity of RSGs and SGB stars.

We have searched in *Gaia* DR2 (Gaia Collaboration et al. 2018) for matches to the $\approx$ 1400 candidate Galactic RSGs collected and listed by Skiff (2014). We refer to these stars as candidate RSGs because they are reported in the literature at least once as cold stars of luminosity class I. In Messineo & Brown (2019) we published the catalog of known K–M class I stars with good quality Gaia DR2 parallaxes. We cross-matched the catalog with historical catalogs of RSGs, such as those of Humphreys (1978), Elias et al. (1985), and Jura & Kleinmann (1990) (the references are listed in the catalog). An average spectral type or recently revised spectral type was adopted for every entry, and the stellar temperature was estimated by assuming the temperature scale of Levesque et al. (2005). Parallaxes were found for 1342 stars, but after having applied a data filtering (RUWE $<$ 2.7 and $\varpi/\sigma_\varpi > 4$,see Lindegren et al. 2018)*), the sample was reduced to 889 stars.

Photometric measurements were retrieved from the 2MASS, CIO, MSX, WISE, MIPSGAL, GLIMPE and NOMAD catalogues; to validate the matches, we used positional distances as well as a visual inspection of the stellar energy distribution. By combining those magnitudes with the *Gaia* parallaxes, we were able to estimate the luminosities of the stars. We classified 30% of the stars as giants because their luminosities were fainter than the tip of the red-giant branch. We counted 43 stars (5%) brighter than $\log(\frac{L}{L_\odot})= 4.74$ (i.e., $M_{\rm bol}=-7.1$ mag), which is the AGB luminosity limit. By using the stellar tracks of Ekström et al. (2012) we estimated that at least the 41% of the stars that were brighter than $M_{\rm bol}= -5.0$ mag and of spectral type earlier than M4 were probably more massive than 7 $M_\odot$, making them probable RSGs. The catalogue treats the stars individually, but lists known associations with stellar clusters. Associations have traditionally been used to locate definite RSGs (e.g. Levesque et al. 2005), in the sense that a luminous and bright late-type star associated with a

[1] CAS Key Laboratory for Research in Galaxies and Cosmology, Department of Astronomy, University of Science and Technology of China, 96 Jinzhai Road, Hefei 230026, China

[2] Leiden University, Leiden Observatory, P.O. Box 9513, 2300 RA Leiden, The Netherlands

*see the online documentations *https://www.cosmos.esa.int/web/gaia/dr2-known-issues#AstrometryConsiderations*

population of evolved OB stars is certainly a massive star. Among the 889 stars with good parallaxes, 93 (10%) were associated with OB groups. Only 13% of all 1406 stras considered were reported as members.
The main focus of our exercise was to extract from *Gaia* DR2 a genuine sample of bright, luminous, cold stars. We derived the average magnitudes per spectral type and found that the stellar bolometric magnitudes correlated linearly with temperature in the range 3950–3600 K (see Fig. 1). We found that only 90 out of the 889 stars with good parallaxes (about 10%) were flagged as variables (Holl et al. 2018). Those variables tended to have later spectral types (K5–M7). 89 of them were classified automatically by the *Gaia* pipeline as long-period variables, showing an average variation in the G-band of 0.51 mag with a dispersion around the mean of 0.38 mag.

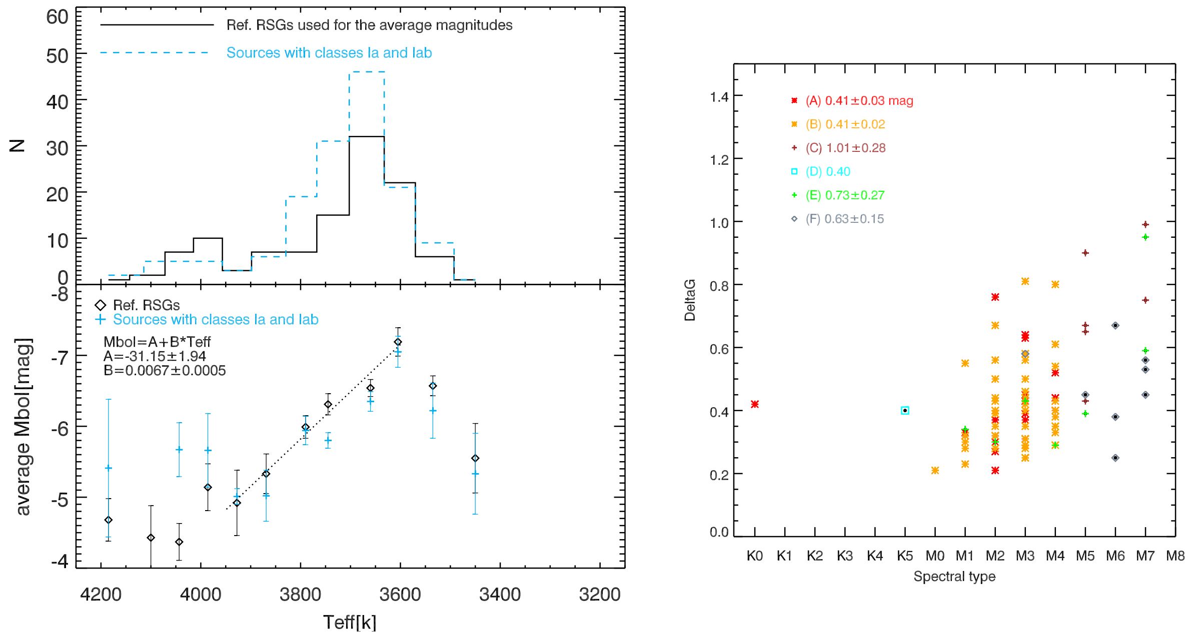

Fig. 1. Left Bottom panel: Average $M_{\rm bol}$ *vs.* $T_{\rm eff}$. Cyan crosses show the values for class Ia and Iab stars. Black diamonds indicate the values for the reference RSGs. **Left Top panel:** Histogram of the stars used to estimate the average magnitude per spectral type from stars with good parallaxes and $M_{\rm bol} < -3.6$ mag. **Right panel:** Differences beween the maximum and minimum magnitudes measured in G-band *vs.* spectral type. The legends list the average ΔG measured in the areas of the H–R diagram defined by Messineo & Brown (2019)

References

Ekström, S., Georgy, C., Eggenberger, P., et al. 2012, A&A, 537, A146
Elias, J. H., Frogel, J. A., & Humphreys, R. M. 1985, ApJS, 57, 91
Gaia Collaboration, Brown, A. G. A., Vallenari, A., et al. 2018, A&A, 616, A1
Holl, B., Audard, M., Nienartowicz, K., et al. 2018, A&A, 618, A30
Humphreys, R. M. 1978, ApJS, 38, 309
Iben, I., J. 1974, ARA&A, 12, 215
Jura, M. & Kleinmann, S. G. 1990, ApJS, 73, 769
Levesque, E. M., Massey, P., Olsen, K. A. G., et al. 2005, ApJ, 628, 973
Lindegren, L., Hernández, J., Bombrun, A., et al. 2018, A&A, 616, A2
Messineo, M. & Brown, A. G. A. 2019, AJ, 158, 20
Skiff, B. A. 2014, VizieR Online Data Catalog, B/mk

THE PULSATION SPECTRUM OF A MASS-ACCRETING COMPONENT OF AS ERI

D. Mkrtichian[1], K. Gunsriwiwat[2], C. Engelbrecht[3], N. A-thano[4], H. Lehmann[5], P. Lampens[6], J. Matthews[7], E. Rodriguez[8] and A. Kusakin[9]

Abstract. We present the results of pulsational analysis of ground-based multi-site and space (TESS and MOST) photometric and high-resolution spectroscopic (using SALT) observations of a mass-accreting pulsating A3V primary component of the semidetached Algol-type system AS Eri. We report about spectroscopic detection of high-degree nonradial modes in AS Eri.

Keywords: Stars: binaries: eclipsing, oscillations

1 Introduction

The 24.39 min pulsations of the primary component of the semi-detached 2.664148-day Algol-type system AS Eri have been discovered by Gamarova et al. (2000) and confirmed by Mkrtichian et al. (2004). The pulsator belongs to the class of mass-accreting pulsating components of Algols (so called oEA stars) (Mkrtichian et al. 2018) currently representing a group of over 100 pulsators (Mkrtichian et al. 2020).

2 Preliminary results of pulsational analysis

In 2013, AS Eri was observed during 41 days (582 orbits) by the MOST space telescope; these observations sampled only 10-15 % of orbital time. These observations in 2013 have been supported by two follow-up ground-based multisite photometric campaigns, first in 2014 (68 nights) was carried out using Skynet Robotic Telescope Network and second in 2018 (30 nights) using Prompt-8 telescope at CTIO, and finally completed by 27-day TESS observations. The analysis of TESS light curves revealed multi-periodic non-radial pulsations(NRPs). Fig. 1 shows the DFT spectrum of the pure pulsational light curve. We revealed a regular spacing of the six dominant modes with 3.75 c/d which is ten times the orbital/rotation frequency f_{orb}. The 2013 MOST and 2014 campaign data confirmed the results of TESS photometry.

High- and medium-resolution spectroscopic time series of AS Eri collected using 10m SALT/HRS and 2.4m Thai National Telescopes show strong line profile variations caused by high-degree non-radial modes (see Fig. 2). The full analysis of Least Square Deconvolved (LSD) line-profiles and the mode identification is in progress. One short run of SALT spectroscopy in 2018 has been obtained simultaneously with TESS telescope observations.

We found orbital phase dependent variability of the intensity and shape of the He I lines. The existence of strong He I is a good spectroscopic indicator of a hot turbulent zone in the upper atmosphere caused by interaction of a gas stream with the atmosphere of the pulsating gainer. Gas stream-atmosphere interaction is in good agreement with expectations from our 3-D hydrodynamic simulations of mass-transfer, which will be the topic of the future paper.

[1] National Astronomical Research Institute of Thailand, 50180 Chiang Mai, Thailand
[2] Department of Physics and Materials Science, Faculty of Science, Chiang Mai University, Thailand
[3] Department of Physics, University of Johannesburg, PO Box 524, Auckland Park, Johannesburg, South Africa
[4] Institute of Astronomy, National Tsing Hua University, Hsinchu 30013, Taiwan
[5] Thuṙinger Landessternwarte, D-07778 Tautenburg, Germany
[6] Koninklijke Sterrenwacht van Belgie, Brussel 1180, Belgium
[7] Department of Physics and Astronomy, University of British Columbia, Vancouver, BC V6T 1Z1, Canada
[8] Instituto de Astrofisica de Andalucia-CSIC, Glorieta de la Astonom'ia S/N, E-18008 Granada, Spain
[9] National Space Agency of the Republic of Kazakhstan, Fesenkov Astrophysical Institute, 050020, Kazakhstan

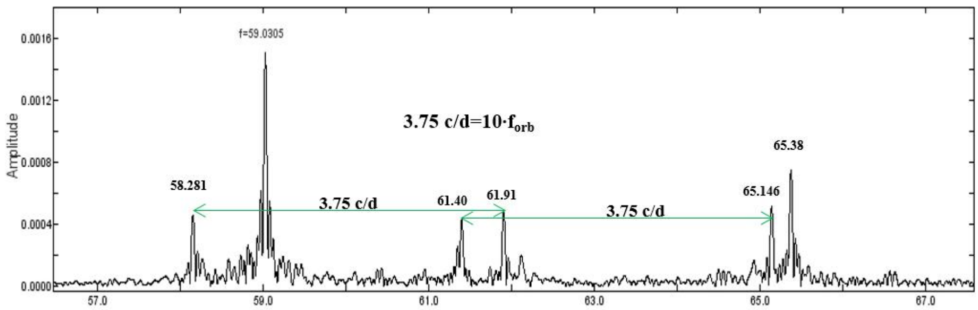

the ABSENCE of the extension .pdf !

Fig. 1. The DFT spectrum of the residual pulsational light curve of AS Eri

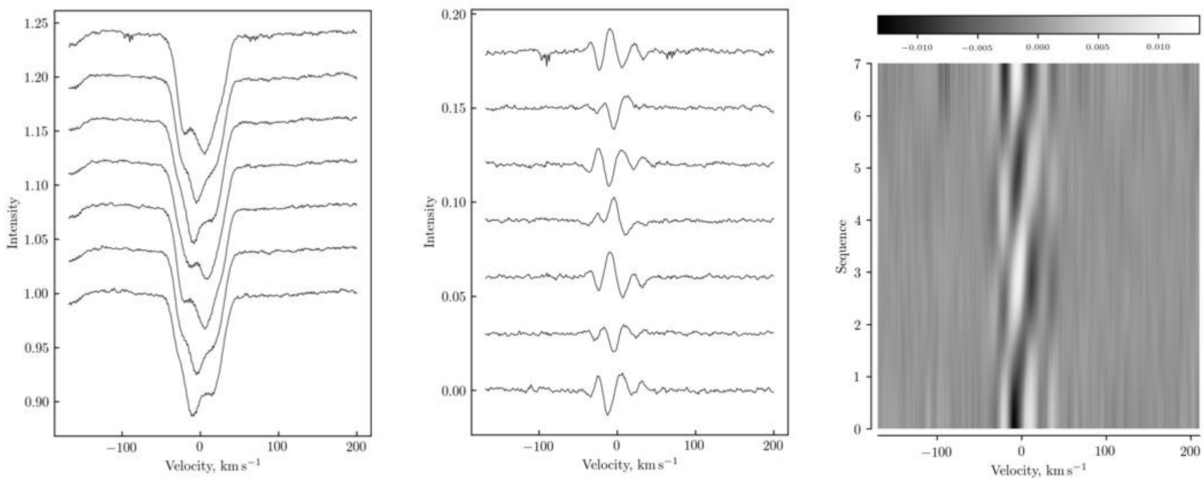

Fig. 2. The high-degree NRPs detected in LSD profiles of primary component of AS Eri

3 Conclusions

The photometric and spectroscopic line-profile analysis of AS Eri revealed the rich spectrum of low- and high degree non-radial modes. We found that the strong orbital phase dependent variability of He I lines is a sensitive indicatior of the mass-transfer and the gas stream atmosphere interaction.

References

Gamarova, A. Y., Mkrtichian, D. E., & Kusakin, A. V. 2000, IBVS, 4837, 1

Mkrtichian, D. E., Gunsriwiwat, G., & et al. 2020, (in preparation)

Mkrtichian, D. E., Kusakin, A. V., Rodriguez, E., et al. 2004, A&A, 419, 1015

Mkrtichian, D. E., Lehmann, H., Rodríguez, E., et al. 2018, MNRAS, 475, 4745

CEPHEIDS NEAR AND FAR

D. Tarczay-Nehéz[1,2], L. Szabados[1,2] and Z. Dencs[1,3]

Abstract. Cepheid variable stars play a fundamental role in astronomy because they are standard candles for calibrating the cosmic distance scale via the period-luminosity relationship. As of October 2019, Cepheids have been discovered in 97 galaxies beyond the Milky Way. The total number of known Cepheid variable stars now exceeds 20 000 (not counting the newly discovered ones announced in Gaia DR2). In this paper we presented our online database maintained at the web site of the Konkoly Observatory*.

Keywords: Stars: variables: Cepheids, Astronomical databases: miscellaneous, Galaxies: statistics, Stars: statistics, Galaxy: stellar content, (Cosmology:) distance scale

1 Introduction

Cepheid variable stars are pulsating supergiant stars, and are found in the classical instability strip of the Hertzsprung-Russell diagram. The first Cepheids in the Milky Way were discovered in the late 1700s by Pigott (1785) and Goodricke (1786). The first extragalactic Cepheids were discovered by Leavitt (1908). In the last hundred or more years a huge number of Cepheids have been discovered within about 40 Mpc. As their pulsation periods and luminosities are related through the so-called period-luminosity relationship (see Leavitt & Pickering 1912), they constitute the basis of the cosmic distance ladder.

A list of the hosting galaxies, their distance from the Milky Way and the number of known Cepheids (N) they contain is given in Table 1. In Fig. 1 the left panel shows the number of host galaxies as a function of distance. The riht panel indicates that the number of known Cepheids is inversely proportional to the distance of the galaxy; however, this is a selection effect caused by the fact that the discovery of brightness variability depends on the limiting magnitude of the photometry. The most distant galaxy known to host Cepheids is at about 40 Mpc from our Galaxy.

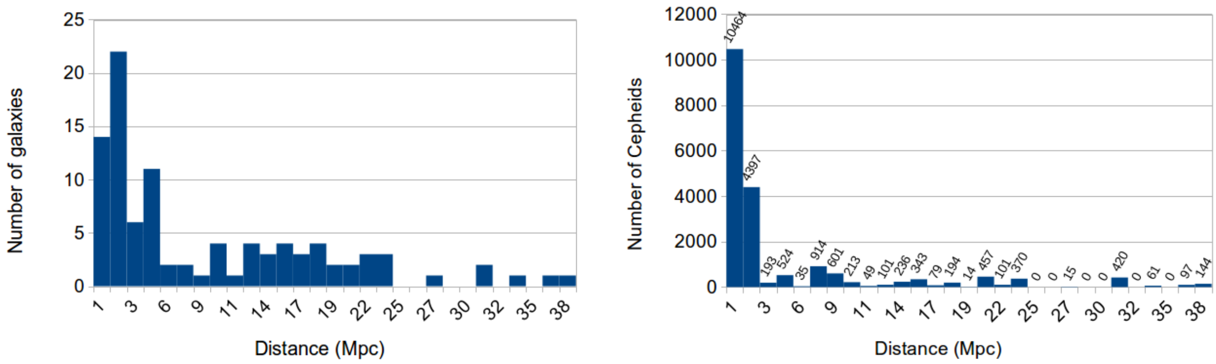

Fig. 1. Left: The number of host galaxies as a function of distance. **Right:** The number of known Cepheids beyond the Milky Way as a function of distance.

[1] Konkoly Observatory, Research Centre for Astronomy and Earth Sciences, MTA Centre of Excellence, Konkoly Thege Miklós 15-17, H-1121
[2] MTA CSFK Lendület Near-Field Cosmology Research Group
[3] Department of Astronomy, Eötvös University, H-1117
*`https://cepheids.konkoly.hu`

Galaxy	N	Distance (Mpc)	Galaxy	N	Distance (Mpc)	Galaxy	N	Distance (Mpc)
Milky Way	2807		NGC 3370	348	30.03	DDO 155	1	2.42
LMC	5122	0.03	NGC 3447	126	13.48	DDO 187	2	2.20
SMC	5102	0.05	NGC 3621	69	6.74	DDO 193	32	39.83
NGC 55	134	2.14	NGC 3627 (M66)	68	9.50	DDO 210	75	0.98
NGC 147	7	0.79	NGC 3972	78	12.87	DDO 216	39	0.92
NGC 185	13	0.63	NGC 3982	72	20.87	IC 10	5	0.67
NGC 205 (M110)	7	0.82	NGC 4038	58	13.79	IC 342	24	3.28
NGC 224 (M31)	2686	0.77	NGC 4258 (M106)	601	8.00	IC 1613	209	0.73
NGC 247	26	3.37	NGC 4321 (M100)	52	16.85	IC 4182	28	5.21
NGC 300	151	1.86	NGC 4395	11	4.29	Andromeda II	1	0.68
NGC 598 (M33)	747	0.84	NGC 4414	11	19.09	Andromeda III	5	0.75
NGC 925	80	9.28	NGC 4424	7	5.21	Andromeda VI	6	0.78
NGC 1015	27	36.15	NGC 4496A	95	22.67	Andromeda XIX	8	0.92
NGC 1309	172	36.76	NGC 4527	86	14.98	Andromeda XXI	9	0.86
NGC 1313	26	4.29	NGC 4535	50	16.59	Andromeda XXV	3	0.80
NGC 1326A	17	15.99	NGC 4536	153	14.92	Canes Venatici I	3	0.22
NGC 1365	95	20.83	NGC 4548 (M91)	24	19.30	Carina	22	0.03
NGC 1425	29	21.14	NGC 4571	3	17.77	Cetus	3	0.75
NGC 1448	89	16.85	NGC 4603	61	32.78	Draco	8	0.08
NGC 1637	41	9.19	NGC 4639	64	22.37	Fornax	31	0.14
NGC 2090	34	12.26	NGC 4725	20	12.26	Leo I	12	0.27
NGC 2366	6	3.06	NGC 5128 (Cen A)	51	4.29	Leo II	4	0.21
NGC 2403	17	2.45	NGC 5235 (M83)	112	4.60	Phoenix	24	0.44
NGC 2442	433	20.01	NGC 5253	15	3.34	Sagittarius	1	1.04
NGC 2541	34	12.26	NGC 5457 (M101)	845	6.43	Sculptor	4	3.49
NGC 2841	26	14.09	NGC 5584	212	22.06	Sextans	6	0.09
NGC 3021	72	30.64	NGC 5917	15	26.04	Sextans A	92	1.32
NGC 3031 (M81)	141	3.68	NGC 6822	157	0.49	Sextans B	8	1.36
NGC 3109	120	1.29	NGC 7250	29	15.32	Tucana	6	0.98
NGC 3198	78	14.40	NGC 7331	13	12.26	Ursa Minor	6	0.06
NGC 3319	33	16.24	NGC 7793	17	3.89	Wolf-Lundmark-Melotte	61	0.93
NGC 3351 (M95)	49	10.11	Holmberg II	7	3.37			
NGC 3368 (M96)	24	9.50	Leo A	156	0.80	I Zwicky 18	3	18.08

Table 1. Numbers of known Cepheids (N) in host galaxies, and the distances of the galaxies (Mpc).

2 Galactic Cepheids

Almost 15% (2807) of the known Cepheid variables have been found in the Milky Way Galaxy (Udalski et al. 2018). The distribution of Galactic Cepheids is shown in Fig. 2; however, that distribution does not include the newly discovered Cepheids announced in Gaia DR2 [†] (see Gaia Data Release 2 in Gaia Collaboration, Brown et al 2018).

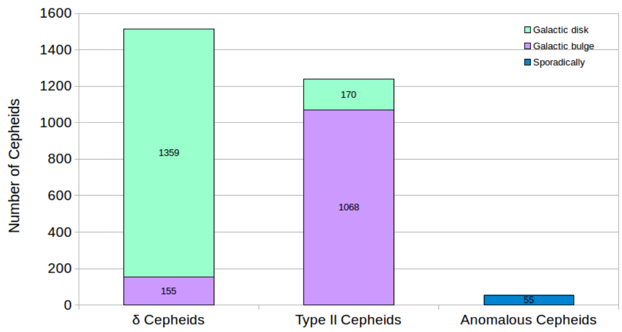

Fig. 2. Location of the known Cepheids in the Milky Way system.

- δ **Cepheids:** 54% (1514) of the Cepheids in the Milky Way are classical Cepheids and are mainly located in the Galactic disk.

[†]`https://www.cosmos.esa.int/web/gaia/dr2`

- **Type II Cepheids:** 44% (1238) of the Cepheids in the Milky Way are metal-poor type II Cepheids, and are located mainly in the Galactic bulge.

- **Anomalous Cepheids:** 2% (55) of the Cepheids in the Milky Way are anomalous Cepheids, and are located sporadically in the Galaxy.

3 Extragalactic Cepheids

The number of known Cepheid variables as a function of distance is shown in the right panel of Fig. 1. It can easily be seen that almost 75% (~15000) of the Cepheids beyond the Milky Way are found in the Local Group. More than 51% (10224) of the known extragalactic Cepheid variables are located in the Magellanic Clouds. As to the numbers of known Cepheids, the 10 host galaxies beyond the Milky Way containing the most Cepheidsare listed in Table 2.

Galaxy	N	% of $N_{\rm all}$ [a]	Distance (Mpc)
LMC	5122	25.6	0.03
SMC	5102	25.5	0.05
M31	2686	13.4	0.77
M101	845	4.2	6.43
M33	747	3.7	0.84
M106	601	3	8.00
NGC 2442	433	2.1	20.01
NGC 3370	348	1.7	30.03
NGC 5584	212	1.1	22.06
IC 1613	209	1	0.73

[a] Percentages of the known extragalactic Cepheids: $N/N_{\rm all}$.

Table 2. The ten galaxies beyond the Milky Way containing the largest number of known Cepheids.

4 Conclusion

When investigating the periods of Cepheids in each host galaxy, we found that the more distant the galaxy, the longer the mean value of the period of Cepheids (see Fig. 3). However, that effect can be explained as a selection effect in the way the Cepheids were discovered. According to the period-luminosity relation, the more luminous the Cepheid, the longer its pulsation period. That emphasizes the importance of observing distant galaxies with higher sensitivity in order to search for short-period Cepheids among the fainter stars.

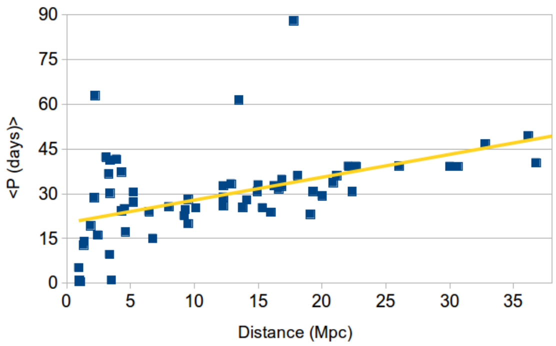

Fig. 3. The distribution of the mean values of periods of Cepheids per galaxy as a function of distance.

Technical help from Nikolett Szalai, András Holl and Mihály Váradi is gratefully acknowledged. We also acknowledge financial support from the Momentum grant No. LP2018-7/2019 of the Hungarian Academy of Sciences. We are also grateful for financial support of the Hungarian OTKA Grant No. 119993 and the Hungarian NKFIH projects K-115709 and K-129249.

References

Gaia Collaboration, Brown, A. G. A., Vallenari, A., et al. 2018, A&A, 616, A1
Goodricke, J. 1786, Philosophical Transactions of the Royal Society of London Series I, 76, 48
Leavitt, H. S. 1908, Annals of HCO, 60, 87
Leavitt, H. S. & Pickering, E. C. 1912, HCO Circular, 173, 1
Pigott, E. 1785, Philosophical Transactions of the Royal Society of London Series I, 75, 127
Udalski, A., Soszyński, I., Pietrukowicz, P., et al. 2018, Acta Astron., 68, 315

Stars and their variability observed from space
C. Neiner, W. W. Weiss, D. Baade, R. E. Griffin, C. C. Lovekin, A. F. J. Moffat (eds)

SCIENCE WITH BRITE-CONSTELLATION AT THE UNIVERSITY OF INNSBRUCK

K. Zwintz[1], R. Kuschnig[2], C. Arnold[1], F. Brüser[1], M. J. Dornacher[1], S. Gössl[1], A. Ivanov[1], M. Mayerl[1], M. Müller[1], M. Müllner[1], S. Panny[1], A. M. Stanciu[1], T. Steindl[1], A. Thaler[1], D. Weßmayer[1] and S. Zieba[1]

Abstract. At the University of Innsbruck, BRITE-Constellation data of several types of variable stars are analyzed together with students as part of their bachelor theses or as course work during lectures. Here we show an overview of our recent team work including γ Doradus and δ Scuti stars as well as some stars showing variability caused by spots.

Keywords: Stars: variables: delta Scuti, Stars: variables: gamma Doradus, Stars: rotation

1 Data Reduction & Analysis

The raw BRITE photometry was corrected for instrumental effects including outlier rejection, and 1D and 2D decorrelations with all available parameters, in accordance with the procedure described by Pigulski (2018). The frequency analysis of the reduced and decorrelated BRITE photometric time series was performed using the software package Period04 (Lenz & Breger 2005). Frequencies were prewhitened and considered to be significant if their amplitudes exceeded 3.8 times the local noise level in the amplitude spectrum (e.g., Kuschnig et al. 1997). The analysis was verified using the iterative prewhitening method based on the Lomb-Scargle periodogram (Van Reeth et al. 2015).

2 γ Doradus stars

Three seasons of BRITE-Constellation observations of QW Puppis (HD 55892) were obtained in 2015, 2016/17, and 2017/18 with time bases of ~78 days, ~225 days, and ~167 days. 20 g-mode pulsation frequencies ranging from 0.7 to 3.6 d^{-1} were identified. A first investigation yielded a clear period spacing pattern with a mean ΔP of 3246 seconds.

For 39 Pegasi (HD 213617) single season observations in 2017 provided a time base of ~88 days. First signs for g-mode period spacings can be seen, but a longer time base is needed for a more detailed investigation.

3 δ Scuti stars

3.1 The δ Scuti star β Pictoris

β Pictoris was observed in two colors in the same three subsequent seasons by BRITE-Constellation as QW Puppis, i.e., from 2015 to 2018 with time bases of ~78 days, ~225 days, and ~167 days (see Zwintz et al. 2019). 15 significant pulsation frequencies were identified from the BRITE data. Additionally, a variability of the amplitudes of two of the pulsation frequencies was detected (Zwintz et al. 2019).

3.2 δ Scuti stars in the Taurus field

BRITE-Constellation observations of the Taurus field collected from September 2017 to March 2018 included nine δ Scuti stars. One of the δ Scuti pulsators in the Taurus field is the A7 star θ^2 Tauri with 14 identified pulsation frequencies in the range from 10 to 15 d^{-1}. (M. Müller, Bachelor thesis, University of Innsbruck).

[1] Universität Innsbruck, Institut für Astro- und Teilchenphysik, Technikerstraße 25, A-6020 Innsbruck, Austria
[2] Institut für Kommunikationsnetze und Satellitenkommunikation, Technical University Graz, Inffeldgasse 12, A-8010 Graz, Austria

4 Spotted stars

In the 45 fields observed by BRITE-Constellation since 2013, a wealth of stars showing rotational modulation caused by spots on the surfaces was observed. Many of these objects lacked precise photometric time series to derive the rotation periods. Such data are necessary to plan further spectroscopic and spectropolarimetric observations to study the distribution of chemical abundances on the surfaces, investigate chemical peculiarities, and measure potential magnetic fields. All present data have been downloaded from the BRITE-Constellation Public Data Archive*. 13 stars showing rotational modulation were analyzed as course work by a team of enthusiastic students that are also listed as co-authors of this article. Figure 1 shows the BRITE-Constellation data for five of these stars as examples. Future work will focus on the analysis of complementary spectroscopic data and a common interpretation with the BRITE photometry.

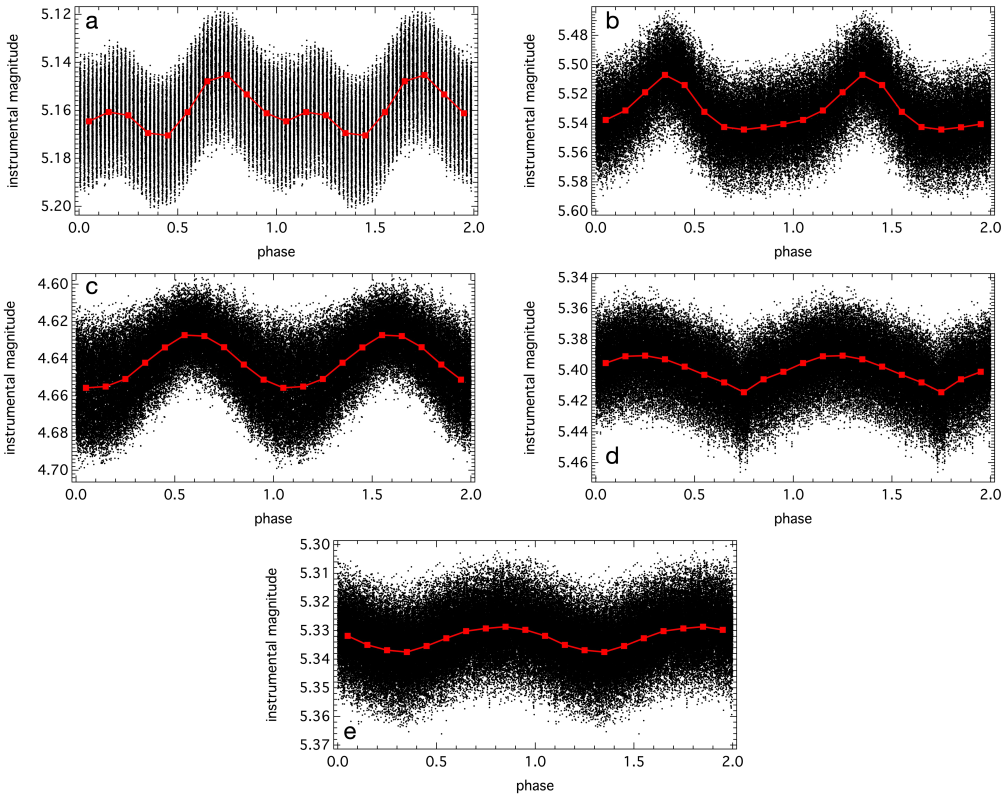

Fig. 1. Examples of spotted stars observed with BRITE-Constellation: Phase plots for the stars (a) HD 54118 (A0pSi), (b) HD 92664 (ApSi), (c) HD 64503 (B2), (d) HD 69144 (B2.5), (e) HD 99556 (B3).

References

Kuschnig, R., Weiss, W. W., Gruber, R., Bely, P. Y., & Jenkner, H. 1997, A&A, 328, 544
Lenz, P. & Breger, M. 2005, Communications in Asteroseismology, 146, 53
Pigulski, A. 2018, in 3rd BRITE Science Conference, Vol. 8, 175–192
Van Reeth, T., Tkachenko, A., Aerts, C., et al. 2015, A&A, 574, A17
Zwintz, K., Reese, D. R., Neiner, C., et al. 2019, A&A, 627, A28

*https://brite.camk.edu.pl/pub/index.html

Stars and their variability observed from space
C. Neiner, W. W. Weiss, D. Baade, R. E. Griffin, C. C. Lovekin, A. F. J. Moffat (eds)

LONG-TERM *BRITE* AND *SMEI* SPACE PHOTOMETRY OF γ CAS (B0.5 IVe)

C. C. Borre[1], D. Baade[2], A. Pigulski[3], A. Weiss[4], T. Rivinius[5] and The BRITE Team

Abstract. For years, the first Be star discovered, γ Cas, had only one short period known. Because that period falls into the range of possible rotation periods, it was assumed that it was really the rotation period. Space photometry has now found multiperiodicity that is best understood as multi-mode nonradial pulsation, thereby leaving the rotational hypothesis (and other assumptions built around it) less well founded.

Keywords: Stars: emission-line, Be, oscillations, individual: γ Cas

1 Introduction

Classical Be stars rotate typically at ∼80% of the critical velocity (Rivinius et al. 2013), eject material when multiple nonradial pulsation (NRP) modes interact (Baade et al. 2018), form Keplerian decretion disks from the ejecta in a viscous process (Lee et al. 1991), and exhibit no large-scale magnetic fields (0/97 detections by Wade et al. 2016). γ Cas was the first emission-line star discovered (Secchi 1866); it possesses an unseen $\sim 1\,M_\odot$ companion in a circular 203.5-d orbit (Nemravová et al. 2012), is the prototype of a ∼1% sub-population of Be stars with peculiar hard X-ray emission and spectral types B0.5–B1.5 (Smith et al. 2016), and has for years exhibited optical mmag variability with a frequency of 0.82 c/d (Henry & Smith 2012). Smith et al. (2016) have suggested that 0.82 c/d is the frequency of (critical) rotation. They went on to assume the existence of two magnetic fields, one due to a subsurface convection zone in the star and the other produced by magneto-rotational instability (MRI) in the circumstellar disk. In the picture painted by Smith et al. (2016), X-rays are produced when particles hit the star after the two magnetic fields have reconnected after a temporary rupture, and thereby accelerate matter. The stellar property that is thought to be modulated by rotation and giving rise to the 0.82 c/d photometric variability is left unidentified, and the spatial scales of the two magnetic fields are stated to be too small to be detectable. It is therefore, by design, impossible to design an observational experiment that can verify or falsify the proposed rotation-based and magnetic description of γ Cas.

Most Be stars pulsate in multiple NRP modes (Rivinius et al. 2003). The range in amplitude is large, and amplitudes can vary on time-scales of weeks to years so non-detections may only be a matter of insufficient sensitivity and/or time coverage. In many of these stars, the observed NRP frequencies straddle the range into which global stellar parameters would place the rotation frequency (e.g., Baade et al. 2017; Semaan et al. 2018); however, in no case has it been possible to prove that a frequency is actually rotational. Therefore, if it can be shown that γ Cas, also exhibits multiple frequencies, NRP would be the most likely common interpretation, and it would be less justified to assign a completely different nature to one of them. In any event, if stellar frequencies differ by a large factor, not all of them can be due to (differential) rotation. For the detection of multiple low-amplitude variabilities, the method of choice is photometry from space.

2 Observations and analysis

Observations by the Automated Photometric Telescope (APT) (∼7,800 and ∼7,900 measurements in the B and V passbands, respectively), which were obtained between 1997 and 2011 and analyzed by Henry & Smith (2012), were downloaded through VizieR (Ochsenbein et al. 2000). Even without a comprehensive and very complex preprocessing similar to that applied by Henry & Smith (2012), the 0.82 c/d frequency (referred to

[1] Stellar Astrophysics Centre, Aarhus University, Denmark; e-mail: cborre@phys.au.dk
[2] European Organisation for Astronomical Research in the Southern Hemisphere (ESO), Garching b. München, Germany
[3] Instytut Astronomiczny, Uniwersytet Wrocławski, Poland
[4] Max-Planck-Institut für Astrophysik, Garching b. München, Germany
[5] European Organisation for Astronomical Research in the Southern Hemisphere (ESO), Santiago, Chile

below as f_1) was easily recovered. However, there were no other significant peaks in the APT power spectrum thus calculated. In addition, archival observations with SMEI (Jackson et al. 2004), which extending from 2004 to 2011 (and therefore fully overlapping the APT data) were also studied. The SMEI database, kindly made available (to D.B.)by B. Jackson, permits the observations to be investigated separately for the three cameras. The Camera 3 data were discarded because the noise was too high. In the 38,500 or so measurements with the other two cameras, f_1 was clearly detected, and the strong decline in amplitude reported by Henry & Smith (2012) was confirmed. Furthermore, another frequency appeared in the analysis at $f_2 \sim 1.25\,\mathrm{c/d}$ with Camera 2 but only marginally in Camera 1. More periodic variabilities may exist but do not stand out strongly above the presumed noise.

New observations were obtained with *BRITE*-Constellation (Weiss et al. 2014). All five *BRITE* satellites (up to three in parallel) observed γ Cas in four seasons from 2015–2018/19 and accumulated a total of ~4,500 orbit-averaged data points. Frequency f_1 had not returned at the time of these observations, but there were hints of f_2. By far the strongest signal persisted at $f_3 = 2.48\,\mathrm{c/d}$. Because the data strings are long, the frequency determinations are precise enough to establish the following numerical inequalities: $f_3 \neq 3 \times f_1$ and $f_3 \neq 2 \times f_2$. That is, there are no harmonic relations between these three frequencies.

3 Discussion and conclusions

Although the individual datasets used in this study do not have ideal noise properties (most notably for SMEI), the detection of all frequencies with completely independent equipment leaves little room for doubts as to their reality. Their values are consistent with NRP frequencies found in other early-type Be stars (e.g., Baade et al. 2017; Semaan et al. 2018). The simultaneous presence of frequencies differing by a large factor demonstrates that at least two of them are, in fact, due to nonradial pulsations. Since rotational modulation is not an established property of Be stars, the rotational-modulation hypothesis for γ Cas is not convincing. In that regard, γ Cas therefore no longer differs from the large majority of Be stars. Accordingly, γ Cas might once more be considered prototypical of Be stars; the explanation of the peculiar X-ray properties may be found in its binary evolution (Langer et al. 2019). High-cadence spectroscopy is the most promising method for determining the nature of f_1 unambiguously.

A full account of this work, which also includes the recovery of the orbital 203.5-d period from a time-series analysis of 300+ archival Hα profiles, has been submitted to *Astronomy & Astrophysics*.

Based on data collected by the BRITE Constellation satellite mission, designed, built, launched, operated and supported by the Austrian Research Promotion Agency (FFG), the University of Vienna, the Technical University of Graz, the University of Innsbruck, the Canadian Space Agency (CSA), the University of Toronto Institute for Aerospace Studies (UTIAS), the Foundation for Polish Science & Technology (FNiTP MNiSW), and the National Science Centre (NCN).

References

Baade, D., Rivinius, T., Pigulski, A., et al. 2017, in Second BRITE-Constellation Science Conference: Small satellites—big science, Vol. 5, 196–205

Baade, D., Rivinius, T., Pigulski, A., et al. 2018, in 3rd BRITE Science Conference, Vol. 8, 69–76

Henry, G. W. & Smith, M. A. 2012, ApJ, 760, 10

Jackson, B. V., Buffington, A., Hick, P. P., et al. 2004, Sol. Phys., 225, 177

Langer, N., Baade, D., Bodensteiner, J., et al. 2019, arXiv e-prints, arXiv:1911.06508

Lee, U., Osaki, Y., & Saio, H. 1991, MNRAS, 250, 432

Nemravová, J., Harmanec, P., Koubský, P., et al. 2012, A&A, 537, A59

Ochsenbein, F., Bauer, P., & Marcout, J. 2000, A&AS, 143, 23

Rivinius, T., Baade, D., & Štefl, S. 2003, A&A, 411, 229

Rivinius, T., Carciofi, A. C., & Martayan, C. 2013, A&A Rev., 21, 69

Secchi, A. 1866, AN, 68, 63

Semaan, T., Hubert, A. M., Zorec, J., et al. 2018, A&A, 613, A70

Smith, M. A., Lopes de Oliveira, R., & Motch, C. 2016, Advances in Space Research, 58, 782

Wade, G. A., Petit, V., Grunhut, J. H., Neiner, C., & MiMeS Collaboration. 2016, in ASP Conf. Series, Vol. 506, Bright Emissaries: Be Stars as Messengers of Star-Disk Physics, ed. T. A. A. Sigut & C. E. Jones, 207

Weiss, W. W., Rucinski, S. M., Moffat, A. F. J., et al. 2014, PASP, 126, 573

Variability other than pulsation

Stars and their variability observed from space
C. Neiner, W. W. Weiss, D. Baade, R. E. Griffin, C. C. Lovekin, A. F. J. Moffat (eds)

CHEOPS & STARS (& ASTEROSEISMOLOGY)

S. Barceló Forteza[1], A. Moya[2], A. Bonfanti[3], S.J.A.J. Salmon[3], V. Van Grootel[3] and D. Barrado[1]

Abstract. The characterization of exoplanets has been considerably improved during the last decade mainly through space missions (*Kepler*/*K2*, *CoRoT*) and also the characterization of their host stars by stellar seismology. Nowadays, *TESS* and *CHEOPS* are the only two important missions that will provide short-cadence high-precision photometric time-series for a large amount of targets. This project explored the asteroseismic potential of *CHEOPS* light-curves. For that purpose, we analysed the probability of detecting solar-like pulsations, and the accuracy we could obtain for estimates of the seismic indices for the expected targets, observing time and expected duty cycle of this mission. Our results suggested that we can determine the frequency at maximum power for evolved and/or massive F-G-K solar-like stars with an uncertainty better than 5%. Asteroseismology therefore enables us to decrease age, mass, radius and density uncertainties significantly in the characterization of exoplanet host stars.

Keywords: stars: fundamental parameters, stars: solar-type, asteroseismology

1 Introduction

CHEOPS (Fortier et al. 2014) will be the next ESA space mission to study transiting exoplanetary systems accurately. Moya et al. (2018) explored the asteroseismic potential of this mission. Asteroseismology enables us to determine the structural parameters of the host stars with higher precision than do other techniques, improving the characterization of the exoplanetary system. For that reason, we estimated the detectability potential of solar-like pulsations in each region of the H–R diagram. In addition, we studied the accuracy we can reach in determining the frequency at maximum power for different observing times and duty cycles. Finally, we analysed the benefits we can derive through accurate seismic analyses with *CHEOPS* light-curves.

2 Detectability potential

To estimate the detectability potential of solar-like pulsations, we analysed the probability of a Gaussian-like power excess to differ statistically from noise in the frequency power spectrum. First of all, using semi-empirical relations and stellar models, we estimated the expected strength of stellar pulsations in the power spectrum:

$$P_{tot} = \frac{1}{2} c A_{\max}^2 \eta^2(\nu_{\max}) D^{-2} \frac{W}{\Delta\nu} \text{ ppm}^2, \tag{2.1}$$

where $\Delta\nu$ is the large separation, $\nu_{\max}$ is the frequency at maximum power, W is the pulsational frequency range, and $A_{\max}$ is the expected maximum amplitude of the radial modes (l = 0) in parts per million (ppm),

$$A_{\max} = A_{\max,\odot} \beta(T_{\rm eff}) \left(\frac{R}{R_\odot}\right)^2 \left(\frac{T_{\rm eff}}{T_{\rm eff,\odot}}\right)^{\frac{1}{2}} \text{ ppm}\,. \tag{2.2}$$

The values of these variables depend on the fundamental parameters of the models such as radius (R) and temperature of the star ($T_{\rm eff}$). The factor c measures the mean number of modes per $\Delta\nu$ segment and depends on the observed wavelength. Since the *CHEOPS* bandpass is similar to that of *Kepler* (see Fig.1 and Gaidos et al. 2017), we have used $c \sim 3.1$ (Chaplin et al. 2011). The attenuation factor, $\eta^2(\nu)$, takes into account the non-zero integration time that affects the measurement of the signal. The dilution factor $D \sim 1$ for an isolated object. In this study we focussed on this isolated star case.

[1] Dpto. Astrofísica, Centro de Astrobiología (CSIC-INTA), ESAC campus, Camino Bajo del Castillo s/n, 28692, Villanueva de la Cañada, Spain.
[2] Electrical Engineering, Electronics, Automation and Applied Physics Department, E.T.S.I.D.I, Polytechnic University of Madrid (UPM), Madrid 28012, Spain
[3] Space sciences, Technologies and Astrophysics Research (STAR) Institute, Université de Liège, Allée du Six Août 19C, B-4000, Liège, Belgium.

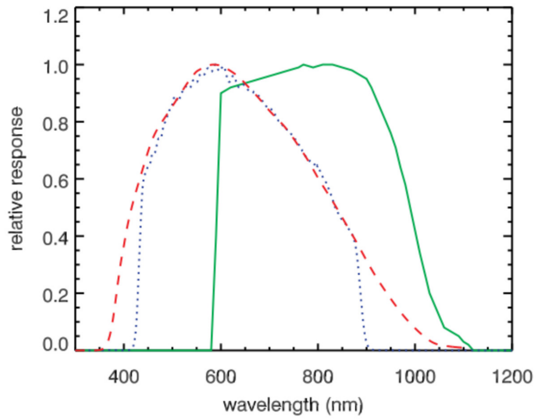

Fig. 1. The predicted or established response functions of *TESS* (solid green), *Kepler* (dotted blue), and *CHEOPS* (dashed red), all normalized to unit maximum. See Gaidos et al. (2017).

Next, we estimated the background power coming from different sources:

$$B_{tot} \approx W\,(b_{instr} + P_{gran})\ ppm^2, \tag{2.3}$$

where b_{instr} is the instrumental noise and P_{gran} the stellar granulation power. The instrumental noise follows the form

$$b_{instr} \approx 2 \times 10^{-6} \sigma \Delta t\, ppm^2 \mu Hz, \tag{2.4}$$

where σ is the *CHEOPS* predicted RMS noise per given exposure time (t_{exp}) and Δt is the integration time. The final RMS noise value mainly depends on the stellar magnitude (*CHEOPS* Red Book, 2013), the exposure time, and the integration time. Since *CHEOPS* adds and downloads images every 60 seconds we worked with only one integration time of 60 sec. Table 1 shows the instrumental RMS for three different stellar magnitudes (V = 6, 9, and 12), with three corresponding exposure times (1, 10, and 60 s, respectively). Those values were our reference values.

Table 1. Instrumental noise of *CHEOPS* for $\Delta t \sim 60$s.

V	t_{exp} (s)	σ (ppm)
6	1	44
9	10	165
12	60	623

To calculate the stellar granulation noise we use

$$P_{gran} = \eta^2(\nu_{\max}) D^{-2} \sum_{i=1}^{2} \frac{\frac{2\sqrt{2}}{\pi}\frac{a_i^2}{b_i}}{1 + (\frac{\nu_{\max}}{b_i})^4}\, ppm^2 \mu Hz \tag{2.5}$$

from Kallinger et al. (2014), where all parameters depend on $\nu_{\max}$ in the following way

$$\begin{aligned} a_i &\propto \nu_{\max}^{-0.6}\,, \\ b_i &\propto \nu_{\max}\,. \end{aligned} \tag{2.6}$$

For a detailed explanation of the origin and assumptions of these expressions, we refer to Moya et al. (2018) for *CHEOPS*, Chaplin et al. (2011) for *Kepler* and Campante et al. (2016) for *TESS*.

Because of the dependencies of the signal-to-noise ratio ($S/N = P_{tot}/B_{tot}$), the probability to detect solar-like oscillations depends on the structural parameters (M, R, $T_{\rm eff}$). But it also depends on the observing time (T), since the number of bins with information on the power excess in the frequency domain is $N = W\,T$. In addition, we want to ensure cover of at least one entire period of each expected solar-like pulsation. Therefore,

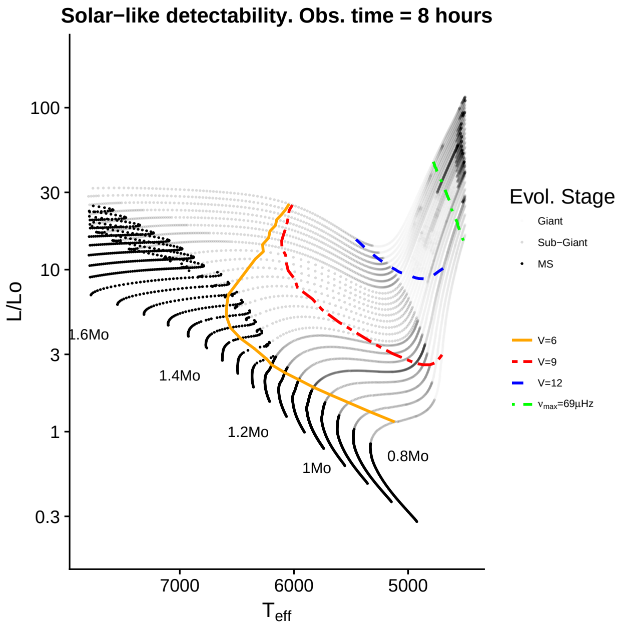

Fig. 2. H–R diagram showing the region where $\nu_{\rm max}$ can be determined, using 8 hours of observing time. Black/dark grey/light grey points are the models of the stars in different evolutionary stages: main-sequence, subgiant and giant stars. The limits of $\nu_{\rm max}$ detections are represented by orange solid/red dashed/blue dashed-dotted lines for different apparent magnitudes ($V \sim 6, 9, 12$). The green line represents the limit for a correct cover of all pulsations.

another condition to study properly the power excess is $T \geq 2/\nu_{\rm max}$.

In that way, we calculated for each model the probability of a given excess to differ statistically from noise; Fig. 2 shows the detection limits for $T \sim 8$ hours and our three reference values of stellar magnitude. Each star inside the limited regions has a potentially detectable $\nu_{\rm max}$. We note that the largest regions of the H–R diagram can be analysed for the brightest stars. In the opposite way, we can make the same study but for fixed stellar magnitude and variable observing times (see Fig. 3). For the longest observing times, the largest regions can then be studied and the longest periods can also be analysed. Fig. 3 also shows (green triangles) the position in the H–R diagram of the 169 exoplanet host-stars located in the ecliptic plane and which can be studied by *CHEOPS*, and weakly covered by *TESS* if so. Each of its panels shows those stars with apparent magnitudes between those presented in the plot (big triangles) and those of the following plot (small triangles).

In summary, *CHEOPS* can potentially obtain the seismic index $\nu_{\rm max}$ for post- and main -sequence F-G-K stars. Depending on the observing time, tens of stars with planets can be properly characterized.

3 Impact of duty cycle on determinations of $\nu_{\rm max}$

The observing time T has a major impact on the information obtained in the frequency domain. Since the time per target will be of the order of hours or a few days, it is not possible to obtain the parameters of individual modes. Nevertheless, it is sufficient for obtaining the frequency of maximum power. In addition, the duty cycle produces spurious signals that, *a priori*, may affect the determination of this seismic index. We studied the impact of the observing time and duty cycle upon the determination of $\nu_{\rm max}$.

To study the dependencies of the accuracy upon those parameters, we analysed a group of short-cadence (SC) *Kepler* light-curves of well-studied stars in different evolutionary stages. From those, we could simulate shorter light-curves with lower duty cycles from 60 to 90%. We used CHEOPSim tool in order to obtain the expected duty cycle produced by the South Atlantic Anomaly and Earth occultation. We filled each of the gaps with a linear fit.

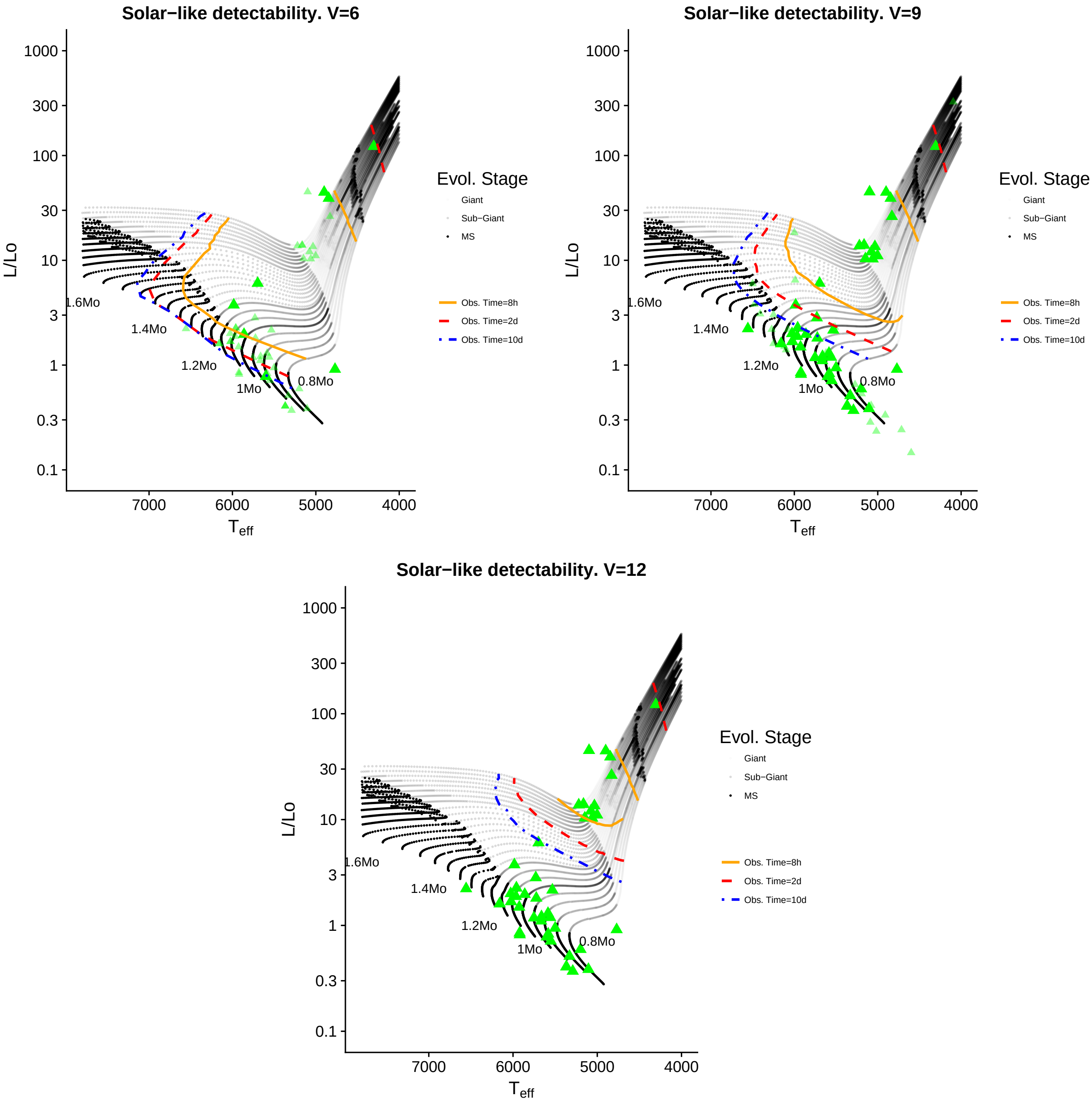

Fig. 3. Top left panel: Same as Fig. 2 but with the stellar magnitude fixed at $V \sim 6$, and using different observing times. The limits of $\nu_{\rm max}$ detection are represented by orange solid/red dashed/blue dashed-dotted lines for observing times of 8 hours, 2 days, and 10 days, respectively. Big green triangles indicate the positions of the currently known planet-hosting stars in the ecliptic plane, with $V < 6$. Small and more transparent green triangles are host stars with magnitudes between $6 < V < 9$. **Top right and bottom panel:** Same as top left panel but for stars with $V \sim 9$ and $V \sim 12$, respectively. The big/small green triangles are brighter/fainter than the specified magnitudes.

To calculate $\nu_{\rm max}$, we used the weighted mean frequency (Kallinger et al. 2010):

$$\nu_{\rm max} = \frac{\sum A_i \nu_i}{\sum A_i}\,, \tag{3.1}$$

where ν_i and A_i are the frequency and the amplitude of each peak of the power excess. We tested the accuracy of the method by comparing the results with the values in the literature for the stars in our sample (e.g. Lund et al. 2017). Fig. 4 shows the relative error of $\nu_{\rm max}$ for three different stars, one per evolutionary stage tested, in 1-day runs with an 80% duty cycle. Although some measurements can have a considerably large relative error, the mean relative error is appropriate (the red lines in this Figure).

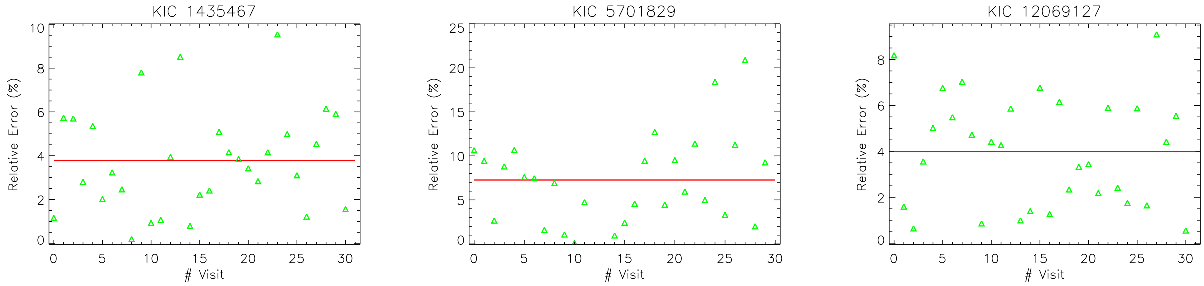

Fig. 4. Relative error of $\nu_{\max}$ calculated for 1-day runs with an 80% duty cycle. Shown here are the results for a main-sequence star, a subgiant and a red giant, respectively. Each green triangle points to significant detections. The red line represents the mean relative error of $\nu_{\max}$ for each star.

Once we had calculated the mean relative error for all stars, we repeated the process for several observing times and duty cycles (see Fig. 5). Our results showed that, in general, the longer the duty cycle and the observing time, the smaller the mean and maximum relative error. The mean relative error ranges from ∼2% for 30-day and 100% duty cycle to ∼4% in the case of 1-day run and 60% duty cycle. The mean maximum error is 11% in this last case. There are no large variations in accuracy for different observing times or duty cycles. However, planning several runs is recommended in order to discard individual measurements that may have large errors. Moreover, it is not worth proposing observing ranges longer than 4 days if several runs are planned. The improvement of maximum and mean relative errors achieved in those cases is non-significant*.

4 Benefits of asteroseismology

To characterize a star, we want to obtain its parameters such as effective temperature (T_{eff}), metallicity ([Fe/H]), and surface gravity ($\log g$), usually from spectroscopy. Using asteroseismic $\nu_{\max}$ with a mean relative error of 5%, we can obtain an independent measure of $\log g$ that is four times more accurate than the spectroscopic value (Moya et al. 2018). Moreover, it is also possible to improve the mean uncertainties of other stellar parameters such as mass (from 2.1% to 1.8%), radius (from 1.8% to 1.6%), density (from 5.6% to 4.7%), and age (from 52% to 38%). These improvements become more significant if we study star-by-star, especially ones beyond the main-sequence turn-off. For example, KIC 5701829 has an age uncertainty of 45% from spectroscopy but only 18% from asteroseismology. Apart from improvements in stellar uncertainties, asteroseismology enables us to remove stellar pulsation signals, so this technique is also useful for improving the accuracy of modelling exoplanet transits.

5 Conclusions

Asteroseismology offers us an open window for improving the characterization of some exoplanet(s)-hosting stars and their observed transits. The main advantage is that the seismic analysis can be done with the planned observing strategy and technical characteristics of *CHEOPS*. However, it is only possible for massive and/or post-MS stars. As expected, the longer the observing time, the larger the range of stars that can potentially be characterised with asteroseismology.
The large accuracy achieved for $\nu_{\max}$ measurements is sufficient to determine stellar $\log g$ and other stellar characteristics such as age, mass and radius precisely. Unfortunately, this is the only seismic parameter measurable. In any case, it will be helpful for removing the main pulsational signal from the time series.
There are two observational strategies possible: to use comprehensive monitoring of some targets with potentially observable pulsations, and to fill some gaps by monitoring the most interesting targets when not in transit

*We repeated this analysis for δ Scuti stars instead of solar-like pulsators. The mean relative error was around 5% for observing times down to a few hours and duty cycles higher than 70%. A relative error lower than 10% (5%) was guaranteed for 1-(2-)day light-curves. See Moya et al. (2018) for further details.

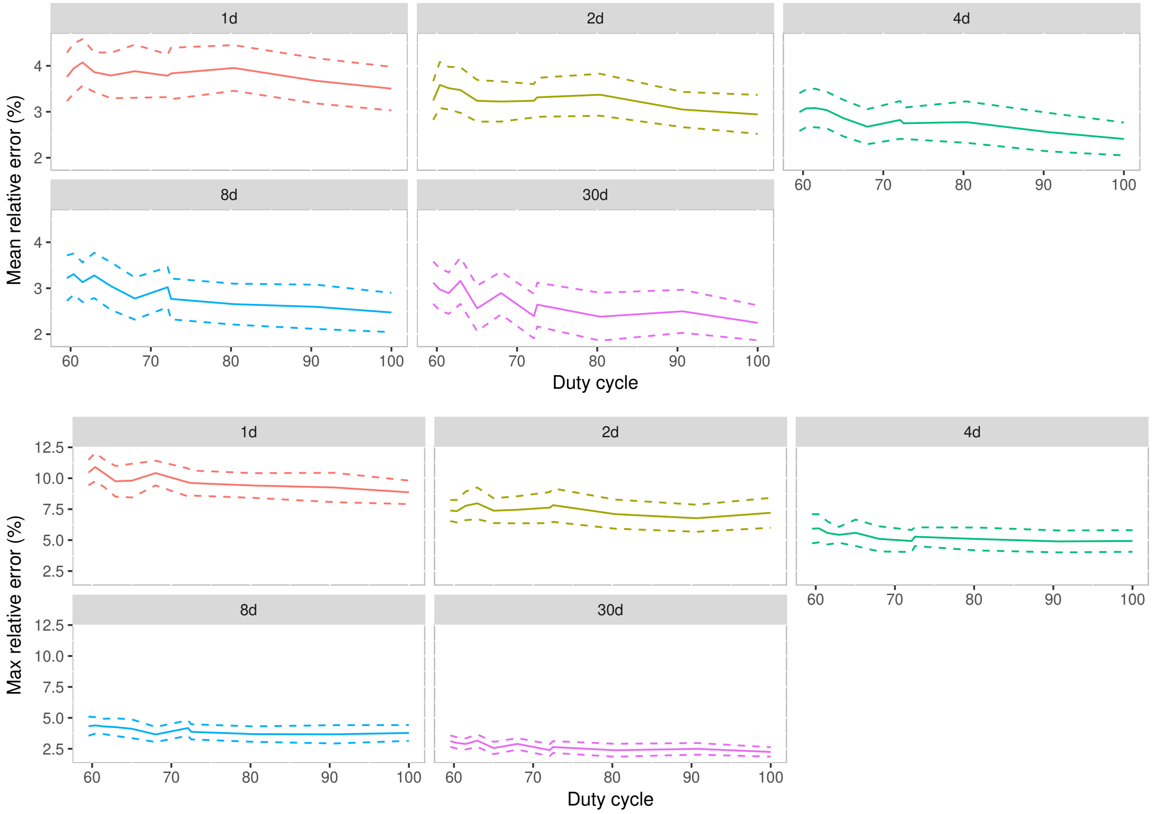

Fig. 5. Top (Bottom) panels: Mean (maximum) relative error according to the duty cycle for different observing times. Dashed lines are their standard deviations.

for at least 8 hours.

SBF and DB acknowledge support by the Spanish State Research Agency (AEI) Projects No.ESP2017-87676-C5-1-R and No. MDM-2017-0737 Unidad de Excelencia María de Maeztu- Centro de Astrobiología (INTA-CSIC). AM acknowledges funding from the EU Horizon 2020 research and innovation programme under the Marie Curie grant agreement no. 749962 (project THOT).

References

Campante, T. L., Schofield, M., Kuszlewicz, J. S., et al. 2016, ApJ, 830, 138

Chaplin, W. J., Kjeldsen, H., Bedding, T. R., et al. 2011, ApJ, 732, 54

Fortier, A., Beck, T., Benz, W., et al. 2014, in SPIE Conference Series, Vol. 9143, Proc. SPIE, 91432J

Gaidos, E., Kitzmann, D., & Heng, K. 2017, MNRAS, 468, 3418

Kallinger, T., De Ridder, J., Hekker, S., et al. 2014, A&A, 570, A41

Kallinger, T., Weiss, W. W., Barban, C., et al. 2010, A&A, 509, A77

Lund, M. N., Silva Aguirre, V., Davies, G. R., et al. 2017, ApJ, 835, 172

Moya, A., Barceló Forteza, S., Bonfanti, A., et al. 2018, A&A, 620, A203

Stars and their variability observed from space
C. Neiner, W. W. Weiss, D. Baade, R. E. Griffin, C. C. Lovekin, A. F. J. Moffat (eds)

EARLY-TYPE MAGNETIC STARS: THE ROTATION CHALLENGE

G. Mathys[1]

Abstract. Large-scale organised magnetic fields of the order of kG are present in 5–10% of upper main-sequence stars. The rotation periods of those stars span up to five or six orders of magnitude, with no evidence for evolution besides conservation of angular momentum during their main-sequence lifetimes. Explaining how period differentiation over such a wide range is achieved in stars that are effectively at the same evolutionary stage represents a major challenge. To address it, improved knowledge of the distribution of the rotation periods is a pre-requisite. Space missions have already enabled considerable progress to be achieved in the study of periods of days to months, and they will continue to do so in the coming years. They can also contribute usefully to the identification of slowly rotating stars. However, ground-based observations lend themselves better to monitoring the longest periods. The most extreme among the latter, which may reach decades to centuries, are of particular interest, but constraining them is also the most challenging endeavour. Recent progress in this area is reviewed, and future prospects and concerns are discussed.

Keywords: Stars: magnetic field, Stars: rotation, Stars: early-type, Stars: chemically peculiar

1 Introduction

Large-scale organised magnetic fields of ∼100 to a few 10^4 G are present in 5–10% of the early-type stars. To first order, in almost all of them the predominant component of the magnetic field resembles a dipole whose axis is inclined at an angle β to the stellar rotation axis. Periodic magnetic variations are observed as the result of the changing aspect of the visible stellar hemisphere as the start rotates, but the fields do not show any intrinsic variations on time-scales of many stellar rotation periods. The magnetic fields of the early-type stars are generally believed to be fossil fields, that is, fields that were acquired at the time of the formation of the stars, or during their early pre-main-sequence evolution, and frozen in.

The magnetic early-type stars rotate more slowly on average than the non-magnetic stars of the same spectral types. Their rotation periods can be determined directly from consideration of their magnetic variations and/or of related variations of other observables, such as their magnitude in various photometric bands and the intensities of their spectral lines. Indeed, to a large extent, the magnetic field defines inhomogeneities of stellar properties such as brightness and elemental abundances over the stellar surface. These inhomogeneities also have a certain degree of symmetry about the magnetic axis, the magnetic early-type stars are oblique rotators. As a result, the changing aspect of the visible stellar hemisphere as the star rotates manifests itself observationally through strictly periodic photometric, spectroscopic and magnetic variations, whose single common period is the rotation period of the star.

The rotation periods of the magnetic early-type stars range from a fraction of a day to several centuries. To first order, their distribution is similar for the different types of magnetic early-type stars: the Ap and Bp stars, the early-type B stars, and the O-type stars (Shultz et al. 2018). The five to six orders of magnitude spanned by this distribution represent a major challenge for theory: how and when does the period differentiation take place? Answering this question is relevant for the understanding of the formation and evolution of *all* early-type stars.

The Ap (and Bp) stars constitute the best studied group of early-type magnetic stars. They were the first stars, apart from the Sun, in which magnetic fields were detected (Babcock 1947), and for several decades they remained the only non-degenerate stars in which the presence of such fields was definitely established. They still represent, by far, the largest fraction of the magnetic early-type stars that are known to this day, and the number of them whose rotation periods have been determined accurately vastly exceeds the number of other magnetic early-type stars with a known rotation period.

[1] European Southern Observatory, Alonso de Cordova 3107, Vitacura, Santiago, Chile

This review therefore discusses relevant aspects of our current knowledge of the "classical" Ap stars, most of which have spectral types between F0 and B8, in relation to the challenge of understanding the differentiation of their rotation. To a large extent, the insight that is gained from consideration of these stars should be applicable to all magnetic early-type stars.

It has long been known that, as a group, Ap stars rotate more slowly than superficially normal stars with similar temperatures (e.g., Preston 1974, and references therein). The existence of Ap stars with very long periods, from more than 100 d to several years, was also recognised long ago (Preston 1970a). This realisation was made possible by the fact that Ap stars are oblique rotators. The anticorrelation between the variation period and the stellar equatorial velocity was demonstrated convincingly by Preston (1971).

That the rotation rates of the Ap stars can be determined directly from the observation of their periodic variations contrasts with the prevailing situation for most other stellar types, for which the knowledge of rotation is based on the consideration of the projected equatorial velocity, $v \sin i$, and is therefore limited by the ambiguity introduced through the inclination (i) of the rotation axis to the line of sight, since it is generally unknown. Furthermore, the lowest value of $v \sin i$ that can be determined reliably with a typical high-resolution spectrograph ($R \sim 10^5$) is of the order of $3\,\mathrm{km\,s^{-1}}$. For an Ap star, that corresponds to a rotation period that does not exceed ∼50 d. In what follows, we refer to Ap stars with rotation periods longer than 50 d as the 'super-slowly rotating' Ap (ssrAp) stars.

2 Period distribution

The number of Ap stars for which the rotation period is known has increased dramatically in recent years through the exploitation of the results of various photometric surveys. That includes both ground-based surveys such as ASAS-3 (Bernhard et al. 2015a; Hümmerich et al. 2016) and SuperWASP (Bernhard et al. 2015b), and space surveys such as *STEREO* (Wraight et al. 2012), *Kepler* (Hümmerich et al. 2018), and *TESS* (Sikora et al. 2019), for which data acquisition is still on-going and exploitation of the results is only starting. While the most recent systematic study of the distribution of the rotation periods of Ap stars (Netopil et al. 2017) confirms that the majority have rotation periods between 2 and 10 days, it also clearly shows an extended, nearly flat, tail of super-slow rotators. However, ivestiations of photometric variation are poorly suited to study this long-period tail, which (as explained above) is also beyond the reach of spectroscopic line-broadening studies.

With Doppler broadening below the spectroscopic resolution limit, the spectral lines of stars that have strong enough magnetic fields are resolved observationally into their magnetically split components. The wavelength separation is proportional to the mean magnetic field modulus $\langle B \rangle$, that is, the average over the visible stellar disk of the modulus of the magnetic vector, weighted by the local emergent line intensity. The value, already realised 50 years ago (Preston 1970b), of studying the rotational variation of $\langle B \rangle$ to constrain the geometrical structure of the magnetic fields of Ap stars, motivated the undertaking of systematic efforts to identify Ap stars with resolved magnetically split lines and to study the variations of their mean magnetic field moduli over their rotation periods (Mathys et al. 1997; Mathys 2017, and references therein).

While the existence of ssrAp stars had already been recognised by Preston (1970a), the number of such stars that were known remained small for a long time. Many more have been identified in the past two decades, mostly among the newly found stars with magnetically resolved lines. The majority of the latter are genuine slow rotators (as opposed to faster rotating stars seen at a low inclination angle i). From consideration of the distribution of their periods, Mathys (2017) concluded that several percent of all Ap stars must have rotation periods longer than 1 yr, that the periods of some of them must definitely be of the order of 300 yr, and that there may even exist Ap stars with much longer rotation periods, perhaps ∼1000 yr or more. Since the periods of the fastest rotating Ap stars are of the order of half a day (Netopil et al. 2017), this implies that the rotation periods of the Ap stars span five to six orders of magnitude.

Ap stars lose at most a small amount of their angular momentum on the main sequence (Kochukhov & Bagnulo 2006; Hubrig et al. 2007). The evolutionary changes of their rotation periods during their main-sequence lifetimes do not exceed a factor of 2, so the differentiation of their periods must mostly have been achieved before they arrived on the main sequence, or even before their progenitors become observable as magnetic Herbig Ae/Be stars (Alecian et al. 2013). The way in which this happens is unclear, and more observational constraints are needed to guide the theoretical developments. The differentiation of the rotation in Ap stars is potentially one of the main keys to the understanding of their origin and of the origin of their magnetic fields.

Within this context, the study of the ssrAp stars is particularly valuable, not only to characterise better the long-period tail of the distribution of the rotation periods, but also because, as the most extreme examples of the slow rotation of Ap stars, they have the potential to provide the most valuable insight into the mechanisms responsible for this generic property of the class.

3 The longest periods

The first determination of the period of variation of an Ap star (α^2 CVn = HD 112413, $P_{\rm rot} = 5.5$ d) was achieved just over one century ago (Belopolsky 1913). Hardly more than 70 years have elapsed since the first detection of a magnetic field in a star of this type (78 Vir = HD 118022, Babcock 1947). It has been almost 50 years since Preston (1970c) compiled the first list of Ap stars that may have long periods, raising the interest in studying such stars. The systematic study of the Ap stars with resolved magnetically split lines led to the conclusion that the ssrAp stars represent a more considerable fraction of the Ap population than was generally believed until then (Mathys 2017). The initiation of this project itself arose from the realisation a little more than 25 years ago of the potential interest of the many Ap stars with magnetically resolved lines that had not been identified yet, much less studied in detail (Mathys & Lanz 1992). These time-scales are longer than the time-bases over which observations have been obtained until now for most ssrAp stars, but still considerably shorter than the rotation periods of many of them. Accordingly, to date only a limited fraction of the super-slow rotators have been observed over a full cycle (or more), making an accurate determination of their rotation periods possible. For the others, still in majority, only lower limits of the periods are currently known, and those must be of the same order as the time-base of the available observations.

More specifically, to the best of our knowledge accurate periods have been determined for 33 ssrAp stars (Mathys 2019). Eight of those periods are longer than 1000 d (Mathys et al. 2019c); the 29 yr period of HD 50169 (Mathys et al. 2019a) is the longest of them. This is at least ten times shorter than the period lengths of 300 yr or more whose occurrence appears inescapable from statistical arguments (Mathys 2017). Among the stars for which only a lower limit of the value of the period is known until now, HD 201601 (= γ Equ) has been monitored for the longest time; the available magnetic measurements span $\sim$70 years. Extrapolating from them suggests that the rotation period of this star cannot be significantly shorter than 97 yr (Bychkov et al. 2016). Consideration of these numbers emphasises the incompleteness of our current knowledge of the distribution of the periods of the most slowly rotating Ap stars. Progress in this area will, by nature, be incremental, because the only way to increase the time base over which relevant observations are available is to await the passage of time. But as observations covering a full rotation cycle are obtained for a growing number of stars, each increase in the value of the longest accurately-determined period will be of the order of a few years. However, in the meantime, it should be possible, and valuable, to improve considerably our knowledge of the distribution of the less extreme rotation periods – say, between 50 days and ten years.

Of the 33 ssrAp stars whose rotation periods have been determined accurately, 18 show resolved magnetically split lines. The spectral lines of another four are definitely very sharp, and do not show any hint of resolution into their magnetic components. We could not find any published measurements of the magnetic field of the remaining 11 stars, nor any high spectral-resolution observation in public observatory archives. The longest rotation period that has been derived to date for an Ap star in which magnetically resolved lines have not been observed (yet) is 236.5 d. The 13 longest periods that have been determined accurately to this day pertain to Ap stars with resolved magnetically split lines. There are different factors that may account for this situation, either individually or in combination with each other.

The vast majority of the known rotation periods of Ap stars have been determined through analyses of their photometric variations. As already stated, this technique is ill-suited for long periods. The latter are best derived from consideration of the variations of the mean magnetic-field modulus, or of the mean longitudinal magnetic field ($\langle B_z \rangle$, the line-intensity weighted average, over the visible stellar disk, of the component of the magnetic vector along the line of sight), or of both. Indeed the ratio of the amplitude of variation of these field moments to the uncertainties affecting their measurements is in general much higher than the ratio of the photometric variation amplitudes to the photometric measurement errors. Furthermore, the magnetic measurements are seldom affected by long-term drifts or other lack of reproducibility that tend to occur frequently in photometric observations. This is especially true for $\langle B \rangle$ determinations, which are obtained from straightforward measurements of relative wavelength shifts of line components in classical high-resolution spectra. As $\langle B_z \rangle$ is diagnosed from the circular polarisation of spectral lines, the derived values may occasionally be affected by systematic instrumental effects, especially when combining observations obtained with different instruments. But for slowly rotating stars, these systematic effects tend to be limited and are often considerably smaller than the variation amplitudes.

Naturally, the stronger the magnetic field, the easier its detection and the higher the relative precision with which it can be measured. Therefore, using magnetic variation curves to constrain the rotation periods of the most strongly magnetic Ap stars is particularly convenient. Conversely, the scientific interest of Ap stars with spectral lines resolved into their magnetically split components and the systematic efforts that were made to identify and study such stars (see Sect. 2) led to the discovery of a large number of super-slow rotators, whose sometimes extremely long periods rather exceeded expectation. Undoubtedly, the combination of these two factors implies that the distribution of the magnetic fields in the ssrAp stars that are currently known is significantly biased towards the stronger ones. However, this does not rule out the possible existence of a difference between strongly and weakly magnetic Ap stars with respect to the rate of occurrence of super-slow rotation. In the course of our systematic search for Ap stars with resolved magnetically split lines, we identified a considerable number of stars whose spectral line profiles hardly differ, if at all, from the instrumental profile of the spectrograph used for their observation. In other words, the spectra of those stars do not show any significant Doppler or magnetic line broadening. If – as appears to be the case for Ap stars with magnetically resolved lines – the inclination angles of the rotation axes of these stars with respect to the line of sight are random, then the majority of them must be super-slow rotators. These stars may potentially represent a significant fraction of the group of ssrAp stars, which has been mostly overlooked until now. The distribution of their rotation periods may or may not be similar to that of their more strongly magnetic counterparts. In particular, the question is open as to whether some of the weakly magnetic stars have periods reaching several hundred years. This question is particularly relevant in relation to the apparent exclusion of very strong magnetic fields in Ap stars whose rotation periods exceed ∼150 d, for which very strong statistical evidence was presented by Mathys et al. (1997) and by Mathys (2017).

More generally, any correlation that may exist between the rotation period and the magnetic properties of the ssrAp stars may potentially provide essential clues for the theoretical understanding of the formation and evolution of these stars. This requires the distribution of the rotation periods to be constrained across the whole range of magnetic field strengths, including the lowest ones. Together with S. Hubrig, we recently recorded circularly polarised HARPS spectra of a number of the above-mentioned Ap stars with very sharp, unresolved lines that we had identified in our systematic search for Ap stars with resolved magnetically split lines. All of them show very definite Stokes V signatures, which confirmed fully the feasibility of using the variations of their mean longitudinal magnetic fields to constrain their rotation periods. We are now preparing to undertake a project to carry out systematic, multi-epoch $\langle B_z \rangle$ determinations of all the known Ap stars with sharp, unresolved spectral lines, with a view to constraining the distribution of their rotation periods.

4 Rate of occurrence of super-slow rotation

Our current knowledge of the overall rate of occurrence of ssrAp stars is limited by the biases affecting the existing studies of the longest period stars, which were discussed in Sect. 3. This has significantly hampered theoretical developments, as a complete and accurate knowledge of the distribution of the rotation periods represents an essential constraint for the models. The *TESS* Mission has presented an opportunity to overcome those biases to a large extent. Indeed, an exhaustive list of Ap stars was proposed for observation by *TESS* during the nominal mission (Cunha et al. 2019). Ultimately not all were observed, but the selection was based on the overall priorities of the mission, not on the properties of the Ap targets, so it is unbiased with respect to those properties. ny inference about the longest-period Ap stars that is derived from the *TESS* observations is representative of their actual rate of occurrence. In particular, all stars are dealt with in the same way, regardless of the strengths of their magnetic fields. This ensures that weakly magnetic stars are duly included in the statistics.

As part of a project in collaboration with D. Kurtz and D. Holdsworth, we have started to identify the Ap stars that do not show evidence of photometric variations of rotational nature in the 27-d-long data sets recorded in each of the *TESS* sectors. The vast majority of these stars very probably have rotation periods considerably longer than 27 d. The main exceptions should be the ones whose rotation axis lies almost exactly along the line of sight. There should be very few such stars; under the assumption that the inclination angles of the rotation axes with respect to the line of sight are random, these angles would be less than 5° for less than 1% of the stars. We checked that the adopted strategy identified successfully almost all the known ssrAp stars present in the fields observed. The rare exceptions all seemed to be cases where apparent variations with periods shorter than 27 d that were detected by *TESS* could plausibly be attributed to contamination by the light of another, unresolved, neighbouring source.

We propose to record high-resolution spectra of all the new long-period candidates identified through the search described above, in order to confirm that they are Ap stars with low projected equatorial velocities. The resulting sample will presumably include a mix of stars with resolved magnetically split lines corresponding to a range of field strengths and of stars showing sharp spectral lines with little or no evidence of a magnetic effect. Further follow-ups of these stars will be carried out to constrain their rotation periods. Ultimately, this study will enable us to characterise the distribution of the ssrAp stars both in terms of period and in terms of magnetic field strength.

5 Final remarks

How the differentiation of the rotation rates of the Ap stars over five to six orders of magnitude is achieved is one of the outstanding unsolved questions of stellar physics. Answering it is essential for understanding the formation of these stars, and the origin of their magnetic fields. More generally, it is relevant for the knowledge of the physical processes that are at play in the formation and evolution of all the early-type stars. This relevance is emphasised by the similarity, recently evidenced, between the distributions of the rotation periods of Ap (and Bp) stars, the magnetic early B-type stars and the magnetic O stars (Shultz et al. 2018).

Knowledge of the distribution of the rotation periods of Ap stars, and in particular of its long-period tail, is essential as input for theoretical developments aimed at explaining the evolution of rotation in these stars. In recent years, the exploitation of the results of several extensive ground- and space-based photometric surveys has led to a considerable increase in the number of well-determined short periods of up to 2–3 weeks. The corresponding part of the distribution is, accordingly, very well defined. By contrast, for more slowly rotating stars the current knowledge of the period distribution remains biased and incomplete.

Some of these shortcomings can now be addressed. This presentation has showed how the "non-variable" Ap stars in the *TESS* database can be exploited to constrain the rate of occurrence of ssrAp stars. In particular, considering them will allow us to identify, and to characterise, the weakly magnetic ssrAp stars, which to date have never been studied systematically. This represents a good illustration of the way in which advantage can be taken of observations from space in order to complement ground-based studies and provide valuable additional scientific insight besides the obvious straightforward exploitation of space-based photometric surveys for systematic determinations of short to intermediate periods for large samples of stars.

However, for the longest periods there is a fundamental limitation that can only be overcome by the passing of time. Namely, no period can be determined accurately that is longer than the time-base over which suitable observations of the star of interest have been obtained. Currently, the longest period that has been determined accurately is that of HD 50169, $P_{\rm rot} = 29\,{\rm yr}$. Most likely, the star that will some day overturn HD 50169 as the longest-period Ap star with full coverage of the variation curve of one of its observables will only have a rotation period a few years longer. Such increments are small compared to the century-scale periods of the most slowly rotating stars. With respect to the latter, we are responsible for ensuring that no gaps are left in the coverage of their variation curves. Decades or centuries may elapse before a critical phase that is missed now can be re-observed.

References

Alecian, E., Wade, G. A., Catala, C., et al. 2013, MNRAS, 429, 1027

Babcock, H. W. 1947, ApJ, 105, 105

Belopolsky, A. 1913, AN, 195, 159

Bernhard, K., Hümmerich, S., Otero, S., & Paunzen, E. 2015a, A&A, 581, A138

Bernhard, K., Hümmerich, S., & Paunzen, E. 2015b, AN, 336, 981

Bychkov, V. D., Bychkova, L. V., & Madej, J. 2016, MNRAS, 455, 2567

Cunha, M. S., Antoci, V., Holdsworth, D. L., et al. 2019, MNRAS, 487, 3523

Hubrig, S., North, P., & Schöller, M. 2007, AN, 328, 475

Hümmerich, S., Mikulášek, Z., Paunzen, E., et al. 2018, A&A, 619, A98

Hümmerich, S., Paunzen, E., & Bernhard, K. 2016, AJ, 152, 104

Kochukhov, O. & Bagnulo, S. 2006, A&A, 450, 763

Mathys, G. 2017, A&A, 601, A14

Mathys, G. 2019, arXiv e-prints, arXiv:1912.06107

Mathys, G., Hubrig, S., Landstreet, J. D., Lanz, T., & Manfroid, J. 1997, A&AS, 123, 353

Mathys, G., Khalack, V., & Landstreet, J. D. 2019c, A&A, submitted

Mathys, G. & Lanz, T. 1992, A&A, 256, 169

Mathys, G., Romanyuk, I. I., Hubrig, S., et al. 2019a, A&A, 624, A32

Netopil, M., Paunzen, E., Hümmerich, S., & Bernhard, K. 2017, MNRAS, 468, 2745

Preston, G. W. 1970a, in IAU Colloq. 4: Stellar Rotation, ed. A. Slettebak, 254
Preston, G. W. 1970b, ApJ, 160, 1059
Preston, G. W. 1970c, PASP, 82, 878
Preston, G. W. 1971, PASP, 83, 571
Preston, G. W. 1974, ARA&A, 12, 257
Shultz, M. E., Wade, G. A., Rivinius, T., et al. 2018, MNRAS, 475, 5144
Sikora, J., David-Uraz, A., Chowdhury, S., et al. 2019, MNRAS, 487, 4695
Wraight, K. T., Fossati, L., Netopil, M., et al. 2012, MNRAS, 420, 757

Be STAR VARIABILITY AS SEEN FROM GROUND-BASED AND SPACE PHOTOMETRY

J. Labadie-Bartz[1] and A. C. Carciofi[1]

Abstract. Recent progress in understanding and modelling Be-star disk evolution is reviewed. Calculations of the angular momentum carried away by the disk provide a unique way to test certain predictions of stellar evolution models dealing with angular momentum transport. Knowing reasonably well how a disk behaves over months and years once formed, we can turn to recent and ongoing space photometry to classify Be star variability on shorter time-scales. Results from space missions have revealed that typically Be stars have much more complex frequency spectra than their non-Be siblings, showing features that, even though shared by other types of objects, are probably unique to Be stars in how they combine. From an initial analysis of 254 light-curves of southern Be stars observed by *TESS* with a 2-min cadence during its first year of operations, we identified 8 types of variability features, according to the properties of their light-curves and frequency spectra, and assigned each one visually to one or more of those types. By far the most common type of variability, present in 57–86% of the stars (depending on the spectral sub-type) is the presence of frequency groups. Other common features include isolated single frequencies and prominent stochastic variability. This work is a first step towards attempting to understand the complex frequency spectra of Be stars and their relation to what has so far been an elusive mass-loss mechanism operating in them.

Keywords: Techniques: photometric, stars: emission-line, Be, mass-loss, oscillations

1 Introduction

-Be stars are non-supergiant, non-radially pulsating, B-type stars that are rotatig near the critical limit. Their spectra exhibit emission lines which arise in a viscous, Keplerian, circumstellar "decretion" disk formed from ejected stellar mass in discrete events called "outbursts." These disks appear and disappear, and can be variable on time-scales from hours to decades. Be stars are valuable astrophysical laboratories for studying the effects of rapid rotation on stellar structure and evolution, pulsation-driven mass loss, the physics of viscous disks, and the transport of angular momentum from the stellar interior to the outer layers and to its removal from the system via the decretion disk (*e.g.*, Rivinius et al. 2013; Rímulo et al. 2018).

This contribution discussed recent advances in Be research stimulated by the availability of good-quality light-curves. On the one hand, ground-based observations provide the long time-baselines needed to track the entire process of disk formation and dissipation. The large number of light-curves available from surveys such as OGLE (Udalski et al. 1997) enable us to select a sizable sample of Be light-curves with simple, well-isolated disk events (see Sect. 2. On the other hand, space photometry delivers both the high degree of precision and the high cadence to reveal the minute changes in brightness associated with stellar pulsation. This is important because nonradial pulsation is often thought to play an integral role on how Be stars eject mass, possibly through interaction of multiple modes (Baade et al. 2016; Kurtz et al. 2015).

2 Current understanding of Be star disks

The disks of Be stars are their most defining characteristic. A significant amount of research has been dedicated to observing, modelling, and interpreting the growth, dynamics and dissipation of the line-emitting gas in the circumstellar environment (Rivinius et al. 2013). The Viscous Decretion Disk model (VDD; Lee et al. 1991; Carciofi 2011) has emerged as the best explanation for the various observed phenomena. In the VDD model, the process of building a disk begins with material being somehow ejected from the star. Viscous diffusion then acts to transport matter and angular momentum outwards, causing the disk to grow (at the expense of some material losing angular momentum and falling back onto the star). With a constant mass injection rate the

[1] Instituto de Astronomia, Geofísica e Ciências Atmosféricas, Universidade de São Paulo, São Paulo, Brazil

disk grows towards a steady state; is geometrically thin, rotates in a nearly Keplerian fashion, has roughly a power-law radial density profile, and has a complicated temperature structure. The main free parameters in the VDD model are viscosity (according to the alpha disk theory), and the injection rate of mass and angular momentum into the disk (which can be, and often is, highly variable with time).

Be star disks are the brightest and most accessible systems for studying disk physics, owing to the fact that Be stars are common (comprising ∼20% of all main-sequence B stars) and show variability on accessible time-scales. Lessons learned about viscosity from Be star disks are relevant for astrophysical disks at all scales, including protostellar disks, AGN and accretion disks. Modelling the time-dependent structure of Be star disks provides measurements of the viscosity parameter, which is an integral aspect of all astrophysical disks as it controls the time-scales over which the disk evolves.

In the context of stellar evolution, Be star disks have relevance in that they transport angular momentum out of the system. Stellar evolution theory predicts that as a massive star evolves, its convective core contracts and spins up, and if there is sufficient coupling between the core and envelope, angular momentum will be transported radially outwards. By the creation of a disk, angular momentum is removed from the outer layers of the star and carried out of the system entirely, whereby the star avoids super-critical rotation. In this scenario, the angular momentum transported from the core should match the angular momentum lost from the disk. The Geneva stellar-evolution models account for this (Granada et al. 2013) and predict angular momentum loss rates as a function of stellar mass averaged over the main-sequence life-time. Modelling Be star disks provides a way to test those predictions. Fig. 1 shows an example model light-curve for a Be star with varying mass and angular momentum loss rates, and the total amount of angular momentum lost by the star through the disk in those episodes.

VDD theory has been used to model disk events by involving a large grid of hydrodynamic models and a Monte Carlo Markov Chain (MCMC) radiative transfer code to compute a grid of synthetic light-curves. The latter were then fitted to photometric OGLE data (Udalski et al. 1997) through an MCMC technique, whereby the viscosity parameter and angular momentum flux through the build-up and dissipation of the disk were calculated (Rímulo et al. 2018). Figure 2 shows an example disk event that was modelled in that fashion. A key result of the work by Rímulo et al. (2018) was that the angular momentum loss rates measured in disk events may be up to ∼100 times smaller than predicted by the Geneva models. The predictions of those models are compared to the calculated angular momentum loss rates of Be stars in the SMC and LMC (and one in the Milky Way) in Fig. 3. The discrepancy is made worse by the fact that Be stars are observed to spend only a fraction of their main-sequence life-time building disks (i.e., their duty cycle is approximately 10–20% from a preliminary analysis of OGLE data of LMC stars; A. Figueiredo, priv. comm.). Since the efficiency of angular momentum transport in stellar-evolution models is a free parameter, it is possible that it has been overestimated in the case of rapidly rotating stars. Further modelling of the light-curves of Be stars may provide the means to calibrate the angular momentum transport efficiency empirically in such evolutionary models.

3 Interpreting observations of Be star systems

tBoth the central star and the disk are interesting astrophysical systems to study. The previous section relies on observations and models of the disk. While the star forms the disk, the evolution of the disk is largely independent of the star itself, being primarily influenced by the gravitational and radiation fields of the star. Once a disk is formed, the material forgets its history and evolves mainly through viscous forces. Meanwhile, the central star represents the best opportunity to study the physics of rapidly rotating main-sequence pulsating stars. In order to learn from the star or the disk, it is necessary to disentangle their relative contributions to a given observable. For example, in the disk modelling method outlined in the previous section, the photometric excess arising from circumstellar material is the relevant quantity. For such methods to succeed, the brightness of the star must first be subtracted. Likewise, studies involving the star itself must account properly for any observational contributions from the disk.

Certain observed variations can be attributed confidently to either the star or the disk. In terms of photometry, brightening or fading events that occur on time-scales of months or years are understood to be due to disk growth or dissipation (e.g. Fig. 2), while coherent, stable periodic signals on time-scales of around one day are best attributed to stellar pulsation. There are, however, many cases where the origins of photometric signals are ambiguous. The stellar rotation period, orbital period in the close circumstellar environment, and possible pulsational periods, are all very similar. Since many factors can influence the total brightness of the system (and other observables) in often complex and time-variable ways, care must be taken in interpreting photometric data.

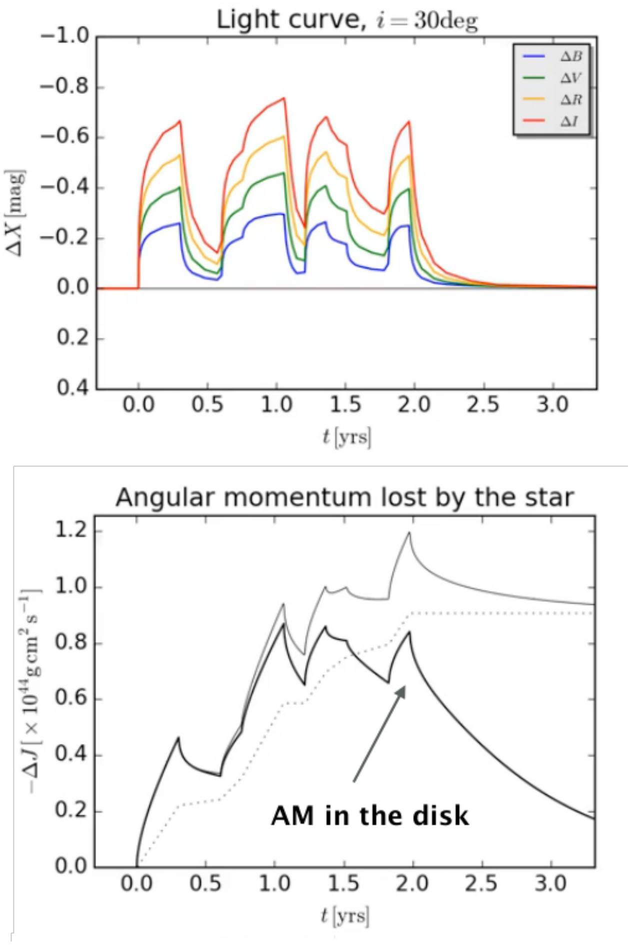

Fig. 1. Top: Simulated light-curve of a Be star with variable mass-loss rates, for several photometric bands, as indicated. When the brightness is increasing the Be star is ejecting mass and the disk is being built up. **Bottom:** The amount of angular momentum in the disk (solid black line) and the amount of angular momentum lost by a star (solid grey line) with the above simulated mass-loss history. As the disk dissipates it carries angular momentum out of the system.

Despite these complications, space photometry is a powerful tool that has opened a new window into understanding Be stars. In the following sections, we summarize recent progress and ongoing work from space photometry.

4 Space photometry of Be stars: recent highlights

Space photometry has led to significant advances in the field of classical Be stars in recent years. Analyses of space-based photometry have revealed that pulsation is ubiquitous among classical Be stars, and that they pulsate primarily in low order g-modes (Rivinius et al. 2003), similar to the class of Slowly Pulsating B (SPB) stars (Walker et al. 2005). Analyses of photometry from *MOST, BRITE, Kepler* and *CoRoT* have shown that the frequency spectra of Be stars are often complex relative to other B-type main-sequence pulsators (the β Cephei and SPB stars), typically exhibiting multiperiodicity, groups of closely spaced frequencies (as well as isolated frequencies), and signatures of stochastic variability (Baade et al. 2017, 2018; Rivinius et al. 2016; Semaan et al. 2018).

Frequency groups often appear in sets of three – one at low frequencies ($\sim$0.03 c d^{-1}), one at mid frequencies ($\sim$2 c d^{-1}), and the third at higher frequencies ($\sim$4 c d^{-1}). The high-frequency group is usually about twice the frequency of the mid-frequency group. Sometimes the mid-frequency group has two dominant frequencies whose difference roughly corresponds to the low-frequency group. While this general pattern is found in many Be stars, there are numerous exceptions. Nevertheless, in stars with these frequency groups, there can appear correlations between the frequencies and episodes of mass ejection (Baade et al. 2016), and are therefore prime

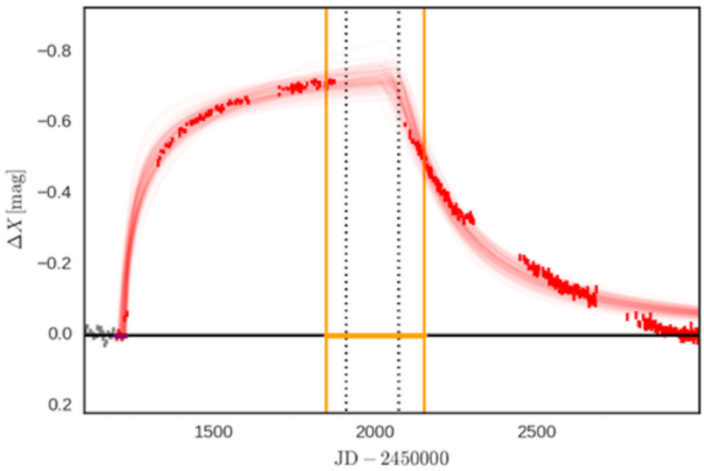

Fig. 2. Light-curve (red points; I band) of a disk event of an SMC star as seen with OGLE; the red lines represent 100 randomly chosen models from the MCMC routine. The vertical lines mark the range within which the MCMC sampler fits the transition of the disk phase from build-up to dissipation. Figure adapted from Rímulo et al. (2018).

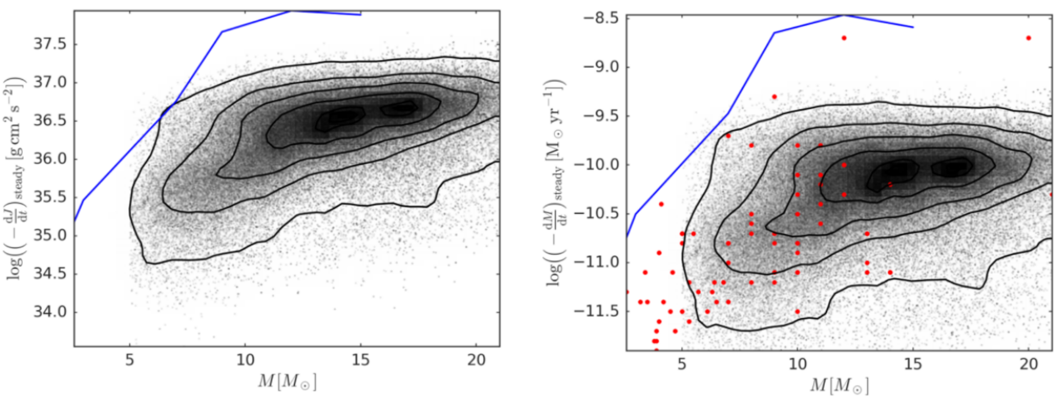

Fig. 3. Distributions of the steady-state mass (right) and angular momentum (left) loss rates for the sample of 54 Be stars from the SMC observed with OGLE. The blue curves show the predictions of the Geneva models for SMC metallicity from Granada et al. (2013) averaged over the main sequence life-time due to disk events. The red dots in the upper panel were computed for Galactic Be stars from Vieira et al. (2017). Figure reproduced from Rímulo et al. (2018).

objects for studying the mass ejection mechanism. One plausible hypothesis is that resonant mode coupling of pulsation modes can lead to combination frequencies with higher amplitudes than the sum of the base frequencies, which is somehow related to mass ejection (Rivinius et al. 2016).

It is well known that variability in both the stellar photosphere and the circumstellar environment can contribute to brightness changes and signals in the frequency spectrum. The frequency spectra often change drastically during active mass ejection episodes, with many transient modes appearing, variable amplitudes of the persistent modes, and characteristic signals at slightly lower frequencies than the stellar rotation (Semaan et al. 2018). An inhomogeneous distribution of recently ejected circumstellar material orbiting the star can leave such imprints on the frequency spectrum, but it is also possible that multiple transient pulsation modes are associated with these mass ejection events. From photometry alone it is difficult or impossible to disentangle the contributions from the photosphere and the circumstellar gas.

Great care must be taken in interpreting the frequency spectra as seen from space, since they are almost always time-variable. For example, it has been observed that during outbursts (here understood as an active disk-feeding phase), the amplitude of some modes increase, whereas in some modes the amplitude, frequency and phase may change (e.g., as seen in α Eri by Goss et al. 2011). Whether these changes in the frequency spectra are a cause or a consequence of the outbursts remains unknown. The disk may therefore add a layer of complication to the frequency spectrum that can only be investigated if the dynamical state of the disk (e.g., stability *versus* build-up *versus* dissipation) is understood properly. However, that can only be achieved if long-term multi-technique data are available.

5 Be stars with *TESS*

TESS is a space-based photometric mission designed to discover Earth-sized transiting exoplanets orbiting relatively bright stars by surveying nearly the whole sky. Launched on 2018 April 18, the nominal 2-year mission is dedicated to observing the southern ecliptic hemisphere for 1 year, followed by 1 year observing the northern ecliptic hemisphere. Each hemisphere is observed in 13 sectors, each with a 27 day base-line (but in overlap regions between sectors stars can be observed for many consecutive months, up to a full year). For stars brighter than $V = 8$ the typical precision is approximately 50 parts per million for 1 hour of observing. The observing cadence is 2 minutes for pre-selected targets (which can be requested through Guest Investigator programmes), and 30 minutes for the Full Frame Images (FFIs).

TESS is a unique space photometry mission for a number of reasons, but of particular relevance for massive stars is its nearly all-sky coverage and its focus is on bright stars ($5 < \mathrm{V} < 10$). While other space photometry missions such as *Kepler* and *CoRoT* observed some massive stars, the number is very small and the targets are faint, making detailed spectroscopic studies difficult or impossible. During its first two years *TESS* will observe approximately 1300 bright Be stars – a significantly greater number than all previous and current space missions combined. *TESS* therefore represents the best opportunity in the foreseeable future to study massive stars that vary on time-scales of days to weeks with photometry from space, since no similar missions are planned.

Our main goal in this section is to give a brief overview of the variability captured in the *TESS* light-curves of Be stars observed in the first year of the *TESS* mission. First, we identify and describe several characteristic features that appear in *TESS* data for our sample. Then we examine the light-curve and frequency spectrum for each object and record the types of signals shown. That provides us with information regarding the fraction of our sample showing various signals, and enables us to compare the features of the frequency spectra of the sample as a whole.

5.1 *Characteristic features of Be stars in TESS*

We begin by analyzing the light-curves of 254 classical Be stars observed with 2-minute cadence in the southern ecliptic in the first year of the *TESS* mission (Guest Investigator project ID G011204). For each light-curve, the Lomb-Scargle (LS) periodogram is also calculated as a measure of the frequency spectrum. While each light-curve and frequency spectrum is unique, there are certain features that are common among many members of the sample. Figure 4 shows examples of Be stars that exhibit these characteristic features, which are listed and described below.

- Type 1 – flickers: loosely defined as features in the light-curve whereby the brightness increases by a few percent over a few days, followed by a return towards the base-line. Some flickers show a precursor phase, i.e., a dimming before the rise in brightness, and some are accompanied by a temporary increase of the amplitude of higher-frequency signals (or their emergence if not already present). The largest amplitude features in panel B of Fig. 4, especially in the first half of the data, are examples of this. Flickers are not an oscillation around the mean brightness (like in panel A), but are rather a marked departure from the base-line brightness.

- Type 2 – Low-frequency signals dominate: the most prominent have frequencies lower than 0.5 c d^{-1} . Panels A and B in Fig. 4 show examples of stars with this characteristic.

- Type 3 – Stochastic variation: non-periodic, and a significant feature of the data. Stochastic signals can appear as extra noise in the frequency spectrum (as opposed to coherent periodic signals, which exist at a single frequency). However, this noise is astrophysical, and arises from genuine variability, which is not periodic. Wavelet analysis of these light-curves sometimes reveals real modes, albeit with varying amplitudes and frequencies. Panel C shows an example of this. The frequency spectrum between 0–2 c d^{-1} is characterized by stochastic variability in the data. There are also coherent and isolated signals at higher frequencies. Stochastic signals are likewise evident in the data in panel A, especially after removing the low-frequency signals ($<$ 0.5 c d^{-1}) from the data (grey lines in Fig. 4), and to a slightly lesser extent in panel B.

- Type 4 – Frequency groups: many closely-spaced frequencies that often form groups in the frequency spectra of Be stars. The light-curve in panel D shows three groups near 0.05, 1, and 2 c d^{-1} , panel E shows two groups near 3 and 6 c d^{-1} , and Panel B shows frequency groups where the first group at the lowest frequencies is highest in amplitude, and the other two groups centred around 1.5 and 2.5 c d^{-1} are relatively wide (and are more obvious after removing the low-frequency signals). The Be star in panel F also shows two prominent groups near 2.5 and 5 c d^{-1} .

- Type 5 – Single, isolated frequencies: single and well-defined in contrast to groups. There are many isolated frequencies in the periodogram of panel F, and also some in panel C.

- Type 6 – High-frequency signals: shown by some Be stars in contrast to theusual level, which is similar to that of the Slowly Pulsating B (SPB) stars, in that it is a g-mode pulsation with typical frequencies around 0.5–3 c d^{-1} . In this initial classification scheme, we have chosen 6 c d^{-1} as the defining level. Panel F shows a star with many high-frequency signals, while panels C and E are also examples that meet this criterion.

- Type 7 – Harmonics: a second frequency (or group) in the frequency spectrum occurs at twice the frequency of another signal. Some are exact, others are approximate. In panel D the group near 2 c d^{-1} could be considered the near harmonic of the group near 1 c d^{-1} , and likewise with the two groups in panel E. An exact harmonic is seen in panel F, where the lowest frequency, $f_0 = 1.684$ c d^{-1} has a first harmonic at $2{\times}f_0 = 3.368$ c d^{-1} .

- Type 8 – No variability: nothing above the *TESS* noise level in small fraction of the stars in the sample.

5.2 *Analysis*

We identified characteristic features of interest in the light-curves and frequency spectra, and inspected plots for the sample visually in order to determine which of the characteristics (above) could be attributed to each star. During this process we recorded the number of frequency groups and individual frequencies in each periodogram, and the frequency and amplitude of all significant signals* (having an S/N rate >4 using a 1.0 c d^{-1} window centred on the frequency in question). In all cases, versions of the periodogram were calculated both with and without frequencies lower than 0.5 c d^{-1} , since in many systems low frequencies dominate, and make the detection of higher-frequency signals more difficult if they are not first removed.

The sample was also subdivided according to a rough spectral-type designation from the literature. "Early-B" stars have a spectral type of B3 and earlier, "mid-B" stars have spectral types of B4–B6, and "late-B" stars are B7 and later. Of the 254 Be stars in this sample, 12 do not have a spectral type in the literature adequate for classifying them in that detail (e.g., an assigned type is "Be").

5.3 *Results*

As is clear from the examples in Fig. 4, a given Be star can display many of the characteristic features listed above: see Table 1. Figure 5 displays histograms showing the number of frequency groups in the sample. The dominant frequencies of each star in the sample are shown in Fig. 6, ordered by the frequency of the signal with the highest amplitude (after removing low frequencies); the three smaller panels show the same plot split along the spectral-type categories.

Table 1, Fig. 5 and Fig. 6 leads to the following conclusions. We found that early-type stars tend to show the most dramatic variability on time-scales accessible with *TESS*, and are the most likely to show flickers (11%) and high-amplitude low-frequency variations (33%), in accordance with previous results showing that early-type Be stars are much more active than late-type ones (*e.g.*, Labadie-Bartz et al. 2017). They usually have frequency groups (86%), 3 groups being the most typical configuration. However, frequency groups are also very common in mid-type stars (79%), and in late-type stars to a slightly lesser extent (57%). Isolated single frequencies are more common towards later spectral sub-types. High frequencies have a more or less uniform incidence across spectral types (∼23%), which is somewhat surprising since high frequency β Cephei-type pulsation is generally found only in early B stars. Only two stars were apparently without any signals above the noise level of *TESS*;

*Some discretion must be applied, because frequency groups can be wide and populated with many peaks of similar amplitudes. The signal-to-noise ratio (S/N) of any particular peak in such a group may be low according to the usual conventions, even when the group as a whole is clearly far above the noise level.

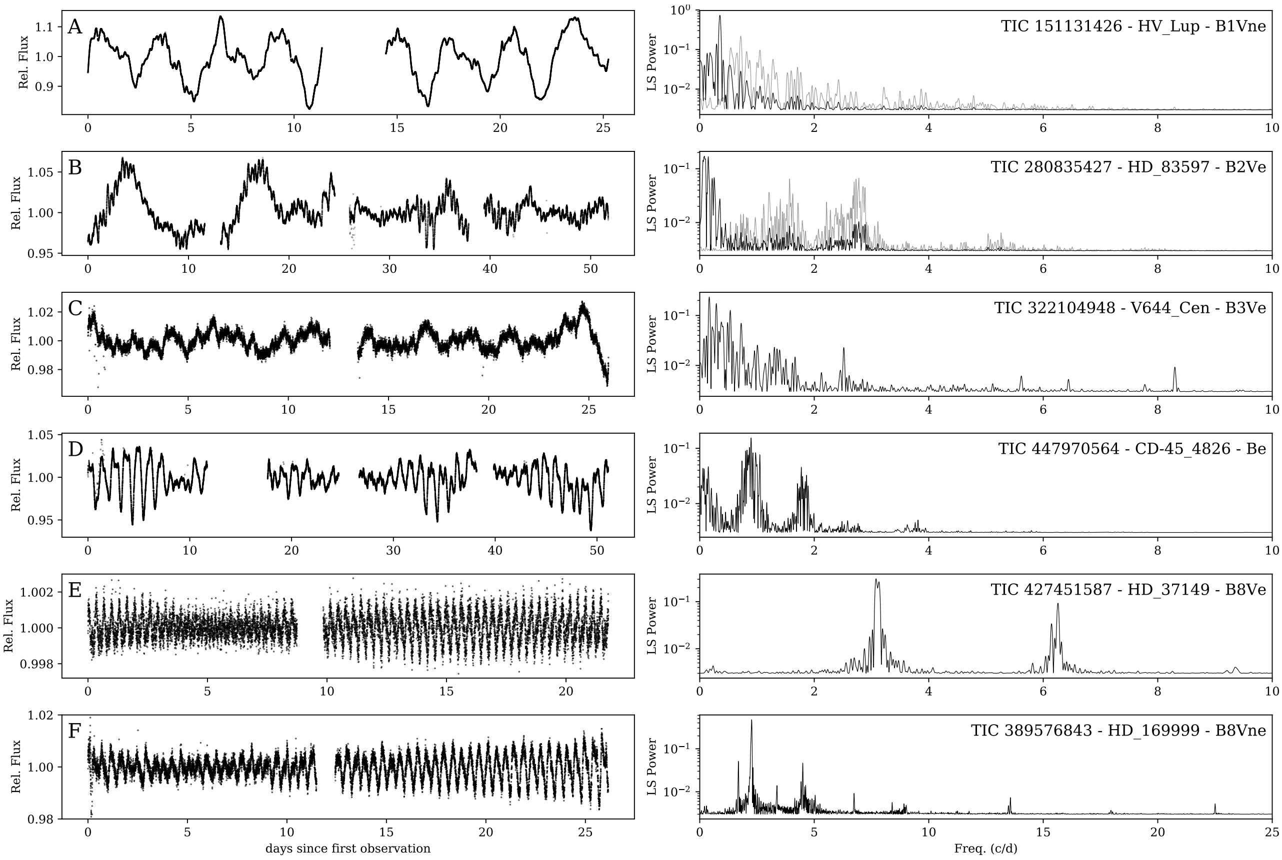

Fig. 4. *TESS* light-curves (**left**) and Lomb-Scargle periodograms (**right'**) for a representative selection of Be stars that show certain characteristic features, as described in the text. For the top two cases, the periodogram is re-calculated after removing the low frequency (< 0.5 c d^{-1}) signals and is shown in a lighter grey colour. Panels B and D show two sectors of *TESS* data; the rest have only one *TESS* sector of observations. The x-axis of the periodogram in panel F is extended to include the high frequencies. Signals at frequencies higher than 10 c d^{-1} are absent in all other stars shown here.

they require further analysis to derive upper limits to potential pulsational amplitude. Five stars appear to be mono-periodic, in that only a single frequency was found (with no harmonics) and they were without other types of variation. However, the short observational base-line of *TESS* and the possibility of signals below the detection threshold mean these are not necessarily purely single-mode pulsators.

Figure 6 shows a nearly linear crest between 0.5 and about 2.5 c d^{-1} . It means that within that frequency range the strongest frequencies seem to exist along a continuum, without any strong preference around any particular value. Groups associated with the strongest signal extend to both higher and lower values, but tend to have a longer tail towards lower frequencies. It is common for another group to exist at approximately twice the frequency of the dominant group. Exact harmonics of single frequencies are most common in the late-type stars, but it should be noted that late-type stars are less likely to have groups and more likely to have isolated frequencies dominant in their periodograms. Given frequency groups that do not have a single dominant frequency, it is difficult to distinguish the difference between exact harmonics and near harmonics. This introduces a bias in our analysis of harmonics in stars with frequency groups that has not yet been accounted for.

6 Conclusions

Ground-based photometric surveys have provided long-baseline light-curves of Be stars in the Galaxy, the SMC and the LMC. Some of the available light-curves are particularly well suited for disk studies, as they reveal the entire process of disk formation and dissipation. Recent such studies (Rímulo et al. 2018; Ghoreyshi et al. 2018) used these light-curves to determine the rate of angular momentum loss from the star in order to compare it

Table 1. Percentages showing variability classifications

	All (254)	*Early (126)*	*Mid (53)*	*Late (63)*
Flickers	7% (17)	11% (14)	6% (3)	0% (0)
Dominated by low freq. var.	22% (57)	33% (42)	19% (10)	6% (4)
Prominent stochastic variability	25% (63)	30% (38)	21% (11)	18% (11)
Frequency groups	77% (196)	86% (108)	79% (42)	57% (36)
Isolated single frequencies	40% (101)	33% (41)	43% (23)	50% (32)
High frequencies (> 6 c d^{-1})	23% (58)	22% (28)	23% (12)	24% (15)
Exact harmonics	15% (37)	9% (11)	17% (9)	25% (16)
No variability	1% (2)	0% (0)	1% (1)	1% (1)

Fraction of stars showing each type of variability, according to their spectral type. The category 'all' includes early-, mid-, and late-type stars, as well as 12 stars without a known spectral sub-type.

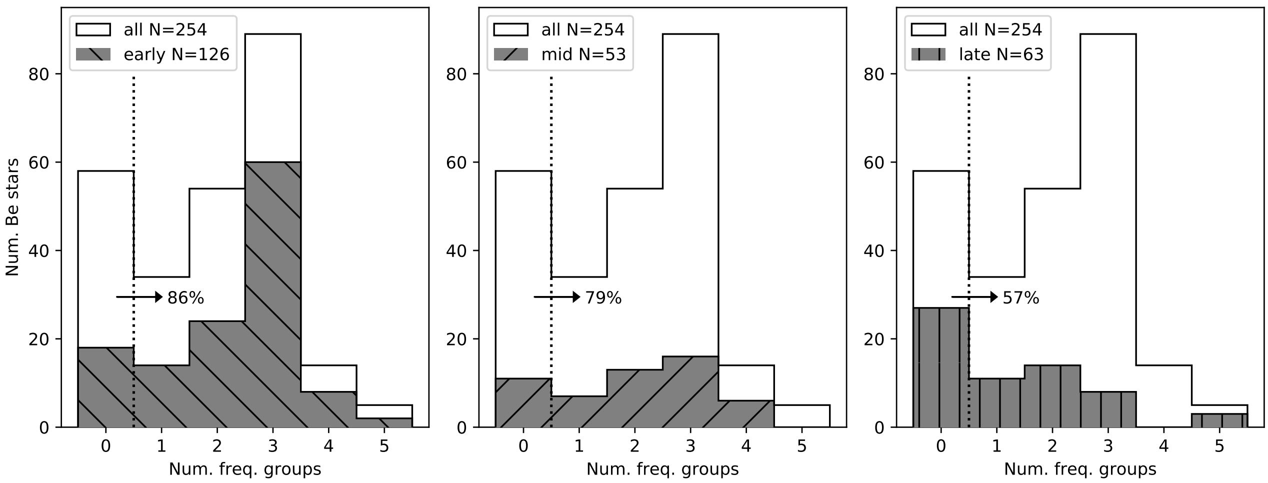

Fig. 5. Number of frequency groups in the Lomb-Scargle periodograms, split according to spectral sub-type. The black outline shows the distribution for the entire sample. In early-, mid-, and late-type stars, 86%, 79%, and 57%, respectively, show one or more frequency group.

with theoretical calculations from stellar evolution models of fast-spinning stars. The main result is that, even though the models do reproduce the observed trend of higher angular momentum loss rate for more massive stars, they predict rates that are up to 100 times larger than the observations reveal.

TESS promises to continue the legacy of massive-star photometry from space by providing by far the largest sample to date of high-precision, near-continuous data across nearly the entire sky. This is especially important for classical Be stars. Because Be star variability is so diverse and the phenomenon extends across a large range of spectral sub-types (late O to early A), large samples are needed to describe the behaviour of the Be-star population. This work takes a first step in that direction, by identifying characteristic signals that are seen in Be stars by *TESS*, and analyzing a subset of the southern Be stars observed in year 1 of *TESS* and ascribing their characteristics to each star (with most stars showing multiple features). Further work is being undertaken to define these characteristic signals more rigorously, to increase the sample size by including all southern Be stars (and not just 2-min cadence targets), to incorporate information from archived multi-year ground-based light-curves, spectroscopy, and the literature, and to acquire new spectra simultaneous with *TESS* observations to disentangle variability that arises in the photosphere rather than in the circumstellar environment.

J. L.-B. acknowledges support from FAPESP (grant 2017/23731-1). A. C. C acknowledges support from CNPq (grant 307594/2015-7) and FAPESP (grant 2018/04055-8).

References

Baade, D., Pigulski, A., Rivinius, T., et al. 2018, A&A, 610, A70

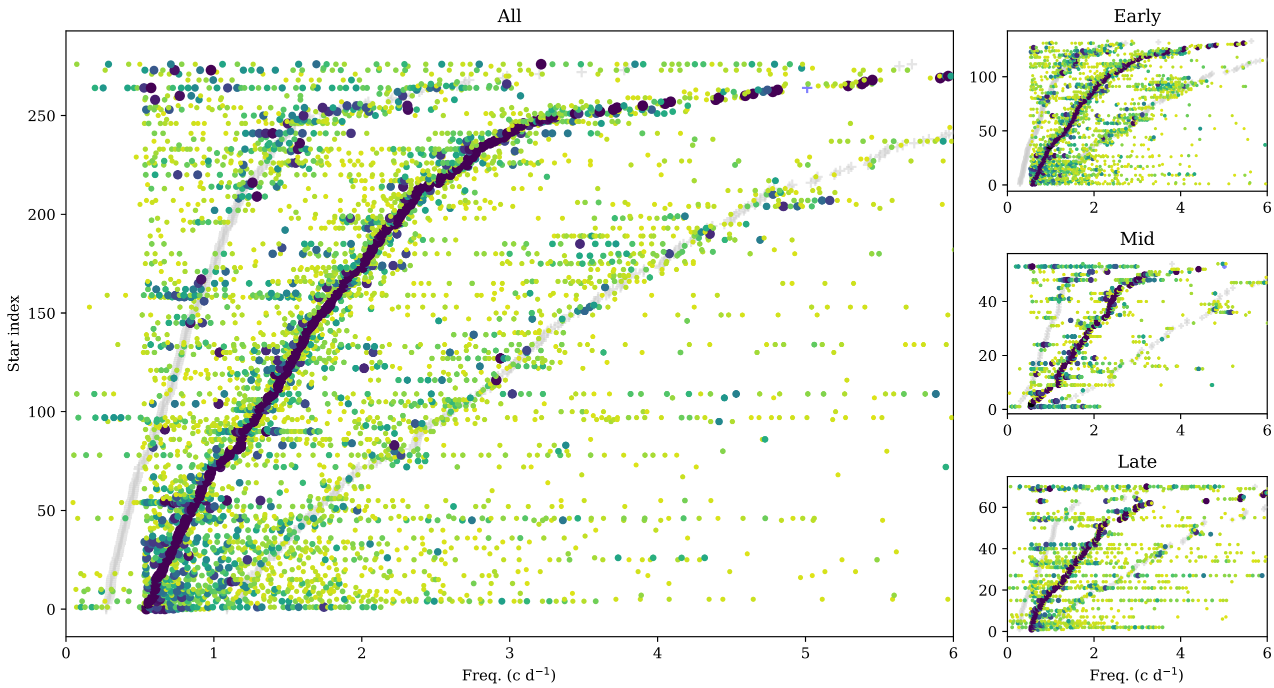

Fig. 6. Plots showing the strongest frequencies for the whole sample, sorted by spectral type. Each row in the plot shows the frequencies for one object. The stars are ordered according to their strongest frequency, increasing upwards. These frequencies are from a Lomb-Scargle periodogram, calculated after removing frequencies lower than 0.5 c d^{-1} . The grey lines to the left and right of the main frequency sequence are at 0.5 and 2*times* the strongest frequency, to help visualise signals that are near harmonics. Marker sizes and colour are proportional to the amplitude of the signal, relative to the strongest signal in each star (darker and larger symbols mean larger amplitude). There are many signals past the x-axis cutoff of 6 c d^{-1} but tend to be weaker, and the purpose of this plot is to show how frequencies lower than 6 c d^{-1} are distributed in the sample.

Baade, D., Rivinius, T., Pigulski, A., et al. 2017, in Second BRITE-Constellation Science Conference: Small Satellites - Big Science, Vol. 5, 196–205

Baade, D., Rivinius, T., Pigulski, A., et al. 2016, A&A, 588, A56

Carciofi, A. C. 2011, in IAU Symposium, Vol. 272, Active OB Stars: Structure, Evolution, Mass Loss, and Critical Limits, ed. C. Neiner, G. Wade, G. Meynet, & G. Peters, 325–336

Ghoreyshi, M. R., Carciofi, A. C., Rímulo, L. R., et al. 2018, MNRAS, 479, 2214

Goss, K. J. F., Karoff, C., Chaplin, W. J., Elsworth, Y., & Stevens, I. R. 2011, MNRAS, 411, 162

Granada, A., Ekström, S., Georgy, C., et al. 2013, A&A, 553, A25

Kurtz, D. W., Shibahashi, H., Murphy, S. J., Bedding, T. R., & Bowman, D. M. 2015, MNRAS, 450, 3015

Labadie-Bartz, J., Pepper, J., McSwain, M. V., et al. 2017, AJ, 153, 252

Lee, U., Osaki, Y., & Saio, H. 1991, MNRAS, 250, 432

Rímulo, L. R., Carciofi, A. C., Vieira, R. G., et al. 2018, MNRAS, 476, 3555

Rivinius, T., Baade, D., & Carciofi, A. C. 2016, A&A, 593, A106

Rivinius, T., Baade, D., & Štefl, S. 2003, A&A, 411, 229

Rivinius, T., Carciofi, A. C., & Martayan, C. 2013, A&A Rev., 21, 69

Semaan, T., Hubert, A. M., Zorec, J., et al. 2018, A&A, 613, A70

Udalski, A., Kubiak, M., & Szymanski, M. 1997, Acta Astron., 47, 319

Vieira, R. G., Carciofi, A. C., Bjorkman, J. E., et al. 2017, MNRAS, 464, 3071

Walker, G. A. H., Kuschnig, R., Matthews, J. M., et al. 2005, ApJ, 635, L77

BRITENESS VARIATIONS OF THE BRITEST HOT STARS

T. Ramiaramanantsoa[1] and A. F. J. Moffat[2]

Abstract. We and our collaborators have been using *BRITE-Constellation* since the beginning of the mission to observe some of the intrinsically and apparently brightest hot stars in the sky. This includes O stars, luminous blue variables (LBVs) and Wolf-Rayet (WR) stars, which share the feature of driving strong winds and ending in a supernova explosion yielding mainly a black hole, or a neutron star in some cases, or even no remnant at all. As such, O stars and their descendant LBVs and WR stars are tied to gamma-ray bursts and gravitational wave sources, as well as to the first stars to form in the Universe which were predominantly very massive. We present two key cases for O and WR stars observed by *BRITE*, with their implications for hot star winds and internal structure. In particular, contrary to expectations, hot luminous stars (especially the most extreme among them) tend to show hydrostatic-surface, semi-stable bright spots that betray the stellar rotation. Such bright spots are found to drive large-scale, spiral-shaped, wind features known as co-rotating interaction regions (CIRs), so far regarded as virtually present in all O-star and some WR-star winds. These bright spots are likely the direct result of a distinct layer of subsurface convection, as proposed by recent theoretical investigations. This layer may also be the ultimate source of shorter-lived stochastic perturbations in the photosphere, which are found to drive clumping in the inner part of O-star and very likely also WR winds.

Keywords: Stars: massive, Stars: rotation, (Stars:) starspots, Stars: Wolf-Rayet, Stars: winds, outflows, Turbulence, Techniques: photometric, Space vehicles

1 Introduction

BRIght Target Explorer (*BRITE-Constellation*; Weiss et al. 2014; Pablo et al. 2016) is a fleet of five independent nanosatellites each equipped with a 30-mm telescope and CCD detector to carry out precision, time-dependent optical photometry of bright stars down to $4-6$ visual apparent magnitude. *BRITE* is well adapted to observe massive stars in particular because (1) satellite pointing constraints favour the higher stellar density of apparently bright stars towards the Galactic plane, where massive stars also tend to lie, and (2) *BRITE* can observe for long, uninterrupted intervals of up to six months, well matched to the relatively long variability timescales encountered in massive stars.

Massive stars have initial masses $\mathrm{M_i} \gtrsim 8\mathrm{M_\odot}$ and explode as core-collapse or pair-instability supernovae at the end of their short lives. Very massive stars (VMS) are taken to be massive stars with strong stellar winds and $\mathrm{M_i} \gtrsim 20\mathrm{M_\odot}$, and include all O-type stars on the main sequence plus all of their descendants, mainly luminous blue variables (LBVs) and Wolf-Rayet (WR) stars. Compared to solar-like stars, VMS, while much rarer and shorter-lasting, dominate the luminosities and especially the mass-loss in star-forming regions like the spiral arms of spiral galaxies.

In the Hertzsprung-Russell diagram, O stars lie just above the β Cep instability strip, which includes mostly early-B stars. However, this instability strip spills over to higher luminosity and includes some of the latest-type, O9 stars. A good example of this is the O9.5V star ζ Oph, with clear β Cep-type pulsations as revealed most clearly by *BRITE*'s precursor, the *MOST (Microvariability and Oscillations of STars)* microsatellite mission (Walker et al. 2005), as well as other space-based observatories (Howarth et al. 2014).

On the other hand, early O-type stars show fewer pulsations, if any (section 1.1 in Ramiaramanantsoa et al. 2018a for a recent review). Instead, they are found to exhibit both stochastic and cyclic variability at their photosphere and in their wind, possibly ultimately connected to a subsurface convection zone caused by partial ionization of iron atoms with their prolific number of atomic transitions, despite their relatively low abundance (Cantiello et al. 2009; Cantiello & Braithwaite 2011). Massive He-burning WR stars have even

[1] School of Earth and Space Exploration, Arizona State University, 781 E. Terrace Mall, Tempe, AZ, USA 85287-6004
[2] Département de physique, Université de Montréal, CP 6128, Succursale Centre-Ville, Montréal, Québec, H3C 3J7

hotter hydrostatic surface temperatures than (H-burning) O stars (Hamann et al. 2019). Those WR stars with the coolest temperatures tend to be more variable (Michaux et al. 2014), because the subsurface iron convection zone is located deeper into the star and involves more driving mass. Here we concentrate on two prime examples, both single, one a well-known early-O supergiant, and the other a strongly variable WR star. Both serve as good proxies of other stars in their class.

2 The O4I(n)fp star ζ Puppis

The very well-known hot massive O-type supergiant ζ Pup [O4I(n)fp] has been studied at many wavelengths as a standard for its type. This may be somewhat surprising, given its runaway nature and possibility of surface pollution. The most likely scenario explaining its current runaway status is that it might have been the secondary in a massive binary, in which the primary exploded as a supernova, likely leaving behind a black hole moving in the opposite direction to ζ Pup. Such a scenario explains its high projected rotational velocity (for a supergiant) of $v \sin i = 219 \pm 18$ km s^{-1} as a result of the spin-up expected in the Roche-lobe overflow (RLOF) stage of the pre-runaway process.

Several studies geared to exploring the variability of ζ Pup have led to periodicities ranging from 8.5 h to 5 d. Our recent investigation (Ramiaramanantsoa et al. 2018a) using *BRITE* is arguably the most far-reaching to date. We discovered for the very first time a direct link via variability between the surface of a massive, hot star and its strong wind. With 56M$_{\odot}$, ζ Pup is the most massive star observed so far by *BRITE*, although a recent revision of its distance decreases this mass somewhat (Howarth & van Leeuwen 2019). The *BRITE* light curve extends non-stop (except for odd gaps) over almost 6 months in both the blue and red *BRITE* optical filters. With orbit-binned cadence of $\sim$ 100 min, the blue and red light curves (varying at the 10 mmag level compared to the instrumental level of just over 1 mmag) are highly correlated, both supporting its reality and suggesting that the stellar surface source of continuum variability is either of similar temperature to (but brighter than) the rest of the stellar surface, or is much hotter than the surrounding photosphere (although the observations are not sensitive to a difference in temperature at the Rayleigh-Jeans tail far from the UV peak emission).

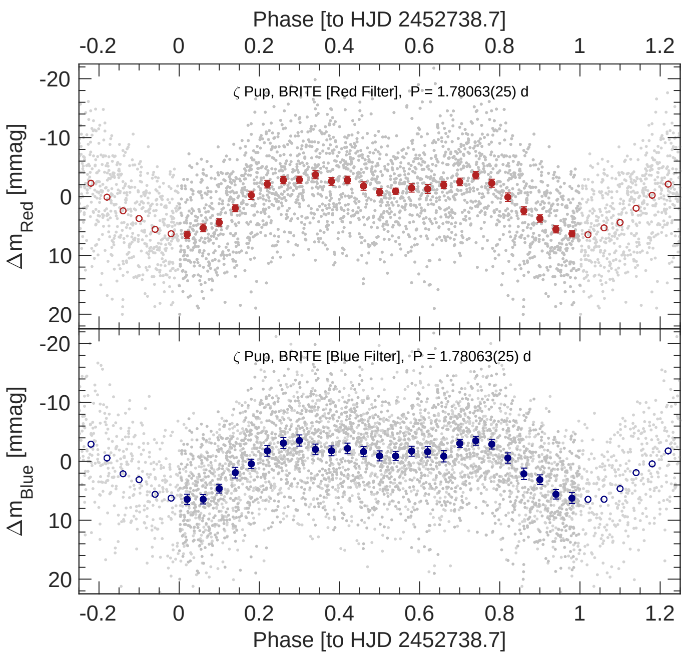

Fig. 1. *BRITE* light curves of ζ Pup phased with the 1.78-d period found to be the stellar rotation period. The scatter around the binned values is intrinsic, given the observed precision of $1 - 2$ mmag per datapoint.

2.1 Light variability arising from bright photospheric spots

The Fourier analysis of the whole *BRITE* light curves of ζ Pup reveals a period of 1.78 d, identical to that found from lower-precision but more voluminous, earlier *Coriolis/SMEI* satellite data (Howarth & Stevens

2014). Fig. 1 shows the orbit-binned light curve in each filter, phased with the 1.78 d period. While Howarth & Stevens (2014) found a single-peaked phased light curve, we now clearly see double (or even multiple) peaks. Also, in the frequency domain, while only the peak corresponding to the 1.78 d periodicity was present during the epoch of the *Coriolis/SMEI* observations, the first harmonic of that signal also appeared during the *BRITE* observing run.

The shape-changing behaviour of the observed phased light curve and the behaviour of its periodogram are indicative of rotational modulation due to localized brightness enhancements in the stellar photosphere from where $\gtrsim 99\%$ of the optical continuum light is arising. We then carried out a light-curve inversion to locate the bright spots on the stellar surface using the algorithm developed by Harmon & Crews (2000). We found that, depending on the epoch of observation, two to three bright spots are required along with slow variability in relative strength to reproduce the observed light curve. We also found that the spots grow and fade on timescales of weeks.

Such spots may be the footprint seeds of the well-observed CIRs (or their projected UV resonant-line P Cygni absorption manifestations called discrete absorption components) in the wind of ζ Pup (e.g. Howarth et al. 1995), with two dominating and spaced typically about 20 h (about half a 1.78 d rotation period) apart. Our ground-based high S/N contemporaneous optical spectra bear this out, showing that we see the same 1.78 d periodicity in the strongest optical He II λ4686 emission line from the inner wind (see Fig. 2). Further modeling of this spectral recombination line with CIRs at three distinct intervals of the *BRITE* observations corroborate this idea for the origin of the 1.78 d period as due to rotation of slowly varying bright spots fixed in the rotating frame of the stellar surface. We also detected rotation-phase delays for different wind lines formed at different distances from the central star.

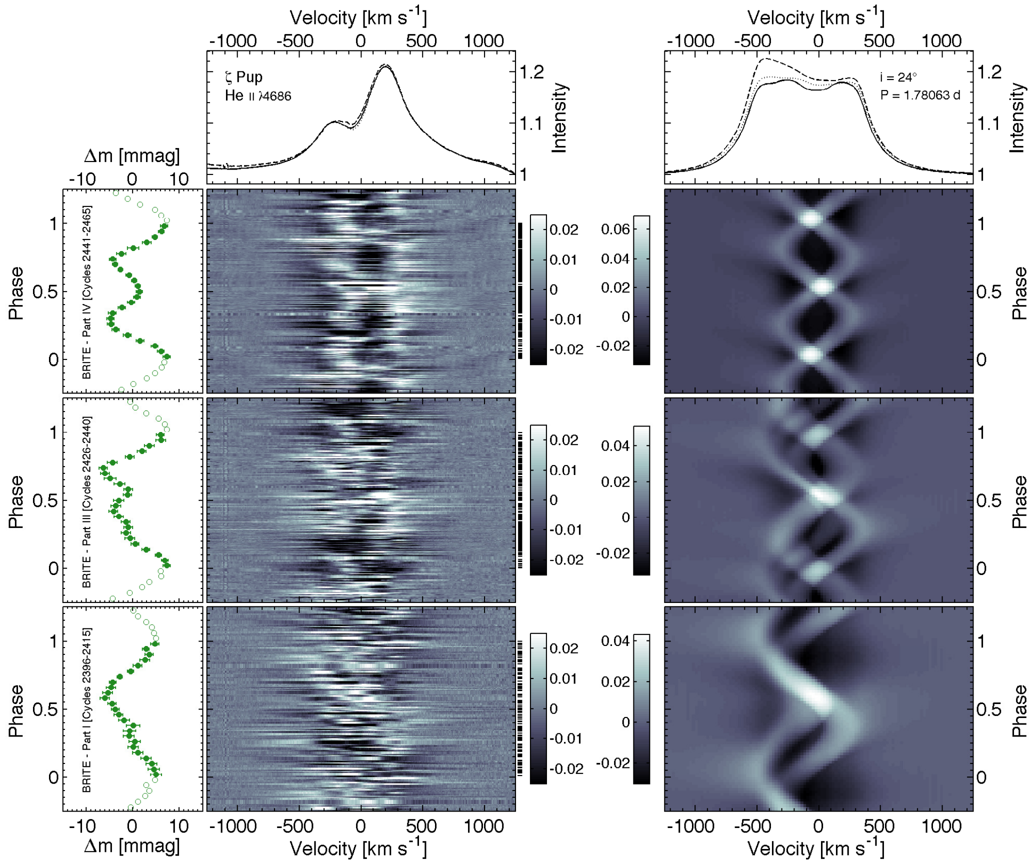

Fig. 2. *BRITE* light curve of ζ Pup and variations in its He II λ4686 emission line phased with the 1.78-d period (left), along with models of wind emission line-profile variations due to arms of CIRs.

If indeed the 1.78 d periodicity is identified as the rotation period, this leads to a rather low rotation-axis inclination of 24^{+10}_{-6} degrees. In this case, the true equatorial rotation speed would be just over 500 km/s, making ζ Pup an extreme rotator, likely spun up in a pre-separation RLOF process.

2.2 Stochastic photospheric light variability

Of equal interest as the cyclic light variations due to localized bright surface spots is the fact that the *BRITE* scatter around the 1.78 d binned light curve depicted in Fig. 1 is quite real, with variation amplitude comparable to that of the periodic signal. This appears to be the first time such apparently random variability has been unequivocally seen in ζ Pup, facilitated by the contemporaneous observations by three independent *BRITE* satellites in two distinct optical filters, allowing one to better assess the potential contribution of instrumental errors.

After removing the slowly varying 1.78 d signal from the observed light curve, we see no significant periodicity in either filter, rather just stochastic variations at the ± 10 mmag level (same as for the 1.78 d modulation) coherent over several hours (Fig. 3). These are likely relatively short-lived randomly-triggered photospheric perturbations whose origin may lead back to stochastically-triggered oscillations in the iron subsurface convection zone and/or gravito-inertial waves generated at the interface between any convection and radiative zones (see also e.g. Aerts & Rogers 2015; Ramiaramanantsoa et al. 2018b). Given the correlation between these random surface variations seen by *BRITE* and variations in the wind-line of He II λ4686, we propose that the random photospheric perturbations act as drivers to form the (largest visible) clumps in ζ Pup's wind.

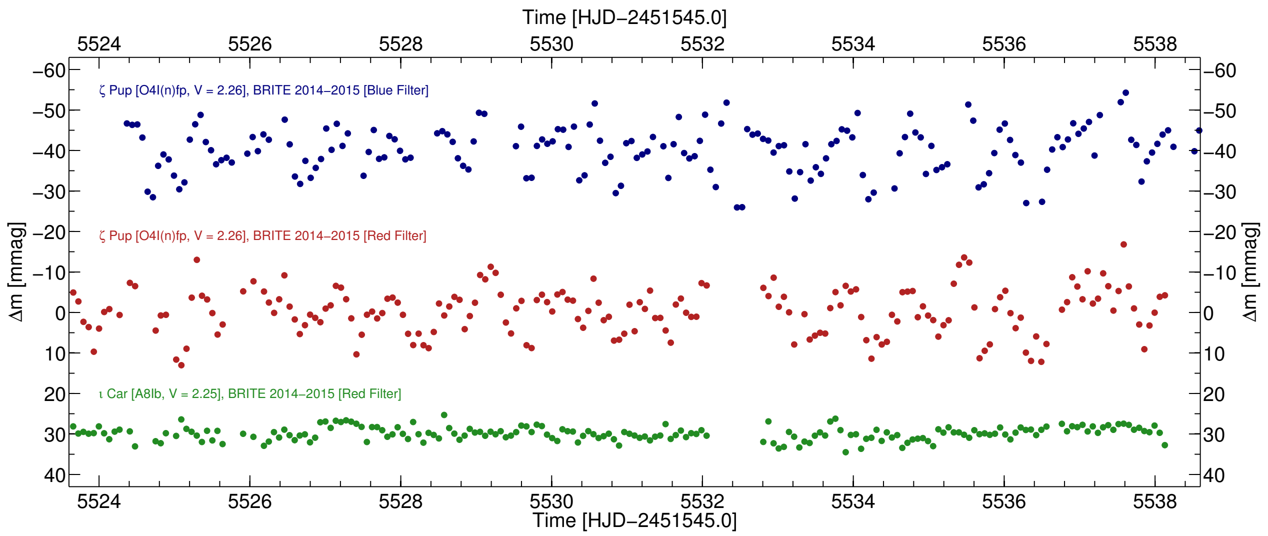

Fig. 3. Residual *BRITE* light curves of ζ Pup after removal of the 1.78 d variability.

3 The WN8h star WR 40

Among WR stars, those of the cooler nitrogen-sequence of type WN8 generally show the strongest light variability, normally completely stochastic in nature. The apparently brightest WN8 star in the sky is the V=7.7 mag WN8h ("h" means with some hydrogen left in its wind) star WR 40 = HD 96548. On the other hand, WR 40 is by far the faintest star observed intentionally by *BRITE* so far (Ramiaramanantsoa et al. 2019). However, its faintness is made up for by its relative isolation as a runaway in the sky (as are most, if not all, WN8 stars) and its high level of variability as known from previous ground-based observations (e.g. Marchenko et al. 1998). Such ground-based observations are always severely limited by day-night rhythms and weather, making space photometry a welcome tool.

Fig. 4 shows the complete *BRITE* light curve of WR 40, obtained only in the red filter. The peak-to-valley amplitude exceeds 100 mmag compared to the typical *BRITE* orbital mean bins with 5 mmag rms instrumental noise. Fig. 5 shows the overall and time-dependent Fourier transform of the *BRITE* data, revealing no outstanding Fourier peaks among a "forest" of peaks at low frequency. While short observing runs from the ground generally do show a small number of dominating power peaks, with a very long data-string such a forest would degenerate into a very broad Fourier power excess centered at around 0.2 d^{-1} in frequency (~ 5 d in period), presumably the dominant timescale of the variations.

The time-dependent Fourier transform bears this out, with stochastically triggered signals that are present for typically $4 - 10$ days (Fig. 5). We simulated this light curve using stochastic clumps that define the wind

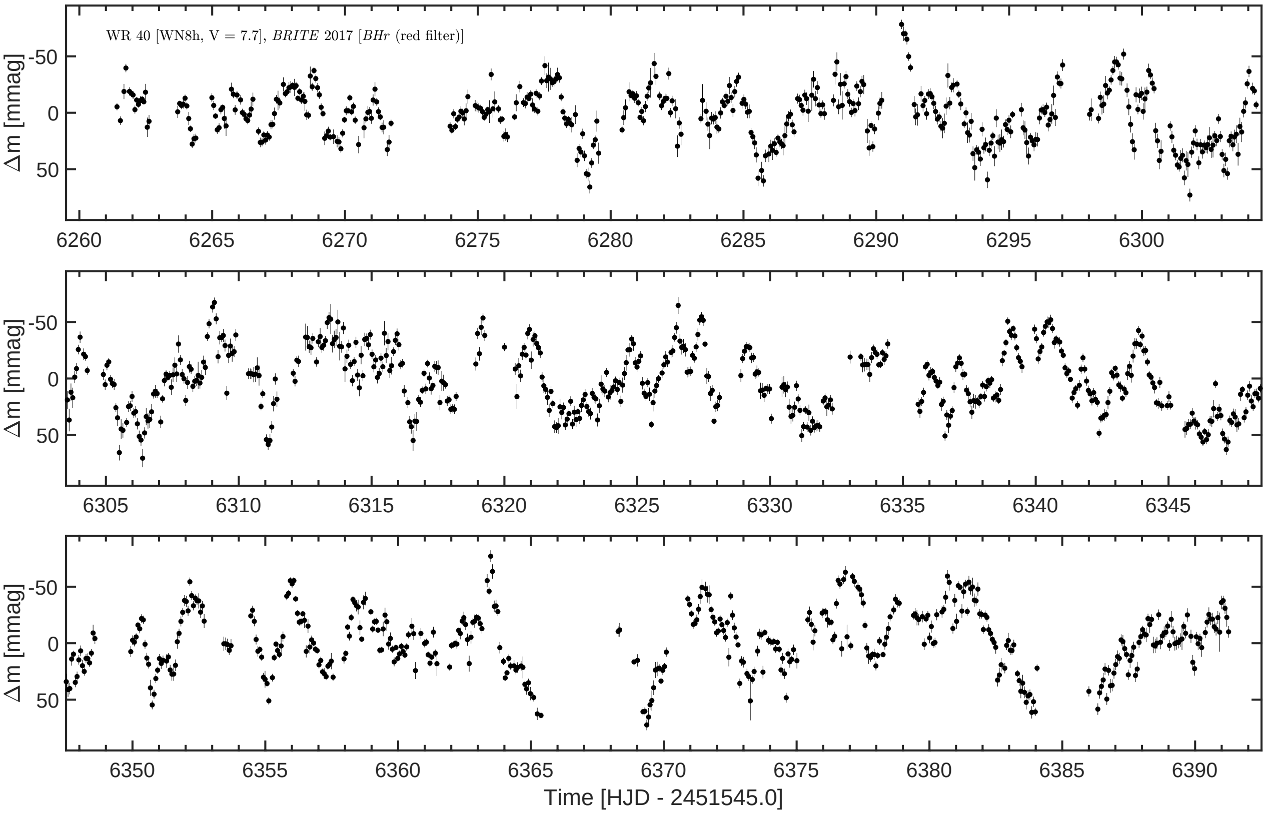

Fig. 4. Four-month long *BRITE* light curve of WR 40.

and electron-scattered light into the observer's direction. Somewhat surprisingly, both a turbulent power-law and a constant clump-size distribution yield qualitatively similar model light curves, compared to both each other and to the data. This may be a fundamental limitation of one-dimensional light curves. However, the effective higher dimension of analysis of WR 40's (and other WR stars') spectroscopic variations does favour the power law generated by the plausible presence of compressible turbulence (Moffat 1994). In any case, it seems likely that the light and spectral variations of WR 40 in particular and WN8 stars in general are dominated by random clumps being created and fading away as they propagate outward in the wind. By analogy with their progenitor O-stars, it also seems likely that the clumps are created at their hydrostatic surfaces, with enhancement possibly occurring in the wind via line-driving instability (Sundqvist & Owocki 2013).

4 Conclusions

The two highlighted massive stars illustrate:

1. how the variability of hot O-stars, with ζ Pup as a proxy, is dominated by surface features:
   (a) stochastic short-lived photospheric perturbations leading to the creation of wind clumps;
   (b) longer-living bright spots driving corotating interaction regions (CIRs) in the wind.
2. how the intrinsic variability of WR stars, with WR 40 as a proxy, is dominated by short-lived stochastic clumps.

Another WR star (WR6; St-Louis, these proceedings) is dominated by longer-living CIRs (uncertain if universal in WR stars), with clumps playing a secondary role. Both WR wind structures are likely associated with photospheric features similar to those seen in O-type stars, but unfortunately the hydrostatic stellar surfaces of WR stars are hidden by their opaque inner wind.

Although these *BRITE* observations illustrate new variability effects in just one O and one WR star, we believe that there is no reason not to expect to see similar behaviour in virtually all other early-type O stars

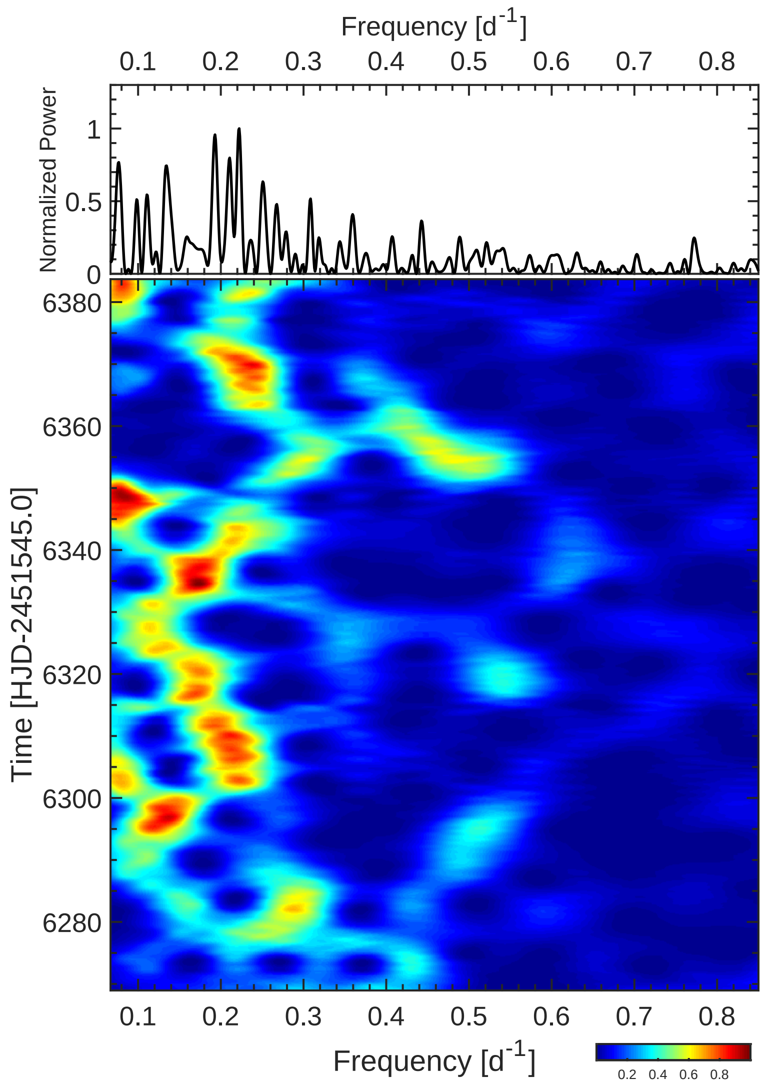

Fig. 5. Sliding windowed (15 d) Fourier transform of the *BRITE* light curve of WR 40.

and wind-dominated single WR stars. In the case of ζ Pup, we see a direct link both between bright (probably magnetic) spots in the photosphere and semi-periodic CIRs, and between randomly-triggered photospheric perturbations and stochastic clumps in the wind. In the case of WR 40 where we are limited to seeing only the wind, we do not see any indication of a periodicity, rather random variability that must be linked to the strong stochastic variability of clumps, as seen in virtually all hot-star winds.

This may be the long-sought answer for the origin of both semi-periodic (CIR-related) variations in O-star and some WR winds, and stochastic clumping variations in the winds of all massive hot stars.

Based on data collected by the BRITE-Constellation satellite mission, designed, built, launched, operated and supported by the Austrian Research Promotion Agency (FFG), the University of Vienna, the Technical University of Graz, the University of Innsbruck, the Canadian Space Agency (CSA), the University of Toronto Institute for Aerospace Studies (UTIAS), the Foundation for Polish Science & Technology (FNiTP MNiSW), and National Science Centre (NCN). AFJM is grateful to NSERC (Canada) for financial aid.

References

Aerts, C. & Rogers, T. M. 2015, ApJ, 806, L33

Cantiello, M. & Braithwaite, J. 2011, A&A, 534, A140

Cantiello, M., Langer, N., Brott, I., et al. 2009, A&A, 499, 279

Hamann, W. R., Gräfener, G., Liermann, A., et al. 2019, A&A, 625, A57

Harmon, R. O. & Crews, L. J. 2000, AJ, 120, 3274
Howarth, I. D., Goss, K. J. F., Stevens, I. R., Chaplin, W. J., & Elsworth, Y. 2014, MNRAS, 440, 1674
Howarth, I. D., Prinja, R. K., & Massa, D. 1995, ApJ, 452, L65
Howarth, I. D. & Stevens, I. R. 2014, MNRAS, 445, 2878
Howarth, I. D. & van Leeuwen, F. 2019, MNRAS, 484, 5350
Marchenko, S. V., Moffat, A. F. J., van der Hucht, K. A., et al. 1998, A&A, 331, 1022
Michaux, Y. J. L., Moffat, A. F. J., Chené, A.-N., & St-Louis, N. 2014, MNRAS, 440, 2
Moffat, A. F. J. 1994, Reviews in Modern Astronomy, 7, 51
Pablo, H., Whittaker, G. N., Popowicz, A., et al. 2016, PASP, 128, 125001
Ramiaramanantsoa, T., Ignace, R., Moffat, A. F. J., et al. 2019, MNRAS, 490, 5921
Ramiaramanantsoa, T., Moffat, A. F. J., Harmon, R., et al. 2018a, MNRAS, 473, 5532
Ramiaramanantsoa, T., Ratnasingam, R., Shenar, T., et al. 2018b, MNRAS, 480, 972
Sundqvist, J. O. & Owocki, S. P. 2013, MNRAS, 428, 1837
Walker, G. A. H., Kuschnig, R., Matthews, J. M., et al. 2005, ApJ, 623, L145
Weiss, W. W., Rucinski, S. M., Moffat, A. F. J., et al. 2014, PASP, 126, 573

Stars and their variability observed from space
C. Neiner, W. W. Weiss, D. Baade, R. E. Griffin, C. C. Lovekin, A. F. J. Moffat (eds)

SHINE BRITE: SHEDDING LIGHT ON STELLAR VARIABILITY THROUGH ADVANCED MODELS

D. Fabbian[1], F. Kupka[2], D. Krüger[1,2,3], N. M. Kostogryz[2] and N. Piskunov[4]

Abstract. The correct interpretation of the large amount of complex data from next-generation (in particular, space-based) observational facilities requires a very strong theoretical underpinning. One can predict that, in the near future, the use of atmospheric models obtained with three-dimensional (3-D) radiation magneto-hydrodynamics (RMHD) codes, coupled with advanced radiative transfer treatment including non-local thermodynamic equilibrium (non-LTE) effects and polarisation, will become the norm. In particular, stellar brightness variability in cool stars (i.e., spectral types F– M) can be caused by several different effects besides pulsation. In this review we have briefly discussed some published results, and mentioned aspects of recent progress. It then attempted to peek into what the future may hold for understanding this important aspect of the lives of stars.

Keywords: Method: magnetohydrodynamics (MHD), radiative transfer, stars: variables: general

1 Introduction

Numerical radiation (magneto-)hydrodynamic simulations of stellar atmospheres provide a strong basis for a multitude of studies of different aspects of (in particular) cool stars. One of the topics of great interest is understanding why many – if not all – of them undergo some amount of variation in their brightness with time. Owing to its proximity, one particularly well-studied case is that of the Sun. However, because its periodic brightness variation is small (about 0.1%) and has a relatively long period of 11 years, it was discovered only relatively recently compared to the variations observed in other stars (intrinsic variables such as pulsating, eruptive or cataclysmic/explosive stars, or extrinsic variables such as eclipsing or rotating stars), which in some cases have been known for many centuries.

In this contribution we have provided a very brief discussion of some recent results of interest, and some conclusions.

2 Discussion

"Box in a star" numerical simulations of stellar atmospheres, based on solving the (numerical) radiation (magneto-)hydrodynamics equations, aim at reproducing and understanding features of (magneto-)convection as observed by ground- and space-based instruments.

These type of simulations are well-tested, and are capable of reproducing observations such as solar granulation and stellar spectral lines. Moreover, they are useful for gaining physical insight into convective heat transport and the interaction of convection with pulsation modes.

***Figure 1 shows the temperature for a snapshot from the ~ 21 solar h of statistically-stable evolution of a solar-like simulation of ~ 3.7 Mm vertical extent and of 6.0 Mm extent in each horizontal direction.

Improvements in the treatment of radiative transfer and in the starting input for the modelling have recently been implemented in the code, plus the possibility of using, where appropriate, the (non-grey, 3-D) Eddington approximation for faster calculations (see, e.g., Krüger et al. (2019); Kupka (2018); Kostogryz et al. (2019)).

The ANTARES code has recently been applied successfully by our group to perform long-duration 3-D simulations of solar and stellar convection, for studying p-mode excitation and damping processes. The spectral

[1] Georg-August-Universität Göttingen, Institut für Astrophysik, Friedrich-Hund-Platz 1, D-37077 Göttingen, Germany
[2] MPI für Sonnensystemforschung, Justus-von-Liebig-Weg 3, D-37077 Göttingen, Germany
[3] Universität Wien, Fakultät für Mathematik, Oskar-Morgenstern-Platz 1, A-1090 Wien, Austria
[4] Uppsala University, Department of Physics and Astronomy, Regementsvägen 1, SE-752 37 Uppsala, Sweden

power of vertical velocity in the solar granulation simulation performed with this code shows eigenmode frequencies with the correct shape. Scaling has to be carried out to account for the limited size and depth coverage of the simulated model (i.e., for the relative shallowness of the "box in a star" geometry compared to the whole star).

Apart from the necessary scaling, it is important (as presented by F. Kupka, [PAGE]) that the 3-D hydrodynamical simulations have sufficient spatial and temporal resolution, spatial vertical and horizontal extent and time duration, for successful application to asteroseismology studies such as excitation and damping of solar-like p-modes. In particular (as is the case for our simulations) they must be able to describe well the properties of the superadiabatic layer, one of the crucial aspects for matching observed p-mode characteristics (*viz.*,frequency, amplitude and line shapes) in the power spectra of solar-like oscillating stars. It will of course be interesting to see MHD models applied for this purpose in the future for understanding the influence of magnetism on stellar atmospheric plasma, as discussed briefly below.

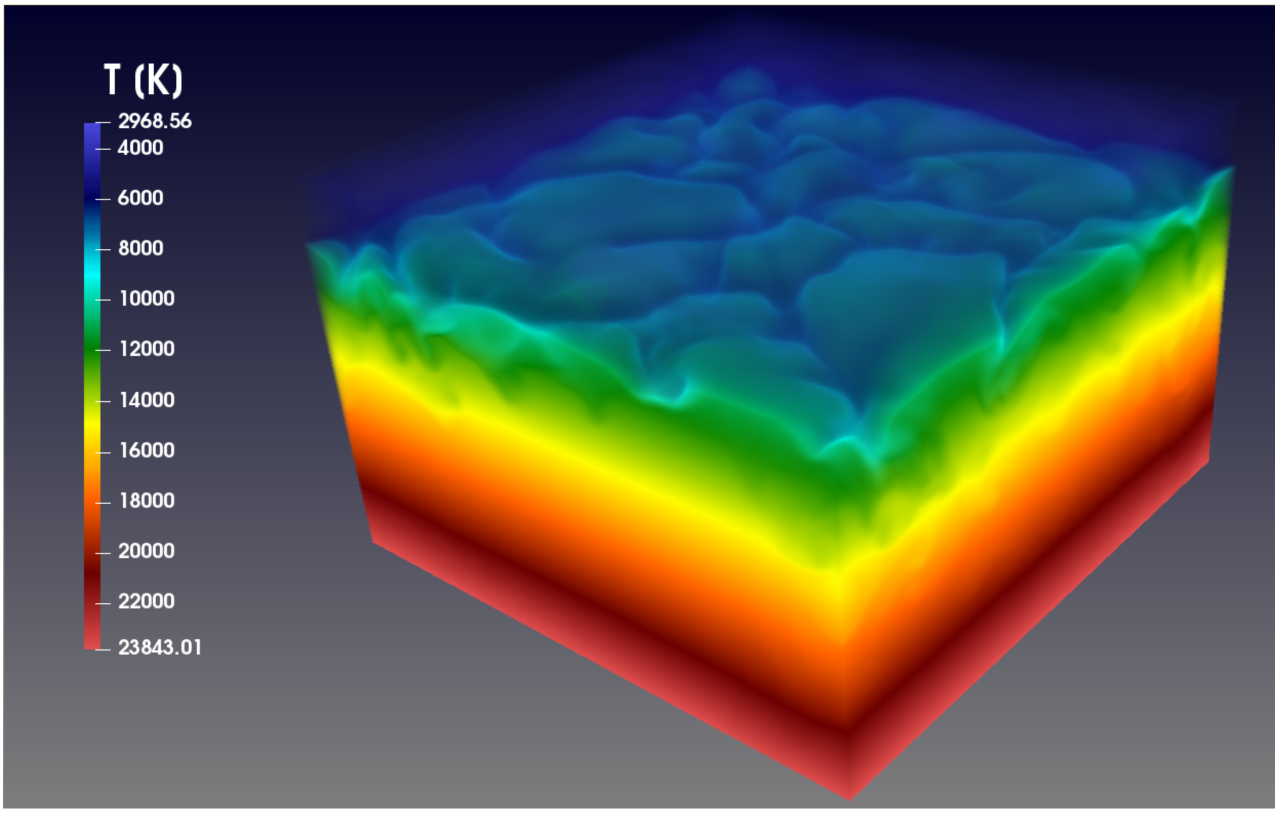

Fig. 1. Temperature (in K units) for a snapshot of the solar-like simulation "SLOPMD1" performed with the code ANTARES and visualised using ParaView (`https://www.paraview.org/`). This is the snapshot used as input to obtain the synthetic spectrum shown in Fig. 3.

Brightness variations observed in the light curve of different stars can, however, at least in part, be caused by processes other than solar-like oscillations (i.e., those excited by convective motions).

Granulation is the clearest visual manifestation of the process of convection at the surface of stars. Owing to the stochastic nature of convection, the granulation pattern produces micro-variations of the emerging radiation with time. Once p-mode oscillations (manifested as discrete peaks) are removed from the solar power spectrum, for example, it is mostly this granulation signal (the so-called "granulation background") which is left.

One sub-category of cool stars is particularly interesting, namely, stars on the main sequence and broadly similar to the Sun (spectral types F–K), so-called solar-type stars. The variability of their magnetic activity has recently been reviewed e.g. in Fabbian et al. (2017).

For the Sun, observations show a steeply-decreasing granular signal power at high frequencies ($\sim 1-8$ mHz), while the roughly constant power around ~ 0.2 mHz is followed by a rise with decreasing frequencies below ~ 0.1 mHz, caused by solar magnetic activity. Using the CO^{5}BOLD code, Ludwig et al. (2009) showed that atmospheric models from 3-D radiation hydrodynamic (RHD) simulations, while able to reproduce the power spectrum of granulation-related brightness fluctuations at intermediate and high frequencies reasonably well, contain (as to be expected, being representative of the pure non-magnetic case) less power at low frequencies than in the observational data. They found a puzzling discrepancy with the observed granulation background for F-type dwarfs, in that it was only after scaling the power and frequency of their predicted granulation-related brightness fluctuations to account (e.g.) for possible uncertainties in stellar parameter determinations, and after adding an *ad hoc* power-law magnetic activity signal, that the mismatch could be resolved – at least to a significant extent. The authors then performed 2-D RMHD solar simulations, assuming different levels of initial magnetic field strength. They found that observations have a low level of granulation-related brightness fluctuations around 1 mHz compared to their 2-D RMHD predictions. By virtue of the very similar topology of granular flows among solar-type stars, they made the hypothesis that the rise at low frequency in the temporal power spectrum of F-type dwarfs may be an indication of some type of magnetic activity in those stars too, analogous to what was hinted in the case of observational data for the Sun. However, their 2-D results – see their derived temporal power spectra of resulting emergent intensity in Fig. 2 – exclude local dynamo action in the granular flow as the source of magnetism producing the mismatch between predictions and observations. That leaves the existence of a ubiquitous, larger-scale magnetic field of several hundred G (though not yet detected by observations) as the only plausible cause able to affect the dynamics of granulation to an extent of the order needed to reduce the predicted brightness fluctuations to the observed low level.

It remains to be seen if switching to RMHD simulations in 3-D, for solar-type stars that have very precise stellar parameter determinations, can clarify the appearance of the brightness fluctuations power spectra for solar-type stars other than the Sun, or whether observations will confirm the presence of a strong magnetic field organised on a larger scale, or whether other explanations may be required.

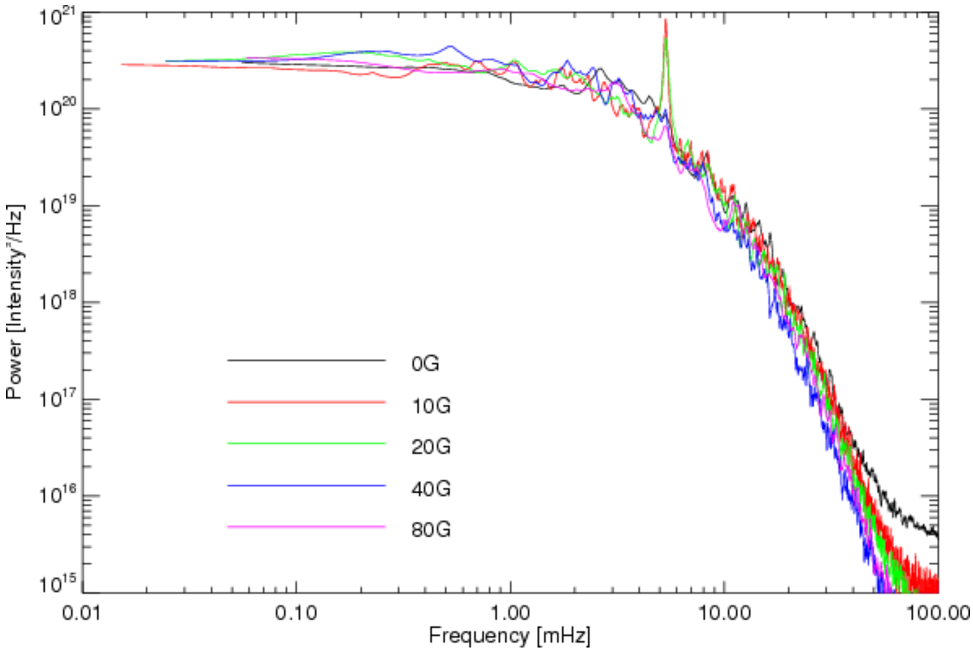

Fig. 2. Temporal power spectra of the horizontally-averaged vertically-emergent intensity of different MHD runs (solid curves in different colours) with solar atmospheric parameters (image adapted from Fig. 5 of Ludwig et al. (2009)).

Tools for calculating the synthetic spectrum on the basis of the multi-dimensional stellar photosphere simulations enable one to compare with, and check against, observations. Figure 3 gives an example of a synthetic spectrum computed on the basis of a solar granulation model, from an ANTARES radiation hydrodynamic photospheric simulation having "Model S" Christensen-Dalsgaard et al. (1996) as its starting input model and then relaxed as described by Kupka & Muthsam (2017).

Fabbian et al. (2010, 2012); Fabbian & Moreno-Insertis (2015) showed that the presence of magnetic fields can have a significant effect on the formation of Fe and O spectral lines in 3-D MHD solar simulations, affecting their profiles and intensities and thence the photospheric chemical abundances inferred from a fit to the observations.

Some spectral lines are particular sensitive to the level of solar and stellar activity (see, e. g., Vitas et al. (2009)).

Concerning the Sun, very recently Criscuoli et al. (2019) performed a thorough study comparing the results of different commonly-employed radiative transfer codes. They showed the importance of being aware of the

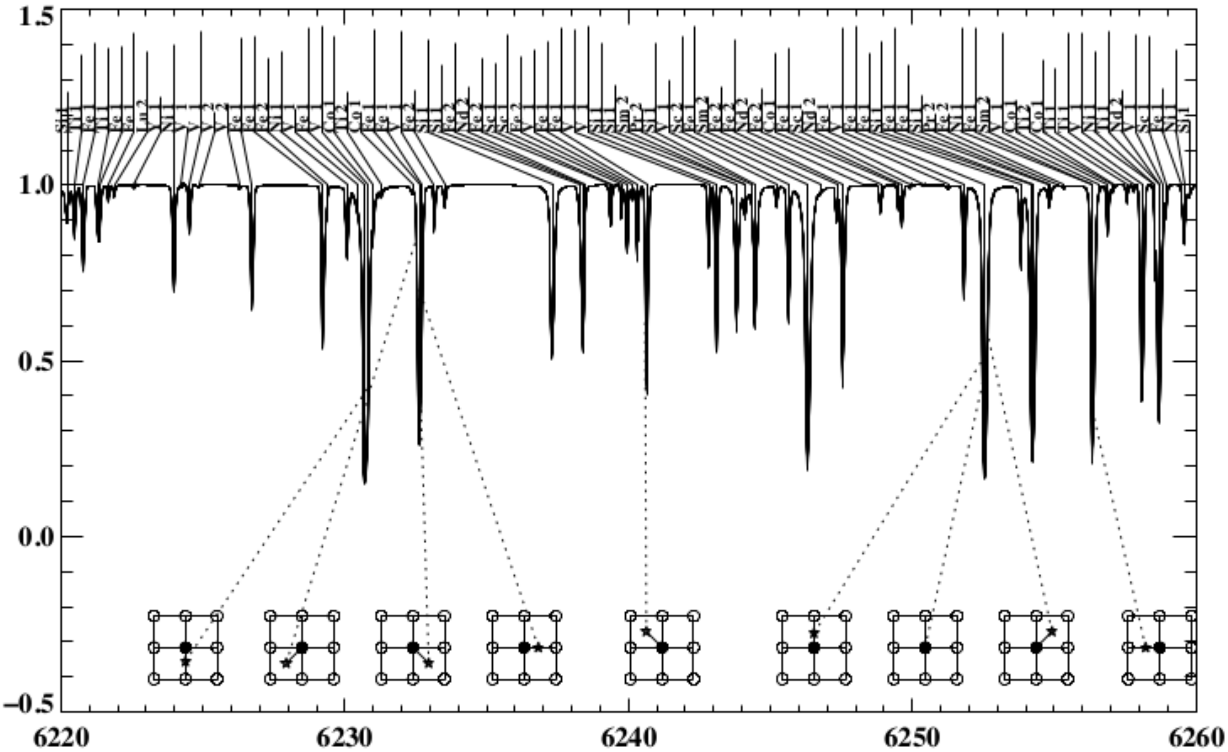

Fig. 3. Disk-centre intensity for the synthetic spectrum obtained for the region $\lambda\,6220$–$6260\,\text{Å}$, based on a 3-D RHD solar simulation performed with the ANTARES code. The calculation used as input the snapshot shown in Fig. 1.

relevant techniques, approximations and uncertainties involved, for explaining the subtle differences they found between the synthetic quiet-Sun spectra in order to reproduce well the solar irradiance measurements and to understand which features contribute the most to solar variability.

An effort on the part of theoretical and experimental physicists to achieve more accurate atomic and molecular data is of particular help. Databases listing their most recent data and compilations, e.g. VALD3 (the current version of the VALD online database, as described in Pakhomov et al. (2017)) are of great help for improving atmospheric and spectral synthesis modelling, and should be strongly supported by the stellar astrophysical community.

3 Conclusions

In this review we have discussed briefly some issues related to understanding stellar brightness variability. Cool stars show variability with periods ranging from very short to very long time-scales, with variations of different types often overlapping so the physical causes of their different variations are not easy to disentangle. One main point is that 3-D RMHD stellar atmospheric models, being based on first-principles and updated micro- and macro-physics and being able to withstand demanding tests against observations, are sufficiently well-developed nowadays to be employed in this field as the required input.

That naturally suggests that the application of advanced stellar atmospheric simulations, including the ever-more-complete treatment of relevant physical processes, is one of the main avenues for understanding better this aspect of the lives of stars, and that it will become more widespread and common practice to replace outdated and over-simplified modelling restricted to the limitations of one-dimensional, plane-parallel, static, gray atmospheres that neglect scattering and magnetic fields.

DF, FK, and DK gratefully acknowledge support by the Austrian Science Fund (FWF) through project P29172-N27, and they also thank the Vienna Scientific Cluster VSC-3 (project 70950) and the Faculty of Mathematics at the University of Vienna for granting computing resources. FK acknowledges partial support through the European Research Council Synergy Grant WHOLE SUN #810218. NMK is supported by the German space agency (Deutsches Zentrum für Luft- und Raumfahrt) under PLATO Data Center grant 50OO1501.

References

Christensen-Dalsgaard, J., Dappen, W., Ajukov, S. V., et al. 1996, Science, 272, 1286

Criscuoli, S., Rempel, M., Haberreiter, M., et al. 2019, Sol. Phys., *accepted*

Fabbian, D., Khomenko, E., Moreno-Insertis, F., & Nordlund, Å. 2010, ApJ, 724, 1536

Fabbian, D. & Moreno-Insertis, F. 2015, ApJ, 802, 96

Fabbian, D., Moreno-Insertis, F., Khomenko, E., & Nordlund, Å. 2012, A&A, 548, A35

Fabbian, D., Simoniello, R., Collet, R., et al. 2017, AN, 338, 753

Kostogryz, N. M., Kupka, F., Piskunov, N., et al. 2019, Sol. Phys., *in prep.*

Krüger, D., Kostogryz, N., Fabbian, D., & Kupka, F. 2019, in Journal of Physics Conference Series, Vol. 1225, Journal of Physics Conference Series, 012017

Kupka, F. 2018, in Astronomy in Focus, IAU Focus Meeting FM9, XXXth IAU GA, Vienna (Austria), ed. G. Kopp & A. Shapiro, Vol. 1, *in press*

Kupka, F. & Muthsam, H. J. 2017, Living Reviews in Computational Astrophysics, 3, 1

Ludwig, H. G., Samadi, R., Steffen, M., et al. 2009, A&A, 506, 167

Pakhomov, Y., Piskunov, N., & Ryabchikova, T. 2017, ASPCS, Vol. 510, VALD3: Current Developments (San Francisco: ASP), 518

Vitas, N., Viticchiè, B., Rutten, R. J., & Vögler, A. 2009, A&A, 499, 301

Stars and their variability observed from space
C. Neiner, W. W. Weiss, D. Baade, R. E. Griffin, C. C. Lovekin, A. F. J. Moffat (eds)

RIEGER-TYPE PERIODICITY IN THE ACTIVITY OF SOLAR-TYPE STARS

E. Gurgenashvili [2,3], T.V. Zaqarashvili[2,1], V. Kukhianidze[2], A. Reiners [3] and T. Reinhold[4]

Abstract. Rieger type periodicity occurs in many indices of solar magnetic activity such as: sunspots, solar flares, CME-s, etc. Our recent analysis of long- term sunspot data showed that observed Rieger-type periods correlate with solar cycle strength so that the stronger cycles show shorter periods. This finding allowed us to estimate the magnetic field strength in the solar dynamo layer. Some solar-type stars show short-term variations in magnetic activity, which might correspond to the solar Rieger-type periodicity. We study Kepler light curves to search the periodicities on solar-like stars at different evolutionary stages and use them for an estimation of the stellar dynamo magnetic field.

Keywords: Stars: activity, Stars: magnetic field

1 Introduction

Short-term variations of 155-200 days known as Rieger-type periodicity occur in many indices of solar activity Rieger et al. (1984); Oliver et al. (1998); Zaqarashvili et al. (2010). Our recent analysis of long-term sunspot data showed that observed Rieger periods correlate with solar cycle strength: stronger cycles show shorter periods and this periodicity is smaller in the more active hemisphere in each cycle Gurgenashvili et al. (2016, 2017).

Our main goal during this investigation of stellar activity is to search for Rieger type periodicity, which may give us information regarding the magnetic activity of stars in different phase of evolution. The recent Kepler space mission collected huge amounts of data about stellar activity, which gives an excellent basis to search for Sun-like periodicities in other stars. Observed periodicities in solar-like stars with different rotational periods are very important to understand the development of dynamo activity during stellar evolution.

2 Short-term periods in the activity of Kepler-observed Sun-like stars

Using Kepler data, McQuillan et al. (2014) created a catalogue of more than 34 000 stars with determined rotation periods, where Sun-like stars could be selected by different criteria, such as effective surface temperature (5500-6000 Kelvin for the Sun), stellar surface gravity, log_g (4.2 for the Sun), and rotation period, which varies between 0.5-80 days. As the Rieger type periodicity is 5-6 times longer than the rotation period for the Sun (P_{rot} is 27 days and the Rieger type periodicity is around 150-170 days), therefore we were interested in stars where we could find periods several times longer than the stellar P_{rot}.

From thousands of Sun-like stars we chose one solar type star, with rotation period of about 9.5 days, which shows very clear periodicity of 60-61 days. This star is a younger analog of our Sun. The effective temperature of this star is 5601 K and the (log) surface gravity is 4.906. First we investigated the rotation period of this star quarter by quarter to study the variation of the stellar differential rotation period in detail. Then we performed different types of analysis to justify that the period of 60-61 days really is associated with the stellar activity. We found that this periodicity has stronger power during the first half of the observing interval; it is not instrumental and CCD-dependent and therefore it is related to stellar activity.

[1] University of Graz, Graz, Austria
[2] Abastumani Astrophysical Observatory, Ilia State University, Georgia
[3] Georg-August-Universitt Gttingen, Germany
[4] Max Planck Institute for Solar System Research, Germany

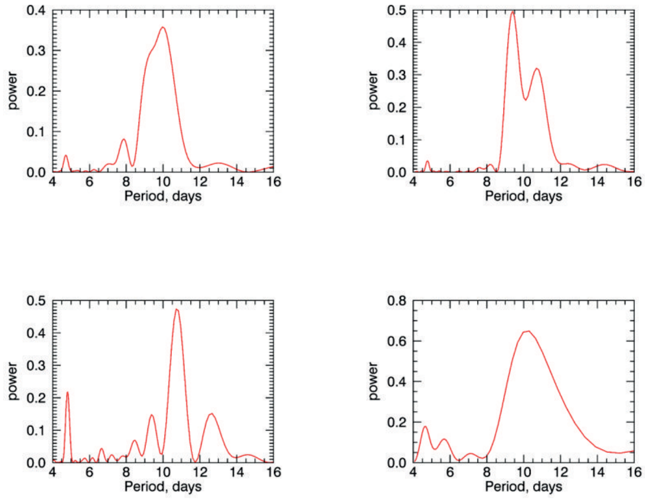

Fig. 1. GLS analysis of a Kepler Sun-like star which is a younger solar analog with rotation period of about 9.5 days. The rotational period is well defined in some quarters and mixed in others, very similar to the Sun. Therefore, the rotation periods might reflect the different phases of stellar activity.

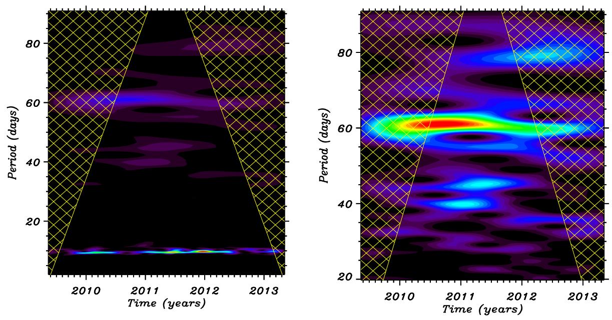

Fig. 2. The 9.5d rotating Kepler Sun-like star. Left panel: full range of periods. Right panel: selected range between 20-90 days. The chosen star shows a period of 60 days, which takes place during the first 8-9 quarters, after which it became less evident.

3 Conclusions

We investigated a Kepler solar-type star which shows similar behavior as the Sun, as the rotation period changes from 9 to 11 days. The rotation period varies in different quarters with various amplitudes. The variation of P_{rot} might mean that it reflects the different phases of stellar magnetic activity. We found very clear periodicity of 58-61 days in the light curve, which is probably due to stellar activity variations and not instrumental. This periodicity has stronger power during the first half of the observational interval, then it disappears.

This work was supported by Georgian SRNSF projects (217146, N04/46, project number N93569) and funded by the Volkswagen Foundation . This paper resulted from discussions at workshops of the ISSI team Rossby waves in astrophysics organized in Bern, Switzerland.

References

Gurgenashvili, E., Zaqarashvili, T. V., Kukhianidze, V., et al. 2016, ApJ, 826, 55

Gurgenashvili, E., Zaqarashvili, T. V., Kukhianidze, V., et al. 2017, ApJ, 845, 137

McQuillan, A., Mazeh, T., & Aigrain, S. 2014, ApJS, 211, 24

Oliver, R., Ballester, J. L., & Baudin, F. 1998, Nature, 394, 552

Rieger, E., Kanbach, G., Reppin, C., et al. 1984, Nature, 312, 623

Zaqarashvili, T. V., Carbonell, M., Oliver, R., & Ballester, J. L. 2010, ApJ, 709, 749

SUPERFAST SPECTRAL VARIATIONS OF OBA STARS

A.A. Batrakov[1], A.F. Kholtygin[1], S. Hubrig[2], S. Fabrika[3], A.F. Valeev[3] and A.E. Kostenkov[1]

Abstract. Results of our recent search for superfast line-profile variations (LPVs) in spectra of the bright OBA stars HD 93521 (O9.5III), ρ Leo (B1Iab), α^2 CVn, and γ UMi are presented. The spectra were obtained using the multi-mode focal reducer SCORPIO on the Russian 6-m telescope. Both regular LPVs with periods from 2 to 90 minutes and non-regular LPVs on time-scales of seconds were detected. Such short-term spectral variability in massive OBA stars has not been studied systematically before. These studies can be crucial for understanding the physics of type-II supernova and for improved modelling of stellar evolution.

Keywords: Stars: early-type, variables: general, line profiles

1 Introduction

Regular variations of line profiles with periods ranging from several hours to days in spectra of all types of OBA stars have been well studied. Recent observations by Hubrig et al. (2014) of the A0 supergiant HD 92207 using the focal-reducer, low-dispersion spectrographs FORS 2 in spectropolarimetric mode showed moderate line-profile variations (LPVs) of various lines on a time-scale of minutes.

This paper presented the continuation of studies of superfast LPVs in spectra of early-type stars as published by Batrakov et al. (2019); Kholtygin et al. (2018). A log of observations for all the programme stars and their measured *rms* magnetic field strengths $\mathcal{B}$ was taken from a review by Tsiopa et al. (2019) and is listed in the Table.

Star	Sp.Class	Year, month	N_{sp}	Exp (s)	$\mathcal{B}$, G
		6-m telescope, SCORPIO			
ρ Leo	B1Iab	Jan. 2015	1271	1	~ 50
HD 93521	O9Vp	Jan. 2015	529	3	~ 130
α^2 CVn	A0spe	Jan. 2015	387	1	~ 1100
γ UMi	A2III	Jan. 2015	249	3	suspected
HD 21389	A0Ia	Sep. 2016	284	11	not detected
		VLT, FORS2			
HD 92207	A0Iae	2011–2012	32	~ 60	~ 225
λ Eri	B2III(e)p	2011–2012	155	~ 3	~ 150

2 Results and discussion

In spectra of all of the stars observed with the SCORPIO spectrograph at the 6-meter telescope, regular components of LPVs were detected with periods from ~ 30 to ~ 90 min using the CLEAN method by Roberts et al. (1987). These components extend to higher frequencies the sequence of non-radial pulsation (NRP) harmonics already known for these stars, and may be connected with NRP modes $l = 6 - 12$.

In order to reveal any high-frequency components of LPVs, a Fourier transform with Hamming window of width ΔT was applied. Details of this technique are given by Batrakov et al. (2019). The windowed Fourier-transform maps of LPVs for the Hγ line in the spectra of the programme OBA stars are shown in Figs. 1-2.

[1] Saint-Petersburg University, Saint-Petersburg, Russia
[2] Leibniz-Institut für Astrophysik, Potsdam, Germany
[3] Special Astrophysical observatory, Nizhnii Arhyz, Russia

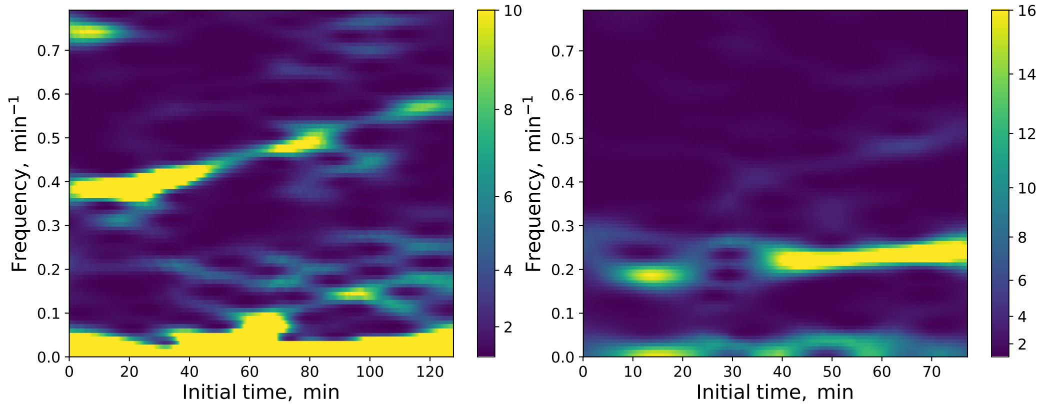

Fig. 1. Left: map of the windowed Fourier transform with Hamming window width $\Delta T = 40$ min for the Hγ line in the spectra of ρ Leo. **Right:** the same as in the left panel, but for HD 93521 and $\Delta T = 30$ min.

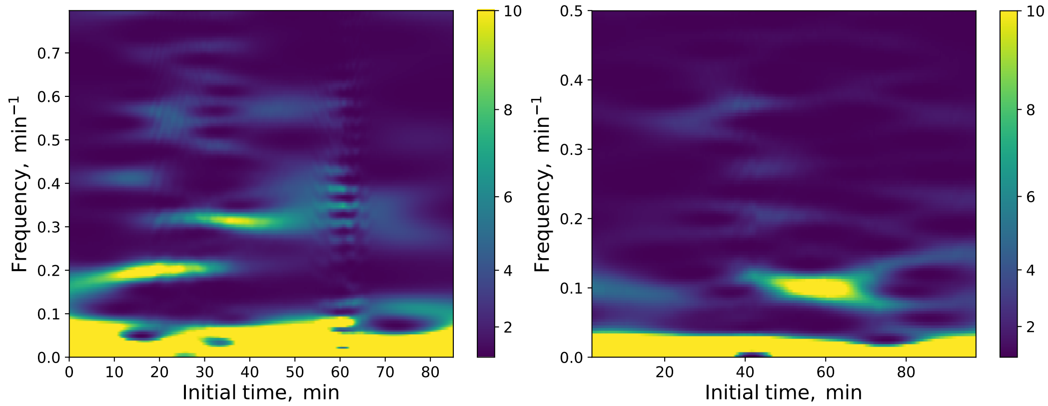

Fig. 2. Left: the same as in Fig. 1 but for α^2 CVn and $\Delta T = 35$ min. **Right:** the same as in the left panel, but for γ UMi and $\Delta T = 50$ min.

Very short period harmonics in the frequency interval $\nu \in [0.1 - 0.7]$ min^{-1} were detected. They appear to be unstable on time-scales of tens of minutes. A similar pattern of LPVs was also revealed for other H and He lines. At the same time, such short-scale LPVs were not detected in spectra of HD 21389.

One can presume that the presence of such intriguing components of LPVs can be explained by the instability of high modes of NRPs over short time intervals ($10 - 100$ min). The stars in which short time-scale LPVs were detected have spectral types from A to O and are of various luminosity classes; they are also magnetic, or suspected to be so. It can indicate that this kind of LPVs can hardly be explained by the properties of the stars themselves, but could be related to their magnetic fields.

The authors acknowledge support from RFBR grant 19-02-00311 A.

References

Batrakov, A. A., Kholtygin, A. F., Fabrika, S., & Valeev, A. 2019, ASP Conference Series, Vol. 518, (San Francisco: ASP), 153

Hubrig, S., Schöller, M., & Kholtygin, A. F. 2014, MNRAS, 440, 1779

Kholtygin, A. F., Batrakov, A. A., Fabrika, S. N., et al. 2018, Astrophysical Bulletin, 73, 471

Roberts, D. H., Lehar, J., & Dreher, J. W. 1987, AJ, 93, 968

Tsiopa, O. A., Batrakov, A. A., Kholtygin, A. F., et al. 2019, Astronomical Journal of Azerbaijan, in press

Stars and their variability observed from space
C. Neiner, W. W. Weiss, D. Baade, R. E. Griffin, C. C. Lovekin, A. F. J. Moffat (eds)

RESULTS OF LIGHT-CURVES ANALYSES FOR THE DWARF NOVA EX DRA

I. Voloshina[1] and T. Khruzina[1]

Abstract. The results of a long-term photometric observations of the cataclysmic variable EX Dra acquired between 2014 and 2016 in Crimea (24 nights, more than 10500 measurements) are presented. The observations were performed using CCD photometers mounted on 50-cm and 60-cm telescopes in the visible and red, during both quiescent and active states. These observations were used to derive the orbital period of the system. A combined model that takes into account the radiation fluxes from the gaseous stream and a hot spot on the lateral surface of the accretion disk was used to determine the parameters of the system components (white dwarf, red dwarf, accretion disk and hot spot, and gaseous stream). Variations of the parameters when the system changes from one activity state to the other were considered. Six light-curves displaying an unsatisfactory disagreement between the observed and theoretical light-curves can be fitted successfully using a version of the combined model that includes hot spots on the secondary's surface. That model is able to reproduce qualitatively a secondary minimum in the light-curves that exhibits shifts of this minimum from phase 0.5. The parameters of dark spots on the red-dwarf surface were determined. The data obtained indicate that the outbursts in the EX Dra are related to instabilities in the matter outflowing from the secondary.

Keywords: photometry, cataclysmic variables, dwarf novæ, light-curves

The cataclysmic variable EX Dra (HS1804+6753, $\alpha = 18^h04^m14.11^s$ and $\delta = +67°54'12.2''$), which has an orbital period of about 5 h and deep eclipses $\sim 1.5^m$, was detected in the Hamburg Quasar Survey (Bade et al. 1989). It was shown to be an eclipsing dwarf nova by Barwig et al. (1993). Outbursts occurs every $\sim 10 - 30^d$ with durations up to $\sim 10^d$. The brightness at outburst is about 13.5^m, and 15^m at quiescence.

Observations of EX Dra were made with two telescopes of Sternberg Astronomical Institute in Crimea: the 60-cm with a CCD detector Apogee 47 in 2014–2015 (17 observational sets), and the 50-cm with a CCD detector Apogee Alta U8300 in 2015–2016 (7 observational sets). The accuracy of our data is $0.02 - 0.06^m$.

Parameters of EX Dra were derived from the light-curves using a "combined" model that takes into account the presence of a hot spot on the lateral surface of the geometrically thick disk and of a region of enhanced energy release near the disk edge, at the base of the gas flow (the so-called "hot line"). The shape of the few light-curves obtained in quiescence could not be described in sa tandard model, so we added the presence of dark spots on the secondary surface. The non-ellipsoidal contribution of secondary radiation enabled us to describe anomalous minima at phases ~ 0.2 and ~ 0.7 (Fig. 2, right).

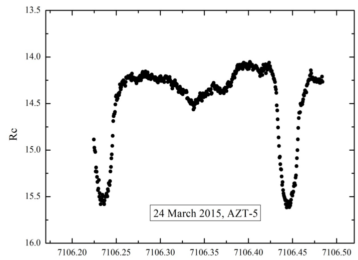

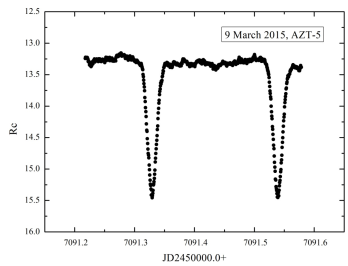

Fig. 1. Photometric observations of EX Dra obtained with the SIA 50-cm telescope: **Left:** Quiescence. **Right:** Outburst.

Our results:

The value of the orbital period of the EX Dra system was derived from our numerous new observations of this system in the quiet state. This value, $P_{orb} = 0^d.2099366(6)d$, coincides with the previous value obtained from spectroscopic observations of the star.

[1] Sternberg Astronomical Institute, Moscow State university, 119234, Moscow, Russia

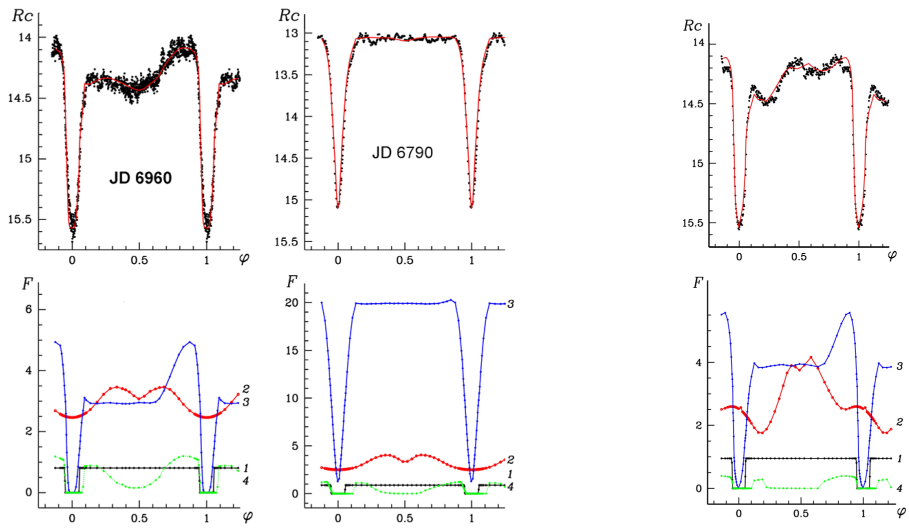

Fig. 2. Left: Typical light curves of EX Dra. Left: light-curves during quiescence; right: during outburst. Observations are shown as points, theoretical curves as the red line. The contribution of different components to the total luminosity is indicated by the white dwarf (1), red dwarf (2), disk with hot spot(3), hot line (4). **Right:** The same for one of the abnormal light-curves.

Table 1. Accretion disk and hot line parameters of EX Dra in the *Rc* band

Parameter	Inactive state	Active state
R_d, accretion disk radius in a_0	0.16−0.32	0.31−0.36
e, eccentricity	0.003−0.3	0.003−0.3
$0.5\beta_d$, thickness of the outer edge of accretion disk, °	0.5−1.7	0.6−1.6
T_{in}, temperature of inner regions of the disk, K	19 100−25 700	24 200−33 400
γ, parameter showing temperature changes along the radius of the disc	0.43−0.58	0.24−0.42
T_{ww}, temperature of windward side of gaseous stream, K	29 000−75 600	33 600−86 500
T_{lw}, temperature of leeward side of gaseous stream, K	31 800−66 500	30 600−78 900

A combined model that takes into account the presence of a hot spot on the lateral surface of the accretion disk and the contribution of light from a gaseous stream near the outer edge of the disk can be applied successfully to determine the main parameters of EX Dra in its different states of activity, at least for most of the light-curves studied (Khruzina 2011). A few of the light-curves observed could not be fitted satisfactorily with theoretical ones in the combined model. We therefore added to that model one or two dark spots on the surface of the secondary. Taking the existence of dark spots into account, we were able to reproduce qualitatively the shift of the secondary minimum from $\varphi \sim 0.5$.

The outbursts in the EX Dra system are related to the instability of the matter outflowing from the secondary (MTIM model), according to Baptista (2012).

This study was carried out with the support of RFBR grant N 17-52-53200. The authors are grateful to Dr. Sementsov for discussions. .

References

Bade, N., Hagen, H. J., & Reimers, D. 1989, in ESA Special Publication, Vol. 1, Two Topics in X-Ray Astronomy, Volume 1: X Ray Binaries. Volume 2: AGN and the X Ray Background, ed. J. Hunt & B. Battrick, 883

Baptista, R. 2012, Mem. Soc. Astron. Italiana, 83, 530

Barwig, H., Fiedler, H., Reimers, D., & Bade, N. 1993, in IAU Symposium 165: Compact Stars in Binary Systems, ed. H. van Woerden (Kluwer, Dordrecht), 89

Khruzina, T. S. 2011, Astronomy Reports, 55, 425

INSTRINSIC X-RAY VARIABILITY OF O STARS AND WOLF-RAYET STARS

A.M.T. Pollock[1]

Abstract. X-rays are produced in the radiatively-driven winds of O stars and Wolf-Rayet stars and show irregular variability of a few per cent amplitude on time scales of hours and days. How this slow X-ray chaos relates to the lower amplitude, more rapid optical chaos being revealed by TESS is not known.

Keywords: X-rays: stars, Stars: early-type, Stars: Wolf-Rayet, Stars: variables: general

1 X-rays from massive stars

Only a handful of single O stars and Wolf-Rayet stars are bright enough with current technology to have high-resolution X-ray spectra. The broad emission lines with widths about $\frac{3}{4}$ of the UV terminal velocities show that the X-rays are produced out in the supersonic stellar winds. The most popular theory, although incomplete, appeals to microscopic shocks that develop from instabilities in the wind line-driving mechanism. Accumulated intermittently over several years as part of XMM-Newton calibration, the aggregated 1 Ms high-resolution X-ray spectrum shown in Figure 1 of the single O4 supergiant ζ Puppis by the Reflection Grating Spectrometer (RGS) shows strong lines from highly-ionised abundant elements and little or no electron continuum. Apart from its unusually strong lines of NVI and NVII, testament to a high nitrogen abundance, it is typical of the soft X-ray spectra intrinsic to single massive O stars and Wolf-Rayet stars.

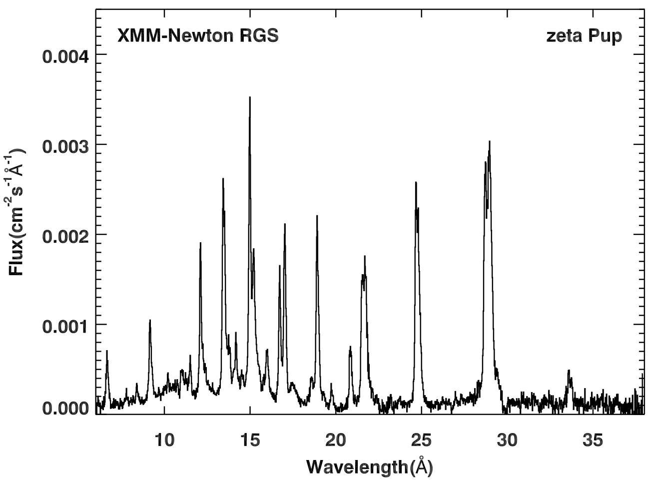

Fig. 1. XMM-Newton RGS high-resolution X-ray spectrum of the single O4 supergiant ζ Puppis.

2 X-ray variability instrument of choice

The ideal instrument combines linearity and stability with high sensitivity. The XMM-Newton EPIC-pn instrument acting as an imaging photometer is by far the best currently available. It also has the advantage of working alongside the other XMM instruments including the RGS. The pn's exceptional instrumental stability at a level of about 0.1% is demonstrated through repeated observations over many years of the very X-ray bright LMC SNR N132D shown in Figure 2.

[1] Department of Physics and Astronomy, University of Sheffield, Sheffield S3 7RH, UK

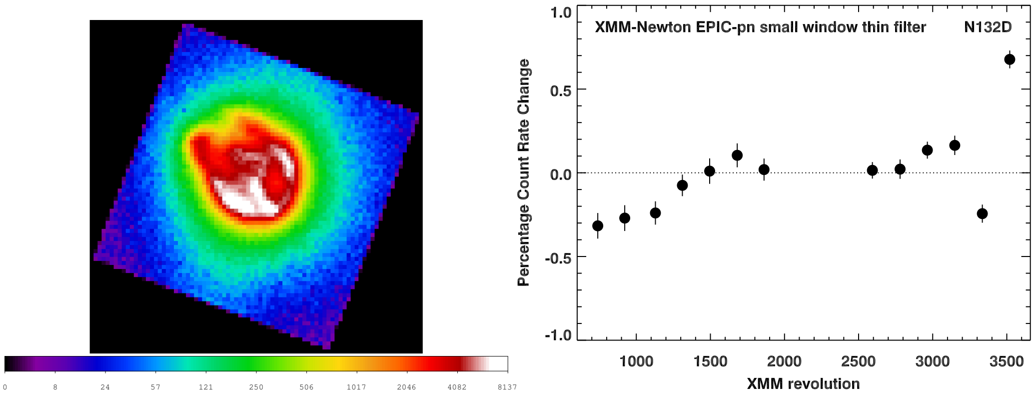

Fig. 2. XMM-Newton EPIC-pn observations of the LMC SNR N132D with the image left and the long-term light curve right.

3 X-ray variability

Even fewer massive stars have variability measurements. These all show that the X-ray brightness is not constant. XMM-Newton EPIC-pn light curves of the single O4 supergiant ζ Puppis show smooth irregular changes with an amplitude of a few percent on time-scales generally of a few days. This type of variability that might be classified as slow chaos has also been observed in all other hot stars with suitable data including δ Orionis and EZ CMa = WR6. Accumulated over several years by the EPIC-pn in parallel with the RGS spectrum above, the X-ray light curve of ζ Puppis of 1ks resolution on the left of Figure 3 has the unobserved gaps greatly reduced between typically annual observations. The Median Absolute Deviation measure of variability, or MAD, is only 3%, too small for other instruments to measure. There is no periodic signal with variations appearing stochastic or chaotic.

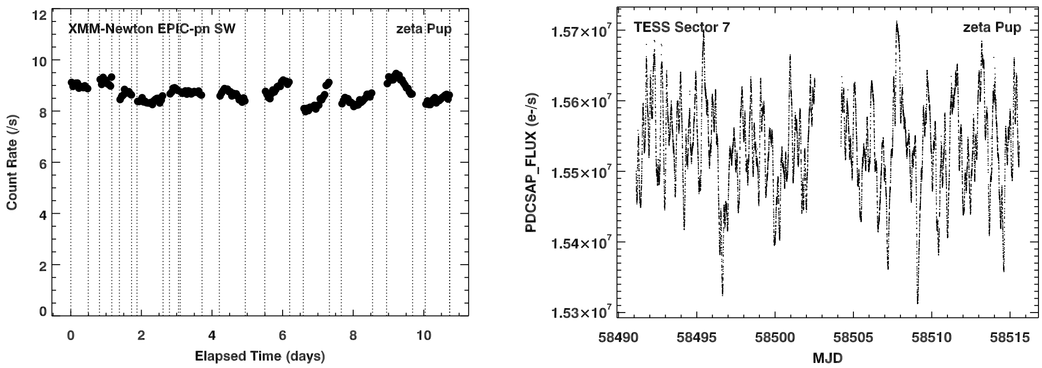

Fig. 3. Comparative X-ray and optical light curves of the O4 supergiant ζ Puppis from XMM-Newton EPIC-pn on the left and TESS on the right.

4 Towards a coherent physical synthesis

The well-developed theory of mass loss in hot stars holds that the powerful supersonic winds in O stars and Wolf-Rayet stars are driven by radiation pressure. TESS data have recently revealed the variability of the driving force through the beautiful material freely available in exemplary fashion through the MAST Archive as shown on the right of Figure 3 for ζ Puppis in one of two sectors. Here the MAD is 0.29%, an order of magnitude smaller in amplitude than in X-rays on time scales similarly perhaps an order of magnitude faster. It seems at least plausible that instead of responding to instabilities that X-rays are produced by interacting shocks out in the wind responding to variable radiation pressure. One of many unknowns concerns X-ray variability time scales because no observations have ever been long enough, a circumstance that will only be resolved through concerted community efforts.

Stars and their variability observed from space
C. Neiner, W. W. Weiss, D. Baade, R. E. Griffin, C. C. Lovekin, A. F. J. Moffat (eds)

ASTRONOMICAL POTENTIAL OF SATELLITE STAR TRACKERS

A.M.T. Pollock[1]

Abstract. An initiative is proposed to develop photometric data from satellite star trackers for astronomical use. A feasibility study undertaken for XMM-Newton shows clearly the enormous potential of the high cadence and long exposures of the bright guide stars used for the purposes of ensuring stable satellite pointing. Calibration is required to ensure photometric integrity and allow routine generation of science-ready data products for ultimate distribution to the astronomical community through archives.

Keywords: Stars: variables: general, Instrumentation: photometers, Astronomical databases: miscellaneous

1 The Star Tracker aboard the XMM-Newton satellite

One of the vital operational components of the European Space Agency's XMM-Newton X-ray Observatory satellite is the so-called AOCS system that ensures stable pointing during observations of the sky. In common with most space observatories, this is partly achieved with the use of a Star Tracker designed specifically to lock on to bright stars in its own field-of-view which is much larger than those of the X-ray instruments. Data pertaining to the set of bright stars forms part of the telemetry data stream and finds its quiet way into material delivered to observers through archive services. Measurements of stellar brightness in magnitude units and position within the Star Tracker field-of-view are reported every 0.5 s for many hours at a time to a precision of 0.05 mag. Despite these limitations, combinations of 50 or 100 successive points, for example, increases the precision of the measurements.

1.1 Chandra Variable Guide-Star Catalog

In 2010, XMM's US counterpart the Chandra X-ray Observatory published a catalogue by Nichols and colleagues `http://cxc.harvard.edu/vguide/index.php` confined to the 827 guide stars which showed significant variability along similar, if more limited, lines to the work proposed here ultimately to be fully integrated into routine pipeline and archive services of all space missions both past and present.

2 Astronomical potential of the XMM-Newton Star Tracker

In addition to their operational use, data of this type constitute a photometric sampling density and length of exposure of bright stars over the whole sky essentially otherwise unknown in routine astrophysics, certainly before TESS, as other missions often deal with generally fainter stars. The XMM Star Tracker could offer rich possibilities to observers of investigating uncharted parts of the time domain of whatever bright stars were used in an observation for pointing purposes. The tens of thousands of guide stars used over the course of the 20 years of the XMM mission have covered the magnitude range between 2.4 and 8.5 about a median of 7.4; spectral types between O6 and M5; and luminosity classes I-V. About 5000 light curves provide continuous uninterrupted coverage for longer than 1 day. The total body of data is an untapped astronomical resource of extraordinary value for stellar astronomy for both research and teaching purposes and likely to be of interest to communities in many of the dozens of variability classifications in one of the key resources in stellar astronomy, the General Catalogue of Variable Stars.

[1] Department of Physics and Astronomy, University of Sheffield, Sheffield S3 7RH, UK

2.1 Scientific rationale

XMM-Newton has been observing 5 bright stars on a more-or-less continuous basis for the 20 years since launch and will probably continue to do so for many years to come. In an initial feasibility study performed without access to documentation other than definition of telemetry contents, light curves have been extracted for 44128 XMM guide stars in public data of which 38510 have been assigned preliminary SIMBAD identifications on the basis of their reported star-tracker coordinates. Inspection of the light curves accumulated in intervals of 25 or 50 seconds reveals many examples of variability in the optical relevant to the study of a full variety of variable systems from eclipsing binaries through rotation and various forms of pulsations to stochastic changes of uncertain origin. Their potential value is demonstrated by considering a few examples identified from a short initial more-or-less random inspection of the tens of thousands of light curves available.

Shown in Figure 1 are three stars that illustrate the possibilities for binary systems; for pulsators; and for simultaneous X-ray and optical observations. Among binaries, ellipsoidal variables are tidally-distorted close systems without eclipses: TV Pic, shown on the left, was perfectly captured by the XMM-Newton Star Tracker. The central plot shows the light curve of the newly-discovered rapidly variable F0 IV star HR 1882 in 1 of 14 separate observations that showed remarkable long-term modulations. The target of an X-ray observation was also selected by accident as a guide star including the prominent Wolf-Rayet star EZ CMa whose optical light curve shown on the right was obtained precisely simultaneously with the star's X-ray light curve in a way otherwise almost impossible to obtain.

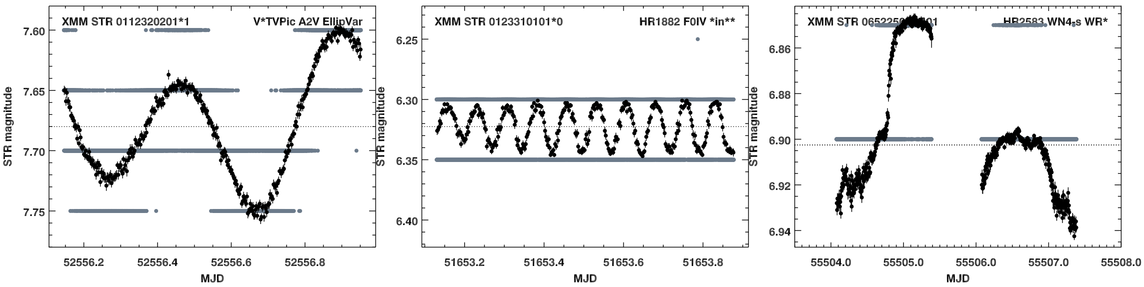

Fig. 1. Examples of optical light curves from the XMM-Newton Star Tracker. **Left:** TV Pic. **Centre:** HR 1882. **Right:** EZ CMa. The grey points show raw photometric measurements accurate to 0.05 magnitudes, the black points show the higher precision achievable with longer-term averages.

3 A Simple and profound conclusion

In the era of the Open Science data revolution, all space missions old and new should calibrate and publish all Star Tracker photometry.

Stars and their variability observed from space
C. Neiner, W. W. Weiss, D. Baade, R. E. Griffin, C. C. Lovekin, A. F. J. Moffat (eds)

EM CEP – AN INTERESTING BE STAR

N. Kochiashvili[1], I. Kochiashvili[1], R. Natsvlishvili[1], S. Beradze[1,2] and M. Vardosanidze[1,2]

Abstract. On the basis of $UBVR$ photometric data, obtained at Abastumani Astrophysical Observatory during 1991–1999, a very interesting and unusual flare in the Be star EM Cep was detected. An increase in brightness in the R band was observed, together with a simultaneous decrease in brightness in the U-band. The duration of the flare was over two hours. We estimated the percentage of brightness increase during the flare and the brightness decrease of the corresponding anti-flare, and the minimum amount of mass lost during this event. Different explanations for the nature of the star were investigated, from a binary companion to a pulsating star to a magnetic reconnection event. The present data point to the star probably being a single magnetic Be star; however, new observations are required to settle the question of the nature of EM Cep finally.

Keywords: $UBVR$ photometry, stellar flare, Be star

1 Introduction

We observed the B-type giant EM Cep at Abastumani Observatory from 1991 to 1999 (Kochiashvili 1999). At that time it was believed to be a bright ($V = 7.03$) short-period variable of spectral type BI IV+?. The amplitude of its variability is 0.15 mag; the period is P = 0.806187 days. Some investigators have considered the star to be a close binary system; some have regarded it as a non-radial pulsator (See Kochiashvili (1999) and literature cited therein). According to her observations, Rachkovskaya (Rachkovskaya 1977)concluded that EM Cep is either a β Cep-type variable or an oblique rotator. As Hα emission lines have been observed in its spectrum (Plaskett & Pearce (1931); Merril et al. (1925); Rachkovskaya (1977)), EM Cep must be a Be-type star. The character of the changes in its light-curves leads us to suggest that it maybe a λ Eri-type short-period Cepheid (Kochiashvili et al. (2007); Bakış et al. (2007); Kochiashvili & Kochiashvili (2008)). We also examined the case of binarity for the star (Kochiashvili & Kochiashvili 2008).

2 The Flare

It is known that O and B stars display flare activity. Two to three decades ago flares were rarely mentioned in the context of early spectral type stars, but according to more recent data such types do in fact belong to the most active class of variables in the Universe. A very interesting "unusual" flare was revealed in EM Cep in 1991. During photometric $UBVR$ observations eith the 48-cm Abastumani reflector a flare was detected in the R band, with a simultaneous anti-flare in the U band (Kochiashvili 1999). The increase in luminosity during the flare in the R band was approximately 24% of the total luminosity of the star; the simultaneous decrease in luminosity in the U-band was about 10%.

3 New findings by Bulgarian astronomers

New spectral observations were carried out during 2004–2015 with the 2-m RCC Rozhen telescope in Bulgaria, with a resolving power of 16 400; most spectra have a S/N ratio of 150–250. EM Cep was initially observed in a spectral region centred on Hα, but after 2005 July the region was changed to include the He I line at λ 6678 Å (Kjurkchieva et al. 2016). According to the new spectral data, EM Cep switches between B-star and Be-star states, as revealed by the level of Hα emission, but spends most of its time in the B-star state.

[1] Abastumani Astrophysical Observatory, Ilia State University, Mt. Kanobili, 0301 Adigeni, Georgia
[2] Samtskhe-Javakheti State University, 0800, Akhaltsikhe, Georgia

4 Conclusions

Be stars and their massive extension, the Oe stars, may prove to be progenitors of late stages of massive-star evolution connected to rapid rotation, such as S Dor variables, or even the long GRBs. A full extension of Be star research to extragalactic environments will only be reached with future facilities, such as extremely large telescopes (Rivinius et al. 2013). There are some unsolved problems concerning S Dor and Be stars that could be related to each other. We believe observations of bright stars of both types with small telescopes is an advantage, so we are continuing to observe EM Cep using the same 48-cm Cassegrain telescope (now furnished with a new CCD), with standard $UBVRI$ filters (see a V light-curve in Fig. 1). We hope to find observational evidence for stellar pulsations, if they occur. One of the aims for these observations is to monitor flare activity of EM Cep.

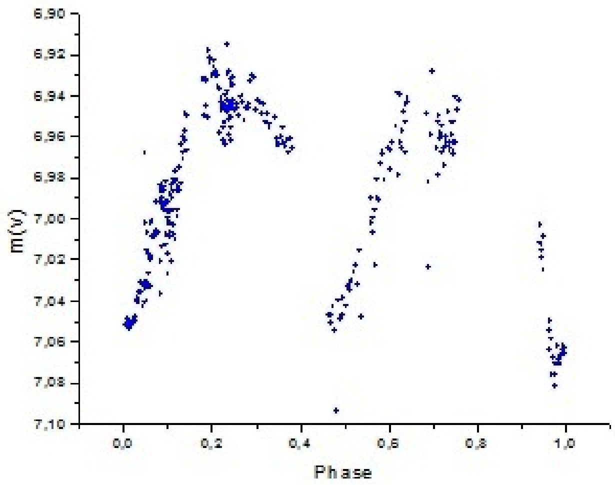

Fig. 1. Observations of EM Cep, V band, made in 2018

This work was supported by Shota Rustaveli National Science Foundation (SRNSF), grant No 218070.

References

Bakış, V., Bakış, H., Eker, Z., & Demircan, O. 2007, MNRAS, 382, 609

Kjurkchieva, D., Marchev, D., Sigut, T. A. A., & Dimitrov, D. 2016, AJ, 152, 56

Kochiashvili, I. & Kochiashvili, N. 2008, Romanian Astronomical Journal, 18, 61

Kochiashvili, N., Natsvlishvili, R., Bakis, H., & Tanriver, M. 2007, Astronomical and Astrophysical Transactions, 26, 113

Kochiashvili, N. T. 1999, Astrophysics, 42, 399

Merril, P. W., Humason, M. L., & Burwell, C. G. 1925, Contributions from the Mount Wilson Observatory / Carnegie Institution of Washington, 294, 1

Plaskett, J. S. & Pearce, J. A. 1931, Publications of the DAO Victoria, 5, 1

Rachkovskaya, T. M. 1977, Izvestiya Ordena Trudovogo Krasnogo Znameni Krymskoj Astrofizicheskoj Observatorii, 56, 11

Rivinius, T., Carciofi, A. C., & Martayan, C. 2013, A&A Rev., 21, 69

Stars and their variability observed from space
C. Neiner, W. W. Weiss, D. Baade, R. E. Griffin, C. C. Lovekin, A. F. J. Moffat (eds)

OLD AND NEW OBSERVATIONAL DATA FOR P CYGNI

S. Beradze[1,2], N.Kochiashvili[1], I.Kochiashvili[1], R.Natsvlishvili[1] and M.Vardosanidze[1,2]

Abstract. We present results of old and new photometric observations of P Cygni. The old data (1951–1983) were collected by E. Kharadze and N. Magalashvili at the Abastumani Astrophysical Observatory, Georgia; we recovered and recalculated them, and concluded that the star should undergo its next great eruption in some 100 years. New observations, obtained in 2014 using the Abastumani 48-cm Cassegrain telescope, demonstrated interesting behaviour in the light-curve.

Keywords: UBV photometry, stars: Luminous Blue Variable Stars, individual: P Cygni

1 Introduction

P Cygni, the massive early-type Luminous Blue Variable with a history of some 400 years of investigations, had been observed photoelectrically with the 33-cm reflector of the Abastumani Astrophysical Observatory from its very establishment. The telescope was equipped with an electro-photometer which had a maximum spectral sensitivity at 4350 AA. The photometric system was similar to that of Johnson (Beradze et al. 2015). From 1951 N. Magalashvili and E. Kharadze observed P Cyg regularly with this telescope, using B and V filters from 1951–1960 and UBV filters after 1961. Kharadze and Magalashvili continued observing the star until 1983. From 1968 they used the same filters and the same photometer but on the Abastumani 48 cm Cassegrain telescope. We had the opportunity to process those observations and to calculate reliable brightness variations of the target star using 36 Cyg as comparison star; see Fig.1 (Beradze et al. 2018) (Kochiashvili et al. 2018). At first glance we can see that during 1974–1983 the star dimmed in the U band while brightening in the B and V bands (the last third part of Fig. 1). The middle part of the figure represents the time interval of 1961–1967, when the colour behaviour of the star was different; whilst brightening in V, the star became fainter in B and U.

2 Colour behaviour of P Cygni

Long-term photometric observations of P Cyg have given us an opportunity to trace its $B-V$ colour variability. It is known that the star is gradually reddening; however, that behaviour is particularly impressive as seen in the observations of Kharadze and Magalashvili, because after correcting for an initial reddening of 0.5 in $B-V$, the $B-V$ values vary from –0.5 to –0.1 between 1951 and 1983. Those colour indices correspond to an early-B type (Kochiashvili et al. 2017).

3 Photometric observations of P Cygni in 2014

We observed P Cygni on 2014 July 23–October 20 with the 48-cm Cassegrain telescope and standard B, V, R, I filters. HD 228793 (V=9.9, B=10.16) was used as a comparison star (see Fig. 2). During those observations P Cyg underwent light variations with a mean amplitude of ∼0.1 mag in all pass-bands, during a period of ∼68 days (Beradze et al. 2018) (Kochiashvili et al. 2017).

[1] E.Kharadze Abastumani Astrophysical Observatory, Mt. Kamobili, 0301 Adigeni
[2] Samtskhe-Javakheti State University, 0800. Akhaltsikhe, Georgia

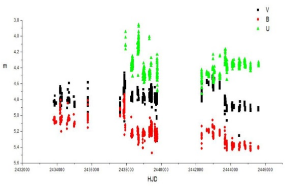

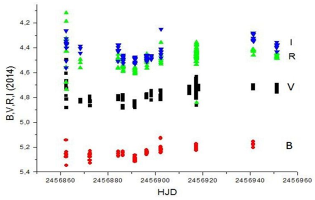

Fig. 1. Left: *UBV* observations of P Cyg made by E. Kharadze and N. Magalashvili during 1951–1983. 36 Cygni (HD 193369) was used as a comparison star. **Fig.2 Right:** Observations of P Cyg in 2014.

4 Conclusions

We have presented observations of P Cyg obtained between 1951–1983 and in 2014 at the Abastumani Astrophysical Observatory, including unpublished observations obtained by Kharadze and Magalashvili. These observations are very significant for the following reasons: 1. they represent homogenous data of more than 30 years; 2. The simultaneous *UBV* observations enable us to trace the colour behaviour of the star; 3. The observations by Kharadze and Magalashvili are unique because they are the only existing data of P Cyg observed with *UBV* filters between 1951 and 1983. But we still need more observational data and detailed analyses, because some questions still remain unanswered, e.g. concerning a possible binary nature of the star. The mechanism of the great eruptions in P Cyg and other LBVs are still not established. The connection between stellar rotation, pulsation and magnetic fields in P Cyg are (so far) also not very clear.

5 Acknowledgements

This work was supported by the Shota Rustaveli National Science Foundation (SRNSF) Grant - No PHDF/ 18-1327, Project Title - Modeling of P Cygni on the basis of existing and newly obtained photometric and spectral observations.

References

Beradze, S., Kochiashvili, N., Natsvlishvili, R., et al. 2015, in Wolf-Rayet Stars, ed. W.-R. Hamann, A. Sander, & H. Todt, 353

Beradze, S., Kochiashvili, N., Natsvlishvili, R., Kochiashvili, I., & Vardosanidze, M. 2018, Communications of the Byurakan Astrophysical Observatory, 65, 255

Kochiashvili, N., Beradze, S., Kochiashvili, I., Natsvlishvili, R., & Vardosanidze, M. 2017, in IAU Symposium, Vol. 329, The Lives and Death-Throes of Massive Stars, ed. J. J. Eldridge, J. C. Bray, L. A. S. McClelland, & L. Xiao, 415–415

Kochiashvili, N., Beradze, S., Natsvlishvili, R., et al. 2018, Astrophysics, 61, 22

Stars and their variability observed from space
C. Neiner, W. W. Weiss, D. Baade, R. E. Griffin, C. C. Lovekin, A. F. J. Moffat (eds)

DISCOVERY OF THE FIRST AP STAR IN AN ECLIPSING BINARY SYSTEM

M. Skarka[1], P. Kabáth[2], E. Paunzen[1], M. Mašek[3], J. Žák[1] and J. Janík[1]

Abstract. We report the discovery of a very special object, the first star of its kind. HD 99458 appeared to be a chemically peculiar star of Ap type, showing overabundances of Si, Ti and other heavy elements which are concentrated into spots. The spots produce rotational modulation of light variations. In addition, the star shows pulsations of a δ Scuti type, which has never before been reported in Ap stars. The star is in a binary system with a red-dwarf companion, which is also very rare among magnetic chemically-peculiar stars. In this paper we discuss new observations and results concerning the pulsation period and chemical peculiarity of this object.

Keywords: Stars: chemically peculiar, inidividual: HD 99458, binaries: eclipsing

1 Introduction

HD 99458 was originally identified as a candidate exoplanetary host star by Barros et al. (2016). We report here on the analysis performed by Skarka et al. (2019). We utilized *Kepler/K2* data (Howell et al. 2014) and new radial-velocity (RV) observations gathered in the Czech and Slovak Republic to confirm the exoplanetary nature of the companion. We found that the companion is a low-mass red-dwarf star of mass $0.45\,\mathrm{M}_\odot$ and not an exoplanet. High-resolution spectra enabled us to perform a basic chemical-abundance analysis; it revealed that the primary star in the binary system shows overabundance of Si, Ti and other elements. We explain the out-of-transit variations with a period of 2.722 days, which is the same as the orbital period, to be a consequence of chemical spots. The primary of HD 99458 is therefore a magnetic chemically-peculiar star (CP2 type, Preston 1974).

CP2 stars are only rarely reported to be found in binary systems (e.g. Carrier et al. 2002; Mathys 2017). Some unknown process is expected in close binaries that removes the magnetic field, which is necessary to sustain the chemical spots. This makes HD 99458 a special case, and the first A-type CP2 star known to be bound in a close binary system. The analysis of the photometric *K2* data revealed multi-mode stellar oscillations of δ Scuti type, with a dominant frequency at 19.2 c/d (period of 0.052 days). This phenomenon is also rarely reported among A-type CP2 stars (Bowman et al. 2018). The basic parameters of the binary, (taken from Skarka et al. 2019), are summarized in Table 1.

2 New results and conclusions

In 2019 we obtained new photometry with 60-cm telescope at Mt. Suhora Observatory (Poland) and with the 25-cm FRAM telescope at La Palma (Spain). The photometry in Strömgren filters supplemented with a g2 filter at Mt. Suhora, enabled us to estimate the $\Delta a = +35(3)$ mmag index. That value is typical for stars of the CP2 type (Paunzen et al. 2005). The photometry from the FRAM telescope (Janeček et al. 2019) revealed that the dominant frequency detected in *K2* data by Skarka et al. (2019) was actually the Nyquist reflection of the true dominant frequency, which is 27.72 c/d (0.036 days; see Fig. 1). Fututre stages in the investigation of HD 99458 will feature detailed spectroscopic and spectropolarimetric analyses.

MS acknowledges the OP VVV project Postdoc@MUNI No. CZ.02.2.69/0.0/0.0/16-027/0008360. This work is supported by MEYS (Czech Republic) under the projects MEYS LM2015046, LTT17006 and EU/MEYS CZ.02.1.01/0.0/0.0/16_013/0001403. PK would like to acknowledge grant GACR 17-01752J

[1] Department of Theoretical Physics and Astrophysics, Masaryk University, Kotlářská 2, 611 37 Brno, Czech Republic
[2] Astronomical Institute of the Czech Academy of Sciences, Fričova 298, 251 65 Ondřejov, The Czech Republic
[3] Institute of Physics, Czech Academy of Sciences, Na Slovance 1999/2, CZ-182 21 Praha, Czech Republic

Table 1. Basic parameters of the HD 99458 system. Values are taken from (Skarka et al. 2019), T_0 was adopted from Barros et al. (2016).

P (d)	2.722045(9)	i (deg)	73.2(6)
T_0 (HJD)	2456814.4918	R_1 ($R_\odot$)	3.47(16)
a ($R_\odot$)	11.28(5)	R_2 ($R_\odot$)	$0.59^{+0.06}_{-0.14}$
$q = M_2/M_1$	0.21(1)	$\log g_1$ (cgs)	3.70(5)
K_1 (km s^{-1})	35.2(3)	$\log g_2$ (cgs)	4.55(5)
M_1 ($M_\odot$)	2.15(5)	M_2 ($M_\odot$)	0.45(2)

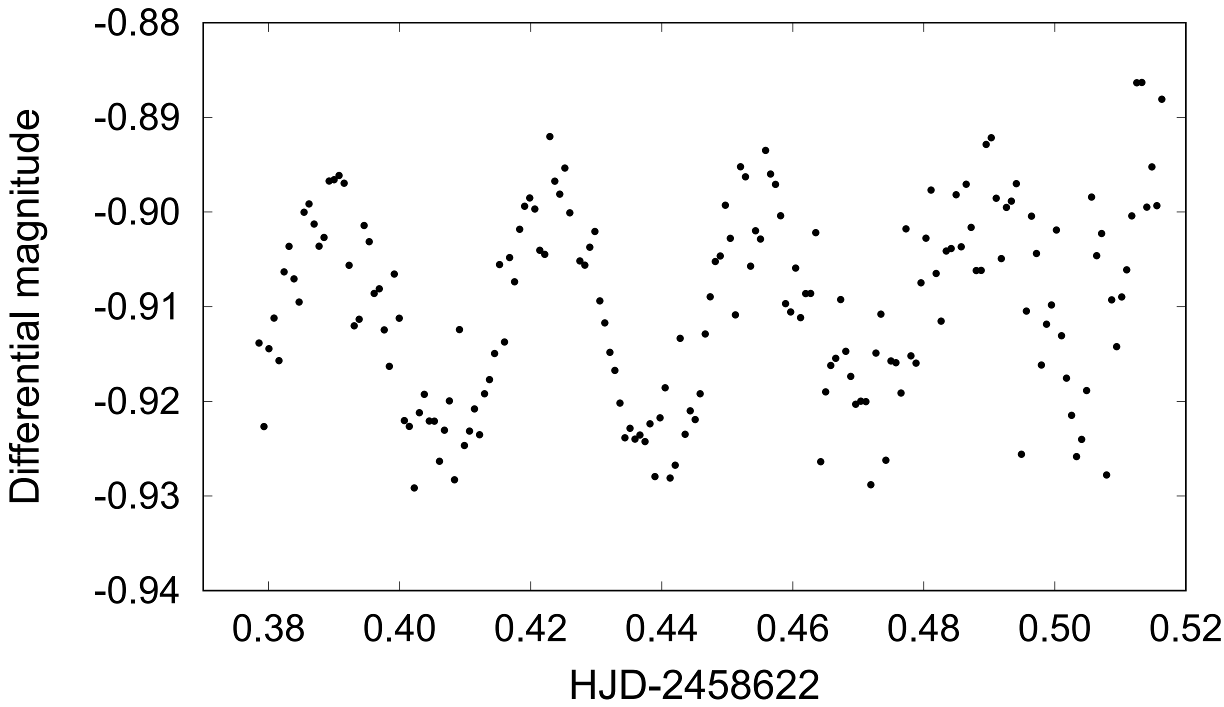

Fig. 1. Observations in Johnson B taken with the FRAM telescope.

References

Barros, S. C. C., Demangeon, O., & Deleuil, M. 2016, A&A, 594, A100

Bowman, D. M., Buysschaert, B., Neiner, C., et al. 2018, A&A, 616, A77

Carrier, F., North, P., Udry, S., & Babel, J. 2002, A&A, 394, 151

Howell, S. B., Sobeck, C., Haas, M., et al. 2014, PASP, 126, 398

Janeček, P., Ebr, J., Juryšek, J., et al. 2019, in EPJ Web of Conferences, Vol. 197, EPJ Web of Conferences, 02008

Mathys, G. 2017, A&A, 601, A14

Paunzen, E., Stütz, C., & Maitzen, H. M. 2005, A&A, 441, 631

Preston, G. W. 1974, ARA&A, 12, 257

Skarka, M., Kabáth, P., Paunzen, E., et al. 2019, MNRAS, 487, 4230

Stars and their variability observed from space
C. Neiner, W. W. Weiss, D. Baade, R. E. Griffin, C. C. Lovekin, A. F. J. Moffat (eds)

MOBSTER*: SEARCH FOR PERIOD EVOLUTION IN ORION'S MAGNETIC B-TYPE STARS

M. E. Shultz[1], A. David-Uraz[1], J. Labadie-Bartz[2], Z. Mikulášek[3] and V. Petit[1]

Abstract. Magnetic hot stars are expected to spin down through angular momentum loss via their magnetospheres, but the small number of magnetic early-type stars for which period change has been measured directly yields ambiguous results. We aim to utilize *TESS* data in conjunction with archived photometric and magnetic measurements to constrain period changes in a larger sample of stars.

Keywords: Stars: individual: HD 35298, HD 36526, HD 37017, rotation, magnetic field, early-type

1 Introduction

Magnetic wind confinement greatly increases the moment arm of a star, and is therefore expected to lead to angular momentum loss (Weber & Davis 1967; ud-Doula et al. 2009). Magnetic hot stars are consequently expected to be slower rotators than hot stars without magnetic fields, and this is indeed observed to be the case (e.g. Alecian et al. 2013; Shultz et al. 2018). Furthermore, the rotation periods of magnetic B-type stars increase rapidly with fractional main-sequence age (Shultz et al. 2019b). Despite this strong supporting evidence for magnetic spindown at the population level, direct measurements of period changes have so far yielded contradictory results; σ Ori E is spinning down at the expected rate (Townsend et al. 2010), HD 142990 is spinning *up* (Shultz et al. 2019a), and CU Vir and Landstreet's Star (HD 37776) are both exhibiting complex patterns of alternating spin-down and spin-up (Mikulášek et al. 2011; Mikulášek 2016; Mikulášek et al. 2017).

2 Expanding the sample

We obtained *TESS* light-curves for the Orion magnetic B-type stars HD 35298 (B5p V), HD 36526 (B5p V), and HD 37017 (B2p V). Multi-year light-curves from the Kilodegree Extremely Little Telescope (KELT; Pepper et al. 2007, 2012) are available for all the stars, as are high-quality magnetic measurements obtained by the MiMeS programs with the ESPaDOnS spectropolarimeter. We then obtained all available photometric (North 1984; van Leeuwen 2007; Mikulášek et al. 2007) and magnetic (Borra & Landstreet 1979; Bohlender et al. 1987; Yakunin 2013; Romanyuk et al. 2016; Shultz et al. 2018) data. For each star, the total dataset spans between about 30 and 45 years.

Periods were determined independently from each dataset (top panels of Fig. 1), and do not show any evidence of a systematic change with time for any of the stars. The photometric data, which are available in much greater abundance, were then used to calculate observed minus calculated ($O-C$) diagrams by shifting the model light-curve obtained from a harmonic fit to the *TESS* data in phase in order to obtain the best match of the harmonic fit to each time-binned subset of the total photometric time-series. Those are shown in the second row of Fig. 1. $O-C$ uncertainties were determined via bootstrapping, and period change rates were determined from parabolic fits to each bootstrapping iteration (third row of Fig. 1). HD 35298 and HD 36526 respectively show very slight evidence of period decrease and period increase, albeit much slower than in previously reported cases of period change. The light-curve of HD 37017's is consistent with no change in period.

The bottom rows of Fig. 1 show the phase-binned photometric and longitudinal magnetic field $\langle B_z \rangle$ measurements, folded with constant periods determined via minimizing the slopes of the $O-C$ diagrams. In all three cases the photometric and magnetic variations can plausibly be phased with a constant period.

*Magnetic OB[A] Stars with TESS: probing their Evolutionary and Rotational properties; David-Uraz et al. (2019); see also David-Uraz et al., these proceedings.

[1] Department of Physics and Astronomy, University of Delaware, 217 Sharp Lab, Newark, Delaware, 19716, USA

[2] Instituto de Astronomia, Geofísica e Ciencias Atmosféricas, Universidade de Sáo Paulo, Rua do Matão 1226, Cidade Universitãria, Sáo Paulo, SP 05508-900, Brazil

[3] Department of Theoretical Physics and Astrophysics, Masaryk University, Kotlsk 2, CZ 611 37, Brno, Czech Republic

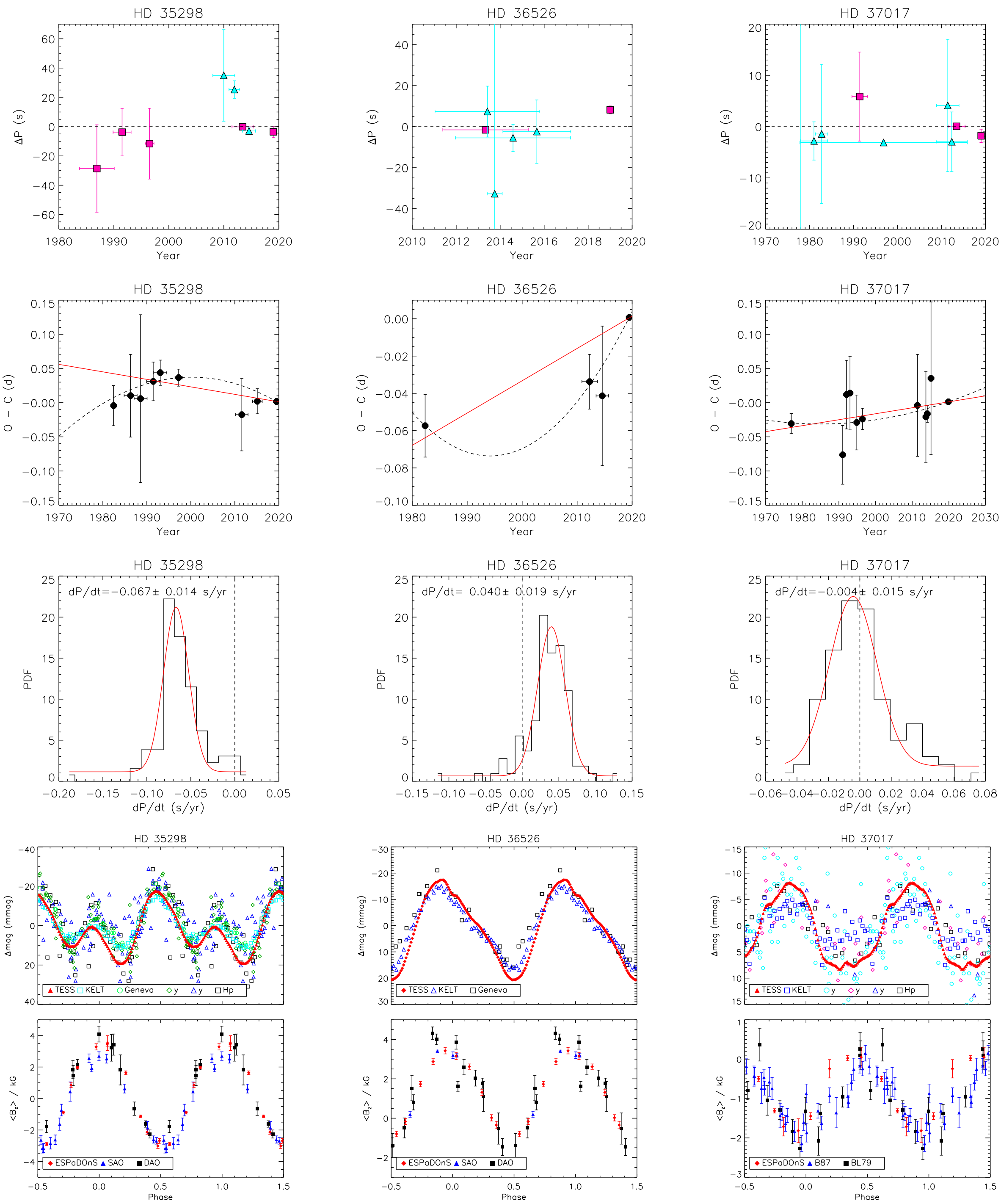

Fig. 1. *Top*: Periods as a function of time. Periods from magnetic data as blue triangles; photometric data as magenta squares. *Second row*: Photometric $O - C$ diagrams with parabolic and linear fits. *Third row*: $\dot{P}$ determined from parabolic fits to bootstrapped $O - C$ iterations. Dashed lines indicate $\dot{P} = 0$. *Bottom rows*: phase-binned photometric and magnetic data folded with the best (constant) periods determined via $O - C$ minimization.

3 Conclusions

While there is some evidence of period change in the $O - C$ diagrams of HD 35298 and HD 36526, the photometric and magnetic time-series of all three stars can be phased with constant periods. There is therefore no strong evidence of period change over the past 4 decades in any of these three stars.

MES acknowledges financial support from the Annie Jump Cannon Fellowship, supported by the University of Delaware and endowed by the Mount Cuba Astronomical Observatory. ADU acknowledges financial support from the Natural Sciences and Engineering Research Council of Canada (NSERC). ZM was supported by GAR grant 18-05665S.

References

Alecian, E., Wade, G. A., Catala, C., et al. 2013, MNRAS, 429, 1027

Bohlender, D. A., Landstreet, J. D., Brown, D. N., & Thompson, I. B. 1987, ApJ, 323, 325

Borra, E. F. & Landstreet, J. D. 1979, ApJ, 228, 809

David-Uraz, A., Neiner, C., Sikora, J., et al. 2019, MNRAS, 487, 304

Mikulášek, Z. 2016, Contributions of the Astronomical Observatory Skalnate Pleso, 46, 95

Mikulášek, Z., Janík, J., Zverko, J., et al. 2007, AN, 328, 10

Mikulášek, Z., Krtička, J., Henry, G. W., et al. 2011, A&A, 534, L5

Mikulášek, Z. Z., Krtička, J., Janík, J., et al. 2017, in ASPCS, Vol. 510, Stars: From Collapse to Collapse, ed. Y. Y. Balega, D. O. Kudryavtsev, I. I. Romanyuk, & I. A. Yakunin, 220

North, P. 1984, A&AS, 55, 259

Pepper, J., Kuhn, R. B., Siverd, R., James, D., & Stassun, K. 2012, PASP, 124, 230

Pepper, J., Pogge, R. W., DePoy, D. L., et al. 2007, PASP, 119, 923

Romanyuk, I. I., Semenko, E. A., Yakunin, I. A., Kudryavtsev, D. O., & Moiseeva, A. V. 2016, Astrophysical Bulletin, 71, 436

Shultz, M., Rivinius, T., Das, B., Wade, G. A., & Chand ra, P. 2019a, MNRAS, 486, 5558

Shultz, M. E., Wade, G. A., Rivinius, T., et al. 2019b, MNRAS, 490, 274

Shultz, M. E., Wade, G. A., Rivinius, T., et al. 2018, MNRAS, 475, 5144

Townsend, R. H. D., Oksala, M. E., Cohen, D. H., Owocki, S. P., & ud-Doula, A. 2010, ApJ, 714, L318

ud-Doula, A., Owocki, S. P., & Townsend, R. H. D. 2009, MNRAS, 392, 1022

van Leeuwen, F. 2007, A&A, 474, 653

Weber, E. J. & Davis, Jr., L. 1967, ApJ, 148, 217

Yakunin, I. A. 2013, Astrophysical Bulletin, 68, 214

Stars and their variability observed from space
C. Neiner, W. W. Weiss, D. Baade, R. E. Griffin, C. C. Lovekin, A. F. J. Moffat (eds)

,

THE STRANGE CASE OF HD 65987, A MAGNETIC BP STAR WITH TWO PERIODS

J. D. Landstreet[1,2], A. David-Uraz[3], O. Kochukhov[4], C. Neiner[5], P. Nelson[1] and G. Wade[6]

Abstract. *TESS* photometry of the magnetic chemically peculiar star HD 65987, a member of the open cluster NGC 2516, shows clear photometric variability with a period of 1.45 d. However, new magnetic and spectroscopic measurements of this star reveal a magnetic field varying with a stellar rotation period of about 7.7 d. The origin of the 1.45 d variations is suggested to be stellar pulsations.

Keywords: Stars: chemically peculiar, magnetic field, individual: HD 65987

1 Introduction

HD 65987 is a member of the open cluster NGC 2516, a cluster with an unusually large number of magnetic stars. Its membership was confirmed by data of the cluster and surroundings in *Gaia* given in DR2. Its parallax and proper motions are in good agreement with mean values for the cluster. The star's position within the main sequence in a *uvby* H–R diagram supports its cluster membership.

A longitudinal magnetic field was detected in HD 65987 with the FORS1 spectropolarimeter at the ESO VLT (Bagnulo et al. 2006). The field was detected twice at about the 6–7σ level. The star is clearly magnetic, and has a longitudinal field that reverses sign.

2 *TESS* photometry

Light variability of this star was observed by *TESS* (Ricker et al. 2015). Several groups have concluded that its light varies with a small amplitude and a period of 1.44 to 1.46 d, and that the variations are what would be expected for rotational variability of a magnetic Bp star (Balona et al. 2019; David-Uraz et al. 2019; Cunha et al. 2019). This range of periods is in good agreement with the photometric observations by North (1984). One 27 d–long *TESS* light-curve (of seven available) is shown in Fig. 1.

3 New magnetic observations

The magnetic field of HD 65987 was measured from seven new polarised spectra obtained during a 10-night run with the HARPSpol spectropolarimeter at ESO's La Silla Observatory during 2016 February. The values of $\langle B_z \rangle$ were measured as described by Landstreet et al. (2015), using only the cores of the Hα, Hβ, and Hγ Balmer lines in order to minimise the effects of abundance patchiness over the surface. The new data confirm that the strength of the $\langle B_z \rangle$ field reaches several hundred G, and that it reverses sign.

However, when the $\langle B_z \rangle$ values are plotted on the photometric period, they form a scatter plot. No smooth regular variation of $\langle B_z \rangle$ with photometric period is observed. The magnetic observations have therefore been searched for periodic variations using a χ^2 minimisation strategy. The data strongly suggest a period of about (7.7 ± 0.6) d, or perhaps the 1/day alias of this period at 1.15 d, but are *completely inconsistent* with variations in the 1.45 d photometric period.

[1] Department of Physics & Astronomy, University of Western Ontario, London, Ontario, Canada
[2] Armagh Observatory & Planetarium, Armagh, UK
[3] Department of Physics & Astronomy, University of Delaware, Newark, Delaware, USA
[4] Department of Physics & Astronomy, Uppsala University, Uppsala, Sweden
[5] LESIA, Paris Observatory, PSL University, CNRS, Sorbonne University, Université de Paris, 5 place Jules Janssen, 92195 Meudon, France
[6] Department of Physics & Space Science, Royal Military College of Canada, Kingston, Ontario, Canada

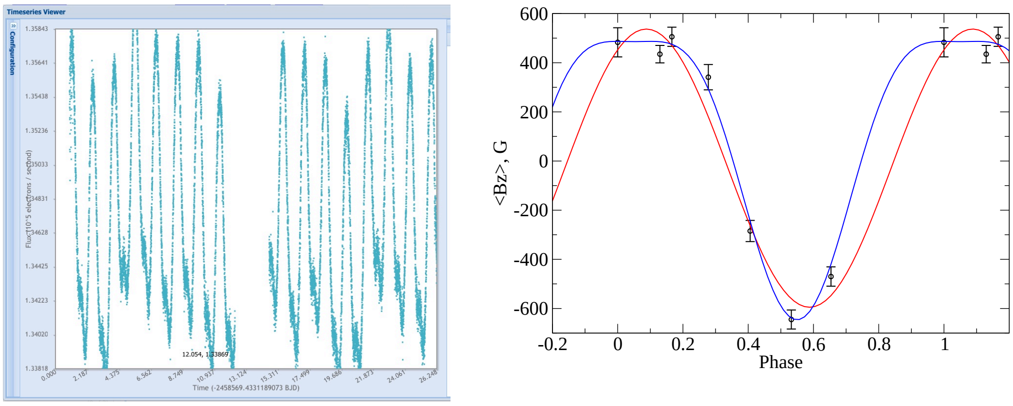

Fig. 1. Left: *TESS* light-curve from a single 27-day observation block with 120 s cadence starting, on 2019 March 26. The separation between successive peaks in the obvious light variations implies a period of about 1.45 d. **Right**: New magnetic field ($\langle B_z \rangle$) measurements, phased with period $P = 7.73$ d. The smooth curves are a sine wave fit (red), and a higher-order fit (blue).

4 Discussion

It is clear from the above descriptions that the $P = 1.45$d light variations do not represent the rotation period of HD 65987. There is no obvious signature of any $P \approx 7.7$ d magnetic field variations as in the observed light variations. This is probably consistent with the low amplitude of line-strength variations observed in the spectra.

So – what is causing the light variations?

Light variablity of HD 65987 with $P = 1.456$ d was observed in *seven* different 27 d series of observations obtained with *TESS*. It seems extremely unlikely that the variations are the result of an instrumental artefact.

There is no hint of a second star in the modern data. No eclipse-like light variations are seen. No radial-velocity variations larger than about 1 km/s are observed on time-scales of days, months, or years (González & Lapasset 2000). Although the spectrum of HD 65987 is quite complex, all the apparently unblended or weakly blended lines in the optical spectrum have widths consistent with the rotational velocity ($v \sin i = 21$ km/s) of a single star. There are no hints of a secondary spectrum.

The most probable explanation for this period discrepancy is that HD 65987 is a *Slowly Pulsating B Star* or SPB star. Such stars show low-amplitude light variations of 0.1 mag or less, and periods typically of one to a few days (Lata et al. 2016, and references therein). HD 65987 lies in the instability region for such pulsations (Miglio et al. 2007), and its light variability has the appropriate amplitude and frequency. The light-curve appears to vary somewhat in amplitude, and could conceal multiple frequencies. In other words, HD 65987 shows *rotational* variability via the magnetic data, and *pulsational* variability via photometry.

JDL, ADU and GW acknowledge support from the Natural Sciences and Engineering Research Council of Canada.

References

Bagnulo, S., Landstreet, J. D., Mason, E., et al. 2006, A&A, 450, 777
Balona, L. A., Handler, G., Chowdhury, S., et al. 2019, MNRAS, 485, 3457
Cunha, M. S., Antoci, V., Holdsworth, D. L., et al. 2019, MNRAS, 487, 3523
David-Uraz, A., Neiner, C., Sikora, J., et al. 2019, MNRAS, 487, 304
González, J. F. & Lapasset, E. 2000, AJ, 119, 2296
Landstreet, J. D., Bagnulo, S., Valyavin, G. G., et al. 2015, A&A, 580, A120
Lata, S., Pandey, A. K., Panwar, N., et al. 2016, MNRAS, 456, 2505
Miglio, A., Montalbán, J., & Dupret, M.-A. 2007, MNRAS, 375, L21
Ricker, G. R., Winn, J. N., Vanderspek, R., et al. 2015, JATIS, 1, 014003

MULTI-INSTRUMENT ANALYSIS OF GAIA, KEPLER K2, ASAS-SN, AND ASAS OBSERVATIONS OF LONG-PERIOD VARIABLES

E. Hartig[1], T. Lebzelter[2] and K.H. Hinkle[3]

Abstract. Several sky-monitoring projects provide the possibility to search for variations of long-period variables (LPVs) on a large combined photometric data-set. We used the newly published results from *Gaia* Data Release 2 together with the *Kepler* K2 survey and the earth-based observations of the All-Sky Automated Survey for Supernovae (ASAS-SN). In addition, we added information from ASAS observations starting from 1997, the database of the American Association of Variable Stars Observers (AAVSO), the International Variable Star Index (VSX) and the HIgh Precision PARallax COllecting Satellite (Hipparcos) to explore long-term trends. Using this combination of observation data we could finally calculate secondary periods, which are typical for long-period variables.

Keywords: stars: variables: general, stars: oscillations, telescopes, space vehicles: instruments

1 Introduction

The *Gaia* Data Release 2 (Gaia DR 2) provided details of 151,761 LPVs: Gaia Collaboration et.al. (2018). The All-Sky Automated Survey for Supernovae (ASAS-SN) V-band survey delivered light curves of 421 000 variable stars in the VSX Catalog. The *Kepler* K2 SFF data provided high quality light-curve details restricted to roughly 80 days' length: Huber et al. (2016). These three data sets have been obtained with some overlap in time, and thus allow a direct comparison of the obtained light curves. We selected a set of LPVs from our own *Kepler* K2 program for this study. We ran tests on several automated data-analysis tools for the Kepler data: Hartig et al. (2014), decided to use the *Kepler* High Level Science Products (K2HLSP) and selected the Self-flat-fielding tool (K2SFF) as the best suited for the LPV process: Vanderburg & Johnson (2014). The other data sets were taken as published in the corresponding catalogues. The prerequisite for the combination of several data sets are high precision photometric data. In this paper we discuss a selection of adjustment methods for the zero points of the various data sets and the problems encountered when looking for the most appropriate solution. We explore the effect of zero-point settings on the calculated periods of the combined data sets, in particular for cases with multiple periods. First results for a few showcases are presented.

2 Multi-instrumental Survey

To search the combined datasets for LPV candidates, an automated process for the combination of the various parts of the light curves is essential. This provides a particular challenge for stars crossing the sensitivity limit during their light change (ASAS) and data sets where only short fragments of time-series (*Kepler* K2 data) are available.

We first analyzed all data points of all data-sets using their catalogue zero-points; two examples are presented in the top left (**BW Sco**) and bottom left diagram (**UZ Sco**) of Fig. 1. Very long periods would become visible as an asymmetric distribution of the data points. In those cases we interactively varied their zero-points and found the best fit indicated by least-square fitting, which is also confirmed by the disappearance of extremely long, fake periods, often significantly longer than 1000 days, in our data analysis (see Fig. 1 left and middle diagram). The phase diagram, bottom right, confirms the quality and necessity of our adjustment. Fig. 1, right panel, shows the overall details of our first five targets. Our first search delivered 28 targets for which observations from multiple data sets exist. For ten of them we got both *Gaia* and *Kepler* K2 data in addition to the ground-based observations. Their properties and the three main periods resulting from our Fourier analysis are shown in table 1. For ten (four) more objects no *Gaia* (*Kepler*) data are available.

[1] University of Vienna, Department of Astrophysics, Austria, erich.hartig@univie.ac.at
[2] University of Vienna, Department of Astrophysics, Austria
[3] National Optical Astronomy Observatories, P.O. Box 26732, Tucson, AZ 85726 USA

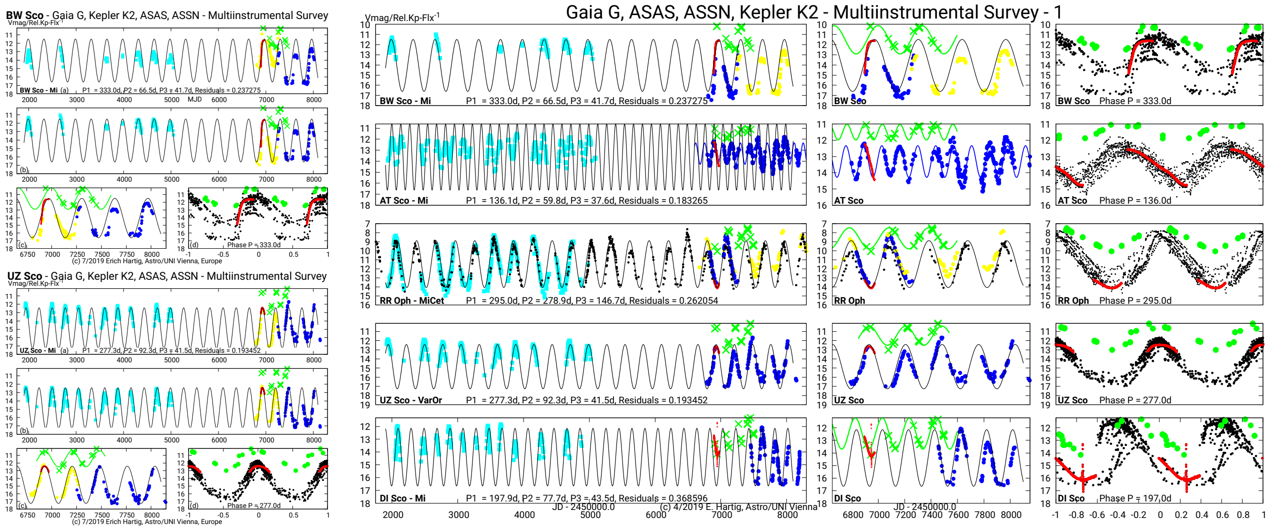

Fig. 1. Top Left: BW Sco, **Bottom left:** UZ Sco: Raw data (left top), 0-Point adjusted (left middle), zoom (bottom left), phase (bottom right). **Figure Right:** Five Observations: all adjusted data (left), zoom (middle), phase for P1 (right); Colors: *Gaia* G (green), *Kepler* K2 (red), ASAS (light blue), ASAS-SN (blue/yellow), P1 (black line); Phase Diagram: all ground based (black); RR Oph: AAVSO (black)

3 Preliminary conclusions

In all tested cases, the light curves were found in good agreement between the various surveys and confirm the reliability of each data set for the study of LPV light changes. This holds also when comparing data sets of very high photometric precision with data sets of medium photometric accuracy. Therefore, a combination of the data sets seems feasible allowing one to study long-term trends in these light-curves, both in terms of long secondary periods and in terms of period changes. We will soon extend our analysis to our full sample and explore the possibilities of combining data-sets from multiple missions for further light-curve studies.

Table 1. Summary of *GAIA* (G), ASAS (AS), AAVSO, ASAS-SN (SN), *Kepler* K2 (Kp) data, and the final results.

#	Name	*Kepler* EPIC	Gper	ASAS	AS-SN	G-P1	AS-P1	SN-P1	Kp-P1	ALL-P1	
	Typ	Gaia Id		AAVSO		G-P2	AS-P2	SN-P2	Kp-P2	ALL-P2	ALL-P3
1	BW-Sco	K2-C2 203748709	335.0	330.0	377.5	336.6	330.7	323.2	189.3	333.0	
	Mi	6048860248373535744				6.2	145.7	168.9	74.9	66.5	41.7
2	AT-Sco	K2-C2 202913758	133.9	136.3	133.7	136.1	135.8	136.3	117.0	136.1	
	Mi	6044303249415452800				158.6	1.0	158.0	67.6	59.8	37.6
3	RR-Oph	K2-C2 205087771	297.7	299.0	289.9	300.2	299.3	291.3	334.1	293.4	
	MiCet	4130587357014777088		294.3		2.4	148.9	387.8	209.4	321.8	47.4
4	UZ-Sco	K2-C2 203763661	252.7	271.2	276.1	255.5	277.0	274.1	76.3	277.3	
	VarOr	6049609015792443008				50.3	295.5	532.9	75.9	92.3	41.5
5	DI-Sco	K2-C2 203795904	206.9	197.5	197.5	397.9	198.0	200.8	318.4	197.9	
	Mi	6046766086744209280				1.5	1.0	683.8	46.7	77.7	43.5

References

Gaia Collaboration et.al. 2018, A&A, 616, 25

Hartig, E., Cash, Jennifer Hinkle, K. H., Lebzelter, T., Mighell, K. J., & Walter, D. K. 2014, AJ, 148, 123

Huber, D., Bryson, S. T., & Haas et.al., M. R. 2016, ApJS, 224, 17

Vanderburg, A. & Johnson, J. A. 2014, PASP, 126, 948

THE IMPOSTER Be STAR HD 19818: SUPERFLARES IN A COOL GIANT?

J. Labadie-Bartz[1] and A. C. Carciofi[1]

Abstract. Classical Be stars are identified by certain observational features, most notably the presence of hydrogen emission. However, in samples of Be stars there is often contamination by other systems that mimic the observables that are generally attributed to Be stars. This paper discussed one such system, HD 19818, and argued that it is an imposter Be star that is actually a close binary comprised of a B9/A0V star and an unusually active cool-giant component that exhibits highly energetic superflares.

Keywords: Techniques: photometric, stars: emission-line, Be, flare, binaries: spectroscopic, individual: HD 19818

1 Introduction

Classical Be stars are near-main-sequence, very rapidly rotating, B-type stars with a circumstellar "decretion" disk that gives rise to emission lines in their spectra. One difficulty in studying Be stars as a population is that there are many types of astrophysical systems which seem to exhibit the features of classical Be stars (Rivinius et al. 2013) but which are actually quite different physical objects. This paper discussed one such object, HD 19818. It has been classified as a Be star, but a closer look at the data reveals it as more prbably a close binary comprised of a B9/A0V star plus a cooler giant that has dramatic flare events and a high degree of chromospheric activity which causes the Hα emission.

2 HD 19818: a binary with an active giant star masquerading as a Be star

Classical Be stars have many observational features which, taken together, can enable a reliable classification to be made (Rivinius et al. 2013). Common methods of discovering Be stars include analysis of hydrogen emission in spectra, narrow-band photometry (sampling Hα), SED analysis to measure the excess at long wavelengths caused by the disk, photometric variability studies to search for disk-building events, and polarimetric measurements to study the light scattered off the disk. However, most methods for discovering Be stars rely primarily on an incomplete set of these features, which can lead to mis-classification. Samples of Be stars often have some (unknown) degree of contamination from systems that, at first glance, mimic the characteristics of B stars with decretion disks.

HD 19818 is classified as a B9.5Vne star, and has so far been considered to be a classical Be star (Houk & Cowley 1975). It was observed by *TESS* in sectors 2 and 3 (2018 Aug 22–2018 Oct 18) in 2-minute cadence mode as part of a *TESS* GI proposal to study classical Be stars. The most remarkable features seen by *TESS* are two events that resemble flares, with durations of 5–10 hours and amplitudes of ∼1% and ∼6%, superimosed on a 3.34-d periodic signal. The *TESS* data for the two flares are plotted in Fig. 1. To the best of our knowledge, events like this are not seen in any of the other *TESS* Be stars, nor have they been observed in other space photometry of Be stars. That prompted us to obtain high-resolution spectroscopy as a first step towards classifying the system better.

Our first spectrum from the CHIRON spectrograph (on the SMARTS 1.5-m telescope at CTIO) revealed lines from two components (Fig. 2). One component is consistent with a main-sequence B9/A0 star, and the other with a cooler giant (which dominates the optical flux of the system). More recent spectra show clearly the relative motion of those lines, consistent with close binary motion. HD 19818 is also an X-ray source (with an unusually high ratio of X-ray to bolometric luminosity, and a low hardness ratio; Nazé & Motch 2018); the latter is generally inconsistent with later-type Be stars but is consistent with high levels of chromospheric activity in cooler stars. The morphology, amplitude, and time-scale of the two flares are consistent with the "superflares"

[1] Instituto de Astronomia, Geofísica e Ciências Atmosféricas, Universidade de São Paulo, São Paulo, Brazil

in giant stars seen with *Kepler* (Van Doorsselaere et al. 2017; Balona 2015) and in the giant star HK Lac (Katsova et al. 2018). It is possible that tidal interactions have spun up the giant star in HD 19818, thereby enhancing the energy in its magnetic dynamo and driving its chromospheric activity. At $V \sim 9$, this system is bright enough for more detailed spectroscopic studies, and which are not feasible with the *Kepler* superflare giant stars. We are continuing to monitor HD 19818 in order to obtain an orbital solution, to characterize both stellar components, and study the (highly variable) Hα emission.

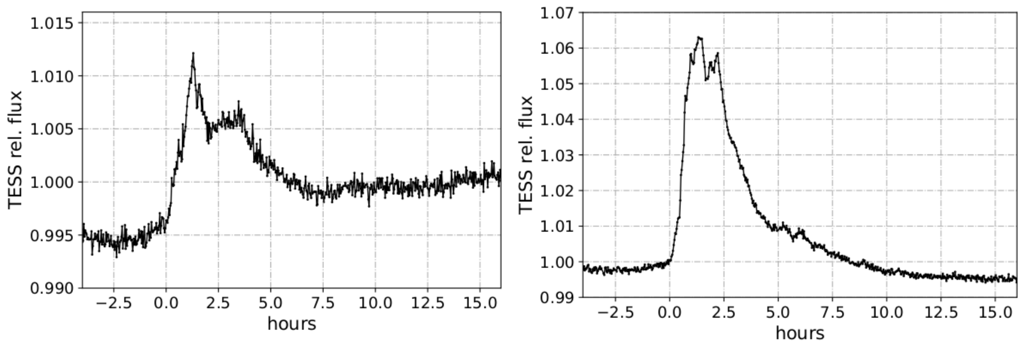

Fig. 1. Sections of the *TESS* 2-minute cadence light-curve for HD 19818, showing the two recorded flares.

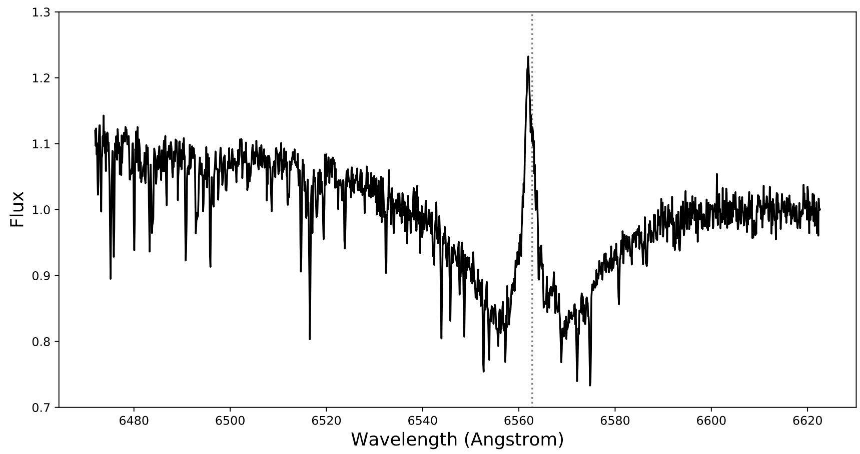

Fig. 2. CHIRON spectrum showing the region around Hα. We attribute the broad Hα absorption to the B9/A0V component. Most of the narrow lines are from the cooler giant, and the emission appears to be correlated with chromospheric activity in the giant star.

3 Conclusions

By studying new data from *TESS* and high-resolution spectroscopy, we could claim that HD 19818 is not a classical Be star but is instead more likely to be a close binary in which the broad hydrogen absorption lines are indeed from a B9/A0 main sequence star but the spectrum also includes lines from a cool giant. The Hα emission, flares seen in *TESS* data, and the observed X-ray flux, can be explained if the system contains a chromospherically-active cool giant that exhibits superflares.

J. L.-B. acknowledges support from FAPESP (grant 2017/23731-1). A. C. C acknowledges support from CNPq(grant 307594/2015-7)

References

Balona, L. A. 2015, MNRAS, 447, 2714

Houk, N. & Cowley, A. P. 1975, University of Michigan Catalogue of two-dimensional spectral types for the HD stars. Volume I. Declinations -90 to -53 f0. (University of Michigan)

Katsova, M. M., Kitchatinov, L. L., Moss, D., Oláh, K., & Sokoloff, D. D. 2018, Astronomy Reports, 62, 513

Nazé, Y. & Motch, C. 2018, A&A, 619, A148

Rivinius, T., Carciofi, A. C., & Martayan, C. 2013, A&A Rev., 21, 69

Van Doorsselaere, T., Shariati, H., & Debosscher, J. 2017, ApJS, 232, 26

Stars and their variability observed from space
C. Neiner, W. W. Weiss, D. Baade, R. E. Griffin, C. C. Lovekin, A. F. J. Moffat (eds)

STEREO OBSERVATIONS OF BE STARS

D. Ozuyar[1] and L. Balona[2]

Abstract. In this study, five-year STEREO data of five bright Be stars were investigated in order to clarify the physical processes in the photospheres of Be stars. All samples were selected from B spectral types in such a way as to cover the entire spectrum from B0 to B9. The analyses were performed with the Lomb-Scargle technique, and time-frequency diagrams were produced. The diagrams showed groups at a fundamental or a harmonic of the fundamental frequency. The phased light-curves that were constructed according to the main frequencies display sinusoidal variations, which can be attributed to rotation. The resulting suggestion, that a localized cloud was formed from ejected material, was discussed as the cause of the modulations.

Keywords: Stars: Be stars, rotation, mass loss, methods: STEREO data, data analysis

1 Introduction

The classical Be stars are dwarf and giant B stars whose Balmer lines (particularly H) show, or have at some time shown, emission in the core of the line (binary interactions are excluded) (Porter & Rivinius 2003). Observations of light and line profile variations indicate that many Be stars are periodic variables. The variability is interpreted in two ways: either pulsation or rotational modulation (Balona 2010). Since the observed period is close to the rotation period, it is difficult to distinguish between the two hypotheses. Pulsation is a rather attractive idea since it offers a plausible trigger for the mass loss. However, the photometric behaviour of these stars seems more simply understood as transient variations. They could easily be interpreted as non-radial pulsations if observed for only a few days, yet the overall shape of the light-curve is consistent with a rotating star where obscuration is present (Balona & Ozuyar 2019). Our aim was therefore to present observations of some Be stars provided by STEREO, in order to assist with clarifying which physical processes are active in the photospheres of these stars.

2 Data and Analyses

The data, which covered the period from 2007–2011, came from the HI-1A instrument of the STEREO-A satellite. Even though the main purpose of this satellite is to track solar mass ejections, it is also able to observing background stars brighter than 12 magnitude for a maximum of 20 days. The cadence of the light-curves is 40 minutes, which provides a maximum of 720 data points in a season. Since the satellite observes the region close to the solar disk, light curves are mostly affected by solar activity. The data are therefore first cleaned from those effects using an IDL code. Changes in the five years of data are represented by a time–frequency diagram. The amplitude of each frequency as a function of time was calculated by applying a sliding window whose length was chosen as five days. The window was shifted with a time-step of one day; in each step a Fourier analysis was performed with the Lomb-Scargle technique, and the results plotted against time.

3 Discussion

A localized cloud of ejected material would presumably cause a signal in the irregular light variations in Be stars, whether the cloud were ejected by pulsation or by some other mechanism. It was therefore quite possible that the periodic variations of the sample stars could arise analogously. The presence of transient frequencies presented in Fig. 1 provides evidence that the periodicities may be a result of rotation rather than pulsation.

[1] Ankara University, Faculty of Science, Department of Astronomy and Space Sciences, Ankara, Turkey
[2] South African Astronomical Observatory, P.O. Box 9, Observatory, Cape 2735, South Africa

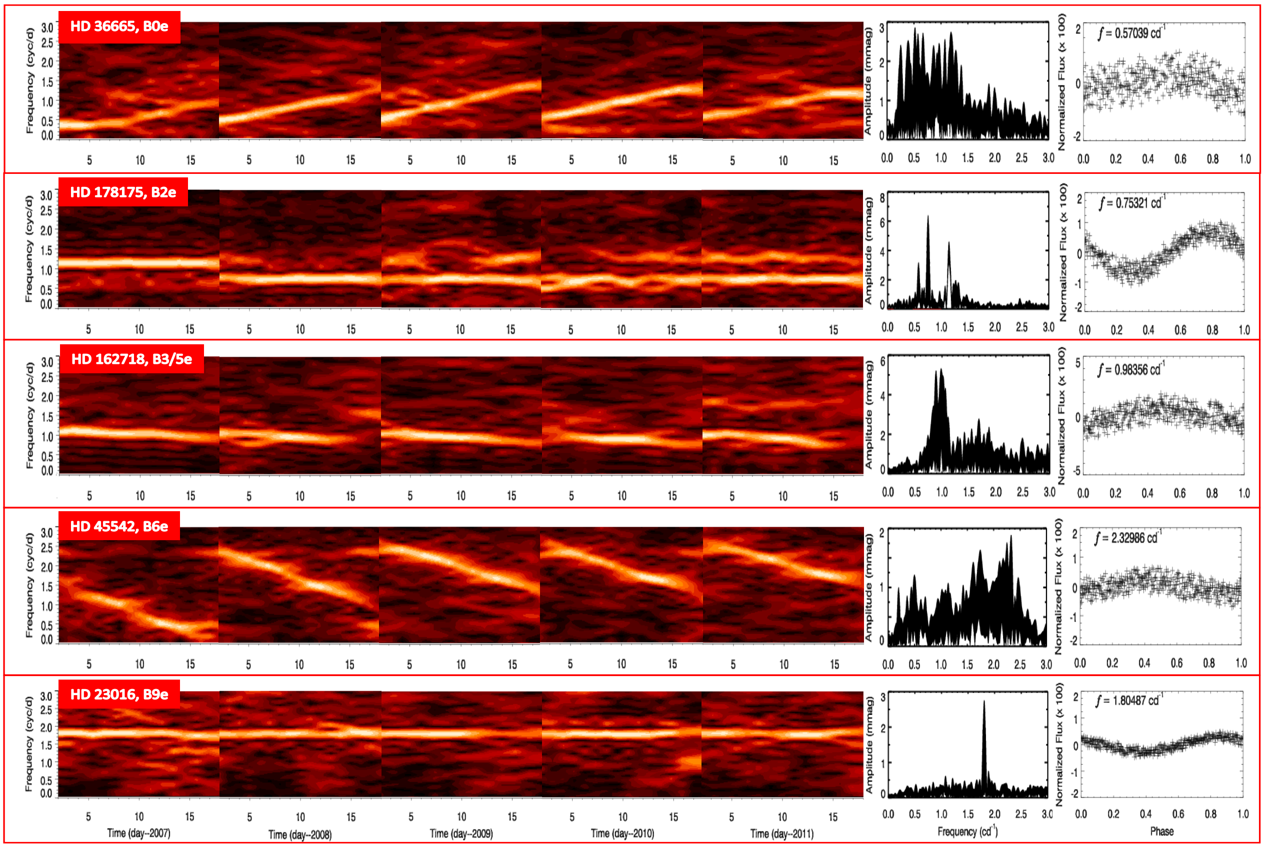

Fig. 1. Time–frequency diagrams, periodograms and phased light-curves of data combined over five years.

Furthermore, the amplitudes of the seasonal frequencies display variations which may be a signature of non-uniformly distributed regions. It is suggested that hose changes are related to a change in the size of the spot regions, or to a possible drift in latitude (Balona et al. 2011). Rotational modulation is supported by the phased light-curves of the five-year combined data (Fig. 1). Starspots on A and B stars, and also flares, have been observed in a large fraction of A and B stars (Balona 2013, 2016; Balona et al. 2019) using *Kepler* and *TESS* data. In a rapidly-rotating star, it is conceivable that such activity can lead to mass loss. Balona & Ozuyar (2019) have shown that mass loss caused by flaring is an impulsive event – which describes Be outbursts rather well. That study stimulated a discussion as to whether the highly-ionized gas released in the process could expand and become trapped in closed magnetic loops. The relative strength of the fundamental and first harmonic depends on the relative amount of gas trapped in the two regions. Gas escapes along open field lines and is dragged and accelerated by the rapid rotation of the star. The gas reaches circular orbital speeds at some distance from the star if it is still ionized, so that depends on the rotational velocity of the star. After some time the gas cools down, becomes neutral, and is then unaffected by the magnetic field; it slowly dissipates into the inner circumstellar disk, rotating at Keplerian velocity.

References

Balona, L. A. 2010, Challenges In Stellar Pulsation (Bentham Science)

Balona, L. A. 2013, MNRAS, 431, 2240

Balona, L. A. 2016, MNRAS, 457, 3724

Balona, L. A., Handler, G., Chowdhury, S., et al. 2019, MNRAS, 485, 3457

Balona, L. A. & Ozuyar, D. 2019, arXiv e-prints, arXiv:1911.03068

Balona, L. A., Pigulski, A., De Cat, P., et al. 2011, MNRAS, 413, 2403

Porter, J. M. & Rivinius, T. 2003, PASP, 115, 1153

VARIABILITY OF WOLF-RAYET STARS THROUGH MOST(LY) BRITE EYES

G. Lenoir-Craig[1], N. St-Louis[1], A.F.J. Moffat[1], T. Ramiaramanantsoa[1] and H. Pablo[2]

Abstract. We present preliminary results from *BRITE* and *MOST* photometry of a subset of 8 Wolf-Rayet stars. After allowing for any known periodic variations in binaries, we found only stochastic light variations, for which time-frequency and wavelet analyses reveal an average life-time of around 10 days, with frequencies ranging from 0.05 to 0.5 cycles/day.

Keywords: Stars: Wolf-Rayet, winds, activity, massive, techniques: photometric

1 Introduction

Wolf-Rayet (WR) stars, the descendants of main-sequence O stars, present the densest sustained winds known among all types of massive stars. These hot and luminous stars are known for their variability, both from intrinsic processes such as pulsations (e.g. Hénault-Brunet et al. 2011), wind clumping (e.g. Robert 1992) and rotational modulations (e.g. Morel et al. 1997), as well as from binarity. Those dense winds prevent us from seeing the surface of the star where the wind driving occurs. There is little consensus as to the source of the short-term variability observed, and the lack of periodicity complicates the task of identifying it. This contribution presented preliminary results from an attempt to characterize those variations better.

2 Data Reduction and Results

This study of the short-term variability of 8 WR stars of various subtypes was conducted using *BRITE*-Constellation (Weiss et al. 2014) and *MOST* (Walker et al. 2003) data. They were de-correlated against the various satellite parameters to clean the observed fluxes from instrumental biases. Our datasets are presented in Table 1.

A period search was carried out on each light-curve using a Fourier transform time-frequency analysis with a sliding, tapered window. (The periodic eclipses in WR22 were subtracted away before this analysis). Stochastic light variations were found in all the stars in our sample, corresponding to significant features in the time-frequency diagram. The average life-time of the features measured along the time axis had a mean value of ∼10 days, with frequencies ranging from 0.05 to 0.5 cycles/day. As an example, the time-frequency analysis of 2017 data sets for WR22 and WR24 are presented in Figure 1.

The time-frequency analysis allows one to characterize temporal changes of the frequencies in a variable signal, but does not allows one to detect abrupt changes in a signal due to the constant size of the sliding window (Mallat 2000). On the other hand, a wavelet analysis, which relies on a mother function localized in timescale parameter space, is more efficient at finding sudden changes by providing information on the powers and periods of the wavelets used to analyze the signal. Therefore, we performed multiple wavelet analysis of our sample light-curves. As presented in Figure 2, a much better resolution was reached for longer periods/shorter frequencies. The results of that analysis support our previous ones, namely, that stochastic variations with time-scales of 2–20 days were detected, with some signals surviving as long as 40 days before disappearing.

3 Conclusions

The physical processes causing these variations and the time-scales driving their temporal evolution have not yet been identified. Being stochastic in nature, however, does narrow down the choices, with wind clumping currently popular. We are presently carrying out a more thorough analysis of these data using Gaussian processes with different Kernels, and also a Bayesian analysis. Stochastic clumping models are being explored too, as are the *TESS* light-curves of WR stars.

[1] Département de physique, Université de Montréal, C.P. 6128, Succ. Centre-Ville, Montréal, Québec H3C 3J7, Canada
[2] American Association of Variable Star Observers, 49 Bay State Road, Cambridge, MA 02138, USA

Table 1. Our WR datasets analyzed so far. B-Hz stands for BRITE-Heweliusz and B-Tr stands for BRITE-Toronto.

Star (year if available)	Spectral Type	Observing Interval (days)	Satellite
WR22 (2017, 2018)	WN7h+O9III-V	153	B-Hz
WR24 (2016, 2017, 2018)	WN6ha	163, 153, 62	B-Tr, B-Hz, B-Tr
WR71	WN6o	27	MOST
WR92	WC9	26	MOST
WR115	WN6o	38	MOST
WR119	WC9d	48	MOST
WR120	WN7o	38	MOST
WR121	WC9d	47	MOST

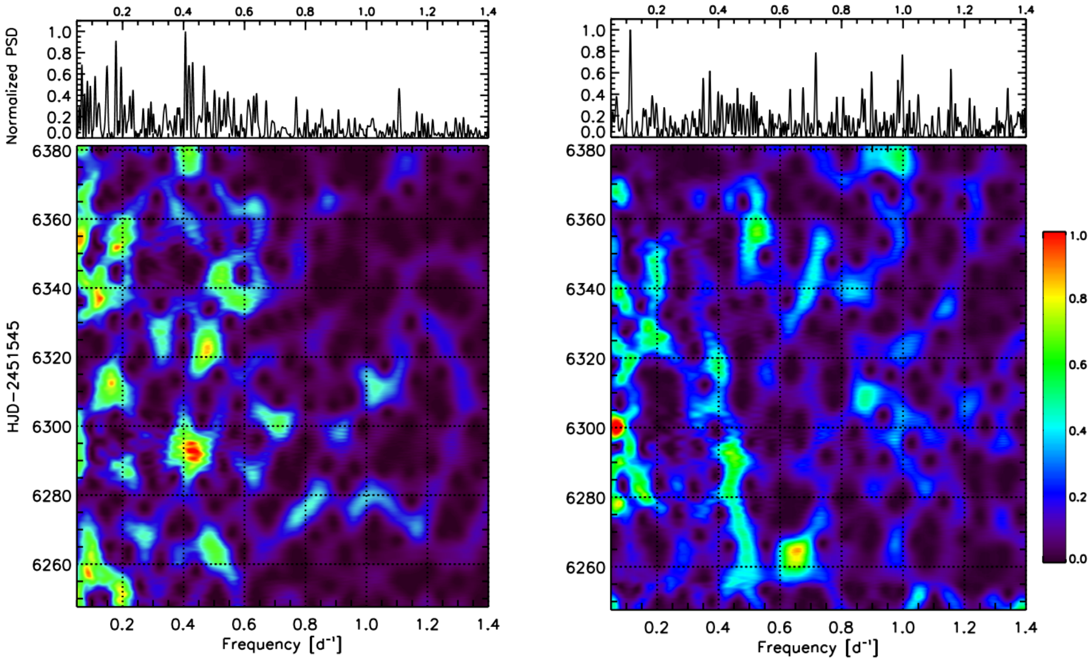

Fig. 1. Left: Time-frequency analysis of the 2017 data set of WR22. **Right:** Time-frequency analysis of the 2017 data set of WR24.

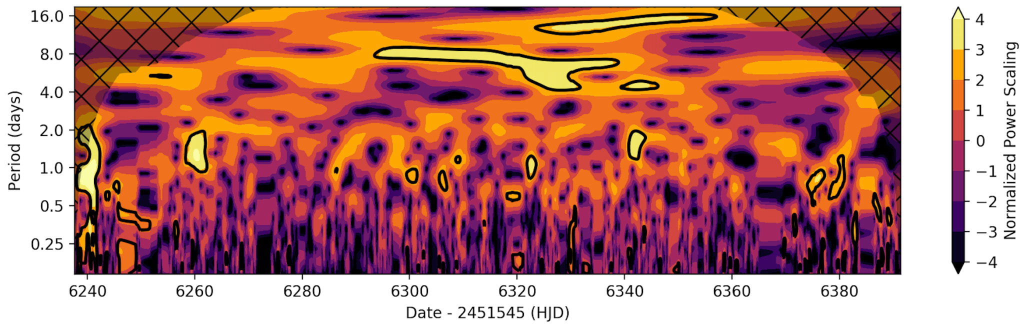

Fig. 2. Wavelet analysis of the 2017 data set of WR24.

References

Hénault-Brunet, V., St-Louis, N., Marchenko, S. V., et al. 2011, ApJ, 735, 13

Mallat, S. 2000, Une exploration des signaux en ondelettes (Les Editions de l'Ecole Polytechnique)

Morel, T., St-Louis, N., & Marchenko, S. V. 1997, ApJ, 489, 1004

Robert, C. 1992, PhD thesis, Universit de MontralL (Canada).

Walker, G., Matthews, J., Kuschnig, R., et al. 2003, PASP, 115, 1023

Weiss, W. W., Rucinski, S. M., Moffat, A. F. J., et al. 2014, PASP, 126, 573

Stars and their variability observed from space
C. Neiner, W. W. Weiss, D. Baade, R. E. Griffin, C. C. Lovekin, A. F. J. Moffat (eds)

SIMULTANEOUS PHOTOMETRIC AND SPECTROSCOPIC ANALYSIS OF A NEW OUTBURST OF V1686 CYG

H.R. Andreasyan[1]

Abstract.
This poster presented an analysis of optical observations of the Herbig AeBe star V1686 Cyg. This object usually demonstrates slow brightness variations with irregular Algol-type minima. Our observations were obtained with the Byurakan 2.6-m telescope between 2015–2017. During that period we obtained direct images and 14 medium- and low-resolution spectra of V1686 Cyg. In the course of the observations we noticed that it underwent an atypical brightness outburst. After reducing the data we found that the full rise and decline of the star's brightness had an amplitude of almost 3 mags, and lasted about 3 months. We were also able to trace changes in the stellar spectrum during the outburst; they were correlated with the photometric variations.

Keywords: stars: pre-main-sequence, variables: T Tauri, Herbig Ae/Be

1 Introduction

In our project we were studying a group of HAe Be stars in the vicinity of the bright star BD+40°4124, also a Herbig Be star and with a very strong Hα emission line. One of group was LkHα 224, another HAe Be star. Those two stars, and the nearby star LkHα 225, were mentioned for the first time by Herbig (1960) in his much-acclaimed study of Ae/Be stars connected to bright nebulosities. Photometric variability of LkHα 224 was detected by Wenzel (1980) and being a variable it received the designation V1686 Cyg. The most complete information about its photometric behaviour so far has been collected in the papers by Shevchenko et al. (1991, 1993) and Herbst & Shevchenko (1999). Estimates of its spectral type have varied from B2 to F9 (see Hernandez et al. 2004, and references therein). In 2015 we started observing the field around BD+40°4124, since a new outburst of V1318 Cyg S had been detected (Magakian et al. 2019). In parallel to those investigations, V1686 Cyg was also observed photometrically and spectroscopically. Its unusual and unsuspected brightening by nearly 3 mag was discovered, and tracked.

2 Results

2.1 The new outburst of V1686 Cyg

During the period from 2015 September to 2016 August no significant photometric variability was detected in V1686 Cyg. But in 2016 August we noticed that the star's brightness rose significantly. During a period of (probably) several months its brightness increased unexpectedly by more than 2 mag in V, which is an unusually high amplitude, and then gradually returned to its previous level. The light-curve is shown in Fig. 1.

2.2 The spectrum of V1686 Cyg

2.2.1 Quiescent stage

Spectra taken before the outburst are quite typical for this star. In the red spectral region the most conspicuous line is a broad and strong Hα emission, flanked by a weak, blue-shifted absorption feature. By 2016 November–December, after the end of the outburst, the spectrum had returned to the same appearance. In general, during the time of our observations the spectral type of V1686 Cyg could be classified as an early Ae star, judging from the broad wings of Balmer absorptions and the absence of the He I line at $\lambda\,5876\,\text{Å}$.

[1] Byurakan Observatory NAS Armenia, Byurakan, Aragatsotn prov., 0213, Armenia

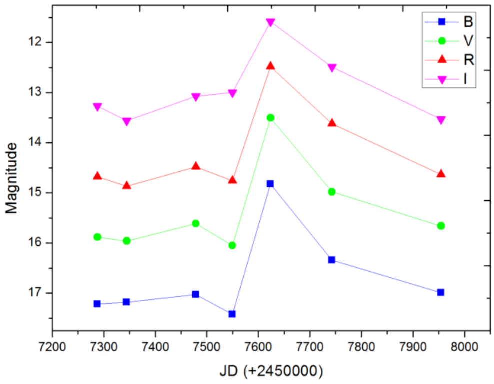

Fig. 1. *BVRI* light-curve of V1686 Cyg during the period 2015–2017.

2.2.2 During the outburst

Significant spectral changes could first be seen in the spectra of the star before any photometric variations were detected. Its maximum brightness was reached in 2016 August. To represent the changes better, we have shown parts of the normalized V1686 Cyg spectrum in Fig. 3 in the region up to Hα, in various periods; variations in the Hα profile are presented in Fig. 2.

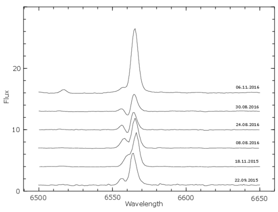

Fig. 2. Strong variations in the profile of Hα in the spectrum of V1686 Cyg. During the outburst, the absorption component became rather intense and is even below the continuum.

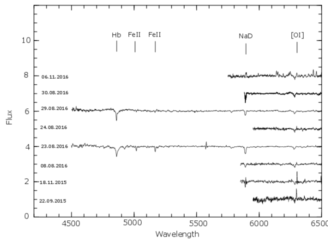

Fig. 3. Variations of the V1686 Cyg spectrum in 2015–2016 in the region λ 4500–6500 Å. At the shorter wavelengths Hβ and Fe II absorptions are prominent. There is an obvious increase in chromospheric emission on 2016 November 6.

3 Conclusion

These observations fully confirm pronounced changes in the strengths of certain absorption and emission lines, which easily explain the large range of spectral types assigned to this star. V1686 Cyg is actually one of the most variable of the HAe Be stars in both photometry and spectroscopy, and (at least in this case) we can see that its spectroscopic and photometric variations are directly related. As already stated, the rapidity of the brightening which we observed is not typical of V1686 Cyg. At least, similar events could not be found on the previous long time-span light-curve presented by Herbst & Shevchenko (1999). The brightening was not considered an outburst, because the accompanying spectroscopic changes could be interpreted as the formation of a dense expanding envelope around the star, with subsequent dissipation over several months. This envelope, emitting mainly in the continuum, hid the lower layers of the stellar chromosphere, making the metallic emissions invisible and diminishing even the very strong emission component of the Hα line. On the other hand, the envelope was sufficiently dense to produce absorption lines with negative radial velocity. It is not known how long V1686 Cyg will remain in its present low-brightness state. Only new photometric observations will clarify the situation. This star definitely deserves continuing monitoring Several authors make analogies between the rapid dimming of V1686 Cyg and similar events that occur in UX Ori-type variables. However, this question remains to be investigated. This star could also be an object which combines two types of PMS variability.

References

Herbig, G. H. 1960, ApJS, 4, 337
Herbst, W. & Shevchenko, V. S. 1999, AJ, 118, 1043
Hernandez, J., N., C., C., B., L., H., & P., B. 2004, AJ, 127, 1682
Magakian, T. Y., Movsessian, T. A., Andreasyan, H. R., & Gevorgyan, M. H. 2019, A&A, 625, 8
Shevchenko, V. S., Grankin, K. N., Ibragimov, M. A., Mel'Nikov, S. Y., & Yakubov, S. D. 1993, Ap&SS, 202, 121
Shevchenko, V. S., Ibragimov, M. A., & Chenysheva, T. L. 1991, Soviet Ast., 35, 229
Wenzel, W. 1980, Mit.VS, 8, 182

Stars and their variability observed from space
C. Neiner, W. W. Weiss, D. Baade, R. E. Griffin, C. C. Lovekin, A. F. J. Moffat (eds)

MAGNETIC FIELD MEASUREMENTS OF KEPLER AP/CP2 STARS

I. I. Romanyuk[1], Z. Mikulášek[2], S. Hümmerich[3], I. Yakunin[1], A. Moiseeva[1], J. Janík[2], K. Bernhard[3], J. Krtička[2], E. Paunzen[2], M. Jagelka[2], M. Zejda[2], and M. Vaňko[4]

Abstract. We present first results of the ongoing search for magnetic fields in eight Ap/CP2 stars and one candidate in the Kepler field using the spectropolarimeter of the 6-meter SAO reflector in Russia. Five stars (KIC 4180396, KIC 5264818, KIC 5473826, KIC 6065699, and KIC 8324268) were found to harbor a strong magnetic field. Very likely, KIC 6864569 is also a magnetic star, but more observations are needed. The status of KIC 8161798 and KIC 10324412 remains as yet unclear; no significant field was detected for the CP2 star candidate KIC 6278403. The resulting sample will facilitate research on the connection between magnetic field topologies and surface chemical structures in mCP stars.

Keywords: Chemically peculiar stars, magnetic field

1 Introduction

We searched for magnetic fields in eight Ap/CP2 stars and one candidate in the Kepler field. These upper main-sequence objects are characterized by peculiar photospheric abundances thought to be produced by selective processes (radiative levitation and gravitational settling) operating in their calm radiative atmospheres. CP2 stars belong to the magnetic chemically peculiar (mCP) stars, which possess strong global magnetic fields, possibly of fossil origin. In many mCP stars, the overabundant chemical elements are concentrated into chemical spots or patches. These objects display strictly periodic light, spectrum and magnetic variations, which can be well described by a rotating star model with a non-axial stable magnetic field and persistent chemical structures. However, the physical connection between the magnetic field topology and the structure of the chemical surface inhomogeneities is not yet understood or well explored. Furthermore, the recent study by Jagelka et al. (2019) indicates that - in contrast to what is generally assumed - the distribution of the chemical spots does not follow the magnetic field topology. Clearly, further investigations into this topic are necessary.

Our intended project "Probing the role of the magnetic fields in the physics of chemically peculiar stars using BTA-6 spectropolarimetry" aims to assess and better comprehend the role of the global magnetic field in the process of the formation and sustaining of the chemical surface abundance inhomogeneities of mCP stars by using high-quality BTA-6 spectropolarimetry and ultra-precise photometric data from the Kepler and TESS satellites. These data will offer unique and detailed information about chemical structures and magnetic field geometry for a representative sample of mCP stars. As a pilot study, we have observed eight Ap/CP2 stars and one candidate in the Kepler field, which were selected from the list of Hümmerich et al. (2018) and unpublished observations. Our data constitute the first spectropolarimetric measurements of these objects.

2 Magnetic fields measurements

In April and May 2019, we obtained a total of 31 spectra for all nine objects using the Zeeman analyzer. Strong magnetic fields were found in five stars: KIC 4180396 = HD 225728 (2 spectrograms), KIC 5264818 = HD 180374 (4), KIC 5473826 = HD 226339 (2), KIC 6065699 = HD 188101 (5), and KIC 8324268 = HD 189160 (5). Very likely, KIC 6864569 = BD+42 3356 (2) is also a magnetic star, but more observations are needed.

The status of KIC 8161798 = BD+43 3223 (only one spectrum), and KIC 10324412 = HD 176436 (5) remains as yet unclear. No significant magnetic field (amplitude 40 ± 140 G) has been detected in the only CP2 star candidate of the sample, KIC 6278403 = HD 181436 (5).

[1] Special Astrophysical Observatory of the RAS, Nizhnii Arkhyz, Karachai-Cherkessian Republic, 369167, Russia
[2] Department of Theoretical Physics and Astrophysics, Masaryk University, Kotlářská 2, 61 387 Brno, Czech Republic
[3] Bundesdeutsche Arbeitsgemeinschaft für Veränderliche Sterne e.V. (BAV), D-12169 Berlin, Germany
[4] Astronomical Institute of the Slovac Academy of Science, Tatranská Lomnica, Slovac Republic

Two of the CP2 stars were observed so well that we can discuss the relationship between their magnetic and light phase curves.

HD 180374 is an A0 IV Si star (Gray et al. 2016), displaying a double wave light curve with effective amplitude of 25.8 mmag and period $P = 1.905\,050\,059(5)$ d (Hümmerich et al. 2018), while the magnetic field dependence $\langle B_z \rangle$ is a pure cosine wave with an amplitude of 4.0 kG and extrema that coincide in phase with the light maxima. Thus, regions of increased silicon content can be expected to be present in the area of the magnetic poles. However, this speculation has yet to be verified spectroscopically.

HD 189160 is an A0 V SiCr star, displaying a single, slightly asymmetric light curve with effective amplitude of 27.1 mmag and period $P = 2.009\,120\,16(7)$ d (Hümmerich et al. 2018), while the magnetic field curve $\langle B_z \rangle$ is also a cosine wave with an amplitude of 1.25 kG, with a maximum that coincides in phase with the light maximum.

However, both stars show a visible link between the distribution of spots with increased content of optically active chemical elements (such as silicon or iron) and the dipole geometry of the magnetic field found. This, however, contradicts our recent finding (Jagelka et al. 2019) that the analysis of CP2 star light curves obtained by ASAS 3 (Bernhard et al. 2015) instead suggests that there is no apparent correlation between element distribution and surface magnetic induction.

3 Conclusions

The here presented results from our pilot study in the framework of the proposed Czech-Russian project collaboration are very promising and confirm the feasibility of the chosen approach. With the ongoing collection of more and more spectra, we will be able to significantly enlarge the sample of mCP stars with accurate phase-resolved magnetic measurements. The resulting sample, which will also boast ultra-precise light curves from satellite photometry, will be unique and greatly facilitate further research on the connection between the magnetic fields and other parameters in mCP stars.

ZM, EP, and MZ were granted by Masaryk University Institutional Support of the Research, JK by GAČR 18 - 05665S. IIR, IY, AM acknowledge SAO administration for allocation of additional time for observation with the 6-m telescope.

References

Bernhard, K., Hümmerich, S., Otero, S., & Paunzen, E. 2015, A&A, 581, A138

Gray, R. O., Corbally, C. J., De Cat, P., et al. 2016, AJ, 151, 13

Hümmerich, S., Mikulášek, Z., Paunzen, E., et al. 2018, A&A, 619, A98

Jagelka, M., Mikulášek, Z., Hümmerich, S., & Paunzen, E. 2019, A&A, 622, A199

NEAR-ULTRAVIOLET VARIABILITY IN THE KEPLER FIELD

E. Bertone[1], M. Sachkov[2], D. Olmedo[1], M. Olmedo[1] and M. Chavez[1]

Abstract. We present a large catalog of near-ultraviolet (NUV) light curves for almost 400,000 point sources in the *Kepler* field. It represents one of the largest database for studying NUV variability of a variety of point-like objects (such as pulsating stars, eclipsing binaries, or flare stars) down to a limiting magnitude of NUV$\simeq$21.5. It also allows a complementary characterization of the variability for objects with observations at other wavelengths.

Keywords: catalogs, ultraviolet: stars, stars: variables: general, techniques: photometric

1 The MGCK catalog

The Multi-visit *GALEX*-CAUSE *Kepler* (MGCK) catalog (Olmedo et al. 2020, in preparation) is a database of NUV (1771–2931 Å) light curves of point-like sources in the whole 104 deg^2 *Kepler* field (Borucki et al. 2010). It is based on the previous *GALEX*-CAUSE *Kepler* (GCK) collection of NUV fluxes (Olmedo et al. 2015) of the point sources detected in the observations by *GALEX* (Martin et al. 2005)), within the Complete All-Sky Ultraviolet Survey Extension (CAUSE). The observational program, funded by Cornell University (P.I. James Lloyd), was conducted in August-September 2012 over a period of 46 days, during which *GALEX* scanned several times the *Kepler* field, allowing the construction of time series for a large part of the GCK sources. The MGCK catalog contains the light curves of 385,539 point sources and reaches a limiting magnitude of NUV$\simeq$21.5 at 3σ, as depicted in Fig. 1. The best sampled light curves have 22 data points with signal-to-noise ratio SNR$>3\sigma$; the average number of visits per object is 10, while the median is 11 (Fig. 1). Note that 61,687 sources have just one valid ($> 3\sigma$) detection, therefore no variability can be assessed for this sub-sample. Nevertheless, almost all objects with NUV<18 mag generally have more than 10 points in their light curves, all of them detected with SNR>10.

In Fig. 2, we present two examples of MGCK light curves for a faint object, the star KIC 7731201, and for a brighter source, KOI-671, known to be a rotationally variable star.

The MGCK database has 291,094 sources in common with the *Kepler* Input Catalog (KIC; Brown et al. 2011). As the time period of the *GALEX*-CAUSE observations overlapped with Quarter 14 of the *Kepler* program, the MGCK data can be compared with simultaneous optical data, allowing for multiwavelength analyses. As an example, Fig. 3 shows the simultaneous MGCK and *Kepler* light curves of the eclipsing binary V481 Lyr and of the flare star KIC 7459173. We note that the brightness changes in the NUV are far stronger than the variability shown in the visible interval.

The MGCK catalog will provide a powerful supplement to previous photometric surveys for the study of the space ultraviolet in the time domain (e.g., Gezari et al. 2013; Conti et al. 2014; Miles & Shkolnik 2017)). The complete database of the MGCK catalog will be publicly available at `http://www.inaoep.mx/~modelos/mgck`.

References

Borucki, W. J., Koch, D., Basri, G., et al. 2010, Science, 327, 977
Brown, T. M., Latham, D. W., Everett, M. E., & Esquerdo, G. A. 2011, AJ, 142, 112
Conti, A., Bianchi, L., Chopra, N., Orio, M., & Shiao, B. 2014, Advances in Space Research, 53, 967
Gezari, S., Martin, D. C., Forster, K., et al. 2013, ApJ, 766, 60
Martin, D. C., Fanson, J., Schiminovich, D., et al. 2005, ApJ, 619, L1
Miles, B. E. & Shkolnik, E. L. 2017, AJ, 154, 67
Olmedo, M., Lloyd, J., Mamajek, E. E., et al. 2015, ApJ, 813, 100

[1] Instituto Nacional de Astrofísica, Óptica y Electrónica, Luis E. Erro 1, 72840 Tonantzintla, Puebla, Mexico
[2] Institute of Astronomy, Russian Academy of Sciences, Pyatnitskaya str. 48, 119017 Moscow, Russia

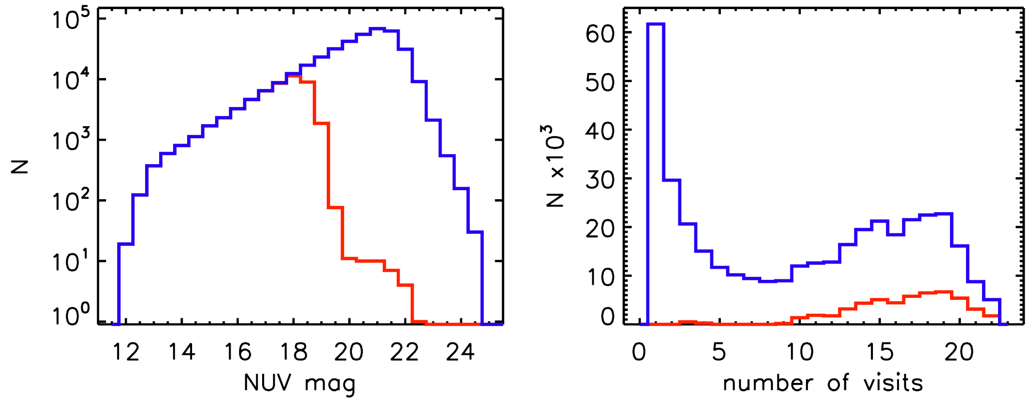

Fig. 1. Left: NUV magnitude (from the GCK catalog) distribution of the MGCK sources with at least one 3σ detection (blue line). The red line shows the distribution of sources that have all light curve points detected at SNR>10. **Right:** Distribution of sources per number of visits. The color code is the same as in the left panel.

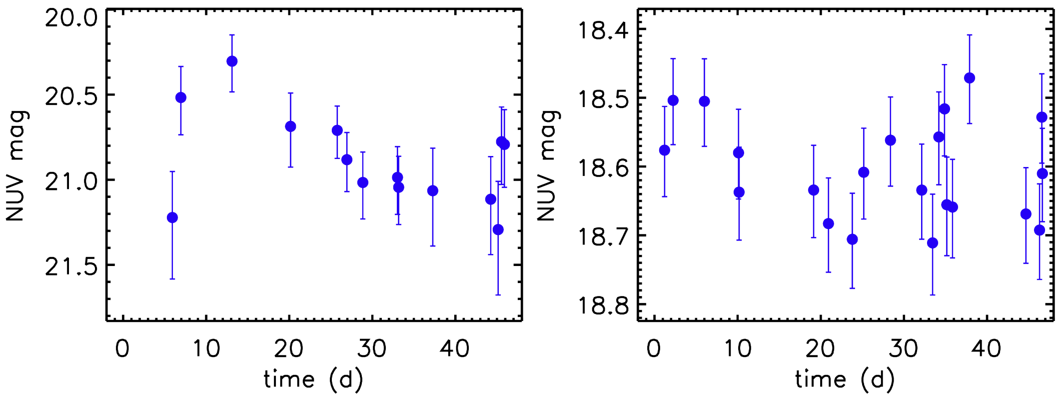

Fig. 2. Left: MGCK light curve of KIC 7731201. **Right:** MGCK light curve of KOI-671.

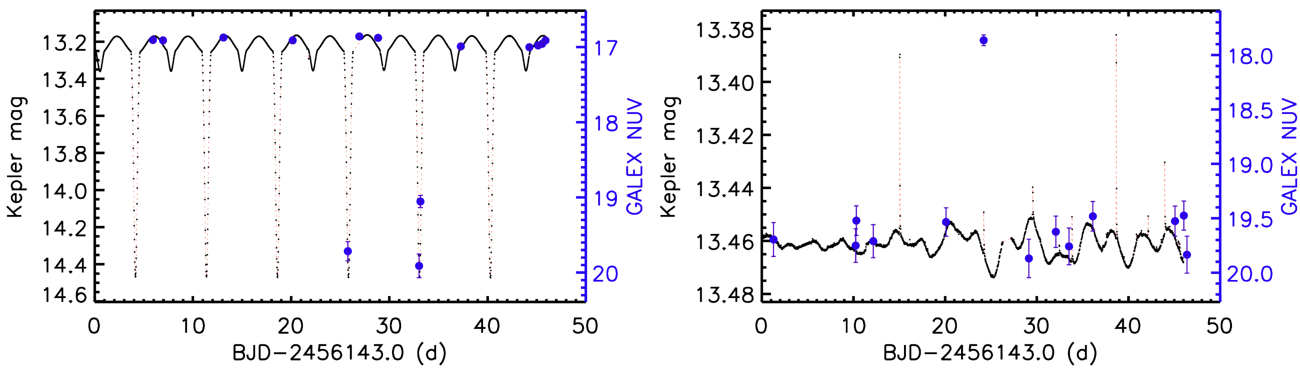

Fig. 3. Left: Simultaneous MGCK (blue points, right axis) and *Kepler* (black points, left axis) light curves of V481 Lyr. **Right:** Same as the left panel, but for KIC 7459173.

Modelling

LISTENING TO THE HEARTBEAT: TIDAL ASTEROSEISMOLOGY IN ACTION

Z. Guo[1]

Abstract. We briefly review the current status of the study of tidally excited oscillations (TEOs) in heartbeat binary stars. Particular attention is paid to correctly extracting the TEOs when the Fourier spectrum also contains other types of pulsations and variabilities. We then focus on the theoretical modeling of the TEO amplitudes and phases. Pulsation amplitude can be modeled by a statistical approach, and pulsation phases can help to identify the azimuthal number m of pulsation modes. We verify the results by an ensemble study of ten systems. We discuss some future prospects, including the secular evolution and the non-linear effect of TEOs.

Keywords: Binary star, tide, oscillation

1 Introduction

More than half of all stars reside in binaries, and tides can have a significant effect on stellar oscillations. In the first version of the classical textbook *Nonradial oscillations of stars*, there is a whole chapter on tidal oscillations (Unno et al. 1979). However, it was removed in the second version (Unno et al. 1989), probably owing to the notion that such oscillations are difficult to be observed in practice.

The direct manifestation of equilibrium and dynamical tides can be seen in the light curves as flux variations. The theoretical foundations were laid out several decades ago, and Kumar et al. (1995) even derived an expression for the observed flux variations from the tidal response. However, it is only because of the *Kepler* satellite that we are able to observe unambiguously such tidally excited oscillations. The prototype system KOI-54 (Welsh et al. 2011), inspired lots of interest in observational (Hambleton et al. 2013, 2016, 2018; Guo et al. 2017, 2019a) and theoretical studies (Fuller & Lai 2012; Burkart et al. 2012; Fuller et al. 2013; O'Leary & Burkart 2014; Fuller 2017; Penoyre & Stone 2019). Thompson et al. (2012) presented tens of such so-called 'heartbeat' stars (HBs) and the Kepler Eclipsing Binary (EB) Catalog (Kirk et al. 2016) now consists of 173 such systems, flagged as 'HBs'. Out of these, about 24 systems show tidally excited oscillations (TEOs), flagged as 'TPs'. Spectroscopic follow-up observations are accumulating (Smullen & Kobulnicky 2015; Shporer et al. 2016). Other space missions such as BRITE revealed more-massive HBs with TEOs (Pigulski et al. 2018), including the O-type binary ι Ori (Pablo et al. 2017). The first sector data of the ongoing TESS mission already offered us a massive HB with TEOs (Jayasinghe et al. 2019).

2 Extracting Tidally Excited Oscillations from Binary Light Curves

To study TEOs, we usually first model the flux variations from the equilibrium tide. Dedicated light-curve synthesis codes are usually used, such as that by Wilson-Devinney (Wilson & Devinney 1971) and its further development in PHOEBE (Prša & Zwitter 2005). In Figure 1, we show sample binary light curve models as red lines. For low inclination systems, the light curves usually contain only one periastron brightening bump. If the binary orbit has a moderate inclination, both a hump and a dip are present. For high inclination systems, the light curves usually contain both a bump and an eclipse. The binary models presented here are either from the simplified light-curve model (Kumar model for KIC 9016693 and KIC 5034333) or from dedicated synthesis codes (KIC 4142768).

After subtracting the binary model, Fourier spectra of the residuals are presented in the right half of Fig 1. Both the low-frequency (g-mode) and high-frequency (p-mode) region can show variability.

[1] Department of Astronomy and Astrophysics, 525 Davey Lab, The Pennsylvania State University, USA

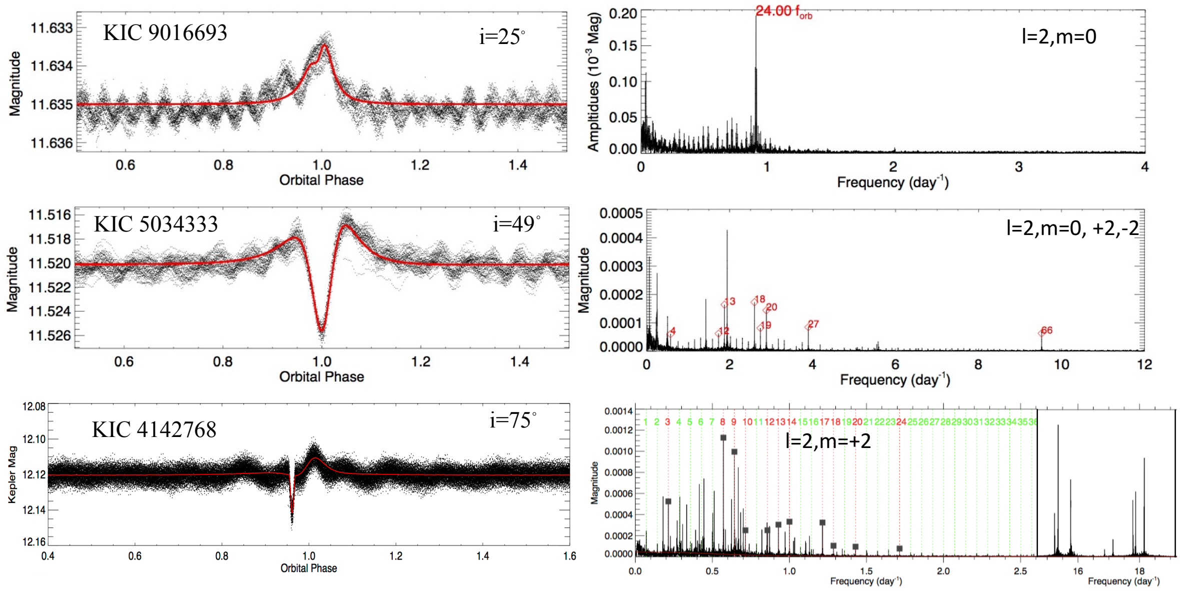

Fig. 1. Phase-folded Kepler light curves of sample heartbeat binaries and their Fourier spectra. Here we show three typical systems of low, moderate, and high orbital inclinations. From top to bottom, $i = 25.6°, 49.9°$, and $75.8°$. The tidally excited oscillations are labeled in the Fourier spectra.

2.1 *Low-frequency Region*

The tidal forcing frequencies from the companion star naturally fall within the low frequency regime. We thus expect the prominent TEOs are low-frequency g modes* with $l = 2$, which are almost always orbital harmonics†. However, in the low-frequency region of the Fourier spectrum, variabilities can also arise from imperfect binary light-curve removal (a series of orbital harmonic frequencies), rotational modulations (usually one or two times the orbital frequency), and γ Dor-type self-excited g modes (usually not orbital harmonics, but quasi-linearly spaced in period). Thus the analysis has to be performed with care. In the right panels of Fig 1, we show the three Fourier spectra. The TEOs have been labeled, and other variablities are mostly from the rotational signal and γ Dor type g modes.

2.2 *High-frequency Region*

Tidally excited oscillations can coexist with high-frequency p modes. These p-modes can be affected by tides. For instance, the δ Scuti type p modes in KIC 4544587 are coupled to the tidally excited g-modes, showing a regular pattern spaced by the orbital frequency (Hambleton et al. 2013). In the circular, close binary HD 74423, the p modes from the near-Roche-lobe filling primary star are magnified and trapped around the inner L1 point (Handler et al., submitted). The pulsation axis is aligned with the tidal force so that the observed p modes show amplitude and phase variations. In the Fourier spectrum, the perturbed p modes also appear as splittings with spacing of the orbital frequency.

3 Modeling the amplitudes and phases of TEOs

3.1 *Pulsation Amplitude: the Statistical Approach by Fuller (2017)*

Unlike self-excited oscillations, linear theory can predict the amplitude of the tidally forced oscillations. This can be achieved by directly solving the forced oscillation equations (Burkart et al. 2012; Valsecchi et al. 2013) or

*However, refer to Fuller et al. (2013) for tidally excited p modes in a triple system. In principle, Rossby modes can also be tidally excited.

†Non-linear effects can generate harmonic TEOs, e.g., those in KOI-54 and KIC 3230227.

by using the mode decomposition method (Schenk et al. 2002; Fuller & Lai 2012). The latter method has been used to calculate the amplitude and phases of TEOs with rotation, nonadiabaticity, and spin-orbit misalignment taken into account (Fuller 2017). The pulsation amplitude sensitively depends on the detuning parameter, i.e., the difference between the forcing frequency and the eigen-frequency of the star, which cannot be determined accurately. It is better to model the TEO amplitude by a statistical approach, treating the detuning as a random variable. Fig 2 shows the TEO amplitude modeling for KIC 4142768 (Guo et al. 2019a). The shaded region indicates the $\pm 2\sigma$ credible region, matching the observed amplitudes (gray squares) very well.

For the modeling of TEOs in resonance locking, special treatment is required: refer to section 5.1 of Fuller (2017). Practical applications can be found in Fuller et al. (2017) for KIC 8164262, and Cheng (2020, in prep.) for KIC 11494130.

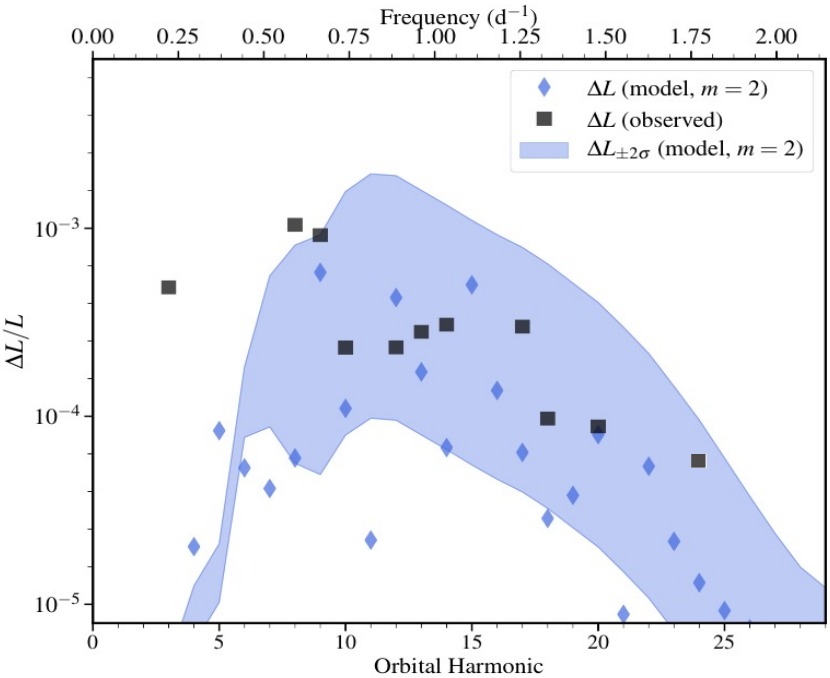

Fig. 2. TEO amplitude modeling of KIC 4142768 assuming a mode identification of $l=2, m=2$. See Guo et al. (2019a) for details.

3.2 Mode Identification from Pulsation Phases

Simply speaking, the theoretical adiabatic pulsation-phase of TEOs depends only on the argument of periastron passage ω_p by the relation $\phi_{l=2,m} = 0.25 + m[0.25 - \omega_p/(2\pi)]$. Fig 3 shows the observed TEO phases of six heartbeat binaries and the theoretical phases (vertical strips) with the corresponding azimuthal number m labeled. The diagrams of KOI-54 and KIC 3230227 are taken from O'Leary & Burkart (2014), and Guo et al. (2017), respectively. It is encouraging to see that they almost all agree within one sigma.

However, as shown in Fig. 4, we also find a large number of heartbeat systems that show significant deviations from the theoretical adiabatic phases (see Guo et al. 2019b for more details). A non-adiabaticity mode and spin-orbit misalignment are likely the reasons behind this. Guo et al. (2019a) considered the mode nonadiabaticity in the theoretical TEO phase calculations, and the theory seems to agree with observations.

We find that low-inclination systems favor the presence of $m = 0$ modes, and very high-inclination systems are more likely to show $|m| = 2$ modes. This is in agreement with the simple geometric interpretation.

4 Discussions and Future Prospects

Other than mode identification, variations of the amplitude and phase of TEOs can offer us information on mode damping and orbital evolution. For KOI-54, it was found that the TEO amplitudes decrease by about $2-3\%$ over three years, which cannot be explained solely by the radiative-mode damping (O'Leary & Burkart 2014). A careful observation of these TEOs can identify modes that are undergoing triple- or multi-mode coupling.

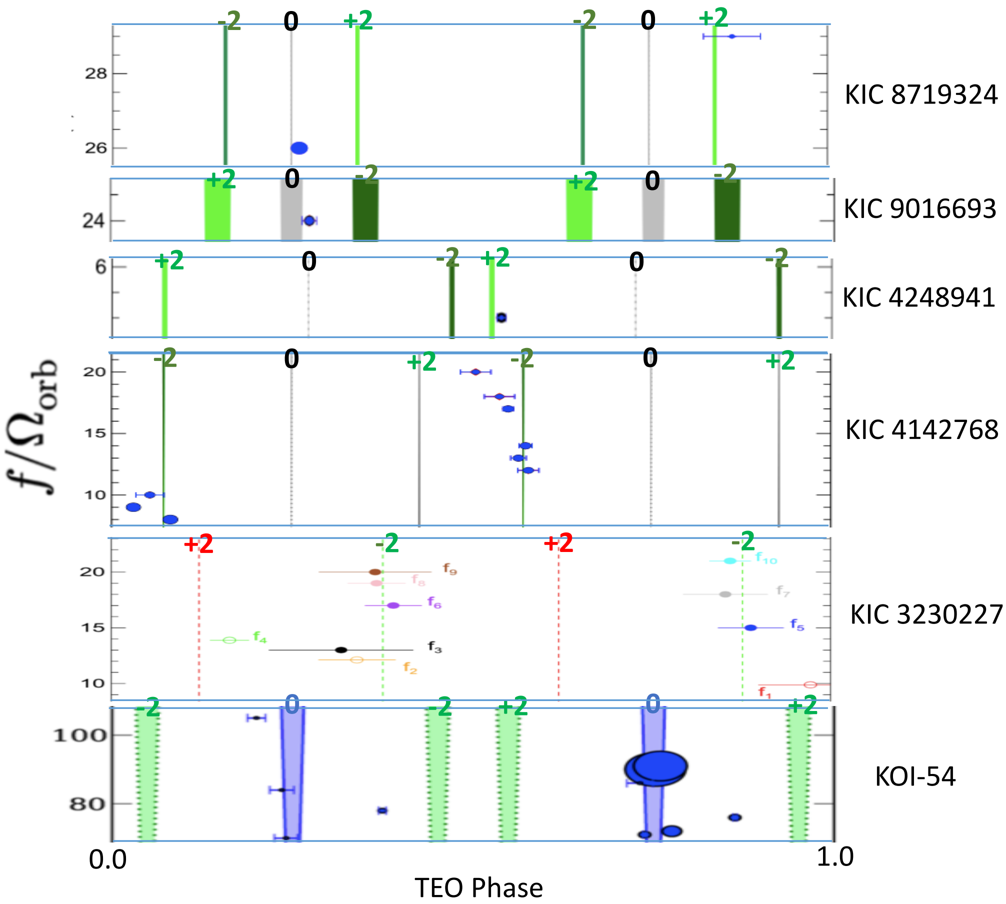

Fig. 3. Pulsation frequencies of TEOs in units of the orbital frequency ($N = f/\Omega_{orb}$) as a function of TEO phases (in units of 2π). These are six heartbeat binaries showing a good match with theoretical predictions for TEO phases. The azimuthal number m is labeled.

Recently, Guo (2019, submitted) found that the non-linear mode coupling in KIC 3230227 has probably settled to the equilibrium state. By utilizing the amplitude equations, a detailed analysis of the non-linear mode coupling can be performed (Weinberg et al. 2012) and is highly desirable. Besides the tidal effect, heartbeat stars are also laboratories for physical processes such as high-eccentricity orbital migration and precession. Their potential has not yet been fully exploited.

I thank the organizers for the invitation, and I am also grateful to Jim Fuller for presenting this work on my behalf. We thank Phil Arras and Nevin Weinberg for helpful discussions on nonlinear tides. We thank Rich Townsend for the development of the GYRE oscillation code.

References

Burkart, J., Quataert, E., Arras, P., & Weinberg, N. N. 2012, MNRAS, 421, 983
Fuller, J. 2017, MNRAS, 472, 1538
Fuller, J., Derekas, A., Borkovits, T., et al. 2013, MNRAS, 429, 2425
Fuller, J., Hambleton, K., Shporer, A., Isaacson, H., & Thompson, S. 2017, MNRAS, 472, L25
Fuller, J. & Lai, D. 2012, MNRAS, 420, 3126
Guo, Z., Fuller, J., Shporer, A., et al. 2019a, ApJ, 885, 46
Guo, Z., Gies, D. R., & Fuller, J. 2017, ApJ, 834, 59
Guo, Z., Shporer, A., Hambleton, K., & Isaacson, H. 2019b, arXiv e-prints, arXiv:1911.08687
Hambleton, K., Fuller, J., Thompson, S., et al. 2018, MNRAS, 473, 5165
Hambleton, K., Kurtz, D. W., Prša, A., et al. 2016, MNRAS, 463, 1199
Hambleton, K. M., Kurtz, D. W., Prša, A., et al. 2013, MNRAS, 434, 925

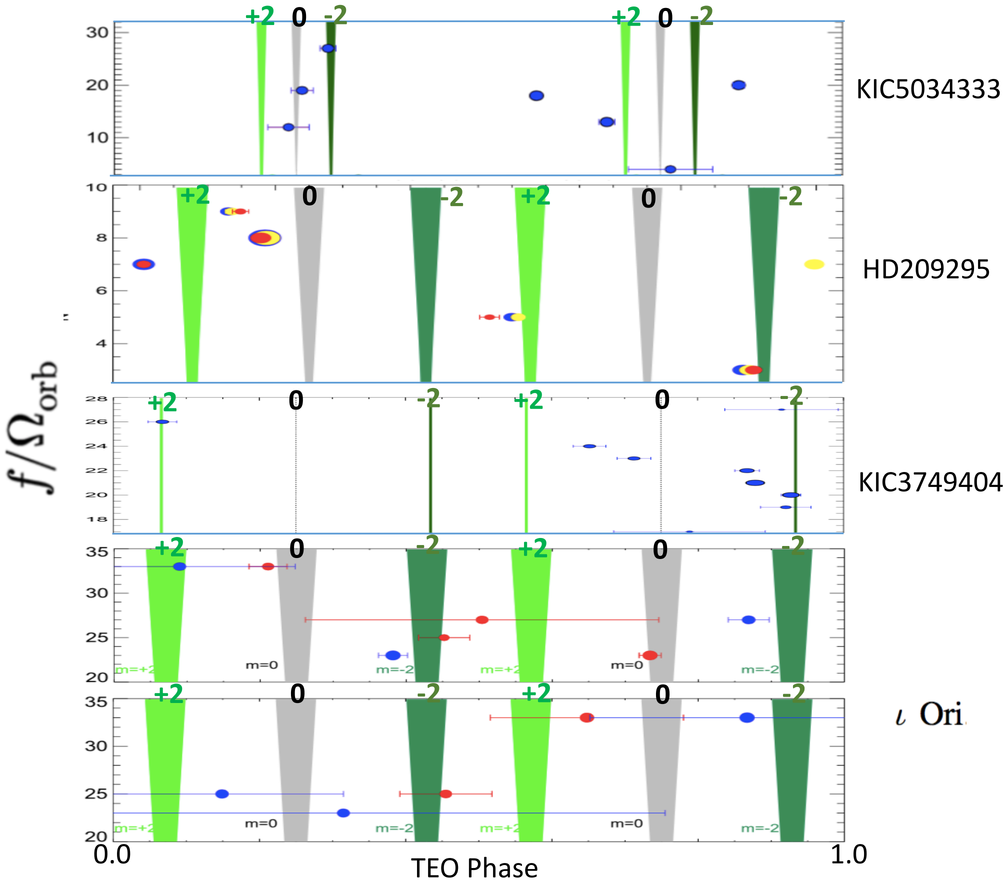

Fig. 4. Same as Fig. 3, but for four systems with significant deviations from theoretical adiabatic phases (vertical strips).

Jayasinghe, T., Stanek, K. Z., Kochanek, C. S., et al. 2019, MNRAS, 489, 4705

Kirk, B., Conroy, K., Prša, A., et al. 2016, AJ, 151, 68

Kumar, P., Ao, C. O., & Quataert, E. J. 1995, ApJ, 449, 294

O'Leary, R. M. & Burkart, J. 2014, MNRAS, 440, 3036

Pablo, H., Richardson, N. D., Fuller, J., et al. 2017, MNRAS, 467, 2494

Penoyre, Z. & Stone, N. C. 2019, AJ, 157, 60

Pigulski, A., Kamińska, M. K., Kamiński, K., et al. 2018, in 3rd BRITE Science Conference, ed. G. A. Wade, D. Baade, J. A. Guzik, & R. Smolec, Vol. 8, 115–117

Prša, A. & Zwitter, T. 2005, ApJ, 628, 426

Schenk, A. K., Arras, P., Flanagan, É. É., Teukolsky, S. A., & Wasserman, I. 2002, Phys. Rev. D, 65, 024001

Shporer, A., Fuller, J., Isaacson, H., et al. 2016, ApJ, 829, 34

Smullen, R. A. & Kobulnicky, H. A. 2015, ApJ, 808, 166

Thompson, S. E., Everett, M., Mullally, F., et al. 2012, ApJ, 753, 86

Unno, W., Osaki, Y., Ando, H., Saio, H., & Shibahashi, H. 1989, Nonradial oscillations of stars (Tokyo: University of Tokyo Press)

Unno, W., Osaki, Y., Ando, H., & Shibahashi, H. 1979, Nonradial oscillations of stars (Tokyo: University of Tokyo Press)

Valsecchi, F., Farr, W. M., Willems, B., Rasio, F. A., & Kalogera, V. 2013, ApJ, 773, 39

Weinberg, N. N., Arras, P., Quataert, E., & Burkart, J. 2012, ApJ, 751, 136

Wilson, R. E. & Devinney, E. J. 1971, ApJ, 166, 605

Stars and their variability observed from space
C. Neiner, W. W. Weiss, D. Baade, R. E. Griffin, C. C. Lovekin, A. F. J. Moffat (eds)

3D HYDRODYNAMICAL SIMULATIONS OF STELLAR CONVECTION FOR HELIO- AND ASTEROSEISMOLOGY

F. Kupka[1]

Abstract. Hydrodynamical simulations of stellar convection are an essential theoretical tool for gaining insight into the physics of mixing and heat transport by convection, and also into the interaction of convection with pulsation. They are particularly useful for obtaining an accurate description of the structure of the superadiabatic layer, which is important to explain the observed frequencies of p-modes in solar-like oscillating stars. The simulations can also be used to probe analytical models of excitation and damping of modes, and thus explain their amplitudes, and eventually the physical completeness of such models. This presentation discussed general challenges of such 3D hydrodynamical simulations developed for helio- and asteroseismology; it summarized some recent results in this field for the Sun, and which are also relevant to other lower main-sequence stars.

Keywords: convection, hydrodynamics, asteroseismology, turbulence, methods: numerical

1 Introduction

Convective instability in a gravitationally stratified fluid can be derived from considering small vertical perturbations of a fluid element. If adiabatic expansion results in a density ρ_1 of the displaced fluid that is less than the density ρ_2 of its new local environment, the fluid is convectively unstable. Equivalent criteria are those of superadiabaticity ($\nabla > \nabla_{\rm ad}$), or an entropy gradient dropping against the direction of gravitational acceleration (cf. also Kupka & Muthsam 2017). Such an unstable stratification triggers the generation of velocity fields. Those are described by conservation laws (the Navier-Stokes equation, NSE) which enable predictions of heat transport in a fluid, mixing of a fluid, the coupling of convection to pulsation and shear flows, and (since stellar fluids are actually plasmas) their interactions with magnetic fields including, dynamo effects.

Numerical approximations to solutions of the fully compressible Navier-Stokes equation form a powerful tool to model convective flows in stars, and their interactions with various physical processes. If the surface layers are included in such numerical models, radiative transfer has to be accounted for (i.e., *radiation hydrodynamical (RHD) simulations*). They have been developed continuously for the last 40 years or so (cf. Nordlund 1982; for reviews and further references see also Nordlund et al. 2009 and Kupka & Muthsam 2017). *Magnetohydrodynamics (MHD)* (cf. Galtier ???? and Brun & Browning 2017 for reviews and references) and radiation magnetohydrodynamics (RMHD) (see, for instance, Stein 2012) are based on effectively the same physical and numerical concepts, but include magnetic fields generated by, and interacting with, the stellar plasma of the simulation models.

The following considers the non-magnetic case. RHD are now mainly performed for the case of three spatial dimensions (3D), although the case of two dimensions (2D) still has applications where 3D simulations have remained unaffordable. The basic numerical equations of (radiation) hydrodynamics are recalled in Sect. 2, which sets the stage for applications to helio- and asteroseismology. Three important simulation scenarios, plus the methodological limitations of the RHD simulation approach, are summarized in Sect. 3. Further recent results on the damping of solar p-modes by RHD simulations are described in Sect. 4. Conclusions are summarized in Sect. 5.

2 Numerical (radiation) hydrodynamics and its applications to helio- and asteroseismology

Supplemented by the continuity (mass conservation) and energy equation, the *Navier-Stokes equation* in a gravitational field with acceleration $\boldsymbol{g}$ and with radiation but without a magnetic field, reads

$$\partial_t \rho + \operatorname{div}(\rho \boldsymbol{u}) = 0, \tag{2.1}$$

[1] MPI for Solar System Research, Justus-von-Liebig-Weg 3, 37077 Göttingen, Germany

$$\partial_t(\rho \boldsymbol{u}) + \mathrm{div}\,(\rho(\boldsymbol{u} \otimes \boldsymbol{u})) = -\mathrm{grad}\,p + \mathrm{div}\,\boldsymbol{\pi} + \rho\,\boldsymbol{g}\,, \tag{2.2}$$

$$\partial_t\,(\rho E) + \mathrm{div}\,((\rho E + p)\,\boldsymbol{u}) = \mathrm{div}(\boldsymbol{\pi}\boldsymbol{u}) - \mathrm{div}\,\boldsymbol{f}_{\mathrm{rad}} - \mathrm{div}\,\boldsymbol{h} + \rho\boldsymbol{u}\cdot\boldsymbol{g} + q_{\mathrm{nuc}}. \tag{2.3}$$

In addition to density ρ, velocity $\boldsymbol{u}$, gas pressure p and viscous stress tensor $\boldsymbol{\pi}$, the energy equation invokes the conductive heat flux $\boldsymbol{h}$ and the nuclear energy generation rate q_{nuc}, but for *stellar envelopes* both these last two can be neglected. Assuming the radiation field to be sufficiently isotropic, the pressure p is usually considered to represent the sum of the gas pressure and the radiative pressure.

At large optical depths the diffusion approximation of radiative transfer holds:

$$\boldsymbol{f}_{\mathrm{rad}} = -K_{\mathrm{rad}}\,\mathrm{grad}\,T. \tag{2.4}$$

Here, $T = T(\rho, \varepsilon, \mathrm{chemical\,composition})$ is the temperature, $E = \varepsilon + \frac{1}{2}|\boldsymbol{u}|^2$ is the total specific energy without gravitational potential energy, ε is the specific internal energy, and K_{rad} is the *radiative conductivity*,

$$K_{\mathrm{rad}} = \frac{4\mathrm{ac}T^3}{3\kappa\rho} = \frac{16\sigma T^3}{3\kappa\rho}, \tag{2.5}$$

with $\kappa = \kappa_{\mathrm{Ross}}(\rho, \varepsilon, \mathrm{chemical\,composition})$ denoting the Rosseland opacity.

In stellar physics $\boldsymbol{\pi} \approx 0$ as $\nu \ll \chi$, where ν is the kinematic viscosity and χ the radiative heat diffusivity. It is replaced by a *sub-grid scale viscosity* (physical model of numerically unresolved scales, which is commonly associated with the term *large eddy simulations* or *LES*), *artificial viscosity* (numerical scheme stabilizing simulations), or through *numerical viscosity* from the discretization of advection (terms such as $\mathrm{div}\rho(\boldsymbol{u} \otimes \boldsymbol{u})$), as occurs in *implicit large-eddy simulations* or *iLES*.

In *optically thin layers* the radiative flux is computed by integrating the stationary limit of the radiative-transfer equation for the intensity I_ν:

$$\mathbf{r}\cdot\nabla I_\nu = \rho\kappa_\nu(S_\nu - I_\nu). \tag{2.6}$$

Here, S_ν is the source function. Summations over bins of frequency averages assure affordability of *non-grey radiative transfer* (4 to 12 bins are common). Owing to resource constraints, this is done in *local thermal equilibrium, LTE*: $S_\nu = B_\nu$ (the Planck function), with non-LTE effects accounted for only very approximatively, if at all.

Angular integration to compute div $\boldsymbol{f}_{\mathrm{rad}}$ is performed by integrating over a (necessarily heavily undersampled) set of rays (as done in most such codes), or by a truncated moment expansion approach (such as the 3D Eddington approximation by Unno & Spiegel (1966) to yield:

$$J_\nu = \frac{1}{4\pi}\int I_\nu(\mathbf{r})d\omega, \qquad \text{and} \tag{2.7}$$

$$q_{\mathrm{rad}} = -\mathrm{div}\,\boldsymbol{f}_{\mathrm{rad}} = 4\pi\rho\int_\nu \kappa_\nu(J_\nu - B_\nu)d\nu. \tag{2.8}$$

To complete the setup of a numerical simulation, the physical problem has to be defined. To that end, the microphysical properties are specified by an equation of state and opacity data, usually given in tabulated form. The chemical composition of the fluid has to be defined, and because a numerical simulation can only account for a finite spatial domain, the latter has to be constructed by choosing a specific volume and the local spatial resolution. Initial conditions are often taken from a 1D model. The environment of this domain is specified through boundary conditions, which may either be open (to allow for inflow and outflow of fluid), closed (to allow only for inflow and outflow of energy), or periodic (usually in horizontal directions). The evolution of this system with time is performed to find a statistically quasi-stationary state. This relies on a quasi-ergodic hypothesis which enables computing ensemble averages from time averages to describe the system through its basic statistical properties. This is also useful for comparisons with 1D models.

The choice of a particular discretization approach requires specifying the numerical grid and its associated coordinate system (Cartesian, polar/spherical/cylindrical, mapped or irregular), the discretization of various terms in the underlying hydrodynamical equations (conservative or non-conservative with respect to mass, momentum and energy, specification of dissipation at small scales and subgrid scale physics), the method of time integration (explicit or (semi)-implicit, multi-stage or multi-step, etc.), and whether the grid values are considered to be interpolated (as in a finite difference method) or volume averages (as in a finite volume approach).

The following applications of 3D RHD of stellar convection are of particular interest in the context of helio- and asteroseismology. First, 1D stellar models can be calibrated, based on data obtained from 3D RHD. This can improve models of convective stellar envelopes and atmospheres (e.g. Magic et al. 2015; Tanner et al. 2016). Secondly, more realistic mean structures can be derived from the RHD simulations for the (near) surface layers of stars. To that end the 3D model is averaged to compute a new mean structure. The latter can be "patched" on top of 1D stellar structure and stellar evolution models. The new 1D model obtained this way can be used for further research. This procedure has been used, for example to study near surface effects of convection on solar-like oscillations in stars (Rosenthal et al. 1999; Sonoi et al. 2015). Finally, quantities of interest can be evaluated directly from the 3D RHD simulation. This approach is of particular interest in the study of mode excitation and mode damping (Stein & Nordlund 2001; Belkacem et al. 2019; Yixiao et al. 2019).

3 Simulation scenarios and methodological limitations

Surface convection zones in main-sequence stars and white dwarfs can be studied with 3D RHD simulations performed for the box-in-a-star scenario. This is based upon the fact that, for those stars, the surface pressure scale-height $P/(\rho\, g) = H_p \ll R$, where R is the stellar radius. Hence, the curvature of mass shells along the radius of such a star, which supposedly rotates slowly enough to be roughly spherically symmetric, is small along a vertical extent of 10 to 12 pressure scale-heights centred around the stellar surface. Cartesian box geometry with a constant vertical gravitational acceleration then allows a good approximation for a set of mass shells along the stellar radius. The horizontal extent of such a simulation box is chosen to be large enough so that near the bottom of the box, where H_p and thus convective flow structures are largest, periodic boundary conditions in the lateral directions do not constrain constrain the flow significantly. In this case structural sizes, such as the width of granules at the stellar surface, are not influenced by introducing this simulation geometry.

The 3D RHD simulations provide numerical solutions for this scenario on a grid in space and time. That enables us to compute mean structures and perform a patching of the averaged 3D structure on top of a 1D stellar structure model. Using an earlier version of the STAGGER code (see also Magic et al. 2015) Rosenthal et al. (1999) demonstrated that the differences in frequencies between solar observations and 1D models such as the famous "model S" by Christensen-Dalsgaard et al. (1996) can partially be explained by effects not accounted for in the standard 1D models: turbulent pressure and radiative cooling in a horizontally inhomogeneous medium. That explains the *structural part of the near surface effect*, the discrepancy between observed and predicted p-mode frequencies at high radial order, n. Using a grid of numerical simulations constructed with the CO5BOLD code Sonoi et al. (2015) studied the dependency of this structural near-surface effect for various stellar spectral types (F to K for main-sequence stars and the lower part of the red giant branch). They noticed a significant variation of the effect with $T_{\rm eff}$ and $\log(g)$. It was confirmed by Ball et al. (2016), who used the MuRAM code for F–K main-sequence stars and also included effects on low-degree non-radial modes (ℓ of up to 3) in their analysis. For a summary of the contributions that appear in addition to these structural effects, i.e. the so called *modal effects*, the review by Houdek & Dupret (2015) provides further insights (and are also a topic in the presentations by G. Houdek [PAGE] and J. Schou [PAGE]). Online resources using the patching of 3D RHD simulations can be found at a webpage on the TOP tool, a Python library for asteroseismology published by Reese, Ballot & Putigny at `https://top-devel.github.io/top/index.html`, with examples given at `https://top-devel.github.io/top/examples.html#surface` based on the ANTARES code (Muthsam et al. 2010; see also Belkacem et al. 2019).

Apart from investigating structural effects upon p-mode frequencies, 3D RHD can also be used to study the near-surface part of the eigenfunctions of high-order radial p-modes. The restriction to high radial order is caused by the slow decay of eigenfunction amplitudes and their contributions inside the star for lower-order modes and the large computational costs of deep 3D RHD simulations with sufficient spatial resolution, thermal relaxation, and long statistical sampling times for resolving p-mode damping and computing work integrals.

For the Sun, that implies $n \gtrsim 15$ (or perhaps somewhat less), $n \gtrsim 7$ (or perhaps a bit larger) for late Am/Fm stars, and $n \gtrsim 50$ for DA white dwarfs with $T_{\rm eff} \sim 12000\,{\rm K}$, (note the latter have not been detected yet in stars). The study of vertical eigenmodes in RHD simulations of the solar surface has been pioneered by Stein & Nordlund (2001), who compared the properties of such modes with the upper part of radial eigenmodes derived from full solar-structure 1D models, which requires scaling of mode amplitudes for reasons explained in further detail by Belkacem et al. (2019).

Alternatively, one can compute work integrals directly from the RHD simulations. Antoci et al. (2014) and Smalley et al. (2017) have demonstrated that an accurate calculation of the turbulent pressure contributions to the work integral is key to understanding which modes are excited in cool Am and Fm stars. This is particularly challenging for 1D models, as they have to be based on a non-local model of convection. For 3D RHD simulations of such objects one would have to ensure that the damping and driving regions of intrinsically unstable modes (e.g., for $n \gtrsim 4$) fit (mostly) into the box to allow reliable work integral computations (especially for $n \gtrsim 7$ in the cases discussed in those papers). Otherwise, polar geometry and deeper domains would be needed, and would lead to even higher computational costs.

Not all the box modes present in 3D RHD are actually observable in stars. An example is p-modes of DA white dwarfs with shallow convection zones and effective temperatures close to 12000 K, where the equivalent of high radial order p-modes are clearly visible in the numerical simulations (cf. Kupka et al. 2018) though no observations have been reported yet. This is due partlyto the technical challenge of detecting modes in the 4 Hz region for faint stars. and partly to the fact that the amplitudes in the simulation boxes are related to their much smaller mode masses which they have, compared to those of full stellar structures.

To study the interaction of envelope convection zones with low radial-order modes, such as in the case of classical variables, much larger fractions of the stellar volume have to be accounted for. This motivates the use of polar coordinates and simulation boxes that may be called "wedge-in-a-star" (having a fixed azimuthal and/or polar opening angle and laterally periodic boundary conditions), "annulus-in-a-star"(covering all azimuthal angles in 2D), or a "spherical shell-in-a-star" (the 3D counterpart of the former). Global 2D simulations (in "annulus-in-a-star" geometry) of the fundamental mode of a Cepheid and its interaction with the mode-driving convection zone due to ionization of He II have been described by Kupka et al. (2014) with a simulation featuring more than 13000 azimuthal zones. They also support the study of non-radial modes (or, in 2D, their counterparts in cylindrical geometry). The key challenges of such multi-dimensional RHD calculations are the computational costs of a sufficiently high spatial resolution near the surface, and the necessity of a long relaxation time. (The drastic effects of insufficient resolution have been demonstrated by Mundprecht et al. 2013 for a "wedge-in-a-star" simulation of the same object).

It may be tempting to demand global simulations of stars to derive results for the damping of p-modes in solar-like stars or for the main radial modes of classical variables and their interaction with convection or higher-order modes. However, for the case of solar-like stars this is not feasible with present, semi-conductor based technology, as was demonstrated by Kupka & Muthsam (2017) (their Table 2). Such a calculation, at a resolution comparable to that of Belkacem et al. (2019), requires 3×10^6 times more grid points than the former (with a 400 times larger area at the same resolution and a 20 times deeper simulation domain, even with highly adapted spatial grids) and a 5000 times longer integration time (to resolve the solar modes, an integration time similar to the observing time of SOHO can be expected), which results in a computational demand that is more than 10^{10} times greater than the simulations used by Belkacem et al. (2019) and Yixiao et al. (2019), and is several orders of magnitude beyond what we can expect from exascale computers during the next 10 years. Likewise, while an in-depth study of classical variables with 2D RHD for a full annulus has now become feasible, 3D RHD of just a single star of this class will either be severely restricted in integration time, or in resolution, or in both, even if the exascale supercomputers of the next decade were to be used with highly optimized simulation codes.

4 Some recent results on solar p-modes

Recent 3D RHD simulations of the convective surface of the Sun have supported detailed analyses of p-mode damping processes. The simulations have aimed at characterizing the main damping contributions by various physical mechanisms (Belkacem et al. 2019) and at computing the theoretical oscillation amplitude and frequency of maximum power $\nu_{\max}$ (Yixiao et al. 2019), among others. Fig. 1 compares the spectral power of the vertical mean velocity evaluated for the layer where the mean temperature equals the (solar) effective temperature, for two 3D RHD simulation runs with ANTARES. The first one, called cosc13, has been published by Belkacem et al. (2019); the latter, called wide4, has been analyzed in==by Leitner et al. (2017) and Lemmerer et al. (2017). Both simulations have the same resolution (11.1 km vertically, 35.3 km horizontally), the same element abundances, opacity tables and starting model, and are based on a 4-bin averaged non-grey radiative transfer with distinct rays for angular integration (see Belkacem et al. 2019 for details). Limited by the sound speed in deep layers and shock waves near the top, and a Courant number associated with the numerical methods used, the time steps are usually less than 0.2 sec.

However, the two simulations differ in several aspects. Wide4 has a 570 km deeper simulation box, i.e., its total vertical extent is 4.45 Mm compared to the 3.88 Mm of cosc13; it also ranges 600 km further into the quasi-adiabatic part of the convection zone. This explains why the three box vertical p-modes (fundamental one with no node in the interior at the lowest frequency, and the first and second overtones with one and two interior nodes, respectively) appear at lower frequency in the simulation wide4 compared to cosc13. In an analysis they thus have to be compared to different solar radial p-modes (see Belkacem et al. 2019 for details). The

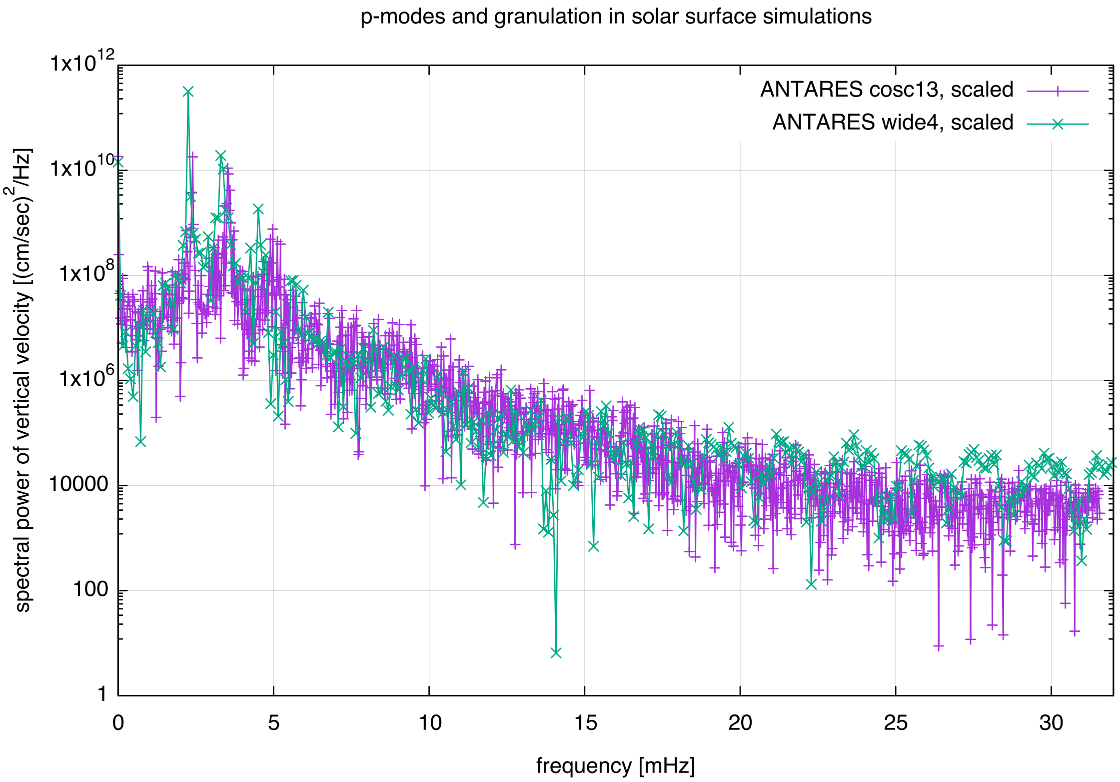

Fig. 1. Spectral power of velocity for two solar granulation simulations performed with ANTARES, evaluated for the layer where the mean temperature equals the (solar) effective temperature. Scaling is necessary to account for the different areas and averaging times of both simulations, but here it was actually set such that both data sets agree in the region from 1–2 mHz with the results obtained by Yixiao et al. (2019) (not shown in the figure).

difference in data output rate (8.54 sec for wide4 and 15.84 sec for cosc13) is less important, as it corresponds to frequencies 100 times smaller than those associated with the simulation time steps, but 10 times larger than the mode frequencies. Fig. 1 therefore truncates the spectrum at about the Nyquist frequency of the lower sampled simulation. The difference in horizontal extent of the simulation domain (18 Mm for wide4 compared to 6 Mm for cosc13) should actually lead to smaller mode power for the simulation with the larger horizontal area (Belkacem et al. 2019). However, the sampling time of wide4 is only 12420 sec (about 3.5 hrs) instead of 40012 sec (about 11 hrs) used for cosc13. Thus, whereas the second mode around 3.5 mHz is resolved in cosc13 (the first one at 2.4 mHz is not), neither is resolved in the case of wide4. The amplitudes obtained are therefore not yet reliable, and the simulation would have to be continued for a longer period of time to obtain more accurate information. between several days and one week of stellar sampling time is necessary to resolve all three modes reliably.

The main conclusion from the study of (Belkacem et al. 2019) has been that, at least for the mode near 3.5 mHz, the different contributions associated with fluctuations of the gas pressure (induced by perturbations of the radiative and enthalpy flux as well as the dissipation rate of turbulent kinetic energy ϵ) can partially cancel each other while being comparable to effects caused by perturbations of the turbulent pressure. In particular, ϵ plays a role that is equally important for the amplitudes of p-modes in the Sun as the other three contributions.

5 Conclusions

The existing simulations used for studying p-modes in solar-like stars are already a very useful tool for gaining insights into the physics of mode amplitudes in addition to mode frequencies. To proceed further, such simulations should be conducted over longer time-scales (a week or a few weeks of solar/stellar time)q at a sufficiently high sampling rate, if the granulation background spectrum should also be investigated with the same numerical data. The influence of boundary conditions, box sizes, and spatial resolution will have to be considered in more detail, and a comparison of simulations based on different discretization methods will be necessary to ensure that the dissipation rate of turbulent kinetic energy is calculated reliably. Evidently, it will be highly informative – and also for gaining a theoretical understanding of the scaling laws used in asteroseismology – to repeat such studies for stars other than the Sun. The main limitation of this approach is the excessive amount of computing resources it requires: simulations have to be planned carefully, to obtain the desired results within an affordable amount of computing time and to avoid unrealistic demands on supercomputing power presently available or during the next decade.

The author gratefully acknowledges partial support through the Austrian Science Fund (FWF) project P29172-N27, and the European Research Council Synergy Grant WHOLE SUN #810218.

References

Antoci, V., Cunha, M., Houdek, G., et al. 2014, ApJ, 796, 118 (8 pp.)

Ball, W. H., Beeck, B., Cameron, R. H., & Gizon, L. 2016, A&A, 592, A159 (8 pp.)

Belkacem, K., Kupka, F., Samadi, R., & Grimm-Strele, H. 2019, A&A, 625, A20 (15 pp.)

Brun, A. & Browning, M. 2017, Living Reviews in Solar Physics, 14:4, 133 pages

Christensen-Dalsgaard, J., Dappen, W., Ajukov, S. V., et al. 1996, Science, 272, 1286

Galtier, S. ???? (Cambridge University Press, Title = Introduction to Modern Magnetohydrodynamics, Year = 2016)

Houdek, G. & Dupret, M.-A. 2015, Living Reviews in Solar Physics, 12:8, 88 pages

Kupka, F., Mundprecht, E., & Muthsam, H. J. 2014, in IAU Symposium, Vol. 301, Precision Asteroseismology, ed. J. A. Guzik, W. J. Chaplin, G. Handler, & A. Pigulski, 177–184

Kupka, F. & Muthsam, H. J. 2017, Living Reviews in Computational Astrophysics, 3:1, 159 pages

Kupka, F., Zaussinger, F., & Montgomery, M. H. 2018, MNRAS, 474, 4660

Leitner, P., Lemmerer, B., Hanslmeier, A., et al. 2017, ApSS, 362, 181 (13 pp.)

Lemmerer, B., Hanslmeier, A., Muthsam, H., & Piantschitsch, I. 2017, A&A, 598, A126 (13 pp.)

Magic, Z., Weiss, A., & Asplund, M. 2015, A&A, 573, A89 (17 pp.)

Mundprecht, E., Muthsam, H. J., & Kupka, F. 2013, MNRAS, 435, 3191

Muthsam, H. J., Kupka, F., Löw-Baselli, B., et al. 2010, New Astronomy, 15, 460

Nordlund, Å. 1982, A&A, 107, 1

Nordlund, Å., Stein, R. F., & Asplund, M. 2009, Living Reviews in Solar Physics, 6:2, 117 pages

Rosenthal, C., Christensen-Dalsgaard, J., Nordlund, Å., Stein, R., & Trampedach, R. 1999, A&A, 351, 689

Smalley, B., Antoci, V., Holdsworth, D. L., et al. 2017, MNRAS, 465, 2662

Sonoi, T., Samadi, R., Belkacem, K., et al. 2015, A&A, 583, A112 (11 pp.)

Stein, R. F. 2012, Living Reviews in Solar Physics, 9:4, 51 pages

Stein, R. F. & Nordlund, Å. 2001, ApJ, 546, 585

Tanner, J. D., Basu, S., & Demarque, P. 2016, ApJ, 822, L17 (5 pp.)

Unno, W. & Spiegel, E. A. 1966, PASJ, 18, 85

Yixiao, Z., Asplund, M., & Collet, R. 2019, ApJ, 880, 13 (10 pp.)

Stars and their variability observed from space
C. Neiner, W. W. Weiss, D. Baade, R. E. Griffin, C. C. Lovekin, A. F. J. Moffat (eds)

CHALLENGES TO MODELLING FROM GROUND-BREAKING NEW DATA OF PRESENT/FUTURE SPACE AND GROUND FACILITIES

G. Clementini[1], M. Marconi[2] and A. Garofalo[1]

Abstract. The sheer volume of high-accuracy, multi-band photometry, spectroscopy, astrometry and seismic data that space missions like *Kepler, Gaia, PLATO, TESS, JWST* and ground-based facilities under development such as MOONS, WEAVE and LSST will produce within the next decade brings big opportunities to improve current modelling; but there are also unprecedented challenges to overcome the present limitations in stelar evolution and pulsation models. Such an unprecedented harvest of data also requires multi-tasking and synergistic approaches to be interpreted and fully exploited. We review briefly the major output expected from ongoing and planned facilities and large sky surveys, and then focus specifically on *Gaia* and present a few examples of the impact that this mission is having on studies of stellar physics, Galactic structure and the cosmic distance ladder.

Keywords: Stars: general, oscillations, distances, Hertzsprung–Russell and C–M diagrams, variables: general, surveys, cosmology: distance scale

1 Introduction

The wealth and variety of datasets produced by ground/space-based facilities and large sky surveys under way or planned for the near future are trning Astronomy into a paradigm of "Big Data" science. Some of these facilities are reviewed briefly to show how their complementary data products can not only advance significantly our knowledge of stellar interiors, evolution and pulsation, but can also help constraining the structure and formation of our Galaxy, enable us to characterise the stellar populations in Galactic and extragalactic environments, and refine the cosmic distance ladder and gauge the expansion rate of the Universe.

Past, ongoing and future space facilities like *WIRE* (Hacking et al. 1999), *MOST* (Walker et al. 2003), *CoRoT* (Baglin 2003), *Kepler* (Koch et al. 2010), it K2 (Howell et al. 2014), *BRITE* (Pablo et al. 2016), *TESS* (Ricker et al. 2015), *Cheops* (Broeg et al. 2013) and *PLATO* (Rauer et al. 2014) are producing unprecedented, accurate light-curves that are revealing a very rich collection of stellar oscillations (gravity-modes, pressure-modes, rotation-related modes, etc.) for stars in different evolutionary stages. Asteroseismology is exploiting these data to provide seismic measurements of radii, masses, ages, distances and positions on the Hertzsprung–Russell diagram for thousands of stars within some tens of kpc. These measurements enable us to test distances derived from parallaxes, such as those measured by *Gaia*; they also provide a unique benchmark for testing and improving models for stellar evolution and pulsation. On the theoretical side, 3D model atmospheres are now starting to become available. They will enable a calibration of the empirical oscillations and convection parameters used in stellar-evolution codes (see e.g. Chaplin & Miglio 2013; Dupret 2019, and various contributions in this conference).

Several physical mechanisms (e.g. rotation and rotationally-induced mixing, magnetic fields, thermohaline mixing, internal gravity waves, mass loss, etc.) are still poorly understood and are not accounted for well in current stellar modelling. Including such effects into models is difficult because they are controlled by several physical parameters. However, it is no longer possible to ignore them if we wish to understand and interpret thoroughly the huge amount of high-accuracy photometric, spectroscopic, astrometric and seismic information that on-going and future surveys are providing. The development of 3-D stellar models and hydro-dynamical codes is also needed to describe convection and other dynamical phenomena realistically as they occur in stars; however, this is a very challenging and computationally expensive task (see e.g. Joyce et al. 2019, and references therein, and a number of talks at this conference).

[1] Osservatorio di Astrofisica e Scienza dello Spazio, Via Piero Gobetti 93/3, 40129 Bologna, Italy
[2] Osservatorio Astronomico di Capodimonte, Via Moiariello 16, 80131, Naples, Italy

Large time-domain photometric surveys such as OGLE (Udalski et al. 1992), MACHO (Alcock et al. 1999), EROS (Tisserand et al. 2007), ASAS (Pojmanski 1997), Pan-STARRS (Chambers et al. 2016), *Hipparcos* (van Leeuwen 2007), SDSS (Stripe82; Annis et al. 2014), Catalina (Drake et al. 2014), PTF (Law et al. 2009), ZTF (Bellm et al. 2019), VVV (Minniti et al. 2010), VMC (Cioni et al. 2011) and *Gaia* (Gaia Collaboration et al. 2016) are providing a census of the variable stars in the Milky Way and its closest companions, revealing new features and new variability types. Starting full science operations in 2023, LSST (Ivezić et al. 2019 and references therein) will be *Gaia's deep complement in the southern hemisphere, providing parallaxes, proper motions and multiband photometry with uncertainties similar to Gaia's faint end (V∼20.5 mag) but reaching to about 5 magnitudes fainter than Gaia can.*

HERE

In parallel, large spectroscopic surveys such as SEGUE (Yanny et al. 2009), RAVE (Steinmetz et al. 2006), GALAH (De Silva et al. 2015), APOGEE (Allende Prieto et al. 2008), LAMOST (Deng et al. 2012) are measuring radial velocities and elemental abundances. Gaia-ESO (Gilmore et al. 2012), the only spectroscopic survey at an 8 m class telescope so far, is providing large samples of heavy-element abundances, both for s-process-dominated (Y-Zr-Ba-La-Ce), r-process-dominated (Sm-Eu), and mixed s&r (Pr-Nd) elements. In the near future, instruments under development such as WEAVE (Bonifacio et al. 2016) at the William Herschel Telescope (WHT), 4MOST (de Jong et al. 2019) at VISTA and MOONS (Cirasuolo et al. 2011) at the VLT will provide a detailed chemical characterisation for millions of stars in the Galactic halo and disk(s) (WEAVE) and accurate chemistry and kinematics for large samples of old giants spanning a wide portion of the red giant branch in the Magellanic Clouds and the Sagittarius dwarf spheroidal (MOONS). Accurate nucleosynthesis predictions, in particular for s-elements, require a detailed modelling of the asymptotic giant branch (AGB) evolutionary phase. The AGB phase is also critical for the interpretation of the infrared observations of the evolved populations in galaxies (e.g. the Magellanic Clouds and Local Group dwarf galaxies) and to study extinction properties. In the future, study of the circumstellar envelopes around massive stars in the Milky Way and in the Local Group will also become possible thanks to the high spatial resolution of next-generation facilities such as ELT in the optical and SKA in the radio. SKA will also allow one to measure the magnetic fields in stars of different evolutionary phases.

Such an unprecedented harvest of data requires synergistic and multivariate approaches to be fully exploited.

2 Gaia, three instruments in one mission: astrometry, (spectro-)photometry, spectroscopy

The stunning revolution being operated by Gaia has often been mentioned during the conference and examples have been shown in a number of talks (see, e.g. Eyer et al. contribution to this proceedings). Here, we would like to address two specific fields where Gaia is really astonishing: (i) the detailed monitoring of stellar populations in different evolutionary phases, and (ii) the distance scale.

The study of stellar populations can rely on Gaia 3-band time-series photometry (G, G_{BP} and G_{RP}) and G_{BP}, G_{RP} spectro-photometry; on spectroscopy from the Radial Velocity Spectrometer (RVS; for sources brighter than G∼ 16-16.5 mag) and on astrometry (positions, proper motions and parallaxes, hence individual distances) for over 1 billion stars, that allow us to build accurate HR diagrams (see left panel of Fig. 1, showing the colour-magnitude diagram of the Large Magellanic Cloud – LMC, from Gaia Data Release 2 – DR2, data) as well as to estimate precise individual and mean distances. On this basis a 3D map of the Milky Way providing insight into the Galactic formation and evolution mechanisms is derived. Gaia is also a most powerful tool to discover and characterise all-sky variable sources, as shown by the catalogue and multiband time-series for more than half a million variables of different types (RR Lyrae stars, Cepheids, Long Period Variables – LPVs, Solar-like stars with rotation modulation, δ Scuti & SX Phoenicis and short period variables) released in Gaia DR2 (Holl et al. 2018). In the right panel of Fig. 1, we show RR Lyrae stars, Cepheids and LPVs released in DR2 which belong to the LMC plotted over the Galaxy CMD.

A noteworthy product released in DR2, is the catalogue of about 150,000 rotational-modulation variable candidates of the BY Draconis class, an unprecedented sample to study stellar rotation, magnetic activity and stellar ages (Lanzafame et al. 2018, 2019).

Gaia DR2 contains also a catalogue of 140,784 confirmed RR Lyrae stars with full characterization: periods, amplitudes, mean magnitudes, Fourier parameters, photometric metal abundances (for a subsample of 64,932 sources) and interstellar absorption (for 54,272 of them) (Clementini et al. 2019). About 50,000 of these RR Lyrae stars are new discoveries by Gaia. In the DR2 variability tables there are more than 9,000 confirmed Cepheids fully characterized and with photometric metal abundances (for 3,738 for sources). About 350 of them are new discoveries by Gaia (Clementini et al. 2019; Ripepi et al. 2019).

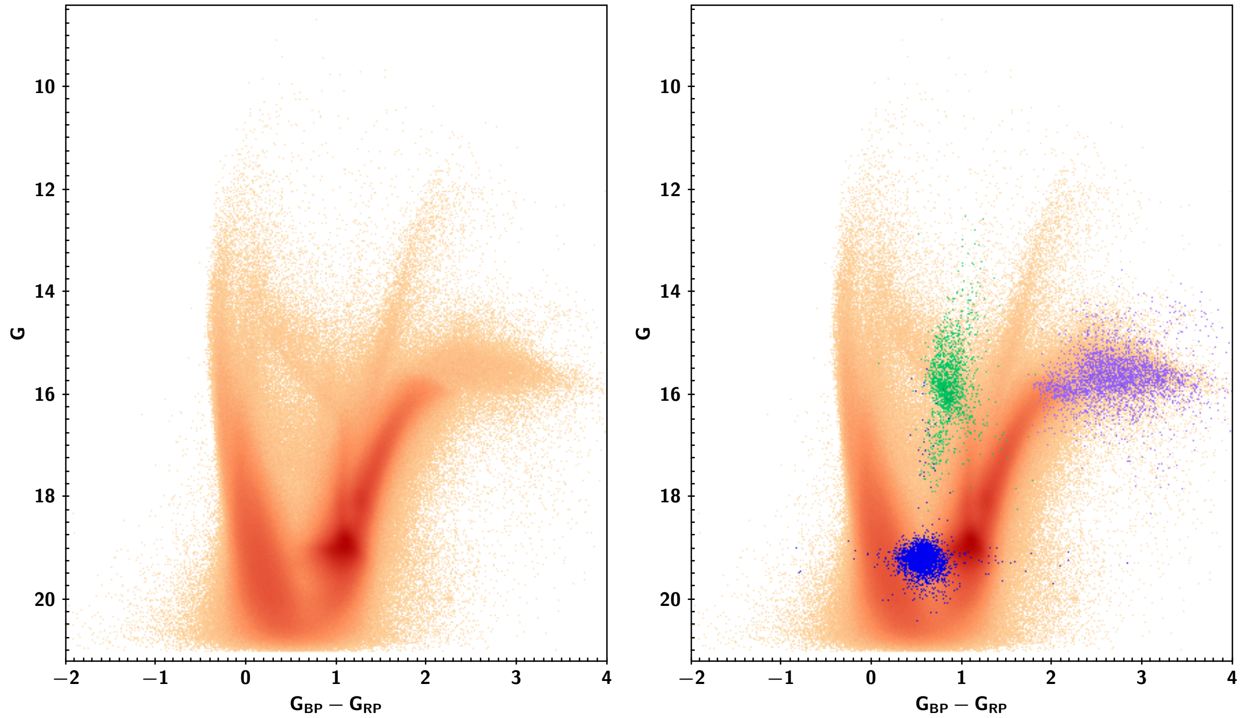

Fig. 1. Left: CMD of sources in the Gaia DR2 catalogue (selected by parallax and proper motions) contained in a region of about 8.8 degrees in radius around the Large Magellanic Cloud centre. Main features corresponding to the different evolutionary phases can be easily recognised: the main sequence, the red giant branch, the red clump, the horizontal branch. A sharp cut on the red giant branch marks the tip of the red giant branch (TRGB). The magnitude of the TRGB, which is set by the luminosity of the He core flash, may serve as a distance indicator for old stellar populations. Also very clearly visible are the blue loops of the core helium-burning evolutionary phase. **Right:** Same as in the right panel but with Cepheids, RR Lyrae stars, and LPVs (Soszyński et al. 2017, 2016, 2009, respectively) that cross-match with variable sources in the DR2 catalogue plotted as green, blue and purple filled circles, respectively, using G, $G_{BP}-G_{RP}$ mean magnitudes and colours from Gaia DR2 variability tables. The bulk of classical Cepheids are located on the central helium burning blue loop evolutionary phase, whereas RRLs nicely trace the LMC horizontal branch. Most of the LPVs are found above the TRGB, in the region of thermally-pulsing AGB stars.

In the case of pulsating stars, the distance information inferred from Gaia parallaxes can be used to provide stringent constraints on other debated quantities and relations such as the efficiency of superadiabatic convection or Mass-Luminosity relations, as well as, once complementary spectroscopic metallicities are available, the Helium to metal enrichment ratio. This will be possible through the comparison between observed and predicted pulsation properties including the model fitting of multi-filter light curves through non-linear convective pulsation models (see e.g. Marconi & Clementini 2005; Keller & Wood 2006; Marconi et al. 2013b,a, and references therein). Figure 2 shows the model fitting of the multiband light curves of the classical Cepheid RS Puppis. The best fit is obtained for a model with $T_{\rm eff} = 4875$ *K,* $\log L/L_\odot = 4.19$, $M/M_\odot$*=9 and mixing-length parameter* $\alpha = 1.5$*. The model fitting provides a parallax of 0.58± 0.03 mas in excellent agreement with the Tycho-Gaia Astrometric Solution (TGAS) parallax released with Gaia DR1 for this star, 0.63± 0.26 mas.*

Furthermore, once the distances are fixed, it will be possible to constrain the coefficients of the adopted extinction laws in current applications of the Period-Wesenheit relations. The comparison between predicted and observed radial velocity curves or Period-Radius relations will also allow us to directly measure the projection factor P, whose value and possible dependence on the pulsation period are debated in the literature.

Gaia distances are also adopted to calibrate Cepheid Period-Luminosity and Period-Wesenheit relations that in turn allow us to calibrate the extra-galactic distance ladder and to evaluate the Hubble constant through the calibration of secondary distance indicators.

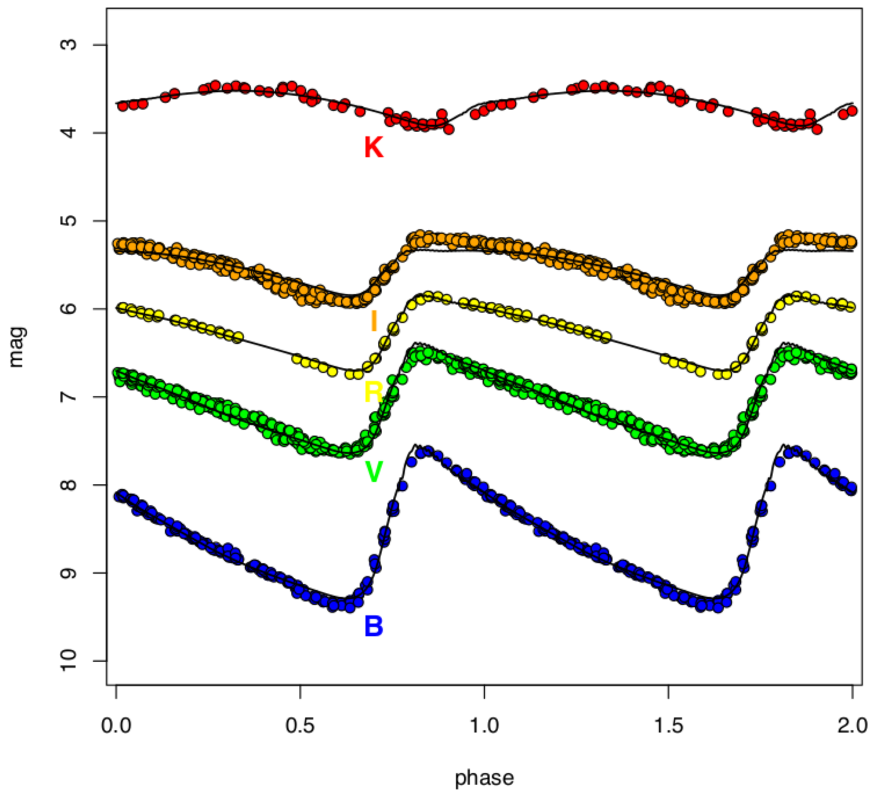

Fig. 2. Model fitting of the multi-wavelength light curves of the fundamental mode classical Cepheid RS Puppis (P=41.528 days) through non-linear convective pulsation models (adapted from Fig. 12 of Gaia Collaboration et al. 2017).

3 Parallaxes - Distances - H_0 and the H_0 'tension'

The Hubble constant, H_0, is the expansion rate of the Universe measured in units of inverse time. There is 'tension' between values of H_0 as derived from measurements of the anisotropy of the cosmic microwave background (CMB) radiation and as measured from a series of distance indicators in the local Universe. The CMB measures the age of the Universe at recombination. The distance ladder measures the age of the Universe now. If the standard model of cosmology is correct, these measurements should agree on the value of H_0 within the errors. Figure 3 summarises values of H_0 based on early- and late-Universe probes presented in the conference: "Tensions between the Early and the Late Universe", held at the Kavli Institute for Theoretical Physics, UC Santa Barbara in July 2019. The figure is an updated version of Fig. 1 in Verde et al. (2019) and shows that currently that 'tension' is between 4σ and 5.8σ. One thing is clear from Fig. 3 the onus to improve the accuracy of the H_0 measurements is on the distance ladder, rather than on the CMB. The error budget of the distance ladder must therefore be fully understood.

The Gaia contribution to understanding and quantifying the H_0 tension, as arising from the distance ladder side, will be unprecedented. This mission will allow us to raise the accuracy of the astronomical distance ladder by specifically tackling uncertainties and systematics in main stellar standard candles in order to cast light on the origin of the tension and at the same time better understand the underlying stellar physics.

The accuracy of local H_0 determinations will be significantly improved already by building on the data products in the forthcoming Gaia Data Releases 3 (EDR3 in the second half of 2020 and DR3 in the second half of 2021), and further boosted by subsequent releases (Gaia DR4, likely to occur in 2024) and the combination with data from TESS, JWST (Beichman et al. 2012) and the LSST.

Gaia will specifically improve the 'Anchors' of the distance ladder by directly measuring their distances through parallaxes. Examples of these improvements were already shown by the TGAS parallaxes released in Gaia

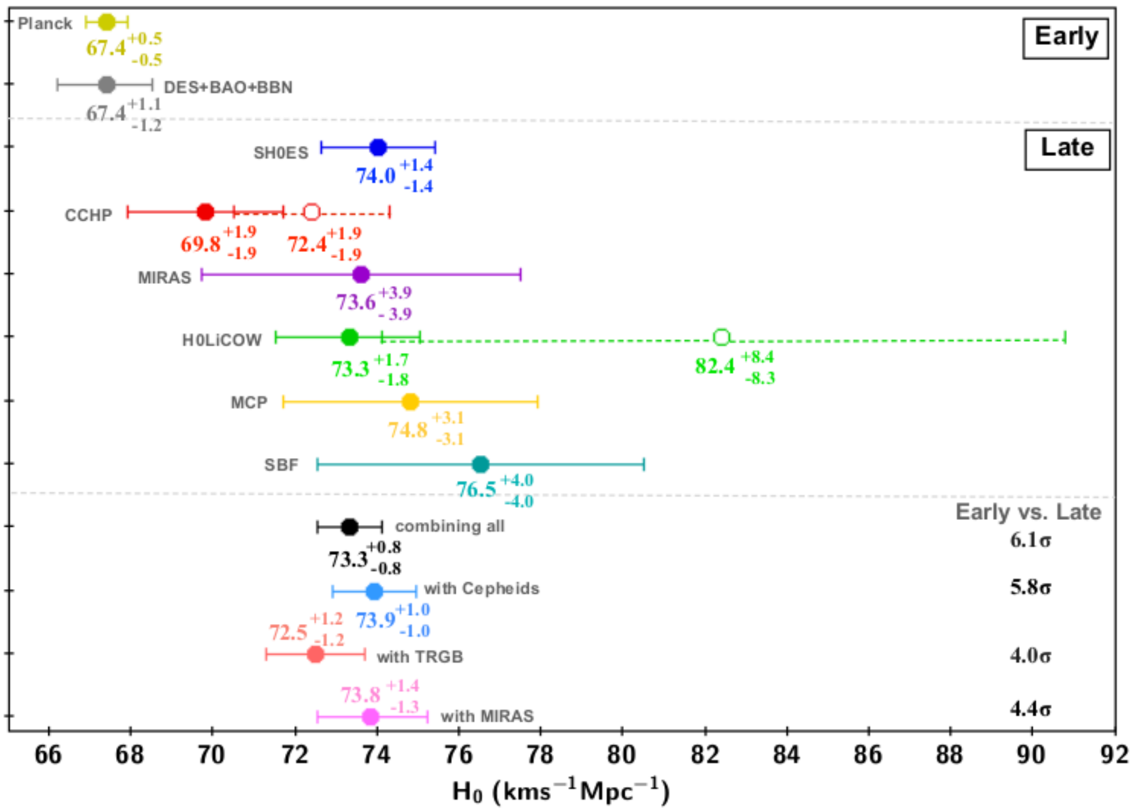

Fig. 3. Predictions and measurements of H_0 based on early- and late-Universe probes (adapted from Fig. 1 in Verde et al. 2019). The two independent predictions based on early-Universe data are from: Planck Collaboration et al. (2018), and Abbott et al. (2018), respectively. Results based on late-Universe data include: Riess et al. (2019) results for the SH0ES collaboration which uses geometric distances to calibrate Cepheids; Freedman et al. (2019) results for the CCHP collaboration which uses the TRGB to connect the distance ladder and, shown by the red dashed line, Jee et al. (2019) revision of the CCHP TRGB-based estimate of H_0; Huang et al. (2018) and Huang et al. (2019) results for Miras in NGC 4258 and NGC 1159, respectively; Wong et al. (2019) for the H0liCOW team that uses strong lensing time delays between multiple images of background quasars and, shown by the green dashed line, the new measurements from strong gravitational lenses by Jee et al. (2019) who recently increased the H_0 value by H0liCOW to H_0=82.4 +8.4/-8.3 km s^{-1} Mpc^{-1} (but note the large uncertainty); new results from the Megamaser Cosmology Project (MCP; Reid et al. 2009) which uses VLBI observations of water masers orbiting around supermassive black holes to measure geometric distances; and, Potter et al. (2018) results from IR Surface Brightness Fluctuations. Not shown in the figure, but potentially an additional tool to measure H_0, are gravitational waves and standard sirens. Recent results from this method were published by Mukherjee et al. (2019) who find $H_0 = 69.3^{+4.5}_{-4.0}$ km s^{-1} Mpc^{-1}.

DR1 (see, e.g. Gaia Collaboration et al. 2017) and by the Gaia-only parallaxes of RR Lyrae stars (Muraveva et al. 2018) and Cepheids (Riess et al. 2018) released in Gaia DR2.

According to current estimates of the error budget associated to each step of the cosmic ladder, the improvement that Gaia is going to provide can allow us to evaluate H_0 to ∼ 1%. This will occur through a number of progressive steps that are briefly listed below:

- *The exploitation of Gaia DR3 parallaxes along with a detailed investigation of the associated systematics, offsets (e.g. the offset with respect to QSOs, see fig. 12 in Lindegren et al. 2018) and relativistic effects, also relying on the comparison with asteroseismic parallaxes from Kepler, K2 and TESS*

- *The use of Gaia parallaxes along with NIR photometry for pulsating stars to re-calibrate Cepheid and RR Lyrae distance scales and their application to measure the distance to stellar systems containing different, independent primary and secondary distance indicators and, at the same time, bridging Gaia's distance range to those of LSST and JWST in a self-consistent path to H_0*

- *The simultaneous development and extension of fine grids of nonlinear convective pulsation models for variable stars in different evolutionary phases and environments that will allow us to theoretically constrain the distances and their dependence on physical and numerical assumptions, with relevant implications for the final error budget associated to H_0*
- *An improved treatment of population effects in various classes of standard candles associated to different stellar populations, namely, Cepheids, RR Lyrae stars, LPVs and the TRGB, directly calibrated through Gaia parallaxes locally, and all well represented in many external systems, like the Magellanic Clouds*
- *The investigation of possible alternative cosmic distance scale anchors to the traditionally adopted LMC, such as M31, and the use of different independent indicators for the same stellar system/anchor*
- *A rigorous quantification of systematic effects associated to the various adopted distance indicators and their impact on the final H_0 derivation.*

4 Conclusions

Synergy between different techniques, instruments and datasets is the key to tackle many of the issues affecting stellar evolution and pulsation modelling as well as to test empirical results (e.g. Gaia parallaxes). A bright future is in front of us thanks to present/future outstanding facilities and surveys, providing an unprecedented wealth of excellent photometry/astrometry/spectroscopy/asteroseismology datasets to challenge stellar evolution and pulsation modelling.

Acknowledgement: This work has made use of data from the European Space Agency (ESA) mission Gaia (https://www.cosmos.esa.int/gaia), processed by the Gaia Data Processing and Analysis Consortium (DPAC, https://www.cosmos.esa.int/web/gaia/dpac/consortium). Funding for the DPAC has been provided by national institutions, in particular the institutions participating in the Gaia Multilateral Agreement. We wish to warmly thank our colleagues and collaborators in the project "SH_0T: the Stellar path to the H_0 Tension with whom many of the ideas presented in this proceedings are being developed.

References

Abbott, T. M. C., Abdalla, F. B., Annis, J., et al. 2018, MNRAS, 480, 3879

Alcock, C., Allsman, R. A., Alves, D. R., et al. 1999, PASP, 111, 1539

Allende Prieto, C., Majewski, S. R., Schiavon, R., et al. 2008, AN, 329, 1018

Annis, J., Soares-Santos, M., Strauss, M. A., et al. 2014, ApJ, 794, 120

Baglin, A. 2003, Advances in Space Research, 31, 345

Beichman, C. A., Rieke, M., Eisenstein, D., et al. 2012, SPIE Conference Series, Vol. 8442, Science opportunities with the near-IR camera (NIRCam) on the James Webb Space Telescope (JWST) (SPIE), 84422N

Bellm, E. C., Kulkarni, S. R., Graham, M. J., et al. 2019, PASP, 131, 018002

Bonifacio, P., Dalton, G., Trager, S., et al. 2016, in SF2A-2016: Proceedings of the Annual meeting of the French Society of Astronomy and Astrophysics, ed. C. Reylé, J. Richard, L. Cambrésy, M. Deleuil, E. Pécontal, L. Tresse, & I. Vauglin, 267–270

Broeg, C., Fortier, A., Ehrenreich, D., et al. 2013, in EPJ Web of Conferences, Vol. 47, EPJ Web of Conferences, 03005

Chambers, K. C., Magnier, E. A., Metcalfe, N., et al. 2016, arXiv e-prints, arXiv:1612.05560

Chaplin, W. J. & Miglio, A. 2013, ARA&A, 51, 353

Cioni, M. R. L., Clementini, G., Girardi, L., et al. 2011, A&A, 527, A116

Cirasuolo, M., Afonso, J., Bender, R., et al. 2011, The Messenger, 145, 11

Clementini, G., Ripepi, V., Molinaro, R., et al. 2019, A&A, 622, A60

de Jong, R. S., Agertz, O., Berbel, A. A., et al. 2019, The Messenger, 175, 3

De Silva, G. M., Freeman, K. C., Bland-Hawthorn, J., et al. 2015, MNRAS, 449, 2604

Deng, L.-C., Newberg, H. J., Liu, C., et al. 2012, Research in A&A, 12, 735

Drake, A. J., Graham, M. J., Djorgovski, S. G., et al. 2014, ApJS, 213, 9

Dupret, M.-A. 2019, arXiv e-prints, arXiv:1901.08809

Freedman, W. L., Madore, B. F., Hatt, D., et al. 2019, ApJ, 882, 34

Gaia Collaboration, Clementini, G., Eyer, L., et al. 2017, A&A, 605, A79

Gaia Collaboration, Prusti, T., de Bruijne, J. H. J., et al. 2016, A&A, 595, A1

Gilmore, G., Randich, S., Asplund, M., et al. 2012, The Messenger, 147, 25

Hacking, P., Lonsdale, C., Gautier, T., et al. 1999, ASPCS, Vol. 177, The Wide-Field Infrared Explore (WIRE) Mission (ASP), 409

Holl, B., Audard, M., Nienartowicz, K., et al. 2018, A&A, 618, A30

Howell, S. B., Sobeck, C., Haas, M., et al. 2014, PASP, 126, 398

Huang, C. D., Riess, A. G., Hoffmann, S. L., et al. 2018, ApJ, 857, 67

Huang, C. D., Riess, A. G., Yuan, W., et al. 2019, arXiv e-prints, arXiv:1908.10883

Ivezić, Ž., Kahn, S. M., Tyson, J. A., et al. 2019, ApJ, 873, 111

Jee, I., Suyu, S. H., Komatsu, E., et al. 2019, Science, 365, 1134

Joyce, M., Lairmore, L., Price, D. J., Mohamed, S., & Reichardt, T. 2019, ApJ, 882, 63

Keller, S. C. & Wood, P. R. 2006, ApJ, 642, 834

Koch, D. G., Borucki, W. J., Basri, G., et al. 2010, ApJ, 713, L79

Lanzafame, A. C., Distefano, E., Barnes, S. A., & Spada, F. 2019, ApJ, 877, 157

Lanzafame, A. C., Distefano, E., Messina, S., et al. 2018, A&A, 616, A16

Law, N. M., Kulkarni, S. R., Dekany, R. G., et al. 2009, PASP, 121, 1395

Lindegren, L., Hernández, J., Bombrun, A., et al. 2018, A&A, 616, A2

Marconi, M. & Clementini, G. 2005, AJ, 129, 2257

Marconi, M., Molinaro, R., Bono, G., et al. 2013a, ApJ, 768, L6

Marconi, M., Molinaro, R., Ripepi, V., Musella, I., & Brocato, E. 2013b, MNRAS, 428, 2185

Minniti, D., Lucas, P. W., Emerson, J. P., et al. 2010, New A, 15, 433

Mukherjee, S., Lavaux, G., Bouchet, F. R., et al. 2019, arXiv e-prints, arXiv:1909.08627

Muraveva, T., Delgado, H. E., Clementini, G., Sarro, L. M., & Garofalo, A. 2018, MNRAS, 481, 1195

Pablo, H., Whittaker, G. N., Popowicz, A., et al. 2016, PASP, 128, 125001

Planck Collaboration, Aghanim, N., Akrami, Y., et al. 2018, arXiv e-prints, arXiv:1807.06209

Pojmanski, G. 1997, Acta Astron., 47, 467

Potter, C., Jensen, J. B., Blakeslee, J., et al. 2018, in AAS Meeting Abstracts, Vol. 232, AAS Meeting Abstracts #232, 319.02

Rauer, H., Catala, C., Aerts, C., et al. 2014, Experimental Astronomy, 38, 249

Reid, M. J., Braatz, J. A., Condon, J. J., et al. 2009, ApJ, 695, 287

Ricker, G. R., Winn, J. N., Vanderspek, R., et al. 2015, JATIS, 1, 014003

Riess, A. G., Casertano, S., Yuan, W., et al. 2018, ApJ, 861, 126

Riess, A. G., Casertano, S., Yuan, W., Macri, L. M., & Scolnic, D. 2019, ApJ, 876, 85

Ripepi, V., Molinaro, R., Musella, I., et al. 2019, A&A, 625, A14

Soszyński, I., Udalski, A., Szymański, M. K., et al. 2009, Acta Astron., 59, 239

Soszyński, I., Udalski, A., Szymański, M. K., et al. 2016, Acta Astron., 66, 131

Soszyński, I., Udalski, A., Szymański, M. K., et al. 2017, Acta Astron., 67, 103

Steinmetz, M., Zwitter, T., Siebert, A., et al. 2006, AJ, 132, 1645

Tisserand, P., Le Guillou, L., Afonso, C., et al. 2007, A&A, 469, 387

Udalski, A., Szymanski, M., Kaluzny, J., Kubiak, M., & Mateo, M. 1992, Acta Astron., 42, 253

van Leeuwen, F. 2007, ASSL, Vol. 350, Hipparcos, the New Reduction of the Raw Data (Springer Netherlands)

Verde, L., Treu, T., & Riess, A. G. 2019, Nature Astronomy, 3, 891

Walker, G., Matthews, J., Kuschnig, R., et al. 2003, PASP, 115, 1023

Wong, K. C., Suyu, S. H., Chen, G. C. F., et al. 2019, arXiv e-prints, arXiv:1907.04869

Yanny, B., Rockosi, C., Newberg, H. J., et al. 2009, AJ, 137, 4377

OPEN PROBLEMS IN HIGH-MASS STELLAR EVOLUTION

S. Ekström[1], G.Meynet[1], C. Georgy[1], R. Hirschi[2], A. Maeder [1], J. Groh[3], P. Eggenberger[1] and G. Buldgen[1]

Abstract. Massive stars can roughly be divided into two categories: the one that will become red supergiants at (or shortly before) the end of their life, and those that will become Wolf-Rayet stars. RSG stars are dominated by convection, and experience a very strong mass loss; WR stars also undergo a strong mass loss, though through another process than RSGs. Both convection and mass loss don't arise naturally in 1D stellar evolution codes, so we rely on prescriptions. On top of that, most massive stars live in multiple systems, which increases even more the complexity of the picture. I will review the current status of massive star modelling, the problems we meet and some solutions that could come, either from 3D modeling, or from surveys.

Keywords: Stars: massive, Stars: evolution, Stars: mass-loss, Stars: binaries: general, Stars: rotation, Convection

1 Introduction

Massive stars are extreme objects that often show an extreme luminosity, bringing them close to the Eddington limit $L_{\rm Edd} = \frac{\kappa_{\rm es}}{4\pi cGM}$ (where $\kappa_{\rm es}$ is the opacity by electron scattering, and other variables have the obvious meaning). They also experience strong mass loss, which imprints the circumstellar/interstellar medium both kinematically and chemically.

If we extend the Conti scenario for the filiation of massive stars spectral types (Conti 1975), we see that we can divide the stars in two categories: the ones that become red supergiants (RSG) at some point in their evolution, and the ones that become Wolf-Rayet stars (WR). Except in a narrow mass range between $30-40\,M_{\odot}$, there is no overlap between the two categories.

$M > 60\,M_{\odot}$:	O → Of/WNL → LBV → WNL → WC → WO	→ SNIbc?	WR
$M = 40-60\,M_{\odot}$:	O → BSG → LBV → WNL → (WNE) → WC	→ SNIbc?	
	→ WC → WO	→ SNIbc?	
$M = 30-40\,M_{\odot}$:	O → BSG → RSG → WNE→ WCE	→ SNIbc	
$M = 25-30\,M_{\odot}$:	O → (BSG) → RSG → (YSG? LBV?)	→ SNII-L/b	RSG
$M = 10-25\,M_{\odot}$:	O/B → RSG → (Ceph. loop for $M < 15\,M_{\odot}$) → RSG	→ SNII-P	

Both RSG and WR are dominated by mass loss, and RSG are moreover dominated by convection, two processes that are absolutely out of reach of 1D stellar evolution codes. For the modelling of the secular evolution of stars, we are restricted to 1D codes and hence rely on prescriptions and recipes to implement these two processes. We will review below the strategies adopted in the case of convection (Sect. 2) and mass loss (Sect. 3). On top of this, two physical ingredients seem to play a major role in massive star evolution: rotation and multiplicity. We will also review the uncertainties and difficulties brought by these two ingredients (Sect. 4 and 5).

[1] Department of astronomy of the University of Geneva, 1290 Versoix,Switzerland
[2] Astrophysics group, Keele University, Keele ST5 5BG, United Kingdom
[3] Trinity College Dublin, The University of Dublin, Dublin, Ireland

2 Convection

Massive stars undergo a succession of core- and shell-burning phases, a large fraction of which are convective. The convective or radiative nature of central C-burning has been evoked as a determinant for the success of a supernova explosion (Timmes et al. 1996). Massive stars that become RSG develop an extended convective envelope. In any case, convection is a non-optional ingredient in the models. The problem we face is that convection is a highly non-1D process, being linked to turbulence.

When implementing convection in 1D codes, the first step we have to take is the definition of the convective zones. Linear perturbation theory shows that a stratified medium becomes unstable when $\nabla_{\rm rad} > \nabla_{\rm ad}$ (Schwarzschild 1958) or alternatively when $\nabla_{\rm rad} > \nabla_{\rm ad} + \frac{\varphi}{\delta}\nabla_\mu$ (Ledoux 1947), with $\nabla_{\rm rad} = \frac{3}{16\pi acG}\frac{\kappa LP}{MT^4}$ the radiative thermal gradient, and $\nabla_{\rm ad} = \frac{P\delta}{C_P\rho T}$ the adiabatic thermal gradient. Note that great care must be taken in the way this determination is done, as shown in Gabriel et al. (2014): the border must be determined from within the convective side of the boundary, not from the radiative side.

The second step is to determine the thermal gradient inside the convective zone. In the deep interior, convection can be reasonably treated as adiabatic, but near the surface, this is not the case. Most 1D codes use the mixing-length theory (Böhm-Vitense 1958, MLT), but more sophisticated, non local theories exist (Shaviv & Salpeter 1973; Maeder 1975; Roxburgh 1978; Bressan et al. 1981; Kuhfuss 1986; Langer 1986; Canuto 1992, 2011a,b,c,d,e; Xiong et al. 1997; Deng et al. 2006; Gabriel & Belkacem 2018).

There are many pieces of observational evidence that the classical Schwarzschild or Ledoux criterion underestimate the size of convective cores: measures of the width of the main sequence (MS, Maeder & Mermilliod 1981), of eclipsing binaries (Claret & Torres 2016), or asteroseismic measures (Aerts et al. 2003; Miglio et al. 2008; Moravveji et al. 2015, 2016, among others). This can be easily understood since of course, convective movements don't stop where the acceleration stops, the matter having still a velocity, as shown recently in 3D modelling (Arnett et al. 2019, see their figure 3). The region where the additional mixing occurs above a convective zone is called *overshoot*. While 3D prescriptions are on their way to help 1D modellers to implement this overshoot better, for now there are usually two different overshoot implementations in 1D stellar codes:

- **penetrative overshoot**, where the core radius is increased by a given fraction of the pressure scale height: $R_{\rm cc} = R_{\rm boundary} + f_{ov}H_P$
- **exponential overshoot**, where the diffusion coefficient in the region is modified with an exponentially decaying factor: $D_{\rm ov} = D_{\rm conv,0}\,\exp\left(-\frac{2\Delta r}{f_{\rm ov}H_P}\right)$

Both these implementations imply a calibration. There are usually two kinds of calibrations: either on the MS width, or on the drop of the surface velocity in a $V\sin(i) - \log(g)$ diagram. In the stellar grids by Brott et al. (2011), they used the second calibration and deduced an overshoot parameter $d_{\rm over} = 0.3\,H_P$. In those by Ekström et al. (2012), we used the first calibration and deduced an overshoot parameter $d_{\rm over} = 0.1\,H_P$. The different physical inputs in the two grids can partially explain the difference found in the value to use, but it might also be linked to the region of the mass domain in which the calibration has been performed. Brott et al. (2011) have used models of 16 $M_\odot$, while Ekström et al. (2012) have calibrated the MS width in the low-mass domain, where neither rotation nor stellar winds play any major role in the evolution. Several observational studies suggest that the overshoot could be mass dependent (Maeder & Mermilliod 1981; Ribas et al. 2000; Castro et al. 2014).

Comparing models computed with different codes shows large differences, especially after the main sequence (Martins & Palacios 2013; Jones et al. 2015). A large part of these differences is linked to the way convection is implemented in the various codes. Some attempts to get help from 3D modelling have been undertaken (see, for instance, Freytag et al. 1996; Arnett et al. 2015; Cristini et al. 2017). The first results show that the convective boundaries are much smoother than usually assumed in 1D codes, and that the bottom boundary is steeper than the top one (Cristini et al. 2017). Also, the simulations show that internal gravity waves are generated above the convective zone and propagate in the radiative zone, waves that could play a role in the angular momentum transport (Edelmann et al. 2019, see next section).

To go from 3D to 1D, the way is paved: we have first to identify the important parameters. A promising variable seems to be the bulk Richardson number: ${\rm Ri_B} = \frac{\Delta B\,\ell}{V_{\rm rms}^2}$, with $\Delta B = \int_{r_c-\Delta r}^{r_c+\Delta r}\left(N^2{\rm d}r\right)$ the buoyancy jump, ℓ the length scale of the fluid element, and $V_{\rm rms} = V_{\rm conv} = \left(\frac{F_{\rm conv}}{\rho}\right)^{1/3}$ the convective velocity. Then we have to test different convection regimes (shell C-, Ne-, O- burning, maybe even He), to check if they behave identically with respect of this parameter. We have to find a formulation adequate for parameters accessible in 1D codes, and finally we have to do tons of tests... It's a long process, but it is on its way, so stay tuned!

3 Mass loss

From the lowest mass B-type main sequence stars to the extreme luminous blue variables (LBV), the mass-loss rates encoutered in massive stars cover about 8 orders of magnitude. One single star during its whole life can experience mass-loss regimes that differ up to about 4 orders of magnitude. When one observes a massive star, the mass-loss rates it is experiencing plays a major role in the stellar type determination.

Mass loss comes in two flavours: steady radiatively-driven winds, and episodic mass-loss events. Radiatively-driven winds can be fast and thin, during the main sequence, or slow and thick in the post-MS phase, while WR stars show very fast and thick winds. Episodic mass-loss events occur in the LBV phase, during the final stage instabilities, or because of binary interactions. The RSG mass loss is probably something inbetween those two flavours, resulting in a slow and thick wind, which nature is not fully understood yet.

The challenge we meet as 1D modellers is that the mass loss doesn't come from first principles in the modelling. We rely on prescriptions (see, for instance, Reimers 1975; de Jager et al. 1988; Kudritzki et al. 1987; Kudritzki & Puls 2000; Nugis & Lamers 2000; Vink et al. 2000, 2001; van Loon et al. 2005; Gräfener & Hamann 2007, among others). 1D models need average rates, they cannot usually follow burst episodes.

The various existing prescriptions often cover only a narrow validity domain, so we have to switch from one to the other along the evolution of a given model. In case two prescriptions overlap, they often differ in their outcome and it is difficult to decide which one we should use. But even a slight change during a limited time can completely modify the endpoint and the stellar track in the Herzsprung-Russell diagram (HRD, see Georgy & Ekström ????, Groh et al. in prep). Actually, comparisons between observations and models for massive stars are rather a check for the mass-loss prescription used than anything else.

Not only the wind prescription is a difficult choice, but also there is some uncertainties due to wind clumping. Wind clumping makes the mass-loss rates observed seem larger than they really are. It has been claimed that we should reduce the mass-loss rates by a factor of 3 to 10 (Bouret et al. 2005; Fullerton et al. 2006). However, the winds might be clumped, but it seems they might be porous as well, and neglecting the porosity of the wind could lead to underestimate the mass-loss rates (Oskinova et al. 2007; Muijres et al. 2011). So all in all, the reduction of the mass-loss rates could be only small.

4 Rotation

All massive stars rotate, many of them rapidly (Mokiem et al. 2006; Huang & Gies 2006; Ramírez-Agudelo et al. 2013; Simón-Díaz & Herrero 2014). The difficulty comes when we want to implement the effects of rotation in 1D codes. Some use a purely diffusive scheme, others use an advecto-diffusive scheme. The diffusive scheme is completely dependent on the choice of the f_C and f_μ values (see Keszthelyi et al. in prep.). When the advective term is taken into account, we meet three different prescriptions for the expression of the horizontal turbulence coefficient (Zahn 1992; Maeder 2003; Mathis et al. 2004), and two different prescriptions for the expression of the shear turbulence (Maeder 1997; Talon & Zahn 1997). Moreover, Maeder et al. (2013) have shown that the different instabilities triggered by rotation cannot be taken into account separately, because they interact one with the others.

The choice of the prescriptions yields large differences in the outcome (stellar tracks in the HRD, rotation velocity evolution, chemical enrichment, etc. see Chieffi & Limongi 2013; Meynet et al. 2013).

Moreover, rotation can induce magnetic instability, which brings an additional coupling inside the star. The basic developements have been proposed by Spruit (1999, 2002). Maeder & Meynet (2004) have added the condition that the differential rotation must be large enough for triggering the magnetic instability. On the observational side, the MiMes survey have found that around 7% of OB stars present detectable magnetic fields (Grunhut et al. 2011; Wade et al. 2014, 2016). Of course, this number counts only the stars that have a surface magnetic field, and one strong enough to be detected, so it must be considered as a lower limit.

An indirect observational constraint comes from the rotation rates of white dwarfs or neutron stars. According to Suijs et al. (2008), it is clear that models without magnetic fields cannot reproduce the slow rotation of observed stellar remnants, while the inclusion of the magnetic coupling marginally helps reconcile with the observation. While for the neutron star, the explosion episode could modify the angular momentum budget one way or another, the white dwarfs experience a much smoother transition from stellar life to remnant, and hence represent strong constraints. The need for a stronger coupling has been also highlighted by asteroseismic measurements of differential rotation inside red giants (Mosser et al. 2012; Cantiello et al. 2014). Several studies have started to pave the way towards a solution (Eggenberger et al. 2012; Cantiello et al. 2014; Fuller et al. 2019; Edelmann et al. 2019). Thanks to the Kepler satellite, a handful of red subgiants have been observed and for six of them, exquisite core and surface rotation determinations were made possible. It seems from those measurements that the coupling increases with mass but decreases with the evolution during the subgiant phase (Eggenberger et al. 2019), which is in contrast with the behaviour found for the giants, in which the coupling seems to increase with the evolutionary stage. Could this be the sign of different mechanisms at play? We definitely need more subgiant measurements before we can draw firm conclusions.

5 Multiplicity

Most massive stars don't live alone. Sana et al. (2012) find that 70% of O-type stars are in binaries. From the apparently single stars, only 48% of them would be real single stars, the 52% left being either merger products, or pre-, or post-interacting binaries (de Mink et al. 2014).

This fact complicates the picture in an indescribable way. Binaries are at least as complicated as two single stars, bearing the same uncertainties on convection, mass loss, rotation for each component. But binaries are more than two single stars, since they also come with additional uncertainties linked to their binary nature (Georgy & Ekström ????).

They might undergo mass-transfer episodes, being the donor or the gainer (sometimes the two situations successively during their lifetime). It is a tricky episode to model, since we do not now exactly how much of the matter released in the Roche lobe overflow should fall on the gainer and how much could be lost by the system.

Binarity complicates the rotation picture of the component, since it might induce tidal interaction, modifying the way the stars are mixed internally and the way the rotation velocity evolves (Song et al. 2016). If they undergo mass transfer episodes, their angular momentum should change accordingly, but it is not clear how to handle that aspect, what fraction of angular momentum could be really transferred, or if it could become a barrier to mass transfer.

While single star evolution can be explored with three parameters (M, Z, and Ω), when it comes to binaries, an almost infinite parameter space opens, since to the three basic parameters one needs to add the separation (that can take almost any value) and mass ratio (that can be anything between 0 and 1). There are basically two different approaches to this problem. For specific cases, detailed binary models will be computed, with the simultaneous evolution of both components, and with more or less full binary physics (Cantiello et al. 2007; Eldridge et al. 2008; Eldridge & Stanway 2009). However to explore more widely the parameter space, a population synthesis is used, based often on single star models, with the help of binary prescriptions for the period and mass ratio distributions, for the mass and angular momentum transfer efficiency, or the tidal influence on rotation (de Mink et al. 2013). It must be kept in mind that stellar evolution shows often non linear behaviours, that could be completely missed by the simplifications needed to handle such a huge parameter space. Some assumptions that are usually made in these cases are sometimes questionable. For instance, immediate synchronisation is assumed most of the time, while in models computed with tidal mixing and all the other internal mixing processes, the result is that synchronisation is achieved only temporarily, but soon the natural evolution of the star overcomes this forcing and the velocity of the star drops below the orbital angular velocity (Song et al. 2016). Careful observations of the velocity of the two components of a binary also shows that synchronisation might not be the rule (Martins et al. 2017; Putkuri et al. 2018). Another assumption is that during the common envelope phase, the envelope is completely ejected. 3D simulations do not show this, with only about 10% of the envelope ejected very early in the spiral-in phase (Ricker & Taam 2008, 2012; Passy et al. 2012; Ohlmann et al. 2016). Of course, 3D simulations do not cover long timescales, so it might be that the envelope is ejected on longer, thermal timescales. Also most of the simulations do not take into account the recombination processes, which could play a role in the ejection (Nandez et al. 2015). However this shows that some caution is still needed when pondering the results of binary population synthesis.

6 Conclusions

Our understanding of massive star evolution still faces many open problems. Some of them concern very basic physical inputs (convection, mass loss), some concern more sophisticated (but essential) modelling ingredients (rotation $\pm$ magnetic fields, multiplicity).

Some help can come from 3D modelling, studying short phases or parts of stars. It could in particular give us prescriptions for the treatment of convection, the inclusion of internal gravity waves, and help us understand what occurs in weird phases of binary evolution. Unfortunately, the computational cost of multi-D modelling prevents us from using them to study the secular evolution of stars.

To make further progress, we need large surveys with exquisite precision and consistent analysis. Unfortunately this is seldom compatible: either we benefit from large survey results, or we benefit from detailed analysis of observational data on a handful of stars.

I take the opportunity here to address a caveat to stellar models users: be careful when mixing models form different codes. We have just seen that the differences in the physical inputs are large and have important consequences on the outcome. Mixing models could however be used to get some sorts of theoretical error bars on the model's predictions.

The authors acknowledge fruitful discussions made possible thanks to the ISSI international team program* (team 367).

References

Aerts, C., Thoul, A., Daszyńska, J., et al. 2003, Science, 300, 1926
Arnett, W. D., Meakin, C., Hirschi, R., et al. 2019, ApJ, 882, 18
Arnett, W. D., Meakin, C., Viallet, M., et al. 2015, ApJ, 809, 30
Böhm-Vitense, E. 1958, Zeitschrift für Astrophysik, 46, 108
Bouret, J.-C., Lanz, T., & Hillier, D. J. 2005, A&A, 438, 301
Bressan, A. G., Chiosi, C., & Bertelli, G. 1981, A&A, 102, 25
Brott, I., de Mink, S. E., Cantiello, M., et al. 2011, A&A, 530, A115
Cantiello, M., Mankovich, C., Bildsten, L., Christensen-Dalsgaard, J., & Paxton, B. 2014, ApJ, 788, 93
Cantiello, M., Yoon, S.-C., Langer, N., & Livio, M. 2007, A&A, 465, L29
Canuto, V. M. 1992, ApJ, 392, 218
Canuto, V. M. 2011a, A&A, 528, A76
Canuto, V. M. 2011b, A&A, 528, A77
Canuto, V. M. 2011c, A&A, 528, A78
Canuto, V. M. 2011d, A&A, 528, A79
Canuto, V. M. 2011e, A&A, 528, A80
Castro, N., Fossati, L., Langer, N., et al. 2014, A&A, 570, L13
Chieffi, A. & Limongi, M. 2013, ApJ, 764, 21
Claret, A. & Torres, G. 2016, A&A, 592, A15
Conti, P. S. 1975, Mémoires of the Société Royale des Sciences de Liège, 9, 193
Cristini, A., Meakin, C., Hirschi, R., et al. 2017, MNRAS, 471, 279
de Jager, C., Nieuwenhuijzen, H., & van der Hucht, K. A. 1988, A&AS, 72, 259
de Mink, S. E., Langer, N., Izzard, R. G., Sana, H., & de Koter, A. 2013, ApJ, 764, 166
de Mink, S. E., Sana, H., Langer, N., Izzard, R. G., & Schneider, F. R. N. 2014, A&A, 782, 7
Deng, L., Xiong, D. R., & Chan, K. L. 2006, ApJ, 643, 426
Edelmann, P. V. F., Ratnasingam, R. P., Pedersen, M. G., et al. 2019, ApJ, 876, 4
Eggenberger, P., Deheuvels, S., Miglio, A., et al. 2019, A&A, 621, A66
Eggenberger, P., Montalbán, J., & Miglio, A. 2012, A&A, 544, L4
Ekström, S., Georgy, C., Eggenberger, P., et al. 2012, A&A, 537, A146
Eldridge, J. J., Izzard, R. G., & Tout, C. A. 2008, MNRAS, 384, 1109
Eldridge, J. J. & Stanway, E. R. 2009, MNRAS, 400, 1019
Freytag, B., Ludwig, H. G., & Steffen, M. 1996, A&A, 313, 497
Fuller, J., Piro, A. L., & Jermyn, A. S. 2019, MNRAS, 485, 3661
Fullerton, A. W., Massa, D. L., & Prinja, R. K. 2006, ApJ, 637, 1025
Gabriel, M. & Belkacem, K. 2018, A&A, 612
Gabriel, M., Noels, A., Montalbán, J., & Miglio, A. 2014, A&A, 569, A63
Georgy, C. & Ekström, S. ???? (Cambridge University Press, Title = Massive star evolution: binaries as two single stars, eds. Boffina, H.M.J. and Beccari, G., Year = 2019)
Gräfener, G. & Hamann, W.-R. 2007, Highlights of Astronomy, 14, 199
Grunhut, J. H., Wade, G. A., & the MiMeS Collaboration. 2011, ArXiv e-prints
Huang, W. & Gies, D. R. 2006, ApJ, 648, 580
Jones, S., Hirschi, R., Pignatari, M., et al. 2015, MNRAS, 447, 3115
Kudritzki, R. P., Pauldrach, A., & Puls, J. 1987, A&A, 173, 293

*`http://www.issibern.ch/program/teams.html`

Kudritzki, R.-P. & Puls, J. 2000, ARA&A, 38, 613
Kuhfuss, R. 1986, A&A, 160, 116
Langer, N. 1986, A&A, 164, 45
Ledoux, P. 1947, ApJ, 105, 305
Maeder, A. 1975, A&A, 40, 303
Maeder, A. 1997, A&A, 321, 134
Maeder, A. 2003, A&A, 399, 263
Maeder, A. & Mermilliod, J. C. 1981, A&A, 93, 136
Maeder, A. & Meynet, G. 2004, A&A, 422, 225
Maeder, A., Meynet, G., Lagarde, N., & Charbonnel, C. 2013, A&A, 553, A1
Martins, F., Mahy, L., & Hervé, A. 2017, A&A, 607, A82
Martins, F. & Palacios, A. 2013, A&A, 560, A16
Mathis, S., Palacios, A., & Zahn, J.-P. 2004, A&A, 425, 243
Meynet, G., Ekström, S., Maeder, A., et al. 2013, in Lecture Notes in Physics, Vol. 865, Studying Stellar Rotation and Convection, ed. M. Goupil, K. Belkacem, C. Neiner, F. Lignières, & J. J. Green, 3
Miglio, A., Montalbán, J., Noels, A., & Eggenberger, P. 2008, MNRAS, 386, 1487
Mokiem, M. R., de Koter, A., Evans, C. J., et al. 2006, A&A, 456, 1131
Moravveji, E., Aerts, C., Pápics, P. I., Triana, S. A., & Vandoren, B. 2015, A&A, 580, A27
Moravveji, E., Townsend, R. H. D., Aerts, C., & Mathis, S. 2016, ApJ, 823, 130
Mosser, B., Goupil, M. J., Belkacem, K., et al. 2012, A&A, 548, A10
Muijres, L. E., de Koter, A., Vink, J. S., et al. 2011, A&A, 526, A32
Nandez, J. L. A., Ivanova, N., & Lombardi, J. C. 2015, MNRAS, 450, L39
Nugis, T. & Lamers, H. J. G. L. M. 2000, A&A, 360, 227
Ohlmann, S. T., Röpke, F. K., Pakmor, R., & Springel, V. 2016, ApJ, 816, L9
Oskinova, L. M., Hamann, W. R., & Feldmeier, A. 2007, A&A, 476, 1331
Passy, J.-C., De Marco, O., Fryer, C. L., et al. 2012, ApJ, 744, 52
Putkuri, C., Gamen, R., Morrell, N. I., et al. 2018, A&A, 618, A174
Ramírez-Agudelo, O. H., Simón-Díaz, S., Sana, H., et al. 2013, A&A, 560, A29
Reimers, D. 1975, Mémoires of the Société Royale des Sciences de Liège, 8, 369
Ribas, I., Jordi, C., & Giménez, Á. 2000, MNRAS, 318, L55
Ricker, P. M. & Taam, R. E. 2008, ApJ, 672, L41
Ricker, P. M. & Taam, R. E. 2012, ApJ, 746, 74
Roxburgh, I. W. 1978, A&A, 65, 281
Sana, H., de Mink, S. E., de Koter, A., et al. 2012, Science, 337, 444
Schwarzschild, M. 1958, Structure and evolution of the stars. (Princeton University Press)
Shaviv, G. & Salpeter, E. E. 1973, ApJ, 184, 191
Simón-Díaz, S. & Herrero, A. 2014, A&A, 562, A135
Song, H. F., Meynet, G., Maeder, A., Ekström, S., & Eggenberger, P. 2016, A&A, 585, A120
Spruit, H. C. 1999, A&A, 349, 189
Spruit, H. C. 2002, A&A, 381, 923
Suijs, M. P. L., Langer, N., Poelarends, A.-J., et al. 2008, A&A, 481, L87
Talon, S. & Zahn, J.-P. 1997, A&A, 317, 749
Timmes, F. X., Woosley, S. E., & Weaver, T. A. 1996, ApJ, 457, 834
van Loon, J. T., Cioni, M.-R. L., Zijlstra, A. A., & Loup, C. 2005, A&A, 438, 273
Vink, J. S., de Koter, A., & Lamers, H. J. G. L. M. 2000, A&A, 362, 295
Vink, J. S., de Koter, A., & Lamers, H. J. G. L. M. 2001, A&A, 369, 574
Wade, G. A., Grunhut, J., Alecian, E., et al. 2014, in IAU Symposium, Vol. 302, IAU Symposium, 265
Wade, G. A., Neiner, C., Alecian, E., et al. 2016, MNRAS, 456, 2
Xiong, D. R., Cheng, Q. L., & Deng, L. 1997, ApJS, 108, 529
Zahn, J.-P. 1992, A&A, 265, 115

Stars and their variability observed from space
C. Neiner, W. W. Weiss, D. Baade, R. E. Griffin, C. C. Lovekin, A. F. J. Moffat (eds)

INTERNAL STELLAR MAGNETIC FIELDS

J. Fuller[1]

Abstract.

The past five years have seen a remarkable growth in our understanding of internal stellar magnetic fields. The largest advances have occurred for low-mass red-giant stars, for which space-based photometry has yield thousands of detections of mixed modes that penetrate into their radiative cores. Advances in theory have shown how these modes provide tight constraints on the rotation and magnetic field strengths of their degenerate cores. Core rotation rates may be determined by magnetic torques, providing additional insight into evolutionary phases where data are not available.

Keywords: Stars: magnetic fields, interiors

1 Introduction

The ongoing asteroseismic renaissance has led to a paradigm shift in our understanding of internal stellar magnetic fields. Unlike surface fields, which can be probed with Zeeman splitting and polarimetry, little was previously known about internal fields. Prior constraints (e.g., those from helioseismology) were weak because acoustic modes are only sensitive to magnetic fields that contribute significantly to the internal stellar pressure, i.e., magnetic pressure comparable to thermal pressure. Such field strengths ($B > 1$ MG) in main-sequence stars imply implausibly large and theoretically unexpected magnetic fluxes, so those constraints have not been particularly useful.

2 Magnetic fields through an asteroseismic lens

Recent asteroseismic data have been much more useful, because gravity modes are a much more sensitive probe of internal magnetic fields. Unlike pressure modes that are sensitive only to near-equipartition field strengths, gravity modes are sensitive to fields whose magnetic tension restoring force competes with buoyancy forces. High-order g modes, like the mixed modes that propagate in the cores of red giants, are thus sensitive to fields far below equipartition. Fuller et al. (2015) showed that magnetic fields with radial components

$$B > B_{\rm crit} = \sqrt{\frac{\pi\rho}{2}}\frac{\omega^2 r}{N} \qquad (2.1)$$

will affect g modes strongly, where ω is the mode's angular frequency and N is the Brunt-Väisälä frequency. In typical red giants, fields in excess of $\sim 10^5$ G near the hydrogen-burning shell will affect the mixed modes strongly and are hence readily observable. These magnetic fluxes are comparable to those in other magnetic stars and to those produced in convective dynamos (e.g., Augustson et al. 2016, so we might expect them to be prevalent in stellar interiors.

To understand the observable signature of magnetic fields, the interaction of gravity waves and magnetic fields have been studied in several recent works. Fuller et al. (2015) showed that gravity waves become evanescent for field strengths in excess of equation 2.1. That work also showed that the wave-field interaction would increase greatly the wavenumber of the mode, transferring power to high angular wavenumbers ℓ, such that the scattered mode would be trapped within the radiative core of a red giant in a so-called "magnetic greenhouse" effect. Hence, any g mode propagating into a strongly magnetized core of the star would not be able to tunnel back towards the surface of the star, so mixed modes would be suppressed and would not be observable in the star's power spectrum.

[1] TAPIR, Mailcode 350-17, California Institute of Technology, Pasadena, CA 91125, USA

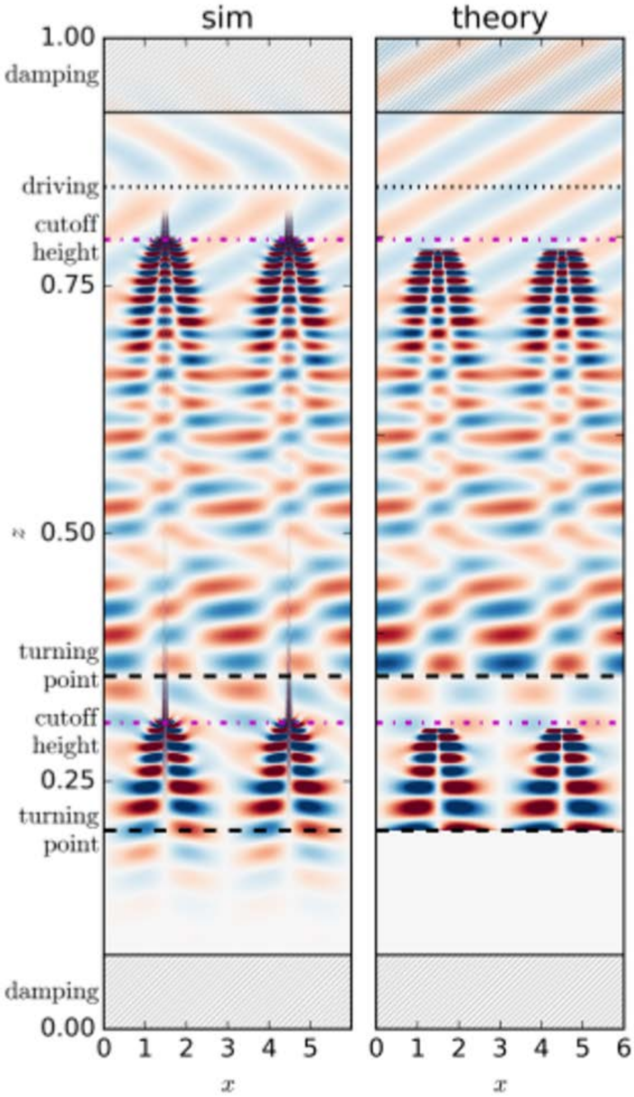

Fig. 1. Left panel: Simulation, **right panel:** analytic calculation, of gravity waves interacting with a magnetic field, colour-coded by horizontal velocity, taken from Lecoanet et al. (2017). The turning points correspond to an analytic prediction, similar to that of equation 2.1, for waves of differing parity. The cutoff heights are where the magnetically refracted Alfvén waves reach infinite wavenumber and the waves damp.

Lecoanet et al. (2017) performed a more rigorous calculation of the wave–field interaction that occurs in stellar interiors, finging that for radial field strengths in excess of B_c in equation 2.1 (with weak dependence on magnetic geometry), incident gravity waves would be totally converted into outgoing Alfvén-like waves (Fig. 1). The angular and radial wavenumber of the Alvén waves diverges, causing the waves to be completely damped within the star such that no gravity wave escapes the radiative core and no mixed modes can be formed. The star's dipole mode power would be heavily suppressed relative to radial modes (which do not propagate as gravity waves and do not interact with internal fields) in a very predictable way.

Indeed, Stello et al. (2016) showed that this dipole mode suppression is relatively common and is observed in roughly 20% of red giants in the *Kepler* field (see Fig. 2). These "depressed dipole mode stars" had already been noted by Mosser et al. (2012) and García et al. (2014) but the mechanism had not then been identified. Stello et al. (2016) showed that the level of suppression matches closely the predictions of Fuller et al. (2015) based on core magnetic fields, lending credence to the magnetic hypothesis. Moreover, Stello et al. (2016) showed that dipole mode suppression is very sensitive to stellar mass, occurring in roughly 50% of stars with $M > 1.5\,M_{\odot}$, and almost never occurring for $1\,M_{\odot}$ stars. They interpreted the suppression as arising from core magnetic fields left over from magnetic dynamos in the convective cores of the main-sequence progenitors of red giants.

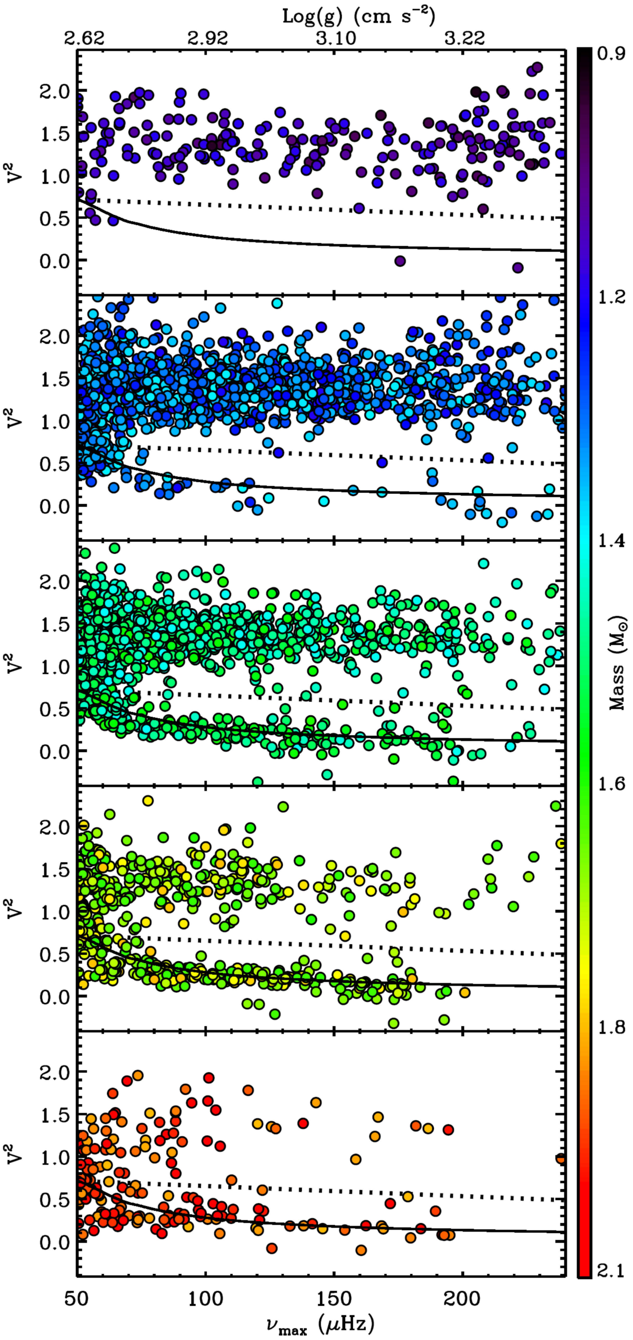

Fig. 2. Dipole mode power compared to radial mode power in a large sample of red giants with *Kepler* data from Stello et al. (2016). Each point corresponds to a different star with frequency of maximum power $\nu_{\max}$ and colour-coded mass. The prediction for magnetic suppression from Fuller et al. (2015) is shown by the solid line.

Cantiello et al. (2016) examined the implications of that model and the constraints on magnetic fields possible for a variety of pulsating stars.

That interpretation of Stello et al. (2016) has been challenged by Mosser et al. (2017), who found that the suppressed modes still show signatures of being mixed modes, i.e., there are multiple mixed-mode components surrounding each dipole p mode in the power spectra (see Fig. 3). Mosser et al. (2017) also found evidence of frequency bumping (implying the existence of mixed modes) even when mixed modes are not detectable directly. This contradicts the prediction from Fuller et al. (2015) that strong magnetic fields prevent coherent g modes from existing in the power spectra, and that only a suppressed envelope p mode should be observed.

Currently this issue remains controversial. A counterpoint to Mosser et al. (2017) is that most of the stars

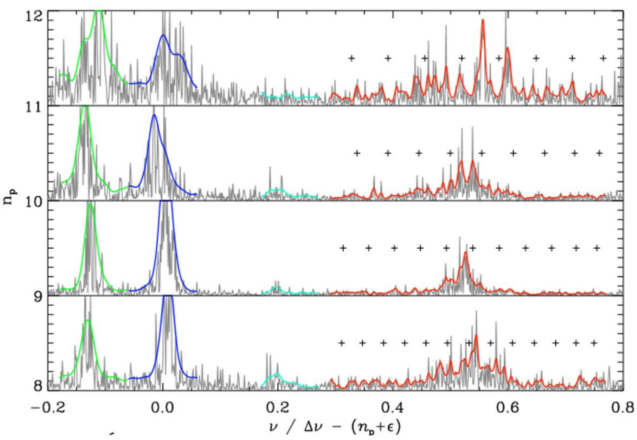

Fig. 3. From Mosser et al. (2017), the power spectrum of a star with low dipole mode amplitude, yet still with possible evidence for dipole mixed modes (red part of the power spectrum). Crosses show the expected period spacing of dipole mixed modes. The magnetic suppression model of Fuller et al. (2015) predicts a single, very broad, Lorentzian profile for dipole modes, similar to (but broader than) that of the radial modes (dark blue line). From Mosser et al. (2017); ©ESO, reproduced with permission.

where depressed mixed modes appear to be observed are either ordinary clump stars (they lie at the left edge of Fig. 2), or they have larger dipole visibilities than most red giants with suppressed dipole modes and could simply be ordinary red giants with weaker dipole modes (they lie near the dotted line in Fig. 2). Both groups agree that the clear presence of mixed modes in a red giant excludes the presence of core magnetic fields with radial components exceeding equation 2.1.

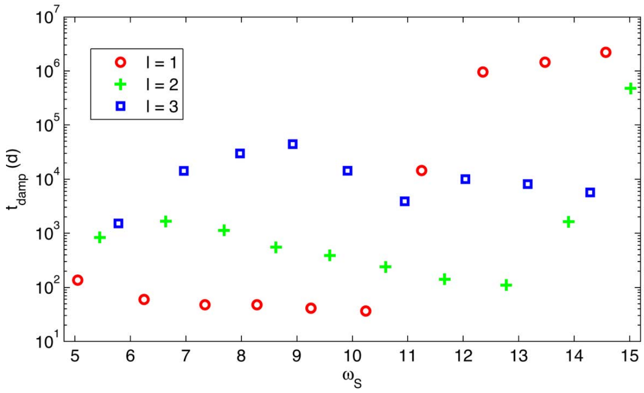

Fig. 4. From Loi & Papaloizou (2017), the damping time of mixed modes of acoustic degree ω_S in a red giant, due to interaction with strong toroidal magnetic fields. Larger field strengths (and lower mode fequencies) produce efficient damping when the toroidal field strength roughly exceeds equation 2.1.

If mixed modes do exist in stars with suppressed dipole modes, another damping mechanism must be at play. The suppressed modes are most evident in stars low on the red-giant branch and for which radiative damping and non-linear damping effects (Weinberg & Arras 2019) are inadequate. The most likely alternative is strong toroidal magnetic fields (i.e., those with a much smaller radial component relative to the horizontal component). Such fields were investigated in a series of papers by (Loi & Papaloizou 2017, 2018, 2019), who showed that gravity-wave energy is sapped by the excitation of Alfvén waves that propagate along the magnetic field lines. Magnetic fields with strengths comparable to equation 2.1 cause the most efficient damping because the phase speed of gravity waves and Alfvén waves are comparable at those field strengths. Fig. 4 shows that, for a given magnetic field strength, the damping is efficient for modes whose frequencies lie below that of equation 2.1, and inefficient for higher-frequency modes. Crucially, because the modes are damped but not totally destroyed, mixed modes would still be apparent in the spectrum, but with suppressed amplitude owing to the extra magnetic damping in the core.

We note that both plausible models of dipole-mode suppression involve strong magnetic fields in the radiative cores of red giants. The question is whether the fields have significant radial components (as examined by Fuller et al. 2015 and Lecoanet et al. 2017), or whether they are nearly toroidal so that the mechanism of Loi & Papaloizou (2017) can operate without complete magnetic suppression of mixed modes. Additional studies of the power spectra of stars with suppressed dipole modes should be performed in order to constrain rigorously and statistically the presence of mixed modes in these stars.

3 Magnetic effects on internal stellar rotation

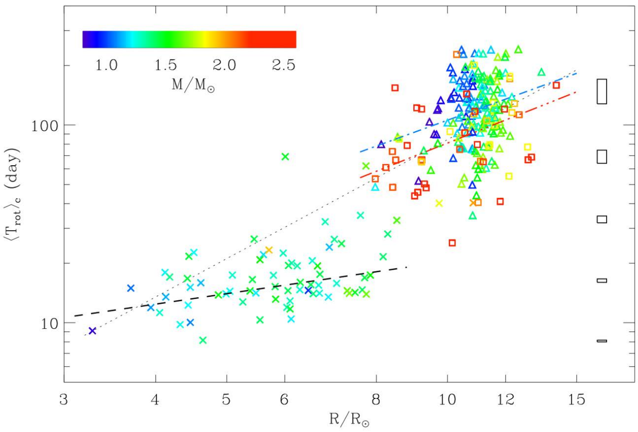

Fig. 5. Asteroseismically measured core rotation periods of a large sample of red giants as a function of stellar radius, colour-coded by mass. From Mosser et al. (2012); ©ESO, reproduced with permission.

Magnetic fields almost certainly have a huge impact on angular momentum transport and the internal rotation profiles of stars. Asteroseismic measurements of core rotation rates of red giants from Mosser et al. (2012); Gehan et al. (2018) reveal core rotation periods of ∼15 days on the red-giant branch, and ∼ 100 days on the clump, with considerable scatter (Fig. 5). Although the cores rotate much faster than the stellar surfaces (see, e.g., Beck et al. 2012; Deheuvels et al. 2014), they rotate much slower than predicted by the most popular pre-existing angular momentum transport models (see Fig. 6 and Cantiello et al. 2014) based on the magnetic Tayler-Spruit dynamo (Spruit 2002).

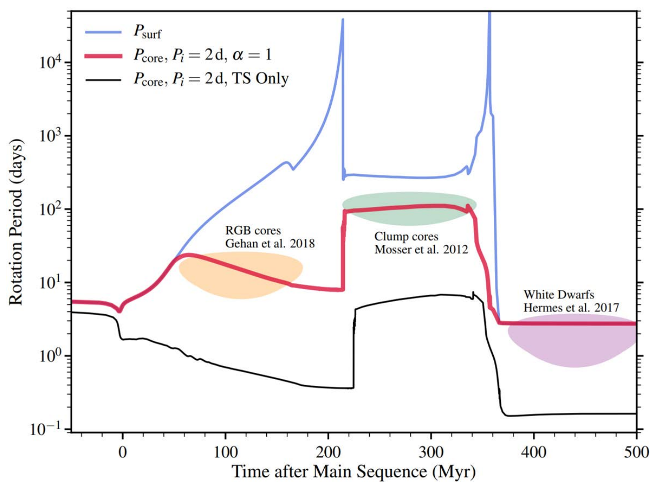

Fig. 6. From Fuller et al. (2019), a model of the core rotation rate of a 1.6 $M_\odot$ star evolving from the main sequence to the white-dwarf stage. The blue line shows the model's surface rotation period, while the red line shows the core rotation period with an updated angular momentum transport prescription based on the Tayler instability. The black line is the core rotation period using the Tayler-Spruit dynamo (Spruit 2002). Shaded ovals indicate typical core rotation rates measured by Mosser et al. (2012), Gehan et al. (2018), and Hermes et al. (2017).

Fuller et al. (2019) re-examined the Tayler instability in stellar interiors, arguing that energy is dissipated more slowly than the model of Spruit (2002). That would allow the magnetic fields to become larger in amplitude and exert stronger magnetic torques and transport more angular momentum. Applying their model to the MESA stellar evolution code (Paxton et al. 2011), they found core rotation rates much more compatible with asteroseismic data for red giants, clump stars and white dwarfs (Fig. 6). The most plausible alternative to this model is that nearly rigid core rotation is enforced by magnetic fields too strong to be wound up by differential rotation. In that case, strong differential rotation must exist within the convective envelopes of those stars (with inner rotation rates a factor of 10–100 larger than surface rotation rates), as advocated by Kissin & Thompson (2015). Detailed modelling of sub-giant stars (as in Eggenberger et al. 2019), where both core and surface rotation rates can be measured, will help to distinguish between the models, and will be enabled by upcoming *TESS* data.

4 Conclusions

Asteroseismology has delivered a wealth of surprising new insights on the magnetic fields that lurk deep within stellar cores. These fields manifest themselves by suppressing gravity modes, or by altering internal rotation rates. Internal magnetic fields could also suppress g-mode oscillations in many types of stars that would otherwise pulsate, such as stars in the γ-Doradus, SPB, and ZZ-Ceti instability strips. More detailed modelling of magnetic impacts on stellar pulsations (e.g., Prat et al. 2019) and new data from *TESS* on a variety of stellar pulsators (especially sub-giant stars) will shed new light on magnetic fields hidden deep within stars of all types.

I thank the organizers for inviting me to give a keynote presentation, and for all their hard work organizing the conference.

References

Augustson, K. C., Brun, A. S., & Toomre, J. 2016, ApJ, 829, 92
Beck, P. G., Montalban, J., Kallinger, T., et al. 2012, Nature, 481, 55
Cantiello, M., Fuller, J., & Bildsten, L. 2016, ApJ, 824, 14
Cantiello, M., Mankovich, C., Bildsten, L., Christensen-Dalsgaard, J., & Paxton, B. 2014, ApJ, 788, 93
Deheuvels, S., Doğan, G., Goupil, M. J., et al. 2014, A&A, 564, A27
Eggenberger, P., den Hartogh, J. W., Buldgen, G., et al. 2019, A&A, 631, L6
Fuller, J., Cantiello, M., Stello, D., Garcia, R. A., & Bildsten, L. 2015, Science, 350, 423
Fuller, J., Piro, A. L., & Jermyn, A. S. 2019, MNRAS, 485, 3661
García, R. A., Pérez Hernández, F., Benomar, O., et al. 2014, A&A, 563, A84
Gehan, C., Mosser, B., Michel, E., Samadi, R., & Kallinger, T. 2018, A&A, 616, A24
Hermes, J. J., Gänsicke, B. T., Kawaler, S. D., et al. 2017, ApJS, 232, 23
Kissin, Y. & Thompson, C. 2015, ApJ, 808, 35
Lecoanet, D., Vasil, G. M., Fuller, J., Cantiello, M., & Burns, K. J. 2017, MNRAS, 466, 2181
Loi, S. T. & Papaloizou, J. C. B. 2017, MNRAS, 467, 3212
Loi, S. T. & Papaloizou, J. C. B. 2018, MNRAS, 477, 5338
Loi, S. T. & Papaloizou, J. C. B. 2019, MNRAS, 2592
Mosser, B., Belkacem, K., Pinçon, C., et al. 2017, A&A, 598, A62
Mosser, B., Goupil, M. J., Belkacem, K., et al. 2012, A&A, 548, A10
Paxton, B., Bildsten, L., Dotter, A., et al. 2011, ApJS, 192, 3
Prat, V., Mathis, S., Buysschaert, B., et al. 2019, A&A, 627, A64
Spruit, H. C. 2002, A&A, 381, 923
Stello, D., Cantiello, M., Fuller, J., et al. 2016, Nature, 529, 364
Weinberg, N. N. & Arras, P. 2019, ApJ, 873, 67

SEARCH FOR QUIET STELLAR-MASS BLACK HOLES BY ASTEROSEISMOLOGY FROM SPACE

H. Shibahashi[1] and S. J. Murphy[2]

Abstract.
It is thought that stars with an initial mass more than $\sim 25\,\mathrm{M}_\odot$ ultimately become black holes. Stellar-mass black holes should therefore be ubiquitous, but fewer than 20 have been found in our Galaxy to date, and all of them have been found through their X-ray emission. In most cases these are soft X-ray transients – low-mass X-ray binaries whose optical counterparts are late-type stars filling their Roche lobes, giving rise to accretion onto black holes. In one case the stellar-mass black hole is in a high-mass X-ray binary whose optical counterpart is an early-type star. Its strong stellar winds are accreted by the black hole, producing X-ray emission. It follows that X-ray-quiet stellar-mass black holes exist in wide binary systems. The discovery of black holes in the optical region through their gravitational interactions would be a major scientific breakthrough. Recent space-based photometry has made it possible to measure phase or frequency modulations of pulsating stars to extremely high precision. Such modulations are caused by orbital motion, and analyses offer a lower limit for the mass of the companion to the pulsating star. If the companions are non-luminous and if their masses exceed the mass limit for neutron stars ($\sim 3\,\mathrm{M}_\odot$), they should be black holes. We review the methodology, and demonstrate analyses of some encouraging cases.

Keywords: Asteroseismology, Binaries: general, Stars: black holes, oscillations

1 Introduction

It is thought that stars with an initial mass more than $\sim 25\,\mathrm{M}_\odot$ ultimately become black holes. Though the mass thresholds are dependent on the metallicity of the stars and are currently uncertain, stars with an initial mass in the range ~ 25–$40\,\mathrm{M}_\odot$ are expected to form black holes following a supernova explosion. Even more massive stars collapse to black holes without a spectacular explosion (Heger et al. 2003). These events are thought to correspond to the observed phenomena known as "failed supernovæ", in which sudden brightening occurs – as in the early stage of a supernova – but does not develop to full supernova luminosity (Adams et al. 2017). Stellar-mass black holes should therefore be ubiquitous. Population statistics of these stellar-mass black holes in our Galaxy may be estimated with a reasonable initial mass function, star formation rate, and assumptions of the density structure of the Galaxy. The uncertainty is large, but it is estimated that more than 100 million black holes reside in our Galaxy (Brown & Bethe 1994; Mashian & Loeb 2017; Breivik et al. 2017; Lamberts et al. 2018; Yalinewich et al. 2018; Yamaguchi et al. 2018).

Clearly there is no way to observe black holes directly. However, if a black hole is in a close binary system with an ordinary star, its presence can manifest itself in X-ray emission. If the black hole swallows gas from the companion star, a huge amount of potential energy is liberated, ultimately emitting X-rays that are detectable from space. However, X-ray binaries are not limited to systems containing a black hole. In general, they are close binaries composed of a compact object (a neutron star or a black hole) which is accreting mass from a companion donor star. Spectroscopic radial-velocity (RV) measurements of the optically visible donor enable us to deduce the lower limit of the invisible compact object, even if the latter is not itself visible. According to current theory, a neutron star more massive than $3\,\mathrm{M}_\odot$ is unstable and will collapse into a black hole. Therefore, a mass function that corresponds to a companion exceeding this critical mass is considered to be reliable evidence of a black hole. This is how stellar-mass black holes have been detected and confirmed (e.g., Cowley 1992; Remillard & McClintock 2006; Casares & Jonker 2014). Yet despite those estimates of 10^8 black holes in our Galaxy, fewer than 20 have so far been confirmed (Corral-Santana et al. 2016; Torres et al. 2019). If X-ray emission resulting from accretion only occurs in close binaries, quiescent stellar-mass black holes that show no X-ray emission would be limited to widely separated binaries.

[1] Department of Astronomy, School of Science, University of Tokyo, Tokyo 113-0033, Japan
[2] Sydney Institute for Astronomy, School of Physics, University of Sydney, NSW 2006, Australia

2 Black-hole X-ray binaries

About one third of X-ray binaries are not steadily visible but are detected as transient sources. Except for Cyg X-1, the Galactic stellar-mass black holes have so far been detected as transient X-ray sources in binaries with low-mass K- or M-dwarf companions (Tanaka & Shibazaki 1996). Figure 1 shows the γ-ray light-curve, obtained by the (*Swift* satellite) (Gehrels et al. 2004; Barthelmy et al. 2005), of such a low-mass X-ray binary, a *Ginga* source (GS 2023+338). Though their light-curves are individually different, these systems are often called X-ray novæ because of their X-ray brightening. The outbursts are caused by mass transfer instabilities in an accretion disc, which is fed by a low-mass dwarf (Mineshige & Wheeler 1989). During the γ-ray (and X-ray) outburst in 2015, the optical counterpart (known as V404 Cyg) brightened by ~ 6 mag in V. Such optical outbursts, labelled Nova Cygni 1938 by A. A. Wachmann, seem to be caused by reprocessing of X-ray photons in the accretion disk. In some other X-ray transients, the sudden optical brightening has also been classified as a nova (like Nova Vel 1993 in the case of GRS 100 9−45). The naming is misleading, since a classical nova is caused by a thermonuclear flash triggered by the accumulation of accreted gas on the surface of a white dwarf.

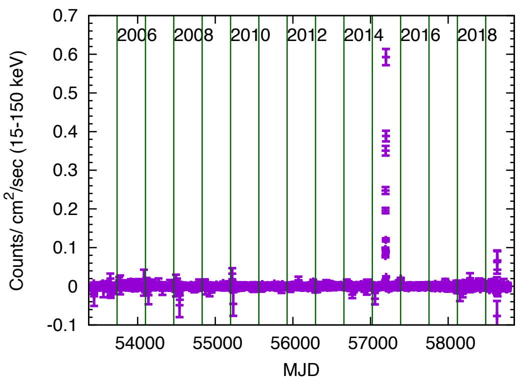

Fig. 1. γ-ray light-curve of GS 2023+338 obtained by *Swift*. Data were taken from the Swift archives.

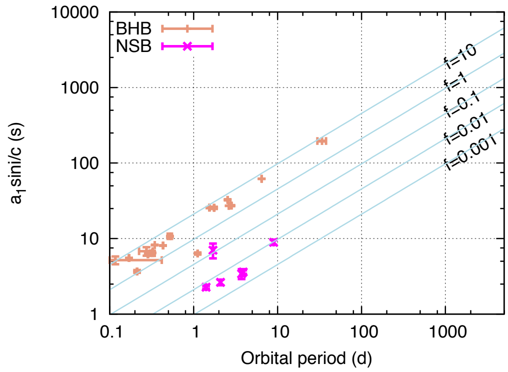

Fig. 2. Orbital period vs projected semi-major axis of X-ray binary systems.

In the X-ray quiescent phase between outbursts of GS 2023+338, V404 Cyg is as faint as $V \sim 18$ mag, and the optical source is the low-mass donor star itself (Casares et al. 2019); RV measurements therefore become possible and the orbital elements are deduced from them. The mass function giving the lower limit of the invisible compact object is determined from the orbital period $P_{\rm orb}$, the amplitude of RV variation $K_{\rm opt}$, and the eccentricity e:

$$f(M_{\rm opt}, M_{\rm X}, \sin i) \quad := \quad \frac{M_{\rm X}^3 \sin^3 i}{(M_{\rm opt} + M_{\rm X})^2} = \frac{1}{2\pi G} P_{\rm orb} K_{\rm opt}^3 \left(1 - e^2\right)^{3/2}, \tag{2.1}$$

where $M_{\rm X}$ and $M_{\rm opt}$ denote the masses of the X-ray emitting, but optically invisible, compact object and of the optical counterpart, respectively, i is the inclination angle of the orbit, and G is the gravitational constant.

For V404 Cyg, the orbital period is 6.5 d and the amplitude of (almost sinusoidal) RV variations is $\sim 200\,{\rm km\,s^{-1}}$, so the mass function is $\sim 6\,{\rm M_\odot}$, giving a companion mass $M_{\rm X}$ much larger than the critical mass for a neutron star. This binary system therefore contains a stellar-mass black hole (Casares et al. 1992).

Besides GS 2023+338, 16 X-ray binaries have been confirmed, via spectroscopic RVs of the optical counterparts, to be composed of a late-type low mass star and a stellar-mass black hole. In addition, the presence of a stellar-mass black hole has been confirmed in Cyg X-1, whose optical counterpart is an early-type star (Webster & Murdin 1972; Bolton 1972). Its strong stellar winds are accreted by the black hole, producing X-ray emission. The binary properties of all of these Galactic black holes given in the literature are listed in Table 1 (Corral-Santana et al. 2016 and references therein). For each X-ray binary system, the projected semi-major axis of the optical counterpart, in units of light-seconds, is plotted versus the orbital period in Fig. 2, where both axes use a logarithmic scale. Here, the semi-major axis is

$$\frac{a_{\rm opt} \sin i}{c} = \frac{1}{2\pi c} P_{\rm orb} K_{\rm opt} \left(1 - e^2\right)^{1/2}, \tag{2.2}$$

Table 1. Binary properties of the dynamically confirmed black-hole X-ray binaries in our Galaxy.

X-ray source	Opt.	Sp. Type	$P_{\rm orb}$ (h)	$f(M)$ ($M_\odot$)	$M_{\rm BH}$ ($M_\odot$)
Cyg X-1	HDE226868	O9Iab	134.4	0.244 ± 0.006	14.8 ± 1.0
GROJ0422+32	N. Per	M4-5V	5.09	1.19 ± 0.02	2 – 15
3A0620−003	N. Mon	K2-7V	7.75	2.79 ± 0.04	6.6 ± 0.3
GRS1009−45	N. Vel 93	K7-M0V	6.84	3.2 ± 0.1	> 4.4
XTEJ1118+480		K7-M1V	4.08	6.27 ± 0.04	6.9 – 8.2
GRS1124−684	N. Mus 91	K3-5V	10.38	3.02 ± 0.06	3.8 – 7.5
GS1354−64	BW Cir	G5III	61.07	5.7 ± 0.3	> 7.6
4U1543−475	IL Lup	A2V	26.79	0.25 ± 0.01	8.4 – 10.4
XTEJ1550−564		K2-4IV	37.01	7.7 ± 0.4	7.8 – 15.6
XTEJ1650−500		K4V	7.69	2.7 ± 0.6	< 7.3
GROJ1655−40	N. Sco 94	F6IV	62.92	2.73 ± 0.09	6.0 ± 0.4
1HJ1659−487	GX 339-4	> GIV	42.14	5.8 ± 0.5	> 6
H1705−250	N. Oph 77	K3-M0V	12.51	4.9 ± 0.1	4.9 – 7.9
SAXJ1819.3−2525	V4641 Sgr	B9III	67.62	2.7 ± 0.1	6.4 ± 0.6
XTEJ1859+226	V406 Vul	K5V	6.58	4.5 ± 0.6	> 5.42
GRS1915+105		K1-5III	812	7.0 ± 0.2	12 ± 2
GS2000+251	QZ Vul	K3-7V	8.26	5.0 ± 0.1	5.5 – 8.8
GS2023+338	V404 Cyg	K3III	155.31	6.08 ± 0.06	$9.0^{+0.2}_{-0.6}$

where c is the speed of the light. Systems of the same mass function would form a line with an inclination of 2/3. In the same diagram, some representative data for neutron-star X-ray binaries are plotted. As expected, most of the black-hole binaries (BHB) have a mass function larger than $1\,M_\odot$, while the neutron-star binaries (NSB) have substantially smaller values.

Since the low-mass star is tidally locked, the spin period is the same as the orbital period. Hence the rotation velocity and the orbital velocity differ only by the factor of the ratio of the size of the star and the size of the orbit. The star fills its Roche lobe, so the size of the star is the Roche lobe size. The Roche lobe size relative to the binary separation is determined by the mass ratio (Paczyński 1971). Hence, the ratio of the rotation velocity to the orbital velocity gives the mass ratio. With a reasonable estimate for the mass of the low-mass star from its spectrum, the mass of the invisible object is thus observationally determined. The results taken from the literature are illustrated in Fig. 3 (Corral-Santana et al. 2016 and references therein). The X-ray objects with estimated masses in the range of 1.5–3 $M_\odot$ are neutron stars. X-ray transient systems containing an invisible object having a mass higher than $3\,M_\odot$ are considered to be the best signatures of stellar-mass black holes.

X-ray binaries containing black holes are mostly distinguishable from those with neutron stars by their X-ray spectra. The former are characterised by an ultrasoft thermal component ($\lesssim 1.2$ keV), accompanied by a hard tail and seen after the flux reaches to the maximum, while the latter show a slightly harder ($\sim$ a few

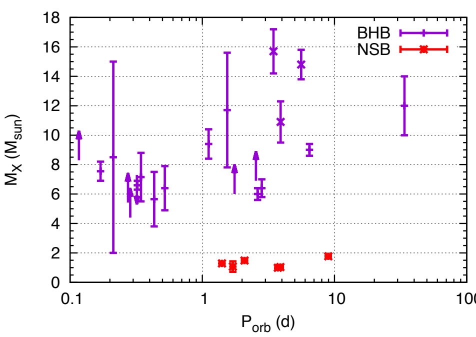

Fig. 3. Mass of the invisible compact object vs orbital period of X-ray binary systems.

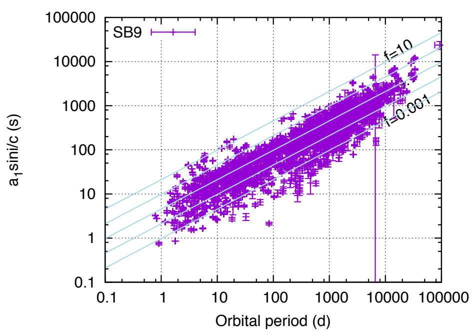

Fig. 4. Orbital period vs projected semi-major axis of binary systems listed in the *Ninth Catalogue of Spectroscopic Binary Systems* (SB9) (Pourbaix et al. 2004). Mass functions are shown in units of $M_\odot$.

keV) black-body component, which is thought to be from the neutron star envelope, and a softer but still a bit harder component than the black-hole X-ray binaries, most probably from the accretion disk. Ultrasoft X-ray transient sources are regarded as a signature of binaries containing a black hole. There are ~ 60 such X-ray sources suspected to be black hole binaries from their spectra, and classified as "black-hole candidates", but not yet dynamically confirmed, so less secure (Corral-Santana et al. 2016 and references therein).

3 Search for quiet black holes in single-lined spectroscopic binaries

Quiescent black holes in wide binary systems may be found in RV surveys by searching for single-lined systems with high mass functions. Such an attempt was proposed by Guseinov & Zel'dovich (1966), who selected 7 plausible candidates in an attempt to detect "collapsed stars". Their attempt was later followed by Trimble & Thorne (1969) (see also Trimble & Thorne 2018) using the sixth catalogue of the orbital elements of spectroscopic binary systems (Batten 1967). For each system the mass of the primary star was estimated from its spectral type, and an approximate lower limit to the mass of the unseen companion was then calculated from the observed mass function. Trimble & Thorne (1969) listed 50 systems that had an unseen secondary star more massive than the Chandrasekhar mass limit for a white dwarf.

Figure 4 shows the distribution of spectroscopic binaries listed in SB9 (Pourbaix et al. 2004) in the plane of orbital period versus semi-major axis. More than 50 systems are found to have a mass function larger than $1\,\mathrm{M}_\odot$. However, in most cases careful follow-up observations unveiled the presence of a fainter secondary star of larger mass (e.g. Stickland 1997). A plausible scenario is that the primary was originally more massive than the secondary and it had evolved faster than the secondary. A substantial amount of mass loss in the red-giant phase made the primary significantly less massive than the secondary, which is still in the main-sequence phase and relatively much fainter than the evolved primary. Generally, a larger and more homogeneous sample of main-sequence stars is favourable; however, such a sample has been difficult to procure in practice. Spectroscopic data have to be collected as time-series covering the orbital phase of each binary system, often obtained one by one from ground-based observing sites with a large amount of observing time, and often with large telescopes for fainter stars. This forms a bottle-neck to such binary studies.

Since this conference, Thompson et al. (2019) found a black hole–giant star binary (2MASS J05215658+4359220), from multi-epoch RVs acquired by the APOGEE survey (Majewski et al. 2017). The system has a nearly circular orbit with $P_{\mathrm{orb}} = 83.2 \pm 0.06\,\mathrm{d}$, a semi-amplitude $K_{\mathrm{opt}} \simeq 44.6 \pm 0.1\,\mathrm{km\,s^{-1}}$ and a mass function of $0.766 \pm 0.006\,\mathrm{M}_\odot$. The photometric data vary periodically in step with the RV variations, implying spin-orbit synchronisation of the star. A combination of the measured projected spin velocity and the period leads to $R_{\mathrm{opt}} \sin i \simeq 23 \pm 1\,\mathrm{R}_\odot$; the mass of the giant star is estimated to be $M_{\mathrm{opt}} \sin^2 i \simeq 4.4^{+2.2}_{-1.5}\,\mathrm{M}_\odot$ from this radius and the spectroscopically estimated $\log g$. An independent combination of the apparent luminosity, the spectroscopically determined effective temperature and *Gaia* distance measurements gives $R_{\mathrm{opt}} = 30^{+9}_{-6}\,\mathrm{R}_\odot$, which is consistent with the value based on the spin velocity. As a consequence, from the aforementioned mass function, the minimum mass of the unseen companion is estimated to be $\sim 2.9\,\mathrm{M}_\odot$, marginally exceeding the critical mass for a neutron star. This is likely to be the first success at finding an X-ray quiet black hole lurking in a binary system, though within the uncertainties the companion could be a neutron star instead.

4 Search for quiet black holes based on phase modulations of pulsating stars in binaries

From *MOST* (Walker et al. 2003) to *CoRoT* (Auvergne et al. 2009), *Kepler* (Koch et al. 2010), *TESS* (Ricker et al. 2015) and *BRITE*-Constellation (Weiss et al. 2014), space-based photometry with extremely high precision over long time-spans has led to a drastic change of this situation, and has revolutionized our view of variability of stars. Some variability has been detected in almost all stars, and thousands of pulsating stars plus hundreds of eclipsing binaries (Kirk et al. 2016) have been newly discovered. *Kepler*'s 4-year simultaneous monitoring of nearly 200,000 stars also opened a new window onto a statistical study of binaries (Murphy et al. 2018; Murphy 2018; Shibahashi & Murphy 2019). This pedigree will be augmented further by *PLATO**.

Binary orbital motion causes a periodic variation in the path length of light travelling to us from a star, so if the star is pulsating, the time delay manifests itself as a periodically varying phase-shift in the form of the product with an intrinsic angular frequency (Shibahashi & Kurtz 2012; Shibahashi et al. 2015). The light arrival-time delay can then be measured by dividing the observed phase variation by the frequency (Murphy et al. 2014). The light-time effect upon the observed times of maxima in luminosity, which vary over the orbit,

*http://sci.esa.int/plato/59252-plato-definition-study-report-red-book/

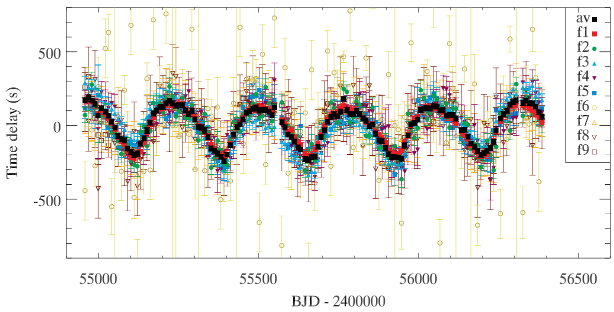

Fig. 5. An example of a time-delay curve (KIC 9651065) using 9 different pulsation modes. The weighted average is shown as filled black squares. Adopted from Murphy & Shibahashi (2015).

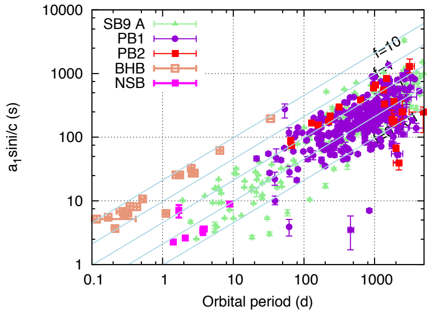

Fig. 6. Orbital period vs projected semi-major axis of newly discovered δ Sct binary systems, together with binaries having an A-type primary (as catalogued in SB9). Mass functions are shown in units of $\mathrm{M}_\odot$.

has been used to find unseen binary companions (the so-called *O-C* method; e.g. Sterken 2005 and papers cited therein). Such a method works well in the case of stars pulsating with a single mode, since the intensity maxima are easy to track and any deviations from precise periodicity are fairly easy to detect. However, if the pulsating star is multiperiodic (as in the case of most objects observed from space), the situation is much more complex, and it is more suitable measure the time delay by careful analysis of phase modulation. Figure 5 shows a time-delay curve calculated with *Kepler* data. It immediately provides us with qualitative information about the orbit (Murphy & Shibahashi 2015; Murphy et al. 2016).

Murphy et al. (2018) applied this technique to all targets in the original *Kepler* field with effective temperatures ranging from 6600–10000 K, and discovered 341 new binary systems containing δ Scuti stars (main-sequence A stars pulsating in pressure modes). Importantly, many of those binaries would not have been detectable by other techniques, because A stars are often rapid rotators (Royer et al. 2007), making spectroscopic RVs difficult to measure. Using space-based photometry to measure the phase modulation of pulsating stars is a very efficient way of creating a homogeneous sample of binary systems. Indeed, these asteroseismically detected binaries tripled the number of intermediate-mass binaries with full orbital solutions, and, importantly, provided a homogeneous dataset for statistical analyses.

The newly detected binaries are plotted in the (P_{orb}-$a_1 \sin i/c$)-diagram shown as Fig. 6, and (for comparison) the black-hole X-ray binaries listed in Table 1 and 162 spectroscopic binaries listed in the SB9 (2004) Catalogue having primary stars of similar spectral type (A0–F5). Only systems with full orbital solutions plus uncertainties were selected. The following should be noted: Binaries with orbital periods shorter than 20 d were not found by the asteroseismic method. This is because the light-curve is divided into short segments, such as 10 d, in order to measure the phases of pulsation modes of close frequencies. It is then unfavourable to deal with binary stars with orbital periods shorter than the segment size dividing the observational time span, which is typically $\sim$10 d. With short-period binaries also having smaller orbits (hence smaller light travel times), the binaries with periods in the range of 20–100 d are difficult to detect by the asteroseismic method and the sample in this period range must be considerably incomplete. It is also in this period range that binaries are most likely to exhibit eclipses, but eclipsing binaries were removed from the asteroseismic sample so as to avoid biasing the detection (Murphy et al. 2018).

The mass range of δ Scuti type stars used by Murphy et al. (2018) is $1.8 \pm 0.3\,\mathrm{M}_\odot$. Those systems having a mass function larger than $\sim 1\,\mathrm{M}_\odot$ are therefore thought to have a binary counterpart more massive than the neutron-star mass threshold, $\sim 3\,\mathrm{M}_\odot$ and they may be regarded as systems containing a stellar-mass black hole. As shown in Fig. 6, several systems with large mass functions have been found. Those with a mass function larger than $1\,\mathrm{M}_\odot$ are listed in Table 2. However, the seemingly massive secondary could itself be double or multiple, rendering each component less massive and fainter than expected. Indeed, some systems with large mass functions were eventually found to be triples, via follow-ups with ground-based RV observations made by Lehman, Murphy and their many collaborators (in preparation). In some other cases of highly eccentric orbits, the RV observations clarified the suspicion that the amplitude of phase modulation was simply overestimated (see Fig. 7). Nevertheless, there still remain a few systems that are found to be single-lined spectroscopic binaries with large mass functions. They could be systems with a massive white dwarf or a neutron star. Further detailed observations are required before conclusions can be considered definite.

Table 2. Binary properties of δ Sct stars in the *Kepler* field having a mass function larger than $1\,\mathrm{M}_\odot$.

KIC	$P_{\rm orb}$ (d)	$a_1 \sin i/c$ (s)	e	ϖ_1 (rad)	$f(M)$ ($\mathrm{M}_\odot$)
5219533	$1571.0^{+15.0}_{-13.0}$	$1367.0^{+11.0}_{-10.0}$	$0.5767^{+0.0081}_{-0.0081}$	$0.478^{+0.016}_{-0.013}$	$1.111^{+0.032}_{-0.032}$
8459354	$53.559^{+0.020}_{-0.022}$	$276.0^{+57.0}_{-76.0}$	$0.9809^{+0.0062}_{-0.0180}$	$6.085^{+0.034}_{-0.078}$	$7.9^{+4.9}_{-6.5}$

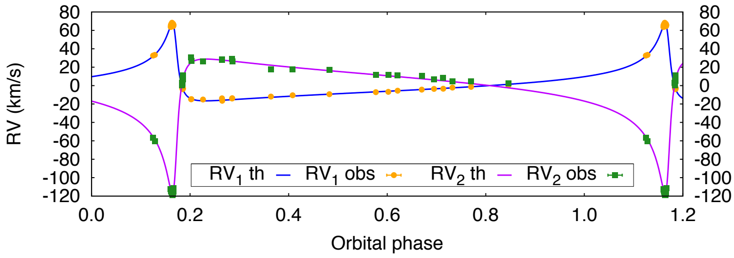

Fig. 7. An example of systems with highly eccentric orbits for which the RV observations confirmed that the amplitude of phase modulation was simply overestimated.

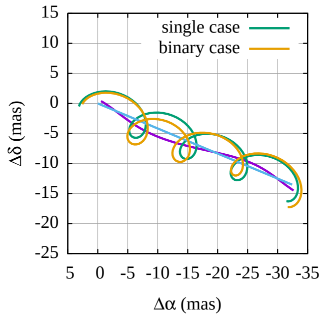

Fig. 8. Projected motion of a single star, and of a star in a binary system with an unseen companion.

5 Self-lensing black-hole binaries

In the case of an edge-on black-hole binary system (whose orbital axis is almost perpendicular to the line-of-sight), evidence for a lurking black hole would be available in addition to its large mass function. At superior conjunction, when the black hole transits in front of the optical companion, contrary to the case of an ordinary eclipsing binary, a luminosity brightening is induced by the gravitational microlensing (Einstein 1936; Leibovitz & Hube 1971; Maeder 1973). In the general case, the characteristic size of this lens (called the Einstein radius, $R_{\rm E}$) is given by

$$R_{\rm E} := \sqrt{\frac{4GM_{\rm BH}}{c^2}\frac{d_{\rm S}}{d_{\rm L}}(d_{\rm S}-d_{\rm L})} \tag{5.1}$$

with the notation described in Gould (2000), where G is the gravitational constant, $M_{\rm BH}$ is the mass of the black hole, and $d_{\rm S}$ and $d_{\rm L}$ denote the distances to the source and to the lens, respectively. For the present case, $d_{\rm S} = d_{\rm L} + a(1-e^2)/(1-e\sin\varpi_{\rm opt})$, where $a := a_{\rm opt} + a_{\rm BH}$ is the summation of the semi-major axes of the two components and $\varpi_{\rm opt}$ is the argument of the periapsis of the optical companion. Hence the Einstein radius, in units of light-seconds, is

$$\frac{R_{\rm E}}{c} = 4.44\times10^{-2}\left(\frac{a/c}{100\,\mathrm{s}}\right)^{1/2}\left(\frac{M_{\rm BH}}{\mathrm{M}_\odot}\right)^{1/2}\left(\frac{1-e^2}{1-e\sin\varpi_{\rm opt}}\right)^{1/2}\ \mathrm{s}. \tag{5.2}$$

This is only a few percent of one solar radius, so the geometry for the lensing is narrowly restricted to the edge-on case; the inclination angle, i, should be in the range $\pi/2-(R_{\rm opt}/a)\le i\le \pi/2+(R_{\rm opt}/a)$.

The tangential velocity of the black hole relative to the optical component at the superior conjunction is

$$\frac{v_{\rm t}}{c} = \frac{2\pi(a/c)}{P_{\rm orb}}\frac{(1-e\sin\varpi_{\rm opt})}{\sqrt{1-e^2}}. \tag{5.3}$$

The duration of the transit is then given by

$$\begin{aligned} t_{\rm trans} &:= \frac{2\sqrt{R_{\rm opt}^2 - a^2\cos^2 i}}{v_{\rm t}} \\ &= \frac{P_{\rm orb}}{\pi}\left\{\left(\frac{R_{\rm opt}}{a}\right)^2-\cos^2 i\right\}^{1/2}\frac{\sqrt{1-e^2}}{1-e\sin\varpi_{\rm opt}}. \end{aligned} \tag{5.4}$$

Luminosity brightening repeats at every superior conjunction, i.e., once per orbital period. Similar self-lensing systems containing white dwarfs have so far been found for five cases (Kruse & Agol 2014; Kawahara et al. 2018;

Masuda et al. 2019), so the probability to detect such a rare but physically important event is not necessarily hopeless (Masuda & Hotokezaka 2019).

The brightness enhancement of the microlens during the transit is $A(R_{\rm E}/R_{\rm opt})^2$, where we estimate A to be 1.27 by integrating light emitted from points behind the Einstein radius using equation 5 of Paczyński (1986). Therefore, the luminosity enhancement during the black-hole transit is of the order of a few percent in the case of $R_{\rm E}/R_{\rm opt} = 1/10$. The transit light curves (magnification versus time) of microlensing events resemble inverted planetary transits.

6 Search for quiet black holes by astrometry

Another promising method for finding quiet black-hole binaries uses *Gaia* astrometry, which is extremely sensitive to non-linear proper motions of astrometric binaries with periods in the range 0.03–30 years. Targets are not restricted to pulsating stars. *Gaia* is expected to detect "approximately 60% of the estimated 10 million binaries down to 20 mag closer than 250 pc"[†]. Like a simulation illustrated in Fig. 8, the orbital motion in each astrometric binary system can be seen directly, leading to the orbital elements and the mass functions. *Gaia* simultaneously carries out spectroscopic observations, though not for all stars. If the target has spectroscopy, the mass of the star can be estimated independently once its temperature is determined spectroscopically. If one component is unseen, its mass is deduced from the mass function and the spectroscopic mass of the optical counterpart. The unseen single companion should be either a white dwarf, a neutron star or a black hole, depending on its mass.

7 Sumary

(a) X-ray quiet BHBs are expected to be present. (b) Searching for X-ray quiet BHBs is challenging, but worth pursuing. (c) Space-based asteroseismology and the measurements of light arrival-time delays opened a new window on binary statistics. (d) Binary systems with unseen companions and high mass functions could result from the secondary being a black hole. (e) Self-lensing BHBs are expected to show periodic brightening. (f) Space-based astrometry also opens another window on binary statistics.

8 Acknowledgements

The authors thank the organizing committee of the conference, led by Werner Weiss, for their excellent organization, resulting in a fruitful meeting. This work was partly supported by the JSPS Grant-in-Aid for Scientific Research (16K05288).

References

Adams, S. M., Kochanek, C. S., Gerke, J. R., & Stanek, K. Z. 2017, MNRAS, 469, 1445

Auvergne, M., Bodin, P., Boisnard, L., et al. 2009, A&A, 506, 411

Barthelmy, S. D., Barbier, L. M., Cummings, J. R., et al. 2005, Space Sci. Rev., 120, 143

Batten, A. H. 1967, Publications of the DAO Victoria, 13, 119

Bolton, C. T. 1972, Nature Physical Science, 240, 124

Breivik, K., Chatterjee, S., & Larson, S. L. 2017, ApJ, 850, L13

Brown, G. E. & Bethe, H. A. 1994, ApJ, 423, 659

Casares, J., Charles, P. A., & Naylor, T. 1992, Nature, 355, 614

Casares, J. & Jonker, P. G. 2014, Space Sci. Rev., 183, 223

Casares, J., Muñoz-Darias, T., Mata Sánchez, D., et al. 2019, MNRAS, 488, 1356

Corral-Santana, J. M., Casares, J., Muñoz-Darias, T., et al. 2016, A&A, 587, A61

Cowley, A. P. 1992, ARA&A, 30, 287

Einstein, A. 1936, Science, 84, 506

Gehrels, N., Chincarini, G., Giommi, P., et al. 2004, ApJ, 611, 1005

Gould, A. 2000, ApJ, 542, 785

Guseinov, O. K. & Zel'dovich, Y. B. 1966, Soviet Astronomy, 10, 251 (Astronomicheskii Zhurnal, 43, 313)

Heger, A., Fryer, C. L., Woosley, S. E., Langer, N., & Hartmann, D. H. 2003, ApJ, 591, 288

[†] https://sci.esa.int/web/gaia/-/31441-binary-stars

Kawahara, H., Masuda, K., MacLeod, M., et al. 2018, AJ, 155, 144
Kirk, B., Conroy, K., Prša, A., et al. 2016, AJ, 151, 68
Koch, D. G., Borucki, W. J., Basri, G., et al. 2010, ApJ, 713, L79
Kruse, E. & Agol, E. 2014, Science, 344, 275
Lamberts, A., Garrison-Kimmel, S., Hopkins, P. F., et al. 2018, MNRAS, 480, 2704
Leibovitz, C. & Hube, D. P. 1971, A&A, 15, 251
Maeder, A. 1973, A&A, 26, 215
Majewski, S. R., Schiavon, R. P., Frinchaboy, P. M., et al. 2017, AJ, 154, 94
Mashian, N. & Loeb, A. 2017, MNRAS, 470, 2611
Masuda, K. & Hotokezaka, K. 2019, ApJ, 883, 169
Masuda, K., Kawahara, H., Latham, D. W., et al. 2019, ApJ, 881, L3
Mineshige, S. & Wheeler, J. C. 1989, ApJ, 343, 241
Murphy, S. J. 2018, arXiv e-prints, arXiv:1811.12659
Murphy, S. J., Bedding, T. R., Shibahashi, H., Kurtz, D. W., & Kjeldsen, H. 2014, MNRAS, 441, 2515
Murphy, S. J., Moe, M., Kurtz, D. W., et al. 2018, MNRAS, 474, 4322
Murphy, S. J. & Shibahashi, H. 2015, MNRAS, 450, 4475
Murphy, S. J., Shibahashi, H., & Bedding, T. R. 2016, MNRAS, 461, 4215
Paczyński, B. 1971, ARA&A, 9, 183
Paczyński, B. 1986, ApJ, 304, 1
Pourbaix, D., Tokovinin, A. A., Batten, A. H., et al. 2004, A&A, 424, 727
Remillard, R. A. & McClintock, J. E. 2006, ARA&A, 44, 49
Ricker, G. R., Winn, J. N., Vanderspek, R., et al. 2015, JATIS, 1, 014003
Royer, F., Zorec, J., & Gómez, A. E. 2007, A&A, 463, 671
Shibahashi, H. & Kurtz, D. W. 2012, MNRAS, 422, 738
Shibahashi, H., Kurtz, D. W., & Murphy, S. J. 2015, MNRAS, 450, 3999
Shibahashi, H. & Murphy, S. J. 2019, arXiv e-prints, arXiv:1909.07595
Sterken, C. 2005, The Light-Time Effect in Astrophysics: Causes and cures of the O-C diagram, ASP Conf. Ser., 335
Stickland, D. J. 1997, The Observatory, 117, 37
Tanaka, Y. & Shibazaki, N. 1996, ARA&A, 34, 607
Thompson, T. A., Kochanek, C. S., Stanek, K. Z., et al. 2019, Science, 366, 637
Torres, M. A. P., Casares, J., Jiménez-Ibarra, F., et al. 2019, ApJ, 882, L21
Trimble, V. & Thorne, K. S. 2018, arXiv e-prints, arXiv:1811.04310
Trimble, V. L. & Thorne, K. S. 1969, ApJ, 156, 1013
Walker, G., Matthews, J., Kuschnig, R., et al. 2003, PASP, 115, 1023
Webster, B. L. & Murdin, P. 1972, Nature, 235, 37
Weiss, W. W., Rucinski, S. M., Moffat, A. F. J., et al. 2014, PASP, 126, 573
Yalinewich, A., Beniamini, P., Hotokezaka, K., & Zhu, W. 2018, MNRAS, 481, 930
Yamaguchi, M. S., Kawanaka, N., Bulik, T., & Piran, T. 2018, ApJ, 861, 21

Stars and their variability observed from space
C. Neiner, W. W. Weiss, D. Baade, R. E. Griffin, C. C. Lovekin, A. F. J. Moffat (eds)

ACCRETION SIMULATIONS OF η CARINAE AND IMPLICATIONS FOR THE EVOLUTION OF MASSIVE BINARIES

A. Kashi[1]

Abstract. This contribution presented high-resolution numerical simulations of the colliding wind system η Carinae, showing accretion of the primary wind onto the secondary star close to periastron passage. We found that the stellar winds collide and develop instabilities, mainly the non-linear thin shell instability, and form filaments and clumps. We also found that a few days before periastron passage the dense filaments and clumps flow towards the secondary as a result of its gravitational attraction, and are then accreted onto the secondary. We ran our simulations for a conventional model of stellar masses, $M_1 = 120$ M$_\odot$ and $M_2 = 30$ M$_\odot$, and for the high-mass model, $M_1 = 170$ M$_\odot$ and $M_2 = 80$ M$_\odot$, that was proposed to fit better the history of giant eruptions in the 19$^{\text{th}}$ Century, as well as radial-velocity variations of spectral lines during recent spectroscopic events. The results of the simulations show that the accretion process is more pronounced in the high-mass model, and that the amount of mass accreted, as well as the duration of the accretion, are also fitted much better. Our findings establish η Car as the most massive binary system in the Galaxy. As our simulations demonstrate, the presence of a binary companion can have a huge influence on the evolution of massive stars, especially at later stages where it may undergo giant episodes of mass loss.

Keywords: Stars: massive, mass-loss, winds, outflows, accretion, accretion disks, binaries: general

1 Introduction

Massive stars involve physical processes that are not often seen in low mass stars, such as rotation at almost critical speeds, strong winds and eruptive outbursts (e.g., Heger & Langer 2000; Heger et al. 2000; Kudritzki & Puls 2000; Puls et al. 2008; Meynet et al. 2009; Davidson & Humphreys 2012; Vink et al. 2015). Perhaps the most interesting phenomena observed in massive stars are related to ithe fact that most of them ($\approx 70\%$ according to Sana et al. 2012) share their lives with a companion star, which may influence their evolution considerably (e.g., De Marco & Izzard 2017; Eldridge 2017; van den Heuvel 2017).

The massive binary system η Carinae is composed of a primary which is a very massive star at a late stage of its evolution, and a secondary which is a hotter and less luminous evolved main-sequence (MS) star (e.g., Davidson & Humphreys 1997, 2012). (e.g., Davidson & Humphreys 1997; Davidson et al. 2017), and strong winds (Pittard & Corcoran 2002; Akashi et al. 2006), resulting in a unique phase of strong interaction every 5.54 years during periastron passage known as the "spectroscopic event". During the event many spectral lines and emission at practically all wavelengths show rapid variability (e.g., Nielsen et al. 2007; Damineli et al. 2008b,a; Davidson et al. 2015; Mehner et al. 2015, and many refs. therein). The X-ray intensity, which also serves as an indicator of the intensity of wind interaction, drops for a few weeks, changing from one spectroscopic event to the other (Corcoran et al. 2015).

Soker (2005a) developed a model to interpret the line variations during the spectroscopic event as a result of accreting clumps of gas onto the secondary near periastron passages, disabling its wind. The suggestion was later developed into a detailed model accounting for various observations (Akashi et al. 2006; Kashi & Soker 2009b). An estimate of the amount of accreted mass during the spectroscopic event was first obtained by Kashi & Soker (2009a), who performed a detailed calculation, integrating over time and volume of the density within the Bondi–Hoyle–Lyttleton accretion radius around the secondary. Kashi & Soker (2009a) found that accretion should take place close to periastron, and that the secondary should accrete $\sim$ few $\times$ 10^{-6} M$_\odot$ each cycle.

The last three spectroscopic events, 2003.5, 2009 and 2014.6, were different from each other, and reflected a trend in the intensities of various lines (Mehner et al. 2015). Observations of spectral lines during the 2014.6 event were interpreted as weaker accretion onto the secondary close to periastron passage compared to previous events, indicating a decrease in the mass loss rate from the primary star. This 'change of state' of the primary

[1] Ariel University, 4070000 Ariel, Israel ; Email: kashi@ariel.ac.il ; ORCID:0000-0002-7840-0181

was identified by Davidson et al. (2005) and also predicted from numerical simulations by Kashi et al. (2016). Further indications of the change of state was found by comparing UV emission lines at similar orbital phases separated by two orbital revolutions, at positions far from periastron passage (Davidson et al. 2018).

Older grid-based simulations (Parkin et al. 2009, 2011) and Smoothed Particle Hydrodynamics (SPH) simulations (Okazaki et al. 2008; Madura et al. 2013) of the colliding winds did not accretion onto the secondary. Teodoro et al. (2012) and Madura et al. (2013) argued against the need for accretion to explain the spectroscopic event. But in spite of those claims, Parkin et al. (2011) simulated stationary colliding winds at the time of periastron and showed that unstable wind and clumps were formed and reached to distance that was very near the secondary. Since their simulations were unable to reach high resolution they could not obtain a clear picture of accretion, but they postulated that high-resolution simulations with "switching off" the initiation of the wind will be able to reveal a wind "collapse". These simulations did not include the gravity of the secondary either, but it was later found to be important for accretion to take place.

Akashi et al. (2013) also simulated the wind interaction, and found that clumps of gas were formed a few days before periastron passage owing to instabilities in the colliding winds structure, in agreement with X-ray flares observed at that time (Moffat & Corcoran 2009). Some of the clumps moved towards the secondary, and reached one grid cell from the secondary wind injection zone, implying accretion. However, the resolution of these simulations was not fine enough to see the accretion itself.

The simulations presented below extend those of Akashi et al. (2013) in the sense that they include (1) higher resolution that could trace the flow better, allow the development of instabilities, and reveal final details, and (2) more detailed physical treatment. The following discusses the results of our simulation and their implications for massive-star research.

2 Simulations and Results

The simulations were described in detail by Kashi (2017) and Kashi (2019). The final evidence for accretion came from the simulations of Kashi (2017) that included many more physical effects (e.g., gravity of the two stars, radiative cooling, radiation transfer, artificial viscosity), and showed the destruction of the colliding winds structure into filaments and clumps that later were accreted onto the secondary. They demonstrated that dense clumps are crucial to the onset of the accretion process. The clumps were formed by the smooth colliding stellar winds that developed instabilities, (mainly the non-linear thin shell instability, NLTI: Vishniac 1994)) that later grew into clumps (no artificial clumps were seeded). This confirmed the preceding theoretical arguments by Soker (2005a,b) who suggested accretion of clumps. Furthermore, as the simulations in Kashi (2017) included a radiation transfer unit which treats the photon-gas interaction, so the momentum of the accreted gas is being changed appropriately along its trajectory. It thus quantitatively showed that radiative braking cannot prevent the accretion, thereby confirming theoretical arguments given by Kashi & Soker (2009a). Kashi (2019) extended the simulations to treat *the response of a wind blowing star to mass that arrives with strong momentum and is accreted onto its surface.* Figure 1 shows the results for one of our simulations.

We found that accretion is obtained for both the conventional mass model ($M_1 = 120$ M$_\odot$, $M_2 = 30$ M$_\odot$) and the high mass model ($M_1 = 170$ M$_\odot$, $M_2 = 80$ M$_\odot$). For the high mass model the stronger secondary gravity attracts the clumps and we get higher accreted mass of $M_{\rm acc} \simeq$ few$\times 10^{-6}$ M$_\odot$ yr^{-1} and longer accretion periods, in the order of a month, which more closely match the observed ones. We also calculated the increase in optical depth in any line of sight and the reduction in the effective temperature ($T_{\rm eff}$) as a result. Observations of lines during the spectroscopic event indicate ionizing radiation from the secondary equivalent to that of a star with $T_{\rm eff} \lesssim 25\,000$ K. For reasonable and even high mass loss rates, only the high mass model we tested matched the observed decline in $T_{\rm eff}$ (Figure 2, right panel).

We ran a number of simulations with varying parameters (Figure 2, left panels). An important parameter we studied is the mass loss rate of the primary (see Kashi 2017). We found that the mass loss rate of the primary affects the accretion rate of the secondary in a non-linear way, and found a strong dependency between the accreted mass and the mass loss rate of the primary. The simulations showed that if the mass loss rate of the primary is lowered by a factor of a few the accretion can stop. Thwrefore, they supported the claim of Mehner et al. (2015), who suggested that, if the mass loss rate of the primary continues to decrease, future spectroscopic events will be very weak or might not occur at all (though a recent paper argues differently; Mehner et al. 2019).

Another parameter we varied is the eccentricity, for which we also tested $e = 0.85$. This value was favored by Davidson et al. (2017) because it gives the smallest possible separation distance at the beginning of the spectroscopic event. It was therefore expected that $e = 0.85$ would produce earlier accretion compared to $e = 0.9$, even though the periastron distance is 50% larger for the smaller eccentricity. Figure 2 shows our results, confirming that for $e = 0.85$ the accretion duration is indeed longer, and more mass was accreted. Run

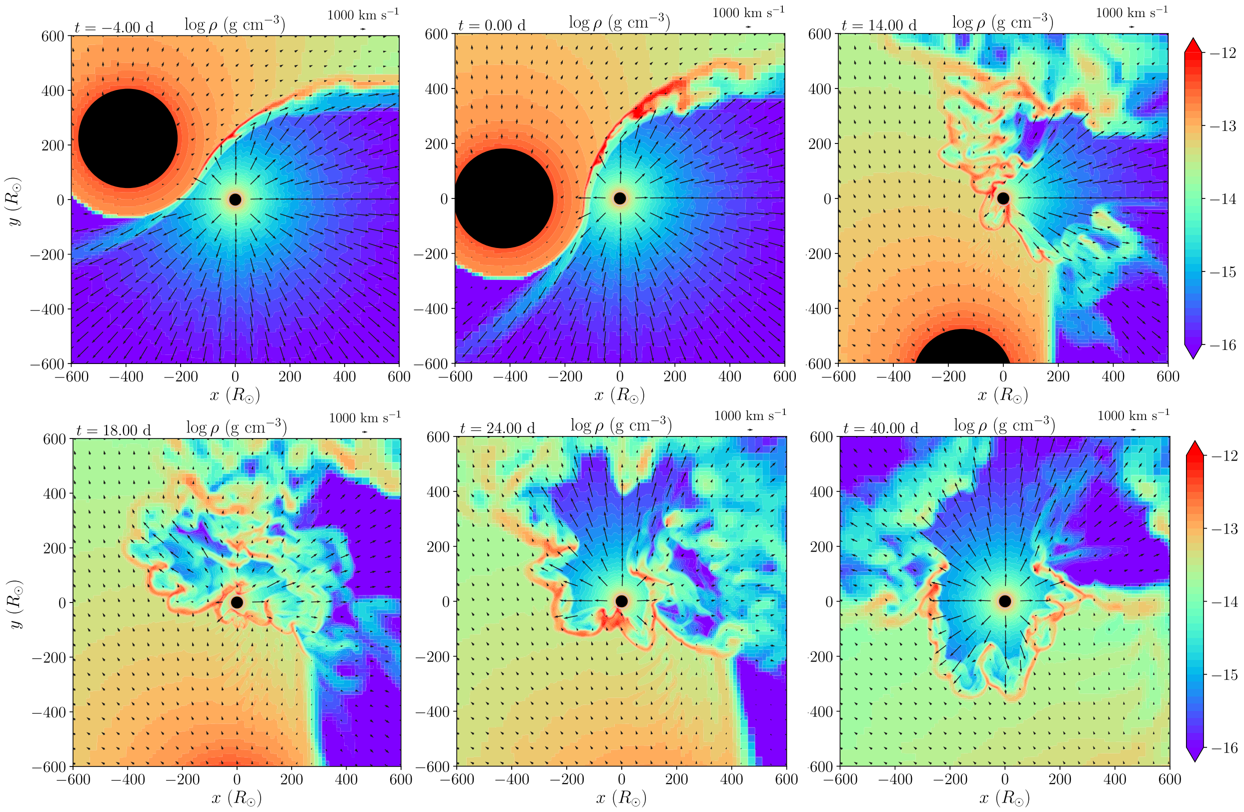

Fig. 1. Density maps with velocity vectors, sliced in the orbital plane ($z = 0$), for one of our runs with the high mass model for η Car, $M_1 = 170$ M$_\odot$ and $M_2 = 80$ M$_\odot$. The secondary is at the center (small black circle) while the primary (large black circle) orbits it counter-clockwise. Periastron passage occurs at $(x, y, z) \simeq (-1.9 \text{ au}, 0, 0)$ and $t = 0$. The colliding wind structure is destructed by instabilities and gas is accreted onto the secondary. The simulation shows how the secondary star wind is restored as the stars move away from each other after periastron passage.

M6 (high mass model, lower e) also showed early accretion exactly as expected by Davidson et al. (2017). For the conventional mass model (run C6) we did not see this behavior, because the larger periastron distance and smaller secondary mass combined to reduce the gravitational attraction of the secondary and therefore early accretion could not occur.

3 Conclusions

Our simulations prove that accretion takes place close to periastron passage. As expected from the studies of Soker (2005a) and Kashi & Soker (2009a), we found in Kashi (2019) that accretion causes the secondary star to stop, at least partially, blowing its wind. Quantifying the effect for a large parameter space requires an extensive effort of running many simulations and advanced post-processing of the results. So far we ran a number of cases that partially cover the parameter space (Figure 2). Our results support the high mass model for η Car, with a combined mass of 250 M$_\odot$, a result that was also supported by other considerations, such as the timings of periastron passages during the 1839–1858 Great Eruption (Kashi & Soker 2009a), and fitting radial velocity variations of spectral lines for present-day observations during the orbital motion, and especially close to periastron passage. (Kashi & Soker 2016).

As accretion takes place presently it certainly has occured during the Great Eruption of η Car, when the mass loss rate of the primary was at least a few thousand times larger than today. This makes the accretion model (Soker 2004; Kashi & Soker 2009a) the most probable scenario for the Great Eruption of η Car, and the formation of the Homunculus nebula. Very briefly, according to the accretion model an instability in the primary was amplified by the gravity of the secondary at periastron, hereby causing the eruption. The energy then comes from mass accreting onto the secondary, and the jets launched by the secondary shape the bipolar nebula. Many questions still remain, the most curious one is what instability was amplified. But despite of the unknowns, it is clear that the primary star could not have undergone this eruption without the help of the

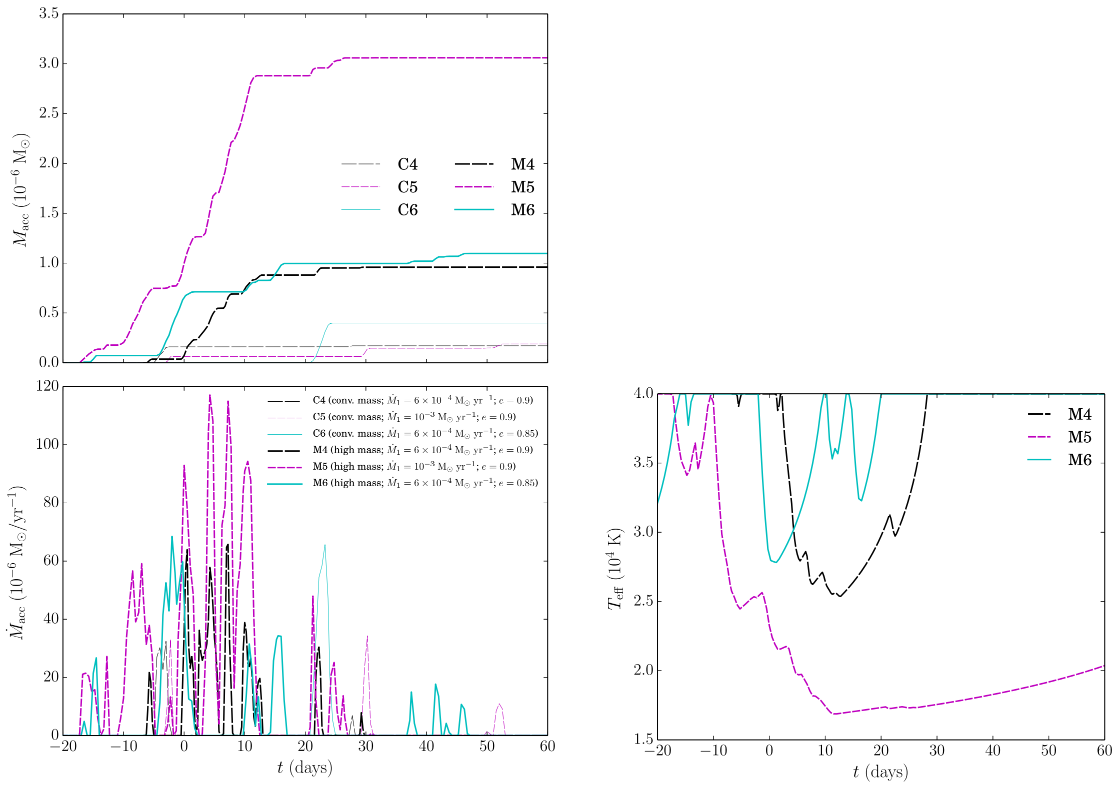

Fig. 2. **Left:** The accreted mass (upper panel) and the accretion rate (lower panel) for our simulations. Parameters are listed within the figure. It can be seen that for the high mass model (M-runs) much more mass is accreted onto the secondary. The main reason is the stronger gravity of the secondary. It is also very clear that a stronger mass loss rate of the primary (runs C5 and M5) causes a large increase in the accreted mass. The dependence on eccentricity is more complicated as lower eccentricity (runs C6 and M6) means larger periastron distance but also longer periastron passage. These two effects can combine in different ways, making the results difficult to predict. **Right:** The direction-averaged reduction in the effective temperature of the secondary.

secondary.

Accretion against ejected wind may seem to be a simple process, but in fact it is a problem with many fine details that requires a special code, careful parameter study, and high resolution simulations. The accretion may seem to be a small effect in one orbit, but in massive binary stars accretion is a process that may have a significant influence on the evolution of the stars, as the accreted massed can play a major role. For the duration of a few million years of evolution, a few $\mathrm{M}_\odot$ can be transferred between the stars. The influence is significant both for the donor and the gainer, and both stars are expected to undergo a different evolutionary path than their single counterparts. As mentioned earlier, it also determines the stellar mass before collapse and consequently what kind of compact remnant will be formed. The effects of losing and especially gaining a lot of mass will be important for the next generation of stellar evolution codes, a generation that moves from using theoretical models that are parameterized and often simplified, to relying on results of advanced 3D simulations.

This work used the Extreme Science and Engineering Discovery Environment (XSEDE) TACC/Stampede2 at the service-provider through allocation TG-AST150018. This research was enabled in part by support provided by Compute Canada (`www.computecanada.ca`), thanks to the sponsorship of Prof. A. Skorek. We acknowledge PRACE for awarding us access to the national supercomputer Cray XC40 at the High Performance Computing Center Stuttgart (HLRS) under the grant number PrcPA4873/ipramkas. We acknowledge support from the Chairman of the Department of Physics in Ariel University, Prof. Y. Raichlin, and the R&D authority.

References

Akashi, M., Soker, N., & Behar, E. 2006, MNRAS, 368, 1706

Akashi, M. S., Kashi, A., & Soker, N. 2013, New A, 18, 23

Corcoran, M. F., Hamaguchi, K., Liburd, J., et al. 2015, in AAS Meeting Abstracts, Vol. 225, 344.15

Damineli, A., Hillier, D. J., Corcoran, M. F., et al. 2008a, MNRAS, 386, 2330
Damineli, A., Hillier, D. J., Corcoran, M. F., et al. 2008b, MNRAS, 384, 1649
Davidson, K. & Humphreys, R. 2012, ASSL, 384
Davidson, K. & Humphreys, R. M. 1997, ARA&A, 35, 1
Davidson, K., Ishibashi, K., & Martin, J. C. 2017, Research Notes of the AAS, 1, 6
Davidson, K., Ishibashi, K., Martin, J. C., & Humphreys, R. M. 2018, ApJ, 858, 109
Davidson, K., Martin, J., Humphreys, R. M., et al. 2005, AJ, 129, 900
Davidson, K., Mehner, A., Humphreys, R. M., Martin, J. C., & Ishibashi, K. 2015, ApJ, 801, L15
De Marco, O. & Izzard, R. G. 2017, PASA, 34, e001
Eldridge, J. J. 2017, Population Synthesis of Massive Close Binary Evolution, in Handbook of Supernovae (Springer), 671
Heger, A. & Langer, N. 2000, ApJ, 544, 1016
Heger, A., Woosley, S. E., & Langer, N. 2000, New A Rev., 44, 297
Kashi, A. 2017, MNRAS, 464, 775
Kashi, A. 2019, MNRAS, 486, 926
Kashi, A., Davidson, K., & Humphreys, R. M. 2016, ApJ, 817, 66
Kashi, A. & Soker, N. 2009a, New A, 14, 11
Kashi, A. & Soker, N. 2009b, MNRAS, 397, 1426
Kashi, A. & Soker, N. 2016, ApJ, 825, 105
Kudritzki, R.-P. & Puls, J. 2000, ARA&A, 38, 613
Madura, T. I., Gull, T. R., Okazaki, A. T., et al. 2013, MNRAS, 436, 3820
Mehner, A., Davidson, K., Humphreys, R. M., et al. 2015, A&A, 578, A122
Mehner, A., de Wit, W. J., Asmus, D., et al. 2019, arXiv e-prints, arXiv:1908.09154
Meynet, G., Ekström, S., Georgy, C., Chiappini, C., & Maeder, A. 2009, Reviews in Modern Astronomy, 21, 97
Moffat, A. F. J. & Corcoran, M. F. 2009, ApJ, 707, 693
Nielsen, K. E., Corcoran, M. F., Gull, T. R., et al. 2007, ApJ, 660, 669
Okazaki, A. T., Owocki, S. P., Russell, C. M. P., & Corcoran, M. F. 2008, MNRAS, 388, L39
Parkin, E. R., Pittard, J. M., Corcoran, M. F., & Hamaguchi, K. 2011, ApJ, 726, 105
Parkin, E. R., Pittard, J. M., Corcoran, M. F., Hamaguchi, K., & Stevens, I. R. 2009, MNRAS, 394, 1758
Pittard, J. M. & Corcoran, M. F. 2002, A&A, 383, 636
Puls, J., Vink, J. S., & Najarro, F. 2008, A&A Rev., 16, 209
Sana, H., de Mink, S. E., de Koter, A., et al. 2012, Science, 337, 444
Soker, N. 2004, ApJ, 612, 1060
Soker, N. 2005a, ApJ, 635, 540
Soker, N. 2005b, ApJ, 619, 1064
Teodoro, M., Damineli, A., Arias, J. I., et al. 2012, ApJ, 746, 73
van den Heuvel, E. P. J. 2017, Supernovae and the Evolution of Close Binary Systems, in Handbook of Supernovae (Springer), 1527
Vink, J. S., Heger, A., Krumholz, M. R., et al. 2015, Highlights of Astronomy, 16, 51
Vishniac, E. T. 1994, ApJ, 428, 186

Stars and their variability observed from space
C. Neiner, W. W. Weiss, D. Baade, R. E. Griffin, C. C. Lovekin, A. F. J. Moffat (eds)

FROM THE SUN TO SOLAR-LIKE STARS: HOW DOES THE SOLAR MODELLING PROBLEM AFFECT OUR STUDIES OF SOLAR-LIKE OSCILLATORS?

G. Buldgen[1], C. Pezzotti[1], M. Farnir[2], S.J.A.J. Salmon[2] and P. Eggenberger[1]

Abstract. Since the first observations of solar oscillations in 1962, helioseismology has probably been one of the most successful fields of astrophysics. Besides the improvement of observational data, solar seismologists developed sophisticated techniques to infer the internal structure of the Sun. Back in the 1990s these comparisons showed a very high agreement between solar models and the Sun. However, the downward revision of the CNO surface abundances in the Sun in 2005, confirmed in 2009, induced a drastic reduction of this agreement leading to the so-called solar modelling problem. More than ten years later, in the era of the space-based photometry missions which have established asteroseismology of solar-like stars as a standard approach to obtain their masses, radii and ages, the solar modelling problem still awaits a solution. I will briefly present the results of new helioseismic inversions, discuss the current uncertainties of solar models and possible solutions to the solar modelling problem. I will also discuss how the solar problem can have significant implications for asteroseismology as a whole by discussing the modelling of the exoplanet-host star Kepler-444, thus impacting the fields requiring a precise and accurate knowledge of stellar masses, radii and ages, such as Galactic archaeology and exoplanetology.

Keywords: Stars: interiors, Stars: oscillations, Stars: fundamental parameters, Asteroseismology

1 Introduction

The advent of space based photometry missions such as CoRoT (Baglin et al. 2009), *Kepler* (Borucki et al. 2010), TESS (Ricker et al. 2015) and the BRITE constellation (Weiss et al. 2014) has enabled us to thoroughly test the physical ingredients of theoretical stellar models using asteroseismology. In this era of precision stellar physics, various modelling strategies can be adopted to derive fundamental stellar parameters, e.g. fitting of individual frequencies and frequency combinations or of global asteroseismic indices. Ultimately, the derived precision and accuracy of such inferences is not limited by the propagation of the observational uncertainties on the stellar properties, but by the limitations of theoretical stellar models.

A good illustration of the current shortcomings of stellar models is the so-called "solar modelling problem" which stems from the downward revision of the solar metallicity by Asplund et al. (2009). In this context, we show that varying the ingredients entering the standard solar model while still following its framework, we find a significant contribution to the uncertainties of the fundamental parameters of Kepler-444 at the level of precision of *Kepler* observations. The full results of our study are presented in Buldgen et al. (2019a). This paper is the first of a series aiming at a detailed characterization of the evolution of the planetary system of Kepler-444, following the methodology of Privitera et al. (2016b,c,a); Meynet et al. (2017); Rao et al. (2018).

In addition, we show the need for non-standard ingredients to fully reproduce seismic observations by *Kepler* for this well-known planet host star.

2 The solar modelling problem and its contributors

The solar modelling problem, resulting from the revision of the solar abundances by Asplund et al. (2009), has been the subject of long standing debates in the stellar modelling community (see e.g. Bahcall et al. 2005; Montalban et al. 2006; Antia & Basu 2005; Guzik 2008; Basu & Antia 2008, and references therein). To this day, no unequiivocal solution to the issue has been found, as multiple contributions can be at play to explain the observed disagreement between the new generation of standard solar models and helioseismic constraints.

In Fig. 1, we illustrate the impact of varying the opacity tables and abundance tables on the inversion of the entropy proxy defined in Buldgen et al. (2017b).

[1] Observatoire de Genève, Université de Genève, 51 Ch. Des Maillettes, CH1290 Sauverny, Suisse
[2] STAR Institute, Université de Liège, Allée du Six Août 19C, B4000 Liège, Belgium

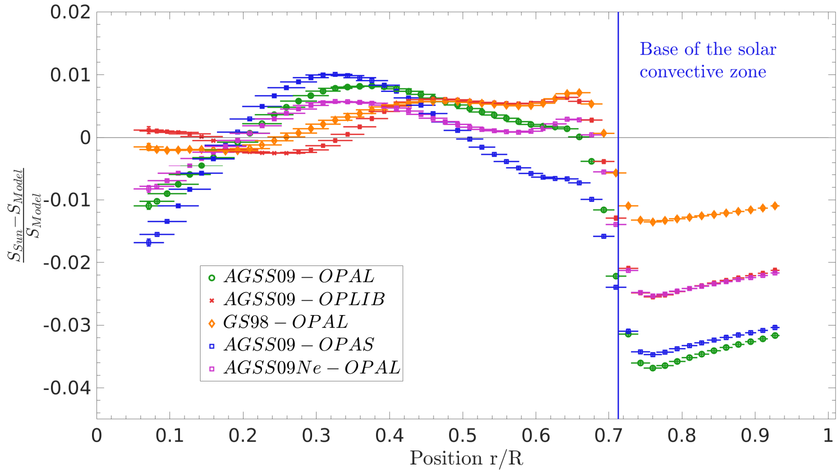

Fig. 1. Inversion of the entropy proxy for various standard solar models, built varying the opacity and chemical abundance tables.

These modifications are only few of many examples of physical ingredients that are uncertain. Others include: the chemical mixing at the base of the convective envelope, strongly related to the missing dynamical processes in standard solar models; recently, Zhang et al. (2019) put forward the combined effects of such additional mixing to early accreation and mass-loss to erase the discrepancies; Ayukov & Baturin (2017) computed modified solar models in extended calibration procedures by allowing opacity modifications and nuclear reaction rates modification, leading to similar results. Buldgen et al. (2019b) carried out an extensive comparison varying the equation of state, opacity tables, formalism for microscopic diffusion and convection and concluded on the necessity for a combination of opacity increase and mixing at the base of the convective zone. Similar results were obtained by Christensen-Dalsgaard et al. (2018) and opacity modifications were foreseen early on as a potential solution. The inadequacy between recently published opacity tables and the experimental measurements of Bailey et al. (2015); Nagayama et al. (2019) seems to also point towards further revision of radiative opacities in the future and sparked intense discussions in the community.

3 Implication for the modelling of Kepler-444

Given the very high precision of *Kepler* data, the limitations of stellar seismic modelling for the best targets are not only related to observational uncertainties but rather to the shortcomings of stellar models. In the case of Kepler-444, various existing studies have been carried out to determine its fundamental properties. In this section, we compute a full seismic modelling of Kepler-444 and discuss the implication of modifying the ingredients of the models on the final precision of the modelling results. We combine seismic data from Campante et al. (2015) to revised spectroscopic parameters (Mack et al. 2018) and GAIA DR2 parallaxes in our revised modelling (Evans et al. 2018; Gaia Collaboration et al. 2018).

3.1 *Tests of standard physics*

The details of the modelling procedure are given in Buldgen et al. (2019a); we recall here only a few key points. The first step of the modelling is carried out assuming a given set of physical ingredients and seismic and non-seismic constraints, using the AIMS software (Rendle et al. 2019) to compute the relevant probability distributions for the model parameters.

The second step of the seismic modelling procedure is carried out using a Levenberg-Marquardt minimization technique to test the variations in the optimal stellar parameters under the effects of changes to the model physical ingredients.

As a third step, we carry out seismic inversions of the mean density to further constrain the mass range of acceptable models of our sample. The results of the seismic inversion procedure are illustrated in Fig. 2. It is clear from this plot that the main dispersion of the results stems from the impact of the reference model and of the surface effect correction (see Buldgen et al. (2019a) for a detailed discussion). This is a general result of linear seismic inversions based on individual frequencies as shown in (Buldgen et al. 2015, 2016a,b, 2017a, 2018)).

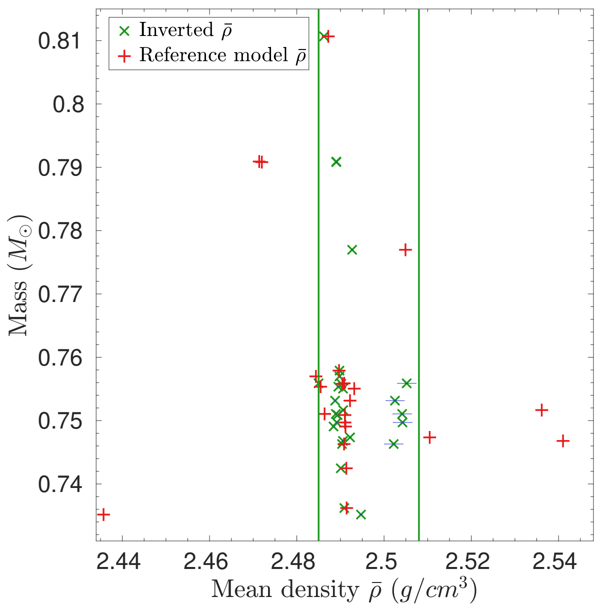

Fig. 2. Results of mean density inversions for the optimal Kepler-444 models in our study.

Based on this inversion procedure, we have built a reduced sample of reference models and obtained the following values for the mass, radius and age estimates of Kepler-444: 0.754 ± 0.030 $M_\odot$, 0.753 ± 0.010 $R_\odot$ and 11.00 ± 0.8 Gy. These uncertainties are slightly lower than those of Campante et al. (2015) who used multiple pipelines to determine the stellar fundamental parameters. Our study thus demonstrates the need to take such biases into account when carrying out detailed modelling of *Kepler* targets. Such aspects are also of paramount importance if seismic inversions of the structure are undertaken, as the trade-off between precision and accuracy is a key factor to avoid overinterpretations of the results.

3.2 Non-standard processes acting in Kepler-444

In addition to testing "standard" ingredients of stellar models, we also observed that a significant improvement of the agreement with the frequency ratios could be obtained when taking into account convective overshooting during the evolution of the transitory convective core at the beginning of the main-sequence. The inclusion of overshooting allows for ^{3}He out-of-equilibrium burning for up to 8 Gy. As the temperature dependency of out-of-equilibrium burning of ^{3}He is much higher than that of the equilibrium burning, a convective core is maintained throughout this phase. This was already seen in the CoRoT target HD203608 which has kept a convective core up to its present age (Deheuvels et al. 2010).

In the case of Kepler-444, the convective core has already disappeared but the sound-speed profile has kept a trace of this phase, as can be seen in the left panel of Fig. 3. This is then seen in the frequency ratios (as defined in Roxburgh & Vorontsov 2003) of Kepler-444, which are better reproduced when the overshooting is included, as shown in Fig. 3. This result is independent of the "standard" input physics used for the model.

As seen from Fig. 4, the key element is to maintain the convective core by keeping the ^{3}He abundance above its equilibrium value. Once this condition is not fulfilled, the convective core disappears. Thus, the chemical mixing of ^{3}He is the key aspect that is missing in the standard models and this may not necessarily be achieved only through convective overshooting, as rotation or even non-linear effects of gravity modes (Sonoi & Shibahashi 2012) may be at the origin of the mixing.

4 Conclusions

In our study, we have carried out a detailed seismic modelling of Kepler-444, building on our knowledge of the solar modelling problem to characterize the spread in fundamental parameters occurring from the uncertainties on key physical ingredients.

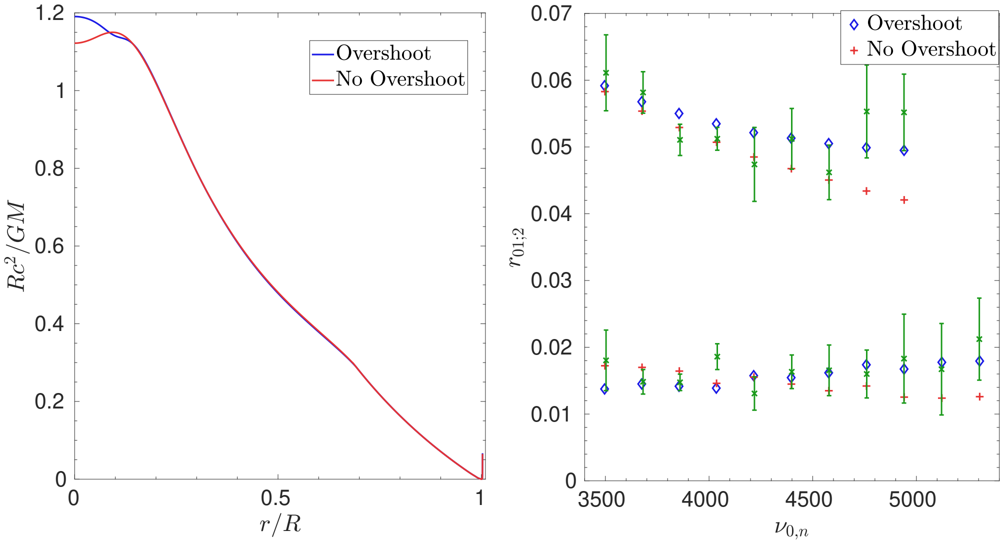

Fig. 3. Left panel: Sound speed profile of models of Kepler-444 built with and without core overshooting. Right panel: Frequency ratios for the models built with and without core overshooting.

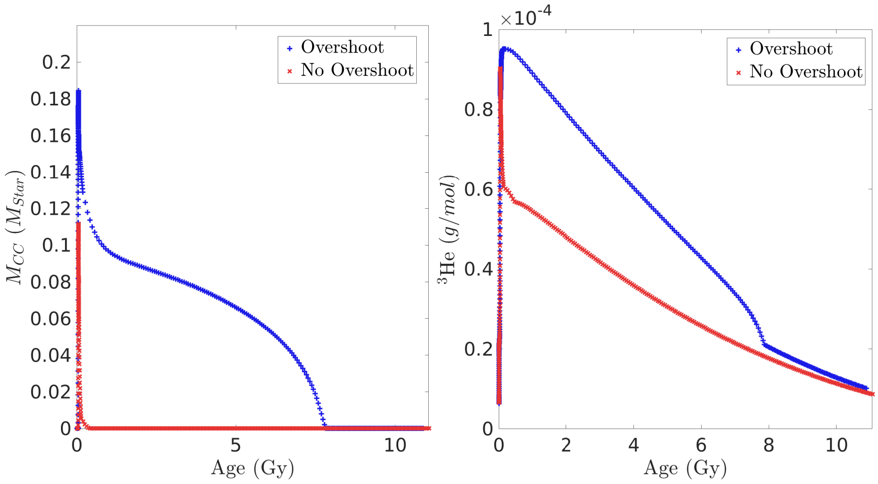

Fig. 4. Left panel: evolution of the mass of the convective core as a function of age for models of Kepler-444 with and without overshooting. Right panel: Central abundance of ^{3}He for models of Kepler-444 with and without overshooting.

We used a combination of global and local minimization techniques supplemented by inversions of the stellar mean density to determine precise and accurate stellar fundamental parameters for Kepler-444. In addition, we have shown that this low-mass star bore a convective core during a significant fraction of its life, namely 8 out of 11 Gy.

We have shown that the presence of the convective core is a result of out-of-equilibrium burning of ^{3}He, maintained through the additional mixing, bringing fresh fuel in the deep layers. While the presence of mixing seems required to fit the seismic data, its nature is still to be determined. In that sense, the very high quality of seismic data provided by space-based photometry missions provides an unprecedented opportunity to test the limitations of standard stellar models. In parallel, our study shows that not taking such limitations and the resulting biases into account may lead to clear overestimations of the precision of seismic modelling.

This work is sponsored by the Swiss National Science Foundation (project number 200020 − 172505). M.F. is supported by the FNRS (“Fonds National de la Recherche Scientifique”) through a FRIA (“Fonds pour la Formation la Recherche dans l’Industrie et l’Agriculture”) doctoral fellowship. S.J.A.J.S. is funded by the Wallonia-Brussels Federation ARC grant for Concerted Research Actions. This article used an adapted version of InversionKit, a software developed within the HELAS and SPACEINN networks, funded by the European Commissions’s Sixth and Seventh Framework Programmes.

References

Antia, H. M. & Basu, S. 2005, ApJ, 620, L129

Asplund, M., Grevesse, N., Sauval, A. J., & Scott, P. 2009, ARA&A, 47, 481

Ayukov, S. V. & Baturin, V. A. 2017, Astronomy Reports, 61, 901

Baglin, A., Auvergne, M., Barge, P., et al. 2009, in IAU Symposium, Vol. 253, IAU Symposium, ed. F. Pont, D. Sasselov, & M. J. Holman, 71–81

Bahcall, J. N., Basu, S., Pinsonneault, M., & Serenelli, A. M. 2005, ApJ, 618, 1049

Bailey, J. E., Nagayama, T., Loisel, G. P., et al. 2015, Nature, 517, 3

Basu, S. & Antia, H. M. 2008, Phys. Rep., 457, 217

Borucki, W. J., Koch, D., Basri, G., et al. 2010, Science, 327, 977

Buldgen, G., Farnir, M., Pezzotti, C., et al. 2019a, A&A, 630, A126

Buldgen, G., Reese, D., & Dupret, M.-A. 2017a, in EPJ Web of Conferences, Vol. 160, EPJ Web of Conferences, 03005

Buldgen, G., Reese, D. R., & Dupret, M. A. 2015, A&A, 583, A62

Buldgen, G., Reese, D. R., & Dupret, M. A. 2016a, A&A, 585, A109

Buldgen, G., Reese, D. R., & Dupret, M. A. 2018, A&A, 609, A95

Buldgen, G., Salmon, S. J. A. J., Noels, A., et al. 2019b, A&A, 621, A33

Buldgen, G., Salmon, S. J. A. J., Noels, A., et al. 2017b, A&A, 607, A58

Buldgen, G., Salmon, S. J. A. J., Reese, D. R., & Dupret, M. A. 2016b, A&A, 596, A73

Campante, T. L., Barclay, T., Swift, J. J., et al. 2015, ApJ, 799, 170

Christensen-Dalsgaard, J., Gough, D. O., & Knudstrup, E. 2018, MNRAS, 477, 3845

Deheuvels, S., Michel, E., Goupil, M. J., et al. 2010, A&A, 514, A31

Evans, D. W., Riello, M., De Angeli, F., et al. 2018, A&A, 616, A4

Gaia Collaboration, Brown, A. G. A., Vallenari, A., et al. 2018, A&A, 616, A1

Guzik, J. A. 2008, MmSAI, 79, 481

Mack, C. E., Strassmeier, K. G., Ilyin, I., et al. 2018, A&A, 612, A46

Meynet, G., Eggenberger, P., Privitera, G., et al. 2017, A&A, 602, L7

Montalban, J., Miglio, A., Theado, S., Noels, A., & Grevesse, N. 2006, Communications in Asteroseismology, 147, 80

Nagayama, T., Bailey, J. E., Loisel, G. P., et al. 2019, Phys. Rev. Lett., 122, 235001

Privitera, G., Meynet, G., Eggenberger, P., et al. 2016a, A&A, 593, L15

Privitera, G., Meynet, G., Eggenberger, P., et al. 2016b, A&A, 591, A45

Privitera, G., Meynet, G., Eggenberger, P., et al. 2016c, A&A, 593, A128

Rao, S., Meynet, G., Eggenberger, P., et al. 2018, A&A, 618, A18

Rendle, B. M., Buldgen, G., Miglio, A., et al. 2019, MNRAS, 484, 771

Ricker, G. R., Winn, J. N., Vanderspek, R., et al. 2015, JATIS, 1, 014003

Roxburgh, I. W. & Vorontsov, S. V. 2003, A&A, 411, 215

Sonoi, T. & Shibahashi, H. 2012, MNRAS, 422, 2642

Weiss, W. W., Rucinski, S. M., Moffat, A. F. J., et al. 2014, PASP, 126, 573

Zhang, Q.-S., Li, Y., & Christensen-Dalsgaard, J. 2019, ApJ, 881, 103

Stars and their variability observed from space
C. Neiner, W. W. Weiss, D. Baade, R. E. Griffin, C. C. Lovekin, A. F. J. Moffat (eds)

ASTEROSEISMIC BINARIES AS NON-SOLAR MIXING LENGTH CALIBRATORS

M. Joyce[1]

Abstract. We report on a preliminary investigation into the utility of various binary systems exhibiting solar-like oscillations as empirical calibrators of the convective mixing length parameter, $\alpha_{\rm MLT}$, in one dimensional (1-D) stellar models.

Keywords: Stars: evolution, asteroseismology, convection

1 Introduction

Asteroseismic binaries, especially those systems comprising solar analogs, are ideal laboratories in which to test our stellar modeling formalisms. One such formalism under recent scrutiny is the ad hoc adoption of a solar-calibrated value of the one-dimensional convective mixing length parameter, $\alpha_{\rm MLT}$, in models of highly non-solar stars.

The recent work of Joyce & Chaboyer (2018b) and Joyce & Chaboyer (2018a) has demonstrated that the assumption of solar-calibrated $\alpha_{\rm MLT}$ no longer constitutes a reliable method in 1-D stellar evolution modeling. This calls into question the use of current stellar evolution databases, all of which assume solar-calibrated mixing lengths in their isochrones.

These calibrations, however, require tight constraints and thus rely on high precision observations in many arenas: classical brightness measurements, interferometry, spectroscopy, and asteroseismology. In light of unprecedented observational scope and precision—thanks to Gaia, TESS, and stable, high resolution spectroscopy—the number of candidates for non-solar calibration is increasing.

Among recent, successful candidates for empirical mixing length calibrations are the metal-poor subgiant HD 140283 and α Centauri A and B (Creevey et al. 2015, 2017; Joyce & Chaboyer 2018b,a). This proceeding discusses the methods used to perform these calibrations, the necessary observational constraints, and the feasibility of extending this analysis to future TESS targets and members of known doubly oscillating or eclipsing binary systems, especially Procyon A.

2 Modeling technique

In Joyce & Chaboyer (2018b), it was discovered that the best-fitting mixing lengths for high-precision, 1-D stellar evolution models of α Cen A and B differed systematically at the level of $10 - 30\%$. This finding was robust against changes in the adopted surface boundary conditions, efficiency of diffusion, and use of convective overshoot in the models, all of which were computed with the Dartmouth Stellar Evolution Program (DSEP; Dotter et al. 2008).

Before seismic considerations were applied, models were optimized in accordance with classical observational constraints (e.g. radius, luminosity, surface abundance) and binary considerations: common initial helium and heavy metal abundances and a common present-day age. In requiring only that independently run grids of models for α Cen A and α Cen B satisfy their respective photometric, spectroscopic, and interferometric constraints at any common age, we discovered a clear bifurcation in the best-fitting convective mixing lengths for both stars, regardless of the other assumptions in the modeling physics. This behavior is shown in Figure 1.

The application of seismic constraints reduced the viable parameter space considerably, producing a set of fundamental parameter estimates for the α Cen system that is highly consistent with the literature. The impact of including a seismic agreement criterion in the reduced χ^2 score on the viable age range is shown in Figure 2.

[1] Research School of Astronomy and Astrophysics, Australian National University, Canberra, ACT 2611, Australia

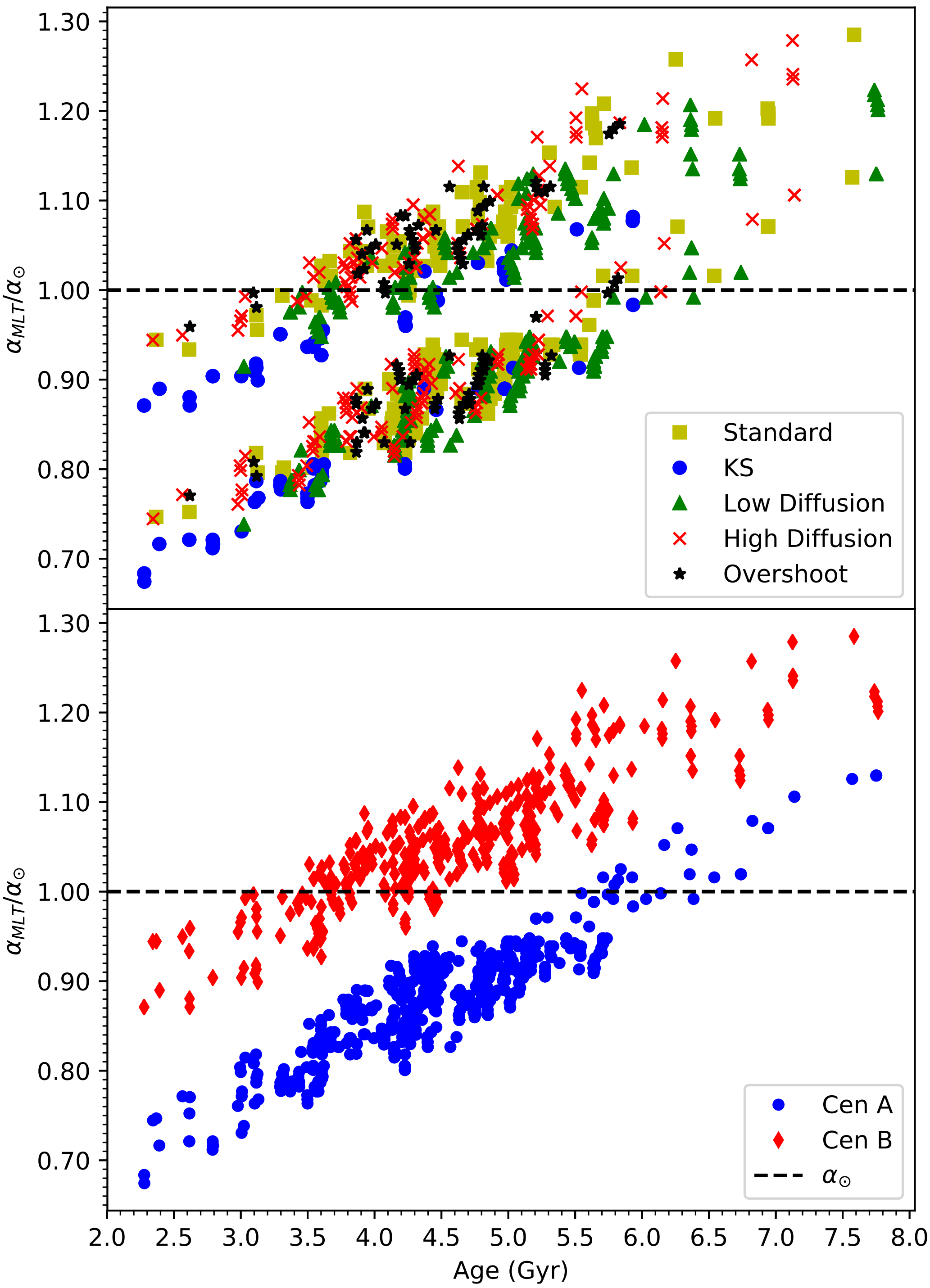

Fig. 1. Bifurcation of the optimal mixing length for α Cen A and B is found regardless of age at which their respective classical parameters are satisfied in large grids of stellar tracks. This figure was originally used in Joyce & Chaboyer (2018a).

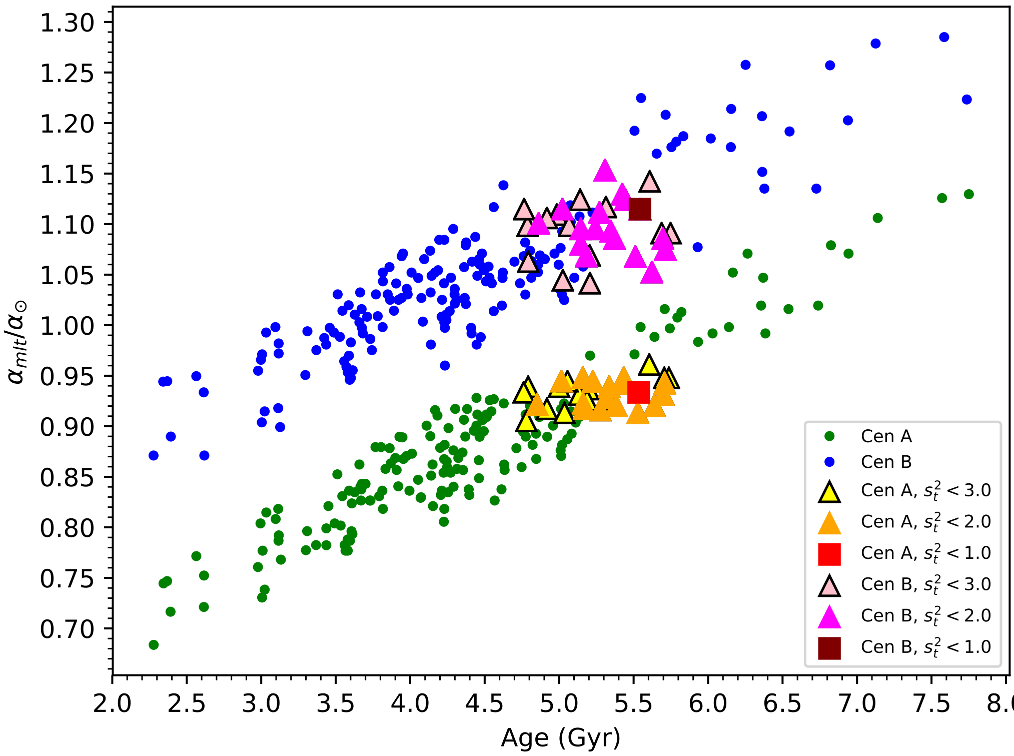

Fig. 2. Impact on Figure 1 of the inclusion of seismic constraints for both stars. This figure was originally used in Joyce & Chaboyer (2018a).

3 Necessity of high-precision observational constraints

The successful characterization of α Cen A and B and subsequent discovery of a robust bifurcation in optimal $\alpha_{\rm MLT}$between the two stars was made possible by a confluence of excellent observational measurements. We obtained the masses of α Cen A and B kinematically, the radii interferometrically, the luminosities from photometry, the shared surface abundance from high resolution spectroscopy, and the stellar interior constraints from asteroseismic analysis of p-mode frequencies.

This set of inference methods is, unfortunately, not reproducible for any other system at this time. Contenders we have investigated include doubly-oscillating *Kepler* targets, catalogs of eclipsing binaries, and catalogs of low-mass stars with interferometry. In all cases where the precision of some observational quantity is sufficient, other types of observations are missing.

Though we cannot rebuild the full suite of constraints available for α Cen A and B for any other candidate, we anticipate that some candidates fulfill enough of the requirements that meaningful inferences about their interior mixing can still be made. We believe the most effective candidates for follow-up are Procyon A and 16 Cyg A and B. In the case of Procyon A, we must grapple with difficulties in reproducing the observed seismic signature, which is more physically complex than for α Cen A or B (Compton et al. 2019). In the case of 16 Cyg A and B, preliminary tests have suggested that its observational constraints are simply too weak to restrict the domain of consistency of $\alpha_{\rm MLT}$, as shown in Figure 3. These setbacks aside, our modeling efforts are ongoing.

4 Conclusions

We are unable to reproduce the seismic analysis performed on α Cen A and B for Procyon A using similar methods at this time. However, we are continuing our search for other viable candidates and exploring adjustments to the modeling methodology such that it may be become better adapted to stars with weaker (and

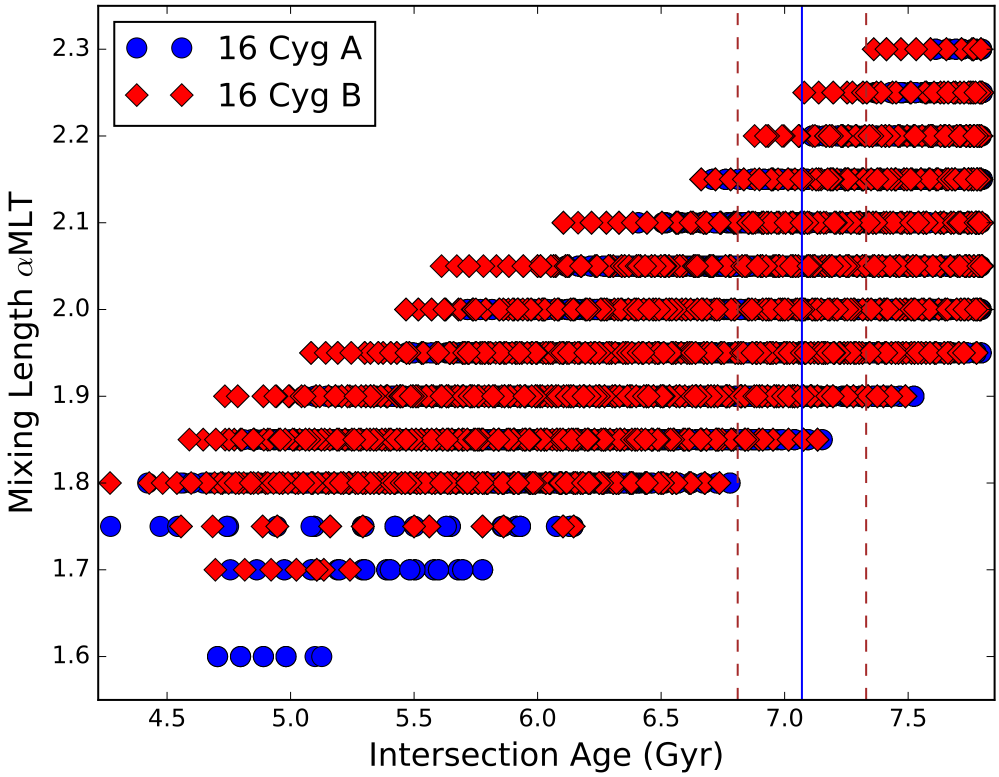

Fig. 3. Lack of $\alpha_{\rm MLT}$ bifurcation across wide age range for 16 Cyg A and B, likely due to relative weakness of observational constraints compared to α Cen A and B. Vertical lines mark literature age estimates and their uncertainty.

fewer) observational constraints.

An understanding of the relationships between $\alpha_{\rm MLT}$ and other fundamental stellar parameters, grounded by direct observational data, will contribute to the development of more sophisticated stellar tracks and isochrones. Such science is necessary to maintain the utility of 1-D stellar structure and evolution models in the current observational landscape.

M. Joyce acknowledges Martin Asplund and Australian Research Council grant No. DP150100250 for supporting this ongoing research. M. Joyce likewise acknowledges Tim Bedding and Tim R. White for support of this work and resources at the University of Sydney and Thomas Nordlander for providing high-precision spectroscopic constraints of a number of preliminary candidates.

References

Compton, D. L., Bedding, T. R., & Stello, D. 2019, MNRAS, 485, 560

Creevey, O. L., Metcalfe, T. S., Schultheis, M., et al. 2017, A&A, 601, A67

Creevey, O. L., Thévenin, F., Berio, P., et al. 2015, A&A, 575, A26

Dotter, A., Chaboyer, B., Jevremović, D., et al. 2008, ApJS, 178, 89

Joyce, M. & Chaboyer, B. 2018a, ApJ, 864, 99

Joyce, M. & Chaboyer, B. 2018b, ApJ, 856, 10

Stars and their variability observed from space
C. Neiner, W. W. Weiss, D. Baade, R. E. Griffin, C. C. Lovekin, A. F. J. Moffat (eds)

UNBIASED SEISMIC MODEL FITTING

T. Kallinger[1]

Abstract. The unprecedented quality of data from space missions like Kepler and TESS enables detailed seismic studies of the interiors of many stars. However, such studies often require the computation of theoretical frequencies and the imperfect modelling of the star's near-surface layers introduces systematic uncertainties that hamper a direct comparison with the observations. To overcome this, various corrections have been introduced to reduce the systematic shifts between observed and model frequencies. Even though such corrections generally improve the analysis, they still bear unpredictable systematics and therefore prevent us from making the best use of the observations. I present here a new approach that uses probabilistic methods to marginalise the surface effect. This therefore enables an unbiased search for a best-fit model by using only the observed frequencies and without the need to correct for the surface effect. The approach is tested with Kepler data of the red giant component in the eclipsing binary system KIC 8410637 and gives accurate stellar fundamental parameters that are in agreement with independent measurements.

Keywords: stars: late-type – stars: oscillations (including pulsations) – stars: fundamental parameters – stars: solar-type – stars: individual: KIC 8410637

1 Introduction

Asteroseismology is a major part of the space photometry revolution. The detection of solar-type oscillations in hundreds of sun-like stars and thousands of evolved cool giants has triggered many breakthroughs in stellar astrophysics (e.g. Bedding et al. 2011; Beck et al. 2012; Kallinger et al. 2010b). The availability of photometric time-series data of unprecedented duration and quality should enable precise determination of both the global stellar parameters and interiors by comparing the observed oscillations to the eigen-frequencies of stellar models.

However, such an approach still suffers from uncertainties in the models, like the insufficient treatment of convection. The resulting systematic shifts in the theoretical frequencies complicate a direct comparison between observed and model frequencies. This so-called seismic surface effect was first recognised for the Sun (e.g. Brown 1984) and has since been extensively investigated (e.g. Houdek et al. 2017). Lacking a definitive conclusion, Kjeldsen et al. (2008) proposed to empirically model the surface effects as a power law in frequency. They calibrated the power-law exponent to the difference between the observed solar frequencies and theoretical frequencies computed from a standard solar model. Such a correction is indeed required to avoid matching the observed frequencies to a model with systematically incorrect properties and interior structure. However, their correction over-estimates the effect at low frequencies and assumes that the frequency shifts follow the same power law in all stars.

Ball & Gizon (2014) proposed to model the surface effect as a combination of an inverse and cubic frequency term normalised by the mode inertia, which does not rely on a solar calibration. This improved the correction for the Sun but is likely also not universally applicable. In fact, Gruberbauer et al. (2013) showed that the surface effect significantly varies across the HR-diagram and Sonoi et al. (2015) argued that instead of calibrating it to the Sun, the surface corrections should be constrained from realistic physical modelling as provided by 3D hydrodynamical simulations.

Even though standard surface corrections have extensively been used (e.g. Mathur et al. 2012) it is not yet understood if they are actually applicable for stars different from the Sun. To verify this is quite difficult as one needs accurate independent measurements for the stellar properties, which are usually not available for the mostly faint stars targeted by photometric space missions like *Kepler*. Rare exceptions are eclipsing binary systems with at least one oscillatory component, for which precise and accurate dynamic masses and radii can be determined from radial velocity and photometric eclipse observations (e.g. Gaulme et al. 2016). Ball et al. (2018) investigated three such systems with a red giant component and found that none of the available surface corrections are sufficient to seismically model the stars in agreement with the dynamic parameters.

[1] Institut für Astrophysik, Universität Wien, Türkenschanzstrasse 17, 1180 Vienna, Austria

Here, I introduce a new method that allows for unbiased seismic forward modelling without the need to explicitly correct the model frequencies for the surface effect. The method defines the search for a match between a set of observed and the corresponding model frequencies in a Bayesian framework. It thereby introduces an additional frequency offset parameter, which is then marginalised without the need to explicitly know its value.

2 Bayesian asteroseismic forward modelling

In seismic forward modelling the search for a best fit is usually quantified by minimising the sum of the squared differences between the observed and model frequencies. However, to consistently encode possibly available prior information and to make use of all advantages that come with Bayesian statistics it is more convenient to perform the model fitting in a probabilistic framework. Kallinger et al. (2010a) formulated asteroseismic model fitting in terms of Bayes' theorem,

$$p(\mathcal{M}|\mathcal{D},\mathcal{I}) = \frac{p(\mathcal{M}|\mathcal{I}) \cdot p(\mathcal{D}|\mathcal{M},\mathcal{I})}{p(\mathcal{D},\mathcal{I})}. \tag{2.1}$$

The prior probability $p(\mathcal{M}|\mathcal{I})$ is for a specific model ($\mathcal{M}$) for which one can encode prior information ($\mathcal{I}$) on, e.g., the fundamental parameters of the star. The likelihood function,

$$p(\mathcal{D}|\mathcal{M},\mathcal{I}) = \prod_{\mathrm{i}}^{N_{\mathrm{obs}}} \frac{1}{\sigma_{\mathrm{i}}\sqrt{2\pi}} \exp\left(\frac{-(\nu_{\mathrm{i,obs}} - \nu_{\mathrm{i,mod}})^2}{2\sigma_{\mathrm{i}}^2}\right), \tag{2.2}$$

combines the probability that a given model frequency ν_{mod} matches an observed frequency ν_{obs}, which follows from the Gaussian distribution of the uncertainties $\sigma^2 = \sigma^2_{\mathrm{obs}} + \sigma^2_{\mathrm{mod}}$. The denominator in Eq. 2.1 is a normalisation factor for the specific model probability in the form of $p(\mathcal{D},\mathcal{I}) = \sum_{\mathrm{i}} p(\mathcal{M}_{\mathrm{i}}|\mathcal{I}) \cdot p(\mathcal{D}|\mathcal{M}_{\mathrm{i}},\mathcal{I})$. By maximising Eq. 2.1 one can identify a best match between the observed and model frequencies and determine the best-fit model parameters and their uncertainties from the marginal distribution of the corresponding parameter.

Even though the Bayesian approach allows for a realistic error determination and statistically correct comparison of different solutions, it still suffers (in its current form) from systematic errors in the model frequencies. However, one of the major strengths of the probabilistic framework is the marginalisation of model parameters. Any parameter θ, needed to describe a model, can be marginalised by applying the sum rule of probability theory (Jaynes ????), which in the case of continuous parameters, turns into an integral. By integrating the full posterior over the parameter range of θ, one obtains the marginal posterior that still retains the overall effects of including θ in the model, but is independent of any particular choice of its value.

Gruberbauer et al. (2012) have shown that this "Bayesian trick" can perfectly be applied to the unknown systematic errors in seismic model fitting. They showed that, if Δ_{i} is the systematic shift of an individual model frequency, Eq. 2.2 can be modified as

$$p(\mathcal{D}|\mathcal{M},\mathcal{I}) = \prod_{\mathrm{i}}^{N_{\mathrm{obs}}} \int_{\Delta_{\mathrm{i,min}}}^{\Delta_{\mathrm{i,max}}} p(\Delta_{\mathrm{i}}|\mathcal{I}) \times \frac{1}{\sigma_{\mathrm{i}}\sqrt{2\pi}} \exp\left(\frac{-(\nu_{\mathrm{i,obs}} - \nu_{\mathrm{i,mod}} - \Delta_{\mathrm{i}})^2}{2\sigma_{\mathrm{i}}^2}\right) d\Delta_{\mathrm{i}}, \tag{2.3}$$

to marginalise (i.e., to remove) the influence of the surface effect in the model search. Even though Δ_{i} remains an unknown parameter, its influence is fully considered in the probabilistic analysis as long as its upper and lower boundaries can be roughly estimated. Here, $p(\Delta|\mathcal{I})$ encodes prior information about the expected behaviour of the surface effect, with $\int p(\Delta_{\mathrm{i}}|\mathcal{I}) d\Delta_{\mathrm{i}} = 1$. Gruberbauer et al. (2012) suggested a parameter-free beta prior $p(\Delta_{\mathrm{i}}|\mathcal{I}) = 2(\Delta_{\mathrm{i,max}} - \Delta_{\mathrm{i}})/\Delta^2_{\mathrm{i,max}}$, leading to a linearly decreasing probability density with the advantage of being properly normalised, and of reaching zero at $\Delta_{\mathrm{i}} = \Delta_{\mathrm{i,max}}$. Finally, $\Delta_{\mathrm{i,min}}$ is set to zero and $\Delta_{\mathrm{i,max}} = a \cdot \Delta\nu \left(\nu_{\mathrm{i,obs}}/\nu_{\mathrm{max}}\right)^b$, where a and b are fixed to 0.3 and 4.9, respectively. In fact, the latter are not very critical as long as it is ensured that the real Δ_{i} is covered by the range. Similar values of a and b or even a different functional form of $\Delta_{\mathrm{i,max}}$ (e.g., a Lorentzian) give similar results.

The above-described surface-correction independent approach correctly identifies the mean density of a star but has only low discriminative power to disentangle its mass and radius (see Fig. 1a). This is not surprising since the marginalisation of Δ_{i} gives similar weight to a relatively broad range of models. Gruberbauer et al. (2013) overcame this problem by encoding prior information about the star's fundamental parameters. However, this should be avoided, since the model's $M - L - T_{\mathrm{eff}}$ relation very much depends on the adopted mixing length parameter and primordial chemical composition, and is therefore highly model-dependent. Instead, I aim to constrain the models by using *only* the observed frequencies.

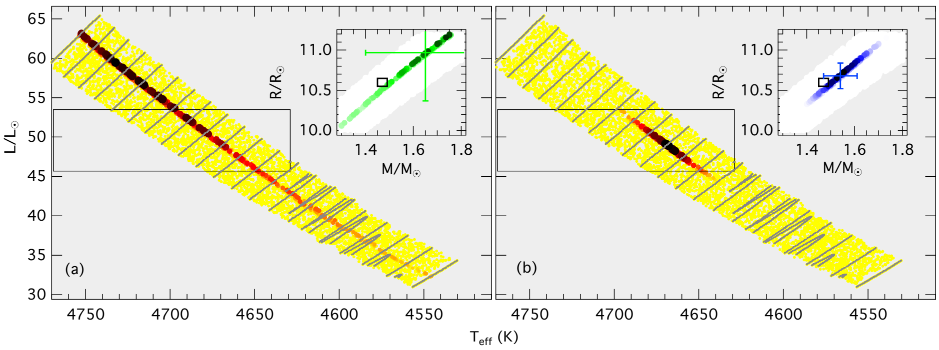

Fig. 1. HR diagram showing the uncertainty box of KIC 8410637 and a subset of the stellar model grid used to fit the observed frequencies. Grey dots indicate the original grid and colored dots are interpolated models with the color scale indicating the goodness of the fit (the darker the better). Panels (b) and (c) show posterior model probabilities from the surface-correction independent Bayesian forward modelling based on Eq. 2.3 and 2.5, respectively. Inserts show the same in the $M - R$ plane and the corresponding best-fit values and uncertainties. The black error box shows the dynamic solution from Themeßl et al. (2018).

It is well-known that periodic deviations from the regular mode pattern are the signature of acoustic glitches (e.g. Gough 1990) due to sharp structural variations in the stellar interior. While the modulation period is related to the sound-travel time from the structural feature to the stellar surface, its amplitude depends on the width of the glitch. In red giants, the main source of observable discontinuities is the 2nd helium ionisation zone, and Miglio et al. (2010) found that its relative acoustic radius varies with mass (in their models). It should therefore be possible to use the glitch signal to disentangle the mass and radius in the above fit.

Apart from the glitch signal, the oscillation modes of a red giant are also modulated by the so-called curvature, which can be described by a second-order development of the asymptotic theory and is presumably due to hydrogen ionisation just below the stellar surface. To disentangle the glitch and curvature signal in the observed and model frequencies (which also contain a modulation from the surface effect!), I follow Kallinger et al. (2018) and compute a second-order polynomial fit and subtract it from the original frequencies as,

$$\nu'(n) = \nu(n) - \left[\nu_{\rm c} + \Delta\nu_{\rm cor}\left(n - n_{\rm c} + \frac{\alpha}{2}(n - n_{\rm c})^2\right)\right], \tag{2.4}$$

where $\nu_{\rm c}$ and $n_{\rm c}$ are the frequency and radial order of the central radial mode, respectively, α is the curvature parameter, and $\Delta\nu_{\rm cor}$ the curvature-corrected large separation. One can now add a term to Eq. 2.3,

$$p(\mathcal{D}|\mathcal{M},\mathcal{I}) = \prod_{\rm i}^{N_{\rm obs}} \int_{\Delta_{\rm i,min}}^{\Delta_{\rm i,max}} \frac{p(\Delta_{\rm i}|\mathcal{I})}{\sigma_{\rm i}\sqrt{2\pi}} \exp\left(\frac{-(\nu_{\rm i,obs} - \nu_{\rm i,mod} - \gamma\Delta_{\rm i})^2}{2\sigma_{\rm i}^2}\right) d\Delta_{\rm i} \frac{1}{\sigma'_{\rm i}\sqrt{2\pi}} \exp\left(\frac{-(\nu'_{\rm i,obs} - \nu'_{\rm i,mod})^2}{2\sigma'^2_{\rm i}}\right), \tag{2.5}$$

which also compares the glitch contributions of the observed and model frequencies, where the uncertainties σ' result from Eq. 2.4.

3 The test case KIC 8410637 and conclusions

To demonstrate the abilities of the Bayesian asteroseismic forward modelling I use the *Kepler* data of KIC 8410637, which is a detached eclipsing binary system consisting of a RGB and MS component, that circle each other in a 408-day orbit (Hekker et al. 2010; Frandsen et al. 2013). Themeßl et al. (2018) determined the mass and radius of the RGB component to be $1.47 \pm 0.02\,\mathrm{M}_\odot$ and $10.60 \pm 0.05\,\mathrm{R}_\odot$, respectively, and found the system to have a near solar chemical composition. The photometry of KIC 8410637 reveals a clear red-giant oscillation spectrum, which makes the system an ideal target for testing various asteroseismic applications, (Kallinger et al. 2018; Ball et al. 2018; Li et al. 2018; Buldgen et al. 2019). To extract the mode frequencies from the *Kepler* data I follow the approach of Kallinger (2019) and determine a sequence of six consecutive radial modes with frequencies in agreement with the measurements of Themeßl et al. (2018) and Li et al. (2018).

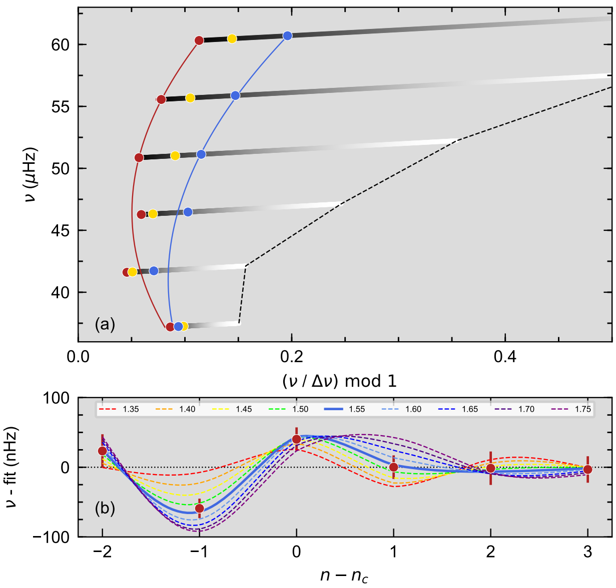

Fig. 2. Echelle diagram of KIC 8410637. Panel (a) shows the observed (red symbols) and best-fit model frequencies, where yellow and blue symbols correspond to fits based on Eq. 2.3 and 2.5, respectively. Red and blue lines give second-order polynomial fits to the frequencies (i.e. curvature). The grey-shaded trails indicate the prior probability density for varying Δ_i, with black and white corresponding to a probability of one and zero, respectively. The dashed line gives $\Delta_\mathrm{i,max}$. Panel (b) gives the curvature-corrected observed frequenices and a sequence of models (colored lines), where instead of the actual model frequencies, spline fits are shown for better visibility.

The stellar models used in this analysis are computed with `MESA`* (Paxton et al. 2011) for an initial chemical composition of (Y, Z) = (0.286, 0.023) and $\alpha_\mathrm{MLT} = 2.1$ and cover a mass ranging from 1 to 2 $\mathrm{M}_\odot$ in steps of 0.05 $\mathrm{M}_\odot$ from the early giant branch ($\log g \leq 3.4$) to after the core-He burning phase. Overshooting and mass loss are turned off. Adiabatic mode frequencies for the roughly 110 000 RGB and post-RGB models are then computed with the `GYRE`† stellar oscillation code (Townsend & Teitler 2013), using an outer mechanical boundary condition as described by Christensen-Dalsgaard (2008).

A fit to the observed frequencies based on Eq. 2.3 results in a precise mean stellar density of $1.260 \pm 0.006 \times 10^{-3} \rho_\odot$, which is also in good agreement with the dynamic solution. The mass and radius are, however, only poorly constrained and in principle overestimated in comparison to the dynamic values (see Fig. 1a). Considering also the glitch signal (fit based on Eq. 2.5) significantly changes the situation and reveals a much better defined mass and radius of $1.54 \pm 0.07\,\mathrm{M}_\odot$ and $10.68 \pm 0.17\,\mathrm{R}_\odot$, respectively (see Fig. 1b), which agree to within -5 ± 5 and $0.7 \pm 1.6\%$ with the dynamic measurements of Themeßl et al. (2018). The observed and best-fit model frequencies are illustrated in Fig. 2. As a byproduct, the fit also allows one to quantify the actual surface effect of the best-fit model frequencies, which is inconsistent with predictions from the widely used surface corrections of Kjeldsen et al. (2008) and Ball & Gizon (2014). More details about this are, however, beyond the scope of this proceedings paper and will soon be presented in a separate article (Kallinger, A&A submitted).

References

Ball, W. H. & Gizon, L. 2014, A&A, 568, A123

Ball, W. H., Themeßl, N., & Hekker, S. 2018, MNRAS, 478, 4697

Beck, P. G., Montalban, J., Kallinger, T., et al. 2012, Nature, 481, 55

Bedding, T. R., Mosser, B., Huber, D., et al. 2011, Nature, 471, 608

Brown, T. M. 1984, Science, 226, 687

Buldgen, G., Rendle, B., Sonoi, T., et al. 2019, MNRAS, 482, 2305

*http://mesa.sourceforge.net

†https://bitbucket.org/rhdtownsend/gyre/wiki/Home

Christensen-Dalsgaard, J. 2008, Ap&SS, 316, 113
Frandsen, S., Lehmann, H., Hekker, S., et al. 2013, A&A, 556, A138
Gaulme, P., McKeever, J., Jackiewicz, J., et al. 2016, ApJ, 832, 121
Gough, D. O. 1990, in Lecture Notes in Physics, Berlin Springer Verlag, Vol. 367, Progress of Seismology of the Sun and Stars, ed. Y. Osaki & H. Shibahashi, 283
Gruberbauer, M., Guenther, D. B., & Kallinger, T. 2012, ApJ, 749, 109
Gruberbauer, M., Guenther, D. B., MacLeod, K., & Kallinger, T. 2013, MNRAS, 435, 242
Hekker, S., Debosscher, J., Huber, D., et al. 2010, ApJ, 713, L187
Houdek, G., Trampedach, R., Aarslev, M. J., & Christensen-Dalsgaard, J. 2017, MNRAS, 464, L124
Jaynes, E. T. ???? (Cambridge: Cambridge University Press, timestamp = 2011-05-10T10:42:42.000+0200, title = Probability theory: The logic of science, year = 2003)
Kallinger, T. 2019, arXiv e-prints, arXiv:1906.09428
Kallinger, T., Beck, P. G., Stello, D., & Garcia, R. A. 2018, A&A, 616, A104
Kallinger, T., Gruberbauer, M., Guenther, D. B., Fossati, L., & Weiss, W. W. 2010a, A&A, 510, A106
Kallinger, T., Mosser, B., Hekker, S., et al. 2010b, A&A, 522, A1
Kjeldsen, H., Bedding, T. R., & Christensen-Dalsgaard, J. 2008, ApJ, 683, L175
Li, T., Bedding, T. R., Huber, D., et al. 2018, MNRAS, 475, 981
Mathur, S., Metcalfe, T. S., Woitaszek, M., et al. 2012, ApJ, 749, 152
Miglio, A., Montalbán, J., Carrier, F., et al. 2010, A&A, 520, L6
Paxton, B., Bildsten, L., Dotter, A., et al. 2011, ApJS, 192, 3
Sonoi, T., Samadi, R., Belkacem, K., et al. 2015, A&A, 583, A112
Themeßl, N., Hekker, S., Southworth, J., et al. 2018, MNRAS, 478, 4669
Townsend, R. H. D. & Teitler, S. A. 2013, MNRAS, 435, 3406

Stars and their variability observed from space
C. Neiner, W. W. Weiss, D. Baade, R. E. Griffin, C. C. Lovekin, A. F. J. Moffat (eds)

THE RELEVANCE OF PARTIAL IONIZATION IN THE OUTER LAYERS OF F STARS

A. Brito[1,2] and I. Lopes[1]

Abstract. The present-day quality of asteroseismic data enables us to probe the complex outer layers of Sun-like stars. F stars are particularly interesting, given their diversity of magnetic and rotational behaviours. Using a seismic diagnostic based on the phase shift of the acoustic waves, we found a trend, in the form of a power-law dependence, that correlates the ionisation processes occurring in these external layers with the rotation periods of the stars. In addition, we have studied the internal structure of the outer layers of 10 main-sequence F stars; we found that the rotational characteristics of those stars can be distinguished by the relative location of the partial ionisation region of heavy elements and the base of the convective zone. Since the region near the base of the convective zone (the tachocline) is known to have a strong influence in the expected dynamo-driven mechanism, these results might be important for improving and extending our understanding of the relations between magnetism and rotation in those stars.

Keywords: Chemical processes: partial ionisation, stars: rotation, oscillations, low-mass stars

1 Introduction

Main-sequence stars of spectral type F exhibit a diversity of rotational and magnetic properties that makes them interesting targets for studies of stellar structure and evolution. Late-F stars are generally slow rotators ($P_{\rm rot} \gtrsim 10$ days) whereas early-F stars are generally rapid rotators ($P_{\rm rot} \lesssim 10$ days). These two distinct rotational regimes for stars on the main sequence were observed and studied by Kraft (1967). The transition between the two regimes occurs around type F5, and can be considered abrupt since it consists of a decrease in rotational velocity from $\sim$20 to $\sim$80 km s^{-1} for stars with masses in the range $1.2 - 1.4$ M$_\odot$. Concerning magnetic activity, slow rotators are usually less active than rapid rotators. It is also worth remembering that we are dealing with stars with convective external envelopes for which the magnetic field is thought to be amplified by a dynamo mechanism acting at the tachocline – the shear layer located between the radiative and convective zones (e.g., Spiegel & Zahn 1992; Brun & Browning 2017).

In this work, we probe the outer convective layers of 10 main-sequence F-type stars using a seismic diagnostic that is particularly sensitive to partial ionisation processes occurring in their more external layers. The stars were chosen from the *Kepler Legacy* sample (Lund et al. 2017). We separated the stars into two subgroups. One consists of the cooler stars, the other consists of the hotter stars – as shown in Table 1. The non-linear seismic diagnostic used to analyse the 10 stars is a robust one based on the phase shift of the acoustic waves reflected by the surface of the star. This phase shift $\alpha(\omega)$ enters the eigenfrequency equation resulting from the asymptotic analysis (e.g., Duvall 1982)

$$F(W) = \pi \left(\frac{\alpha(\omega) + n}{\omega} \right) , \tag{1.1}$$

where ω is the angular frequency, $W = \omega/(l + 1/2)$ determines the penetration depth of the acoustic mode, l is the degree and n the radial order of the mode. The function $F(W)$ is determined by the profile of the speed of sound in the stellar interiors. After some manipulation of the eigenfrequency equation 1.1, it is possible to define a non-linear seismic diagnostic (Brodskii & Vorontsov 1987),

$$\beta(\omega) = \frac{\omega - n\left(\frac{\partial\omega}{\partial n}\right) - L\left(\frac{\partial\omega}{\partial L}\right)}{\left(\frac{\partial\omega}{\partial n}\right)} , \tag{1.2}$$

that is suitable for obtaining information about the relevant partial ionisation processes occurring in the outer stellar convective layers. This diagnostic was studied extensively in the solar case (e.g., Vorontsov & Zharkov

[1] CENTRA - center for astrophysics and gravitation, Instituto Superior Técnico, University of Lisbon, Portugal
[2] ISG – Business & Economics School, Department of Mathematics, Lisbon, Portugal

Table 1. Observational parameters

Star Id.	T_{eff} (K)	[Fe/H] (dex)
C1	6033 ± 77	-0.23 ± 0.1
C2	6177 ± 77	-0.07 ± 0.1
C3	6122 ± 77	-0.08 ± 0.1
C4	6140 ± 77	-0.19 ± 0.1
C5	6179 ± 77	-0.08 ± 0.1
H1	6479 ± 77	0.01 ± 0.1
H2	6344 ± 77	0.02 ± 0.1
H3	6326 ± 77	0.01 ± 0.1
H4	6538 ± 77	0.16 ± 0.1
H5	6331 ± 77	-0.05 ± 0.1

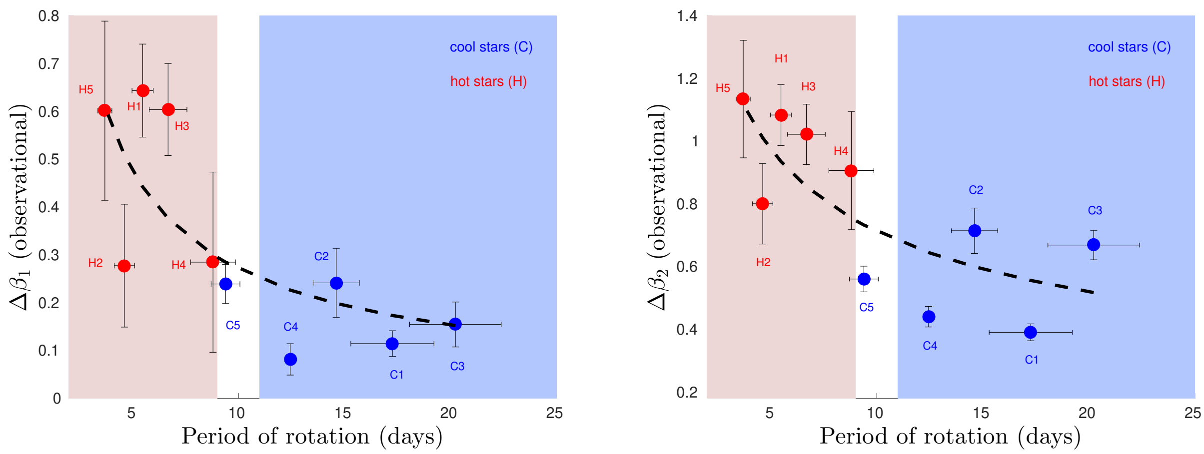

Fig. 1. The ionisation indices $\Delta\beta_1$ and $\Delta\beta_2$ plotted against the rotation period of the selected stars. The dashed line represents the result of a power law fit, $\Delta\beta_i = a \times P_{\mathrm{rot}}^{b}$ to the data ($i = 1, 2$). Specifically, $\Delta\beta_1 = 1.777 \times P_{\mathrm{rot}}^{(-0.8176)}$ and $\Delta\beta_2 = 2.023 \times P_{\mathrm{rot}}^{(-0.4536)}$. The vertical white bar signalises the values of the rotation period around which the transition between the two rotational regimes on the main sequence occurs (the Kraft break). Rotation periods were taken from Benomar et al. (2015) and Kiefer et al. (2017).

1989; Lopes & Gough 2001), enabling a measurement of the solar helium abundance and contributing to the calibration of the equation of state (Pamiatnykh et al. 1991). More recently, Brito & Lopes (2017a), studying the theoretical envelopes of *Kepler* F stars, used the diagnostic $\beta(\omega)$ to define two seismic ionisation indices ($\Delta\beta_1$ and $\Delta\beta_2$) that can be related to the magnitude of the partial ionisation processes in the envelopes of Sun-like stars. It was noticed that the ionisation indices have larger values for hot stars than for cool ones. Owing to the differences in the rotational behaviours of cool and hot stars we plotted the ionisation indices against the rotation period of the stars being studied and found a correlation in the form of a power law (Fig. 1) which strongly suggests that partial ionisation might be acting as an important factor for understanding better the complex relations between rotation and magnetism.

2 How partial ionisation correlates with the rotational regimes for main-sequence F stars

In order to explore further the importance of partial ionisation and how it might influence the macroscopic properties of stars, we need new tools. To that end, we defined a mean effective ionic charge, $\overline{Q}$, (Brito & Lopes 2017b), which is simply the sum of the average ionic charges of each atomic species considered in the theoretical models of our sample of 10 main-sequence F stars. For computating $\overline{Q}$ in this particular case, we considered three heavy elements (carbon, nitrogen, and oxygen) alongside hydrogen and helium,

$$\overline{Q} = \langle Q_{\mathrm{H}} \rangle + \langle Q_{\mathrm{He}} \rangle + \langle Q_{\mathrm{C}} \rangle + \langle Q_{\mathrm{N}} \rangle + \langle Q_{\mathrm{O}} \rangle, \tag{2.1}$$

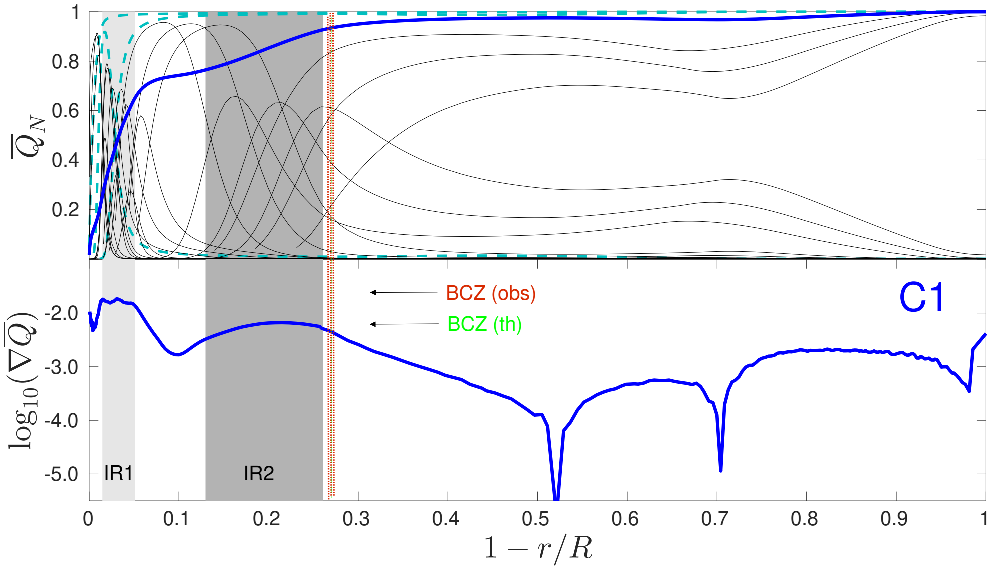

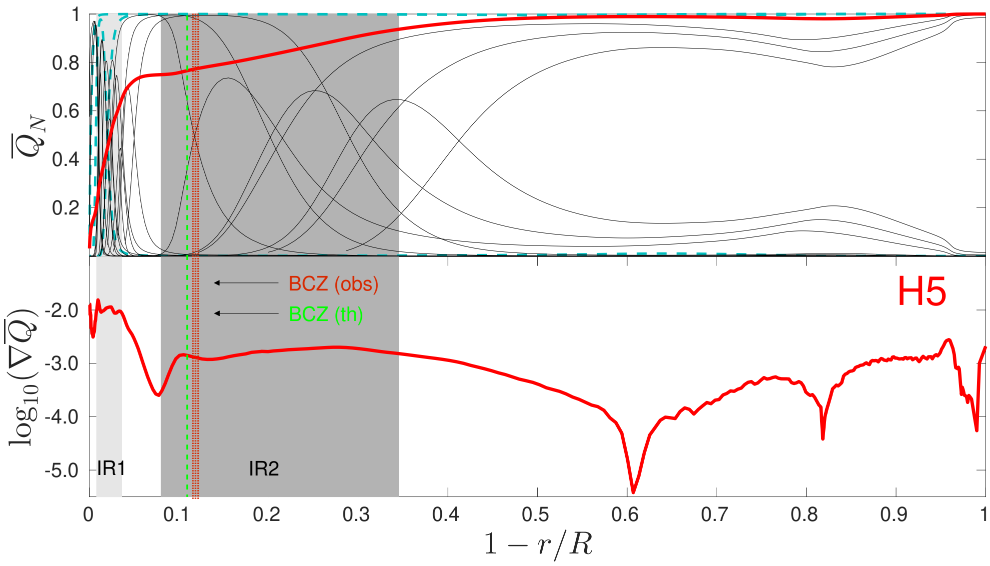

Fig. 2. Detailed representation of the partial ionisation processes occurring in the interior of a cool star (top; in blue) and of a hot star (bottom; in red). The ionisation fractions of light elements (H, He) are indicated by dashed lines, and the ionisation fractions of heavy elements are indicated with thin solid black lines (see Brito & Lopes 2017b). The mean effective ionic charge normalised to its maximum value, $\overline{Q}_N = \overline{Q}/\max\overline{Q}$, is given by the thick solid lines (blue, red) in each case. Below, the corresponding gradient of the ionic charge is also given by a thick solid line in each case. The partial ionisation regions IR1 and IR2 represent the locations where the effective mean ionic charge increases significantly. IR1 coincides with the partial ionisation region of helium, while IR2 is associated with partial ionisation of heavier elements. Both regions are marked with vertical grey bars. The locations of the base of the convective envelopes for both stars are also shown. The red vertical dashed line represents the observed value. The thickness of the line indicates $r_{\rm bcz}$ approximately within a 1-σ error bar. Dashed vertical green lines represent the theoretical value of $r_{\rm bcz}$. All quantities are plotted as a function of the star's fractional radius.

where

$$\langle Q_{\rm elem}\rangle \equiv \sum_{j=1}^{q_{\rm elem}} j\, x_{j,{\rm elem}}\ , \tag{2.2}$$

is the mean ionic charge of each element. $x_{j,{\rm elem}}$ is the number of atoms of element "elem" in the ionisation state j divided by the total number of atoms of the element "elem". By taking the gradient of $\overline{Q}$ it is possible

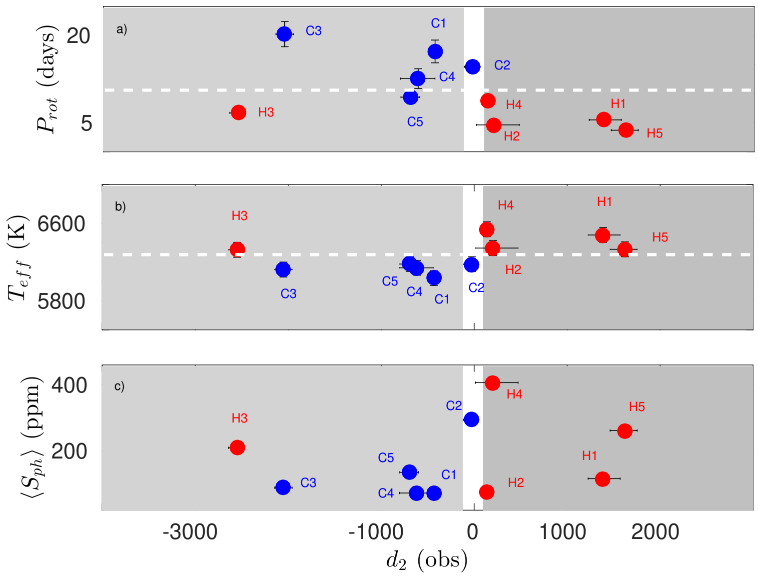

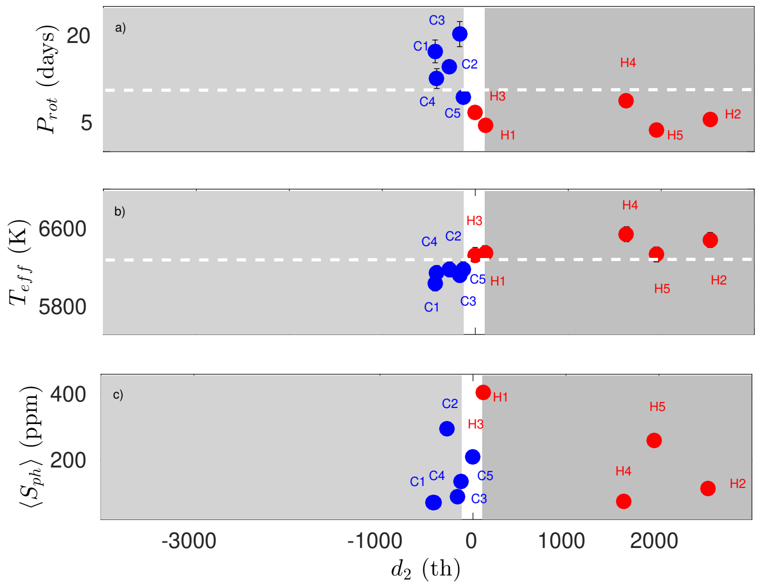

Fig. 3. d_2 represents the difference between the acoustic depths of the location of the region IR2 and the acoustic depth of the location of the BCZ (Eq. 2.3). A negative value means that the location of the region IR2 is above the base of the convective zone, i.e., IR2 is closer to the surface than the BCZ. A zero value occurs when the two zones coincide. A positive value means that the region IR2 is located (mostly) below the BCZ. The white vertical bar marks the overlap of IR2 (at its central point) and BCZ. White horizontal dashed lines correspond to the threshold values of the Kraft break for the rotation period ($\sim$ 10 days) and $T_{\rm eff}$ ($\sim$ 6250 K). d_2 is plotted against: a) the rotation period ($P_{\rm rot}$), b) the effective temperature ($T_{\rm eff}$), and c) the magnetic photometric index ($S_{\rm ph}$). Top panel: The observed value for the location of the base of the convective zone was used. Bottom panel: The theoretical value for the location of the base of the convective zone was used.

to identify and locate the relevant ionisation zones in stellar interiors. Fig. 2 shows the mean effective ionic charge for a representative cool star (top panel) and for a representative hot star (bottom panel) in our sample. These figures are very interesting, for several reasons. First, they illustrate that in the more external regions of these stars we can see the influence of two main ionisation regions. IR1 corresponds to a region where hydrogen and helium are the main contributors to the variation of the ionic charge, and we therefore named IR1 as the partial ionisation region of light elements. The other relevant ionisation region represented, IR2, is completely dominated by the ionisation of heavy elements, because at that depth light elements are already fully ionised. We therefore named IR2 as the partial ionisation region of heavy elements. Secondly, another aspect that stands out in these figures is the location of the base of the convective zone. For cool stars, the base of the convective zone is located predominantly *outside* the ionisation region IR2, whereas for hot stars the base of the convective zone is located predominantly *inside* the ionisation region IR2.

Finally, this interesting structural detail that differentiates the two subgroups of stars, cool and hot, can be quantified by the introduction of an indicator that we called the acoustic distance d_2. This indicator gives us the relative position between the region IR2 and the base of the convective zone. We define it as follows,

$$d_2 = \tau_{\mathrm{IR2}} - \tau_{\mathrm{BCZ}} \,. \tag{2.3}$$

With the help of this indicator we can distinguish the rotational regimes for main-sequence F stars. Thus, the structure of a slowly-rotating F star is characterised by a negative value of d_2 ($d_2 < 0$), whereas the structure of a rapidly-rotating F star is characterised by a positive value of d_2 ($d_2 > 0$). The most interesting case is the transitional one, where the transition between the two main rotational regimes occurs. This case corresponds to $d_2 \approx 0$, meaning that the base of the convective zone is located well within the central region of the partial ionisation zone of heavy elements. To investigate this relation further, we plotted the effective temperatures, the rotation periods, and a photometric activity index (Mathur et al. 2014) against the distance d_2 (Fig. 3). It is noteworthy that this Figure shows that the distance d_2 does indeed separate the two main rotational regimes for our sample of 10 main-sequence F stars. The different types of stellar structure and rotational regime thus appear to be related to the microphysics of stellar interiors, specifically to the partial ionisation processes occurring in the upper layers.

3 Conclusions

In this work we studied the internal ionisation profiles of a sample of 10 main-sequence F stars and correlate them with the two distinct rotational regimes observed among these stars. More specifically, we relate the two rotational regimes with the relative location of the base of the convective zone and the region where heavy elements ionise. For a detailed reading about this result we refer to the paper Brito & Lopes (2019).

From a physical standpoint we would like to highlight that the relevant regions of partial ionisation are regions of large variations of ionic charges. At the same time it is well-known that electric charges are among the main ingredients needed for the generation of magnetic fields, and that these play an important role in the mechanisms of redistribution of angular momentum (e.g., Aerts et al. 2019). Also interesting is the fact that there is an overlapping of T_{eff} and mass for the hotter stars in this study and γ Doradus stars. The latter are known to be gravity mode oscillators with the pulsations being driven by the convective flux blocking mechanism at the base of their convective envelope (e.g., Guzik et al. 2000; Samadi et al. 2015). Therefore, the relative location of partial ionisation zones and convective boundaries seems to be worthy of special attention in future studies of stellar interiors.

The computation of the observed seismic diagnostic used in this work to establish a connection between ionisation and rotation greatly benefits from a large number of high-precision detected oscillation mode frequencies. We hope that in a nearby future, the observational data from the TESS (Ricker et al. 2014) and PLATO (Rauer et al. 2014) missions allow us to extend this study to other spectral types and probe further for this connection between ionisation, rotation and magnetism.

We are grateful to Conny Aerts for drawing our attention to F-type gravity-mode pulsators that, we hope, will allow us to place this study in a broader context in the future.

References

Aerts, C., Mathis, S., & Rogers, T. M. 2019, ARA&A, 57, 35

Benomar, O., Takata, M., Shibahashi, H., Ceillier, T., & García, R. A. 2015, MNRAS, 452, 2654

Brito, A. & Lopes, I. 2017a, ApJ, 843, 75

Brito, A. & Lopes, I. 2017b, MNRAS, 466, 2123

Brito, A. & Lopes, I. 2019, MNRAS, 488, 1558

Brodskii, M. A. & Vorontsov, S. V. 1987, Soviet Astronomy Letters, 13, 179

Brun, A. S. & Browning, M. K. 2017, Living Reviews in Solar Physics, 14, 4

Duvall, T. L., J. 1982, Nature, 300, 242

Guzik, J. A., Kaye, A. B., Bradley, P. A., Cox, A. N., & Neuforge, C. 2000, ApJ, 542, L57

Kiefer, R., Schad, A., Davies, G., & Roth, M. 2017, A&A, 598, A77

Kraft, R. P. 1967, ApJ, 150, 551

Lopes, I. P. & Gough, D. 2001, MNRAS, 322, 473

Lund, M. N., Silva Aguirre, V., Davies, G. R., et al. 2017, ApJ, 835, 172

Mathur, S., García, R. A., Ballot, J., et al. 2014, A&A, 562, A124

Pamiatnykh, A. A., Vorontsov, S. V., & Dappen, W. 1991, A&A, 248, 263

Rauer, H., Catala, C., Aerts, C., et al. 2014, Experimental Astronomy, 38, 249

Ricker, G. R., Winn, J. N., Vanderspek, R., et al. 2014, SPIE Conference Series, Vol. 9143, Transiting Exoplanet Survey Satellite (TESS), 914320

Samadi, R., Belkacem, K., & Sonoi, T. 2015, in EAS Publications Series, Vol. 73-74, EAS Publications Series, 111–191

Spiegel, E. A. & Zahn, J. P. 1992, A&A, 265, 106

Vorontsov, S. V. & Zharkov, V. N. 1989, Astrophys. Space Phys. Res., 7, 1

Stars and their variability observed from space
C. Neiner, W. W. Weiss, D. Baade, R. E. Griffin, C. C. Lovekin, A. F. J. Moffat (eds)

KIC 11971405 - THE SPB STAR WITH THE FOUR ASYMPTOTIC SEQUENCES OF G MODES

W. Szewczuk[1], P. Walczak[1] and J. Daszyńska-Daszkiewicz[1]

Abstract. We re-analsed all *Kepler* photometric data of the fast rotating B-type pulsator KIC 11971405; we extracted pulsation frequencies, and found five period spacing patterns, i.e. sequences of frequencies quasi-equally spaced in period.

Our modelling shows that four sequences could be associated with prograde sectoral modes with the degrees $\ell = 1, 2, 3, 4$; the fifth sequence is most probably accidental. Fitting the four g-mode sequences simultaneously offers a unique opportunity to obtain constraints on the internal processes described by the free parameters, e.g., convective overshoot and other types of mixing. We found that at least moderate overshoot from a convective core is reqired, but a high amount of mixing in the radiative zone is not supported.

In addition we confirmed a need to revise the opacity data. In order to obtain unstable theoretical counterparts of the observed modes, a significant increase in the opacity coefficient in the driving zone appeared necessary.

Keywords: stars: early-type, individual: KIC 11971405, oscillations, rotation, atomic data: opacities

1 Introduction

KIC 11971405 is a B5 IV-Ve star observed by *Kepler* during its nominal mission. Pápics et al. (2017) analysed *Kepler* spectroscopic observations and photometric data. The values they derived for the effective temperature and gravity are $T_{\rm eff} = 15\,100 \pm 200$ and logg= 3.94 ± 0.06, respectively, thus placing the star in the middle of the Slowly Pulsating B-type (SPB) instability strip (see e. g., Walczak et al. 2015; Szewczuk & Daszyńska-Daszkiewicz 2017). Pápics et al. (2017) also concluded that the star is a fast rotator with $V_{\rm rot} \sin i = 242 \pm 14\,{\rm km\,s^{-1}}$.

The *Kepler* light-curve of the star shows high complexity. The analysis by Pápics et al. (2017) revealed several photometric outbursts, and a rich oscillation spectrum. They found three period spacing patterns which, according to asymptotic theory (see e.g. Tassoul 1980; Bouabid et al. 2013), can be interpreted as high radial-order gravity (g) modes with consecutive radial orders.

Our re-analysis of *Kepler* data is described in Section 2, and the results of seismic modelling in Section 3. Conclusions end the paper.

2 Frequency analysis

Observations of KIC 11971405 spanning the whole duration of the nominal mission of *Kepler* (i.e., Q0–17) are available in the public domain. To extract the light-curve from target pixel files we proceeded in a similar manner as in the case of KIC 3240411 (Szewczuk & Daszyńska-Daszkiewicz 2018). As before, we used *PyKE* package (Vinícius et al. 2017; Still & Barclay 2012).

We ended up with 60874 data points, and followed a standard pre-whitening procedure until the S/N ratio of the highest peak in the periodogram was above four. We found 188 frequencies, and noticed that in some parts of the residues the variance was much higher than the average for the whole data set, especially at time when outbursts occurred. We decided to remove those parts, leaving 36009 data points spanning 867 days. We then repeated the pre-whitening procedure on that data set and found 1131 frequencies, among which 1096 seemed to be independent.

We looked for patterns in period, and found five such structures, three already found by Pápics et al. (2017) and two additional ones. Fig. 1 shows four of patterns which we were able to associate with high radial-order g modes with consecutive degrees $\ell = 1$, 2, 3 and 4 (see the next Section). The one not shown in the figure was most probably accidental.

[1] Astronomical Institute of the Wroclaw University, Kopernika 11, 51-622 Wrocław, Poland

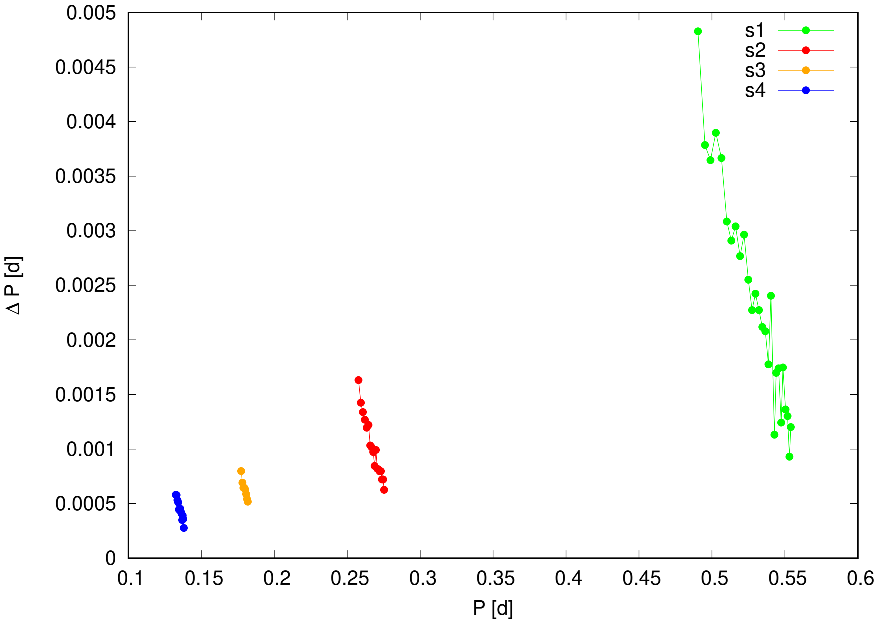

Fig. 1. 4 out of 5 period spacing patterns we found are shown in this plot of P vs ΔP. The two sequences with periods less than 0.2 d are new ones.

3 Seismic modelling

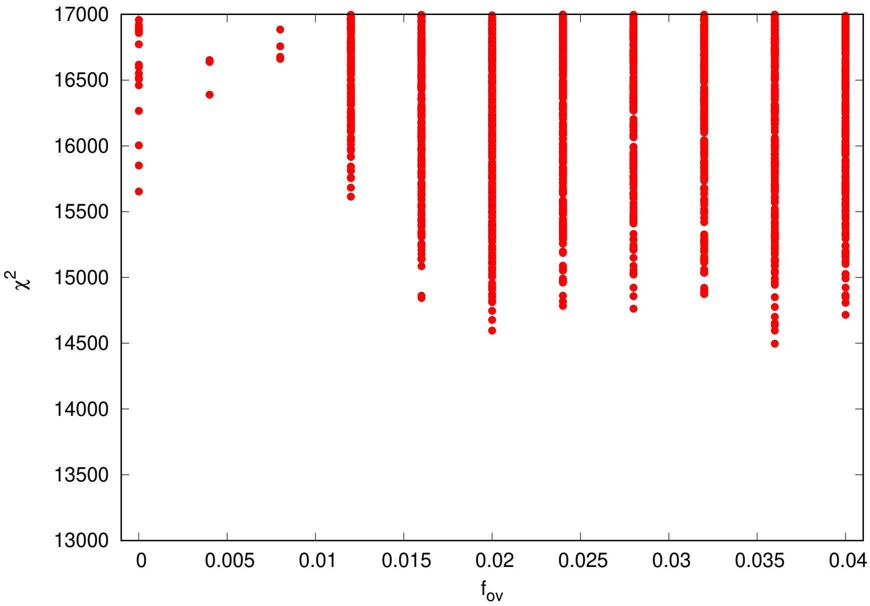

Fig. 2. The discriminant χ^2 as a function of overshoot parameter, $f_{\rm ov}$, in the set of models calculated with the standard OPLIB opacity data.

The main goal of our seismic analysis was to estimate the amount of internal mixing in the KIC 11971405. We therefore constructed a grid of stellar and oscillation models and compared them with observations using the χ^2 discriminant (see e.g., Szewczuk & Daszyńska-Daszkiewicz 2018).

Evolutionary calculations were carried out with the MESA package (see e.g., Paxton et al. 2011, 2013, 2015, 2018). We calculated models inside 3σ error box in effective temperature and gravity, with a step in mass of $\Delta M = 0.05 \mathrm{M}_\odot$, rotation velocity $\Delta V_{\rm rot} = 10 \mathrm{km\,s^{-1}}$ (in the range 220 - 400 $\mathrm{km\,s^{-1}}$) and an overshoot parameter from convective core in its exponential description $\Delta f_{\rm ov} = 0.004$ (in the range $0 - 0.04$). In these

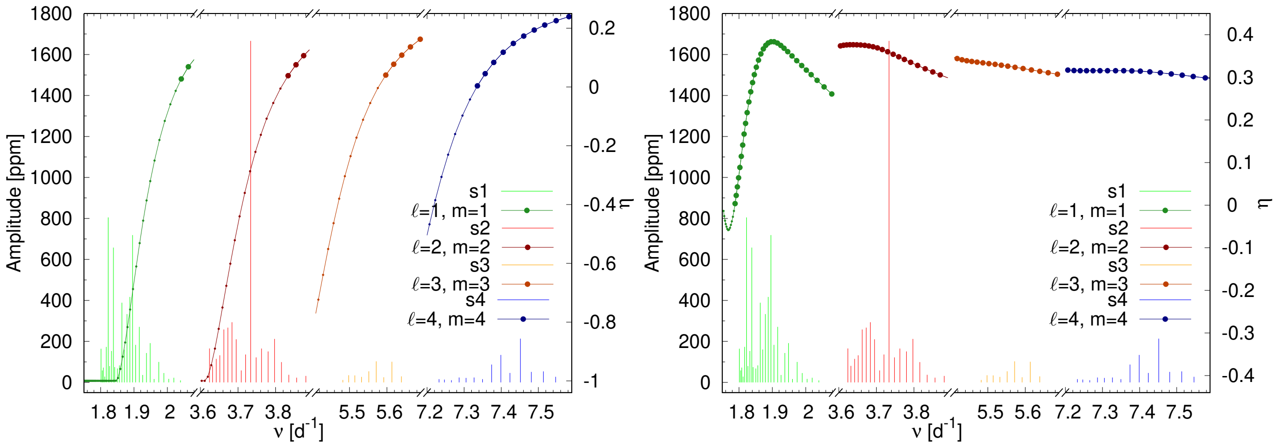

Fig. 3. Left: Comparison of the observed and theoretical frequencies in the best model. Observed frequencies with their amplitudes are marked by continuous vertical lines (left y-axis). Theoretical frequencies with their instability parameter, η, in the best model calculated with the standard OPLIB opacity data are marked by dots (right y-axis). Bigger symbols denote unstable modes, i.e with $\eta > 0$. Smaller symbols are stable modes. **Right:** The same as in the left panel but for the best model calculated with the modified opacity data.

computations we assumed rigid rotation, a AGSS09 chemical mixture (Asplund et al. 2009), OPLIB opacity data (Colgan et al. 2015, 2016) and an initial amount of hydrogen, $X = 0.71$. We tested a few values of metallicity $Z = 0.013$, 0.014, 0.0148, 0.0149, 0.0150, 0.0151, 0.0152, 0.016 and extra mixing in the radiative zone (described in terms of mixing coefficient min_D_mix = 0, 50, 100, 500, 1000, 5000, 10000 $\mathrm{cm^2\,s^{-1}}$). In order to include the effects of rotation on pulsations we adopted the traditional approximation. We used customized oscillation code of Prof. Dziembowski (see e.g., Dziembowski et al. 2007). At this stage the step in the rotation velocity was reduced to $\Delta V_{\rm rot} = 0.05\,\mathrm{km\,s^{-1}}$.

Mode identification was carried out simultaneously with seismic modelling, i.e., we compared the values of χ^2 for models from our grid and the given pattern (s1, s2, s3 and s4) for different pairs of (ℓ, m) numbers. The best fitting was reached when the sequence s1 corresponded to the modes ($\ell = 1, m = +1$), s2 to the modes (2, 2), s3 to the modes (3, 3), and s4 to the modes (4, 4). The remaining sequence not depicted in Fig. 1 is most probably composed of modes with various (ℓ, m) numbers and/or a combination of frequencies. Furthermore, we found that the overshoot parameter, $f_{\rm ov}$, should be approximately higher than 0.016 (see Fig. 2). Moreover, we do not see the need for very efficient mixing in the radiative zone. The best models in the sense of low χ^2 were with min_D_mix = 0, 50 and 100 with the minimum reached for 50. There is also no strong dependence on metallicity.

One of the best models from our grid has the following parameters: $M = 4.65\mathrm{M}_\odot$, $V_{\rm rot} = 267\,\mathrm{km\,s^{-1}}$ (54% $V_{\rm crit}$), $X = 0.71$, $Z = 0.014$, $f_{\rm ov} = 0.02$, min_D_mix = 50 $\mathrm{cm^2\,s^{-1}}$, $\log T_{\rm eff} = 4.183$, $\log L/\mathrm{L}_\odot = 2.709$ and $\log g = 4.08$. Fig. 3 shows a comparison of the theoretical and observed frequencies. While the frequency values in this model reproduce the observed ones quite well, there was a serious problem with mode excitation.

A common problem with mode excitation in the seismic models of B-type pulsators suggests a need to revise the opacity data (see e.g., Daszyńska-Daszkiewicz et al. 2017b,a). We therefore recalculated our grid of models with modified OPLIB opacity data. As did Szewczuk & Daszyńska-Daszkiewicz (2018), we increased opacity at $\log T = 5.46$ by 200%, at $\log T = 5.22$ by 100%, and decreased it at $\log T = 5.06$ by 50%.

From a grid with modified opacities we identified our best model as having the following parameters: $M = 4.55\mathrm{M}_\odot$, $V_{\rm rot} = 283\,\mathrm{km\,s^{-1}}$ (59% $V_{\rm crit}$), $X = 0.71$, $Z = 0.014$, $f_{\rm ov} = 0.02$, min_D_mix = 50 $\mathrm{cm^2\,s^{-1}}$, $\log T_{\rm eff} = 4.167$, $\log L/\mathrm{L}_\odot = 2.698$ and $\log g = 4.02$. But this time all observed frequencies from the sequences have unstable theoretical counterparts, or in other words their instability parameters, η, are greater than zero (see the right panel of Fig. 3).

4 Conclusions

As far as we know, this is the first attempt to fit simultaneously the four observed sequences of period spacing. These patterns correspond to prograde sectoral modes of consecutive mode degrees $\ell = 1, 2, 3, 4$. In total we fitted 70 frequencies.

On the one hand, we found a need of at least moderate overshooting from the convective core and relatively low mixing in the radiative envelope, and also a need to modify the opacity data. But on the other hand, there is still room to increase the goodness of the model of fitting. In particular, the effect of the amount of hydrogen and different modifications of the opacity data should be tested. Our assumption of rigid rotation may also be inappropriate, and differential rotation should be tested. Finally, we note that the rotation velocities which we consider here place our models on the border of the validity of the traditional approximation.

Clearly, further studies are necessary. More elaborate descriptions of our seismic modelling along with the extended grid of models of KIC 11971405 will be published elsewhere.

This work was supported financially by the Polish National Science Centre grant 2018/29/B/ST9/01940. Calculations were carried out using resources provided by Wroclaw Centre for Networking and Supercomputing (http://wcss.pl), grant no. 265. Funding for the Kepler mission is provided by the NASA Science Mission directorate .Some of the data presented in this paper were obtained from the Multimission Archive at the Space Telescope Science Institute (MAST). STScI is operated by the Association of Universities for Research in Astronomy, Inc., under NASA contract NAS5-26555. Support for MAST for non-HST data is provided by the NASA Office of Space Science via grant NNX09AF08G and by other grants and contracts.

References

Asplund, M., Grevesse, N., Sauval, A. J., & Scott, P. 2009, ARA&A, 47, 481

Bouabid, M. P., Dupret, M. A., Salmon, S., et al. 2013, MNRAS, 429, 2500

Colgan, J., Kilcrease, D. P., Magee, N. H., et al. 2015, High Energy Density Physics, 14, 33

Colgan, J., Kilcrease, D. P., Magee, N. H., et al. 2016, ApJ, 817, 116

Daszyńska-Daszkiewicz, J., Pamyatnykh, A. A., Walczak, P., et al. 2017a, MNRAS, 466, 2284

Daszyńska-Daszkiewicz, J., Walczak, P., Pamyatnykh, A., Jerzykiewicz, M., & Pigulski, A. 2017b, in Second BRITE-Constellation Science Conference: Small Satellites - Big Science, Vol. 5, 138–144

Dziembowski, W. A., Daszyńska-Daszkiewicz, J., & Pamyatnykh, A. A. 2007, MNRAS, 374, 248

Pápics, P. I., Tkachenko, A., Van Reeth, T., et al. 2017, A&A, 598, A74

Paxton, B., Bildsten, L., Dotter, A., et al. 2011, ApJS, 192, 3

Paxton, B., Cantiello, M., Arras, P., et al. 2013, ApJS, 208, 4

Paxton, B., Marchant, P., Schwab, J., et al. 2015, ApJS, 220, 15

Paxton, B., Schwab, J., Bauer, E. B., et al. 2018, ApJS, 234, 34

Still, M. & Barclay, T. 2012, PyKE: Reduction and analysis of Kepler Simple Aperture Photometry data, Astrophysics Source Code Library

Szewczuk, W. & Daszyńska-Daszkiewicz, J. 2017, MNRAS, 469, 13

Szewczuk, W. & Daszyńska-Daszkiewicz, J. 2018, MNRAS, 478, 2243

Tassoul, M. 1980, ApJS, 43, 469

Vinícius, Z., Barentsen, G., Gully-Santiago, M., et al. 2017, KeplerGO/PyKE

Walczak, P., Fontes, C. J., Colgan, J., Kilcrease, D. P., & Guzik, J. A. 2015, A&A, 580, L9

Stars and their variability observed from space
C. Neiner, W. W. Weiss, D. Baade, R. E. Griffin, C. C. Lovekin, A. F. J. Moffat (eds)

THE SLOWLY PULSATING B-STAR 18 PEG: A TESTBED FOR UPPER MAIN SEQUENCE STELLAR EVOLUTION

A. Irrgang[1], P. De Cat[2], A. Pigulski[3], G. Handler[4], A. Tkachenko[5] and the BRITE team

Abstract. The predicted width of the upper main sequence in stellar evolution models depends on the empirical calibration of the convective overshooting parameter. Despite decades of discussions, its precise value is still unknown and further observational constraints are required to gauge it. In 2016, Irrgang et al. discovered that the mid B-type subgiant 18 Peg is one of the most evolved members of the rare class of slowly pulsating B-stars and, thus, bears some potential to derive a tight lower limit for the width of the upper main sequence. Here we report on new photometric and spectroscopic analyses based on follow-up observations obtained with the BRITE-Heweliusz satellite and the HERMES spectrograph, which, among others, led to a revised oscillation frequency as well as to an updated radial-velocity curve of this single-lined spectroscopic binary system.

Keywords: binaries: spectroscopic, stars: early-type, stars: individual: 18 Peg, stars: oscillations

1 Introduction

The phenomenon of slowly pulsating B (SPB) stars is more or less restricted to the main-sequence (MS) phase due to the very strong damping of high-order gravity modes in the interiors of post-MS stars (e.g., Pamyatnykh 1999; Moravveji 2016). The most-evolved SPB stars may thus be used to derive a lower limit on the width of the upper MS, which is an important constraint for stellar evolution models. Irrgang et al. (2016) showed that the program star 18 Peg is one of those very evolved SPB stars that bear such a potential. Triggered by this finding, we have collected follow-up observations with the BRITE-Heweliusz satellite and the HERMES spectrograph to study 18 Peg's properties in further detail.

2 Analyses

For the analysis of the new data, we followed almost exactly the methods applied by Irrgang et al. (2016), which is why we refer the interested reader to that paper for details about the analysis and just focus on the new results here. Please note that all uncertainties given in this work are 1σ.

2.1 Analyses of the light curves

The investigation of the photometric variability of 18 Peg is based on data from the BRITE-Heweliusz satellite (almost continuously observing it for 140 days) as well as on differential Strömgren u and y magnitudes taken with the Automatic Photoelectric Telescope (APT) T6 at Fairborn Observatory in Arizona (471 measurements spread over 90 days). Those data sets constitute a significant improvement over the scarcely sampled Tycho and HIPPARCOS epoch photometry which was used by Irrgang et al. (2016) and which allowed to find a single oscillation frequency of $\sim 0.72\,\mathrm{d}^{-1}$. The new results are illustrated in Figs. 1 and 2 and summarized in Table 1. Owing to the excellent temporal coverage of the BRITE light curve, it is now obvious that the signal at $\sim 0.72\,\mathrm{d}^{-1}$ is actually just a daily alias of the true frequency at $0.28876 \pm 0.00012\,\mathrm{d}^{-1}$, which, like the other detected frequencies at $0.4541 \pm 0.0004\,\mathrm{d}^{-1}$ and $0.1660 \pm 0.0005\,\mathrm{d}^{-1}$, is compatible with an SPB nature of 18 Peg.

[1] Dr. Karl Remeis-Observatory Bamberg & ECAP, Sternwartstr. 7, 96049 Bamberg, Germany (e-mail: andreas.irrgang@fau.de)
[2] Royal Observatory of Belgium, Ringlaan 3, B-1180 Brussels, Belgium
[3] Wroclaw University, Astronomical Institute, Kopernika 11, 51-622 Wroclaw, Poland
[4] Copernicus Astronomical Center, Bartycka 18, 00-716 Warszawa, Poland
[5] Instituut voor Sterrenkunde, KU Leuven, Celestijnenlaan 200D, B-3001 Leuven, Belgium

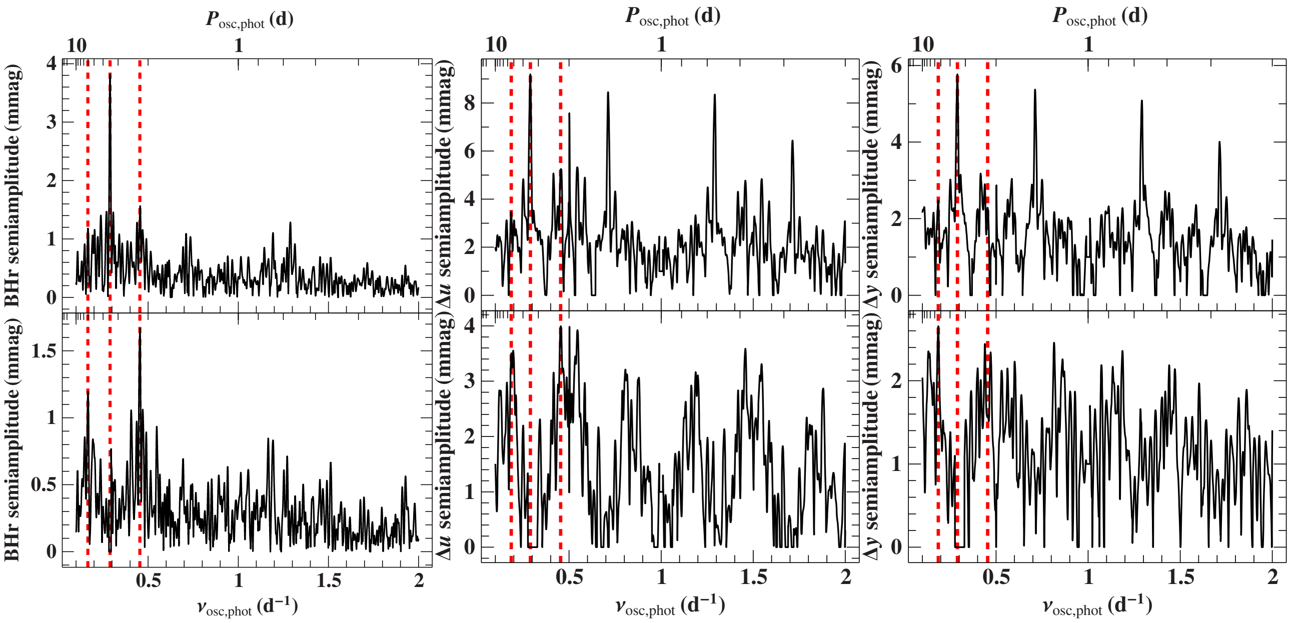

Fig. 1. The frequency spectra derived from photometric data taken with the BRITE-Heweliusz satellite (*left column*) as well as from differential Strömgren u (*middle column*) and y (*right column*) data taken with APT. The curves in the *upper row* are based on the original data while those in the *lower row* have been prewhitened by $\nu_{\rm osc} \sim 0.29\,\mathrm{d}^{-1}$, i.e., the frequency exhibiting the strongest strong signal in the original data. The ground-based data show additional signals from daily aliases of this frequency. The red dashed, vertical lines mark the three detected signals.

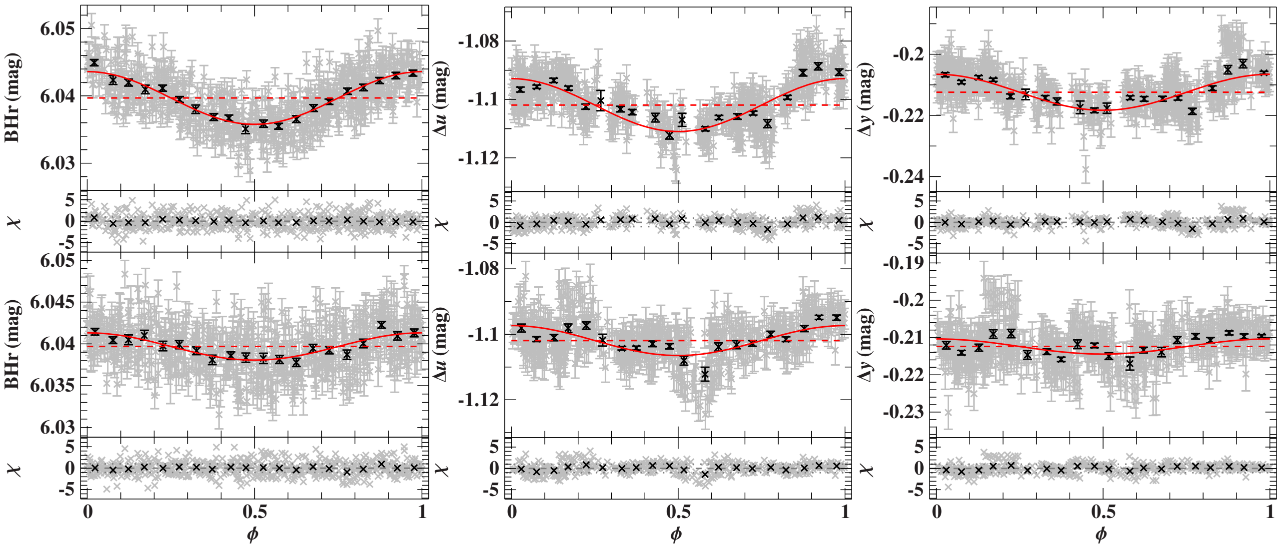

Fig. 2. Phased and prewhitened light-curves of BRITE-Heweliusz (*left column*) and differential Strömgren u (*middle column*) and y (*right column*) data for the first (*upper row*) and second (*lower row*) detected mode ($\phi = 0$ corresponds to the maximum brightness within the pulsation cycle): the measurements are represented by gray crosses with error bars (BRITE-Heweliusz data are orbital averages) while the best-fitting model (see Table 1) is indicated by the red solid curve. The red dashed line marks the derived mean magnitude. The black points are phase-averaged values that were just added to guide the eye. Residuals χ, i.e., the difference between observation and model divided by the respective uncertainty, are shown as well.

2.2 *Analysis of the spectral energy distribution and of the spectra*

Owing to the availability of improved spectral models (Irrgang et al. 2018) and new data, e.g., taken with the Hermes spectrograph, we repeated the analysis of the spectral energy distribution (Fig. 3) and the spectroscopic analysis (Fig. 4). The resulting atmospheric parameters are listed in Table 2 and are now much more consistent with each other and still compatible with an SPB star.

Table 1. Results of the light-curve analysis.

Parameter	Mode 1	Mode 2	Mode 3
BRITE-Heweliusz data:			
Period P_{osc} (d)	$3.4630^{+0.0015}_{-0.0014}$	$2.2020^{+0.0018}_{-0.0017}$	$6.023^{+0.017}_{-0.015}$
Frequency ν_{osc} (d^{-1})	0.28876 ± 0.00012	0.4541 ± 0.0004	0.1660 ± 0.0005
Phase ϕ_{ref} at epoch T_{ref}	$0.697^{+0.010}_{-0.009}$	$0.707^{+0.028}_{-0.026}$	$0.501^{+0.032}_{-0.029}$
BHr semiamplitude (mmag)	3.92 ± 0.11	1.63 ± 0.10	1.17 ± 0.10
BHr mean magnitude (mag)		$6.03969^{+0.00007}_{-0.00008}$	
Differential Strömgren data:			
Period P_{osc} (d)	$3.4470^{+0.0023}_{-0.0030}$	$2.2007^{+0.0013}_{-0.0023}$	$5.373^{+0.007}_{-0.011}$
Frequency ν_{osc} (d^{-1})	$0.29010^{+0.00025}_{-0.00020}$	$0.45440^{+0.00048}_{-0.00025}$	$0.18612^{+0.00038}_{-0.00022}$
Phase ϕ_{ref} at epoch T_{ref}	$0.13^{+0.07}_{-0.05}$	$0.61^{+0.15}_{-0.09}$	$0.915^{+0.028}_{-0.017}$
Δu semiamplitude (mmag)	$9.05^{+0.34}_{-0.30}$	$4.57^{+0.31}_{-0.27}$	$4.18^{+0.35}_{-0.26}$
Δy semiamplitude (mmag)	5.9 ± 0.4	$2.03^{+0.30}_{-0.28}$	$3.00^{+0.33}_{-0.30}$
Δu mean magnitude (mag)		$-1.10191^{+0.00021}_{-0.00026}$	
Δy mean magnitude (mag)		$-0.21242^{+0.00021}_{-0.00025}$	
Fixed reference epoch T_{ref} (HJD−2 400 000.5)		57 939.0	

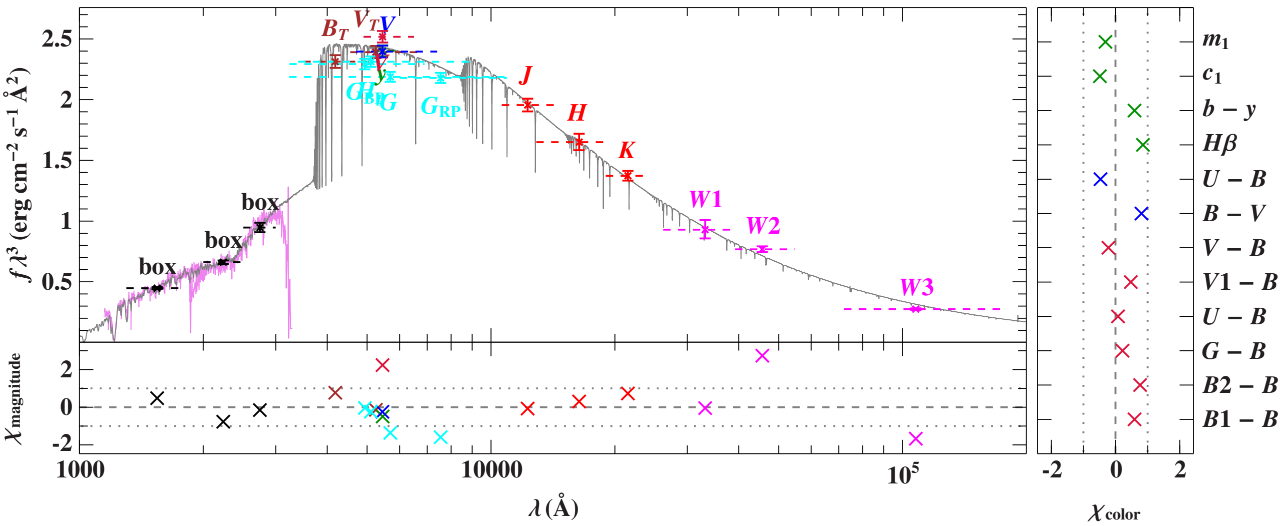

Fig. 3. Comparison of synthetic and observed photometry: The *top panel* shows the spectral energy distribution. The colored data points are filter-averaged fluxes which were converted from observed magnitudes (the respective filter widths are indicated by the dashed horizontal lines), while the gray solid line represents the best-fitting model (see Table 2) degraded to a spectral resolution of 6 Å. The three black data points labeled "box" are fluxes converted from magnitudes computed by means of box filters of the indicated width from IUE spectra (magenta line). The panels at the *bottom* and on the *side* show the residuals for magnitudes and colors, respectively. The photometric systems have the following color code: Tycho (brown); *Gaia* and HIPPARCOS (cyan); Johnson-Cousins (blue); Strömgren (green); Geneva (crimson); 2MASS (red); WISE (magenta).

Table 2. Stellar parameters derived from photometry and spectroscopy.

Parameter	Photometry	Spectrocopy
Angular diameter $\log(\Theta\,(\mathrm{rad}))$	-9.1495 ± 0.0025	...
Color excess $E(B-V)$	0.055 ± 0.006 mag	...
Extinction parameter R_V (fixed)	3.1	...
Effective temperature T_{eff}	$15\,080^{+170}_{-160}$ K	$15\,260 \pm 160$ K
Surface gravity $\log(g\,(\mathrm{cm\,s^{-2}}))$	3.72 ± 0.16	3.59 ± 0.04

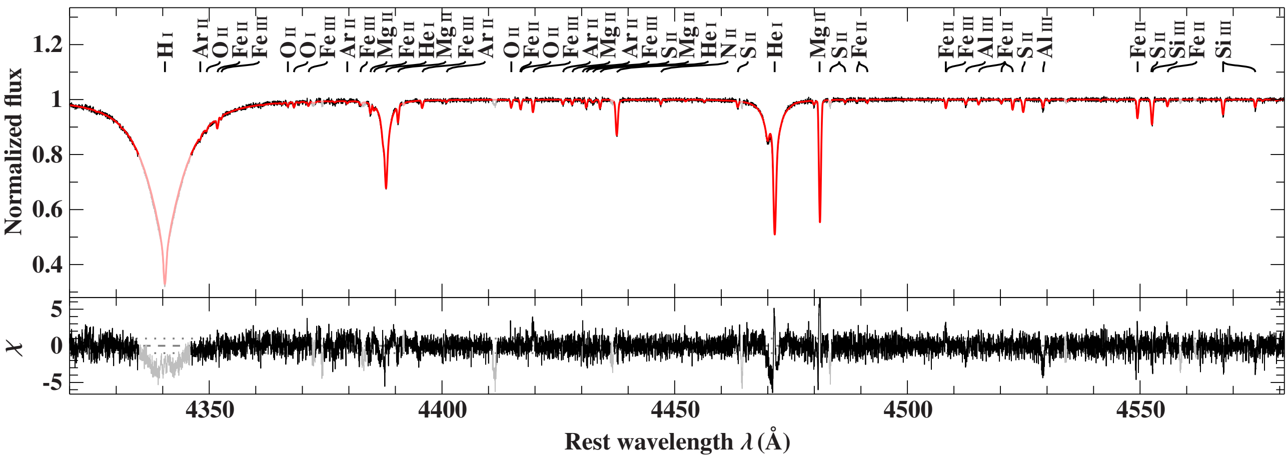

Fig. 4. Exemplary comparison of the best-fitting model spectrum (red line, see Table 2) with one of the re-normalized HERMES spectra (black line). Light colors mark regions that have been excluded from fitting. Residuals χ are shown as well.

2.3 Analysis of the line-profile variations

To study the pulsationally induced temporal distortions of the spectral line profiles, we fitted nine different spectral lines in 59 epochs using a purely dynamical model for the velocity field of an adiabatically pulsating star whose pulsational and rotational axes are aligned (Schrijvers et al. 1997). Two oscillation modes were included in the model. While the observed frequency (for a definition see Ledoux 1951) of the first mode was restricted to a small interval around the result of the light-curve analysis, we left the second one as a free parameter to allow for modes that are only visible in the line-profile variations, e.g., because of cancellation effects of modes with high degree l or azimuthal order m in the light curve. Figure 5 shows an exemplary comparison between observations and best-fitting model. Despite the additional mode, the model is not able to decently reproduce the observations for all epochs, which may be a consequence of all the simplifying assumptions made in the model. Consequently, the parameters of the best-fitting model, which are listed in Table 3 and whose meaning is described in Irrgang et al. (2016), are currently not reliable and a more sophisticated treatment of the line-profile variations is needed.

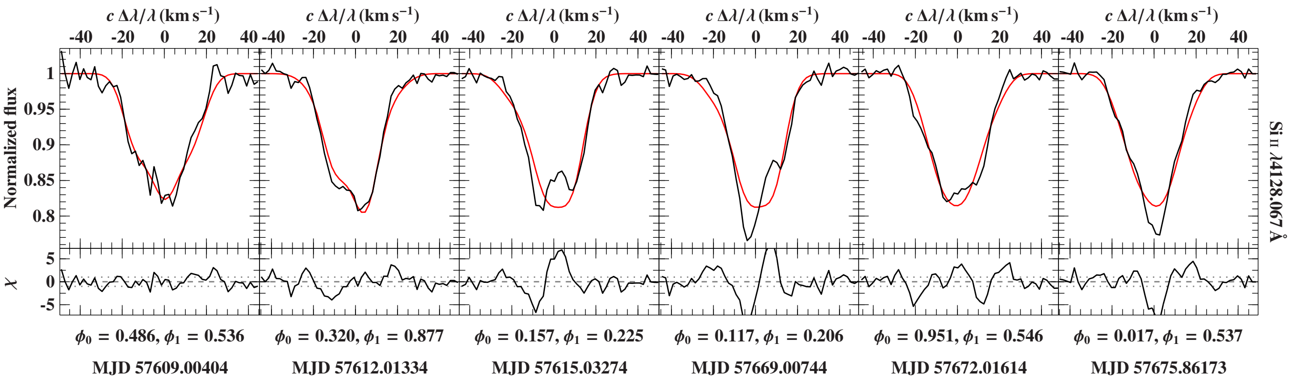

Fig. 5. Spectral modeling of the pulsationally driven line-profile distortions for six exemplary epochs (*columns*) and one exemplary spectral line: the HERMES observations are indicated by a black line, the model (see Table 3) by a red one, and the quality of the fit by the residuals χ. Observed oscillation phases for both modes are listed on the x-axes.

2.4 Analysis of the radial-velocity curve

The updated model for the spectral line-profile variations as well as the new HERMES observations allow us to revise the radial-velocity curve of this single-lined spectroscopic binary system. In contrast to Irrgang et al. (2016), we solely rely here on high-resolution spectra to extract radial velocities. Figure 6 shows the new solution

Table 3. Parameters of the best-fitting model for the line-profile variations.

Most relevant parameters affecting (the)												Derived quantities from (the)										
first mode						second mode				both modes		first mode		second mode				both modes				
l	m	$\langle v_{\mathrm{v}}^2\rangle^{1/2}$	$k^{(0)}$	$\frac{\nu_{\mathrm{rot}}}{\nu_{\mathrm{osc}}^{(0)}}$	$\nu_{\mathrm{osc}}^{\mathrm{obs}}$	l	m	$\langle v_{\mathrm{v}}^2\rangle^{1/2}$	$\nu_{\mathrm{osc}}^{\mathrm{obs}}$	i	$v\sin(i)$	a_{sph}	$\nu_{\mathrm{osc}}^{(0)}$	$k^{(0)}$	$\frac{\nu_{\mathrm{rot}}}{\nu_{\mathrm{osc}}^{(0)}}$	a_{sph}	$\nu_{\mathrm{osc}}^{(0)}$	η	ν_{rot}	M	$R_\star$	$\log(g)$
		$\mathrm{km\,s^{-1}}$			$\mathrm{d^{-1}}$			$\mathrm{km\,s^{-1}}$	$\mathrm{d^{-1}}$	°	$\mathrm{km\,s^{-1}}$	$R_\odot$	$\mathrm{d^{-1}}$			$R_\odot$	$\mathrm{d^{-1}}$		$\mathrm{d^{-1}}$	$M_\odot$	$R_\odot$	cgs
2	+2	0.569	2.46	0.205	0.277	4	−4	0.798	0.778	24.5	19.68	0.12	0.444	2.71	0.215	0.19	0.423	0.02	0.091	7.2	10.3	3.27

whose parameters are listed in Table 4.

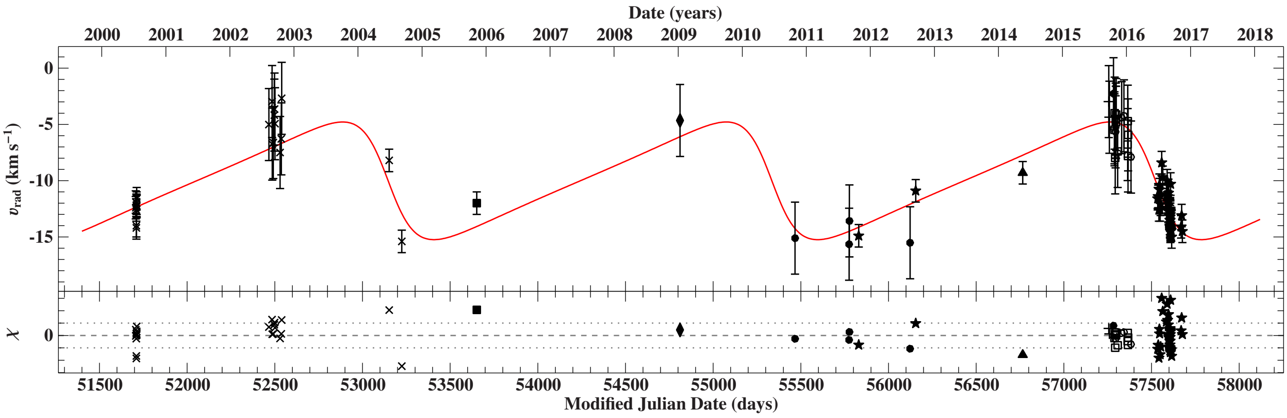

Fig. 6. Updated radial velocity curve of 18 Peg: the measurements are represented by black symbols with error bars while the best-fitting Keplerian model (see Table 4) is indicated by the red solid curve. Residuals χ are shown in the *lower panel*. The symbols identify different instruments, all of which are high-resolution spectrographs.

Table 4. Orbital parameters of the single-lined spectroscopic binary system.

Parameter	Value
Period P	2188 ± 10 d
Epoch of periastron $T_{\mathrm{periastron}}$	$57\,520 \pm 40$ MJD
Eccentricity e	$0.42^{+0.06}_{-0.05}$
Longitude of periastron ω	$90^{+10}_{-\ 9}{}^{\circ}$
Velocity semiamplitude K_1	$5.2 \pm 0.4\,\mathrm{km\,s^{-1}}$
Systemic velocity γ	$-10.02^{+0.28}_{-0.27}\,\mathrm{km\,s^{-1}}$
Derived parameter	**Value**
Mass function $f(M)$	$0.024^{+0.007}_{-0.006}\,M_\odot$
Projected semimajor axis $a_1\sin(i)$	$0.95^{+0.09}_{-0.08}$ AU
Projected periastron distance $r_{\mathrm{p}}\sin(i)$	$118^{+19}_{-18}\,R_\odot$

3 Discussion

Our revised atmospheric parameters still indicate that 18 Peg is one of the most evolved SPB stars known to date. However, as demonstrated in Fig. 7, its surface gravity does not seem to be low enough to put significant new constraints on current stellar models for the upper MS given that the results from line-profile fitting are unreliable because they are based on a model that is probably too simplistic.

APi acknowledges support from the Polish NCN grant no. 2016/21/B/ST9/01126. Based on data collected by the BRITE Constellation satellite mission, designed, built, launched, operated and supported by the Austrian Research Promotion Agency (FFG), the University of Vienna, the Technical University of Graz, the Canadian Space Agency (CSA), the University of Toronto Institute for Aerospace Studies (UTIAS), the Foundation for Polish Science & Technology (FNiTP MNiSW), and National Science Centre (NCN).

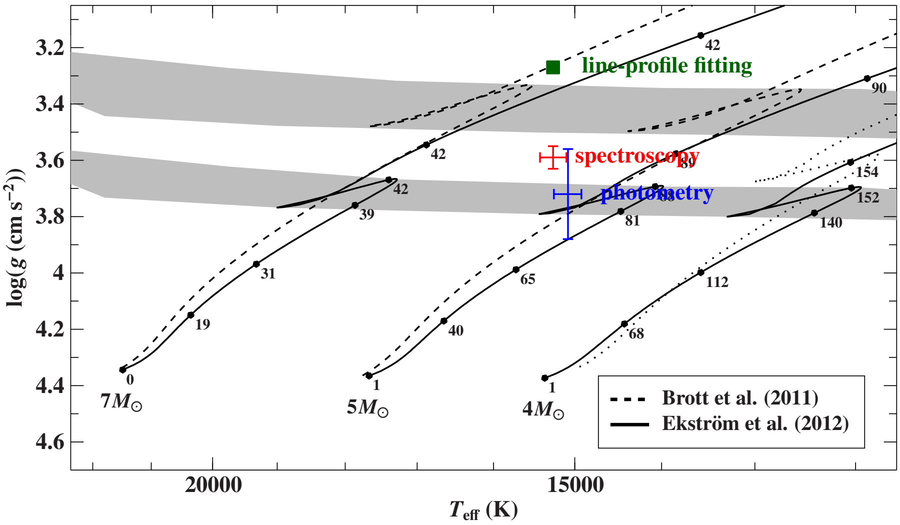

Fig. 7. Position of 18 Peg in a ($T_{\rm eff}$, $\log(g)$) diagram based on spectroscopy, photometry, and fitting of the spectral line-profile variations ($T_{\rm eff}$ taken from spectroscopy). Overlaid are evolutionary tracks for non-rotating stars of solar metallicity and different initial masses by Brott et al. (2011, dashed lines) and Ekström et al. (2012, solid lines). The gray-shaded areas highlight the transition region between MS and post MS for the two different sets of models, which primarily differ in the efficiency of convective overshooting. The impact of stellar rotation is demonstrated via the dotted line, which is an Ekström et al. (2012) track for a rotating ($\Omega/\Omega_{\rm crit} = 0.4$) star with an initial mass of $4\,M_\odot$.

References

Brott, I., de Mink, S. E., Cantiello, M., et al. 2011, A&A, 530, A115
Ekström, S., Georgy, C., Eggenberger, P., et al. 2012, A&A, 537, A146
Irrgang, A., Desphande, A., Moehler, S., Mugrauer, M., & Janousch, D. 2016, A&A, 591, L6
Irrgang, A., Kreuzer, S., Heber, U., & Brown, W. 2018, A&A, 615, L5
Ledoux, P. 1951, ApJ, 114, 373
Moravveji, E. 2016, MNRAS, 455, L67
Pamyatnykh, A. A. 1999, Acta Astron., 49, 119
Schrijvers, C., Telting, J. H., Aerts, C., Ruymaekers, E., & Henrichs, H. F. 1997, A&AS, 121, 343

Stars and their variability observed from space
C. Neiner, W. W. Weiss, D. Baade, R. E. Griffin, C. C. Lovekin, A. F. J. Moffat (eds)

DETERMINATION OF PRECISE STELLAR PARAMETERS OF KEPLER LEGACY TARGETS USING THE WHOSGLAD METHOD

M. Farnir[1], M.-A. Dupret[1], S.J.A.J. Salmon[1], A. Noels[1] and G. Buldgen[2]

Abstract.
We developed a method, WhoSGlAd, that provides a comprehensive adjustment of solar-like oscillation spectra. The method allows for tighter constraints (up to four times smaller standard deviations than those of analogous ones). We take advantage of this new method and of the quality of the *Kepler* LEGACY data to highlight trends in the stellar parameters and the limitations of the current generation of stellar models.

Keywords: Asteroseismology, stars: oscillations, solar-type, abundances, methods: numerical

1 Introduction

In recent years, space missions such as *Kepler* (Borucki et al. 2010), *CoRoT* (Baglin et al. 2009) and *BRITE* (Weiss et al. 2014) have provided a wealth of data of unprecedented quality. This has allowed asteroseismology to become a very efficient tool for constraining stellar structure. Moreover, owing to the high quality of the data, it has become possible to study acoustic glitches. These are oscillating signatures in frequency spectra that are caused by a sharp variation* in the stellar structure. They therefore provide very localized and invaluable information. For example, several studies have taken advantage of the glitches to infer the surface helium content in solar-like pulsators, which cannot be measured by any other technique. The idea to use such glitches to constrain the stellar structure was first formulated by Gough (1990) and Vorontsov (1988). Since then, several studies involving acoustic glitches have been carried out, among which we cite Basu et al. (2004) and Verma et al. (2014). A previous paper (Farnir et al. 2019) presented a new method, WhoSGlAd, to adjust simultaneously the signature of such glitches and the smoothly varying component of the oscillation spectrum. This method has the advantage of providing constraints that are correlated as little as possible, owing to the use of the Gram-Schmidt orthogonalisation procedure. Moreover, the standard deviation of the defined seismic indicators are up to four times smaller than usual. This contribtion recalls briefly the principle of the WhoSGlAd method and present its application to the study of the *Kepler* LEGACY sample (Lund et al. 2017) and to an in-depth study of 16 Cygni A.

2 Principle

2.1 Mathematical description

This section contains a very brief description of the principle of the WhoSGlAd method. More information can be found in Farnir et al. (2019). To describe a set of observed frequencies, ${\nu_{obs}}^{\dagger}$, we built a euclidean vector space of functions. The following scalar product was defined:

$$\langle \boldsymbol{x}|\boldsymbol{y}\rangle = \sum_{i=1}^{N} \frac{x_i y_i}{\sigma_i^2}, \tag{2.1}$$

where $\boldsymbol{x}$ and $\boldsymbol{y}$ are two sets of N frequencies and σ_i are the individual standard deviations. In this vector space we represent the smooth part of the oscillation spectrum as polynomials in the radial order n and the glitch part as oscillating functions linearized to the fitted coefficients. We then used the Gram-Schmidt orthogonalisation

[1] Institut d'Astrophysique et Géophysique de l'Université de Liège, Allée du 6 août 17, 4000 Liège, Belgium
[2] Observatoire de Genève, Université de Genève, 51 Ch. Des Maillettes, 1290 Sauverny, Switzerland
*compared to the wavelength of the incoming wave
†We here denote by the *obs* subscript the frequencies to be adjusted, be they observed or modelled.

procedure to build an orthonormal basis over this vector space. If we write $p_j(n,l)$ as the former basis elements, $q_{j_0}(n,l)$ as the orthonormal basis elements and $R^{-1}_{j,j0}$ as the transformation matrix, we have:

$$q_{j_0}(n,l) = \sum_{j \le j_0} R^{-1}_{j,j_0} p_j(n,l). \tag{2.2}$$

Finally, using the scalar product 2.1, we project the frequencies over the successive basis elements. The fitted frequencies are thus:

$$\nu_f(n,l) = \sum_j a_j q_j(n,l), \tag{2.3}$$

where a_j are the fitted coefficients and $q_j(n,l)$ the orthonormal basis elements. It is essential to note that, owing to the orthonormalisation, all the coefficients a_j are completely independent of each other. Therefore, while the glitch and smooth components are treated simultaneously, they are fully uncorrelated.

HERE

2.2 Useful seismic indicators

Combining in a clever way the adjusted coefficients, we may construct seismic indicators as uncorrelated as possible for the stellar structure that are proxies of the 'usual' ones.

Large separation: At first order, the smooth part of the spectrum is approximated by a straight line. For a given spherical degree, the slope of this line is the large separation for this degree. In our formulation, we obtain[‡]

$$\Delta_l = a_{l,1} R^{-1}_{l,1,1} \tag{2.4}$$

Averaging this quantity over the range of observed spherical degrees, we get:

$$\Delta = \frac{\sum_l a_{l,1}/R^{-1}_{l,1,1}}{\sum_l 1/\left(R^{-1}_{l,1,1}\right)^2} \tag{2.5}$$

Small separation ratios: Analogous to Roxburgh & Vorontsov (2003), we may define averaged small separation ratios as:

$$\hat{r}_{0,l} = \frac{\bar{\nu_0} - \bar{\nu_l}}{\Delta_0} + \bar{n_l} - \bar{n_0} + \frac{l}{2}, \tag{2.6}$$

where the overlined symbols represent the mean value of those quantities calculated using our scalar product. We show in Farnir et al. (2019) that these ratios are almost independent of surface effects, as expected from Roxburgh & Vorontsov (2003).

Large separation ratios: We define:

$$\Delta_{0l} = \frac{\Delta_l}{\Delta_0} - 1 \tag{2.7}$$

It is straightforward to show that this represents the mean slope of r_{010}, which is the combination of the small separation ratios r_{01} and r_{10} (Roxburgh & Vorontsov 2003).

Helium glitch amplitude: We define the amplitude of the helium glitch, $\delta\nu_{\mathrm{He}}$, as the norm of the helium glitch term, i.e.:

$$A_{\mathrm{He}} = \|\delta\nu_{\mathrm{He}}\| = \sqrt{\sum_j a^2_{j,\mathrm{He}}}. \tag{2.8}$$

[‡]Note that, for the smooth part, the j index has been separated into the spherical degree l and the polynomial degree k, as we have different polynomials for each spherical degree.

3 Applications

3.1 Models

Unless specified otherwise, every model was constructed using the CLES stellar evolution code (Scuflaire et al. 2008b) with the AGSS09 solar chemical mixture (Asplund et al. 2009), the OPAL opacity table (Iglesias & Rogers 1996) combined with that of Ferguson et al. (2005) at low temperatures, the FreeEOS software to generate the equation of state table (Cassisi et al. 2003) and the reaction rates prescribed by Adelberger et al. (2011). We also used the mixing length theory (Cox & Giuli 1968), with the solar calibrated value of $\alpha_{\rm MLT} = l/H_p = 1.82$ (where l is the mixing length and H_p the pressure scale height), to parametrize the mixing inside convective regions. The microscopic diffusion of elements was included and treated as in Thoul et al. (1994). Moreover, the temperature conditions above the photosphere were determined using an Eddington $T(\tau)$ relationship, τ being the optical depth. Finally, the model frequencies were calculated using the LOSC oscillation code (Scuflaire et al. 2008a) which were corrected for the surface effects according to Kjeldsen et al. (2008)'s prescription using the a and b coefficients fitted by Sonoi et al. (2015).

3.2 The Kepler LEGACY sample

The *Kepler* LEGACY sample consists of 66 main sequence solar-like stars which have been observed by the *Kepler* telescope for at least one continuous year (Lund et al. 2017). This is therefore the best data available for the asteroseismology of main-sequence solar-like pulsators.

For each star in the sample, we tried to provide a fitted model to the observed seismic indicators defined in the previous section and built over the frequencies from Lund et al. (2017). To do so, we first used the AIMS algorithm (Rendle et al. 2019) to provide initial guesses that were then used as starting points by a Levenberg-Marquardt algorithm.

The constraints used are the following seismic indicators: Δ, $\hat{r}_{01}$, $\hat{r}_{02}$, Δ_{01} and $A_{\rm He}$ and the metallicity. The free parameters are: the mass, age, initial hydrogen and metal abundances and the overshooting parameter.

From the whole sample, only 18 stars were properly fitted, with a $\chi^2 = \sum_i \left(\frac{y_{{\rm th},i} - y_{{\rm obs},i}}{\sigma_{{\rm obs},i}}\right)^2 \leq 40$. The results are shown in Figs. 1 and 2. Figure 1 shows the initial helium content as a function of the initial metallicity. We observe a correlation which could be a clue for a Galactic enrichment. In Fig.2 we show the adjusted overshooting parameter versus the stellar mass. We do not observe a correlation between these two quantities as expected from Claret & Torres (2019). However, the range of masses depicted in their Fig. 10 is much broader than ours and the apparent absence of a correlation could result from our restricted mass range. Therefore, to validate both observations, it will be necessary to provide a proper adjustment for as many stars from the sample as possible.

3.3 Application to 16 Cygni A

In the previous subsection, we showed adjustments that were done by considering only one set of physical ingredients. To properly understand the dependency of the stellar parameters on the physics as well as to provide proper standard deviations for these parameters, one has to test different physical ingredients. This is what we did for the specific case of 16 Cyg A. We show in Fig. 3 the results for the different choices of microphysics we considered. The frequencies from which we built our seismic indicators were those determined by Davies et al. (2015). We calculated the models shown in the figure by changing one microphysical ingredient at a time from the reference described in Sec. 3.1. The reference is shown in black. The considered variations were: the GN93 solar reference (Grevesse & Noels 1993) (in red), the opacity table from the opacity project OP (Badnell et al. 2005) (in green), the LANL/OPLIB opacity table (Colgan et al. 2016) (in blue), the CEFF equation of state (Christensen-Dalsgaard & Daeppen 1992) (in yellow), the OPAL05 equation of state (Rogers & Nayfonov 2002) (in magenta), the inclusion of turbulent mixing (in cyan) following the relation $DDT = D_{\rm turb}\left(\frac{\rho}{\rho_0}\right)^n + D_{ct}$, where ρ is the density, ρ_0 the surface density and $D_{\rm turb}$, n and D_{ct} were fixed at -7500, -3 and 0 respectively (Proffitt & Michaud 1991). A reduced value of 1.7 for the mixing length parameter (in light green) was also considered. We used Δ, $\hat{r}_{01}$, $\hat{r}_{02}$ and $A_{\rm He}$ as constraints and the mass, age, initial helium abundance and metallicity as free parameters.

We observe that, given the current precision of both the data and the method, it becomes possible to discriminate between different choices of input physics. We also show with a grey box the luminosity (deduced from the interferometric radius) and effective temperature (White et al. 2013). These constraints were not

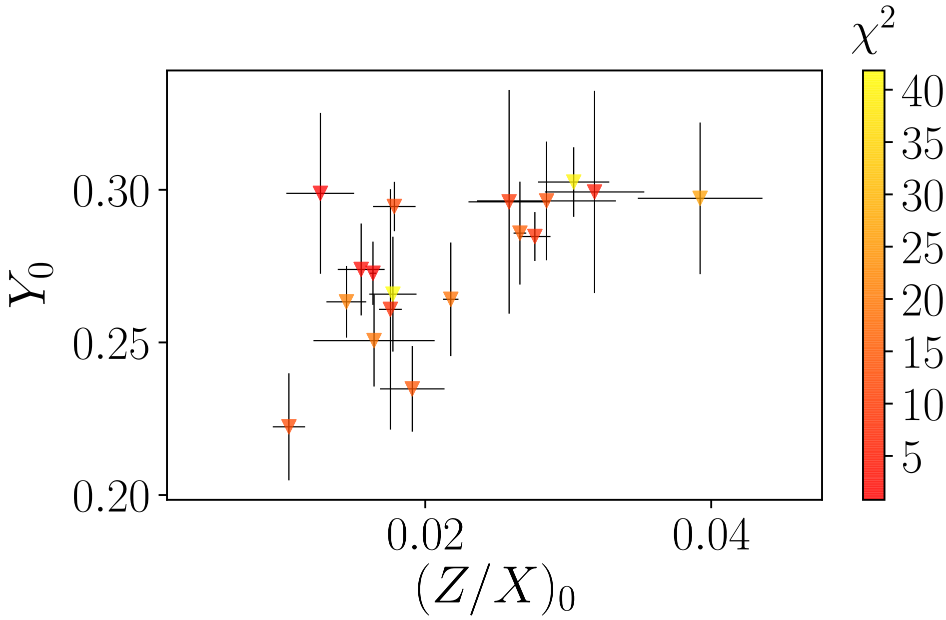

Fig. 1: Best fit values for the initial helium abundance as a function of the initial metallicity. The color code represents the χ^2 value for each model.

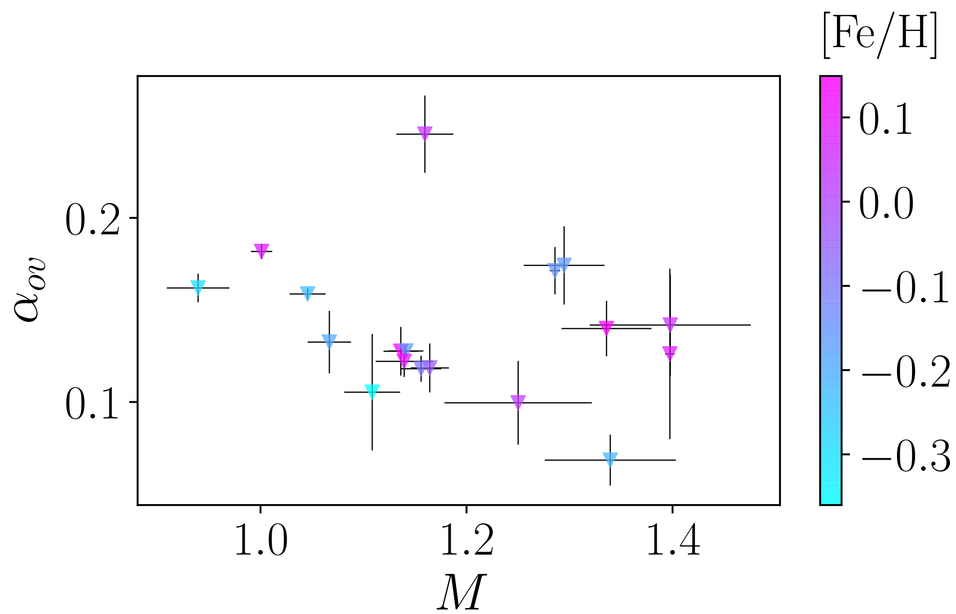

Fig. 2: Best fit values for the step overshooting parameter as a function of the mass. The color code represents the metallicity of the models.

included during the fit; we merely show the discrepancy of the results with them. Only a few models lie in the box, one of them relying on non-classical physics (the cyan model includes turbulent mixing). This clearly illustrates the limitations of the forward approach for the stellar modeling as well as that of our knowledge about the stellar structure. To further improve our results and highlight the necessary improvements to the stellar models, one should consider making use of inverse techniques as in Buldgen et al. (2016).

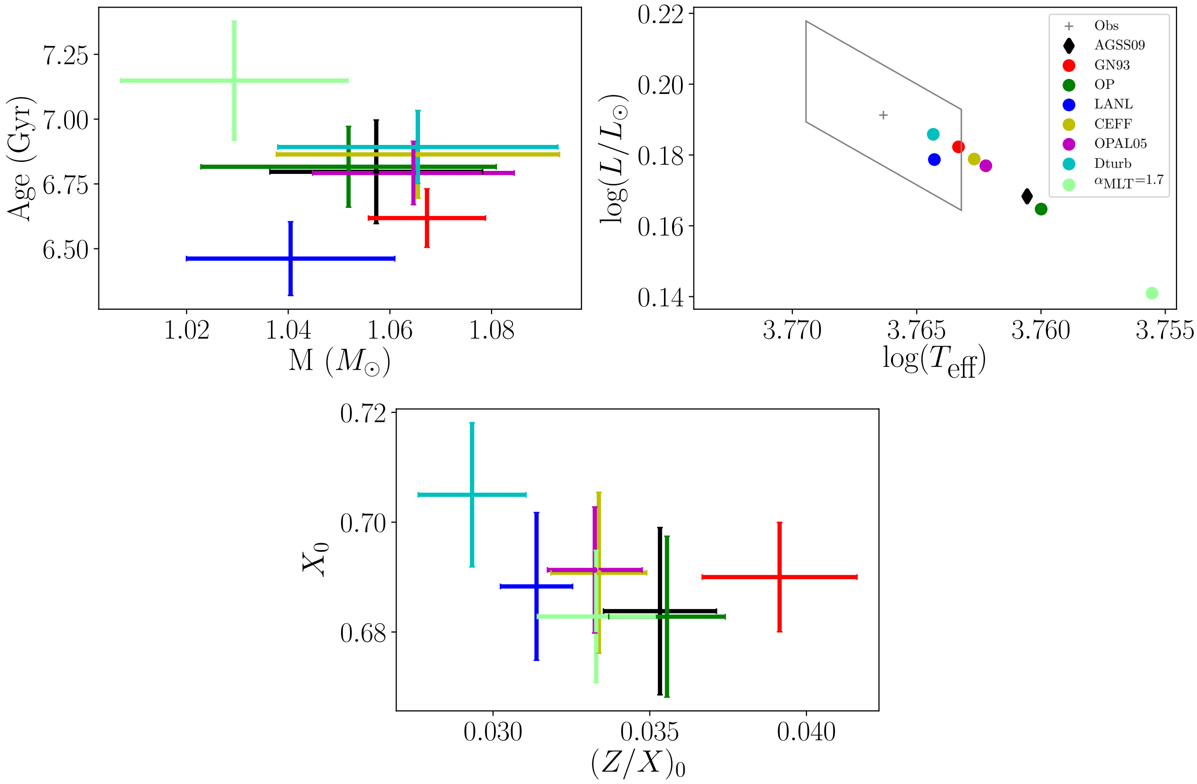

Fig. 3: Ensemble of 16Cyg A best fit models represented in an age - mass diagram (upper left panel), HR diagram (upper right panel) and initial hydrogen - metallicity diagram (lower panel). The different choices of microphysics are represented by the colors. The luminosity (deduced from the interferometric radius) and effective temperature (White et al. 2013) (observed values and standard deviations) are represented by the grey box in the upper right panel.

4 Conclusions

The WhoSGlAd method allows us to provide a comprehensive adjustment of solar-like pulsator oscillation spectra as a whole (glitch and smooth parts) and to put tighter seismic constraints (up to four times smaller than 'classical' values) on the stellar structure. Combined with the precision of the *Kepler* LEGACY data, it becomes possible to observe trends over the whole sample (we note a correlation between the initial helium content and the initial metallicity) as well as the limitations of the current stellar models. It therefore becomes necessary to refine those by, for example, improving the treatment of convection or including non-standard physics (e.g. turbulent mixing, revised abundances and opacities). Moreover, to go even further in the modeling, combining the promising WhoSGlAd method with inverse techniques may be of great help. Finally, the adaptation of the method to the more complex case of subgiants exhibiting mixed modes will be a natural step as they present the regularities of p and g modes, which are well suited for such an approach.

M.F. is supported by the FRIA (Fond pour la Recherche en Industrie et Agriculture) - FNRS PhD grant. S.J.A.J.S. is funded by ARC grant for Concerted Research Actions, financed by the Wallonia-Brussels Federation. G. Buldgen is supported by the Swiss National Science Foundation (project number 200020 172505)

References

Adelberger, E. G., García, A., Robertson, R. G. H., et al. 2011, Reviews of Modern Physics, 83, 195

Asplund, M., Grevesse, N., Sauval, A. J., & Scott, P. 2009, ARA&A, 47, 481

Badnell, N. R., Bautista, M. A., Butler, K., et al. 2005, MNRAS, 360, 458

Baglin, A., Auvergne, M., Barge, P., et al. 2009, in IAU Symposium, Vol. 253, Transiting Planets, ed. F. Pont, D. Sasselov, & M. J. Holman, 71–81

Basu, S., Mazumdar, A., Antia, H. M., & Demarque, P. 2004, MNRAS, 350, 277

Borucki, W. J., Koch, D., Basri, G., et al. 2010, in Bulletin of the AAS, Vol. 42, AAS Meeting Abstracts #215, 215

Buldgen, G., Reese, D. R., & Dupret, M. A. 2016, A&A, 585, A109

Cassisi, S., Salaris, M., & Irwin, A. W. 2003, ApJ, 588, 862

Christensen-Dalsgaard, J. & Daeppen, W. 1992, A&A Rev., 4, 267

Claret, A. & Torres, G. 2019, ApJ, 876, 134

Colgan, J., Kilcrease, D. P., Magee, N. H., et al. 2016, ApJ, 817, 116

Cox, J. P. & Giuli, R. T. 1968, Principles of stellar structure (New York: Gordon and Breach)

Davies, G. R., Chaplin, W. J., Farr, W. M., et al. 2015, MNRAS, 446, 2959

Farnir, M., Dupret, M. A., Salmon, S. J. A. J., Noels, A., & Buldgen, G. 2019, A&A, 622, A98

Ferguson, J. W., Alexander, D. R., Allard, F., et al. 2005, ApJ, 623, 585

Gough, D. O. 1990, in Lecture Notes in Physics, Berlin Springer Verlag, Vol. 367, Progress of Seismology of the Sun and Stars, ed. Y. Osaki & H. Shibahashi, 283

Grevesse, N. & Noels, A. 1993, in Origin and Evolution of the Elements, ed. N. Prantzos, E. Vangioni-Flam, & M. Casse, 15–25

Iglesias, C. A. & Rogers, F. J. 1996, ApJ, 464, 943

Kjeldsen, H., Bedding, T. R., & Christensen-Dalsgaard, J. 2008, ApJ, 683, L175

Lund, M. N., Silva Aguirre, V., Davies, G. R., et al. 2017, ApJ, 835, 172

Proffitt, C. R. & Michaud, G. 1991, ApJ, 380, 238

Rendle, B. M., Buldgen, G., Miglio, A., et al. 2019, MNRAS, 484, 771

Rogers, F. J. & Nayfonov, A. 2002, ApJ, 576, 1064

Roxburgh, I. W. & Vorontsov, S. V. 2003, A&A, 411, 215

Scuflaire, R., Montalbán, J., Théado, S., et al. 2008a, Ap&SS, 316, 149

Scuflaire, R., Théado, S., Montalbán, J., et al. 2008b, Ap&SS, 316, 83

Sonoi, T., Samadi, R., Belkacem, K., et al. 2015, A&A, 583, A112

Thoul, A. A., Bahcall, J. N., & Loeb, A. 1994, ApJ, 421, 828

Verma, K., Faria, J. P., Antia, H. M., et al. 2014, ApJ, 790, 138

Vorontsov, S. V. 1988, in IAU Symposium, Vol. 123, Advances in Helio- and Asteroseismology, ed. J. Christensen-Dalsgaard & S. Frandsen, 151

Weiss, W. W., Rucinski, S. M., Moffat, A. F. J., et al. 2014, PASP, 126, 573

White, T. R., Huber, D., Maestro, V., et al. 2013, MNRAS, 433, 1262

Stars and their variability observed from space
C. Neiner, W. W. Weiss, D. Baade, R. E. Griffin, C. C. Lovekin, A. F. J. Moffat (eds)

FROM LIGHT-CURVES TO FREQUENCIES OF OSCILLATION MODES USING TACO

N. Themeßl[1, 2], J. S. Kuszlewicz[1,2], A. García Saravia Ortiz de Montellano[1,2] and S. Hekker[1,2]

Abstract. The TACO code (**T**ools for **A**utomated **C**haracterization of **O**scillations) has been developed to provide an automated, fast and reliable analysis of solar-like oscillations. We demonstrated its capabilities, based on the asteroseismic study of an open-cluster red giant that has been observed by the *Kepler* space mission. TACO uses as input a light-curve corrected for systematics, and after several analysis steps it provides the characteristics of all statistically-significant oscillation modes, including mode identification.

Keywords: Asteroseismology, Methods: data analysis, Stars: individual: KIC 4937257, Stars: oscillations

1 Introduction

State-of-the-art space missions such as *CoRoT*, *Kepler*, *K2* and *TESS* (e.g., Baglin et al. 2006; Borucki et al. 2010; Howell et al. 2014; Ricker et al. 2015), have been – and are still – providing high-precision photometric light-curves for an unprecedented number of oscillating stars, and with more data coming (e.g., *TESS* extended mission and *PLATO* Rauer et al. 2014). In the case of solar-like oscillations, the modes form a distinctive pattern in the observed frequency spectrum of the star. Several radial orders of low spherical degree modes ($\ell \leq 3$) can be detected; those are suitable for automated procedures to extract their characteristics in the tens of thousands of stars that show solar-like oscillations. General attempts to detect these oscillation frequencies are based on the asymptotic relation (Tassoul 1980), or the so-called "universal pattern" (Mosser et al. 2011). These approaches can be hampered if mode frequencies are below the detection limit; they need careful inspection on a mode-by-mode basis, and are prone to a certain degree of subjectivity.

In order to handle the large number of stars for which we have data, we introduced the TACO code, which consists of a sequence of modules that perform an analysis of solar-like oscillations. We have implemented a data-driven Mexican-hat wavelet-transform based a detection method to search for all the statistically-significant peaks in the observed frequency spectrum (**?**). This algorithm is appropriate for detecting peaks that are approximately symmetric, have a positive peak height, and a finite width, as is the case for solar-like oscillation modes. Commonly used astrophysical concepts are only included in other parts of the analysis; more information will be available in the main TACO paper, which will be submitted soon. The final output is a list of frequencies and mode identifications of the oscillations. As a byproduct, TACO provides some of the global oscillation parameters, among which are the frequency of maximum oscillation power ($\nu_{\rm max}$), the large and small frequency separations, the period spacing and the coupling factor, and also the rotational splitting (if present).

2 Characterization of solar-like oscillations using TACO

Here we present the analysis of the oscillating red-giant star KIC 4937257, which is a member of the open cluster NGC 6819. We focus on two of the modules that are implemented in TACO; they involve background fitting of power density spectra (PDS), including $\nu_{\rm max}$ estimation and automated detection of peaks in the observed frequency range of the oscillations. As a general input, TACO uses light-curve data. Those are first high-pass filtered (default = 40 days), and we then compute a PDS from the filtered light-curve normalized by the window function (see Fig. 1). Next, we obtain estimates of the location of the oscillation power excess, i.e. $\nu_{\rm max}$, from the variance of the photometric time-series and the application of both the Morlet and the Mexican-Hat wavelets to the PDS. A comparison between these three estimates provides a preliminary value of $\nu_{\rm max}$, which will be used to set some priors for subsequently fitting a global model to the PDS. For more information on these modules we refer the interested reader to the main TACO paper.

[1] Max Planck Institute for Solar System Research, Justus-von-Liebig-Weg 3, DE-37077 Göttingen, Germany
[2] Stellar Astrophysics Centre (SAC), Department of Physics and Astronomy, Aarhus University, Ny Munkegade 120, DK-8000 Aarhus C, Denmark

2.1 Global background model fit and determination of $\nu_{\max}$

The next step uses a global fit to estimate the granulation and white noise background level on which the oscillation modes lie. By default, TACO applies a model to the PDS that consists of a Gaussian function to approximate the oscillation power envelope, three granulation background components, and a single parameter to account for the white noise in the data (Fig. 1; for functional forms of the model, see the main TACO paper). To reduce the computation time during the background fitting process, TACO uses a binned version of the PDS with a default set to 300 bins ($\approx 0.94\,\mu$Hz-wide bins). By basing this on a Bayesian Markov Chain Monte Carlo (MCMC) framework with affine-invariant ensemble sampling (EMCEE; Foreman-Mackey et al. 2013), we obtain posterior probability distributions for the fitted parameters and adopt the medians of those distributions as estimates of the expectation values and their $16^{\mathrm{th}}/84^{\mathrm{th}}$ percentiles as uncertainties. In Figure 2 we show the results for the background fits based on different binnings and their influences on the estimates of $\nu_{\max}$.

The following arguments can be applied to optimize the output from this module: the number of walkers (chains) for the fit (default = 50), the number of steps for the MCMC warm-up (default = 1000), the minimum number of steps for the MCMC estimation (default = 2000), the maximum number of steps for the whole MCMC run (default = 5000) and the binning of the PDS for the fitting process*.

2.2 Automated detection of significant peaks and mode identification

First, we divide the PDS by the background model which is comprised of the granulation and white noise components. A Mexican-hat wavelet-transform based algorithm then searches for the significant peaks in the predefined area of $\nu_{\max} \pm 3$ times the width of the Gaussian function fitted to the oscillation power excess. Next, we optimize simultaneously the parameters of all the detected oscillation modes through maximum likelihood estimation, using a global model fit. From that fit, TACO provides a list of frequencies, amplitudes and linewidths. Those oscillation parameters are subsequently used for mode identification.

This part of the analysis can be applied iteratively in order to achieve an optimal result. For KIC 4937257, we first searched for the resolved peaks in the spectrum, which were then fitted with Lorentzian functions. We then used the mode identification module to detect the $\ell = 0, 2$ modes in that preliminary list of frequencies by using well-established relations for solar-like oscillations (such as the "universal pattern"). We divided the PDS by a global model fit, including only the even modes, and reran the peak detection method. This time, we used TACO to detect both resolved and unresolved peaks, where the latter are fitted with sinc^2 functions. The final step was to combine the lists to obtain all the frequencies of statistically-significant oscillation modes. We have reported these results in Table 1. Figure 3 shows the different steps of the peak detections for KIC 4937257.

For the peak detection module, the optimization parameters are the minimum signal-to-noise ratio of the wavelet for resolved peaks (set to 1.3) plus the maximum search line-width for resolved peaks in the continuous wavelet transform (set to $0.4\,\mu$Hz) and the minimum (most frequent) probability threshold for unresolved peaks (default = 0.0001).

After obtaining the final list of frequencies, TACO evaluates the dipole modes ($\ell = 1$), and a period spacing is estimated (if present). Finally, for the rotationally-split modes the azimuthal orders are identified and the rotational splitting is determined. A more detailed description of these remaining analysis modules can be found in our main TACO paper (in preparation).

3 Conclusions

With more asteroseismic data becoming available in the near future, TACO can provide an important step towards an automated and reliable asteroseismic study of solar-like oscillations in main-sequence, subgiant and red-giant stars. Owing to its modular design, each part of the analysis can be used separately and new modules can be included without much effort. For example, the module to detect significant peaks in a frequency spectrum could be very useful for extracting the observed frequencies of classical pulsators. TACO has been tested extensively on 4 years of *Kepler* data (i.e., APOKASC red-giant sample; Pinsonneault et al. 2014, 2018). In addition, we have successfully applied it to study the global oscillations of the Sun using BISON (García Saravia Ortiz de Montellano et al. 2018) and SPM Virgo data (Themeßl et al. in prep.), and also of δ Eridani observed by the SONG network (Bellinger et al., in prep.), the subgiants ν Indi (Chaplin et al., in press) and β Hydri observed by *TESS*.

*To change the number of granulation components to two, substitute the class "KeplerBg3Comp" within the code to "KeplerBg2Comp". Other functional forms of the fit can be implemented as new classes.

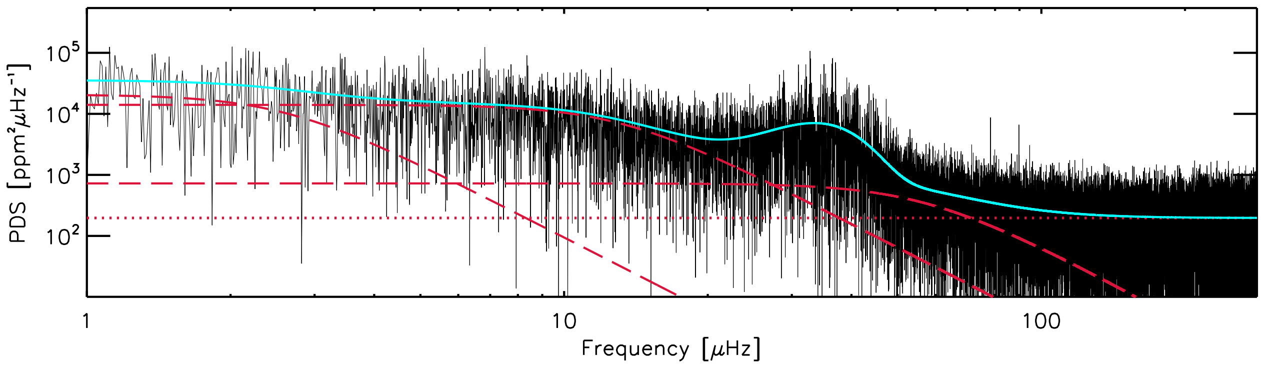

Fig. 1. Power density spectrum (in black) of KIC 4937257 showing our global model fit (in cyan), which comprises three granulation components (red dashed lines), one white noise component (horizontal red dotted line) and a Gaussian fit to the oscillation power excess.

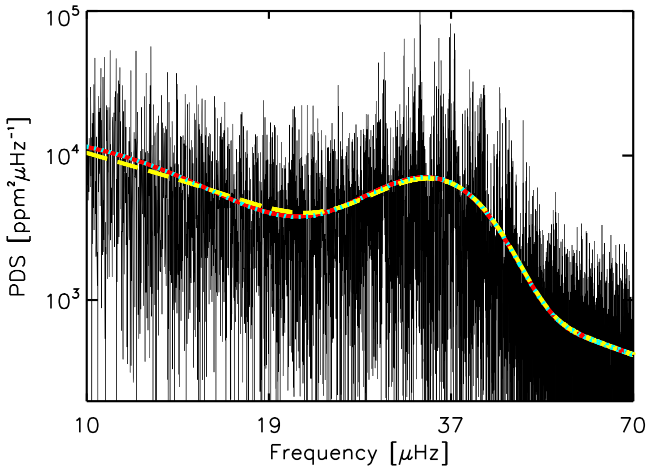

Fig. 2. Part of the power density spectrum of KIC 4937257 around the oscillation power excess is shown. The different colours represent the global fits based on different binnings. The $\nu_{\rm max}$ estimates are: $33.77 \pm 0.27\,\mu$Hz (300 bins, dotted red line), $34.18 \pm 0.38\,\mu$Hz (50 bins, dashed yellow line) and $33.79 \pm 0.26\,\mu$Hz (no binning of the data, dotted cyan line).

This work was funded by the European Research Council under the European Community's Seventh Framework Programme (FP7/2007-2013)/ERC grant agreement No. 338251 (StellarAges).

References

Baglin, A., Auvergne, M., Boisnard, L., et al. 2006, in 36th COSPAR Scientific Assembly, Vol. 36, 3749

Borucki, W. J., Koch, D., Basri, G., et al. 2010, Science, 327, 977

Foreman-Mackey, D., Hogg, D. W., Lang, D., & Goodman, J. 2013, PASP, 125, 306

García Saravia Ortiz de Montellano, A., Hekker, S., & Themeßl, N. 2018, MNRAS, 476, 1470

Howell, S. B., Sobeck, C., Haas, M., et al. 2014, PASP, 126, 398

Mosser, B., Belkacem, K., Goupil, M. J., et al. 2011, A&A, 525, L9

Pinsonneault, M. H., Elsworth, Y., Epstein, C., et al. 2014, ApJS, 215, 19

Pinsonneault, M. H., Elsworth, Y. P., Tayar, J., et al. 2018, ApJS, 239, 32

Rauer, H., Catala, C., Aerts, C., et al. 2014, Experimental Astronomy, 38, 249

Ricker, G. R., Winn, J. N., Vanderspek, R., et al. 2015, JATIS, 1, 014003

Tassoul, M. 1980, ApJS, 43, 469

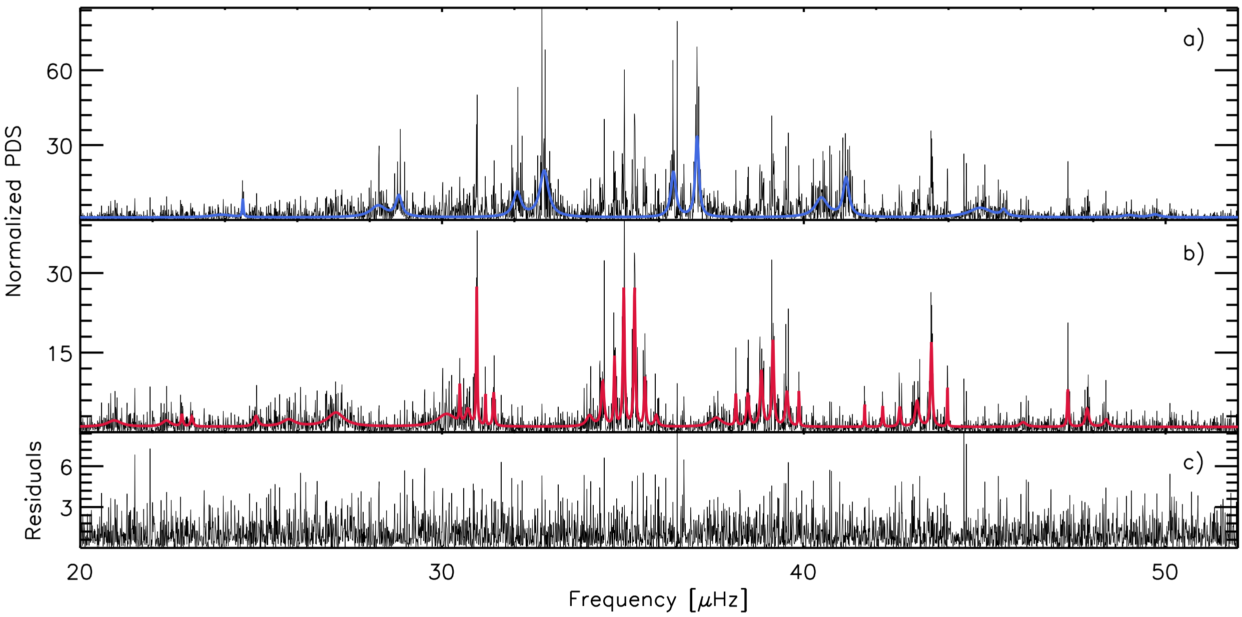

Fig. 3. Panel a): Background-normalized power density spectrum (PDS) covering the oscillation modes of the red giant, with a fit to the even modes (in blue). Panel b): PDS normalized by the global fit from panel a), now including the fit to the odd modes (in red); the residuals are shown in panel c).

Table 1. Characteristics of detected oscillation modes for KIC 4937257.

Frequency [μHz]	Amplitude	Linewidth [μHz]	Spherical degree
20.94 ± 0.08	0.94 ± 0.14	0.24 ± 0.12	1
22.38 ± 0.06	0.71 ± 0.14	0.14 ± 0.09	1
22.81 ± 0.02	0.45 ± 0.13	0.03 ± 0.02	1
23.08 ± 0.03	0.46 ± 0.12	0.04 ± 0.03	1
23.91 ± 0.13	1.13 ± 0.17	0.38 ± 0.16	2
24.49 ± 0.01	0.64 ± 0.14	0.02 ± 0.01	0
24.86 ± 0.03	0.63 ± 0.13	0.06 ± 0.04	1
25.76 ± 0.08	0.95 ± 0.15	0.22 ± 0.11	1
27.07 ± 0.06	1.51 ± 0.12	0.27 ± 0.06	1
28.24 ± 0.05	1.93 ± 0.20	0.26 ± 0.10	2
28.81 ± 0.03	1.59 ± 0.18	0.10 ± 0.04	0
30.12 ± 0.07	1.49 ± 0.14	0.30 ± 0.08	1
30.49 ± 0.01	0.56 ± 0.20	0.01 ± 0.01	1
30.71 ± 0.04	0.78 ± 0.19	0.07 ± 0.06	1
30.96 ± 0.01	1.14 ± 0.21	0.02 ± 0.01	1
31.20 ± 0.01	0.48 ± 0.15	0.01 ± 0.01	1
31.43 ± 0.01	0.70 ± 0.13	0.02 ± 0.01	1
32.08 ± 0.03	1.99 ± 0.18	0.13 ± 0.04	2
32.82 ± 0.02	2.90 ± 0.19	0.14 ± 0.03	0
34.08 ± 0.04	0.81 ± 0.14	0.10 ± 0.06	1
34.44 ± 0.02	1.11 ± 0.14	0.05 ± 0.02	1
34.77 ± 0.01	0.95 ± 0.16	0.02 ± 0.01	1
35.02 ± 0.01	1.44 ± 0.20	0.03 ± 0.01	1
35.32 ± 0.01	1.43 ± 0.20	0.02 ± 0.01	1
35.61 ± 0.01	0.85 ± 0.14	0.03 ± 0.01	1
35.92 ± 0.04	0.57 ± 0.13	0.05 ± 0.03	1
36.40 ± 0.02	2.19 ± 0.19	0.08 ± 0.02	2
37.05 ± 0.01	2.46 ± 0.23	0.06 ± 0.02	0
37.58 ± 0.06	0.99 ± 0.13	0.19 ± 0.08	3
38.12 ± 0.01	0.59 ± 0.15	0.02 ± 0.02	1
38.45 ± 0.02	0.86 ± 0.14	0.04 ± 0.02	1
38.83 ± 0.01	1.15 ± 0.15	0.04 ± 0.02	1
39.15 ± 0.01	1.28 ± 0.17	0.03 ± 0.01	1
39.53 ± 0.02	0.97 ± 0.13	0.05 ± 0.02	1
39.87 ± 0.01	0.55 ± 0.13	0.01 ± 0.01	1
40.48 ± 0.04	2.24 ± 0.16	0.21 ± 0.05	2
41.17 ± 0.02	2.17 ± 0.18	0.10 ± 0.02	0
41.68 ± 0.01	0.39 ± 0.11	0.01 ± 0.01	1
42.18 ± 0.01	0.47 ± 0.12	0.02 ± 0.01	1
42.65 ± 0.02	0.60 ± 0.12	0.03 ± 0.02	1
43.13 ± 0.02	0.95 ± 0.12	0.06 ± 0.02	1
43.53 ± 0.01	1.20 ± 0.16	0.03 ± 0.01	1
43.97 ± 0.01	0.52 ± 0.13	0.01 ± 0.01	1
44.88 ± 0.07	2.13 ± 0.15	0.38 ± 0.08	2
45.53 ± 0.06	0.81 ± 0.19	0.08 ± 0.05	0
46.06 ± 0.09	0.53 ± 0.13	0.10 ± 0.07	3
47.30 ± 0.01	0.70 ± 0.13	0.02 ± 0.01	1
47.83 ± 0.03	0.76 ± 0.12	0.05 ± 0.03	1
48.36 ± 0.04	0.56 ± 0.13	0.07 ± 0.05	1
48.98 ± 0.11	0.81 ± 0.18	0.24 ± 0.16	2
49.71 ± 0.07	0.74 ± 0.16	0.15 ± 0.11	0
53.03 ± 0.17	0.91 ± 0.19	0.38 ± 0.24	2

Stars and their variability observed from space
C. Neiner, W. W. Weiss, D. Baade, R. E. Griffin, C. C. Lovekin, A. F. J. Moffat (eds)

A NOVEL MODELING OF MAGNETO-ROTATING STELLAR EVOLUTION

K. Takahashi[1]

Abstract. About 10% of massive and intermediate-mass main-sequence stars possess strong surface magnetic fields, and the magnetic massive stars may be progenitors of strongly magnetized neutron stars known as magnetars. However, the evolution of magnetic fields in stellar interiors remains a big open question for stellar evolution theory. We have developed a new stellar evolution code that is capable to follow a long-timescale evolution of stellar magnetism. First, the structure of the stellar field is significantly simplified to have axially symmetric toroidal + poloidal components. Then the evolution of the two-component magnetic field is described by the mean-field dynamo equation. The new formalism self-consistently includes the effects of the Ω-dynamo, which results from large scale shear in the rotation flow, magnetic dissipation, and angular momentum transfer due to magnetic stress. We will present our preliminary results and discuss how the model can be verified by observations.

Keywords: Stars: evolution — Stars: magnetic field — Stars: rotation

1 Introduction

Magnetic stars account for about ∼10% of radiative main sequence stars of OBA types (Landstreet 1992). Their strong (typically ∼100-1000 G) fields are characterized by a large-scale (∼dipole) structure and long-timescale (∼10 yr) stability (Wade et al. 2000; Silvester et al. 2014). No correlations between the field strength and fundamental parameters have been found so far. These properties would be compatible with a fossil field, i.e., a remnant of star formation that survives in a stable configuration (Braithwaite & Spruit 2017).

The evolution of radiative main sequence stars, which are the progenitors of magnetic white dwarfs and neutron stars, can be significantly affected by strong magnetic fields. Because of the intrinsically strong stellar wind, the magnetic breaking for massive OB type stars can be significant enough to be observed (e.g., σ-Ori E; Townsend et al. 2010). Strong surface fields can even trap the wind material into a corotating magnetosphere, which provides substantial understanding for X-ray emission of IQ Aur (Babel & Montmerle 1997) or phase variations of Balmer-line emissions of σ-Ori E (Townsend & Owocki 2005). Besides, strong magnetic stress that is furnished by the internal field may account for the efficient angular momentum transfer in a radiatively stratified region (Spruit 1999).

The purpose of this work is to present a new framework of stellar evolution modeling, in which the evolution of stellar magnetic fields and rotation is treated in a physically consistent manner. The axisymmetric dipole approximation is applied to the magnetic field structure. The field evolution equation is formulated starting from the mean-field MHD equation. We utilize a path integral for the averaging, which yields the conservation law of magnetic flux in the case of no dissipation. Also, the angular momentum transfer due to the Lorentz force is expressed by defining the Maxwell stress tensor, which naturally yields a conservative expression for the magnetic angular momentum transfer.

In this proceedings, simulation results of the code test as well as the magneto-rotating stellar evolution of intermediate-mass radiative stars are presented. The detailed information will be reported in Takahashi & Langer (2019).

2 Field evolution coupled with stellar rotation

2.1 Magnetic flux conservation

We have calculated a 1.5 $M_\odot$ stellar evolution with a magnetic field but switching off the magnetic dissipation and the Ω-effect. The evolution is followed from the zero age main sequence (ZAMS) phase until the star starts core helium burning and enters into the red clump in the Hertzsprung-Russell Diagram.

[1] Max-Planck-Institut für Gravitationsphysik / Albert-Einstein-Institut, Am Mülenberg 1, 14476 Potsdam-Golm, Germany

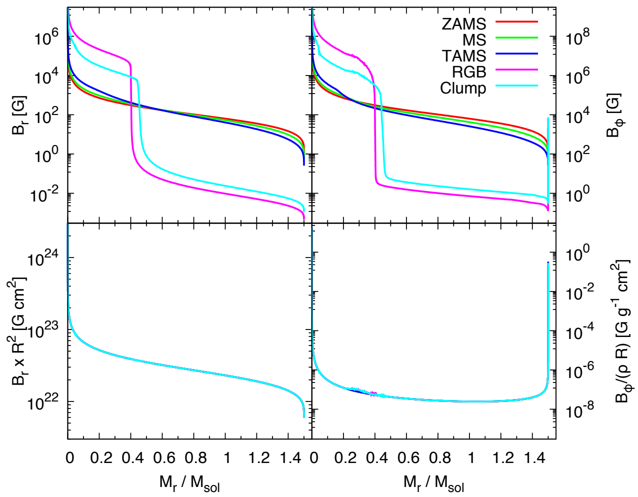

Fig. 1. Evolution of the internal magnetic fields at the ZAMS (red), at the middle of the main sequence phase (MS; green), at TAMS (blue), at the middle of the red giant phase (RG; magenta), and at the red clump phase (Clump; cyan). The top two panels show the evolution of the radial component (B_r; left) and the toroidal component (B_ϕ; right). The bottom two panels show the evolution of conserved quantities, $B_r r^2$ at the left and $B_\phi/\rho r$ at the right.

Figure 1 shows the resulting evolution of the internal magnetic field. The top two panels, which show radial and toroidal magnetic field components, exhibit the effect of contraction and expansion during stellar evolution. They show that the magnetic field in the central core of $<\sim 0.4$ M$_\odot$ is amplified by about two orders of magnitude, while that in the outer envelope is reduced by about four orders of magnitude. Nevertheless, the two quantities which are shown in the bottom panels, are entirely conserved during the whole evolutionary phases. Only a small fluctuating deviation is seen for $B_\phi/\rho r$ at $\sim$0.3–0.4 M$_\odot$. This results from automated mesh refinement, which is done to capture the thin structure of the hydrogen-burning shell that surrounds the helium core.

2.2 *Torsional wave solution*

Differential rotation winds up the poloidal magnetic field to produce a toroidal component. As the toroidal component gets strong, the magnetic stress increases as well, counteracting to reduce the differential rotation. We have found that the basic equations that describe the evolution of the toroidal field component and the angular momentum can be approximated by a set of hyperbolic differential equations. Therefore, we can expect that a wave that propagates with the speed of about the Alfvén velocity is formed in this system.

Taking the 1.5 M$_\odot$ main-sequence stellar structure as the background, which has a radius of $\sim$ 1.5 R$_\odot$, we have calculated the coupled evolution of the toroidal field and the rotation frequency, taking the Ω-effect and the magnetic stress into account, but turning the viscosity and the magnetic diffusivity off. A uniform $B_r = 500$ G is applied. A step-function distribution of $\Omega = 10^{-4}$ rad s^{-1} for $M \leq 1$ M$_\odot$, or $\Omega = -10^{-4}$ rad s^{-1} otherwise, is applied for the initial Ω distribution. B_ϕ is set uniformly to be zero.

Figure 2 shows the result. As we have expected, the formation and propagation of torsional waves are well captured by the simulation. The wave velocity becomes $c \sim 80$ cm s^{-1}, and correspondingly, the wave-crossing time from the center to the surface becomes $\sim 1.3 \times 10^9$ s $\sim$ 41 yr. We have noticed that the torsional wave results in two important outcomes. The first is that the wave accounts for the significantly efficient angular momentum transport. When the dissipations in both mechanical and magnetic components are switched on, the wave propagates through the stellar interior while it dissipates to distribute the angular momentum to other regions. The model finally reaches rigid rotation. The second outcome is that the star starts to oscillate torsionally during the transitional period towards rigid rotation. The oscillation frequency is comparable to the wave-crossing time. This torsional oscillation may be compatible with the period change of stellar rotation observed in several B-type stars (Krtička et al. 2017; Shultz et al. 2018, 2019).

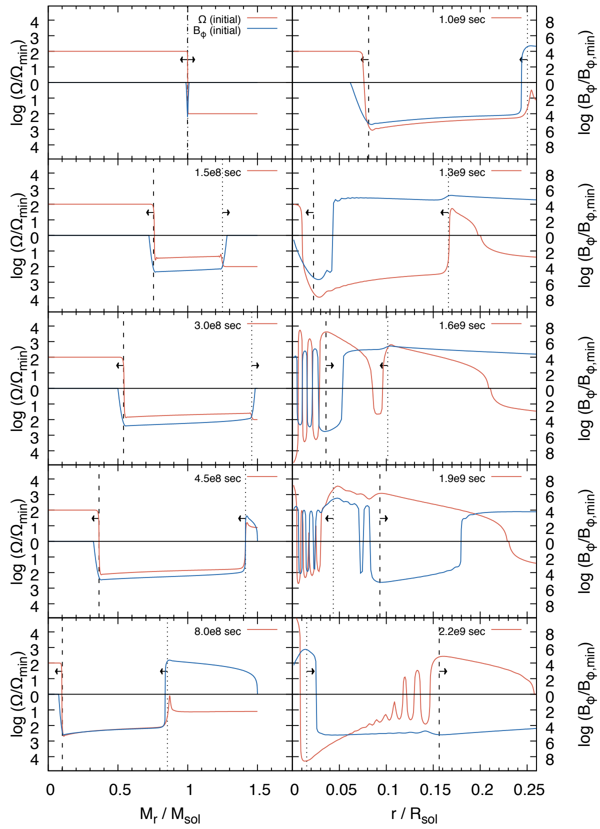

Fig. 2. Wave propagation illustrated by 10 different time snapshots. The logarithm of Ω or B_ϕ is shown by either a red or a blue line. The horizontal axis for the left panels, in which waves before 8×10^8 s are shown, is the enclosed mass. For the right panels, in which waves after 1×10^9 s are shown, the radius is taken as the horizontal axis. The black dashed and black dotted lines show the estimated positions of the wave fronts, and arrows indicate directions of the propagation. Critical values of $\Omega_{\rm min} = 1 \times 10^{-6}$ rad s^{-1} and $B_{\phi,\rm min} = 1 \times 10^3$ G are used.

3 Evolution toward a red giant

As a demonstration of the capability of our method, we have calculated the stellar evolution up to the central helium ignition of a solar metallicity 1.5 $M_\odot$ magneto-rotating star. For the initial distributions of rotation and magnetic field, rigid rotation with $\Omega = 5.0 \times 10^{-5}$ rad s^{-1} (equivalent to $P_{\rm rot} = 1.4$ d), zero toroidal field component of $B_\phi = 0$, and a uniform radial component of $B_r = 10$ G are applied. In this calculation, we test two types of angular velocity profiles in a convective region. The first one is the rigid rotation, $\Omega(r) \sim r^0$, and the other is $\Omega(r) \sim r^{-1}$.

Evolution of the surface and core rotation periods are shown in Fig. 3. The core spin period of the Ω-constant model, which is shown by the red solid line, agrees with the surface periods shown by the black dashed line up to the point of $\log R/R_\odot = 1.7$. Meanwhile, not only the core rotation period but also the surface period of the $\Omega \sim r^{-1}$ model simultaneously explain the observations.

4 Conclusions

We have developed a new framework to follow the evolution of magneto-rotating stars. The time-dependent and global basic equations have the torsional wave solution. We predict that a magnetic star can oscillate torsionally, which may be compatible with the observed rotational period change. Moreover, the dissipating wave can account for the efficient angular momentum transport inside the star. We plan to apply this new formulation to general purpose stellar evolution simulations in the future.

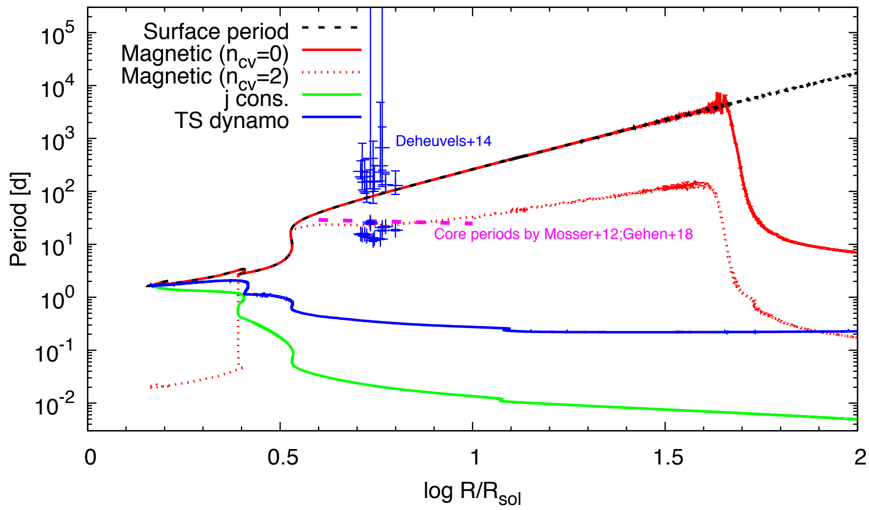

Fig. 3. Period evolution of the 1.5 $M_\odot$ stellar models. Surface and core rotation periods of the $\Omega \sim r^0$ model are shown by black dashed and red solid lines, and the core rotation period of the $\Omega \sim r^{-1}$ model is shown by the red dotted line. Core periods of models with no angular momentum transfer and with transfer due to the Tayler-Spruit dynamo are shown by green and blue solid lines. Theoretical models are compared with the observations of the core rotation periods by Mosser et al. (2012); Gehan et al. (2018) (purple dashed line) and of both the surface and the core periods by Deheuvels et al. (2014) (blue pluses).

References

Babel, J. & Montmerle, T. 1997, A&A, 323, 121

Braithwaite, J. & Spruit, H. C. 2017, Royal Society Open Science, 4, 160271

Deheuvels, S., Doğan, G., Goupil, M. J., et al. 2014, A&A, 564, A27

Gehan, C., Mosser, B., Michel, E., Samadi, R., & Kallinger, T. 2018, A&A, 616, A24

Krtička, J., Mikulášek, Z., Henry, G. W., Kurfürst, P., & Karlický, M. 2017, MNRAS, 464, 933

Landstreet, J. D. 1992, A&A Rev., 4, 35

Mosser, B., Goupil, M. J., Belkacem, K., et al. 2012, A&A, 548, A10

Shultz, M., Rivinius, T., Das, B., Wade, G. A., & Chand ra, P. 2019, MNRAS, 486, 5558

Shultz, M. E., Wade, G. A., Rivinius, T., et al. 2018, MNRAS, 475, 5144

Silvester, J., Kochukhov, O., & Wade, G. A. 2014, MNRAS, 440, 182

Spruit, H. C. 1999, A&A, 349, 189

Takahashi, K. & Langer, N. 2019, in prep.

Townsend, R. H. D., Oksala, M. E., Cohen, D. H., Owocki, S. P., & ud-Doula, A. 2010, ApJ, 714, L318

Townsend, R. H. D. & Owocki, S. P. 2005, MNRAS, 357, 251

Wade, G. A., Donati, J. F., Landstreet, J. D., & Shorlin, S. L. S. 2000, MNRAS, 313, 851

NEW FULLY EVOLUTIONARY MODELS FOR ASTEROSEISMOLOGY OF ULTRA-MASSIVE WHITE-DWARF STARS

A. H. Córsico[1, 2], F. C. De Gerónimo[1,2], M. E. Camisassa[1,2] and L. G. Althaus[1,2]

Abstract. Ultra-massive hydrogen-rich white dwarf (WD) stars of spectral type DA ($M_\star > 1M_\odot$) coming from single-star evolution are expected to harbour cores made of ^{16}O and ^{20}Ne, resulting from semi-degenerate carbon burning when the progenitor star evolved through the super-asymptotic giant branch phase. These stars are expected to be crystallized by the time they reach the ZZ Ceti instability strip ($T_{\rm eff} \sim 12\,500$ K). Theoretical models predict that crystallization leads to a separation of ^{16}O and ^{20}Ne in the core of ultra-massive WDs, which has an impact on their pulsational properties. That property offers a unique opportunity to study the processes of crystallization. This paper presented the first results of a detailed asteroseismic analysis of the best-studied ultra-massive ZZ Ceti star, BPM 37093. As a second step, we plan to repeat the analysis using ultra-massive DA WD models with C/O cores in order to study the possibility of elucidating the core chemical composition of BPM 37093 and shed some light on its evolutionary origin. We also plan to extend this kind of analysis to other stars observed from the ground and with space instruments like *Kepler* and *TESS*.

Keywords: tars: pulsations, interiors, white dwarfs

1 Input physics, evolution/pulsation codes, and stellar models

In this project, evolutionary models were generated by Camisassa et al. (2019) employing the `LPCODE` evolutionary code. They are shown in Fig. 1. The input physics of `LPCODE` is described by Camisassa et al. (2019), where details can be found. Of particular importance in this work is the treatment of crystallization. Cool WD stars are believed to crystallize through the strong Coulomb interactions in their very dense interiors (van Horn 1968). In our models, crystallization set in when the energy of the Coulomb interaction between neighbouring ions was much higher than their thermal energy. The release of latent heat, and the release of gravitational energy associated with changes in the chemical composition profile induced by crystallization, were taken into account consistently. The chemical redistribution due to phase separation and the associated release of energy were considered following Althaus et al. (2010), appropriately modified by (van Horn 1968) for ONe plasmas. To assess the enhancement of ^{20}Ne in the crystallized core, we used the azeotropic-type phase diagram of Medin & Cumming (2010). The pulsation code used to compute nonradial g(gravity)-mode pulsations was the adiabatic version of the `LP-PUL` pulsation code described by Córsico & Althaus (2006). To account for the effects of crystallization on the pulsation spectrum of g modes, we adopted the "hard sphere" boundary conditions (see Montgomery & Winget 1999). Our ultra-massive WD models have stellar masses $M_\star = 1.10, 1.16, 1.22$, and $1.29 M_\odot$. They result from the complete evolution of the progenitor stars through the super-asymptotic giant branch phase. The core and inter-shell chemical profiles of our models at the start of the WD cooling phase were obtained from Siess (2010).

2 Chemical profiles and the Brunt-Väisälä frequency

The cores of our models are composed mostly of ^{16}O and ^{20}Ne, plus and smaller amounts of ^{12}C, ^{23}Na, and ^{24}Mg. Since element diffusion and gravitational settling operate throughout the WD evolution, our models develop pure H envelopes. The He content of our WD sequences is given by the evolutionary history of progenitor star, but instead, the H content of our canonical envelopes [$\log(M_{\rm H}/M_\star) = -6$] has been set by imposing that the further evolution does not lead to H thermonuclear flashes on the WD cooling track. We have expanded our grid

[1] Facultad de Ciencias Astronómicas y Geofísicas, Universidad Nacional de La Plata, Paseo delBosque s/n, (1900), La Plata, Argentina
[2] Instituto de Astrofísica de La Plata, IALP, CONICET-UNLP, La Plata, Argentina

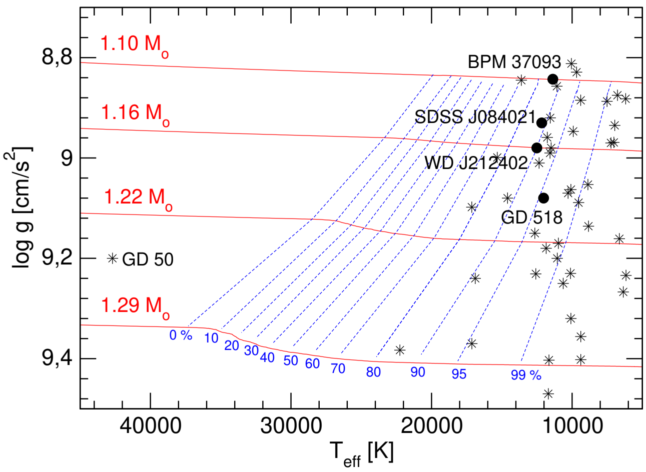

Fig. 1. Evolutionary tracks (red solid lines) of the ultra-massive DA WD models computed by Camisassa et al. (2019) in the $T_{\rm eff} - -\log g$ plane. Blue dashed lines indicate 0, 10, 20, 30, 40, 50, 60, 70, 80, 90, 95 and 99% of crystallized mass. The location of ultra-massive DA WD stars are indicated by black star symbols, and the ultra-massive ZZ Ceti stars are shown as black dots.

of models by generating new sequences artificially with thinner H envelopes [$\log(M_{\rm H}/M_\star) = -7, -8, -9, -10$], for each value of stellar mass. This procedure was done at high-luminosity stages of the WD evolution. The temporal changes of the chemical abundances due to element diffusion were assessed by using a new fully-implicit treatment for time-dependent element diffusion (Althaus et al. 2019, submitted).

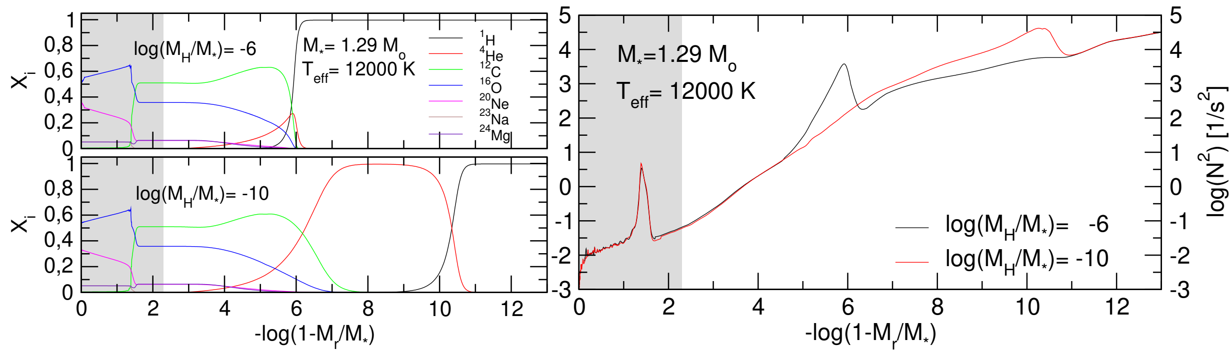

Fig. 2. Left: Abundances of the different chemical species by mass, as a function of the fractional mass, corresponding to ONe-core WD models with $M_\star = 1.29 M_\odot$, $T_{\rm eff} \sim 12\,000$ K and two different H-envelope thicknesses, as indicated. The percentage of crystallized mass fraction of the models is 99.5% (grey region). **Right:** Logarithm of the squared Brunt-Väisälä frequency, corresponding to the same ONe-core WD models with $M_\star = 1.29 M_\odot$, $T_{\rm eff} \sim 12\,000$ K and $\log(M_{\rm H}/M_\star) = -6$, and -10 that are shown in the left panel.

The chemical profiles in terms of the fractional mass for $1.29 M_\star$ ONe-core WD models at $T_{\rm eff} \sim 12\,000$ K and H envelope thicknesses $\log(M_{\rm H}/M_\star) = -6$ and -10 are shown in the left panel of Fig. 2. A pure He buffer develops as we consider thinner H envelopes. At this effective temperature, the chemical rehomogenization due to crystallization has already finished, giving rise to a core where the abundance of ^{16}O (^{20}Ne) increases (decreases) outwards. The right panel of Fig. 2 shows the logarithm of the squared Brunt-Väisälä frequency corresponding to the same models shown in the left panel. The peak at $-\log(1 - M_r/M_\star) \sim 1.4$, which is due to the abrupt step at the triple chemical transition between ^{12}C, ^{16}O and ^{20}Ne, is within the solid part of the core, so it has no relevance for the mode-trapping properties of the models. This is because, according to the hard-sphere boundary conditions adopted for the pulsations, the eigenfunctions of g modes do not penetrate the crystallized region. In this way, the mode-trapping properties are entirely determined by the presence of the He/H transition, which is located in more external regions for thinner H envelopes. The pulsation properties of these models have been explored by De Gerónimo et al. (2019) and Córsico et al. (2019, submitted).

Table 1. Frequencies and periods of BPM 37093 (Metcalfe et al. 2004), together with the theoretical periods, harmonic degrees, radial orders and period differences of our best-fitting model.

$\Pi^{\rm O}$ [sec]	ν [μHz]	$\Pi^{\rm T}$ [sec]	ℓ	k	δ_i [sec]
511.7	1954.1	512.4	2	29	−0.7
531.1	1882.9	531.9	1	17	−0.8
548.4	1823.5	548.1	2	31	0.3
564.1	1772.7	565.3	2	32	−1.2
582.0	1718.2	583.0	2	33	−1.0
600.7	1664.9	599.9	2	34	0.8
613.5	1629.9	613.8	1	20	−0.3
635.1	1574.6	632.2	2	36	2.9

Table 2. The main characteristics of BPM 37093

Quantity	Spectroscopy	Asteroseismology
$T_{\rm eff}$ [K]	$11\,370 \pm 500$	$11\,650 \pm 40$
$M_\star/M_\odot$	1.098 ± 0.1	1.16 ± 0.014
$\log g$ [cm/s^2]	8.843 ± 0.05	8.970 ± 0.025
$\log(L_\star/L_\odot)$	—	-3.25 ± 0.01
$\log(R_\star/R_\odot)$	—	-2.234 ± 0.006
$\log(M_{\rm H}/M_\star)$	—	-6 ± 0.26
$\log(M_{\rm He}/M_\star)$	—	-3.8
$M_{\rm cr}/M_\star$	0.935	0.923
$X_{^{16}{\rm O}}$ cent.	—	0.52
$X_{^{20}{\rm Ne}}$ cent.	—	0.34
Quantity	**Measured**	**Asteroseismology**
$\overline{\Delta\Pi}_{\ell=1}$ [s]	—	29.70
$\overline{\Delta\Pi}_{\ell=2}$ [s]	17.3 ± 0.9	17.63
Quantity	**Astrometry (*Gaia*)**	**Asteroseismology**
d [pc]	14.81	11.32
π [mas]	67.5	88.3

3 Application: asteroseismological analysis of the ultra-massive ZZ‘Ceti star BPM 37093

BPM 37093 is the first ultra-massive ZZ Ceti star discovered by Kanaan et al. (1992). It is characterized by $T_{\rm eff} = 11\,370$ K and $\log g = 8.843$ (Nitta et al. 2016). We searched for a pulsation model that matches the individual pulsation periods of BPM 37093 best. The goodness of the match between the theoretical pulsation periods ($\Pi_k^{\rm T}$) and the observed periods ($\Pi_i^{\rm O}$) is measured by means of a merit function defined as $\chi^2(M_\star, M_{\rm H}, T_{\rm eff}) = \frac{1}{N}\sum_{i=1}^{N} \min[(\Pi_i^{\rm O} - \Pi_k^{\rm T})^2]$, where N is the number of observed periods. The WD model that shows the lowest value of χ^2, if it exists, is adopted as the “best-fitting model”. We assumed two possibilities for the mode identification: (i) that all of the observed periods correspond to g modes with $\ell = 1$, and (ii) that the observed periods correspond to a mix of g modes with $\ell = 1$ and $\ell = 2$. We considered the eight periods employed by Metcalfe et al. (2004) (see Table 1). Case (i) did not show clear solutions compatible with BPM 37093 in relation to its spectroscopically-derived effective temperature. Rather, case (ii) resulted in a clear seismological solution for a WD model with $M_\star = 1.16 M_\odot$, $T_{\rm eff} = 11\,650$ K and $\log(M_{\rm H}/M_\star) = -6$. Table 1 shows the periods of the best-fitting model along with the harmonic degree, radial order, and the period differences (theoretical minus observed). Most of the periods of BPM 37093 were identified as $\ell = 2$ modes. That was not expected, owing to geometric cancellation effects (that is, $\ell = 1$ modes should be more easily detectable than $\ell = 2$ modes). Table 2 lists the main characteristics of the best-fitting model for BPM 37093. Its parameters are in agreement with the spectroscopically-derived ones. The asteroseismological distance is also in line with the astrometric distance obtained from *Gaia*.

A.H.C. warmly thanks the Local Organising Committee, in particular Prof. Werner W. Weiss, for support that allowed him to attend this conference.

References

Althaus, L. G., García-Berro, E., Renedo, I., et al. 2010, ApJ, 719, 612
Camisassa, M. E., Althaus, L. G., Córsico, A. H., et al. 2019, A&A, 625, A87
Córsico, A. H. & Althaus, L. G. 2006, A&A, 454, 863
De Gerónimo, F. C., Córsico, A. H., Althaus, L. G., Wachlin, F. C., & Camisassa, M. E. 2019, A&A, 621, A100
Kanaan, A., Kepler, S. O., Giovannini, O., & Diaz, M. 1992, ApJ, 390, L89
Medin, Z. & Cumming, A. 2010, Phys. Rev. E, 81, 036107
Metcalfe, T. S., Montgomery, M. H., & Kanaan, A. 2004, ApJ, 605, L133
Montgomery, M. H. & Winget, D. E. 1999, ApJ, 526, 976
Nitta, A., Kepler, S. O., Chené, A.-N., et al. 2016, IAU Focus Meeting, 29B, 493
Siess, L. 2010, A&A, 512, A10
van Horn, H. M. 1968, ApJ, 151, 227

Stars and their variability observed from space
C. Neiner, W. W. Weiss, D. Baade, R. E. Griffin, C. C. Lovekin, A. F. J. Moffat (eds)

MAGNETO-ROSSBY WAVES AND SHORT-TERM PERIODICITY IN SOLAR-TYPE STARS

T. Z. Zaqarashvili[1]

Abstract. Magnetic activity and variations of solar-type stars are governed by dynamo layers below or inside the convection zone. This layer is supposed to be much shorter than the stellar radius, so large-scale magneto-Rossby waves can be trapped inside. The waves may cause variations in the dynamo magnetic field and can thus can trigger quasi-periodic eruptions of magnetic flux towards the surface, which will modify stellar light-curves seen in *Kepler, CoRoT* and *TESS* data. The spherical harmonics of magneto-Rossby waves of different order and degree can lead to multiple short-term periodicities in the light-curves. Theoretical oscillation spectra of magneto-Rossby waves and the short periods observed in stellar activity will allow us to estimate the magnetic field strength in the dynamo layer. The seismology of stellar interiors, combined with magneto-Rossby wave theory in solar-type stars having different rotation periods, opens a new domain of research into understanding stellar evolution.

Keywords: Stars: activity, magnetic field

1 Introduction

Chromospheric activity in main-sequence stars based on Mount Wilson Ca II H and K observations has solar cycle-like periodicity (Wilson 1978). The empirical relation between cyclic (P_{cyc}) and rotational (P_{rot}) periods shows clearly an increase in P_{cyc} with increasing P_{rot} (Saar & Brandenburg 1999). Recent *Kepler* and *CoRoT* collected huge amounts of data on stellar activity, thus offering an excellent basis to search for Sun-like periodicities in other stars. The main period in solar activity is around 11 years, which means that the ratio of cyclic to rotational periods is approximately 150 for the Sun (the solar rotational period is around 26 days). On the other hand, solar activity also displays a shorter periodicity of 150–180 days ("Rieger-type" periodicity), which is actually correlated with solar-cycle strength (Gurgenashvili et al. 2016). Several stars from *CoRoT* (Lanza et al. 2009) and *Kepler* (Bonomo & Lanza 2012) data showed $P_{cyc}/P_{rot} \sim 4-6$, which is within the range of Rieger periodicity in the Sun. The two cases cited clearly indicate the existence of periodicity in stellar activity, and to the need for further systematic and comprehensive analyses. The most plausible mechanism for solar Rieger-type periodicity is connected with magneto-Rossby waves in the internal dynamo layer (Zaqarashvili et al. 2010), which enables us to probe the layer of the observed periodicity in solar activity (Gurgenashvili et al. 2016; Zaqarashvili & Gurgenashvili 2018). This technique of seismology can also be applied to solar-like stars at different stages of evolution by searching for short term periodicity in their light-curves.

2 Magneto-Rossby waves and seismology of dynamo layers in solar-like stars

The dispersion relation of magneto-Rossby waves in the internal dynamo layers can be written as follows (Gachechiladze et al. 2019):

$$\omega = -\frac{2m\Omega}{3l(l+1)}\left(1+2\sqrt{1+\frac{81}{8}l(l+1)\frac{B^2}{4\pi\rho\Omega^2R^2}}\right) \tag{2.1}$$

where Ω is the stellar angular velocity, B the magnetic field strength in the layer, ρ the layer density, R the distance of the layer from the stellar centre, m is the order and l is the degree of spherical harmonics of the magneto-Rossby waves. The dispersion relation shows that the periodicity depends on angular velocity and magnetic field strength, as well as the spherical harmonic order and degree (see Fig. 1). Periods determined from observations therefore enable us to estimate the magnetic field strength in a star's dynamo layers.

[1] IGAM, Institute of Physics, University of Graz, Austria and
Abastumani Astrophysical Observatory at Ilia State University, Tbilisi, Georgia

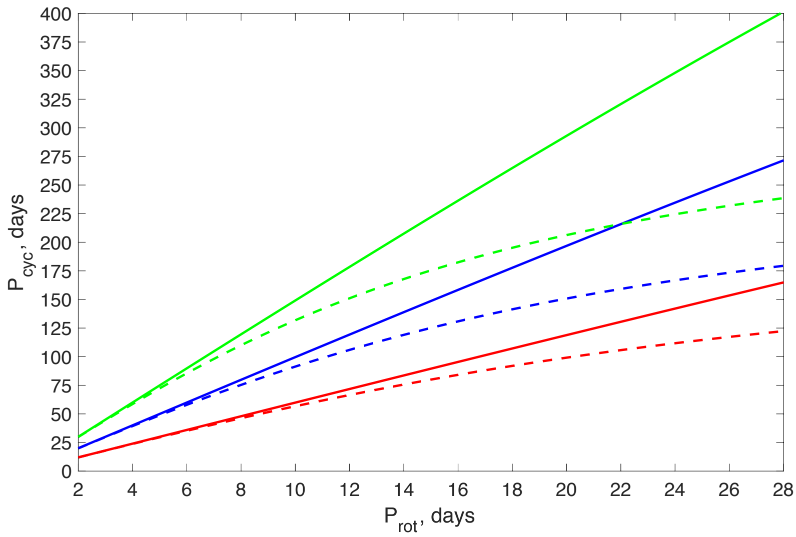

Fig. 1. Periods of magneto-Rossby wave spherical harmonics *vs.* stellar rotation period. Red, blue and green lines show the spherical harmonics of degree l=3, 4 and 5, respectively. Solid and dashed lines correspond to magnetic field strengths of 10 kG and 50 kG. The spherical harmonic order is $m = 1$.

3 Conclusions

Magneto-Rossby waves in dynamo layers of solar-like stars may lead to periodic variations in the dynamo magnetic field strength. Those variations may trigger quasi-periodic eruptions of magnetic flux towards the surface, which can modulate stellar light-curves and could be observed in *Kepler, CoRoT* and *TESS* data. Spherical harmonics of magneto-Rossby waves with different degrees have different periods, and could lead to multiple periodicities in light-curves. The periods of magneto-Rossby waves depend on the magnetic field strength (see Fig. 1), so periods determined from observations (given a theoretical dispersion relation) may allow us to probe the dynamo layers of solar-like stars. Stars having different rotation periods will then indicate how the star's dynamo magnetic field has evolved. The seismology of stellar interiors using magneto-Rossby waves can thus open up a new research area for studying stellar evolution.

This work was supported by the Austrian Science Fund (FWF) project P30695-N27 and by Georgian SRNSF project 217146. This paper resulted from discussions at workshops of the ISSI team, "Rossby waves in astrophysics" organized in Bern, Switzerland.

References

Bonomo, A. S. & Lanza, A. F. 2012, A&A, 547, A37
Gachechiladze, T., Zaqarashvili, T. V., Gurgenashvili, E., et al. 2019, ApJ, 874, 162
Gurgenashvili, E., Zaqarashvili, T. V., Kukhianidze, V., et al. 2016, ApJ, 826, 55
Lanza, A. F., Pagano, I., Leto, G., et al. 2009, A&A, 493, 193
Saar, S. H. & Brandenburg, A. 1999, ApJ, 524, 295
Wilson, O. C. 1978, ApJ, 226, 379
Zaqarashvili, T. V., Carbonell, M., Oliver, R., & Ballester, J. L. 2010, ApJ, 709, 749
Zaqarashvili, T. V. & Gurgenashvili, E. 2018, Frontiers in Astronomy and Space Sciences, 5, 7

A SOLUTION TO THE "SOLAR ABUNDANCE" PROBLEM

Q.-S. Zhang[1], Y. Li [1] and J. Christensen-Dalsgaard[2]

Abstract. We report a solution to the long-standing "solar abundance" problem. Solar models that include three extra physical processes (convective overshoot, solar wind and PMS accretion) which are missing from standard solar models are shown to be consistent simultaneously with helioseismic inferences (the depth and helium abundance of the convection zone and profiles of sound speed and density), the observed solar Li abundance, and solar neutrino fluxes.

Keywords: Convection, the Sun: abundances, the Sun: interior

1 The "solar abundance" problem

The standard solar model with revised solar composition (AGSS09, Asplund et al. (2009)) cannot be consistent with helioseismic inferences (sound speed and density profiles, $R_{\rm bc}$, and $Y_{\rm S}$). This is called the "solar abundance" problem. The recent measurement of Ne abundance by Young (2018) showed an enhancement of $\sim 40\%$ in the solar photospheric Ne abundance, denoted as AGSS09Ne composition. However, revising the Ne abundance still does not solve the problem.

Since 2004 many extra mechanisms have been tested, but no satisfactory solution has been found. This contribution proposed a different mechanism. If solar models (e.g., Model TWA) can include convective overshooting, PMS helium-poor accretion and a helium-poor solar-wind mass loss, they then show very good agreement simultaneously with helioseismic inferences: sound speed and density profiles, $R_{\rm bc}$, and $Y_{\rm S}$), the solar lithium abundance, and solar neutrino fluxes.

Model TWA is a typical improved solar model that includes the extra physical processes described below. Neither opacity nor micro diffusion enhancement is assumed.

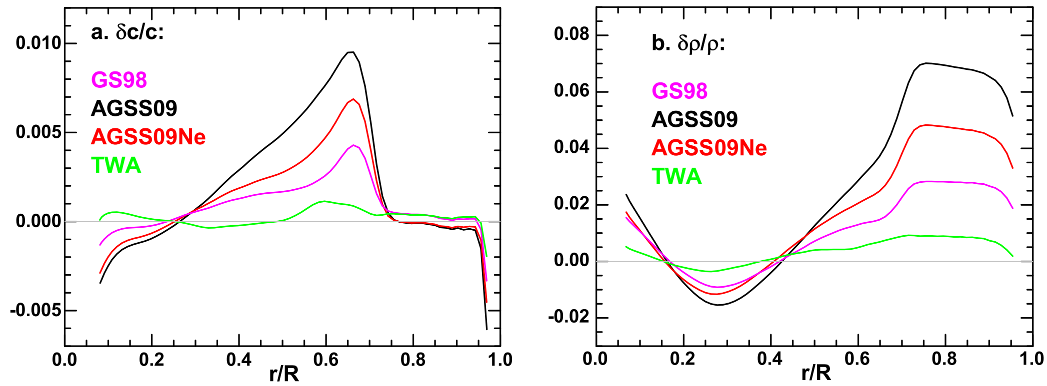

model	GS98	AGSS09	AGSS09Ne	TWA	the Sun
$M_{\rm acc}/M_\odot$	——	——	——	0.0585	——
$M_{\rm L}/M_\odot$	——	——	——	0.0028	0.001−0.03
$Y_{\rm S}$	0.2453	0.2381	0.2405	0.2450	0.2485(35)
$(Z/X)_{\rm S}$	0.0229	0.0181	0.0188	0.0188	0.0188(12)
$R_{\rm bc}/R_\odot$	0.7152	0.7239	0.7207	0.7110	0.713(1)
A(Li)	2.44	2.73	2.60	0.82	1.05(10)
neutrino fluxes in ($\rm cm^{-2}s^{-1}$)					
^{7}Be (10^9)	4.91	4.63	4.70	4.84	4.80(5%)
^{8}B (10^6)	5.35	4.74	4.89	5.13	5.16(2.2%)

[1] Yunnan Observatories, Chinese Academy of Sciences, China; zqs@ynao.ac.cn, ly@ynao.ac.cn
[2] Department of Physics and Astronomy, Aarhus University, Denmark; jcd@phys.au.dk

2 Extra physical processes in Model TWA

2.1 Convective overshoot below the convection envelope

Convective overshoot has two effects: the kinetic energy flux below the base of the convection zone (CZ), and overshoot mixing. A simple model to describe the kinetic energy flux of the overshoot below the CZ base is

$$L_{\rm K}(r) = -\beta L(r)[\frac{P(r)}{P_{BCZ}}]^{(-1/\theta)}, \text{for } r \leq r_{BCZ}, \tag{2.1}$$

where P_{BCZ} is the pressure at the base of the CZ r_{BCZ}, $\beta = 0.13$ and $\theta = 0.2$ (based on helioseismic inferences). The kinetic energy flux in the CZ has little effect on solar models, sp there is an arbitrariness to set $L_{\rm K}$ in the CZ. To retain a smooth profile for $L_{\rm K}$, it is set as

$$L_{\rm K} = -\beta L(r) \exp\left(\frac{x}{\sqrt{x^2+1}}\right) f(\log T(r), 5.7, 6.2), \text{for } r > r_{BCZ}, \tag{2.2}$$

where $x(r) = \ln[P(r)/P_{BCZ}]$ and

$$f(y,a,b) = \begin{cases} 1, y > b \\ \frac{1}{2} + \frac{1}{2}\sin[(\frac{y-a}{b-a} - \frac{1}{2})\pi], a \leq y \leq b \\ 0, y < a \end{cases}. \tag{2.3}$$

The diffusion coefficient for the overshoot mixing is modelled as (Zhang 2013):

$$D_{\rm OV} = C_{\rm X}\frac{\varepsilon_{\rm turb}}{N^2} = -\frac{C_{\rm X} g L_{\rm K}}{4.4\pi\theta r^2 P N^2}, \tag{2.4}$$

where $\varepsilon_{\rm turb}$ is the rate of dissipation of turbulent kinetic energy, and $C_{\rm X} = 5 \times 10^{-4}$ (based on the solar lithium abundance).

2.2 Solar wind

Observations have shown that the helium abundance in the solar wind is about half its abundance in the CZ, owing to the effect of the first ionization potential (FIP). The solar-wind mass-loss rate was estimated as $\mathrm{d}M/\mathrm{d}t \propto t^{-2.00\pm0.52}$ and reaches saturation before 0.1 Gyr (Wood et al. 2002).

The adopted solar-wind mass-loss rate is

$$\frac{\mathrm{d}M}{\mathrm{d}t} = -Ct^{\gamma}, \text{for } t > 0.1\text{Gyr}, \tag{2.5}$$

where adjustments in C and γ have been based on the total mass loss of $0.0028M_{\odot}$ and the present solar-wind mass-loss rate, $\mathrm{d}M/\mathrm{d}t = -2 \times 10^{-14} M_{\odot}\mathrm{yr}^{-1}$. The composition of the solar wind, based on its helium-poor property, is then set as

$$(X_{\rm L}, Y_{\rm L}, Z_{\rm L}) = \frac{(X_{\rm S}, 0.5Y_{\rm S}, Z_{\rm S})}{X_{\rm S} + 0.5Y_{\rm S} + Z_{\rm S}}, \tag{2.6}$$

2.3 PMS accretion

PMS accretion is a common property in solar-mass stars. The mass accretion rate, adopted from (Hartmann et al. 2016), is

$$\log[\frac{d(M/M_{\odot})}{d(t/\mathrm{yr})}] = -1.32 - 1.07\log(t/\mathrm{yr}) + 2.1\log(\frac{M/M_{\odot}}{0.7}). \tag{2.7}$$

The accretion starts at age 2Myr and ends at 12Myr, with a total accreted mass of $0.0585M_{\odot}$. The composition of the accreted materials is assumed to be $Z_{\rm acc} = 0.015$ and $Y_{\rm acc} = 0.07$. We also assumed that accretion in the PMS magnetosphere is ion-dominated, so the FIP effect could lead to inhomogeneous accretion. The composition of the accreted materials could therefore be different from the primordial composition.

3 Link to publication

A paper on this topic has been published by Zhang, Li, & Christensen-Dalsgaard, in ApJ 881, 103, 2019.

References

Asplund, M., Grevesse, N., & Sauval, A. J. 2009, ARA&A, 47, 481
Hartmann, L., Herczeg, G., & Calvet, N. 2016, ARA&A, 54, 135
Wood, B. E., Müller, H.-R., & Zank, G. P. 2002, ApJ, 574, 412
Young, P. R. 2018, ApJ, 855, 15
Zhang, Q. S. 2013, ApJS, 205, 18

Stars and their variability observed from space
C. Neiner, W. W. Weiss, D. Baade, R. E. Griffin, C. C. Lovekin, A. F. J. Moffat (eds)

THE AGE OF ZERO AGE MAIN SEQUENCE STARS AS AN ANALYTIC FUNCTION OF MASS

T. Steindl[1] and K. Zwintz[1]

Abstract. We discuss the need for an improved theoretical definition of the zero age main sequence (ZAMS) for stellar evolution models. We show that this may be achieved by creating an analytic function of the ZAMS age as a function of stellar mass by investigating the hydrogen abundance throughout the star. To achieve this, the most probable ZAMS model for different stellar masses in the range 0.5–6.0 $M_\odot$ is determined. The corresponding ages are then fitted with a piecewise power law function.

Keywords: Stars: pre-main sequence, methods: numerical

1 Introduction

The computation of stellar models is very important for the understanding of stellar structure and evolution. The typical approach is to create stellar models for different sets of input physics that define the characteristics of each evolutionary calculation. Different stellar models, calculated with two distinct sets of such input physics, are compared at the same relative evolutionary stage so as to infer information about the structure of a star.
During evolution on the main sequence, the core hydrogen abundance may be used as a proxy for age and therefore relative evolutionary stage, as has been demonstrated in the past (e.g. Aerts et al. 2018). Pre-main-sequence stars do not exhibit full equilibrium hydrogen burning and therefore a similar approach can not be applied to infer relative ages.
For the study of pre-main-sequence stars it is important to find stellar properties that can play the same role as the central hydrogen abundance does for main-sequence stars. This may be achieved by considering stellar properties relative to their values at the zero age main sequence (ZAMS) as a reference point, where the pre-main-sequence phase ends. We therefore need a reliable definition of the ZAMS. Any such method should be reliable for the whole mass range of pre-main-sequence stars.
Different definitions of the ZAMS have been considered in the past. We find that they all show problems for stars in specific mass ranges. We discuss how the hydrogen profile throughout the star in element diffusion-free models may be used to infer the most probable ZAMS model for pre-main sequence models of any mass in the range 0.5–6.0 $M_\odot$. All of our models have been calculate using version 11701 of the stellar-evolution code "Modules for Experiments in Stellar Astrophysics" (`MESA`) (Paxton et al. 2011, 2013, 2015, 2018, 2019).

2 ZAMS age as an analytic function of mass

Stars originate from clouds of molecular matter. It is therefore reasonable to assume uniform element abundances at the beginning of their evolution. Those abundances become changed by different physical mechanisms, e.g. nuclear reactions or chemical mixing. Furthermore, dynamical instability leads to constant abundances in convective regions and therefore to discontinuities of the hydrogen abundance at convective boundaries.
Figure 1 shows the hydrogen abundance X_H towards the end of the pre-main-sequence lifetime. Hydrogen burning in a convective stellar centre introduces a discontinuity in the hydrogen profile. A subsequent change of the position of the convective boundary then introduces multiple discontinuities (in this case two as depicted in Fig. 1). Mixing gradually reduces the size of the discontinuity until the hydrogen profile is again continuous. The right panel of Fig. 1 shows only one discontinuity at the convective boundary; it corresponds to a main-sequence star.
As this effect is present in all our stellar models, we use it to define the ZAMS. The most probable ZAMS model is therefore the first stellar model that shows no discontinuities (apart from the convective core) in the

[1] Institute for Astro and Particle Physics, 6020 Innsbruck, Austria

hydrogen profile.

We acknowledge the fact that more efficient mixing or the inclusion of element diffusion and gravitational settling might induce changes to the profiles identified as the most probable ZAMS model. It remains to be seen if this influences the hydrogen profile to such an extent that it renders that definition unfeasible, but at this stage we have no reason to believe so.

We have calculated a total of 100 stellar models, and searched for the most probable ZAMS model. The resulting ages seem to be described well by a piecewise power law. Fitting a piecewise power law function then provides the ZAMS age as an analytic function of mass. We find that the resulting ages agree well with previous definitions for corresponding mass ranges.

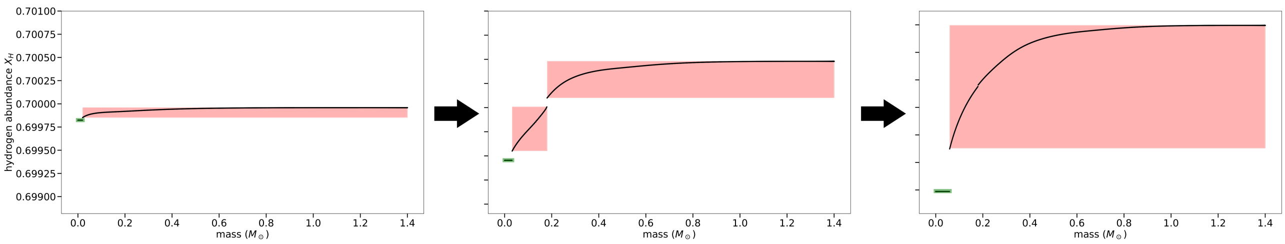

Fig. 1. The hydrogen abundance (black) as a function of mass for a $1.4\,M_\odot$ star. The green area shows the convective region; non-convective zones of continous hydrogen abundance are shaded in red. The hydrogen burning convective centre introduces a change in the hydrogen abundance. The moving position of the convective boundary then lets discontinuities appear. The hydrogen abundance of main-sequence stars shows no discontinuities, apart from the convective core.

3 Conclusions

We provided a possible new definition of the ZAMS age for stellar models. It relies on the hydrogen profile throughout the star to define the most probable ZAMS model for a MESA evolution of a pre-main-sequence star. While it remains to be shown that this methodology works for models that include higher amount of mixing as well as element diffusion and gravitational settling, it provides a reliable way of inferring ZAMS ages for all masses in the range 0.5–6.0 $M_\odot$.

References

Aerts, C., Molenberghs, G., Michielsen, M., et al. 2018, ApJS, 237, 15
Paxton, B., Bildsten, L., Dotter, A., et al. 2011, ApJS, 192, 3
Paxton, B., Cantiello, M., Arras, P., et al. 2013, ApJS, 208, 4
Paxton, B., Marchant, P., Schwab, J., et al. 2015, ApJS, 220, 15
Paxton, B., Schwab, J., Bauer, E. B., et al. 2018, ApJS, 234, 34
Paxton, B., Smolec, R., Schwab, J., et al. 2019, ApJS, 243, 10

Stars and their variability observed from space
C. Neiner, W. W. Weiss, D. Baade, R. E. Griffin, C. C. Lovekin, A. F. J. Moffat (eds)

STUDY OF CONVECTION IN ONE AND MULTI-DIMENSIONAL PULSATING MODELS

G. B. Kovács[1,2,3], R. Szabó[2,3] and J. Nuspl[2]

Abstract. The handling of convection is one of the open questions in numeric modelling. Since convection is a genuine multi-dimensional phenomenon, one-dimensional simulations can only approximately (and inadequately) describe its complexity and effects. We investigated the accuracy of these approximations through the use of the multi-dimensional code SPHERLS.

Keywords: Convection, Hydrodynamics, stars: oscillations, variables: RR Lyrae

1 Introduction

In this study we compared selected results of two distinct hydrodynamical pulsation codes. For the first we used the one-dimensional (1D) Budapest–Florida code (Buchler et al. 1997) which contains 7 parameters to describe the effects of turbulent convection (Yecko et al. 1998). For the second (2D calculations) we used the multi-dimensional pulsation code SPHERLS (Geroux & Deupree 2011). The latter programme applies a hybrid technique to ensure that no free parameters are required to account for convection. We applied our calculations to an RR Lyrae model with the following parameters: $L = 50L_\odot$, $M = 0.7M_\odot$, $T_{\mathrm{eff}} = 6300\mathrm{K}$, $X = 0.75$, $Z = 0.0005$.

2 Comparing the 2D and 1D model results

The periodic boundary conditions at the edges of the computed sector might influence the nature of the convective cells in 2D; it is therefore mandatory to investigate its effects. In Fig. 1 we present a 6- and a 12-degree-wide 2D model with convective cells reaching down to a temperature of 50000 K. The convection alters the shape of the ionisation front at a temperature of 10000 K but the size of the convective cells remains the same in both cases. We can therefore conclude that the boundary condition has no effects on the convection.

We compared the light-curves of the two models, and found that the 1D model has higher amplitude by a factor of two (See Fig. 2, left panel). Note, however, that its parameters were adjusted to fit the observations instead of the 2D results. We also studied the pressure, temperature and radial-velocity profiles (See Fig. 2, right panel). In the first two cases the profiles are similar, with only slight differences in the temperature. On the contrary, the two models have very different radial-velocity profiles, while the 1D model has higher velocities in the partially ionized zones.

3 Conclusions

We investigated the 1D approximation of convection in the Budapest–Florida code compared to 2D computations. Our test case was an RR Lyrae type pulsator, and we found that the amplitude of the pulsation is greater in the 1D case. However, the 1D model is calibrated to observations, so we will check the results of the 2D model before further calibrations are made. Kupka & Muthsam (2017) suggested that time-varying α parameters throughout the calculations could be a better approximation for the 1D problem.

To get a better understanding of this problem and the relevant physical phenomena, we will continue the investigation of one and multi-dimensional computations, comparing different prescriptions for convection including, (e.g.) the hydrocode of Smolec & Moskalik (2008) since they use a different approach.

This study has been supported by the Lendület Program of the Hungarian Academy of Sciences, grant No. LP2018-7/2019, and grant NKFIH K-115709 of the Hungarian National Research, Development and Innovation Office.

[1] ELTE, Eötvös Loránd University, Budapest, Hungary
[2] Konkoly Observatory, CSFK, Budapest, Hungary
[3] MTA CSFK Lendület Near-Field Cosmology Research Group

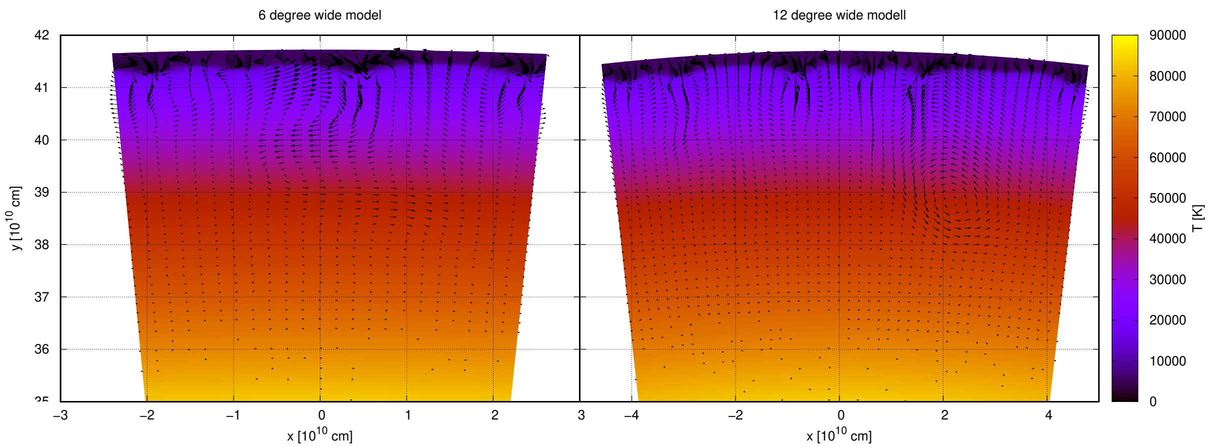

Fig. 1. A 6-degree (**left**) and a 12-degree (**right**)-wide 2D model computed by SPHERLS. The colour bar shows the temperature of the model at a given point; the arrows are the normalized velocity. As can be seen, the size of the convective cells are the same in both models.

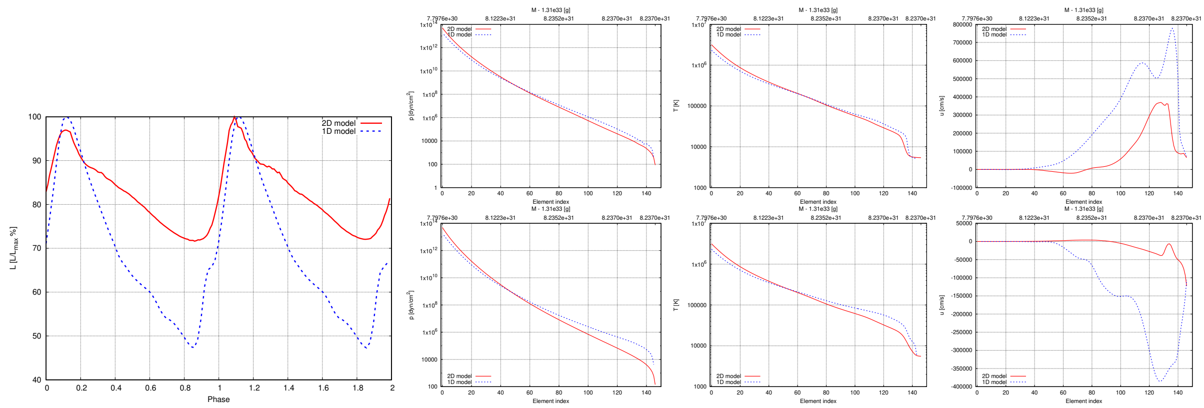

Fig. 2. Left: Phase-folded normalized light-curves of the SPHERLS (red) and Budapest–Florida (blue) models. It is clear that the former produces smaller amplitudes. **Right:** Profiles of the pressure, temperature and radial-velocity (from left to right) near the luminosity maximum (top row) and minimum (bottom row). The pressure and temperature profiles are similar, but the velocity profiles are very different in the two models.

References

Buchler, J. R., Kolláth, Z., & Marom, A. 1997, ApSS, 253, 139

Geroux, C. M. & Deupree, R. G. 2011, ApJ, 731, 18

Kupka, F. & Muthsam, H. J. 2017, Living Reviews in Computational Astrophysics, 3, 1

Smolec, R. & Moskalik, P. 2008, ActAA, 58, 193

Yecko, P. A., Kollath, Z., & Buchler, J. R. 1998, AAP, 336, 553

Stars and their variability observed from space
C. Neiner, W. W. Weiss, D. Baade, R. E. Griffin, C. C. Lovekin, A. F. J. Moffat (eds)

CONVECTION IN ROTATING STARS: CONVECTIVE PENETRATION AND MIXING

K. C. Augustson[1] and S. Mathis[1]

Abstract. This poster examined a model for rotating convection in stars and planets. The convection model is used as a boundary condition for a first-order expansion of the equations of motion in the transition region between convectively unstable and stably-stratified regions, estimating the depth of convective penetration into the stable region and establishing a relationship between that depth and the local convective Rossby number. Several models for the mixing in such a region were considered.

Keywords: stars: convection, rotation, mixing

1 Introduction

Convective flows cause mixing not only in regions of superadiabatic temperature gradients but in neighboring subadiabatic regions as well, as motions from the convective region contain sufficient inertia to extend into those regions before being braked buoyantly or eroded turbulently (e.g., Miesch 2005; Lecoanet et al. 2015; Viallet et al. 2015). This convective penetration and turbulence can thus alter the chemical composition and thermodynamic properties in those regions (e.g., Zahn 1991; Augustson et al. 2016; Pratt et al. 2017a). One such convection model has been described in Paper I (Augustson & Mathis 2019). The motivation for taking rotation into account in this model was the numerical work of Käpylä et al. (2005) and Barker et al. (2014), who found that the rotational scaling of the amplitude of the temperature, its gradient, and the velocity field compared well with those derived by Stevenson (1979). Moreover, the analysis by Howard (1963) showed that a principle of heat-flux maximization provided a sound basis for the description of Rayleigh–Bénard convection, triggering its use here. Thus, two hypotheses underlie the convection model: the Malkus conjecture that convection arranges itself to maximize the heat flux, and that the nonlinear velocity field can be characterised by the dispersion relationship of the linearised dynamics. Constructing the model of rotating convection then consists of three steps: first, to derive a dispersion relationship that links the normalized growth rate $\hat{s} = s/N_*$ to $q = N_{*,0}/N_*$, which is the ratio of superadiabaticity of the nonrotating case to that of the rotating case, where $N_*^2 = |g\alpha_T\beta|$ is the absolute value of the square of the Brunt-Väisälä frequency, g is the magnitude of the gravity, α_T is the coefficient of thermal expansion, and β is the temperature gradient. The next is to apply the normalized wavevector $\xi^3 = k^2/k_z^2$ (where $k_z = \pi/l$, with l being the depth of the convective layer) to maximize the heat flux with respect to ξ. The last is to assume an invariant maximum heat flux that closes this three-variable system.

To that end, a local region was considered, as in Paper I, where a small 3D section of the spherical geometry was the focus of the analysis. As shown in figure 1 of that Paper, this region covers a portion of both convectively stable and unstable zones, where the setup is configured for a low-mass star with an external convective envelope. Those regions may be exchanged when considering an early-type star with a convective core. In this local frame, there is an angle between the effective gravity $\mathbf{g}_{\text{eff}}$ and the local rotation vector that is equivalent to the co-latitude, θ. The Cartesian coordinates are defined such that the vertical direction z is anti-aligned with the gravity vector, the horizontal direction y lies in the meridional plane and points toward the north pole defined by the rotation vector, and the horizontal direction x is equivalent to the azimuthal direction. The assumption of this convection model is that the magnitude of the velocity is defined as the ratio of the maximizing growth rate and wavevector. With that approximation, the velocity amplitude can be defined relative to the case of nondiffusive and nonrotating scales without a loss of generality, as

$$\frac{\mathrm{v}}{\mathrm{v}_0} = \frac{k_0}{s_0}\frac{s}{k} = \frac{5}{\sqrt{6}}\frac{N_*}{N_{*,0}}\frac{\hat{s}}{\xi^{3/2}} = \frac{5}{\sqrt{6}}\frac{\hat{s}}{q\xi^{3/2}} = \left(\frac{5}{2}\right)^{\frac{1}{6}}\xi^{-\frac{1}{2}}. \tag{1.1}$$

[1] AIM, CEA, CNRS, Université Paris-Saclay, Université Paris Diderot, Sorbonne Paris Cit, F-91191 Gif-sur-Yvette, France

Only the maximising wavevector therefore needs to be determined in order to ascertain the relative velocity amplitude. From all those equations, the horizontal wavevector may be seen to be roots of the fourteenth-order polynomial:

$$\xi^3\left(V_0\xi^2+\tilde{s}\right)^2\left[3V_0K_0\xi^4\left(2\xi^3-3\right)+\tilde{s}\xi^2(V_0+K_0)\left(4\xi^3-7\right)+\tilde{s}^2\left(2\xi^3-5\right)\right]$$
$$-\frac{6\cos^2\theta}{25\pi^2\mathrm{Ro}_\mathrm{c}^2}\left[2\tilde{s}\left(K_0-V_0\right)+3\tilde{s}^2\xi+\tilde{s}\left(K_0+5V_0\right)\xi^3+3K_0V_0\xi^5\right]=0,, \tag{1.2}$$

where V_0 and K_0 are the non-dimensional diffusivities and $\tilde{s}$ is a numerical factor. To ascertain the maximising wavenumber, and thus the velocity, of the motions that maximise the heat flux, one therefore supplies the co-latitude, θ, and the convective Rossby number of the flow, Ro_c.

Once the quantities relating to the convection model have been defined, the impact of rotation on the convective penetration can be characterised. Following Paper I, we determined that the depth of convective penetration scaled as $L_P/L_{P,0}=(\mathrm{v}/\mathrm{v}_0)^{3/2}$. Then, considering the extreme-value models of penetration developed by Pratt et al. (2017b), one can improve the initial estimate of Baraffe et al. (2017). Using the above extension of the Zahn (1991) model, one could then estimate both the penetration depth and the level of diffusive turbulent mixing. Taking the parameters of the Gumbel distribution as in Pratt et al. (2017a) yields the following description of the radial dependence of the diffusion: coefficient

$$D_\mathrm{v}\left(r\right)=\left(\frac{5}{2}\right)^{\frac{1}{6}}\frac{\alpha H_{P,0}\mathrm{v}_0h}{3\sqrt{z}}\left\{1-\exp[-\exp\left(\left(r-r_c\right)/\lambda L_P+\mu/\lambda\right)]\right\},, \tag{1.3}$$

where r_c is the base of the convection zone and $\mu=5\times10^{-3}$ and $\lambda=6\times10^{-3}$ are the empirically determined parameters from Baraffe et al. (2017). Likewise, following the analysis of Korre et al. (2019), one can find that

$$D_\mathrm{v}\left(r\right)=\left(\frac{5}{2}\right)^{\frac{1}{6}}\frac{\alpha H_{P,0}\mathrm{v}_0h}{3\sqrt{z}}\exp\left(-\frac{\left(r-r_c\right)^2}{2\delta_G^2}\right),\quad\text{where}\quad\delta_G=1.2\frac{\mathrm{v}}{\mathrm{v}_0}\left(\frac{E_0P_r}{SRa_0}\right)^{1/2},, \tag{1.4}$$

where S is the stiffness of the stable interface, Ra_0 is the Rayleigh number, P_r is the Prandtl number, and E_0 is the energy in the nonrotating convection. These models have now to be implemented in stellar evolution codes (Michielsen et al. 2019), and to be assessed with seismic constraints and the observed surface abundances.

K. C. Augustson and S. Mathis acknowledge support from the ERC SPIRE 647383 grant.

References

Augustson, K. C., Brun, A. S., & Toomre, J. 2016, ApJ, 829, 92
Augustson, K. C. & Mathis, S. 2019, ApJ, 874, 83
Baraffe, I., Pratt, J., Goffrey, T., et al. 2017, ApJ, 845, L6
Barker, A. J., Dempsey, A. M., & Lithwick, Y. 2014, ApJ, 791, 13
Howard, L. N. 1963, Journal of Fluid Mechanics, 17, 405
Käpylä, P. J., Korpi, M. J., Stix, M., & Tuominen, I. 2005, A&A, 438, 403
Korre, L., Garaud, P., & Brummell, N. H. 2019, MNRAS, 484, 1220
Lecoanet, D., Le Bars, M., Burns, K. J., et al. 2015, Phys. Rev. E, 91, 063016
Michielsen, M., Pedersen, M. G., Augustson, K. C., Mathis, S., & Aerts, C. 2019, A&A, 628, A76
Miesch, M. S. 2005, Living Reviews in Solar Physics, 2, 1
Pratt, J., Baraffe, I., Goffrey, T., et al. 2017a, A&A, 604, A125
Pratt, J., Busse, A., Müller, W.-C., Watkins, N. W., & Chapman, S. C. 2017b, New Journal of Physics, 19, 065006
Stevenson, D. J. 1979, Geophysical and Astrophysical Fluid Dynamics, 12, 139
Viallet, M., Meakin, C., Prat, V., & Arnett, D. 2015, A&A, 580, A61
Zahn, J.-P. 1991, A&A, 252, 179

Stars and their variability observed from space
C. Neiner, W. W. Weiss, D. Baade, R. E. Griffin, C. C. Lovekin, A. F. J. Moffat (eds)

GRAVITY OFFSET AND COUPLING FACTOR OF MIXED MODES IN RGB STARS

C. Pinçon[1]

Abstract. The space-borne missions CoRoT and *Kepler* provided us with exquisite photometric data for thousands of red giant stars. The observation of mixed modes in the oscillation spectra of these stars brought stringent constraints on their deep interiors. In this short article, we discuss the potential of two seismic parameters associated with mixed modes, namely, the gravity offset, $\varepsilon_{\rm g}$, and coupling factor, q, to probe the internal structure of red giants. The observed variations in these parameters along the red giant branch (hereafter, RGB) are interpreted by means of a simple analytical model. Their sensitivity to the extra mixing at the base of the convective envelope (hereafter, BCZ) is emphasized.

Keywords: asteroseismology, stellar interior, stellar modeling

1 Mixed-mode frequency pattern

Owing to the high density contrast between the core and the envelope of red giant stars, stochastically-excited oscillation modes can propagate in two resonant cavities: a central one where they behave as gravity waves, and an external one where they behave as acoustic waves. Both resonant cavities are coupled by an intermediate region where the modes are evanescent (hereafter, ER for evanescent region), that is, where the mode frequency is larger than the Brunt-Väisälä frequency but smaller than the Lamb frequency. Such modes constitue the so-called mixed modes (e.g., Hekker & Christensen-Dalsgaard 2017, for a recent review). Guided by the asymptotic theory (i.e., in the short-wavelength approximation) of stellar oscillations (e.g., Shibahashi 1979; Tassoul 1980; Takata 2016a), observations showed that the frequency pattern of mixed modes is ruled at leading order by the implicit quantization condition (e.g., Mosser et al. 2012, 2018)

$$\cot\left[\pi\left(\frac{1}{\nu\Delta\Pi}-\varepsilon_{\rm g}\right)\right]\tan\left[\pi\left(\frac{\nu}{\Delta\nu}-\varepsilon_{\rm p}(\nu)\right)\right]=q\ , \tag{1.1}$$

where ν is the mode frequency, and $\Delta\Pi$, $\Delta\nu$, q, and $\varepsilon_{\rm g}$ are frequency-independent parameters representing the period spacing, large frequency separation, coupling factor and gravity offset, respectively. Besides, the acoustic offset $\varepsilon_{\rm p}(\nu)$ is supposed to follow the quadratic universal red-giant oscillation pattern for pressure modes (e.g., Mosser et al. 2011).

According to the asymptotic theory of mixed modes, $\Delta\Pi$ and $\Delta\nu$ are related to the "size" (i.e., as seen by waves) of the internal and external cavities, respectively. Moreover, q measures the transmission of the wave energy from one cavity to the other one through the intermediate ER, while $\varepsilon_{\rm g}$ and $\varepsilon_{\rm p}$ are sensitive to the phase lags induced at the wave reflection near the boundaries of the inner cavity (i.e., at the center and the inner edge of the ER) and those of the external cavity (i.e., at the outer edge of the ER and at the surface), respectively (e.g., Takata 2016b). The mixed-mode frequency pattern has thus the potential to bring us information on the properties of the whole structure of RGB stars, that is, of their core, envelope, and mid-layers. As an illustration, a synthetic frequency spectrum obtained by solving Eq. (1.1) with typical parameters is represented in a period-échelle diagram and plotted in Fig. 1 (left panel).

Before going further, it is worth mentioning that Eq. (1.1) is an approximate form of the asymptotic expression of mixed modes over a narrow frequency range around $\nu_{\rm max}$, the frequency at maximum oscillation power (e,g, Belkacem et al. 2011). Interpreting the fitted values of the parameters within the asymptotic framework is thus relevant if the observational error bars are larger than the error made when approximating the asymptotic expression by Eq. (1.1). We assume in the following that this condition is always met, given that the typical observed frequency ranges in red giant stars are quite narrow around $\nu_{\rm max}$ (e.g., see Fig. 5 of Mosser et al. 2013).

[1] STAR Institute, Université de Liège, 19C Allée du 6 Août, B-4000 Liège, Belgium

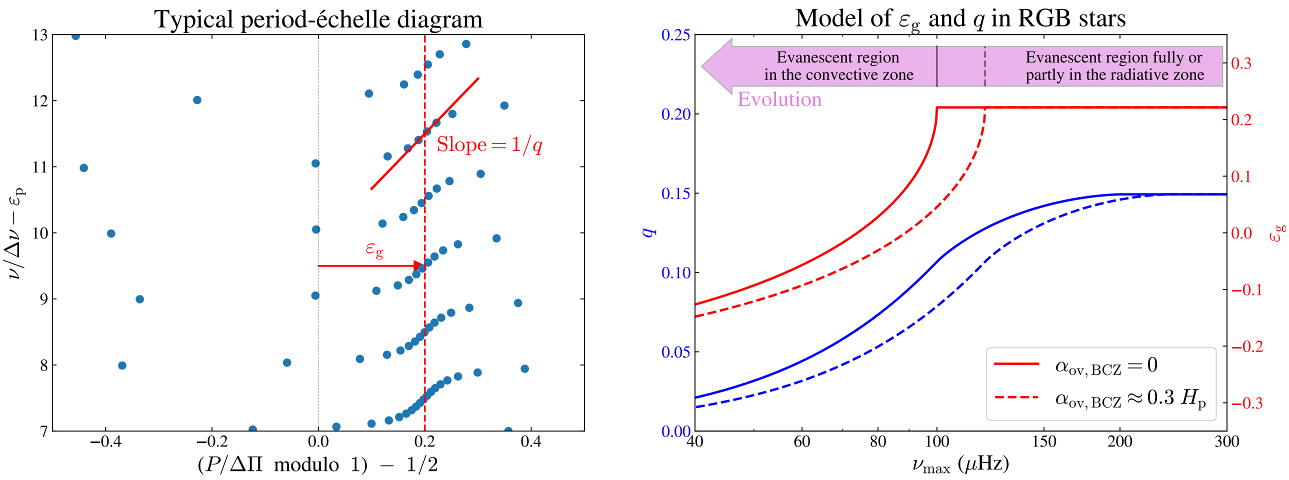

Fig. 1. Left: Period-échelle diagram obtained by solving Eq. (1.1) for a typical Red Giant where $\Delta\nu = 10$ μHz, $\nu_{\rm max} = 100$ μHz, $\Delta\Pi = 100$ s, $\varepsilon_{\rm g} = 0.2$, $q = 0.12$ and $\varepsilon_{\rm p}$ is frequency-dependent. Each blue dot represents an oscillation mode. The influence of $\varepsilon_{\rm g}$ and q on the shape of the spectrum is emphasized. **Right:** Model for the coupling factor and gravity offset on the RGB (blue and red, respectively) for typical values of $\nu_{\rm max}$. Evolution goes from the right to the left. Dashed lines represent the predictions when an adiabatic overshooting region is included at the BCZ.

2 Physical interpretation of the observed values of $\varepsilon_{\rm g}$ and q

2.1 Asymptotic predictions in a simple model

The asymptotic expressions of q and $\varepsilon_{\rm g}$ essentially depend on the properties of the ER. As shown by typical stellar models, the intermediate ER is located in the upper part of the radiative zone at the beginning of the RGB, that is, between the hydrogen-burning shell and the BCZ. As $\nu_{\rm max}$ decreases during the evolution on the RGB, the ER progressively migrates toward the lower part of the convective region (e.g., Hekker et al. 2018; Pinçon et al. 2019b). In order to explicitly express the asymptotic forms of these parameters as a function of the stellar properties, reasonable assumptions about the structure of the ER can be made along the evolution on the RGB. We note that this study implicitly focuses on dipolar modes since they are the most easily observable and were detected for a large sample of stars.

First, owing to the high density contrast between the core and surface of RGB stars, the internal structure (i.e., pressure, density,...) can be supposed in a good approximation to follow power laws with respect to radius in the ER. In these considerations, the Brunt-Väisälä frequency is about twice lower than the Lamb frequency, but their power-law exponents are similar and close to $-3/2$, except for the Brunt-Väisälä frequency in the convective zone that vanishes. Second, the ER can be supposed to be thick and the low-coupling formalism of Shibahashi (1979) has to be considered. Moreover, guided by stellar models, we assume that the envelope expansion is so predominant that the changes in the properties of the ER are much more related to its progressive migration during the RGB (owing to the rapid decrease in $\nu_{\rm max}$) rather than the slower evolution of the mid-layer structure. Finally, the ER is assumed to become fully located in the lower part of the convective envelope when $\nu_{\rm max} \lesssim 100$ μHz. We refer the reader to Pinçon et al. (2019a) for more details. Using this modeling, Pinçon et al. (2019a,b) could predict the evolution of the asymptotic expressions of q and $\varepsilon_{\rm g}$ on the RGB.

As shown in Fig. 1 (right panel), the model predicts that the gravity offset remains about equal to 0.22 in the first part of the RGB when the ER is located in the radiative region (i.e., for 100 μHz $\leq \nu_{\rm max} \lesssim$ 300 μHz). This is a direct consequence of the power-law behavior of the structure. As soon as the ER arrives in the convective zone, the asymptotic value of $\varepsilon_{\rm g}$ sharply drops; it then continues to progressively decrease during the rest of the evolution on the RGB. This sudden change originates from the abrupt kink of the profile of the Brunt-Väisälä frequency at the BCZ. These predictions are in global agreement with the observations of Mosser et al. (2018): the drop in the observed value of the gravity offset around $\nu_{\rm max} \sim 100$ μHz can therefore be interpreted as the signature of the arrival of the whole ER in the lower part of the convective envelope.

In contrast, Fig. 1 (right panel) shows that q is expected to smoothly decrease during the evolution on the RGB. More precisely, for 200 μHz $\lesssim \nu_{\rm max} \lesssim$ 300 μHz, q remains equal to about 0.14 as a result, again, of the power-law behavior of the structure in the ER. Later on the RGB, that is, for 100 μHz $\lesssim \nu_{\rm max} \lesssim$ 200 μHz, q starts decreasing slowly, because of the progressive migration of the ER in the vicinity of the BCZ. When the ER becomes fully located in the convective zone, that is, for $\nu_{\max} \lesssim 100\ \mu$Hz, the predicted decrease in q results from the continuous increase in the radial thickness of the ER as $\nu_{\max}$ decreases, so that the coupling between the two resonant cavities lowers. These predictions turn out to be in qualitative agreement with the observations of Mosser et al. (2017). The decreasing trend in the observed values of the coupling factor can therefore be interpreted as the result of either the progressive migration of the ER from the radiative to the convective regions for $\nu_{\max} \gtrsim 100\ \mu$Hz, or the increase in the thickness of the ER for $\nu_{\max} \lesssim 100\ \mu$Hz. We nevertheless note that the model predicts too small values of q compared to observations in evolved red giant stars (i.e., for $\nu_{\max} \lesssim 100\ \mu$Hz). This quantitative discrepancy could result from an observational bias, buoyancy glitches, or the frequency dependence of q over the observed frequency range (e.g., Cunha et al. 2019; Pinçon et al. 2019a).

2.2 Influence of overshooting at the BCZ

At a given evolutionary state (i.e., at a given value of $\nu_{\max}$), accounting for overshooting moves the BCZ toward deeper layers. As a result, the ER reaches the convective zone earlier on the RGB. Using typical stellar models, Pinçon et al. (2019b,a) found that including an adiabatic overshooting region over about $0.3H_{\rm p}$ at the BCZ, with $H_{\rm p}$ the local pressure scale height, increases the value of $\nu_{\max}$ at which the whole ER arrives in the convective zone from about 100 μHz to about 120 μHz. We note that Khan et al. (2018) demonstrated that such a value of overshooting is needed to fit the luminosity bump on the RGB. We can see in Fig. 1 (right panel) that overshooting tends to decrease the values of $\varepsilon_{\rm g}$ and q at a given value of $\nu_{\max}$. Moreover, the characteristic sharp decrease in $\varepsilon_{\rm g}$ occurs at higher values of $\nu_{\max}$. These predictions clearly demonstrate the potential of these parameters to probe the convective mixing processes at the BCZ.

3 Concluding remarks

The link between the global variations observed in q and $\varepsilon_{\rm g}$ and the migration of the ER from the radiative to the convective regions on the RGB is now demonstrated. The sensitivity of these parameters to the extra mixing at the BCZ is clearly emphasized. As a next step, a more detailed study of q and $\varepsilon_{\rm g}$ in grids of stellar models or in observed RGB stars with high signal-to-noise ratio will have to be performed to assess quantitatively and practically the potential of these parameters as seismic diagnoses of the stellar interior.

C. P. warmly thanks M. Takata, B. Mosser, M.-J. Goupil and K. Belkacem for fruitful discussions about the present topic, as well as M. Farnir for his careful reading of the paper. During this work, C. P. was funded by a postdoctoral fellowship from F.R.S.-FNRS.

References

Belkacem, K., Goupil, M. J., Dupret, M. A., et al. 2011, A&A, 530, A142

Cunha, M. S., Avelino, P. P., Christensen-Dalsgaard, J., et al. 2019, MNRAS, 2220

Hekker, S. & Christensen-Dalsgaard, J. 2017, A&A Rev., 25, 1

Hekker, S., Elsworth, Y., & Angelou, G. C. 2018, A&A, 610, A80

Khan, S., Hall, O. J., Miglio, A., et al. 2018, ApJ, 859, 156

Mosser, B., Belkacem, K., Goupil, M. J., et al. 2011, A&A, 525, L9

Mosser, B., Gehan, C., Belkacem, K., et al. 2018, A&A, 618, A109

Mosser, B., Goupil, M. J., Belkacem, K., et al. 2012, A&A, 540, A143

Mosser, B., Pinçon, C., Belkacem, K., Takata, M., & Vrard, M. 2017, A&A, 600, A1

Mosser, B., Samadi, R., & Belkacem, K. 2013, in SF2A-2013: Proceedings of the Annual meeting of the French Society of Astronomy and Astrophysics, ed. L. Cambresy, F. Martins, E. Nuss, & A. Palacios, 25–36

Pinçon, C., Goupil, M. J., & Belkacem, B. 2019a, submitted to A&A

Pinçon, C., Takata, M., & Mosser, B. 2019b, A&A, 626, A125

Shibahashi, H. 1979, PASJ, 31, 87

Takata, M. 2016a, PASJ, 68, 109

Takata, M. 2016b, PASJ, 68, 91

Tassoul, M. 1980, ApJ, 43, 469

Stars and their variability observed from space
C. Neiner, W. W. Weiss, D. Baade, R. E. Griffin, C. C. Lovekin, A. F. J. Moffat (eds)

BETTER PHYSICS FOR MODELLING STARS AND THEIR OSCILLATIONS

R. Trampedach[1], G. Houdek[2] and W. Däppen[3]

Abstract. Our interpretation of stellar observations can only be as good as our stellar models and the strong constraints provided by asteroseismology demand very good models indeed. We have approached modelling improvements from three angles: Including effects of realistic 3D convection on the structure of stellar surface layers, including non-adiabatic effects of that convection on oscillations, and finally improving and modernising the equation of state for stellar plasmas. We present a review of our progress on all three fronts.

Keywords: Equation of state, Convection, Asteroseismology, Stars: atmospheres, Stars: oscillations

1 Convective Effects on Modes and Stellar Atmosphere Structure

The structure of atmospheres of late-type stars are governed by interactions between turbulent convection and radiative transfer in three dimensions. This has consequences for both the outer boundary conditions of stars (Trampedach et al. 2014a), determining which atmospheric parameters correspond to a given interior model and what will be observed; and also for the acoustic cavity trapping the observed oscillation modes inside the star, affecting their frequencies through the *structural surface effect* (Trampedach et al. 2017). Direct interactions between modes and convection gives rise to coherent mode-damping and frequency shifts (*modal surface effect*) which also manifest as a component of the pressure fluctuations that is out of phase with the density fluctuations (adiabatic modes are in phase) shown in Fig. 1 (Houdek et al. 2018). This modelling effort is in progress.

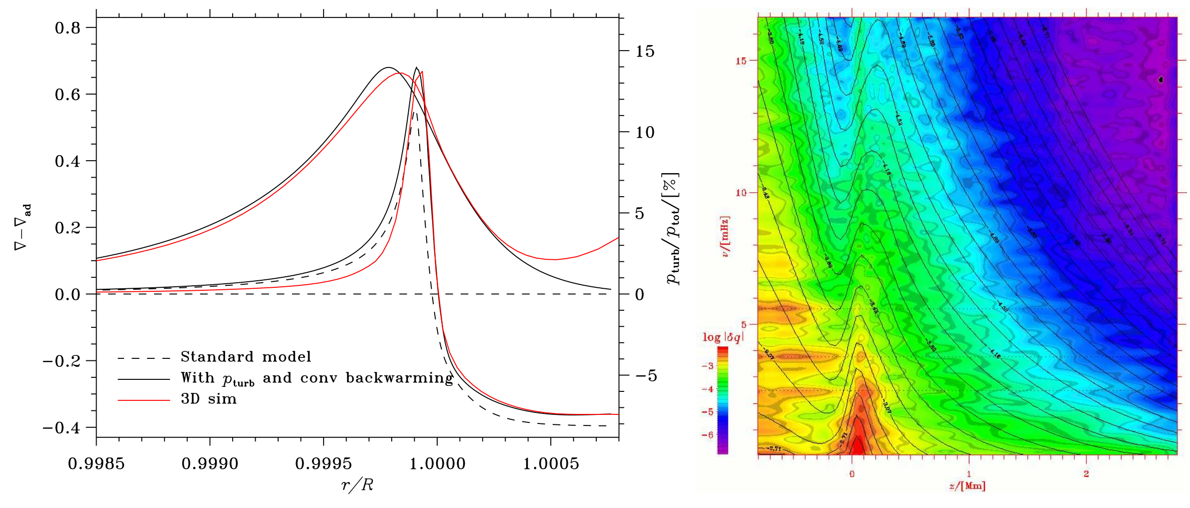

Fig. 1. Left: The turbulent to total pressure ratio (broad peak) in a 3D solar simulation (red) and reproduced in a 1D model (black). Convective backwarming affects the super-adiabatic gradient (narrow peak) A model without those two effects is shown for reference (dashed) (Trampedach et al. 2014b). **Right:** Interactions between modes and convection are quantified through the non-adiabatic pressure fluctuations, shown as function of depth and frequency in a solar sim.

[1] Space Science Institute, 4765 Walnut Street, Boulder, CO 80301, U.S.A.
[2] Stellar Astrophysics Centre, Department of Physics and Astronomy, Aarhus University, 8000 Aarhus C, DK
[3] Department of Physics and Astronomy, University of Southern California, Los Angeles, CA 90089, USA

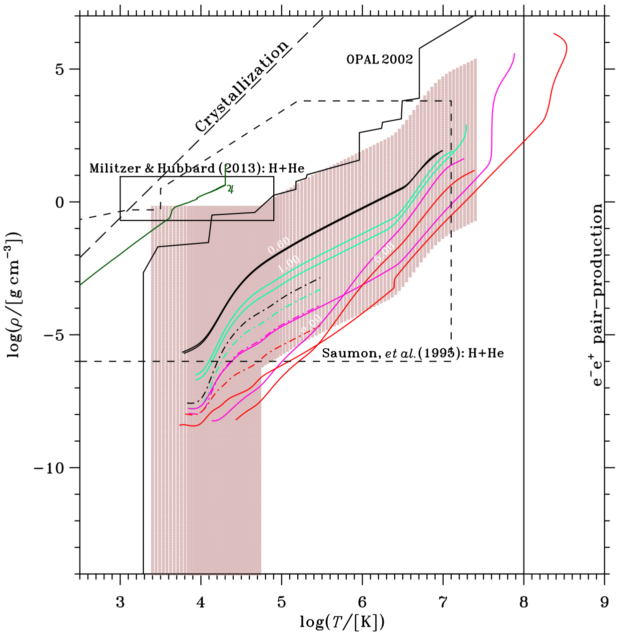

Fig. 2. The extent of various current EOS, compared with constraints on the present work: Lack of crystallisation at high density, lack of electron-positron pair-production at high T and limits to molecular partition functions at low T. The original MHD is shown in grey (Hummer & Mihalas 1988; Mihalas et al. 1988). The black outline shows the extent of the OPAL EOS by Rogers & Nayfonov (2002), and a few high-density EOS that are only evaluated for H+He mixtures are also shown. A few stellar structure tracks are shown for 0.6, 1.0, 2.0 and 5.0 M⊙ (colour coded) and each shown for three stages of their evolution.

2 A New Equation of State

The Mihalas-Hummer-Däppen (MHD) equation of state (EOS) by Hummer & Mihalas (1988); Mihalas et al. (1988) is missing a number of physical processes, only includes six elements and has a fairly limited extent in temperature T and density ϱ. An extensive update addressing those three issues is close to complete. A total of 27 elements are now included (H He Li Be B C N O Ne Na Mg Al Si P S Cl Ar K Ca Ti V Cr Mn Fe Co Ni Zr), making it uniquely suitable as a basis for opacity calculations and addressing some of the opacity issues raised by Lynas-Gray et al. (2018). Out of these 27 elements, 187 molecules form (based on partition functions by Barklem & Collet (2016)), beyond the H_2 and H_2^+ molecules included in the original MHD EOS, making this EOS very relevant for stellar atmosphere modelling.

The update also includes a much improved model of the distribution function of electric fields around atoms and ions in the plasma, which perturbs bound electrons and gives rise to pressure ionization. The hard-sphere approximation of interactions between neutral atoms has been abandoned and substituted for a model where the nuclear charges are screened by their bound electrons. The Debye-Hückel theory for weakly coupled plasmas has been amended with results from plasma simulations making it, if not accurate then at least applicable, all the way to the point of crystallisation (see Fig. 2). Relativistically degenerate electrons are included, as are quantum diffraction and exchange interactions among them.

References

Barklem, P. S. & Collet, R. 2016, A&A, 588, A96:1

Houdek, G., Lund, M. N., Trampedach, R., et al. 2018, MNRAS, (in progress)

Hummer, D. G. & Mihalas, D. 1988, ApJ, 331, 794

Lynas-Gray, A. E., Basu, S., Bautista, M. A., et al. 2018, in Workshop on Astrophysical Opacities, ed. C. Mendoza, S. Turck-Chièze, & J. Colgan, ASP Conf. Ser. No. 515 (San Francisco: ASP), 301–318

Mihalas, D., Däppen, W., & Hummer, D. G. 1988, ApJ, 331, 815

Rogers, F. J. & Nayfonov, A. 2002, ApJ, 576, 1064

Trampedach, R., Aarslev, M. J., Houdek, G., et al. 2017, MNRAS, 466, L43

Trampedach, R., Christensen-Dalsgaard, J., Nordlund, Å., Asplund, M., & Stein, R. F. 2014a, MNRAS, 442, 805

Trampedach, R., Christensen-Dalsgaard, J., Nordlund, Å., Asplund, M., & Stein, R. F. 2014b, MNRAS, 445, 4366

Binaries and clusters

Stars and their variability observed from space
C. Neiner, W. W. Weiss, D. Baade, R. E. Griffin, C. C. Lovekin, A. F. J. Moffat (eds)

R-MODE OSCILLATIONS IN ECLIPSING BINARIES

H. Saio[1]

Abstract. The presence of r-mode oscillations (global modes of Rossby waves coupled with buoyancy) in an eclipsing binary is recognized as frequency groups in a frequency-amplitude diagram obtained from a Fourier analysis of Kepler light curve data. The frequency at the upper bound of an r-mode frequency group is close to the rotation frequency of the star. Analysing about eight hundred Kepler light curves of eclipsing binaries finds about seven hundred cases showing the signature of r modes. Sometimes two sets of the frequency groups are found, which indicates the two component stars to have slightly different rotation frequencies. Plotting the so obtained rotation frequencies with respect to orbital frequencies, we find that rotation is roughly synchronous to the orbital frequency if the latter is larger than about 1 c/d, while some stars rotate super-synchronously in systems with longer orbital periods.

Keywords: Stars:binaries:eclipsing, Stars:oscillations, Stars:rotation

1 Introduction

The possible presence of r-mode oscillations (global modes of Rossby waves coupled with buoyancy; sometimes called ‘rossby modes’) in rotating stars has been discussed theoretically for a long time (e.g., Papaloizou & Pringle 1978; Provost et al. 1981; Saio 1982). But the first clear evidence of r modes was discovered only recently by Van Reeth et al. (2016) in Kepler data of rapidly rotating γ Dor variables; the evidence of r modes is the period-spacing increasing with period, while the period spacing of prograde g modes decreases with period. Later, from the period-spacing property Li et al. (2019a,b) found r modes in a large fraction of rapidly rotating γ Dor stars.

Another property of r modes is a frequency group located just below the rotation frequency in frequency-amplitude diagrams, which is useful to identify r modes when each frequency in the group cannot be resolved. From this property Saio et al. (2018); Saio (2018) found r modes in Kepler data for spotted early-type stars, binary stars, chemically-peculiar stars, and Be stars. Saio (2019) discusses that short period oscillations observed in accreting white dwarfs in cataclysmic variables are consistent with r mode oscillations. We note that this possibility was already discussed more than 40 years ago by Papaloizou & Pringle (1978).

Here, we discuss r mode oscillations in eclipsing binaries adopting from the Kepler Eclipsing Binary Catalog (KEBC) V3 maintained by the eclipsing binary working group (e.g. Kirk et al. 2016; Matijevič et al. 2012; Slawson et al. 2011; Prša et al. 2011, `http://keplerebs.villanova.edu/`). We identify r modes from the property of frequency groups in frequency-amplitude diagrams, which will be discussed below.

2 Basic properties of r modes

R-modes are normal modes of large-scale Rossby waves, which have nearly toroidal motions but couple with buoyancy due to the effect of the Coriolis force. In the co-rotating frame, r modes are retrograde modes and have frequencies smaller than the rotation frequency. Therefore, in the inertial frame, r modes are observed as prograde modes with phase speeds less than the rotation speed, and the frequencies of r modes with azimuthal order m (> 0; we adopt in this paper the convention that $m > 0$ for retrograde modes in the co-rotating frame) are less than $m\nu_{\rm rot}$ with $\nu_{\rm rot}$ being the cyclic frequency of rotation. Period spacing in the co-rotating frame is roughly constant (see e.g. Saio et al. 2018, for details), while in the inertial frame, period spacing, ΔP, decreases with frequency (Fig. 1), or increases with period. The sign of the slope of ΔP with respect to frequency (or period) of r modes in the inertial frame is opposite to that of g modes. From this fact r modes can be detected convincingly if each r-mode frequency is resolved as in many amplitude-period diagrams obtained from Kepler data for γ Dor stars (Van Reeth et al. 2016; Li et al. 2019a,b).

[1] Astronomical Institute, Tohoku University, Sendai, Japan

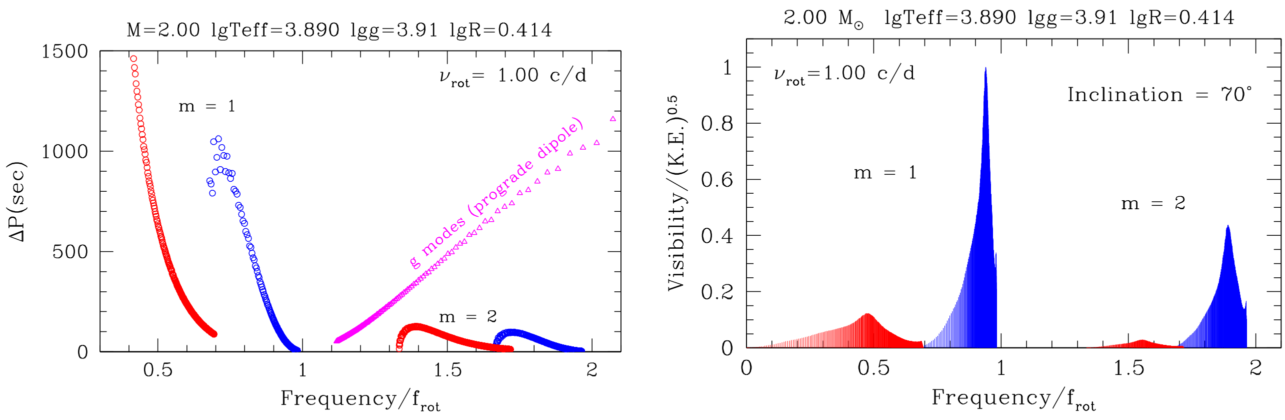

Fig. 1. Left: Period spacings versus frequency of r modes (and dipole prograde g modes - magenta triangles - for comparison) in the inertial frame. Although period spacing is usually plotted as a function of period, here it is given as a function of frequency for better correspondence to the diagram on the right side. Blue and red colors are used for even and odd (with respect to the equator) r modes. **Right:** Visibility distribution of r modes (arbitrarily normalized) expected for energy equipartition as a function of frequency in the inertial frame.

For other types of variables, however, each r-mode frequency is not resolved, but r modes appear as dense frequency groups in frequency-amplitude diagrams. As seen in the right panel of Fig. 1, even (i.e., symmetric with respect to the equator) r modes, in particular the $m = 1$ mode-group, are most visible, whose frequencies are slightly lower than $m\nu_{\rm rot}$. In other words, if we find an r-mode frequency group of $m = 1$, we can estimate an approximate rotation frequency as the frequency at the upper bound of the group.

3 R modes in eclipsing binaries

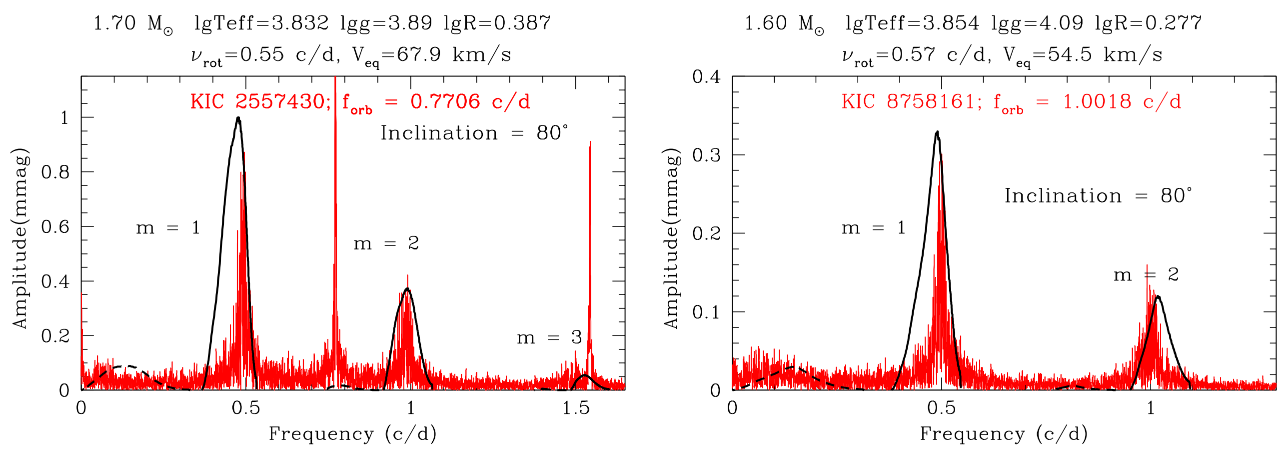

Fig. 2. Left: Frequency-amplitude relation (red lines) of the eclipsing binary KIC 2557430 with an orbital frequency of 0.771 c/d is fitted with the theoretical r-mode visibility predicted for a 1.70 $M_\odot$ model at a rotation frequency of 0.55 c/d, where solid and dashed lines are for even and odd modes, respectively. **Right:** Similar to the left diagram but for KIC 8758161 with an orbital frequency of 1.00 c/d fitted with the theoretical r-mode visibility of a 1.6 $M_\odot$ model at a rotation frequency of 0.57 c/d.

From the Kepler Eclipsing Binary Catalog V3 (KEBC), 837 binaries have been chosen in a range of orbital frequencies from 0.2 to 2.5 c/d, under the condition that they were observed by Kepler longer than 3 quarters, and the primary's effective temperatures are higher than 4000 K.

For each case, the mean light curve of eclipses is subtracted from the original Kepler light-curve data using the polynomial fit given in the KEBC. A Fourier analysis by the software PERIOD04 (Lenz & Breger 2005) for the residual data yields a frequency-amplitude diagram, which is searched by eye for frequency groups attributable to r modes. R-mode features are found in 737 binaries, and among them, 320 cases show r-mode features from both components. Figs. 2 and 3 show four examples of frequency-amplitude diagrams and fits with theoretical visibility distributions of r modes (solid and dashed lines) derived from models with best-fit rotation frequencies, where model parameters were adopted by referring to the effective temperatures obtained by Armstrong et al. (2014). We note that the frequency-amplitude diagram in the right panel of Fig. 3 is an example showing r modes from both component stars rotating at slightly different rates from each other.

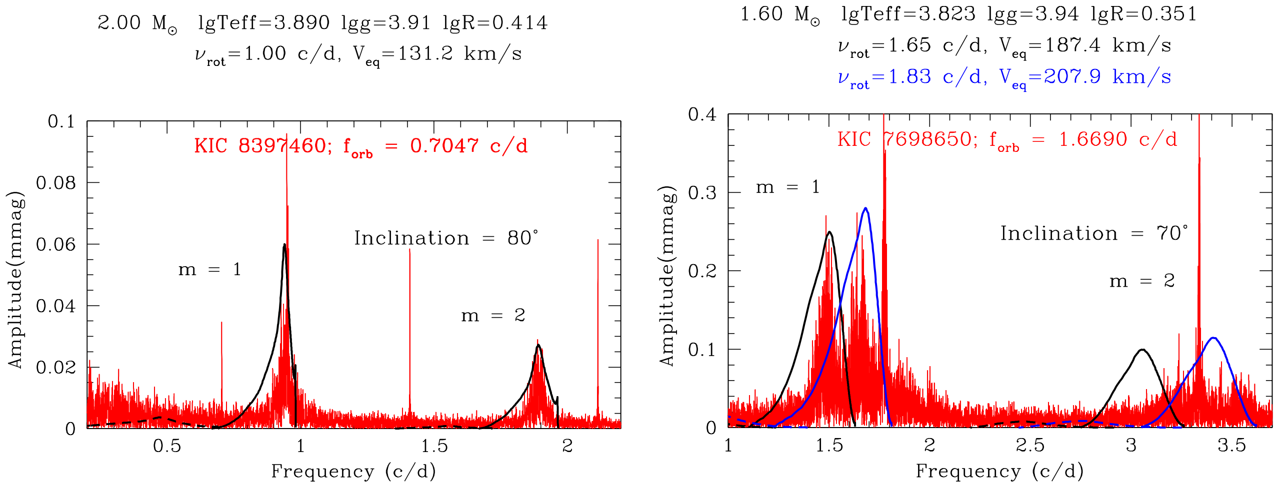

Fig. 3. Left: Similar to Fig. 2 but for KIC 8397460 with an orbital frequency of 0.70 c/d fitted with the theoretical visibility prediction of r modes for a 2.0 $M_\odot$ model at a rotation frequency of 1.00 c/d. **Right:** Similar to the left panel but for the eclipsing binary KIC 7698650 with an orbital frequency of 1.67 c/d. There are two closely-separated frequency groups around ~ 1.5 c/d and ~ 1.7 c/d. They are fitted with r-mode visibility models of 1.6 $M_\odot$ with rotation frequencies of 1.65 c/d and 1.83 c/d, respectively. These two frequency groups correspond to r mode oscillations in the two components of the binary.

4 Rotation frequencies of stars in eclipsing binaries

In the left panel of Fig. 4, an open circle gives the ratio of the frequency at the upper bound of the r-mode frequency group (which should be similar to the rotation frequency) to the orbital frequency of an eclipsing binary. Non-detection cases lie on the horizontal axis. This figure indicates that stars in eclipsing binaries with orbital frequencies larger than about 1 c/d tend to rotate more-or-less synchronously to the orbital motion, while in some longer-period binaries rotation frequencies are considerably higher than orbital frequencies.

The right panel of Fig. 4 is the same as the left panel but for the eclipsing binaries which show two sets of closely separated r mode frequency groups which should correspond to r modes in each component star. If the orbital frequency is less than about 1 c/d, rotation frequencies of the two component stars sometimes differ considerably from each other.

5 Conclusions

We found that r-mode oscillations are present frequently in eclipsing binaries (737 cases are found among 837 samples), which suggests that fluid motions arising by tidal force should generate Rossby waves and hence r-mode oscillations. Detecting r-mode frequency groups is useful to obtain a rotation frequency of a star or sometimes rotation frequencies of both components in eclipsing binaries. These rotation frequencies relative to orbital frequencies would give insight about the orbit-rotation interaction in close-binary stars.

Although the results presented in this paper are still preliminary, they seem to indicate that in binary systems whose orbital periods are shorter than about one day, stellar rotation is more-or-less synchronized, while in systems with longer orbital periods, stellar rotation periods can be considerably shorter than the orbital periods. Further analysis is needed to gain a clearer picture on the orbit-rotation interactions in close binaries.

The author is very grateful to the Kepler Eclipsing Binary working group for their maintenance of the Kepler Eclipsing Binary Catalog.

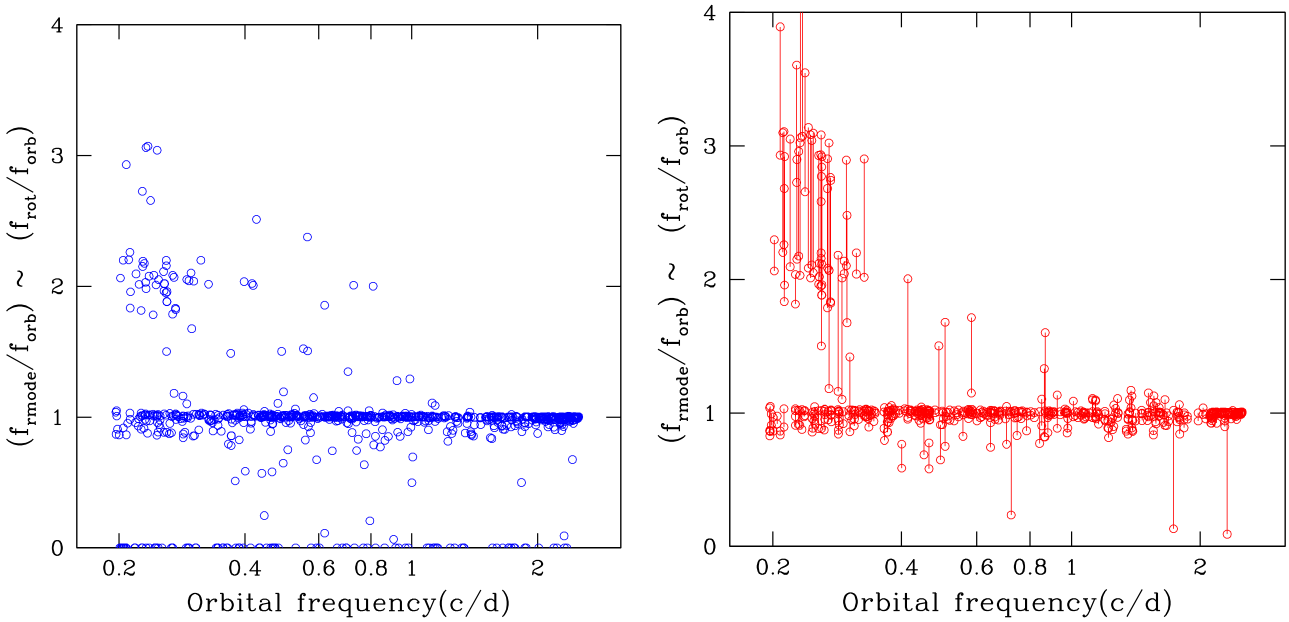

Fig. 4. Left: Frequencies at upper bounds of $m = 1$ r-mode frequency groups, which should be close to the rotation frequencies, relative to orbital frequencies for eclipsing binaries selected from the KEBC. Points on the horizontal axis are cases in which no r modes are detected. **Right:** The same as the left panel but for the cases in which r-mode frequencies of both components (connected by vertical lines) are detected.

References

Armstrong, D. J., Gómez Maqueo Chew, Y., Faedi, F., & Pollacco, D. 2014, MNRAS, 437, 3473

Kirk, B., Conroy, K., Prša, A., et al. 2016, AJ, 151, 68

Lenz, P. & Breger, M. 2005, Communications in Asteroseismology, 146, 53

Li, G., Van Reeth, T., Bedding, T. R., Murphy, S. J., & Antoci, V. 2019a, MNRAS, 487, 782

Li, G., Van Reeth, T., Bedding, T. R., et al. 2019b, MNRAS, 2517

Matijevič, G., Prša, A., Orosz, J. A., et al. 2012, AJ, 143, 123

Papaloizou, J. & Pringle, J. E. 1978, MNRAS, 182, 423

Provost, J., Berthomieu, G., & Rocca, A. 1981, A&A, 94, 126

Prša, A., Batalha, N., Slawson, R. W., et al. 2011, AJ, 141, 83

Saio, H. 1982, ApJ, 256, 717

Saio, H. 2018, arXiv e-prints, arXiv:1812.01253

Saio, H. 2019, MNRAS, 487, 2177

Saio, H., Kurtz, D. W., Murphy, S. J., Antoci, V. L., & Lee, U. 2018, MNRAS, 474, 2774

Slawson, R. W., Prša, A., Welsh, W. F., et al. 2011, AJ, 142, 160

Van Reeth, T., Tkachenko, A., & Aerts, C. 2016, A&A, 593, A120

Stars and their variability observed from space
C. Neiner, W. W. Weiss, D. Baade, R. E. Griffin, C. C. Lovekin, A. F. J. Moffat (eds)

STELLAR INCLINATION ANGLES FROM BE STAR Hα EMISSION-LINE PROFILES

T. A. A. Sigut[1], A. K. Mahjour[2] and C. Tycner[3]

Abstract.
Radiative transfer modelling of the Hα emission-line profile of a Be star can be used to extract a reliable estimate of the angle between the observer's line-of-sight and the central B star's rotation axis, commonly called the stellar inclination angle. We verify this radiative transfer approach by comparing two inclination angles derived geometrically for a sample of eleven Be stars with interferometric observations that resolve the star's disk light distribution on the sky. With this Hα profile-fitting technique, we can use Be stars as probes in young open clusters to detect potential correlations between the orientation of stellar spins.

Keywords: Stars: emission-line, Be, rotation, open clusters and associations: general

1 Introduction

Stellar rotation axes are usually assumed to be randomly oriented in space, and in that case a distant observer will measure inclination angles i (the angle between the line-of-sight and the stellar rotation axis) that satisfy a $\sin i$ distribution Gray (1992). As it is difficult to measure the angle i for any individual star, the $\sin i$ distribution is usually assumed to be valid and is often used to derive other quantities, such as the distribution of stellar equatorial speeds. Nevertheless, most (perhaps all) OB stars are born in clusters, originating from the gravitational collapse of the parent molecular cloud (Lamb et al. 2010). The details of this collapse, and the interplay between gravity, rotation, turbulence, and magnetic fields, ultimately sets the angular momentum acquired by individual stars. Given the complexity of this process, it is not *a priori* obvious that the individual stellar spins will be randomized. Numerical simulations (Rey-Raposo & Read 2018) suggest that strongly-aligned stellar spins can result if more than $\approx 40\%$ of the initial kinetic energy of the parent cloud is in the form of rotation.

There are several possible approaches to determining the inclination angles of individual stars in order to test the assumption of random orientations; a measurement of the projected equatorial rotational speed ($v \sin i$) from the broadening of spectral lines plus an estimate of the star's underlying rotation period from photometric or magnetic variations can be used to extract i (Abt 2001, for example,). Very rapid stellar rotation leads to gravitational darkening in which the star becomes oblate, with a temperature variation over its surface (Collins 1965); as the star's spectrum then depends on how it is viewed, an estimate of i can be extracted from carefully modelling its spectrum (Zorec et al. 2016, and references within). Another interesting approach is the use of asteroseismology (Gizon & Solanki 2003). Using this method, Corsaro et al. (2017) have recently detected the first observational evidence of strong spin alignment between red giants in two old Galactic open clusters, NGC 6791 and NGC 6819, based on three years of *Kepler* data. Nevertheless, all three of these methods are data intensive and require extensive time series and/or high signal-to-noise observations. In this paper we propose a simpler method of overcoming these limitations based on the spectra of Be stars.

2 Method

A Be star is a rapidly-rotating, B-type, main-sequence star surrounded by a circumstellar disk. The most widely accepted disk formation model invokes episodes of near critical rotation of the central B star, in which material is ejected from the stellar equator into a disk (Granada et al. 2013). The disk then spreads outward by the action of turbulent viscosity, forming a viscous decretion disk (Rivinius et al. 2013). The spectra of Be stars

[1] Department of Physics & Astronomy/ Western Institute for Earth & Space Exploration, The University of Western Ontario, London, Ontario, Canada: asigut@uwo.ca
[2] Department of Physics & Astronomy, The University of Western Ontario, London, Ontario, Canada
[3] Department of Physics, Central Michigan University, Mt Pleasant, Michigan, USA

show emission in the hydrogen Balmer series, most notably Hα. It has long been known that the morphology of the Hα emission line reflects the inclination angle of the central B-type star (Porter & Rivinius 2003), from singly-peaked emission for $i \approx 0°$ (pole-on star and face-on disk), to double-peaked emission for intermediate i, to doubly-peaked emission with strong central (shell) absorption for $i \approx 90°$ (equator-on star and edge-on disk). This suggests that detailed profile fitting of the Hα emission line based on radiative transfer modelling may be able to extract a reliable measure of the stellar inclination angle.

We have used the `Beray` radiative transfer code (Sigut 2011, 2018) to compute theoretical Hα profiles for a large number of Be-star models. The thermal structure of the circumstellar disk was determined using the `Bedisk` code (Sigut & Jones 2007) which enforces radiative equilibrium in a gas of solar chemical composition heated by the photoionizing radiation of the central B star. The disk density was taken to fall with radius as a power-law of index n, starting from a value ρ_0 at the stellar surface. For each spectral type of the central B-type star, the Hα line profile is a function of four model parameters: the base disk density, ρ_0 (range 10^{-12}–10^{-10} gm cm^{-3}), the power-law index, n (range 1.5–4.0), the outer disk radius, R_d (range 5–65 $R_\odot$), and the system viewing inclination, i (range 0°–90°). Models were computed for eleven spectral types between B0 and B9, making a total Hα library of over 231,000 profiles.

To extract the inclination angle for a Be star, its observed Hα line profile is compared to model profiles in the line library of the appropriate spectral type. The comparison uses a figure-of-merit, taken to be the absolute percentage difference between the observed profile and the model profile, and the disk parameters (ρ_0, n, R_d, i) of the profile that minimize the figure-of-merit are adopted as representing the star best. One potential issue is that there may be degeneracies among the four model parameters such that a wide range of model inclinations i may fit the observed profile equally well by adjusting the values of the other parameters (ρ_0, n, R_d). We tested this issue extensively via Monte Carlo simulations, in which simulated observed Hα profiles were generated with $S/N = 10^2$ and resolution $\mathcal{R} = \lambda/\Delta(\lambda) = 10^4$ (both typical of Be star observations) and fitted them to the Hα profile libraries. In examining the distributions of the (ρ_0, n, R_d) parameters corresponding to the best 15% of fits to each simulated profile, we found that the inclination angle was robustly recovered, typically to within $\pm 10°$. This issue is discussed further in the following section, where we use observed, and not simulated, profiles.

3 Comparison with interferometric observations

To test how the Hα profile-fitting method performs, we assembled a sample of eleven Be stars with published interferometric visibilities from the Naval Precision Optical Interferometer (Armstrong et al. 1998). Interferometric observations can resolve the Be star disk on the sky, and purely geometric models can be fitted to the light distribution. A particularly simple and successful model is an elliptical Gaussian disk (Tycner et al. 2003). In it, four parameters are fitted to the observed visibilities: a major axis (a), a minor axis (b), a position angle on the sky (χ), and a brightness ratio between the disk and the central star (c_*). As Be star disks are equatorial and circular, the observed axial ratio is simply due to projection through the stellar inclination angle, i.e. $r \equiv b/a = \cos i$; hence, the system inclination can be recovered geometrically from the interferometric observations in a manner that is independent of any radiative transfer modelling. Of course, the simple relation $r = \cos i$ must fail for sufficiently large i, as the disk's minor axis will be limited by its finite scale height; however, simulated images computed with `Beray` suggest that this only occurs for $i > 80°$.

The following eleven Be stars (with references to the available interferometry) form our sample: γ Cas (Tycner et al. 2003); η Tau, β CMi (Tycner et al. 2005); ϕ Per (Tycner et al. 2006); κ Dra, υ Cyg, β Psc (Jones et al. 2008); χ Oph (Tycner et al. 2008), o Aqr (Sigut et al. 2015), 48 Per (Jones et al. 2017), and ϕ Per (Sigut *et al.* 2019, private communication). Observed Hα line profiles were taken from observations at the John S. Hall telescope at Lowell Observatory; all spectra have $S/N = 10^2$ and $\mathcal{R} = 10^4$.

Fits to all eleven observed Hα line profiles, along with the best-fitting disk parameters and inclinations, are shown in the left panel of Fig. 1. It most cases the fits are good; however, in some cases (ϕ Per, for example) there is clearly a systematic difference between the available models and the observations. In addition, the profiles in this sample are nearly symmetric, whereas many Be stars show asymmetric profiles with V/R variations, i.e. sizable differences between the height of the red (R) and blue (V) emission peaks (Stefl et al. 2009). In tests, we have had success in fitting the red and blue sides of asymmetric Hα profiles separately, extracting a consistent i from both fits; however, this is outside the scope of the current project.

The right panel of Fig. 1 shows the fits to the observed interferometric visibilities presented as axial ratios $r \equiv b/a$ as a function of the reduced χ^2 of the fit. The cloud of points for each star represents 500 bootstrap Monte Carlo re-samplings of the interferometric data, and the cloud of points gives a visual representation of the uncertainties. Also shown in each stellar panel is the histogram of model inclinations for all library profiles that

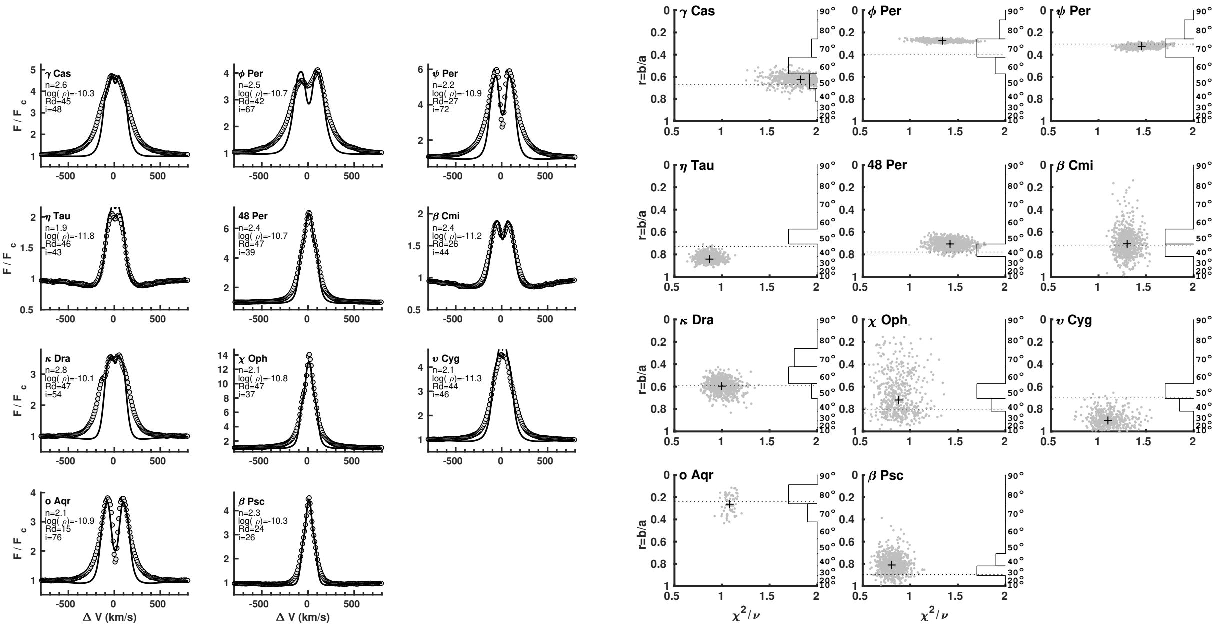

Fig. 1. Left: Hα library profile fits to the sample of Be stars. The observed Hα profile for each star is shown by the circles, and the best-fitting model profile by a solid line. The adopted disk parameters and inclination are indicated for each star. **Right:** Interferometric axial ratios $r = b/a$ as a function of the reduced χ^2 of the fit for the sample Be stars. The cross in each panel is at the median axial ratio and fit reduced χ^2. Histograms on the right of each stellar panel give the distribution of inclinations of all model Hα profiles that have a fit with a figure-of-merit within 15% of the best-fitting profile.

fittted the observed Hα line profile with a figure-of-merit within 15% of the best-fitting profile. These histograms show visually the degeneracy in the spectroscopic viewing inclination over the other model parameters. The horizontal dotted line in each panel is a "refined" inclination found via interpolation in the library models. In all of these panels, axial ratios and inclination angles have been related using $r = \cos i$. The difference between the spectroscopic inclinations and interferometric inclinations is consistent with a normal distribution of mean $\mu = -1^\circ$ and a standard deviation of $\sigma = 7^\circ$. Thus, based on this sample, stellar inclinations of an accuracy of $\approx \pm 10^\circ$ are obtainable from Hα line-profile fitting.

Another important characteristic of Be stars is their variability (Porter & Rivinius 2003). Be star disks are often observed to form and dissipate on time-scales of several years to decades, as set by the disk's viscous time-scale. An example of disk dissipation is shown in Fig. 2 for the star κ Dra (HD 109387); over nearly 14 years of observations, its Hα profile shows a factor of 5 decrease in emission strength. We have fitted all 85 Hα profiles in this time-series using the methods outlined above to extract the system inclination at each epoch – which we expect to be unchanging, despite the disappearance of the disk. As shown in Fig. 2, all profiles are consistent with a system inclination of $i = 54^\circ \pm 4^\circ$, independent of the strength of the Hα emission.

4 Conclusions

We have demonstrated that an observation of the Hα emission-line profile of a single Be star (with moderate signal-to-noise and resolution) is sufficient to constrain the inclination angle of the central B-type star to within $\approx \pm 10^\circ$. As Be stars comprise upwards of one-fifth of all main-sequence B stars (Zorec & Briot 1997), Be stars provide a promising avenue to look for possible spin-correlations between massive stars in young open clusters.

Finally, we note another intriguing possibility. The stellar inclination angle i constrains the star's rotation axis to lie along a cone of opening angle i around the line of sight. However, Be stars offer the possibility to obtain the position angle of the rotation axis within this cone via polarization measurements. The continua of Be stars are weakly polarized owing to electron scattering from the circumstellar disk. The position angle of the polarization vector is perpendicular to the scattering plane, i.e., the disk, and in the direction of the stellar rotation axis. Hence, Hα profile fitting combined with polarization measurements for Be stars will enable the reconstruction of the 3D orientation of the central B star's rotational axis.

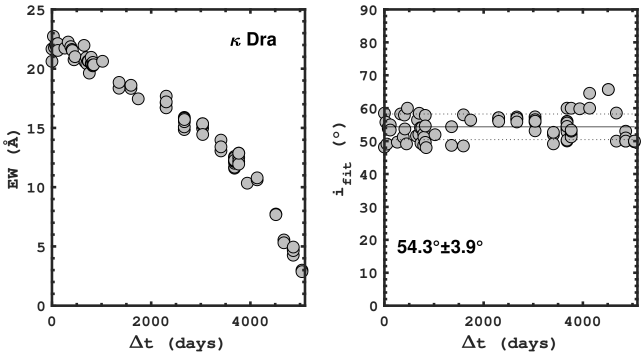

Fig. 2. Left: Hα equivalent widths as a function hof time (days since first observation) for the Be star κ Dra. A positive equivalent width indicates emission. The initial observation was on 2005 March 3. **Right:** Recovered stellar inclination for the central B star of κ Dra as a function of time, based on Hα line profile fitting. The solid line is the mean inclinaton; the dotted lines give the 1σ variation.

T. A. A. Sigut thanks the National Sciences and Engineering Research Council of Canada for supporting this research through a Discovery Grant.

References

Abt, H. A. 2001, AJ, 122, 2008

Armstrong, J. T., Mozurkewich, D., Rickard, L. J., et al. 1998, ApJ, 496, 550

Collins, II, G. W. 1965, ApJ, 142, 265

Corsaro, E., Lee, Y.-N., García, R. A., et al. 2017, Nature Astronomy, 1, 0064

Gizon, L. & Solanki, S. K. 2003, ApJ, 589, 1009

Granada, A., Ekström, S., Georgy, C., et al. 2013, A&A, 553, A25

Gray, D. F. 1992, Cambridge Astrophysics, Vol. 20, The observation and analysis of stellar photospheres. (Cambridge University Press, adsurl = https://ui.adsabs.harvard.edu/abs/1992oasp.book.....G, adsnote = Provided by the SAO/NASA Astrophysics Data System)

Jones, C. E., Sigut, T. A. A., Grzenia, B. J., Tycner, C., & Zavala, R. T. 2017, ApJ, 843, 24

Jones, C. E., Tycner, C., Sigut, T. A. A., Benson, J. A., & Hutter, D. J. 2008, ApJ, 687, 598

Lamb, J. B., Oey, M. S., Werk, J. K., & Ingleby, L. D. 2010, ApJ, 725, 1886

Porter, J. M. & Rivinius, T. 2003, PASP, 115, 1153

Rey-Raposo, R. & Read, J. I. 2018, MNRAS, 481, L16

Rivinius, T., Carciofi, A. C., & Martayan, C. 2013, A&A Rev., 21, 69

Sigut, T. A. A. 2011, in IAU Symposium, Vol. 272, Active OB Stars: Structure, Evolution, Mass Loss, and Critical Limits, ed. C. Neiner, G. Wade, G. Meynet, & G. Peters, 426–427

Sigut, T. A. A. 2018, in ASPCS, Vol. 515, Workshop on Astrophysical Opacities, ed. C. Mendoza, S. Turck-Chiéze, & J. Colgan, 213

Sigut, T. A. A. & Jones, C. E. 2007, ApJ, 668, 481

Sigut, T. A. A., Tycner, C., Jansen, B., & Zavala, R. T. 2015, ApJ, 814, 159

Stefl, S., Rivinius, T., Carciofi, A. C., et al. 2009, A&A, 504, 929

Tycner, C., Gilbreath, G. C., Zavala, R. T., et al. 2006, AJ, 131, 2710

Tycner, C., Hajian, A. R., Mozurkewich, D., et al. 2003, AJ, 125, 3378

Tycner, C., Jones, C. E., Sigut, T. A. A., et al. 2008, ApJ, 689, 461

Tycner, C., Lester, J. B., Hajian, A. R., et al. 2005, ApJ, 624, 359

Zorec, J. & Briot, D. 1997, A&A, 318, 443

Zorec, J., Frémat, Y., Domiciano de Souza, A., et al. 2016, A&A, 595, A132

BINARY STARS: A CHEAT SHEET

J. Southworth[1]

Abstract. This talk presented a brief summary of three different types of binary star – astrometric, spectroscopic and eclipsing – and tabulated the properties of these systems that can be determined directly from observations. Eclipsing binary stars are the most valuable, as they are our main source of direct mass and radius measurements for normal stars. In good cases, masses and radii can be obtained to better than 1% precision and accuracy using only photometry, spectroscopy and geometry. These measurements constitute vital empirical data aginst which theoretical models of stars can be verified and improved. It gave examples of the use of these systems for constraining stellar theory and the distance scale, and concluded with a presentation of preliminary results for the solar-type eclipsing binary 1SWASP J034114.25+201253.5.

Keywords: Stars: binaries: visual, spectroscopic, eclipsing, fundamental parameters

1 Introduction

Binary stars are one of the classical subject areas of *astronomy*, as they represent the only way of determining the masses and radii of normal stars to high precision and accuracy. This makes them *astrophysically* vital: the properties of stars in binary systems are used to calibrate theoretical stellar models, determine the distances to nearby galaxies, and support asteroseismology studies.

This review summarised the various types of binary star, the history of their study, and what physical properties can be obtained from them. It then presented some new work in progress on the eclipsing binary 1SWASP J034114.25+201253.5, detected using SuperWASP data and observed using the NASA K2 mission.

2 Binary stars

Table 1 summarises the properties directly measurable for different types of binary star. Both their symbols and names are given. The organisation of the table follows the observational techniques used–a convenient way of considering these systems.

2.1 Visual binaries

The first type of binary star to be observed was the *spatially-resolved* binary. These are also called visual binaries (because they can be identified by eye) and astrometric binaries (because it is possible to determine their orbits from measurements of the relative positions of the two stars).

Visual binaries were shown to be real, rather than chance alignments of stars at different distances, on statistical grounds, by the Revd. John Michell (1767). William Herschel (1802) introduced the term *binary star* and spent many years proving that some visual doubles show orbital motion. Herschel (1803) found that the double star Castor, with a separation of $3.9''$, is a binary system with a period of 342 yr, relatively close to the "modern" value of 420 yr (Rabe 1958). Visual binaries are usually close to Earth and have a large orbital separation (and thus a long orbital period) in order for the stars to be far enough apart on the sky to be resolved.

The equations of an astrometric orbit were established by Félix Savary in 1827. From observations of the motion of one of the stars relative to the other, it is possible to determine several of the properties of the orbit (P, e, ω, a). The semimajor axis a that can be found is the *angular size*, not the true length (Table 1). The properties ω, Ω and i can also be measured; they give the orientation of the orbit relative to the observer, so are not intrinsic properties of the system.

If we know the distance to the system, usually via a parallax from the *Hipparcos* or *Gaia, we can convert a from angular units to length units. As this is the semimajor axis of the* relative orbit*, it can be used to find the sum of the masses (via Kepler's Third Law) but not the individual masses.*

[1] Astrophysics Group, Keele University, Staffordshire, ST5 5BG, UK

Table 1. Symbols and names of quantities measurable from various types of binary star.

		Astrometric binary			Spectroscopic binary		Eclipsing binary		
Name	Symbol	alone	with distance	with RVs	SB1	SB2	alone	with RVs (SB1)	with RVs (SB2)
Orbital parameters									
Orbital period	P	*	*	*	*	*	*	*	*
Orbital eccentricity	e	*	*	*	*	*	*	*	*
Argument of periastron	ω	*	*	*	*	*	*	*	*
Longitude of ascending node	Ω	*	*	*					
Projected semimajor axis	$a \sin i$		*	*		*			*
True semimajor axis	a (au)		*	*					*
Orbital inclination	i	*	*	*			*	*	*
Distance	d			*					*
Spectroscopic parameters									
Velocity amplitude of star 1	K_1			*	*	*		*	*
Velocity amplitude of star 2	K_2			*		*			*
Systemic velocity	V_γ			*	*	*		*	*
Mass function	$f(M)$				*	*		*	*
Mass ratio	$q = M_2/M_1$			*		*			*
Mass sum	$M_1 + M_2$		*	*		*			*
Minimum masses	$M_{1,2} \sin^3 i$			*		*			*
Mass of primary star	M_1			*					*
Mass of secondary star	M_2			*					*
Size parameters									
Fractional radii	r_1 and r_2						*	*	*
Radius of primary star	R_1								*
Radius of secondary star	R_2								*
Surface gravity of primary	$\log g_1$								*
Surface gravity of secondary	$\log g_2$							*	*
Density of primary star	ρ_1								*
Density of secondary star	ρ_2								*
Radiative parameters									
Temperature of primary star	$T_{\rm eff,1}$	*	*	*	*	*		*	*
Temperature of secondary star	$T_{\rm eff,2}$	*	*	*		*			*
Luminosity of primary star	L_1			*					*
Luminosity of secondary star	L_2			*					*

If we obtain radial-velocity (RV) observations of the two stars and fit a spectroscopic orbit (see below), we can convert a from angular units to length units, measure the distance to the system (without needing its parallax) and also calculate the individual masses of the stars. We can therefore use these systems as distance indicators (e.g. Torres et al. 1997) and to constrain the predictions of theoretical models of stellar evolution (e.g. Torres et al. 2009).

2.2 Spectroscopic binaries

Spectroscopic binaries are those found from changes in the RVs of the stars due to orbital motion. The first known spectroscopic binary was Algol (β Persei), which was already known to be an eclipsing binary (see below). Vogel (1890) observed the brighter of the two components to be moving away from Earth before primary eclipse and moving towards Earth after primary eclipse. Rudolf Lehmann-Filhés established the equations of a spectroscopic orbit in their current form in 1894.

For a "single-lined" spectroscopic binary system (SB1) – one where we can measure RVs for only one component – we can measure the quantities P, e, ω, K_1 and V_γ (Table 1). From these we can in turn calculate the mass function $f(M)$ and a lower limit to the semimajor axis of the barycentric orbit of the star, $a_1 \sin i$.

For a "double-lined" spectroscopic binary system (SB2) – where RVs are measurable for both components – we can obtain all the quantities for an SB1 system, plus the minimum masses ($M_1 \sin^3 i$ and $M_2 \sin^3 i$) and a *lower limit to the semimajor axis ($a \sin i$). As the orbital inclination i is not known, the true values of these three quantities are not accessible.*

Spectroscopic binaries are easier to study if they have short orbital periods, large masses and a high i, in order to maximise the amplitude of the RV variation. On the other hand, it is more difficult to measure RVs for massive stars because they have few spectral lines and high rotational velocities (see Southworth & Clausen 2007). Spectroscopic binaries are useful for measuring the multiplicity fraction of stars (e.g. Duquennoy & Mayor 1991), which varies as a function of mass (Duchêne & Kraus 2013), age (Jaehnig et al. 2017) and chemical composition (Badenes et al. 2018), and can be used to probe the star-formation process (e.g. Bate 2009).

2.3 Eclipsing binaries

These are the most useful kind of binary star because of the huge number of physical properties that can be measured to high precision and accuracy (Table 1). Goodricke (1783) is generally credited as the first to advance the hypothesis of eclipses in order to explain the dimming of the "demon star" Algol every 2.87 days. These eclipses are even recorded in the Ancient Egyptian Calendar dating from around 1100 B.C. (Jetsu & Porceddu 2015). The first eclipsing binary system to be characterised properly was β Aurigae, by Stebbins (1911); the values found for its masses and radii agree reasonably well with modern values (Southworth et al. 2007a). The mathematical framework for eclipse calculations was laid out by Russell (1912a,b); see also Kopal (1959).

The light-curve of an eclipsing binary depends on the fractional radii *of the two stars ($r_1 = \frac{R_1}{a}$ and $\frac{R_2}{a}$), so cannot be used in isolation to obtain the full physical properties of the system (Table 1). The orbital eccentricity e and argument of periastron ω can also be found, because $e \cos \omega$ depends on the time of secondary eclipse relative to primary eclipse, and $e \sin \omega$ depends on the relative durations of the eclipses.*

If we add RVs of one star to the light-curve of an EB we can measure the mass function, $f(M)$, but not the actual masses of the stars. The surface gravity of the secondary star (the one for which we have no RVs) can also be calculated (Southworth et al. 2004b), something that can also be applied to transiting planets (Southworth et al. 2007b).

If RVs are available for both stars, then the full physical properties of the system can be obtained: the true masses and radii of both stars, which in turn give the surface gravities and densities. In the best cases these quantities can be measured to a precision of 0.5% or better (e.g. Hełminiak et al. 2019). It is usually the case that the temperatures of the stars are known, from spectroscopy plus the surface brightness ratio measured from the light-curve. In this case the luminosities of the stars can be calculated from $L = 4\pi R^2 \sigma T_{\rm eff}^{\,4}$, and the distance to the system can be obtained. EB-based distance estimates have been published for nearby galaxies: the LMC (Pietrzyński et al. 2019), SMC (North et al. 2010) and M33 (Bonanos et al. 2006).

For the case of SB2 EBs we can measure the masses, radii and luminosities of two stars of the same age and chemical composition. Such information is valuable for calibrating theoretical stellar models (e.g. Andersen et al. 1990; Pols et al. 1997; Claret 2007), if the two stars have not undergone mass transfer and thus have evolved as single stars. Claret & Torres (2016, 2018) have used a large sample of SB2 EBs to calibrate the strength of convective core overshooting as a function of mass, finding a ramp-up from $1.2\,M_\odot$ to $2.0\,M_\odot$. However, this approach has been challenged by Valle et al. (2016) on account of possible biases in the method, and by Constantino & Baraffe (2018) about the reproducibility of the results.

It is possible to add interferometry of SB2 EBs and obtain highly precise distances and physical properties of individual systems (Gallenne et al. 2016, 2019). The study of EBs with pulsating components is a very promising possibility for constraining the interior and atmospheric structure of stars (Debosscher et al. 2013; Aerts 2013; Tkachenko et al. 2014; Themeßl et al. 2018). Catalogues of EBs from photometric surveys are useful for determining the multiplicity fraction of stars, as have been achieved for M-dwarfs by Shan et al. (2015) and for solar-type stars by Moe et al. (2019).

2.3.1 DEBCat: the Detached Eclipsing Binary Catalogue

DEBCat (Southworth 2015) is a catalogue of EBs suitable for comparison with predictions from theoretical stellar models. It includes all EBs for which there is no evidence for current or past mass transfer, and with mass and radius measurements to precisions of 2% or better. The full physical properties of the systems are collected (mass, radius, surface gravity, temperature, luminosity, orbital period, metallicity) and can be downloaded in ascii format. At the time of writing (2019/12/01) DEBCat contains 239 systems.*

---

*`https://www.astro.keele.ac.uk/jkt/debcat/`

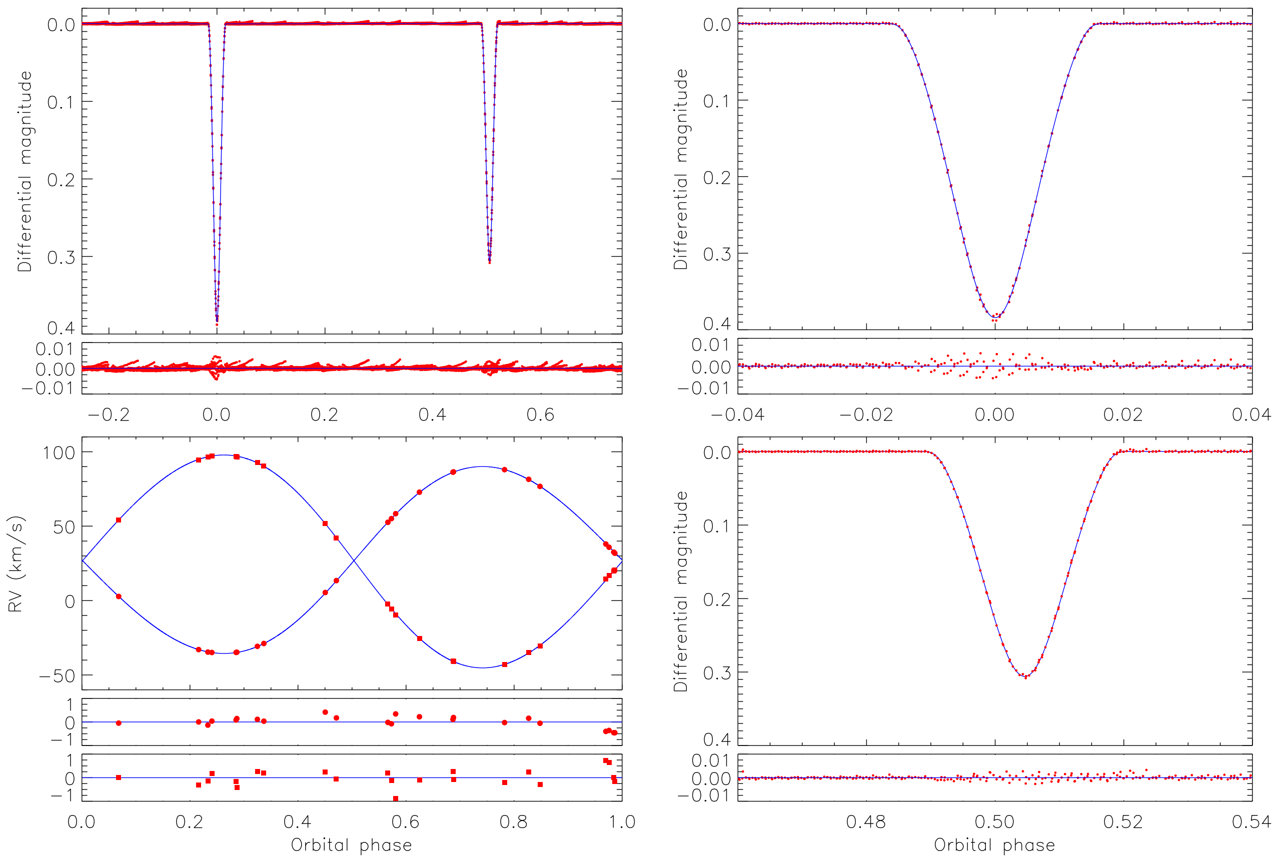

Fig. 1. Observational data for WASP J0341. Top left: *K2* light-curve versus orbital phase. Top right: primary eclipse. Bottom right: secondary eclipse. Bottom left: RV curves.

3 1SWASP J034114.25+201253.5

We now present some preliminary work on the solar-type eclipsing binary system 1SWASP J034114.25+201253.5 (hereafter WASP J0341), performed in collaboration with P. Maxted (Keele), G. Torres (CfA) and K. Pavlovski (Zagreb). WASP J0341 was identified as an eclipsing binary in the vicinity of the Pleiades open cluster by using photometric data from the SuperWASP database (Pollacco et al. 2006). Because of the scientific importance of eclipsing binaries that are cluster members (e.g. Southworth et al. 2004a; Brogaard et al. 2011) we proceeded to obtain several sets of additional observations. We were awarded observations of WASP J0341 from the K2 mission, which observed it in long cadence for 71 days during Campaign 4. The PDC light-curve from the Kepler data reduction pipeline is shown in Fig. 1; more sophisticated reductions of these data exist and will be used for future analyses.

We also obtained a set of 30 high-resolution spectra of this system from the 1.5 m TRES spectrograph on the 1.5 m Tillinghast telescope at FLWO. RVs from these data are shown in Fig. 1. A joint fit of these RVs and the K2 light-curve using the JKTEBOP *code (Southworth 2013) yielded masses of 1.08 and 0.95 $M_\odot$ and radii of 1.21 and 0.93 $R_\odot$, all measured to a precision of 0.5% or better. We have also obtained a set of six high-S/N spectra from VLT/UVES that will be used to measure the chemical composition of the two stars, yielding an even more precise test of theoretical models.*

WASP J0341 has an 8-day orbital period and a small eccentricity, so tidal effects in this system are small. Its properties will therefore serve as an excellent test of theoretical models of solar-type stars. A careful inspection of Fig. 1 shows that the scatter of the data increases during both eclipses. This is an indication of temporal and spatial changes in the flux from the stellar surfaces, which is likely due to starspots. Our UVES data do show weak emission in the centres of the Ca H & K lines, a good indicator of magnetic activity in the stars (Baliunas et al. 1995).

4 Conclusions

Binary systems are a common result of the star formation process and offer the only known way of determining the masses of stars directly. Their frequency of occurrence offers a way to probe the star formation process. Eclipsing binary systems are those which can be characterised in detail; precise measurements of their properties enable an exacting assessment of the predictive power of theoretical stellar models, and provide one of the lower rungs of the cosmological distance ladder.

The advent of space satellites has revolutionised the study of eclipsing binaries, with the discovery of several thousand examples in data from CoRoT (Deleuil et al. 2018) and Kepler (Kirk et al. 2016). TESS is currently providing new data for the great majority of known eclipsing binaries, and in future PLATO will provide unparalleled photometric observations of many known and new examples.

I thank the organisers of the conference for their invitation to give this review talk, my many collaborators on eclipsing binaries, and the students of the PHY-30024 module who are gradually and uncomplainingly weeding out all the typographical and mathematical errors in my lecture notes on binary stars and extrasolar planets.

References

Aerts, C. 2013, in EAS Publications Series, Vol. 64, EAS Publications Series, ed. K. Pavlovski, A. Tkachenko, & G. Torres, 323–330
Andersen, J., Clausen, J. V., & Nordström, B. 1990, ApJL, 363, L33
Badenes, C., Mazzola, C., Thompson, T. A., et al. 2018, ApJ, 854, 147
Baliunas, S. L., Donahue, R. A., Soon, W. H., et al. 1995, ApJ, 438, 269
Bate, M. R. 2009, MNRAS, 392, 590
Bonanos, A. Z., Stanek, K. Z., Kudritzki, R. P., et al. 2006, ApJ, 652, 313
Brogaard, K., Bruntt, H., Grundahl, F., et al. 2011, A&A, 525, A2
Claret, A. 2007, A&A, 475, 1019
Claret, A. & Torres, G. 2016, A&A, 592, A15
Claret, A. & Torres, G. 2018, ApJ, 859, 100
Constantino, T. & Baraffe, I. 2018, A&A, 618, A177
Debosscher, J., Aerts, C., Tkachenko, A., et al. 2013, A&A, 556, A56
Deleuil, M., Aigrain, S., Moutou, C., et al. 2018, A&A, 619, A97
Duchêne, G. & Kraus, A. 2013, ARA&A, 51, 269
Duquennoy, A. & Mayor, M. 1991, A&A, 248, 485
Gallenne, A., Pietrzyński, G., Graczyk, D., et al. 2016, A&A, 586, A35
Gallenne, A., Pietrzyński, G., Graczyk, D., et al. 2019, A&A in press, arXiv1910.03393
Goodricke, J. 1783, Philosophical Transactions of the Royal Society of London Series I, 73, 474
Hełminiak, K. G., Konacki, M., Maehara, H., et al. 2019, MNRAS, 484, 451
Herschel, W. 1802, Philosophical Transactions of the Royal Society of London Series I, 92, 477
Herschel, W. 1803, Philosophical Transactions of the Royal Society of London Series I, 93, 339
Jaehnig, K., Bird, J. C., Stassun, K. G., et al. 2017, ApJ, 851, 14
Jetsu, L. & Porceddu, S. 2015, PLoS ONE, 10, 44140
Kirk, B., Conroy, K., Prša, A., et al. 2016, AJ, 151, 68
Kopal, Z. 1959, Close binary systems (The International Astrophysics Series, London: Chapman & Hall, 1959)
Michell, J. 1767, Philosophical Transactions of the Royal Society of London Series I, 57, 234
Moe, M., Kratter, K. M., & Badenes, C. 2019, ApJ, 875, 61
North, P., Gauderon, R., Barblan, F., & Royer, F. 2010, A&A, 520, A74
Pietrzyński, G., Graczyk, D., Gallenne, A., et al. 2019, Nature, 567, 200
Pollacco, D. L., Skillen, I., Cameron, A. C., et al. 2006, PASP, 118, 1407
Pols, O. R., Tout, C. A., Schroder, K.-P., Eggleton, P. P., & Manners, J. 1997, MNRAS, 289, 869
Rabe, W. 1958, AN, 284, 97
Russell, H. N. 1912a, ApJ, 35, 315
Russell, H. N. 1912b, ApJ, 36, 54
Shan, Y., Johnson, J. A., & Morton, T. D. 2015, ApJ, 813, 75
Southworth, J. 2013, A&A, 557, A119

Southworth, J. 2015, in ASPCS, Vol. 496, Living Together: Planets, Host Stars and Binaries, ed. S. M. Rucinski, G. Torres, & M. Zejda, 321

Southworth, J., Bruntt, H., & Buzasi, D. L. 2007a, A&A, 467, 1215

Southworth, J. & Clausen, J. V. 2007, A&A, 461, 1077

Southworth, J., Maxted, P. F. L., & Smalley, B. 2004a, MNRAS, 349, 547

Southworth, J., Wheatley, P. J., & Sams, G. 2007b, MNRAS, 379, L11

Southworth, J., Zucker, S., Maxted, P. F. L., & Smalley, B. 2004b, MNRAS, 355, 986

Stebbins, J. 1911, ApJ, 34, 112

Themeßl, N., Hekker, S., Southworth, J., et al. 2018, MNRAS, 478, 4669

Tkachenko, A., Degroote, P., Aerts, C., et al. 2014, MNRAS, 438, 3093

Torres, G., Claret, A., & Young, P. A. 2009, ApJ, 700, 1349

Torres, G., Stefanik, R. P., & Latham, D. W. 1997, ApJ, 485, 167

Valle, G., Dell'Omodarme, M., Prada Moroni, P. G., & Degl'Innocenti, S. 2016, A&A, 587, A16

Vogel, H. C. 1890, PASP, 2, 27

Stars and their variability observed from space
C. Neiner, W. W. Weiss, D. Baade, R. E. Griffin, C. C. Lovekin, A. F. J. Moffat (eds)

HOT SUBDWARF STARS AND BINARY EVOLUTION

D. Brown[1]

Abstract. Hot subdwarf B stars are extreme horizontal-branch core-helium burning stars having masses of about $0.5\,\mathrm{M}_{\odot}$, and surrounded by very thin inert hydrogen envelopes of mass of $M_{\mathrm{env}} \leq 0.02\,\mathrm{M}_{\odot}$. They are thought to be formed when they lose most of the their hydrogen envelopes during the RGB phase of evolution, just before they ignite their He cores. The mechanism by which such rapid mass loss occurs is still not fully determined, but it is suspected that binary interactions via RLOF play an important role in their formation, at least in the formation of hot subdwarf stars in the Galactic field, where most sdB stars are found in binary systems. However, the fraction of binary sdB stars in globular clusters is very small, so other mechanisms, perhaps He enhancement via AGB-star ejecta in clusters that have multiple populations, might play a role in their formation, this time from single-star progenitors. Studies carried out using binary population synthesis from a theoretical point of view, following that of Han et al. (2002, 2003) and Han et al. (2007), can reveal much about the formation channels of such EHB stars, and the study described here builds on that, taking into account different chemical abundances (metallicities). Asteroseismological studies of pulsating sdB stars have also contributed greatly to the determination of sdB star parameters, especially stellar masses, which has greatly helped astronomers to understand such stars. A comparison with theory is carried out using high-speed photometry.

Keywords: Stars: sdB, binary, methods: asteroseismology

1 Introduction

The formation mechanism(s) of extreme horizontal branch (EHB) hot subdwarf (sdB/sdO) stars in the Galactic field or in globular clusters (GCs). Such stars typically have He-core masses of about $M_{\mathrm{c}} \sim 0.50\,\mathrm{M}_{\odot}$ (depending on metallicity, Z) and are surrounded by very thin inert hydrogen envelopes of $M_{\mathrm{env}} \leq 0.02\,\mathrm{M}_{\odot}$. Han et al. (2002, 2003) have presented a persuasive analysis of the binary channels suspected of producing sdB stars: 1) the CE (common envelope) binary channel, whereby the sdB progenitor experiences unstable mass transfer and produces a CE which is later ejected, and which tends to produce sdBs in binary systems with short periods of about 0.1 d–10 d, substantiated by observations from Maxted et al. (2001); 2) the stable RLOF (Roche-lobe overflow) channel, where mass transfer is stable from donor to gainer, resulting in longer-period binaries with periods peaking at about 830 d, some having orbital periods $>$ 1100 d (Chen et al. 2013); and, 3) the merger of two He WDs (white dwarfs) in a binary to produce an sdB star. Han et al. (2002, 2003) find that the sdB mass distribution, though sharply peaking at about $0.45 - 0.5\,\mathrm{M}_{\odot}$, can be much broader, with a range of 0.3 – $0.8\,\mathrm{M}_{\odot}$. Using asteroseismology methods to study pulsating sdB stars such as EC 14026 pulsators, Fontaine et al. (2012) obtained an empirical mass distribution, including a low-mass wing component, to constrain and verify such theoretical models. Moreover, data from *Kepler/K2* (and also from *CoRoT*) have provided the precision and resolution in photometry necessary to identify pulsation modes, and thence to probe the internal structure of pulsators and determine other stellar properties. Among the many interesting findings that may fit with theoretical predictions is one dealing with intermediate-mass sdB progenitors. One possible evolutionary scenario of a low-mass sdB + WD close binary (Silvotti et al. 2012) along with asteroseismological studies by Hu et al. (2008) indicates a progenitor intermediate-mass star of mass $2.0\,\mathrm{M}_{\odot} - 2.5\,\mathrm{M}_{\odot}$. Binary population synthesis simulations at different Z carried out by Brown and building on – and in collaboration with – Han et al. (2002, 2003) and Han et al. (2007) for Z=0.02, indicate a moderate number of low-mass hot subdwarf stars evolving from intermediate mass progenitor stars, as seen in areas below the ZAHeMS (in $\log_{10} g$ - T_{eff} diagrams).

[1] Vatican Observatory, V-00120 Città del Vaticano, Europe

2 Methodology

Detailed single and binary evolutionary and binary population synthesis calculations have been conducted by Brown following the methodology of Han et al. (2002, 2003), done originally for Z =0.02 and for sdBs in the Galactic field, in order to explore a greater range of metallicities: Z =0.0001, 0.001, 0.02, 0.03, 0.04, 0.05, mainly to examine EHB and sdB formation in different chemical environments, such as in the Galactic field. Stellar models (MS-RGB-HB-AGB phases, along with specially constructed EHB models with different core and envelope masses) have been constructed and calculations performed for the evolution of single stars and single binaries using an updated version of the stellar evolution code of Eggleton (1971, 1972, 1973), supplemented by the opacity tables of Chen & Tout (2007). The resulting grid of stellar models, for each Z, then serves as input for the binary population synthesis code of Han (1995, 2000), which is able to evolve an entire stellar population over time, including binaries, by using an interpolation routine to account for mass loss through RLOF. In this study, the best fitting parameters of Han et al. (2002, 2003) are then used to examine the evolution of a population of given metallicity Z.

3 Results

Simulations have been conducted using simple stellar populations, and then using the methodology of Han et al. (2002, 2003), first of all to construct a composite population (consisting of one population at 13 Gyr with a 5 Gyr sub-population) in order to study the Galactic field. They yield a high number (75–90%) of hot subdwarf stars in binary systems for Z=0.02, comparable to that of Han et al. (2002, 2003). With selection effects taken into account, their results are consistent with those of Maxted et al. (2001) and Napiwotzki et al. (2004) which indicate a substantial number of hot subdwarf stars in binary systems – of the order of 70% and 42%, respectively. One application of the simulations at different Z is the ability to account for non-canonical-mass hot subdwarf stars that are found below the zero age He main sequence (ZAHeMS), such as those seen in Fig. 1 (left). The Figure shows two ages (for a Z = 0.03 single stellar population [SSP]: 1.995 Gyr and 11.220 Gyr, respectively) for which low-mass sdBs in their post He-core burning phase of evolution are present below the ZAHeMS. Such objects are produced through the 1RLOF, 1CE+, 1CE-, 2CE+, 2CE-, 2RLOF, or merger channels, from progenitor stars of masses close to the transition between low-mass and intermediate-mass stars, which itself depends on metallicity. This suggests that low-mass sdB stars ($0.30 - 0.40\,\mathrm{M_\odot}$) form from intermediate-mass ($\sim 2.0\,\mathrm{M_\odot}$) stars which have ignited their non-degenerate He-cores. Asteroseismology studies from Hu et al. (2008), detecting differences in pulsation modes among various pulsating sdB stars, suggest progenitor intermediate-mass stars as a source of these non-canonical mass sdBs.

4 Conclusions

Given the wealth of information that asteroseismology methods can yield with regard to stellar parameters, such as the mass of a star, an ongoing study (such as that by *TESS*) of pulsating sdB stars promises to yield greater clarity about the evolutionary channels of sdB stars, including those in binary systems. To this end, more observations are needed. Brown and Boyle have studied the possibility of using the Specola Vaticana's VATT telescope on Mt. Graham in Arizona (USA) to study pulsating sdB stars. With photometry, the VATT's two CCD imagers can be used: 1) the VATT 4k CCD camera, or 2) the GUFI (Galway Ultra Fast Imager) L3CCD system, with a readout time of 2 ms and high time-resolutions of up to 400 images per second (subframed). A preliminary run has in fact been conducted using the 4k CCD camera, the hope being to achieve milli-mag pulsation resolution. The preliminary results are shown in the Figure below for PG 1047+003 (Fig. 1, right), as a test case in comparison with other observations already conducted by O'Donoghue et al. (1998). The sdB star PG 1419+081 has also been observed with the VATT. We coclude that much work needs to be done to achieve results.

Special thanks to Drs. Zanwhen Han, Philipp Podsiadlowski and Richard Boyle for their generous assistance.

References

Chen, X., Han, Z., Deca, J., & Podsiadlowski, P. 2013, MNRAS, 434, 186

Chen, X. & Tout, C. A. 2007, ChJAA, 7, 2, 245

Edelmann, H., Heber, U., Hagen, H.-J., et al. 2003, A&A, 400, 939

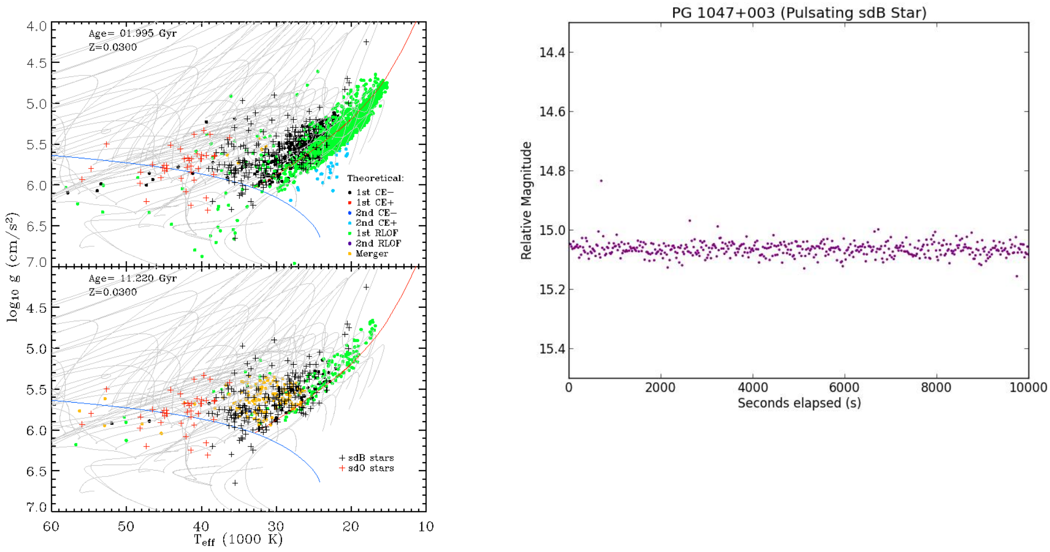

Fig. 1. Left: Shown above are Kiel diagrams for two ages (1.995 Gyr and 11.220 Gyr) for the $Z = 0.03$ SSP for which hot subdwarf stars appear below the ZAHeMS. Data from Saffer et al. (1994), Edelmann et al. (2003), Lisker et al. (2005), and Stroeer et al. (2007) are also plotted using the + symbols. EHB tracks (shown in grey) for core masses $0.35\,\mathrm{M}_\odot$, $0.40\,\mathrm{M}_\odot$, $0.45\,\mathrm{M}_\odot$, $0.50\,\mathrm{M}_\odot$, $0.55\,\mathrm{M}_\odot$, $0.60\,\mathrm{M}_\odot$, $0.65\,\mathrm{M}_\odot$, $0.70\,\mathrm{M}_\odot$, and $0.75\,\mathrm{M}_\odot$ are shown going from right to left along the ZAHeMS, while for each core mass, the tracks for envelope masses of $0.00\,\mathrm{M}_\odot$, $0.001\,\mathrm{M}_\odot$, and $0.002\,\mathrm{M}_\odot$, $0.005\,\mathrm{M}_\odot$, $0.007\,\mathrm{M}_\odot$, and $0.010\,\mathrm{M}_\odot$ are shown going from bottom to top. **Right:** A preliminary sample of the light-curve obtained for PG 1047+003 from the VATT telescope.

Eggleton, P. P. 1971, MNRAS, 151, 351
Eggleton, P. P. 1972, MNRAS, 156, 361
Eggleton, P. P. 1973, MNRAS, 163, 279
Fontaine, G., Brassard, P., Charpinet, S., et al. 2012, A&A, 539, A12
Han, Z. 1995, PhD thesis, University of Cambridge
Han, Z. 2000, Binary Population Synthesis Code, Tech. rep., Cambridge Institute of Astronomy; Yunnan Observatory
Han, Z., Podsiadlowski, P., & Lynas-Gray, A. E. 2007, MNRAS, 380, 1098
Han, Z., Podsiadlowski, P., Maxted, P., & Marsh, T. 2003, MNRAS, 341, 669
Han, Z., Podsiadlowski, P., Maxted, P., Marsh, T., & Ivanova, N. 2002, MNRAS, 336, 449
Hu, H., Dupret, M. A., Aerts, C., et al. 2008, A&A, 490, 243
Lisker, T., Heber, U., Napiwotzki, R., et al. 2005, A&A, 430, 223
Maxted, P., Heber, U., Marsh, T., & North, R. 2001, MNRAS, 326, 1391
Napiwotzki, R., Karl, C., Lisker, T., et al. 2004, Ap&SS, 291, 321
O'Donoghue, D., Koen, C., Lynas-Gray, A. E., Kilkenny, D., & van Wyk, F. 1998, MNRAS, 296, 306
Saffer, R. A., Bergeron, P., Koester, D., & Liebert, J. 1994, ApJ, 432, 351
Silvotti, R., Østensen, R. H., Bloemen, S., et al. 2012, MNRAS, 424, 1752
Stroeer, A., Heber, U., T., L., et al. 2007, A&A, 462, 269

Stars and their variability observed from space
C. Neiner, W. W. Weiss, D. Baade, R. E. Griffin, C. C. Lovekin, A. F. J. Moffat (eds)

ECLIPSING BINARIES WITH POSSIBLE β CEPHEI VARIABLES

F. Kahraman Aliçavuş[1,2] and G. Handler[1]

Abstract. In this study, we present the result of our candidate β Cephei stars search in eclipsing binary systems. Candidate eclipsing binary systems were selected from the catalog given by Avvakumova et al. (2013). Using the available public data of 29 systems, the binarity effects from the light curves were removed after a light-curve analysis and to disclose possible pulsations, a frequency analysis was carried out on the residuals. As regards to pulsation, some candidate slowly pulsating B (SPB) variables were revealed, but no convincing detection of new β Cephei stars was achieved.

Keywords: stars: general – stars: binaries: eclipsing – stars: fundamental parameters – stars: β Cephei

1 Introduction

The existence of pulsating stars in eclipsing binary systems has been known for decades. These systems are astrophysically valuable because their pulsation and binary characteristics allow us to obtain accurate fundamental stellar parameters (mass, radius) and to probe their interior structures. B type pulsating variables, in particularly β Cephei stars, in eclipsing binaries are useful objects to understand the evolution from the main-sequence to supergiants via their binary nature as well as pressure and gravity modes. However, the known number of these variables is small. Therefore in this study, we present a search for β Cephei variables in eclipsing binaries (BCEB) to reveal new candidates and to understand the pulsational behaviour in these eclipsing binary member pulsators. We selected the candidates considering the following conditions. First, stars having spectral type B5 and earlier were selected as candidate BCEB stars from the most recent eclipsing binary catalog of Avvakumova et al. (2013). Second, T_{eff} values of the candidates were estimated using the relation between spectral type and T_{eff} (Gray & Corbally 2009). Third, luminosity values were calculated using mostly the Gaia (Gaia Collaboration et al. 2016, 2018), but also the *Hipparcos* (van Leeuwen 2007) parallaxes. As a final step, we plotted the candidate stars on the Hertzsprung-Russell (H-R) diagram (Fig. 1). The stars inside the β Cephei instability strip were selected as target objects.

2 Light Curve and Frequency Analysis

The photometric data of the selected candidate BCEB stars were retrieved from the SuperWASP and ASAS archives. Only 29 candidate β Cephei stars have available photometric data. These data were used for the light curve and frequency analyses. First, binary light curve analysis was performed by using the Wilson-Devinney code (Wilson & Devinney 1971). Second, the data of individual stars were cleaned from the binarity effects by using our binary light curve models. Third, a frequency analysis was carried out to the residuals using the Period04 (Lenz & Breger 2005) program to detect β Cephei type pulsators. As a result, we classified some candidate SPB variables. No convincing β Cephei candidate was found.

3 Conclusions

In this study, the result of our research for candidate BCEB stars is presented. We discovered a few SPB candidates, while no β Cephei candidates were found. To confirm the SPB type variability of the candidate stars and to find new β Cephei stars in eclipsing binaries, we plan to examine high-quality TESS data with the same methods as well. Some of the candidate BCEB and SPB systems have been already observed by TESS and most of the remaining systems will be observed during the mission. The high-quality TESS data will allow

[1] Nicolaus Copernicus Astronomical Center, Bartycka 18, PL-00-716 Warsaw, Poland
[2] Çanakkale Onsekiz Mart University, Faculty of Sciences and Arts, Physics Department, 17100, Çanakkale, Turkey

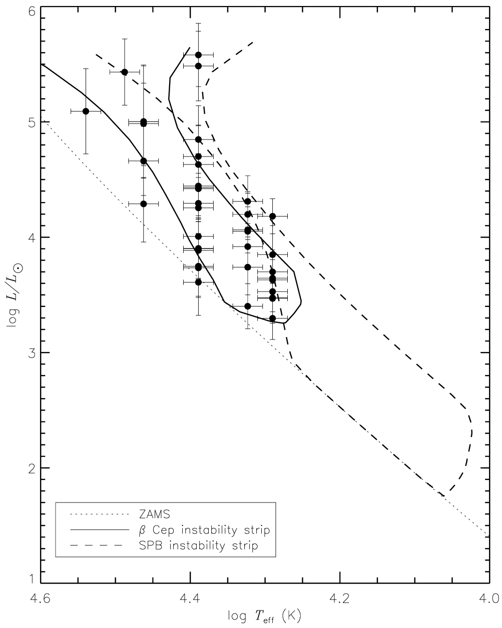

Fig. 1. The position of candidate β Cephei stars in eclipsing binary systems in the H-R diagram. The theoretical instability strips of β Cephei and slowly pulsating B (SPB) stars are from Pamyatnykh (1999).

us to confirm the pulsational variability in the candidate stars. There is one system in our sample, δ Pic, which was defined as a BCEB star using BRITE data (Pigulski et al. in preparation). This system was also observed by TESS and the pulsations were detected clearly. In further work, we will analyse available TESS data of the systems to reveal their oscillations, if they exist. As a result of this study, we aim to understand the pulsational behavior of β Cephei and SPB stars in eclipsing binary systems. Additionally, the fundamental parameters (mass, radius) of BCEB and SPB stars can be derived precisely and be used as input parameters in theoretical studies.

We thank the Polish National Center for Science (NCN) for supporting the study through grant 2015/18/A/ST9/00578. This study makes use of data from the first public release of the WASP data (Butters et al. 2010) as provided by the WASP consortium and services at the NASA Exoplanet Archive, which is operated by the California Institute of Technology, under contract with the National Aeronautics and Space Administration under the Exoplanet Exploration Program. This work has made use of data from the European Space Agency (ESA) mission Gaia (http://www.cosmos.esa.int/gaia), processed by the Gaia Data Processing and Analysis Consortium (DPAC, http://www.cosmos.esa.int/web/gaia/dpac/consortium). Funding for the DPAC has been provided by national institutions, in particular the institutions participating in the Gaia Multilateral Agreement. This research has made use of the SIMBAD data base, operated at CDS, Strasbourq, France.

References

Avvakumova, E. A., Malkov, O. Y., & Kniazev, A. Y. 2013, AN, 334, 860

Butters, O. W., West, R. G., Anderson, D. R., et al. 2010, A&A, 520, L10

Gaia Collaboration, Brown, A. G. A., Vallenari, A., et al. 2018, A&A, 616, A1

Gaia Collaboration, Brown, A. G. A., Vallenari, A., et al. 2016, A&A, 595, A2

Gray, R. O. & Corbally, Christopher, J. 2009, Stellar Spectral Classification (Princeton University Press)

Lenz, P. & Breger, M. 2005, Communications in Asteroseismology, 146, 53

Pamyatnykh, A. A. 1999, Acta Astron., 49, 119

van Leeuwen, F. 2007, A&A, 474, 653

Wilson, R. E. & Devinney, E. J. 1971, ApJ, 166, 605

Stars and their variability observed from space
C. Neiner, W. W. Weiss, D. Baade, R. E. Griffin, C. C. Lovekin, A. F. J. Moffat (eds)

RESULTS OF THE ENSEMBLE ASTEROSEISMOLOGY OF B-TYPE STARS IN OPEN CLUSTER NGC 6910

D. Moździerski[1], A. Pigulski[1], Z. Kołaczkowski[1,2], G. Michalska[1], G. Kopacki[1], F. Carrier[3], P. Walczak[1], A. Narwid[1], M. Stęślicki[1,4], J.-N. Fu[5], X.-J. Jiang[6], Ch. Zhang[5], J. Jackiewicz[7], J. Telting[8], T. Morel[3,9], S. Saesen[3,10], E. Zahajkiewicz[1], P. Bruś[1], P. Śródka[1], M. Vučković[3,11], T. Verhoelst[3,12], V. Van Helshoecht[3], K. Lefever[3,12], C. Gielen[3], L. Decin[3], J. Vanautgaerden[3] and C. Aerts[3,13]

Abstract. We present the results of ensemble asteroseismology of B-type pulsating stars in the NGC 6910 open cluster. Ensemble asteroseismology turns out to be very useful for examination of the instability strip, mode identification and testing the excitation of the modes. It also helps to constrain parameters of the cluster, its age in particular. The outcome shows the large potential of this method, especially when used with space telescopes, e.g. Kepler or TESS, that can provide precise photometry for cluster members.

Keywords: asteroseismology, stars: fundamental parameters, open clusters and associations: individual: NGC 6910

1 Introduction

NGC 6910 is a young open cluster located in the Cygnus constellation. Its age is estimated at 6 $\pm$ 2 Myr (Kołaczkowski et al. 2004) and distance of 1.1 - 1.5 kpc (Kharchenko et al. 2005, 2013). The cluster is known as one of the reachest open clusters in β Cep-type pulsating stars (Kołaczkowski et al. 2004; Pigulski 2008; Moździerski et al. 2018), which makes it a very good target for performing the modeling called ensemble asteroseismology. Here we present some results of the ensemble asteroseismology procedure which we developed for hot, pulsating stars in NGC 6910 cluster. Details of the procedure and full results were published by Moździerski et al. (2019).

2 Observations and analysis

Photometric and spectroscopic observations were obtained at 12 observatories, during two campaigns; in the years 2005 – 2007 (11 observatories) and in 2013 (2 observatories). For the purpose of our work, we chose only the longest and best-quality photometric data obtained in three observatories; Białków Observatory, Xinglong Observatory and ORM (Mercator telescope). In total, we obtained about 3800 CCD frames in B, 19 800 in

[1] Instytut Astronomiczny, Uniwersytet Wrocławski, Kopernika 11, 51-622 Wrocław, Poland
[2] Nicolaus Copernicus Astronomical Center, Polish Academy of Sciences, Bartycka 18, 00-716 Warszawa, Poland
[3] Instituut voor Sterrenkunde, KU Leuven, Celestijnenlaan 200D, 3001 Leuven, Belgium
[4] Space Research Centre, Polish Academy of Sciences, Kopernika 11, 51-622 Wrocław, Poland
[5] Department of Astronomy, Beijing Normal University, 100875 Beijing, PR China
[6] National Astronomical Observatories, Chinese Academy of Sciences, 20A Datun Road, Chaoyang District, 100012 Beijing, PR China
[7] Department of Astronomy, New Mexico State University, Las Cruces, NM 88003, USA
[8] Nordic Optical Telescope, Rambla José Ana Fernández Pérez 7, 38711 San Antonio, Breña Baja, Santa Cruz de Tenerife, Spain
[9] Space sciences, Technologies and Astrophysics Research (STAR) Institute, Université de Liège, Quartier Agora, Allée du 6 Août 19c, Bât. B5C, B4000-Liège, Belgium
[10] Département d'Astronomie, Université de Genève, Chemin des Maillettes 51, 1290 Versoix, Switzerland
[11] Instituto de Física y Astronomía, Universidad de Valparaíso, Casilla 5030, Valparaíso, Chile
[12] Royal Belgian Institute for Space Aeronomy, Ringlaan 3, 1180 Brussels, Belgium
[13] Department of Astrophysics, IMAPP, Radboud University Nijmegen, 6500 GL Nijmegen, The Netherlands

V, 5800 in I_{C} and 1350 CCD frames through U_{G} filter. The data were collected during 138 observing nights between August 2005 and October 2007 in Białków and Xinglong, and during 116 nights between April 2005 and August 2007 in ORM. Spectroscopic observations were obtained with 2.56-m Nordic Optical Telescope of ORM (the year 2007), 1.93-m telescope of OHP (the year 2007) and APO 3.5-m Astrophysical Research Consortium telescope (the year 2013). Fourier analysis of V-band observations allowed us to detect, in all nine examined B-type pulsating stars (NGC6910-14, -16, -27, -18, -25, -41, -34, -38 and -36), 40 frequencies, of which 37 are intrinsic. We determined atmospheric parameters for all of these stars using our spectroscopy and Strömgren photometry available in the literature. U_{G}, B, V and I_{C} photometry was used for photometric identification of modes with the method developed by Daszyńska-Daszkiewicz et al. (2002, 2005). We also made use of the FPF method (Zima 2006) implemented in the FAMIAS package (Zima 2008) for spectroscopic mode identification of the highest amplitude modes in NGC6910-14 and -18.

3 Ensemble asteroseismology and the results

Our method is based on iterative constraining of the cluster age, and assumed coevality of member stars. We defined a grid of parameters for evolutionary and pulsational models and used identified modes to put limits on the cluster age. Then, we derived parameters of the stars and iteratively narrow down these parameters and the cluster age. In parallell, we gained more constraints on mode identification (ensemble identification). As the final result, we determined the age of NGC 6910 as 10.6 ± 0.9 Myr, and we constrained parameters for all nine B-type pulsating stars. Our modeling allowed us to distinguish p, g and mixed modes. It proved that some modes of high frequency are in fact g - modes (in NGC6910-34, -38 and -36). This shows that period alone cannot be always used to distinguish between β Cep and SPB stars. We also found that NGC6910-38 is a β Cep star with unusually low mass, about 5.6 $\mathrm{M}_{\odot}$. This star is decreasing the low-mass boundary of the excited p-modes of B-type stars, compared to the state-of-the-art theoretical predictions (Fig. 1). Our results present promising perspectives for the use of ensemble asteroseismology when many modes are detected for many stars. Such possibilities are provided by the new observations of space telescopes, e.g. Kepler or TESS.

Based on observations obtained with the Apache Point Observatory 3.5-meter telescope, which is owned and operated by the Astrophysical Research Consortium, Nordic Optical Telescope, operated by the Nordic Optical Telescope Scientific Association at the Observatorio del Roque de los Muchachos, La Palma, Spain, of the Instituto de Astrofísica de Canarias, and Mercator Telescope, operated on the island of La Palma by the Flemish Community, at the Spanish Observatorio del Roque de los Muchachos of the Instituto de Astrofísica de Canarias. We thank Eva Bauwens, Bart Vandenbussche, Alexander Eigenbrod, Christoffel Waelkens, Pieter Deroo, Erik Broeders, Djazia Ladjal, Wim De Meester, Cezary Kułakowski, Evelien Vanhollebeke, Rik Huygen, Rachel Drummond, Roy Østensen, Matthieu Karrer, Elena Puga Antolín, Laurent Le Guillou, and Rosa María Domínguez Quintero for making some observations of NGC 6910. This work was supported by the NCN grants 2012/05/N/ST9/03898 and 2016/21/B/ST9/01126 and has received funding from the European Community's Seventh Framework Programme (FP7/2007-2013) under grant agreement no. 269194. PW acknowledges support from NCN grants 2013/08/S/ST9/00583 and 2015/17/B/ST9/02082. JNF acknowledges the support from the National Natural Science Foundation of China (NSFC) through the grants 11833002 and 11673003. TM acknowledges financial support from the European Space Agency through a Postdoctoral Research Fellow grant and from the Research Council of Leuven University through grant GOA/2003/04. CA and CG receive funding from the European Research Council (ERC) under the European Union's Horizon 2020 research and innovation programme (grant agreement N°670519: MAMSIE). This research has made use of the WEBDA database, operated at the Department of Theoretical Physics and Astrophysics of the Masaryk University.

References

Daszyńska-Daszkiewicz, J., Dziembowski, W. A., & Pamyatnykh, A. A. 2005, A&A, 441, 641

Daszyńska-Daszkiewicz, J., Dziembowski, W. A., Pamyatnykh, A. A., & Goupil, M.-J. 2002, A&A, 392, 151

Kharchenko, N. V., Piskunov, A. E., Röser, S., Schilbach, E., & Scholz, R.-D. 2005, A&A, 438, 1163

Kharchenko, N. V., Piskunov, A. E., Schilbach, E., Röser, S., & Scholz, R.-D. 2013, A&A, 558, A53

Kołaczkowski, Z., Pigulski, A., Kopacki, G., & Michalska, G. 2004, Acta Astron., 54, 33

Moździerski, D., Pigulski, A., Kołaczkowski, Z., et al. 2019, A&A, 632, A95

Moździerski, D., Pigulski, A., Kołaczkowski, Z., et al. 2018, in XXXVIII Polish Astronomical Society Meeting, ed. A. Różańska, Vol. 7, 213–215

Pigulski, A. 2008, Journal of Physics Conference Series, 118, 012011

Walczak, P., Fontes, C. J., Colgan, J., Kilcrease, D. P., & Guzik, J. A. 2015, A&A, 580, L9

Zima, W. 2006, A&A, 455, 227

Zima, W. 2008, Communications in Asteroseismology, 155, 17

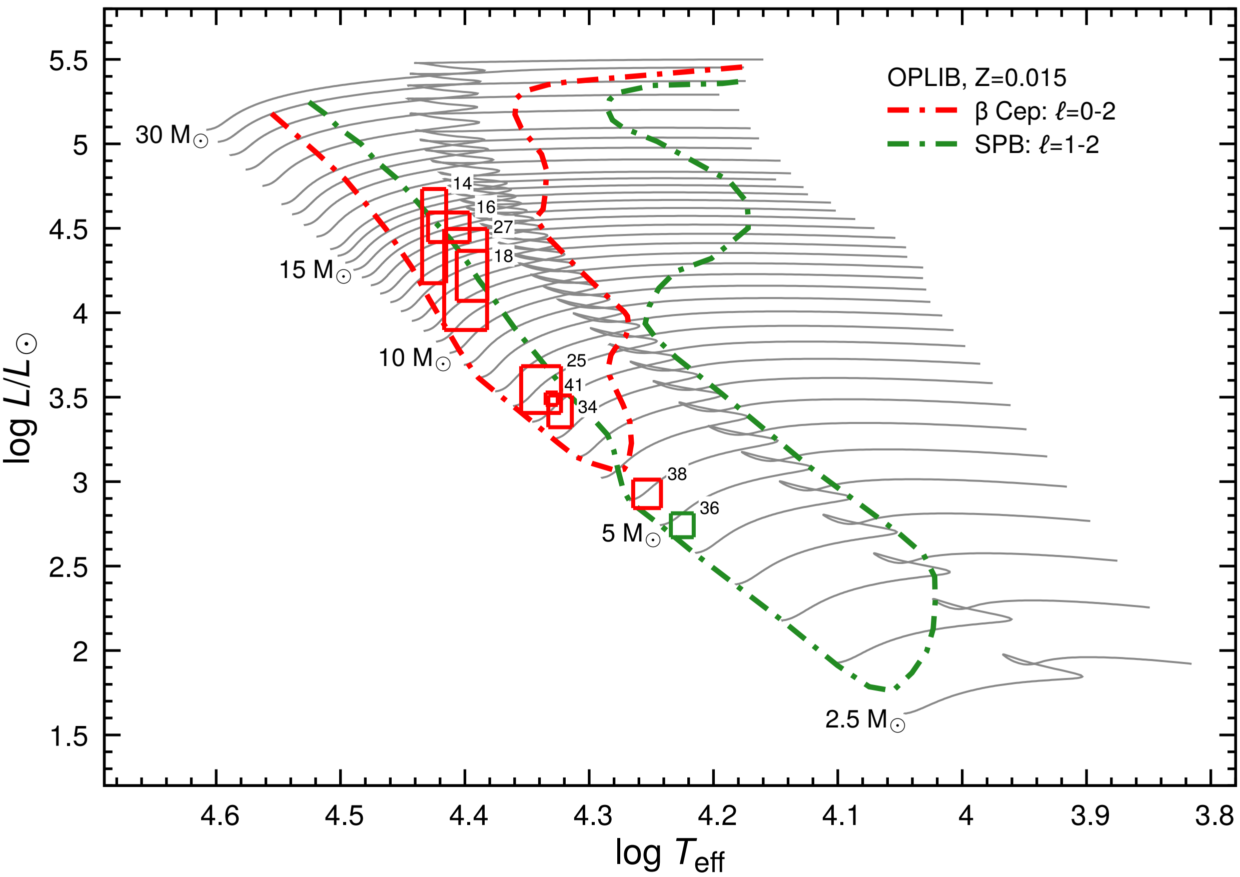

Fig. 1. Location of error boxes, obtained with ensemble asteroseismology, of the nine examined B-type pulsating stars, on the HR diagram, with evolutionary tracks and instability strips taken from Walczak et al. (2015). β Cep stars are marked with red error boxes and the one SPB star is marked with a green error box. All stars are labelled with WEBDA numbers.

Stars and their variability observed from space
C. Neiner, W. W. Weiss, D. Baade, R. E. Griffin, C. C. Lovekin, A. F. J. Moffat (eds)

β-CEP PULSATOR IN THE ECLIPSING BINARY V381 CAR: MODE IDENTIFICATION AND SEISMIC MODELLING

A. Miszuda[1], J. Daszyńska-Daszkiewicz[1] and W. Szewczuk[1]

Abstract.
We re-determine the binary orbit of the single-line eclipsing binary V381 Car. After subtracting the fitted eclipse light-curve, we performed a Fourier analysis in each Strömgren passband. We found 5 independent frequencies, and made mode identifications from the photometric observables and from the spectroscopic IPS diagrams. We identified three frequencies; ν_1 and ν_2 are prograde quadrupole modes, and ν_4 is a dipole zonal mode. Another two frequencies were most probably higher-degree modes.
We constructed preliminary seismic models to fit the dominant frequency and to investigate instability of the whole frequency range observed.

Keywords: stars: early-type, oscillations, binaries: eclipsing,

1 Introduction

HD 92024 (B1 III) is a single-lined (SB1) eclipsing binary with $m_V = 9.02$ mag, located in the open cluster NGC 3293. It was found by Balona (1977) that the system undergoes eclipses and that its light exhibits variations of β Cephei type. Engelbrecht & Balona (1986) subsequently detected two oscillation frequencies, $\nu_1 = 5.640\,\mathrm{d}^{-1}$, $\nu_2 = 7.669\,\mathrm{d}^{-1}$, and after re-examining the data Engelbrecht (1986) detected a third frequency $\nu_3 = 7.17\,\mathrm{d}^{-1}$. Jerzykiewicz & Sterken (1992) acquired *uvby* photometry, and confirmed ν_1 and ν_3. The authors derived an orbital period, $P = 8.3245 \pm 0.0001$ d, for the system

Freyhammer et al. (2005) observed V381 Car for 15 nights between 2002 December and 2003 April. We combined those data with previous observations from Jerzykiewicz & Sterken (1992) and Engelbrecht & Balona (1986), and collected 1617 observational points through *uvy* filters and 1690 through a *b* filter. With the FEROS echelle spectrograph we also acquired 103 high-resolution spectra, and found that V381 Car is an SB1 system. We derived the parameters of the system by combining the spectroscopic and photometric data. The primary has a mass of about 15 $M_\odot$, while the secondary has a much lower mass ($\sim 3\ M_\odot$) and contributes only about 2% to the total flux.

2 Binary modelling and pulsational analysis

Using observations collected by Freyhammer et al. (2005), we recalculated the binary model. Since we did not acquire any new observations we used orbital parameters from Freyhammer et al. (2005) to correct the photometric observations for variability caused by orbital motion. The contribution of the secondary to the total light is only about 2%, so we could assume that the pulsations originated in the primary. In order to detect the light variations that were not affected by the secondary's contribution, we extracted from the light-curve the primary eclipses observed with the *b* filter, obtaining 1293 data points. We performed a Fourier analysis on those data points, and found 5 frequencies with S/N > 3.8 (see Table1̃). One of the frequencies that we found could be a high-order radial *g* mode.

2.1 Mode identification

Following the mode identification technique based on phase differences and amplitude ratios from multi-colour photometry (see e.g. Balona & Stobie 1979; Stamford & Watson 1981; Daszyńska-Daszkiewicz et al. 2002), we attempted to determine the spherical harmonic degree for each frequency. In this study we used a set of

[1] Astronomical Institute, University of Wrocław, ul. Kopernika 11, 51-662 Wrocław, Poland

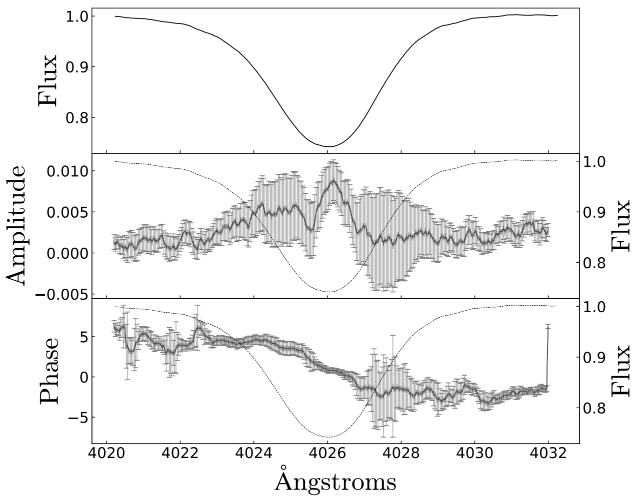

Fig. 1. IPS diagram calculated for the He I line $\lambda\,4026.191$ Å. The mean profile is shown in the top panel; amplitude and phase diagrams for the ν_1 frequency are in the middle and bottom panels, respectively.

	Frequency	S/N	ℓ	m
ν_1	5.6406	7.4	2	+1, +2
ν_2	6.6563	6.1	2	+1, +2
ν_3	8.1624	5.7	2,4,6	–
ν_4	0.5117	4.9	1	0
ν_5	1.0703	3.9	2,4,6	–

Table 1. Frequencies of V381 Car extracted from the Strömgren b passband (second column). The signal-to-noise ratio and the results of the mode identifications are given in the last three columns. The angular degree ℓ was obtained from photometry, and the azimuthal order (m) from spectroscopy.

evolutionary and oscillation models along with Strömgren photometry. Only for three out of five frequencies did we find an unambiguous identification of ℓ (see Table 1).

To determine the azimuthal order (m), we constructed IPS diagrams (Intensity Period Search diagrams, see Gies & Kullavanijaya 1988; Telting & Schrijvers 1997). We analysed 10 smoothed points in the He I (4026.191 Å) line (see Fig 1). From phase changes along the profile of that line we determined that ν_1 and ν_2 are prograde modes, while ν_4 is a zonal mode. We were not able to identify m for ν_3 and ν_5. The results of all the mode identifications are given in Table 1.

2.2 Seismic modelling

In order to find the best seismic models we calculated a grid of models with masses in the range $M = 13.1$–$15.3\,M_\odot$ in incremental steps of $dM = 0.2\,M_\odot$, rotation $V_{\rm rot} = 70$–$150\,{\rm km\ s^{-1}}$, with steps of $dV_{\rm rot} = 10\,{\rm km\ s^{-1}}$, and overshooting from the convective core, $f_{\rm ov}$, taking the values 0.01–0.04, with $df_{\rm ov} = 0.01$. We assumed an initial hydrogen abundance $X_0 = 0.71$ and metallicity $Z = 0.02$. The value of the metallicity was chosen to be equal to Z derived for NGC 3293 which hosts V381 Car (Trundle et al. 2007).

Frequency $\nu_4 = 0.5117$ is the centroid mode, so at first a set of models fitting this frequency was selected. Unfortunately, frequencies ν_1 and ν_2 do not have unambiguous identification of m, therefore instead of fitting models to the centroid we have to consider different m values. Using $\nu_m \approx \nu_0 + m\nu_{\rm rot}$ one can impose a condition that $|m_1|(\nu_{1,obs} - \nu_{1,m_1}) = |m_2|(\nu_{2,obs} - \nu_{2,m_2})$ where m_1 and m_2 are equal to 1 or 2. From our set of models only three of them met our condition with an accuracy better than 0.01. We found that $V_{\rm rot} \geq 100\,{\rm km\ s^{-1}}$and $f_{\rm ov} \geq 0.02$ are preferred.

3 Conclusions

This work presented an analysis of multi-colour photometric and spectroscopic data of the eclipsing binary V381 Car. We re-determined the observed frequencies, identified the mode degree (ℓ), and determined constraints on the azimuthal order (m) for three out of the five frequencies observed.

We constructed preliminary seismic models, and obtained some promising results, especially some constraints on rotation and overshooting from the convective core. However, in order to reproduce fully the pulsational observables we will have to extend our studies.

This work was supported financially by the Polish National Science Centre, grant 2018/29/B/ST9/02803.

The authors thank Prof. K. Pavlovski for providing us with observations, both photometric and spectroscopic, of the V381 Car system.

References

Balona, L. A. 1977, MmRAS, 84, 101

Balona, L. A. & Stobie, R. S. 1979, MNRAS, 189, 649

Daszyńska-Daszkiewicz, J., Dziembowski, W. A., Pamyatnykh, A. A., & Goupil, M. J. 2002, A&A, 392, 151

Engelbrecht, C. A. 1986, MNRAS, 223, 189

Engelbrecht, C. A. & Balona, L. A. 1986, MNRAS, 219, 449

Freyhammer, L. M., Hensberge, H., Sterken, C., et al. 2005, A&A, 429, 631

Gies, D. R. & Kullavanijaya, A. 1988, ApJ, 326, 813

Jerzykiewicz, M. & Sterken, C. 1992, MNRAS, 257, 303

Stamford, P. A. & Watson, R. D. 1981, Ap&SS, 77, 131

Telting, J. H. & Schrijvers, C. 1997, A&A, 317, 723

Trundle, C., Dufton, P. L., Hunter, I., et al. 2007, A&A, 471, 625

Stars and their variability observed from space
C. Neiner, W. W. Weiss, D. Baade, R. E. Griffin, C. C. Lovekin, A. F. J. Moffat (eds)

KIC 10661783 – BINARY SYSTEM WITH A δ SCT TYPE COMPONENT

A. Miszuda[1], W. Szewczuk[1] and J. Daszyńska-Daszkiewicz[1]

Abstract. We present the analysis of KIC 10661783, an eclipsing binary system with a δ Scuti component. We use all available *Kepler* data from both short and long cadences to model the binary system and to subtract the calculated theoretical eclipsing light curve from the original data.

The Fourier analysis of the light curve corrected for the binarity effects shows a rich oscillation spectrum with most prominent peaks concentrated in the range of 20 - 30 d^{-1}. We find small-amplitude signals in the low-frequency range that can be a manifestation of high-radial order g-mode pulsations.

Keywords: stars: binaries: eclipsing, stars: binaries: spectroscopic, stars: low-mass, stars: oscillations

1 Introduction

KIC 10661783 (A5IV) is located in the original *Kepler* field of view and was found to be an eclipsing binary by Pigulski et al. (2009). Its *Kepler* light curve was analysed for the first time by Southworth et al. (2011). The authors found 55 independent pulsational frequencies from SC Q2.3 and LC Q0-1 *Kepler* data and assigned them to the primary component of the system.

Subsequently, Lehmann et al. (2013) obtained 85 spectra and derived atmospheric parameters for each component. Combining spectroscopic data and *Kepler* photometric observations (SC Q 2.3) they obtained an orbital solution of the system and found that KIC 10661783 is a post-mass transfer detached binary. The authors determined the masses and radii of both components to be $M_A = 2.100 \pm 0.028$ $\mathrm{M}_\odot$, $R_A = 2.575 \pm 0.015\, R_\odot$ for the primary and $M_B = 0.1913 \pm 0.0025$ $\mathrm{M}_\odot$, $R_B = 1.124 \pm 0.019\, R_\odot$ for the secondary.

2 Observations and binary modelling

KIC 10661783 was observed by the *Kepler* satellite for nearly 1500 days. The data have been collected in both SC mode (Q2.3, Q6.1-Q8.3 and Q10.1-Q10.3) and LC mode (Q0-Q17), resulting in over 470 000 (SC) and 58 000 (LC) observational points (see left panel of Fig. 1). Having a much longer time span of the observations, we were able to redetermine parameters of the system. Using the Wilson-Devinney (`WD`, see Wilson & Devinney 1971; Wilson 1979) code we derived a precise orbital period, $P = 1.2313632588 \pm 0.0000000326$ d using all available LC observations. Then we modelled the system using SC data in a detached mode. This allowed us to correct the light curve for the variability caused by binarity.

3 Pulsational analysis

With the observations corrected for the binary orbit we performed a Fourier analysis. Periodograms (for SC data) calculated up to the Nyquist frequency ($\sim$680 d^{-1}) with the iterative pre-whitening procedure allowed us to find 750 frequencies with $S/N > 4.0$ (415 with $S/N > 5.0$); 167 of them seem to be independent frequencies. The most prominent frequency peaks are concentrated between $20 - 30\,\mathrm{d}^{-1}$ and no peaks were detected above 200 d^{-1} (see right panel of Fig. 1). Over 85 d^{-1} we observe only high harmonics of the orbital frequency. Moreover, in the case of the highest-amplitude peaks we found an amplitude modulation with the orbital period. Since this effect is also visible outside eclipses it cannot be caused by eclipsing of the stars.

[1] Astronomical Institute, University of Wrocław, ul. Kopernika 11, 51-662 Wrocław, Poland

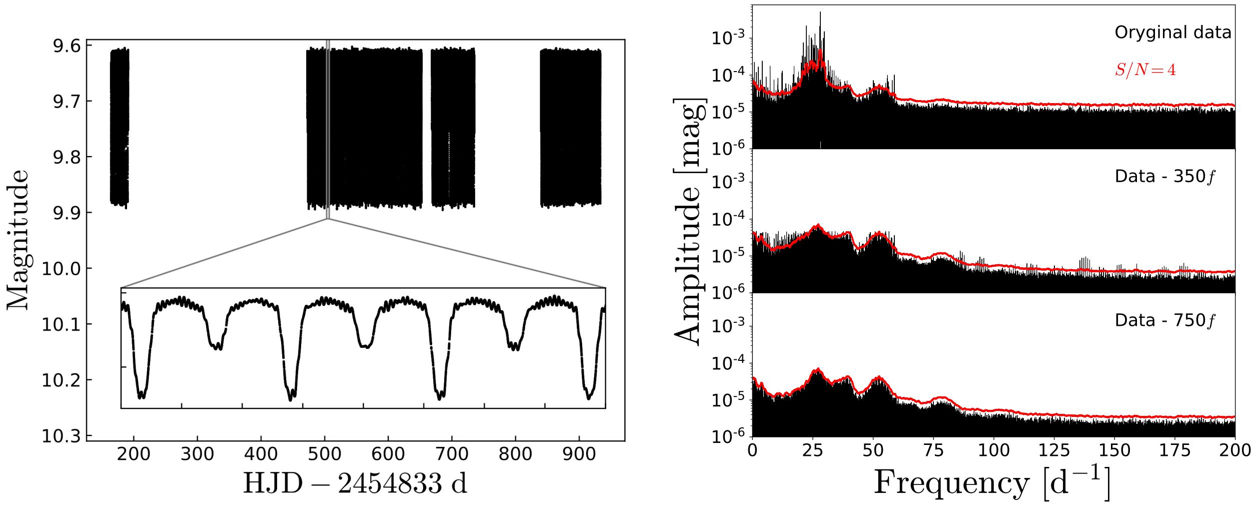

Fig. 1. Left panel: The full *Kepler* short-cadence light curve of KIC 10661783 covering over 473 000 observational points spanning over two years of observations. The inset shows the zoomed area covering 4 days in order to visualize both binary and pulsation variability. **Right panel:** Periodograms calculated for the *Kepler* SC observations corrected for the binary orbit. The amplitude spectra for the original data are shown in the top, after pre-whitening for 350 frequencies in the middle, while pre-whitened for all significant frequencies in the bottom panel. 4×S/N level is marked by red lines.

4 Conclusions

We present the analysis of all available *Kepler* photometric data of KIC 10661783. Using these data we redetermined the orbital elements of this system. Based on Fourier analysis we found 750 frequencies in the range of $0 - 200\,\mathrm{d}^{-1}$ from which 167 are independent. The highest-amplitude peaks concentrate in the range of $20 - 30\,\mathrm{d}^{-1}$. In addition to frequencies in the p-mode regime which are typical for δ Sct pulsators we found low frequency signals that can be interpreted as high-radial order g-modes.

We found that the amplitude of the most prominent frequencies is modulated with the orbital period. This can be caused by amplitude changes over the surface of the star.

This work was financially supported by the Polish National Science Centre grant 2018/29/B/ST9/02803.
Calculations have been carried out using resources provided by Wroclaw Centre for Networking and Supercomputing (http://wcss.pl), grant no. 265.
Funding for the *Kepler* mission is provided by the NASA Science Mission directorate. Some of the data presented in this paper were obtained from the Multi mission Archive at the Space Telescope Science Institute (MAST). STScI is operated by the Association of Universities for Research in Astronomy, Inc., under NASA contract

References

Lehmann, H., Southworth, J., Tkachenko, A., & Pavlovski, K. 2013, A&A, 557, A79
Pigulski, A., Pojmański, G., Pilecki, B., & Szczygieł, D. M. 2009, Acta Astron., 59, 33
Southworth, J., Zima, W., Aerts, C., et al. 2011, MNRAS, 414, 2413
Wilson, R. E. 1979, ApJ, 234, 1054
Wilson, R. E. & Devinney, E. J. 1971, ApJ, 166, 605

Stars and their variability observed from space
C. Neiner, W. W. Weiss, D. Baade, R. E. Griffin, C. C. Lovekin, A. F. J. Moffat (eds)

KIC 9163796 – A BENCHMARK BINARY FOR AGE DETERMINATION

D. H. Grossmann[1], P. G. Beck[1,2,3] and A. Hanslmeier[1]

Abstract. Binary systems constitute a valuable tool in astrophysics for gaining a deeper understanding of stellar evolution and determining stellar ages. That is particularly true for the double-lined binary KIC 9163796, which has a mass ratio of almost unity but varies significantly in temperature, luminosity and Lithium abundance. This paper outlined our approach to generate a combined stellar model for it using the MESA stellar-evolution code. By combining the available observational data with the models we derived, we aimed to find the best-fitting models for both components and to extrapolate the system's age from them.

Keywords: stars:binaries, evolution, solar-type, individual: KIC 9163796

1 Introduction

Gravitationally-bound binary stars provide valuable constraints on stellar models because we can assume that the two stars share characteristics such as age, initial metallicity and distance. The key difference between the two stellar components is mass, since that is the parameter which sets the pace for stellar evolution. Even in the case of non-eclipsing binary systems, the unprojected mass ratio of both binary components is conveyed by the ratio of the radial-velocity amplitudes. Our poster discussed an ongoing)modelling analysis of KIC 9163796. It consists of two oscillating red-giant stars orbiting each other with a period of ∼120 days ($e = 0.692 \pm 0.002$). They have a mass ratio of 1.5 ± 0.5 % (Beck et al. 2018). While such stars would appear on the main sequence as almost indistinguishable stellar twins, the increased pace of stellar evolution leads to substantial differences in effective temperature, luminosity and lithium abundance on the low-luminosity section of the red-giant branch (Fig. 1).

2 Modelling with MESA

This work used the 1-D stellar evolution package MESA (Modules for Experiments in Stellar Astrophysics, Paxton et al. 2011) to model the evolution of the components of the binary system. We began calculating a grid for stellar masses and metallicities in the realm of the observed values and their uncertainties. Starting from the pre-main sequence models, we evolved each model through the observed position in the Hertzsprung–Russel diagramm (Fig. 1). Within the grid, the models will then be compared to the parrameters inferred from spectroscopy and seismology through a figure of merit. We plan to achieve this by implementing a χ^2-test on the calculated models, which first have to be interpolated to correct for the different step sizes in each model. The boundary conditions, implied through membership in a binary system will furthermore guide the pre-selection of tracks. the resulting best fitting models will ultimately furnish us with an estimate of the age of the binary system.

3 The System

Although the two components of KIC 9163796 are very similar in mass and composition, they differ significantly in temperature (∼15%), surface gravity (∼50%) and luminosity ratio (60:40). Both stars undergo the First-Dredge up (FDU), however the primary is in a more advanced state of FDU than the secondary (Beck et al. 2018). Observations from *Kepler* (Borucki et al. 2010) and the HERMES Spectrograph (Raskin et al. 2011), the double-lined binary (SB2) system has a mass ratio $q = 1.015 \pm 0.005$, where the primary mass is $M_1 = 1.39 \pm 0.06\, M_\odot$. The primary has a Lithium abundance of 1.31 ± 0.08 dex, while for the secondary it is 2.55 ± 0.07 dex (Beck et al. 2018). This system constitutes a perfect example of the effects of a small mass difference on the evolution of a star.

[1] Institute of Physics, University of Graz, NAWI Graz, Universitaetsplatz 5/II, 8010 Graz, Austria
[2] Instituto de Astrofsica de Canarias, 38200 La Laguna, Tenerife, Spain
[3] Departamento de Astrofsica, Universidad de La Laguna, 38206 La Laguna, Tenerife, Spain

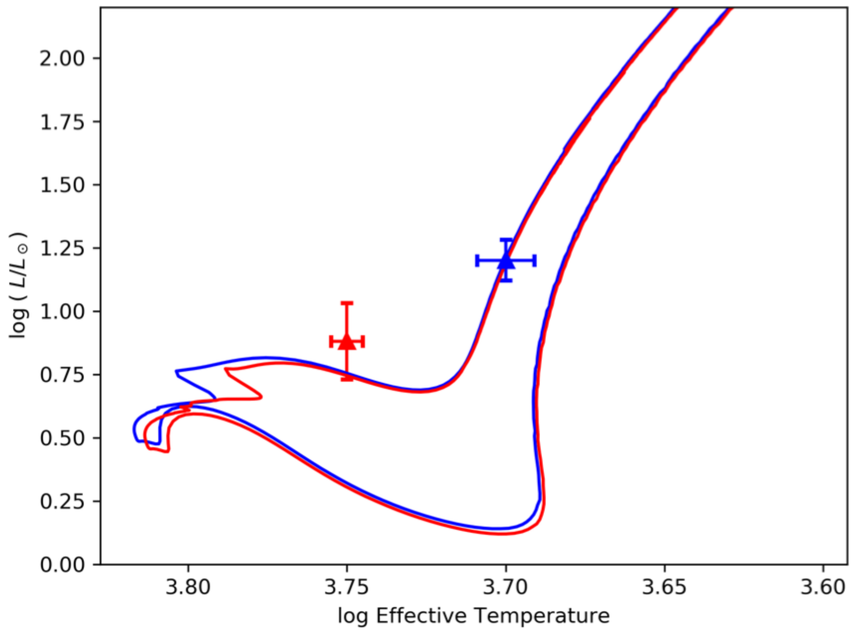

Fig. 1. H–R Diagram showing two stellar models from MESA having a mass ratio of 1.015 (red and blue lines), plus the observed positions of the primary and secondary components of KIC 9163796 including their uncertainties (blue and red triangles).

4 Conclusions

This study has shown that double-lined highly-constrained binaries contribute to our knowledge about stellar evolution, and thereby act as a benchmark for stellar astrophysics. In particular, systems like KIC 9163796 enable us to constrain stellar ages much more precisely than for single stars.

We acknowledge the whole community behind the stellar-evolution code MESA. The most recent version and documentation of MESA can be downloaded at `http://mesa.sourceforge.net`.

References

Beck, P. G., Kallinger, T., Pavlovski, K., et al. 2018, A&A, 612, A22
Borucki, W. J., Koch, D., Basri, G., et al. 2010, Science, 327, 977
Paxton, B., Bildsten, L., Dotter, A., et al. 2011, ApJS, 192, 3
Raskin, G., van Winckel, H., Hensberge, H., et al. 2011, A&A, 526, A69

THE SPECTROSCOPIC MULTIPLICITY FRACTION IN A SAMPLE OF A/F-TYPE (CANDIDATE) HYBRID STARS FROM THE *KEPLER* MISSION

P. Lampens[1], L. Vermeylen[1], P. De Cat[1], Á. Sodór[2], Zs. Bógnar[2], Y. Frémat[1], M. Skarka[3],[4], H. Lehmann[5], A. Samadi[6], L. Fox-Machado[7] and S. Joshi[8]

Abstract. By means of a study based on multi-epoch high-resolution spectra of 83 A–F-type candidate hybrid pulsating stars from the *Kepler* mission, collected at various observatories, we derive a (lower) estimate of the fraction of hybrid stars which belong to spectroscopic binary and multiple systems. In the first part of the study (49 hybrid stars) we derived a global spectroscopic multiplicity fraction of 27% (Lampens et al. 2018). In the second part we intend to obtain the same information for another 46 candidates. From a preliminary classification of 43 new targets, we are finding a spectroscopic multiplicity fraction of ∼30%. Spectroscopic observations are on-going. As a bonus, we identified systems for which a combined analysis of time delays (TDs) with radial velocities (RVs) enable one to derive accurate orbital elements and mass ratios and also an identification of the pulsating component. Furthermore, we will analyse the low-frequency regions of the periodograms of these stars using the exquisite data collected by *Kepler*.

Keywords: technique: spectroscopy, stars: spectroscopic systems, oscillations

1 Introduction

Our goal is to characterize the spectroscopic variability of an unbiased sample of *Kepler* hybrid pulsators in the γ Dor–δ Sct region. We need at least 4–6 spectra per target to be able to detect binarity or multiplicity at different time-scales, with orbital periods ranging from a few days to several years, and to establish a meaningful classification. We aimed to determine the orbits for systems having good phase coverage. The acquisition of the spectra was, and is, performed with telescopes at different sites equipped with an échelle spectrograph: Hermes (La Palma, Spain) (Raskin et al. 2011), ACE spectrograph (Piszkés-tető Observatory, Hungary) (Derekas et al. 2017), TCES (Thüringer Landessternwarte, Tautenburg, Germany), OES (Ondřejov Observatory, Czech Republic) (Kabáth et al., in prep.) and at the Observatorio Astronómico Nacional (San Pedro Mártir, México).

2 The spectroscopic multiplicity fraction

We completed an extensive study of a first sample from the *Kepler* mission (49 A–F *bona fide* hybrid stars and one cool hybrid object from Table 3 in Uytterhoeven et al. (2011)). In this report we have identified 10 spectroscopic systems (3 single-lined or SB1, 4 double-lined or SB2, 3 triple-lined or SB3), and 3 objects with long-term RV variations (VAR). Two other hybrid stars may have a companion or a shell (CMP). Including the known *Kepler* eclipsing binary, we found a global multiplicity fraction of *at least* 27% (Fig. 1, left) (Lampens et al. 2018). The distribution of detected orbital periods is dominated by those in the range 1500–2500 days (based on the 13 new systems). Our second sample of A–F candidate hybrid stars was based on a re-analysis of all *Kepler* targets with $5500 < T_{\rm eff} < 10000$ K. That sample consisted of 46 poorly-studied hybrid stars satisfying Kp < 10.5 mag. Among 43 objects we identified 9 SBs, 2 objects with long-term RV variations (VAR) and 2 targets with a companion or a shell (CMP). We derived a spectroscopic multiplicity fraction of ∼30% (Fig. 1, right).

[1] Royal Observatory of Belgium, Ringlaan 3, 1180 Brussels - Belgium
[2] Konkoly Observatory, Konkoly Thege M. u. 15-17 H-1121 Budapest - Hungary
[3] Astronomical Institute, Czech Academy of Sciences, Fričova 1, CZ-25165 Ondřejov
[4] Department of Theoretical Physics and Astrophysics, Masaryk Univerzity, Kotlářská 2, CZ-61137 Brno - Czech Republic
[5] Thüringer Landessternwarte Tautenburg, Sternwarte 5, 07778 Tautenburg - Germany
[6] Núcleo de Astronomía, Fac. de Ingeniería y Ciencias, Univ. Diego Portales, Av. Ejército Libertador 441, Santiago - Chile
[7] Instituto de Astronomía, Universidad Nacional Autónoma de México, Ensenada - México
[8] Aryabhatta Research Institute of Observational Sciences, Manora peak, Nainital 263002, India

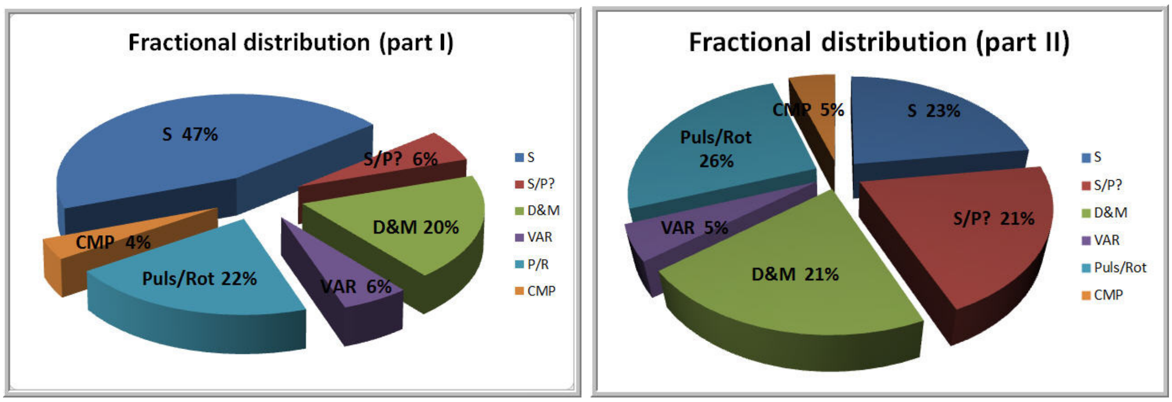

Fig. 1. Classification results based on 83 (candidate) hybrid pulsators. Classes are S: stable, S/P?: stable or pulsating?, D&M: binary/multiple, CMP: composite, Puls/Rot: pulsating/rotating star, VAR: with long-term RV variability. **Left:** Part I. **Right:** Part II. Note: this is *on-going work*.

3 Conclusions

- At least **one out of four** *Kepler* hybrid stars is part of a binary/multiple system. The multiplicity fraction derived from two samples of A/F-type hybrid stars is in excellent agreement with the results obtained by Nemec et al. (2017) (i.e. 33% of binary/multiple systems in a sample of SX Phe stars). *For an asteroseismologist, whether or not the (hybrid) pulsator is in a binary or multiple system matters.*

- The TDs obtained from the *Kepler* light curves and the RVs obtained from the spectroscopic monitoring provide the long time base needed for a precise determination of the orbits. This in turn allows one to derive fundamental-component properties (e.g. the mass function or mass ratio). In addition, we can identify the pulsating component(s). Armed with this information as well as with improved atmospheric parameters and $v \sin i$, our study provides crucial knowledge for a future asteroseismic modelling of some truly interesting hybrid pulsators.

- Immediate objectives for this project are to perform combined (RV+TD) analyses as well as frequency-searches of the *Kepler* data (low-frequency regime); to determine the (global) multiplicity fraction and to spectroscopically follow up on particularly worthwhile long-term targets.

This study is based on spectra obtained with (i) the HERMES spectrograph installed on the Mercator telescope, operated by the IvS, KULeuven, funded by the Flemish Community and located at the Observatorio del Roque de los Muchachos, La Palma, Spain of the Instituto de Astrofísica de Canarias, (ii) the ACE spectrograph of Konkoly Observatory, Piskés-tető, Hungary, and (iii) the coudé spectrograph on the 2-m Alfred Jensch telescope of the Thüringer Landessternwarte, Tautenburg, Germany.
ÁS and ZsB acknowledge support from the Lendület Program of the Hungarian Academy of Sciences, no. LP2018-7/2019. MS acknowledges the Postdoc@MUNI project, no. CZ.02.2.69/0.0/0.0/16_027/0008360. LFM acknowledges the grant PAPIIT, np. IN100918. We are grateful for the support received from the Belgo-Indian Network for A&A (BINA), and for Simbad, CDS, France.

References

Derekas, A., Plachy, E., Molnár, L., et al. 2017, MNRAS, 464, 1553
Lampens, P., Frémat, Y., Vermeylen, L., et al. 2018, A&A, 610, A17
Nemec, J. M., Balona, L. A., Murphy, S. J., Kinemuchi, K., & Jeon, Y.-B. 2017, MNRAS, 466, 1290
Raskin, G., van Winckel, H., Hensberge, H., et al. 2011, A&A, 526, A69
Uytterhoeven, K., Moya, A., Grigahcène, A., et al. 2011, A&A, 534, A125

Stars and their variability observed from space
C. Neiner, W. W. Weiss, D. Baade, R. E. Griffin, C. C. Lovekin, A. F. J. Moffat (eds)

POSSIBLE CONNECTION BETWEEN P CYGNI AND NEIGHBORING OPEN CLUSTERS

S. Beradze[1,2] and N. Kochiashvili[1]

Abstract. According to earlier investigations by Turner and co-authors, P Cygni could be a member of a hypothetical, sparsely-populated open cluster. The star lies near the east boundary of this hypothetical cluster. There is another, but known open cluster IC 4996 on the vicinity of P Cygni. The same authors believe that the above mentioned two clusters are connected to each other and they could represent a double cluster. As P Cygni is a hypergiant and consequently has very a strong and variable stellar wind, so a cluster membership can enable us to determine the age, distance, and reddening of the star relatively precisely. We used new data of different catalogues, for example, PPMXL and GAIA and tried to resolve the problem.

Keywords: Open clusters, LBV, P Cygni

1 Introduction

Early-B (B1Ia) spectral type hypergiant star P Cygni, a Luminous Blue Variable (LBV) (Conti 1984) has been well-known since its 1600 eruption, when it suddenly brightened like a Nova. During decades many authors made photometric and spectral observations of P Cyg to explain its real nature. But still its evolutionary status is not certain. The characteristic prototype "P Cygni" profiles of its spectral lines indicate an outflow of material from the star and is characteristic for Novae, Wolf-Rayet stars and LBVs. P Cyg has three different types of variation: 1. Short, 17-day variation; 2. 100-day variation, which is also observed in other Luminous Blue Variables; 3. Long-period variation of several years duration. P Cygni is the nearest LBV, at a distance of about 1.7 kpc (1.3 kpc according Gaia DR2). It has the following properties: T_{eff}=18200 K; L=$5.6{\cdot}10^5 L_{\odot}$; R=75 $R_{\odot}$; M=30 $M_{\odot}$ (Najarro et al. 1997). A. Kashi (Kashi 2010) suggested that P Cyg′s 17-th century eruption can be explained by mass transfer to a B-type binary companion. He found that the mass of the companion is approximately 3-6 $M_{\odot}$ and the orbital period is about 7 years. Using photometric observations taken from AAVSO and photometric data from Abastumani Astrophysical Observatory (obtained during 1951-1983 by Magalashvili and Kharadze; Kochiashvili et al. (Kochiashvili et al. 2018); Michaelis, Amir; Kashi, Amit and Kochiashvili, Nino (Michaelis et al. 2018) found that the orbital period of P Cyg′s companion is about 4.7 years.

2 "P Cygni cluster"

P Cygni - 34 Cyg ($20^h\ 17^m\ 47^s.2\ +38^{\circ}\ 01'\ 58''.5$) is a member of the Cyg OB1 association. This region is abundant with deep-sky objects, has active star formation, contains Wolf-Rayet stars and other early-type massive stars and also young open clusters. Open clusters are very important objects for studying stellar evolution. Because all the stars in an open cluster have the same age and chemical composition, all the properties of their stars are much easier to study than when they are isolated stars. There are many open clusters around P Cyg: NGC 6910, M 29, NGC 6883, IC 4996 and so on.

Several authors believe that P Cyg and stars around it belong to an anonymous open cluster "P Cygni Cluster" (Turner (1985); Turner et al. (2001)). We attempt here to check this hypothesis. For this we used the Clusterix program. "Clusterix is a web-based, interactive application that allows the computation of membership probabilities from proper motions through a fully non-parametric method and also allows the possibility of gathering physical parameters (parallaxes, radial velocities)" (Balaguer-Núnez et al. 2017). We use the GAIA/DR2 catalogue and choose a 5-arcmin radius around P Cyg with magnitude limits from 4 to 16 and found 211 stars.

After that we tried to find stars with similar proper motions to that of P Cyg (-3.18; -6.45). From these selected 211 objects we find 172 possible cluster-member stars (Fig. 1). If they really are members of the cluster, than P Cygni probably is located near the center of it.

[1] Abastumani Astrophysical Observatory, Ilia State University, Mt. Kanobili, 0301 Adigeni, Georgia
[2] Samtskhe-Javakheti State University, 0800, Akhaltsikhe, Georgia

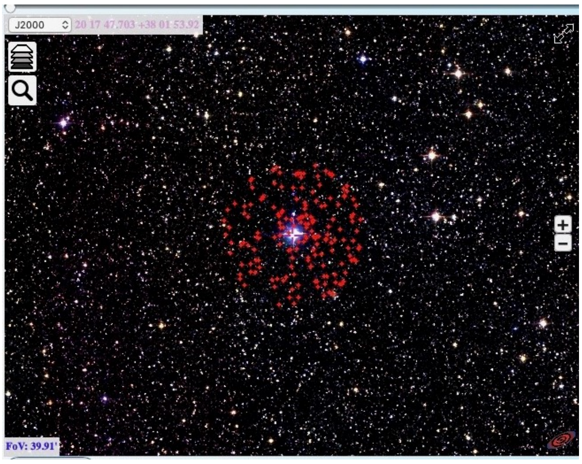

Fig. 1. 172 stars which have similar proper motions to that of P Cyg from the GAIA/DR2 catalogue

Turner and co-authors obtained a similar result according to the photometric study of stars in the vicinity of P Cyg (Turner et al. 2001).
IC 4996 is the nearest open cluster to P Cygni. It is predicted that it forms a double cluster with "P Cygni cluster" ((Turner et al. 2001). According to the proper motion data from GAIA/DR2 catalogue it seems that this hypothesis could be true. The distance of IC 4996 from various sources covers the range from 1.67 kpc to 2.40 kpc, and the ages of the cluster are given from 6 Myr to 9 Myr (Straižys et al. 2019).

3 In Future

We are going to analyze data on all these 211 stars around P Cyg. We will check if the "P Cygni cluster" really does exist and if there is any connection with the young open cluster IC 4996. Then we will construct an HR-diagram, which will give us the possibility to determine precisely the parameters of P Cyg, like - mass, distance, age and luminosity.

This work was supported by Shota Rustaveli National Science Foundation (SRNSF), grant No 218070, The Next Possible Outburst of P Cygni.

References

Balaguer-Núnez, L., Casamiquela, L., Jordana, N., et al. 2017, in Highlights of Spanish Astrophysics IX, ed. S. Arribas, A. Alonso-Herrero, F. Figueras, C. Hernández-Monteagudo, A. Sánchez-Lavega, & S. Pérez-Hoyos, 493

Conti, P. S. 1984, in IAU Symposium, Vol. 105, Observational Tests of the Stellar Evolution Theory, ed. A. Maeder & A. Renzini, 233

Kashi, A. 2010, MNRAS, 405, 1924

Kochiashvili, N., Beradze, S., Natsvlishvili, R., et al. 2018, Astrophysics, 61, 22

Michaelis, A. M., Kashi, A., & Kochiashvili, N. 2018, New A, 65, 29

Najarro, F., Hillier, D. J., & Stahl, O. 1997, A&A, 326, 1117

Straižys, V., Boyle, R. P., Milašius, K., et al. 2019, A&A, 623, A22

Turner, D. G. 1985, A&A, 144, 241

Turner, D. G., Welch, G., Graham, M., et al. 2001, Journal of the AAVSO, 29, 73

Stars and their variability observed from space
C. Neiner, W. W. Weiss, D. Baade, R. E. Griffin, C. C. Lovekin, A. F. J. Moffat (eds)

PARAMETERS OF DETACHED O- AND B-TYPE ECLIPSING BINARIES IN THE LMC

M. Taormina[1]

Abstract.

Detached eclipsing double-lined spectroscopic binaries (SB2) offer a unique opportunity to measure directly, and accurately, stellar parameters like masses, luminosities and radii of the component stars. Such accurate parameters are very important for constraining evolutionary models, especially of early-type stars for which such knowledge is lacking. SB2 eclipsing binaries are also very good distance indicators, and are being used successfully to measure distances in the Galaxy and beyond. Here we present our solution for two O and B-type massive detached SB2 systems in the Large Magellanic Cloud (LMC). The masses of the components of these binaries are about 20 M⊙ and 14 M⊙, respectively, and were determined with an accuracy of 1%. We compared our solution with different evolutionary models and found that the one with higher overshooting agrees better with our results.

Keywords: Eclipsing binaries, early-type stars, Large Magellanic Cloud

1 Observational Data

The two systems that we analyzed, OGLE-LMC-ECL-22270 (hereafter BLMC-01) and OGLE-LMC-ECL-06782 (hereafter BLMC-02), are located close to the centre of the LMC. They have not been analyzed previously, and nothing was known about their physical properties except for a very rough spectral type for BLMC-01 (Muraveva et al. 2014; Evans et al. 2015).

For the purpose of the current analysis we collected photometric data available in the literature, mostly from the OGLE project (Udalski et al. 2008) but also fr om the MACHO and EROS projects.

We also acquired high-resolution optical spectra using the UVES spectrograph (VLT, Paranal Observatory, Chile) and MIKE spectrograph (Magellan telescope, Las Campanas Observatory, Chile).

2 Analysis and results

The radial velocities (RV) of the components (see Fig. 1) were obtained using the Broadening Function technique (Rucinski 1999) implemented in the `RaveSpan` code (Pilecki et al. 2017). Spectra of standards similar to those of our system were used as templates. During these processes, rotational velocities (v_{rot} sin$i$) were also measured.

A preliminary light-curve solution was obtained using the `JKTEBOP` (Southworth et al. 2007) modelling tool, scanning the parameter space through a wide range of parameters. This solution was subsequently employed as a starting point for more sophisticated modelling of both RV and light-curves using the `Wilson-Devinney` code (Wilson & Devinney 1971) with the `Phoebe GUI` (Prša & Zwitter 2005). We modeled all the photometric bands simultaneously (IVK in the case of BLMC-01 and IVR for BLMC-02). The best-fitting orbital solutions are presented in Fig. 1; the light-curve solutions for all the bands used are shown in Fig. 2.

We then calculated the physical properties of the components; they have been published in Table 4 of Taormina et al. (2019).

The reddening was estimated using both the reddening map from Haschke et al. (2011), and directly to the object from the analysis of interstellar sodium lines. For BLMC-01 we found a reddening of $E(B-V)$=0.193, and $E(B-V)$=0.082 for BLMC-02. BLMC-01 is located in 30 Doradus region, so greater reddening is expected there.

[1] Centrum Astronomiczne im. Mikołaja Kopernika PAN, Bartycka 18, 00-716 Warsaw, Poland

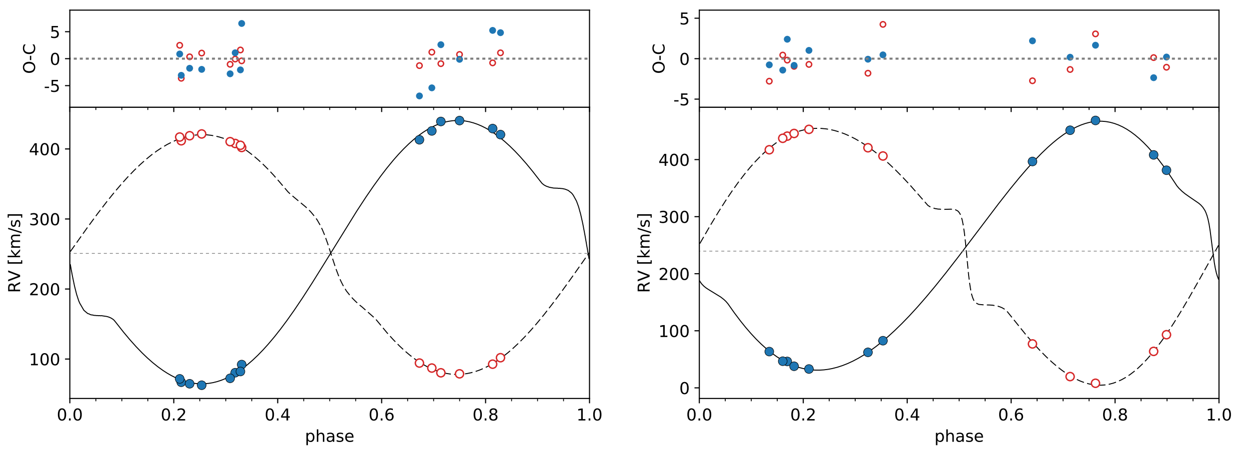

Fig. 1. Orbital solution from the `WD` code (lines) and the RV measurements (circles) from `Ravespan` for BLMC-01 (left) and BLMC-02 (right). Residuals are shown in the upper panels.

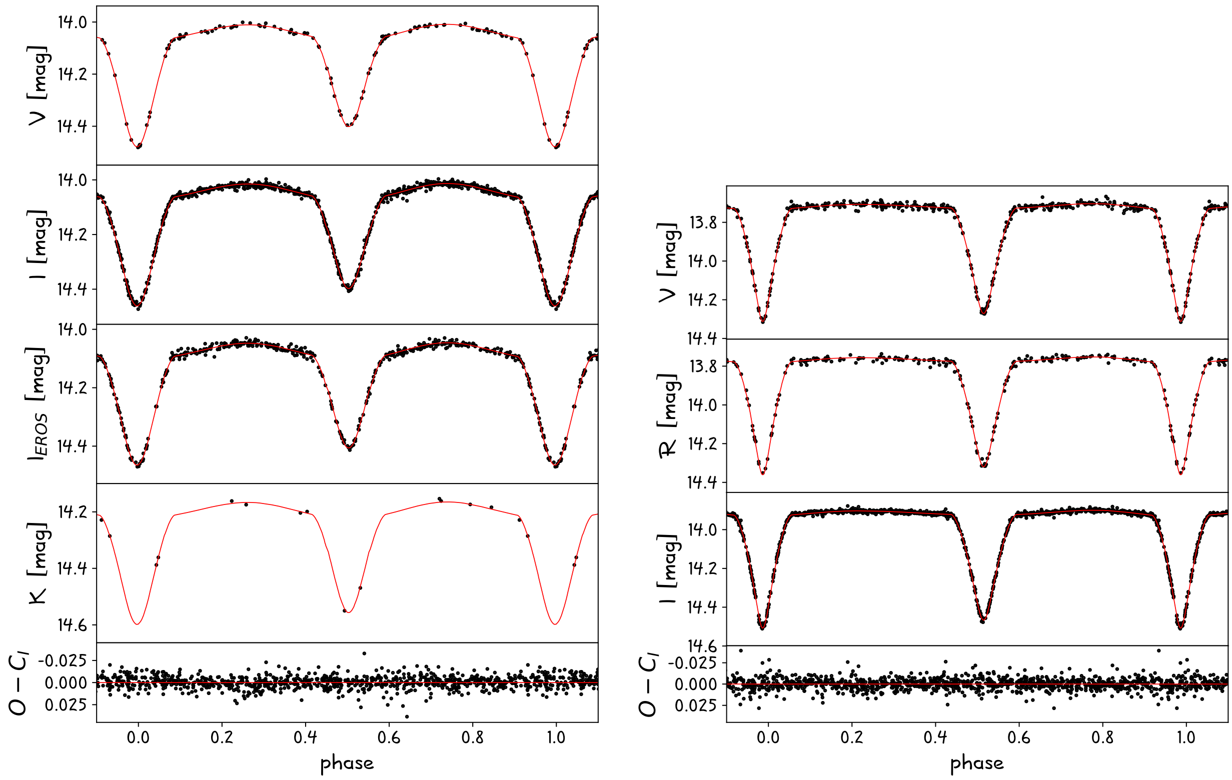

Fig. 2. Light-curves for BLMC-01 (left) and BLMC-02 (right). Data (points) and the model (red line) are plotted. The bottom panels show the I-band residual light-curves.

3 Evolutionary status

The evolution of early-type stars is not well understood, and discrepancies are often found between the observations and models. We used our results for BLMC-01 to test two different sets of evolutionary tracks, calculated for different sets of parameters.

In the left panel of Fig. 3 we compare our measurements with the tracks of Choi et al. (2016). We used a set of models for the LMC metallicity and masses from 13 to 16 M⊙, and also two interpolated tracks for the masses of the components of BLMC-01. These models were calculated with overshooting $\alpha = 0.2$.

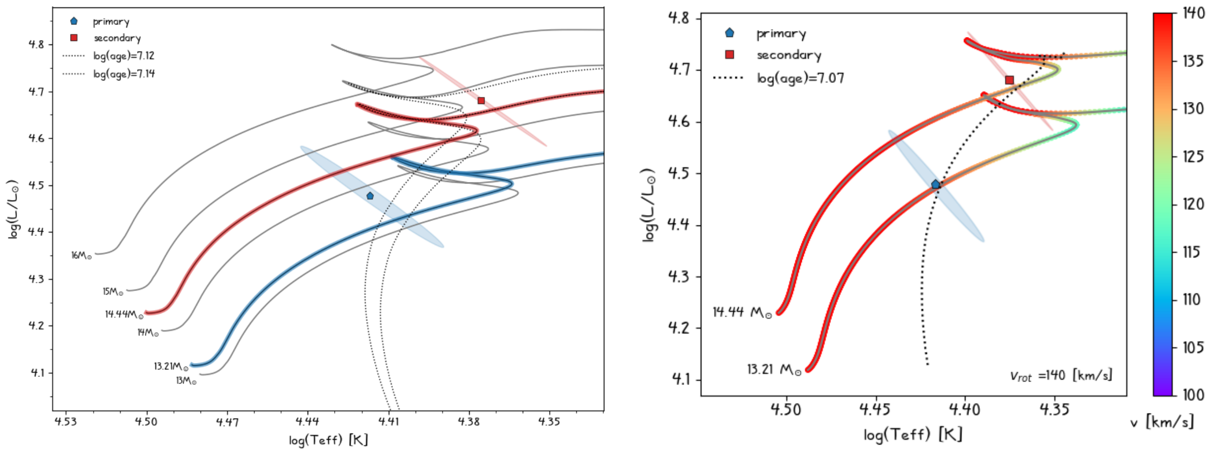

Fig. 3. H–R diagram showing the positions of the components of BLMC-01, on a grid of evolutionary tracks of Choi et al. (2016) (**left**) and evolutionary models from Brott et al. (2011) (**right**). All tracks start at the zero-age main sequence. Error ellipses are shown for the components.

In the right panel of Fig. 3 we show the evolutionary tracks of Brott et al. (2011). This grid covers a wide range of surface rotation velocities and masses. The overshooting used in these models is higher (α=0.335). We chose models with the LMC metallicity and an initial velocity of $\sim$ 140 km/s, consistent with measured current rotational velocities. We note that for different initial velocities the consistency with our results is lower.

As one can see, models of Brott et al. (2011) are more consistent with the results and predict both components to be on the main sequence, which is more probable than the results from Choi et al. (2016). Furthermore, although the uncertainty of the temperature determinations is large, the ratio of the two temperatures is very well constrained so both models should appear at the same distance from the tracks, which is not the case for the models of Choi et al. (2016).

From this comparison we conclude that models with higher overshooting describe our measurements better. The rotation has a lower, but also significant, effect on the results.

For more details regarding the results and analysis of the systems presented here, please refer to Taormina et al. (2019).

MT gratefully acknowledges financial support for this work from the Polish National Science Center grant PRELUDIUM 2016/21/N/ST9/03310.

References

Brott, I., de Mink, S. E., Cantiello, M., et al. 2011, A&A, 530, A115

Choi, J., Dotter, A., Conroy, C., et al. 2016, ApJ, 823, 102

Evans, C. J., van Loon, J. T., Hainich, R., & Bailey, M. 2015, A&A, 584, A5

Haschke, R., Grebel, E. K., & Duffau, S. 2011, AJ, 141, 158

Muraveva, T., Clementini, G., Maceroni, C., et al. 2014, MNRAS, 443, 432

Pilecki, B., Gieren, W., Smolec, R., et al. 2017, ApJ, 842, 110

Prša, A. & Zwitter, T. 2005, ApJ, 628, 426

Rucinski, S. 1999, in ASPCS, Vol. 185, IAU Colloq. 170: Precise Stellar Radial Velocities, ed. J. B. Hearnshaw & C. D. Scarfe, 82

Southworth, J., Bruntt, H., & Buzasi, D. L. 2007, A&A, 467, 1215

Taormina, M., Pietrzyński, G., Pilecki, B., et al. 2019, ApJ, 886, 111

Udalski, A., Szymanski, M. K., Soszynski, I., & Poleski, R. 2008, Acta Astron., 58, 69

Wilson, R. E. & Devinney, E. J. 1971, ApJ, 166, 605

Other and more challenges

Stars and their variability observed from space
C. Neiner, W. W. Weiss, D. Baade, R. E. Griffin, C. C. Lovekin, A. F. J. Moffat (eds)

PROTOSTELLAR ACCRETION BURSTS AND THEIR EFFECT ON PRE-MAIN-SEQUENCE STELLAR EVOLUTION

E. Vorobyov[1, 2] and V. Elbakyan[2]

Abstract. The pre-main-sequence evolution of low-mass stars and brown dwarfs has been studied numerically by considering the accretion of mass onto the central object. Stellar evolution was computed using the STELLAR evolution code developed by Yorke & Bodenheimer. Mass accretion rates were taken from numerical hydrodynamics models of Vorobyov & Basu. We found that mass accretion can have a strong effect on the subsequent evolution of young stars and brown dwarfs. Accreting and non-accreting models disagree with each other, and the extent of the disagreement depends notably on the thermal efficiency of accretion. The largest mismatch is found for the cold accretion case. In the hot and hybrid accretion cases the disagreement between accreting and non-accreting models is less pronounced, but still remains noticeable for 1.0 M-yr-old objects. A wrong age estimate for objects of (sub-)solar mass is possible if isochrones based on non-accreting models are used.

Keywords: accretion, stars: formation, low-mass, brown dwarfs, pre-main sequence

1 Introduction

The evolution of pre-main-sequence (PMS) stars has been studied for decades by various authors (e.g., Baraffe et al. 1998; Palla & Stahler 2000), but only recently has it become possible to study stellar evolution starting from the very early stages of star formation and taking the main accretion phase into account. Solar-type stars form through gravitational collapse of molecular cloud cores, and circumstellar disks form because of the near-conservation of the angular momentum in the collapsing cores. In the early embedded phase of protostellar disk evolution the disks are often prone to gravitational instability (Vorobyov & Basu 2009), which results in very time-dependent mass accretion histories, the episodic accretion histories repeating short accretion bursts and relatively longer quiescent phases (Vorobyov & Basu 2010, 2015; Machida et al. 2011). Other mechanisms, such as the magneto-rotational and thermal instabilities, planet-disk interactions and close stellar encounters, can also produce episodic accretion bursts in both the embedded and T Tauri phases of disk evolution (see Audard et al. (2014) for a review). Various observational signatures of this episodic accretion have also been reported for low-mass protostars (e.g., Dunham et al. 2010; Liu et al. 2016). The effects of such variable mass accretion have recently been included in the stellar evolution calculations focussing on the early (Vorobyov 2016) and late stellar evolutionary phases (e.g., Baraffe et al. 2009, 2012, 2017; Hosokawa et al. 2013).

Those studies revealed that the PMS tracks of accreting stars can differ from the non-accreting tracks that have routinely been used to estimate stellar ages and masses of young clusters. In particular, the age of a star as inferred from non-accreting tracks can be considerably overestimated. We show that the thermal efficiency of accretion, i.e., the fraction of accretion energy retained by the star (normally incorporated as a free parameter of the model), can affect the stellar evolution tracks of accreting stars appreciably. It is therefore still quantitatively uncertain to what extent non-accreting isochrones are reliable after all, and whether it is accretion variability or thermal efficiency of accretion that plays the main role in PMS evolution.

2 Numerical model

2.1 Hydrodynamics code

Mass accretion histories were computed using the numerical hydrodynamics models of star and disk evolution described in detail in Vorobyov & Basu (2010). We started our numerical simulations from the gravitational

[1] University of Vienna, Department of Astrophysics, Vienna 1180, Austria
[2] Research Institute of Physics, Southern Federal University, Stachki Ave. 194, Rostov-on-Don 344090, Russia

collapse of a gravitationally contracting cloud core, continued into the embedded phase of star formation during which star, disk and envelope are formed, and terminated our simulations after the point corresponding to 1.0–2.0 Myr of evolution, depending on the model and available computational resources. We assumed that in subsequent evolution the mass accretion rate declines linearly to zero during another 1.0 Myr. That effectively sets a disk dispersal time of 1 Myr and a total disk age of about 2.0–3.0 Myr in our models. Those values are in general agreement with the disk ages inferred from observations of star-forming regions (Williams & Cieza 2011).

2.2 Stellar evolution code

We computed the evolution of low-mass stars and higher-mass brown dwarfs using the evolution code STELLAR originally developed by Yorke & Bodenheimer (2008). We started our computations from a protostellar seed, continued through the main accretion phase where the growing star accumulates most of its final mass, and ended the computations when the star approached the main sequence. We used the protostellar accretion rates obtained from the numerical hydrodynamics simulations of pre-stellar core collapse described in Sect.2.1.

2.3 Thermal efficiency of accretion

During the evolution calculations we assumed that a fraction α of the accretion energy $\epsilon G M_* \dot{M}/(2R_*)$ is absorbed by the protostar, while a fraction $1-\alpha$ is radiated away and contributes to the accretion luminosity of the star. M_* and R_* are the mass and radius of the central star, and $\dot{M}$ is the mass accretion rate. Here we consider three models for the thermal efficiency of accretion: (i) cold accretion with a constant $\alpha = 10^{-3}$, meaning that practically all accretion energy is radiated away and little is absorbed by the star, (ii) hot accretion with a constant $\alpha = 0.1$, and (iii) a hybrid scheme defined as follows:

$$\alpha = \begin{cases} 10^{-3}, & \text{if } \dot{M} < 10^{-7}\ M_\odot\ \mathrm{yr}^{-1}\ , \\ \dot{M} \times 10^{4} \left[\frac{\mathrm{yr}}{M_\odot}\right], & \text{if } 10^{-7}\ M_\odot\ \mathrm{yr}^{-1} \le \dot{M} \le 10^{-5}\ M_\odot\ \mathrm{yr}^{-1}, \\ 0.1, & \text{if } \dot{M} > 10^{-5}\ M_\odot\ \mathrm{yr}^{-1}. \end{cases} \tag{2.1}$$

3 Hybrid accretion

This section presents our results for the hybrid accretion model, in which the value of α depends on the mass accretion rate. The computed stellar evolution sequences of the total (accretion plus photospheric) luminosity L_* *vs.* effective temperature $T_{\rm eff}$ for 31 models are shown as the dots in the left panel of Fig. 1. The zero point of the stellar age (zero age) is defined as the instance when the growing star accumulates 95% of its final mass. The green symbols mark the reference ages of 1 Myr, 10 Myr, and 25 Myr for each model. The black solid lines present the isochrones for the same ages but derived from the non-accreting stellar evolution models of Yorke & Bodenheimer (2008) (hereafter, the non-accreting isochrones).

The left panel of Fig. 1 indicates that young 1-Myr-old stellar objects show a noticeable deviation from non-accreting isochrones of the same age. This is especially evident for models with effective temperatures of $\log T_{\rm eff} \ge 3.5$, which lie significantly lower than the 1.0-Myr-old isochrone, meaning that these objects appear older on the L_*–$T_{\rm eff}$ diagram than they truly are.

4 Hot accretion

This section discusses the results for the hot accretion model, in which α is set to 0.1 during the entire evolution period. For the models with the hot accretion scenario there again exists a moderate deviation between the accreting and non-accreting 1.0-Myr-old models as concerns the total luminosity and stellar radius, but this disagreement diminishes for 10-Myr-old and 25-Myr-old models. All in all, the behaviour of the hybrid and hot accretion models is similar, in agreement with the previous work of Baraffe et al. (2012).

5 Cold accretion

This section presents our results for the cold accretion model, in which α is always set to the small value of 10^{-3} independent of the actual value of the mass accretion rate, meaning that almost all accretion energy is radiated away and only a tiny fraction is absorbed by the protostar. The right panel of Fig. 1 shows the stellar

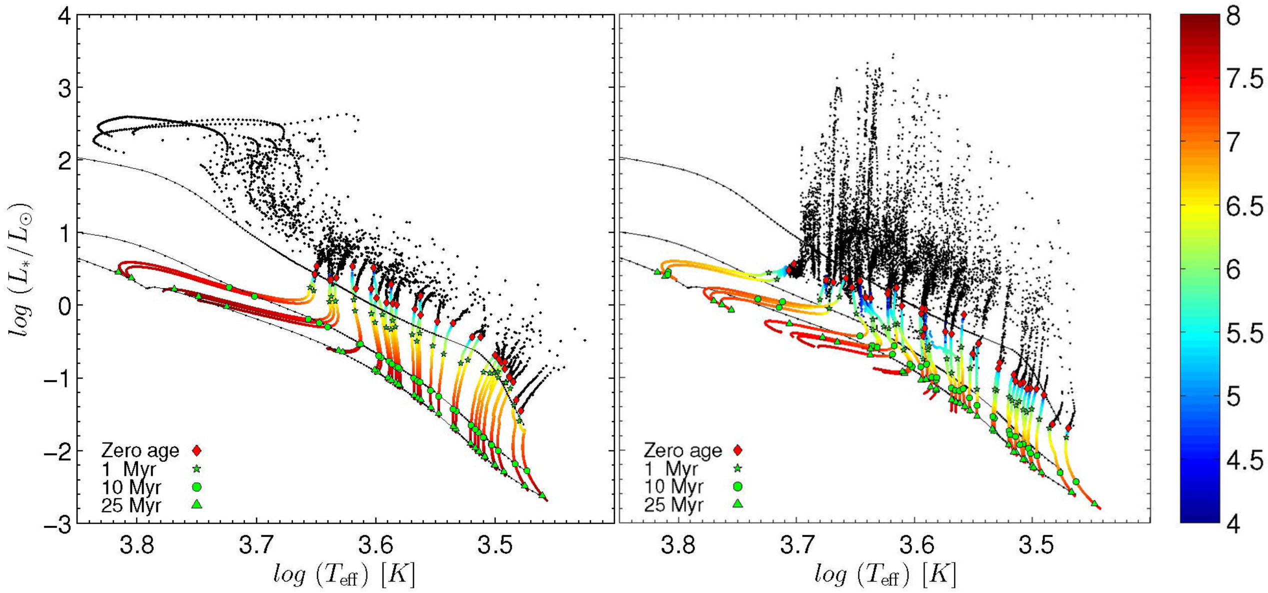

Fig. 1. Left: Stellar evolution sequences in the total luminosity L_* – effective temperature $T_{\rm eff}$ diagram for hybrid accretion models. The dots of various colours present the model tracks. The zero-point age for each model is marked by red diamonds. Green symbols mark the reference ages (as indicated in the bottom left corner) that have elapsed since the zero-point age of each object. The black solid lines indicate the isochrones for stellar ages of 1 Myr, 10 Myr and 25 Myr (from top to bottom) derived from the non-accreting stellar evolution models of Yorke & Bodenheimer (2008). **Right:** Similar to the left panel, but for the cold accretion model.

evolutionary sequences for all models. The meaning of the symbols and lines is the same as in the left panel of Fig. 1.

In general, the disagreement between the cold accretion models of a certain age and the corresponding non-accreting isochrones of Yorke & Bodenheimer has increased as compared to the case of hybrid (or hot) accretion. To quantify this disagreement, the red solid lines in Fig. 2 represent the non-accreting isochrones that best fit our 1 Myr-old stars. The resulting ages of these non-accreting isochrones are 1.5 Myr for hybrid accretion (top panel) and 4.5 Myr for cold accretion (bottom panel). The black lines show the non-accreting isochrones of 1 Myr age. This exercise demonstrates that 1-Myr-old accreting models can be fitted erroneously to 1.5-Myr-old or even 4.5-Myr-old non-accretion isochrones, meaning that the non-accreting isochrones can be unreliable for the stellar age estimates.

6 Conclusions

Our key findings can be summarized as follows:

- In the hybrid accretion case, young 1.0-Myr-old objects show substantial deviations from the non-accreting isochrones for both low-mass stars and brown dwarfs.
- The hot accretion case is qualitatively similar to hybrid accretion, but shows somewhat smaller deviations for L_* and R_*.
- The cold accretion case features the largest deviations from the non-accreting models of Yorke& Bodenheimer.
- As a result of this mismatch, the use of the L_*–$T_{\rm eff}$ diagram may lead to false age estimates for objects with $T_{\rm eff} > 3500$ K, as was also previously noted in Baraffe et al. (2009) and Hosokawa et al. (2011).

This project was supported by the Russian Ministry of Education and Science Grant 3.961.2014/K. The simulations were performed on the Vienna Scientific Cluster (VSC-2 and VSC-3) and on the Shared Hierarchical Academic Research Computing Network (SHARCNET).

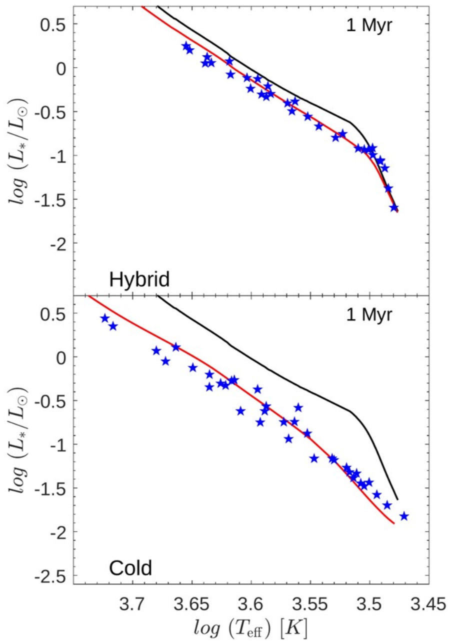

Fig. 2. Total luminosity–effective temperature diagram in the hybrid and cold accretion models. The star symbols represent our 1.0-Myr-old accreting models. The black solid lines are the isochrones (of the corresponding age) derived from the non-accreting models of Yorke & Bodenheimer (2008), while the red solid lines represent the non-accreting isochrones of Yorke & Bodenheimer that fit our model data best. The red solid lines represent the 1.5 Myr isochrone in the top panel and the 4.5 Myr isochrone in the bottom panel.

References

Audard, M., Ábrahám, P., Dunham, M. M., et al. 2014, in Protostars and Planets VI, ed. H. Beuther, R. S. Klessen, C. P. Dullemond, & T. Henning, 387

Baraffe, I., Chabrier, G., Allard, F., & Hauschildt, P. H. 1998, A&A, 337, 403

Baraffe, I., Chabrier, G., & Gallardo, J. 2009, ApJ, 702, L27

Baraffe, I., Elbakyan, V. G., Vorobyov, E. I., & Chabrier, G. 2017, A&A, 597, A19

Baraffe, I., Vorobyov, E., & Chabrier, G. 2012, ApJ, 756, 118

Dunham, M. M., Evans, II, N. J., Terebey, S., Dullemond, C. P., & Young, C. H. 2010, ApJ, 710, 470

Hosokawa, T., Offner, S. S. R., & Krumholz, M. R. 2011, ApJ, 738, 140

Hosokawa, T., Yorke, H. W., Inayoshi, K., Omukai, K., & Yoshida, N. 2013, ApJ, 778, 178

Liu, H. B., Takami, M., Kudo, T., et al. 2016, Science Advances, 2, e1500875

Machida, M. N., Inutsuka, S.-i., & Matsumoto, T. 2011, ApJ, 729, 42

Palla, F. & Stahler, S. W. 2000, ApJ, 540, 255

Vorobyov, E. I. 2016, A&A, 590, A115

Vorobyov, E. I. & Basu, S. 2009, MNRAS, 393, 822

Vorobyov, E. I. & Basu, S. 2010, ApJ, 719, 1896

Vorobyov, E. I. & Basu, S. 2015, ApJ, 805, 115

Williams, J. P. & Cieza, L. A. 2011, ARA&A, 49, 67

Yorke, H. W. & Bodenheimer, P. 2008, in ASPCS, Vol. 387, Massive Star Formation: Observations Confront Theory, ed. H. Beuther, H. Linz, & T. Henning, 189

Stars and their variability observed from space
C. Neiner, W. W. Weiss, D. Baade, R. E. Griffin, C. C. Lovekin, A. F. J. Moffat (eds)

RECENT ADVANCES IN NUMERICAL MODELS THAT INCLUDE ATOMIC DIFFUSION IN STARS

G. Alecian[1]

Abstract.
Atomic diffusion in stars is efficient in changing the distribution of elements slowly but strongly in any radiative zone. The process may produce detectable effects, over time-scales stretching from a few decades to star's lifetime, according to the depth of the radiative zones. The main consequences are that superficial abundances may depart from standard values, but also that internal structure and seismic diagnostics are affected owing to changes in local opacities. The main difficulty of including atomic diffusion in numerical models comes from radiation force (the dominant force acting on atoms within the layers concerned), which is specific to chemical species through their atomic properties, and which makes the process of abundance stratification strongly non-linear in usual situations (especially in atmospheres). This talk presented recent improvements that involve a fast method for calculating radiative accelerations in stellar interiors, and described progress in the modelling of stellar atmospheres.

Keywords: Processes: Diffusion, stars: abundances, chemically peculiar, magnetic field, mass-loss

1 Introduction

Atomic diffusion is a slow process that competes (with difficulty) with large-scale motions (mixing, mass loss, etc.). Separation of the chemical elements occurs inside stars in any stable (radiative) zone. Among the main difficulties of modelling these processes two can be emphasised: (1) calculating radiative accelerations that requires heavy computations of the total momentum acquired by atoms from the radiation field, and (2) estimating the strength of large-scale motions (convection and mass loss, for instance) that prevent element separation. Michaud et al. (2015) have given a detailed and exhaustive discussion on the subject. This talk presented some recent advances concerning the computation of radiative acceleration in a stellar interior, and numerical models of atmospheres including atomic diffusion and mass loss.

Even though the physics is basically the same, the calculation of atomic diffusion effects in stellar interiors and in stellar atmospheres is very different. That is mainly due to radiation transfer computation, which is carried out with very efficient approximations in stellar interiors but which are impossible to apply to stellar atmospheres, where the radiation transfer equation must be solved in detail. In addition, the characteristic time-scales are very different, since in the interior they are comparable to the stellar evolution time-scale, while they may be as short as a year in the atmosphere (Alecian 2013). Both cases were, until the present, considered separately in numerical codes. We should add that processes of atomic diffusion in stellar interiors concern the radiative zones of any type of star (for layers with diffusion time-scales smaller than the age of the star in question), while in an atmosphere they geneally concerns Ap/Bp chemically-peculiar stars (magnetic stars, HgMn, He-weak) and He-rich stars.

2 Improvement of SVP tables

There are several methods for computing radiative accelerations in stellar interiors: (i) the detailed method, which uses atomic transition tables directly, (ii) the opacity sampling method, which uses monochromatic opacity tables, and (iii) a parametric method. The first (i) is in principle the most accurate, but is rarely used because of its heaviness and the very large amount of data to handle (nevertheless, such an approach has to be used for atmospheres). The second approach (ii) is *widely* used (Vick et al. 2011; LeBlanc et al. 2000; Richer et al. 1998; Seaton 1997, 2007), but necessitates having monochromatic opacity tables for elements for which atomic

[1] LUTH, CNRS, Observatoire de Paris, PSL University, Université Paris Diderot, 5 Place Jules Janssen, F-92190 Meudon, France

diffusion is computed. The parametric method (iii) (*SVP*, for Singled-Valued Parameters) is less accurate than the other two methods but is extremely fast for numerical applications (Alecian & LeBlanc 2002; LeBlanc & Alecian 2004) and can be used for elements for which the usual opacity databanks do not provide any data (like Sc, for instance Alecian et al. 2013).

The *SVP* method can only be used in optically thick regions, and for stars with masses larger than, or equal to, approximately one solar mass. It has the advantage of calculating radiative acceleration ($g_{\rm rad}$) from pre-tabulated parameters (6 parameters per ion) without having to access complete atomic data or detailed monochromatic opacities. A first release of tables of parameters is available via the website `http://gradsvp.obspm.fr` for the computation of $g_{\rm rad}$ for various elements (C, N, O, Ne, Na, Mg, Al, Si, S, Ar, Ca and Fe). A forthcoming release (early 2020) will extend the tables to other elements, and will support the computation of radiative accelerations for main-sequence stars with masses from $0.9 - 10\,M_{\odot}$. In addition, Fortran routines to help easy implementation into existing codes will be provided.

The parameters in this forthcoming release are also improved. An example of $g_{\rm rad}$ obtained by the improved *SVP* tables (though still provisional here) is shown in Fig. 1.

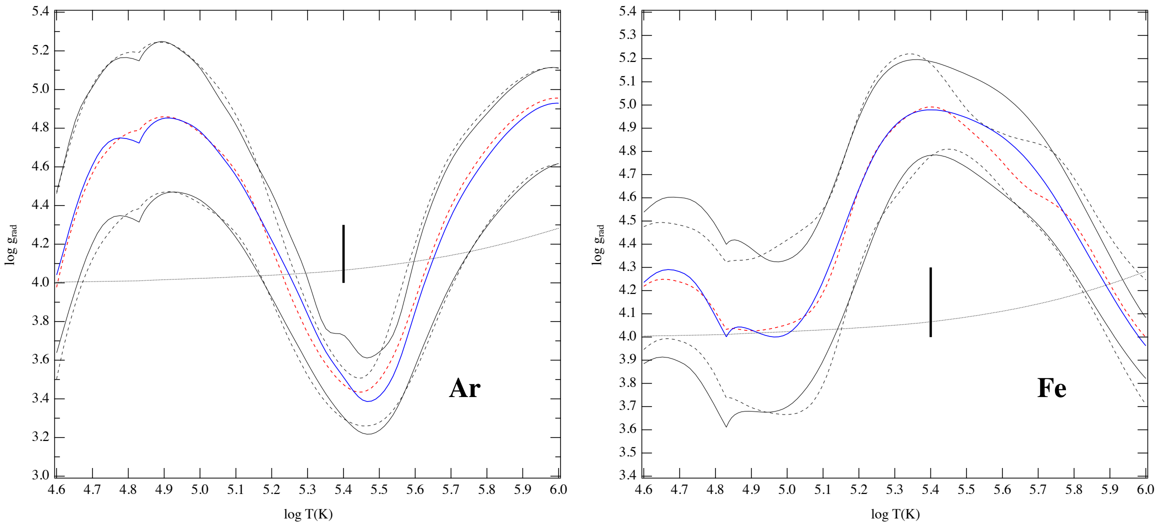

Fig. 1. Radiative accelerations obtained using the *SVP* method. This work is still in progress (see text). **Left**: Argon, radiative acceleration with respect to depth [in $\log T(K)$] in a $2 - M_{\odot}$ model obtained through the *SVP* method (dashed lines), and through the procedure proposed by the Opacity Project (OPCD 3.3, solid lines) for three concentrations of Ar from 10^{-1} (the upper curves) to 10 times the solar value. The blue and red lines are for solar abundances. The vertical bar represents 0.3 dex (the maximum error above which we decided to reject the parameters), and the pointed curve is the local gravity. **Right**: Same as the left panel but for iron.

3 Recent results for atmospheres of CP stars

Among chemically-peculiar (CP) main-sequence stars, Ap/Bp stars (including roAp) often have very strong magnetic fields. Atomic diffusion is very efficient in their atmospheres, and produces non-uniform distributions of chemical elements (element spots and/or abundance stratification). To compute how diffusion works in those atmospheres, one needs first to compute a detailed solution of the polarized radiation transfer equation, and then compute element stratification build-up. We have developed the Carat family numerical codes (in collaboration with M. Stift), starting from the calculation of radiative accelerations in magnetic atmospheres (Alecian & Stift 2004) to the recent model of 3D abundance distributions (Alecian & Stift 2017) and additional physical processes (Alecian & Stift 2019).

Up to now, all calculations of the distribution of elements in stellar atmospheres (see for instance LeBlanc et al. 2009; Alecian & Stift 2010) were obtained assuming equilibrium solutions; concentrations of elements were such that $g_{\rm rad} = g$ (the gravity) in all layers. However, it is not yet known to what extent such equilibria obtain in real atmospheres. The best approach is to solve the time-dependent continuity equation for concentrations, which is a strong numerical challenge. However, since Alecian et al. (2011), it is being used increasingly.

Recent progress in modelling atomic diffusion in atmospheres includes the first calculation by Alecian & Stift

(2017) of a theoretical 3D map of chromium and iron, assuming a magnetic geometry inspired by an observed magnetic map (non-strictly dipolar). That calculation is shown in Fig. 2, and is still obtained for equilibrium solutions, but a time-dependent calculation is in preparation.

Another recent improvement in modelling atomic diffusion is the addition of a missing physical process in our numerical codes: the global outgoing flow of material caused by mass loss. It is accepted, at least from the work of Vauclair (1975) on helium-rich stars, that mass loss (if present) competes with atomic diffusion. It has certainly been taken into account in evolution codes that include atomic diffusion (Vick et al. 2010), but not for atmospheres. That has now been done, in time-dependent calculations, by Alecian & Stift (2019), as shown in Fig. 3 (left panel). The main result that can be drawn from this calculation is that the observed Mg abundances in HgMn stars cannot be explained without assuming a mass loss of about $5.0\,10^{-14}\,M_{\odot}.y^{-1}$. A second result obtained from such a calculation (right panel of Fig. 3) is that to recover the stratification for phosphorus as observed by Ndiaye et al. (2018) in the atmosphere of HD 53929, one needs to assume that this HgMn star, hitherto generally considered as non-magnetic, should have a small magnetic field (around 100 Gauss).

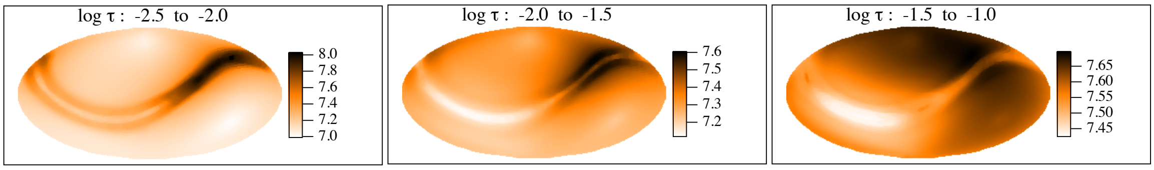

Fig. 2. Tomographic view of the abundance of Cr (Hammer equal-area projection). Three slabs corresponding to three contiguous optical depth ranges (indicated above each projection) are shown. Note that the relation between abundances and colour scale differs from one slab to the other. The solar abundance of Cr is 5.67. See Alecian & Stift (2017) for details.

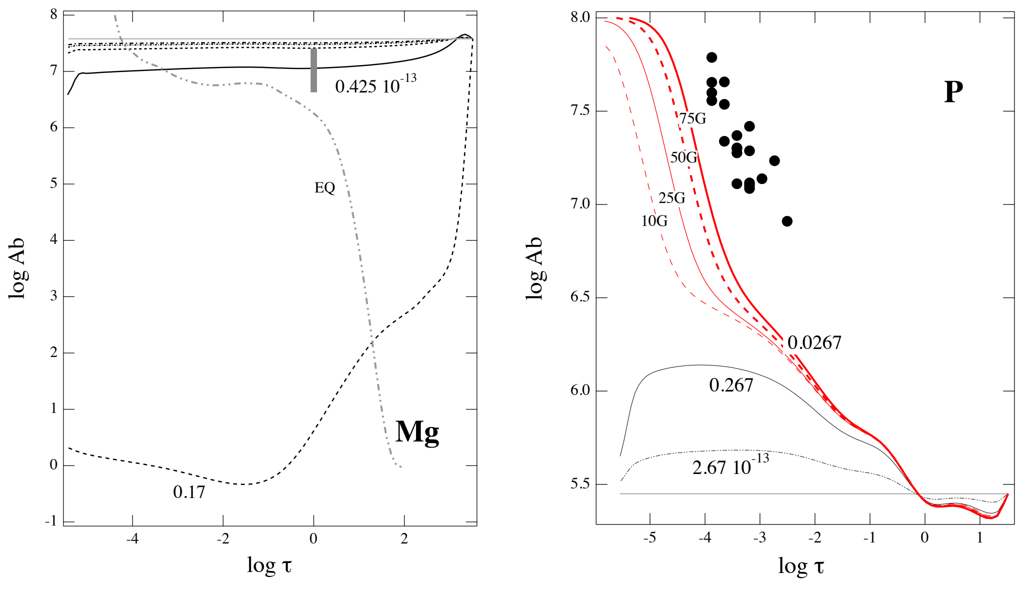

Fig. 3. Left: Stratification of Mg abundance (stationary solutions) *vs.* the logarithm of the optical depth at $\lambda\,5000$ Å as a function of various mass-loss rates (model with $T_{\rm eff} = 12000$ K, and $\log g = 4.0$). The Mg stratification is shown for 5 different mass-loss rates (1.7, 1.28, 0.85, 0.425, 0.17 in units of 10^{-13} solar masses per year). The vertical thick grey bar corresponds to observations of Mg overabundances in HgMn stars having approximately the same $T_{\rm eff}$ and $\log g$. The equilibrium solution (EQ) (heavy dash-dot-dot grey line) is also shown. See Alecian & Stift (2019) for details. **Right:** Stratification of P in the atmosphere of HD 53929. Filled circles show the abundances determined empirically by Ndiaye et al. (2018) from observations. The solid grey line is the solar abundance; the thin solid and dash-dot-dot curves are our stationary non-magnetic solutions for mass-loss rates of 2.67 and $0.267\,10^{-13}$ solar mass per year, respectively. The group of red curves labelled 10 G, 25 G, 50 G and 75 G are the solutions obtained by assuming a weak horizontal magnetic field, and for the lowest mass-loss that ensures convergence of this model ($0.0267\,10^{-13}$). See Alecian & Stift (2017) for details.

4 Conclusions

Recent improvements in the parametric *SVP* method for calculating radiative accelerations for stellar interiors will be available shortly (foreseen for the beginning of 2020), together with Fortran routines, at `http://gradsvp.obspm.fr`.

For stellar atmospheres (with and without magnetic fields), this talk presented the first theoretical 3D calculations of the distribution of elements (at equilibrium), and calculations of time-dependent stratification build-up with mass loss. Two main results can be drawn from those time-dependent calculations; first, mass loss could be considered systematically for all types of CP stars, and secondly, we can justify considering that weak magnetic field may exist in HgMn stars. As a concluding remark, one must admit that numerical models are not yet able to describe detailed abundance distributions modified by atomic diffusion in the atmospheres of individual stars. However, there is a reasonable hope that we will succeed in overcoming this challenge fairly soon through 3D numerical simulations, as long as we also succeed in taking into account all physical processes that make a significant contribution.

All codes that have been used to compute the models for atmospheres have been compiled with the GNAT GPL Edition of the Ada compiler provided by AdaCore and partly performed using HPC resources from GENCI-CINES (grants c2018045021). I acknowledge the financial support of Programme National de Physique Stellaire (PNPS) of CNRS/INSU, France.

References

Alecian, G. 2013, in EAS Publications Series, Vol. 63, 219
Alecian, G. & LeBlanc, F. 2002, MNRAS, 332, 891
Alecian, G., LeBlanc, F., & Massacrier, G. 2013, A&A, 554, A89
Alecian, G. & Stift, M. J. 2004, A&A, 416, 703
Alecian, G. & Stift, M. J. 2010, A&A, 516, A53
Alecian, G. & Stift, M. J. 2017, MNRAS, 468, 1023
Alecian, G. & Stift, M. J. 2019, MNRAS, 482, 4519
Alecian, G., Stift, M. J., & Dorfi, E. A. 2011, MNRAS, 418, 986
LeBlanc, F. & Alecian, G. 2004, MNRAS, 352, 1329
LeBlanc, F., Michaud, G., & Richer, J. 2000, ApJ, 538, 876
LeBlanc, F., Monin, D., Hui-Bon-Hoa, A., & Hauschildt, P. H. 2009, A&A, 495, 937
Michaud, G., Alecian, G., & Richer, J. 2015, Atomic Diffusion in Stars, Astronomy and Astrophysics Library (Springer)
Ndiaye, M. L., LeBlanc, F., & Khalack, V. 2018, MNRAS, 477, 3390
Richer, J., Michaud, G., Rogers, F., et al. 1998, ApJ, 492, 833
Seaton, M. J. 1997, MNRAS, 289, 700
Seaton, M. J. 2007, MNRAS, 382, 245
Vauclair, S. 1975, A&A, 45, 233
Vick, M., Michaud, G., Richer, J., & Richard, O. 2010, A&A, 521, A62
Vick, M., Michaud, G., Richer, J., & Richard, O. 2011, A&A, 526, A37

Stars and their variability observed from space
C. Neiner, W. W. Weiss, D. Baade, R. E. Griffin, C. C. Lovekin, A. F. J. Moffat (eds)

THE PHOTOMETRIC VARIABILITY OF MAGNETIC HOT STARS: DEVIATIONS FROM CENTERED DIPOLES

M. S. Munoz[1] and G. A. Wade[2]

Abstract. Magnetic O-type stars host strong, organized magnetic fields that channel their stellar winds, significantly confining their mass loss and enhancing the shedding of rotational angular momentum. The resultant mass-loss quenching and magnetic braking lead magnetic O-type stars to evolve at higher mass and slower rotation than their non-magnetic kin, making them novel laboratories for the study of high mass stellar evolution. At the root of the magnetic field-stellar wind interaction is the formation of a complex, co-rotating dynamical magnetosphere surrounding the star. The recently developed Analytic Dynamical Magnetosphere (ADM) model (Owocki et al. 2016) provides a straightforward description of the temperature, density, and velocity fields predicted to occur in these magnetospheres, allowing computationally efficient calculation of observable quantities needed for the determination of magnetospheric physical characteristics and for the testing of theoretical limitations. In earlier papers (e.g. Munoz 2019), we have exploited the ADM model to compute photometric observables of magnetic Of?p stars, to test geometric models inferred from magnetometry (for Galactic targets) and to place constraints on as-yet-undetectable magnetic fields (for extra-Galactic targets). In the following, we focus on the light curve of LMCe136-1, an Of?p-type star from the Large Magellanic Cloud, which manifests a clear asymmetry in its light curve that cannot be reproduced by an axisymmetric pure dipole model. For this purpose, we consider offset dipoles and significant quadrupoles components as possible magnetic field geometries for the star. Both topologies yield light curves that can reproduce the observed photometric variability of LMCe136-1.

Keywords: Stars: magnetic field, Stars: massive, Stars: mass-loss

1 Introduction

Stellar magnetic fields can significantly affect the evolution and fate of massive stars. For instance, their rotation rates can be substantially decreased via magnetic braking (e.g. Townsend et al. 2010) and their longevity can be substantially increased via magnetic quenching of mass loss (e.g. Petit et al. 2017). Understanding the nature of these magnetic fields is therefore an important component that plays into the general understanding of massive stars.

The magnetic properties of the known Galactic magnetic O-type stars are generally well described by an obliquely rotating, predominantly dipolar and strong magnetic field. As the star rotate, their observable quantities are expected to manifest periodic variability in accordance to the oblique magnetic rotator paradigm.

The purpose of this investigation is to gain insight on the physical processes that occur within the magnetospheres of magnetic massive stars. To this end, we attempt to model, reproduce and analyse the photometric variability of magnetic O-type stars as a means to characterise the structure and geometry of their magnetic fields.

The photometric modelling of such stars has already been analysed by Munoz et al. (2019) under the assumption of a pure dipolar field topology. Here, we consider more exotic magnetic field topologies, namely, offset dipoles and quadrupoles.

In Section 2, we describe the methodology behind the photometric and polarisation models. In Section 3, we present the light curve of LMCe136-1, a Magellanic Of?p-type star, that may be indicative of deviations from a typical dipolar field geometry. We conclude in the final section.

[1] Department of Physics, Engineering Physics and Astronomy, Queen's University, 64 Bader Lane, Kingston, K7L 3N6, ON, Canada
[2] Department of Physics and Space Science, Royal Military College of Canada, PO Box 17000, Stn Forces, Kingston, K7K 7B4, ON, Canada

2 Numerical Method

2.1 The magnetosphere model

The magnetospheres of slowly rotating O-type stars are expected to behave within the dynamical magnetosphere regime (Petit et al. 2013). Globally, such magnetospheres appear as stable, rigidly rotating structures that are held in magnetic confinement. However, locally, they are complex dynamical structures.

The complexities present in the dynamical magnetospheres of magnetic massive stars can be formally solved utilizing sophisticated 3D magnetohydrodynamic (MHD) simulations (Ud-Doula & Owocki 2002; Ud-Doula et al. 2008, 2009, 2013). However, their steady-state properties can be approximated with an analytical dynamical magnetosphere (ADM) model that was recently developed by Owocki et al. (2016).

The ADM model is capable of quickly computing the density, velocity and temperature structure of dynamical magnetospheres. Although the model was initially designed for pure magnetic dipoles, we have recently extended the model to consider offset dipoles and (linear) quadrupoles. Figure 1 showcases the density structure computed with ADM for three magnetic field geometries: a pure dipole, a decentered dipole and a quadrupole. In all cases the magnetic field axis (shown in pink) is inclined by 45° with respect to the rotation axis (shown in purple). The density structure is computed with input parameters based on the prototypical magnetic massive star HD 191612: $T_{\rm eff} = 35\,{\rm kK}$, $R_* = 14.5\,R_*$, $M_* = 30\,M_*$, $v_\infty = 2700$ km s^{-1}, $\dot{M}_{B=0} = 10^{-6}\,M_\odot{\rm yr}^{-1}$ and $B_{\rm d} = 2.5 \pm 0.4\,{\rm kG}$. In all three cases, we can see over-density structures along the apex of each closed loop. This is an expected result. As material follows the magnetic field lines, they collide and deposit matter near the magnetic equator.

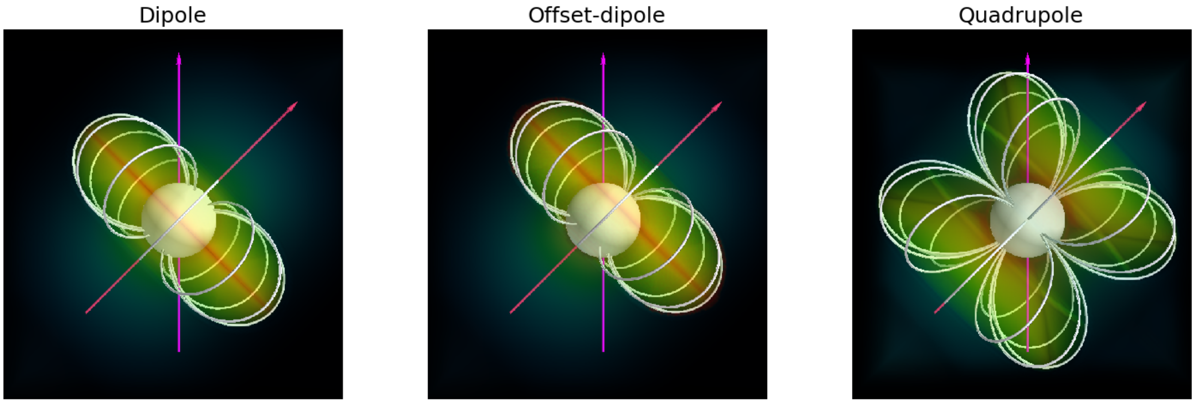

Fig. 1. 3D rendering of the density structure computed with the ADM model for three simple magnetic field topologies: Pure dipole, offset-dipole and linear quadrupole (from left to right). In each panel, the magnetic field axis (inclined pink arrow) is tilted by 45° with respect to the rotation axis of the star (vertical purple arrow) and the field lines of the magnetic topology are overplotted. Red regions are high in density while green regions are low in density.

2.2 The photometric and linear polarisation model

The photometric variability of an oblique magnetic rotator is expected to arise from the periodic occultations of its own magnetosphere. For hot stars, the amount of occulted light can be quickly estimated in the single-electron scattering regime. In such a case, the amount of occultation is predominantly determined by the column density along the line-of-sight of the observer. In order to estimate the optical depth, we exploit the ADM model as a means to quickly obtain the density structure of the magnetosphere.

Figure 2 shows sample light curve morphologies expected from the different magnetic field topologies illustrated in Fig. 1. For a pure dipole, the light curves are either single-dipped (if $i + \beta < 90°$) or double-dipped (if $i + \beta > 90°$). An axisymmetric magnetic field topology will always yield a symmetric light curve (i.e. the light curve is mirrored across the rotational phase 0.5). Deviations from this paradigm may be attributed to more exotic magnetic field topologies. For instance, a dipole offset or a significant quadrupolar component may cause asymmetries to be present in the light curve. Under certain configurations, a light curve produced from an offset-dipole topology may be degenerate from one produced from a dipole plus quadrupole topology. This is

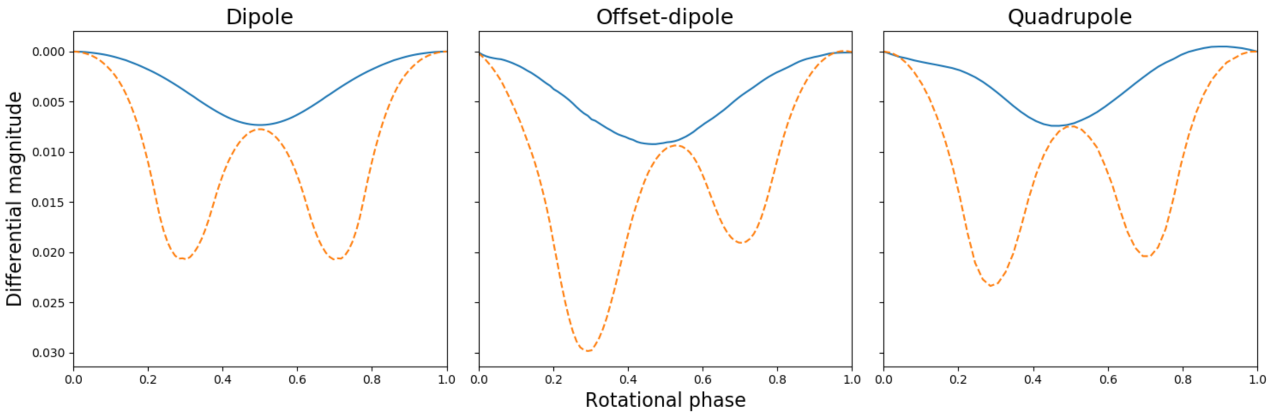

Fig. 2. Photometric variability obtained from the configurations shown in Fig. 1. The solid (blue) curve corresponds to an inclination of $i = 15^\circ$ while the dashed (orange) curve corresponds to an inclination of $i = 75^\circ$. In all cases, the magnetic obliquity is fixed to $\beta = 45^\circ$.

problematic as it may not always be possible to discern the magnetic topology from the observed photometric variability.

3 Application to LMCe136-1

LMCe136-1 was recently identified as an Of?p type star in the Large Magellanic Cloud by Neugent et al. (2018). A photometric light curve was obtained from the Optical Gravitational Lensing Experiment (OGLE) project which revealed a distinctive periodic signal of 18.914 ± 0.004 d.

The phased light curve for LMCe136-1 is displayed in Fig. 3. Since a definitive ephemeris is not yet constrained for this star, the rotational phase $\phi = 0$ was arbitrarily placed to correspond to a maximum in photometric brightness. An interesting feature in the phased light curve is a clear asymmetry present near $\phi = 0.4$ and $\phi = 0.6$.

To account for the asymmetry present in the phased light curve, we attempt to model the photometric variability with a decentered dipole. The curve of best-fit is shown in Fig. 3 (left panel, red curve) with best-fitted parameters listed in Table 1. The photometric variability can be well reproduced with a dipole offset of $a = -0.21^{+0.03}_{-0.03}\,R_*$ (perpendicular to the magnetic axis), a dipolar field strength of $B_\mathrm{d} = 5.6^{+4.1}_{-1.9}$ kG, an inclination angle of $i = 57^{+21\circ}_{-19}$ and a magnetic obliquity of $\beta = 51^{+20\circ}_{-21}$.

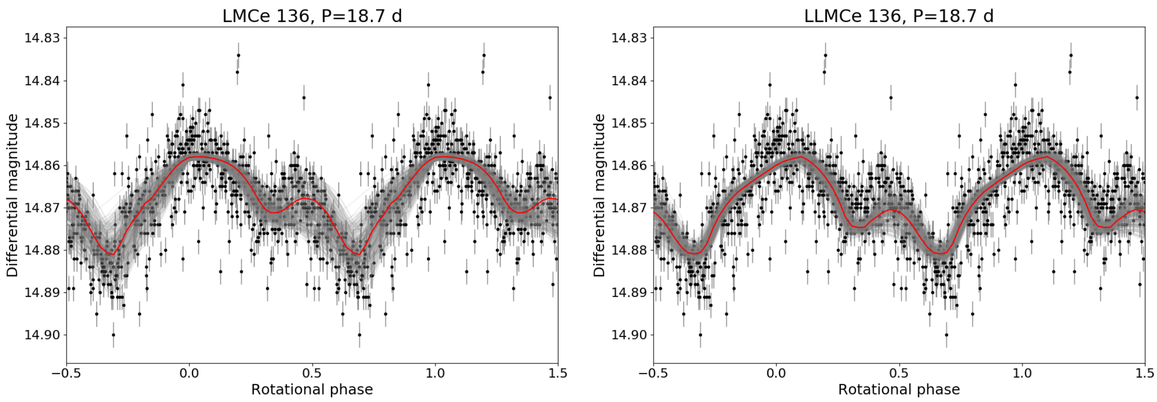

Fig. 3. The photometric variability of LMCe136-1. **Left:** Offset-dipole model. **Right:** Dipole plus quadrupole model. The curves of best-fit are overplotted in red (bold solid lines). Curves that span the 1 σ error bars on the best-fit parameters are overplotted in gray (thin solid lines).

Another magnetic field geometry to consider is a dipole plus quadrupole model. With this configuration, the parameters of best-fit are: $i = 70^{+7\circ}_{-7}$, $\beta_1 = 35^{+9\circ}_{-6}$, $\beta_2 = 30^{+8\circ}_{-6}$, $\Delta\phi = 0.25^{+0.06}_{-0.08}$, $B_\mathrm{d} = 5.0^{+0.6}_{-0.8}$ kG and

Table 1. Best-fit parameters to the OGLE photometry with an offset-dipole and dipole + quadrupole model

Model	i [deg]	β_1 [deg]	β_2 [deg]	$\Delta\phi$	B_d [kG]	B_q [kG]	Δm_0 [mmag]	a [$R_\odot$]
Offset-dipole	57^{+21}_{-19}	51^{+20}_{-21}	-	-	$5.6^{+4.1}_{-1.9}$	-	14858^{+1}_{-1}	$a = -0.21^{+0.03}_{-0.03}$
Dipole + quadrupole	70^{+7}_{-7}	35^{+9}_{-6}	30^{+8}_{-6}	$0.25^{+0.06}_{-0.08}$	$5.0^{+0.6}_{-0.8}$	$6.5^{+1.5}_{-1.5}$	14860^{+2}_{-2}	-

† Δm_0 corresponds to a vertical offset in the differential magnitude (assumed constant).

$B_\mathrm{q} = 6.5^{+1.5}_{-1.5}$ kG (see Fig. 2 and Table 1). Here, β_1 is the magnetic obliquity of the dipolar component, β_2 is the magnetic obliquity of the quadrupolar component, $\Delta\Phi$ is a rotational phase shift between both components, B_d is the dipolar magnetic field strength and B_q is the quadrupolar field strength. Although we can obtain an adequate fit for the photometric variability of LMCe136-1, we obtain a magnetic field strength for the quadrupolar component that is greater than the dipolar component which is unprecedented.

4 Conclusions

To summarise, we have explored the photometric variability produced from a pure dipole, an offset dipole and a dipole plus quadrupole. The light curves were synthesised under the single-electron scattering limit while utilizing the density structure computed from the ADM model. For a pure dipole, the light curve is symmetric about rotation phase $\phi = 0.5$. The implementation of an offset dipole or a significant quadrupolar component introduces asymmetries in the light curve.

For the Of?p-type star LMCe136-1 in the Large Magellanic Cloud, its photometric variability cannot be explained under the assumption of a pure dipolar magnetic field topology. Instead, the light curve could be reproduced with a dipole offset of $a \sim -0.21\,R_*$ or with a quadrupolar field strength of $B_q \sim 6.5$ kG. Unfortunately, we could not rule out one geometry over the other. This is not unexpected, as degeneracy between these two field topologies has been noticed when trying to model longitudinal fields or the magnetic field modulus in Ap-type stars (e.g. Landstreet 1980).

References

Landstreet, J. D. 1980, AJ, 85, 611
Neugent, K. F., Massey, P., & Morrell, N. 2018, ApJ, 863, 181
Owocki, S. P., ud-Doula, A., Sundqvist, J. O., et al. 2016, MNRAS, 462, 3830
Petit, V., Keszthelyi, Z., MacInnis, R., et al. 2017, MNRAS, 466, 1052
Petit, V., Owocki, S. P., Wade, G. A., et al. 2013, MNRAS, 429, 398
Townsend, R. H. D., Oksala, M. E., Cohen, D. H., Owocki, S. P., & ud-Doula, A. 2010, ApJ, 714, L318
Ud-Doula, A. & Owocki, S. P. 2002, ApJ, 576, 413
Ud-Doula, A., Owocki, S. P., & Townsend, R. H. D. 2008, MNRAS, 385, 97
Ud-Doula, A., Owocki, S. P., & Townsend, R. H. D. 2009, MNRAS, 392, 1022
Ud-Doula, A., Sundqvist, J. O., Owocki, S. P., Petit, V., & Townsend, R. H. D. 2013, MNRAS, 428, 2723

Stars and their variability observed from space
C. Neiner, W. W. Weiss, D. Baade, R. E. Griffin, C. C. Lovekin, A. F. J. Moffat (eds)

FROM ANCESTORS TO OFFSPRING: TRACING THE CONNECTION BETWEEN MAGNETIC FLUXES OF OB AND NEUTRON STARS

E. I. Makarenko[1], A. P. Igoshev[2] and A.F. Kholtygin[3]

Abstract.
The origin and evolution of magnetic fields (MFs) of young neutron stars (NSs) is an open question. MFs could be generated through a dynamo during the formation of NSs, or they could be a relic of a pre-supernova magnetic field. We want to test whether MFs of young NSs are the relics of their progenitors, massive OB stars. This could happen through magnetic flux conservation; the MF of massive stars is core confined, so the collapsed core might keep exactly the same magnetic flux as the whole star. Only 5–7% of massive OB stars have well-measured magnetic fields (reaching tens of kG). They can be divided into two groups: highly magnetic stars (B $>$ 20 G) and weakly magnetic stars (B $<$ 20 G). NSs are also divided into normal pulsars (B $\sim 10^{12}$ G) and magnetars (B $> 4 \cdot 10^{13}$ G). We therefore assume that normal pulsars are descendants of weakly magnetic stars, while magnetars originate from highly-magnetic OB stars. To test this hypothesis, our population synthesis code takes into account some severe selection effects in the NS sample, and enables us to compare observed fractions of pulsars and magnetars with the observed fractions of weakly magnetic and highly magnetic OB stars. We also investigated independently the distribution of MFs of massive stars using the maximum likelihood technique.

Keywords: Stars: massive, magnetars, magnetic field, neutron, Methods: statistical

1 Maximum likelihood estimate

We have continued the work of Kholtygin & Makarenko (2019) of testing whether the NS magnetic fields are relics of their progenitor magnetic fields or whether they are generated through a dynamo mechanism during the supernova explosion. To do that, we selected only newer measurements of stellar magnetic fields (MFs), starting from 2006, and mainly from Shultz et al. 2018; Sikora et al. 2019; Chojnowski et al. 2019; Aurière et al. 2007; Freyhammer et al. 2008 as they had relative errors less than 0.5. The corresponding distributions are shown on the left panel of Fig. 1.

We used the maximum likelihood technique to estimate the parameters of the distribution of MFs because it treats properly the observational uncertainties in centring errors in the actual (unknown) values. For the initial distribution of MFs we chose the log-normal distribution having a mean μ_B and standard deviation σ_B. The result of the calculations is presented in Table 1. The log-normal distribution describes very well the values of the measured magnetic fields for B stars; no significant deviations in the cumulative distributions can be seen (right panel of Fig. 1).

We then performed a preliminary optimisation of the pulsar population synthesis model developed by Igoshev & Kholtygin (2011), using parameters mostly similar to those in Faucher-Giguère & Kaspi (2006), and found the initial log-normal distribution for magnetic fields had $\log_{10} B/\mathrm{G} = 13.1$ and $\sigma = 0.7$. In order to trace the magnetic field back to the surface magnetic field of a massive star, we assumed a pure relic origin and occupying a fraction of the core that was 0.2 that of the star.

$$B_{p,\mathrm{B2V}} = B_{\mathrm{NS}} \left(\frac{R_{\mathrm{NS}}}{R_{\mathrm{B2V}}} \right)^2 \frac{R_{\mathrm{core}}}{R_{\mathrm{B2V}}} \approx 18 \text{ G}, \tag{1.1}$$

where B_{NS} is the NS surface dipolar magnetic field, R_{NS} is NS radius, R_{B2V} is a typical radius of a B2 main-sequence star, and R_{core} is the core radius of the massive star. The magnetic field value is given by eq. (1.1) and is similar to ones measured for the weakly magnetic massive stars.

[1] I. Physics Institute, Department of Physics, University of Cologne, Germany
[2] University of Leeds, the United Kingdom
[3] Saint Petersburg State University, Russia

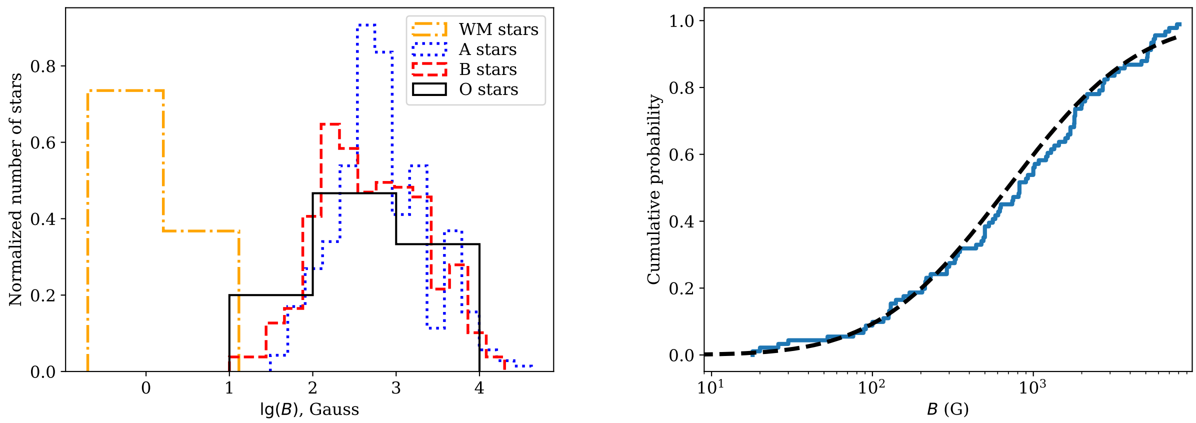

Fig. 1. Left: Histogram of magnetic field strengths for O, B, A and weakly magnetic (WM) stars in our sample. **Right**: Cumulative probability for measured magnetic fields for B stars (blue solid line), and for the best model (dashed black line).

Spectral type	N	μ_B	σ_B
		$\log_{10}$ [G]	
O	11	2.62 ± 0.16	0.25 ± 0.24
B	92	2.84 ± 0.1	0.64 ± 0.08
A	97	3.05 ± 0.11	0.65 ± 0.07
Weakly magnetic	9	0.15 ± 0.47	$0.65^{+0.57}_{-0.26}$

Table 1. Result of the maximum likelihood analysis. N is the number of stars of a particular spectral type.

2 Conclusions

- We performed statistical tests to check which stars are progenitors of different types of neutron stars, using recent observations and considering only stars with confirmed magnetic fields.
- All massive OB stars could be divided into two large groups: weakly magnetic and strongly magnetic.
- The existing code for the pulsar and massive star population synthesis (NINA) has been improved and expanded to include the evolution of magnetars.
- We concluded that it is plausible that normal pulsars are descendants of weakly magnetic OB stars. The precursors of magnetars are magnetic OB stars.

E.I.M. and A.F.K. are grateful for the support of RFBR grant 19-02-00311 A. E.I.M. acknowledges funding by the European Research Council through the its Starting Grant No. 679852 'RADFEEDBACK'. In this research we used the population synthesis code NINA (Nova Investigii Neutronicorum Astrorum – New Study of Neutron Stars): `https://github.com/ignotur/NINA`.

References

Aurière, M., Wade, G. A., Silvester, J., et al. 2007, A&A, 475, 1053
Chojnowski, S. D., Hubrig, S., Hasselquist, S., et al. 2019, ApJ, 873, L5
Faucher-Giguère, C.-A. & Kaspi, V. M. 2006, ApJ, 643, 332
Freyhammer, L. M., Elkin, V. G., Kurtz, D. W., Mathys, G., & Martinez, P. 2008, MNRAS, 389, 441
Igoshev, A. P. & Kholtygin, A. F. 2011, AN, 332, 1012
Kholtygin, A. F. & Makarenko, E. I. 2019, ASP Conference Series, Vol. 518 (San Francisco: ASP), 108
Shultz, M. E., Wade, G. A., Rivinius, T., et al. 2018, MNRAS, 475, 5144
Sikora, J., Wade, G. A., Power, J., & Neiner, C. 2019, MNRAS, 483, 3127

Stars and their variability observed from space
C. Neiner, W. W. Weiss, D. Baade, R. E. Griffin, C. C. Lovekin, A. F. J. Moffat (eds)

ROTATIONAL INVERSIONS ALONG THE LOWER PART OF THE RED-GIANT BRANCH

F. Ahlborn[1,2], E. P. Bellinger[3], S. Hekker [2,3], S. Basu[4] and G. C. Angelou[1]

Abstract. This poster illustrated the results of an investigation into how the accuracy of internal rotation rates, estimated asteroseismically, change as stellar models with varying mass and metallicity evolve along the red-giant branch. A range of increased sensitivity to the surface rotation just below the red-giant bump was found.

Keywords: Asteroseismology, stars: rotation, oscillations, interiors

1 Introduction

Stellar rotation has a substantial impact on the structure and evolution of a star, as it affects internal processes like rotational mixing and the transport of angular momentum. However, it has been shown that hydrodynamic means of angular momentum transport *as currently included* are not sufficient to reproduce core-rotation rates estimated asteroseismically for stars on the red-giant branch (RGB) (Fuller et al. 2019; Ouazzani et al. 2019; Eggenberger et al. 2017; Spada et al. 2016; Marques et al. 2013; Ceillier et al. 2013; Eggenberger et al. 2012). The internal rotation of a star splits its non-radial oscillation modes into multiplets. The frequency difference between subsequent multiplet components is called *rotational splitting.* The advent of high-precision photometric space missions like *CoRoT* (Baglin et al. 2006) and *Kepler* (Borucki et al. 2008) enabled one to resolve rotational splittings in red-giant stars and to probe their internal rotation rates (Beck et al. 2012; Mosser et al. 2012; Gehan et al. 2018; Beck et al. 2014, 2018). To estimate internal rotation rates as a function of radius, so-called asteroseismic *rotational inversions* have been performed for a number of red giants (Deheuvels et al. 2012, 2014; Di Mauro et al. 2016, 2018; Triana et al. 2017). Our poster described results from a study of the asteroseismic sensitivity to internal rotation along the RGB (Ahlborn et al. 2019, submitted).

2 Synthetic Data and Rotational Inversions

We prepared different synthetic data sets to study the behaviour of asteroseismic rotational inversions along the lower part of the RGB. We constructed five different stellar evolution tracks from the pre-main-sequence to beyond the luminosity bump using Modules for Experiments in Stellar Astrophysics (MESA,version r8845, (Paxton et al. 2019), and references therein). To perform rotational inversions, we selected models from the base of the RGB up to the luminosity bump. We investigated models with inital masses of 1, 1.5 and 2 $M_\odot$, and metallicities of [Fe/H] $= -0.2, 0.0$, and 0.2. We used the stellar oscillation code GYRE (Townsend & Teitler 2013; Townsend et al. 2018) to compute the oscillation frequencies and rotational kernels for the combine the individual rotational kernels linearly from the data set to form so-called *averaging kernels* $K(r, r_0)$ localised at a chosen target-radius r_0. For each selected model we performed a rotational inversion and computed a core-averaging kernel (target radius $r_0/R = 0.003$) and a surface-averaging kernel ($r_0/R = 0.98$), and an estimate of the core- and surface-rotation rates. To analyse the inversion results, we computed the sensitivity of the core-averaging kernel in the core ($\beta_{\rm core}$) and the sensitivity of the surface-averaging kernel in the envelope ($\beta_{\rm surf}$):

$$\beta_{\rm core} = \int_0^{r_{\rm core}} K(r, 0.003)\mathrm{d}r; \quad \beta_{\rm surf} = 1 - \int_0^{r_{\rm core}} K(r, 0.98)\mathrm{d}r\,. \tag{2.1}$$

[1] Max Planck Institute for Astrophysics, Karl-Schwarzschild-Straße 1, 85748 Garching, Germany, e-mail: `fahlborn@mpa-garching.mpg.de`

[2] Max Planck Institute for Solar System Research, Justus-von-Liebig-Weg 3, 37077 Göttingen, Germany

[3] Stellar Astrophysics Centre, Department of Physics and Astronomy, Aarhus University, Ny Munkegade 120, DK-8000 Aarhus C, Denmark

[4] Department of Astronomy, Yale University, New Haven, CT 06520, USA

The radius $r_{\rm core}$ indicates the integration boundary between the core and the envelope in terms of the internal rotation profile. It does not need to be the actual radius of the stellar core.

3 Results and Conclusions

The left panel of Fig. 1 shows the core and the surface sensitivities, $\beta_{\rm core}$ and $\beta_{\rm surf}$, for a 1 $M_\odot$ model in blue and red dots, respectively in; the base of the convective envelope was adopted as $r_{\rm core}$. The computed values of the core sensitivities showed that the sensitivity of the core-averaging kernels is almost entirely confined below the base of the convection zone for all models under consideration. This means that the computed core-averaging kernels are well localised at the radius of the chosen target. However, the computed surface sensitivities showed a substantially different behaviour. First they decrease until they reach a minimum at about 19 $L_\odot$. From there on there is a narrow range of increased sensitivity to the surface rotation, just below the luminosity bump. The minimum surface sensitivity of about 70% translates into a 30% sensitivity to the core rotation in the estimated surface-rotation rate. Even at the base of the RGB, the estimated surface-rotation rates showed about a 5% sensitivity to the core rotation.

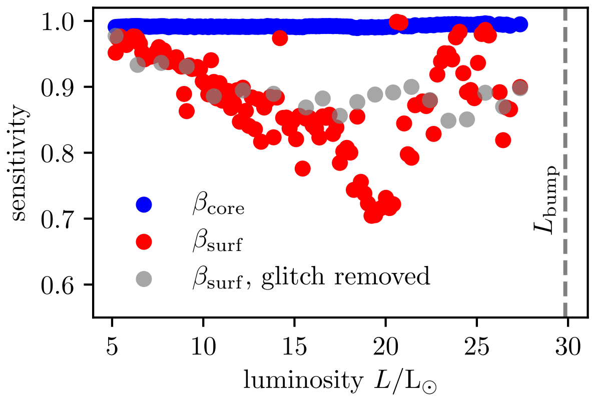

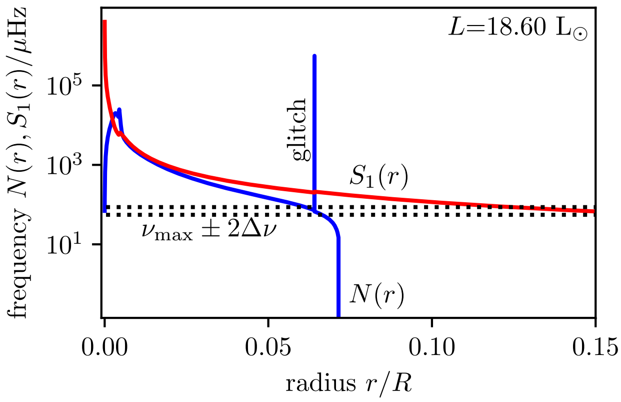

Fig. 1. Left: Core (blue) and surface (red) sensitivities $\beta_{\rm core}$ and $\beta_{\rm surf}$ for a solar metallicity, 1 $M_\odot$ model. Grey dots indicate inversion results for models where the peak associated with the composition discontinuity has been removed manually from the buoyancy frequency. **Right:** Propagation diagram for a 1.0 $M_\odot$ model in the vicinity of the surface-sensitivity minimum. N indicates the buoyancy frequency, and S_1 the Lamb frequency, for $l = 1$ modes. The frequency range of the dipole modes used for the rotational inversions is indicated by two horizontal dotted lines.

The increased surface sensitivity below the bump indicates that there is a theoretical possibility to estimate surface-rotation rates in red giants close to the luminosity bump with an accuracy similar to that at the base of the RGB. The same qualitative behaviour was found for all the masses and metallicities under consideration. The glitch in the buoyancy frequency (Fig. 1, right panel) could be responsible for the decrease and subsequent increase in surface sensitivities. As long as the glitch is in the range of frequencies used, the surface sensitivity decreases. When the glitch moves out of the frequency range, the surface sensitivity increases again. We recomputed some of the rotational inversions for models from the 1 $M_\odot$ track in which we removed the glitch artificially, and found that the minimum in sensitivity is no longer present, and that the overall decrease in surface sensitivity is more gentle (grey dots, left panel of Fig. 1).

The research leading to these results received funding from the European Research Council under the ECs Seventh Framework Programme (FP7/2007-2013)/ERC, grant no. 338251, a "Stellar Ages"). SB acknowledges partial funding from NASA grant NNX16A109G and NSF grant AST-1514676.

References

Baglin, A., Auvergne, M., Barge, P., et al. 2006, in ESA Special Publication, Vol. 1306, The CoRoT Mission Pre-Launch Status - Stellar Seismology and Planet Finding, ed. M. Fridlund, A. Baglin, J. Lochard, & L. Conroy, 33

Beck, P. G., Hambleton, K., Vos, J., et al. 2014, A&A, 564, A36

Beck, P. G., Kallinger, T., Pavlovski, K., et al. 2018, A&A, 612, A22

Beck, P. G., Montalban, J., Kallinger, T., et al. 2012, Nature, 481, 55

Borucki, W., Koch, D., Basri, G., et al. 2008, in IAU Symposium, Vol. 249, Exoplanets: Detection, Formation and Dynamics, ed. Y.-S. Sun, S. Ferraz-Mello, & J.-L. Zhou, 17–24

Ceillier, T., Eggenberger, P., García, R. A., & Mathis, S. 2013, A&A, 555, A54

Deheuvels, S., Doğan, G., Goupil, M. J., et al. 2014, 564, A27

Deheuvels, S., García, R. A., Chaplin, W. J., et al. 2012, ApJ, 756, 19

Di Mauro, M. P., Ventura, R., Cardini, D., et al. 2016, ApJ, 817, 65

Di Mauro, M. P., Ventura, R., Corsaro, E., & Lustosa De Moura, B. 2018, ApJ, 862, 9

Eggenberger, P., Lagarde, N., Miglio, A., et al. 2017, A&A, 599, A18

Eggenberger, P., Montalbán, J., & Miglio, A. 2012, ApJ, 544, L4

Fuller, J., Piro, A. L., & Jermyn, A. S. 2019, MNRAS, 485, 3661

Gehan, C., Mosser, B., Michel, E., Samadi, R., & Kallinger, T. 2018, A&A, 616, A24

Marques, J. P., Goupil, M. J., Lebreton, Y., et al. 2013, A&A, 549, A74

Mosser, B., Goupil, M. J., Belkacem, K., et al. 2012, 548, A10

Ouazzani, R. M., Marques, J. P., Goupil, M. J., et al. 2019, A&A, 626, A121

Paxton, B., Smolec, R., Schwab, J., et al. 2019, ApJSS, 243, 10

Spada, F., Gellert, M., Arlt, R., & Deheuvels, S. 2016, A&A, 589, A23

Townsend, R. H. D., Goldstein, J., & Zweibel, E. G. 2018, MNRAS, 475, 879

Townsend, R. H. D. & Teitler, S. A. 2013, MNRAS, 435, 3406

Triana, S. A., Corsaro, E., De Ridder, J., et al. 2017, A&A, 602, A62

ANALYSIS OF PHOTOMETRY OF STARS FROM SPACE AND GROUND-BASED SURVEYS

D. E. Tvardovskyi[1,2,3], I. L. Andronov[2], K. D. Andrych[1,2] and L. L. Chinarova[1,2]

Abstract. Methods for extended analysis of signals with irregularly spaced times are discussed with an application to variable stars of different types: eclipsing, cataclysmic, symbiotic, short- and long- periodic pulsating variables. Some of the methods are realized in the "Multi-Column Viewer" (MCV, Andronov & Baklanov 2004) and in a newly developed program MAVKA (Andrych & Andronov 2019). This code realizes 9 methods for approximations of the near-extremum parts of the light curve. We made tests of all of these methods with artificial data sets (both symmetric and asymmetric). Then we chose best methods for each shape of minimum and obtained moments of extrema for 16 randomly chosen stars from sector 11, observed by TESS. Totally, we got 262 extrema. As well, MAVKA was used in several other of our researches and there we got 1030 minima using AAVSO observations.

Keywords: variable stars - photometric observations - visual observations - brightness extrema

1 Introduction

MAVKA is the software for extrema approximation of stellar light curves developed by Andrych & Andronov (2019). MAVKA is used at the "near-extremum" parts of the light curve. The main aim is to determine the moment of extremum with best accuracy. Currently there are 11 methods included in MAVKA, i.e.: algebraic polynomial in general form, "Symmetrical" algebraic polynomial, "New Algol Variable" (NAV) (Andronov et al. 2016), the modified function of Mikulášek (2015), "Asymptotic Parabola" (AP) (Andrych et al. 2015), "Wall-Supported Parabola" (WSP), "Wall-Supported Line" (WSL), "Wall-Supported Asymptotic Parabola" (WSAP) (Andrych et al. 2017), and "Parabolic Spline of defect" (spline). In previous research (Andrych et al., in press) we made analysis of approximation accuracy of methods for generated signals with various parameters and shapes. In this research, we present a practical part of our calculations.

2 AAVSO observations

MAVKA was used in several articles: Savastru et al. (2017) - 1 star, 4 extrema; Tvardovskyi et al. (2017) - 6 stars, 235 extrema; Tvardovskyi et al. (2018) - 2 stars, 20 extrema; Tvardovskyi et al. (in press)- 7 stars, 549 extrema; Tvardovskyi (in press) - 5 stars, 222 extrema and Andrych et al. (in prep.). We used our own and the AAVSO observations of different observers. All these data were used for further O-C analysis.

3 TESS observations

We randomly chose 16 stars from the 11th sector of the TESS observation fields. 15 of them are pulsating variables of different types and one is an eclipsing binary. We split the data into separate near-extrema (both maxima and minima). After that, we processed all of them with 9 methods. We plot a histogram to investigate which method is the best for pulsating variables.

[1] Odessa I. I. Mechnikov National University, Odessa, Ukraine
[2] Department Mathematics, Physics and Astronomy, Odessa National Maritime University, Odessa, Ukraine
[3] Université de Mocton, Moncton, New Brunswick, Canada

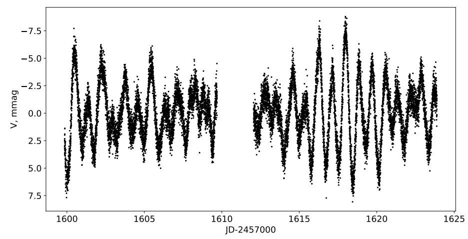

Fig. 1. Light curve of TIC 340176098 observed by TESS in sector 11.

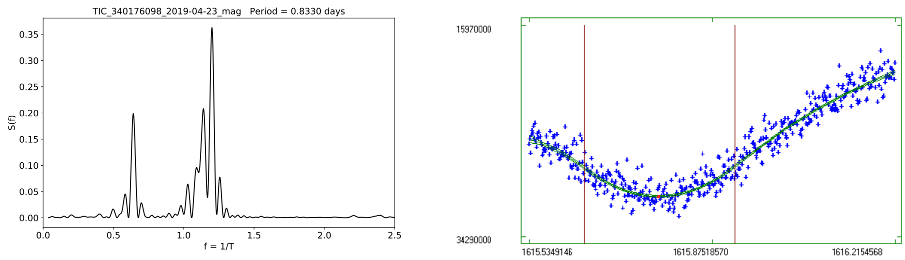

Fig. 2. Left: the periodogram $S(f)$ of TIC 340176098 obtained with the software MCV. Right: an example of extremum approximation made by using MAVKA.

4 Conclusions

As a result of the testing, we determined the best methods for several general shapes of extrema:

- symmetric (not total eclipse/transit) - polynomial, symmetric polynomial, NAV, Mikulášek;
- pulsating in general case - polynomial, parabolic spline, asymptotic parabola;
- asymmetric - asymptotic parabola, parabolic spline, polynomial;
- extremely sharp - asymptotic parabola;
- eclipsing or transit - WSP, WSL, WSAP;

Not recommended to use:

- for pulsating stars - WSP, WSL, WSAP;
- clearly asymmetric and insufficient number of points on one of the branches - polynomial.

We sincerely thank the organizers of this conference "Stars and their variability observed from space" (Vienna, Austria, 19-23 August 2019) for the possibility to present and publish the results of this research. In addition, we are grateful to the AAVSO observers and TESS mission for providing the data.

References

Andronov, I. L. & Baklanov, A. V. 2004, Astronomical School's Report, 5, 264

Andronov, I. L., Chinarova, L. L., Kudashkina, L. S., Marsakova, V. I., & Tkachenko, M. G. 2016, ASPCS, Vol. 505, Statistically Optimal Approximations of Astronomical Signals: Implications to Classification and Advanced Study of Variable Stars (ASP), 101

Andrych, K. D. & Andronov, I. L. 2019, Open European Journal on Variable Stars, 197, 65

Andrych, K. D., Andronov, I. L., & Chinarova, L. L. 2017, Odessa Astronomical Publications, 30, 57

Andrych, K. D., Andronov, I. L., Chinarova, L. L., & Marsakova, V. I. 2015, Odessa Astronomical Publications, 28, 158

Mikulášek, Z. 2015, A&A, 584, A8

Savastru, S. V., Marsakova, V. I., Andrych, K. D., & Dubovsky, P. 2017, Odessa Astronomical Publications, 30, 126

Tvardovskyi, D. E., Marsakova, V. I., & Andronov, I. L. 2017, Odessa Astronomical Publications, 30, 135

Tvardovskyi, D. E., Marsakova, V. I., Andronov, I. L., & Shakun, L. S. 2018, Odessa Astronomical Publications, 30, 103

FROM MONITORING SURVEY OF VARIABLE RED GIANT STARS TO THE EVOLUTION OF THE GALAXY: ANDROMEDA VII

M. Navabi[1], M. Noori[2], E. Saremi[1], A. Javadi[1], J. van Loon[3] and H. Khosroshahi[1]

Abstract.
We have observed the Andromeda VII dwarf galaxy (And VII) using optical multi-epochs with the Isaac Newton Telescope (INT), in order to identify AGB stars. Among AGB stars, we concentrated on long-period variable stars (LPVs) with the largest amplitudes at optical wavelengths. Because these stars are cool at the end of their evolution and their luminosities reach maxima, their birth mass is directly related to luminosity by employing theoretical evolutionary tracks. Since the periods of LPVs are months to years, we have taken t10 epochs from And VII during the period $2015-2017$, spaced by a month or more in the i- and V-bands, plus one epoch in the I-band, to find these variable stars. As a result, a catalogue of $10,000$ stars and 48 LPVs was identified within two halflight radii of And VII. The $i-$band amplitude of variability for our LPV stars ranged from 0.2–1.6 mag. We used the luminosity distribution of those stars to reconstruct their star formation history, employing a method that we have applied in the cases of other Local Group galaxies. By using as well the Spitzer catalogues at mid-IR wavelengths, we constructed a detailed map of the mass feedback into the interstellar medium (ISM).

Keywords: Galaxies: Andromeda VII, stars: variable, AGB, LPV, techniques: photometric

1 Introduction

The low-mass dwarf galaxies are the most abundant and nearest targets in which to study star formation history (SFH) on a galactic scale. For probing the star formation and evolution of the And VII dwarf galaxy, we identified LPV stars that trace stellar populations as young as ~ 30 Myr to as old as ~ 10 Gyr. And VII, also known as the Cassiopeia Dwarf, was discovered 20 years ago (Karachentsev et al. 1999). The distance of And VII was obtained from different photometric methods. From the Padova stellar models and colour–magnitude diagram (CMD), Weisz et al computed $\mu = 24.58$ mag, which we have adopted in this paper (Weisz et al. 2014).

AGB stars with low or medium mass $(0.8-8M_{\odot})$ typically become LPV stars in the final stages of evolution, and reach a high luminosity ($\approx 1000 - 60000L_{\odot}$) and low temperature ($T \approx 3000 - 4500K$) in their lifetime (Yuan et al. 2018; Goldman et al. 2019). They are also prominent in the near-IR, where the effects of dust in the form of extinction and reddening are relatively small. These cool evolved stars start to produce dust through radial pulsations of their atmospheric layers, so they shed their mass (up to 80%) into the ISM (Javadi et al. 2015; Boyer et al. 2017). This paper identified LPVs in And VII and estimated the distribution of their amplitudes in the i-band. That was the first step in obtaining mass–age and mass–pulsation relations for the AGB stars, in order to reconstruct the SFH of this dwarf galaxy.

2 Observation and Data analysis

The Wide Field Camera (WFC) is an optical mosaic camera on the INT (La Palma, Spain). It consists of four 2048×4096 CCDs, with a pixel size of 0.33 arcsec/pixel. We used the WFC between 2015–2017 for identifying LPV stars in And VII. We determined the amplitude and mean brightness of LPVs that are variable on time-scales from ≈ 100 days (for low-mass AGB stars) to ≈ 1300 days for the dustiest massive AGB stars. For this purpose, observations were made over 7 epochs, spaced by one month or more, with the WFC Sloan i filter, one epoch with the WFC RGO I filter and 3 epochs with the Harris V filter, to obtain colour information. The data reduction was performed by the THELI pipeline, and we used DAOPHOT II (Stetson 1987) for Point Spread Function photometry (Saremi et al. 2017, 2019a).

[1] School of Astronomy, Institute for Research in Fundamental Sciences (IPM), Tehran, 19395-5531, Iran
[2] Department of Physics, University of Zanjan, University Blvd., P.O. Box: 45371-38791, Zanjan, Iran
[3] Lennard-Jones Laboratories, Keele University, ST5 5BG, UK

3 Search of variable stars

To identify variable stars, we used a method similar to the NEWTRIAL programme described by Welch & Stetson (1993) and developed further by Stetson (1996) to derive variability indices (J, K and L) for stars. We found the optimal variability threshold for identifying LPVs from histograms of the variability index L (Javadi et al. 2011a,b; Saremi et al. 2017). Most of the LPVs in And VII have i-band magnitudes between 20–22 mag and are located inside two half-light radii of the galaxy.

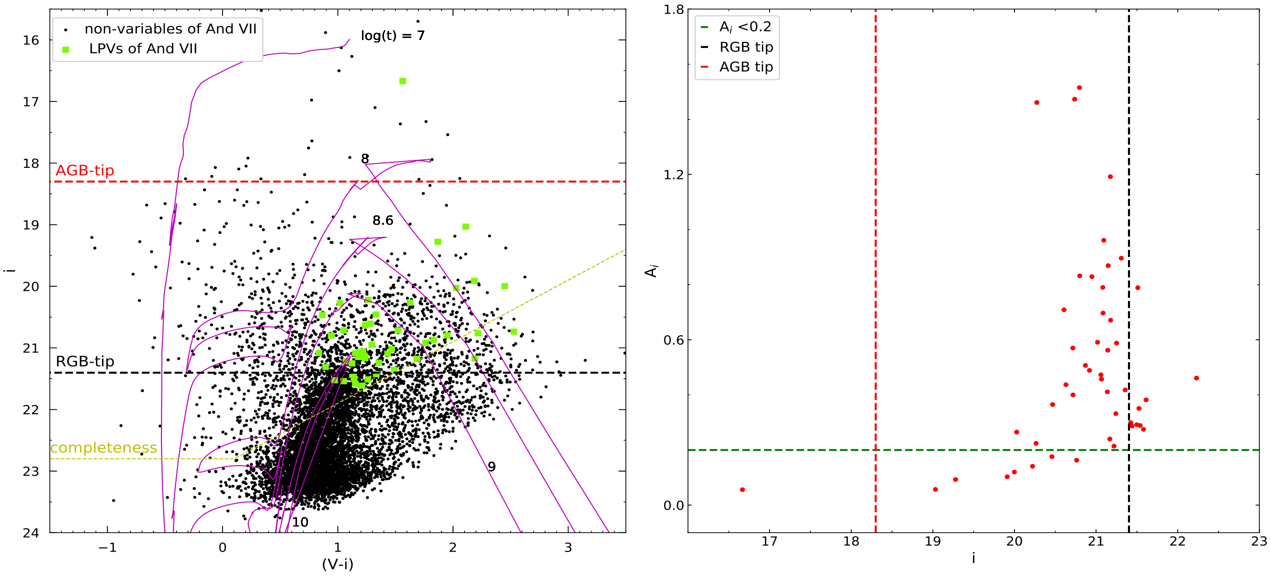

Fig. 1. Left: LPVs are displayed as green points, with isochrones from Marigo et al. (2017) overlaid. **Right:** Estimated A_i of LPVs *vs.* i-band magnitude; dashed lines define the amplitude of $A_i < 0.2$ mag.

Figure 1 (left panel) presents the colour magnitude diagram (CMD) of And VII in the i-band versus $V - i$ colours, with our identified LPV stars in green. Overplotted are isochrones from Marigo et al. (2017). The AGB-tip and RGB-tip are illustrated as red and black dashed lines, respectively. The 50% completeness limit of our photometry is determined from a simple simulation (Saremi et al. 2017). The right panel of Fig. 1 shows that the estimated i-band amplitudes of LPVs are increasing as their brightness decreases, down to near $A_i = 1.6$ mag. We consider only the candidates with $A_i > 0.2$ mag to be LPVs.

4 Ongoing work

We are extending the study of And VII to derive the star-formation history of the dwarf galaxy by applying a method used by Javadi et al. (2011c, 2015, 2017); Rezaeikh et al. (2014); Hamedani Golshan et al. (2017); Hashemi et al. (2019); Saremi et al. (2019b). We will then model the spectral energy distributions of variable stars obtained by a combination of nearIR and optical data (our catalogue) and midIR data (Spitzer catalogues) to estimate the mass-loss rate and chemical enrichment of the galaxy (Javadi et al. 2013).

I would like to thank the conference organizers for their support.

References

Boyer, M. L., McQuinn, K. B. W., Groenewegen, M. A. T., et al. 2017, ApJ, 851, 152

Goldman, S. R., Boyer, M. L., McQuinn, K. B. W., et al. 2019, ApJ, 877, 49

Hamedani Golshan, R., Javadi, A., van Loon, J. T., Khosroshahi, H., & Saremi, E. 2017, MNRAS, 466, 1764

Hashemi, S. A., Javadi, A., & van Loon, J. T. 2019, MNRAS, 483, 4751

Javadi, A., Saberi, M., van Loon, J. T., et al. 2015, MNRAS, 447, 3973

Javadi, A., van Loon, J. T., Khosroshahi, H., & Mirtorabi, M. T. 2013, MNRAS, 432, 2824

Javadi, A., van Loon, J. T., Khosroshahi, H. G., et al. 2017, MNRAS, 464, 2103

Javadi, A., van Loon, J. T., & Mirtorabi, M. T. 2011a, ASPCS, Vol. 445, Infrared Survey of Pulsating Giant Stars in the Spiral Galaxy M 33: Dust Production, Star Formation History, and Galactic Structure (San Francisco: ASP), 497

Javadi, A., van Loon, J. T., & Mirtorabi, M. T. 2011b, MNRAS, 411, 263

Javadi, A., van Loon, J. T., & Mirtorabi, M. T. 2011c, MNRAS, 414, 3394

Karachentsev, I., Aparicio, A., & Makarova, L. 1999, A&A, 352, 363

Marigo, P., Girardi, L., Bressan, A., et al. 2017, ApJ, 835, 77

Rezaeikh, S., Javadi, A., Khosroshahi, H., & van Loon, J. T. 2014, MNRAS, 445, 2214

Saremi, E., Javadi, A., van Loon, J., Khosroshahi, H., & Torki, M. 2019a, in IAU Symposium, Vol. 339, Southern Horizons in Time-Domain Astronomy, ed. R. E. Griffin, 336–339

Saremi, E., Javadi, A., van Loon, J. T., et al. 2017, in Journal of Physics Conference Series, Vol. 869, Journal of Physics Conference Series, 012068

Saremi, E., Javadi, A., van Loon, J. T., et al. 2019b, in IAU Symposium, Vol. 344, Dwarf Galaxies: From the Deep Universe to the Present, ed. K. B. W. McQuinn & S. Stierwalt, 125–129

Stetson, P. B. 1987, PASP, 99, 191

Stetson, P. B. 1996, PASP, 108, 851

Weisz, D. R., Dolphin, A. E., Skillman, E. D., et al. 2014, ApJ, 789, 147

Welch, D. L. & Stetson, P. B. 1993, AJ, 105, 1813

Yuan, W., Macri, L. M., Javadi, A., Lin, Z., & Huang, J. Z. 2018, AJ, 156, 112

Stellar spheres of influence

Stars and their variability observed from space
C. Neiner, W. W. Weiss, D. Baade, R. E. Griffin, C. C. Lovekin, A. F. J. Moffat (eds)

DISKS AROUND BE STARS AND COMPLEX RADIATION EFFECTS

N. D. Kee[1]

Abstract. Observations of classical Be stars show significant variability in the signatures arising from their circumstellar disks on relatively short (month to year) times-cales. Indeed, it is even inferred that these stars are able to construct and fully destroy their disks in those short times. Given the high luminosity of the massive stars at the centre of the systems, interpreting and understanding the observations requires detailed modelling of the often quite complex interplay of stellar irradiation with disk material. This paper discusses recent efforts in that modelling, including the treatment of radiative acceleration of disk material, the thermal structure of the disk, and the role that these effects play in the observed variability of classical Be stars.

Keywords: Processes: hydrodynamics, radiative transfer, stars: circumstellar matter, emission-line, Be, winds, outflows

1 Introduction

In addition to their intrinsic stellar variability, classical Be stars also drive significant variations in their near-star environments by sculpting, constructing, and destroying their circumstellar disks on time-scales of a month to a year (Rivinius et al. 2013). It is this variability of the "stellar sphere of influence" that is addressed here. Even within this category of variations in the circumstellar environment, however, a wide variety of signatures are observed or expected from theory, and include photometric, spectroscopic and polarimetric variability, as well as combinations thereof. Therefore, in order to prioritize a detailed discussion over a broad overview, we are emphasising two active areas of study: (1) spectro-polarimetric diagnostics of the disk temperature and density structure, and (2) UV radiation-driven disk destruction.

For both of these sub-topics, the irradiation from the star itself is a key factor in driving the variability and forming the observable signatures. The following discussion is therefore centred around radiation transfer and radiation hydrodynamics. The primary focus is on the role of the stellar illumination in irradiating and heating the disk to generate the observed spectropolarimetric signatures. In Section 3, it is the role of UV irradiation to impart momentum to the disk material, and the attendant disk destruction mechanism that is emphasised.

2 Diagnosing disk density, size, and temperature with spectropolarimetry

To set up a discussion of the predicted spectropolarimetric signatures and how they depend on disk structure, it is first important to highlight the overall morphology of such signatures as observed in classical Be stars. For the purposes of this discussion, we focus on the region of the Balmer and Paschen jumps, specifically from about $\lambda\,3000$–$9000\,\text{Å}$. As shown in Fig. 1 (adapted from Quirrenbach et al. 1997, their Figure 6), the characteristic polarization signature in this region is at a level of a few percent, with a saw-tooth pattern imprinted onto it by the unpolarized hydrogen bound-free opacity.

By comparing these observations to theoretical predictions of the spectropolaremetric signature, as shown in Fig. 2 (adapted from Halonen & Jones 2013, their Figures 1, 4, 5, and 7), we see that theoretical models reproduce that general morphology of a saw-toothed pattern, and also the few-percent level of polarization. Additionally, taking each panel of Figure 2 individually, we also see that varying the disk size, density and thermal structure all introduce marked differences into the spectropolarimetric signature, much larger than the errors in the observed polarization signatures shown in Fig. 1. Conversely, from a comparison of all four panels of Fig. 2, we also see that there are degeneracies between the impact these different physical variations have on the spectropolarimetric signatures. The long history of studies of classical Be stars has revealed a plethora of

[1] Institute of Astronomy, KU Leuven, Celestijnenlaan 200D, B-3001 Leuven, Belgium
e-mail: dylan.kee@kuleuven.be

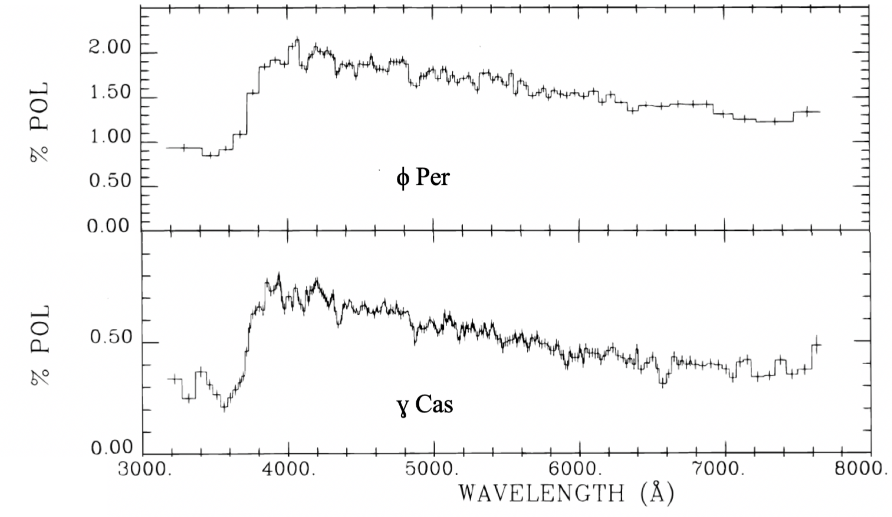

Fig. 1. Spectropolarimetric observations of two classical Be stars, showing the percentage of polarization as a function of wavelength across the Balmer jump. Adapted from Quirrenbach et al. (1997).

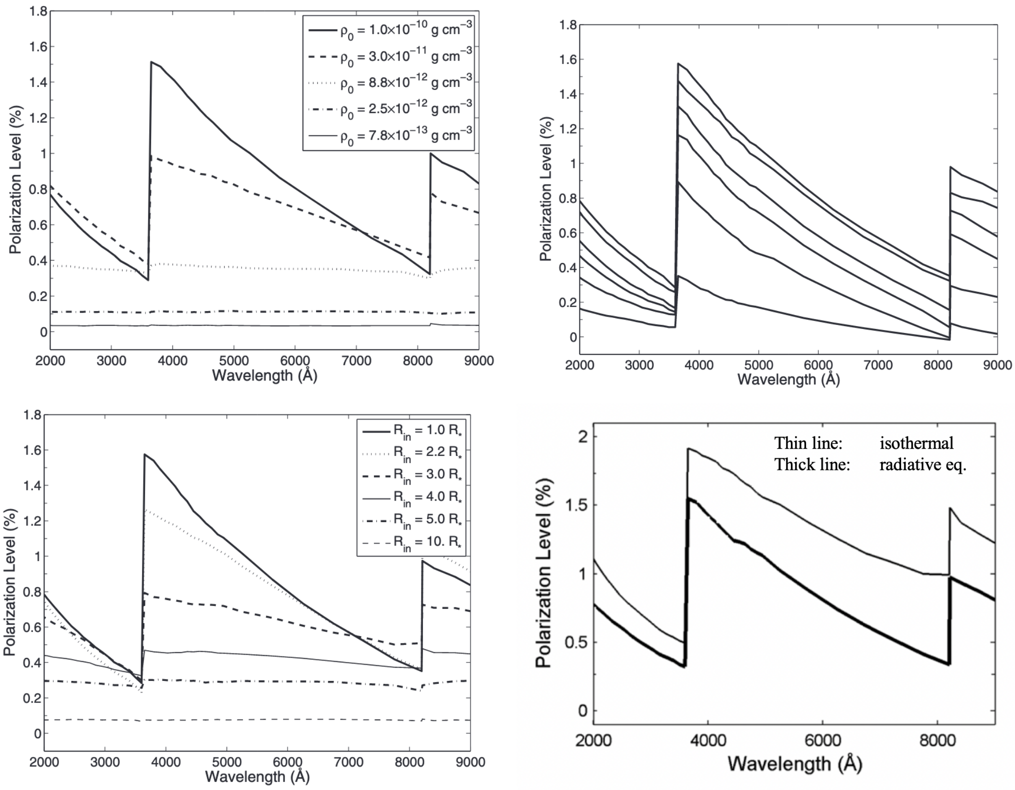

Fig. 2. Effects on the predicted polarization degree across the Balmer and Paschen jumps for a B2 star arising from varying **Top Left:** disk density (increasing density from bottom to top), **Top Right:** size of the disk (outer radius increasing from bottom to top), **Bottom Left:** the size of the gap between the disk inner edge and the star (increasing from top to bottom), and **Bottom Right:** the thermal structure of the disk, specifically here whether the disk is in radiative equilibrium or is isothermal at 0.6 times the stellar effective temperature. Adapted from Halonen & Jones (2013).

additional information derived from spectroscopy and photometry of classical Be stars (see, e.g. Rivinius et al. 2013, for a review); however, that synergizes well with the information available through spectopolarimetry, and simultaneous modelling of the spectropolarimetric signature alongside other observational diagnostics may lift this degeneracy

In addition to spectropolarimetric observations of fixed axisymmetric disks, time-resolved observations of the signatures from asymmetric disks can also assist in interpreting the morphology of classical Be stars. As shown by Marr et al. (2018), even simplified models for warping and over/under-densities in the disk generate noticeable variations in both the overall level of polarization and the strength of the Balmer/Paschen jumps. Figure 3 (adapted from Marr et al. 2018, their Figure 2) emphasises this point by showing the phased variation in both overall polarization (measured in the V band as an average of the polarization at $\lambda\,5250$ and $5750\,\text{Å}$) and the change in polarization over the Balmer jump for disks with a $10\times$ over-density in an azimuthal segment of 45, 90, 180 or 270 degrees, as labelled in the Figure. Both these signatures can clearly be seen to vary considerably with the phased viewing position of the disk, emphasising the additional information embedded in such time-resolved signatures.

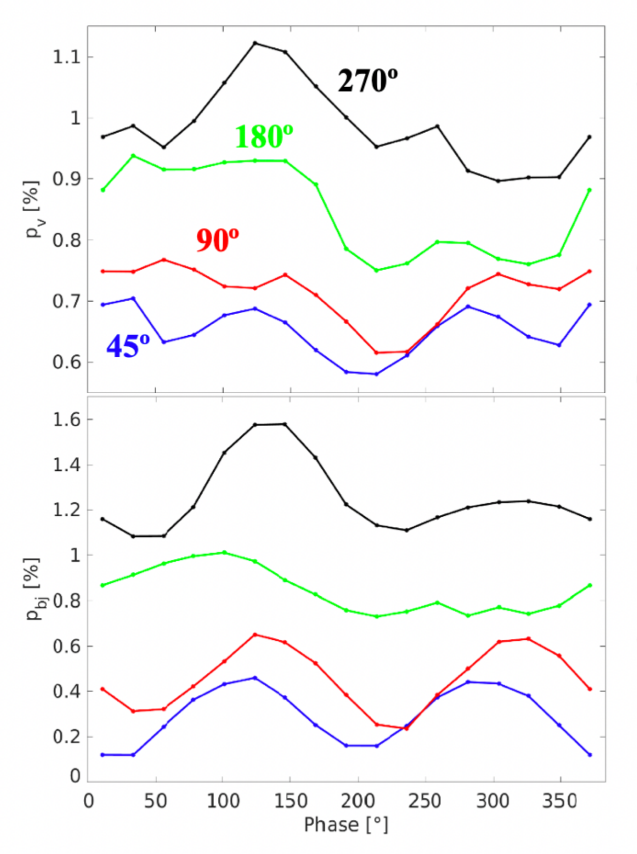

Fig. 3. Phase dependence of the polarization degree (**Top**, averaged from $\lambda\,5250$ and $5750\,\text{Å}$) and change in polarization across the Balmer jump (**Bottom**, difference between $\lambda\,3800$ and $3600\,\text{Å}$) for a simple model of an over-dense wedge in a disk of angular extent 45°, 90°, 180°, or 270° in azimuth, as labelled in the Figure. Adapted from Marr et al. (2018).

3 Disk destruction by UV line-driven disk ablation

We now turn our attention to studies of disk destruction, attempting to understand the rapid times – a month to a year – in which classical Be stars are able to lose their disks. Again motivated by the brightness of the central star, we emphasise the role that stellar irradiation may play in this process. This section actually parallels the discussion of UV line-driven disk ablation introduced by Kee et al. (2016).

The central concept here is that the standard model of UV line-driven winds as introduced by Castor et al. (1975) allows for the computation of acceleration from a local velocity gradient. When one accounts for the non-radial photons near the stellar surface that arise because of the finite size of the star, such velocity gradients can arise from the projection of non-radial motions, e.g. Keplerian rotation of the disk, onto the flight direction of the photon, thereby allowing photons from the star to drive acceleration of disk material. As shown by Fig. 4

(adapted from Kee et al. 2016, their Figures 5 and 6), this results in the acceleration of disk material in thin sheets along the surfaces of the disk to high velocities comparable with the speed of the wind.

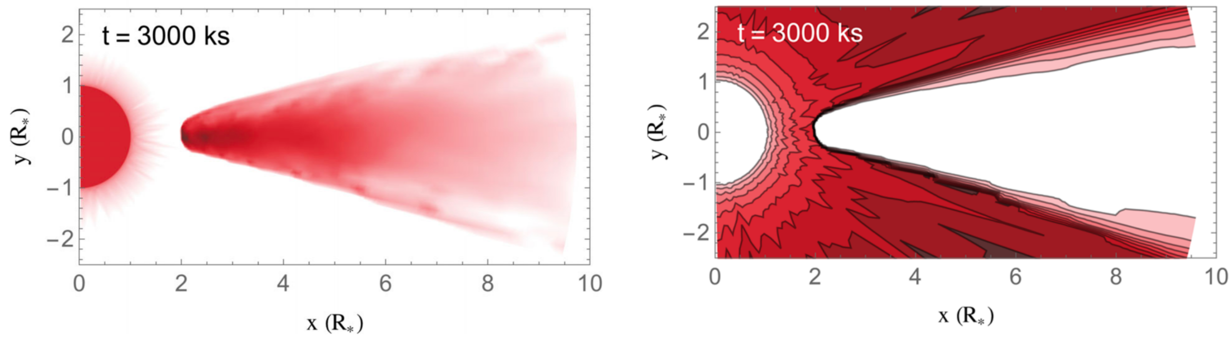

Fig. 4. Morphology of disk ablation shown in **Left:** density and **Right:** radial velocity, emphasising that the thin ablation layer is at disk-like densities but wind-like velocities. Adapted from Kee et al. (2016).

While these sheets of material are geometrically thin, their high density and velocity combine to allow them to carry substantial amounts of material away from the disk. This is emphasised by Figure 5 (Kee et al. 2016, Figure 14), which shows the rate of change of mass in the simulation volume for disks around Be stars. Since the wind away from the disk is steady-state, this is the rate at which the disk loses mass by ablation. For all simulations we see that the disk ablation rate reaches a factor of an order of unity times the spherically symmetric wind mass loss rate. For later spectral types, this can be sustained due to the lower wind mass loss rate, while for the earliest spectral types considered it results in the disk being ejected dynamically from the simulation, shedding some light on the relative rareness of classical Oe stars in general and the tendency to find them in lower-metallicity environments where the stellar wind is weaker.

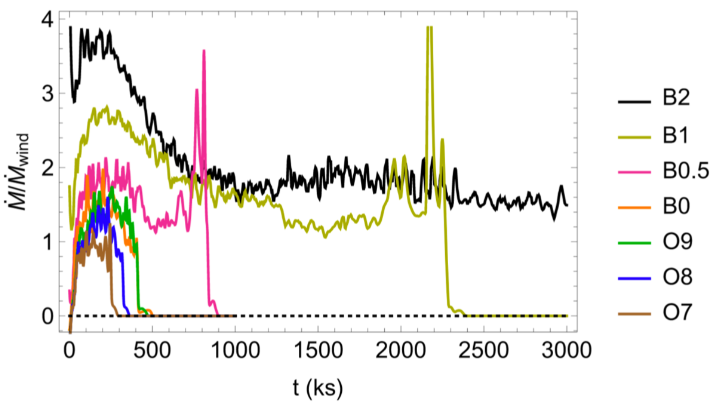

Fig. 5. Rate of disk destruction in the radiation-hydrodynamic simulations in units of the analytic, spherically-symmetric wind mass loss rate, $\dot{M}_{\rm wind}$. Adapted from Kee et al. (2016).

Looked at in a different way, we can instead quantify the time that the star will take to lose its disk. Motivated by the rates found in Figure 5, a good first order estimate should be the total mass of the disk divided by the wind mass loss rate. This is plotted in Fig. 6 (Kee et al. 2016, their Figure 15) with the actual disk destruction time from the simulations plotted for comparison. Given the generally good agreement between this estimate and the simulation results, we can take this one step further and compare it to photometric variability time-scales in observations of classical Be stars.

As an example, we can make a comparison with the recently published light-curve and model of ω CMa by Ghoreyshi et al. (2018). The model of the light-curve indicates that the disk loses $\sim 3 \times 10^{-9} M_\odot$ in each dissipation event, and from the stellar parameters provided the star has a mass loss rate $\sim 6 \times 10^{-10} M_\odot$ yr^{-1}. Taken together, this implies a disk ablation time of ~ 5 yr, well in line with the observed disk dissipation time for this star. From the modelling by Ghoreyshi et al. (2018), however, the observed light-curve is fitted well by

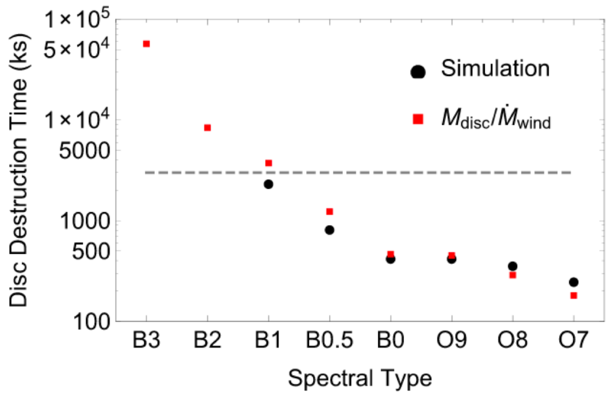

Fig. 6. Disk destruction time in the radiation-hydrodynamic simulations compared to a simple estimate given by the ratio of the disk mass, $M_{\rm disk}$, to the wind mass loss rate, $\dot{M}_{\rm wind}$. The grey dashed line shows the duration of the simulation. Adapted from Kee et al. (2016).

a viscous dissipation of the disk, highlighting the need for additional work to determine the interplay of these physical mechanisms in describing classical Be star disk destruction.

4 Conclusions

As emphasised by the two ongoing research areas discussed above, many efforts are currently under way to understand the structure of classical Be-star disks and the physical processes that govern them. The talk has also emphasised that these interpretations often require detailed, fully three-dimensional, radiation-hydrodynamics and radiation-transport models owing to the complex nature of the interplay between stellar irradiation and circumstellar disk material. Given the wealth of observational data that continues to flow in from observing missions like *BRITE*, however, the advancement of such models can proceed in step with the observational data to give us an ever improving view of the nature of these intriguing objects.

NDK would like to acknowledge funding from NASA ATP grant NNX11AC40G, under which a portion of the work presented here was completed, and the KU Leuven C1 grant MAESTRO for ongoing support.

References

Castor, J. I., Abbott, D. C., & Klein, R. I. 1975, ApJ, 195, 157
Ghoreyshi, M. R., Carciofi, A. C., Rímulo, L. R., et al. 2018, MNRAS, 479, 2214
Halonen, R. J. & Jones, C. E. 2013, ApJ, 765, 17
Kee, N. D., Owocki, S., & Sundqvist, J. O. 2016, MNRAS, 458, 2323
Marr, K. C., Jones, C. E., & Halonen, R. J. 2018, ApJ, 852, 103
Quirrenbach, A., Bjorkman, K. S., Bjorkman, J. E., et al. 1997, ApJ, 479, 477
Rivinius, T., Carciofi, A. C., & Martayan, C. 2013, A&A Rev., 21, 69

Stars and their variability observed from space
C. Neiner, W. W. Weiss, D. Baade, R. E. Griffin, C. C. Lovekin, A. F. J. Moffat (eds)

TRACING STELLAR WIND VARIABILITY FROM SPACE

J. Krtička[1] and A. Feldmeier[2]

Abstract. Mass-loss by winds constitute one of the crucial processes that determine the evolution and fate of stars. The amount of mass lost by a star per unit of time (the mass-loss rate) and its dependence on stellar parameters is therefore one of the crucial ingredients of any stellar evolutionary model. Being derived either from observation or theory, wind mass-loss rates are highly uncertain, in many cases by a factor of a few. The uncertainty in a determination of the mass-loss rate is to a large extent connected with the variability of the wind. We discuss how the observation of stellar winds from space can help trace the wind's variability and its origin, and how that knowledge can be used to derive more precise wind mass-loss rates.

Keywords: Stars: winds, outflows, mass-loss, early-type, variables, hydrodynamics

1 Introduction

Stars lose mass during their evolution, and there are many different ways in which single stars do so. In general they can be divided into explosive events (e.g., supernovæ and LBV-type eruptions) and quasi-stationary outflows (winds and disks). The outflowing disks are discussed elsewhere within these proceedings (Baade, Carciofi & Labadie-Bartz, Sigut, and Kee [PAGE]). This contribution discussed the variability of three main types of stellar winds: line-driven winds of hot luminous stars, dust-driven winds from AGB stars, and coronal winds from cool stars.

Mass loss by winds has important consequences for different fields of astrophysics. Winds affect stellar evolution (De Loore et al. 1977; Maeder 1981), contribute to the mass and momentum input into the interstellar medium, and redistribute heavier elements created during stellar nucleosynthesis. Furthermore, the interaction zone between a wind and the interstellar medium is an important source of galactic cosmic-ray particles (Aharonian et al. 2019).

Stellar winds may be studied from different aspects, but the "holy grail" of wind studies is to understand how the wind *mass-loss rate* (amount of mass lost per unit of time) varies as a function of stellar parameters:

$$\dot{M} = \dot{M}(L, T_{\mathrm{eff}}, M, Z, \dots) \qquad [M_\odot\,\mathrm{yr}^{-1}]. \tag{1.1}$$

Although other wind parameters (for example, wind terminal velocity, wind angular momentum loss or wind X-ray emission) are important for specific issues, the wind mass-loss rate is indisputably the most important one. Despite significant efforts of many astronomers over last few decades, the wind mass-loss rates are not known with a precision sufficient for many applications. Below we discuss why that is the case, and how observations of wind variability can improve the situation.

2 Hot-star winds

Winds from hot stars are mostly driven by the light absorption (scattering) in the lines of "heavy" elements such as carbon, nitrogen, oxygen, silicon and iron (Castor et al. 1975). This type of stellar wind, which is propelled by stellar radiation, can be found in hot stars in various evolutionary phases, including main-sequence stars, OBA supergiants, hot subdwarfs, central stars of planetary nebulæ and Wolf-Rayet stars. Although theoretical predictions of mass-loss rates exist for all these stellar types (e.g., Vink et al. 2001; Krtička & Kubát 2017), they differ from one another by factor of a few, and they also differ significantly from observational estimates.

[1] Masaryk University, Brno, Czech Republic
[2] Potsdam University, Potsdam-Golm, Germany

2.1 Hot-star wind mass-loss rate estimates and the influence of clumping

There are several methods that enable us to derive wind mass-loss rates from observations. However, there is no direct way of estimating those rates. Every method uses models or physical assumptions that enable us to quantify the amount of mass loss. As a result, significant discrepancies may exist between individual methods.

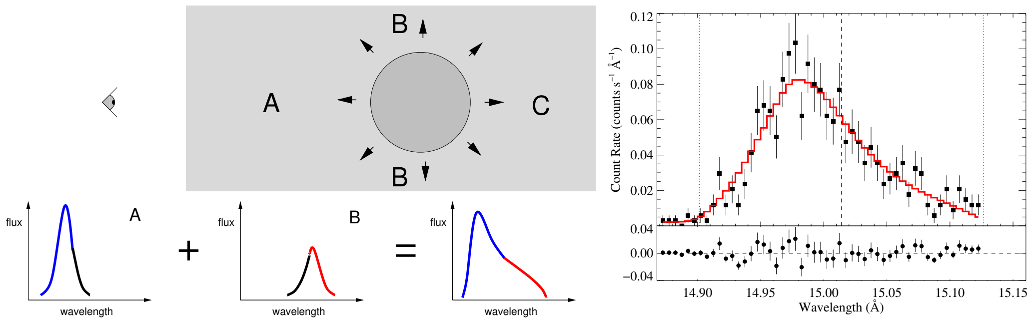

Fig. 1. X-ray line formation. **Left:** Lines originate from the whole wind volume, but the emission from part B is more absorbed on its way towards the observer than the emission from part A. **Right:** Observed profile (Leutenegger et al. 2013). © AAS. Reproduced with permission.

As a result of their supersonic nature, hot-star winds emit strong X-rays. Most X-rays are emitted by hot, shock-heated material at frequencies corresponding to individual line transitions. However, the bulk of the wind material is relatively cool and absorbs the X-rays in the continuum. Owing to the asymmetry of wind X-ray absorption (the X-rays emitted from the opposite hemisphere being more strongly absorbed than X-rays emitted in the hemisphere that faces the observer), the wind X-ray profiles become asymmetric (see Fig. 1). The level of asymmetry is a measure of the wind mass-loss rate (Owocki & Cohen 2001; Ignace & Gayley 2002).

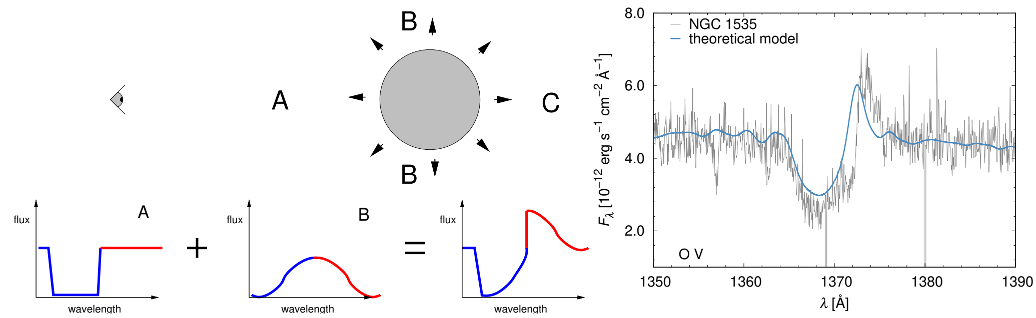

Fig. 2. Origin of P Cygni line profiles. **Left:** The P Cygni line profile is formed from an absorption component, which originates from intervening material in region A, and an emission component from material in regions A and B. Adopted from Owocki (2000). **Right:** Comparison of observed and theoretical P Cygni line profiles.

P Cygni and emission line profiles provide another mass-loss rate characteristic in the ultraviolet and optical domains. There, the strength of the emission-line components and the depth of unsaturated absorption components are proportional to the mass-loss rate (see Fig. 2).

Wind material causes a continuum excess that is especially strong in the infrared and radio domains (Fig. 3, Bieging et al. 1989; Scuderi et al. 1998). The amount of excess leads to another measure of the mass-loss rate.

The comparison of theoretical and observed mass-loss rate estimates in Fig. 4 (left) shows an order-of-magnitude discrepancy between individual values. From the point of view of observations, this discrepancy is probably caused by the influence of inhomogeneities (clumping) that may mimic higher mass-loss rates (in the case of optically thin clumps, e.g., Puls et al. 2006; Bouret et al. 2012) or decrease the absorption due to porosity effects in the case of optically thick clumps (Oskinova et al. 2007; Sundqvist et al. 2010; Šurlan et al. 2013).

The level of the influence which clumping can have upon observed characteristics is unclear. However, inhomogeneities also cause wind variability. The study of the wind variability using different wind observables may therefore help to constrain the structure of inhomogeneities and their influence on the mass-loss rate indicators.

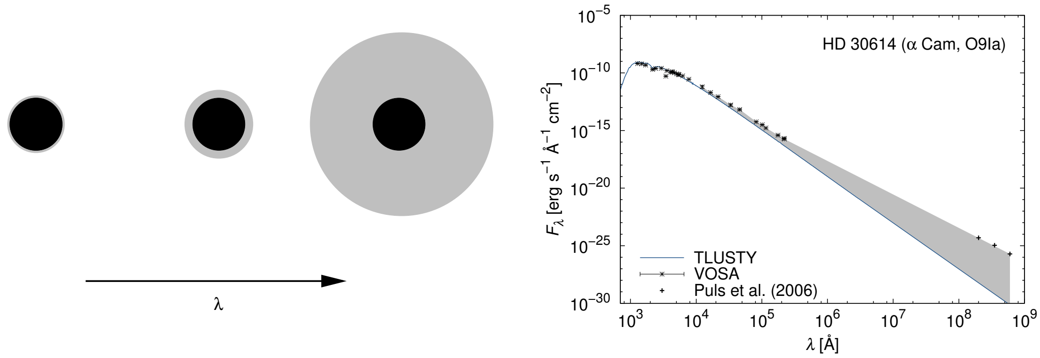

Fig. 3. Infrared and radio excess due to a stellar wind. **Left:** The radius of the optically thick region increases with increasing wavelength (adopted from Lamers & Cassinelli 1999). **Right:** Observed spectral energy distribution (VOSA and Puls et al. 2006) compared to the radiative flux from hydrostatic model atmospheres (Lanz & Hubeny 2007).

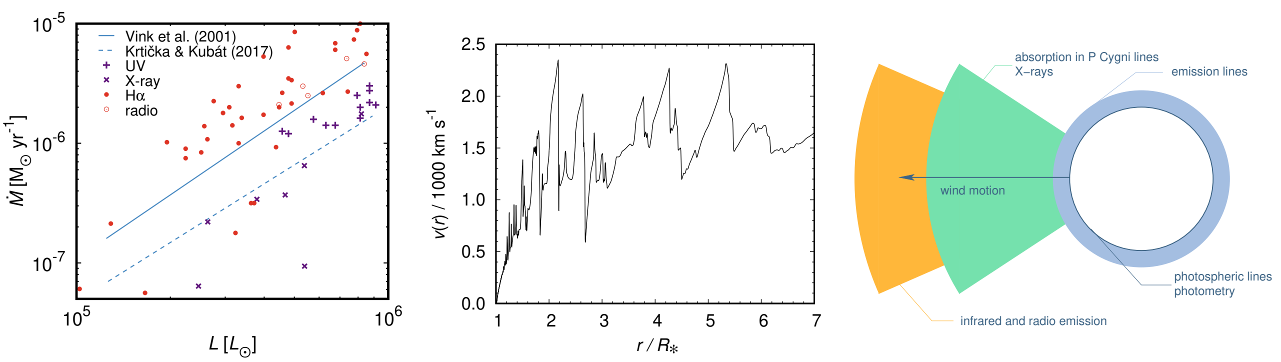

Fig. 4. Left: Comparison of theoretical (Vink et al. 2001; Krtička & Kubát 2017) and observed (Scuderi et al. 1998; Mokiem et al. 2007; Bouret et al. 2012; Šurlan et al. 2013; Cohen et al. 2014) mass-loss rate determinations of O stars. **Middle:** A snapshot of simulations of hydrodynamical wind instability by Feldmeier et al. (1997), showing a radial dependence of velocity. **Right:** Origin of different observables in the winds of hot stars.

Different observables originate at different locations in the wind (Fig. 4, right). While optical photometry relates to the stellar atmosphere and at the wind base, Hα emission comes from wind regions relatively close to the star. The X-ray emission and the absorption part of the P Cygni line profiles trace the supersonic part of the wind, up to the speed equal to its terminal velocity. The infrared and radio emission originate in an extended envelope at large distances from the star. Different origins of wind observables enables us to trace the wind structure from its possible origin at the stellar surface, through the development of strong inhomogeneities in the supersonic part of the wind, and up to the free movement of those clumps at large distances from the star.

2.2 *Large scale wind structure: corotating interacting regions*

Large-scale wind structure is the easiest to study. Its appearance is manifested as deep additional absorption components moving in blue parts of P Cygni line profiles (discrete absorption components, DACs, Fig. 5). The speed of the DACs, as inferred from their slope in the time *versus* Doppler-shift diagram (Fig. 5, right), is lower than the speed of the wind. A possible interpretation is that the evolution of DACs is the result of a projection effect of dense streams (corotating interacting regions) spiralling in the wind through stellar rotation (Fig. 5).

There are several effects that can test this model of corotating interacting regions. Overdensity implies a stronger radiative force across a small portion of the stellar surface. The radiative force can most easily be modulated by bright surface spots, which should in turn show up in the photometry. Indeed, many hot stars show periodic light variability with the same periods in which DACs appear. This was found from MOST observations of WR 110 (Chené et al. 2011) and ξ Per (O7.5 III(n)((f)), Ramiaramanantsoa et al. 2014), and from K2 photometry of ρ Leo (B1 Iab, Aerts et al. 2018). The agreement is not always perfect, as shown from

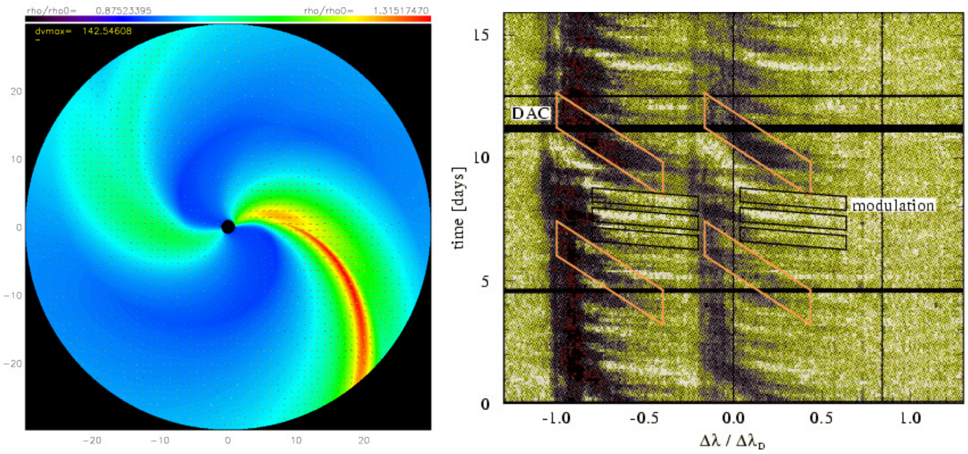

Fig. 5. Left: Origin of large-scale wind structure. Surface spots generate dense streams, which (owing to velocity plateaux and overdensities) lead to discrete absorption components (DACs, Cranmer & Owocki 1996; Lobel & Blomme 2008). © AAS. Reproduced with permission. **Right:** Time development of P Cygni line profiles. The abscissa shows the wavelength (or wind velocity); the ordinate shows time. Individual horizontal slices correspond to stellar spectra taken at different times with colour coded absorption. Deep, slowly moving absorption components (DACs) are superimposed on weak structures. The graph shows a doublet, so the structure consequently repeats at two different wavelengths. Credit: Hamann et al. (2001), reproduced with permission © ESO.

SMEI and BRITE observations of ζ Pup (O4I(n)fp, Howarth & Stevens 2014; Ramiaramanantsoa et al. 2018). On the other hand, the fact that theoretical models show that the detected level of light variability is able to account for the observed strength of DACs (David-Uraz et al. 2017) does support the model of corotating interacting regions.

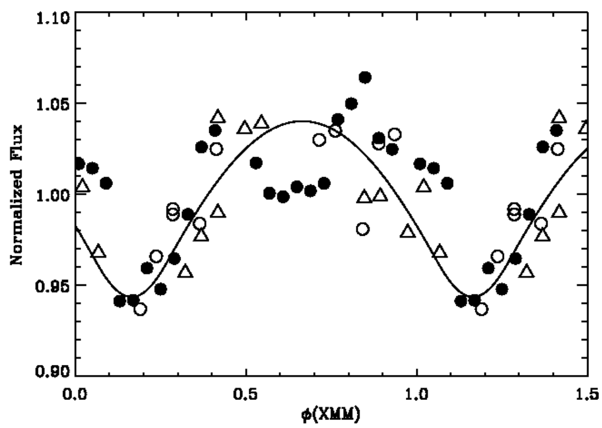

Fig. 6. O7.5 III(n)((f)) star ξ Per: X-ray flux (filled symbols) compared with UV data (open symbols). CIR variability of UV lines, Hα emission, and X-ray flux are modulated with the same period (de Jong et al. 2001; Massa et al. 2019). © AAS. Reproduced with permission.

As the overdensities connected with corotating interacting regions move through the wind, they also affect other observable characteristics. They become visible in Hα first (see Fig. 4 right), followed by the appearance as DACs (Kaper et al. 1997). The modulation of X-ray emission at the same period as that of DACs nicely completes the picture (Massa et al. 2019, Fig. 6).

2.3 *Small scale wind structure: the effect of clumping*

While the large-scale wind structure causes the most prominent observational effects, the small-scale structure has very important consequences for the mass-loss rate determination. The inhomogeneities due to the small-scale wind structure influence significantly the wind observables, and are likely to cause the disagreement between theory and observations (Fig. 4, left). However, while the model of corotating interacting regions provides a consistent picture of large-scale wind structure, the model of small-scale wind structure does not seem to be so successful.

The small-scale wind structure (clumping) is probably caused by line-driven wind instability (Fig. 4, middle, Lucy & Solomon 1970; Owocki et al. 1988; Feldmeier & Thomas 2017), which either amplifies the photospheric perturbations seeded by subsurface turbulent motions (Feldmeier et al. 1997), or is self-initiated in the wind (Sundqvist et al. 2018). The aim of observational studies of wind clumping is to trace the inhomogeneities as they originate in the photosphere (or close to it) and develop in the wind, influencing different observables.

Multiple wind observations point to the existence of a small-scale stochastic wind structure. Very precise photometry from satellites like *Kepler, CoRoT* and BRITE show stochastic low-amplitude light variations in O stars (e.g., Blomme et al. 2011; Briquet et al. 2011; Aerts et al. 2017). The variations are attributed to sub-surface convection and to stellar oscillations, but part may also originate through wind blanketing and the line-driven wind instability, which had already developed in the stellar photosphere (Krtička & Feldmeier 2018) if the base perturbation is large enough. The surface velocity fields are expected to cause not only photometric variability but also photospheric line-profile variability. Aerts et al. (2017) indeed found similar frequencies in photometric and spectroscopic observations, but without a strong correlation.

As the perturbations propagate into the wind, they affect wind-line profiles. The effect of inhomogeneities (clumping) most likely leads to discordances in individual mass-loss rate determinations (Fig. 4, left). However, time-resolved observations do not show any obvious link between photospheric and wind variability from optical lines (Martins et al. 2015). It may be difficult to trace individual inhomogeneities, owing to their small masses, but this result shows that more research is needed in order to understand the connection between surface perturbations and wind inhomogeneities.

In a supersonic wind the instabilities steepen into shocks and cause X-ray emission (Owocki et al. 1988; Feldmeier et al. 1997, middle panel of Fig. 4). As a result of the stochastic nature of instabilities, one should expect some X-ray variability. However, such variability is not observed, implying that a large number of independent shocks contribute to the X-ray emission (Nazé et al. 2013).

3 Dust-driven winds of luminous cool stars

The acceleration of dust-driven winds of luminous cool stars is the result of a three-step process (Gilman 1972; Bowen 1988; Woitke 2006; Höfner & Olofsson 2018). Stellar pulsations cause large amounts of stellar material to be transported outwards and deposited at distances where the dust particles can condensate. The radiation then takes over and accelerates the wind by radiative forces on the dust particles. The bulk of the wind that is composed of hydrogen and helium is accelerated by collisions with dust particles.

Stellar variability is therefore a prerequisite for the formation of the wind. As the pulsation period is related to the stellar luminosity, one can expect some relation between the mass-loss rate and the pulsation period (or luminosity). This was indeed found for different types of AGB stars by Uttenthaler (2013).

4 Coronal winds of cool main-sequence stars

Cool solar-type stars have coronal winds through thermal expansion of the stellar corona (Parker 1958). While the mechanism of the coronal heating is still somewhat unclear (see Sakaue, [PAGE], for a recent model), it is clear that the heating process is closely related to stellar activity. For example, it explains the relation between time-series of the Ca II H and K lines and *ROSAT* X-ray fluxes (Hempelmann et al. 2003).

Mass-loss due to a *magnetized* stellar wind causes magnetic rotational braking (Weber & Davis 1967; Skumanich 1972; Kawaler 1988). With proper calibration, this can be used to estimate stellar ages from photometric periods (Angus et al. 2015).

5 Conclusions

Every estimate of a wind mass-loss rate is relatively uncertain. To a large extent, it is connected to small-scale wind structure, which leads to wind variability. We have shown here how wind variability can be used as a tracer of wind structure, so the study of wind *variability* can therefore improve our knowledge of the wind *structure*, leading to more reliable estimates of wind mass-loss rates.

JK was supported by grant GA ČR 18-05665S.

References

Aerts, C., Bowman, D. M., Símon-Díaz, S., et al. 2018, MNRAS, 476, 1234

Aerts, C., Símon-Díaz, S., Bloemen, S., et al. 2017, A&A, 602, A32

Aharonian, F., Yang, R., & de Oña Wilhelmi, E. 2019, Nature Astronomy, 3, 561

Angus, R., Aigrain, S., Foreman-Mackey, D., & McQuillan, A. 2015, MNRAS, 450, 1787

Bieging, J. H., Abbott, D. C., & Churchwell, E. B. 1989, ApJ, 340, 518

Blomme, R., Mahy, L., Catala, C., et al. 2011, A&A, 533, A4

Bouret, J.-C., Hillier, D. J., Lanz, T., & Fullerton, A. W. 2012, A&A, 544, A67

Bowen, G. H. 1988, ApJ, 329, 299

Briquet, M., Aerts, C., Baglin, A., et al. 2011, A&A, 527, A112

Castor, J. I., Abbott, D. C., & Klein, R. I. 1975, ApJ, 195, 157

Chené, A. N., Moffat, A. F. J., Cameron, C., et al. 2011, ApJ, 735, 34

Cohen, D. H., Wollman, E. E., Leutenegger, M. A., et al. 2014, MNRAS, 439, 908

Cranmer, S. R. & Owocki, S. P. 1996, ApJ, 462, 469

David-Uraz, A., Owocki, S. P., Wade, G. A., Sundqvist, J. O., & Kee, N. D. 2017, MNRAS, 470, 3672

de Jong, J. A., Henrichs, H. F., Kaper, L., et al. 2001, A&A, 368, 601

De Loore, C., De Greve, J. P., & Lamers, H. J. G. L. M. 1977, A&A, 61, 251

Feldmeier, A., Puls, J., & Pauldrach, A. W. A. 1997, A&A, 322, 878

Feldmeier, A. & Thomas, T. 2017, MNRAS, 469, 3102

Gilman, R. C. 1972, ApJ, 178, 423

Hamann, W. R., Brown, J. C., Feldmeier, A., & Oskinova, L. M. 2001, A&A, 378, 946

Hempelmann, A., Schmitt, J. H. M. M., Baliunas, S. L., & Donahue, R. A. 2003, A&A, 406, L39

Höfner, S. & Olofsson, H. 2018, A&A Rev., 26, 1

Howarth, I. D. & Stevens, I. R. 2014, MNRAS, 445, 2878

Ignace, R. & Gayley, K. G. 2002, ApJ, 568, 954

Kaper, L., Henrichs, H. F., Fullerton, A. W., et al. 1997, A&A, 327, 281

Kawaler, S. D. 1988, ApJ, 333, 236

Krtička, J. & Kubát, J. 2017, A&A, 606, A31

Krtička, J. & Feldmeier, A. 2018, A&A, 617, A121

Lamers, H. J. G. L. M. & Cassinelli, J. P. 1999, Introduction to Stellar Winds (Cambridge University Press, adsurl = https://ui.adsabs.harvard.edu/abs/1999isw..book.....L, adsnote = Provided by the SAO/NASA Astrophysics Data System)

Lanz, T. & Hubeny, I. 2007, ApJS, 169, 83

Leutenegger, M. A., Cohen, D. H., Sundqvist, J. O., & Owocki, S. P. 2013, ApJ, 770, 80

Lobel, A. & Blomme, R. 2008, ApJ, 678, 408

Lucy, L. B. & Solomon, P. M. 1970, ApJ, 159, 879

Maeder, A. 1981, A&A, 99, 97

Martins, F., Marcolino, W., Hillier, D. J., Donati, J. F., & Bouret, J. C. 2015, A&A, 574, A142

Massa, D., Oskinova, L., Prinja, R., & Ignace, R. 2019, ApJ, 873, 81

Mokiem, M. R., de Koter, A., Vink, J. S., et al. 2007, A&A, 473, 603

Nazé, Y., Oskinova, L. M., & Gosset, E. 2013, ApJ, 763, 143

Oskinova, L. M., Hamann, W.-R., & Feldmeier, A. 2007, A&A, 476, 1331

Owocki, S. 2000, Radiatively Driven Stellar Winds from Hot Stars (Bristol: Institute of Physics Publishing), 1887

Owocki, S. P., Castor, J. I., & Rybicki, G. B. 1988, ApJ, 335, 914

Owocki, S. P. & Cohen, D. H. 2001, ApJ, 559, 1108

Parker, E. N. 1958, ApJ, 128, 664

Puls, J., Markova, N., Scuderi, S., et al. 2006, A&A, 454, 625

Ramiaramanantsoa, T., Moffat, A. F. J., Chené, A.-N., et al. 2014, MNRAS, 441, 910

Ramiaramanantsoa, T., Moffat, A. F. J., Harmon, R., et al. 2018, MNRAS, 473, 5532

Scuderi, S., Panagia, N., Stanghellini, C., Trigilio, C., & Umana, G. 1998, A&A, 332, 251

Skumanich, A. 1972, ApJ, 171, 565

Sundqvist, J. O., Owocki, S. P., & Puls, J. 2018, A&A, 611, A17
Sundqvist, J. O., Puls, J., & Feldmeier, A. 2010, A&A, 510, A11
Uttenthaler, S. 2013, A&A, 556, A38
Šurlan, B., Hamann, W.-R., Aret, A., et al. 2013, A&A, 559, A130
Vink, J. S., de Koter, A., & Lamers, H. J. G. L. M. 2001, A&A, 369, 574
Weber, E. J. & Davis, Leverett, J. 1967, ApJ, 148, 217
Woitke, P. 2006, A&A, 452, 537

Stars and their variability observed from space
C. Neiner, W. W. Weiss, D. Baade, R. E. Griffin, C. C. Lovekin, A. F. J. Moffat (eds)

STAR–PLANET MAGNETIC INTERACTIONS

A. F. Lanza[1]

Abstract. This paper reviews briefly the observation and theory of magnetic interactions between stars and their nearby planets, focussing on systems with hot Jupiters and considering phenomena observed in the atmospheres of the host stars. These interactions can provide an indirect method to measure the magnetic fields of hot Jupiters, opening a new window on the magnetohydrodynamics and thermodynamics of their interiors. Statistical analyses of the signatures of star–planet interactions in the coronal emission and in the rotation of planet-hosting stars are also considered, with the main emphasis on some specific cases that may shed light on the complex interplay between stars and their nearby planets.

Keywords: planetary systems; stars: activity, late-type, magnetic fields, planets and satellites: magnetic fields

1 Introduction

The magnetic fields of planets play a fundamental role in several important processes that shape their structure and evolution. They reduce the evaporation rate of nearby planets (e.g., Adams 2011) and protect them from coronal mass ejections; they affect the habitability of the planetary environments (e.g., Airapetian et al. 2019) and provide us with information on the planetary interiors, where magnetic fields are generated by hydromagnetic dynamos (e.g. Driscoll 2018). The interactions between the magnetic fields of late-type stellar hosts and their planets can in principle be observed, but a combination of ground-based and space-born observations is crucial for obtaining a complete descriptions of these phenomena, whose detection is often at the limit of presently available instruments. This contribution focussed on the effects which might be observed in the host star.

2 Types of magnetic interactions

In the solar system planets orbit in the super-Alfvénic region of the solar wind, where the wind velocity $v_{\rm w}$ is greater than the local Alfvén velocity $v_{\rm A} \equiv B/\sqrt{\mu\rho}$; B is the intensity of the magnetic field in the wind, μ is the magnetic permeability of the plasma, and ρ its density. In this regime, a perturbation generated by the planet in the wind magnetic field and propagating at the Alfvén velocity is blown away by the faster-moving wind. On the other hand, in the case of nearby planets (representing the majority of known extrasolar planets), the planet orbits so close to its host that the stellar wind is likely to be in a sub-Alfvénic regime, that is, $v_{\rm w} < v_{\rm A}$. In that regime, a perturbation excited by the motion of the planet through the wind magnetic field can propagate back to the atmosphere of the host star. Specifically, a planet excites Alfvén waves that move along characteristics, that is, lines that are everywhere tangent to the vectors $\mathbf{c}_{\rm w}^{\pm} = \mathbf{v}_{\rm w} \pm \mathbf{v}_{\rm A}$, where $\mathbf{v}_{\rm w}$ is the velocity of the wind flow and $\mathbf{v}_{\rm A} = \mathbf{B}/\sqrt{\mu\rho}$ is the vectorial Alfvén velocity. One of the characteristics may reach the host star, thus allowing the Alfvén waves to dissipate their energy in its chromosphere and corona (Saur 2018).

The available power can be computed using the *Alfvén-wing model,* originally developed in the case of the interaction between Jupiter and its moon Io (Neubauer 1980). It orbits inside Jupiter's magnetosphere and produces bright spots in the auroral ovals of the planet that are observed in the ultraviolet and move in phase with the orbital motion of the satellite rather than with the rotation period of Jupiter. A detailed analysis of this phenomenon has been given by Saur et al. (2013), who presented model applications to hot Jupiters and found powers up to $10^{18} - 10^{19}$ W in the most favourable cases. Numerical magnetohydrodynamic (MHD) models by Strugarek (2016, 2018) confirmed these results, and showed the importance of the relative orientation of the planetary field with respect to the stellar field in determining the dissipated power.

[1] INAF-Osservatorio Astrofisico di Catania, Via S. Sofia, 78 – 95123 Catania, Italy – email: antonino.lanza@inaf.it

Inspired by the observations of Io's bright spots in the atmosphere of Jupiter, Shkolnik et al. (2003, 2005) looked for chromospheric hot spots in stars with hot Jupiters moving in phase with the orbits of the planets rather than with stellar rotation. The observed signatures are not steady and have a flux of less that $\sim 1\%$ of the chromospheric emission, making their confirmation difficult (Shkolnik et al. 2008). Nevertheless, further evidence of this phenomenon was recently obtained in the case of HD 189733 (Cauley et al. 2018). Cauley et al. (2019) measured the excess fluxes coming from chromospheric hot spots in HD 179949, HD 189733, τ Bootis and υ Andromedae, finding mean irradiated powers between $(0.28 \pm 0.07) \times 10^{20}$ W and $(1.53 \pm 0.27) \times 10^{20}$ W. Given the impossibility of accounting for such powers with the Alfvén-wing model, other models were explored to interpret the observations.

A simple model of the star–planet interaction assumes that coronal magnetic fields at the distance of their nearby planets have an energy density much larger than the thermal energy density and the kinetic energy density of the plasma, that is, $B^2/2\mu \gg p, \rho v^2/2$, where p is the plasma pressure, ρ its density, and v its velocity. (We have neglected the gravity because of the very low density of the plasma). We considered a stationary system and filtered out Alfvén waves, since their dissipated power is insufficient by at least 1 or 2 orders of magnitude to account for the observations.

This model extends the MHD regime (as usually adopted to model stellar coronal fields) up to the distance of hot Jupiters (Wiegelmann et al. 2017), which is not unreasonable in the case of stars such as HD 189733, whose level of magnetic activity is remarkably greater than that of our Sun. The situation has been explored in detail in a series of papers by Lanza (2008, 2009, 2012, 2013, 2018). Since pressure forces and gravity are too small to balance the Lorentz force in the regime considered, a stationary configuration is possible only if the Lorentz force vanishes:

$$\mathbf{J} \times \mathbf{B} = \frac{1}{\mu}(\nabla \times \mathbf{B}) \times \mathbf{B} = 0, \tag{2.1}$$

where we have expressed the current density $\mathbf{J} = (1/\mu)(\nabla \times \mathbf{B})$ by means of Ampere's law because the displacement current is negligible in MHD given the very small speed of the plasma in comparison with the speed of light. A magnetic field satisfying equation (2.1) is said to be *force-free.* We can recast equation (2.1) as

$$\nabla \times \mathbf{B} = \alpha \mathbf{B}, \tag{2.2}$$

where α is a scalar that is in general a function of position. By taking the divergence of both sides of equation (2.2) and considering that $\nabla \cdot \mathbf{B} = 0$, we obtain:

$$\mathbf{B} \cdot \nabla \alpha = 0, \tag{2.3}$$

telling us that α is constant along magnetic field lines.

In the framework of this simplified model, a magnetic field that interconnects the star with the planet has α constant along the interconnecting field lines. The magnetic field of the planet is potential because in the nearly neutral planetary atmosphere electric currents cannot propagate, implying $\mathbf{J} = 0$, that is, $\nabla \times \mathbf{B} = 0$, giving $\alpha = 0$ (cf. equation 2.2). An interconnecting field line therefore has $\alpha = 0$, implying that the stellar magnetic field is also potential along all the interconnecting structure. In general, the magnetic field of a stellar corona is not potential because the field stores energy in excess of the minimum corresponding to the potential field under the action of the stresses produced by photospheric motions. As a consequence, the stellar coronal field is generally topologically disconnected from the planetary field and the two fields interact only in the region of space where they come into contact (see Fig. 1), producing a release of power by magnetic reconnection P_{rec} given by:

$$P_{\mathrm{rec}} = \gamma \frac{\pi}{2\mu} B^2(a) R_{\mathrm{m}}^2 v_{\mathrm{rel}}, \tag{2.4}$$

where $0 < \gamma < 1$ is a factor depending on the angle between the field lines of the stellar and planetary fields, $B(a)$ is the stellar coronal field at the separation a of the planet, R_{m} the radius of the planetary magnetosphere, and v_{rel} the relative velocity between the field lines of the star and of the planet (see Lanza 2009, 2012). The power released by magnetic reconnection in the case of two topologically separated star–planet flux systems is $P_{\mathrm{rec}} \sim 10^{16} - 10^{19}$ W, assuming the stellar fields were measured by means of spectropolarimetric techniques in the above stars (Moutou et al. 2018) and a magnetic field strength of the hot Jupiters of the order of $\sim 10 - 100$ G.

When the stellar coronal field is potential, the formation of an interconnecting loop joining the stellar and planetary fields is possible (see Fig. 2). In this case the footpoints on the star and on the planet move with a relative velocity $v \approx v_{\rm orb}$, where $v_{\rm orb}$ is the orbital velocity of the planet and the power dissipated into the interconnecting loop is:

$$P_{\rm inter} \simeq \frac{2\pi}{\mu} f_{\rm AP} B_{\rm p}^2 R_{\rm p}^2 v, \tag{2.5}$$

where $f_{\rm AP}$ is the fraction of the planet's surface covered with the interconnecting field lines, $B_{\rm p}$ the strength of the planetary field at its poles, and $R_{\rm p}$ the radius of the planet (Lanza 2013). The dissipated power is of the order of $10^{21} - 10^{22}$ W in the case of the systems considered above, assuming $B_{\rm p} \sim 10 - 100$ G. This model is therefore a candidate for accounting for the observed power radiated by chromospheric hot spots, while the model based on the reconnection between two separated flux systems provides insufficient power, as in the case of the Alfvén-wing model.

By applying equation (2.5), Cauley et al. (2019) derived the first indirect estimates of the planetary magnetic fields in the four systems considered above, finding $B_{\rm p}$ between 20–120 G. They assumed that $\approx 0.2\%$ of the dissipated power $P_{\rm inter}$ was radiated by chromospheric hot spots in the Ca II H&K lines – an estimate based on observations of solar flares. Such magnetic field strengths are in agreement with a model proposed by Yadav & Thorngren (2017), which assumes that a fraction of the stellar insolation received by the planet is conveyed into the planetary interior, where it provides energy to power the planetary dynamo. It is interesting to note that the same extra power could provide an explanation for the inflated radii of hot Jupiters (for an introduction to this problem, see Laughlin 2018).

Numerical models of star-planet magnetic interactions that include the effects of plasma pressure and gravity have been presented by Cohen et al. (2009, 2011) and generally confirm the existence of interconnecting field configurations that can release large amounts of energy, sufficient to account for the power radiated by chromospheric hot spots. Models of stellar winds, including interactions with nearby planets, have been considered by, e.g., Vidotto et al. (2010, 2012, 2014); Cohen et al. (2014); Strugarek et al. (2017, 2019) and illustrate cases in which a planet passes from sub-Alfvénic to super-Alfvénic regimes along its orbit, and *vice versa*. This produces remarkable variations in the interaction strength and in the efficiency of the evaporation of the planetary atmosphere.

A classification of the different cases of interaction, based on the relative intensities of tides, winds and magnetic fields, has been proposed by Matsakos et al. (2015), and shows the important role of the evaporation of the planetary atmospheres in shaping the circumstellar environments in systems with hot Jupiters. The material evaporated from the planet can fall on the star, producing an energy release at specific orbital phases that can account for the flares observed preferentially just after the occultation of the planet in HD 189733 (Pillitteri et al. 2014, 2015, but see Lanza (2018) for an alternative explanation). In a different regime, the evaporated material can form a torus encircling the star, similar to what the simulations by Debrecht et al. (2018) show.

3 Statistical analyses of star–planet interactions, and some specific cases

In principle, the effects of the energy dissipated by nearby planets into the outer atmospheres of stars could be detected in a statistical study that considered planets at different separations and with different masses, because the interaction strength is expected to depend on those two parameters. Miller et al. (2015) reviewed previous investigations and performed a detailed analysis that looked for such a statistical correlation, but they obtained a generally negative result. A similar conclusion was reached in a more recent study by France et al. (2018). Nevertheless, Miller et al. (2015) found a subset of stars with hot Jupiters that showed a potentially significant correlation. Those stars do not usually show anomalously high activity in comparison to the expected level according to their rotation periods; nevertheless, their coronal emissions appear to be correlated with measures of the interaction strength such as $M_{\rm p} a^{-2}$ or a^{-1}, where $M_{\rm p}$ is the mass of the planet and a its separation from the star.

Some active stars with hot Jupiters, such as HD 189733 and CoRoT-2, have visual companions whose X-ray emission can be used to estimate the ages of the systems. The intriguing result is that the age found for both of them is of the order of several Gyrs, while their levels of activity point to much younger ages of $1.5 - 2.0$ and 0.5 Gyr, respectively (Poppenhaeger & Wolk 2014). Statistical studies of the rotation of stars with hot Jupiters indicate that they may be rotating faster than single stars of the same age (Pont 2009; Lanza 2010; Maxted et al. 2015). Tidal interactions do not appear capable of maintaining such a relatively rapid rotation in all the observed stars (Lanza 2010; Maxted et al. 2015), and it has therefore been suggested that a nearby massive planet may reduce the efficiency of the stellar wind responsible for braking the stellar rotation during their main-sequence life-times (Lanza 2010; Cohen et al. 2010).

The effect of a nearby massive planet on its host is not always that of increasing its rotation and activity level. The WASP-18 system is an example of a massive ($\sim 10.4 \pm 0.4$ $\mathrm{M_{Jup}}$), very close ($a \sim 0.0205$ AU) hot Jupiter orbiting an F6 V star that has a relatively normal rotation ($v \sin i \sim 10.9 \pm 0.7$ km s^{-1}) but whose level of activity is much lower than expected on the basis of its spectral type and rotation rate. The X-ray emission of WASP-18 is not detectable, i.e., it is at least two orders of magnitude lower than expected in a star in which the strength of Lithium absorption in its spectrum and its rotation rate (Pillitteri et al. 2014; Fossati et al. 2018) indicate an estimated age that is younger than ~ 1 Gyr. The conclusion is that the massive and very close planet is somehow quenching the stellar dynamo, although a detailed model of such a phenomenon has not yet been proposed.

In view of these observations, the lack of a general correlation between the level of stellar activity and the parameters measuring the strength of the star–planet interaction could be the result of considering together systems in which opposite effects manifest themselves. A more detailed investigation is clearly needed before we can exclude any possible effects of nearby planets on stellar activity. More specifically, a better understanding of the physical mechanisms through which nearby planets affect their hosts is required.

In this context, it is worth mentioning the intriguing correlation found by Hartman (2010), and confirmed by Figueira et al. (2014), between the chromospheric stellar emission as measured by the index $\log R'_{\mathrm{HK}}$ and the gravity of a transiting planet that can be derived directly from the measurements of the stellar radial velocity and the depth of the transit, without the need for any specific stellar model (Sozzetti et al. 2007). According to such a correlation, stars with nearby planets having a stronger gravity are statistically more active. Lanza (2014) proposed an explanation based on the evaporation of the planetary atmosphere producing an accumulation of plasma in a torus encircling the star, thus generalizing the model proposed by Fossati et al. (2013) in the case of WASP-12. Plasma condensations forming inside the torus can absorb selectively the flux in the cores of the Ca II *H&K* lines, reducing the observed chromospheric emission. Planets with a stronger gravity have a lower evaporation rate, leading to smaller absorption by the circumstellar torus and an apparent higher level of activity. A more detailed investigation by Fossati et al. (2015) gave support to this interpretation, although an alternative explanation has been proposed by Collier Cameron & Jardine (2018).

Collier Cameron & Jardine (2018) showed that more massive nearby planets are statically younger than less massive planets, and are therefore found preferentially around more active stars because the level of stellar activity declines with stellar age. Since the radius of massive planets is more or less independent of their mass, more massive planets generally have a stronger gravity, and that could explain the observed correlation. In the framework of this interpretation, the correlation between $\log R'_{\mathrm{HK}}$ and M_{p} should be stronger than the correlation between the chromospheric index and the surface gravity of the planets, yet the observations show the opposite (Hartman 2010; Fossati et al. 2015), giving more support to the other interpretation.

The possibility of photospheric activity phenomena produced by the interaction with a nearby planet is based on circumstantial evidence, mainly coming from the modelling of the observations obtained with *CoRoT* and *Kepler*. CoRoT-2 (Lanza et al. 2009) and CoRoT-6 (Lanza et al. 2011) show evidence of a short-term activity cycle and an active longitude, respectively, that could be related to star–planet interactions (see Lanza 2011, for details). Kepler-17 (Désert et al. 2011) and HAT-P-11 (Béky et al. 2014) show spots that rotate with periods commensurable with the orbital periods of their hot Jupiters, respectively. Sound conclusions cannot be based on a few cases, especially because we lack a theoretical framework for understanding the processes that could be responsible for such phenomena. We therefore hope to make decisive progress in this field with *PLATO* (Rauer et al. 2014), which should provide us with a larger sample of systems upon which to base our investigations of these effects.

4 Conclusions

Some recent results in the field of star–planet magnetic interactions have been reviewed, focussing on the relevant observations and some analytical or numerical models proposed for their interpretation. This is a rapidly growing field that promises to shed light on the processes occurring in the interiors of exoplanets, mainly hot Jupiters, where magnetic fields are generated, and on the effects produced by a nearby planet on the stellar hydromagnetic dynamo and chromospheric or coronal heating.

AFL is grateful to the Scientific Organizing Committee for their kind invitation to attend the Conference and deliver a keynote talk on the topic of this paper.

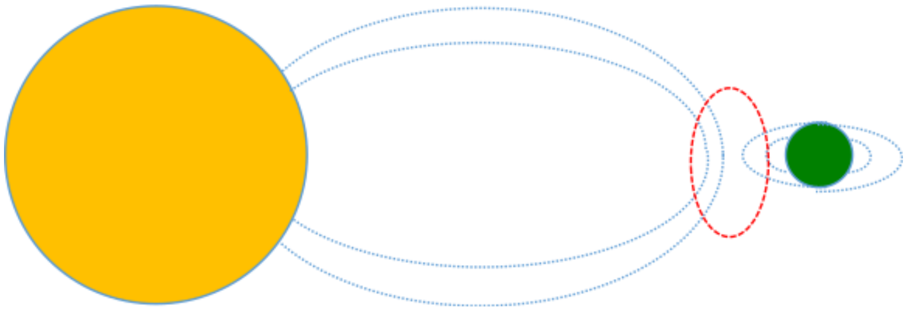

Fig. 1. Sketch of a configuration with separate flux systems for the star and the planet. Some magnetic field lines are indicated by the dotted blue lines. This configuration typically occurs when the stellar field in our simplified model is non-potential. The section of the star is rendered in yellow-orange, while the planet is in green, and the region where the magnetic fields of the stellar and planetary flux systems interact is encircled by the dashed red line. Magnetic reconnection occurs inside that region (see text for more detail).

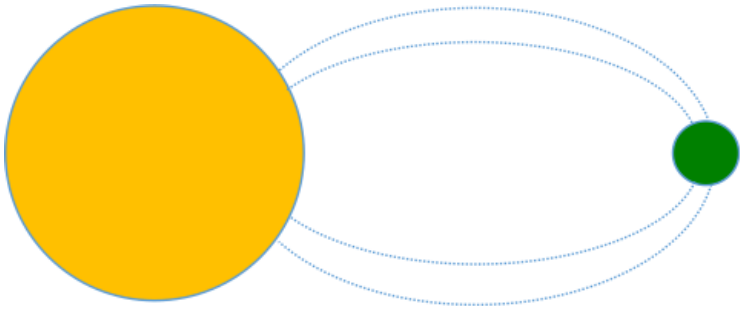

Fig. 2. Sketch of a magnetic loop connecting the stellar coronal field with a nearby planet (see Fig. 1 for more details). In the framework of the simplified model introduced in the text, this configuration is possible when the stellar magnetic field is potential. The planet field is connected directy with the stellar field without any ionosphere that prevents the field from reaching the planetary surface.

References

Adams, F. C. 2011, ApJ, 730, 27

Airapetian, V. S., Barnes, R., Cohen, O., et al. 2019, arXiv e-prints, arXiv:1905.05093

Béky, B., Holman, M. J., Kipping, D. M., & Noyes, R. W. 2014, ApJ, 788, 1

Cauley, P. W., Shkolnik, E. L., Llama, J., Bourrier, V., & Moutou, C. 2018, AJ, 156, 262

Cauley, P. W., Shkolnik, E. L., Llama, J., & Lanza, A. F. 2019, Nature Astronomy, 408

Cohen, O., Drake, J. J., Glocer, A., et al. 2014, ApJ, 790, 57

Cohen, O., Drake, J. J., Kashyap, V. L., et al. 2009, ApJ, 704, L85

Cohen, O., Drake, J. J., Kashyap, V. L., Sokolov, I. V., & Gombosi, T. I. 2010, ApJ, 723, L64

Cohen, O., Kashyap, V. L., Drake, J. J., Sokolov, I. V., & Gombosi, T. I. 2011, ApJ, 738, 166

Collier Cameron, A. & Jardine, M. 2018, MNRAS, 476, 2542

Debrecht, A., Carroll-Nellenback, J., Frank, A., et al. 2018, MNRAS, 478, 2592

Désert, J.-M., Charbonneau, D., Demory, B.-O., et al. 2011, ApJS, 197, 14

Driscoll, P. E. 2018, Planetary Interiors, Magnetic Fields, and Habitability, in Handbook of Exoplanets, H. Deeg and J. A. Belmonte (Eds.) (Springer), 76

Figueira, P., Oshagh, M., Adibekyan, V. Z., & Santos, N. C. 2014, A&A, 572, A51

Fossati, L., Ayres, T. R., Haswell, C. A., et al. 2013, ApJ, 766, L20

Fossati, L., Ingrassia, S., & Lanza, A. F. 2015, ApJ, 812, L35

Fossati, L., Koskinen, T., France, K., et al. 2018, AJ, 155, 113

France, K., Arulanantham, N., Fossati, L., et al. 2018, ApJS, 239, 16

Hartman, J. D. 2010, ApJ, 717, L138

Lanza, A. F. 2008, A&A, 487, 1163

Lanza, A. F. 2009, A&A, 505, 339
Lanza, A. F. 2010, A&A, 512, A77
Lanza, A. F. 2011, Ap&SS, 336, 303
Lanza, A. F. 2012, A&A, 544, A23
Lanza, A. F. 2013, A&A, 557, A31
Lanza, A. F. 2014, A&A, 572, L6
Lanza, A. F. 2018, A&A, 610, A81
Lanza, A. F., Bonomo, A. S., Pagano, I., et al. 2011, A&A, 525, A14
Lanza, A. F., Pagano, I., Leto, G., et al. 2009, A&A, 493, 193
Laughlin, G. 2018, Mass-Radius Relations of Giant Planets: The Radius Anomaly and Interior Models, in Handbook of Exoplanets, H. Deeg and J. A. Belmonte (Eds.) (Springer), 1
Matsakos, T., Uribe, A., & Königl, A. 2015, A&A, 578, A6
Maxted, P. F. L., Serenelli, A. M., & Southworth, J. 2015, A&A, 577, A90
Miller, B. P., Gallo, E., Wright, J. T., & Pearson, E. G. 2015, ApJ, 799, 163
Moutou, C., Fares, R., & Donati, J.-F. 2018, Magnetic Fields in Planet-Hosting Stars, in Handbook of Exoplanets, H. Deeg and J. A. Belmonte (Eds.) (Springer), 21
Neubauer, F. M. 1980, J. Geophys. Res., 85, 1171
Pillitteri, I., Maggio, A., Micela, G., et al. 2015, ApJ, 805, 52
Pillitteri, I., Wolk, S. J., Sciortino, S., & Antoci, V. 2014, A&A, 567, A128
Pont, F. 2009, MNRAS, 396, 1789
Poppenhaeger, K. & Wolk, S. J. 2014, A&A, 565, L1
Rauer, H., Catala, C., Aerts, C., et al. 2014, Experimental Astronomy, 38, 249
Saur, J. 2018, Electromagnetic Coupling in Star-Planet Systems, in Handbook of Exoplanets, H. Deeg and J. A. Belmonte (Eds.) (Springer), 27
Saur, J., Grambusch, T., Duling, S., Neubauer, F. M., & Simon, S. 2013, A&A, 552, A119
Shkolnik, E., Bohlender, D. A., Walker, G. A. H., & Collier Cameron, A. 2008, ApJ, 676, 628
Shkolnik, E., Walker, G. A. H., & Bohlender, D. A. 2003, ApJ, 597, 1092
Shkolnik, E., Walker, G. A. H., Bohlender, D. A., Gu, P. G., & Kürster, M. 2005, ApJ, 622, 1075
Sozzetti, A., Torres, G., Charbonneau, D., et al. 2007, ApJ, 664, 1190
Strugarek, A. 2016, ApJ, 833, 140
Strugarek, A. 2018, Models of Star-Planet Magnetic Interaction, in Handbook of Exoplanets, H. Deeg and J. A. Belmonte (Eds.) (Springer), 25
Strugarek, A., Bolmont, E., Mathis, S., et al. 2017, ApJ, 847, L16
Strugarek, A., Brun, A. S., Donati, J. F., Moutou, C., & Réville, V. 2019, ApJ, 881, 136
Vidotto, A. A., Fares, R., Jardine, M., et al. 2012, MNRAS, 423, 3285
Vidotto, A. A., Jardine, M., Morin, J., et al. 2014, MNRAS, 438, 1162
Vidotto, A. A., Opher, M., Jatenco-Pereira, V., & Gombosi, T. I. 2010, ApJ, 720, 1262
Wiegelmann, T., Petrie, G. J. D., & Riley, P. 2017, Space Sci. Rev., 210, 249
Yadav, R. K. & Thorngren, D. P. 2017, ApJ, 849, L12

Stars and their variability observed from space
C. Neiner, W. W. Weiss, D. Baade, R. E. Griffin, C. C. Lovekin, A. F. J. Moffat (eds)

DYNAMICS OF STAR-DISK INTERACTION PROCESSES IN YOUNG, LOW-MASS STARS AS SEEN FROM SPACE

L. Venuti[1]

Abstract. High-precision time series photometry provides a unique window into the dynamics of the inner disk regions (< 1 AU) around young stars (< 5-10 Myr), at spatial scales hardly accessible via direct imaging techniques. In this review, we discuss the breakthrough brought in by space-based missions in our understanding of the physics and characteristic timescales of variability of protoplanetary disks in connection with their host stars. Our review is based on several young clusters and star-forming regions monitored with the *CoRoT* (NGC 2264) and *Kepler*/K2 (ρ Ophiuchus, Upper Scorpius) satellites. These regions virtually cover every stage of the disk lifetimes. In each region, hundreds of young, low-mass stars with disks were monitored nearly continuously for 30 to 80 days. The precision and homogeneity of such space-borne data allowed us to identify several distinct classes of young star-disk variables: spotted, quasi-periodic, stochastic, bursters, and dippers. The intrinsic timescales of variability that pertain to each light-curve class are indicative of the characteristic timescales of interaction between the stars and their inner disks, which are in turn related to the dynamical evolution of inner disk structures. The observed photometric behaviors can be associated with at least two distinct paradigms of star-disk interaction: an unstable regime, with erratic flux variations that trace intense and short-lived bursts of mass accretion onto the star, and a stable regime, with ordered accretion streams from the inner disk onto the star. These distinct scenarios may be related to different stages of the inner disk evolution, in an interplay with external and environmental conditions.

Keywords: Accretion, accretion disks – Stars: low-mass – Stars: pre-main sequence – Stars: variables: T Tauri – Open clusters and associations: individual: NGC 2264, ρ Ophiuchus, Upper Scorpius

1 Introduction

Over the last few years, our view of protoplanetary disks around pre–main sequence (PMS; ∼1–10 Myr–old) stars has undergone a dramatic revolution, thanks in particular to the advent of the ALMA telescope, which revealed their varied morphologies (rings, gaps, cavities, shadows) in astounding detail. However, even for the protoplanetary disks closest to us (e.g., TW Hydrae; Andrews et al. 2016), the spatial scales (∼0.1 AU) of the region around the central star, where the magnetospheric star–disk interaction develops, fall well below the limiting resolution that can be achieved in those images. Monitoring the photometric variability of young stars therefore provides the most direct observational approach to unveil the nature and characteristic timescales of the physical processes that govern the inner disk regions. While the variable nature of young stars has been known for decades (Joy 1945; Herbig 1962, and references therein), only in recent years have the exquisite photometric precision, sampling, and time coverage brought in by space–based observatories (MOST, *Spitzer*, *CoRoT*, *Kepler*) enabled appreciating the wide range of distinct photometric behaviors that PMS stars with disks can exhibit. In this contribution, we review the main drivers of variability in young, low–mass stars, and discuss what their light curves reveal on the structure and dynamical evolution of the inner disk environment.

2 The variability of young, low–mass stars

The distinctive variable nature of young solar–type stars (T Tauri stars, TTS; $M_\star \lesssim 1-2\ M_\odot$) can be associated with a variety of mechanisms. At the very basic level, photometric variability on rotational timescales (i.e., days to weeks; see, e.g., Venuti et al. 2017; Roquette et al. 2017) is driven by the presence of unevenly–distributed

In collaboration with A. M. Cody (NASA Ames Research Center, CA, USA), J. R. Stauffer (Spitzer Science Center, IPAC, Caltech, CA, USA), L. M. Rebull (Infrared Science Archive, IPAC, Caltech, CA, USA), J. Bouvier (Institut de Planétologie et d'Astrophysique de Grenoble, France), S. H. P. Alencar (Universidade Federal de Minas Gerais, Brazil), S. B. Howell (NASA Ames Research Center, CA, USA), CSI2264 Team, and *Kepler*/K2 Team.

[1] NPP fellow, NASA Ames Research Center, Moffett Field, CA 94035, USA

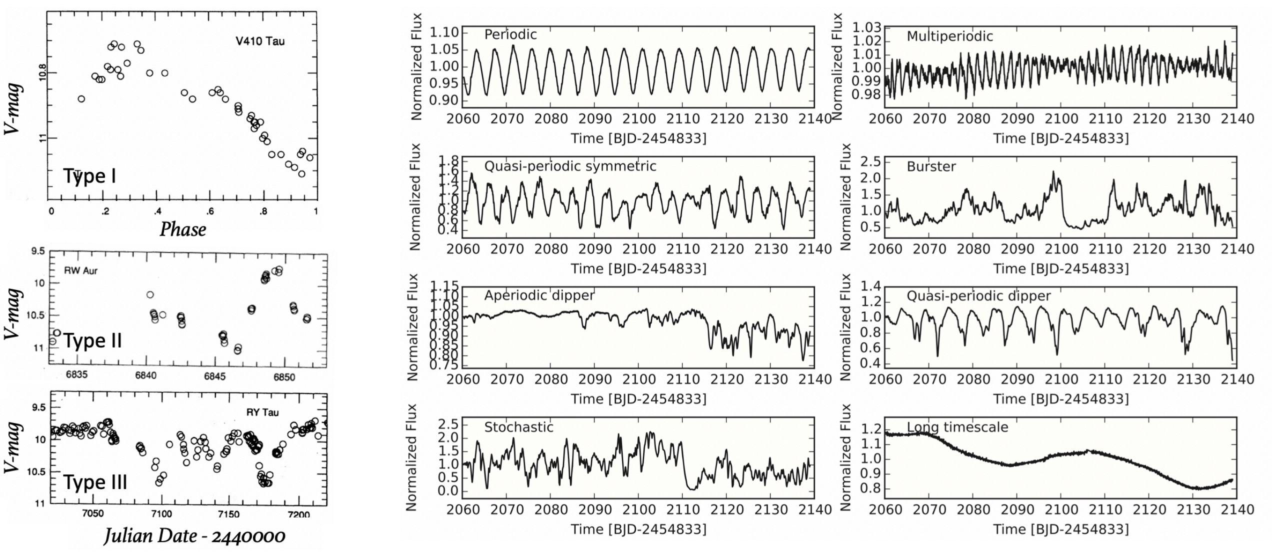

Fig. 1. *Left*: Examples of the three different types of TTS variability identified by Herbst et al. (1994) from ground–based data: cold spot modulation (Type I), mix of cold spots and accretion shocks (Type II), and circumstellar obscuration (Type III). Adapted from Herbst et al. (1994). *Right*: Different classes of variability identified among disk–bearing stars in ρ Ophiuchus and Upper Scorpius from *Kepler*/K2 data. Reproduced from Cody & Hillenbrand (2018).

dark spots at the stellar surface, which are produced by enhanced magnetic activity of the same type observed in our Sun. More intense, and often irregular, variability can be contributed by the process of magnetically–driven interaction between the central star and the inner disk, regulated in particular by accretion of material from the disk onto the star (see Hartmann et al. 2016 for a recent review). The rapidly–evolving accretion shocks that form when the accretion stream impacts the star modulate the luminosity of the star on timescales varying between their intrinsic lifetimes and the stellar rotation timescales. A key role in the observed variability properties is also played by the specific geometry of the star–disk system (from edge–on to face–on) with respect to the observer's line-of–sight, which determines what features of the system come into view.

2.1 TTS variability: a ground–based perspective

A first morphological classification of the different types of variability that TTS can exhibit was presented in the seminal work by Herbst et al. (1994), who identified three distinct variability classes (Fig. 1, *left*). The first type of variability, predominantly associated with TTS with no evidence of ongoing mass accretion (weak–lined T Tauri stars, WTTS), manifested as periodic flux variations that could be explained by rotational modulation by cold surface spots. The second type of variability, characteristic of T Tauri stars actively accreting from their disks (classical T Tauri stars, CTTS), manifested as "generally irregular variations on timescales as short as hours", with larger variability amplitudes than those measured for variables of the first type, and likely driven by a changing mix of magnetic spots and accretion shocks at the stellar surface. The third type of variability, also associated with disk–bearing objects, manifested as irregular and asymmetric flux variations on timescales of days to weeks, with pronounced fading events interspersed with a more slowly–varying luminosity continuum, and was tentatively attributed to variable circumstellar obscuration. However, the sparseness of ground–based observations hampered the identification of the distinct characteristic timescales of variability that pertain to young stars, and the limitedness of the early stellar samples prevented a statistical appreciation of how common different types of variability are among TTS.

2.2 The space–borne revolution in studies of TTS variability

Over the last decade, dedicated space–based monitoring campaigns have dramatically changed our understanding of TTS variability. Thanks to photometric precisions of the order of mmag, and to nearly continuous monitoring with a cadence of minutes over baselines of months, such campaigns enabled a synoptic view of TTS behavior over the time domain on all timescales from several hours (sensitive to short–term variations in accretion) to several rotational cycles (sensitive to dynamic changes in the innermost disk regions, near the co-rotation radius).

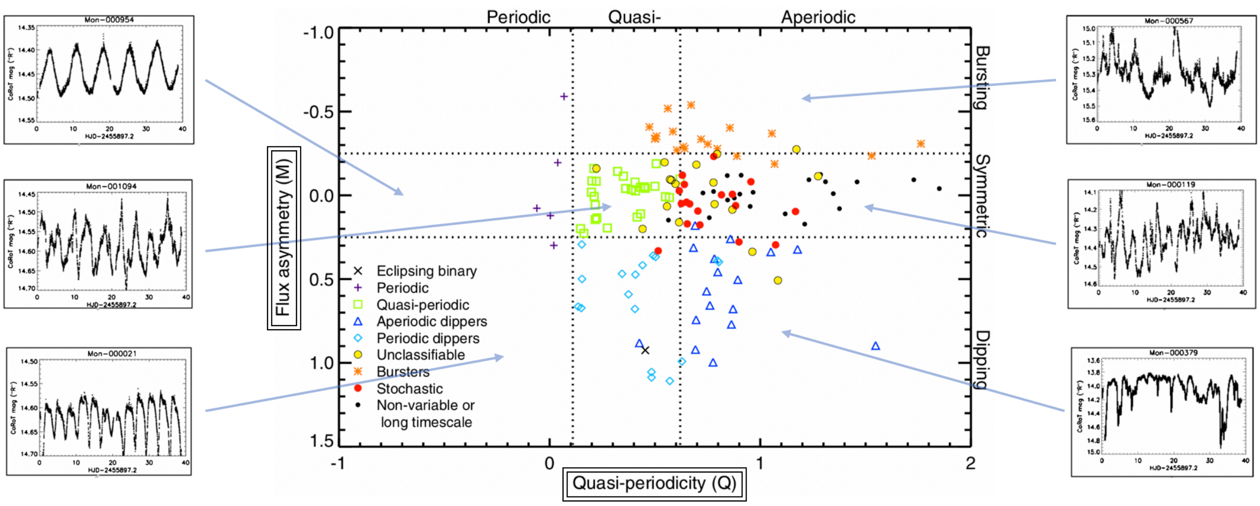

Fig. 2. Metrics defined in Cody et al. (2014) to categorize the variability behaviors of CTTS, applied to NGC 2264 members monitored with *CoRoT*. The side panels show selected examples of light curves for different classes: periodic (left, top), quasi–periodic (left, middle), periodic dipper (left, bottom), burster (right, top), stochastic (right, middle), and aperiodic dipper (right, bottom). Adapted from Cody et al. (2014).

A main revelation brought in by high–precision space photometry is that the actual variety of time behaviors observed among CTTS extends well beyond the broad classes identified from the ground (Fig. 1, *right*). The first large–scale monitoring campaign of thousands of TTS in 12 star–forming regions, the Young Stellar Object VARiability project (YSOVAR; Morales-Calderón et al. 2011; Rebull et al. 2014), was conducted in the early 2010s with *Spitzer*/IRAC at mid-infrared wavelengths, sensitive to the thermal emission from the inner disk. At the end of 2011, the scope of the YSOVAR project was expanded into the Coordinated Synoptic Investigation of NGC 2264 (CSI2264; Cody et al. 2014), a dedicated campaign of variability monitoring across the wavelength and time domains for over 500 TTS in the NGC 2264 region (∼3–5 Myr; Dahm 2008), employing the *CoRoT* (optical), *Spitzer* (mid-infrared), and Chandra (X-rays) satellites, in addition to several other telescopes and instruments (e.g., CFHT/MegaCam, VLT/Flames), from ground and from space.

CSI2264 enabled a first statistical definition of metrics to classify the variability behaviors exhibited by CTTS (Cody et al. 2014), according to how periodic (or aperiodic) the light curve patterns are, and to how symmetric (or asymmetric) the flux variations are with respect to the typical luminosity state of the star (Fig. 2). Based on these parameters, the original classification into three types of variability for TTS could be expanded into eight distinct classes among CTTS alone: *periodic* (with stable light curve patterns over timescales of months), *quasi–periodic symmetric* (with small–scale irregular variability superimposed over an overall periodic light curve pattern), *multiperiodic* (which may exhibit a beating or pulsating pattern, or recurring eclipses added to the "continuum" variability), *bursters* (irregular variability with a preference for brightening events above the light curve continuum), *periodic dippers* (with flux dips regularly spaced over a flatter continuum), *aperiodic dippers* (which exhibit prominent dimming events with no obvious periodicity), *stochastic* (irregular variability with no preference for brightening events over dimming events or vice versa), and *long-timescale* variables (with a light-curve pattern that appears to change across the whole duration of the time series). These distinct behaviors are likely associated with different properties of the circumstellar environment and different modes of star–disk interaction, as discussed in the following section. It is not uncommon for individual CTTS to also switch between different types of photometric behaviors on timescales as short as years, perhaps as a result of more dramatic changes in the inner disk structure on hundreds of rotational timescales (Sousa et al. 2016).

3 Young star variability and star–disk interaction

In the currently accepted paradigm of magnetospheric accretion in CTTS, the stellar magnetosphere connects and drives the interaction between the central star and the inner disk, truncated at a distance of a few stellar radii from the stellar surface. Columns of material are lifted from the disk midplane and channeled along the magnetic field lines until they impact the star in localized regions close to the stellar poles. The hot accretion shocks generated at the stellar surface modulate the observed luminosity of the star, with an overall stable

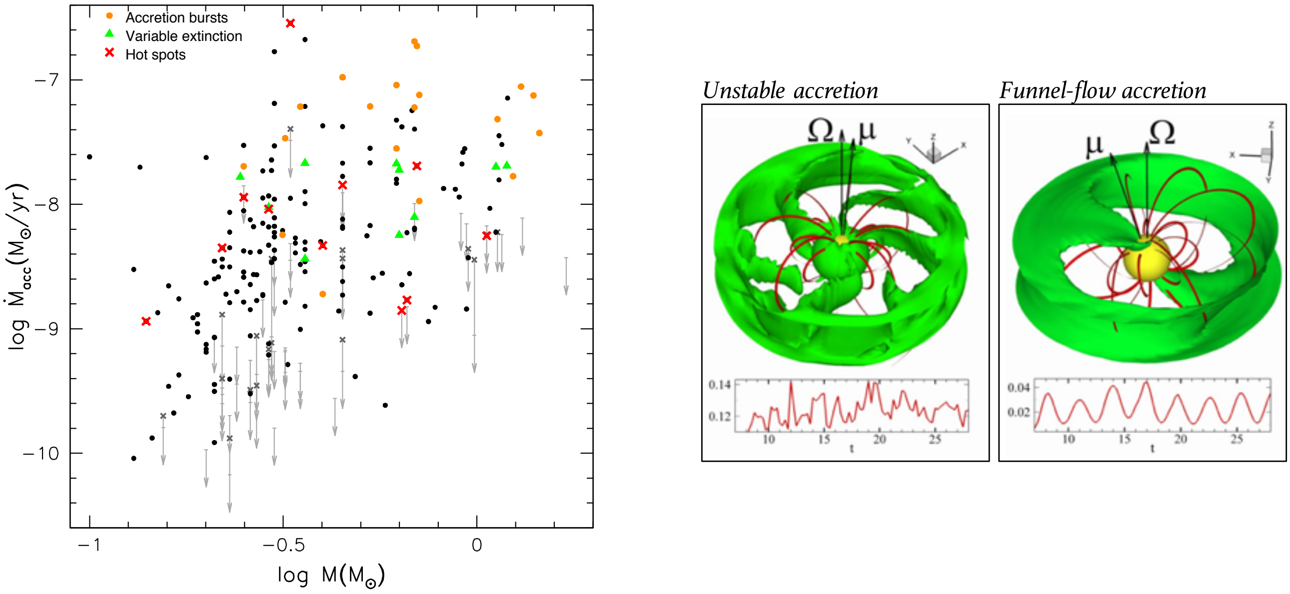

Fig. 3. *Left*: Accretion rates measured, as a function of mass, for CTTS in NGC 2264. Orange circles, green triangles, and red crosses highlight the accretion properties for stars that exhibit a bursting, dipping, or periodic behavior, respectively. Adapted from Venuti et al. (2014). *Right*: Models of CTTS accreting in an unstable or in a stable regime, and corresponding variability predicted for the star on rotation timescales. Adapted from Kulkarni & Romanova (2008).

pattern over several rotational cycles (e.g., Romanova et al. 2004). However, theoretical models also predict different scenarios of star–disk interaction, driven by instabilities at the disk–magnetosphere interface. In these cases, accretion does not proceed in an ordered fashion, but rather in stochastic tongues of material that impact the star surface at random locations, producing intense accretion events and rapidly evolving accretion features (e.g., Kulkarni & Romanova 2008; Fig. 3, *right*). Very different photometric variability signatures are expected in these two scenarios; however, the irregular and short–lived nature of the phenomena associated with an unstable regime of star–disk interaction hampered the identification of such scenarios from the ground.

Thanks to the cadence and duration of space–based data, and to the coordinated exploration of variability across the wavelength domain, CSI2264 was the first campaign to provide observational evidence for the coexistence of distinct modes of star–disk interaction among a given CTTS population. Accretion and disk properties were shown to be the discriminating factor between irregular and regular variability (Venuti et al. 2014; Sousa et al. 2016; Stauffer et al. 2016). Burster stars, in particular, were found to be associated with the strongest accretion rates detected (Fig. 3, *left*), and their light curve patterns were shown to match the theoretical predictions for young stars accreting in an unstable regime (Stauffer et al. 2014). Dipper stars (McGinnis et al. 2015) and periodic or quasi–periodic stars, instead, were found to correspond to more moderate levels of accretion, similar to each other. These photometric behaviors are interpreted to both arise in a scenario of ordered funnel–flow accretion, for different geometries of the star–disk system: in highly inclined systems, the inner disk warp at the base of the accretion columns may periodically occult part of the stellar photosphere, therefore producing the observed flux dips (Bodman et al. 2017); in low–inclination systems, instead, the line–of–sight to the star is not obstructed by inner disk structures, and the observed variability is dominated by accretion hotspot modulation. A bursting behavior is statistically found among CTTS with the thickest inner disks, while less conspicuous infrared excesses are statistically found among dipper stars and quasi–periodic stars.

4 Young star variability and disk evolution

Over the past five years, the *Kepler* repurposed mission, K2 (Howell et al. 2014), has provided an excellent opportunity to extend the census of CTTS photometric behaviors, established during CSI2264, to several other star–forming regions: ρ Ophiuchus and Upper Scorpius (1–3 Myr and 5–10 Myr, respectively; Cody et al. 2017; Cody & Hillenbrand 2018), the Lagoon Nebula (∼2 Myr; Venuti et al., in preparation), and Taurus (∼2 Myr; Rebull et al., in preparation; Cody et al., in preparation). These regions span the entire age range during which

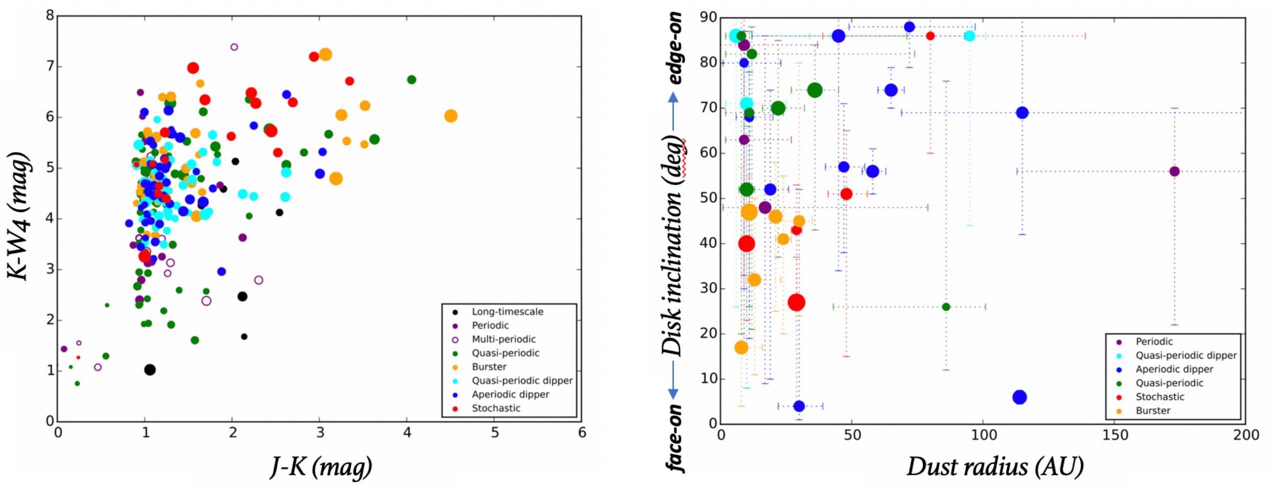

Fig. 4. *Left*: Near- and mid-infrared color properties for CTTS in the ρ Ophiuchus and Upper Scorpius regions, distinguished according to the morphology class of their K2 light curves. Adapted from Cody & Hillenbrand (2018). *Right*: Distribution of CTTS in ρ Ophiuchus and Upper Scorpius, sorted according to their photometric behaviors, as a function of disk inclination and inner disk radius, measured from ALMA data. Adapted from Cody & Hillenbrand (2018).

circumstellar disks are statistically observed to evolve and disperse (e.g., Fedele et al. 2010); therefore, they represent an ideal sample to investigate how the dynamics of interaction between the star and the inner disk regions changes in the course of disk evolution and as a function of the environment.

At the end of the K2 mission, and midway through the analysis of its legacy dataset on young star clusters, the global picture of CTTS variability that is emerging indicates that around 50% of young stars with disks typically exhibit repeated variability patterns, with a periodicity that can be clearly extracted from months–long monitoring data. This suggests that dynamic changes in the inner disk region typically take place over timescales of several rotational cycles. Irregular variability behaviors (bursting, stochastic) appear to be consistently associated with stars that exhibit larger amounts of infrared emission (indicative of more conspicuous inner disks) than dipper stars and quasi–periodic variables (Fig. 4, *left*). Interestingly, the distinction in infrared properties between irregular and regular variables appears to be more marked well into the mid–infrared regime ($\sim$20 μm) than in the near– or early mid–infrared. This indicates that disk instabilities that drive an irregular variability behavior may originate beyond the innermost, and hottest, disk regions (Cody & Hillenbrand 2018).

Preliminary statistics may indicate an overall increase in the occurrence of quasi-periodic and dipping behaviors, and a decrease in the fraction of stochastic behaviors, with cluster age. This would suggest that, as the disks become more evolved, more moderate and stable regimes of star–disk interaction are favored over unstable patterns. However, no obvious trends with the average cluster age are revealed by current data on the fraction of burster stars among CTTS ($\sim$13%). These statistics might be reconciled with the suggestion of a global evolutionary trend by assuming a non–negligible age spread among the population of a given cluster; in each cluster, a bursting behavior may be associated with the youngest, most strongly accreting members (e.g., Venuti et al. 2014, in the NGC 2264 region). However, no clear evidence of such an effect could be deduced for the ρ Opiuchus and Upper Scorpius populations (Cody et al. 2017).

Dipper stars are especially interesting targets to probe the inner disk structure and variability. The large number of dipper stars documented during the K2 mission, combined with the results from ALMA surveys of protoplanetary disks in young star clusters in the solar neighborhood (e.g., Barenfeld et al. 2016), has enabled a direct confirmation of the fact that CTTS with a dipping behavior tend to exhibit highly inclined disks (Fig. 4, *right*), which supports the interpretation of their photometric behavior in terms of inner disk warp occultation. However, this dataset also unveiled several remarkable cases of a dipping behavior found in stars whose outer disks (imaged with ALMA) are observed nearly face–on (e.g., Ansdell et al. 2016). The only scenario where a highly–inclined inner disk and a nearly face–on outer disk can be reconciled is a picture where the initial disk evolves into disconnected and misaligned inner and outer disks, perhaps as a result of dynamical interactions with a stellar companion (Facchini et al. 2018) or a gap–carving protoplanet. More investigations are required to assess how common such scenarios may be during disk evolution, and the potential impact on the host star.

5 Conclusions

Space-based monitoring of young stars has been pivotal in revealing the structure and characteristic timescales of the inner circumstellar environment. Large–scale surveys conducted, among others, with *CoRoT* and *Kepler* have documented a large diversity of photometric behaviors for young stars with disks, from periodic to stochastic and from bursting to dipping. Such photometric behaviors provide the most direct observational signatures of distinct modes of interaction between the stars and their inner disks, ranging from stable and ordered to unstable and chaotic. The typical timescales of variability observed for young stars indicate that structural changes in the inner disk can take place on characteristic timescales of several rotation periods (i.e., weeks). Shorter timescales of variability are instead associated with erratic accretion events, often aperiodic but recurring. The breakthroughs achieved during the past decade have demonstrated the great potential of coordinated efforts which combine multiple diagnostics to unveil the nature and interplay of the different processes that govern the complex star–disk environment. Numerous open questions remain, such as on the connection between stellar, inner disk, and outer disk evolution, and on the link between different timescales of variability, from hours, to weeks, to several years. Current and future missions like TESS, PLATO, and LSST will be key to continuing the exploration of young star variability as a function of stellar mass, age, and external environment, in order to unveil what parameters may drive different patterns of star–disk evolution and planet formation.

References

Andrews, S. M., Wilner, D. J., Zhu, Z., et al. 2016, ApJ, 820, L40
Ansdell, M., Gaidos, E., Williams, J. P., et al. 2016, MNRAS, 462, L101
Barenfeld, S. A., Carpenter, J. M., Ricci, L., & Isella, A. 2016, ApJ, 827, 142
Bodman, E. H. L., Quillen, A. C., Ansdell, M., et al. 2017, MNRAS, 470, 202
Cody, A. M. & Hillenbrand, L. A. 2018, AJ, 156, 71
Cody, A. M., Hillenbrand, L. A., David, T. J., et al. 2017, ApJ, 836, 41
Cody, A. M., Stauffer, J., Baglin, A., et al. 2014, AJ, 147, 82
Dahm, S. E. 2008, The Young Cluster and Star Forming Region NGC 2264, Vol. 4 (ASP Monograph Publications), 966
Facchini, S., Juhász, A., & Lodato, G. 2018, MNRAS, 473, 4459
Fedele, D., van den Ancker, M. E., Henning, T., Jayawardhana, R., & Oliveira, J. M. 2010, A&A, 510, A72
Hartmann, L., Herczeg, G., & Calvet, N. 2016, ARA&A, 54, 135
Herbig, G. H. 1962, Advances in Astronomy and Astrophysics, 1, 47
Herbst, W., Herbst, D. K., Grossman, E. J., & Weinstein, D. 1994, AJ, 108, 1906
Howell, S. B., Sobeck, C., Haas, M., et al. 2014, PASP, 126, 398
Joy, A. H. 1945, ApJ, 102, 168
Kulkarni, A. K. & Romanova, M. M. 2008, MNRAS, 386, 673
McGinnis, P. T., Alencar, S. H. P., Guimarães, M. M., et al. 2015, A&A, 577, A11
Morales-Calderón, M., Stauffer, J. R., Hillenbrand , L. A., et al. 2011, ApJ, 733, 50
Rebull, L. M., Cody, A. M., Covey, K. R., et al. 2014, AJ, 148, 92
Romanova, M. M., Ustyugova, G. V., Koldoba, A. V., & Lovelace, R. V. E. 2004, ApJ, 610, 920
Roquette, J., Bouvier, J., Alencar, S. H. P., Vaz, L. P. R., & Guarcello, M. G. 2017, A&A, 603, A106
Sousa, A. P., Alencar, S. H. P., Bouvier, J., et al. 2016, A&A, 586, A47
Stauffer, J., Cody, A. M., Baglin, A., et al. 2014, AJ, 147, 83
Stauffer, J., Cody, A. M., Rebull, L., et al. 2016, AJ, 151, 60
Venuti, L., Bouvier, J., Cody, A. M., et al. 2017, A&A, 599, A23
Venuti, L., Bouvier, J., Flaccomio, E., et al. 2014, A&A, 570, A82

Stars and their variability observed from space
C. Neiner, W. W. Weiss, D. Baade, R. E. Griffin, C. C. Lovekin, A. F. J. Moffat (eds)

CEPHEID SPHERES OF INFLUENCE

N. R. Evans[1], H. M. Günther[2], H. E. Bond[3], G. H. Schaefer[4], B. D. Mason[5], M. Karovska[1], E. Tingle[1], S. Wolk[1], S. Engle[6], E. Guinan[6], I. Pillitteri[7], C. Proffitt[8], P. Kervella[9] and A. Gallenne[10]

Abstract. Satellite data from *HST*, *Chandra*, *XMM*, *IUE*, and *Gaia* have provided important information for multiple systems containing Cepheids in order to supplement ground-based light and velocity studies. Since systems containing massive stars frequently have multiple components, many approaches are needed to derive the parameters of the components. The distribution of separations and mass ratios are of particular interest here. The final segment of the *HST* WFC3 survey (companions between 0.5 and 5.0″) identifies companions between 100 and 2000 AU. They have the unusual property that *all* have an inner binary as well. This is in contrast to the overall Cepheid population in which 29% are spectroscopic binaries, suggesting that the dynamical evolution of these triple systems plays a part in setting the configuration.

Keywords: Stars: Cepheids, companions, star formation, massive stars

1 Introduction

Like many stars with intermediate or large masses, Cepheids (typically 5 $M_\odot$ stars) are frequently found in binary and multiple systems. Multiple systems such as these provide observational input for investigating many topics:

1. Star formation: the formation of multiple components involves processes such as core fragmentation and disk fragmentation; the resulting properties are functions of the total mass of the system and the separation between components.

2. Dynamical evolution: dynamical interaction between components can occur either before the system settles into an hierarchical configuration or through the Kozai-Lidov mechanism.

3. Mergers: Cepheid progenitors (B stars) include a high fraction of binaries with periods as short as a few days. Post-red-giant Cepheids do not have orbits shorter than one year, implying that shorter orbits have undergone Roche Lobe overflow (RLOF) after their main-sequence phases, and many have merged.

4. Exotic end stage objects: Cepheids are destined to become compact objects, many in multiple systems. Multiple systems containing a compact object (a white dwarf in the case of a Cepheid) give rise to objects such as high-mass X-ray binaries, cataclysmic variables and (in more massive systems) supernovæ. The properties of Cepheid multiple systems furnish the ingredients for these outcomes.

2 Surveys

Studies in recent years have provided detailed information about the components of Cepheid multiple systems. We now have surveys (each containing an average of 70 stars) of spectroscopic binaries (Evans et al. 2015), hot companions observed with *IUE* (Evans 1992), resolved companions (Evans et al. 2016a) and *Gaia* proper motions (Kervella et al. 2019), plus a number of close systems resolved by interferometry (Gallenne et al. 2018).

[1] Smithsonian Astrophysical Observatory, MS 4, 60 Garden St., Cambridge MA, 02138 USA
[2] MIT, 77 Massachusetts Avenue, NE83-557,Cambridge, MA 02139 USA
[3] Dept. Astronomy and Astrophysics, Pennsylvania State Univ., University Park, PA, 16802, USA
[4] The CHARA Array, Georgia State University, P.O. Box 3965, Atlanta GA 30302-3965, USA
[5] US Naval Observatory, 3450 Massachusetts Ave., NW, Washington, D.C. 20392-5420, USA
[6] Department of Astronomy and Astrophysics, Villanova University, 800 Lancaster Ave., Villanova, PA, 19085, USA
[7] INAF-Osservatorio di Palermo, Piazza del Parlamento 1,I-90134 Palermo, Italy
[8] Space Telescope Science Institute, 3700 San Martin Drive, Baltimore, MD 21218, USA
[9] LESIA, Observatoire de Paris, Université PSL, CNRS, Sorbonne Université, Univ. Paris Diderot, Sorbonne Paris Cité, 5 place Jules Janssen, 92195 Meudon, France
[10] Université Cote d'Azur, OCA, CNRS, Lagrange, Parc Valrose, Bat. Fizeau, 06108 Nice Cedex 02, France

This suite of programmes has provided coverage of parameter space wider than the orbital destruction limit of one year and mass ratios M_2/M_1 down to 0.4. The *IUE* survey, for instance, identified companions with no separation-dependent bias.

The *HST* imaging survey is just being completed. Data were observed with Wide Field Camera 3 (WFC3) in two filters which transform to V and I. The first segment (Evans et al. 2016a) covered companions more than 5" from the much brighter Cepheid. That was followed with *XMM* X-ray observations of 14 out of 39 Cepheids with resolved companion candidates to identify X-ray activity in stars young enough to be Cepheid companions, as opposed to old field stars (Evans et al. 2016b). In that sample, one young star (R Cru) was identified has having a separation of 7.6". S Nor was noted as a system whose young companion was at the greatest separation (14.6"), but since it is in a cluster, the companion could be another cluster member rather than a gravitationally bound companion. Closer companions require careful point spread function (psf) correction. Fig. 1 illustrates that for V659 Cen. Full details are to be given in (Evans, et al, 2020 in preparation), and will concentrate on systems whose companions are found within 5" of the Cepheid.

3 Results

The most surprising result concerned the 7 systems systems which have resolved companions within 2" (roughly 500 au) of the Cepheid. Each of the 7 systems with a resolved companion also has an inner spectroscopic binary. This is in sharp contrast to the result from the sample of 70 Cepheids (Evans et al. 2015), where less than one third occur in spectroscopic binaries. There are two possibilities that could explain how this unusual property in the sample with resolved companions might arise.

One possibility is star formation itself; the other is dynamic evolution within these multiple star systems. A number of complex processes which are involved in these intermediate-mass multiple systems are mentioned above: star formation, dynamical evolution within the system, or possibly that some of the components had undergone RLOF that resulted in mergers in some cases. Is it possible to disentangle these complex processes? The finding that wide companions seem to require an inner binary provides a clue to a dominant process. In a model of sequential star formation, outer components are formed first, and inner components form subsequently through disk fragmentation. This sequence seems unlikely to produce wide components *only* if an inner binary is going to be formed, since the outer components will not be able to anticipate that there will in the future be an inner binary formed. On the other hand, dynamical evolution of the system seems consistent with other systems that contain both a resolved companion and a spectroscopic binary, i.e., three stars were formed but the ultimate location of the components was set by interactions among the components of a triple system.

4 Conclusions

Observations have provided good distributions of the separations and mass ratios in Cepheids. As with other systems containing reasonably massive stars, the components can be tricky to disentangle, particularly since many systems contain more than two stars. However the Cepheid studies from *HST*, *Chandra*, *XMM*, *IUE* and *Gaia* are providing data on the distributions of separations and mass ratios. In particular, they provide clues to star formation, yieldibng the implication that the dynamical evolution of the systems is important.

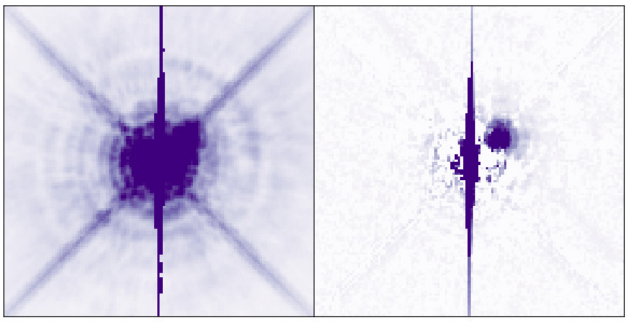

Fig. 1. Left: *HST* image of V659 Cen, showing a square of ∼6" around the Cepheid. The companion is visible, but the image is very complicated. **Right:** The remaining image after point-spread-function correction. The companion is now seen clearly.

Support for this work was provided by NASA through grants from the STScI (GO-12215.01-A and GO-13368.01-A), which is operated by the Association of Universities for Research in Astronomy, Incorporated, under NASA contract NAS5-26555. Support for this work was also provided from the Chandra X-ray Center, NASA Contract NAS8-03060. This work has made use of data from the ESA mission *Gaia* (`https://www.cosmos.esa.int/gaia`), processed by the *Gaia* Data Processing and Analysis Consortium (DPAC, `https://www.cosmos.esa.int/web/gaia/dpac/consortium`). Funding for the DPAC has been provided by national institutions, in particular those participating in the *Gaia* Multilateral Agreement.

References

Evans, N. R. 1992, ApJ, 384, 220

Evans, N. R., Berdnikov, L., Lauer, J., et al. 2015, AJ, 150, 13

Evans, N. R., Bond, H. E., Schaefer, G. H., et al. 2016a, AJ, 151, 129

Evans, N. R., Pillitteri, I., Wolk, S., et al. 2016b, AJ, 151, 108

Gallenne, A., Kervella, P., Evans, N. R., et al. 2018, ApJ, 867, 121

Kervella, P., Gallenne, A., Remage Evans, N., et al. 2019, A&A, 623, A116

Stars and their variability observed from space
C. Neiner, W. W. Weiss, D. Baade, R. E. Griffin, C. C. Lovekin, A. F. J. Moffat (eds)

THE DISTANCE OF THE LONG-PERIOD CEPHEID RS PUPPIS FROM ITS REMARKABLE LIGHT ECHOES

P. Kervella[1]

Abstract. The Milky Way Cepheid RS Puppis is a particularly important calibrator for the Leavitt law (the Period–Luminosity relation). It is a rare long-period pulsator ($P = 41.5$ days), and a good analogue of the Cepheids observed in distant galaxies. It is the only known Cepheid that is embedded in a large (≈ 0.5 pc) dusty nebula which scatters the light from the pulsating star. DOwing to the light travel time-delay introduced by scattering on the dust, the brightness and colour variations of the Cepheid imprint spectacular light echoes on the nebula. This brief overview of the studies of this phenomenon focus in particular on polarimetric imaging obtained with the HST/ACS camera. These observations enabled us to determine the geometry of the nebula and the distance of RS Pup. That distance determination is important in the context of calibrating both the Baade-Wesselink technique and the Leavitt law.

Keywords: stars: distances, distance scale, variables: Cepheids, techniques: polarimetric, scattering, photometric

1 Introduction

The high intrinsic brightness and the tight relation between period and luminosity established by the Leavitt law (Leavitt 1908; Leavitt & Pickering 1912) make long-period Cepheids the most precise standard candles for the determination of extragalactic distances. Their relatively high mass ($m \approx 10 - 15\,M_\odot$) together with the brevity of their passage across the instability strip combine to make them very rare stars. As a result, only a handful of long-period Cepheids ($P > 30$ d) are located within a few kiloparsecs of the Sun. RS Puppis (HD 68860) (period $P = 41.5$ d) is among the most luminous Cepheids in the Milky Way. This article presents the remarkable light echoes that occur in its circumstellar nebula, and how the distance to the Cepheid can be derived from observating them. It also describes how modelling of the pulsation of RS Pup, and the calibration of the Baade-Wesselink projection factor have been carried out.

2 Light echoes in the nebula of RS Puppis

The circumstellar dusty nebula of RS Puppis was discovered by Westerlund (1961). This author proposed that the presence of the dusty environment results in the creation of “light echoes” of the photometric variations of the Cepheid (see, e.g., Sugerman (2003) for a review of this phenomenon). The variable illumination wavefronts emitted by the Cepheid propagate in the nebula, where they are scattered by dust grains. The additional optical path of the scattered light compared to the light coming directly from the Cepheid causes the appearance of a time delay (and therefore a phase difference) between the Cepheid cycle as observed directly and the photometric variation of the dust in the nebula.

The first detection of the light echoes of RS Pup was achieved by Havlen (1972). More than 30 years later CCD observations were collected by Kervella et al. (2008) using the EMMI imager on the 3.6-m ESO NTT. Those authors derived a distance based on the phase lag of selected dust knots with respect to the Cepheid. However, Bond & Sparks (2009) objected that the hypothesis of coplanarity of the selected dust knots was probably incorrect (see also Feast (2008)), and that a determination of the 3D structure of the dust is necessary to derive the distance using the echoes. To measure that distribution, polarimetric imaging has been shown to be a powerful technique, as applied for instance on V838 Mon by Sparks et al. (2008) (see also Sparks (1994)). Using that technique, Kervella et al. (2012) determined the structure of the nebula from ground-based observations with VLT/FORS. The dust is distributed over a relatively thin ovoidal shell, probably swept away by the strong radiation pressure from the Cepheid’s light. They concluded that the mass of the dust in the

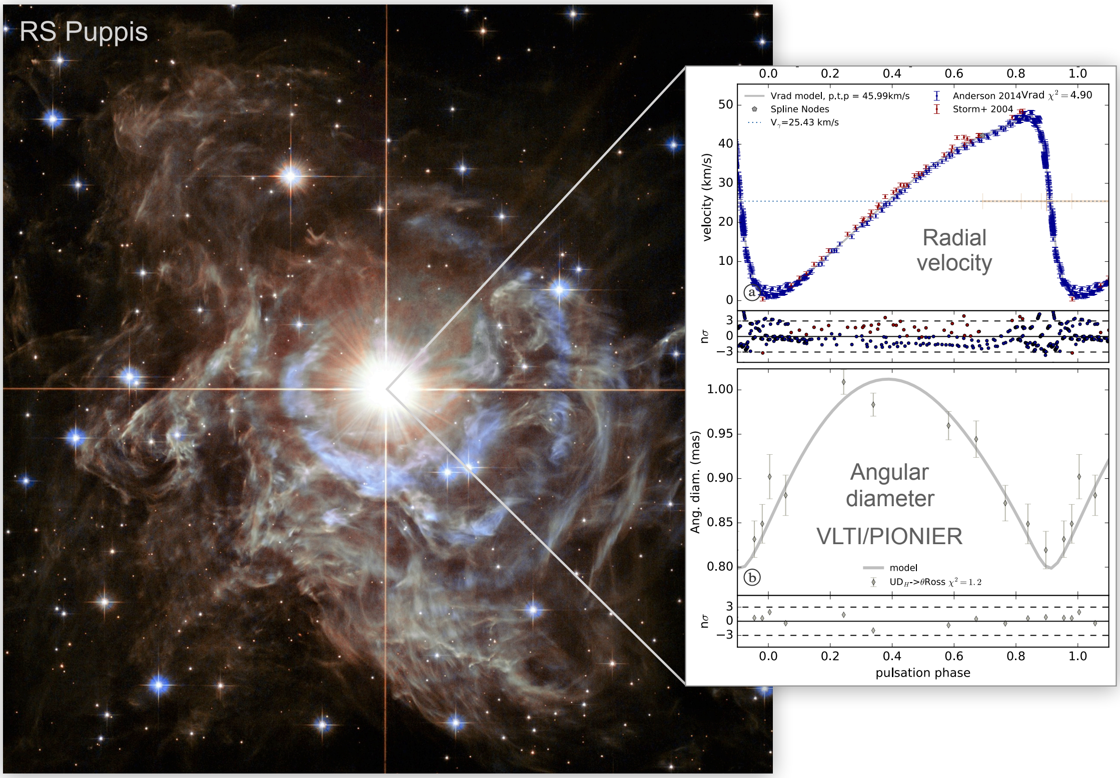

Credit: NASA, ESA, and the Hubble Heritage Team

Fig. 1. Left: HST/ACS colour image of the RS Pup nebula (Kervella et al. 2014). The light echoes of the maximum light phase are visible as irregular blue rings caused by the hotter temperature of the star at its maximum light. **Right:** Radial-velocity and angular-diameter data used for modelling the pulsation of the Cepheid (Kervella et al. 2017).

nebula is too large to be explained by mass loss from the Cepheid itself, and that the nebula is a pre-existing interstellar dust cloud in which the Cepheid is temporarily embedded.

However, the VLT/FORS polarimetric images are seeing-limited and could not provide a sufficiently detailed map of the structure of the nebula. A time-sequence of polarimetric images of RS Pup was therefore obtained by Kervella et al. (2014) using the HST/ACS. They showed in spectacular detail the structure of the nebula (Fig. 1 left panel), and the propagation of the echoes (Fig. 2; see also `https://vimeo.com/108581936` for a video of the light echoes), and the degree of linear polarization of the scattered light across the nebula.

The combination of the polarization information and the phase delay of the light echoes across the nebula result in a distance of 1910 ± 80 pc (4.2%), equivalent to a parallax of $\varpi = 0.524 \pm 0.022$ mas (Kervella et al. 2014). That value is significantly different from the parallax of RS Pup $\varpi_{\mathrm{GDR2}} = 0.613 \pm 0.026$ mas (adopting a *Gaia* parallax shift of $+29\,\mu$as) reported in the second *Gaia* data release (Gaia Collaboration et al. 2018). The parallax of a field star interacting with the RS Pup nebula (labelled S1, $\varpi[\mathrm{S1}] = 0.532 \pm 0.048$ mas; Kervella et al. (2019)) is, however, consistent with the distance of the light echo to the Cepheid.

3 Pulsation modelling and the projection factor

The classical Baade-Wesselink (BW) distance determination technique (also known as the parallax-of-pulsation) is based on a comparison of the linear amplitude of the radius variation of a pulsating star with its angular amplitude (see, e.g., Groenewegen (2008)). The SPIPS approach is a recent BW implementation presented by Mérand et al. (2015) that uses a combination of spectroscopic radial velocity, multi-band photometry and interferometric angular diameters to build a consistent model of the pulsating photosphere of the star.

[1] LESIA, Observatoire de Paris, Université PSL, CNRS, Sorbonne Université, Univ. Paris Diderot, Sorbonne Paris Cité, 5 place Jules Janssen, 92195 Meudon, France

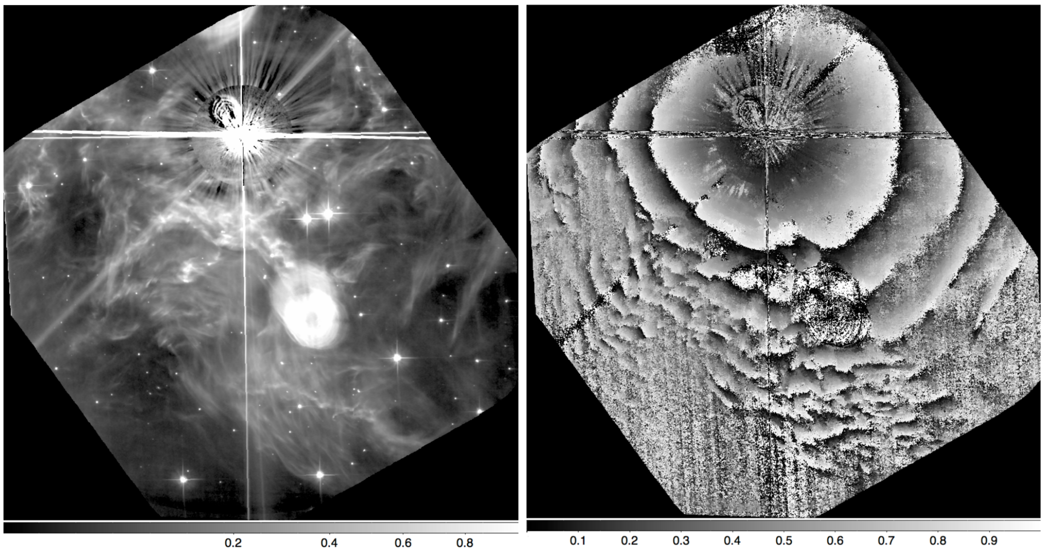

Fig. 2. Left: Mean scattered light intensity around RS Pup (Kervella et al. 2014) (arbitrary grey scale). **Right:** Phase delay of the light variation across the nebula with respect to the Cepheid cycle.

A strong limitation of the BW technique comes from the fact that the distance and the spectroscopic projection factor (p-factor) are fully degenerate. The p-factor is defined as the ratio between the photospheric velocity and the disk-integrated radial velocity measured from spectroscopy (Nardetto et al. 2014). The p-factor is presently the major limiting factor in terms of accuracy for the application of the BW technique; research is particularly active on this topic (Groenewegen 2007; Storm et al. 2011a; Ngeow et al. 2012; Pilecki et al. 2013; Breitfelder et al. 2015, 2016; Nardetto et al. 2017; Nardetto 2018). Using the VLTI/PIONIER optical interferometer, Kervella et al. (2017) measured the changing angular diameter of RS Pup over its pulsation cycle (Fig. 1, right panel). Those measurements, together with the light-echo distance from the HST/ACS observations, enabled those authors to resolve the degeneracy between the distance and the p-factor, and to obtain a p-factor value of $p = 1.25 \pm 0.06$ for RS Pup.

4 Conclusion

The determination of an accurate distance to RS Pup using its light echoes is an important step towards a reliable calibration of the Leavitt law, as it is still, even after the second *Gaia* data release (Gaia Collaboration et al. 2018), the most accurate distance estimate today to a long-period Cepheid. Moreover, this original technique is independent of the trigonometric parallax, enabling an independent validation. The light-echo distance can also be employed to calibrate the Baade-Wesselink method, especially the p-factor. A reliable calibration of this classical technique provides a solid basis for estimating the distances of Cepheids that are too far for direct trigonometric parallax measurements with *Gaia*. While BW analyses of individual Cepheids is accessible at present only out to the LMC and SMC (Storm et al. 2004, 2011b; Gallenne et al. 2017), it could soon become possible, with extremely large telescopes like the E-ELT or the TMT, to determine the distances of individual Cepheids in significantly more distant galaxies of the Local Group.

The research leading to these results has received funding from the European Research Council (ERC) under the EU's Horizon 2020 research and innovation programme (grant agreement No. 695099, project CepBin). Support for Program number GO-13454 was provided by NASA through a grant from the STScI, which is operated by the Association of Universities for Research in Astronomy, Incorporated, under NASA contract NAS5-26555. Some of the data presented in this paper were obtained from the Multimission Archive at the STScI (MAST). Support for MAST for non-HST data is provided by the NASA Office of Space Science via grant NAG5-7584, and by other grants and contracts.

References

Bond, H. E. & Sparks, W. B. 2009, A&A, 495, 371

Breitfelder, J., Kervella, P., Mérand, A., et al. 2015, A&A, 576, A64

Breitfelder, J., Mérand, A., Kervella, P., et al. 2016, A&A, 587, A117

Feast, M. W. 2008, MNRAS, 387, L33

Gaia Collaboration, Brown, A. G. A., Vallenari, A., et al. 2018, A&A, 616, A1

Gallenne, A., Kervella, P., Mérand, A., et al. 2017, A&A, 608, A18

Groenewegen, M. A. T. 2007, A&A, 474, 975

Groenewegen, M. A. T. 2008, A&A, 488, 25

Havlen, R. J. 1972, A&A, 16, 252

Kervella, P., Bond, H. E., Cracraft, M., et al. 2014, A&A, 572, A7

Kervella, P., Gallenne, A., Evans, N. R., et al. 2019, A&A, 623, A117

Kervella, P., Mérand, A., Szabados, L., et al. 2008, A&A, 480, 167

Kervella, P., Mérand, A., Szabados, L., et al. 2012, A&A, 541, A18

Kervella, P., Trahin, B., Bond, H. E., et al. 2017, A&A, 600, A127

Leavitt, H. S. 1908, Annals of HCO, 60, 87

Leavitt, H. S. & Pickering, E. C. 1912, HCO Circular, 173, 1

Mérand, A., Kervella, P., Breitfelder, J., et al. 2015, A&A, 584, A80

Nardetto, N. 2018, in IAU Symposium, Vol. 330, Astrometry and Astrophysics in the Gaia Sky, ed. A. Recio-Blanco, P. de Laverny, A. G. A. Brown, & T. Prusti, 335–336

Nardetto, N., Poretti, E., Rainer, M., et al. 2017, A&A, 597, A73

Nardetto, N., Storm, J., Gieren, W., Pietrzyński, G., & Poretti, E. 2014, in IAU Symposium, Vol. 301, IAU Symposium, ed. J. A. Guzik, W. J. Chaplin, G. Handler, & A. Pigulski, 145–148

Ngeow, C.-C., Neilson, H. R., Nardetto, N., & Marengo, M. 2012, A&A, 543, A55

Pilecki, B., Graczyk, D., Pietrzyński, G., et al. 2013, MNRAS, 436, 953

Sparks, W. B. 1994, ApJ, 433, 19

Sparks, W. B., Bond, H. E., Cracraft, M., et al. 2008, AJ, 135, 605

Storm, J., Carney, B. W., Gieren, W. P., et al. 2004, A&A, 415, 531

Storm, J., Gieren, W., Fouqué, P., et al. 2011a, A&A, 534, A94

Storm, J., Gieren, W., Fouqué, P., et al. 2011b, A&A, 534, A95

Sugerman, B. E. K. 2003, AJ, 126, 1939

Westerlund, B. 1961, PASP, 73, 72

Stars and their variability observed from space
C. Neiner, W. W. Weiss, D. Baade, R. E. Griffin, C. C. Lovekin, A. F. J. Moffat (eds)

BRITE PHOTOMETRIC VARIABILITY OF THE INTRIGUING WOLF-RAYET STAR WR6: ROTATIONAL OR BINARY MODULATIONS?

N. St-Louis[1], A.F.J Moffat[1], T. Ramiaramanantsoa[2] and G. Lenoir-Craig[1]

Abstract. This paper presented preliminary results from a simultaneous photometric and spectroscopic observing campaign of the WR star WR6, of spectral subtype WN4b. The combination of BRITE-Constellation photometry over a time-interval of nearly 160 days and optical spectroscopy over more than 100 days led to a unique dataset, both in time coverage and temporal resolution.

Keywords: Stars: Wolf-Rayet, rotation , winds, outflows

1 Introduction

WR6 is a Wolf-Rayet (WR) star of subtype WN4b; it exhibits a mass-loss rate of $\dot{M}$=6.3×10^{-5} M$_\odot$yr^{-1} (Hamann et al. 2019) and a terminal velocity of 1900 kms^{-1} (Prinja et al. 1990). It has long been known to present periodic variability in spectroscopy (e.g. St-Louis et al. 1995; Morel et al. 1997), photometry and polarimetry (e.g. Robert et al. 1992) with a period of 3.77 days but without any clear evidence of a massive companion. Although periodic, the changes have been shown to be *epoch-dependent* (e.g. Robert et al. 1992) and there is therefore certainly a transient phenomenon involved in the process of generating the variability.

The two most common interpretations for the periodic nature of the variability are (a) the presence of large-scale structures in the wind (e.g. St-Louis et al. 2018) in the form of Corotation Interaction Regions (CIRs, Cranmer & Owocki 1995) and (b) a binary system with a low-mass companion (e.g. Schmutz & Koenigsberger 2019). We discuss briefly the BRITE-Constellation observations of WR6 and simultaneous optical spectroscopy obtained by amateur astronomers as members of the Southern Astro Spectroscopy Email Ring (SASER) collaboration.

2 BRITE Photometry

Figure 1 presents the complete light-curve of WR6 obtained between 2015 October 18 and 2016 April 16 by the BRITE-Toronto satellite equipped with a red optical filter. The mean error for these observations is 0.0037 mag. Large-amplitude variability can clearly be seen, with a peak-to-peak amplitude of $\Delta m \sim$0.08.

A period search using the Discrete Fourier Transform technique included in the Period04 package (Lenz & Breger 2005) yielded one independant frequency (ν_1= 0.26712±00013) and at least three different harmonics (ν_2= 0.53199±0.00012, ν_3= 0.78729±0.00016, ν_4= 1.06399±0.00022), indicating (as Fig. 1 shows) that the curve is highly non-sinusoidal. By combining all those harmonics, we calculated a mean period of 3.768 days; we adopt that in this paper.

As the variations are known to be epoch dependent, we carried out a time-frequency analysis of our data using a tapered sliding window covering a time interval of 25 days with an overlap of 50%. We found that the result of this analysis was not very sensitive to either the size of the sliding widow or the overlap interval. Our results are shown in the left panel of Figure 2. The epoch-dependent nature of the variability can clearly be seen, with different combinations of harmonics dominating at different times. The typical stability of a given variability pattern seems to be roughly 30–40 days. The right panel shows a dynamic plot illustrating the evolution of the light-curve as a function of cycle number. Each row presents the light-curve for a given cycle; the magnitudes that are smaller than the global mean are plotted in progressive shades of blue and those higher in progressive shades of red. The curve changes from having one or two peaks whose widths and separation also evolve.

[1] Département de physique, Université de Montréal, C.P. 6128, Succ. Centre-Vile, Montréal (QC), H3C 3J7, Canada
[2] Arizona State University, School of Earth and Space Exploration, 781 Terrace Mall, Rm 770A Tempe, AZ 85287, USA

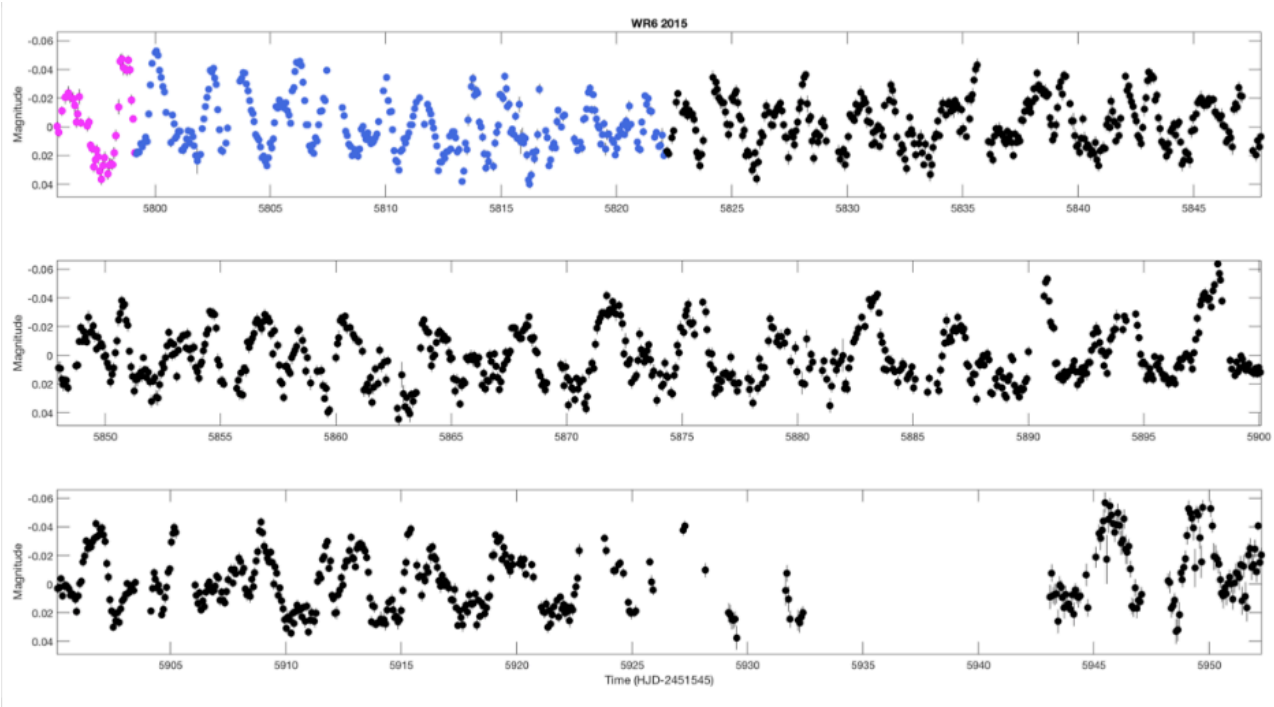

Fig. 1. BRITE light-curve of WR6 obtained by BRITE-Toronto. Satellite-orbital mean fluxes were calculated and the overall mean flux was removed. Various instrument settings (change in the observing conditions; see Popowicz et al. 2017) are plotted in different colours.

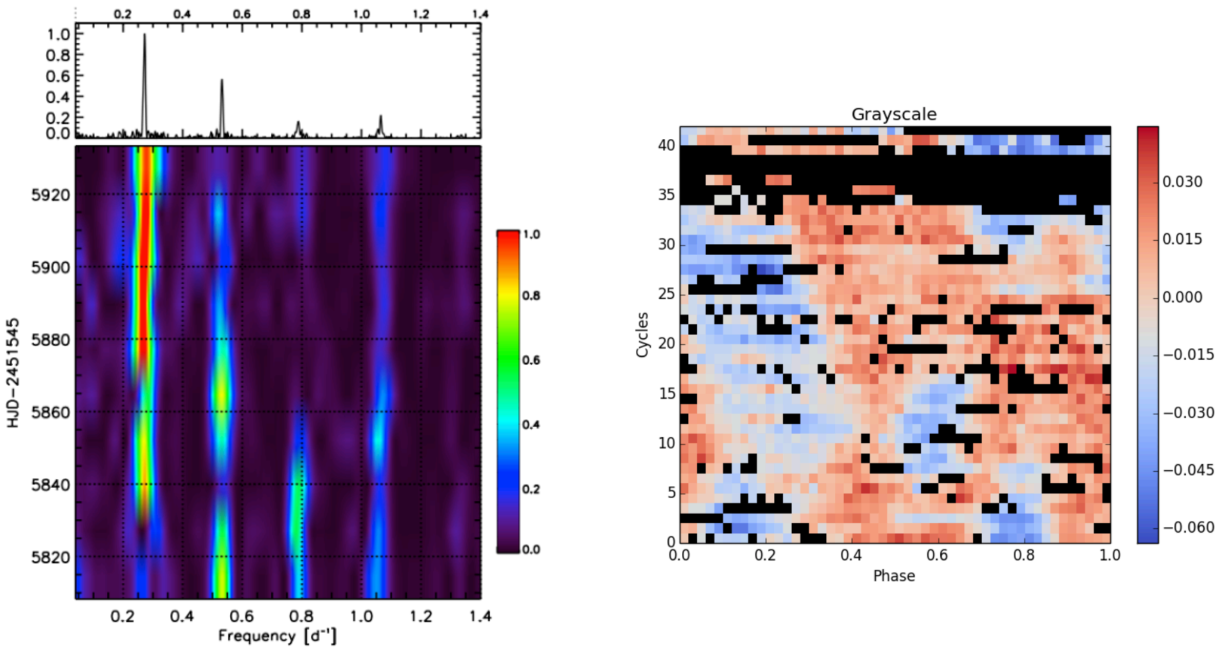

Fig. 2. Left: Time-frequency Fourier transform analysis of our BRITE light-curve of WR6. **Right**: Dynamic plot showing the evolution over time of the periodic variability of WR6. The black regions indicate data gaps.

3 Optical Spectroscopy

Through a fruitful collaboration with a group of four amateur astronomers from the SASER collaboration (Paul Luckas, Paulo Cacella, Bernard Heathcote and Terry C. Bohlsen), we were able to secure 105 optical spectra

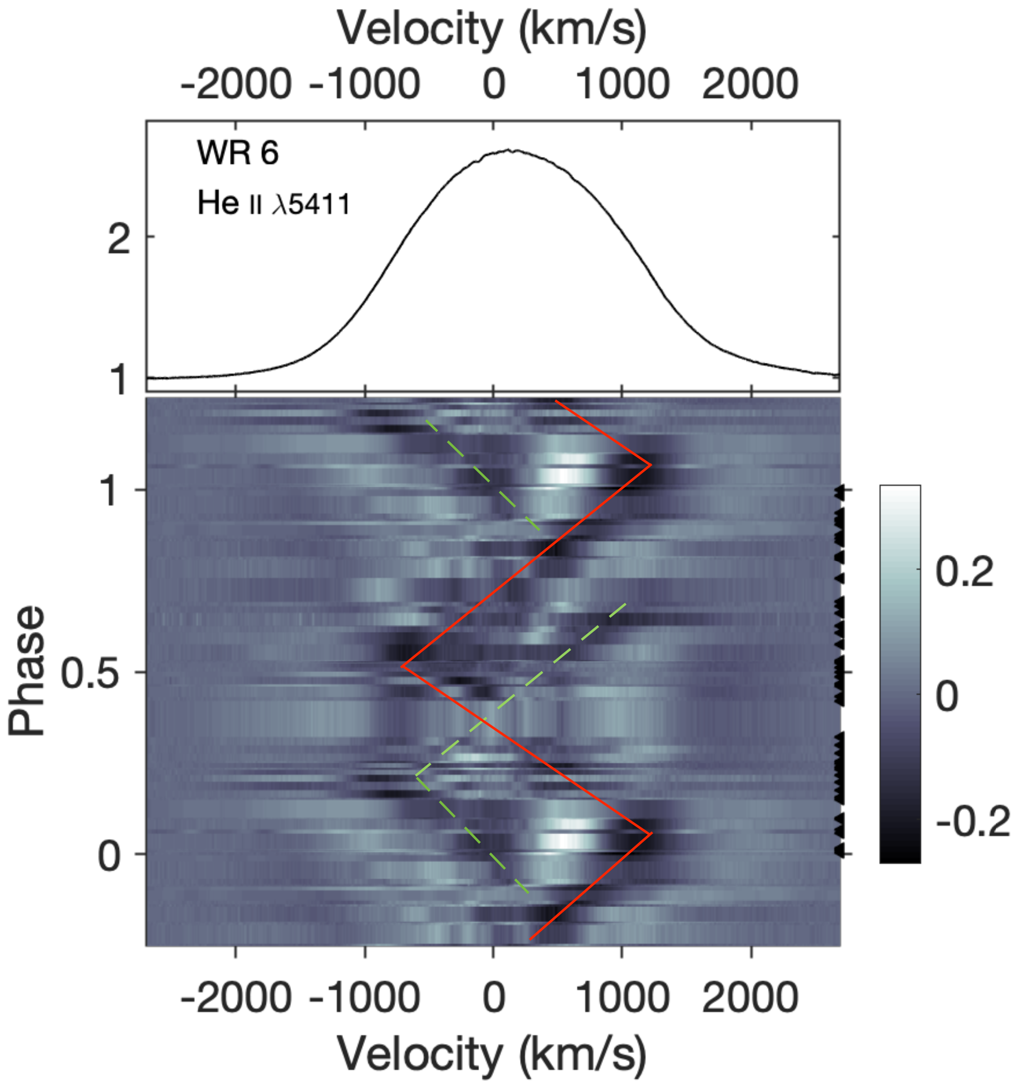

Fig. 3. Dynamic plot showing differences from the global mean of a subset of our optical spectra around the HeIIλ5411 transition as a function of phase of the 3.768-day period.

centred on the HeIIλ5411 emission line between 2016 January 15 to April 28, in parallel with the BRITE observations. A wavelength-dependent CLEAN Fourier analysis of the spectroscopic time-series revealed a period of 3.73±0.06 days and its first three harmonics across the extent of the HeIIλ5411 line profile, which is compatible – within the errors – with our adopted photometric period. A careful analysis of the spectroscopic variability revealed that the nature of the variability changeed over the 104 days of our observing period. We therefore chose a smaller time-interval to present the spectroscopic variability as a function of phase for our adopted 3.768-day period.

We selected a time-interval of slightly more than 50 days (∼15 cycles of the 3.768-day period) corresponding approximately to the middle panel of Fig. 1. A dynamic plot of the differences between the observed emission lines and the global mean as a function of phase (arbitrary zero point) is presented in Figure 3. The variations are characteristic of the changes expected from CIRs in the wind of a massive star as predicted by Dessart & Chesneau (2002), namely, a characteristic S-Shape feature in the dynamic plot. In our dataset, we found one main dark S-shape feature that reached its maximum negative velocity around phase 0.5 and its maximum positive velocity around phase 0. We have added a red solid line to the plot to indicate the location of that feature. A fainter structure, shifted to lower phases by about 0.2, can also be distinguished (indicated by the dashed green line). During the 15 cycles, most of the light-curve presented only one peak, with a second peak appearing towards the end of the time period (right panel of Figure 2). This is compatible with the variations detected by spectroscopy.

4 Discussion and Conclusions

As mentioned above, the simultaneous photometric and spectroscopic variability we detected during these observations had characteristics that are compatible with CIRs in the wind of a massive star. The periodic but epoch-dependent nature of the variability, the presence of a number of harmonics associated with the periodic phenomenon, and the spectroscopic characteristics of the line-profile changes, are all expected within the framework of that model.

The binary scenario presented by Schmutz & Koenigsberger (2019) involves light variations with an orbital period of 3.63 days and a fast apsidal motion from a putative third star on a timescale of ∼100 days. The resulting sidereal period is the well-known 3.77-day period. The variability is mostly caused by two eclipses per cycle by either the WR star (20 $M_\odot$) or its yet undetected low-mass companion (1.5 $M_\odot$), of shocked WR wind as it collides with the surface of its low mass companion, contributing about 15% of the total flux. To estimate the minimum period of the outer body causing the fast apsidal motion, one must assume a mass for this third body. If the mass of the third body is equal to that of the WR star, the outer period is estimated to P_{out}=22 days, while if the mass of the third body dominates, the outer period would be 31 days. We note that there is no sign of such periods from a period-search analysis.

A more careful analysis is required to determine which model reproduces best the entirety of the data obtained for this star over the years. The correlated ultraviolet continuum and line-flux variability accompanied by blue edge P Cygni absorption component changes (St-Louis et al. 1995), the broadband continuum polarimetric variability (e.g. St-Louis et al. 2018), the correlated optical continuum and line flux changes (e.g. Morel et al. 1997) and the lack of correlation between the optical photometric changes and X-ray variability (Huenemoerder et al. 2015) are examples of phenomena that will need to be reproduced by the models.

References

Cranmer, S. R. & Owocki, S. P. 1995, ApJ, 440, 308
Dessart, L. & Chesneau, O. 2002, A&A, 395, 209
Hamann, W. R., Gräfener, G., Liermann, A., et al. 2019, A&A, 625, A57
Huenemoerder, D. P., Gayley, K. G., Hamann, W.-R., et al. 2015, ApJ, 815, 29
Lenz, P. & Breger, M. 2005, Communications in Asteroseismology, 146, 53
Morel, T., St-Louis, N., & Marchenko, S. V. 1997, ApJ, 482, 470
Popowicz, A., Pigulski, A., Bernacki, K., et al. 2017, A&A, 605, A26
Prinja, R. K., Barlow, M. J., & Howarth, I. D. 1990, ApJ, 361, 607
Robert, C., Moffat, A. F. J., Drissen, L., et al. 1992, ApJ, 397, 277
Schmutz, W. & Koenigsberger, G. 2019, A&A, 624, L3
St-Louis, N., Dalton, M. J., Marchenko, S. V., Moffat, A. F. J., & Willis, A. J. 1995, ApJ, 452, L57
St-Louis, N., Tremblay, P., & Ignace, R. 2018, MNRAS, 474, 1886

Stars and their variability observed from space
C. Neiner, W. W. Weiss, D. Baade, R. E. Griffin, C. C. Lovekin, A. F. J. Moffat (eds)

DO PLANET SYSTEMS INFLUENCE THE HOST STAR ATMOSPHERIC ABUNDANCES ?

T. Ryabchikova[1]

Abstract. The question of how planet formation affects the host-star atmosphere was widely discussed during the last years. We performed a comparative abundance analysis of a sample of stars with and without planets. The observed trends with condensation temperature, relative to the solar atmospheric abundances, are more closely connected to the overall metallicity of the star than to planet formation. Abundance differences for pairs of stars with and without planets but with similar metallicities in the range of −0.15 +0.34 with respect to the Sun do not show any significant trend with the condensation temperature.

Keywords: Spectroscopy, stars, atmospheric parameters, chemical abundances, exoplanets

1 Introduction

The discovery of differences between atmospheric abundances in the Sun and nearby solar twins (Meléndez et al. 2009), and in particular, of differences between abundances in solar analogs hosting giant planets and those without planets triggered massive differential abundance studies of stars hosting planets (see, for example, Schuler et al. 2011b). Meléndez et al. (2009) found a dependence of the abundance differences on the condensation temperature. Fig. 1 (left panel) represents the reconstruction of the abundance correlations found by Meléndez et al. (2009) (Fig. 5 in their paper) in slightly different form where the mean relative-to-solar atmospheric abundances in a group of solar analogs hosting planets shows a clear dependence on the condensation temperature, while the same dependence for non-planet solar analogs is weak/insignificant. The main characteristic of the observed correlation is an increase of the refractory elements relative to the volatile ones in comparison with the Sun. Abundance differences between stars without planets and those hosting giant planets also show a weak correlation with the condensation temperature (Fig. 1 – right panel). These correlations were interpreted as an influence of the planet formation on the host-star atmospheric abundances. An excellent possibility to study in detail the effects of planet formation on host-star atmospheres is provided by the differential analysis of wide binary systems in which one of the components hosts a planet and the other one does not. The best candidate is the 16 Cyg system where the secondary is a planet-hosting star (Cochran et al. 1997). I present the results of abundance analyses of both components performed with different combinations of the components' atmospheric parameters. The effect of the overall stellar metallicity on the abundance correlation with the condensation temperature is also studied.

2 Sample of stars, observations and data analysis

For the analysis we chose a sample of three pairs of stars with similar metallicities [M/H] in the range of −0.17 to +0.34 dex. One pair represents the binary system 16 Cyg. The list of the stars with the derived atmospheric parameters is given in Table 1.

Spectra were obtained with the ESPaDONs spectrograph at the Canada-France-Hawaii Telescope* (CFHT) of 16 Cyg and HD 149026 and with the Keck HiReS spectrograph (Howard et al. 2010) of the other stars. Details of the reduction procedure and atmospheric parameter determination are given by Ryabchikova et al. (2016). We used the Spectroscopy Made Easy (SME) package (Valenti & Piskunov 1996; Piskunov & Valenti 2017) with the LLmodels (Shulyak et al. 2004) grid for 16 Cyg, HD 149026, and with the MARCS model grid (Gustafsson et al. 2008) for the other stars. Abundances of 25 elements including ions were derived from the line-profile fitting of about 350 spectral lines.

[1] Institute of Astronomy, Russian Academy of Sciences, Pyatnitskaya 48, 119017 Moscow, Russia
*http://www.cadc-ccda.hia-iha.nrc-cnrc.gc.ca/en/cfht/

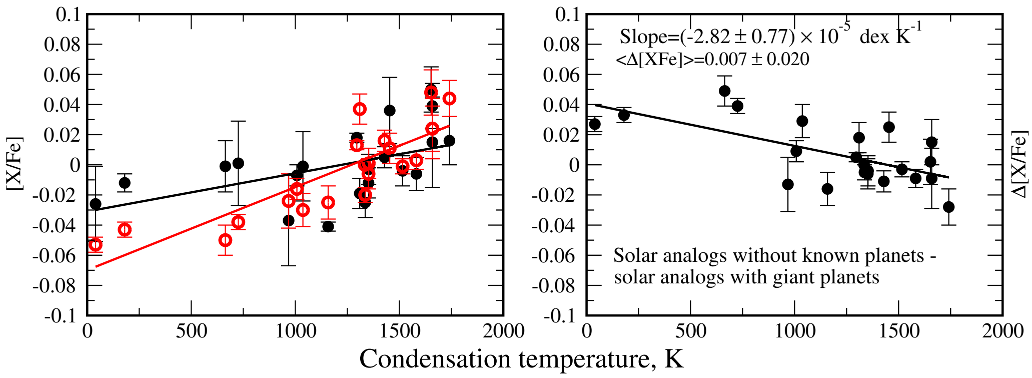

Fig. 1. Left: Differences [X/Fe] between the mean metallicity values in solar analogs and in the Sun as a function of element condensation temperature. Stars hosting planets are shown by black filled circles and those without detected planets are shown by red open circles. Linear regressions for both groups are indicated by lines. Based on the data from Fig. 5 of Meléndez et al. (2009). **Right:** Abundance differences between both groups.

Table 1. Parameters of the programme stars. The errors are given in parentheses.

Stars without planets				Stars with planets			
Star	$T_{\rm eff}$,K	$\log g$	[M/H]	Star	$T_{\rm eff}$,K	$\log g$	[M/H]
HD 107211	5789(80)	4.20(29)	0.34(06)	HD 149026	6074(82)	4.18(29)	0.24(06)
16 Cyg A	5829(39)	4.30(11)	0.09(03)	16 Cyg B	5773(40)	4.38(09)	0.07(03)
HD 209203	6160(80)	4.29(29)	-0.17(09)	HD 50554	5972(80)	4.31(30)	-0.12(07)

3 Abundance correlations

3.1 16 Cyg

First, we consider the binary system 16 Cyg, which has nearly identical components with atmospheric parameters close to the solar ones. In this case we can perform a differential analysis of the components directly not involving the Sun to see if there is any abundance difference between component 16 Cyg A without planet and 16 Cyg B hosting a giant planet. Note, that both components are considered to have formed from the same material.

In 2011, Ramírez et al. (2011) and Schuler et al. (2011a) performed abundance analyses of the 16 Cyg system. They found a correlation of the abundances with the condensation temperature in both components similar to that shown in Fig. 1 (left panel) but no correlation in abundance differences between components A and B. Later, a very careful abundance study of 16 Cyg was performed by Tucci Maia et al. (2014); Maia et al. (2019). They found abundance correlations in both components as well as a correlation of abundance difference with condensation temperature. Their results are represented in Fig. 2 (left panel). Atmospheric parameters derived in both papers are given in Table 2. We also add $T_{\rm eff}$ obtained from interferometry (White et al. 2013) and $\log g$ obtained from asteroseismology (Metcalfe et al. 2015) as independent parameter determinations through direct methods. Then we performed abundance analyses of the components of 16 Cyg by the methods given above using our spectroscopically determined atmospheric parameters and those derived by the direct methods. Note that we employed the same spectra as Tucci Maia et al. (2014). Differential abundances (averaged line-by-line differences) as a function of the condensation temperature are shown in Fig. 2. The plots demonstrate the variations of the slope of the linear correlation with the temperature difference between the components. While $T_{\rm eff}$ of the primary is practically the same in all investigations, 5834±4 K, for the secondary we have a range of 5750≤ $T_{\rm eff}$ ≤5809. With the largest temperature difference of 80 K, derived by Tucci Maia et al. (2014), we have a positive correlation, while the interferometric estimates give us the minimal temperature difference, 30 K, and produce a negative correlation. Our own analysis results in a temperature difference of 56 K, and any correlation is practical absent. If the overall abundance difference of 0.02 dex found by us is considered significant, the planet formation around 16 Cyg B has resulted in a negligible depletion of the atmosphere of 16 Cyg B in all elements.

Table 2. Parameters of the 16 Cyg system from different studies

	T_{eff},K	$\log g$	[M/H]	T_{eff},K	$\log g$	[M/H]	T_{eff},K	$\log g$
16 Cyg A	5830(11)	4.30(02)	0.101(008)	5834(5)	4.330(013)	0.103(005)	5839(42)	4.292(003)
16 Cyg B	5751(11)	4.35(02)	0.054(008)	5749(4)	4.360(011)	0.052(003)	5809(39)	4.358(002)
Reference		1			2		3	4

References: (1) Tucci Maia et al. (2014); (2) Maia et al. (2019); (3) White et al. (2013); (4) Metcalfe et al. (2015)

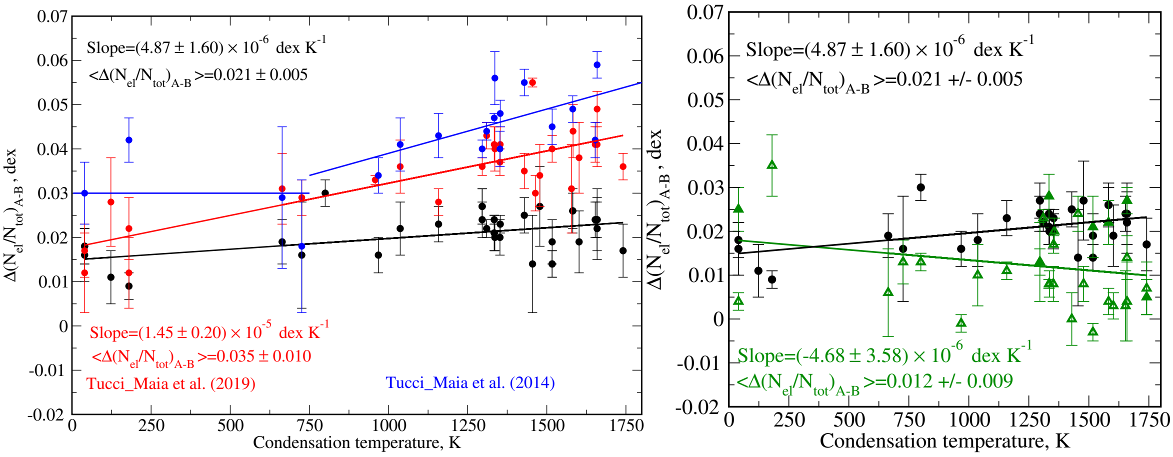

Fig. 2. Left: Differential abundances in the 16 Cyg system as a function of the condensation temperature. Results of the present study are shown by filled black circles, while blue and red filled circles represent the results from Tucci Maia et al. (2014) and Maia et al. (2019), respectively. Linear regression lines, the slopes and the mean abundance differences are indicated by the corresponding colours. The masses of the planets are given. **Right:** Same as left panel except for atmospheric parameters determined by the direct methods of interferometry and asteroseismology (green triangles).

3.2 *Metallicity effect*

From six selected stars, we formed three pairs by metallicity. The results of the pairwise differential analyses are plotted on Fig. 3. One can see large abundance variations (relative to the Sun) with the condensation temperature for high-metallicity stars and a de facto absence of such variations for low-metallicity stars, independently of the presence of a planet. At the same time, line-by-line abundance differences between stars with and without planets do not show any significant dependence on the condensation temperature, and their average values simply reflect differences in overall stellar metallicity.

4 Conclusions

Our analysis shows that the observed variations of the atmospheric abundances (relative to the Sun) with condensation temperature are similar for the planet/non-planet stars of similar metallicities. The amplitude of these variations depends on the metallicity, coming close to zero at low metallicity. We did not find any significant trends in atmospheric abundances differences with the condensation temperature for stars having giant planets and without detected planets. We propose that the observed abundance trends are rather connected with the overall metallicity of the star than with planet formation, although more extensive studies are required to support this result.

References

Cochran, W. D., Hatzes, A. P., Butler, R. P., & Marcy, G. W. 1997, ApJ, 483, 457

Gustafsson, B., Edvardsson, B., Eriksson, K., et al. 2008, A&A, 486, 951

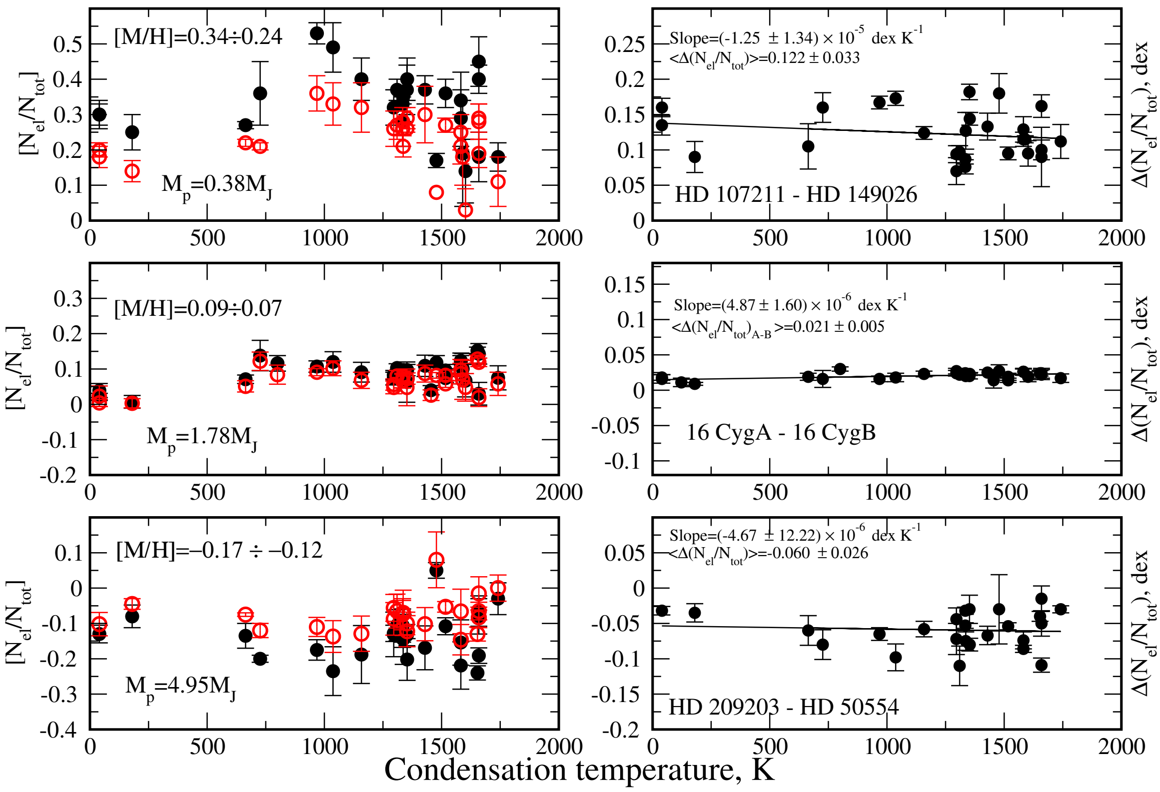

Fig. 3. Left: Differential atmospheric abundances of the programme stars relative to the Sun as a function of condensation temperature. Star without detected planets are shown by filled black circles, those with giant planets by open red circles. **Right:** Line-by-line differences between stars without detected planets and with giant planets as a function of the condensation temperature. The slopes and mean difference are given for each pair of stars.

Howard, A. W., Johnson, J. A., Marcy, G. W., et al. 2010, ApJ, 721, 1467
Maia, M. T., Meléndez, J., Lorenzo-Oliveira, D., Spina, L., & Jofré, P. 2019, A&A, 628, A126
Meléndez, J., Asplund, M., Gustafsson, B., & Yong, D. 2009, ApJ, 704, L66
Metcalfe, T. S., Creevey, O. L., & Davies, G. R. 2015, ApJ, 811, L37
Piskunov, N. & Valenti, J. A. 2017, A&A, 597, A16
Ramírez, I., Meléndez, J., Cornejo, D., Roederer, I. U., & Fish, J. R. 2011, ApJ, 740, 76
Ryabchikova, T., Piskunov, N., Pakhomov, Y., et al. 2016, MNRAS, 456, 1221
Schuler, S. C., Cunha, K., Smith, V. V., et al. 2011a, ApJ, 737, L32
Schuler, S. C., Flateau, D., Cunha, K., et al. 2011b, ApJ, 732, 55
Shulyak, D., Tsymbal, V., Ryabchikova, T., Stütz, C., & Weiss, W. W. 2004, A&A, 428, 993
Tucci Maia, M., Meléndez, J., & Ramírez, I. 2014, ApJ, 790, L25
Valenti, J. A. & Piskunov, N. 1996, A&AS, 118, 595
White, T. R., Huber, D., Maestro, V., et al. 2013, MNRAS, 433, 1262

Stars and their variability observed from space
C. Neiner, W. W. Weiss, D. Baade, R. E. Griffin, C. C. Lovekin, A. F. J. Moffat (eds)

FLARES OF M STARS IN THE UPPER SCORPIUS REGION AND FLARES/CMES OF THE ACTIVE M-STAR AD LEO

E. W. Guenther[1], D. Wöckel[1] and P. Muheki[2]

Abstract. Using *Kepler K2* data, we studied the flare activity of young K and M stars in the Upper Sco region and found that they have 10000–80000 times as many super-flares with ($E \geq 5\,10^{34} erg$) than solar-like stars. The power-law index for flares is $dN/dE \sim E^{-1.2}$ for K-stars, $dN/dE \sim E^{-1.4}$ for early M-stars and $dN/dE \sim E^{-1.3}$ for late M-stars, which is about the same as for the Sun. We also observed the active star AD Leo.

1 Low-mass planets, flares and CMEs of M-stars

Searching for planets around M-stars has recently become fashionable because it is relatively easy to detect low-mass planets in the so-called habitable zone (HZ) of these stars. However, planets in the HZ of M-stars are exposed to radiation from flares and to Coronal Mass-Ejections (CMEs). A large flare and CME rate could be critical, because the X-ray and UV-radiation from flares together with the CMEs might erode a planetary atmosphere. In less extreme cases, flares and CMEs still affect the photochemistry of the atmospheres. Particularly important are the first few 100 Myrs, which is the main erosion phase of planetary atmospheres. This presentation gave the first result of our study of flares and CMEs on young M stars.

2 Flares on M stars in Upper Scorpius

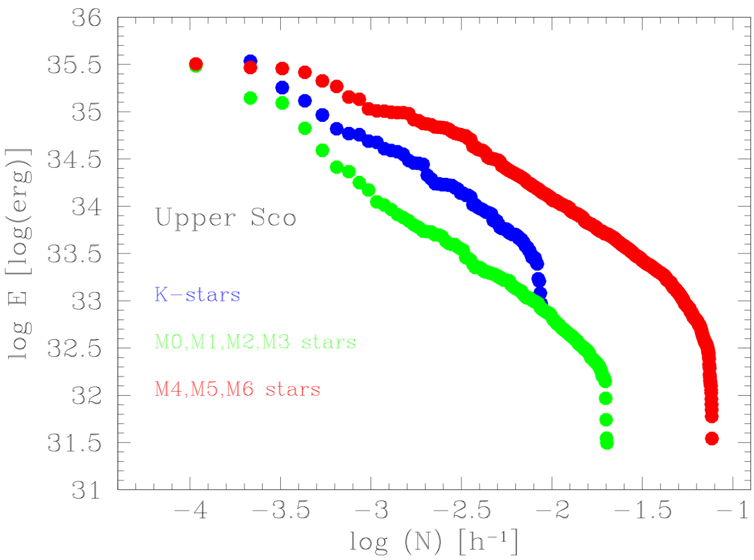

Fig. 1. Cumulative frequency diagram for K and M stars in Upper Sco.

Using light-curves obtained from *Kepler K2* data, we studied the flare activity of M stars in the Upper Scorpius OB association, which has an age of 6–11 Myr (Fang et al. 2017). At that age planets will just have

[1] Thüringer Landessterwarte Tautenburg, Sternwarte 5, 07778 Tautenburg, Germany
[2] Mbarara University of Science and Technology, P.O Box 1410, Mbarara, Uganda.

formed, and should be in the main erosion phase of their atmospheres. About 100 M stars in Upper Sco have been observed, but we focus here on those 41 stars which we confirmed as being members according to VLT-FLAMES spectra. Of those, 5 are K stars, 17 are early M stars (M0–M3) and 19 are late M stars (M4–M6). One particularly remarkable case is the M1 star 2M161115.3-175721, where we detected 138 flares during the 78 days of monitoring. The radius of this star is 1.30 R_{sun}, and its mass 0.85 M_{sun}. 2M161115.3-175721 will eventually become a late-G or early-K star. Its X-ray brightness is log(Lx) = 30.2 log(ergs^{-1}) and it has a rotation period of 6.03 days. For comparison, the Sun has log(Lx) = 26.4–27.7 log(ergs^{-1}), while the value for solar-like stars in the Pleiades is 29.1–29.6 log(ergs^{-1}) (Giardino et al. 2008). The X-ray flux thus is 300–6000 times larger than that of the Sun. The largest flare emitted $3.3\,10^{30}$ erg in the *Kepler* band (4200–9000 Å), and the smallest one 10^{27} erg.

Summing up the observing times for all stars in each class, we monitored K stars for 9273 hours (1.01 years), early M stars for 31527 hours (3.6 years), and late-M stars for 35236 hours (4.0 years). We detected 81 flares in K stars, 711 in early-M stars and 188 in late-M stars. The power-law index of the distribution was $dN/dE \sim E^{-1.2}$ for K stars (log(E) = 33.8–35.5), $dN/dE \sim E^{-1.4}$ for early M stars (log(E) = 32.4–34.2), and dN/dE $\sim$ E$-^{1.3}$ (log(E)33.2–35.0 log(erg)) (Fig. 1). For comparison the Sun has dN/dE $\sim$ E$^{-1.5}$ for flares (Crosby et al. 1993), and $dN/dE \sim E^{-1.8}$ for nanoflares (Aschwanden et al. 2000). Flares larger than $5\,10^{34}$ erg are usually called super-flares. Compared to solar-like stars, the rate of super-flares was 20000 times greater for the K stars in Upper Sco, 80000 times greater for the early-M stars, and 10000 times greater for the late-M stars (Notsu et al. 2019).

3 The frequency of coronal mass ejections in AD Leo

Coronal Mass Ejections (CMEs) can be detected in stars as blue-shifted components in the spectrum that have velocities larger than the escape velocity of the star. For our study, we selected the M4 star AD Leo, which has an age of 20–300 Myr. The escape velocity from this star is 580 km s^{-1}. We observed it for 222 hours with the echelle spectrograph of the 2-m Alfred Jensch Telescope in Tautenburg, and detected 22 flares. The largest of them emitted $2.9\,10^{31}$ erg in Hα and $1.8\,10^{32}$ erg in $H\beta$. We estimated the XUV-flux to be about $2\,10^{33}$ erg for this flare from the Hα and $H\beta$ fluxes. If M stars have the same CME-to-flare ratio as the Sun, we expect to see a number of CMEs with masses up to $2 - 3\,10^{17}$ g. So far we have not detected a blue-shifted component with $V \geq 600 km\,s^{-1}$, but we did observe velocities up to 200 km/s. It thus looks as though the frequency of CMEs on AD Leo is lower than expected, unless they escaped detection through having a very high velocity.

4 Summary and conclusions

- Young K and M stars have 10000–80000 times as many super-flares ($E \geq 5\,10^{34} erg$) as solar-like stars.
- This enormous activity will certainly affect the evolution and habitability of M-star planets.
- The power-law index for flares was found to be $dN/dE \sim E^{-1.2}$ for K-stars, $dN/dE \sim E^{-1.4}$ for early-M stars and $dN/dE \sim E^{-1.3}$ for late-M stars, which is about the same as that for the Sun.
- We observed AD Leo spectroscopically for 222 hours to search for CMEs. A total of 22 flares was observed, but none showed a clear CME signature.

References

Aschwanden, M. J., Tarbell, T. D., Nightingale, R. W., et al. 2000, ApJ, 535, 1047

Crosby, N. B., Aschwanden, M. J., & Dennis, B. R. 1993, Sol. Phys., 143, 275

Fang, Q., Herczeg, G. J., & Rizzuto, A. 2017, ApJ, 842, 123

Giardino, G., Pillitteri, I., Favata, F., & Micela, G. 2008, A&A, 490, 113

Notsu, Y., Maehara, H., Honda, S., et al. 2019, ApJ, 876, 58

Stars and their variability observed from space
C. Neiner, W. W. Weiss, D. Baade, R. E. Griffin, C. C. Lovekin, A. F. J. Moffat (eds)

STARSPOTS AND ROTATION VELOCITIES OF NORMAL A- AND AM- STARS

O. Trust[1], E. Jurua[1], P. De Cat[2] and S. Joshi[3]

Abstract. Using the "hump and spike" features, we computed the rotation frequencies and amplitudes. The corresponding equatorial rotational velocity (V_{rot}) and spot size were estimated. On fitting the auto-correlation functions of the light-curves with the appropriate model, we obtained the starspot decay-time scale. The V_{rot} agrees well with the projected rotational velocity ($\nu \sin i$) in the literature. Considering a single circular and black spot, we estimate its radius from the amplitude of the "spike". No evidence for a significant difference in the average "spike" amplitude and spot radius was found for Am/Fm and normal A stars. Indeed, we derived an average value of $\sim 21 \pm 2$ and $\sim 19 \pm 2$ ppm for the photometric amplitude and of 1.01 ± 0.13 and $1.16 \pm 0.12\,R_E$ for the spot radius (where R_E is the Earth radius), respectively. We do find a significant difference for the average spot decay-time scale, which amounts to 3.6 ± 0.2 and 1.5 ± 0.2 days for Am/Fm and normal A stars, respectively. In general, spots on normal A stars are similar in size to those on Am/Fm stars, and both are weaker than previously estimated. The existence of the "spikes" in the frequency spectra may not be strongly dependent on the appearance of starspots on the stellar surface. In comparison with G, K and M stars, spots in normal A and Am/Fm stars are weak which may indicate the presence of a weak magnetic field.

Keywords: stars: photometry, stars: chemically peculiar, stars: rotation, stars: starspots

1 Introduction

Rotation is one of the most important phenomena in stellar physics. Thanks to the availability of high-precision and almost continuous photometric data from space missions like *Kepler*/K2 and *TESS*, precise rotation periods can be obtained. Balona (2013) derived rotation periods of a large number of A-type stars from the original *Kepler* field based on spot induced rotational modulation. The spot based rotational modulation in these stars was unexpected, since they possess a thin sub-surface convective envelope. Balona (2013) observed in the frequency spectra of 135 stars of the 875 normal A-stars a sharp peak ("spike") on the high frequency side of a broad hump of very close frequencies ("hump"). Balona et al. (2015) observed the same scenario in some Am/Fm stars. Balona (2014) suspected the sharp peak corresponds to the rotational frequency and its amplitude to be related to the starspot size, but the hump remained unexplained. Recently, Saio et al. (2018) named these stars "hump and spike" stars. Saio et al. (2018) reported that the broad humps as observed for these stars are induced by Rossby modes (r modes) and the spike structures are the rotation frequencies induced by one or more spots. This has improved estimates of rotational velocities and spot sizes of such stars.

2 Methods and Results

We studied a total of 170 "hump and spike" stars of which 131 are part of the normal A stars reported by Balona (2013), 3 are within the sample studied by Balona et al. (2015), and 36 are from Gray et al. (2016). We used all the available quarters (Q_0 upto Q_{17}) of the long-cadence *Kepler* data processed by the pre-search data conditioning (PDC) pipeline. We calculated the frequency spectra using the discrete Fourier fitting technique.

We derived the luminosity from GAIA parallaxes, reddening from a 3D model and adopted the effective temperature from the revised catalog of *Kepler* targets for Q_{1-17} by Mathur et al. (2017) which were used to calculate the stellar radius. Using the rotation frequencies (spike frequency) and stellar radius, we computed the rotational velocities from the standard relation. The average rotational velocity of Am/Fm and normal A stars is 105 ± 3 km s^{-1} and 161 ± 3 km s^{-1}, respectively.

[1] Department of Physics, Mbarara University of Science and Technology, P.O. Box 1410, Mbarara, Uganda
[2] Royal Observatory of Belgium, Ringlaan 3, B-1180 Brussel, Belgium
[3] Aryabhatta Research Institute of Observational Sciences, Manora Peak, Nainital- 263002, India

From the frequency spectra, we obtained and considered the amplitudes of the spikes to be the photometric amplitudes (A_{rot}) associated with rotation. The average A_{rot} of Am/Fm and normal A stars was found to be $\sim 21 \pm 2$ ppm and $\sim 19 \pm 2$ ppm, respectively. For simplicity, we assume that the stars are spherical and that a single, circular and black spot reproduces the amplitude of the spike. This is identical to determining the size of an exoplanet from a transit. We computed the radius of the spot (R_{spot}) from the standard relation, $R_{spot} = \sqrt{A_{rot}}R$. The average spot radius is 1.01 ± 0.13 and $1.16 \pm 0.12\,R_E$ for Am/Fm and normal A stars, respectively.

We computed autocorrelation function (ACFs) for the combined *Kepler* light-curves. To estimate the decay-time scale of the active regions, we fitted the ACFs with a model for an under-damped simple harmonic oscillator, as shown in Fig. 1. About 40% of the ACFs do not show any significant peaks. This points towards a short decay-time and low amplitudes, so it suggests very weak or the absence of starspots and co-rotating structures. However, the "hump and spike" features exist in their frequency spectra. The majority of the stars have decay-time scales of a few days or less. The average decay-time in Am and normal A stars is 3.6 ± 0.2 and 1.5 ± 0.2 days, respectively.

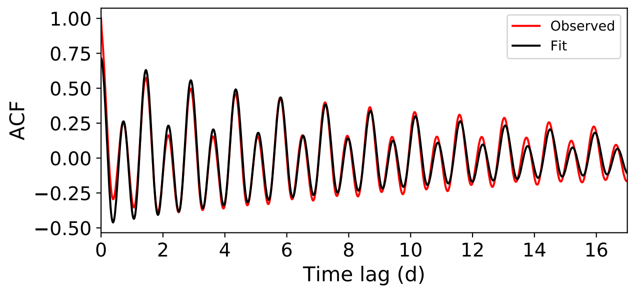

Fig. 1. An ACF for KIC 5121064. The second local maximum corresponds to the rotation period (P_{ACF}) while a lower local maximum is observed at almost half the rotation period. This indicates that there is(are) weak starspot(s) opposite to the stellar face with the dominant starspot(s).

3 Conclusions

Am/Fm stars rotate slowly relative to normal A stars. This confirms the conclusion from several studies (e.g, Abt & Morrell 1995). The starspot size in normal A and Am/Fm stars is smaller than previously estimated by Balona (2013) and Balona et al. (2015) by about 38 %. This implies that the activity in Am/Fm and normal A stars is weaker than previously suggested by these studies. Finally, significantly large starspots may not be required to produce the existing spikes in the frequency spectra.

The International Science Program (ISP) of Uppsala University financed the study. The part of work presented here is supported by the Belgo-Indian Network for Astronomy & Astrophysics (BINA), approved by the International Division, Department of Science and Technology (DST, Govt. of India; DST/INT/Belg/P-02) and the Belgian Federal Science Policy Office (BELSPO, Govt. of Belgium; BL/33/IN12).

References

Abt, H. A. & Morrell, N. I. 1995, ApJS, 99, 135

Balona, L. A. 2013, MNRAS, 431, 2240

Balona, L. A. 2014, MNRAS, 441, 3543

Balona, L. A., Catanzaro, G., Abedigamba, O. P., Ripepi, V., & Smalley, B. 2015, MNRAS, 448, 1378

Gray, R. O., Corbally, C. J., De Cat, P., et al. 2016, AJ, 151, 13

Mathur, S., Huber, D., Batalha, N. M., et al. 2017, ApJS, 229, 30

Saio, H., Kurtz, D. W., Murphy, S. J., Antoci, V. L., & Lee, U. 2018, MNRAS, 474, 2774

Stars and their variability observed from space
C. Neiner, W. W. Weiss, D. Baade, R. E. Griffin, C. C. Lovekin, A. F. J. Moffat (eds)

ULTRAVIOLET VARIABILITY OF B, BE, AND B[E] STARS

I. Krtičková[1] and J. Krtička[1]

Abstract. We study the ultraviolet variability of evolved B[e], Be, and B stars from our Galaxy and from the Magellanic Clouds. We use IUE observations to derive fluxes of individual stars in the selected bands in the near-UV and far-UV regions. We diagnose the variability in the lines and the total flux variability. We discuss the origin of the UV light variability of studied stars. We detected pulsations in B[e] star HD 50138, LBV-type variations in HD 34664, and constant luminosity for a group of B[e] supergiants.

Keywords: stars: early-type, stars: emission-line, Be, stars: variables: general, stars: oscillations

1 Introduction

The study of stellar variability in non-optical domains is complicated by the lack of suitable data. Here we show how the archival ultraviolet (UV) spectra of B stars can be used to study their variability.

We used UV fluxes $F(\lambda)$ observed by IUE to construct the broad-band fluxes $F_c = \int_0^\infty \Phi_c(\lambda) F(\lambda)\,\mathrm{d}\lambda$. Here $\Phi_c(\lambda)$ is a Gauss function centered on wavelength c. We selected $c = 1500\,\text{Å}$ to study the flux in the far-UV region and $c = 2175\,\text{Å}$ and $c = 2500\,\text{Å}$ for the near-UV region. To describe the variations of emission lines as a whole, we integrated the flux above and below the continuum and derived the total flux in emission lines F_{em}.

2 LBV-type variations in HD 34664 and pulsations in B[e] star HD 50138

The UV fluxes from HD 34664 (LHA 120-S 22) significantly decreased between MJD 45 000 and 48 000 (Fig. 1, see also Shore 1990). The decrease is stronger in the far-UV than in the near-UV. This can be explained by the change of the effective temperature. Such variations are typical for LBV stars. The total emission-line flux decreased in HD 34664 during the IUE observations. This also corresponds to the decrease of the effective temperature. The decrease of the emission-line flux during the period of constant broad-band flux after MJD 48 000 indicates that the emission lines and continuum originate in different regions.

The IUE fluxes of HD 50138 (V743 Mon) are variable with the period $1.194 \pm 0.006\,\mathrm{d}$ (see Fig. 2). Borges Fernandes et al. (2012) detected line profile variations in this star with a period significantly shorter than the rotational period of 3.6 d. These variations are attributed to pulsations. To our knowledge, this is the first detection of pulsations in B[e] stars.

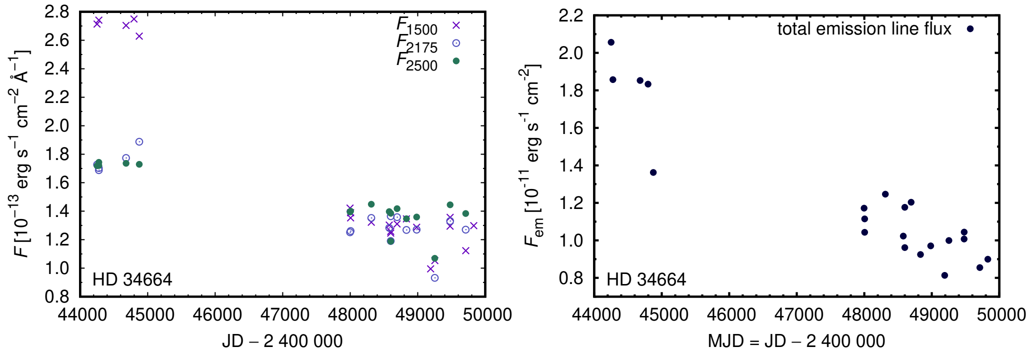

Fig. 1. Variations in B[e] star HD 34664. **Left:** Long-term flux variations. **Right:** Total emission line flux variations.

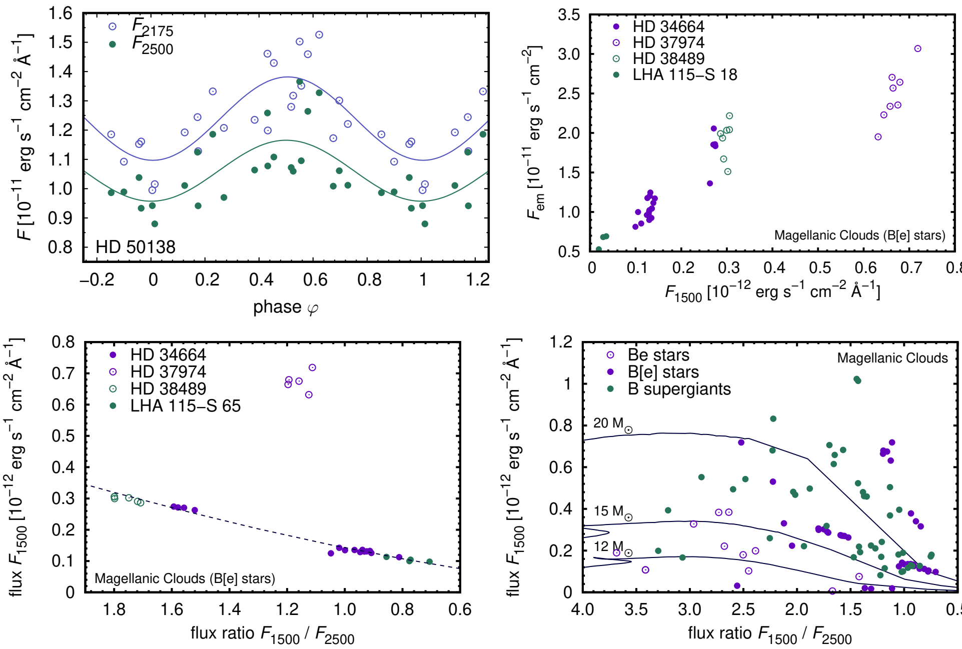

Fig. 2. Top Left: Pulsations in HD 50138. **Top Right:** Relation between the emission-line and the far-UV fluxes for B[e] stars. **Bottom Left:** Correlation between the far-UV flux and the time variable flux ratio for selected B[e] supergiants. **Bottom Right:** UV variant of the color-magnitude diagram for B supergiants from the Magellanic Clouds.

3 General relations between fluxes

The far-UV and emission-line fluxes correlate for the Magellanic Cloud B[e] stars (Fig. 2). This most likely results from geometrical causes. With larger disk column density (or for disks seen edge-on) the continuum flux is more absorbed and becomes lower. However, line emitting regions of the envelope are visible even when the disk is seen edge-on; consequently, the emission-line flux is nonzero even for very low continuum fluxes.

Be stars and B[e] supergiants occupy different parts of the flux vs. flux ratio diagram in Fig. 2, while B supergiants are distributed more uniformly with enhanced density in two perceptible branches. Similarly, B[e] stars divide into different possible groups. Comparison with evolutionary tracks shows that the studied stars are in a post main-sequence stage with typical initial mass of $10 - 30\,M_\odot$.

There is a correlation between the flux and flux ratio for a group of B[e] supergiants. The relation can be fitted by model-atmosphere emergent fluxes assuming constant luminosity and variable temperature and radius (dashed line in Fig. 2). From this it follows that these stars have the same luminosity of about $(1.9{\pm}0.4){\times}10^5\,L_\odot$.

4 Conclusions

We have studied UV variability of B-type stars (Krtičková & Krtička 2018). We detected LBV-type variations in HD 34664 and pulsations of B[e] star HD 50138 with the period 1.194 d. The correlation of fluxes implies the luminosity $1.9 \times 10^5\,L_\odot$ for a group of B[e] supergiants suggesting their similar origin.

This work was supported by grant GA ČR 18-05665S.

References

Borges Fernandes, M., Kraus, M., Nickeler, D. H., et al. 2012, A&A, 548, A13

Krtičková, I. & Krtička, J. 2018, MNRAS, 477, 236

Shore, S. N. 1990, IAU Circ., 5005, 1

[1] Department of Theoretical Physics and Astrophysics, Masaryk University, Brno, Czech Republic

Stars and their variability observed from space
C. Neiner, W. W. Weiss, D. Baade, R. E. Griffin, C. C. Lovekin, A. F. J. Moffat (eds)

TYPE II CEPHEIDS IN THE KEPLER K2 MISSION

M. I. Jurkovic[1, 2], E. Plachy[2, 3], L. Molnár[2,3], M. A. T. Groenewegen[4] and R. Szabó[2,3]

Abstract.
Type II Cepheids (T2Cs) are old, low-mass (0.5 $M_\odot$) stars. They mainly pulsate in a radial mode, but recent discoveries have shown that there are first overtone pulsators among them, and they can exhibit a phenomenon called "period-doubling". They are separated into three subgroups according to their pulsation periods: BL Her, 1 < P [d] < 4, W Vir: 5 < P [d] < 20, RV Tau: 20 < P [d] < 150. Anomalous Cepheids (ACs) have an average mass of 1.2 $M_\odot$, and they pulsate in a fundamental mode and/or[?] in the first overtone. Their periods are in the range from 0.4 to 2.4 days. The Kepler space telescope's original field contained only a single RV Tau star, DF Cyg, but that changed during the K2 mission. Here we present the 12 stars that were observed in Campaigns 1 – 14 of the K2 mission. We have found Type II Cepheids in the sample that show "period doubling", and four possible anomalous Cepheids among the 12 stars.

Keywords: Stars: variables: Cepheids

1 Introduction and Data

The data for the Kepler K2 mission were downloaded from the Mikulski Archive for Space Telescopes database (MAST, `https://archive.stsci.edu`) and analysed with the Extended Aperture Photometry (EAP, Plachy et al. 2017). For each star, an individual aperture was applied, as seen in Figure 1 on the right for the star 218128117 from Campaign 7, where the telescope made significant jumps during the observing run. We have also used the magnitudes from the EPIC Variability Extraction and Removal for Exoplanet Science Targets (EVEREST, Luger et al. (2016)) pipeline for comparison. Table 1 gives the basic information about each star in the sample.

Table 1. The stars identified as T2Cs and ACs in the K2 mission.

Cycle	EPIC ID	RA (2000)	DEC (2000)	P [d]	<Kp> [mag]	Notes
2	202862302	16 36 52.85	-28 05 34.26	1.956	12.926	V1287 Sco: W Vir
4	210622262	04 20 01.80	+17 16 45.80	16.657	16.882	W Vir with PD
7	217235287	19 16 10.99	-20 55 55.86	1.259	15.155	V527 Sgr: BL Her
7	215881928	18 59 37.24	-23 21 52.27	1.835	14.606	V839 Sgr: BL Her
7	217987553	19 06 26.95	-19 36 35.25	13.448	12.482	V1077 Sgr: W Vir with cycle-to-cycle variations
7	218642654	19 06 03.14	-18 25 41.62	13.758	12.166	V410 Sgr: W Vir with PD?
7	217693968	18 48 09.79	-20 07 35.61	16.215	13.289	V377 Sgr: W Vir with PD
7	218128117	19 34 34.67	-19 21 39.96	2.119	12.735	AC?
12	246015642	23 39 54.14	-09 05 01.81	1.071	15.399	AC
12	246385425	23 15 26.54	-01 22 28.73	1.502	17.972	AC
12	246333644	23 22 33.11	-02 23 40.13	1.287	17.792	AC
13	247445057	05 05 14.27	+21 45 48.93	13.944	12.355	VZ Tau: W Vir with PD?

[1] Astronomical Observatory Belgrade, 11060 Belgrade, Serbia, Konkoly Observatory
[2] Research Centre for Astronomy and Earth Sciences, H-1121 Budapest, Hungary
[3] MTA CSFK Lendület Near-Field Cosmology Research Group
[4] Koninklijke Sterrenwacht van Belgie, 1180, Brussels, Belgium

2 Results

Our results can be summarized as follows:

- We have found four anomalous Cepheids (see Fig. 1).
- Two W Virginis stars show "period doubling" (PD). Star 217987553 does not show PD, but it does have an additional modulation (cycle-to-cycle variation).
- For two additional stars further analysis needs to be done to confirm if there is a PD in their light curves.

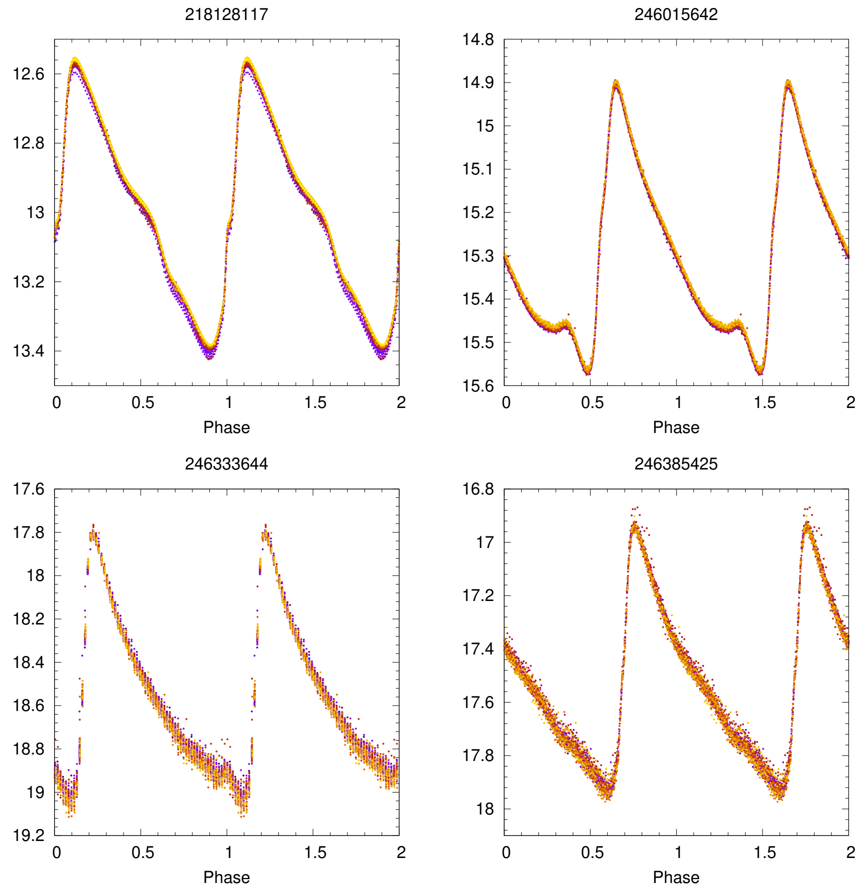

Fig. 1. The phased light curves of ACs in the K2 mission previously identified as T2Cs.

This project has been supported by the NKFIH K-115709 and PD-121203 grants of the Hungarian National Research, Development and Innovation Office and the Lendület program of the Hungarian Academy of Sciences, project No. Lendület LP2018-7/2019. MIJ acknowledges financial support from the Ministry of Education, Science and Technological Development of the Republic of Serbia through the project 176004. Research partially supported by the Délvidékért Kiss Foundation and Maria Lugaro's OTKA/NKFI-6 grant. LM was supported by the Premium Postdoctoral Research Program, EP by the János Bolyai Research Scholarship of the Hungarian Academy of Sciences.

References

Luger, R., Agol, E., Kruse, E., et al. 2016, AJ, 152, 100

Plachy, E., Klagyivik, P., Molnár, L., Sódor, Á., & Szabó, R. 2017, in EPJ Web of Conferences, Vol. 160, EPJ Web of Conferences, 04009

Stars and their variability observed from space
C. Neiner, W. W. Weiss, D. Baade, R. E. Griffin, C. C. Lovekin, A. F. J. Moffat (eds)

TRANSITING EXOCOMETS DETECTED IN BROADBAND LIGHT BY *TESS* IN THE β PICTORIS SYSTEM

S. Zieba[1], K. Zwintz[1], M. A. Kenworthy[2] and G. M. Kennedy[3]

Abstract. We present the first broadband detections of exocomets crossing the disk of β Pictoris. We use photometric data obtained by the *TESS* satellite over a time-base of 105 days, and pre-whiten the 54 identified δ Scuti p-modes of the star. The residual photometric time-series show three distinct dipping events. These dips have depths from 0.5 to 2 millimag, durations of up to 2 days for the largest dip, and are asymmetric in nature. This detection complements the predictions made 20 years earlier. Furthermore they confirm the spectroscopic detection of exocomets in Calcium II H and K lines that have been seen in high-resolution spectroscopy.

Keywords: Comets: general, stars: planetary systems, individual: β Pictoris, Techniques: photometric, circumstellar matter

β Pictoris (HD 39060) is a bright ($m_V = 3.86$), close (19.76 pc; Brown et al. 2018) and young ($\sim$23 Myr; Mamajek & Bell 2014) exoplanet host star showing δ Scuti pulsations. Ferlet et al. (1987) detected absorption features in the spectrum of the star that changed with time, and which have been attributed to Falling Evaporting Bodies (FEBs, also known as exocomets). Similar signatures have been detected around other stars, such as HD 172555 (Kiefer et al. 2014). The first exocomets to be seen photometrically were discovered in *Kepler* data by Rappaport et al. (2018) around the two stars KIC 3542116 and KIC 11084727. Kennedy et al. (2019) developed an algorithm to search for asymmetric, exocomet-like dips in light-curves, retriving those two events and finding a third around HD 182952. The deep and irregular dimming events seen in KIC 8462852 (Boyajian's star or Tabby's star) have also been interpreted as having a cometary origin (Boyajian et al. 2016; Wyatt et al. 2018).

Zieba et al. (2019) presented observations of β Pictoris from *TESS*, and showed that the duration and depth of a dipping event in Sector 6 (see Fig. 1) are consistent with the transit of an exocomet, and also agree with the predictions made by Lecavelier Des Etangs et al. (1999). Two smaller dips in Sector 5 are visible (see Fig. 1) after the subtraction of 54 identified δ Scuti p-modes of the star (see Fig. 2 and 3).

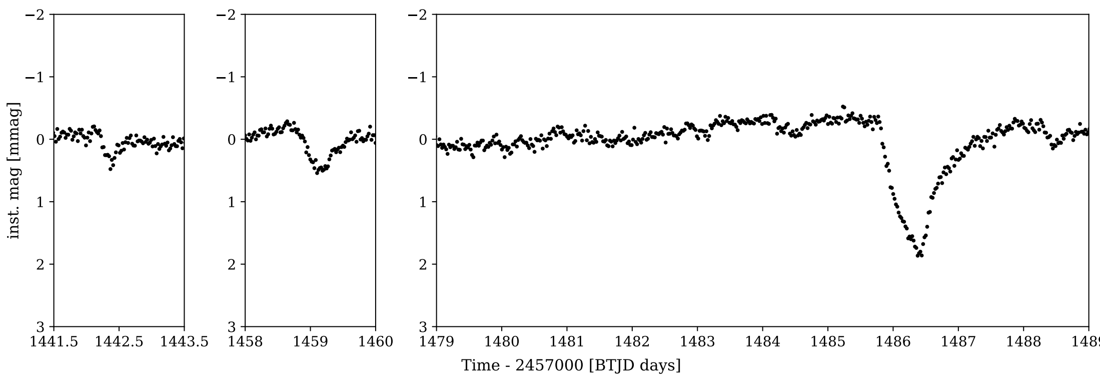

Fig. 1. Enlargement of the three events in the 30-min binned light-curve, after subtraction of the pulsational signal. The two smaller dips in the left and middle panels occurred in *TESS* Sector 5. The bigger event in the right panel was in Sector 6.

[1] Universität Innsbruck, Institut für Astro- und Teilchenphysik, Technikerstraße 25, A-6020 Innsbruck
[2] Leiden Observatory, Leiden University, P.O. Box 9513, 2300 RA Leiden, The Netherlands
[3] Department of Physics, University of Warwick, Gibbet Hill Road, Coventry CV4 7AL, UK

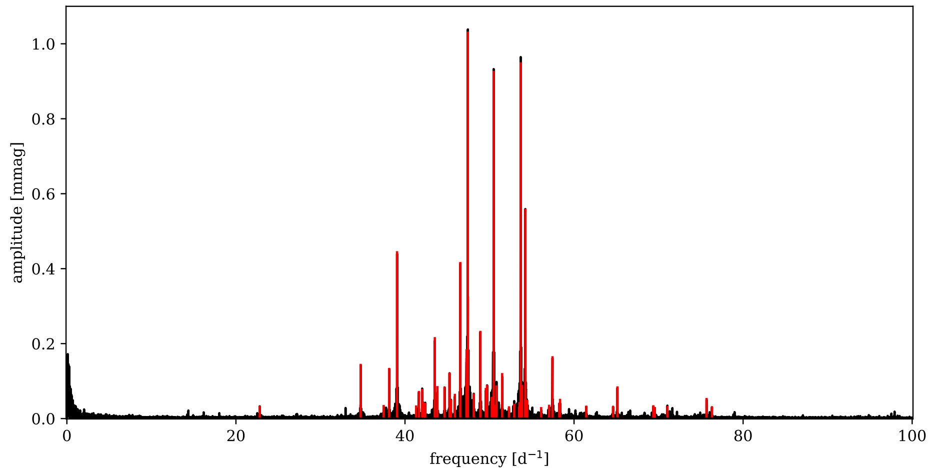

Fig. 2. Original amplitude spectrum of the full β Pictoris light-curve collected by *TESS* in black, and the 54 identified δ Scuti pulsations in red.

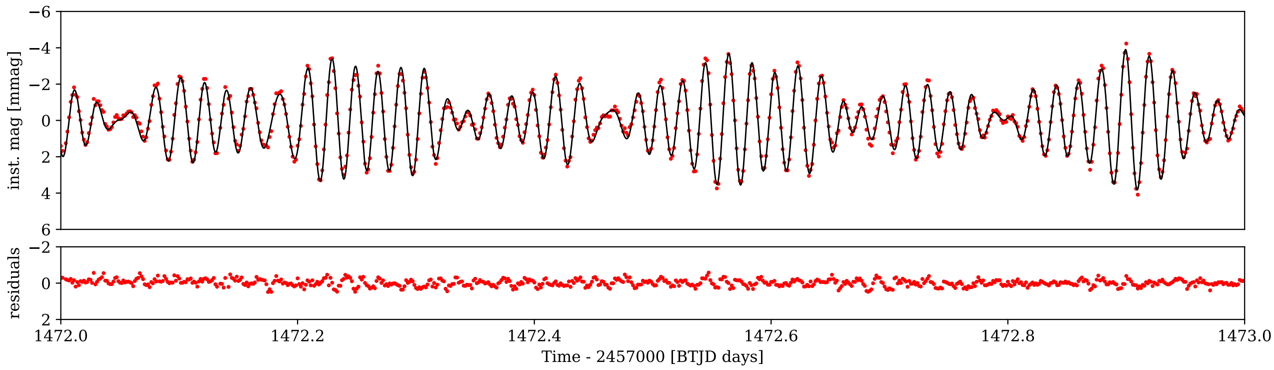

Fig. 3. One-day enlargement of the β Pictoris light-curve. *Upper panel: TESS* photometric time-series (red points) and multi-sine fit, using the 54 identified δ Scuti frequencies (black line). *Lower panel:* Residual time-series after subtracting the multi-sine fit using all 54 identified pulsation frequencies.

References

Boyajian, T. S., LaCourse, D. M., Rappaport, S. A., et al. 2016, MNRAS, 457, 3988
Brown, A. G. A., Vallenari, A., Prusti, T., et al. 2018, A&A, 616, A1
Ferlet, R., Hobbs, L. M., & Madjar, A. V. 1987, A&A, 185, 267
Kennedy, G. M., Hope, G., Hodgkin, S. T., & Wyatt, M. C. 2019, MNRAS, 482, 5587
Kiefer, F., Lecavelier des Etangs, A., Augereau, J.-C., et al. 2014, A&A, 561, L10
Lecavelier Des Etangs, A., Vidal-Madjar, A., & Ferlet, R. 1999, A&A, 343, 916
Mamajek, E. E. & Bell, C. P. M. 2014, MNRAS, 445, 2169
Rappaport, S., Vanderburg, A., Jacobs, T., et al. 2018, MNRAS, 474, 1453
Wyatt, M. C., van Lieshout, R., Kennedy, G. M., & Boyajian, T. S. 2018, MNRAS, 473, 5286
Zieba, S., Zwintz, K., Kenworthy, M. A., & Kennedy, G. M. 2019, A&A, 625, L13

Stars and their variability observed from space
C. Neiner, W. W. Weiss, D. Baade, R. E. Griffin, C. C. Lovekin, A. F. J. Moffat (eds)

THE INFLUENCE OF STELLAR X-RAY AND UV RADIATION ON EXOPLANETS

S.R.G. Joyce[1], J.P. Pye[1], J.D. Nichols[1] and The Exoplanets-A consortium[2]

Abstract. The Exoplanets-A project is a collaboration comprised of 7 institutions in Europe to study exoplanets and their host stars. The project aims to develop new tools for modelling exoplanet atmospheres. Itk includes improving our understanding of the stellar radiation environment through gathering observations and creating models of stellar atmospheres. Variability of stellar XUV radiation on short (days) to long (Gyr) time-scales can have a profound influence on the evolution and potential habitability of orbiting exoplanets. Data, models and software developed during the project will be made publicly available to aid the next stages of exoplanet research with JWST and beyond.

Keywords: X-rays:stars, Ultraviolet:stars, Planet–star interactions

1 Introduction

We have identified 113 stars known to have transiting exoplanets, and which have been observed with HST and/or Spitzer. Many of these stars are prime candidates for additional transit spectroscopy, providing detailed characterisation of the exoplanet atmosphere. Atmospheric modelling requires knowledge of the host-star spectrum, in particular the high-energy XUV which can influence the planetary atmosphere's temperature, structure and composition. For example, some hot-Jupiters show evidence of rapid atmospheric evaporation caused by intense X-ray irradiation (e.g. Lalitha et al. 2018). As a first step we have identified existing X-ray and UV data available for 113 stars from HST, XMM-Newton, Galex, Swift and other X-ray/UV observatories (Fig. 1). These data will be combined with new analyses to construct a database of the XUV properties of transiting exoplanet host stars (Pye et al. 2019).

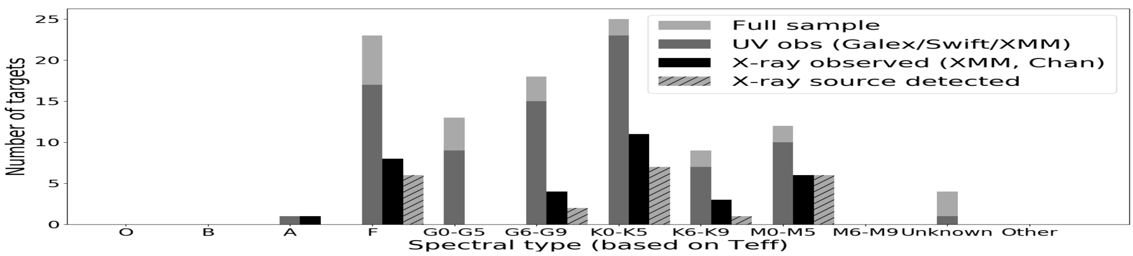

Fig. 1. The spectral type distribution of the 113 stars in the sample. Light grey indicates the total number of stars in each spectral-type range. A total of 94 stars, or 83% of the sample, have existing UV data (dark grey). 38 have been observed by X-ray satellites (black), resulting in 24 positive detections (striped bars).

2 X-ray and UV radiation from host stars

Individual measurements of a star's X-ray and UV luminosity are useful for estimating the flux received by its planets. However, the intrinsic variability of phenomena which produce XUV radiation, such as flares, and the

[1] School of Physics and Astronomy, University of Leicester, Leicester, UK
[2] Exoplanet Atmosphere New Emission Transmission Spectra Analysis : CEA Saclay, Paris, France; CAB-INTA, Madrid, Spain; MPIA, Heidelberg, Germany; University College London, U.K.; University of Leicester, U.K.; SRON, Utrecht, NL; Universitat Wien, Austria.

longer term changes due to active-region evolution and possible activity cycles, limit the usefulness of a single measurement. If a flare occurred during the observation it could increase the measured luminosity significantly. A number of planet-hosting stars have been observed multiple times by Galex, Swift (UVOT) and XMM (Optical Monitor) at UV wavelengths (Fig. 2). Similarly, multiple observations exist at X-ray wavelengths from XMM, Rosat, Chandra and other observatories. Compiling these observations will make it possible to estimate variability over approximately 2 decades. Repeated measurements also help to establish the average luminosity of a star, highlighting those observations which may have been affected by flaring activity. Estimating the frequency of flares for stars of different spectral types and ages is also important for taking into account the effects these high energy events may have on planets.

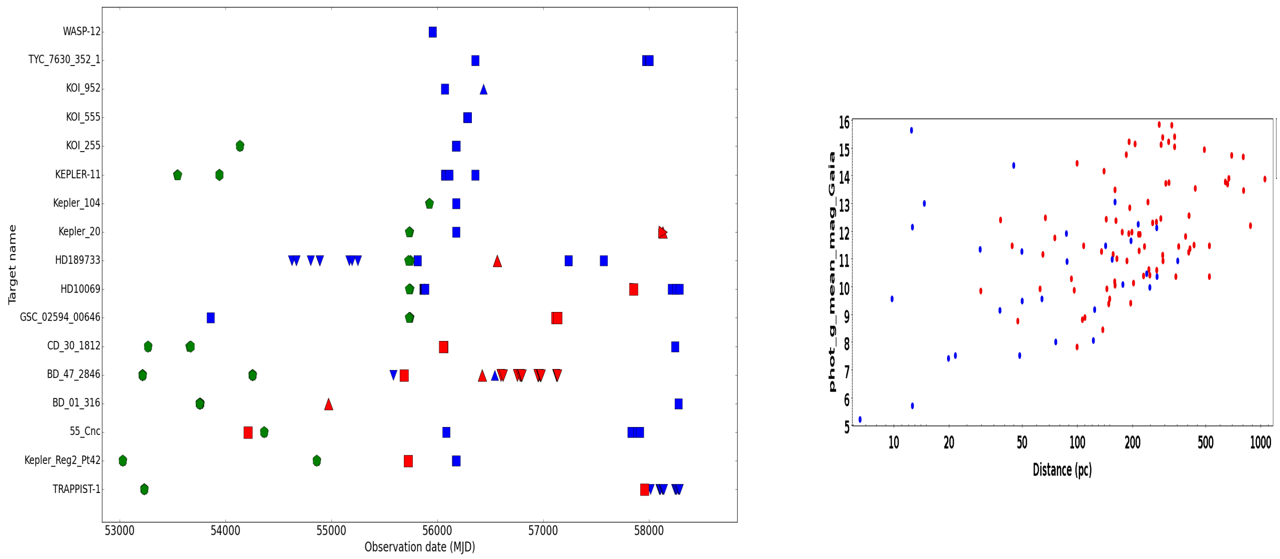

Fig. 2. Left: Timeline of UV observations covering approximately 20 years. Some stars have been observed by Galex (green), Swift UVOT (blue) and the XMM-Newton optical monitor (red), producing in total a longer timeline than any single observatory. **Right:** The distribution of the 113 host stars according to *Gaiag* magnitude (optical) and distance. Targets with available X-ray data are highlighted in blue.

The combination of detailed characterisation of host stars, together with analyses of existing and upcoming transit spectroscopy of the exoplanet atmospheres, will make it possible to investigate the links between stellar activity and the evolution of planetary atmospheres. Many questions remain about the early formation of planets which takes place when young stars are at their most active magnetically. Data gathered by this project will be made available online, providing a valuable database for use in investigations of the evolution of stars, planets and the influences that stars have on habitability.

Acknowledgements : The ExoplANETS-A project has received funding from the EU's Horizon-2020 programme; Grant Agreement no. 776403. https://cordis.europa.eu/project/rcn/212911 en.html

References

Lalitha, S., Schmitt, J. H. M. M., & Dash, S. 2018, MNRAS, 477, 808

Pye, J. P., Barrado, D., Garcia, R. A., et al. 2019, arXiv e-prints, arXiv:1903.00234

Stars and their variability observed from space
C. Neiner, W. W. Weiss, D. Baade, R. E. Griffin, C. C. Lovekin, A. F. J. Moffat (eds)

THE ONDŘEJOV EXOPLANET GROUP

M. Blažek[1, 2], P. Kabáth[1], M. Skarka[1,2], T. Klocová[1], M. Špoková[1,2], J. Šubjak[1, 3], J. Dvořáková[1, 4], J. Žák[2], D. Dupkala[1,4] and E. Plávalová[5]

Abstract. Ground-based telescopes are an integral part of exoplanetary space missions. Our poster presented results from the high-resolution Ondřejov Echelle Spectrograph (OES) installed at the Perek 2-m telescope in Ondřejov, Czech Republic and operated by the Czech Academy of Sciences. We focussed on results from monitoring Kepler/K2 and *TESS* objects during 2018–2019, and other activities and collaborations carried out by the group.

Keywords: Telescopes, Instrumentation: spectrographs, Planetary systems, Eclipses.

1 Introduction

The exoplanet group at the Astronomical Institute of the Czech Academy of Sciences was formed in 2015; more than ten members belong to the group. The research is dedicated to radial-velocity (RV) follow-up observations of exoplanetary candidates, and the characterisation of exoplanetary atmospheres.

The main scientific topics are:

- Radial-velocity follow-ups
- Detection and characterisation of exoplanetary atmospheres
- Space missions and ground-based instrumentation

2 Radial-velocity follow-ups

We are using the 2-m Perek telescope and its échelle spectrograph to characterise the host star of a candidate system and to measure RVs. We are following up planetary candidates from Kepler/K2 missions. In 2019 we started to perform ground-based follow-up observations for the *TESS* space mission, and in the future we plan to follow up candidates from the *PLATO* space mission too.

The main characteristics of the OES are as follows:

- Spectral resolving power: 50,000
- Wavelength coverage: 370–850 nm
- Detector: CCD 2048 × 2048 pix
- Calibration lamp: Th/Ar

[1] Astronomical Institute of the Czech Academy of Sciences, Fričova 298, 251 65 Ondřejov, Czech Republic
[2] Department of Theoretical Physics and Astrophysics, Masaryk University, Kotlářská 2, 611 37 Brno, Czech Republic
[3] Astronomical Institute, Charles University, Faculty of Mathematics and Physics, V Holešovičkách 2, 180 00 Praha 8, Czech Republic
[4] Institute of Physics, Faculty of Philosophy and Science, Silesian University in Opava, Bezručovo nám. 13, 746 01 Opava, Czech Republic
[5] Astronomical Institute, Slovak Academy of Sciences, Štefánikova 49, 811 04 Bratislava 1, Slovak Republic

We also plan a ground-based RV follow-up facility at the 1.52-m telescope at La Silla. A state-of-the-art échelle spectrograph *PLATOSpec* will be built and operated by a consortium led by the Astronomical Institute of the Czech Academy of Sciences, with Thüringer Landessternwarte Tautenburg and Universidad Catolica de Chile as partners. This new instrument, which will have a spectral resolving power of 70,000, will be dedicated to ground-based support of *TESS, PLATO*, and (later) *ARIEL*. More information about *PLATOSpec* can be found at `https://stelweb.asu.cas.cz/plato/index.html`.

To highlight the most recent results, we mention the discovery of the first brown dwarf, observed by *TESS*, which is orbiting a metallic-line A star. A paper on this discovery has been submitted to the AJ (Šubjak et al. 2019), and is the result of a collaboration between Harvard University, PRL India, and the KESPRINT consortium. We have also published an article about the Ap star HD 99458 as being the first ever δ Scuti pulsator in a short-period eclipsing binary./ That research was mainly based on observations with the OES (Skarka et al. 2019, see also Skarka et al., [PAGE).

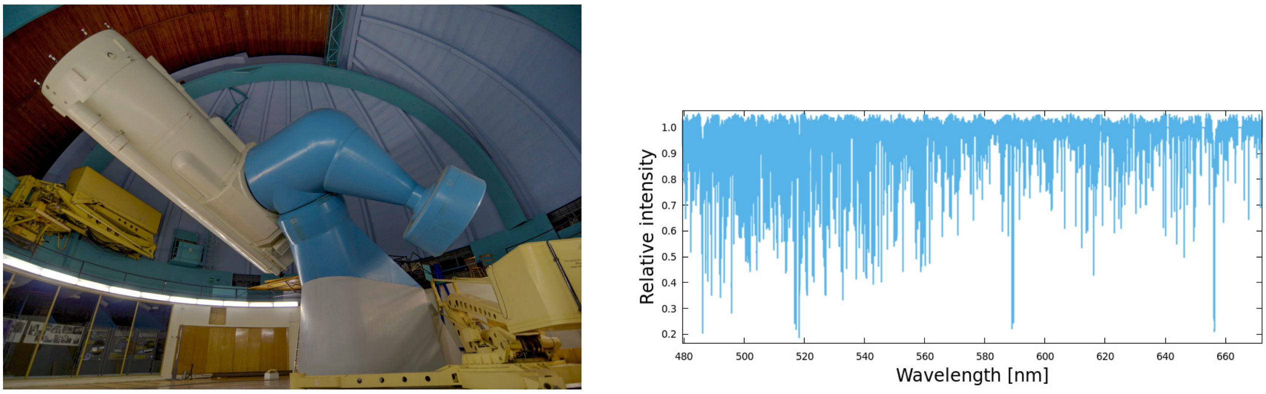

Fig. 1. Left: The Ondřejov 2-m telescope, Czech Republic. **Right**: Part of the spectrum of HD 109358 (G0V, V = 4.25 mag) obtained with the OES in an exposure of 600 seconds.

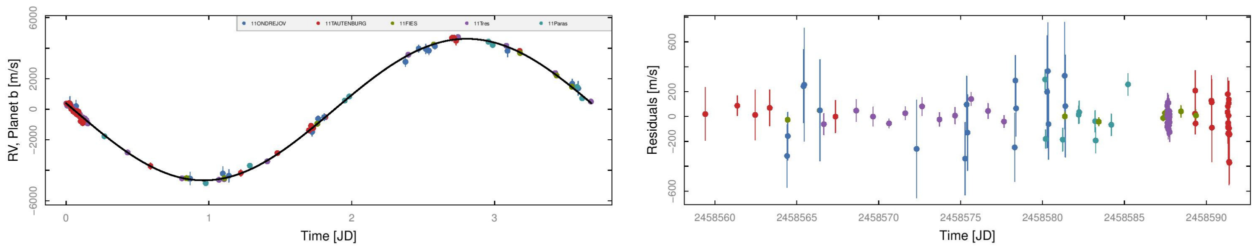

Fig. 2. Left: Example of a radial-velocity curve obtained with the OES (blue circles) and other instruments. **Right**: Residuals from the same RV curve, after removing the orbital model.

3 Exoplanetary atmospheres

Our group uses large telescope facilities (such as ESO Paranal) to detect and characterise exoplanetary atmospheres via transmission spectroscopy and emission photometry (Kabáth et al. 2019; Kabáth et al. 2019b; Žák et al. 2019), Blažek et al., in prep.). We are also involved in investigating the profiles of spectral lines and their impact on those characterizations.

4 Space missions

Our group is involved in the *PLATO* scientific programme. We are members of the PLATO Mission Consortium and are coordinating the Czech contribution to *PLATO*. The OES will be used to observe planetary candidates in the northern hemisphere, and will act as a follow-up instrument for that mission. We will also perform an initial screening of the candidates and the characterisation of hot Jupiters.

5 Collaborations

We are collaborating with Tautenburg Observatory (Germany) on RV follow-ups of *TESS* targets (Sabotta et al. 2019). We are also working closely with AI SAS (Gajdoš et al. 2019; Skarka & Kabáth 2019; Kabáth et al. 2019a), and are a member of the KESPRINT consortium(Gandolfi et al. 2019; Persson et al. 2019).

P. Kabáth, M. Blažek, M. Špoková, and J. Šubjak acknowledge grant GAČR 17-01752J. M. Skarka acknowledges the support from an OP VVV PostdocMUNI (No. CZ.02.2.69/0.0/0.0/16_027/0008360).

References

Gajdoš, P., Vaňko, M., Pribulla, T., et al. 2019, MNRAS, 484, 4352

Gandolfi, D., Fossati, L., Livingston, J. H., et al. 2019, ApJ, 876, L24

Kabáth, P., Skarka, M., Sabotta, S., & Guenther, E. 2019a, Contributions of the Astronomical Observatory Skalnate Pleso, 49, 462

Kabáth, P., Žák, J., Boffin, H. M. J., et al. 2019b, PASP, 131, 085001

Kabáth, P., Zak, J., Boffin, H., Ivanov, V. D., & Skarka, M. 2019, in AAS/Division for Extreme Solar Systems Abstracts, Vol. 51, 326.28

Persson, C. M., Csizmadia, S., Mustill, A. e. J., et al. 2019, A&A, 628, A64

Sabotta, S., Kabáth, P., Korth, J., et al. 2019, MNRAS, 489, 2069

Skarka, M. & Kabáth, P. 2019, Contributions of the Astronomical Observatory Skalnate Pleso, 49, 137

Skarka, M., Kabáth, P., Paunzen, E., et al. 2019, MNRAS, 487, 4230

Šubjak, J., Sharma, R., Carmichael, T. W., et al. 2019, arXiv e-prints, arXiv:1909.07984

Žák, J., Kabáth, P., Boffin, H. M. J., Ivanov, V. D., & Skarka, M. 2019, AJ, 158, 120

Stars and their variability observed from space
C. Neiner, W. W. Weiss, D. Baade, R. E. Griffin, C. C. Lovekin, A. F. J. Moffat (eds)

SOUTHERN BP-E STAR HD124448

M. Zboril[1]

Abstract. The atmospheres of early-type He-rich stars are believed to be non-standard in several respects. The He-rich star HD 124448 also shows UV and visual emissions. Perhaps it is the reason for the large uncertainty in its basic stellar parameters. Using both UV and ground-based observations, basic stellar parameters, evolutionary status, $v \sin i$ and elemental abundances are re-examined.

Keywords: Stellar atmosphere, stellar activity, stellar parameters

1 Introduction

He-rich stars (also called intermediate helium stars) typically posses light variations that are often supported by variations in the mean magnetic field. These stars are approximately B2 main-sequence stars. Besides having non-standard He atmospheres, they are likely to display both azimuthal and vertical He inhomogeneities. The abundance of helium and its evolutionary status were studied by Zboril et al. (1997), and a number of suspected He stars (HD 124448, HD 56139, HD 105435, CpD -62 2124) were found in our sample with emission at visual wavelengths (hydrogen profile). In an attempt to start studying these emissions we selected the Bp star HD 124448 from the sample.

2 Observations

To study helium stars, 155 spectra for 24 stars were obtained with the ESO 1.5-m telescope and the Boller-Chivens spectrograph. The spectra of HD 124448 were obtained over 4 nights (between January 5 and January 9 1993). It is important to note that emission in the hydrogen profiles (Hβ, Hγ, Hδ) was recognised in all spectra. The emission was constant and at the level of continuum. The *IUE* archive contains 7 low-resolution (swp) spectra that were obtained since 1978; variable emission in the Lyman-α profile was clearly detected in data.

3 Analysis and results

The basic characteristics of this star are certainly non-standard. It has unusual colour indices, a broad interval of spectral type and luminosity class, metallicity, a perhaps unknown projected $v \sin i$ and a small parallax of order 0.57 mas: see Table 1.

$(U-B)$	$(B-V)$	V	$T_{\rm eff}$	$logg$	$v \sin i$	[Fe/H]	note
-0.80	-0.09	9.98	16-27000 K	2-4	-	0.2 - 1.0	Simbad
-	-	-	16 000	4.0	44	0.8 He	this work

However, these characteristics are actually more complicated. For example, narrow-band and UBV photometry suggest that the effective temperature is of the order of 23000 K. A near-solar helium abundance and a large stellar radius (13 $R_{\rm sol}$) were reported for this star by Schoenberner & Wolf (1974),while oxygen underabundance and a hint of a cool circumstellar shell was proposed by Hill (1965). Furthermore, as the emission fills in the hydrogen profile, it is not possible to study the profile and adopt suitable model atmosphere. Strong UV resonance lines of Al and Si are not present in absorption.

We recall that an adequate model atmosphere for a star should undergo the following criteria: an agreement of absolute fluxes with observations at around 555.6 nm, relative fluxes at 120–500 nm, bound–bound hydrogen profiles, and fluxes in the infrared region. Our study was therefore very limited with respect to calculating a model atmosphere for the photosphere; the study consisted of the following steps: distance modulus $m - M$ (for

[1] Slovakia

the stellar radius), effective temperature from the radius and the absolute magnitude, synthetic UV spectra and observations for spectral type and metallicity, synthetic visual spectra and detailed line profiles for metallicity, individual abundances and projected $v \sin i$. The $v \sin i$ value was also studied in the Fourier domain.

The calculations were performed with the following software: an early PC version of the NLTE Synspec code (original reference: Hubeny (1992), Zboril (1996)) and adopted LTE model atmospheres, up-dated versions of our own software (Convol for a convolution, Sigma6 for Fourier transforms).

The basic stellar properties for the star were found to be:

- $T_{\rm eff} = 16\,000\,K$, $R/R_{\rm sol} = 4.07$, log g=3.9, $R/R_{\rm zams} = 1.19$ ($m - M$ modulus) inter-stellar absorption less than 0.3/kpc
- $T_{\rm eff}\,16\,000\,K$, log g 2.5-4.0, C, Si abundance non-solar (UV region)
- $T_{\rm eff}\,16000K$, log g=4.0, $A_{\rm C}$=2.4e-2, Mg=1.8e-4, Si=1.7e-4 (vis. region) He=0.8, Fe=4.8e-4, O=8.3e-3
- He I 4009, 4471, 4438 and 4713 give preliminary $A_{\rm He} = 0.83$

  In addition, rotational broadening is dominant; $v \sin i = 44$ km/s; there are variable emissions – hydrogen profiles and resonance UV transitions, and extra absorption is present in He line profiles and in a number of spectral type tracers (Mg II 4481, C II 4267, N II 4601), indicating possibly binary status or multiplicity for this star.

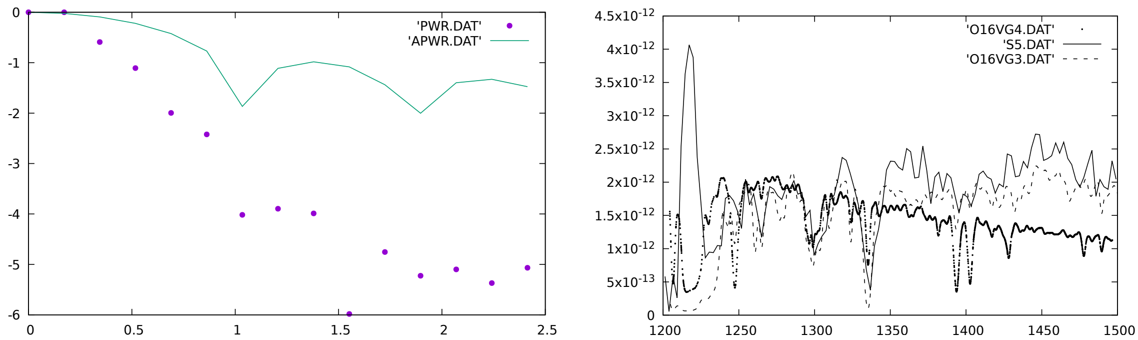

Fig. 1. Left: C II 4267 Å profile in the Fourier domain (dots); projected vsini value (solid line). **Right:** *IUE* swp 5789l spectrum (solid line); synthetic spectrum from a model for 16000 K, log g of 4 (dashed line), and model for 27000 K, log g of 4 (dots).

4 Conclusions

This star displays not only helium overabundace but overabundances of some light elements as well. According to the projected $v \sin i$ value, it belongs to the class of slower rotators. It is reported that the star is also pulsating. The overabundance seems to be better understood through the construction of an overall active atmosphere or shell joining the stellar photosphere.

I thank Vienna Observatory for financial support, and J. Krtička for his help in the final version of the poster. This work is based on observations obtained at ESO and with *IUE* (operated by NASA, SERC and ESA). This research has made use of the Simbad database, Strasbourg, France.

References

Hill, P. 1965, MNRAS, 129, 137
Hubeny, I. 1992, priv.com
Schoenberner, D. & Wolf, R. E. A. 1974, A&A, 37, 87
Zboril, M. 1996, ASP. Conf. Ser., 108, 193
Zboril, M., North, P., Glagolevskij, Y. V., & Betrix, F. 1997, A&A, 324, 949

Lessons learned

Stars and their variability observed from space
C. Neiner, W. W. Weiss, D. Baade, R. E. Griffin, C. C. Lovekin, A. F. J. Moffat (eds)

BRITE-CONSTELLATION OPERATIONS AND DATA COLLECTION

R. Kuschnig[1]

Abstract. BRITE-Constellation (BRight Target Explorer) consists of six nano-satellites aiming to study the variability of the brightest stars in the sky. Austria, Poland, and Canada contribute two spacecraft each all launched into low earth orbits. The satellites have the same structure: they are 20 cm cubes, 7kg mass, with a CCD photometer fed by 3 cm aperture telescopes. The main difference between pairs of satellites is the instrument passband which is set to blue (400-450nm) or red (550-700nm). The core scientific objective is to obtain high-precision two-color photometry, with a time base of up to 180 days, of stars brighter than 4.5 mag in order to study stellar pulsations, spots, and granulation, eclipsing binaries, search for planets and more. Since the launch of the first two BRITE satellites in February 2013 more than 6 and a half years of experiences in space have been gathered to run the mission and a summary of lessons learned is presented. By now more than 30 peer-reviewed scientific articles have been published based on data collected by BRITE-Constellation satellites in space and most results presented therein benefited greatly from supplementary spectroscopy obtained by meter-size ground-based telescopes. In addition the synergy potential with the 2018 launched NASA TESS mission is outlined.

Keywords: Techniques: photometric, Methods: observational

1 BRITE-Constellation overview

The acronym BRITE stands for BRIght Target Explorer. BRITE-Constellation is a fleet of six nano-satellites with each of three pairs funded and built in Austria, Canada and Poland. The primary goal of the BRITE mission is to collect high precision photometry from selected very bright stars in the sky with limiting magnitude of 4.5. Measurements are collected over a time span of up to 6 months and for most objects in two colors. Exposure times are typically set between 0.1 and 5 seconds. Three images of 16-30 stars in the instant field of view per minute are collected during 15-30 minutes of each satellite orbit. The aim is to achieve milli-magnitude precison photometry on orbital means. A comprehensive overview of the technical design of the satellites was provided by (Weiss et al. 2014) and of the BRITE mission operations by (Kuschnig 2017). This article is focused on developments and updates during the past two years.

Even after more than six-and-a-half years of operations of the two Austrian satellites and more than five years of the other spacecraft, five of the six units of BRITE-Constellation are collecting scientifically useful data. Table 1 comprises the main properties of the BRITE satellites.

Table 1. BRITE-Constellation satellites.

Country	Name	ID	Launch Date	Period [min]	Filter
Austria	UniBRITE	UBr	25-02-2013	100.37	RED
	BRITE-Austria	BAb	25-02-2013	100.36	BLUE
Poland	BRITE-Heweliusz	BHr	19-08-2014	97.10	RED
	BRITE-Lem	BLb	21-11-2013	99.57	BLUE
Canada	BRITE-Toronto	BAb	19-06-2014	98.24	RED
	BRITE − Montreal	*BMb*	19-06-2014	*n/a*	*BLUE*

While BRITE-Montreal did not separate from the launch vehicle and hence was never operational, all other BRITE satellites which where designed for a nominal productive lifetime of two years are still working very well three times longer then base-lined. Therefore, the BRITE satellites are perfect examples for nano-satellites that can be utilized for front-edge science extending over several years of productive lifetime, something often critized of such small platforms in space.

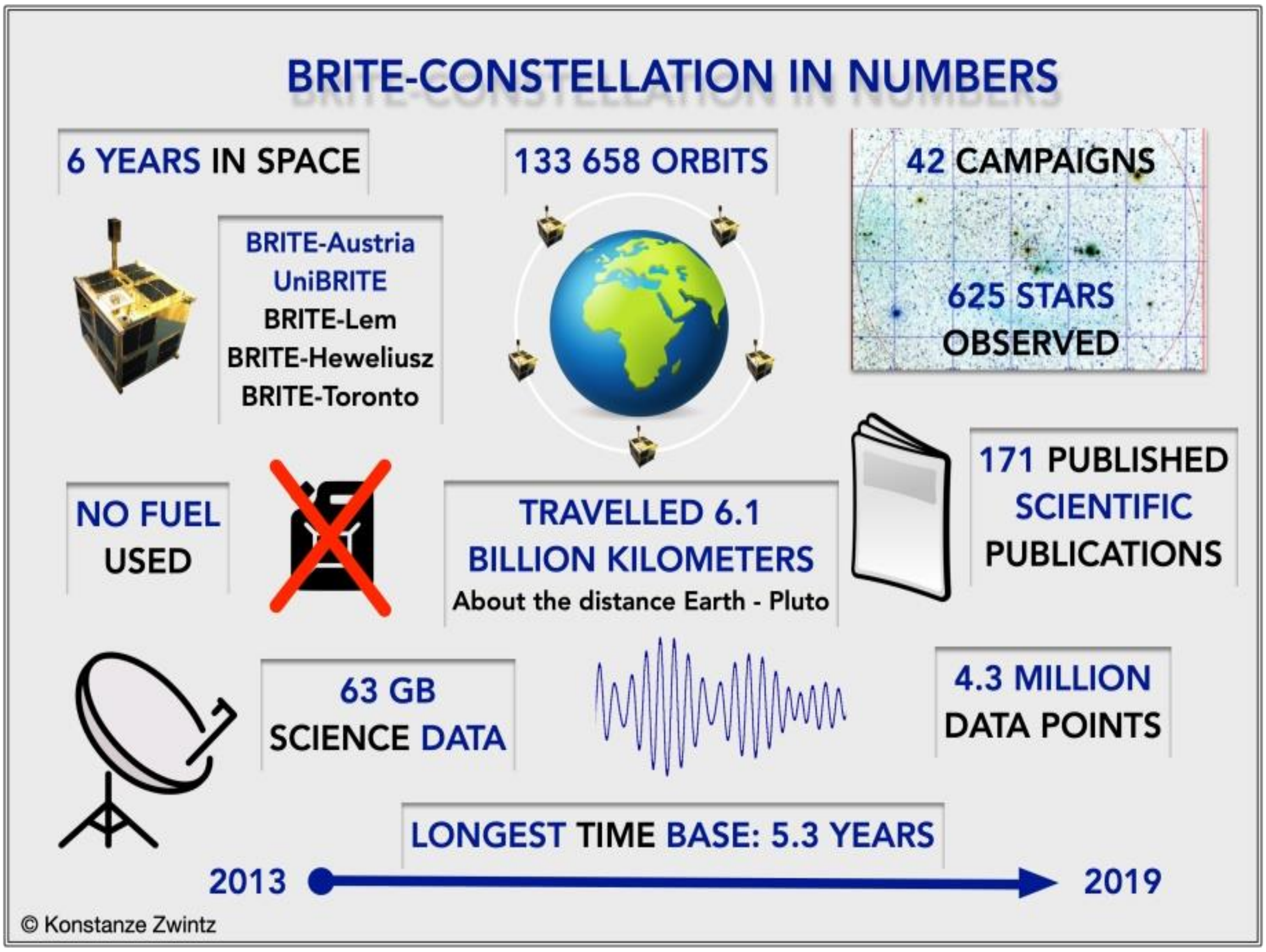

Fig. 1. BRITE-Constellation in numbers.

In total at the time of the conference, BRITE-Constellation satellites have observed 625 individual stars during 42 campaigns. More numbers and stats are shown in Figure 1 .

The observation fields and selected target stars within are shown in Figure 2 Apparently most observed fields were placed at or close to the Galactic plane due to the fact that many bright stars are found there on the sky. In particular many primary targets like bright O, B and Be stars can be placed in the 24 deg wide focal plane when selecting those orientations.

Many of the 625 stars were observed multiple times during the past six-and-a-half years since December 2013 when the first two BRITE satellites began regular science observations. Most notably, the brightest stars in the Orion field have essentially been measured during 5 campaigns even in two colors.

2 Performance over time

As reported in the past, the BRITE CCDs (Kodak,KAI 11002-M) are subject to radiation degradation where pixels and even whole columns had elevated dark (thermal) signals, 'hot pixels' and 'warm columns'. These defects emerge across the whole detector and progressively increase over time. The cause is bombardment of the CCD chip with high energy protons and electrons mainly during passages through the SAA (South Atlantic Anomaly), which occur every day in low earth orbit. While 'warm columns' have only modest effects on the quality of BRITE photometry, the number of 'hot pixels' which are generated at a rate of 1.7 percent per year (at 20C CCD operating temperature) and which merge with the stellar PSFs are a substantial source of noise.

[1] Institut für Kommunikationsnetze und Satellitenkommunikation, Technical University Graz, Inffeldgasse 12, A-8010 Graz, Austria

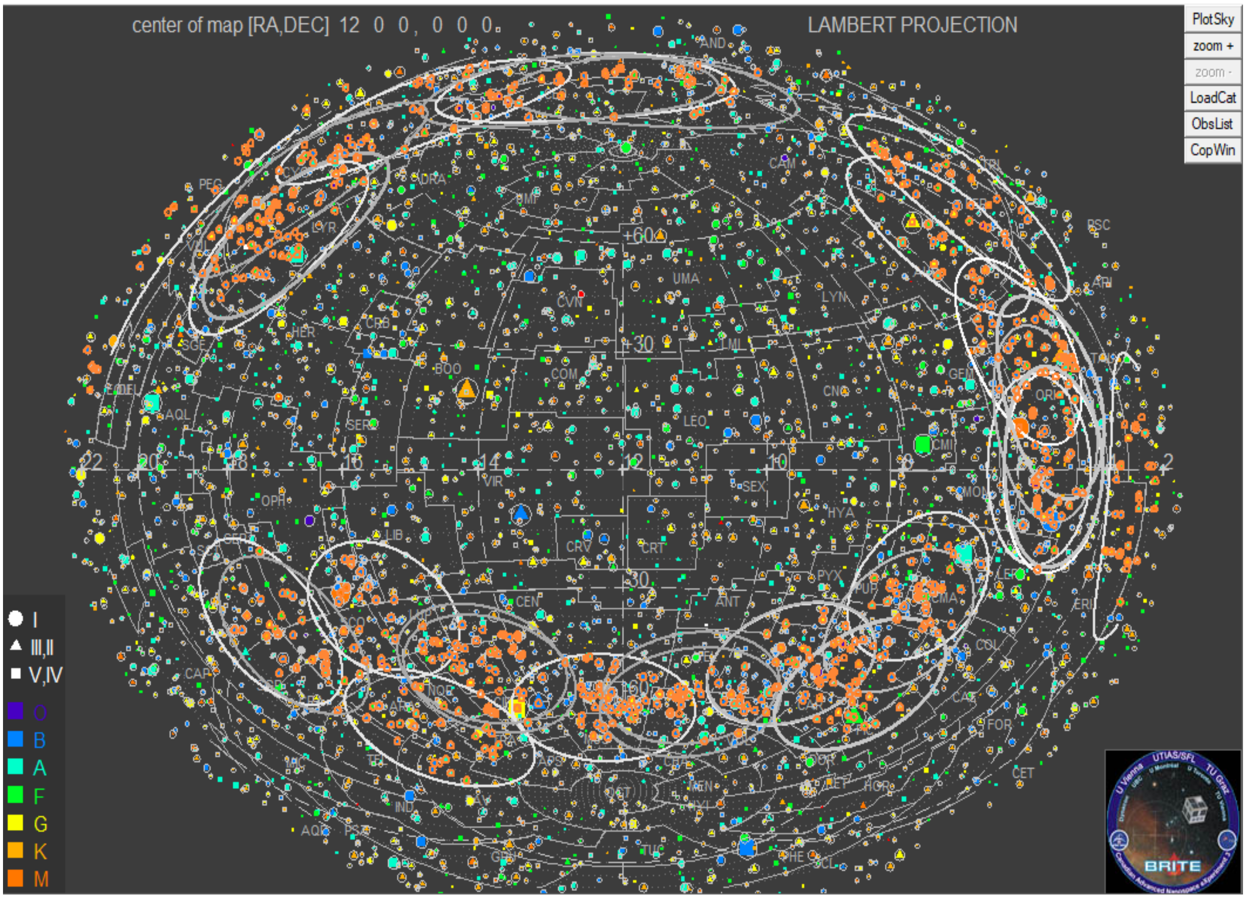

Fig. 2. BRITE-Constellation stars and observation fields

To compensate for that the operating scheme was changed in the fall of 2014 such that the position of the stars between each exposure changed from a position A to B and back to A and so forth by about 30 pixels along CCD rows. Subtracting images obtained from subsequent exposures for a star removes to a large degree the signal offsets of hot pixels when applying aperture photometric reduction to the collected data ((Popowicz et al. 2017)).

Up to the present four of the five BRITE satellites reveal a fraction of 'hot pixels' in excess of 12 percent. Only BRITE-Heweliusz (BHr) the second Polish satellite, which has a slightly different instrument design including specifically introduced radiation shielding of the detector housing has a significantly lower damage by a factor of four due to that foresight.

To evaluate the photometric performance over time during the past six years, the photometric scatter of stars can be calculated as shown in Figure 3

The photometric noise obtained based on BAb from ϵ and σ Orionis over the past six years shows in both cases only a modest increase. The past current and in the future projected 'hot pixel' fraction of the BRITE-Austria CCD has also been determined as shown in Figure 3. The residual 'problem pixel' fraction after applying the reduction pipeline is also drawn as solid bars. The photometric performance development over time here presented just for one satellite (BAb) is in fact consistent with UBr, BTr and BLb. BHr which is less affected by radiation damage reveals thus far no significant loss of data quality since launch in August 2014.

3 BRITE and TESS

TESS (https://tess.gsfc.nasa.gov/) is a NASA mission launched in April 2018 to search for planets around nearby stars across almost the full sky. While TESS photometry is more precise than BRITE photometry, about 90 percent of TESS targets will only be observed for 27 days. BRITE, however, can observe up to 180

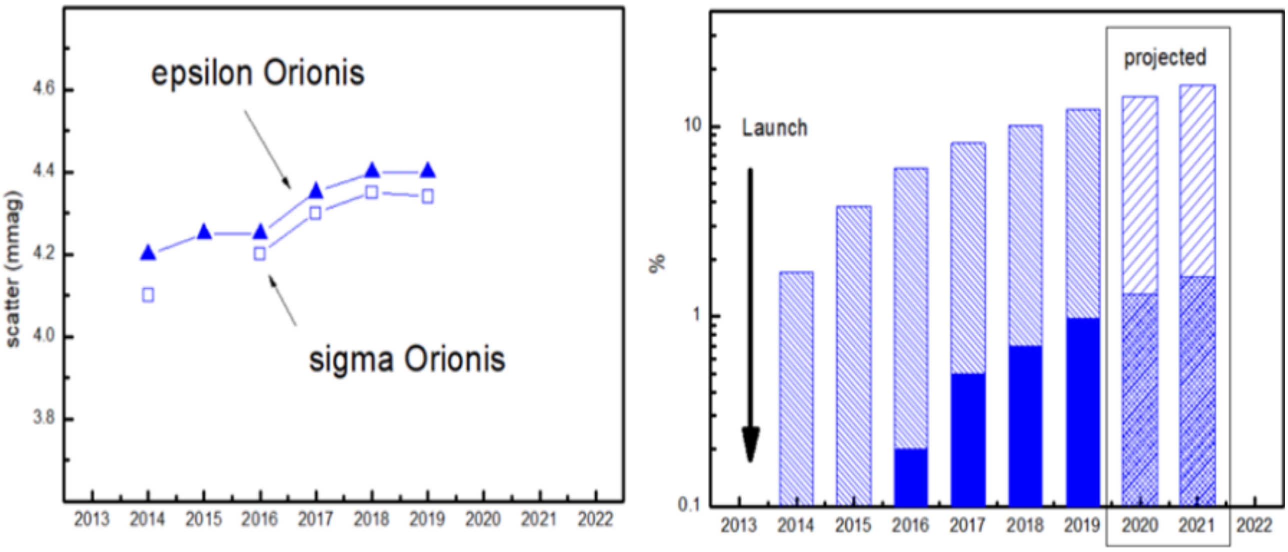

Fig. 3. (Left panel) BRITE-Austria photometric scatter (noise) values plotted over the past 6 observing campaigns of ϵ Ori and σ Ori. (Right panel) BRITE-Austria percentage of hot pixels in the past, current and projected till 2021. The solid blue bars indicate the residual pixel percentage when applying the chopping scheme.

days in a single observing campaign and additionally in two colours. Almost all stars in the BRITE program will be also observed by TESS, often even contemporaneously. Combining data sets from both missions opens up unique scientific opportunities.

TESS science data gathering started in July 2018. The observing plan started in the southern hemisphere split up in 13 segments each observed by four cameras for about 28 days. In parallel the BRITE observing plan also included southern fields and in December 2018 it started to overlap in time. As an example the contemporaneous photometric data collection of η Orionis is portrayed in Figure 4.

From the comparison of just that one case it is evident that combining both data sets for that one star collected in a blue passband (BLb) and the red range of TESS can be of particular value for the analysis of this complex multiple star system. The ultra-high precision of TESS data can reveal much more spurious variations which may be present in the BRITE data at very low signal-to-noise levels. However, the much longer time base of the BRITE data be used for much better frequency resolution in the Fourier analysis.

From December 2018 onwards, BRITE and TESS were observing more than 60 stars in common at least during 28 days contemporaneously. Among these were many different types of variable stars from hot massive O and B stars to cool Red Giants. Some of those were observed by two BRITE satellites in red and blue bands and in one band with TESS.

4 Summary and Outlook

The BRITE-Constellation satellites are still working well. Despite being six years in space, three times longer than the anticipated lifetime, high-precision photometric data from selected bright stars are still collected on a daily basis. Based on the current condition and performance of the hardware, despite significant radiation degradation of the CCD detectors, the mission can continue at least until the end of 2021 without severely compromised quality.

Many outstanding results based on BRITE data have furthered the understanding of physical processes acting in many different types of stars. Furthermore, a rare Nova eruption was recently monitored by BRITE satellites with unprecedented quality and time coverage. The overall scientific analysis has currently led to 31 refereed articles in highly-ranked journals, along with three international science conferences and their proceedings, adding up to a total of more than 170 publications to date. A recent highlight was this international conference Stars and their Variability, Observed from Space Celebrating BRITEConstellation with more than 260 scientist from across the globe coming together in Vienna.

The future activities of BRITEConstellation will focus, among various priorities, on the synergy of BRITE and TESS space photometry with ground based spectroscopy, collected contemporaneously by instruments such as SONG.

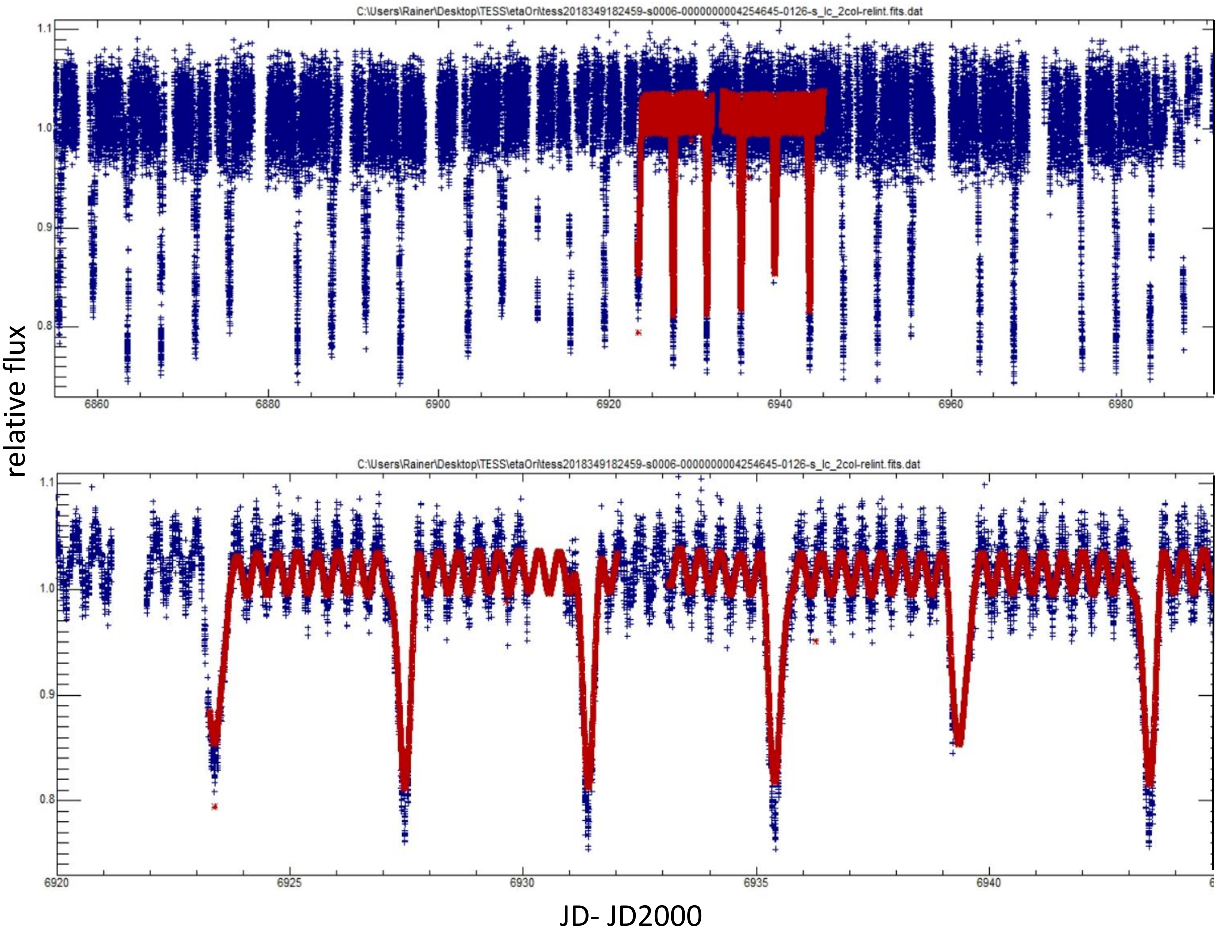

Fig. 4. top: complete 137-day long η Orionis light-curves obtained by BRITE-LEM (BLb) in blue and by TESS in red (21 days). bottom: closeup look at the period of contemporaneous observations

References

Kuschnig, R. 2017, in Second BRITE-Constellation Science Conference: Small Satellites - Big Science, ed. K. Zwintz & E. Poretti, Vol. 5, 15–25

Popowicz, A., Pigulski, A., Bernacki, K., et al. 2017, A&A, 605, A26

Weiss, W. W., Rucinski, S. M., Moffat, A. F. J., et al. 2014, PASP, 126, 573

Stars and their variability observed from space
C. Neiner, W. W. Weiss, D. Baade, R. E. Griffin, C. C. Lovekin, A. F. J. Moffat (eds)

SOLAR-LIKE OSCILLATIONS: LESSONS LEARNED & FIRST RESULTS FROM TESS

D. Huber[1], K. Zwintz[2] and the BRITE team

Abstract. Solar-like oscillations are excited in cool stars with convective envelopes, and provide a powerful tool to constrain fundamental stellar properties and interior physics. We provide a brief history of the detection of solar-like oscillations, focussing in particular on the space-based photometry revolution started by the *CoRoT* and *Kepler* Missions. We discuss some of the lessons learned from those missions, and highlight the continued importance of smaller space telescopes such as the BRITE Constellation to characterize very bright stars with independent observational constraints. As an example, we use BRITE observations to measure a tentative surface rotation period of 28.3 ± 0.5 days for α Cen A, which has so far been only poorly constrained. We also discuss the expected yields of solar-like oscillators from the *TESS* Mission, demonstrating that *TESS* will complement *Kepler* by discovering oscillations in a large number of nearby subgiants, and we present first detections of oscillations in *TESS* exoplanet host stars.

Keywords: Stars: oscillations, fundamental parameters, Planets and satellites: fundamental parameters

1 Introduction: A Brief History of Solar-like Oscillations

Solar-like oscillations in cool stars are excited by turbulent convection in the outer layers (e.g. Houdek et al. 1999), and most commonly described by a spherical degree l (the total number of node lines on the surface), azimuthal order $|m|$ (the number of node lines that cross the equator), and radial order n (the number of nodes from the surface to the centre of the star). Modes with higher spherical degrees penetrate to shallower depths within the star, and thus the detection of radial ($l = 0$) and non-radial ($l > 0$) modes provides a diagnostic for the interior structure and fundamental properties of stars. Solar-like oscillators typically exhibit a rich oscillation spectrum with regular spacings, enabling mode identification through simple pattern recognition (see e.g. Bedding 2011; Aerts 2019, for introductory reviews).

Following the discovery of oscillations in the Sun in the 1960s (Leighton et al. 1962), early efforts to detect oscillations in other stars focussed on ground-based radial-velocity (RV) observations. The first confirmed detection of oscillations in a star other than the Sun was made in Procyon by Brown et al. (1991), followed by the first detection of regularly spaced frequencies in η Boo by Kjeldsen et al. (1995). The greatly improved RV precision for detecting exoplanets enabled the detection of oscillations in several nearby main-sequence and subgiant stars such as β Hyi (Bedding et al. 2001; Carrier et al. 2001), α Cen A (Bouchy & Carrier 2001; Butler et al. 2004) and B (Carrier & Bourban 2003; Kjeldsen et al. 2005), and in red giant stars such as ξ Hya (Frandsen et al. 2002) and ϵ Oph (De Ridder et al. 2006).

Some of the first space-based photometric observations of solar-like oscillations were obtained by the Canadian space telescope *MOST* (Microvariability and Oscillations in Stars, Walker et al. 2003; Matthews 2007), which initially yielded a non-detection in Procyon (Matthews et al. 2004) but later confirmed a detection that was consistent with RV observations (Guenther et al. 2008; Huber et al. 2011). *MOST* also detected oscillations in red giants (Barban et al. 2007), including observational evidence for non-radial modes (Kallinger et al. 2008). Space-based observations of solar-like oscillations were also performed using the startracker of the *WIRE* (Wide-field InfrRed Explorer) satellite (Schou & Buzasi 2001; Retter et al. 2003; Bruntt et al. 2005; Stello et al. 2008), the *SMEI* (Solar Mass Ejection Imager) experiment (Tarrant et al. 2007) and the *Hubble Space Telescope* (Edmonds & Gilliland 1996; Gilliland 2008; Stello & Gilliland 2009; Gilliland et al. 2011). In total, ground and space-based observational efforts prior to 2009 yielded detections in ~ 20 stars (see left panel of Figure 1).

A major breakthrough, which is now widely recognized as the beginning of the space photometry revolution of asteroseismology, was achieved by the French-led *CoRoT* (Convection, Rotation and planetary Transits) satellite. *CoRoT* detected oscillations in a number of main-sequence stars (e.g. Appourchaux et al. 2008; Michel

[1] Institute for Astronomy, University of Hawai'i, 2680 Woodlawn Drive, Honolulu, HI 96822, USA
[2] Institut für Astro- und Teilchenphysik, Universität Innsbruck, Technikerstrae 25, A-6020 Innsbruck

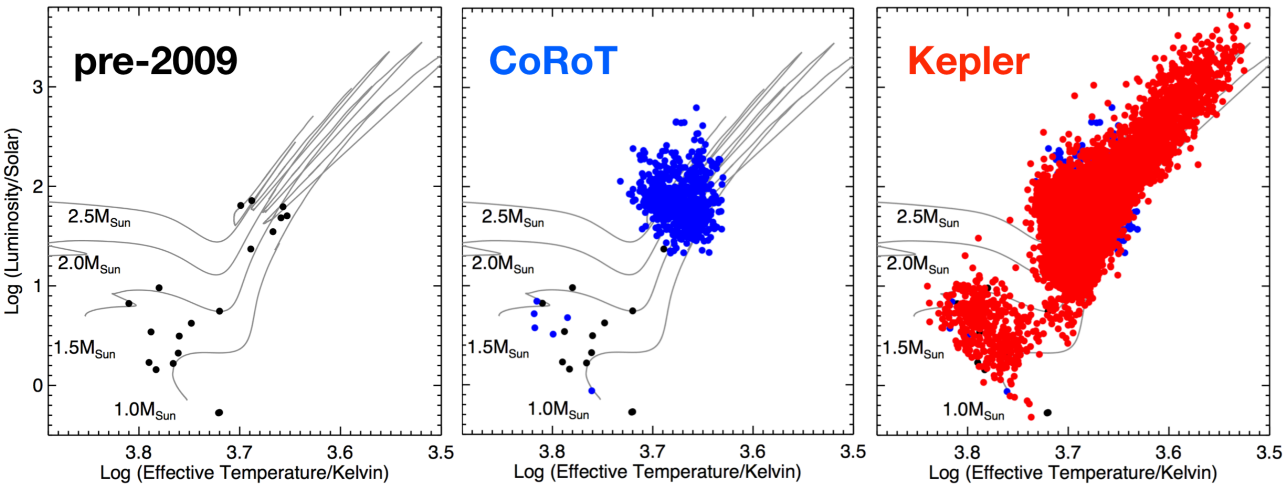

Fig. 1. H–R diagram showing stars with detected solar-like oscillations prior to 2009 (left panel), and after adding detections by the *CoRoT* (middle panel) and *Kepler* (right panel) missions. Grey lines show evolutionary tracks for solar-metallicity with masses as marked. The space-photometry revolution has increased the number of solar-like oscillators by three orders of magnitude over the past decade.

et al. 2008) and several thousands of red-giant stars (e.g. Hekker et al. 2009) (middle panel of Figure 1). In particular, *CoRoT* demonstrated unambiguously, for the first time, that red giants oscillate in non-radial modes (De Ridder et al. 2009), a result which opened the door for detailed studies of the interior structure of red giants (see Hekker & Christensen-Dalsgaard 2017, for a recent review).

Kepler, launched in 2009, completed the revolution of asteroseismology by covering the low-mass H–R diagram with detections. It detected oscillations in over 500 main-sequence and subgiant stars (Chaplin et al. 2014) and over twenty thousand red giants (Hekker et al. 2011; Stello et al. 2013; Yu et al. 2016), enabling the study of oscillations across the low-mass H–R diagram (right panel of Figure 1). The larger number of red giants with detected oscillations is due to a combination of two effects. First, oscillation amplitudes increase with luminosity (Kjeldsen & Bedding 1995), making a detection easier at a given apparent magnitude. Secondly, the majority of targets were observed with 30-minute sampling, setting an upper limit of $\log g \sim 3.5$ (since less evolved stars oscillate above the Nyquist frequency).

2 Lessons Learned from CoRoT and Kepler

CoRoT and *Kepler* yielded numerous breakthroughs for solar-like oscillators. One of the most influential discoveries was that scaling relations for global asteroseismic observables such as the frequency of maximum power, the large frequency separation, and oscillation amplitudes – all of which can be measured trivially from power spectra – are remarkably precise across nearly the entire low-mass H–R diagram (e.g. Stello et al. 2009; Huber et al. 2011; Mosser et al. 2012). The use of these scaling relations started the era of "ensemble asteroseismology" through the large-scale determination of stellar radii and masses (Kallinger et al. 2009), paving the way for the now widely successful synergy between asteroseismology and galactic archeology (Miglio et al. 2013, e.g.). Furthermore, the systematic discovery of mixed modes and rotational splittings opened up numerous breakthrough studies of the interior structure and rotation of subgiants and red giants (e.g. Beck et al. 2011; Bedding 2014; Mosser et al. 2014; Stello et al. 2016).

Space-based observations of solar-like oscillators also uncovered several new challenges. For example, *CoRoT* and *Kepler* demonstrated that mode lifetimes decrease strongly for hot stars, causing an increase in the line-widths which hampers identification of radial and non-radial modes. The "bloody F star" problem has been partially addressed through the phase offset ϵ (White et al. 2012), but remains a major obstacle for carrying out asteroseismology of hot stars. In addition, the transition of solar-like oscillators to classical pulsators remains only poorly understood, and causes major uncertainties when predicting amplitudes and thus detection yields for current and future space-based missions such as *TESS* and PLATO.

Another major challenge for *Kepler* was that the majority of oscillating stars are relatively faint, and thus lack independent observational constraints that are required to fully exploit the information provided by individual frequencies. For example, the potential of the *Kepler* "legacy" sample to constrain the convective

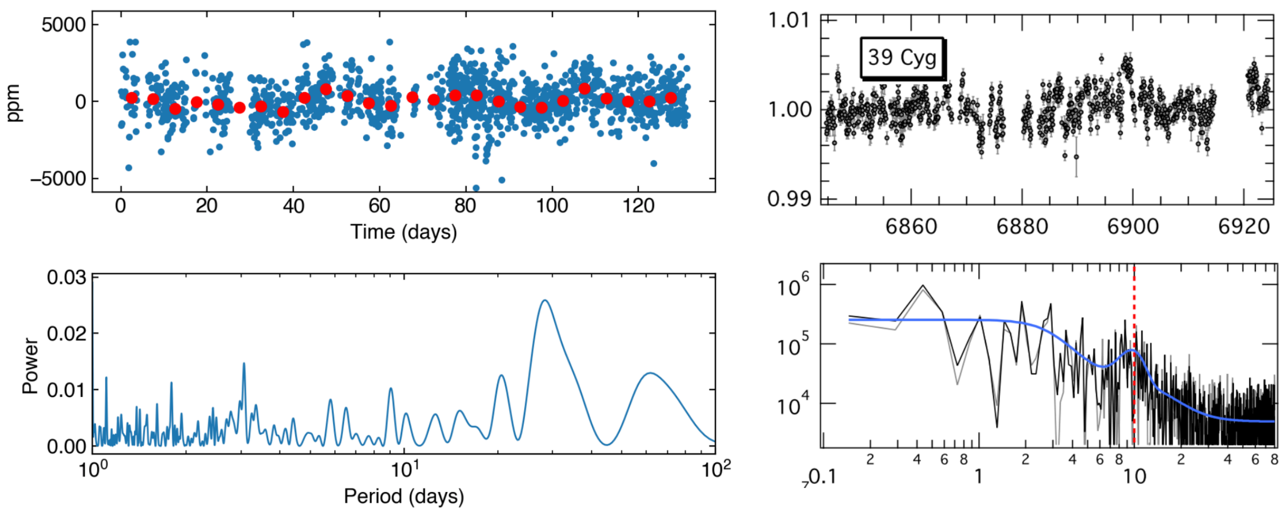

Fig. 2. *Left:* BRITE Constellation light curve of α Cen obtained in 2014 (top), binned into one-orbit (blue circles) and one-day (red circles) averages. A periodogram shows a significant peak at 28.3 ± 0.5 days, which may correspond to the rotation period of α Cen A (see text). *Right:* BRITE Constellation light-curve and power spectrum of the red giant 39 Cyg, showing the clear detection of solar-like oscillations. Adapted from Kallinger et al. (2019).

mixing length parameters (Silva Aguirre et al. 2017) and initial Helium abundances (Verma & Silva Aguirre 2019) is at times limited by the lack of fundamental constraints such as temperatures, radii and masses from interferometry and/or binary systems.

Small space telescopes such as BRITE Constellation play an important role by filling the gap left by the inability of most space instruments to observe very bright stars. A prominent example is α Cen: while fundamental properties of both components have been exceptionally well constrained using astrometry and asteroseismology, their rotation periods still remain a matter of debate. Figure 2a shows the BRITE light-curve of α Cen obtained 2014. The continuous coverage over 120 days reveals variability with a period of 28.3 ± 0.5 days. α Cen is not resolved in BRITE observations, but – based on the activity cycle of both components (Ayres 2018) – the period that is observed probably corresponds to α Cen A. That period is consistent with, but significantly more precise than, previous estimates from asteroseismic splittings (21 ± 9 days, Fletcher et al. 2006), and when dilution by component B is taken into account the amplitude of the spot modulation (~ 370 ppm) is consistent with that of relatively quiescent solar-type stars (van Saders et al. 2019). BRITE follow-up observations in 2018 provided only a preliminary confirmation of this signal, tentatively attributed to change in the spot coverage. The period identified in the 2014 dataset should therefore be viewed with caution.

BRITE has also detected oscillations in bright red giants such as 39 Cyg (Fig. 2, right, Kallinger et al. 2019). 39 Cyg ($V = 4.4$) is eight magnitudes brighter than the average *Kepler* red giant, thus providing an excellent opportunity to study oscillations in red giants with well determined independent parameters.

3 First Results from the *TESS* Mission

3.1 Target Selection

The NASA *TESS* Mission (Ricker et al. 2014) was launched in April 2018. Located in a 2:1 lunar resonance orbit, *TESS* observes 24×96 degree fields for 27 days, with continuous coverage near the ecliptic poles. In addition to downloading the entire FOV every 30-minutes (full-frame images, FFIs), *TESS* also observes a subset of targets in a 2-minute cadence, which is suitable for the detection of oscillations in solar-type stars.

The selection of asteroseismology targets for the *TESS* prime mission was coordinated within the TESS Asteroseismic Science Consortium (TASC). To select solar-like oscillators, we calculated a detection probability given estimates of effective temperature, luminosity, apparent *TESS* magnitude and the expected number of observed sectors for all stars in Hipparcos and Gaia DR2 following the method by Chaplin et al. (2011), modified for the *TESS* mission. The resulting Asteroseismic Target List (ATL) for the *TESS* mission is described in detail in Schofield et al. (2019).

Figure 3 shows an expected representative yield of solar-like oscillators from *TESS* compared to ground-

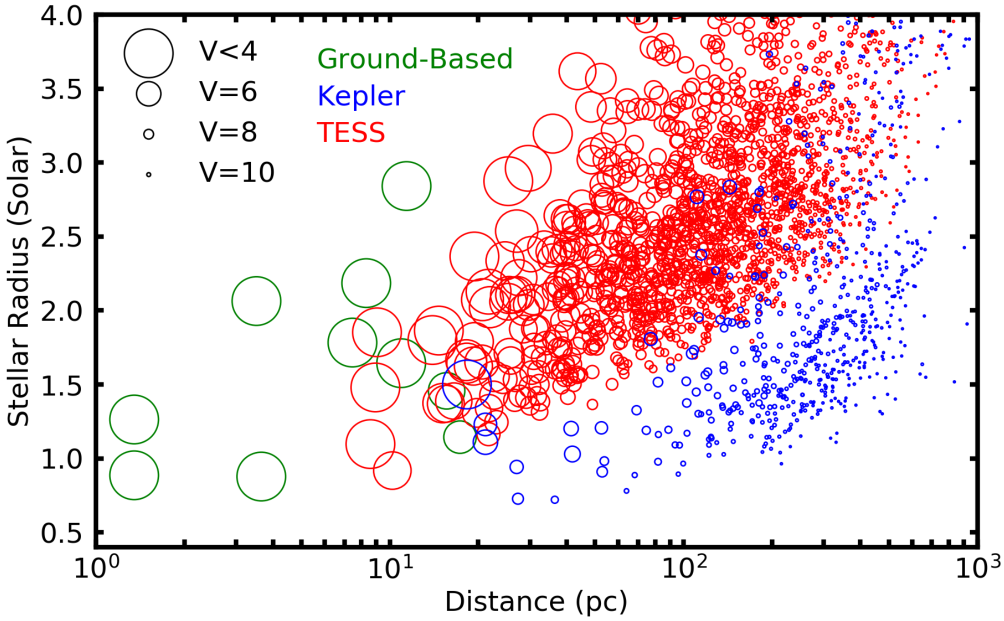

Fig. 3. Stellar radius versus distance for solar-like oscillators detected using ground-based observations (green circles), *Kepler* (blue circles), and a representative expected yield from *TESS* (red circles) based on the *TESS* Asteroseismic Target List (ATL, Schofield et al. 2019). Symbol sizes scale with the apparent V-band magnitude, as indicated on the plot. The brightest and closest *Kepler* detections are θ Cyg (Guzik et al. 2016) and 16 Cyg A and B (Metcalfe et al. 2015). *TESS* is expected to complement the *Kepler* yield by detecting oscillations in bright, evolved stars.

based observations and the *Kepler* mission. Owing to its smaller aperture, the average *TESS* detection is expected to be ~ 5 magnitudes brighter, more evolved, and closer compared to *Kepler*. *TESS* is thus expected to complement the parameter space explored by *Kepler* which yielded a substantial number of solar-type stars that were relatively faint. Based on preliminary performance, the total yield of solar-like oscillators from *TESS* in the prime mission is expected to range between 1000–2000 stars, a 2–4-fold increase in yield over the *Kepler* mission.

3.2 Asteroseismology of TESS Exoplanet Host Stars

The search for solar-like oscillations with *TESS* initially focussed on exoplanet host stars, for which light-curves were first made publicly available to facilitate ground-based follow-up observations. The first claimed detection of oscillations was made for the solar-type star π Men (Gandolfi et al. 2018), which hosts the first transiting exoplanet discovered by *TESS* (Huang et al. 2018). Subsequent analysis of the π Men light-curve showed that the power spectrum noise level is twice as large as the predicted oscillation amplitude*, thus demonstrating that the claimed detection of oscillations by Gandolfi et al. (2018) could not have been correct.

The first confirmed detection by *TESS* of solar-like oscillations was made in the exoplanet host-star HD 221416 (TESS Object of Interest 197, TOI-197), a $V = 8.2$ mag late subgiant star (Huber et al. 2019). The power spectrum (Figure 4, left) shows a clear detection of mixed dipole modes. Asteroseismic modelling combined with spectroscopic $T_{\rm eff}$ metallicity and *Gaia* luminosity yielded a precise characterization of the host-star radius ($R_\star = 2.943 \pm 0.064 R_\odot$), mass ($M_\star = 1.212 \pm 0.074 M_\odot$) and age ($4.9 \pm 1.1$ Gyr), and demonstrated that it has just started ascending the red-giant branch. The combination of asteroseismology with transit modelling and RV observations showed that the planet is a "hot Saturn" ($R_{\rm p} = 9.17 \pm 0.33 R_\oplus$) with an orbital period of ~ 14.3 days, irradiance of $F = 343 \pm 24 F_\oplus$, moderate mass ($M_{\rm p} = 60.5 \pm 5.7 M_\oplus$) and density ($\rho_{\rm p} = 0.431 \pm 0.062\,{\rm g\,cm^{-3}}$). The properties of HD 221416 b showed that the correlation between host-star metallicity and planet mass found in sub-Saturns (Petigura et al. 2017) does not extend to larger radii, indicating that planets in the transition between sub-Saturns and Jupiters follow a relatively narrow range of densities. With a density measured to $\sim 15\%$, HD 221416 b is one of the most carefully characterized Saturn-sized planets

*`https://exofop.ipac.caltech.edu/tess/edit_obsnotes.php?id=261136679`

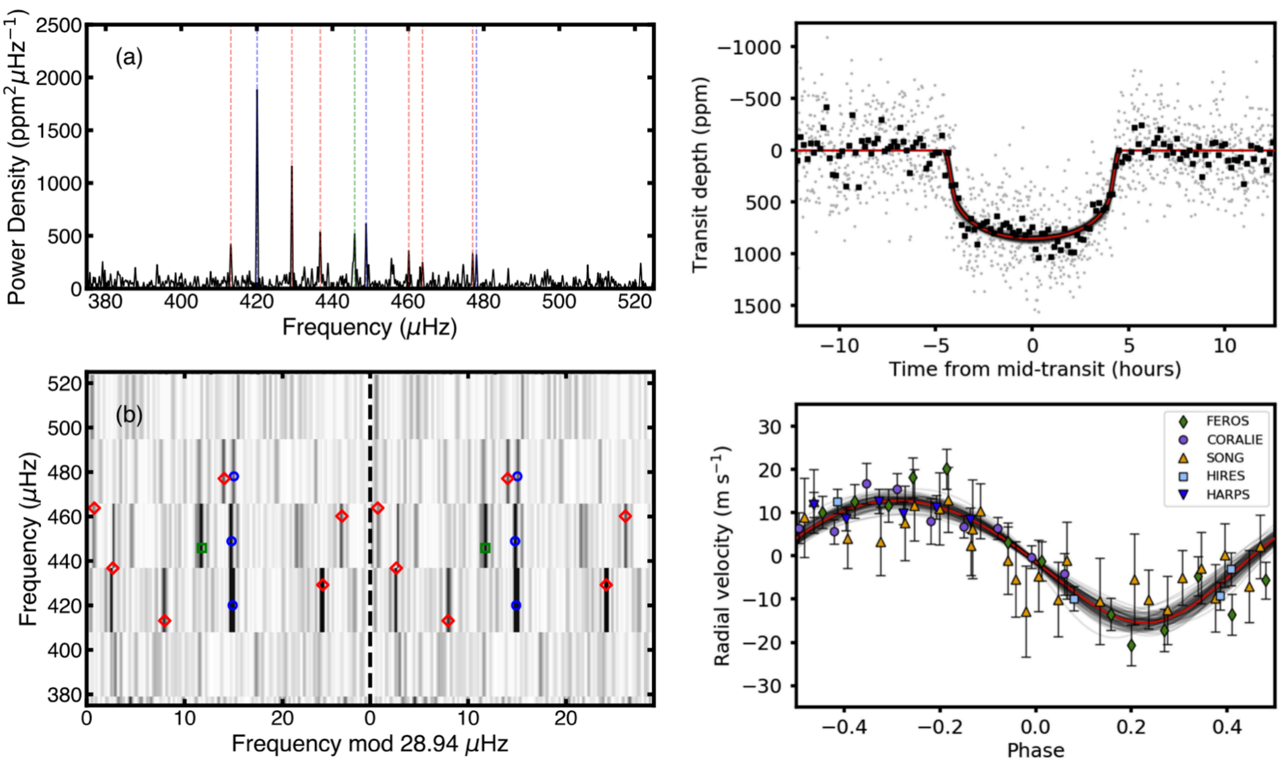

Fig. 4. Detection of solar-like oscillations in HD 221416 (TESS Object of Interest 197, TOI-197), the first *TESS* asteroseismic exoplanet host star. Left: power spectrum and echelle diagram of the *TESS* time-series after removing the planetary transits. From Huber et al. (2019); © AAS, reproduced with permission. Right: Phase-folded transit light-curve and RV follow-up observations using six different instruments. The combination of asteroseismology, transits and RV measurements constrained the density of the planet to ~15%, making the planet one of the most carefully characterized Saturn-sized planets to date.

to date.

In addition to recognizing stars that are hosting transiting planets, *TESS* has detected oscillations in stars previously known to host planets and which were discovered using the Doppler method (e.g. Campante et al. 2019). *TESS* is expected to yield a significant number of both new and known exoplanet hosts that are amenable to asteroseismic characterization (Campante et al. 2016), including new discoveries of transiting planets around oscillating red-giant-branch stars (e.g. Grunblatt et al. 2019).

4 Conclusions

Asteroseismology of solar-like oscillators has undergone an exciting revolution over the past decade. This review has discussed how small space-based missions such as the BRITE Constellation is, and will remain, a critical component in characterizing the brightest stars, as akready achieved (for example) through measuring the poorly constrained rotation period of α Cen A, or asteroseismology of bright red giants. Current and future large space-based mission such as *TESS* and PLATO will continue the *CoRoT* and *Kepler* legacies, filling in the parameter space of nearby solar-like oscillators including the systematic characterization of exoplanet host stars.

It is a pleasure to thank DH's first academic mentor, Werner Weiss, and the whole LOC for a memorable conference in Vienna. We thank Eliana Amazo-Gomez, Tim Bedding, Travis Metcalfe, Bert Pablo, Andrzej Pigulski, and Jen van Saders for discussions on the rotation period of alpha Cen. DH acknowledges support by the National Aeronautics and Space Administration (80NSSC19K0379) through the TESS Guest Investigator Program.
Based on data collected by the BRITE Constellation satellite mission: designed, built, launched, operated and supported by the Austrian Research Promotion Agency (FFG), the University of Vienna, the Technical University of Graz, the University of Innsbruck, the Canadian Space Agency (CSA), the University of Toronto Institute for Aerospace Studies (UTIAS), the Foundation for Polish Science & Technology (FNiTP MNiSW), and the National Science Centre (NCN).

References

Aerts, C. 2019, arXiv e-prints, arXiv:1912.12300

Appourchaux, T., Michel, E., Auvergne, M., et al. 2008, A&A, 488, 705

Ayres, T. R. 2018, Research Notes of the AAS, 2, 17

Barban, C., Matthews, J. M., De Ridder, J., et al. 2007, A&A, 468, 1033

Beck, P. G., Bedding, T. R., Mosser, B., et al. 2011, Science, 332, 205

Bedding, T. R. 2011, ArXiv e-prints (arXiv:1107.1723)

Bedding, T. R. 2014, Solar-like oscillations: An observational perspective (Cambridge University Press, adsurl = https://ui.adsabs.harvard.edu/abs/2014aste.book...60B, adsnote = Provided by the SAO/NASA Astrophysics Data System), 60

Bedding, T. R., Butler, R. P., Kjeldsen, H., et al. 2001, ApJ, 549, L105

Bouchy, F. & Carrier, F. 2001, A&A, 374, L5

Brown, T. M., Gilliland, R. L., Noyes, R. W., & Ramsey, L. W. 1991, ApJ, 368, 599

Bruntt, H., Kjeldsen, H., Buzasi, D. L., & Bedding, T. R. 2005, ApJ, 633, 440

Butler, R. P., Bedding, T. R., Kjeldsen, H., et al. 2004, ApJ, 600, L75

Campante, T. L., Corsaro, E., Lund, M. N., et al. 2019, ApJ, 885, 31

Campante, T. L., Schofield, M., Kuszlewicz, J. S., et al. 2016, ApJ, 830, 138

Carrier, F., Bouchy, F., Kienzle, F., et al. 2001, A&A, 378, 142

Carrier, F. & Bourban, G. 2003, A&A, 406, L23

Chaplin, W. J., Elsworth, Y., Davies, G. R., et al. 2014, MNRAS, 445, 946

Chaplin, W. J., Kjeldsen, H., Bedding, T. R., et al. 2011, ApJ, 732, 54

De Ridder, J., Barban, C., Baudin, F., et al. 2009, Nature, 459, 398

De Ridder, J., Barban, C., Carrier, F., et al. 2006, A&A, 448, 689

Edmonds, P. D. & Gilliland, R. L. 1996, ApJ, 464, L157

Fletcher, S. T., Chaplin, W. J., Elsworth, Y., Schou, J., & Buzasi, D. 2006, MNRAS, 371, 935

Frandsen, S., Carrier, F., Aerts, C., et al. 2002, A&A, 394, L5

Gandolfi, D., Barragán, O., Livingston, J. H., et al. 2018, A&A, 619, L10

Gilliland, R. L. 2008, AJ, 136, 566

Gilliland, R. L., McCullough, P. R., Nelan, E. P., et al. 2011, ApJ, 726, 2

Grunblatt, S. K., Huber, D., Gaidos, E., et al. 2019, AJ, 158, 227

Guenther, D. B., Kallinger, T., Gruberbauer, M., et al. 2008, ApJ, 687, 1448

Guzik, J. A., Houdek, G., Chaplin, W. J., et al. 2016, ApJ, 831, 17

Hekker, S. & Christensen-Dalsgaard, J. 2017, A&A Rev., 25, 1

Hekker, S., Gilliland, R. L., Elsworth, Y., et al. 2011, MNRAS, 414, 2594

Hekker, S., Kallinger, T., Baudin, F., et al. 2009, A&A, 506, 465

Houdek, G., Balmforth, N. J., Christensen-Dalsgaard, J., & Gough, D. O. 1999, A&A, 351, 582

Huang, C. X., Burt, J., Vanderburg, A., et al. 2018, ApJ, 868, L39

Huber, D., Bedding, T. R., Arentoft, T., et al. 2011, ApJ, 731, 94

Huber, D., Chaplin, W. J., Chontos, A., et al. 2019, AJ, 157, 245

Kallinger, T., Beck, P. G., Hekker, S., et al. 2019, A&A, 624, A35

Kallinger, T., Guenther, D. B., Weiss, W. W., et al. 2008, Communications in Asteroseismology, 153, 84

Kallinger, T., Weiss, W. W., De Ridder, J., Hekker, S., & Barban, C. 2009, in ASPCS, Vol. 404, The Eighth Pacific Rim Conference on Stellar Astrophysics: A Tribute to Kam-Ching Leung, ed. S. J. Murphy & M. S. Bessell, 307

Kjeldsen, H. & Bedding, T. R. 1995, A&A, 293, 87

Kjeldsen, H., Bedding, T. R., Butler, R. P., et al. 2005, ApJ, 635, 1281

Kjeldsen, H., Bedding, T. R., Viskum, M., & Frandsen, S. 1995, AJ, 109, 1313

Leighton, R. B., Noyes, R. W., & Simon, G. W. 1962, ApJ, 135, 474

Matthews, J. M. 2007, Communications in Asteroseismology, 150, 333

Matthews, J. M., Kusching, R., Guenther, D. B., et al. 2004, Nature, 430, 51

Metcalfe, T. S., Creevey, O. L., & Davies, G. R. 2015, ApJ, 811, L37

Michel, E., Baglin, A., Auvergne, M., et al. 2008, Science, 322, 558

Miglio, A., Chiappini, C., Morel, T., et al. 2013, MNRAS, 429, 423

Mosser, B., Benomar, O., Belkacem, K., et al. 2014, A&A, 572, L5

Mosser, B., Elsworth, Y., Hekker, S., et al. 2012, A&A, 537, A30

Petigura, E. A., Sinukoff, E., Lopez, E. D., et al. 2017, AJ, 153, 142

Retter, A., Bedding, T. R., Buzasi, D. L., Kjeldsen, H., & Kiss, L. L. 2003, ApJ, 591, L151

Ricker, G. R., Winn, J. N., Vanderspek, R., et al. 2014, in SPIE Conference Series, Vol. 9143, Proceedings of the SPIE, 20

Schofield, M., Chaplin, W. J., Huber, D., et al. 2019, ApJSS, 241, 12

Schou, J. & Buzasi, D. L. 2001, in ESA Special Publication, Vol. 464, SOHO 10/GONG 2000 Workshop: Helio- and Asteroseismology at the Dawn of the Millennium, ed. A. Wilson & P. L. Pallé, 391–394

Silva Aguirre, V., Lund, M. N., Antia, H. M., et al. 2017, ApJ, 835, 173

Stello, D., Bruntt, H., Preston, H., & Buzasi, D. 2008, ApJ, 674, L53

Stello, D., Cantiello, M., Fuller, J., et al. 2016, Nature, 529, 364

Stello, D., Chaplin, W. J., Bruntt, H., et al. 2009, ApJ, 700, 1589

Stello, D. & Gilliland, R. L. 2009, ApJ, 700, 949

Stello, D., Huber, D., Bedding, T. R., et al. 2013, ApJ, 765, L41

Tarrant, N. J., Chaplin, W. J., Elsworth, Y., Spreckley, S. A., & Stevens, I. R. 2007, MNRAS, 382, L48

van Saders, J. L., Pinsonneault, M. H., & Barbieri, M. 2019, ApJ, 872, 128

Verma, K. & Silva Aguirre, V. 2019, MNRAS, 489, 1850

Walker, G., Matthews, J., Kuschnig, R., et al. 2003, PASP, 115, 1023

White, T. R., Bedding, T. R., Gruberbauer, M., et al. 2012, ApJ, 751, L36

Yu, J., Huber, D., Bedding, T. R., et al. 2016, MNRAS

Stars and their variability observed from space
C. Neiner, W. W. Weiss, D. Baade, R. E. Griffin, C. C. Lovekin, A. F. J. Moffat (eds)

RR LYRAE AND CEPHEID VARIABLES WITH *TESS*

E. Plachy[1,2] and TASC WG6

Abstract. The space-based photometry revolution that started with *MOST, CoRoT, Kepler* and *BRITE* is being continued with *TESS*. The scope of *TESS* is different from that of its predecessors, in that it monitors the whole sky on shorter time-scales instead of observing selected fields for longer. This approach provides us with new possibilities – and challenges – to investigate variable stars of any type. This paper focussed on RR Lyrae and Cepheid stars, and summarizes our preliminary conclusions as to how these stars can benefit from *TESS* data. The first results from *TESS* observations of RR Lyrae and Cepheid stars will not be discussed here, as they will be presented in detail in the near future, in collaboration with *TESS* Asteroseismic Science Consortium Working Group 6.

Keywords: Stars: variables: RR Lyrae, Stars: variables: Cepheids, techniques: photometric

1 Introduction

RR Lyrae and Cepheid stars are key objects in many fields of astronomy: stellar structure and evolution, distance determinations, population studies and pulsation theory and, as such, are well-studied variables. A simplified view of these stars is that they exhibit radial pulsations (usually in the fundamental mode, less frequently in the first overtone mode, or simultaneously in both), with only rare cases where higher overtone pulsation occurs. However, the contemporary picture is much more complex, and many additional phenomena exist in these stars that can often only be recovered from high-precision light-curves. Many of these more recent discoveries still await theoretical explanation.

2 Hot topics

This section is a collection of the most relevant topics that challenge our theories, and where *TESS* observations will provide us with important new knowledge.

2.1 Pulsation properties

The oldest and most famous problem concerning RR Lyrae stars was described long before the start of space-based observations. Many examples of amplitude and phase modulations have been reported and studied in detail, and in a statistical sense since the discovery paper of Blažko (1907). For the state of the art concerning the Blazhko effect we refer to the latest studies by Smolec (2016); Prudil & Skarka (2017); Jurcsik et al. (2018); Netzel et al. (2018). Continuous space-based measurements were needed to reveal an additional phenomenon, *viz.* period doubling, which has been observed only in Blazhko RR Lyrae stars so far (Szabó et al. 2010). This effect is the sign of nonlinear dynamics in the pulsation caused by a resonance with a high-order mode (Kolláth et al. 2011; Smolec & Moskalik 2012). The occurrence rate, duration and stability of period doubling, and its relation to the modulation or pulsation properties, are as of now mostly unknown. Period doubling is manifested as an amplitude alternation in the light-curve and as a series of small frequency peaks in the Fourier transform, midway between the harmonics of the pulsation frequency. But other small-amplitude frequency components may also appear in the Fourier spectra, be they fundamental (RRab), overtone (RRc) or double-mode (RRd) RR Lyrae stars, modulated or non-modulated (Benkő et al. 2014, 2019; Netzel & Smolec 2019). The positions of these peaks in RRc stars are near where high-order nonradial modes should be excited (Dziembowski 2016). The first and second radial overtone frequencies can be identified tentatively among the low-amplitude peaks in RRab stars, but the origin of many other peaks remains unknown (Molnár et al. 2017b).

[1] Konkoly Observatory, Research Centre for Astronomy and Earth Sciences, Konkoly Thege Miklós út 15-17, H-1121 Budapest, Hungary
[2] MTA CSFK Lendület Near-Field Cosmology Research Group

Cepheid stars also exhibit all the phenomena mentioned above, but with some differences in strength and occurrence within the types and subtypes. The modulation in classical Cepheids is not as prominent as in RR Lyrae stars (Derekas et al. 2017), though many examples of weak modulation were found in the Magellanic Clouds durinig a systematic search through OGLE observations (Smolec 2017). The only exception, where modulation reaches a high amplitude, is V473 Lyr (Molnár et al. 2017a). This unique star exhibits period doubling, too. Period doubling and modulation were also reported in each subtype of the Type II Cepheid class (Smolec et al. 2018). Quasi-periodic modulation often co-exists with further irregular variations in the pulsation period and/or phase in these stars. Period doubling seems to be common among the long-period Type II Cepheids, so much so that amplitude alternations are considered to be the main characteristic of the RV Tauri type. Period doubling appears to be common as well in intermediate-period, or W Vir stars, for pulsation periods greater than 15 days; those stars may belong to an older population than the rest (Soszyński et al. 2019b). In contrast, only a handful of period-doubled stars were found among the short-period BL Her-type pulsators. The distribution of non-radial modes in overtone Cepheids shows strong similarities to that of the RRc stars when visualized in the Petersen diagram, where clear sequences, potentially connected to different spherical degrees, can be distinguished (Smolec & Śniegowska 2016). On the other hand, additional modes in the fundamental-mode classical Cepheids seem to show no pattern at all (Süveges & Anderson 2018), in contrast to the clear regions of peaks in RRab stars (Molnár et al. 2017b). Instabilities and cycle-to-cycle variation in the pulsation is common in Type II Cepheids: the longer the period the stronger the effect. However, this phenomenon is very weak in the classical Cepheids. Before the era of space-based photometry, those stars were considered to be clockwork pulsators, but the photometric accuracy of *Kepler* and *MOST* showed that that is not the case (Derekas et al. 2012; Evans et al. 2015).

The most pressing questions concerning pulsation—nonlinear effects (modulation, period doubling), low-amplitude additional modes (overtones and non-radial modes), and other instabilities (period jitter, cycle-to-cycle changes)—all require high-precision, continuous, and long observations.

2.2 Proper classification

Better knowledge of the pulsation properties helps us distinguish between various subtypes and filter out the non-pulsating impostors. Classification algorithms applied to sparsely sampled photometric surveys are often confused by other high-amplitude variables (Drake et al. 2017; Udalski et al. 2018; Rimoldini et al. 2019). The confusion usually occurs between variable types that have a common period range and similar light-curve shapes, such as W UMa eclipsing binaries and RRc stars, or rotational variables and Cepheid stars. The fraction of non-Cepheid stars among Cepheid candidates can be exceptionally large. Similarly, short-period Cepheids can easily be confused with RR Lyrae stars. One-day aliases in ground-based measurements may cause mis-identifications between BL Her stars and RR Lyrae stars.

Identifying anomalous Cepheids in the Galactic field is also challenging, since their period range overlaps both those of the Cepheids and the RR Lyrae stars (Jurkovic 2018). However, they differ in luminosity, and have their own period–luminosity relations for the fundamental and first overtone stars, respectively, which could be utilized to find them. Unfortunately, the *Gaia* DR2 parallaxes are not precise enough to classify individual pulsating variables yet (Ripepi et al. 2019), but we hope that the situation will change with the next data release. For the moment, light-curve morphology seems to be a more reliable classifier. The Fourier parameters (R_{21}, R_{31}, ϕ_{21} and ϕ_{31}), determined by (Simon & Lee 1981), provide quantitative measures of the light-curve shape, and by plotting them as a function of the period we can identify groups of the different types of variable. That method has also been used in the OGLE classification, and turned out to be successful in identifying anomalous Cepheids (Soszyński et al. 2017).

Single-mode overtone pulsation in Type II Cepheids is very rare; the first two such objects have been found only recently (Soszyński et al. 2019a) through careful analysis of the OGLE collection. This research was inspired by the recent discovery of the first double-mode BL Her stars (Udalski et al. 2018). The results show nicely that a statistically large sample of high-quality light-curves can still be used to recover new subtypes among radial pulsators.

2.3 Physical properties

Asteroseismology became an important tool for determining fundamental stellar parameters in the era of space-based photometry, and it is now common practice to estimate mass, radius and age from solar-like oscillations of main-sequence and evolved stars (Chaplin et al. 2014; Yu et al. 2018). A similar breakthrough has not yet been achieved for radial pulsators, but our increasing knowledge of pulsation properties, along with state-of-the-art pulsation and evolution models, has the potential to extraact physical properties from light-curves in the future. Promising steps have recently been taken to constrain the model parameters mass, metallicity and temperature from multi-colour light-curve data (Bhardwaj et al. 2017). It has also been shown that, besides the pulsation period, the light-curve structure can play a statistically significant role in determining global stellar parameters (Bellinger et al., in prep.). Further effort is required to map these connections among observations and model light-curves. An important and essential part of that work is to recover the differences and similarities in the light-curve properties between populations and subtypes.

Until then we can rely on binarity, which offers another great opportunity to determine stellar parameters accurately. Seeking eclipsing binary candidates among Cepheids and RR Lyrae stars is therefore an important task. A few systems containing Cepheid members have already been analyzed in detail in the Magellanic Clouds (Pilecki et al. 2018) and within the Galaxy (Gallenne et al. 2019). Several new binary candidates have been proposed recently from proper-motion anomalies detected in *Gaia* DR2 (Kervella et al. 2019). The latter study also contains binary RR Lyrae candidates. The expected binary fraction among RR Lyraes stars is significantly smaller (~7%) than in Cepheids (~80%), but because they are much more numerous we have good chances of finding multiple examples. The (O–C) technique is an effective tool for searching for companions; however, the light-travel time effect causes cyclical variations in the (O–C) diagram similar to Blazhko modulation; it therefore gives reliable results only for non-modulated stars (Prudil et al. 2019).

3 Observing with TESS

The main goal of the *TESS* mission is to discover the nearest exoplanets that orbit relatively close to their host stars (Ricker et al. 2015), but as with *CoRoT, Kepler* and *K2* it is expected to be a significant contributor to the fields of asteroseismology and stellar variability, including heat-driven pulsating stars. *TESS* was designed to be an all-sky survey, and in its 2-year prime mission it is already covering most of the sky, dividing the field of view into 26 partially overlapping sectors that rotate around the ecliptic poles. The telescope has a 21"/px angular resolution. A milli-magnitude level of accuracy can be achieved for stars brighter than 12th magnitude in the *TESS* passband (T_{mag}); the photometric precision drops to about 1% per long-cadence data point for a 16-T_{mag} star. The next Section discusses how Cepheid and RR Lyrae investigations are constrained by the properties of *TESS*, and what data products are available.

3.1 Benefits

The undoubted strength of the *TESS* ission is the size of the area observed. Such a large part of the sky has never been observed continuously from space. Each of the sectors is monitored for 27 days, a length that is adequate for recognizing RR Lyrae and even short-period Cepheid pulsations. Only a handful of Cepheid stars have been observed continuously from space so far; thus, a big step will be taken with *TESS* inasmuch as it is able to observe all Cepheids in the Galaxy and the bright ones in the Magellanic System as well. With its faint limit we are only able to sample the RR Lyrae population in the solar neighbourhood. The benefits of high-precision, continuous space-based photometric data are clear: from precise light curves we can determine accurate Fourier parameters and (O–C) diagrams, and recover low-amplitude modes and other weak changes in pulsations. *TESS* data will enable us to study many of the hot topics mentioned in Section 2 in a huge sample of classical variables. A significant fraction of Cepheid and RR Lyrae targets are in the overlapping areas of the sectors or (as for the Large Magellanic Cloud) in the continuous viewing zone. The latter area is being observed for nearly a year, providing an opportunity to study the longer-period Cepheids and the Blazhko effect in RR Lyrae stars.

3.2 Limitations

As for all space missions, *TESS* also has some inherent limitations. Perhaps the most constraining feature is the low angular resolution. The image of a stellar object has a diameter of 2–3 pixels in *TESS* images. Given the 21-″ pixel size, many blends are observed. The contamination is especially critical in dense stellar fields such as the Magellanic Clouds, the Galactic bulge and even the Galactic plane; those areas are where most of the Cepheids can be found (Fig. 1).

Contamination can cause several problems in an analysis, even if the brightness variation of the blended star is negligible. The extra flux may change the shape of the ligh-curve, and thence the Fourier parameters. Blends may therefore affect classification and other studies that use those parameters, such as the estimation of photometric metallicity. When the contaminating star is itself a variable, extra peaks may appear in the

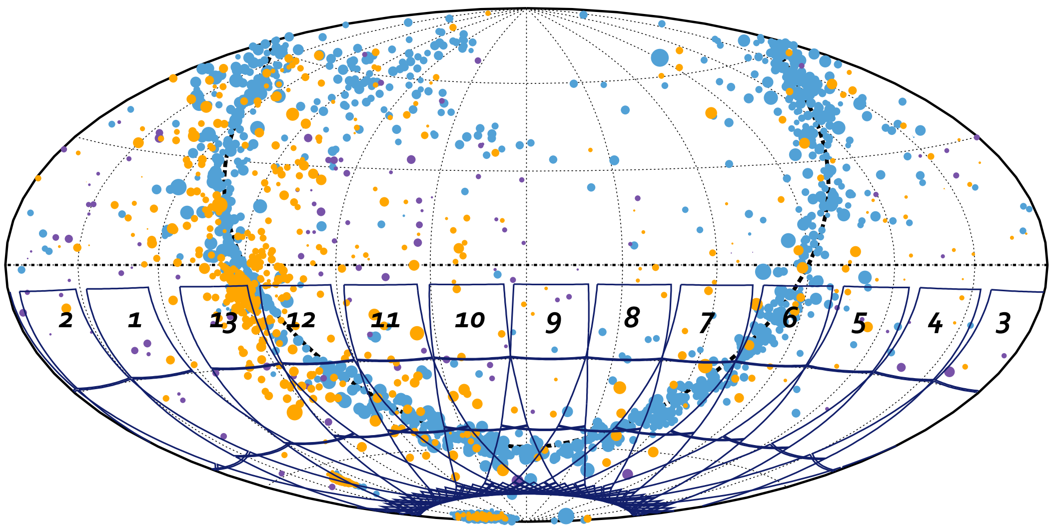

Fig. 1. Distribution of Cepheid stars in the ecliptic coordinate system: classical Cepheids (blue), Type II Cepheids (orange), anomalous Cepheids (purple). The southern *TESS* sectors are also marked.

composite Fourier transform, and which can easily be misidentified as additional pulsation modes. Moreover, in dense stellar fields it is possible that more than one Cepheid star can fall within the same aperture. Blends are able to cause fake cycle-to-cycle variations and features that resemble amplitude modulation.

The targets observed in multiple sectors can have extended light-curves after stitching the data sets together. The technique of stitching is not straightforward. A similar problem was experienced with the original *Kepler* mission as a consequence of rotation of the telescope, when data of different campaigns were joined: the average flux and the pulsation amplitudes were different owing to differences in pixel sensitivity (Benkő et al. 2014). No perfect solution has been developed for this problem. In the case of *TESS*, this issue is even more pressing because the contaminating stars in the large pixels can differ significantly in each sector, and may prevent us from studying cycle-to-cycle variations and other low-amplitude features in crowded areas.

The 27-day-long observation is fine for unmodulated RR Lyrae stars, but nearly half of the fundamental-mode stars are Blazhko stars, and the period of the Blazhko modulation is rarely shorter than 27 days. We may therefore not be able to study the Blazhko effect in detail, or even recognize a long-period modulation extending to hundreds or thousands of days in a single-sector light-curve. Those can only be achieved in the continuous viewing zone. We face a similar situation for the Cepheid stars, too. In contrast to RR Lyrae stars that have pulsation periods shorter than a day, the range of Cepheid periods extends up to a hundred days, so we expect more success when observing the shorter-period stars. However, owing to the Cepheid period–luminosity relation, shorter-period objects are fainter, and that is critical in the Magellanic Clouds and the Bulge, where visibility is seriously constrained by this confusion. Fortunately, a period range where Cepheids can still be fruitfully studied can nevertheless be found.

Finally, we ask how the faintness of RR Lyraes affects investigations. The brightness distribution of Galactic RR Lyrae stars that were recently identified in *Gaia* DR2 by Clementini et al. (2019) showed that the majority of RR Lyrae stars are fainter than $T_{mag} = 16$ (Fig 2). This raises the question of how deep we can go with *TESS* photometry, and what we can achieve with noisy data. Preliminary tests suggest that the RR Lyrae variability is still recognizable at 17.5 T_{mag}, suggesting that these data are still useful in classification and validation of RR Lyrae catalogues based on sparsely-sampled data, but modulation or additional modes cannot be recovered any more.

3.3 Data availability

The *TESS* mission* provides target pixel files and light-curves produced by the Science Processing Operations Center (SPOC) at NASA Ames Research Center, for the pre-selected 2-minute cadence targets, which are

*https://heasarc.gsfc.nasa.gov/docs/tess/

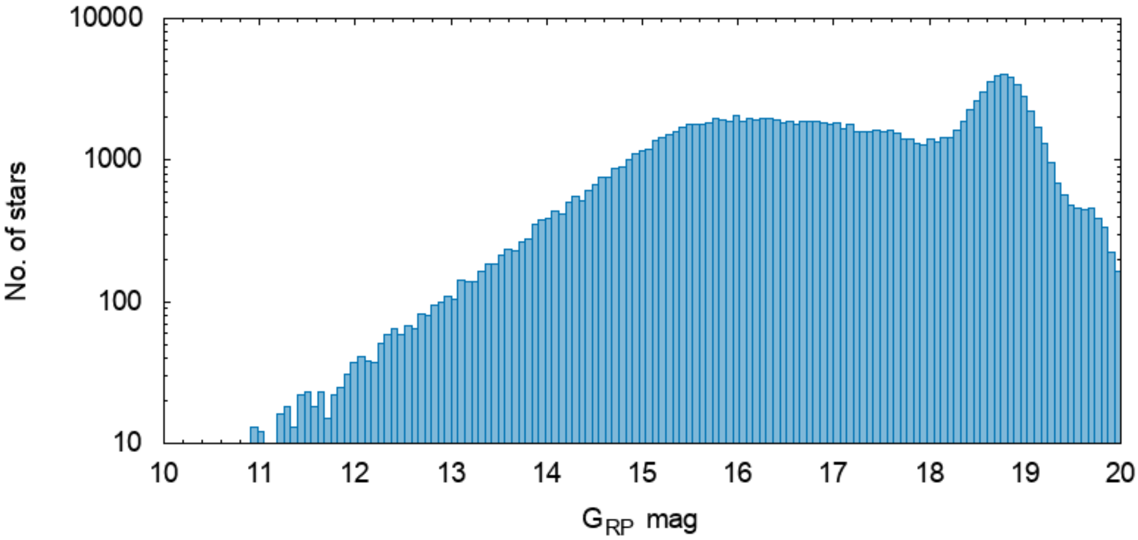

Fig. 2. Brightness distribution of RR Lyrae stars in *Gaia* DR2 in the G_{RP} passband, which is similar to that of *TESS*.

available at the MAST Archive †. The working groups (WGs) of the *TESS* Asteroseismic Science Consortium (TASC) proposed almost 38 thousand asteroseismic targets for the 2-minute cadence in the prime mission. WG6 focuses on RR Lyrae and Cepheid stars, and proposed 89 important or peculiar targets for the short-cadence mode. All other RR Lyrae and Cepheid targets are in the full-frame images (FFIs) that are taken with a 30-minute cadence. The mission does not provide light-curves for the ∼150 million stars (< 16 T_{mag}) in the FFIs; that task has to be organised by the scientific community, by using separate pipelines or open-source codes developed for *TESS* photometry – for example, `eleanor` (Feinstein et al. 2019) and `lightkurve` (Lightkurve Collaboration et al. 2018). Data releases are in progress by the *TESS* Data for Asteroseismology (TDA) Coordinated Activity of TASC at the *TESS* Asteroseismic Science Operations Center (TASOC) and by other groups too (Oelkers & Stassun 2019). To get a first look at *TESS* RR Lyrae and Cepheid stars we have prepared difference-imaging aperture photometry using the FITSH package (Pál 2012) developed at Konkoly Observatory. The pipeline corrects many of the instrumental and intrinsic differences between the target frames and the reference frame (differential velocity aberration, spacecraft jitter, background and stray-light variations, strap reflection, momentum wheel dumps), and provides suitably high-quality data to search for low-amplitude phenomena.

4 Conclusions

The *TESS* mission will be a determining factor in space-based photometry in the following years. It is hard to estimate how many new important results will come out from *TESS* observations, but we can definitely predict that, after *Kepler* revolutionized RR Lyrae and Cepheid investigations through its unprecedented photometric precision, *TESS* will revolutionize the field again because of the high number of stars observed. However, we have to be very careful with the analysis of low-amplitude signals because of the strong contamination from nearby objects.

This work has been supported by Lendület LP2014-17 and LP2018-7/2018 grants and the János Bolyai Research Scholarship of the Hungarian Academy of Sciences. This work presents results from the ESA mission *Gaia*. *Gaia* data are being processed by the Gaia Data Processing and Analysis Consortium (DPAC). Funding for DPAC is provided by national institutions. I thank László Molnár and Róbert Szabó for proofreading this manuscript.

† https://archive.stsci.edu/tess/

References

Benkő, J. M., Jurcsik, J., & Derekas, A. 2019, MNRAS, 485, 5897
Benkő, J. M., Plachy, E., Szabó, R., Molnár, L., & Kolláth, Z. 2014, ApJS, 213, 31
Bhardwaj, A., Kanbur, S. M., Marconi, M., et al. 2017, MNRAS, 466, 2805
Blažko, S. 1907, AN, 175, 325
Chaplin, W. J., Basu, S., Huber, D., et al. 2014, ApJS, 210, 1
Clementini, G., Ripepi, V., Molinaro, R., et al. 2019, A&A, 622, A60
Derekas, A., Plachy, E., Molnár, L., et al. 2017, MNRAS, 464, 1553
Derekas, A., Szabó, G. M., Berdnikov, L., et al. 2012, MNRAS, 425, 1312
Drake, A. J., Djorgovski, S. G., Catelan, M., et al. 2017, MNRAS, 469, 3688
Dziembowski, W. A. 2016, Commmunications of the Konkoly Observatory Hungary, 105, 23
Evans, N. R., Szabó, R., Derekas, A., et al. 2015, MNRAS, 446, 4008
Feinstein, A. D., Montet, B. T., Foreman-Mackey, D., et al. 2019, PASP, 131, 094502
Gallenne, A., Kervella, P., Borgniet, S., et al. 2019, A&A, 622, A164
Jurcsik, J., Hajdu, G., Dékány, I., et al. 2018, MNRAS, 475, 4208
Jurkovic, M. I. 2018, Serbian Astronomical Journal, 197, 13
Kervella, P., Gallenne, A., Remage Evans, N., et al. 2019, A&A, 623, A116
Kolláth, Z., Molnár, L., & Szabó, R. 2011, MNRAS, 414, 1111
Lightkurve Collaboration, Cardoso, J. V. d. M. a., Hedges, C., et al. 2018, Lightkurve: Kepler and TESS time series analysis in Python
Molnár, L., Derekas, A., Szabó, R., et al. 2017a, MNRAS, 466, 4009
Molnár, L., Plachy, E., Klagyivik, P., et al. 2017b, in EPJ Web of Conferences, Vol. 160, EPJ Web of Conferences, 04008
Netzel, H. & Smolec, R. 2019, MNRAS, 487, 5584
Netzel, H., Smolec, R., Soszyński, I., & Udalski, A. 2018, MNRAS, 480, 1229
Oelkers, R. J. & Stassun, K. G. 2019, Research Notes of the AAS, 3, 8
Pál, A. 2012, MNRAS, 421, 1825
Pilecki, B., Gieren, W., Pietrzyński, G., et al. 2018, ApJ, 862, 43
Prudil, Z. & Skarka, M. 2017, MNRAS, 466, 2602
Prudil, Z., Skarka, M., Liška, J., Grebel, E. K., & Lee, C. U. 2019, MNRAS, 487, L1
Ricker, G. R., Winn, J. N., Vanderspek, R., et al. 2015, JATIS, 1, 014003
Rimoldini, L., Holl, B., Audard, M., et al. 2019, A&A, 625, A97
Ripepi, V., Molinaro, R., Musella, I., et al. 2019, A&A, 625, A14
Simon, N. R. & Lee, A. S. 1981, ApJ, 248, 291
Smolec, R. 2016, in 37th Meeting of the Polish Astronomical Society, ed. A. Różańska & M. Bejger, Vol. 3, 22–25
Smolec, R. 2017, MNRAS, 468, 4299
Smolec, R. & Moskalik, P. 2012, MNRAS, 426, 108
Smolec, R., Moskalik, P., Plachy, E., Soszyński, I., & Udalski, A. 2018, MNRAS, 481, 3724
Smolec, R. & Śniegowska, M. 2016, MNRAS, 458, 3561
Soszyński, I., Smolec, R., Udalski, A., & Pietrukowicz, P. 2019a, ApJ, 873, 43
Soszyński, I., Udalski, A., Szymański, M. K., et al. 2019b, Acta Astron., 69, 87
Soszyński, I., Udalski, A., Szymański, M. K., et al. 2017, Acta Astron., 67, 297
Süveges, M. & Anderson, R. I. 2018, MNRAS, 478, 1425
Szabó, R., Kolláth, Z., Molnár, L., et al. 2010, MNRAS, 409, 1244
Udalski, A., Soszyński, I., Pietrukowicz, P., et al. 2018, Acta Astron., 68, 315
Yu, J., Huber, D., Bedding, T. R., et al. 2018, ApJS, 236, 42

MAGNETIC OB[A] STARS WITH TESS: PROBING THEIR EVOLUTIONARY AND ROTATIONAL PROPERTIES - THE MOBSTER COLLABORATION

A. David-Uraz[1], C. Neiner[2], J. Sikora[3], J. Barron[4,5], D. M. Bowman[6], P. Cerrahoğlu[1], D. H. Cohen[7], C. Erba[1], V. Khalack[8], O. Kobzar[5], O. Kochukhov[9], H. Pablo[10], V. Petit[1], M. E. Shultz[1], A. ud-Doula[11], G. A. Wade[5] and the MOBSTER Collaboration

Abstract. In this contribution, we present the MOBSTER Collaboration, a large community effort to leverage high-precision photometry from the Transiting Exoplanet Survey Satellite (*TESS*) in order to characterize the variability of magnetic massive and intermediate-mass stars. These data can be used to probe the varying column density of magnetospheric plasma along the line of sight for OB stars, thus improving our understanding of the interaction between surface magnetic fields and massive star winds. They can also be used to map out the brightness inhomogeneities present on the surfaces of Ap/Bp stars, informing present models of atomic diffusion in their atmospheres. Finally, we review our current and ongoing studies, which lead to new insights on this topic.

Keywords: Techniques: photometric, Stars: magnetic field, Stars: rotation

1 Introduction

Magnetism is found in stars across the Hertzsprung–Russell diagram. However, while low-mass stars generate magnetic fields contemporaneously via strong surface dynamos powered by rotation and convection, stars across the OBA spectral type range lack the ingredients actively to create and sustain a large-scale magnetic field. Despite that fact, as evidenced by results from recent large spectropolarimetric surveys (e.g. MiMeS, BOB, BinaMiCS and LIFE; Wade et al. 2016; Morel et al. 2015; Alecian et al. 2015; Martin et al. 2018), a small fraction ($\lesssim 10\%$) of these stars exhibits the presence of strong, globally-organized magnetic fields on their surfaces. Even more remarkably, this incidence rate appears to be flat across a wide range of stellar masses, and the magnetic characteristics of these stars appear to be uncorrelated with their physical properties. The prevailing hypothesis to explain these observations is that the field is of *fossil* origin, meaning that it was formed at an earlier stage of evolution (Borra et al. 1982), although there remains a debate as to what that earlier stage might be (Neiner et al. 2015).

The presence of a surface magnetic field influences several aspects of OBA stars that are crucial to their evolution. In the more massive O- and early B-type stars magnetism can spin the star down significantly (e.g. ud-Doula et al. 2009) and confine its wind, leading to much lower effective mass-loss rates (ud-Doula & Owocki 2002). These effects greatly impact the evolution of magnetic OB stars, and are starting to be included in evolutionary codes (e.g. Keszthelyi et al. 2019). The latter effect might even provide a possible channel to form heavy stellar-mass black holes (e.g. Liu et al. 2019), such as those whose coalescence was detected by LIGO (Abbott et al. 2016), at solar metallicity (Georgy et al. 2017; Petit et al. 2017).

[1] Department of Physics and Astronomy, University of Delaware, Newark, DE 19716, USA
[2] LESIA, Paris Observatory, PSL University, CNRS, Sorbonne University, Université de Paris, 5 place Jules Janssen, 92195 Meudon, France
[3] Physics and Astronomy Department, Bishop's University, Sherbrooke, QC J1M 1Z7, Canada
[4] Department of Physics, Engineering Physics & Astronomy, Queen's University, 64 Bader Lane, Kingston, ON K7L 3N6, Canada
[5] Department of Physics and Space Science, Royal Military College of Canada, PO Box 17000 Kingston, ON K7K 7B4, Canada
[6] Institute of Astronomy, KU Leuven, Celestijnenlaan 200D, B-3001 Leuven, Belgium
[7] Department of Physics and Astronomy, Swarthmore College, Swarthmore, PA 19081, USA
[8] Département de Physique et d'Astronomie, Université de Moncton, Moncton, NB E1A 3E9, Canada
[9] Department of Physics and Astronomy, Uppsala University, Box 516, 75120, Uppsala, Sweden
[10] American Association of Variable Star Observers (AAVSO), 49 Bay State Rd., Cambridge, MA 02138, USA
[11] Penn State Scranton, 120 Ridge View Drive, Dunmore, PA 18512, USA

In later B- and A-type stars, magnetic fields affect atomic diffusion processes in the atmosphere, leading to anisotropic chemical abundances on the stellar surface. This causes spectral peculiarities, as noted in the spectral types of many of these objects: the so-called "Ap/Bp" stars. When compared to other stars of similar spectral type, they are found to exhibit slower rotation rates as a population (Abt & Morrell 1995). In both cases, a further examination into the detailed interaction between magnetic fields and the atmospheres (and extended atmospheres) of these stars will constrain better their overall evolution and observable properties.

To this extent, we propose to take full advantage of the unique opportunity offered by the Transiting Exoplanet Survey Satellite (*TESS*; Ricker et al. 2015). While it was originally designed, as its name suggests, for the detection and characterization of exoplanets via the transit method, the high-precision, high-cadence data that it provides for objects covering ∼85% of the sky represent a veritable treasure trove for the field of stellar astrophysics. Below we describe briefly what kind of photometric signatures can be expected from magnetic massive and intermediate-mass stars, what kind of physical insights we can expect to gain by analyzing *TESS* data, and the ways in which we can increase that gain by combining them with various other observational diagnostics.

2 General phenomenology

Magnetic OBA stars tend to present a common photometric behaviour. Their light curves are recognizable owing to periodic rotational modulation. For the earlier spectral types, that is due to the magnetically confined wind material which scatters continuum light. Since this material is distributed non-axisymmetrically around the star and the magnetic and rotation axes are generally not aligned, a varying column density intersects the line of sight throughout a rotational cycle.

However, as already mentioned, slightly cooler magnetic stars have abundance patches on their surfaces. Flux redistribution (Krtička et al. 2007) also leads to brightness inhomogeneities on the stellar surface which appear and disappear as the star rotates, causing periodic photometric variations.

Both of these phenomena manifest themselves in a light-curve periodogram as a well-defined peak in a reasonable frequency range that might be associated with the rotation of the star; there is at least one harmonic (typically the first one; Bowman et al. 2018), although occultation by magnetospheric material can, in some cases, lead to the presence of more harmonics and a rather complex light-curve (Townsend 2008). This phenomenology can be used to select highly probable magnetic candidates (Buysschaert et al. 2018). However, the method must be used with caution since other mechanisms can lead to a similar observational signature (e.g. eclipsing binaries, ellipsoidal variations, etc.), and should be ruled out before the frequencies are ascribed to a rotational origin.

3 Physical insights obtained from photometry

3.1 O and early B stars

The circumstellar *magnetospheres* formed by the interaction between a surface magnetic field and a strong stellar wind around OB stars have been studied in great detail over the past two decades. State-of-the-art magnetohydrodynamic simulations (ud-Doula & Owocki 2002; ud-Doula et al. 2008, 2009) have provided us with unprecedented insights into their structure and their influence on a star. Simpler parametrizations have also been developed, both for fast (Townsend & Owocki 2005) and slow (Owocki et al. 2016) rotators, which enable us to define a density and velocity at any given point in the magnetosphere. Coupled with an appropriate radiative transfer scheme (e.g. Hennicker et al. 2018), these models can reproduce a large swath of multi-wavelength observations to great accuracy (e.g. Nazé et al. 2014; David-Uraz et al. 2019a). They can also be confronted with optical photometry, as was done with great success with MOST data to explain the light-curve of σ Ori E (Townsend et al. 2013). Ongoing efforts also aim to derive magnetospheric parameters using photometry (Munoz et al. 2019). Measuring period changes in magnetic OB stars can validate or challenge our current understanding of their rotational evolution (e.g. Townsend et al. 2010; Mikulášek et al. 2011; Shultz et al. 2019a).

3.2 Late B and A stars

Photometric time-series can be used to map brightness spots on the surface of a star using various light-curve inversion techniques, as exemplified by the work that Weiss et al. (2016) have done with BRITE data to map the surface of α Cir. The maps can then be compared to elemental abundance maps derived from applying

Doppler Imaging to well-sampled time-series of high-resolution spectroscopy (e.g. Khokhlova & Riabchikova 1975). Furthermore, information about the abundance and vertical stratification of different chemical elements can be obtained by performing a detailed analysis of their line profiles, as has been achieved by the VeSElkA project (Khalack et al. 2017). There is a clear synergy between that endeavour and the core goals of the MOBSTER Collaboration, leading to a more complete picture of the atmosphere of Ap/Bp stars – as evidenced by studies conducted in common by both groups (Khalack et al. 2019).

4 Progress to date

To date our collaboration has published three refereed articles; more are planned. Paper I (David-Uraz et al. 2019b) looked at the morphology of the photometric variations for known magnetic B- and A-type stars in sectors 1 and 2, and concluded that most were compatible with rotational modulation. It also derived refined periods for them.

In Paper II (Sikora et al. 2019) we detected rotational modulation in the light-curves of many A-type stars observed by *TESS* in sectors 1 to 4. Interestingly, the properties of the variations (e.g., period and amplitude) appear to differ between the population of stars identified as chemically peculiar (Ap) and the population of stars that are not identified as such. This might be providing us with a clue as to the underlying physical mechanisms.

In Paper III (Shultz et al. 2019b) we discuss the puzzling case of an eclipsing B-type binary system, HD 62658. Careful modelling of its light-curve, and examining its spectroscopic and spectropolarimetric data, suggests that only one of the stars is magnetic, even though the mass ratio is almost unity and the stars appear otherwise to be nearly identical. This poses a particular challenge to theories of the origin of magnetic fields in such stars ... The plot thickens even further.

5 Conclusions, and future work

The MOBSTER Collaboration groups both observers and theorists together with the goal of maximizing the scientific output of the *TESS* mission with respect to magnetism in massive and intermediate-mass stars. As elaborated above, the high-precision light-curves produced by *TESS* enable us to constrain the physics of the atmosphere and winds of these stars, leading to a deeper understanding of their evolution. While some work has already been done, there remain many questions to be answered. So far we have only skimmed the surface of this data bounty; we have focused mainly on 2-minute cadence data (which are obtained for somewhere between 200,000 and 400,000 objects), but full-frame image data (30 minute cadence) should be available for over 500 million point sources (Stassun et al. 2018). Much work thus remains to unlock the truly transformative potential of the MOBSTER project in the field of magnetism in OBA stars.

ADU, VK and GAW acknowledge support from the Natural Sciences and Engineering Research Council of Canada (NSERC). Some of the research leading to these results has received funding from the European Research Council (ERC) under the European Union's Horizon 2020 research and innovation programme (grant agreement No. 670519: MAMSIE). CE acknowledges a graduate assistant salary from the Bartol Research Institute in the Department of Physics, University of Delaware, and support from program HST-GO-13629.002-A provided by NASA through a grant from the Space Telescope Science Institute. MES acknowledges financial support from the Annie Jump Cannon Fellowship, endowed by the Mount Cuba Observatory and supported by the University of Delaware. AuD acknowledges support from NASA through Chandra Award number TM7-18001X issued by the Chandra X-ray Observatory Center, which is operated by the Smithsonian Astrophysical Observatory for and on behalf of NASA under contract NAS8-03060.

References

Abbott, B. P., Abbott, R., Abbott, T. D., et al. 2016, Phys. Rev. Lett., 116, 061102

Abt, H. A. & Morrell, N. I. 1995, ApJS, 99, 135

Alecian, E., Neiner, C., Wade, G. A., et al. 2015, in IAU Symposium, Vol. 307, New Windows on Massive Stars, ed. G. Meynet, C. Georgy, J. Groh, & P. Stee, 330–335

Borra, E. F., Landstreet, J. D., & Mestel, L. 1982, ARA&A, 20, 191

Bowman, D. M., Buysschaert, B., Neiner, C., et al. 2018, A&A, 616, A77

Buysschaert, B., Neiner, C., Martin, A. J., et al. 2018, MNRAS, 478, 2777

David-Uraz, A., Erba, C., Petit, V., et al. 2019a, MNRAS, 483, 2814

David-Uraz, A., Neiner, C., Sikora, J., et al. 2019b, MNRAS, 487, 304

Georgy, C., Meynet, G., Ekström, S., et al. 2017, A&A, 599, L5

Hennicker, L., Puls, J., Kee, N. D., & Sundqvist, J. O. 2018, A&A, 616, A140
Keszthelyi, Z., Meynet, G., Georgy, C., et al. 2019, MNRAS, 485, 5843
Khalack, V., Gallant, G., & Thibeault, C. 2017, MNRAS, 471, 926
Khalack, V., Lovekin, C., Bowman, D. M., et al. 2019, MNRAS, 490, 2102
Khokhlova, V. L. & Riabchikova, T. A. 1975, Ap&SS, 34, 403
Krtička, J., Mikulášek, Z., Zverko, J., & Žižňovský, J. 2007, A&A, 470, 1089
Liu, J., Zhang, H., Howard, A. W., et al. 2019, arXiv e-prints, arXiv:1911.11989
Martin, A. J., Neiner, C., Oksala, M. E., et al. 2018, MNRAS, 475, 1521
Mikulášek, Z., Krtička, J., Henry, G. W., et al. 2011, A&A, 534, L5
Morel, T., Castro, N., Fossati, L., et al. 2015, in IAU Symposium, Vol. 307, New Windows on Massive Stars, ed. G. Meynet, C. Georgy, J. Groh, & P. Stee, 342–347
Munoz, M. S., Wade, G. A., Nazé, Y., et al. 2019, MNRAS, 2573
Nazé, Y., Petit, V., Rinbrand, M., et al. 2014, ApJS, 215, 10
Neiner, C., Mathis, S., Alecian, E., et al. 2015, in IAU Symposium, Vol. 305, Polarimetry, ed. K. N. Nagendra, S. Bagnulo, R. Centeno, & M. Jesús Martínez González, 61–66
Owocki, S. P., ud-Doula, A., Sundqvist, J. O., et al. 2016, MNRAS, 462, 3830
Petit, V., Keszthelyi, Z., MacInnis, R., et al. 2017, MNRAS, 466, 1052
Ricker, G. R., Winn, J. N., Vanderspek, R., et al. 2015, JATIS, 1, 014003
Shultz, M., Rivinius, T., Das, B., Wade, G. A., & Chandra, P. 2019a, MNRAS, 486, 5558
Shultz, M. E., Johnston, C., Labadie-Bartz, J., et al. 2019b, MNRAS, 490, 4154
Sikora, J., David-Uraz, A., Chowdhury, S., et al. 2019, MNRAS, 487, 4695
Stassun, K. G., Oelkers, R. J., Pepper, J., et al. 2018, AJ, 156, 102
Townsend, R. H. D. 2008, MNRAS, 389, 559
Townsend, R. H. D., Oksala, M. E., Cohen, D. H., Owocki, S. P., & ud-Doula, A. 2010, ApJ, 714, L318
Townsend, R. H. D. & Owocki, S. P. 2005, MNRAS, 357, 251
Townsend, R. H. D., Rivinius, T., Rowe, J. F., et al. 2013, ApJ, 769, 33
ud-Doula, A. & Owocki, S. P. 2002, ApJ, 576, 413
ud-Doula, A., Owocki, S. P., & Townsend, R. H. D. 2008, MNRAS, 385, 97
ud-Doula, A., Owocki, S. P., & Townsend, R. H. D. 2009, MNRAS, 392, 1022
Wade, G. A., Neiner, C., Alecian, E., et al. 2016, MNRAS, 456, 2
Weiss, W. W., Fröhlich, H. E., Pigulski, A., et al. 2016, A&A, 588, A54

Stars and their variability observed from space
C. Neiner, W. W. Weiss, D. Baade, R. E. Griffin, C. C. Lovekin, A. F. J. Moffat (eds)

TOSC: AN ALGORITHM FOR THE TOMOGRAPHY OF SPOTTED TRANSIT CHORDS

G. Scandariato[1]

Abstract. Photometric observations of planetary transits may show localized bumps, called transit anomalies, due to the possible crossing of photospheric starspots. The aim of this work is to analyze the transit anomalies and derive the temperature profile inside the transit belt along the transit direction. We have developed the algorithm TOSC, a tomographic inverse-approach tool which, by means of simple algebra, reconstructs the flux distribution along the transit belt. Here we test TOSC against some simulated scenarios. We find that TOSC provides robust results for light curves with photometric accuracies better than 1 mmag, typical of current and future space photometers, returning the spot-photosphere temperature contrast with an accuracy better than 100 K. TOSC is also robust against the presence of unocculted spots, provided that the apparent planetary radius given by the fit of the transit light curve is used in place of the true radius. The analysis of space-borne and ground-based real data with TOSC returns results consistent with previous studies.

Keywords: methods: data analysis, methods: numerical, techniques: photometric, stars: activity, stars:atmospheres, stars: starspots

1 Introduction

During a planetary transit, the observed flux of the star decreases because part of the stellar disk is blocked by the planetary disk. It is possible to analyze the transit light-curve (LC), and to characterize the stellar surface. In particular, if the planet transits in front of starspots, an apparent rebrightening (called "transit anomaly") of the star is observed while the spot is being crossing: the brightening corresponds to an increase of the flux received from the unocculted stellar surface because a darker area is being occulted.

The analysis of transit anomalies has been approached using various methods. Some authors fit the transit anomaly with a given analytical model to retrieve the size of the spots and their contrast with respect to the photosphere (e.g., Sanchis-Ojeda & Winn 2011; Nascimbeni et al. 2015). Others have developed more sophisticated codes, which fit the LCs by means of Monte Carlo algorithms (e.g., Tregloan-Reed et al. 2013; Béky et al. 2014). In both cases, some assumptions about the shape and distribution of the spots over the stellar disk are needed.

Scandariato et al. (2017) presented the Tomography Of Spotted transit Chords (TOSC) code, a new and fast algorithm which reconstructs the flux distribution inside the area of the stellar surface crossed by the transiting planet, namely the "transit chord". The main advantage of our code is that it only needs a few assumptions about the geometry of the planetary system and the stellar spectrum. In other words, TOSC does not assume any *a priori* parameter of the photospheric starspots such as shape, size or temperature.

2 The model

The transit chord is divided into adjacent rectangular cells. For each photometric point recorded during the planetary transit at time t, the flux occulted by the planet $F_{occ}(t)$ corresponds to the sum of the fluxes radiated by the corresponding cells F, weighted by the fractional overlap area $w(t)$ between the cells and the planetary disk (see Fig. 1).

Each photometric point corresponds to the weighted sum of the unknown fluxes F_i. The sample of photometric points gives the system of linear equations in Eq. 2.1. TOSC inverts this system and returns the flux,

[1] c/o Oss. Astr. Catania, via S. Sofia 78, 95123 Catania (Italy)
gaetano.scandariato@inaf.it

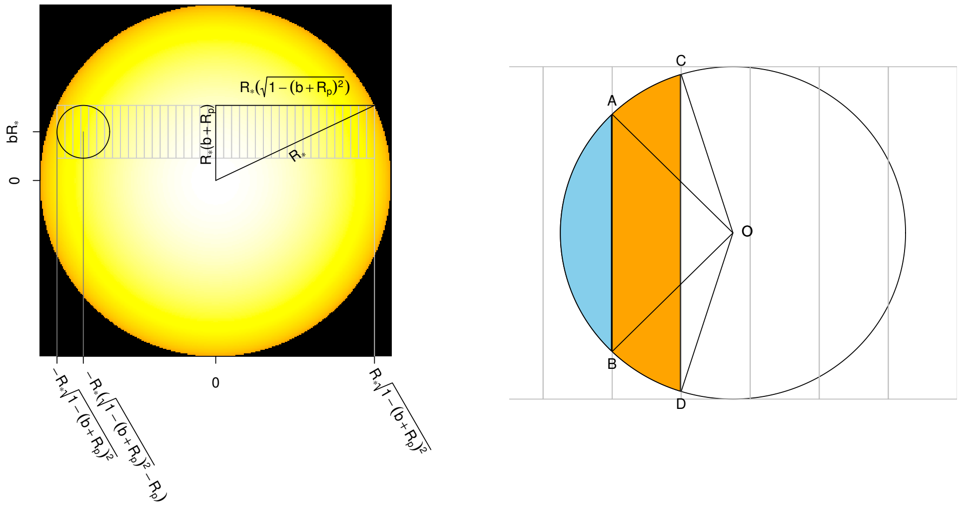

Fig. 1. Left: Schematic representation of the geometry discussed in the text. The circle represents the transiting planet, while the grid rectangles shows the cells used in the chord reconstruction.. **Right:** Graphical representation of the computation of the weights $w(t)$. The circle is the planetary disk centered at O, while the gray grid shows the cells drawn on the stellar disk partially covered by the planetary disk.

and thus the temperature, along the transit chord. Since the system inversion is an ill-posed problem from a mathematical point of view, TOSC uses Tikhonov's method to regularize the inversion algorithm.

$$\begin{bmatrix} w_1(t_1) & \cdots & w_N(t_1) \\ \vdots & \ddots & \vdots \\ w_1(t_M) & \cdots & w_N(t_M) \end{bmatrix} \cdot \begin{bmatrix} F_1 \\ \vdots \\ F_N \end{bmatrix} = \begin{bmatrix} F_{occ}(t_1) \\ \vdots \\ F_{occ}(t_M) \end{bmatrix} \tag{2.1}$$

3 Examples of applications

TOSC has been tested against different simulated scenarios, and it has proved to return the expected temperature profile of the chord within ∼100 K as long as the photometric precision of the LCs is better than 1 mmag.

We also tested TOSC against some actual datasets. HAT-P-11 is a V=9.6 K4 dwarf (T_{eff}=4780 K) in the Kepler field (Borucki et al. 2010), orbited by a hot Neptune every 4.9 days (Bakos et al. 2010). We analyzed the Kepler photometry of the transit occurring at BJD=2454967.6 (Fig. 2). The reconstructed chord (green line in the top panel) shows a cool spot centered at $\simeq$0.3 R_* and is $\simeq$0.15 R_* wide. The fitted spot-photosphere temperature contrast is $\Delta T \simeq$-900 K (bottom panel). These results are in line with previous results (Béky et al. 2014).

4 Conclusions

Extensive tests have shown that TOSC can reconstruct the crossed spots to give a photometric accuracy better than 1 mmag, and that the temperature contrast is returned with an uncertainty <100 K. TOSC is consistent with previous approaches available in literature, and also with more sophisticated algorithms. For a complete description of TOSC (e.g. Tychonov's regularization, treatment of unocculted spots and limb darkening, etc.), please see Scandariato et al. (2017).

TOSC is available as a web interface at `www.oact.inaf.it/tosc`, where the user can run the algorithm feeding a few input files and retrieving the output in table format complemented by quick-look plots. It is also possible to run multiple transit LCs in one go. The web page contains extensive instructions and some sample data. The source code is available for download too. For support, please contact the authors.

I acknowledge financial support from " Accordo ASI–INAF" n. 2013-016-R.0 July 9, 2013.

I dedicate this work to my father, after whom TOSC is named.

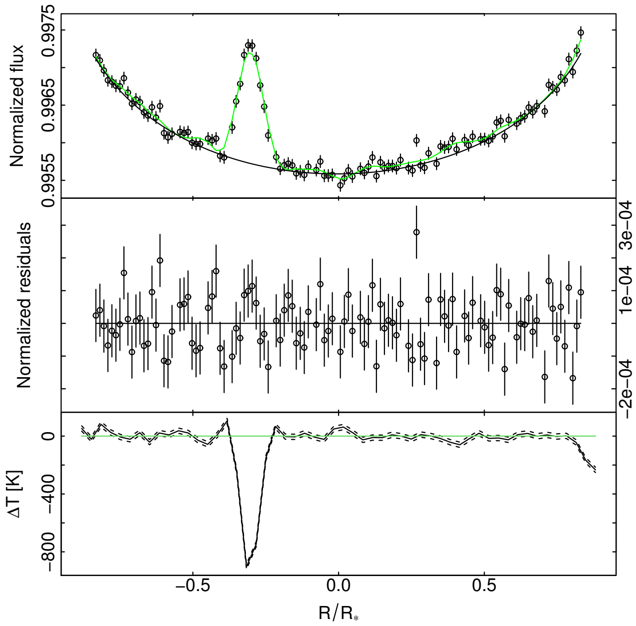

Fig. 2. *Top panel* - Kepler LC of HAT-P-11b. The "unspotted" transit model and the "spotted" transit fit are represented by the solid black line and the solid green line respectively. *Middle* - Residuals of the transit fit. *Bottom* - The reconstructed temperature profile of the transit chord with the uncertainty in the reconstruction shown by dashes.

References

Bakos, G. Á., Torres, G., Pál, A., et al. 2010, ApJ, 710, 1724
Béky, B., Kipping, D. M., & Holman, M. J. 2014, MNRAS, 442, 3686
Borucki, W. J., Koch, D., Basri, G., et al. 2010, Science, 327, 977
Nascimbeni, V., Mallonn, M., Scandariato, G., et al. 2015, A&A, 579, A113
Sanchis-Ojeda, R. & Winn, J. N. 2011, ApJ, 743, 61
Scandariato, G., Nascimbeni, V., Lanza, A. F., et al. 2017, A&A, 606, A134
Tregloan-Reed, J., Southworth, J., & Tappert, C. 2013, MNRAS, 428, 3671

ASTEROSEISMIC ANALYSIS OF THE SPB STAR HD 54967 OBSERVED BY *TESS*

P. Walczak[1], W. Szewczuk[1] and J. Daszyńska-Daszkiewicz[1]

Abstract. HD 54967 was observed by *TESS* with a 2-min cadence in Sectors 1 and 2. Its light-curve revealed a rich frequency spectrum, mostly in the region of high-order *g*-modes. That meant that the star is a Slowly Pulsating B-type pulsator. Our frequency analysis indicated the presence of quasi-equal period spacings, which support mode identification and detailed seismic modelling. We present the results of our initial analysis of the star. Further studies should supply constraints on physical processes occurring inside it, including various types of mixing processes.

Keywords: Stars: individual: HD 54967, variables: general, asteroseismology

1 Introduction

The luminosity of the star was calculated from the Gaia DR2 parallax (Gaia Collaboration et al. 2016, 2018; Lindegren et al. 2018), and bolometric correction from Flower (1996). The evolutionary tracks shown in the H–R diagram in the left panel of Fig. 1 were calculated with the MESA code (MESA Paxton et al. 2011, 2013, 2015, 2018), version 11701. We adopted a metallicity $Z = 0.010$, an exponential overshooting parameter $f_{\rm ov} = 0.01$ from the hydrogen-burning convective core (Herwig 2000), a hydrogen abundance $X = 0.7$ and the OPLIB opacity tables (Colgan et al. 2015, 2016). Two values for the rotational velocity were studied, $V_{\rm rot} = 0$ km s^{-1} and 200 km s^{-1}.

From the *TESS* light-curve of HD 54967 we derived about 200 independent frequencies. Most of them occupy the low-frequency region, but there are frequencies as high as 10 d^{-1}. The frequency spectrum is shown in the upper right panel of Fig. 1.

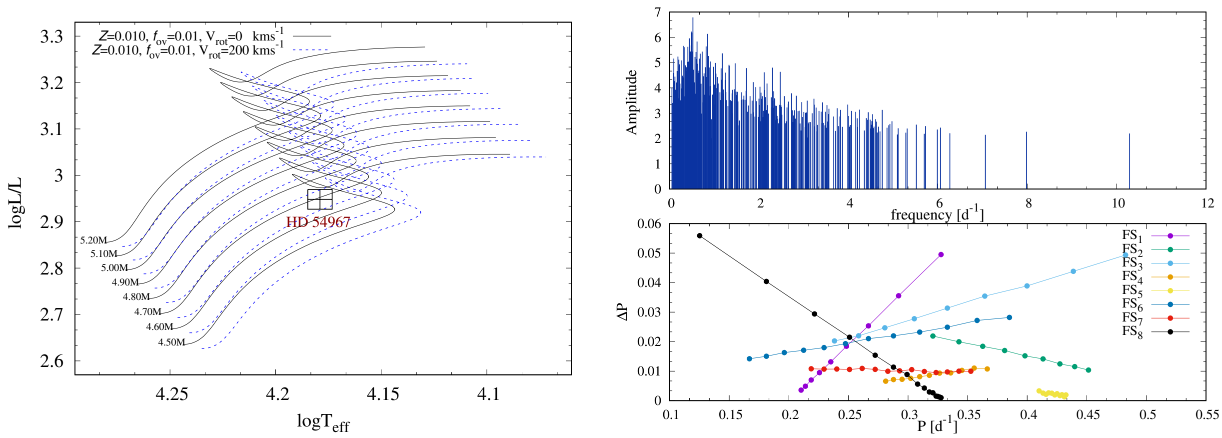

Fig. 1. Left: H–R diagram showing the position of the target star HD 54967. The evolutionary tracks were calculated for masses from 4.5M$_\odot$ to$_\odot$, and for different rotational velocities: $V_{\rm rot} = 0$ and 200 km s^{-1}. We also assumed metallicity Z = 0.01 and an exponential overshooting parameter $f_{\rm ov} = 0.01$. Right (upper): Frequency spectrum derived from *TESS* data. Right (lower): Diagram showing frequency sequences in the period vs. period differences

The frequency spectrum is very dense, and there are no obvious quasi-equal period spacings. However, a more detailed analysis revealed some regular structures. The lower right panel of Fig. 1 shows the most interesting frequency sequences in the diagram of period vs. period difference.

[1] Astronomical Institute Wrocław University, ul. Kopernika 11, 51-622 Wrocław, Poland

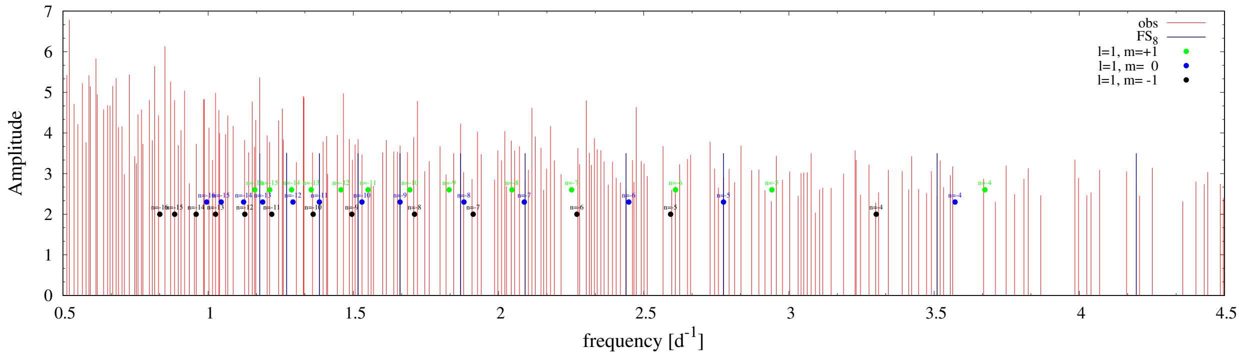

Fig. 2. A model example that fits some frequencies from frequency sequence No. 8.

Some of the sequences we found may be accidental. A detailed analysis consisting of simultaneous mode identification and frequency fitting is required in order to establish physical sequences of frequencies with the same degree and consecutive radial orders. For more information on the subject see Szewczuk & Daszyńska-Daszkiewicz (2018).

Here we present the result of a very preliminary analysis. The model fits frequencies from frequency sequence No. 8 under the assumption that it is a dipole mode series. We derived the following parameters: mass $M = 4.716 M_\odot$, rotational velocity $V_{\rm rot} = 70$ km s^{-1}, effective temperature $\log T_{\rm eff} = 4.1778$ and luminosity $\log L/L_\odot = 2.9206$.

2 Conclusions

Analysis of the *TESS* data obtained for HD 55967 resulted in the detection of a large number of pulsational frequencies. Most of them are low frequencies (g-modes) typical of SPB type stars. A detailed study of the frequency spectrum revealed a few frequency series that can be associated with consecutive radial orders of modes with a given mode degree (ℓ) and azimuthal number(m). Further seismic modelling of the star should yield constraints on different mixing processes that take place inside the star.

This work was supported financially by the Polish National Science Centre under grants 2013/08/S/ST9/00583 and 2015/17/B/ST9/02082. The calculations were partly carried out using resources provided by Wroclaw Centre for Networking and Supercomputing (http://www.wcss.pl), under grant no. 265. This paper includes data collected by *TESS*, whose funding is provided by the NASA Explorer Program. This work made use of data from *Gaia* (`https://www.cosmos.esa.int/gaia`), and processed by the *Gaia* Data Processing and Analysis Consortium (DPAC, `https://www.cosmos.esa.int/web/gaia/dpac/consortium`). Funding for DPAC has been provided by national institutions, in particular the institutions participating in the *Gaia* Multilateral Agreement.

References

Colgan, J., Kilcrease, D. P., Magee, N. H., et al. 2015, High Energy Density Physics, 14, 33

Colgan, J., Kilcrease, D. P., Magee, N. H., et al. 2016, ApJ, 817, 116

Flower, P. J. 1996, ApJ, 469, 355

Gaia Collaboration, Brown, A. G. A., Vallenari, A., et al. 2018, A&A, 616, A1

Gaia Collaboration, Prusti, T., de Bruijne, J. H. J., et al. 2016, A&A, 595, A1

Herwig, F. 2000, A&A, 360, 952

Lindegren, L., Hernández, J., Bombrun, A., et al. 2018, A&A, 616, A2

Paxton, B., Bildsten, L., Dotter, A., et al. 2011, ApJS, 192, 3

Paxton, B., Cantiello, M., Arras, P., et al. 2013, ApJS, 208, 4

Paxton, B., Marchant, P., Schwab, J., et al. 2015, ApJS, 220, 15

Paxton, B., Schwab, J., Bauer, E. B., et al. 2018, ApJS, 234, 34

Szewczuk, W. & Daszyńska-Daszkiewicz, J. 2018, MNRAS, 478, 2243

Stars and their variability observed from space
C. Neiner, W. W. Weiss, D. Baade, R. E. Griffin, C. C. Lovekin, A. F. J. Moffat (eds)

ECLIPSING BINARIES HIDING IN THE BACKGROUND: THE *KEPLER* PIXEL PROJECT

A. Forró[1,2,3] and R. Szabó[1,3]

Abstract. The aim of the Kepler pixel project is to discover new pulsating and other types of variable stars in the individual pixels of the original *Kepler* mission. In the framework of the project, 1272 eclipsing binary candidates were identified in the background pixels. After eliminating false positives and those stars that are already present in the *Kepler* Eclipsing Binary Catalog, we were left with 776 new eclipsing binaries. This is a substantial and significant addition to the 2922 eclipsing binaries present in the catalogue. The methods applied are automatic, and can therefore be used in the future for exploring the vast amounts of data that other space missions (e.g. *TESS*, later *PLATO*) produce.

Keywords: Stars: binaries, methods: photometry

1 Introduction

During its original mission, the *Kepler* space telescope measured the brightness of more than 150000 stars, producing quasi-continuous 4-year-long observations with unprecedented photometric precision. Though usually the main targets, those that are listed in the *Kepler* Input Catalog (Brown et al. 2011) were already investigated, but more findings indicate that even the background pixels of *Kepler*'s data hold interesting new information waiting to be mined.

2 The *Kepler* Pixel Project

The aim of the *Kepler* Pixel Project (Szabó 2018) was to discover new pulsating and other types of variable stars in the original *Kepler* field. Since Q4 was a relatively quiescent observing period, we decided to start our search using its dataset.

We downloaded each individual pixel of the long-cadence (30 min) files, which resulted in more than 6 million light-curves. All the pixels were examined, regardless of whether or not they belonged to a main (KIC) target. The initial goal was to look for faint background RR Lyrae stars, so we specified the filtering criteria accordingly. Those pixels were included in our potential candidate list whose light-curves showed a period between 0.25 and 1 day, and whose Fourier spectra exhibited at least two harmonics of the main frequency with decreasing amplitude.

3 Results

The above criteria yielded $\sim$12500 candidate pixels. However, one pixel does not equal one candidate, and in the majority of cases a couple of pixels were available for each candidate. Despite our specific criteria, $\sim$90% of our candidates were eclipsing binary stars. We identified successfully 1272 target pixel files containing an eclipsing binary candidate; in most cases they were located in the background.

Since the goal was to find new variable stars in the field, those candidates that are already listed in the *Kepler* Eclipsing Binary Catalog (Prša et al. 2011; Abdul-Masih et al. 2016) were excluded. This cross-match left us with 777 candidates. One of our candidates' light-curve was in fact the result of contamination by a neearby bright star, so that was removed from our candidate list too. The final list of potentially new eclipsing binaries in the original *Kepler* field had 776 candidates, consisting of 2778 individual pixels in total. Figure 1 shows one of our eclipsing binary candidates (DR2 2073865026641810944). It was found in the background of not just one but two main targets, namely KIC 5898935 and KIC 5898983.

[1] Konkoly Thege Miklós Astronomical Institute, Research Centre for Astronomy and Earth Sciences
[2] Eötvös Loránd University, Department of Astronomy
[3] MTA CSFK Lendület Near-Field Cosmology Research Group

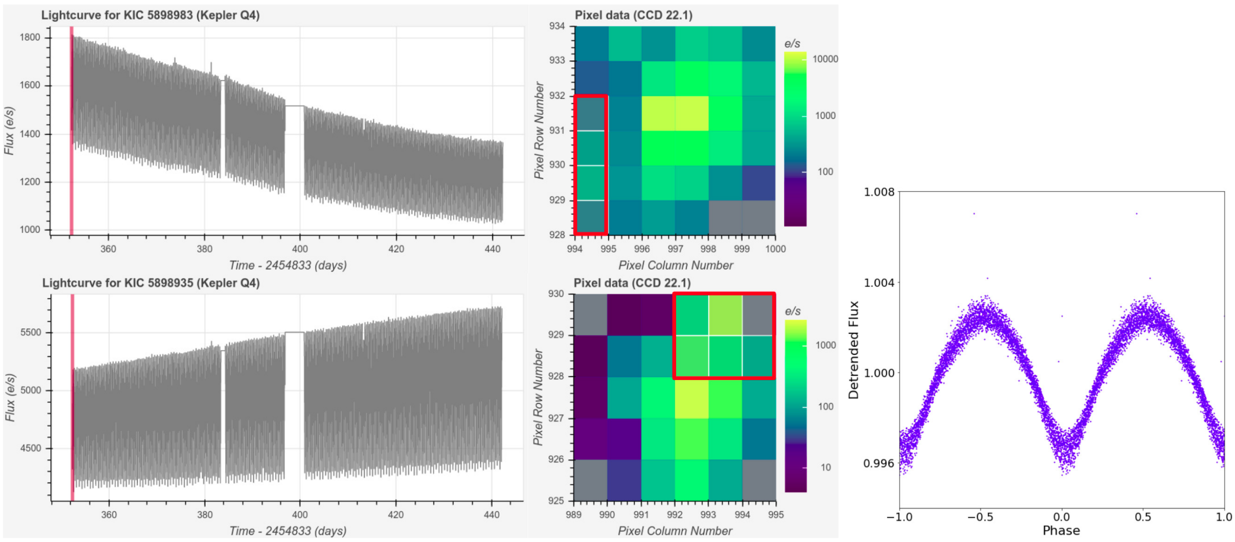

Fig. 1. Left: Light-curves of the candidate, as observed in Q4. The pixels containing the signal of the eclipsing binary are marked with red edges. The candidate is located near two apparently close main targets, so it is present in the background of both target pixel files. **Right:** Folded light-curve of the candidate.

4 Conclusions

By investigating each individual pixel of the original *Kepler* mission's Q4 quarter, the *Kepler* Pixel Project succeeded in finding 1272 new eclipsing binary candidates in the original *Kepler* data, of which 776 turned out to be new candidates. We also btained data from the other quarters for the candidates, thereby creating 4-year-long light-curves. The unprecedented photometric precision enabled us to investigate the systems we had discovered in more detail. The algorithms developed for the project can be used analogously for exploring other space-mission data as well (e.g. *TESS*, later *PLATO)*.

The research leading to these results has received funding from the LP2018-7/2019 Lendlet grant of the Hungarian Academy of Sciences and from the NKFIH K-115709 grant of the National Research, Development and Innovation Office of Hungary. It made use of Lightkurve, a Python package for Kepler and TESS data analyses (Lightkurve Collaboration et al. 2018).

References

Abdul-Masih, M., Prša, A., Conroy, K., et al. 2016, AJ, 151, 101

Brown, T. M., Latham, D. W., Everett, M. E., & Esquerdo, G. A. 2011, AJ, 142, 112

Lightkurve Collaboration, Cardoso, J. V. d. M., Hedges, C., et al. 2018, Lightkurve: Kepler and TESS time series analysis in Python, Astrophysics Source Code Library

Prša, A., Batalha, N., Slawson, R. W., et al. 2011, AJ, 141, 83

Szabó, R. 2018, in The RR Lyrae 2017 Conference. Revival of the Classical Pulsators: from Galactic Structure to Stellar Interior Diagnostics, ed. R. Smolec, K. Kinemuchi, & R. I. Anderson, Vol. 6, 119–123

Conclusion

CELEBRATING FIVE YEARS OF *BRITE*-CONSTELLATION WITH GOOD GOOD GOOD, GOOD VIBRATIONS DURING THE END-OF-CONFERENCE SUMMARY PARTY

C. Aerts[1]

How does one summarize 87 talks and 118 poster presentations in half an hour while keeping the attention of the participants, most of whom have trains or flights to catch? Surely not by going over each contribution with a boring sequence of 8-seconds-per-presentation statements. I therefore decided to run a different *once-in-a-lifetime* show, building up a science story from (sometimes scientific) quotes of statements that were made by participants during the conference. There were plenty of quotes available, including Laurent Eyer's "*Gaia* brings stars (and us!) in motion", so two of them got an upgrade by being coupled to a musical (dancing) intermezzo (see Fig. 1).

The first quote came from the editor's choice for the front page of *Nature Astronomy*, Volume 3, issued just before the conference (August 2019) and triggered by Gerald Handler on the fourth day of the meeting: "Good vibrations" (`https://www.nature.com/natastron/volumes/3/issues/8`), referring to gravity waves detected in numerous O-type stars and blue supergiants from *K2* and *TESS* space photometry (Bowman et al. 2019). One of my favourite songs, "Good, good, good, good vibrations" from *The Beach Boys*, hence kick-started the talk on the major topic of angular momentum transport. Various contributions touched upon improving the theory of stellar interiors to eliminate the current discrepancies between theory and observations for the slow core rotation of stars and the near-rigidity of the rotation in phases when stars have a convective core. Given that several of the OBA-type variables observed with *BRITE* and *TESS* are known to be magnetic (e.g., David-Uraz et al. 2019), a second musical band passed the stage: *The Magnetic Fields* (their music causing mood depression of the author). Numerous contributions on magnetism were presented during the conference, connected to angular momentum transport, magnetic braking and rotation, stellar winds and mass loss, and dipole mode depression in red giants. If the observed phenomenon of mode depression is due to magnetism, then it is required half of the F-type dwarfs to have a strong interior magnetic field (Stello et al. 2016). However, several (all?) dipole modes with depressed amplitudes are mixed modes (Mosser et al. 2017), so nonlinear resonant mode coupling offers a promising alternative and not mutually exclusive explanation (Weinberg & Arras 2019). This is particularly attractive, since nonlinear mode behaviour is omnipresent in space asteroseismology, across almost all masses and evolutionary stages. Notable contributions to this topic from *BRITE* studies of Be stars were presented during the meeting (following earlier findings, e.g., Baade et al. 2017).

Given the *Kepler* space photometry programme and the convenient and easy-to-use scaling relations, much emphasis on asteroseismology has been injected into research of low- and intermediate-mass stars during the past decade. The repurposed *K2* mission added their remnants as popular asteroseismology targets (Hermes et al. 2017). We have thus reached the stage of having a complete evolutionary path, at least of stellar birth to death, covered with asteroseismic data to rely upon for the improvement of the theory of stellar interiors. Much modelling work is yet to be done and new theories are to be developed, guided by the asteroseismic results. A wealth of information can be found in the recent extensive reviews by García & Ballot (2019) for dwarfs, Hekker & Christensen-Dalsgaard (2017) for red giants, and Córsico et al. (2019) for white dwarfs. Aerts et al. (2019) has united all those evolutionary stages into one global picture of angular momentum transport, but we still lack the pre-birth phase. Asteroseismic tuning of the transport of chemical elements is a lot harder, but various contributions during the conference revealed that it too is also coming along, and demonstrating a clear need to have more massive cores in models of intermediate- and high-mass stars across their evolution. It was stressed during the meeting how important are the ongoing and future studies of high-mass stars by *BRITE, TESS* and *PLATO* for covering their evolution and calibrating their interiors in the presence of rotation, magnetism, and a variable wind. Several neat results from *BRITE*–*TESS* bi-satellite campaigns on B-type single and binary pulsators were presented. And of course *BRITE* occupies an immense niche for the highest-mass stars in the

[1] Institute of Astronomy, KU Leuven, Belgium

Universe, whose winds are so strong that the detection of asteroseismic signals remains challenging, if not impossible.

Many of the topics treated during the conference have been included in general reviews written for a broad readership by Aerts (2020), with numerous references to recently published work that had been highlighted in talks and posters. In particular, the glorious future of asteroseismology, as emphasised during the last day of the conference, gave rise to a poll in between the dancing. The audience was asked to vote, from several options, where our focus should lie and our attention should go with the highest priority in our community. The reader will find the outcome of the poll in Sections IV and V of the review by Aerts (2020).

Fig. 1. The show at the end of the conference on "5 years of *BRITE*" featured scientific highlights intertwined with acts involving the audience. Here, Werner Weiss and Conny Aerts are dancing with help from the song, "Good, good, good, good vibrations" by *The Beach Boys*, with encouragements from members of the *BRITE* Executive Science Team (BEST). Photo credit: @Herbst-Kiss.

The author is much indebted to the audience for their cooperation and activities during this end-of-conference talk. The act will not be repeated for those who were absent or left early.

References

Aerts, C. 2020, RvMP, in press, arXiv:1912.12300

Aerts, C., Mathis, S., & Rogers, T. M. 2019, ARA&A, 57, 35

Baade, D., Rivinius, T., Pigulski, A., et al. 2017, in Second BRITE-Constellation Science Conference: Small Satellites - Big Science, ed. K. Zwintz & E. Poretti, Vol. 5, 196–205

Bowman, D. M., Burssens, S., Pedersen, M. G., et al. 2019, Nature Astronomy, 3, 760

Córsico, A. H., Althaus, L. G., Miller Bertolami, M. M., & Kepler, S. O. 2019, A&A Rev., 27, 7

David-Uraz, A., Neiner, C., Sikora, J., et al. 2019, MNRAS, 487, 304

García, R. A. & Ballot, J. 2019, Living Reviews in Solar Physics, 16, 4

Hekker, S. & Christensen-Dalsgaard, J. 2017, A&A Rev., 25, 1

Hermes, J. J., Gänsicke, B. T., Kawaler, S. D., et al. 2017, ApJS, 232, 23

Mosser, B., Belkacem, K., Pinçon, C., et al. 2017, A&A, 598, A62

Stello, D., Cantiello, M., Fuller, J., et al. 2016, Nature, 529, 364

Weinberg, N. N. & Arras, P. 2019, ApJ, 873, 67

Author Index